ACS SYMPOSIUM SERIES 1120

Proteins at Interfaces III
State of the Art 2012

EDITED BY

Thomas Horbett, John L. Brash, and
Willem Norde

Downloaded by FORDHAM UNIV on December 13, 2012 | http://pubs.acs.org
Publication Date (Web): December 12, 2012 | doi: 10.1021/bk-2012-1120.fw001

Proteins at Interfaces III
State of the Art 2012

Downloaded by FORDHAM UNIV on December 13, 2012 | http://pubs.acs.org
Publication Date (Web): December 12, 2012 | doi: 10.1021/bk-2012-1120.fw001

In Proteins at Interfaces III State of the Art 2012; Horbett, T., et al.;
ACS Symposium Series; American Chemical Society: Washington, DC, 2012.

Downloaded by FORDHAM UNIV on December 13, 2012 | http://pubs.acs.org
Publication Date (Web): December 12, 2012 | doi: 10.1021/bk-2012-1120.fw001

ACS SYMPOSIUM SERIES **1120**

Proteins at Interfaces III
State of the Art 2012

Thomas Horbett, Editor
University of Washington
Seattle, Washington

John L. Brash, Editor
McMaster University
Hamilton, Ontario, Canada

Willem Norde, Editor
Wageningen University
Wageningen, The Netherlands
and
University Medical Center Groningen and
University of Groningen
Groningen, The Netherlands

Sponsored by the
ACS Division of Colloid and Surface Chemistry

American Chemical Society, Washington, DC

Distributed in print by Oxford University Press, Inc.

In Proteins at Interfaces III State of the Art 2012; Horbett, T., et al.;
ACS Symposium Series; American Chemical Society: Washington, DC, 2012.

Downloaded by FORDHAM UNIV on December 13, 2012 | http://pubs.acs.org
Publication Date (Web): December 12, 2012 | doi: 10.1021/bk-2012-1120.fw001

Library of Congress Cataloging-in-Publication Data

Library of Congress Cataloging-in-Publication Data

Proteins at interfaces III : state of the art 2012 / Thomas Horbett, editor, University of Washington, Seattle, Washington ; John L. Brash, editor, McMaster University, Hamilton, Ontario ; Willem Norde, editor, Wageningen University, Wageningen, The Netherlands and University Medical Center Groningen and University of Groningen, Groningen, The Netherlands ; sponsored by the ACS Division of Colloid and Surface Chemistry.
pages cm. -- (ACS symposium series, ISSN 0097-6156 ; 1120)
Includes bibliographical references and index.
ISBN 978-0-8412-2796-5 (alk. paper)
1. Proteins--Congresses. 2. Surface chemistry--Congresses. 3. Biological interfaces--Congresses. I. Horbett, Thomas A., 1943- editor of compilation. II. American Chemical Society. Division of Colloid and Surface Chemistry. III. Title: Proteins at interfaces three. IV. Title: Proteins at interfaces 3.
QP551.P6977822 2012
612′.01575--dc23
2012043084

The paper used in this publication meets the minimum requirements of American National Standard for Information Sciences—Permanence of Paper for Printed Library Materials, ANSI Z39.48n1984.

Copyright © 2012 American Chemical Society

Distributed in print by Oxford University Press, Inc.

All Rights Reserved. Reprographic copying beyond that permitted by Sections 107 or 108 of the U.S. Copyright Act is allowed for internal use only, provided that a per-chapter fee of $40.25 plus $0.75 per page is paid to the Copyright Clearance Center, Inc., 222 Rosewood Drive, Danvers, MA 01923, USA. Republication or reproduction for sale of pages in this book is permitted only under license from ACS. Direct these and other permission requests to ACS Copyright Office, Publications Division, 1155 16th Street, N.W., Washington, DC 20036.

The citation of trade names and/or names of manufacturers in this publication is not to be construed as an endorsement or as approval by ACS of the commercial products or services referenced herein; nor should the mere reference herein to any drawing, specification, chemical process, or other data be regarded as a license or as a conveyance of any right or permission to the holder, reader, or any other person or corporation, to manufacture, reproduce, use, or sell any patented invention or copyrighted work that may in any way be related thereto. Registered names, trademarks, etc., used in this publication, even without specific indication thereof, are not to be considered unprotected by law.

PRINTED IN THE UNITED STATES OF AMERICA

Downloaded by FORDHAM UNIV on December 13, 2012 | http://pubs.acs.org
Publication Date (Web): December 12, 2012 | doi: 10.1021/bk-2012-1120.fw001

Foreword

The ACS Symposium Series was first published in 1974 to provide a mechanism for publishing symposia quickly in book form. The purpose of the series is to publish timely, comprehensive books developed from the ACS sponsored symposia based on current scientific research. Occasionally, books are developed from symposia sponsored by other organizations when the topic is of keen interest to the chemistry audience.

Before agreeing to publish a book, the proposed table of contents is reviewed for appropriate and comprehensive coverage and for interest to the audience. Some papers may be excluded to better focus the book; others may be added to provide comprehensiveness. When appropriate, overview or introductory chapters are added. Drafts of chapters are peer-reviewed prior to final acceptance or rejection, and manuscripts are prepared in camera-ready format.

As a rule, only original research papers and original review papers are included in the volumes. Verbatim reproductions of previous published papers are not accepted.

ACS Books Department

Downloaded by FORDHAM UNIV on December 13, 2012 | http://pubs.acs.org
Publication Date (Web): December 12, 2012 | doi: 10.1021/bk-2012-1120.pr001

Preface

This book is based on the Proteins at Interfaces III symposium held at the 243rd American Chemical Society meeting in San Diego March of 2012. The symposium was sponsored by the Colloid and Surface Science division, whose support and help we gratefully acknowledge, especially the warm welcome and continuous aid given to us by the program chairman Ramanathan Nagarajan. We also wish to thank the American Chemical Society book division for agreeing to publish this volume, in particular our editor Timothy Marney who helped us throughout to keep on time with the many tasks involved in preparing this volume. Ms. Arlene Furman was our invaluable assistant editor throughout the process, and we are especially grateful for her thorough work in guiding us through the many steps involved in getting each manuscript through the review process. The authors who contributed chapters are thanked again for their willingness to share their knowledge of Proteins at Interfaces. Finally, we wish to acknowledge the contribution of Dr. Dan Li, Soochow University, who provided the cover art.

The chapters in the book are grouped into five general areas: physical chemistry, computer simulation, biological effects, protein resistant surfaces, and techniques for the study of protein adsorption and adsorbed proteins. We considered these to be major categories into which the research in this area falls; the introductory chapter is organized along the same lines. We also wish to point out that the various chapters typically include elements that represent more than one of these areas; we placed them in the topic area we felt they were most closely related to.

As the book's title indicates, this is the third volume of its type to appear. The prior two also originated from symposia sponsored by the ACS Colloid and Surface Science division, and were published by ACS books division: ACS Symposium Series Vol. 343, *Proteins at Interfaces, Physicochemical and Biochemical Studies*, J. L. Brash and T. A. Horbett, editors, American Chemical Society, Washington, D.C., 1987; ACS Symposium Series Vol. 602, *Proteins at Interfaces II: Fundamentals and Applications*, T. A. Horbett and J. L. Brash, editors, ACS Books, Washington, D.C., 1995. The general intent for all three initiatives was the same, namely to bring together the many groups around the world working on proteins at interfaces to share their ideas and knowledge, and to document the current state of the art in the resulting publication.

Thomas A. Horbett
Departments of Bioengineering and Chemical Engineering
University of Washington
Seattle, Washington 98195

John L. Brash
School of Biomedical Engineering, Department of Chemical Engineering
McMaster University
Hamilton, Ontario, Canada L8S 4L8

Willem Norde
Department of Biomedical Engineering
University Medical Center Groningen
Groningen, The Netherlands

Laboratory of Physical Chemistry and Colloid Science
Wageningen University
The Netherlands

Downloaded by FORDHAM UNIV on December 13, 2012 | http://pubs.acs.org
Publication Date (Web): December 12, 2012 | doi: 10.1021/bk-2012-1120.pr001

Editors' Biographies

Thomas A. Horbett

Thomas A. Horbett (Ph.D., University of Washington) is currently a professor emeritus in Bioengineering and Chemical Engineering at the University of Washington in Seattle, where he spent his entire career doing research on the interactions of biomaterials with blood and soft tissue. His research was supported for many years by grants from the National Institute of Health. Specific research areas he has worked in include protein adsorption, cell interactions, blood compatibility, the foreign body reaction, and controlled delivery of insulin and other drugs from polymers. He is the recipient of the 1989 Society for Biomaterials Clemson Award for Basic Research. He was the Distinguished Lecturer in Controlled Drug-Delivery,1994 College of Pharmacy, Rutgers University, and is a Fellow, Society for Biomaterials (1994); Fellow, American Institute of Medical and Biological Engineering (1995); and Fellow, Biomaterials Science Engineering (FBSE) of the World Biomaterials Congress (1996). He has authored or co-authored 125 journal articles, and co-edited 3 books, including *Proteins at Interfaces I* and *II*. He has also organized or co-organized 5 symposia at national meetings since 1975. He is a long-standing member of the editorial board of the *Journal of Biomedical Materials Research*, the *Journal of Biomaterials Science, Polymer Edition*, and the *Journal of Colloids and Surfaces B: Biointerfaces*.

John L. Brash

John Brash is Distinguished University Professor, McMaster University, in the Department of Chemical Engineering and the School of Biomedical Engineering. He has worked in biomaterials and biocompatibility research for most of his career, with emphasis on materials for use in blood contact, which are required for devices such as vascular grafts, coronary stents, and heart valves. He is the author of over 200 peer-reviewed journal publications, most of which are in the biomaterials area with a strong focus on protein–surface interactions. His work has involved collaborations with groups in Canada, the United States, Germany, France, Sweden, Australia, and China. Honors include: Fellow, Royal Society of Canada (FRSC); Fellow, Biomaterials Science and Engineering (FBSE), International Union of Societies for Biomaterials Science and Engineering; Clemson Award for Basic Research, U.S. Society for Biomaterials; Founders Award, U.S. Society for Biomaterials; Chair Professor, Soochow University, Suzhou, China; R.S. Jane Memorial Award, Canadian Society for Chemical Engineering; Docteur Honoris Causa, Université de Paris (XIII); and Chair,

In Proteins at Interfaces III State of the Art 2012; Horbett, T., et al.;
ACS Symposium Series; American Chemical Society: Washington, DC, 2012.

Gordon Research Conference on Biocompatibility and Biomaterials. He is a present or past member of several editorial boards, including those of the *Journal of Biomedical Materials Research, Biomaterials*, *Journal of Biomaterials Science Polymer Edition*, *Journal of Colloid and Interface Science*, and *Biointerphases*. He is currently an editor of *Colloids and Surfaces B: Biointerfaces*.

Willem Norde

Willem Norde (Ph.D., Wageningen University, The Netherlands) is professor emeritus in Bionanotechnology at Wageningen University and professor in Colloid and Interface Science at the University Medical Center Groningen and the University of Groningen, The Netherlands. He has a long and internationally acknowledged expertise in studying interactions among different types of (bio)particles, in particular proteins and micro-organisms, and between such particles and surfaces. He has (co-)authored about 250 peer-reviewed publications; his H-index is 55. He wrote several book chapters, edited *Physical Chemistry of Biological Interfaces* (Marcel Dekker, 2000), *Nanotechnology in the Agri-Food Sector* (Wiley-VCH, 2011) and is author of the book *Colloids and Interfaces in Life Sciences and Bionanotechnology* (CRC Press, 2011). He is member of the editorial board of *Colloids and Surfaces B: Biointerfaces*, and a member of the International Association of Colloid and Interface Scientists, the European Colloid and Interface Society, the Royal Dutch Chemical Society, and the Dutch Society for Biotechnology. He has been visiting professor at various universities around the world.

Chapter 1

Proteins at Interfaces III: Introductory Overview

Willem Norde,[1,2] Thomas A. Horbett,[3] and John L. Brash*,[4]

[1]Department of Biomedical Engineering, University Medical Center Groningen, Groningen, The Netherlands
[2]Laboratory of Physical Chemistry and Colloid Science, Wageningen University, The Netherlands
[3]Departments of Bioengineering and Chemical Engineering, University of Washington, Seattle, Washington 98195
[4]School of Biomedical Engineering, Department of Chemical Engineering, McMaster University, Hamilton, Ontario, Canada L8S 4L8
***E-mail: brashjl@mcmaster.ca**

Downloaded by UNIV OF SUSSEX on December 13, 2012 | http://pubs.acs.org
Publication Date (Web): December 12, 2012 | doi: 10.1021/bk-2012-1120.ch001

In this chapter, we provide a review of current research on proteins at interfaces under the headings: physicochemical aspects, computer simulation of protein adsorption, biological function of adsorbed proteins, resistance to protein adsorption, and experimental techniques for the study of protein surface interactions. All of these areas are represented in the various chapters in the book. This chapter gives a broader context into which the individual, specialized chapters can be placed and we have attempted to point out the connections. We intend this chapter to be of help to the community at large, and in particular to beginning students and new investigators wishing to make a contribution to the field.

1. Physicochemical Aspects

Proteins are very complex polymers. They are polyamino acids built from twenty two different amino acids, linked together via peptide bonds. They vary in size, polarity and charge. Depending on the distribution of the polar and apolar amino acids along the polyamino acid chain, the protein molecule is more or less amphiphilic. This is one of the more general or overriding reasons why

In Proteins at Interfaces III State of the Art 2012; Horbett, T., et al.;
ACS Symposium Series; American Chemical Society: Washington, DC, 2012.

Downloaded by UNIV OF SUSSEX on December 13, 2012 | http://pubs.acs.org
Publication Date (Web): December 12, 2012 | doi: 10.1021/bk-2012-1120.ch001

proteins are very surface active. Furthermore, some amino acids in the polymer chain contain a cationic group, some an anionic group, and others are uncharged. Proteins may therefore be classified as polyampholytes. Just as an almost infinite number of words can be written by using the twenty six letters of the alphabet, an endless number of polyamino acids may be formed using the twenty two amino acids, each one with its own amino acid composition and distribution. As with words, only a fraction (but still amounting to millions) of all possible sequences are “meaningful”, that is, are represented in nature as proteins, each with its own specific function.

Understanding the behavior of proteins at interfaces may start from that of the simple, coiled polymers. First, like the simple polymers, proteins adsorb by attaching several segments to a surface (like a centipede on a fly trap) resulting in a poor ability to desorb (*1–3*). When the affinity for attachment of the various molecular segments is sufficiently reduced by environmental changes (*e.g.,* temperature, pH, ionic strength, *etcetera*), the protein may leave the surface. Also, protein molecules may be displaced from the surface by adding components that have a higher affinity to adsorb. Second, because of their ionic groups proteins show adsorption patterns typical for polyampholytes, that is, strong pH-dependence, the more so the lower the ionic strength, with a maximum adsorbed amount at isoelectric conditions (*4*).

In other aspects the adsorption behavior of most proteins deviates from that of the simple polymers. In solution the simple polymers adopt flexible high-entropy structures, but when adsorbed at an interface their entropy is lower. In proteins, in particular globular proteins in an aqueous medium, the polyamino acid chain is folded up to shield the apolar moieties from contact with water resulting in a more or less compact structure of which the exterior is relatively hydrophilic and the interior more hydrophobic. Obviously, the ionic groups reside primarily at the water-exposed surface of the protein molecule. Thus, unlike the simple polymers, proteins have limited conformational freedom or, in other words, are low-entropy structures (*5*). For reasons explained under “Protein adsorption affinity”, upon adsorption the protein may undergo structural rearrangements towards a higher conformational entropy.

Against this background we will discuss some theoretical and phenomenological aspects of protein adsorption and its applications.

1.1. Protein Adsorption Affinity

Adsorption data are often presented in the form of adsorption isotherms, where, for constant temperature, the adsorbed amount Γ per unit mass or, preferably, per unit surface area of the sorbent, is plotted against the protein concentration c_p in solution, after adsorption. Protein adsorption isotherms tend to belong to the “high affinity” category, displaying a steep initial rise and a strong resistance to desorption by dilution. There is no reason to expect the isotherms to be of the Langmuirian type, because the premises of the Langmuir theory are usually not fulfilled: the adsorption is not at all or only partly reversible, lateral interactions cannot be excluded, and the attachment is usually not site-determined (*6*). The observation that adsorption isotherms for (globular) proteins show well-developed plateau values, unlike the isotherms for coiled polymers that tend to increase with increasing concentration in solution, suggests that, even though structural changes may occur, the protein molecules do not unfold to attain a loopy structure at the sorbent surface. Indeed, different experimental approaches, such as ellipsometry, optical waveguide spectroscopy, quartz crystal microbalance, and AFM spectroscopy, point to relatively compact adsorbed protein layers (*7–10*).

In some cases protein adsorption isotherms do follow a Langmuir pattern. This may be due to variation of the sorbent surface area occupied per protein molecule with varying protein concentration in solution. This phenomenon is discussed in more detail in section "Kinetics and dynamics of protein adsorption" as well as in reference (*11*). Obviously, analysis of the isotherm using the Langmuir theory (or modifications thereof) yields misleading conclusions, because the underlying conditions of that theory are not obeyed.

Because of their complex nature, *i.e.,* amphiphilicity, ambivalency, and structural features, adsorption of proteins is an intricate phenomenon involving different types of interactions. The main contributions to the adsorption process are from electrostatic, dispersion and hydrophobic forces, and, in many cases, from rearrangements in the structure of the protein molecules (*6*).

The distance over which electrostatic interaction is effective, the so-called Debye length (*12*), is in the range of a few nm, depending on the ionic strength. More specifically, in a medium of 0.01 M ionic strength the Debye length is 3 nm and in 0.1 M ionic strength it is 1 nm. Dispersion forces between proteins and sorbents interacting across an aqueous medium are usually attractive but small, because of the small dimensions of protein molecules and the low value of the Hamaker constant pertaining to such systems (*12*, *13*). When the protein and the sorbent are in close proximity (say, ≤ 0.5 nm) changes in the hydration of both components may strongly affect the adsorption. When the surfaces of the protein and the sorbent are both polar it is probable that some hydration water is retained in the contact zone between the two. However, if the surface of the protein and/or the sorbent is primarily apolar, dehydration strongly favors adsorption. Thus, when the protein and the sorbent repel each other electrostatically adsorption may occur because of overruling attractive forces. More quantitatively, the Gibbs energy of dehydration of one CH_2 group is about 1 k_BT, which corresponds to the Gibbs energy of adsorption of one monovalent ion at a surface having a potential of 25 mV. Still, because of the larger range of operation, electrostatic repulsion may give rise to an energy barrier that the protein has to surpass prior to deposition at the sorbent surface.

Rearrangements in the protein structure may occur when a protein molecule encounters an interface where it can turn one side away from the aqueous solution. Then, upon adsorption the protein may be able to present part of its hydrophobic interior at the sorbent surface without exposing apolar residues to the water. As a consequence, intramolecular hydrophobic interactions become less important as a factor stabilizing the protein structure. Because hydrophobic interactions in the protein's interior support the formation of ordered secondary structures (α-helices and β-sheets) (*5*), a reduction of these interactions destabilizes such structures. A decrease of α-helix and/or β-sheet content is therefore expected if the peptide units released from these structures can form hydrogen bonds with the

Downloaded by UNIV OF SUSSEX on December 13, 2012 | http://pubs.acs.org
Publication Date (Web): December 12, 2012 | doi: 10.1021/bk-2012-1120.ch001

Downloaded by UNIV OF SUSSEX on December 13, 2012 | http://pubs.acs.org
Publication Date (Web): December 12, 2012 | doi: 10.1021/bk-2012-1120.ch001

sorbent surface, as is the case for oxides like glass, silica, and metal oxides, or with remaining surface-bound water molecules. The decrease of ordered structure implies a higher conformational entropy and thus favors adsorption, possibly up to tens of k_BT per protein molecule (*6*). If, however, in the non-aqueous contact zone no hydrogen bonding with the surface is possible, which is the case for apolar surfaces, adsorption may induce extra peptide-peptide hydrogen bonds promoting the formation of α-helices and β-sheets (*14*). Thus, whether or not adsorption at an apolar surface leads to an increased or decreased order in the protein structure depends on a subtle balance between energetically favorable intramolecular interactions (notably hydrogen bonding) and the ensuing changes in the conformational entropy of the protein. In this context the terms "hard" and "soft" have been introduced (*15*) to indicate the strength of the internal structural coherence in the protein molecule and, hence, its resistance against adsorption-induced conformational changes.

The main conclusion is that interfaces cannot easily resist the adsorption of proteins. When the sorbent surface is hydrophobic, adsorption of any type of protein is very likely because dehydration of that surface easily outweighs electrostatic repulsion. When the sorbent is hydrophilic electrostatic interaction and/or protein structural changes may facilitate adsorption. Only when the surface is hydrophilic and the protein hard can electrostatic repulsion prevent adsorption from occurring. To achieve protein resistance, surfaces are modified, *e.g.,* by applying a coating of hydrophilic strongly hydrated polymers or zwitterionic components. This matter is further discussed in Section 4, Resistance to protein adsorption.

1.2. Kinetics and Dynamics of Protein Adsorption

As adsorption of proteins appears to be irreversible on practical time scales, the characteristics of the adsorbed molecules in their final state depend on their history, that is, on their preceding stages. Kinetics, in particular rates of adsorption relative to rates of structural changes, should be considered.

During the last few decades various models for protein adsorption kinetics have been proposed. Because of the complexity of the protein and, possibly, the sorbent surfaces on the atomic level the models follow a mesoscopic approach, where the protein is considered as a particle and effective rate constants, particle-sorbent and particle-particle interactions are used. The models have in common that they account for the generally observed features of (partial) irreversibility of the protein adsorption process and deceleration of adsorption with increasing coverage of the sorbent surface. The models differ more or less with respect to the underlying assumptions. For instance, Bornzin and Miller (*16*) assume the sorbent surface heterogeneity to cause partial irreversibility, distinguishing regions where the protein molecules stick irreversibly and regions where they attach weakly and desorb upon dilution. Kurrat et al (*17*) interpret reversible and irreversible binding in terms of the number of bonds formed, without indicating whether this variation in the way of binding results from sorbent surface heterogeneity or from different orientations/conformations of the

Downloaded by UNIV OF SUSSEX on December 13, 2012 | http://pubs.acs.org
Publication Date (Web): December 12, 2012 | doi: 10.1021/bk-2012-1120.ch001

adsorbed protein molecule. Obviously, when the sorbent surface is homogeneous the irreversibly adsorbed fraction will increase in time and ultimately the whole protein population at the surface will be irreversibly adsorbed. In the models proposed by Walton and Soderquist (*18*) and Beissinger and Leonard (*19*) time-dependent adaptation of the adsorbed protein structure to optimize interaction with the sorbent surface is accounted for: initially the protein adsorbs reversibly but during contact with the surface the desorption rate decreases gradually with time. Here too, the irreversible nature of the adsorbed layer increases with ongoing contact between the sorbent and the protein solution. The same assumptions, but, furthermore, an increasing molecular area ("footprint") of the adsorbed protein molecule when it relaxes at the sorbent surface, is included in the model presented by Norde (*20*). According to this model, the growing fraction of irreversibly adsorbed, structurally relaxed, molecules at the expense of reversibly adsorbed unperturbed ones may result in an "overshoot" of protein at the surface during the course of the adsorption process (*21–23*).

Perhaps the most successful, at least the most popular, description of protein adsorption is the random sequential adsorption (RSA) model, or modifications thereof (*24–26*). According to the RSA theory a single adsorbed molecule (or, for that matter, particle) that hits the sorbent surface sticks there and defines a zone around that particle that excludes the center of subsequently arriving molecules. Thus, for spheres of radius a each adsorbing particle blocks an area of $\pi(2a)^2$. Therefore, at low surface coverage the area available for adsorption decreases four times faster than when the surface occupancy by the particles themselves is taken into account, with a corresponding decrease in adsorption rate. At higher surface coverage the area available for adsorption should be corrected for overlapping exclusion zones around the particles. For spheres the RSA model predicts adsorption saturation due to jamming at a surface coverage of 55%. For particle geometries deviating from spherical the jamming limit is lower, *e.g.*, 40% for particles having an aspect ratio of 7.5. Experimental values for protein adsorption are usually higher than the jamming limits predicted by RSA. This may be due to the possibility of lateral diffusion of the adsorbed protein molecules, as has been reported by (*27*, *28*) as well as by Sotres et al in Chapter 6. A fundamental problem in applying this or any model to actual data is that the area available to the protein molecule is never well known, because even very small, protein molecule sized deviations from flatness can accommodate protein molecules, yet are easily missed by surface area measuring methods.

The RSA model may be modified to more accurately describe protein adsorption by including surface-induced changes in protein conformation and orientation (*26*). Such changes usually lead to a larger footprint and in the RSA model this is accounted for by an instantaneous and symmetric expansion of the particle to a given pre-set size. If no space is available for that expansion the particle permanently keeps its original dimensions. Further modification includes that, unlike the expanded particle, the non-expanded particles may leave the surface by desorption (*26*). The result could be that, under certain conditions, non-expanded particles are gradually displaced by expanded ones showing up as a maximum in the adsorbed amount ("overshoot") during the sequential adsorption process.

The RSA model has also been adapted to apply to mixtures of different proteins (*26*). Then, the population of each type of protein in the adsorbed layer is determined by its respective adsorption rate and molecular size. However, the outcome is not compatible with the experimentally observed “Vroman effect”, *i.e.*, the transient change in composition of the adsorbed layer due to the displacement one kind of protein by a later arriving kind that has a higher adsorption affinity (*29*, *30*). Indeed, the experimental data on sequential adsorption of antibodies and serum albumin, reported by Dupont-Gillain in Chapter 21, seem to be at odds with the RSA model.

Each of these models is suspect in one way or another. The main problem is related to the complexity and heterogeneity of the protein molecule and the poor understanding of the mechanism underlying the time-dependent desorbability of the protein layer (*31*).

Structural changes in the protein molecules are essential in adsorption kinetics and, because of the irreversibility of the adsorption process, for the final state and, as a consequence, for the biological activity of the adsorbed layer. Therefore, the dynamics of the relaxation of the proteins at the sorbent surface is considered in more detail. Relaxation, which usually implies a certain degree of spreading, leading to lower adsorption saturation Γ^{sat}, occurs with a certain characteristic time τ_r. The extent of spreading depends on the rate of relaxation compared to the time τ_f needed to fill the sorbent surface, in the absence of desorption. The value of τ_r depends on the protein’s resistance against deformation. For a given protein, the internal coherence usually decreases with increasing net charge. Indeed, the maximum value of Γ^{sat} (pH), often observed at the isoelectric point of the protein, may be ascribed to progressive conformational changes at pH values further away from the isoelectric point (*6*). Additionally, τ_r is influenced by properties of the sorbent-water interface, notably its interfacial tension. The higher the interfacial tension is, the stronger is the tendency to spread over it. Examples are given in references (*32*, *33*).

The value of τ_f is controlled by the supply rate (flux) of molecules that arrive at the sorbent surface and are able to deposit. Hence, τ_f scales inversely with the protein concentration in solution and linearly with the resistance to reach the surface (which is composed of the resistance to transport through the solution and the resistance associated with overcoming possible barriers for deposition).

If $\tau_r/\tau_f >> 1$, relaxation is completely inhibited because adjacent surface area is already occupied by newly depositing molecules before the previously adsorbed one has the time to spread. If, conversely, $\tau_r/\tau_f << 1$ all molecules are given time to fully relax and reach their maximally attainable footprint at the sorbent surface. For intermediate cases the adsorbed protein population is partly relaxed. Since τ_f depends on the supply rate, the average degree of spreading and, more importantly, the biological activity of the adsorbed layer, can be manipulated by varying experimental conditions that influence the flux (*e.g.*, protein concentration in solution and flow characteristics) (*34*).

By way of example, results for IgG adsorption on a silica surface are shown in Figure 1, where the surface area per adsorbed molecule is plotted vs. τ_f. For $\tau_f = 0$, where spreading is fully suppressed, the corresponding area may be compared with the dimensions of the native IgG molecule. The part of the curve where the

Downloaded by UNIV OF SUSSEX on December 13, 2012 | http://pubs.acs.org
Publication Date (Web): December 12, 2012 | doi: 10.1021/bk-2012-1120.ch001

molecular area is independent of τ_f and has reached its maximum value reflects full relaxation. It is well known that for many proteins in solution the unfolding is a two-state transition rather than a gradual swelling, and this seems to hold for adsorbed proteins as well (*35*). Then, the τ_f-dependent part of the curve in Figure 1 represents the co-existence of native (N) and spread (S) IgG molecules at the surface.

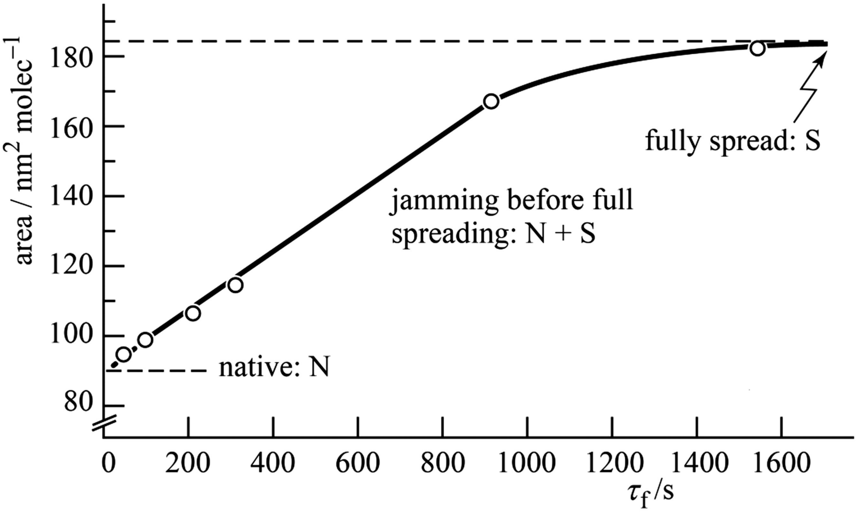

Figure 1. Relaxation of IgG molecules adsorbed at a silica surface. Redrawn from ref. (34).

Clearly, the N/S ratio decreases with increasing τ_f and from that functionality it may be inferred that for IgG the characteristic time of relaxation is of the order of 1000 s. Similarly, for savinase, a much smaller protein molecule, 100 s has been derived for τ_r (*34*), but for serum albumin and fibrinogen relaxation times of more than an hour have been reported (*36*). In contrast to globular proteins, the spreading of simple coiled polymers that adsorb from a good solvent occurs almost instantaneously (*34*).

As expected, the biological activity of adsorbed IgG increases when the fraction of N-molecules in the adsorbed layer is higher (*37*), which may be achieved by increasing the supply rate. In practice, a higher flux is usually realized by choosing a higher protein concentration in solution. Furthermore, even if sufficient time for relaxation is allowed, molecules arriving at a surface that is already crowded with pre-adsorbed molecules may deposit at interstitial sites where no area is left for spreading. Hence, the later arriving molecules may have the highest biological activity. A similar reasoning holds, for other protein/sorbent systems as well (*36*, *38–40*).

As mentioned before, the foregoing discussion of protein adsorption is a mesoscopic one. However, recently more detailed approaches have been more or less successfully followed based on atomistic multilevel simulations either

Downloaded by UNIV OF SUSSEX on December 13, 2012 | http://pubs.acs.org
Publication Date (Web): December 12, 2012 | doi: 10.1021/bk-2012-1120.ch001

or not in synergistic combination with experimental data. The chapters in this book by Bellucci et al (Chapter 10) and by Abramyan et al (Chapter 9) are excellent illustrations of the potential of these methods to understand and predict protein-surface interactions.

2. Computer Simulation of the Adsorption of Proteins to Solid Surfaces and Related Experimental Work

In this section, as an introduction to this area of research, we present some of the reasons for computational approaches to the structure of adsorbed proteins, and some of the barriers that have made this approach develop slowly. In the remainder of the section, three computational studies of adsorbed proteins will be presented, two of which are from this book. As will be seen, each study uses somewhat different approaches.

Downloaded by UNIV OF SUSSEX on December 13, 2012 | http://pubs.acs.org
Publication Date (Web): December 12, 2012 | doi: 10.1021/bk-2012-1120.ch001

2.1. Computational Prediction of Adsorbed Proteins: Rationale and Barriers

The orientation and conformation of adsorbed proteins are fundamental to almost all aspects of protein behavior at interfaces. But experimental techniques to characterize these aspects are mostly limited to indirect measures such as the availability of an antibody binding site or amount of enzyme activity, or global measures of structure such as circular dichroism or the heat of unfolding, in contrast to the exquisitely detailed atomic positions available for crystalline proteins. For small biomineralization proteins like the human salivary phosphoprotein statherin, solid state NMR is capable of giving enough direct information so that computational refinement leads to a high degree of structure determination when these proteins interact with hard tissue minerals (see Chapter 4 by Roehrich et al). However, the structures of statherin and other biomineralization proteins obtained from solid state NMR studies are the only existing example of highly detailed structural information for adsorbed proteins.

The state of the art for adsorbed proteins is thus that highly detailed information about their structure in the adsorbed state is not available, and constitutes a major gap area in this field. To help fill this gap, computational methods are being applied using increasingly powerful computers and novel strategies to sample more structural possibilities. A good appreciation of the power of these methods can be easily obtained by examination of the graphical output of the computations, which shows the location of each atom in the protein and the surface, and can also show the surrounding water (see Figure 5 in Chapter 9 by Abramyan et al). Experimental work needed to support the computational approaches has also led to fundamental information about the strength and type of interactions between each type of amino acid side chain and several types of functional groups at the surface of the adsorbing solid surface. Each approach is fully described in Chapter 9 from Latour's group and also has been reviewed recently (*41*). We therefore limit ourselves here to a brief set of comments on a few more general aspects of computational methods to predict the structure of adsorbed proteins and their orientation.

From the beginning, a central problem of the computational approach has been the absence of known structures for adsorbed proteins, meaning there was no way for a predicted structure to be proven wrong or right and thus no way to be sure the computational methods were accurate. This problem is still an impediment to progress, although it is being addressed in Latour's group with several experimental approaches intended to provide more structural information about adsorbed proteins. Another major problem was the lack of validated force fields for residue-surface interaction calculations, necessitating the use of force fields developed for protein folding calculations. Finally, the ability to include individual water molecules in the calculations, as opposed to a modified force field that implicitly includes the effect of water, have come about only relatively recently, as a result of increased computational power. Another problem with molecular dynamics calculations when done with solvent present is that more or less metastable states can be encountered, although advanced sampling methods are thought to be a feasible way around this problem. It is against this background of major hurdles that computational approaches need to be understood. It is thus not surprising that this approach is still early in its development and far from being fully accepted or appreciated by other workers in the proteins at interfaces field, despite considerable recent progress towards overcoming all these difficulties.

Downloaded by UNIV OF SUSSEX on December 13, 2012 | http://pubs.acs.org
Publication Date (Web): December 12, 2012 | doi: 10.1021/bk-2012-1120.ch001

2.2. Recent Experimental and Computational Studies Related to the Prediction of the Structures of Adsorbed Proteins

2.2.1. Studies from the Latour Group

A major recent achievement of the Latour group has been the collection of extensive experimental data needed to correct the force fields underlying the molecular dynamic (MD) calculations used to calculate protein and peptide interactions with surfaces (see Chapter 9 by Abramyan et al). Existing force fields built into CHARMM and other MD systems are not necessarily correct for protein interactions with surfaces. The experimental data collected by Latour's group consists of free energies of adsorption for a set of 108 peptide–surface combinations collected with SPR methodology. Discrepancies between predicted outcomes based on CHARMM and this experimental data provide the basis for correction of the underlying force fields and for increased accuracy in simulating what peptides and proteins really do at interfaces. In addition, a method was developed that involved AFM tips with covalently bound peptides to measure desorption forces after the tip approached a test surface. A good correlation between the SPR free energy data and desorption forces measured with AFM was found, showing that the AFM method is suitable to measure free energies for peptide-surface systems that are not amenable for evaluation by SPR. The combination of improved computational methods and the experimental peptide adsorption data should lead to much more accurate prediction of protein adsorption behavior and thus provide an invaluable tool in the history of research on protein-surface interactions.

2.2.2. Studies from the Corni Group

While Latour's group has concentrated on simulation of peptide and protein interactions with polymeric surfaces, others have worked on protein interactions with inorganic surfaces. Thus, protein interactions with gold have been simulated (see Chapter 10 by Belluci et al). The authors also use the molecular dynamics method, which employs pre-assigned force fields for all the atoms in the system. The limits of current force fields for simulating protein surface interactions are noted by these authors as well, who thus produced a new force field for gold-protein interfaces which they used to simulate amyloid β (Aβ) peptide interactions with gold. The simulations showed the peptide became trapped near the surface and large conformational rearrangements of the peptide were not observed i.e. the observed structure only depended on how the peptide (randomly) approached the surface. These authors thus also emphasize that enhanced sampling techniques will be necessary to explore the possible adsorption modes and conformations of the biomolecules at the gold/water interface..

2.2.3. Studies from Raffaini and Ganazzoli

Instead of including an ensemble of explicit water molecules in the modeling, with their huge computational burden, as advocated by Latour and others, some workers have used implicit water methods. For example, in a study of the structure of lysozyme adsorbed to graphite, the implicit water method (represented in the model by inclusion of the dielectric constant of the aqueous phase, rather than individual water molecules) predicted a very rapid flattening of the lysozyme molecule (*42*). This group also published a more recent modeling study of an alpha helical albumin subdomain or a beta sheet rich fibronectin module interacting with titanium oxide (*43*). In this study as well, rapid flattening of the protein fragments against most of the polymorphs of titanium oxide was also predicted. Thus, for example, the distance between the backbone center of mass of the albumin domain and the surface decreased from ca. 0.8 to 0.4 nm in the first few nanoseconds of the computational simulation.

However, the accuracy of these predictions is fairly doubtful because the implicit water method may not properly deal with hydrogen bonding or London dispersion interactions between water and the protein or water and the surface (see further discussion in (*41*)). The shortcomings of the implicit water method for studies of proteins at interfaces and doubt about the predictions based on this approach have been discussed by other workers in this field. Yeh et al concluded that "Despite reports that dielectric-screening models in MD simulations can cause significant protein structural distortions, they are still popular among many applications in the literature. ... our results strongly support the notion that the application of these models should be abandoned in large-scale sampling of energy landscapes." (*44*). Latour has concluded that "the use of dielectric constant-based methods alone as an implicit solvation model will give erroneous

Downloaded by UNIV OF SUSSEX on December 13, 2012 | http://pubs.acs.org
Publication Date (Web): December 12, 2012 | doi: 10.1021/bk-2012-1120.ch001

results that have little to do with peptide/protein adsorption behavior and simply should never be used." (*45*). Thus, although the implicit water based calculations are able to predict a final configuration of adsorbing polypeptides even for relatively large peptides like lysozyme and the fibronectin and albumin modules, the accuracy of the computational solutions seems questionable.

3. Biological Function of Adsorbed Proteins

The biological function of adsorbed proteins can be subdivided into two major sub-topics that have received extensive study. The major subtopics are as follows: 1) how the adsorption process affects activities inherent to the protein itself such as enzyme activity or ability of an adsorbed antibody to bind its antigen; 2) how adsorption affects the ability of other agents such as cells or antibodies to bind to the adsorbed protein, especially the adhesion proteins that mediate cell attachment to foreign surfaces. In addition to these two major subtopics, this section also includes shorter sections focused on the following related sub-topics: 3) comments on newer cell interaction studies, including studies from this book as well as others focusing on stem cell growth and differentiation; 4) surface chemistry effects on adhesion proteins; and 5) adsorbed proteins in longer term events. Further discussion of each subtopic is presented below, along with illustrative examples from research presented in this book and from the literature.

Downloaded by UNIV OF SUSSEX on December 13, 2012 | http://pubs.acs.org
Publication Date (Web): December 12, 2012 | doi: 10.1021/bk-2012-1120.ch001

3.1. Adsorbed Enzymes and Antibodies

3.1.1. Enzymes

Immobilized enzymes typically exhibit altered substrate turnover kinetics compared to bulk phase enzymes due to hindered mass transport near the immobilization surface as well as occasional partitioning of the enzyme's substrate by the surface that increases the local concentration. For enzymes with high turnover rates that are adsorbed to porous carriers, the activity is often lower than for the bulk phase enzyme because of mass-transfer limitations, i.e. their turnover rates are "diffusion controlled". Adsorbed enzymes can also have alterations in activity beyond those due to mass transport or partitioning effects, due to either structural changes or to orientations that inhibit access to the active site (reviewed in (*46*)). Changes in adsorbed enzyme activity compared to the bulk phase enzyme's activity thus can give some information on the state of the molecule, although care must be taken to sort out mass transfer effects from those due to molecular changes in the enzyme molecule itself.

Adsorbed or otherwise immobilized enzymes were the subject of intense study and characterization when this technology was first introduced, due to interest in industrial application of immobilized enzymes by chemical engineers and because of their various bioanalytical applications (*46*). Currently, research

Downloaded by UNIV OF SUSSEX on December 13, 2012 | http://pubs.acs.org
Publication Date (Web): December 12, 2012 | doi: 10.1021/bk-2012-1120.ch001

on the use of immobilized enzymes is very active for bioanalytical applications, including biosensors (see recent reviews: (*47*, *48*)) and disposable "bioactive paper" based bioanalytical methods being developed especially for applications in less developed areas (*49*). Immobilized enzymes are a key part of biosensors, and adsorption is one of the immobilization strategies often employed, so new developments in this application area continue to appear. Newer methods include the layer-by-layer adsorption strategy based on alternate layers of polyelectrolyte and enzyme with opposite charges, and Langmuir-Blodgett transfer of enzymes adsorbed to a film formed at the air/water interface to a solid support. The use of high surface area nanomaterials such as multi-walled carbon nanotubes (MWCNT) or gold nanoparticles adsorbed with enzymes to increase sensitivity are also relatively new approaches. Finally, the adsorption of enzymes to conductive polymers that allow electron transfer from the enzyme to the electrode via the conductive polymer has been the subject of many recent studies. The convenience and ease of adsorptive immobilization of enzymes continues to make this method popular, even though many covalent immobilization strategies have also been developed. Finally, we wish to note that because adsorbed enzymes are more properly a subarea of the large field of immobilized enzymes, rather than the field of protein adsorption. Thus, the comments here are necessarily very brief and intended primarily to remind us that adsorbed enzymes are probably the largest single application area for proteins at interfaces.

Probably the most pertinent aspect of enzymes at interfaces to the current book is that their behavior helps us better understand structural changes brought about by adsorption of proteins, since even minor changes in the enzyme's active site are expected to abolish enzyme activity. Adsorbed enzymes typically display reduced enzyme activity compared to the same enzyme in the solution phase. The reduced activity is strongly dependent on surface loading, but this reduction can be mitigated by the inclusion of co-adsorbing proteins such as albumin. The effect of loading levels of the enzyme itself or of co-adsorbed proteins are ascribed to the reduction of enzyme contacts (per molecule of the enzyme) with the substrate so that less conformational distortion of the enzyme occurs. The losses are dependent on both the enzyme and the adsorbent, because some enzymes are less conformationally stable ("softer") than others. All of these aspects of adsorbed enzymes have been described in a recent monograph (*46*).

In the previous volume in this series, stability mutants of T4 lysozyme were used to show the contribution of thermodynamic stability to unfolding rates in the adsorbed enzyme (*31*). In the current volume, the activity of three enzymes adsorbed to four kinds of SAMS varying in terminal functional group has been found to vary greatly (see Chapter 9 by Abramyan et al). In the case of hen egg white lysozyme, the variations in enzyme activity after adsorption to the SAMS were found to be correlated with solvent accessibility of active site tryptophan residues (Abramyan et al Chapter 9). The results indicated that HEWL orientation depended on the hydrophobicity of the adsorbing surface: on a hydrophobic surface, the active site tryptophan in HEWL was not reactive, suggesting that the active site was close to the surface in a non-solvent-accessible manner, while the protein orientation on the OH-SAM surface was such that the bioactive site remained solvent accessible.

3.1.2. Antibodies

Immobilized antibodies are often used in solid phase immunoassays to capture bulk phase antigens. When adsorption is used to immobilize the antibody, typically much less than 100% of the adsorbed antibodies retain the ability to bind antigen. The loss in antigen binding capacity of adsorbed antibodies can be reduced by alteration of the chemical properties of the adsorbing surface so that structural changes are reduced and the binding site is oriented in a more accessible direction. Although recognition of the loss of function in adsorbed antibodies is longstanding (*50*), work continues to the present to overcome this limitation of solid phase immunoassays because of the advantages that the resultant increased sensitivity carry, and the importance of solid phase immunoassay method to disease diagnosis and treatment.

In Chapter 21, Dupont-Gillain describes studies directed towards finding an antibody with a constant part that would be particularly suitable for adsorption in end-on position, which involved evaluating the antigen-binding efficiency of antibodies with different constant parts, i.e. from different species or different isotypes. Surprisingly, for eight antibodies with different constant regions, the antigen binding efficiency varied in only a relatively small range (0.5-1.0 moles antigen per mole antibody).

In Chapter 25 Zhao et al present studies of antibody adsorption at the silica/water interface using a number of interfacial techniques including spectroscopic ellipsometry (SE), neutron reflection (NR), dual polarization interferometry (DPI) and atomic force microscopy (AFM) to determine the interfacial conformations. Packing density of the adsorbed antibodies had a major effect on their ability to bind antigens, due to steric hindrance. This chapter also provides studies of the availability of alpha and gamma chain antibody binding sites in adsorbed fibrinogen, showing them to be highly dependent on the chemistry of the adsorbing surface.

Use of protein engineering methodology that allows insertion of desired amino acids with higher affinity to a chemical moiety on the surface to control protein orientation represents a very sophisticated approach that Baio et al studied (Chapter 35). They hoped it would be useful to improve the antibody capture method's sensitivity. These authors used protein G as a model system to show that controlled orientation is achievable. Cysteine substitutions in the amino acid sequence followed by immobilization to maleimide oligo (ethylene glycol)-functionalized (MEG) substrate were done to alter the orientation of the protein, which was confirmed by changes in the distributions of amino acids detected by TOF-SIMS. TOF-SIMS as well as sum frequency generation spectroscopy (SFG) were used to show differences in amino acid distributions for protein G variants (negatively charged amino acids substitutions for neutral residues) immobilized onto two oppositely charged substrates (COO^- and NH_3^+ functionalized gold).

Jiang's group has also worked extensively to control protein orientation using a "charge-driven protein orientation", using $-NH_2$ (positively charged) and -COOH (negatively charged) terminated self-assembled monolayers (SAMs) (*51*). One of the antibodies studied, an IgG_1 type, had higher antigen binding when adsorbed

Downloaded by UNIV OF SUSSEX on December 13, 2012 | http://pubs.acs.org
Publication Date (Web): December 12, 2012 | doi: 10.1021/bk-2012-1120.ch001

on the NH_2 surface than on a COOH surface, but antigen binding to adsorbed IgG_{2a} was similar on the NH_2- and COOH-terminated surfaces, probably due to the smaller dipole moment of IgG_{2a} compared to IgG_1. This group also used TOF-SIMS on antibodies adsorbed to surfaces to show orientational differences in the adsorbed state of the same antibodies on the -NH_2 and -COOH surfaces (*52*). Jiang's group also used charged SAMS to control the orientation of the cell adhesion proteins osteopontin (*53*) and fibronectin (*54*). Cell adhesion and spreading to OPN or FN adsorbed to the NH_2 surface was much higher than those on the -COOH surface.

3.2. The Adhesion Proteins

3.2.1. The Role of Adhesion Protein Adsorption in Cell Adhesion to Foreign Materials

Downloaded by UNIV OF SUSSEX on December 13, 2012 | http://pubs.acs.org
Publication Date (Web): December 12, 2012 | doi: 10.1021/bk-2012-1120.ch001

The fact that some plasma proteins are specifically bound by integrin receptors on cells is fundamental to understanding the biological role of adsorbed proteins in any setting in which a foreign material interacts with cells, either *in vitro* or *in vivo* and has been reviewed previously (*11*, *55*). Thus it is widely accepted that at least the initial phase of a material's interactions with blood, soft tissue, or bony tissue is largely dictated by adsorbed adhesion proteins. The adhesion proteins include fibrinogen, fibronectin, vitronectin, von Willebrand's factor, and perhaps osteopontin. When adsorbed, the adhesion proteins promote the adhesion of cells to the surface. Most cells have integrin adhesion receptors, including platelets, macrophages, neutrophils, and osteoblasts. Variations in the amount and the adhesive potency of adhesion protein adsorbed to surfaces depends on surface chemistry and adsorption conditions (loading, co-adsorbed proteins, residence time and temperature). The adsorbed adhesion proteins strongly affect short-term cell adhesion, i.e. typically there is little or no cell adhesion unless the surface has at least some adsorbed adhesion protein. Most studies supporting this conclusion are based on *in vitro* study of cell interactions with surfaces exposed to protein containing media such as serum or plasma (for mammalian cells) or saliva (for oral bacteria; see Chapter 16 by Xu et al), but a few *in vivo* studies have also been done.

While much of the early work on the role of adsorbed proteins in cell interactions was done on polymeric surfaces, it is clear that protein adsorption to hard materials also has important biological roles, as shown in the review in this book on protein - interactions with bioceramic materials (see Chapter 3 by Victor and Sharma) and the structural studies of peptides and proteins that affect biomineralization (see Chapter 4 by Roehrich et al). On hard materials, fibronectin adsorption is important, but also bone specific proteins such as bone morphogenic protein (BMP) and osteopontin (OPN) play unique roles in cell interactions with hard materials. Adsorbed proteins also play a key role in hard material morphogenesis, as reflected in this quote from the chapter by Roehrich et al: "The remarkable material properties of shell, bone and teeth thus result from the activities of proteins that function at the organic-inorganic interface." Protein adsorption also plays an important role in another biological process involving hard materials, namely the lubricant properties of adsorbed albumin on artificial joint materials and the apparent importance of the conformation of the albumin adsorbed to different materials in reducing friction (see Chapter 23 by Serro et al).

The key role of adhesion proteins in mediating cell interactions with biomaterials has been demonstrated clearly by preadsorbing a surface with serum or plasma that is missing the protein, which results in a great reduction in adhesion of the target cell. The selectively deficient plasmas and sera used in these studies can be obtained from genetically deficient donors, as in afibrinogenemia (e.g. (*56*)), by selective removal using chromatography over immobilized antibodies (e.g. (*57*)) or by selective enzymatic depletion as done in mice (*58*). In such studies, the role of the depleted protein is typically confirmed by showing that cell adhesion is restored when the depleted protein is added back to the serum or plasma prior to preadsorption of the surface. A recent study of this type is described in Chapter 14 in which the role of both fibrinogen and complement C3 in mediating monocyte/macrophage adhesion to nonfouling and control surfaces was studied with depleted plasma or serum and confirmed by adding back the depleted protein (see Chapter 14 by Szott and Horbett).

Downloaded by UNIV OF SUSSEX on December 13, 2012 | http://pubs.acs.org
Publication Date (Web): December 12, 2012 | doi: 10.1021/bk-2012-1120.ch001

3.2.2. Variations in Adhesion Protein Functional Activity

The many studies with depleted serum or plasma make clear that the adsorption of one (or more) of the adhesion proteins is necessary to promote cell adhesion to the surface, and that most of the proteins that adsorb lack this capability. Thus, variations in the relative amounts of the adhesion proteins in the adsorbed layer on different surfaces would be expected to lead to variations in cell adhesion. For example, the requirement for adsorbed fibrinogen to mediate platelet adhesion to a surface and the fact that most other proteins such as albumin are thought to prevent cell adhesion would suggest that the amount of adsorbed fibrinogen would be well correlated with platelet adhesion. However, several studies have shown that the adsorbed adhesion proteins vary in their adhesive potency, depending on adsorption conditions and the adsorbing surface, so that the total amount of adsorbed adhesion protein is often only poorly correlated with cell adhesion. Instead, cell adhesion correlates with the availability of the cell adhesion motif in the adsorbed adhesion protein, as measured with monoclonal antibodies that bind to this motif. Figure 2 illustrates some of these concepts.

For example, Steele et al found that much higher amounts of fibronectin had to be adsorbed to polystyrene to promote cell adhesion than if the fibronectin were adsorbed to chemically altered “tissue culture” grade polystyrene, and they used the term “molecular potency” to indicate that adsorbed fibronectin could vary in how good it was in supporting cell adhesion (*59*). Subsequently, several studies using monoclonal antibodies to probe for the availability of the cell adhesion motif in adsorbed adhesion proteins have clearly shown that the availability of the adhesion motif varies greatly with chemistry of the surface to which the adhesion protein is adsorbed, explaining the poor correlation with the total amount bound. Good examples are the variations in availability of macrophage binding regions in fibrinogen adsorbed to five different polymers (*60*), and a multivariate study

Downloaded by UNIV OF SUSSEX on December 13, 2012 | http://pubs.acs.org
Publication Date (Web): December 12, 2012 | doi: 10.1021/bk-2012-1120.ch001

of the availability of platelet binding regions in fibrinogen adsorbed to a series of five chemically distinct modified polystyrene surfaces (*61*). In Chapter 14 by Szott and Horbett, the antibody binding method has been used to probe for the availability of monocyte/macrophage binding motifs in fibrinogen adsorbed to plasma deposited tetraglyme protein resistant surfaces. Surprisingly, it was found that even though fibrinogen adsorption to tetraglyme surfaces is low, it may mediate higher than expected monocyte/macrophage adhesion due to higher availability of the cell binding domain in fibrinogen adsorbed to tetraglyme (Chapter 14 by Szott and Horbett). The availability of the platelet binding domains in adsorbed fibrinogen for antibody binding has also been studied using atomic force microscopy (AFM) tips coated with the antibody, as described in Chapter 17 by Xu et al. As these authors state, “The probability of antibody binding correlates well with temporal changes in platelet adhesion to these material surfaces, suggesting that the availability of the γ-chain in fibrinogen is a useful predictor of platelet adhesion.”

Thus, both the older literature and also more recent studies have firmly established the concept that the cell adhesive motifs of adsorbed adhesion proteins vary greatly in regard to their availability to cells attempting to adhere to the surface to which the adhesion protein is adsorbed. These variations in availability have always been assumed to be due to orientations that place the adhesion motif in a position that interferes with access to the cell’s adhesion receptor, or to structural alterations in adsorbed adhesion proteins that cause the adhesion motif to have lower cell binding affinity. A recent study has provided very good evidence for the role of structural variations (*62*). This study found that the correlation between total Fg adsorption and platelet adhesion to SAMs terminated with CH_3, $OCH_2\,CF_3$, NH_2, COOH, or OH was poor ($r^2 = 0.04$), but that there was a very good correlation ($r^2 = 0.96$) between platelet adhesion and loss of alpha helix (measured with circular dichroism, CD). This article and other recent studies on cellular responses to adsorbed proteins were reviewed recently (*55*).

3.3. Some Newer Aspects of Protein Adsorption Effects on Cell Interactions

Almost all studies of the role of adsorbed proteins on cell interactions with materials have been restricted to relatively short times. Thus, what role the adsorbed protein layer plays in cell interactions in the longer term, such as steady state platelet consumption for long term implants in blood, or the development of the fully developed fibrous capsule around implants placed intraperitoneally or subcutaneously, remains poorly understood. It was surprising, for example, to find that plasma deposited tetraglyme coatings that exhibit very low fibrinogen adsorption in short term studies *in vitro* still elicited a typical foreign body capsule after implantation in mice for 30 days (see Chapter 14 by Szott and Horbett). Others have also noted the discrepancy between short term changes in protein and cell interactions caused by surface chemistry changes and lack of an effect on the longer term fibrotic response (see Chapter 15 by Baker and Tang). These workers have taken the approach of trying to increase the surface chemistry effect by increasing surface area using particulate materials or by including topographic cues. Using these approaches, they have been able to show that the fibrotic response appears to be sensitive to surface topography. They have also provided evidence that fibrocytes (circulating fibroblasts), rather than macrophages, appear to be involved in collagen production in fibrosis, and have suggested ways in which topographical cues could affect cell response by alterations in the way the adsorbed proteins cues are perceived by the cells. These authors suggest that increased surface area and protein adsorption may lead to increased cellular adhesion on micropillar substrates over smooth surfaces. They also suggest that increased focal contacts, as a result of changing pillar dimensions, would enhance the mechano-chemical feedback to the cell.

Downloaded by UNIV OF SUSSEX on December 13, 2012 | http://pubs.acs.org
Publication Date (Web): December 12, 2012 | doi: 10.1021/bk-2012-1120.ch001

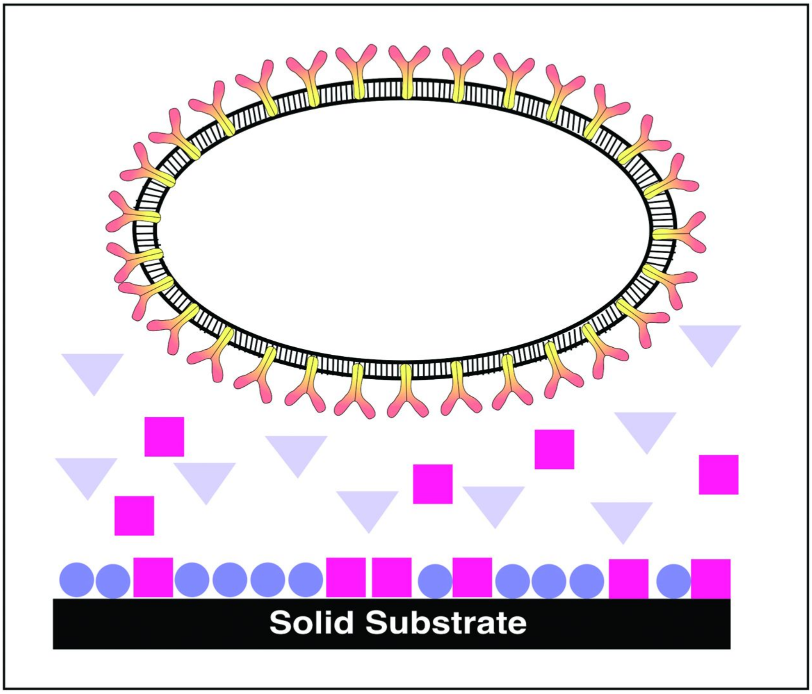

Figure 2. Cell interactions with foreign surfaces are mediated by integrin receptors and adsorbed adhesion proteins that sometimes change their biological activity when they adsorb. The cell is shown as a circular space with a bilayer membrane in which the adhesion receptor protein molecules (the slingshot shaped objects) are partly embedded. The proteins in the extracellular fluid are represented by circles, squares, and triangles. The receptor proteins recognize and cause the cell to adhere to only the surface bound form of one protein, the one represented by a solid dark blue circle. The bulk phase of this same adhesion protein is represented by a lighter blue triangle, indicating that the solution and solid phase forms of this same protein have different structures and cell adhesivity. The figure is schematic and not to scale. (From Biomaterials science, third edition, 2013 in press, with permission. Copyright Elsevier.)

While much of the interest in the role of adsorbed proteins in cell interactions with materials was due to their role in the response to implanted biomedical devices, other application areas included the development of surfaces that would support improved cell growth or migration, e.g. in cell culture or re-endothelialization of vascular grafts. Thus, for example, variations in surface chemistry can lead to enhanced fibronectin adsorption and endothelial cell adhesion and growth (*63*) and corneal cell migration (*64*). However, since fibronectin is often in fibrillar form in natural extracellular matrices, material effects on fibrillogenesis of fibronectin have also been studied recently (see Chapter 22 by Cantini et al). These authors used surface chemistry to promote fibronectin fibril formation and show its effect on cell adhesion and differentiation. Surprisingly, the organization of FN at the material interface on two similar chemistries poly (ethyl acrylate) (PEA) and poly (methyl acrylate) (PMA) was very different: FN fibrils formed on PEA ("material-driven fibrillogenesis"), whereas only dispersed molecules were observed on PMA.

Recently, possible control of stem cell differentiation by variation in surface properties or adsorbed proteins has become of interest because protein adsorption to biomaterials may also elicit alterations in cell fate (see brief review by Szott and Horbett (*55*)). Several studies used combinatorial screening methods to find biomaterials that affect stem cells via their effect on adsorbed Fn and other adhesion factors or immobilized growth factors (*65*, *66*). In the past year, many more studies on using variations in the chemistry of the adsorbing surface to vary stem cell growth and differentiation have appeared, so it is clear that this area represents a growing area of research on the role of adsorbed proteins and cell interactions. One of the more complete studies, in which a synthetic polymer interface for the long-term self-renewal of human embryonic stem cells (hESCs) in defined media was developed, also reported that the key protein in mediating hESC adhesion to the aminopropylmethacrylamide (APMAAm) surface appeared to be bovine serum albumin, rather than the other proteins in the media (transforming growth factor beta and basic fibroblastic growth factor) (*67*).

Downloaded by UNIV OF SUSSEX on December 13, 2012 | http://pubs.acs.org
Publication Date (Web): December 12, 2012 | doi: 10.1021/bk-2012-1120.ch001

3.4. Surface Chemistry Effects on the Adsorbed Adhesion Proteins

From a surface chemistry point of view, it remains difficult to articulate principles that underlie affinity or activity differences in adsorbed adhesion proteins. Thus, experimentation is required with each material to show how well it binds a particular adhesion protein and how much of the adsorbed adhesion protein retains its ability to bind cells. One exception to this generality is of course non-fouling materials, as it is clear that any surface chemistry that reduces protein binding will also reduce cell adhesion, as further discussed elsewhere in this chapter. A seemingly good "theoretical" approach to vastly improved biomaterials stems directly from our current understanding of the role of adsorbed proteins in mediating cell adhesion. Thus if a material could be made that resisted adsorption of all or almost all of the adhesion proteins and also remained highly resistant for long periods in the body, it would be expected to exhibit superior biocompatibility. Protein resistant plasma polymerized tetraglyme coatings on tubes exhibit very little adherent material *in vitro* (*68*) and also after one day exposure to cow blood in an *ex vivo* shunt (Horbett et al, unpublished observations). On the other hand, plasma deposited tetraglyme coated FEP films still elicit a foreign body reaction, possibly because of complement activation (see Chapter 14 by Szott and Horbett). Overall, relatively little long term *in vivo* testing of this or other protein resistant materials has yet been done so it is still unclear whether materials that are persistently protein resistant will improve biocompatibility of implanted medical devices.

3.5. The Role of Adsorbed Proteins in Longer-Term Events

Only a few studies of the adsorbed proteins on surfaces after long contact periods with bodily environment have been published, but they have provided some insight into longer-term events. Extensive degradation of adsorbed proteins on explants has been observed, presumably due to proteolytic digestion. For example, smaller size fragments of proteins have been observed on breast implants (*69*), glucose sensors (*70*) and kidney dialyzers (*71*). Degradation of adsorbed adhesion proteins would be expected to reduce their biological effectiveness and significance to long term implants, but at present this expectation has not been tested. Furthermore, whether intact adhesion proteins adsorb to any extent to the implanted surfaces at later times and thus facilitate adhesion at later times as well has not been studied. Most long-term events around implanted devices remain poorly understood, despite the likelihood that they involve cellular interactions with adsorbed proteins or their degradation products.

The state of the art in regards to the role of adsorbed proteins in reactions to implanted materials is that we now know that the protein layer changes with time in regards to both the types of proteins present as well as their degree of degradation. In the shorter term, the displacement phenomena known as the Vroman effect results in loss of fibrinogen from the adsorbed layer and addition of high molecular weight kininogen (and probably other proteins as well) in the first hour or less after exposure to plasma. At longer times, e.g. after a week or more *in vivo*, explanted devices are coated with heavily degraded proteins, and perhaps lesser amounts of undegraded proteins as well. The short term changes result in declining adhesivity of the surface for platelets and other cells with receptors for fibrinogen, but what the cellular response is to degraded proteins present at later times is not known at all. One may speculate that degradation of the adsorbed proteins leads to release of chemotactic peptides from the surface that draws neutrophils and other phagocytic cells to the implant site to complete the attack process, but no research has yet been done to test this idea.

4. Resistance to Protein Adsorption

Prior to the 1980s research efforts on proteins at interfaces were devoted mainly to elucidating the mechanisms of protein adsorption and to understanding the behavior of proteins once adsorbed. As the problems associated with protein adsorption in various applications became clear, a new focus, namely how to prevent or minimize adsorption, developed, and research on protein resistant

Downloaded by UNIV OF SUSSEX on December 13, 2012 | http://pubs.acs.org
Publication Date (Web): December 12, 2012 | doi: 10.1021/bk-2012-1120.ch001

Downloaded by UNIV OF SUSSEX on December 13, 2012 | http://pubs.acs.org
Publication Date (Web): December 12, 2012 | doi: 10.1021/bk-2012-1120.ch001

surfaces has since become intensive. Such surfaces are thought to be optimal for use in implantable medical devices, biosensors, drug delivery (e.g. liposomes) and other applications. It is however worth noting that devices with protein resistant surfaces have so far received very little testing *in vivo*, so it is not known how much improvement they will actually provide. Moreover, *in vivo* studies to date on protein resistant surfaces suggest much work remains to be done, since two types of surfaces found to be highly resistant to protein adsorption *in vitro* still elicited a nearly normal foreign body reaction *in vivo* (see Chapter 14 by Szott and Horbett). On the other hand, the *in vivo* blood compatibility of plasma deposited tetraglyme coatings appears to be greatly improved (Horbett, unpublished observations).

Proteins are highly surface active macromolecules and, as indicated elsewhere in this chapter, interfaces that resist protein adsorption are rare. Examples may be found in natural systems such as the outer surfaces of some cells, but it seems likely that no synthetic material exists that resists adsorption entirely, i.e. to levels below the limit of detection of current experimental methods. The most resistant material so far reported may be the poly(carboxybetaine) (PCB) surface reported by Jiang et al which showed virtually undetectable adsorption from plasma using surface plasmon resonance (detection limit ~0.0003 $\mu g/cm^2$) (*72*).

It is important to emphasize that we refer in this context to non-specific adsorption, i.e. adsorption occurring via physical interactions as opposed to covalent or biospecific interactions. In the covalent and biospecific cases the interface is usually designed expressly for the purpose of adsorbing (capturing) a "target" protein (see Chapter 12 by Brash for examples). In this section we discuss research on prevention of non-specific adsorption in terms of: (a) approaches to the design of surfaces, and (b) mechanisms of resistance. The reader is referred to recent, more detailed reviews on this topic (*41*, *73*, *74*).

4.1. Design of Protein Resistant Surfaces

4.1.1. Hydrophilic Polymers

Poly(ethylene oxide) (PEO). It is well established that certain hydrophilic polymers, when present at the solid-aqueous interface, cause a reduction in protein adsorption. Polyethylene oxide (PEO), also referred to as polyethylene glycol (PEG), was the first such polymer to be used in this way, and remains as one of the most effective. PEO has been incorporated in a number of ways including surface grafting (chemical, radiation, plasma), blending with a matrix material, and simple coating. Anchoring of PEO to the surface via the adhesive molecule 3,4-dihydroxyphenylalanine (DOPA) has also been used as a preparative method (*75*). PEO-like materials as well as PEO itself have been found to be protein resistant in varying degrees. For example poly(oligoethylene glycol methacrylate) (POEGMA) with short OEG side chains (length 2 to 9) was grafted by atom transfer radical polymerization (ATRP) to polyurethane (*76*). Also protein resistant coatings have been deposited by radio-frequency plasma treatment of tetraglyme (*77*). Different PEO architectures have been investigated in addition to the conventional linear form, especially "star" PEO having multiple "arms" joined at a common terminus (see Chapter 24 by Zieris et al) or dendrimer-like molecules (*78*).

These various approaches have given surfaces of variable performance, expressed as fractional reduction in adsorption compared to an unmodified control or as quantity adsorbed on an absolute scale (typically $\mu g/cm^2$). Ranking by performance, however, is difficult due to variation in the two key parameters that are known to influence protein resistance, i.e. polymer concentration at the interface (often referred to as chain density or grafting density) and polymer chain length. Indeed it is frequently the case that the chain density is unknown. In addition the experiments used to evaluate performance differ significantly from lab to lab. A few examples of high-performing PEO or PEO-like systems follow.

Kenausis et al (*79*) prepared PEO-modified metal oxide surfaces by adsorption of a graft copolymer of PEO on poly(L-lysine). These copolymers have comb-like architecture and are believed to bind to the metal oxide surfaces by electrostatic interactions (positive charge on poly(L-lysine, negative charge on metal oxide). It was shown that modification of TiO_2 reduced adsorption of albumin (1 mg/mL solution) from 200 to <1 ng/cm^2 and deposition from serum (not all due to protein) from 320 to ~20 ng/cm^2. Resistance was strongly dependent on PEO density, controlled by the graft ratio PEO:PLL, and less so on PEO molecular weight.

Zhang et al (*80*) investigated surfaces including oligoethylene glycol (OEG) self assembled monolayers and poly(oligoethylene glycol methacrylate) "brushes" on a gold substrate. Extremely low adsorption levels <0.3 ng/cm^2 were observed from fibrinogen solution and ~10 ng/cm^2 from plasma to the poly(OEGMA) brush surface.

Surfaces prepared by blending a copolymer containing PEO blocks with a polyurethane were shown by Tan et al to be strongly protein resistant in contact with protein solutions (*81*) and with plasma (*82*). On blends containing 20 wt % copolymer, fibrinogen adsorption was found to be reduced by greater than 95% for all PEO block molecular weights from 550 to 5000 Da (*81*). On the 20% blend with PEO block molecular weight 550 Da, fibrinogen, complement C3, albumin and apolipoprotein AI were undetectable by immunoblotting after exposure to plasma for 3 h, suggesting levels <1 ng/cm^2. In this work the unusual observation was made that protein resistance increased with decreasing PEO molecular weight.

PEO modified surfaces are discussed in this book in the chapters by Schilke and McGuire (29), Szott and Horbett (14), Brash (12), Takahashi et al (36), Binazadeh et al (28) and Zieris et al (24).

It is important to point out that PEO may not be suitable for long term applications due to its putative oxidative instability (*73*, *83*). There is thus a need for alternatives.

4.1.2. Other Hydrophilic Polymers

Several other hydrophilic polymers have been investigated as surface modifiers for protein resistance. Among these are polysaccharides (*84–86*) polyacrylamide (*87*) (see Chapter 30 by Liu et al), poly(N-vinylpyrrolidone) (PVP) (*88*), and poly(N-isopropylacrylamide) (PNIPAAm) (*89*). Most of these

Downloaded by UNIV OF SUSSEX on December 13, 2012 | http://pubs.acs.org
Publication Date (Web): December 12, 2012 | doi: 10.1021/bk-2012-1120.ch001

surfaces have been prepared by grafting methods. Layer-by-layer deposition was used by Croll et al for incorporation of chitosan and hyaluronic acid (*86*). As in the case of the PEO, it is difficult to rank these surfaces in terms of performance, and again none of them is completely resistant (adsorbed quantity below the detection limit) especially in contact with "real" biofluids containing many different proteins at high total concentration. It appears also that none of these polymers performs substantially better than PEO, although some of them may have advantages such as ease of surface preparation and improved stability.

4.1.3. Zwitterion

Downloaded by UNIV OF SUSSEX on December 13, 2012 | http://pubs.acs.org
Publication Date (Web): December 12, 2012 | doi: 10.1021/bk-2012-1120.ch001

A second major category of protein resistant surfaces is based on zwitterion-containing materials including phosphobetaines, carboxybetaines and sulfobetaines. In the case of the phosphobetaines this may be seen as a biomimetic approach since, as mentioned, the outer surfaces of cells, consisting largely of phospholipid bilayers (containing phosphocholine zwitterions) along with embedded proteins and polysaccharides are thought to be protein resistant.

The most extensively investigated synthetic material in this category is the carbon chain polymer poly(2-methacryloyloxyethyl phosphorylcholine) (polyMPC) introduced some twenty years ago by Ishihara et al (*90*). This polymer has phosphorylcholine side chains on a methacrylate backbone, and poly MPC-modified surfaces have shown very strong protein resistance *in vitro*. For example, Feng et al (*91*) showed that adsorption of fibrinogen (from 1 mg/mL solution) to poly(MPC)-modified silicon was reduced to levels on the order of 0.01 μg/cm^2, and that adsorption decreased with increasing poly(MPC) molecular weight from ~1500 to 60,000 Da. MPC and its copolymers have been proposed for use in a wide array of medical applications including hip joints, contact lenses, vascular grafts and blood purification systems (see Chapter 27 by Inoue and Ishihara, and reference (*92*) for a review). In certain respects MPC-based materials have advantages over PEO: MPC can be readily copolymerized with other double bond monomers to give materials with a variety of properties; polymer properties such as molecular weight and architecture can be readily varied; and, in the case of grafted surfaces, since the grafting-to method can be used (in contrast to PEO), control of graft density is relatively easy.

Reisch et al (*93*) studied the phosphorylcholine motif in the form of polyelectrolyte multilayer coatings having an outermost layer of polyacrylic acid "grafted" with an oligoethylene glycol-PC moiety. Surfaces of relatively high grafting degree (high PC density) were strongly protein resistant in contact with diluted serum, with some showing zero adsorption based on QCM measurements with detection limit ~0.005 μg/cm^2.

The essential, distinguishing chemical feature of MPC is the phospho-choline zwitterion. Accordingly, other zwitterionic structures have been investigated as protein resistant motifs, notably by Jiang et al (*74*). Among these are poly(sulfobetaines) (PSB) and poly(carboxybetaines) (PCB) which are carbon chain polymers with SB and CB side chains, respectively. PSB and PCB with structures analogous to that of poly(MPC) were shown to be strongly protein resistant. For example a PSB-grafted surface was shown to limit protein adsorption to <0.0003 μg/cm^2, the detection limit of the SPR method used (*94*); and adsorption to a PCB surface from buffer was also undetectable (*95*). In a study of adsorption from serum and plasma, Jiang et al showed that, in a group of resistant surfaces including a PCB, a PSB and a poly(oligoethylene glycol) surface the PCB surface was the most resistant (*72*), with virtually undetectable adsorption from 100% plasma. An advantage of the PCB materials is that they can be readily conjugated to biomacromolecules (e.g. antibodies) to produce surfaces that are both anti-fouling and bioactive. This approach has also been followed using PEO as the anti-fouling component (see Chapter 12 by Brash).

In an extension of the zwitterion concept, Jiang et al have proposed that mixed +/- charges, when balanced precisely, and uniformly distributed at the molecular level, should provide protein resistant surfaces (*96*). They investigated SAMs prepared with glutamic acid (E)- and lysine (K)-based peptides in this regard, and showed that peptides with alternating E and K residues gave surfaces that were highly resistant to fibrinogen, albumin and lysozyme. This approach has particular merit in that the modifiers and their potential degradation products are naturally occurring materials.

Zwitterion-modified surfaces are discussed in this book in the chapters by Binazadeh et al (28), Brash (12), and Inoue and Ishihara (27).

Downloaded by UNIV OF SUSSEX on December 13, 2012 | http://pubs.acs.org
Publication Date (Web): December 12, 2012 | doi: 10.1021/bk-2012-1120.ch001

4.2. Mechanisms of Protein Resistance

The mechanisms by which the surfaces discussed above achieve protein resistance are still a matter of some debate. The debate is generally limited to two possibilities, namely steric effects and water-related effects.

The steric exclusion hypothesis was proposed largely to explain the protein resistance of PEO. It has been observed for grafted PEO surfaces that protein resistance is molecular weight dependent, increasing with increasing PEO molecular weight and leveling off at molecular weight greater than a few thousand Daltons. The PEO chain is flexible compared to an all-carbon chain due to unrestricted rotation around the backbone C-O bonds, suggesting that the chains can be easily compressed. Assuming the graft density is sufficiently high to prevent a protein molecule from accessing the substrate material directly, i.e. that the layer is in the brush regime, with graft spacing less than twice the Flory radius, the protein would tend to compress the PEO as it approaches the surface, implying a loss of conformational entropy, a free energy penalty, and a repulsive interaction. This compression-repulsion effect would increase with increasing chain length consistent with experimental observation. However, chain compression would also entail a loss of PEO-associated water and a corresponding gain of entropy. It is not clear as to the net effect of these opposing entropy effects. In addition it was shown that short chain PEO with as few as two EO monomers conferred protein resistance (*97*). Compression effects for such short chains would not be expected to be significant. Also carbon chain polymers such as PVP (*88*, *98*), with relatively stiff chains, and non-flexible mixed charge SAMs (*99*) have been shown to be protein resistant. It appears, therefore, that steric exclusion is in general not of great importance as a mechanism for protein resistance; it may have a role for flexible chain modifiers like PEO but not for other systems.

The behavior of surface-associated water appears to offer a more plausible mechanism that applies to all surface modifiers including hydrophilic polymers and zwitterions. PEO, for example, associates strongly with water by hydrogen bonding, and zwitterions bind water even more strongly by ionic bonding (*100*). In general the idea is that the structured, bound water effectively creates an energy barrier to adsorption; the water is bound sufficiently tightly that it cannot be displaced by an approaching protein molecule. The existence of bound, structured water in these systems has been confirmed by several groups. For example Morisaku et al (*101*) showed that bound water was in part freezable and nonfreezable and that there were differences in the amounts of these structures associated with poly(MPC) compared to the PEO-containing poly(OEGMA) which accounted for the differences in protein resistance. Other evidence for the role of bound water in PEO systems is the observation that on a gold-PEO surface protein adsorption showed a minimum with increasing PEO chain density (*102*). The increase at higher density was attributed to the "squeezing out" of bound water from the higher density layers.

From all of this evidence, in particular the fact that all known protein resistant motifs have structured water bound more or less tightly, the water barrier mechanism appears to be generally applicable and is thus favored at the present time over steric exclusion. Rosenhahn et al (*103*) have reviewed non-fouling surfaces with particular reference to PEO and have argued in favor of a mechanism based on a stable hydration layer. Water related mechanisms have also been discussed in detail by Chen et al (*73*), by Morra (*104*), and by Hower et al (*105*). The reader is referred to these sources for more details.

As a final comment in this discussion of protein resistance it should be mentioned that guidelines on the maximum adsorbed quantities of proteins compatible with the prevention of biofouling have not been established. Tsai et al (*106*) have suggested in the case of blood-contacting surfaces, that maximal platelet adhesion occurred with as little as 7 ng/cm^2 of adsorbed fibrinogen. Protein resistance of this magnitude is difficult to achieve, and is especially difficult to sustain over time in applications such as those requiring chronic blood and tissue contact. The challenge of extremely protein resistant surfaces thus remains.

Downloaded by UNIV OF SUSSEX on December 13, 2012 | http://pubs.acs.org
Publication Date (Web): December 12, 2012 | doi: 10.1021/bk-2012-1120.ch001

5. Experimental Techniques for the Study of Proteins at Interfaces

The study of proteins at interfaces has been largely experimental as reflected in the content of this book. It is thus appropriate to include a discussion, albeit brief, of this aspect in the introductory chapter. A more detailed discussion of methods (to 1999) may be found in the review by Hlady et al (*107*).

Broadly speaking, experiments on proteins at interfaces are designed to elicit three categories of information: (1) quantity adsorbed, (2) conformation and physical status of the adsorbed protein, and (3) biologic status and function of the adsorbed protein. Biologic status refers largely to enzyme activity, antigen-antibody binding, and the interactions of adsorbed proteins with cells. Experimental methods related to these areas are discussed in this chapter under "Biological function of adsorbed proteins". The discussion in the present section is limited to categories (1) and (2). It should be noted that many of the techniques can be used for more than one purpose.

5.1. Quantity Adsorbed

5.1.1. Single Protein Systems

For systems of one protein, common methods include: solution depletion (*108*), radiolabeling (*82*), and fluorescence labeling (*109*); optical techniques such as ellipsometry (*110*), optical waveguide lightmode spectroscopy (OWLS) (*79*), and surface plasmon resonance (SPR) (*111*); and spectroscopic techniques such as attenuated total reflectance spectroscopy (ATR), e.g. ATR-infrared (*112*), total internal reflection fluorescence spectroscopy (TIRF) (*113*), and X-ray photoelectron spectroscopy (XPS) (*114*). The quartz crystal microbalance (QCM) measures mass adsorbed via the change in frequency of a vibrating quartz crystal as protein accumulates (*115*, *116*). Clearly these methods vary widely in complexity, applicability, sensitivity, detection limit, cost, convenience etc. A few qualitative comments on these aspects are given here.

Solution depletion is perhaps the simplest method to measure quantity adsorbed, but achievement of reasonable sensitivity requires that the substrate have a high surface-to-volume ratio (e.g. microparticles) so that the decrease in concentration due to adsorption is measurable with good precision. Many, perhaps most, materials of interest are not used in this form, so solution depletion is of limited applicability.

Radiolabeling has been widely practiced for many years and has proved to be a veritable "work horse" providing extensive, high quality data on a wide range of materials (see Chapter 12 by Brash and Chapter 14 by Szott and Horbett). The most commonly used isotopes are ^{125}I and ^{131}I both of which are gamma emitters, allowing measurement without separation of surface and protein, though not *in situ* (i.e. solution and surface in contact). Other advantages include: data are obtained in absolute (mass of protein) as opposed to relative terms; one or two proteins can be "traced" in a complex fluid such as blood containing many proteins. Disadvantages include: attachment of the label may affect adsorption behavior, though for most systems studied to date this has not been found to be the case; safety precautions in handling radioactive substances are of strict necessity, and may be limiting in some locations.

Fluorescence labeling is similar in principle to radiolabeling and has been widely practiced (*117*). This method is also useful for studies of conformational change (*108*). In addition to extrinsic labels such as fluorescein isothiocyanate that must be attached to the protein, intrinsic "labels" due to amino acids such as tryptophan can be exploited. Intrinsic fluorescence is less used in adsorption studies due to technical limitations such as low sensitivity. With extrinsic labels

Downloaded by UNIV OF SUSSEX on December 13, 2012 | http://pubs.acs.org
Publication Date (Web): December 12, 2012 | doi: 10.1021/bk-2012-1120.ch001

preferential adsorption of the labeled protein compared to the native protein is likely to occur because the fluorescent labeling is achieved by covalent linking of relatively large hydrophobic moieties such as fluorescein to the lysine residues at the surface of the protein molecule where they would be able to interact with the adsorbing surface. Preferential adsorption of fluorescent proteins does not always occur however (*118*).

Several methods are based on the interactions of light at the solution-solid interface. In ellipsometry, perhaps the oldest of these methods, changes in polarized light reflected from the interface are interpreted in terms of adsorbed layer thickness and refractive index. The data can be converted to mass by use of the de Feijter equation (*119*). In general ellipsometry is limited to reflective, smooth surfaces. Surface plasmon resonance is a widely used optical method and, as for ellipsometry, commercial instruments are readily available. In SPR, light incident at a particular angle on a metal film interacts with delocalized electrons (plasmons) which reduces the reflected light intensity. The angle is shifted when adsorption occurs. Data are rendered in terms of angle shift which can be converted to mass by suitable calibration. Such optical methods have the advantage that adsorption is measured *in situ*, i.e. with the surface and protein solution remaining in contact. This is a considerable benefit since separation and washing generally entail unknown losses of protein.

In spectroscopic methods such as ATR-IR and TIRF radiation of the appropriate wavelength is totally internally reflected at the interface and the generated evanescent wave penetrates and "samples" the adsorbed protein. Spectra of the protein (infrared, fluorescence emission) are generated. These methods provide, in principle, not only information on quantity adsorbed but also on properties of the adsorbed proteins such as conformation and orientation.

XPS gives the atomic composition of the surface from the core electron emission spectra generated by the impact of X-rays. The method is highly surface sensitive with a sampling depth of the order of 2-5 nm; sampling depth varies with emission angle, allowing composition profiling in the depth dimension. In the most basic application of XPS to the measurement of adsorption, protein is detected and quantified based on the nitrogen signal. XPS is not an *in situ* technique; moreover the measurements are typically made under the highly artificial conditions of high vacuum.

The quartz crystal microbalance (QCM) has become a widely used method for measuring adsorbed quantity. As mentioned, the mass of adsorbed protein is available from the decrease in frequency of the vibrating quartz crystal. Modern QCM systems also allow measurement of energy dissipation in the adsorbed layer (QCM-D) by turning off the excitation voltage and observing the decay of the vibrational amplitude. The rate of decay gives a measure of the viscoelastic properties of the layer and can distinguish between, for example, a highly hydrated (rapid dissipation) layer and a non-hydrated layer (slow dissipation) (*115*). The ability to investigate water interactions is an attractive feature of QCM-D. QCM is an *in situ* technique and can give kinetic data in real time with high sensitivity. Unlike optical methods it is not limited to reflective or transmissive materials and has a much wider range of applicability including polymers and ceramics (*116*).

Downloaded by UNIV OF SUSSEX on December 13, 2012 | http://pubs.acs.org
Publication Date (Web): December 12, 2012 | doi: 10.1021/bk-2012-1120.ch001

5.1.2. Systems of Multiple Proteins, Biologic Fluids

Most of the methods discussed above cannot distinguish among different proteins, and thus are not suitable for studies in complex biologic fluids, e.g. blood. Questions such as the magnitude and composition of the protein layer and its evolution over time are of crucial importance for applications such as sensors and biomaterials. Curiously, these important questions have received comparatively little attention, perhaps because of the enormous complexity of the biologic systems. The "proteome" of adsorbed proteins thus remains largely unknown.

Simpler systems of two or perhaps three proteins can be studied using multiple tracer labels, including the radiolabels discussed above (*91*). Methods available for more complex systems are essentially of two types: (1) Elution of adsorbed proteins, separation by gel electrophoresis (eg SDS-PAGE) and identification by immunoblotting; (2) Proteomics-based methods involving separation by electrophoresis and identification by mass spectrometry.

SDS-PAGE/immunoblotting has been used extensively by Brash and coworkers (*120*, *121*) in studies of adsorption from plasma (see Chapter 12). This method provides a highly sensitive, immunologic means of detection and gives the molecular weights of the detected components. The latter is important since adsorbed proteins may undergo degradation or aggregation. The immunoblot data are qualitative in nature although quantitative interpretation is possible using, for example, densitometric scanning calibrated with purified proteins. The methodology has two main shortcomings: first elution may not be complete and proteins that are not eluted will not be detected; second only proteins probed for will be found, leaving many others (on the order of several hundred in the case of most body fluids) as "not tested".

Thanks to technological developments emerging from proteomics research, new methods have become available for the analysis of complex protein mixtures (*122*, *123*) (see Chapter 37 by Fu and Kao). Typically these methods involve separation of the mixture by 2-D gel electrophoresis. The protein spots in the gel are then excised, usually enzyme-digested to yield smaller peptide fragments, and subjected to mass spectrometric analysis (*124*). MALDI (matrix assisted laser desorption ionization) mass spectrometric methods are particularly well adapted to these measurements. The mass spectra give fragmentation patterns that allow the unambiguous identification of the proteins by matching to large data bases. Quantitative analysis is also possible with these methods. Variations adapted to high throughput analysis, and to comparisons between samples have also been developed (*124*). This "proteomics" approach has the advantage that in principle all the components of the mixture are accounted for, whereas in SDS-PAGE/immunoblotting methods only those proteins probed for can be found.

MALDI mass spectrometry has also been used to identify adsorbed proteins directly on the surface without elution. The proteins are sputtered from the surface and ionized by a laser beam. As opposed to proteomics methods where proteins are identified via fragmentation patterns, MALDI-MS detects the parent ion to give

Downloaded by UNIV OF SUSSEX on December 13, 2012 | http://pubs.acs.org
Publication Date (Web): December 12, 2012 | doi: 10.1021/bk-2012-1120.ch001

molecular weight directly. This approach would appear to be relatively simple but again uncertainty arises regarding the removal of the proteins by the laser-matrix combination. The method has been reviewed by Griesser et al (*125*).

5.2. Physical Status: Conformation, Orientation

Conformation refers to the overall shape of the protein. Great importance has been attached to conformational change in the adsorbed state relative to the native state. Several of the experimental methods for the investigation of conformation are based on imaging such as electron microscopy and atomic force microscopy (see Chapter 5 Adamczyk et al). However the ability of these methods to image protein molecules at resolution sufficiently high to give detailed structural information is limited. Most of the literature deals with big proteins such as fibrinogen (*126*), von Willebrand's factor (*127*) and ferritin (*128*).

Fluorescence labeling can provide conformational information both directly from fluorescence images and from energy transfer between fluorescent labels giving a measure of the distance between labels, and thus possible changes in shape of the protein (*108*).

Solid state nuclear magnetic resonance (NMR) is also under investigation as a method for the investigation of adsorbed protein conformation as described in Chapter 4 by Roehrich et al. Sensitivity considerations necessitate that the substrate have a high surface-to-volume ratio to provide sufficient protein for analysis.

Orientation refers to the geometric relation between the adsorbed protein and the surface, most commonly the angle between a principal axis of the protein (assumed to be geometrically asymmetric) and the surface. "Side-on" and "end-on" are frequently used terms to describe orientation angles. Orientation has been less studied than conformation. In addition to its fundamental interest, it is of practical importance for layers of protein that are designed as sensors to interact with components in solution, e.g. solid state immunoassays. For example, antigen-antibody interactions are maximized when the binding site of the adsorbed component is oriented away from the surface and not involved in binding to the surface. A variety of physical methods have been used to study orientation including sum frequency generation (SFG), ToF-SIMS and NMR. Examples can be found in the chapters by Baio et al (35), Takahashi et al (36), Dupont-Gillain (21), Adamczyk et al (5), Kempson et al (33), and Roehrich et al (4).

The secondary structure of adsorbed proteins, i.e., α-helix and β-sheet, has been investigated using circular dichroism spectrometry. This method was limited in earlier work (*129*) by low sensitivity due the inability to generate samples having a sufficient quantity of protein. More recently these limitations have been largely overcome by the use of custom-designed CD cuvettes and other improvements (*130*).

Downloaded by UNIV OF SUSSEX on December 13, 2012 | http://pubs.acs.org
Publication Date (Web): December 12, 2012 | doi: 10.1021/bk-2012-1120.ch001

5.3. Other Methods

Neutron reflectometry (NR) (*131*) is an *in situ* method by which the fully hydrated surface may be studied. The data provide information on the hydrated layer thickness and, uniquely, on the volume fraction of protein as a function of distance from the interface. The hydration state of the adsorbed protein and its variation in the z-dimension can thus be determined. NR has also proved useful in the characterization of protein-resistant materials such as PEO-modified materials and others, again from the point of view of the hydration state of the PEO and its variation with depth (*132*). The technique is highly specialized, requiring access to a neutron facility.

Methods for investigation of the distribution of protein over the surface (patchy, uniform etc.) include AFM, SEM, and fluorescence microscopy as mentioned. The X-ray photoelectron emission microscopy (X-PEEM) techniques developed by Hitchcock et al (see Chapter 34) give the distribution of both the protein and the underlying substrate from "chemical" images. X-PEEM measures the spatial distribution of electrons emitted from a region of the surface by interaction with a beam of soft X-rays. The chemical sensitivity is derived from near edge X-ray absorption fine structure spectroscopy (NEXAFS), typically using the C1s edge at ~285 eV. The sampling depth is of the order of 10 nm and the spatial distribution ~50 nm. This method is highly specialized and requires access to a synchrotron facility.

Downloaded by UNIV OF SUSSEX on December 13, 2012 | http://pubs.acs.org
Publication Date (Web): December 12, 2012 | doi: 10.1021/bk-2012-1120.ch001

References

1. Roe, R. J. *J. Chem. Phys.* **1974**, *60*, 4192–4207.
2. Scheutjens, J. M. H. M.; Fleer, G. J. *J. Phys. Chem.* **1979**, *83*, 1619–1635.
3. Scheutjens, J. M. H. M.; Fleer, G. J. *J. Phys. Chem.* **1980**, *84*, 178–190.
4. Hesselink, F. T. In *Adsorption from Solution at the Solid/Liquid Interface*; Rochester, C. H., Parfitt, G. D., Eds.; Academic Press: New York, 1983.
5. Creighton, T. E. *Proteins: Structures and Molecular Properties*, 2nd ed.; W.H. Freeman: New York, 1993.
6. Haynes, C. A.; Norde, W. *Colloids Surf., B* **1994**, *2*, 517–566.
7. Arwin, H. *Thin Solid Films* **2000**, *377*, 48–56.
8. Höök, F.; Voros, J.; Rodahl, M.; Kurrat, R.; Boni, P.; Ramsden, J. J.; Textor, M.; Spencer, N. D.; Tengvall, P.; Gold, J.; Kasemo, B. *Colloids Surf., B* **2002**, *24*, 155–170.
9. Browne, M. M.; Lubarsky, G. V.; Davidson, M. R.; Bradley, R. H. *Surf. Science* **2004**, *553*, 155–167.
10. You, H. X.; Lowe, C. R. *J. Colloid Interface Sci.* **1996**, *182*, 586–601.
11. Horbett, T. A. In *Biomaterials Science: An Introduction to Materials in Medicine*, 2nd ed.; Ratner, B. H. A., Schoen, F. L. J., Eds.; Academic Press: New York, 2004; pp 237−244.
12. Lyklema, J. *Fundamentals of Interface and Colloid Science*; Academic Press: New York, 1991; Vol. 1.
13. Nir, S. *Prog. Surf. Sci.* **1977**, *8*, 1–58.

14. Norde, W.; Lyklema, J. *J. Biomater. Sci., Polym. Ed.* **1991**, *2*, 183–202.
15. Giacomelli, C. E.; Norde, W. *Macromol. Biosci.* **2005**, *5*, 401–407.
16. Bornzin, G. A.; Miller, I. F. *J. Colloid Interface Sci.* **1982**, *86*, 539–558.
17. Kurrat, R.; Prenosil, J. E.; Ramsden, J. J. *J. Colloid Interface Sci.* **1997**, *185*, 1–8.
18. Soderquist, M. E.; Walton, A. G. *J. Colloid Interface Sci.* **1980**, *75*, 386–397.
19. Beissinger, R. L.; Leonard, E. F. *J. Colloid Interface Sci.* **1982**, *85*, 521–533.
20. Norde, W. *Colloids and Interfaces in Life Sciences and Bionanotechnology*; CRC Press: Boca Raton, FL, 2011; Chapter 15.
21. Van Dulm, P.; Norde, W. *J. Colloid Interface Sci.* **1983**, *91*, 248–255.
22. Walton, A. G.; Soderquist, M. E. *Croat. Chem. Acta* **1980**, *53*, 363–372.
23. Van Tassel, P. R.; Viot, P.; Tarjus, G. *J. Chem. Phys.* **1997**, *106*, 761–770.
24. Schaaf, P.; Talbot, J. *Phys. Rev. Lett.* **1989**, *62*, 175–178.
25. Adamczyk, Z.; Zembala, M.; Siwek, B.; Warszynski, P. *J. Colloid Interface Sci.* **1990**, *140*, 123–137.
26. Talbot, J.; Tarjus, G.; Van Tassel, P. R.; Viot, P. *Colloids Surf., A* **2001**, *165*, 287–324.
27. Tilton, R. A.; Gast, A. P.; Robertson, C. R. *Biophys. J.* **1990**, *58*, 1321–1326.
28. Ravichandran, S.; Talbot, J. *Biophys. J.* **2000**, *78*, 110–120.
29. Vroman, L.; Adams, A. L. *J. Colloid Interface Sci.* **1986**, *111*, 391–402.
30. Pitt, W. G.; Park, K.; Cooper, S. L. *J. Colloid Interface Sci.* **1986**, *111*, 343–362.
31. McGuire, J.; Krisdhasima, V.; Wahlgren, M. C.; Arnebrant, T. In *Proteins at Interfaces II Fundamentals and Applications*; Horbett, T. A., Brash, J. L., Eds.; ACS Symposium Series 602; American Chemical Society: Washington, DC, 1995; pp 52−65.
32. Kleijn, J. M.; Barten, D.; Cohen Stuart, M. A. *Langmuir* **2004**, *20*, 9703–9713.
33. Razumas, V.; Kulys, J.; Arnebrant, T.; Nylander, T. *Elektrokhimiya* **1988**, *24*, 1518–1521.
34. Norde, W.; Giacomelli, C. E. *Macromol. Symp.* **1999**, *145*, 125–136.
35. Zoungrana, T.; Findenegg, G. H.; Norde, W. *J. Colloid Interface Sci.* **1997**, *190*, 437–448.
36. Wertz, C. F.; Santore, M. M. *Langmuir* **1999**, *15*, 8884–8894.
37. Norde, W.; Lyklema, J. *Adv. Colloid Interface Sci.* **2012**, *179-182*, 5–13.
38. Kondo, A.; Murakami, F.; Kawagoe, M.; Higashitani, K. *Appl. Microbiol. Biotechnol.* **1993**, *39*, 726–731.
39. Keitaro, Y.; Motohiko, N.; Sugasawa, H.; Nagasaki, Y. *J. Am. Chem. Soc.* **2010**, *132*, 7982–7989.
40. Nagasaki, Y.; Kobayashi, H.; Katsuyama, Y.; Yomura, T.; Sakura, T. *J. Colloid Interface Sci.* **2007**, *309*, 524–530.
41. Szott, L. M.; Horbett, T. A. *Curr. Opin. Chem. Biol.* **2011**, *15* (5), 683–9.
42. Raffaini, G.; Ganazzoli, F. *Langmuir* **2010**, *26*, 5679–89.
43. Raffaini, G.; Ganazzoli, F. *Philos. Trans. R. Soc., A* **2012**, *370*, 1444–62.
44. Yeh, I. C.; Lee, M. S.; Olson, M. A. *J. Phys. Chem. B* **2008**, *112*, 15064–73.
45. Latour, R. A. *Biointerphases* **2008**, *3*, FC2–12.

Downloaded by UNIV OF SUSSEX on December 13, 2012 | http://pubs.acs.org
Publication Date (Web): December 12, 2012 | doi: 10.1021/bk-2012-1120.ch001

Downloaded by UNIV OF SUSSEX on December 13, 2012 | http://pubs.acs.org
Publication Date (Web): December 12, 2012 | doi: 10.1021/bk-2012-1120.ch001

46. Cao, L. *Carrier-bound immobilized enzymes [electronic resource] : principles, applications and design*; Wiley -VCH: Weinheim, 2005.
47. Sassolas, A.; Blum, L. J.; Leca-Bouvier, B. D. *Biotechnol. Adv.* **2012**, *30*, 489–511.
48. Moyo, M.; Okonkwo, J. O.; Agyei, N. M. *Sensors (Basel)* **2012**, *12*, 923–53.
49. Kong, F.; Hu, Y. F. *Anal. Bioanal. Chem.* **2012**, *403*, 7–13.
50. Butler, J. E.; Ni, L.; Nessler, R.; Joshi, K. S.; Suter, M.; Rosenberg, B.; Chang, J.; Brown, W. R.; Cantarero, L. A. *J. Immunol. Methods* **1992**, *150*, 77–90.
51. Chen, S.; Lingyun, L.; Zhou, J.; Jiang, S. *Langmuir* **2003**, *19*, 2859–2864.
52. Wang, H.; Castner, D. G.; Ratner, B. D.; Jiang, S. *Langmuir* **2004**, *20*, 1877–87.
53. Liu, L.; Chen, S.; Giachelli, C. M.; Ratner, B. D.; Jiang, S. *J. Biomed. Mater. Res., A* **2005**, *74*, 23–31.
54. Wang, H.; He, Y.; Ratner, B. D.; Jiang, S. *J. Biomed. Mater. Res., A* **2006**, *77*, 672–8.
55. Szott, L. M.; Horbett, T. A. *Curr. Opin. Chem. Biol.* **2011**, *15*, 677–82.
56. Tsai, W. B.; Grunkemeier, J. M.; Horbett, T. A. *J. Biomed. Mater. Res.* **1999**, *44*, 130–9.
57. Tsai, W. B.; Grunkemeier, J. M.; McFarland, C. D.; Horbett, T. A. *J. Biomed. Mater. Res.* **2002**, *60*, 348–59.
58. Tang, L.; Eaton, J. W. *J. Exp. Med.* **1993**, *178*, 2147–56.
59. Underwood, P. A.; Steele, J. G.; Dalton, B. A. *J. Cell Sci.* **1993**, *104* (Pt 3), 793–803.
60. Hu, W. J.; Eaton, J. W.; Ugarova, T. P.; Tang, L. *Blood* **2001**, *98*, 1231–8.
61. Tsai, W. B.; Grunkemeier, J. M.; Horbett, T. A. *J. Biomed. Mater. Res., A* **2003**, *67*, 1255–68.
62. Sivaraman, B.; Latour, R. A. *Biomaterials* **2010**, *31*, 832–9.
63. Ertel, S. I.; Ratner, B. D.; Horbett, T. A. *J. Biomed. Mater. Res.* **1990**, *24*, 1637–59.
64. Pettit, D. K.; Horbett, T. A.; Hoffman, A. S. *J. Biomed. Mater. Res.* **1992**, *26*, 1259–75.
65. Nakajima, M.; Ishimuro, T.; Kato, K.; Ko, I. K.; Hirata, I.; Arima, Y.; Iwata, H. *Biomaterials* **2007**, *28*, 1048–60.
66. Yang, J.; Mei, Y.; Hook, A. L.; Taylor, M.; Urquhart, A. J.; Bogatyrev, S. R.; Langer, R.; Anderson, D. G.; Davies, M. C.; Alexander, M. R. *Biomaterials* **2010**, *31*, 8827–38.
67. Irwin, E. F.; Gupta, R.; Dashti, D. C.; Healy, K. E. *Biomaterials* **2011**, *32*, 6912–9.
68. Cao, L.; Chang, M.; Lee, C. Y.; Castner, D. G.; Sukavaneshvar, S.; Ratner, B. D.; Horbett, T. A. *J. Biomed. Mater. Res., A* **2007**, *81*, 827–37.
69. Backovic, A.; Huang, H. L.; Del Frari, B.; Piza, H.; Huber, L. A.; Wick, G. *J. Proteome Res.* **2007**, *6*, 376–81.
70. Gifford, R.; Kehoe, J. J.; Barnes, S. L.; Kornilayev, B. A.; Alterman, M. A.; Wilson, G. S. *Biomaterials* **2006**, *27*, 2587–98.
71. Cornelius, R. M.; Brash, J. L. *J. Biomater. Sci., Polym. Ed.* **1993**, *4*, 291–304.

72. Ladd, J.; Zhang, Z.; Chen, S.; Hower, J. C.; Jiang, S. *Biomacromolecules* **2008**, *9*, 1357–1361.
73. Chen, S.; Li, L.; Zhao, C.; Zheng, J. *Polymer* **2010**, *51*, 5283–5293.
74. Jiang, S.; Cao, Z. *Adv. Mater.* **2010**, *22*, 920–932.
75. Dalsin, J. L.; Hu, B. H.; Lee, B. P.; Messersmith, P. B. *J. Am. Chem. Soc.* **2003**, *125*, 4253–8.
76. Jin, Z.; Feng, W.; Zhu, S.; Sheardown, H.; Brash, J. L. *J. Biomed. Mater. Res.* **2009**, *91A*, 1189–1201.
77. Zhang, M.; Horbett, T. A. *J. Biomed. Mater. Res., A* **2009**, *89*, 791–803.
78. Lapienis, G. *Prog. Polym. Sci.* **2009**, *34*, 852–892.
79. Kenausis, G. L.; Voros, J.; Elbert, D.; Huang, N. P.; Hofer, R.; Ruiz-Taylor, L.; Textor, M.; Hubbell, J. A.; Spencer, N. D. *J. Phys. Chem. B* **2000**, *104*, 3298–3309.
80. Zhang, Z.; Zhang, M.; Chen, S.; Horbett, T. A.; Ratner, B. D.; Jiang, S. *Biomaterials* **2008**, *29*, 4285–4291.
81. Tan, J.; McClung, W. G.; Brash, J. L. *J. Biomed. Mater. Res.* **2008**, *85A*, 873–880.
82. Tan, J.; Brash, J. L. *J. Biomed. Mater. Res.* **2009**, *90A*, 196–204.
83. Roberts, M. J.; Bentley, M. D.; Harris, J. M. *Adv. Drug. Delivery Rev.* **2002**, *54*, 459–476.
84. McArthur, S. L.; McLean, K. M.; Kingshott, P.; St John, H. A. W.; Chatelier, R. C.; Griesser, H. J. *Colloids Surf., B* **2000**, *17*, 37–48.
85. Ruegsegger, M. A.; Marchant, R. E. *J. Biomed. Mater. Res.* **2001**, *56*, 159–167.
86. Croll, T. I.; O’Connor, A. J.; Stevens, G. W.; Cooper-White, J. J. *Biomacromolecules* **2006**, *7*, 1610–22.
87. Xiao, D.; Zhang, H.; Wirth, M. *Langmuir* **2002**, *18*, 9971–9976.
88. Telford, A. M.; James, M.; Meagher, L.; Neto, C. *ACS Appl. Mater. Interfaces* **2010**, *2*, 2399–2408.
89. Yu, Q.; Zhang, Y.; Chen, H.; Wu, Z.; Huang, H.; Cheng, C. *Colloid. Surf., B* **2010**, *76*, 468–474.
90. Ishihara, K.; Ueda, T.; Nakabayashi, N. *Polym. J.* **1990**, *22*, 355–360.
91. Feng, W.; Zhu, S.; Ishihara, K.; Brash, J. L. *Langmuir* **2005**, *21*, 5980–5987.
92. Iwasaki, Y.; Ishihara, K. *Anal. Bioanal. Chem.* **2005**, *381*, 534–546.
93. Reisch, A.; Hemmerle, J.; Voegel, J-C.; Gonthier, E.; Decher, G.; Benkirane-Jessel, N.; Chassepot, A.; Mertz, D.; Lavalle, P.; Mesini, P.; Schaaf, P. *J. Mater. Chem.* **2008**, *18*, 4242–4245.
94. Zhang, Z.; Chen, S. F.; Chang, Y.; Jiang, S. Y. *J. Phys. Chem. B* **2006**, *110*, 10799–10804.
95. Zhang, Z.; Vaisocherova, H.; Cheng, G.; Yang, W.; Xue, H.; Jiang, S. *Biomacromolecules* **2008**, *9*, 2686–2692.
96. Chen, S.; Cao, Z.; Jiang, S. *Biomaterials* **2009**, *30*, 5892–5896.
97. Prime, K.; Whitesides, G. *Science* **1991**, *252*, 1164–1167.
98. Robinson, S.; Williams, P. A. *Langmuir* **2002**, *18*, 8743–8748.
99. Chen, S.; Yu, F.; Yu, Q.; He, Y.; Jiang, S. *Langmuir* **2006**, *22*, 8186–8191.
100. He, Y.; Hower, J.; Chen, S. F.; Bernards, M. T.; Chang, Y.; Jiang, S. Y. *Langmuir* **2008**, *24*, 10358–10364.

Downloaded by UNIV OF SUSSEX on December 13, 2012 | http://pubs.acs.org
Publication Date (Web): December 12, 2012 | doi: 10.1021/bk-2012-1120.ch001

101. Morisaku, T.; Watanabe, J.; Konno, T.; Takai, M.; Ishihara, K. *Polymer* **2008**, *49*, 4652–4657.
102. Unsworth, L. D.; Sheardown, H.; Brash, J. L. *Langmuir* **2005**, *21*, 1036–1041.
103. Rosenhahn, H.; Schilp, S.; Kreuzer, H. J.; Grunze, M. *Phys. Chem. Chem. Phys.* **2010**, *12*, 4275–4286.
104. Morra, M. *J. Biomater. Sci., Polymer Edn.* **2000**, *11*, 547–569.
105. Hower, J. C.; Bernards, M. T.; Chen, S.; Tsao, H. K.; Sheng, Y. J.; Jiang, S. *J. Phys. Chem. B* **2009**, *113*, 197–201.
106. Tsai, W. -B.; Grunkemeier, J. M.; Horbett, T. A. *J. Biomed. Mater. Res.* **1998**, *44*, 130–139.
107. Hlady, V.; Buijs, J.; Jennissen, H. P. *Methods Enzymol.* **1999**, *309*, 402–429.
108. Jennissen, H. P.; Botzet, G. *Int. J. Biol. Macromol.* **1979**, *1*, 171–179.
109. Benesch, J.; Hungerford, G.; Suhling, K.; Tregidgo, C.; Manoa, J. F.; Reis, R. L. *J. Colloid Interface Sci.* **2007**, *312*, 193–200.
110. Elwing, H. *Biomaterials* **1998**, *19*, 397–406.
111. Green, R. J.; Davies, J.; Davies, M. C.; Roberts, C. J.; Tendler, S. J. *Biomaterials* **1997**, *18*, 405–13.
112. Fink, D. J.; Hutson, T. B.; Chittur, K. K.; Gendreau, R. M. *Anal. Biochem.* **1987**, *165*, 147–54.
113. Buijs, J.; Hlady, V. *J. Colloid Interface Sci.* **1997**, *190*, 171–81.
114. McArthur, S. L.; McLean, K. M.; St John, H. A.; Griesser, H. J. *Biomaterials* **2001**, *22*, 3295–3304.
115. Höök, F.; Rodahl, M.; Kasemo, B.; Brzezinski, P. *Proc. Natl. Acad. Sci. U.S.A.* **1998**, *95*, 12271–12276.
116. Becker, B.; Cooper, A. *J. Mol. Recognit.* **2011**, *24*, 754–787.
117. Janot, J. M.; Boissière, M.; Thami, T.; Tronel-Peyroz, E.; Helassa, N.; Noinville, S.; Quiquampoix, H.; Staunton, S.; Déjardin, P. *Biomacromolecules* **2010**, *11*, 1661–1666.
118. Watkins, R. W.; Robertson, C. R. *J. Biomed. Mater. Res.* **1977**, *11*, 915–938.
119. de Feijter, J. A.; Benjamins, J.; Veer, F. A. *Biopolymers* **1978**, *17*, 1759–1772.
120. Sask, K. N.; Berry, L. R.; Chan, A. K. C.; Brash, J. L. *Langmuir* **2012**, *28*, 2099–2106.
121. Cornelius, R. M.; Archambault, J. G.; Berry, L.; Chan, A.; Brash, J. L. *J. Biomed. Mater. Res.* **2002**, *60*, 622–632.
122. Kim, J. K.; Scott, E. A.; Elbert, D. L. *J. Biomed. Mater. Res., A* **2005**, *75*, 199–209.
123. Dukan, S.; Turlin, E.; Biville, E.; Bolbach, G.; Touati, D.; Tabet, J. C.; Blais, J. C. *Anal. Chem.* **2003**, *70*, 4433–4440.
124. Aebersold, R. *J. Infect. Dis.* **2003**, *187*, S315–20.
125. Griesser, H. J.; Kingshott, P.; McArthur, S. L.; McLean, K. M.; Kinsel, G. R.; Timmons, R. B. *Biomaterials* **2004**, *25*, 4861–4875.
126. Yermolenko, I. S.; Lishko, V. K.; Ugarova, T. P.; Magonov, S. N. *Biomacromolecules* **2011**, *12*, 370–9.
127. Kang, I.; Raghavachari, M.; Hofmann, C. M.; Marchant, R. E. *Thrombos. Res.* **2007**, *119*, 731–740.
128. Ho, R. H.; Chen, Y. H.; Wang, C. M. *Colloids Surf., B* **2012**, *94*, 231–235.

Downloaded by UNIV OF SUSSEX on December 13, 2012 | http://pubs.acs.org
Publication Date (Web): December 12, 2012 | doi: 10.1021/bk-2012-1120.ch001

129. McMillin, C. R.; Walton, A. G. *J. Colloid Interface Sci.* **1974**, *48*, 345–49.
130. Sivaraman, B.; Fears, K. P.; Latour, R. A. *Langmuir* **2009**, *25*, 3050–3056.
131. Al-Jawad, M.; Fragneto, G.; Liu, J.; Chang, S. R.; Clarkson, B. *Eur. Phys. J. E.* **2009**, *30*, 175–179.
132. Feng, W.; Nieh, M-P.; Zhu, S.; Brash, J. L.; Harroun, T. A.; Katsaras, J. *Biointerphases* **2007**, *2*, 34–43.

Downloaded by UNIV OF SUSSEX on December 13, 2012 | http://pubs.acs.org
Publication Date (Web): December 12, 2012 | doi: 10.1021/bk-2012-1120.ch001

Chapter 2

Optimizing the Bioaffinity Interaction between His-Tag Proteins and Ni(II) Surface Sites

**Laura E. Valenti,[a] Elisa Herrera,[a] María Fernanda Stragliotto,[a]
Vitor L. Martins,[b] Roberto M. Torresi,[b] and Carla E. Giacomelli*,[a]**

**[a]Instituto de Fisicoquímica de Córdoba (INFIQC-CONICET),
Departamento de Fisicoquímica, Facultad de Ciencias Químicas,
Universidad Nacional de Córdoba. Ciudad Universitaria,
5000 Córdoba, Argentina
[b]Instituto de Química, Universidade de São Paulo,
Av. Prof. Lineu Prestes 748, 05508-000 São Paulo, SP, Brazil
*E-mail: giacomel@fcq.unc.edu.ar**

The bioaffinity interaction between Histidine (His)-tag proteins and Ni(II) surface sites is exploited as a biofunctionalization strategy to achieve a better surface bioactivity than that provided by physical adsorption. This improved functioning is mainly ascribed to the presence of site-oriented proteins on the surface, induced by the interaction between the tag and the Ni(II) sites. In addition to the induced bioaffinity interaction, His-tag proteins are also spontaneously adsorbed (through hydrophobic and electrostatic interactions) on the substrate. These physically adsorbed proteins are randomly oriented and less bioactive, lowering the surface biorecognition capabilities. Therefore, the surface biofunctionalization based on His-Ni(II) interaction requires the optimization of the experimental conditions to promote the bioaffinity interaction while minimizing physical adsorption. This optimization can be achieved by properly selecting the adsorption conditions (solution pH and ionic strength, protein surface coverage, etc.) and the washing agents prior to the detection of the biorecognition event. This chapter is aimed at discussing experimental results related to the optimization of the bioaffinity interaction between a particular recombinant His-tag antigen and Ni(II) surface sites.

In Proteins at Interfaces III State of the Art 2012; Horbett, T., et al.;
ACS Symposium Series; American Chemical Society: Washington, DC, 2012.

Introduction

Biofunctional surfaces refer to the modification of solid substrates with biological systems (like antibodies, enzymes, or single strand DNA) to mimic the sophisticated biorecognition capabilities of native biosystems (*1–3*). The idea behind these applications relies on transferring the biorecognition capabilities (in particular affinity, specificity and selectivity at molecular level) from native biomacromolecules to surface systems. Therefore, the final goal is to biofunctionalize a solid substrate to achieve molecular biorecognition. The need of using solid substrates originates from facilitating the separation between bond and free compounds and providing the support to detect the biorecognition event. In fact, a great variety of detection techniques, ranging from particle agglutination up to very sophisticated optical methods, have been applied to detect the biorecognition event (*4–6*). For that purpose, the substrate is the transducer of the biological activity into a measurable signal. When biomacromolecules are restricted to proteins, mostly enzymes, antibodies or antigens have been used to biofunctionalize solid substrates. On these bases, for example, biosensors and immunosensors are built in which adsorbed enzymes or antibodies/antigens are used as the biorecognition element of a particular analyte in solution. On the other hand, the nature of the substrate has been widely different, going from flat metallic substrates (as electrodes in electrochemical biosensors) to polymer particles (as polystyrene in immuno-agglutination tests).

There are two basic strategies to biofunctionalize sorbent solid substrates with proteins: chemical or physical adsorption. Physical adsorption is easily achieved because most proteins adsorb on most sorbent substrates spontaneously in a short term range, mainly due to electrostatic and hydrophobic interactions (*7*, *8*). Thus, it is a cheap and simple adsorption strategy to prepare biofunctional surfaces. However, the adsorbed molecules are desorbable and randomly oriented, usually with a non-native conformation (*9–11*) which leads to altered (if any) biological activity (*8*, *12*). Chemical interactions have been increasingly incorporated in an attempt to avoid or remove physical adsorption, especially due to the induced conformational changes of adsorbed protein and, hence, their inappropriate molecular recognition capabilities. However, the ratio between the advantages and the disadvantages of both strategies need to be evaluated for each specific protein-substrate system. A rational selection of the appropriate strategy for a particular system relies on understanding the different interactions that play a role in the whole adsorption process in order to minimize those that alter the biological activity, and thus the biorecognition capacity. Therefore, substrate biofunctionalization requires a detailed study of the protein adsorption mechanism (physical, chemical or both). It is important to note that a third emerging strategy would be represented by the application of S-layer fusion proteins carrying functional domains (*13*).

Besides conformational changes upon adsorption, the orientation of the adsorbed protein is the other critical parameter to prepare reliable biofunctional surface. The biorecognition capabilities of the biofunctional surfaces strongly depend on the orientation of the adsorbed protein: the active sites should be free to interact with the specific molecule to be recognized. Adsorption in a particular orientation is achieved both with physical and chemical protein-substrate interactions. In the first case, the substrate is modified in order to induce a particular orientation. As a matter of fact, block copolymers have been used to site-orient antibodies on solid substrates (*14*, *15*). On the other hand, chemical adsorption relies on modifying the substrate, the protein molecules, or both. The most general procedures to induce the proper protein orientation are based on a variety of bioaffinity interactions attained by modifying the protein and the substrate. Among others, the non-covalent interaction of (strept)avidin with biotin and the chelated complexes between polyhistidine (His) tag and metal cations are widely used biofunctionalization strategies (*16–18*). These bioaffinity interactions provide a gentle site-oriented adsorption procedure that have several important advantages over other strategies: a) the attachment is site-specific, relative to the location on the protein sequence where the bond with the sorbent substrate forms; b) the adsorption conditions are mild, which result in a reduced risk of protein denaturation; c) the protein molecules have one orientation and the layer is homogeneous; and d) the sorbent substrate is reusable.

From the great variety of substrate and protein modifications (immunoglobulins (IgG) on protein A/G precoated substrates, oxidized IgG carbohydrate on hydrazine/hydroxylamine functionalized substrates, $F(ab')_2$ IgG fragment on gold or maleimide derivatized substrate, biotinylated proteins on (strept)avidine precoated substrates (*1*)) that can be used to achieve site-oriented molecules, we selected the interaction between His-tag proteins and Ni(II) modified substrate to prepare stable, specific and reusable biofunctional surfaces. The His (usually His_6) tag has been extensively used for site-orienting adsorbed proteins as well as for protein purification by immobilized metal affinity chromatography (IMAC) (*19–21*). The His-tag is genetically introduced into recombinant proteins at one of the N- or C-termini or in an exposed loop of the protein. In fact, one advantage of this biofunctionalization procedure is that many commercially available protein expression plasmid vectors include His_6 tag. This strategy relies on the high affinity of the imidazole groups of the tag for metal cations such as Ni^{2+}, Cu^{2+}, CO_2+ or Zn^{2+} involving a chelate complex formation (*22–25*). Although the tag may be introduced at different positions of the primary structure, His-Ni(II) interaction involves the imidazole nitrogen close to the N-terminal (*22*). Therefore, the tag needs to be engineered on the N-terminal of the protein to induce a stable anchoring to Ni(II) modified substrate. Finally, it is important to emphasize that beside the generated bioaffinity interaction protein molecules also spontaneously adsorb mainly due to electrostatic and hydrophobic interactions. As it was already indicated, these physically adsorbed proteins are mostly avoided when preparing biofunctional surfaces. To this end, the experimental conditions are optimized to promote the bioaffinity interaction while minimizing physical adsorption. This optimization can be achieved by properly selecting the adsorption conditions (solution pH and ionic strength, protein surface coverage, etc.) and the washing agents prior to the detection of the biorecognition event. This optimization may be also attained with protein-repellent substrate coating (like PEG) which implies more steps during the biofunctionalization process (*23*, *24*).

This chapter is organized considering the two basic elements to prepare a biofunctional surface, the protein and the substrate, and the main interactions that drive the adsorption process. The discussed results are based on a particular studied case composed by the H49 antigen (tagged with His_6 during the expression) on Ni(II) modified substrates. The first part provides an overview of the expression, purification and characterization of this particular recombinant protein. The H49 antigen was initially expressed in a Brazilian laboratory and it was reported to be highly specific antigen for Chagas disease, which is endemic in Latin America (*26–28*). Secondly, the substrate modification is briefly discussed considering both the Ni(II) coordination environment and its resulting electrochemical behavior. The third part refers to the bioaffinity and physical interactions between the antigen and the substrate, with a special emphasis on the adsorption mechanisms and desorption behavior upon addition of different agents. This piece of evidence is crucial because it allows optimizing the experimental conditions to prepare stable and specific biofunctional surfaces. Finally, the proposed strategy is extended to a His-tag redox enzyme.

His-Tag H49 Antigen

As stated above, the biorecognition element used to prepare the biofunctional surface is the antigen H49, which is specifically recognized by antibodies in serum of ill people with Chagas disease (*28*). The antigen expression was performed in collaboration with researchers of the Biological Chemistry Department of our Faculty. The gene that encoded for H49 was provided by Dr. Da Silveira from Federal University of São Paulo (Brazil). This gene inserted in a plasmid, was amplified by PCR and was cloned in another plasmid (pGEM-T Easy). Afterwards, the H49 gen was joined to the pET15-B plasmid containing the sequence for the His_6 tag and was used to transform *E. coli* bacteria. The pET15-B plasmid which introduced the histidine residues on the N-terminal of the protein was selected, because the Ni-His_6 interaction was favored when the amino terminal was involved (*22*). After the expression of the foreign protein in bacteria, His-tag H49 was purified by IMAC as it is generally done in biotechnology with recombinant proteins. This purification method also helped to look over the interaction between the expressed His-tag antigen and the surface Ni(II) sites. As expected, H49 was only removed from the column upon the addition of a high imidazole concentration that specifically competed for the Ni(II) sites of the IMAC column. It is important to emphasize that the expression in bacteria resulted in rather small amounts of recombinant proteins (at around 50 mg from 12 L bacteria culture), which represented one disadvantage of using these biomolecules as biorecognition elements.

The biological activity of the recombinant His-tag H49 antigen, checked by western blot with sera with (positive) and without (negative) Chagas antibodies, indicated a high degree of specificity. The protein isoelectric point (IEp) and hidrophobicity profile were calculated with the "protein sequence analysis" software. Based on the amino acid pKa values, the calculated IEp was 5.3.

Hidrophilicity was estimated using the Hopp-Woods scale (*29*); it was in line with the repetitive amino acid sequence (*28*) indicating the presence of five exposed antigenic sites and a rather hydrophilic protein.

Ni(II)-Modified Substrate

In order to modify the solid substrate, we used a rather simple and versatile multi-step strategy based on amino terminated self-assembled monolayer (SAM), e.g. cysteamine on polycrystalline Au or aminopropyltrimethoxysilane on SiO_2, as the first modification step. The purpose of using these two substrates was related to the requirements of studying the adsorption process with a reliable technique and detecting the biorecognition event with a direct method. Modified SiO_2 was the substrate used to study the antigen adsorption-desorption mechanism by reflectometry, while Au was used to evaluate the surface biofunctionality with electrochemical methods. Both solid substrates have been widely used to prepare biofunctional surfaces; Au has been particularly selected as the transducer of different detection techniques such as quartz crystal microbalance (*30*, *31*), surface plasmon resonance (*32*) and electrochemical methods (*33*). Amino surface groups have been attached not only to Au and SiO_2 (*34*) but also to magnetite nanoparticles (*35*), plastic (*36*) and graphite (*37*) as the first step to graft other functionality onto solid substrates. The coordination mode and geometry of the surface Ni(II) sites were studied by X-ray absorption near-edge spectroscopy (XANES) at the Ni-K edge in aqueous solution (*1*), a facility which is available at the National Laboratory of Synchrotron Light in Campinas (Brazil). It is important to note that most XANES studies on SAM modified Au have been performed under high vacuum conditions at the C or O edge (*25*, *38*), whereas nickel coordination compounds in aqueous solution have been previously studied by XANES (*39–44*). The spectral features (pre-edge and edge positions and intensity) of the surface chelate (on both Au and SiO_2) were characteristic of Ni(II) cations in an octahedral environment. The surface complexes were equivalent regardless of the nature of the substrate, emphasizing the versatility of the substrate modification which represented one of the major advantages of this multi-step strategy.

In view of using this substrate modification in combination with the electrochemical detection of the biorecognition event, the electrochemical stability and response of the modified substrate were studied by cyclic voltammetry (CV). These experiments were performed with modified Au as the working electrode in a 50 mmol L^{-1} phosphate buffer pH 8.0 at a scan rate of 100 mV s^{-1} between 0.00 and 0.70 V ($Ag/AgCl/KCl_{sat}$ reference electrode and Pt counter electrode). Figure 1 compares the response of bare Au (solid line) to the first two cycles of CV measurements for Au modified up to the first step (i.e. only the amine terminated SAM) (A) and for Au fully modified (i.e. up to Ni(II) addition) (B). In the presence of cysteamine, the electrochemical signal increased during the first cycle whereas it decreased for the successive cycle, indicating that the SAM was partially removed at the applied potential range. Hence, the electrochemical stability of the cysteamine modified Au was low at potential higher than 0.40 V. Contrarily, the modification processes up to the last step stabilized the Au-SAM interaction, which resulted in a wider available potential range to electrochemically detect biorecognition events. Further, we also determined by XANES that the surface Ni(II) sites were not affected by the potential applied, which indicated that His-tag proteins would remain attached to the substrate under these experimental conditions.

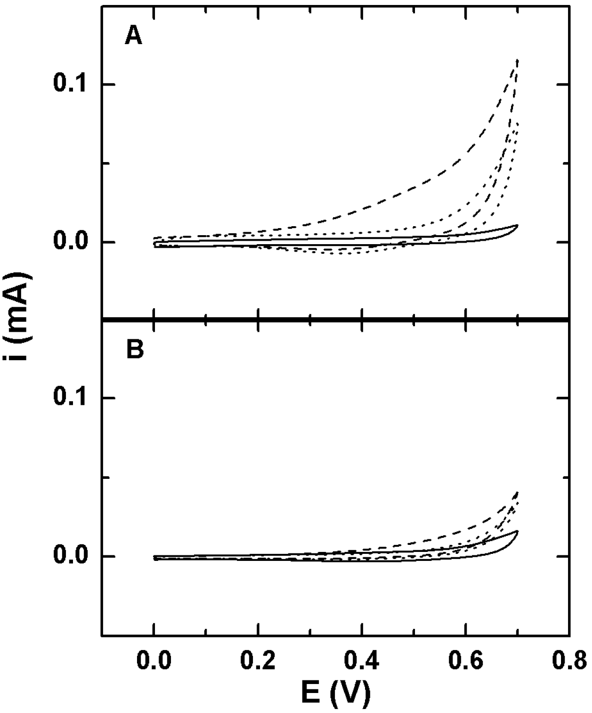

Figure 1. CV of bare (solid line), cysteamine (A) and, Ni(II) (B) modified Au electrodes at the first (dashed line) and second (dotted lines) cycles performed in 50 mmol L^{-1} phosphate buffer pH 8.0 at 100 mV s^{-1} (Ag/AgCl/KCl_{sat}: reference electrode; Pt: counter electrode).

The charge transfer behavior of the modified Au electrode was checked using ferrocene (Fc) as a redox probe. Figure 2 compares the CVs of bare (open symbols) and Ni(II) modified (solid symbols) Au electrodes in the presence of 2.5 mmol L^{-1} Fc (50 mmol L^{-1} phosphate buffer pH 8.0) at 100 mV s^{-1}. Well-defined redox waves corresponding to Fc/Fc^+ redox transformation with a peak separation (ΔE_p) of ~60 mV were observed in the CV of the bare Au, which was indicative of an electrochemically reversible one-electron process. Although the peak separation for the modified Au electrode was greater than 100 mV, the observed electrochemical response was appropriate to detect the biorecognition event. This ΔE_p value can be explained by the decrease of electron-transfer kinetics through the SAM-modified electrode. The electrochemical stability and the electron transfer capabilities of the Ni(II) modified Au substrate imply that this platform can be easily coupled to an electrochemical method to detect the biorecognition event. Moreover, the versatility of the modification procedure allows adding other moieties such as oligoethylenglycol (*38*) (to prevent unspecific adsorption of His-tag proteins) and/or redox probes (*27*) (to improve the biorecognition performance).

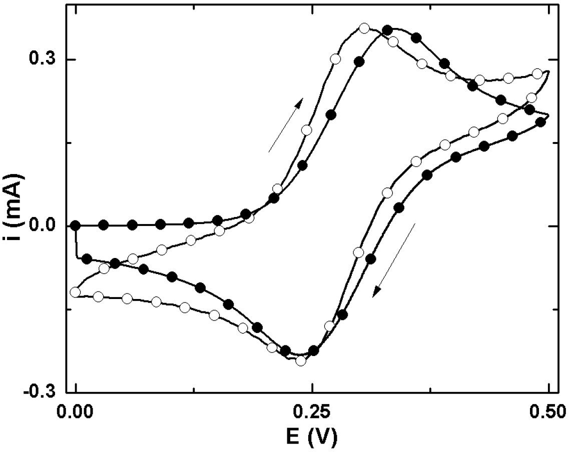

Figure 2. CV of bare (open symbols) and Ni(II) modified (solid symbols) Au electrodes in 50 mmol L^{-1} phosphate buffer pH 8.0 with 2.5 mmol L^{-1} Fc at 100 mV s^{-1} (Ag/AgCl/KCl_{sat}: reference electrode; Pt: counter electrode).

His-Tag H49 Adsorption

The adsorption-desorption process of the His-tag H49 was studied by reflectometry at pH 8.0 (5 mmol L^{-1} phosphate buffer) analyzing both physical and bioaffinity interactions. The pH was selected taking into account two main aspects: provoke the bioaffinity interaction and minimize the physical adsorption. Previously, we studied the complex formation between His_6 and Ni(II) in aqueous solution and we found that the reaction only occurred at pH higher than 4 (*22*). Further, we established that adsorbed His_6 on bare SiO_2 substrates at pH 8 was easily removed by buffer dilution (*45*). Finally, electrostatic interactions between the antigen (IEp 5.3) and the negatively charged (either bare or modified) substrate were also minimized at pH 8. Physical adsorption was evaluated by using a model non-tagged protein and modified SiO_2 in the absence of Ni(II). On the other hand, the His_6-Ni(II) bioaffinity interaction was measured with the His-tag H49 and Ni(II) modified substrate.

Physical Adsorption versus Bioaffinity Interaction

Commercial bovine serum albumin (BSA) was selected as the model non-tagged protein, because of its molecular weight (60 kDa) and IEp (4.8) which roughly coincided with those of the His-tag H49 antigen. The pH and ionic strength conditions of the adsorbing aqueous solution were selected to reduce the electrostatic interactions between the protein and the sorbent substrate. As a matter of fact, figure 3 shows the saturation adsorbed amounts (Γ_{sat}) of the model non-tagged BSA at high (black) and low (light gray) ionic strength. As it was expected for repealing substrate and protein systems, adsorption was minimized when the ionic strength decreased. Furthermore, figure 3 compares the physical adsorption and the bioaffinity interaction of the His-tag antigen (dark gray) at low ionic strength. In the absence of Ni(II), the adsorbed amount of the His-tag H49 had the same magnitude as the non-tagged BSA did, which indicated that the adsorption layer was built in more or less the same fashion in both cases. Moreover, the antigen behaved in the same way as BSA regarding the mechanism of physical interaction (data not shown): attachment-controlled process mainly driven by electrostatic interactions. On the other hand, the antigen adsorbed amount on the Ni(II) modified sorbent was higher than the value measured with BSA, becoming evident the presence of different adsorption features with both proteins. The desorption behavior upon buffer (same pH and ionic strength) addition was also evaluated. Physically adsorbed proteins behaved in a rather different way. BSA was not removed from the substrates while about 20% of H49 was desorbed from the modified SiO_2 in the absence of Ni(II), which suggested a stronger conformational change (i.e. more attached protein segments) of BSA molecules. On the other hand, only 10% of the His-tag antigen was removed from the Ni(II) modified substrate, which indicated that the interaction was stronger when the bioaffinity interactions were possible.

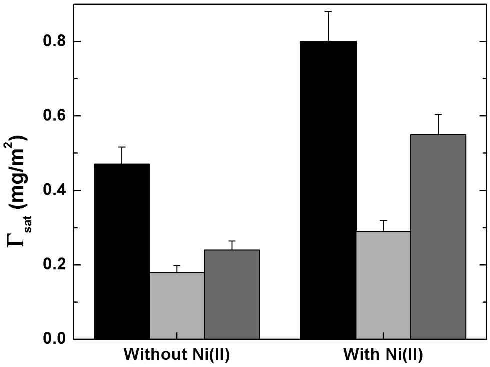

Figure 3. Saturation adsorbed amounts (Γ_{sat}) of BSA at high (black) and low (light gray) ionic strength and His-tag H49 at low ionic strength (dark gray) on modified SiO_2 without or with Ni(II), in 5 mmol L^{-1} phosphate buffer pH 8.0. High ionic strength was achieved by adding 100 mmol L^{-1} NaCl to the buffer. Error bars were calculated from duplicate experiments.

Adsorption Mechanism

From the above discussion, it is clear that when dealing with the His-tag antigen and the Ni(II) modified substrate, both physical and bioaffinity interactions are involved. Usually, the protein adsorption mechanism consists of different stages that are related to the different processes that bring the protein molecules from the solution to the sorbent substrate. Roughly, these stages comprise the transport, attachment and optimization of the protein molecules on the substrate. All these processes may occur in widely different time scales and their relative rates strongly affect the final state (conformation, orientation, etc.) of the adsorbed proteins. Therefore, the adsorption kinetics plays a major role in the final performance of the biofunctional surface. In fact, the optimal conditions to develop biofunctional surface are only determined based on the knowledge of the adsorption-desorption process. As an example, figure 4 compares the adsorption-desorption kinetics of the His-tag antigen adsorbed on modified SiO_2 substrate in the absence (physical) and in the presence of Ni(II) (bioaffinity and physical) at pH 8.0 and low ionic strength (these experiments were performed at least in triplicate and the standard deviation (SD) was always lower than 15%. This SD was strongly reduced when the protein concentration was high and the adsorbed amount was close to the saturation). On the Ni(II) modified substrate the adsorption was faster, the saturation adsorbed amount was higher and the desorbed amount (upon dilution) was lower than those measured in the absence of Ni(II). This trend was observed for different antigen concentrations ranging from 0.1 μg mL^{-1} to 10 μg mL^{-1}. However, all these curves did not merge when the adsorption kinetics plots were normalized by the protein concentration in solution. Hence, the saturation adsorbed amounts were not exclusively determined by the protein concentration. In other words, these amounts were controlled by kinetics rather than thermodynamics reasons (*46*).

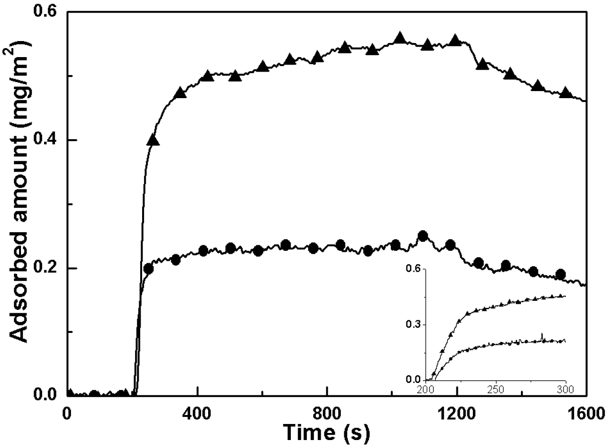

Figure 4. The adsorption-desorption process of 0.01 mg mL^{-1} His-tag H49 on modified SiO_2 without (solid circles) and with Ni(II) (solid triangles) in 5 mmol L^{-1} phosphate buffer pH 8.0 as measured by reflectometry.

The initial adsorption rates (calculated from the initial slopes of Γ vs. t plots, as shown in figure 4) were always lower than the transport rate which indicated that the adsorption process of the His-tag H49 was controlled by the attachment of the protein to both substrates. As stated above, the first contact was ruled by electrostatic interactions even in the presence of Ni(II) surface sites. After this first attachment, protein molecules optimize their interactions with the sorbent substrate. This optimization usually leads to relaxation and spreading when proteins are physically adsorbed (*47*). However, this optimization may be related to bioaffinity interactions when possible (i.e. Ni(II) surface sites and His-tag proteins). The extent of the optimization step depends on the ratio between the optimization rate and the filling rate. When the optimization rate is faster than the filling rate, all the proteins have the same conformation in the final state and the saturation adsorbed amounts do not depend on the supply rate. This is also the case when the optimization process is slower than the filling rate, because the substrate crowding is so fast that prevents protein-substrate optimization. On the other hand, when the characteristic times of both processes are similar, the saturation adsorbed amounts are affected by the supply rate because the optimization step strongly depends on the surface coverage (i.e. the adsorbed amount). It is important to note that the reflectometer set up provides conditions of controlled diffusion layer thickness, but it does not allow varying the flow in a controlled, reproducible way. In order to evaluate the effect of the supply rate on the saturation adsorbed amount, the adsorption kinetics data were normalized by the protein concentration. The fact that these plots did not merge indicated that the filling and optimization rates were similar on both substrates.

From the wide range of possible definitions we used τ_{75} (the time needed to reach 75% of Γ_{sat}) for the characteristic filling time (*9*, *48*), which was reported by Wertz and Santore (*46*). This definition does not assume transport controlled kinetics and it is relatively insensitive to the detailed shapes of the individual adsorption kinetics. Considering that protein molecules continuously attach and optimize (reaching an average surface area per molecule) τ_{75} allows estimating an average filling rate. The characteristic optimization time is estimated by extrapolating to zero the saturation adsorbed amount; in such a situation, a molecule has enough room to optimize its interaction with the substrate and there are no neighboring molecule that hamper the process. Figure 5A shows τ_{75} (on the left) and the percentage of proteins that remained on the substrate after rinsing with buffer (on the right), as a function of Γ_{sat} for purely physical adsorption (these experiments were performed at least in triplicate; SD of τ_{75} was always lower than 20%, while SD of the desorbed amount was lower than 10%). First, the characteristic filling and relaxation times were similar, indicating that these processes occurred at the same time. Secondly, τ_{75} and the percentage of molecules on the substrate after rinsing with buffer linearly diminished as Γ_{sat} increased. Let us remember that the time scales corresponding to the filling and desorbing processes are rather different; the first one represents the initial protein-substrate interaction, while the second one accounts for the strength of the interaction after the optimization stage. Low saturation adsorbed amounts were reached with low protein concentrations, or for that matter, at low supply rate; protein molecules attached to the substrate had enough time and room to spread on the substrate and they were not removable with buffer. When the protein concentration was higher, the supply rate was also higher and some of the attached molecules did not have time and room to relax and were easily desorbed by dilution. Finally, as discussed by Norde et al. (*49*), these data reinforced that idea that Γ_{sat} values were controlled by kinetic rather than thermodynamic.

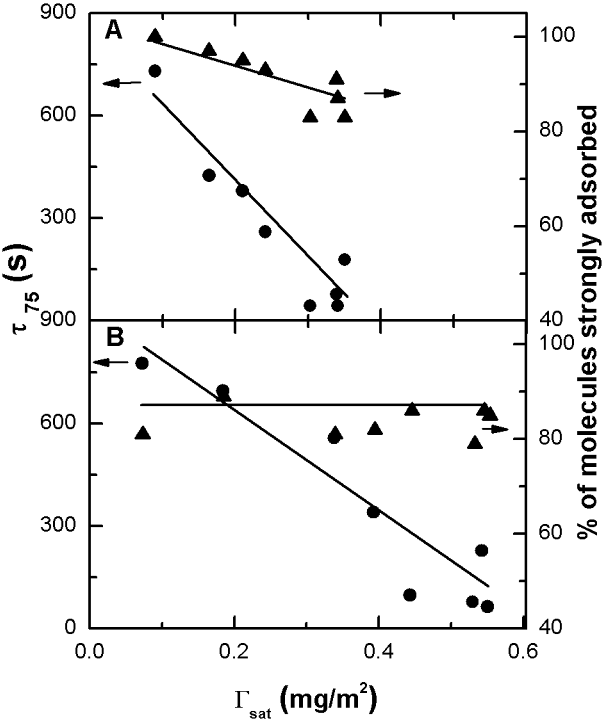

Figure 5. τ_{75} as the characteristic filling time (circles, left axis) and percentage of adsorbed molecules remained on the surface after rinsing with 5 mmol L^{-1} phosphate buffer pH 8.0 (triangles, right axis), as a function of the saturation adsorbed amount (Γ_{sat}) determined for His-tag H49 adsorbed on modified SiO_2 without (A) and with Ni(II) (B).

To summarize, the physical adsorption mechanism of the antigen depended on the supply rate (or the degree of surface coverage): a) at low supply rate, the protein-substrate interaction was optimized by some degree of spreading in such a way that the molecules did not leave the substrate upon dilution; b) at high supply rate, protein molecules were spread to different extent, so a percentage of them were desorbed by adding buffer. Consequently, the His-tag H49 antigen physically adsorbed can be partially removed by rinsing with buffer at high degree of surface coverage.

Figure 5B shows τ_{75} (on the left) and the percentage of proteins that remained on the substrate after rinsing with buffer (on the right) as a function of Γ_{sat} when the His-tag antigen was adsorbed on Ni(II) modified substrates (these experiments

In Proteins at Interfaces III State of the Art 2012; Horbett, T., et al.;
ACS Symposium Series; American Chemical Society: Washington, DC, 2012.

were performed at least in triplicate and SD of τ_{75} was always lower than 20%, while SD of the desorbed amount was lower than 10%). The characteristic filling and optimization times were also similar when the bioaffinity interaction was possible. Further, τ_{75} linearly diminished as Γ_{sat} increased. Thus, there were also two competitive processes which occurred in the same time scale when the His-tag antigen was attached to the Ni(II) modified substrate. On the other hand, the percentage of proteins remained on the surface after desorption (around 85%) did not change with Γ_{sat}. Thus, after the optimization step there were two populations of adsorbed molecules, loosely and strongly bond even at high degree of surface coverage. This behavior suggested that the competitive processes were caused by electrostatic and bioaffinity interactions between the antigen and the Ni(II) modified substrate. Probably, the first contact was through electrostatic interactions and the histidine-Ni(II) coordination developed later due to orientation constrains.

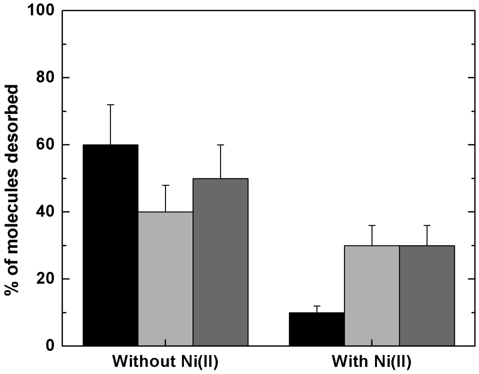

Figure 6. Percentage of desorbed His-tag H49 from modified SiO_2 (without or with Ni(II)) upon rinsing with 0.2 mol L^{-1} NaCl (black), 0.2 mol L^{-1} histidine (light gray), and 0.5 mol L^{-1} imidazole (dark gray) solutions. Error bars were calculated from duplicate experiments.

Desorption

To further evaluate the bioaffinity interaction between Ni(II) surface sites and the histidine residues of the antigen, the desorption behavior of the His-tag protein at high degree of surface coverage was studied with different agents (surfactants, histidine and imidazole). Non-specific washing with surfactant (anionic, cationic or neutral) did not remove neither physical nor chemical adsorbed antigens. Specific desorption was induced with imidazole and histidine solutions because these compounds directly competed with the His-tag protein for the surface Ni(II) sites (*50*). As indicated in figure 6, the effect of 0.2 mol L^{-1} histidine (light gray) or 0.5 mol L^{-1} imidazole (dark gray) solutions was the same as 0.2 mol L^{-1} NaCl (black) solution when treating physically adsorbed H49 (in the absence of Ni(II)). The three desorbing solutions removed around 50% of the adsorbed molecules. When the antigen was adsorbed on the Ni(II) modified substrate, NaCl only removed 10%, while the specific competitors eliminated up to 30%. Physically adsorbed molecules were partially removed with 0.2 mol L^{-1} NaCl in buffer pH 8.0 while the bioaffinity interaction was partially disrupted with specific ligands that compete for the Ni(II) coordination sites. In summary, the physical adsorption of His-tag H49 on Ni(II) modified substrates was reduced by washing with NaCl solution at high degree of surface coverage. Finally, the Ni(II) modified substrate may be re-used after exhausting washing with imidazole and/or histidine solutions that competed with the bioaffinity interaction of the His-tag antigen.

Surface Biofunctionality

The surface biofunctionality was evaluated using CV under the optimal experimental conditions (adsorption at pH 8.0, low ionic strength and high degree of surface coverage; desorption with 0.2 mol L^{-1} NaCl in buffer pH 8.0). The experimental detection set up included the biofunctional surface prepared on Au as a working electrode, Ag/AgCl/KCl_{sat} as a reference electrode, and a Pt counter electrode. The electrodes were immersed in a $K_4Fe(CN)_6/K_3Fe(CN)_6$ redox probe solution which was used to sense the electrochemical response of the biofunctional surface in the absence and in the presence of Chagas antibodies. It is important to note that purified antibodies (mostly used with other immunosensors) were not available to determine the surface activity. The idea behind these activity experiments was that the Chagas antibodies in the positive serum would provoke a surface immunoreaction that reduced the electron-transfer rate at the working electrode (see Figure 2). The redox probe transformation would appear as a less electrochemically reversible one-electron process at a given scanning rate, resulting in larger ΔE_p of the CV. Figure 7 compares the detection parameter ($\Delta(\Delta E_p)$), defined as the difference between ΔE_p before and after the immunoreactions, as a function of the scan rate for positive (black) and negative (white) sera. Although both (positive and negative) sera changed the electron-transfer kinetics (i.e. ΔE_p), the presence of Chagas′ antibodies was differentiate. The observed change with the negative sera may be due to the enormous amount of different compounds in the sample which may be an interference of the redox probe transformation at the working electrode. However, these results clearly indicated that a rather simple and direct electrochemical technique could be coupled to the biofunctional surface to detect Chagas antibodies.

His-Tag Redox Enzyme

Given that the proposed strategy may be extended to other proteins, the same substrate modification was used with His-tag yeast D-amino acid oxidase (*Rg*-DAAO) expressed in bacteria. It is important to emphasize that the efficiency of the expression and purification of this recombinant protein from yeast was higher than found with H49, resulting in higher protein amounts which were more appropriate to prepare biofunctional surfaces. As previously indicated, the adsorption experimental conditions were selected to minimize physical adsorption (due to electrostatic interactions), to induce Ni-histidine coordination and to obtain the best biological activity. On these basis, the biofunctional surface was prepared at pH 8.5 (protein IEp 6.9) and at high *Rg*-DAAO concentration (0.1 mg mL^{-1}). Since this particular redox enzyme catalyses the oxidation of D-amino acids into α-ceto acids and H_2O_2, the enzyme activity on the substrate was followed by amperometry. The stability of the substrate modification (see Figure 1) allowed applying the H_2O_2 oxidation potential (0.45 V vs. Ag/AgCl/KCl$_{sat}$) in order to determine the current change due to the formation of this product. Figure 8 shows the amperometric response (given by the H_2O_2 concentration) as a function of time for three different *Rg*-DAAO modified substrates in the presence of 100 μmol L^{-1} D-Alanine: bare (dashed) and modified Au without (dotted) and with Ni(II) (solid). The only combination that leads to the bioaffinity interaction between *Rg*-DAAO and the solid substrate was represented by the solid curve which showed the best response. Moreover, an analyte concentrations as low as 1 μmol L^{-1} could be detected using this biofunctional surface as working electrode.

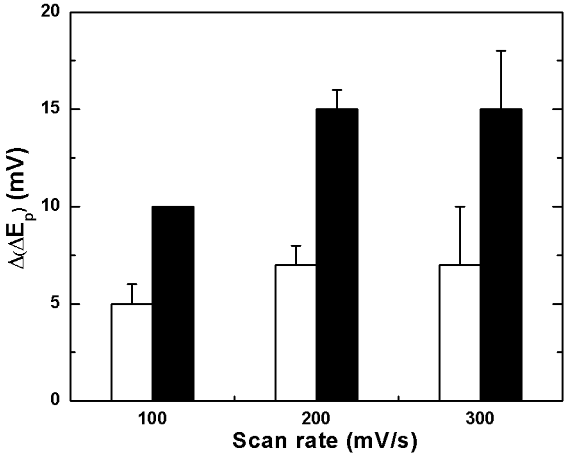

Figure 7. Biorecognition capabilities of the H49 biofunctionalized substrate as determined by CV, measuring the difference between the oxidation and reduction peaks (ΔE$_p$) of $[Fe(CN)_6]^{4-}/[Fe(CN)_6]^{3-}$ redox probe before and after the immunoreactions (Δ(ΔE$_p$)) as a function of the scan rate for positive (black) and negative (white) Chagas sera. (Biofunctional surface: working electrode; Ag/AgCl/KCl$_{sat}$: reference electrode; Pt: counter electrode). Error bars were calculated from duplicate experiments performed with two positive (n=4) and two negative (n=4) Chagas sera.

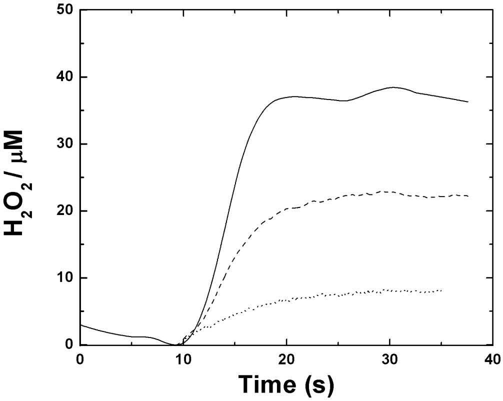

Figure 8. Amperometric response (given by the H_2O_2 concentration) as a function of time for three different Rg-DAAO biofunctionalized substrates in the presence of 100 µmol L^{-1} D-Alanine: bare (dashed) and modified Au electrodes without, (dotted) and with Ni(II) (solid) (Ag/AgCl/KCl_{sat}: reference electrode; Pt: counter electrode).

Conclusions

His-tag proteins adsorb on Ni(II) modified substrates through physical and bioaffinity interactions. The former is minimized by using experimental conditions of electrostatic repulsion (pH and ionic strength), high degree of surface coverage and further removal by washing with unspecific agents (NaCl). Under these conditions all the capabilities of the strong surface chelate which is formed between the Ni(II) surface sites and the histidine residues of the tagged protein are exploited to develop biofunctional surfaces with appropriate biorecognition response.

Acknowledgments

The authors acknowledge CNPq, FAPESP (09/53199-3), FonCyT (PICT 2007-695), SeCyT-UNC (05/C511) and CONICET (PIP 2010 11220090100672) for financial support. VLM thanks FAPESP (09/09209-4), LEV and GEH thank CONICET and MFS thanks FonCyT (PICT 2007-695) for fellowships. LNLS (Campinas, Brazil) is gratefully acknowledged for the use of the X-ray absorption facilities.

References

1. Giacomelli, C. E.; Valenti, L. E.; Carot, M. L. Biomolecules and Solid Substrate Interaction: Key Factors in Developing Biofunctional Surfaces. In *Encyclopedia of Surface and Colloid Science*, 2nd ed.; Taylor & Francis: Philadelphia, 2012; pp 1−16.

2. Kasemo, B. *Surf. Sci.* **2002**, *500* (1-3), 656–677.
3. Wong, L. S.; Khan, F.; Micklefield, J. *Chem. Rev.* **2009**, *109* (9), 4025–53.
4. Algar, W. R.; Tavares, A. J.; Krull, U. J. *Anal. Chim. Acta* **2010**, *673* (1), 1–25.
5. Cao, X.; Ye, Y.; Liu, S. *Anal. Biochem.* **2011**, *417* (1), 1–16.
6. Gonzalez, V. D. G.; Gugliotta, L. M.; Giacomelli, C. E.; Meira, G. R. *J. Mater. Sci.: Mater. Med.* **2008**, *19* (2), 789–795.
7. Valenti, L. E.; Fiorito, P. A.; García, C. D.; Giacomelli, C. E. *J. Colloid Interface Sci.* **2007**, *307* (2), 349–356.
8. Mora, M. F.; Giacomelli, C. E.; Garcia, C. D. *Anal. Chem.* **2009**, *81* (3), 1016–1022.
9. Norde, W.; Giacomelli, C. E. *Macromol. Symp.* **1999**, *145*, 125–136.
10. Vermonden, T.; Giacomelli, C. E.; Norde, W. *Langmuir* **2001**, *17* (12), 3734–3740.
11. Giacomelli, C. E.; Norde, W. *Macromol. Biosci.* **2005**, *5* (5), 401–407.
12. Mora, M. F.; Valenti, L. E.; García, C. D.; Giacomelli, C. E. *Key Eng. Mater.* **2010**, *441*, 75–94.
13. Ilk, N.; Egelseer, E. M.; Sleytr, U. B. *Curr. Opin. Biotechnol.* **2011**, *22*, 824–831.
14. Giacomelli, C. E.; Bremer, M. G. E. G.; Norde, W. *J. Colloid Interface Sci.* **1999**, *220* (1), 13–23.
15. Vermeer, A. W. P.; Bremer, M. G. E. G.; Norde, W. *Biochim. Biophys. Acta, Gen. Subj.* **1998**, *1425* (1), 1–12.
16. Smith, C. L.; Giang, S. M. *Top. Curr. Chem.* **2006**, 63–90.
17. Millner, P.; Hays, H. C. W.; Vakurov; Pchelintsev, N.; Billah, M. M.; Rodgers, M. *Semin. Cell Dev. Biol.* **2009**, *20* (1), 34–40.
18. Hernandez, K.; Fernandez-Lafuente, R. *Enzyme Microb. Technol.* **2011**, *48* (2), 107–22.
19. Jones, C.; Patel, A.; Griffin, S.; Martin, J.; Young, P.; O'Donnell, K. *J. Chromatogr., A* **1995**, *707* (1), 3–22.
20. Nieba, L.; Nieba-Axmann, S. E.; Persson; Hämäläinen, M.; Edebratt, F.; Hansson; Lidholm, J.; Magnusson, K.; Karlsson, F.; Plückthun *Anal. Biochem.* **1997**, *252* (2), 217–28.
21. Ley, C.; Holtmann, D.; Mangold, K.-M.; Schrader, J. *Colloids Surf., B* **2011**, *88* (2), 539–551.
22. Valenti, L. E.; De Pauli, C. P.; Giacomelli, C. E. *J. Inorg. Biochem.* **2006**, *100* (2), 192–200.
23. de Góes, L. C.; Miranda, E. A.; Bueno, S. M. A. *Colloids Surf., A* **2010**, *369* (1-3), 176–185.
24. Cheng, F.; Gamble, L. J.; Castner, D. G. *Anal. Chem.* **2008**, *80* (7), 2564–73.
25. Lata, S.; Reichel, A.; Brock, R.; Tampé, R.; Piehler, J. *J. Am. Chem. Soc.* **2005**, *127* (29), 10205–10215.
26. Cotrim, P. C.; Paranhos, G. S.; Mortara, R. A.; Wanderley, J.; Rassi, A.; Camargo, M. E.; Franco Da Silveira, J. *J. Clin. Microbiol.* **1990**, *28* (3), 519–524.

In Proteins at Interfaces III State of the Art 2012; Horbett, T., et al.;
ACS Symposium Series; American Chemical Society: Washington, DC, 2012.

27. Paranhos-Bacalla, G. S.; Santos, M. R. M.; Cotrim, P. C.; Rassi, A.; Jolivet, M.; Camargo, M. E.; Da Silveira, J. F. *Parasite Immunol.* **1994**, *16* (3), 165–169.
28. Umezawa, E. S.; Bastos, S. F.; Camargo, M. E.; Yamauchi, L. M.; Santos, M. R.; Gonzalez, A.; Zingales, B.; Levin, M. J.; Sousa, O.; Rangel-Aldao, R.; Franco Da Silveira, J. *J. Clin. Microbiol.* **1999**, *37* (5), 1554–1560.
29. Hopp, T.; Woods, E. *Proc. Natl. Acad. Sci. U.S.A.* **1981**, *78*, 3824–3828.
30. Fick, J.; Wolfram, T.; Belz, F.; Roke, S. *Langmuir* **2010**, *26* (2), 1051–6.
31. Boujday, S.; Méthivier, C.; Beccard, B.; Pradier, C.-M. *Anal. Biochem.* **2009**, *387* (2), 194–201.
32. Wang, C.-H. K.; Jiang, S.; Pun, S. H. *Langmuir* **2010**, *26* (19), 15445–52.
33. Balland, V.; Lecomte, S.; Limoges, B. *Langmuir* **2009**, *25* (11), 6532–42.
34. Kim, J.; Cho, J.; Seidler, P. M.; Kurland, N. E.; Yadavalli, V. K. *Langmuir* **2010**, *26* (4), 2599–608.
35. Liao, Y.; Cheng, Y.; Li, Q. *J. Chromatogr., A* **2007**, *1143* (1ï¿½2), 65–71.
36. Maly, J.; Illiano, E.; Sabato, M.; De Francesco, M.; Pinto, V.; Masci, a.; Masci, D.; Masojidek, J.; Sugiura, M.; Franconi, R.; Pilloton, R. *Mater. Sci. Eng., C* **2002**, *22* (2), 257–261.
37. Maly, J.; Di Meo, C.; De Francesco, M.; Masci, a.; Masojidek, J.; Sugiura, M.; Volpe, a.; Pilloton, R. *Bioelectrochemistry* **2004**, *63* (1-2), 271–5.
38. Zwahlen, M.; Herrwerth, S.; Eck, W.; Grunze, M.; Hähner, G. *Langmuir* **2003**, *19* (22), 9305–9310.
39. Colpas, G. J.; Maroney, M. J.; Bagyinka, C.; Kumar, M.; Willis, W. S.; Suib, S. L.; Mascharak, P. K.; Baidya, N. *Inorg. Chem.* **1991**, *30* (5), 920–928.
40. Davidson, G.; Clugston, S. L.; Honek, J. F.; Maroney, M. J. *Biochemistry* **2001**, *40* (15), 4569–4582.
41. Carrington, P. E.; Al-Mjeni, F.; Zoroddu, M. A.; Costa, M.; Maroney, M. J. *Environ. Health Perspect.* **2002**, *110* (s5).
42. Carrington, P. E.; Chivers, P. T.; Al-Mjeni, F.; Sauer, R. T.; Maroney, M. J. *Nat. Struct. Biol.* **2003**, *10* (2), 126–130.
43. Hall, G. *Geochim. Cosmochim. Acta* **2004**, *68* (17), 3441–3458.
44. Huang, H.-c.; Wei, Y.-l.; Yang, Y.-w.; Lee, J.-f. *J. Electron Spectrosc. Relat. Phenom.* **2005**, *147* (3), 825–828.
45. Valenti, L. E. Ph.D. thesis, Facultad de Ciencias Quimicas. Universidad Nacional de Córdoba., Córdoba. Argentina 2008.
46. Wertz, C. F.; Santore, M. M. *Langmuir* **2001**, *17* (10), 3006–3016.
47. Santore, M. M.; Wertz, C. F. *Langmuir* **2005**, *21* (22), 10172–10178.
48. Wertz, C. F.; Santore, M. M. *Langmuir* **1999**, *15* (26), 8884–8894.
49. van der Veen, M.; Stuart, M. C.; Norde, W. *Colloids Surf., B* **2007**, *54* (2), 136–142.
50. Kang, E.; Park, J.-W.; McClellan, S. J.; Kim, J.-M.; Holland, D. P.; Lee, G. U.; Franses, E. I.; Park, K.; Thompson, D. H. *Langmuir* **2007**, *23* (11), 6281–6288.

Chapter 3

Protein−Bioceramic Interactions at the Interface

Sunita Prem Victor and Chandra P. Sharma[*]

**Division of Biosurface technology, Biomedical Technology Wing,
Sree Chitra Tirunal Institute for Medical Science and Technology,
Poojappura, Thiruvananthapuram- 695012 Kerala, India
[*]E-mail: sharmacp@sctimst.ac.in**

Calcium phosphate based ceramics are indispensable in biomaterial and hard tissue application due to their chemical similarity to the mineral component of mammalian bones and teeth. Their interfacial behaviour with proteins determines cellular responses that play a pivotal role in determining the degree of biocompatibility. The control of the cell response to artificial hard tissue substitutes is of crucial importance in terms of biocompatibility. The selective nature of protein adsorption and the functionality of the adsorbed bio molecule are influenced by the physicochemical characteristic of the calcium phosphate material. This chapter focuses on the various factors like ionic composition, surface activity, monolayer adsorption, pH, solution strength and temperature that determine the kinetics of protein adsorption. It also includes the selective adsorption of proteins in competition to nonadhesive proteins to different calcium phosphate surfaces. These interfacial phenomena with the cell adhesion on protein adsorbed calcium phosphate surfaces indicate biocompatibility due to surface properties and have great potential to revolutionize the field of hard tissue engineering.

In Proteins at Interfaces III State of the Art 2012; Horbett, T., et al.;
ACS Symposium Series; American Chemical Society: Washington, DC, 2012.

Introduction

In the last decade the coexistence of biomaterials and tissues has been the focus of attention in biomaterial science, creating new challenges and opportunities. One group of biomaterials; that are of great importance are calcium phosphate based ceramics due to their chemical similarity to the mineral component of mammalian bones and teeth (*1–3*). The bioactive properties of these materials have received most attention in the field of hard tissue replacement. They provide fixation by biological ingrowth of the local tissue through the formation of a biologically active hydroxycarbonate apatite layer (*2*) on their surfaces *in-vivo*. They also have the additional benefits of biocompatibility, bioactivity and nontoxicity (*4*). The calcium phosphates with their varying Ca/P ratio are given in Table 1. However among the various calcium orthophosphates only certain compounds can be utilised for biomedical applications, because those having a Ca/P ionic ratio less than 1 are not suitable for implantation into the body due to their high solubility and acidity (*5*). The stable phases of calcium phosphates depend considerably upon temperature and the presence of water, either during processing or in the environment of its use (*6*). At body temperature, only two calcium phosphates are stable in contact with aqueous media, such as body fluids: at pH < 4.2, the stable phase is $CaHPO_4.2H_2O$ (Dicalcium phosphate, brushite, C_2P), whereas at pH>4.2, the stable phase is $Ca_{10}(PO_4)_6(OH)_2$(Hydroxyapatite, HA). Since body fluids are at pH 7.4 and 37° C, HA is the most stable calcium phosphate phase at that condition (*7*, *8*).

The commonly used bone substitute materials are HA, and tri calcium phosphate (TCP, $Ca_3(PO_4)_2$) which have different characteristics *in-vivo*, although both forms have Ca/P ratios within the range known to promote bone ingrowth (1.50-1.67) (*3*). The HA is known to bond with bone directly and can thus be used as a bone replacing material while the TCP (both α and β phases) is known to be a bone substituting material because it dissolves gradually and new bone will be formed where it is resorbed. The calcium to phosphorous ratio (Ca/P) of HA varies approximately between 1.5 and 1.67. The pH range is 4.6 to 12.4, over which this variable composition is stable at 25° C.

Another attractive member of the calcium phosphate family for medical applications is biphasic calcium phosphates (BCP), which plays an important role as a bioresorbable bioceramic. The BCP ceramic is based on the optimum balance of the most stable HA phase and more soluble TCP phase (*9*). The BCP allows its bioactivity and biodegradation to be controlled by varying the HA to TCP ratio. The BCP ceramic is usually obtained by mixing HA and TCP phases in the required ratio (*10*). These materials transform to carbonate hydroxyapatite, similar to biological apatite either by biodegradation or by bioresorption in the biological medium (*11*). It has been shown that bone in growth into BCP ceramic particles is rapid. Calcium–deficient hydroxyapatite ($Ca_{10-x}(PO_4)_{6-x}(HPO_4)_x(OH)_{2-x}$, $0 \leq x \leq 1$, CDHA) another resorbable ceramic is of greater biological interest, as it has a structure similar to bone mineral with a Ca/P ratio of about 1.5 which is similar to that of TCP but structurally and compositionally similar to stoichiometric HA (*12*). CDHAs play an important role in several processes such as bone remodelling and bone formation. The

In Proteins at Interfaces III State of the Art 2012; Horbett, T., et al.;
ACS Symposium Series; American Chemical Society: Washington, DC, 2012.

CDHAs are more soluble and can be partially decomposed to other phosphate phases at temperatures lower than 900° C (*13*). In addition, CDHAs are more efficient in inducing the precipitation of bone like apatite (*14*).

Table 1. Calcium phosphates with their varying Ca/P ratio

Ca/P Ratio	***Name***	***Formula***	***Acronym***
2.0	Tetracalcium phosphate	$Ca_4O(PO_4)_2$	TTCP
1.67	Hydroxyapatite	$Ca_{10}(PO_4)_6(OH)_2$	HA
1.50	Tricalcium phosphate (ά,β,γ)	$Ca_3(PO_4)_2$	TCP
1.33	Octacalcium phosphate	$Ca_8H_2(PO_4)_65H_2O$	OCP
1.0	Dicalcium phosphate dihydrate	$CaHPO_4.2H_2O$	DCPD
1.0	Dicalcium phosphate	$CaHPO_4$	DCPA
1.0	Calcium pyrophosphate (ά,β,γ)	$Ca_2P_2O_7$	CPP
1.0	Calcium pyrophosphate dihydrate	$Ca_2P_2O_72H_2O$	CPPD
0.7	Heptacalcium phosphate	$Ca_7(P_5O_{16})_2$	HCP
0.67	Tetracalcium dihydrogen phosphate	$Ca_4H_2P_6O_{20}$	TDHP
0.5	Monocalcium phosphate monohydrate	$Ca(H_2PO_4)_2H_2O$	MCPM
0.5	Calcium metaphosphate (ά,β,γ)	$Ca(PO_3)_2$	CMP

Protein adsorption to surfaces of bioceramics is the primary event and an essential aspect of the cascade of biological reactions taking place at the interface between material and the biological environment (*15*). When calcium phosphate particles come in contact with blood a number of events take place; which affect subsequent cell attachment and behaviour. These include apatite layer formation by dissolution and reprecipitation of the ceramic, precipitation solely from the surrounding liquid and protein adsorption (*16*, *17*). Understanding particle-protein interactions, nature and amount of protein adsorbed and their conformation will help in reducing possible adverse effects and directly influence the biocompatibility of the samples with blood. The types and amounts of adsorbed proteins are subsequently recognised by cells that mediate subsequent adhesion, proliferation and differentiation as well as deposition of mineral phases by a complex biological phenomenon (*18–20*). A number of studies have shown that proteins like fibronectin, bone morphogenetic proteins and synthetic peptides can regulate cell adhesion and subsequent tissue attachment to materials used as implants and can lead to an increased rate of normal tissue regeneration (*21–23*)

The sequences of amino acids present in the structure of proteins influence its surface activity and affect protein–surface interactions. The main three proteins present in plasma, albumin, immunoglobulin and fibrinogen are important components of the adsorbed protein layer (*24*). A thin layer of albumin adsorption appears to minimise adhesion and aggregation of platelets, thus determining its *in vivo* fate (*25*). Surfaces pre-coated with albumin have also been associated with lower bacterial adhesion (*26*). Similarly platelet adhesion to surfaces is promoted by prior adsorption of fibrinogen (*27*). Fibronectin is also an important protein that adsorbs to surfaces and promotes platelet adhesion to the subendothelium and nonfibrillar collagen types I and III (*28*). The bigger proteins have more binding sites to interact and have the potential to be adsorbed more on the surface. However protein adsorption mainly follows the Vroman effect (*29*). The more concentrated and smaller proteins that have greater diffusion rate tend to adsorb onto the surface first and are displaced by larger, more strongly interacting proteins that may be adsorbed later. Meanwhile, the hydrophobicity-charged amino acids are generally located on the outside of proteins and are mainly responsible for adsorbing on surfaces. Interestingly, proteins often show greater surface activity near their isoelectric point (*30*). This could be attributed to the weaker interaction between protein molecules at isoelectric point leading to enhanced adsorption.

Factors Affecting Protein Adsorption

Physico-chemically, calcium phosphate surfaces sustain dissolution reprecipitation cascades as the result of exchanges at a solid–liquid interface in supersaturated conditions. In biological systems, this phenomenon is the result of a multi-component dynamic process involving ions and proteins. Proteins become adsorbed to the calcium phosphate particle surface from the surrounding body fluid seconds after they come in contact with biological fluids. Most of the studies concerning biocompatibility of potential biomaterials *invitro* concerns single-protein adsorption (*31*). Unfortunately, there is little correlation between such highly ideal experiments and the real bio environment. Biological fluids contain more than 1000 different components and selective adsorption of proteins from such fluids will thus enhance more-or-less desirable cellular functions. So the competitive adsorption of proteins on the surface of a biomaterial is very similar to the actual conditions *in vivo*. The adsorption of proteins from complex mixtures has therefore become the focus of most of the recent works (*32*). The biocompatibility of calcium phosphates, primarily HA can be attributed to its mild adsorption of proteins. The factors determining which proteins become adsorbed to a substrate are complex; however, it is accepted that properties like surface activity, monolayer adsorption, pH, ionic composition and solution strength, temperature, potential and functional groups of the substrate material and surface morphology determine the kinetics of protein adsorption (Figure 1). Various calcium phosphates have different ability to bind proteins, and different proteins would competitively adhere to the surface. Generally accepted, concentration of signalling molecules such as bone growth factors on the surface has been considered as one of the key factors related to the bioactivity and osteoinduction of calcium phosphates.

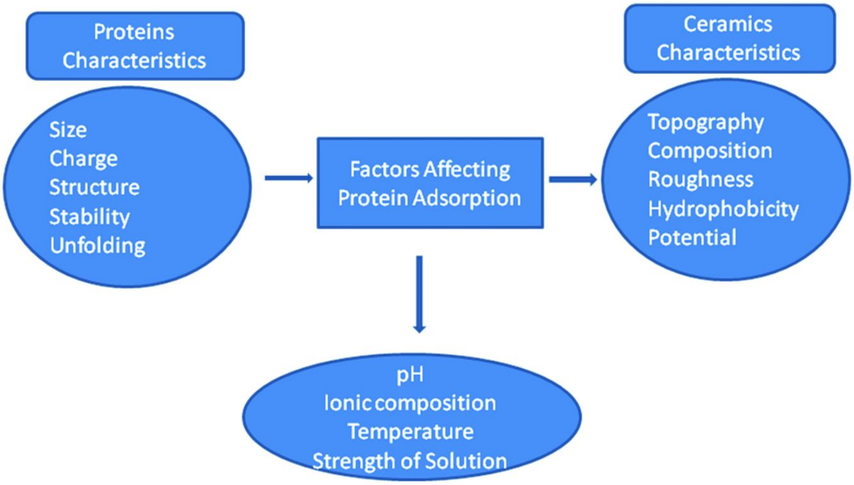
Proteins Characteristics
Size
Charge
Structure
Stability
Unfolding
Factors Affecting Protein Adsorption
Ceramics Characteristics
Topography
Composition
Roughness
Hydrophobicity
Potential
pH
Ionic composition
Temperature
Strength of Solution

Figure 1. Factors affecting Protein adsorption on Ceramics.

Physiochemical Characteristics

The selective nature of protein adsorption and the orientation and conformation of the adsorbed protein have been found to depend on the physiochemical characteristic of the material surface. The different phases of calcium phosphate exhibit variable solubility, roughness, porosity, pore and particle size and are decisive factors of protein adsorption. The composition and crystallinity of these phases play an important role in controlling the initial biological response at the ceramic surface. Rouahi *et al.* (*33*) reported that HA powder having 100 nm particle size having greater surface area led to higher adsorption of proteins when compared to HA powder with 1 µm particle size. Ceramic particles like HA have also been employed to study the adsorption behaviour of proteins from diluted human plasma with regard to total protein binding capacity, relative binding capacity for specific proteins, flowthrough and desorption patterns (*34*). It was characterised regarding chemical composition, specific surface, pore volume and pore size distribution. It was found to adsorb a low amount of plasma proteins, leaving more than 70% of the surface free. It has also been reported that proteins like albumin and lysozyme, can bind to HA just by intimate mixing. HA was found to have higher adsorption and binding capacity of plasma proteins and adsorbed 14% of albumin and 30% of immunoglobulin respectively (*35*). 50% of selective and preferential albumin adsorption was also observed in HA complexed with cyclodextrin (*36*). It has also been observed that immunoglobulin is adsorbed more onto HA and tryptophan modified HA compared to other immunoproteins (*37*).

The effect of porosity on protein adsorption of calcium phosphates has been reviewed in literature. The effects have been considered as an interpretation of their osteoinductive potential after implanting to ectopic sites (*38*, *39*). The porosity in calcium phosphate comprises of microporosity and macroporosity. Microporosity leads to higher surface area which enables increased protein adsorption and subsequent cell attachment (*40*, *41*). The proteins adsorb on porous calcium phosphates by multilayer adsorption process and dense calcium phosphates as a monolayer one (*42*). The roles of the microstructure and phase composition of HA, BCP and TCP particles in the adsorption of various model proteins like fibrinogen, insulin and collagen have been evaluated (*43*). The results showed that BCP always had a higher ability to absorb proteins when compared to HA. The microporosity and micropore size of the particles also had a strong impact on their protein adsorption characteristics. HA and BCP particles with high microporosities having pore size >20 nm in diameter could adsorb more fibrinogen or insulin (*43*). So pore size must correlate with protein size and is very critical for protein adsorption (*44*). Experimental results have validated the fact that protein cannot be adsorbed in the pore if the pore size is smaller than the protein. Contrarily the protein is trapped in the mesopores and thus there is an increase in its adsorption (*45*).

It has also been envisioned that the nanoscale roughness of calcium phosphate can also affect the protein adsorption process (*46*). Surface roughness enhances osteoblast functions while a porous structure improves the osteoinduction properties (*47*). Nanodimensional (size ~67 nm) HA was found to have a higher surface roughness of 17 nm when compared to 10 nm for the submicron-sized (~180 nm) HA. The diameter of individual pores in nanodimensional HA is several times smaller (pore diameter ~6.6 Å) than that in the submicron grain-sized HA compacts (pore diameter within 19.8–31.0 Å) (*48*). Furthermore, nanophase HA has more protein adsorption of fetal bovine serum than submicron sized HA (*49*). However it has been reported that the adsorption of albumin and fibronectin on HA with lower roughness was higher than that observed on TCP (*50*). Another study tried to evaluate the specific role of calcium phosphates surface energy on serum protein adsorption and human osteoblast adhesion, by isolating chemical effects from those caused by topography (*51*). Highly dense HA and TCP presenting two distinct nano roughnesses were produced. The results indicated that the seeding efficacy of osteoblasts was not affected by the topography but the TCP negatively influenced cell spreading. Thus in general the protein adsorption on calcium phosphates was found to increase with an increase in surface area brought about by lesser particle size and higher roughness. Optimum pore size and high micro porosity also leads to an increase in protein adsorption with subsequent increase in cell attachment.

It has also been shown that calcium phosphates can adsorb bone morphogenetic proteins which induce bone formation in a dose dependant manner (*52*). The binding affinity between peptide and HA is the key contributor to both the induction of mineral growth and inhibition of secondary nucleation. The effect of polyelectrolytic peptides on the induction, amorphous phase formation and crystal growth kinetics of HA has been systematically examined (*53*). This study gave support to the notion that the charged noncollagenous proteins present during different stages of bone development might play critical roles in directing hydroxyapatite crystal formation and growth. This ability of bioceramics to instruct cell and tissue development by changing their chemical composition and structural properties was evaluated. The aim of this study was to correlate the osteogenic potential of a variety of porous ceramic materials (HA, BCP and TCP) in vitro to ectopic bone formation in vivo (*54*). TCP was found to have higher stem cell differentiation and osteoinduction invivo. The percentage of bone was also higher in TCP compared to HA. Similar results have been obtained in a previous study wherein a comparison between HA and BCP sintered at same temperature showed more bone formation in BCP which contains highly resorbable TCP (*55*). The above results thus demonstrate that calcium phosphate ceramics with different chemical composition have varying osteoinductive potential.

The adsorption of proteins on calcium phosphate surfaces is a complicated process and leads to conformational changes that influence cellular interactions (*56*). In particular the protein conformational change, which results in entropic gain, is thought to be an important driving force for protein adsorption (*57*). A report on the adsorption of albumin on the surface of HA and Fluorine substituted HA showed that surface composition and structure influenced the kinetics of protein adsorption and the structure of adsorbed protein. The greatest loss in the alpha helix structure of albumin to form random structures was detected on the surface of HA. Similar observations of conformational changes of adsorbed albumin on calcium phosphate surfaces are available in literature (*58*). This loss of alpha helix structure of albumin could also be the result of ionic or electrostatic interactions. The highly ionic surface of calcium phosphates not only attracts the protein but also exerts a greater electrostatic force on the functional groups of protein leading to conformational changes (*59*). The presence of vacancies and defects on HA crystal surface (*60*) and the crystallinity and amorphousness of the surface have also been found to bring about differences in protein adsorption (*61*) and conformational changes. Xie et al. (*62*) showed that there was a conformational change of the adsorbed albumin during the transformation of brushite to HA. Changes in conformation of PRP1a proline-rich acidic salivary protein when adsorbed on HA and carbonated HA has been reported (*63*). The conformational changes in PRP1 adsorbed on carbonated HA and HA were similar in nature; however, the changes were greater in the protein bound to HA. This is attributed to the different distribution of binding sites or electrostatic groups on carbonated HA and HA. However there was no conformational change observed when insulin was adsorbed onto lauric acid modified calcium phosphate nanoparticles (*64*).

Further it has also been observed that the conformation and the structure of residue peptide and protein also affect the nucleation behaviour of calcium phosphates. Molecular dynamic simulations were carried out to study the conformational effect of a proposed nucleating motif of bone Sialoprotein on HA (*65*). The study attempted to see whether a nucleating template for orientated HA could be formed in different peptide conformations. The possibility of promoting template nucleation was seen in alpha helical conformations but not in random coil conformations respectively. Similar studies have also been carried out on Myoglobin adsorption onto HA and HA functionalised with alendronate (*66*) .The results indicate that the interaction with HA alters the coordination state of the iron in the heme .The protein changes conformation upon adsorption onto the HA crystal. However HA functionalised with alendronate does not adsorb the protein but preserves the coordination state of the heme moiety. This Myoglobin behavior toward alendronate-functionalised HA crystals shows that this functionalization imprints surface selectivity to HA and drives the biological environmental response toward them. Further research on the effect of conformational changes of protein on biological responses is necessary to understand the osteoinductivity of calcium phosphates. Table 2 mentions some of the characterisation techniques that have been utilised in literature to study protein adsorption.

Table 2. Characterisation techniques to study protein adsorption

Characterization Technique	*Particle Composition*	*Types of Proteins Adsorbed*	*References*
Poly Acrylamide Gel Electrophoresis	Biphasic Calcium Phosphate, Hydroxyapatite	Bovine serum Albumin, Lysosyme, Serum proteins	(*42*, *76*, *77*, *79*)
Quartz Crystal Microbalance & Fourier Transform Infrared Microscopy	Hydroxyapatite	Fetal Bovine Serum	(*122–124*)
Atomic Force Microscopy	Hydroxyapatite	Bovine serum	(*84*, *86*, *87*, *123*)
BCA Protein Assay	Hydroxyapatite	BMP, bFGF	(*101*, *103*)
Chemiluminesence & gas Chromatography	Hydroxyapatite and Tri Calcium Phosphate	Transferrin	(*105–107*)
Western Blot Analysis	Hydroxyapatite & Polymer scaffold	Fibronectin and Vitronectin	(*66*, *67*)
UV Visible and Surface enhanced Raman spectroscopy	Hydroxyapatite	Myoglobin	(*108*, *109*)
HPLC	Hydroxyapatite	Insulin and Cytochrome C	(*64*, *69*, *72*)
Calorimetric (heat of adsorption)	CDHA	Albumin and lysosyme	(*77*, *109*, *112*)
NMR	HA	Albumin	(*99*)

Chemical Characteristics

Biological responses are determined not only by surface topography but also by chemistry and consequently by the surface energy of the material (*67–69*). The relative effect of either topography or chemistry is generally difficult to discriminate. The chemical properties of the material surface play an important role in determining the amount of protein adsorbed by interaction between the functional groups on substratum and proteins and the efficiency of adsorption. HA possesses two different binding sites, the C and the P sites respectively on its surface and this provide proteins a multiple site binding opportunity (*70*). On dispersion the calcium atoms (C sites) are exposed on the HA surface by dissolution of OH ions at the particle surface. Therefore, the C sites are arranged on ac or bc particle faces in a rectangular manner with the interdistance in the a or b directions equal to 0.943 nm and the interdistance in the c direction equal to 0.344 nm(c/2) (Figure 2). The P sites are arranged hexagonally on the ab particle face with a minimal distance of 0.943 nm (*71*). The C sites are rich in calcium ions or positive charge and thus bind to acidic groups of proteins, but the P sites lack calcium ions or positive charge and therefore attach to basic groups of proteins.

Many fundamental studies on the adsorption of albumin and lysozyme on various kinds of calcium phosphates have been demonstrated (*72*, *73*). The saturated amount of adsorbed albumin was found to depend on the molar ratio of Calcium to Phosphorous (Ca/P) in the materials used and increased with an increase in Ca/P ratio. This was explained by the electrostatic attractive forces between negatively charged BSA and the less negatively charged HA with high Ca/P ratios at pH 6. However, the saturated amounts of adsorbed lysozyme decreased with an increase in the Ca/P ratio (*74*, *75*).

The electrostatic interaction between the surface and proteins could also be affected by the surface charge and protein net charge in different solutions (*76*). The adsorption of albumin onto HA studied by ionic concentration measurements has been found to depend on counter ions complexing to albumin molecules along with the operation of C sites. It has been reported that HA, BCP and TCP had negative surface charge, and preferred to adsorb more basic protein lysozyme than acidic protein albumin in pH 7.4 phosphate-buffered saline (PBS) solution (*77*). HA with higher surface net charge and thus higher value of zeta potential exhibited higher lysozyme adsorption owing to the stronger electrostatic attraction between them (*78*). Another study by the same authors investigates the adsorption of albumin and lysozyme on BCP under various conditions (*79*). The binding energies of Ca and P on BCP showing the alterations of the chemical bonds around Ca or P after albumin adsorption imply that the electrostatic interaction might be a negligible factor for albumin adsorption on BCP. So, the surface charge of BCP has a great influence on the amount of adsorbed BSA on the surface. Further it has also been observed there is coherence between the variation of BSA adsorption and that of the zeta potential of BCP. Besides electrostatic interaction, the driving forces for protein adsorption also come from the hydrophobic interaction between protein molecules and the substrate surface, and the structure stability of protein molecules (*80*). Albumin has a flexible structure and a medium size with a molecular weight of about 67 KDa. Lysozyme has a rigid structure and a lower molecular weight of about 14 KDa. So Lysozyme can't change its conformation as easily as Albumin. The adsorption of Albumin on the BCP surface is mainly driven by the conformation change and the hydrophobic interaction and that of Lysosyme primarily come from the contributions of electrostatic forces. However lysozyme has higher affinity for BCP than albumin and preferentially binds to the surface. This has been explained by the fact that at higher bulk concentrations, less unfolding of albumin occurs due to interaction between albumin molecules resulting in less affinity of albumin for BCP. So the previously adsorbed albumin gets replaced by lysozyme.

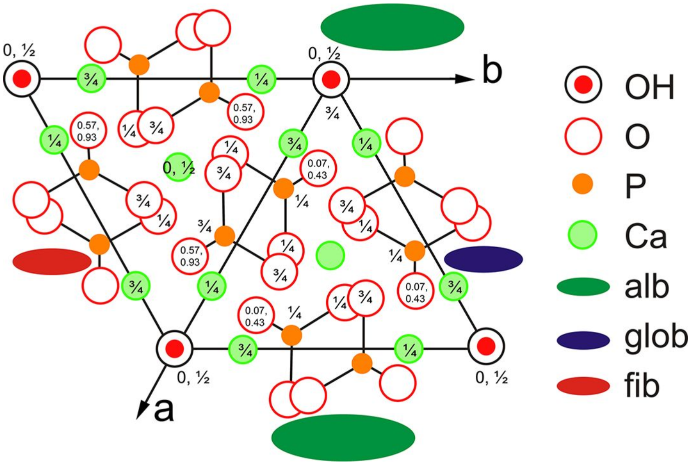

Figure 2. Schematic representation of adsorption of protein on HA crystal.

Computer simulation results have validated the fact that protein interaction with calcium phosphates depends mainly on the electrostatic force and sometimes on the hydrogen bond (*81*). A study investigated the adsorption of the three major amino acids (*82*) glycine, proline, and hydroxyproline, which are constituents of the collagen I protein, at two major hydroxyapatite surfaces, (0001) and (0110). The strength of interaction of the amino acid molecules with the surfaces depends on both the stability of the surface and the capability of the amino acid molecules to form multiple interactions with the surface species, particularly if they can bridge between two or more surface calcium ions. The primary association between amino acids and the HA surfaces is via interactions between carboxyl and surface bound calcium ions but the additional side group interactions have also been found to lead to significant variations in their affinities. Other adsorption mechanisms like ion exchange mechanism and counter ion binding have also been suggested to explain the adsorption of proteins onto the surface of HA (*83*, *84*). Ion exchange between the charged group of the protein and surface ions can occur if they have similar size range. Another study suggested that the acidic peptide or chelators are bound by incorporation of the acidic carboxylic groups into the HA lattice displacing surface phosphate (*85*). It has also been proposed that the binding of proteins takes place through complexing calcium ions adsorbed on the HA particles (*86*). The calcium ions adsorbed on HA surface would bind anionic groups on the proteins. In fact, Lindh et al. reported that the presence of calcium enhances the adsorption of human serum albumin (*82*).

Calcium phosphates with varying structures have specific surface planes which can interact with proteins on a selective basis (*48*). Acidic proteins should preferably be adsorbed on calcium site based surfaces and basic proteins on the phosphorous/hydroxyl site-based surfaces respectively based on electrostatic attractions. This is the reason for acidic proteins being preferentially adsorbed on the (100) face of HA and OCP crystals (*87*). Many of the phosphoproteins that play a key role in bio mineralization are acidic in nature (*88*). These proteins are rich in acidic residues like glutamic acid which bind strongly to 001 face of HA which results in plate like HA. This could be one of the reasons behind the effect proteins have on the morphology, size and orientation of calcium phosphate crystals (*89*).

Hydrophobicity of Calcium Phosphates

Hydrophobic interactions between calcium phosphate surfaces and protein have a direct effect on protein adsorption and subsequent cell adhesion. It has generally been observed that the more hydrophobic a surface, the higher the affinity and the greater the extent of protein adsorption (*90*). However, in the context of protein spreading and specific protein-surface interactions, it is not clear whether higher affinity should always correspond to higher coverage levels. The principal forces responsible for non covalent binding of protein are polar hydrogen bonding forces which are also considered as the main driving force of hydrophobic interactions (*91*). The exposed chemical functional groups determine the distribution and density of these forces, which in turn affect the hydrophobicity of the substrate. The hydrophobic patches of residues present in the protein's amphiphilic structure tend to adsorb on the hydrophobic surface of calcium phosphate. Protein would unfold and spread its hydrophobic core over the surface owing to the thermodynamic driving force to reduce the net hydrophobic surface area of the system exposed to the solvent (*92*) (Figure 3). The charged and polar functional groups of proteins will then subsequently tend to interact with the hydrophilic surface. The hydrophobicity of HA, BCP and TCP are in the order TCP>BCP>HA which subsequently results in BCP having higher ability to adsorb proteins than HA. It has also been reported that the presence of beta-TCP in HA composites influences the surface charge, hydrophobicity, and further increases the protein adsorption of the HA composites (*93*).

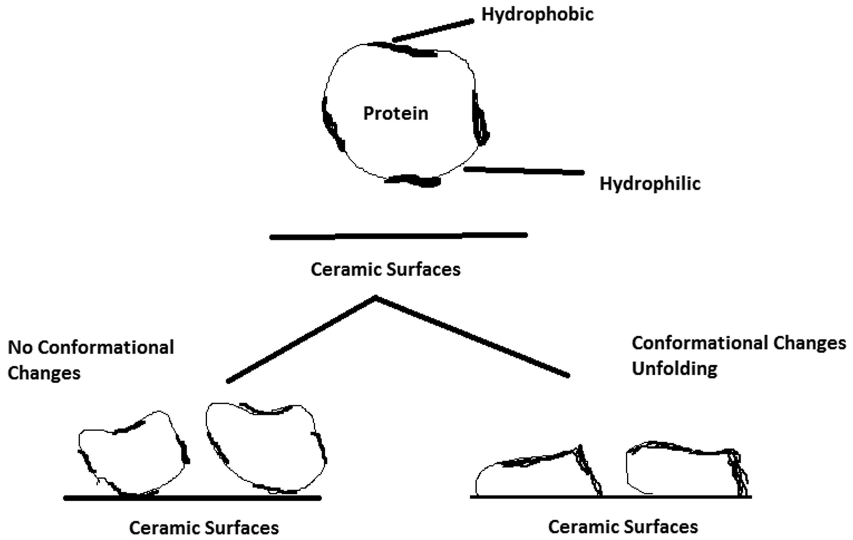

Figure 3. Schematic Illustration of adsorption of proteins on Ceramic surface.

Incubation Solution Characteristics

The incubation environment is an important factor that affects protein adsorption and different solutions could induce different protein adsorption behaviours. It has been accepted that ionic composition, strength of solution, pH and temperature affect the kinetics of protein adsorption (*94*). The different phases of calcium phosphate exhibit variable solubility: HA < β-TCP < α-TCP (*95*). So the different kind of ions that are present in solution, brought about by the dissolution of HA and TCP can alter the surface charge distribution. The overall electrostatic interaction existing between proteins and calcium phosphates depends on the surface and protein charge respectively. So differences in surface charge distribution brought about by incubation can affect protein adsorption. It has been established that the surface charge and the protein charge are functions of pH (*96*). Further protein conformational changes described earlier are also pH dependent and affect the entropy and enthalpy of adsorption.

As mentioned previously on dispersing HA particles in aqueous media, calcium atoms (**C** sites) are exposed on the HA surface by dissolution of hydroxyl ions at the particle surface. Therefore, the **C** sites, rich in calcium ions or positive charge bind to acidic groups of proteins, arranged on the *ac* or *bc* particle face in a rectangular manner with interdistances of 0.943 and 0.344 nm (c/2) for the *a* (or *b*) and *c* directions, respectively (*97*). Chen et al. reported that the -COO- claw of protein grasps the calcium atoms of the HA surface with its two oxygen atoms in a triangle form (*98*). The solid state NMR study also revealed that the -COO- terminus of amelogenin is orientated to the Hap surface (*99*). The **P** sites, lacking calcium ions or positive charge to attach to basic groups of proteins, are arranged hexagonally on the *ab* particle face with a minimal distance of 0.943 nm. The adsorption of bovine serum albumin onto HA has been studied as a function of protein concentration, pH and ionic strength (*100*). The results revealed that amount of albumin adsorbed on HA increased as the pH decreases. The amount of protein adsorbed on the surface was dependent on the magnitude and charge of the both the HA surface and the protein albumin and also the degree of hydration of the protein. The isoelectric point of HA has been found to lie between pH 6.4 to pH 8.5, with the zetapotential being positive in the above range. At lower pH values near the isoelectric point of albumin, the charge on the molecule and the degree of hydration decreases enabling higher adsorption. Similar adsorption studies on HA using human serum albumin and dentine proteins also confirmed an increase in adsorption with decreasing pH (*83*). The ionic strength of the solution was also found to affect albumin adsorption. The ionic strength was varied by the addition of phosphate and calcium both of which affect the surface charge of HA by surface adsorption. Calcium is known to bind to albumin by calcium ion bridging which leads to an increase in albumin adsorption (*101*). However the phosphates being more hydrophilic in nature have a high affinity for HA and they compete with the carboxyl group of the protein to bind onto the HA surface. So there is an observed reduction in albumin adsorption.

The zeta potential measurements of HA particles treated with proteins and polypeptides show that the HA particle reflects the charged environment of the adsorbed molecule and correlate with the number of bacterial cells adhering to the surface (*102*). A basic protein or polypeptide (net positively charged at pH 7.0) produced a positive zeta potential, whereas an acidic protein or polypeptide (net negatively charged at pH 7.0) produced a negative zeta potential. This work reports that protein adsorbed onto the HA surface are involved in both long- and short-range interactions between bacteria and the HA surface (*103*). Acidic proteins reduced the number of bacteria adhering by increasing the repulsion between electrical double layers surrounding the bacterium and the HA. This effect was further modified by the density of nonpolar, acidic and basic amino acids of the adsorbed protein, indicating the involvement of short-range hydrophobic and ionic interactions between adsorbed protein and bacteria.

Another study reports the adsorption of serum proteins from cell culture medium to HA and TCP ceramic powders compared by sodium dodecyl sulphate polyacrylamide gel electrophoresis (*104*). There was a distinct difference in adsorption with higher concentrations of transferrin being adsorbed onto the powders which caused a reduction in the pH of the cell culture medium. Transferrin was also adsorbed to HA in greater concentrations at a lower pH than it was at a higher pH (*105*). Ceramic implant materials have been reported to affect the pH of water due to their dissolution characteristics. But since blood is well buffered and constantly circulating, it is unlikely that large pH changes take place *invivo*. However the interfacial layer created by ions electrostatically bound

In Proteins at Interfaces III State of the Art 2012; Horbett, T., et al.;
ACS Symposium Series; American Chemical Society: Washington, DC, 2012.

to the surface directly adjacent to a ceramic substrate can affect any chemical or biological processes occurring in this layer. So the changes in pH that have been shown to affect protein absorption are also likely to have a direct effect on cell behaviour and consequent tissue response.

Ionic strength is another parameter that affects protein adsorption. Higher the ionic strength in the solution greater is the tendency for the protein to expose more polar ionised residues to the solvent (*106*). So the amount of the protein adsorbed on BCP could be increased by the stronger interaction between protein and the surface-binding sites of BCP, which always has a higher ability to adsorb proteins than HA, considering the effect of topography at the same time (*43*). This also could be the reason behind why BCP has better osteoinductivity than HA.

The sintering temperature of calcium phosphates also affects the solubility of calcium phosphates in the incubation solution due to their differences in thermodynamic properties (*107*). HA and TCP powders heat treated at a range of temperatures from 100 to 1400°C have been found to affect the pH of water, with pH being increased with temperature in both HA and TCP. Higher temperature also leads to higher crystallinity thereby reducing solubility. A study to explore the effects of heat treatment temperature on the protein adsorption behaviour onto HA particles was carried out by systematically heating to 800 degrees (*108*). Albumin, lysozme and Myoglobin were selected as the model proteins respectively. The saturated amounts of adsorbed albumin did not vary on the HA particles after heat treatment at 200 and 400 °C. However, saturated amounts of adsorbed albumin were increased by raising the heat treatment temperature above 600 °C. The adsorption coverage suggests that the albumin molecules are densely adsorbed and a part of the molecule gets adsorbed as end-on type on the HA particle surface or in other words there is a contraction in the albumin molecules. Similar adsorption behaviour was observed on the lysozyme system, but the adsorption coverage was much less than that observed for albumin. On the other hand, no effect of the heat treatment of HA particles was observed on the adsorption of myoglobin. The increases of albumin and lyzozyme adsorption with an increase in temperature were explained by the increase of calcium and phosphate ions in the solutions dissolved from TCP formed after heat treatment of HA, especially at high temperatures. The dissolved calcium and phosphate ions may act as binders between proteins and HA surfaces. Further the adsorption of calcium ions on the HA surface offers an adsorption site for albumin owing to its positive charge. This binding of calcium ions to anionic sites of albumin reduces the inter and intra molecular electrostatic repulsion between albumin segments leading to a dense adsorption of albumin. In the case of adsorption of positively charged lysosyme molecules, phosphate ions act as a binder for adsorption. Since the myoglobin molecules are neutral, no binding effect of either ions were observed. Another study reported that differences in the acid and basic strength in heat treated HA due to their calcium deficiency manifested as different size and morphology in the HA crystal (*109*). This difference in structure further affects observed protein adsorption in calciu, phosphates. A significant amount of research on protein adsorption of calcium phosphates is available in literature and reviews give a comprehensive detail of the same (*110*).

Competitive Adsorption of Proteins

Body fluids like blood contain a large number of proteins. So the competitive adsorption of proteins on the surface of a biomaterial is more close to the actual conditions *invivo*. The competitive adsorption of proteins is highly dependent on the concentration and competing components (*111*, *112*). Brash & Lyman (*113*) demonstrated that protein adsorption is directly proportional to the protein concentration. Moreover, the preferential adsorption of proteins, especially the growth factors, on the implant surface has been considered as one of the key factors related to the bioactivity and osteoinduction of calcium phosphates. When calcium phosphate is implanted into the body, various kinds of proteins will adsorb to the substrate from body fluids. Albumin is the most abundant protein in blood. On the other hand, the proteins relating with bone regeneration are some growth factors which have lower molecular weight and are found in minute amounts in body fluids. So it is very critical to investigate the competitive adsorption of kinds of proteins on calcium phosphates

The competitive adsorption on HA, BCP and TCP ceramics was investigated using conventional protein quantitative analysis with albumin and lysozyme (*114*). Lysozyme was used as the analogue for growth factor due to their similar properties. The three calcium phosphate particles all had negatively surface zeta potentials after being dispersed into pH 7.4 PBS solution. HA had larger absolute value of zeta potential and thus higher surface net charge. It has been observed that lysozyme showed higher affinity for the three calcium phosphate ceramics compared to albumin. Thus it could be inferred that bone growth factors with similar properties as lysozyme might preferentially bind to the surface of calcium phosphate ceramics when implanted into the body. Another study reports the higher affinity of lysozyme for BCP when compared to albumin (*115*); again suggesting that competitive adsorption is undoubtedly important for understanding the mechanism of osteoinduction in calcium phosphates.

Biological Properties of Calcium Phosphates

The bioactivity of calcium phosphate has been related to their propensity to nucleate carbonate apatite crystals analogous to bone minerals. The newly formed bone bonds directly to calcium phosphate materials through a carbonated apatite layer at the bone/material interface. The bioactivity mechanism of calcium orthophosphates has been described as follows (*116*). The partial dissolution of calcium phosphate leads to the release of calcium and phosphate ions that result in an increase in local ionic concentration. The liberated ions increased the supersaturation degree of the biologic fluids, causing precipitation of biological apatite nanocrystals with simultaneous incorporating of various ions presented in the fluids. Ionic exchange takes place leading to the precipitation of carbonated calcium phosphate crystals. The formation of a layer of microcrystals and macrocrystals along with the incorporation of a collageneous matrix leads to bone growth toward the implant. Then bone remodelling takes place. The osteoclasts resorb normal bone by actively secreting hydrogen ions into the extracellular space, creating a local pH of approximately 4.8, and leading to fast resorption of both carbonated HA in bone mineral and the apatite. Finally the bone-implant interface is subjected to further bone ingrowth and remodeling, and a biological fixation can be achieved through the bidirectional growth of a bonding layer. An important study on formation of calcium orthophosphate precipitates on various types of calcium phosphates in simulated body fluid (SBF) and in rabbit muscle sites was performed (*117*). The studies revealed that OCP formation occurred on all apatite surfaces with the exception of TCP, the precipitation was more difficult in-vivo and the partial dissolution of HA lead to apatite formation. The chemical changes that occurring after exposure of a synthetic HA bioceramic to both *in vivo* and *in vitro* conditions were also studied. A small amount of HA was phagocytized but the major remaining part behaved as a secondary nucleator as evidenced by the appearance of a newly formed mineral (*118*). To a certain extent calcium phosphates are also osteoinductive in nature. The apparent osteoinductive property is the ability to concentrate bone growth factors, and induce bone formation. When attached to healthy bones, osteoid is produced directly onto its surfaces in the absence of soft tissue interface. Consequently, the osteoid mineralizes and the resulting new bone undergoes remodelling. The geometry and surface roughness of calcium orthophosphates are critical parameters in bone induction (*119*). Bone formation was found to occur in dog muscle inside porous calcium orthophosphate with surface microporosity, while bone was not observed inside the dense surface of macroporous bioceramics (*120*). Besides, metal implants coated by a microporous layer of OCP was found to induce ectopic bone formation in goat muscle, while a smooth layer of carbonated apatite on these porous metal implants was not able to induce bone formation (*121*).

Interfacial Protein Effect on Apatite Growth

Biological apatite growth from simulated body fluid (SBF) with similar inorganic components of plasma serum is one of the evaluation methods for bioactive materials. This growth was investigated with and without preadsorption of fetal bovine serum protein at the initial nucleation stage using a quartz crystal microbalance technique (*122*). It was observed that during the apatite growth dominated by the interfacial interaction between the ions and substrate surfaces, two processes, which are the heterogeneous nucleation initiating from the protein surfaces and homoepitaxial growth initiating from the already-formed apatite crystals, are competitive. The interfacial viscoelastic changes with the apatite depended on the substrate surfaces; the viscoelastic property and component (IgG/Ab ratio) of the serum adlayer. The interfacial protein effect during the initial crystallization stage could be attributed to the competitive heterogeneous and homoepitaxial ion reactions at the interface which were predominantly attributed to the adsorbed protein species (immunoglobulin (IgG) and albumin) based on the antibody-binding results. Although the serum adlayer clearly inhibits the apatite growth, the relationship between the adsorbed IgG amount and the apatite growth was significantly correlated, indicating that the IgG molecules would promote growth. It was suggested that the interfacial viscoelastic changes with the apatite growth depended on the substrate surface as well as the adsorbed

In Proteins at Interfaces III State of the Art 2012; Horbett, T., et al.;
ACS Symposium Series; American Chemical Society: Washington, DC, 2012.

protein properties. Therefore, the serum adlayer significantly affected the apatite growth at the interface, indicating the importance of the interfacial protein effect.

In another study a quartz crystal microbalance with dissipation (QCM-D) technique was employed to detect the protein adsorption and subsequent osteoblast-like cell adhesion to HA nanocrystals (*123*). The interfacial phenomena with the preadsorption of three proteins albumin, fibronectin and collagen; the subsequent adsorption of fetal bovine serum and the adhesion of the cells were investigated. The results of the protein preadsorption and subsequent cell adhesion showed different behaviour on the surfaces, clearly indicating that the adhesion process was affected by the cell surface interactions through the substrate protein. The different morphological and pseudopod structures formed depend further on the cell adhesion. The preadsorption of proteins has been observed to be accelerated in cell adhesion. Thus the surface modified with the interfacial proteins affected the cytoskeleton changes and the arrangement of the extracellular matrix at the interfaces.

Conclusion

The role of calcium phosphates is changing from a biologically passive, structural role to one in which the properties of the material can orchestrate the process of tissue regeneration. In spite of a long history of research on protein adsorption of calcium orthophosphates, there is still great potential for major advances to be made in the field. There are increasing number of reports demonstrating that cellular behaviour can be modulated by material properties such as surface texture, elasticity, and chemistry. In the restoration of bone defects it has been reported that surface topography influences osteogenesis and proliferation of bone marrow-derived multipotent mesenchymal stromal cells *in vitro* (*124*). Although tissue instructive materials hold great potential, the concept has not progressed beyond the proof-of-concept phase in which *in vitro* assays have demonstrated an effect on cellular differentiation and proliferation. However adsorption of proteins and their interfacial effects are highly complicated and more research is required to understand the mechanisms of adsorption. Resolving the molecular mechanism of osteoinduction will offer tools to develop new osteoinductive materials to meet the challenges of successful bone repair and provide an overall understanding of the fundamentals of biological systems.

References

1. Groot, K. *Biomaterials* **1980**, *1*, 47–50.
2. Hench, L. L. *Biomaterials* **1998**, *19*, 1419–1423.
3. Daculsi, G. *Biomaterials* **1998**, *19*, 1473–1479.
4. Charnley, J. *J. Bone Jt. Surg., Br. Vol.* **1960**, *42*, 28–33.
5. Deb, S.; Aiyathurai, L.; Roether, J. A.; Luklinska, Z. B. *Biomaterials* **2005**, *26*, 3713–3718.
6. Obadia, L.; Amador, G.; Daculsi, G.; Boulder, J. M. *Biomaterials* **2003**, *24*, 1265–1270.

7. Fernandez, E.; Gil, F. J.; Ginebra, M. P.; Driessens, F. C.; Planell, J. A. *J. Mater. Sci.: Mater. Med.* **1999**, *10*, 169–176.
8. Ginebra, M. P.; Fernandez, E.; De Maeyer, E. A.; Verbeeck, R. M.; Boltong, M. G.; Ginebra, J.; Driessens, F. C.; Planell, J. A. *J. Dent. Res.* **1997**, *76*, 905–912.
9. Kannan, S.; Lemos, I. A. F.; Rocha, J. H. G.; Ferreira, J. M. F. *J. Solid State Chem.* **2005**, *178*, 3190–3195.
10. Sampath Kumar, T. S.; Manjubala, I.; Gunasekharan, J. *Biomaterials* **2000**, *21*, 1623–1670.
11. Daculsi, G.; Weiss, P.; Bouler, J. M.; Gauthier, F. M.; Aguado, E. *Biomaterials* **1999**, *25*, 59–64.
12. Mavropoulos, E.; Rossi, A. M.; Nilce, C. C.; Rocha, D.; Gloria, A.; Soares, G. A.; Moreira, J.; Moure, T. G. *Mater. Charact.* **2003**, *50*, 203–207.
13. Monteiro, M. M.; Rocha, N. C. C.; Rossi, A. M.; Soares, G. A. *J. Biomed. Mater. Res.* **2003**, *65*, 299–305.
14. Obadia, L.; Amador, G.; Daculsi, G.; Boulder, J. M. *Biomaterials* **2003**, *24*, 1265–1270.
15. Norde, W. *Cells Mater.* **1995**, *5*, 97–112.
16. Ono, I.; Gunji, H.; Kaneko, F.; Saito, T.; Kuboki, Y. *J. Craniofacial. Surg.* **1995**, *6*, 238–244.
17. Ono, I.; Gunji, H.; Suda, K. *Plastic Reconstructive Surg.* **1995**, *95*, 1265–1272.
18. Andrade, J. D.; Hlady, V. *Adv. Polym. Sci.* **1986**, *79*, l–63.
19. Yan, W. Q.; Oka, M.; Nakamura, T. *J. Biomed. Mater. Res.* **1998**, *42*, 258–265.
20. Puleo, D. A.; Nanci, A. *Biomaterials* **1999**, *20*, 2311–2321.
21. Low, S. B. *Dent. Implantol. Update* **1998**, *9*, 65–67.
22. Daculsi, G.; Pilet, P.; Cottrel, M.; Guicheux, G. *J. Biomed. Mater. Res.* **1999**, *47*, 228–235.
23. Tsortos, A.; Ohki, S.; Zieba, A.; Baier, R. E.; Nancollas, G. H. *J. Colloid Interface Sci.* **1996**, *177*, 257–264.
24. Uniyal, S.; Brash, J. L. *Thromb. Haemostasis* **1982**, *47*, 285–290.
25. Whicher, S. J.; Brash, J. L. *J. Biomed. Mater. Res.* **1978**, *12*, 181–184.
26. Slack, S. M.; Horbett, T. A. *J. Colloid Interface Sci.* **1988**, *124*, 535–539.
27. Beumer, S.; Heijnen, H. F. G.; Ijsseldijk, M. J. W.; Orlando, E.; de Groot, P. G.; Sixma, J. J. *Blood* **1995**, *86*, 3452–3460.
28. Veerman, E. C. L.; Suppers, R. J. F.; Klein, C. P. A. T.; de Groot, K.; Nieuw Amerongen, A. V. *Adv. Biomater.* **1988**, *8*, 33l–335.
29. Jung, S. Y.; Lim, S. M.; Albertorio, F.; Kim, G.; Gurau, M. C.; Yang, R. D.; Holden, M. A.; Cremer, P. S. *J. Am. Chem. Soc.* **2003**, *125*, 12782–12786.
30. Dee, K. C.; Puleo, D. A.; Bizios, R. *Cell Mol. Biol.* **2004**, *8*, 419–425.
31. Zeng, H.; Chittur, K. K.; Lacefield, W. R. *Biomaterials* **1999**, *20*, 377–384.
32. Takami, Y.; Yamane, S.; Makinouchi, K.; Otsuka, G.; Glueck, J.; Benkowski, R.; Nose, Y. *J. Biomed. Mater. Res.* **1998**, *1*, 24–30.
33. Rouahi, M.; Champion, E.; Gallet, O.; Jada, A.; Anselme, K. *Colloids Surf., B* **2005**, *47*, 10–19.

34. Rosengren, A.; Pavlovic, C.; Oscarsson, S.; Krajewski, A.; Ravaglioli, A.; Piancastelli, A. *Biomaterials* **2002**, *23*, 1237–1247.
35. Klein, C.; Ermiden, P. A.; Van Kamp, G. *J. Biomed. Mater. Res.* **1980**, *14*, 705–712.
36. Sunita, P. V.; Sharma, C. P. *Colloids Surf., B* **2011**, *85*, 221–228.
37. Sunita, P. V.; Sharma, C. P. *J. Mater. Sci.: Mater. Med.* **2011**, *22*, 2219–2230.
38. Yuan, H.; Kurashina, K.; De Bruijn, J. D.; Li, Y.; De Groot, K.; Zhang, X. *Biomaterials* **1999**, *20*, 1799–1806.
39. Yuan, H.; Yang, Z.; Li, Y.; Zhang, X.; Bruijn, J. D.; Groot, K. D. *J. Mater. Sci.: Mater. Med.* **1998**, *9*, 723–726.
40. Chevalier, E.; Chulia, D.; Pouget, C.; Viana, M. *J. Pharm. Sci.* **2008**, *97*, 1135–1142.
41. Xu, H. H. K.; Simon, C. G. *J. Orthop. Res.* **2004**, *22*, 535–540.
42. Zhu, X. D.; Fan, H. S.; Xiao, Y. M.; Li, D. X.; Zhang, H. J.; Luxbacher, T.; Zhang, X. D. *Acta Biomater.* **2009**, *5*, 1311–1318.
43. Zhu, X. D.; Zhang, H. J.; Fan, H. S.; Zhang, X. D. *Acta Biomater.* **2010**, *6*, 1536–1541.
44. Fujii, E.; Ohkubo, M.; Tsuru, K.; Hayakawa, S.; Osaka, A.; Kawabata, K.; Bonhomme, C.; Babonneau, F. *Acta Biomater.* **2006**, *2*, 69–74.
45. Takashima, S.; Kusudo, Y.; Takemoto, S.; Tsuru, K.; Hayakawa, S.; Osaka, A. *Key Eng. Mater.* **2001**, *218*, 175–178.
46. Takemoto, S.; Kusudo, Y.; Tsuru, K.; Hayakawa, S.; Osaka, A.; Takashima, S. *J. Biomed. Mater. Res. A* **2004**, *69*, 544–551.
47. Latour, R. A. *Biomater. Biomed. Eng.* **2005**, *1*, 270–278.
48. Addadi, L.; Weiner, S.; Geva, M. *Z. Kardiol.* **2001**, *90*, 92–98.
49. Iijima, M.; Moradian-Oldak, J. *J. Mater. Chem.* **2004**, *14*, 2189–2199.
50. Cai, K.; Frant, M.; Bossert, J.; Hildebrand, G.; Liefeith, K.; Jandt, K. D. *Colloids Surf., B* **2006**, *50*, 1–8.
51. dos Santos, F. A.; Farina, M.; Soares, G. A.; Anselme, K. *J. Mater. Sci.: Mater. Med.* **2008**, *6*, 2307–2316.
52. Sawyer, A.; Hennessy, K.; Bellis, S. *Biomaterials* **2005**, *26*, 1467–1475.
53. Diegmueller, J. J.; Cheng, X.; Akkus, O. *Cryst. Growth Des.* **2009**, *9*, 5220–5226.
54. Yuan, H.; Yang, Z.; Li, Y.; Zhang, X.; Bruijn, J. D.; Groot, K. D. *J. Mater. Sci.: Mater. Med.* **1998**, *9*, 723–726.
55. Yuan, H.; Zou, P.; Yang, Z.; Zhang, X.; Bruijn, J. D.; Groot, K. D. *J. Mater. Sci.: Mater. Med.* **1998**, *9*, 717–721.
56. Yongli, C.; Xiufang, Z.; Yandao, G.; Nanming, Z.; Tingying, Z.; Xinqi, S. *J. Colloid Interface Sci.* **1999**, *214*, 38–45.
57. Kondo, A.; Mihara, J. *J. Colloid Interface Sci.* **1996**, *177*, 214–219.
58. Zeng, H.; Chittur, K. K.; Lacefield, W. R. *Biomaterials* **1999**, *20*, 377–384.
59. Feng, B.; Chen, J.; Zhang, X. *Biomaterials* **2002**, *23*, 2499–2507.
60. Hay, D. I.; Moreno, E. C. *J. Dent. Res.* **1979**, *58*, 930–942.
61. Webster, T. J.; Ergun, C.; Doremus, R. H.; Bizios, R. *J. Biomed. Mater. Res.* **2002**, *59*, 312–317.
62. Xie, J.; Riley, C.; Kumar, M.; Chittur, K. *Biomaterials* **2002**, *23*, 3609–3616.

63. Elangovan, S.; Margolis, H. C.; Oppenheim, F. G.; Beniash, E. *Langmuir* **2007**, *23*, 11200–11205.
64. Paul, W.; Sharma, C. P. *Int. J. Appl. Ceram. Technol.* **2010**, *7*, 129–138.
65. Yang, Y.; Cui, Q. A.; Sahai, N. *Langmuir* **2010**, *26*, 9848–9859.
66. Iafisco, M.; Palazzo, B.; Falini, G.; Di Foggia, M.; Bonora, S.; Nicolis, S.; Casella, L.; Roveri, N. *Langmuir* **2008**, *24*, 4924–4930.
67. Dalby, M. J. *Med. Eng. Phys.* **2005**, *27*, 730–736.
68. Ponsonnet, V.; Comte, A.; Othmane, C.; Lagneau, M.; Charbonnier, M.; Jaffrezic, N. *J. Mater. Sci. Eng. C* **2002**, *21*, 157–164.
69. Wong, J. Y.; Leach, J. B.; Brown, X. Q. *Surf. Sci.* **2004**, *570*, 119–125.
70. Kawasaki, T.; Takahashi, S.; Ikeda, K. *Eur. J. Biochem.* **1985**, *152*, 361–368.
71. Kandori, K; Sawai, S.; Yamamoto, Y.; Saito, H; Ishikawa, T. *Colloids Surf.* **1992**, *68*, 283–289.
72. Kandori, K.; Saito, M.; Saito, H.; Yasukawa, A.; Ishikawa, T. *Colloids Surf., A* **1995**, *94*, 225–230.
73. Kandori, K.; Saito, M.; Takebe, T.; Yasukawa, A.; Ishikawa, T. *J. Colloid Interface Sci.* **1995**, *174*, 124–129.
74. Kandori, K.; Shimizu, T.; Yasukawa, A.; Ishikawa, T. *Colloids Surf., B* **1995**, *5*, 81–87.
75. Kandori, K.; Fudo, A.; Ishikawa, T. *Phys. Chem. Chem. Phys.* **2000**, *2*, 2015–2020.
76. Boontheekul, T.; Mooney, D. J. *Curr. Opin. Biotechnol.* **2003**, *14*, 559–565.
77. Ohta, K.; Monma, H.; Takahashi, S. *J. Biomed. Mater. Res.* **2001**, *55*, 409–414.
78. Kandori, K.; Masunari, A.; Ishikawa, T. *Calcif. Tissue Int.* **2005**, *76*, 194–206.
79. Zhu, X.; Fan, H.; Li, D.; Xiao, Y.; Zhang, X. *J. Biomed. Mater. Res. B* **2007**, *82*, 65–73.
80. Shen, J. W.; Wu, T.; Wang, Q.; Pan, H. H. *Biomaterials* **2008**, *29*, 513–532.
81. Austen, K. F.; Almora-Barrios, N.; De Leeuw, N. H. *Langmuir* **2002**, *25*, 5018–5025.
82. Lindh, L.; Glanz, P. O.; Stromberg, N.; Arnebrant, T. *Biofouling* **2002**, *18*, 87–94.
83. Shimabayashi, S.; Tanizawa, Y. *Chem. Pharm. Bull.* **1992**, *38*, 1810–1814.
84. Juriaanse, A. C.; Booij, M.; Arends, J.; Ten Bosch, J. J. *Arch. Oral Biol.* **1981**, *26*, 91–96.
85. Juriaanse, A. C.; Booij, M.; Arends, J.; Ten Bosch, J. J. *J. Colloid Interface Sci.* **1980**, *76*, 220–226.
86. Bender, S. A; Bumgardner, J. D.; Roach, M. D.; Bessho, K.; Ong, K. L. *Biomaterials* **2000**, *21*, 299–305.
87. Iijima, M.; Moradian-Oldak *J. Mater. Chem.* **2004**, *14*, 2189–2199.
88. George, A.; Sabsay, B.; Simonian, P. A.; Veis, A. *J. Biol. Chem.* **1993**, *268*, 12624–12630.
89. Pan, H.; Tao, J.; Xu, X.; Tang, R. *Langmuir* **2007**, *23*, 8972–8981.
90. Malmsten, M. *J. Colloid Interface Sci.* **1998**, *207*, 186–199.
91. Grunwald, C.; Eck, W.; Opitz, N.; Kuhlmann, J.; Wo¨ll, C. *Phys. Chem. Chem. Phys.* **2004**, *6*, 4358–4362.

92. Silva, R. A.; Urzua, M. D.; Petri, D. F.; Dubin, P. L. *Langmuir* **2010**, *26*, 14–22.
93. Lopes, M. A.; Monteiro, F. J.; Santos, J. D.; Serro, A. P.; Saramago, B. *J. Biomed. Mater. Res.* **1999**, *45*, 370–375.
94. Andrade, J. D.; Hlady, V. *Adv. Polym. Sci.* **1986**, *79*, l–63.
95. Driessens, F. C. M.; Verbeeck, R. M. H. *Adv. Biomater.* **1988**, *8*, 105–111.
96. Schakenraad, J. M.; Stokroos, I.; Busscher, H. J. *Biofouling* **1991**, *4*, 61–70.
97. Kawasaki, T.; Ikeda, K.; Takahashi, S.; Kuboki, Y. *Eur. J. Biochem.* **1986**, *155*, 249–257.
98. Chen, X.; Wang, Q.; Shen, J.; Pan, H.; Wu, T. *J. Phys. Chem. C* **2007**, *207*, 1284–1290.
99. Shaw, W. J.; Campbell, A. A.; Paine, M. L.; Snead, M. L. *J. Biol.Chem.* **2004**, *279*, 40263–40266.
100. Wassell Hughes, D. T.; Hall, R. C.; Embery, G. *Biomaterials* **1995**, *16*, 697–702.
101. Tanaka, H.; Miyajima, K.; Nakagaki, M.; Shimabayashi, S. *Chem. Pharm. Bull.* **1989**, *37*, 2897–2901.
102. Shimabayashi, S.; Tanizawa, Y.; Ishida, K. *Chem. Pharm. Bull.* **1991**, *39*, 2183–2188.
103. Reynolds, E. C.; Wong, A. *Infect. Immun.* **1983**, *3*, 1285–1290.
104. Rolla, G. *J. Swed. Dent.* **1977**, *1*, 241–251.
105. Sharpe, J. R.; Sammons, R. L.; Marquis, P. M. *Biomaterials* **1997**, *18*, 471–476.
106. Wassell, D. T. H.; Hall, R. C.; Embery, G. *Biomaterials* **1995**, *16*, 697–702.
107. Rouahi, M.; Champion, E.; Gallet, O.; Jada, A.; Anselme, K. *Colloids Surf., B.* **2006**, *47*, 10–19.
108. Kandori, K.; Mizumoto, S.; Toshima, S.; Fukusumi, M.; Morisada, Y. *J. Phys. Chem. B* **2009**, *113*, 11016–11022.
109. Akazawa, T.; Kobayashi, M.; Kodaira, T. K. *J. Mater. Sci.* **1998**, *33*, 1927–1931.
110. Wang, K.; Zhou, C.; Hong, Y.; Zhang, X. *Interf. Foc.* **2012**, *2*, 259–277.
111. Barnthip, N.; Parhi, P.; Golas, A.; Vogler, E. A. *Biomaterials* **2009**, *30*, 6495–6513.
112. Noh, H.; Vogler, E. A. *Biomaterials* **2007**, *28*, 405–422.
113. Brash, J. L.; Lyman, D. J. *J. Biomed. Mater. Res.* **1969**, *3*, 175–189.
114. Zhu, X. D.; Fan, H. S.; Zhao, C. Y.; Lu, J.; Ikoma, T.; Tanaka, J.; Zhang, X. D. *J. Mater. Sci.: Mater. Med.* **2007**, *18*, 2243–2249.
115. Zhu, X.; Fan, H.; Li, D.; Xiao, Y.; Zhang, X. *J. Biomed. Mater. Res. B* **2006**, *2*, 65–73.
116. Hench, L. L. *J. Am. Ceram. Soc.* **1991**, *74*, 1482–1489.
117. Xin, R.; Leng, Y.; Chen, J.; Zhang, Q. *Biomaterials* **2005**, *26*, 6477–6485.
118. Orly, M. I.; Gregoire, J.; Menanteau, M.; Heughebaert, B. *Calcif. Tissue Int.* **1989**, *45*, 20–27.
119. Kuboki, Y.; Takita, H.; Kobayashi, D. *J. Biomed. Mater. Res.* **1998**, *39*, 190–198.
120. Yuan, H.; Kurashina, K.; de Bruijn, D. J.; Li, Y.; de Groot, K.; Zhang, X. *Biomaterials* **1999**, *20*, 1799–1806.

121. Barrere, F.; van der Valk, C. M.; Dalmeijer, G.; Meijer, C. A.; Blitterswijk, V.; de Groot, K. *J. Biomed. Mater. Res. A* **2003**, *66*, 779–787.
122. Tagaya, M.; Ikoma, T.; Takeguchi, M.; Hanagata, N.; Tanaka, J. *J. Phys. Chem. C.* **2011**, *115*, 22523–22533.
123. Tagaya, M.; Ikoma, T.; Takemura, T.; Hanegata, N.; Yoshioka, T.; Tanaka, J. *Langmuir* **2011**, *27*, 7645–7653.
124. Yuana, H.; Fernandes, H.; Habibovic, P.; de Boer, J. A.; Barradas, M. C.; de Ruiter, A.; Walsh, W.; van Blitterswijk, C. A.; de Bruijn, J. D. *Proc. Natl. Acad. Sci. U.S.A.* **2010**, *31*, 13614–13619.

Chapter 4

Solid-State NMR Studies of Biomineralization Peptides and Proteins

Adrienne Roehrich,[1] Jason Ash,[1,4] Ariel Zane,[1] David L. Masica,[2] Jeffrey J. Gray,[2] Gil Goobes,[1,3] and Gary Drobny*,[1]

[1]Department of Chemistry, University of Washington, Box 351700, Seattle, Washington 98195
[2]Department of Chemical and Biomolecular Engineering, Johns Hopkins Univeristy, Baltimore, Maryland 21218
[3]Present Address: Department of Chemistry, Bar Ilan University, Israel
[4]Present Address: Center for Materials Science and Engineering, Merck, Rahway, New Jersey 07065
***E-mail: drobny@chem.washington.edu. Phone: (206) 685-2052. Fax: (206) 685-8665**

Nature has evolved sophisticated strategies for engineering hard tissues through the interaction of proteins, and ultimately cells, with inorganic mineral phases. The remarkable material properties of shell, bone and teeth thus result from the activities of proteins that function at the organic-inorganic interface. A better understanding of the biomolecular mechanisms used to promote or retard the formation of mineral-based structures could provide important design principles for the development of calcification inhibitors and promoters in orthopedics, cardiology, urology, and dentistry. In addition to investigating the molecular-level basis for the recognition of biomineral surfaces and the control of hard tissue growth by proteins, the development of materials using biomimetic principles has potential applications in catalysis, biosensors, electronic devices, chromatographic separations, to name only a few.

Despite the high level of interest in elucidating and controlling the structure of proteins at material and biomineral interfaces, there is a decided lack of molecular-level structure information available for proteins at biomaterial interfaces in general, and in particular for mammalian proteins that

In Proteins at Interfaces III State of the Art 2012; Horbett, T., et al.;
ACS Symposium Series; American Chemical Society: Washington, DC, 2012.

directly control calcification processes in hard tissue. The most fundamental questions regarding the secondary and tertiary structures of proteins adsorbed to material surfaces, how proteins catalyze the formation of biomineral composites, or how proteins interact at biomaterial interfaces, remain unanswered, largely due to a lack of methods capable of providing high resolution structural information for proteins adsorbed to material surfaces under physiologically relevant conditions (i.e. fully hydrated).

In order to develop a better understanding of the structure and interactions of proteins in biomaterials, we have begun to utilize solid-state NMR techniques to determine the molecular structure and dynamics of proteins and peptides on inorganic crystal surfaces and within biomineral composites. In this review, we will highlight recent work that is providing insight into the structure and crystal recognition mechanisms of a salivary protein model system, as well as the structure and interactions of a peptide which catalyzes the formation of biosilica composites.

Introduction and Background

Biomineralization is the process by which living organisms control the formation of inorganic materials like hydroxyapatite, calcite and silica into highly intricate and organized structures (*1*). Nature has evolved sophisticated strategies for engineering hard tissues through the interaction of proteins, and other biomolecules, with inorganic mineral phases. The remarkable material properties of bone, shells and teeth thus result in part from the activities of proteins that function at the organic-inorganic interface. A better understanding of the biomolecular mechanisms used to promote or retard mineral growth could provide important design principles for the development of calcification inhibitors and promoters in orthopedics, cardiology, urology, and dentistry (*2*, *3*). A better understanding of how these proteins recognize and assemble in bioactive form on inorganic mineral phases could also aid in the development of surface coatings to improve the biocompatibility of implantable biomaterials and for hard tissue engineering and regeneration technologies. In addition to biomedical applications, current interest in biomineralization also derives from its potential applications in electronics, catalysis, magnetism, sensory devices, and mechanical design (*4–12*), where in contrast to anthropogenic synthesis of hard materials, which requires extremes in temperature, pressure and pH, biological organisms accomplish impressive feats of hard tissue engineering at ambient temperature and at physiological pH.

At the level of fundamental science, it is important to note the paucity of molecular structure information available for biomineralization proteins in general, and in particular for mammalian proteins that directly control calcification processes in hard tissue. Even the most fundamental questions about how the proteins interact at the protein-biomineral interface are yet to be extensively addressed experimentally. These questions include: what is the general structure and orientation of proteins on mineral surfaces or within biomineral composites; what amino acid side chains or structural motifs do proteins use to interact with inorganic phases? In order to develop a better structure-function level understanding of protein-crystal molecular recognition, we have begun to utilize solid-state NMR (ssNMR) techniques to determine the molecular structure of proteins and peptides on calcium phosphate surfaces and within biosilica composites. In this review, we will highlight recent work that is providing insight into the structure and crystal recognition mechanisms of an acidic human salivary phosphoprotein statherin. Providing contrast to the interactions of statherin with hydroxyapatite crystal surfaces, we will also describe the application of solid state NMR to the study of the structure of basic peptides derived from the biosilicification protein silaffin and embedded within biosilica nanoparticles. Silaffin and peptides derived from silaffin catalyze formation of biosilica composites when added to solutions of silicic acid. Here the objective is to use ssNMR to determine the structure of proteins and peptides within biosilica composites, the interactions of these peptides with the surrounding silica, and ultimately the relationship between silaffin peptide secondary structure and biosilica composite morphology.

Principles of Solid-State NMR

Solid state NMR spectra of spin-½ nuclei are dominated by two magnetic interactions, the direct nuclear dipolar interaction and the chemical shift anisotropy (CSA). The dipolar interaction has a straightforward structural interpretation because the dipolar coupling constant is proportional to the inverse cube of the internuclear distance. (See Figure 1, top). As discussed below, although the isotropic chemical shift interaction is valuable as an empirical probe of protein structure, in solid samples the chemical shift anisotropy makes the dominant contribution to the NMR line width. Although the dipolar coupling between two protons separated by a few Angstroms exceeds that proton chemical shift anisotropy, in systems composed of coupled ^{13}C spins, the magnitude of the CSA may exceed the magnitude of the dipolar interaction, and under such circumstances the ^{13}C NMR line shape will be a broad "powder pattern" (see Figure 1, bottom). Therefore the dipolar coupling constant may not be easily discerned in spectral data when the CSA exceeds the dipolar interactions by orders of magnitude. So it is necessary to use NMR methods which suppress one of these interactions thus enabling straightforward detection of the other.

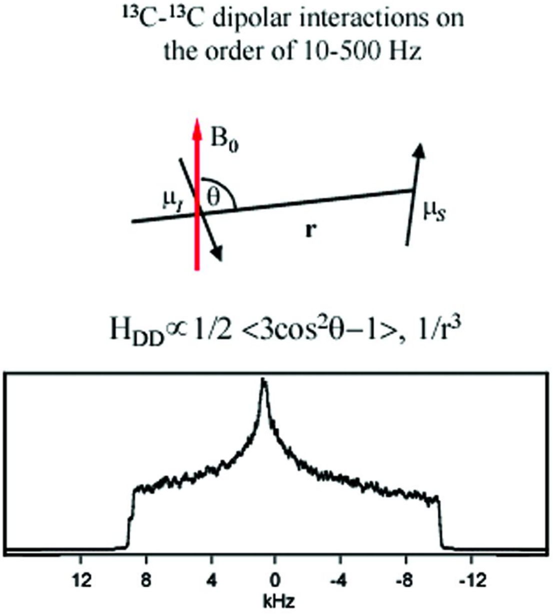
^{13}C-^{13}C dipolar interactions on the order of 10-500 Hz
B_0
μ_I
θ
r
μ_S
$H_{DD} \propto 1/2 <3\cos^2\theta-1>, 1/r^3$
12
8
4
0
-4
-8
-12
kHz

Figure 1. Top: The direct interaction between two spin magnetic dipole moments μ depends upon the angle θ between the internuclear vector and the direction of the magnetic field m and the inverse cube of the internuclear distance r. Bottom: The NMR "powder pattern" lineshape of a spin-½ nucleus where the dominant magnetic interaction is the chemical shift anisotropy (CSA).

Physical rotation of the sample around a goniometer oriented at an angle $\theta_m = 54.74°$ relative to the magnetic field (i.e. Magic Angle Spinning (*13*), MAS, see Figure 2, left) coherently averages spatial parts of the spin magnetic interactions that transform as second rank tensors. If the rate of spinning is less than the anisotropy that underlies the broadened line shape, the powder pattern breaks up into spinning side bands, which appear in Figure 2 as the satellite lines about the isotropic chemical shift signals that are regularly spaced by intervals equal to the spinning rate. Since both the dipolar and the chemical shift Hamiltonians transform as second rank tensors in Cartesian space, MAS removes the effect of both interactions from solid-state NMR spectra.

The objective of dipolar recoupling is to use MAS and radio frequency (r.f.) irradiation in synchrony, with the ultimate objective of suppressing the chemical shift while preserving the dipolar coupling. Because information on internuclear distances can be recovered using dipolar recoupling techniques, these pulse sequences are widely used in structural studies of molecular solids. Solid-state Rotational Echo Double Resonance (REDOR) NMR (*14*) is a high resolution technique employing MAS used to observe heteronuclear dipolar coupling. This method can be applied for either inter- or intramolecular interactions. Appropriate labels, in the case of the work described later in this chapter ^{13}C{^{15}N} and ^{13}C{^{19}F}, are placed either in *i*, *i*+4 residues or on selected side chains of amino acids exposed to the surface. A specific pulse sequence with phase alternation and dependent upon the number of rotor cycles gives carbon signal intensity, *S*. A REDOR plot consists of S/S_0 vs time, where S_0 is obtained without dephasing pulses in the pulse sequence. Experimental data is fit with a simulation curve to determine distances.

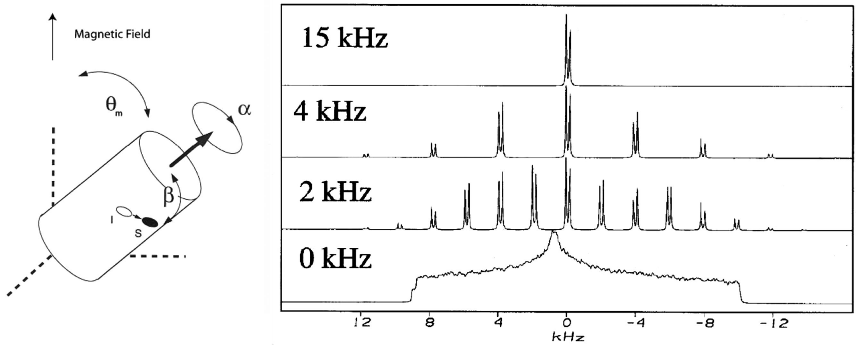

Figure 2. Left: Geometric arrangements in the Magic Angle Spinning (MAS) experiment. An ensemble of randomly oriented dipole-coupled spin-½ nuclear pairs I and S has a NMR powder pattern line shape shown in Figure 1 if the CSA is non-axial and greater than the dipolar coupling If the spin pairs ensemble is spun rapidly around a goniometer whose axis is inclined at $\theta_m = 54.74°$ *the powder pattern breaks up into side band peaks arranged at intervals equal to the spinning rate around a fundamental NMR frequency corresponding to the isotropic chemical shift. Right: Increasing the spinning rate increases the separation between the side bands and decreases the side band intensities. In the limit that the spinning rate exceeds the magnitude of the CSA, the side bands are completely suppressed and only the NMR signal appearing at the isotropic chemical shifts of the I and S spins remain.*

An alternative strategy that has come into wide use in recent years is to use ^{13}C chemical shifts to empirically determine protein secondary structure. The isotropic chemical shifts of the ^{13}CO (i.e. the backbone carbonyl ^{13}C), ^{13}Cα, and ^{13}Cβ spins are known to be dependent upon local secondary structure of the protein. By comparing experimentally observed chemical shifts to an NMR database of known structures, software packages such as TALOS+ are able to predict the φ/ψ torsion angles of a given residue (*15*, *16*). TALOS+ (Torsion Angle Likeliness Obtained from Shift and Sequence Similarity) is a program based on a 200+-protein database for which complete or nearly complete heteronuclear resonance assignments and high resolution X-ray coordinates are available in the protein database (PDB) from the research collaboratory for structural bioinformatics (RCSB) and the biological magnetic resonance bank (BMRB) (*15*, *16*). The TALOS+ software package is based on the principle that homologous sequences give similar shifts (*15*, *16*). The combination of solid-state NMR with backbone torsion angle assignments by the TALOS/+ program has been used to model several peptides including protein G (*17–19*), ubiquitin (*20*), amyloid β (*21–23*), and kaliotoxin (*24*). In the following sections we will show how these two types ssNMR measurements, dipolar couplings and chemical shifts, can be used to determine the structure of proteins at biomineral interfaces.

Solid-State NMR Studies of Salivary Statherin on HAP Crystal Surfaces

Statherin is a small 5.68 kDalton phosphoprotein, and the only salivary protein that has been found to inhibit both the nucleation and the growth of hydroxyapatite (HAP) (*25–30*). Statherin is expressed at its active length and post-translationally phosphorylated at serines 2 and 3 (*31*). It is then excreted by the sublingual and submaxillary salivary glands where it travels to the mouth. Statherin is composed of 43 amino acid residues with primary sequence:

H_2N-DpSpSEEKFLRRIGRFGYGYGPYQPVPEQPLYPQPYQPQYQQYTF-COOOH

In addition to two phosphoserines (i.e. pS) statherin contains four aspartic/glutamic acid residues and four basic amino acids, almost all of which occur close to the N-terminus. Previous studies of statherin fragments by Nancollas and coworkers (*32*, *33*) showed that the N-terminal 15 amino acid fragment (SN-15, H_2N-DpSpSEEKFLRRIGRFG-COOH) is essential for binding to HAP crystal surfaces. SN-15 contains two phosphoserines, three acidic residues, and four basic residues. Removal of the DpSpSE moiety (i.e. resulting in SN-11, EKFLRRIGRFG) reduces the HAP binding affinity by a factor of 4.5 compared to SN-15. Mutation of both phosphoserines to simple serine reduces the HAP binding affinity by a factor of almost nine, while mutation from serine to aspartic acid restores the binding affinity to 70% that of SN-15, indicating that the phosphoserine residues and acidic amino acid side chains are important for the binding of statherin to HAP. Initial ssNMR studies of HAP-bound statherin measured a number of torsion angles and internuclear distances within the N-terminal 15 amino acid segment of native statherin, and within the 15 amino acid SN-15 peptide. These data indicate that the N-terminus in HAP-adsorbed statherin is an α-helix (*34–36*). Subsequent solid state NMR studies of labeled statherin molecules yielded measurements of backbone torsion angles (residues 33-34) and i-i+4 carbonyl-amide distances (residues 34-38) indicating that the C-terminus receptor site for bacterial adhesion adopts an α-helical conformation in statherin adsorbed to hydroxyapatite crystals (*37*). See Figure 3.

In order to define tertiary folding, we also measured long range distances between carbonyl carbons in the C-terminus (residues 33-34) and a fluorine nucleus incorporated into a proline ring (residue 23) showing that this motif closes back onto the protein's proline-rich region (16-28) through a series of backbone turns. These results elucidated the structure of the region in the protein that is recognized by pathogens and provided data on the overall fold of the protein when it binds to its natural solid substrate, hydroxyapatite. Some of these ssNMR data are summarized in Figure 3.

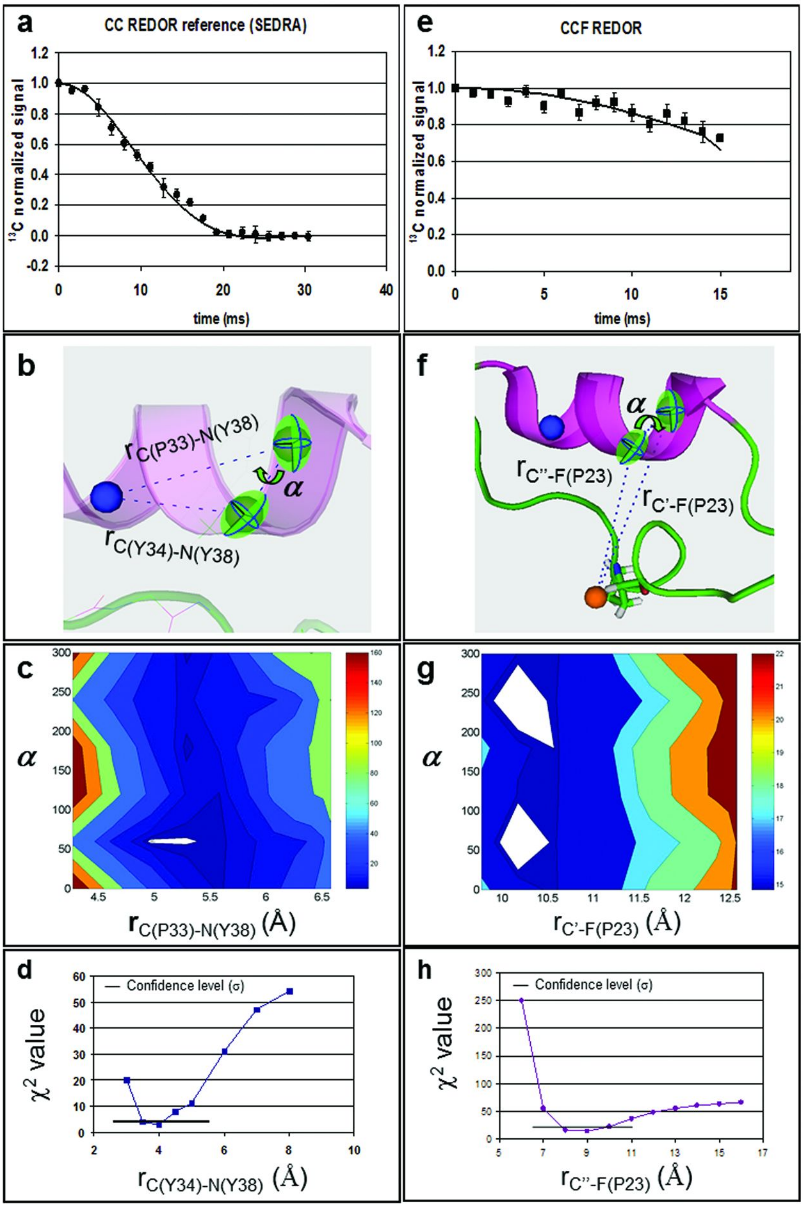

Figure 3. Examples of ssNMR data used to constrain Rosetta simulations. ^{13}C-^{15}N and ^{13}C-^{19}F REDOR decay (S/S_0) curves showing the carbon signal intensity as a function of the length of time the pulses are applied. a) ^{13}C signal decay (S/S_0) from recoupling of the ^{13}C-^{15}N dipolar couplings in a REDOR experiment. e) ^{13}C signal decay (S/S_0) from recoupling of the ^{13}C-^{19}F dipolar couplings in a REDOR experiment. The fits to these decay curves are used to extract the structural parameters. b) Graphic visualization of dipolar interaction parameters in the C(P33)-C(Y34)-N(Y38) spin triad. c) The contour plot of the

$\chi^2(r_{C(P33)-N(Y38)},\alpha)$ function (middle) and d) graph of the $\chi^2(r_{C(Y34)-N(Y38)})$ function showing values for which the CN REDOR data is minimized. f) Dipolar coupling parameters in the C(P33)-C(Y34)-F(P23) spin triad. Here, we denote the two carbons as C′ and C″ since they are indistinguishable in the ^{13}C spectrum. g) Plot of the $\chi^2(r_{C'-F(P23)},\alpha)$ function and h) $\chi^2(r_{C''-F(P23)})$ function demonstrate values for which the CF REDOR data are fit by simulations.

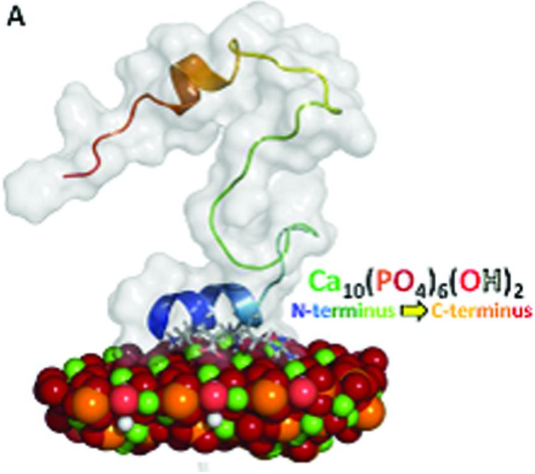

Figure 4. Representative statherin structure from the final phase of ssNMR-constrained RosettaSurface refinement. Opacity represents statherin's molecular shape, ribbons represent regions of helical structure, and individual amino acid side chains within the N-terminus that interact with the surface are shown as stick models. Statherin is shown adsorbed onto the {001} face of hydroxyapatite.

The total number of distances between nuclei within statherin that reflect secondary and tertiary structure in the HAP-bound protein together with distances between nuclear spins in protein side chains ^{31}P spins in the HAP surface that reflect surface proximity and orientation, is insufficient to fully constrain statherin's surface structure. However, the body of ssNMR-derived structural measurements can be used to guide a molecular modeling computation which would provide an experimentally-constrained model of the HAP-bound structure of statherin. Professor Jeffrey Gray and coworkers at Johns Hopkins University have developed a novel algorithm (RosettaSurface.NMR) as part of the Rosetta molecular modeling package for modeling the interactions of proteins with HAP crystal surfaces (i.e.) (*38*). The algorithm uses experimentally derived ssNMR distance data to guide calculation of the structure and orientation of HAP-bound statherin. Using this combined computational-ssNMR approach, analysis wasmade at a sufficiently high resolution to begin understanding residue- and atom-specific contributions to the process of biomineralization and hard tissue formation. Results of the study indicate that when adsorbed onto HAP crystals, statherin has a stable C-terminal helix, and a helical N-terminal HAP-binding domain with a local helix axis oriented more or less perpendicular to the local surface normal, see Figure 4. This domain interacts with the {001} HAP surface via both basic and acidic residues. Predicted by RosettaSurface (*38–40*) and confirmed by our ssNMR (*41*, *42*) and calorimetric measurements (*43–45*), of three acidic and two phosphoserines within this binding helix, only pS3 and E5 interact directly with the HAP surface, while basic residues K6, R9, R10 and perhaps R13 interact directly with phosphate oxygen triads groups within the HAP surface (*38–40*).

To further explore preferential face binding, RosettaSurface.NMR calculations were performed on each at five HAP crystal faces: {001}, {010}, {101}, and two differentially terminated {100} faces ({100}-T1 and {100}-T2), for a range of values of w, the parameter which weights ssNMR experimental constraints in the Rosetta Surface energy functional $E_{\mathrm{constraint}}$. Resulting calculations, shown in Figure 5, indicate significantly greater congruency at three of five tested HAP crystal surfaces, suggesting some specificity. One of the preferred faces is {001}, the kinetically favored growth plane of HAP (*46–49*) and a face to which fluorescence microscopy experiments show HAP regulation proteins like statherin adhere (*48*). We have thus used a ssNMR/computational approach not only to determine the surface structure and orientation of statherin on HAP, but also to determine statherin's face-binding specificity.

With the advent of a combined computational-ssNMR approach, analysis can now be made at a sufficiently high resolution to begin understanding residue- and atom-specific contributions to the process of biomineralization and hard tissue formation. The results presented here indicate that statherin has a stable, folded HAp-binding domain, with the important role of surface recognition involving not simply acidic amino acid and phosphoserine side chains as commonly believed, but primarily the side chains of the basic amino acids. Also, the methods combined here show significantly greater congruency at three of five tested HAp crystal surfaces, suggesting some specificity.

Solid-State NMR Studies of Biosilicification Peptides

Interest in the biomimetic approach to synthesis of silica-based materials derives from numerous technical applications as: catalysts, polymeric fillers, coatings, components in chemical and biological separations, sensors, photonic and electronic devices, bio-encapsulation, enzyme immobilization, bioimaging, drug delivery, insulators, coatings, and cosmetics (*50–53*). Biogenic silica (i.e. biosilica) is the most abundant biomineral with approximately six gigatons of silica produced per year by marine organisms alone. The dominant biosilica producing organism is the diatom, a microalgae characterized by an intricately decorated cell wall (i.e. the frustule) composed of organic material and silica (SiO_2nH_2O) (*54*). Diatoms take in silicon in the form of silicic acid ($Si(OH)_4$), and catalyze its intracellular deposition as silica. As with most biogenic minerals, proteins play an important role in the regulation of silica formation in diatoms.

The dominant protein fraction in the cell wall of the diatom *Cylindrotheca fusiformis* (see Figure 6) consists of a low molecular weight polycationic protein with high affinity for silica called silaffin (*55–59*). It is hypothesized that within the diatom, silaffins self assemble into a matrix which serves as a template for silica deposition. In vitro and in the absence of additional organizing components, addition of silaffins to silicic acid solutions results in the formation of silica nanospheres (*55*).

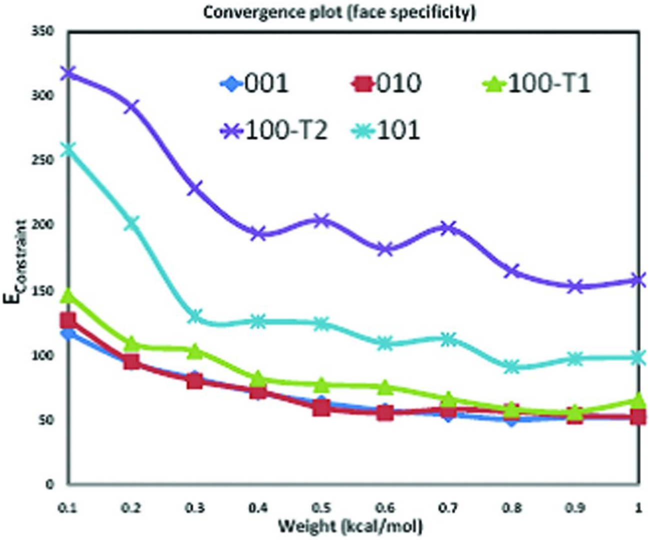

Figure 5. Minimization of $E_{constraint}$ on five HAP surfaces as a function of weighting w. Preferential binding to various crystal faces is indicated.

The primary structure of the silaffin protein (i.e. *sil1p*) has been determined, and contains seven highly homologous peptide domains from residues 108 to 271 labeled R1-R7 (*12*, *55*). These peptide domains, which are to the rich in serine and lysine, are associated with silica formation. Particular has focus been paid to the R5 sequence (SSKKSGSYSGSKGSKRRIL), as this peptide shows in vitro silica nanosphere formation activity (see Figure 7) that is similar native *sil1p* but occurs at neutral pH and without the need for phosphorylation of the serines and alkylation of the lysines, both commonmodifications in *sil1p* (*60–62*). Elucidating the structure of R5 within a biosilica composite is a valuable step toward understanding how small peptides direct the formation of silica structures and thus mimic the behavior of biosilicification proteins like silaffin.

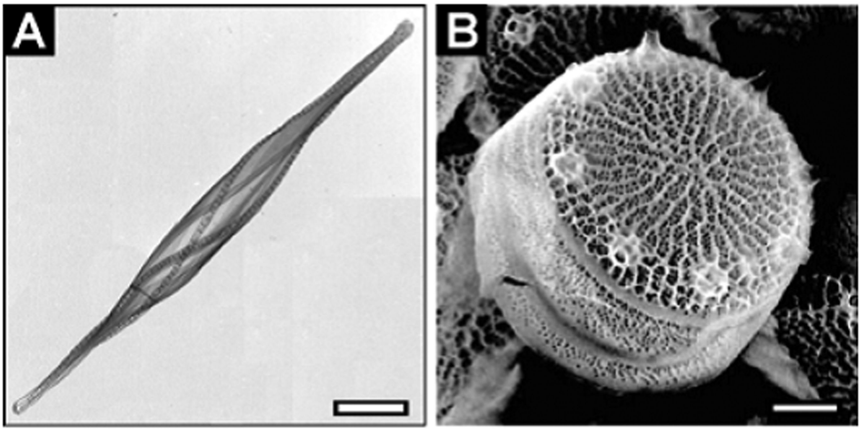

Figure 6. C. fusiformis cell wall (transmission electron micrographs). A) Bar = 2um; B) bar = 0.2um. Reproduced with permission from reference (56). Copyright 2004 The American Society for Biochemistry and Molecular Biology.

Control of silica morphogenesis by silaffin and R5 peptides has been studied at the macroscopic level (*10*, *59*, *62–64*) but atomic level insight into the structure of R5 within biosilica composites and the nature of peptide silica interactions is almost completely lacking. Questions we seek to address regarding peptide-silica interactions in biosilica composites include:

- What is the secondary structure of R5 in the biosilica matrix and to what degree does this structure differ from that of the free peptide?
- What amino acid side chains and functional groups interact with silica?
- How are these side chains arrayed?
- What secondary/tertiary structural motifs are used for this purpose?
- Do the small R5 peptides assemble into higher order structures that act as templates for silica morphogenesis?

In contrast to studies of the biomineralization proteins statherin and amelogenin (*65*) which control crystal growth by adsorbing onto hydroxyapatite surfaces, silaffin and silaffin-derived peptides are embedded within the biosilica matrix rather than being simply adsorbed onto the particle surface. The biosilica microspheres precipitated from silicic acid solutions by R5 (see Figure 7) are about 25-30% peptide by weight. This abundance of peptide within the biosilica composite makes possible the use of two dimensional solid state NMR techniques to obtain ^{13}C and ^{15}N chemical shift measurements from isotopically enriched R5 peptides embedded in biosilica composites. As explained in the section entitled “Principles of Solid State NMR,” chemical shifts obtained via two dimensional ssNMR experiments for the ^{13}CO, $^{13}C\alpha$, $^{13}C\beta$, and the amide ^{15}N spins are sensitive to local secondary structure. Once these chemical shifts are measured, the secondary structure of the peptide within the biosilica composite can be quantified in terms of the backbone φ/ψ angles using the TALOS+ software package. In addition, chemical shifts from ^{13}C spins distally located in protein sides chains (i.e. ^{13}Cγ, ^{13}Cδ, ^{13}Cε, etc.) while not directly correlated with the structure of the protein backbone, are known to be perturbed by proximity to silica interfaces (*66*, *67*).

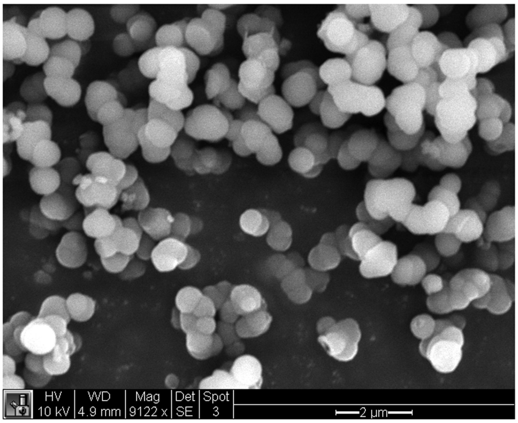

Figure 7. SEM image of the R5-silica co-precipitates, which shows the peptide-catalyzed formation of biosilica microspheres with diameters of 500-750 nm.

The strategy used in the two dimensional ssNMR studies of R5 peptides in biosilica composites starts with synthetic incorporation of uniformly ^{13}C and ^{15}N enriched amino acids into the 19 amino acid R5 peptide. To ensure that the ^{13}CO, ^{13}Cα, and ^{13}Cβ NMR signals can be unambiguously identified with specific amino acids, at most 2-3 isotopically enriched amino acids are incorporated into a R5 peptide sample at a time, making necessary the preparation of seven isotopically enrich R5 samples for study. Where chemical shifts may overlap or have ambiguity in the one dimensional ^{13}C MAS spectrum, ^{13}C two dimensional (i.e.2-D) dipolar assisted rotational resonance (DARR) spectra can clarify spectral assignments (*68*, *69*). DARR is a two dimensional ssNMR method which transfers magnetization from the ^{1}H (protons) to the ^{13}C nuclei, which in turn transfer magnetization to other ^{13}C nuclei which are close in space. Magnetization transfers between ^{13}C spins are indicated in a two dimensional spectrum by "cross peaks", peaks that connect two ^{13}C NMR peaks on the diagonal indicating the ^{13}C spins are thus dipole-dipole coupled and close in space.

Once isotopically enriched R5 peptides are produced, they are incorporated into biosilica composites. R5 was co-precipitated with silica from silicic acid solutions as follows. The peptide was dissolved in a 100 mM phosphate-citrate buffer, pH = 7.0, at 5 mg/mL. Silicic acid was prepared using 1 mL HCl and tetramethyl orthosilicate (TMOS) and was added to the peptide/buffer solution. The R5-silica complex precipitates out in 5-10 minutes. The solution is centrifuged and precipitate collected, then dried overnight under vacuum.

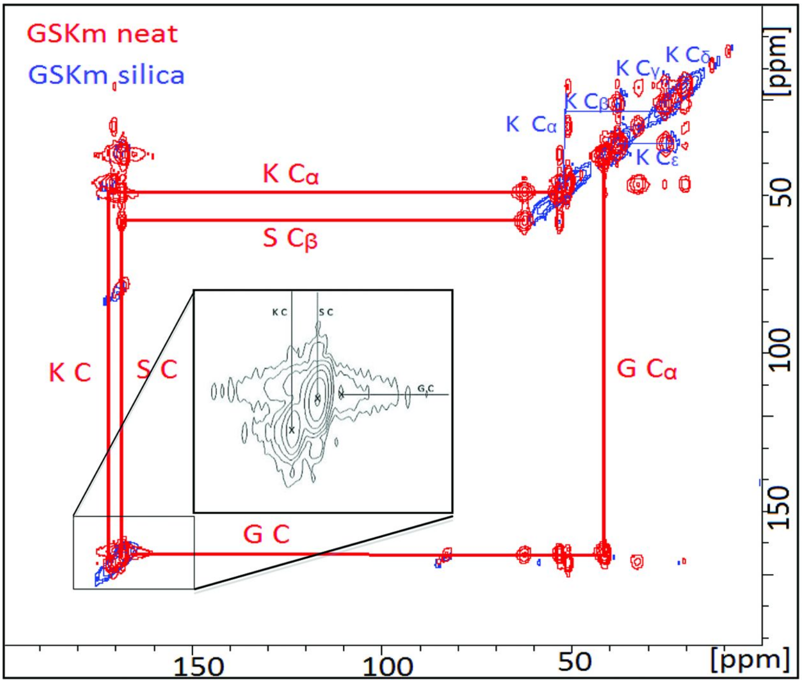

Figure 8. ^{13}C-^{13}C DARR spectrum of the R5 peptide SSKKSGSYSGSKGSKRRIL with uniformly enriched ^{13}C and ^{15}N amino acids incorporated at positions G10, S11, and K12. DARR spectra of the neat R5 peptide and the biosilica incorporated peptide are superimposed to emphasize chemical shift changes that occur due to conformational differences between the free peptide and the peptide in the biosilica composite.

Figure 8 shows the superimposed DARR spectra the neat and biosilica associated R5 peptide with the G10, S11, and K12 residues uniformly enriched with ^{13}C and ^{15}N. The neat peptide is a lyophilized sample while the second sample is precipitated from silicic acid as a silica-R5 complex. NMR peaks on the diagonal occur at the ^{13}C isotropic chemical shift frequencies. Off diagonal peaks indicate the ^{13}C spins are correlated via the dipolar interaction and thus are closely located in space. By following networks of dipolar-coupled ^{13}C spins through the cross peaks in a DARR spectrum (shown as solid vertical and horizontal lines in Figure 8), the NMR peaks with known chemical shifts can be assigned to specific ^{13}C spins within the R5 peptide. Selected assignments are shown for each spectrum. The neat sample shows the ^{13}Cα of the lysine and glycine and the ^{13}Cβ of the serine used to determine the exact peaks of each residue's carbonyl (black inset.) One might note that the serine crosspeak indicated is the ^{13}Cβ to the carbonyl, illustrating the through space contact of DARR. A ^{13}Cα contact for the serine carbonyl and a ^{13}Cβ to ^{13}Cα serine contact are also present in the crosspeaks but not indicated explicitly in the figure.

Besides showing how the cross-peaks in a 2-D spectrum helps elucidate silica sample is labeled to show the differentiation of the lysine sidechain. otherwise ambiguous chemical shifts, this overlay also shows there are perturbations in the chemical shifts occurring at some of the ^{13}C and ^{15}N spins within the silica-associated R5 peptide.

Figure 9 shows the effect on the chemical shifts of the backbone ^{13}C spins (^{13}CO, ^{13}Cα, ^{13}Cβ), amide ^{15}N spins, and side chain ^{13}C spins when the R5 peptide is co-precipitated with silica from silicic acid solutions. The histograms indicate chemical shift changes (i.e. ΔCS) obtained by subtracting the chemical shift of the ^{13}C or ^{15}N spin in the neat peptide from the chemical shift of the same spin in the R5-silica complex. Therefore a positive ΔCS indicates the chemical shift of a given spin has increased (relative to TMS) or been shifted downfield upon complexation with silica. A negative ΔCS indicates the opposite situation: that the ^{13}C or ^{15}N peak has been shifted toward TMS or upfield upon complexation with silica.

Solid state NMR (*70*) and SFG (*71*) studies have shown that peptides interact with silica surfaces via positively charged side chain functional groups, including the NH_3^+ group of the lysine side chain or the guanidinium group of arginine. A recent ^{15}N{^{29}Si} REDOR study shows that monomeric amino acids with nonpolar side chains (i.e. alanine) similarly interact with silica via the NH_3^+ group (*67*). In ^{13}C ssNMR studies of poly-lysine adsorbed onto silica the lysine side chain ^{13}Cε spin's chemical shift shifted by 2 ppm upfield upon adsorption onto silica, an effect attributed to proximity or the side chain of lysine to the negatively charged silica surface (*70*, *72*, *73*). Figure 9 shows that similar upfield shifts can be observed for some, but not all lysine side chains in R5 co-precipitated with silica. For example the ^{13}Cγ, ^{13}Cδ, and ^{13}Cε spins of K3 are all shifted upfield by several ppm when R5 is co-precipitated with silica, while with the exception of ^{13}Cδ, none of the side chain ^{13}C chemical shifts in K4 are affected. Neither do the chemical shifts for the side chain ^{13}C spins of K12 or K15 show significant changes upon co-precipitation with silica. These data indicate that while K3 and to a lesser extent K4 interact with silica, the absence of observable chemical shift changes indicate the side chains of K12 and K15 do not appear to be in proximity to silica.

In Figure 9 it is also clear that the chemical shifts of many of the side chain ^{13}C spins in the C-terminal RRIL moiety are perturbed upon co-precipitation with silica, indicating that there is an environmental change for this moiety as well. The ΔCS data in Figure 9 for R16, R17, and I18 (L19 was tethered to the resin and not labeled) show significant chemical shift changes in many of the side chain ^{13}C spins, although the ΔCS trends indicate more complicated behavior than would be indicated by simple proximity to silica. In R16 the chemical shifts of ^{13}Cγ, ^{13}Cδ, and ^{13}Cζ are moved upfield upon co-precipitation by silica, while R17 and I18 show downfield changes in side chain ^{13}C chemical shifts, the exception being ^{13}Cζ of R17 which shifts upfield upon co-precipitation with silica.

The chemical shift changes observed for selected lysine side chains can be understood as resulting from varying degrees of interaction between positively charged amino acid side chains of aggregated peptides and the silica phase. Studies of silica precipitation by R5 mutants indicate the C-terminal RRIL moiety is necessary for silica formation activity (*60*, *61*). In the presence of RRIL, R5

In Proteins at Interfaces III State of the Art 2012; Horbett, T., et al.;
ACS Symposium Series; American Chemical Society: Washington, DC, 2012.

peptides are observed by light scattering to form aggregates about 825 nm in diameter. Formation of peptide aggregates is considered necessary for silica formation with R5 because when RRIL is omitted silica formation is reduced and no peptides aggregates are formed. The RRIL motif is believed to be involved in the self-assembly of the peptide where the pattern of arginine's positively charged guanidinium groups in proximity to the hydrophobic leucine and isoleucine residues results in a micelle like assembly.

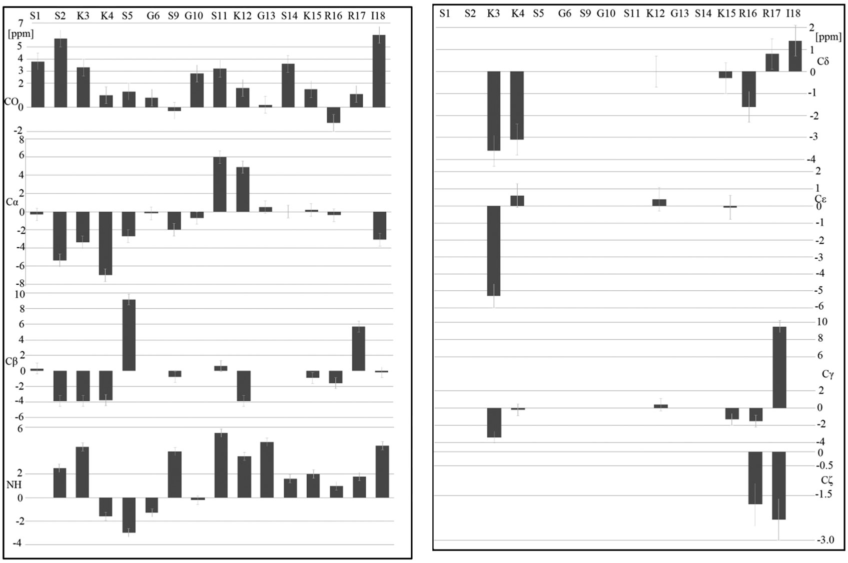

Figure 9. Perturbations of the chemical shifts of the ^{13}CO, ^{13}Cα, ^{13}Cβ and ^{15}N amide nitrogen spins (left) and the sidechain ^{13}C spins (right) in R5 co-precipitated with silica referenced to the native peptide. Vertical scale is graduated in parts per million. Residues 7 and 8 were not labeled due to synthesis errors.

The pattern of chemical shift changes observed in R5 and portrayed in Figure 9, may therefore the result from the formation of micellar-like peptide aggregates where positively-charged amino acid side chains near the peptide N-terminus are exposed at the surface of the aggregate and interact with the surrounding silica matrix. This being the case the side chain of K3 would clearly be most affected, K4 shows less significant perturbations, while K12 and K15 are buried within the aggregate and are removed from the silica matrix. The RRIL chemical shifts are likely due to the effect of peptide-peptide interactions which are the basis for aggregate formation.

Figure 9 also shows that numerous chemical shift changes occur for the ^{15}NH, ^{13}CO, ^{13}Cα, and ^{13}Cβ spins throughout the R5 peptide upon formation of biosilica composites. Interpretation of these chemical shift changes is potentially complicated by the fact that the backbone ^{13}C chemical shifts are sensitive to conformational changes. However, given that biosilica composite formation is only observed in the presence of peptide aggregates, and given that the orientation of the peptides in these aggregates likely leaves amino acid side chains beyond K3 largely removed from the silica matrix, we assume the backbone ^{13}C chemical shift changes observed beyond K3 are largely due to conformational changes. A preliminary evaluation of the carbon-only chemical shifts of CO, Cα and Cβ by TALOS+ shows that while most of the expected angles fall into β-sheet region ($\varphi < 0°$, $\psi > 90°$) for both the neat peptide and the peptide-silica composite, residues K4 goes from α_L-helical ($30° < \varphi < 130°$, $-50° < \psi < 100°$) to a β-sheet region and R17 does the opposite, starting in a β-sheet conformation and moving to a α_L-helical when bound to silica. In general the trend in torsion angles indicate an extension of the peptide, i.e. flattening. This flattening of the peptide in the silica composite may be a form of self-assembly leading to the scaffolding motif seen elsewhere in biomineralization (*74*, *75*). The conformational change near R17 may be associated with peptide interactions that form upon formation of peptide aggregates.

Conclusions

In this chapter, we have shown how solid state NMR techniques can provide information on the structure of proteins and peptides within biomineral composites together with information on protein-inorganic interactions to the level of atomic detail. Such information provides a clear picture of how proteins regulate the formation of these biomineral composites. In the case of statherin adsorbed onto HAP crystal surfaces, direct measurements of distances between ^{13}C and ^{15}N spins within the protein yield constraints for computational modeling of statherin's HAP-bound structure. Direct measurement of distances between nuclear spins in amino acid side chains of statherin and ^{31}P spins in the HAP surface, provide information on statherin's surface orientation and the basis for its face selective binding. Chemical shift measurements obtained by two dimensional ssNMR spectroscopic studies similarly provide information on the nature of peptide aggregates that provide templates for biosilica morphogenesis.

Further work is required to determine the extent to which the protein-mineral interactions derived from solid state NMR studies of statherin-HAP and R5-silica composites varies for other protein- biomineral composites. Besides statherin the only other structure of a HAP-bound protein obtained to date is the ssNMR-derived structure of HAP-bound amelogenin which plays an important role in the formation of tooth enamel (*65*). In contrast to statherin which has a well-structured helical HAP-binding domain and displays a high degree of face binding specificity, amelogenin has a high degree of structural dispersion on HAP to maximize surface coverage and somewhat less face binding specificity. With the two known structures for HAP binding proteins differing to such a significant degree, it is clear that more structures of surface-bound proteins need to be determined before a complete picture can emerge on how acidic proteins regulate HAP growth.

Solid state NMR studies described here for biosilicification peptides mainly focused on studies of secondary structure in silica, but ssNMR methods are ideally suited to determining the structures of protein assemblies. To augment the qualitative chemical shift information presently in Figure 9, ^{13}C{^{29}Si} and ^{15}N{^{29}Si} REDOR experiments can be used to define quantitatively the interactions of the surrounding silica matrix with R5 peptide side chains. Dipolar recoupling ssNMR techniques applied to selectively ^{13}C enriched peptides are widely used to determine the nature of protein assemblies in amyloid fibrils (*76*) and can be similarly applied to R5 peptides in silica matrices to determine the nature of protein aggregates in silica. Promising subjects for future ssNMR studies are silica-forming peptides whose mode of activity seem to differ from silaffins. An example is a class of silica-forming peptides called silacidins (*77*). Although the RRIL moiety appears necessary for R5 self assembly which in turn is required for silica morphogensis, the *direct role* of such arginine-containing repeats has been questioned in the context of the precipitation of silica by silacidins. Wenzl and co-workers (*77*) have shown that similar RRL repeats in silacidins, act as linkers between otherwise polyanionic peptides. They propose that the linkers are removed to render completely anionic chains, which can bind polyamines. It is these complexes that are proposed to template silica. Another very promising direction for future exploration is the use of solid state NMR to determine the role of protein assemblies in the formation of nanostructures based on non-biological materials including TiO_2, GeO_2. Thus we are poised to apply ssNMR techniques to elucidating the structure of proteins in both naturally occurring biological composites as well as non-biological nanostructures prepared using biologically inspired strategies.

Acknowledgments

We would like to acknowledge Matt Power for his contributions to data collection on the R5. Work was supported by the National Institutes of Health (RO1 DE12554).

References

1. *Handbook of Biomineralization*; Wiley VCH: New York, 2007.
2. Schoen, F. J.; Harasaki, H.; Kim, K. M.; Anderson, H. C.; Levy, R. J. *J. Biomed. Mater. Res.* **1988**, *22*, 11–36.
3. Coe, F. L.; Parks, J. H.; Asplin, J. R. *N. Engl. J. Med.* **1992**, *327*, 1141–1152.
4. Dickerson, M. B.; Sandhage, K. H.; Naik, R. R. *Chem. Rev.* **2008**, *108*, 4935–4978.
5. Gordon, R.; Losic, D.; Tiffany, M. A.; Nagy, S. S.; Sterrenburg, F. A. S. *Trends Biotechnol.* **2009**, *27*, 116–127.
6. Losic, D.; Mitchell, J. G.; Voelcker, N. H. *Adv. Mater.* **2009**, *21*, 2947–2958.
7. Parker, A. R.; Townley, H. E. *Nat. Nanotechnol.* **2007**, *2*, 347–353.
8. Sanchez, C.; Arribart, H.; Giraud Guille, M. M. *Nat. Mater.* **2005**, *4*, 277–288.

9. Cha, J. N.; Shimizu, K.; Zhou, Y.; Christiansen, S. C.; Chmelka, B. F.; Stucky, G. D.; Morse, D. E. *Proc. Natl. Acad. Sci. U.S.A.* **1999**, *96*, 361–365.
10. Naik, R. R.; Whitlock, P. W.; Rodriguez, F.; Brott, L. L.; Glawe, D. D.; Clarson, S. J.; Stone, M. O. *Chem. Commun.* **2003**, 238–239.
11. Sandhage, K. H.; Allan, S. M.; Dickerson, M. B.; Gaddis, C. S.; Shian, S.; Weatherspoon, M. R.; Cai, Y.; Ahmad, G.; Haluska, M. S.; Snyder, R. L.; Unocic, R. R.; Zalar, F. M.; Zhang, Y.; Rapp, R. A.; Hildebrand, M.; Palenik, B. P. *Int. J. Appl. Ceram. Technol.* **2005**, *2*, 317–326.
12. Schröfel, A.; Kratošová, G.; Bohunická, M.; Dobročka, E.; Vávra, I. *J. Nanopart. Res.* **2011**, *13*, 3207–3216.
13. Andrew, E. R.; Bradbury, A.; Eades, R. G. *Nature* **1958**, *182*, 1659.
14. Gullion, T.; Schaefer, J. *J. Magn. Reson. (1969)* **1989**, *81*, 196–200.
15. Cornilescu, G.; Delaglio, F.; Bax, A. *J. Biomol. NMR* **1999**, *13*, 289–302.
16. Shen, Y.; Delaglio, F.; Cornilescu, G.; Bax, A. *J. Biomol. NMR* **2009**, *44*, 213–223.
17. Nadaud, P.; Helmus, J.; Jaroniec, C. *Biomol. NMR Assign.* **2007**, *1*, 117–120.
18. Franks, W. T.; Wylie, B. J.; Schmidt, H. L. F.; Nieuwkoop, A. J.; Mayrhofer, R.-M.; Shah, G. J.; Graesser, D. T.; Rienstra, C. M. *Proc. Natl. Acad. Sci. U.S.A.* **2008**, *105*, 4621–4626.
19. Nieuwkoop, A. J. *J. Chem. Phys.* **2009**, *131*, 095101.
20. Zech, S. G.; Wand, A. J.; McDermott, A. E. *J. Am. Chem. Soc.* **2005**, *127*, 8618–8626.
21. Paravastu, A. K.; Leapman, R. D.; Yau, W.-M.; Tycko, R. *Proc. Natl. Acad. Sci. U.S.A.* **2008**, *105*, 18349–18354.
22. Petkova, A. T.; Leapman, R. D.; Guo, Z.; Yau, W.-M.; Mattson, M. P.; Tycko, R. *Science* **2005**, *307*, 262–265.
23. van der Wel, P. C. A.; Lewandowski, J. z. R.; Griffin, R. G. *Biochemistry* **2010**, *49*, 9457–9469.
24. Korukottu, J.; Schneider, R.; Vijayan, V.; Lange, A.; Pongs, O.; Becker, S.; Baldus, M.; Zweckstetter, M. *PLoS One* **2008**, *3*, e2359.
25. Schlesinger, D. H.; Hay, D. I. *J. Biol. Chem.* **1977**, *252*, 1689–1695.
26. Raj, P. A.; Marcus, E.; Sukumaran, D. K. *Biopolymers* **1998**, *45*, 51–67.
27. Schwartz, S. S.; Hay, D. I.; Schluckebier, S. K. *Calcif. Tissue Int.* **1992**, *50*, 511–517.
28. Campbell, A.; Ebrahimpour, A.; Perez, L.; Smesko, S.; Nancollas, G. *Calcif. Tissue Int.* **1989**, *45*, 122–128.
29. Johnsson, M.; Richardson, C. F.; Bergey, E. J.; Levine, M. J.; Nancollas, G. H. *Arch. Oral Biol.* **1991**, *36*, 631–636.
30. Jensen, J. L.; Lamkin, M. S.; Oppenheim, F. G. *Journal of Dental Research* **1992**, *71*, 1569–1576.
31. Minaguchi, K.; Bennick, A. *Journal of Dental Research* **1989**, *68*, 2–15.
32. Wikiel, K.; Burke, E. M.; Perich, J. W.; Reynolds, E. C.; Nancollas, G. H. *Arch. Oral Biol.* **1994**, *39*, 715–721.
33. Richardson, C. F.; Johnsson, M.; Raj, P. A.; Levine, M. J.; Nancollas, G. H. *Arch. Oral Biol.* **1993**, *38*, 997–1002.

34. Shaw, W. J.; Long, J. R.; Dindot, J. L.; Campbell, A. A.; Stayton, P. S.; Drobny, G. P. *J. Am. Chem. Soc.* **2000**, *122*, 1709–1716.
35. Shaw, W. J.; Long, J. R.; Campbell, A. A.; Stayton, P. S.; Drobny, G. P. *J. Am. Chem. Soc.* **2000**, *122*, 7118–7119.
36. Long, J. R.; Shaw, W. J.; Stayton, P. S.; Drobny, G. P. *Biochemistry* **2001**, *40*, 15451–15455.
37. Goobes, G.; Goobes, R.; Schueler-Furman, O.; Baker, D.; Stayton, P. S.; Drobny, G. P. *Proc. Natl. Acad. Sci. U.S.A.* **2006**, *103*, 16083–16088.
38. Makrodimitris, K.; Masica, D. L.; Kim, E. T.; Gray, J. J. *J. Am. Chem. Soc.* **2007**, *129*, 13713–13722.
39. Masica, D. L.; Ash, J. T.; Ndao, M.; Drobny, G. P.; Gray, J. J. *Structure* **2010**, *18*, 1678–1687.
40. Masica, D. L.; Gray, J. J. *Biophys. J.* **2009**, *96*, 3082–3091.
41. Ndao, M.; Ash, J. T.; Stayton, P. S.; Drobny, G. P. *Surf. Sci.* **2010**, *604*, L39–L42.
42. Ndao, M.; Ash, J. T.; Breen, N. F.; Goobes, G.; Stayton, P. S.; Drobny, G. P. *Langmuir* **2009**, *25*, 12136–12143.
43. Goobes, R.; Goobes, G.; Shaw, W. J.; Drobny, G. P.; Campbell, C. T.; Stayton, P. S. *Biochemistry* **2007**, *46*, 4725–4733.
44. Goobes, R.; Goobes, G.; Campbell, C. T.; Stayton, P. S. *Biochemistry* **2006**, *45*, 5576–5586.
45. Srinivasan, S.; Ash, J.; Drobny, G. P.; Stayton, P. S. Unpublished communication..
46. Barnett, B. L.; Strickland, L. C. *Acta Crystallogr., Sect. B* **1979**, *35*, 1212–1214.
47. Margolis, H. C.; Beniash, E.; Fowler, C. E. *J. Dent. Res.* **2006**, *85*, 775–793.
48. Simmer, J. P.; Fincham, A. G. *Crit. Rev. Oral Biol. Med.* **1995**, *6*, 84–108.
49. Zhan, J.; Tseng, Y. H.; Chan, J. C. C.; Mou, C. Y. *Adv. Funct. Mater.* **2005**, *15*, 2005–2010.
50. Neville, F.; Broderick, M. J. F.; Gibson, T.; Millner, P. A. *Langmuir* **2010**, *27*, 279–285.
51. Pouget, E.; Dujardin, E.; Cavalier, A.; Moreac, A.; Valery, C.; Marchi-Artzner, V.; Weiss, T.; Renault, A.; Paternostre, M.; Artzner, F. *Nat. Mater.* **2007**, *6*, 434–439.
52. Kent, M. S.; Murton, J. K.; Zendejas, F. J.; Tran, H.; Simmons, B. A.; Satija, S.; Kuzmenko, I. *Langmuir* **2008**, *25*, 305–310.
53. Cha, J. N.; Stucky, G. D.; Morse, D. E.; Deming, T. J. *Nature* **2000**, *403*, 289–292.
54. Hildebrand, M. *Chem. Rev.* **2008**, *108*, 4855–4874.
55. Kröger, N.; Deutzmann, R.; Sumper, M. *Science* **1999**, *286*, 1129–1132.
56. Kröger, N.; Lorenz, S.; Brunner, E.; Sumper, M. *Science* **2002**, *298*, 584–586.
57. Poulsen, N.; Kröger, N. *J. Biol. Chem.* **2004**, *279*, 42993–42999.
58. Poulsen, N.; Sumper, M.; Kröger, N. *Proc. Natl. Acad. Sci. U.S.A.* **2003**, *100*, 12075–12080.
59. Kröger, N.; Deutzmann, R.; Bergsdorf, C.; Sumper, M. *Proc. Natl. Acad. Sci. U.S.A.* **2000**, *97*, 14133–14138.
60. Knecht, M. R.; Wright, D. W. *Chem. Commun.* **2003**, 3038–3039.

61. Knecht, M. R.; Wright, D. W. *Langmuir* **2004**, *20*, 4728–4732.
62. Rodríguez, F.; Glawe, D. D.; Naik, R. R.; Hallinan, K. P.; Stone, M. O. *Biomacromolecules* **2004**, *5*, 261–265.
63. Zhao, X.; Pan, F.; Xu, H.; Yaseen, M.; Shan, H.; Hauser, C. A. E.; Zhang, S.; Lu, J. R. *Chem. Soc. Rev.* **2010**, *39*, 3480–3498.
64. Xu, H.; Wang, Y.; Ge, X.; Han, S.; Wang, S.; Zhou, P.; Shan, H.; Zhao, X.; Lu, J. R. *Chem. Mater.* **2010**, *22*, 5165–5173.
65. Masica, D. L.; Gray, J. J.; Shaw, W. J. *J. Phys. Chem. C* **2011**, *115*, 13775–13785.
66. Kaplan, S.; Resing, H. A.; Waugh, J. S. *J. Chem. Phys.* **1973**, *59*, 5681–5687.
67. Ben Shir, I.; Kababya, S.; Amitay-Rosen, T.; Balazs, Y. S.; Schmidt, A. *J. Phys. Chem. B* **2010**, *114*, 5989–5996.
68. Takegoshi, K.; Nakamura, S.; Terao, T. *J. Chem. Phys.* **2003**, *118*, 2325–2341.
69. Takegoshi, K.; Nakamura, S.; Terao, T. *Chem. Phys. Lett.* **2001**, *344*, 631–637.
70. Fernandez, V. L.; Reimer, J. A.; Denn, M. M. *J. Am. Chem. Soc.* **1992**, *114*, 9634–9642.
71. Mermut, O.; Phillips, D. C.; York, R. L.; McCrea, K. R.; Ward, R. S.; Somorjai, G. A. *J. Am. Chem. Soc.* **2006**, *128*, 3598–3607.
72. Chiang, C.-H.; Liu, N.-I.; Koenig, J. L. *J. Colloid Interface Sci.* **1982**, *86*, 26–34.
73. Saitô, H. *Magn. Reson. Chem.* **1986**, *24*, 835–852.
74. Patwardhan, S. V.; Maheshwari, R.; Mukherjee, N.; Kiick, K. L.; Clarson, S. J. *Biomacromolecules* **2006**, *7*, 491–497.
75. López-García, M.; Kessler, H. Stimulation of Bone Growth on Implants by Integrin Ligands. In *Handbook of Biomineralization*; Wiley-VCH Verlag GmbH: Weinham, 2008; pp 109−126.
76. Balbach, J. J.; Ishii, Y.; Antzutkin, O. N.; Leapman, R. D.; Rizzo, N. W.; Dyda, F.; Reed, J.; Tycko, R. *Biochemistry* **2000**, *39*, 13748–13759.
77. Wenzl, S.; Hett, R.; Richthammer, P.; Sumper, M. *Angew. Chem.* **2008**, *120*, 1753–1756.

Chapter 5

Mechanisms of Fibrinogen Adsorption on Mica

Zbigniew Adamczyk,[*] Monika Wasilewska, Małgorzata Nattich-Rak, and Jakub Barbasz

J.Haber Institute of Catalysis and Surface Chemistry, Polish Academy of Sciences, ul. Niezapominajek 8, 30-239 Cracow, Poland
[*]E-mail: ncadamcz@cyf-kr.edu.pl. Phone: +4812 6395104. Fax: +4812 4251923

Analysis of experimental data obtained for fibrinogen solutions, obtained by DLS, microelectrophoretic and dynamic viscosity measurements, was performed in terms of the theoretical approach based on bead modeling. The presence of flexible side arms (Aα chains) in the fibrinogen molecule were explicitly considered in these calculations. Two main conformational states of the fibrinogen molecule were predicted, (i) the expanded, prevailing for pH < 4 and lower ionic strength and (ii) the semi collapsed existing under physiological conditions, i.e., pH = 7.4 and 0.15 M NaCl. The latter conformation is characterized by an intrinsic viscosity of 35 and a hydrodynamic radius of 10 nm. Additionally, the interaction energy between the arms and the body of the molecule was predicted to be – 4 kT units, confirming that they are oppositely charged under these conditions, in comparison to the central nodule. This confirms a highly heterogeneous charge distribution over the fibrinogen molecule with the positive charge mostly located at the ends of the Aα chains (for pH up to 9.7), and a negative charge located at the main body of the molecule. However, for pH below 4, the entire molecule becomes positively charged. These predictions were used to quantitatively interpret adsorption kinetics determined by AFM imaging of isolated fibrinogen molecules on mica and by the *in situ* streaming potential measurements. It was confirmed that fibrinogen adsorption for a coverage range below 0.3 proceeds irreversibly according to the side-on mechanism, both at pH 3.5 and 7.4.

In Proteins at Interfaces III State of the Art 2012; Horbett, T., et al.;
ACS Symposium Series; American Chemical Society: Washington, DC, 2012.

The anomalous adsorption at pH = 7.4 was explained in terms of heterogeneous charge distribution. Additionally, colloid deposition experiments (involving negatively charged latex particles) on fibrinogen monolayers were presented. These experiments confirmed the existence of transient states of fibrinogen molecules in the end-on orientation. Based on this hypothesis, a multistage 'hopping' mechanism of colloid particle deposition on fibrinogen monolayers was proposed. It consists of an irreversible immobilization of colloid particles by a few fibrinogen molecules excited to the end-on conformation. This mechanism can also be valid for bioparticle immobilization on fibrinogen monolayers leading to clotting and thrombus formation.

Keywords: adsorption of fibrinogen on mica; bead model of fibrinogen; charge distribution over fibrinogen; conformations of fibrinogen molecule; fibrinogen molecule conformations; hydrodynamic radius of fibrinogen; mechanisms of fibrinogen adsorption

Introduction

Adsorption of proteins is essential for their efficient separation and purification by chromatography, electrophoresis, filtration, biosensing, enzyme immobilization in bioreactors, immunological assays, etc. On the other hand, protein adsorption can be a highly undesirable process initiating biofouling cascades leading to membrane, artificial organ, and contact lense failure, plaque formation, thrombosis, etc.

Numerous studies were devoted to fibrinogen because of its fundamental role in blood clotting, platelet adhesion, thrombosis, angiogenesis, wound healing and tumor growth (*1–5*). The early works (*6–8*) were focused on determining the molecular weight of fibrinogen by measuring its diffusion and sedimentation coefficients.

Reliable data concerning fibrinogen's geometrical dimensions and conformations stem from the electron microscopy studies of Hall and Slayter (*9*) and others (*10–12*). From the micrographs of fibrinogen adsorbed on mica, it was established that its molecule has a co-linear, trinodular shape with a total length of 47.5 nm. The two equal end domains are spherical having a diameter of 6.5 nm; the middle domain has a diameter of 5 nm. These domains are connected by cylindrical rods, having a diameter of 1.5 nm. A schematic view of the fibrinogen molecule derived from the Hall-Slayter model, hereafter referred to as the HS model is shown in Table 1. Interestingly, the HS model's shape and dimensions of fibrinogen agree with the true crystallographic shape derived from X-ray diffraction (*13*), see Table 1.

Table 1. Model shapes of the fibrinogen molecule. Reproduced with permission from Ref. (*24*). Copyright 2012 Elsevier

Model	Shape of Molecule	Remarks, Refs.
Hall and Slyter HS Model	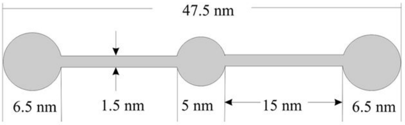 47.5 nm 6.5 nm 1.5 nm 5 nm 15 nm 6.5 nm	$v = 405\ \mathrm{nm}^3$ (anhydrous) (9)
Chemical	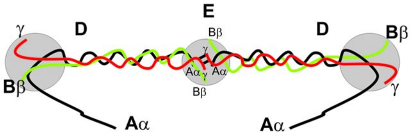 γ D E Bβ D Bβ Bβ γ Aα γ Aα Bβ γ Aα Aα	$M_w = 337{,}897$ (22)
Crystallographic		$\bar{v} = 0.72\ \mathrm{cm}^3\ \mathrm{g}^{-1}$ $\rho_f = 1.38\ \mathrm{g\ cm}^{-3}$ $v_0 = 405\ \mathrm{nm}^3$ (13)
Bead Model A	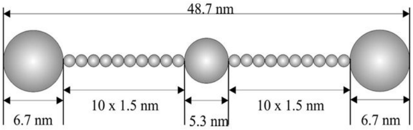 48.7 nm 10 x 1.5 nm 10 x 1.5 nm 6.7 nm 5.3 nm 6.7 nm	$v_A = 428\ \mathrm{nm}^3$ (26)
Bead Model B	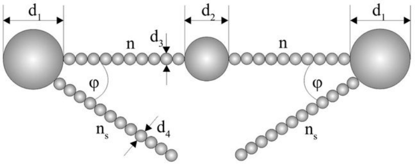 d1 d2 d1 n d3 n φ φ ns d4 ns	$v_B = v_A + 2n_s v_1\ \mathrm{nm}^3$ 428 - 470 (24)

Remarks:
v – molecular volume calculated from geometry
ρ_f - specific density of the fibrinogen molecule (Ref. 32)
$\bar{v}$ - specific volume of the fibrinogen molecule (Ref. 32)
$v_0 = M_w / A_v \rho_f = \bar{v} M_w / A_v$, molecular volume
v_A - molecular volume calculated from geometry for Model A
v_B - molecular volume calculated from geometry for Model B

Similar shape and fibrinogen dimensions were confirmed by numerous studies carried out using atomic force microscopy (AFM) (*14–20*).

As can be seen in Table 1, the fibrinogen molecule is highly anisotropic, characterized by considerable elongation (with the length to width ratio exceeding ten).

It should be mentioned, however, that in these works the shape and dimensions of fibrinogen were determined under dry or vacuum conditions, where the molecule is likely to change its native conformations occurring in the electrolyte solutions, because of a considerable dehydration.

Suggestions that such conformational changes can be essential stem from the chemical amino-acid sequence (primary structure) of fibrinogen determined in the eighties (*21*, *22*). Thus, from the chemical point of view, the fibrinogen molecule is a symmetric dimer composed of three identical pairs of polypeptide chains, refereed to traditionally as Aα, Bβ and γ chains. They are coupled in the middle of the molecule through a few disulfide bridges and forming a central nodule (see Table 1).

The longest Aα chain is composed of 610 aminoacids, the Bβ chain comprises 460 aminoacids and the γ chain 411 aminoacids. Accordingly, the molecular mass of the fibrinogen molecule equals to 337,897 D (*21*). Additionally, from the chemical structure one can deduce that major parts of the Aα chains extends from the core of the molecule forming two polar appendages each having a molecular mass equal to 42,300 D (*5*). These fragments of polypeptide Aα chains are not visible in the crystallographic structure of fibrinogen. Hence, it seems that these chains are collapsed under vacuum conditions. However, they can play an essential role in the hydrodynamic behavior of the molecule in electrolyte solutions because of charging effects.

The essential role of the side ‘arms’ in determining hydrodynamic properties of the fibrinogen molecule was experimentally confirmed in Ref. (*23*). In this work systematic measurements of the diffusion coefficient and the dynamic viscosity of fibrinogen were performed. It was revealed that the diffusion coefficient of fibrinogen changed little with pH and ionic strength, whereas the dynamic viscosity exhibited large variations. These results were interpreted in terms of conformational changes of the fibrinogen molecule induced by increased charging for pH, deviating from the isoelectric point equal to 5.8 (*23*). By adopting the prolate spheroid model of the fibrinogen molecule, it was predicted that its effective length should be 80 nm for $pH < 4$ or $pH > 7.4$ (low ionic strength) and 65 - 68 nm for $pH = 7.4$ and $I = 0.15$ (this corresponds to physiological conditions).

These estimations of the effective length were quantitatively confirmed in Ref. (*24*), where a more realistic bead model of the fibrinogen molecule was developed, which explicitly takes into account the presence of flexible side ‘arms’ (see Table 1).

Knowing bulk fibrinogen properties, especially its conformations, one can attempt to properly interpret its mechanisms of adsorption on various substrates. There are abundant experimental studies of this type, mostly done by ellipsometry (*14*, *15*, *25*) and TIRF (*19*).

A significant spread in the maximum coverage of fibrinogen was reported in these works with the lowest and highest value equal to 1.4 and 11 mg m^{-2}, respectively. It seems that this discrepancy can be attributed to different adsorption mechanisms of fibrinogen on various substrates for various concentration range. For hydrophilic surfaces, and a low concentration regime, fibrinogen adsorption occurs according to the side-on mechanism with the maximum amount of adsorbed protein equal to 1.4 - 1.7 mg m^{-2}, which was confirmed by recent theoretical results discussed in Ref. (*26*)

For hydrophobic surfaces and higher fibrinogen concentrations, the end-on adsorption of the protein becomes feasible with the maximum coverage many times higher than for the side-on configuration. However, since the binding energy in the end-on configuration is much lower than for the side-on orientation, a partial reversibility of adsorption occurred, which can explain the source of the discrepancies. This adsorption regime was theoretically studied in Ref. (*27*)

However, a deeper insight into the mechanism of fibrinogen adsorption and the structure of its monolayers on various substrates is hindered because few experimental methods are available working under wet, *in situ* conditions.

One of few exemptions represent the electrokinetic methods, usually, the streaming potential or streaming current measurements. (*28–30*). Pioneering experiments of this kind were performed by Norde and Rouwendal (*28*). Later on Zembala and Dejardin (*31*) determined variations in the streaming potential of silica capillaries upon fibrinogen adsorption as a function of time for pH = 7.3 and the ionic strength of 10^{-2} M. A systematic increase in the negative potential of the substrate was observed upon fibrinogen adsorption, which was also negatively charged under these conditions.

Thorough streaming potential measurements of fibrinogen adsorption on mica for various ionic strength and pH were reported in Ref. (*32*). The protein coverage was determined by direct AFM imaging of the adsorbed monolayers. Knowing the coverage, these experimental data were successfully interpreted in terms of the electrokinetic model developed for heterogeneous (particle covered) surfaces (*33–35*). The Gouy-Chapman model, based on the concept of a continuous charge distribution, was inadequate to interpret these results. Based on these measurements an irreversible side-on adsorption mechanism of fibrinogen was proposed. Anomalous adsorption of fibrinogen for pH = 7.4 was explained in terms of a heterogeneous charge distribution, characterized by the presence of positive charges on the side arms, and a negative charge on the core part of the molecule as predicted in Ref. (*24*).

More detailed information about fibrinogen monolayers can be gathered using the *in situ* method developed in Refs. (*36–39*) based on the unspecific deposition of colloid particles. The technique, referred to as the colloid enhancement (CE) (*38*, *39*), enables one to determine a unique functional relationship between the amount of adsorbed protein and the amount of adsorbed colloid, which can be quantitatively assessed via optical microscope imaging under wet conditions. Using the colloid deposition method, in conjunction with thorough electrokinetic characteristics of protein covered substrates, one can determine the dynamic behavior of protein monolayers.

The goal of this work is to discuss results pertinent to fibrinogen adsorption on solid substrates, concerning both the theoretical modeling and experimental results acquired by DLS electrophoresis, dynamic viscosity, streaming potential and AFM measurements. Based on an analysis of these data, a unified view of fibrinogen adsorption mechanisms and monolayer behavior is formulated. In particular, when exploiting the CE measurements, a ‘hopping’ mechanism of colloid particle deposition on fibrinogen monolayers is proposed, having significance for bioparticle, e.g., platelet or red blood cell immobilization on protein monolayers.

Theoretical Modeling of Fibrinogen Adsorption

Calculating Bulk Hydrodynamic Properties of the Fibrinogen Molecule

Because of the complicated shape of the fibrinogen molecule, which has no symmetry axis (see Table 1), calculations of its hydrodynamic mobility matrix or intrinsic viscosity, which convey information about the molecule conformations, are not feasible. Therefore, in Ref. (*26*) a bead model of the fibrinogen molecule was proposed to describe adsorption kinetics on solid surfaces. The model, hereafter referred to as Model A, is shown schematically in Table 1. As can be seen, the fibrinogen molecule is approximated as an array of touching beads of various size forming a co-linear conformation. The two external beads have the size of d_1, the central bead has the size of d_2 and the $2n$ remaining, equal-sized beads have the dimension of d_3. For calculations presented in Ref. (*26*), it was assumed that d_1 = 6.7 nm, d_2 = 5.3 nm, d_3 = 1.5 and $2n$ = 20. This gives the overall length of the fibrinogen molecule equal to 48.7 nm. This is slightly larger than in the HS and crystallographic model, due to presence of tightly bound water (hydration effect). Accordingly the volume of the fibrinogen molecule in Model A, v_A, equals to 428 nm^3. This slightly exceeds the molecular volume given by

$$v_0 = M_w / A_v \rho_f = \bar{v} M_w / A_v \quad (1)$$

where M_w is the molecular mass of fibrinogen, A_v is the Avogadro number, ρ_f is the specific density of fibrinogen and $\bar{v}$ is the specific molar volume of fibrinogen.

For the molecular weight M_w = 337,817 derived from the amino acid sequence (see Table 1) and ρ_f = 1.38 g cm^{-3} (*32*) one obtains $\bar{v}$ = 0.72 cm^{-3} g^{-1} and the fibrinogen molecule volume of 405 nm^3.

Model A, due to its simplicity, proved advantageous for performing time consuming MC simulations of fibrinogen adsorption on solid substrates under various orientations (*26*, *27*). However, a limitation of this model is the negligence of side arms in the fibrinogen molecule, which can exert essential influence on its bulk hydrodynamic properties. Therefore, in ref. (*24*) a more realistic model, hereafter referred to as Model B was developed (see Table 2), where the presence of these arms is explicitly considered by introducing two straight sequences of n_s beads of equal size, having the diameter of d_4. These arms form the angle φ with the main body of the fibrinogen molecule. Both the number of beads n_s and the angle φ are variable parameters, which can were optimized in calculations presented in Ref. (*24*). Obviously, for n_s = 0, Model B is reduced to Model A, previously described.

Table 2. Hydrodynamic radii and intrinsic viscosities for model shapes of the fibrinogen molecule. Adapted with permission from Ref. (*24*). Copyright 2012 Elsevier

Shape	Volume [nm^3]	R_H [nm]	[η][1]	Remarks
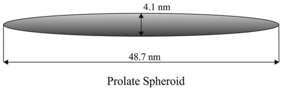 4.1 nm 48.7 nm Prolate Spheroid	428	7.66	17.5	Brenner (40) analytical solution
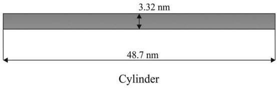 3.32 nm 48.7 nm Cylinder	428	7.25	23.2	Brenner (40) Analytical solution approximate
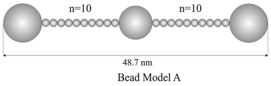 n=10 n=10 48.7 nm Bead Model A	428	8.54	27.1	Ref. (24)
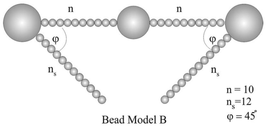 n n φ φ n_s n_s n = 10 n_s=12 φ = 45° Bead Model B	470	10.0	30.9	Ref. (24)
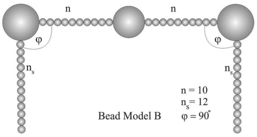 n n φ φ n_s n_s n = 10 n_s= 12 φ = 90° Bead Model B	470	10.8	43.6	Ref. (24)
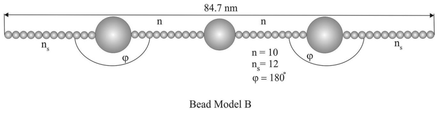 84.7 nm n n n_s n_s φ φ n = 10 n_s= 12 φ = 180° Bead Model B	470	11.0	62.3	Ref. (24)

The volume of the fibrinogen molecule for the Model B is given by the expression

$$v_B = \frac{\pi}{6}\left(2d_1^3 + d_2^3 + 2nd_3^3 + 2n_s d_4^3\right) = v_A + 2n_s v_1 \tag{2}$$

where $v_1 = \frac{\pi}{6} d_4^3$ is the volume of one bead in the side arm.

According to Model B, the fibrinogen molecule has two planes of symmetry, but no symmetry axis, which complicates the hydrodynamic calculations due to the appearance of the coupling between translational and rotational motion.

Using this Model B, extensive calculations were performed in Ref. (*24*) in which the average hydrodynamic mobility <*M*> and the intrinsic viscosity [η] (also called the viscosity increment) were determined for various side arm lengths (number of small beads n_s).

The hydrodynamic mobility <*M*> is a relevant quantity for predicting fibrinogen adsorption kinetics, because it is connected with the orientation averaged translational diffusion coefficient *D* through the Einstein dependence

$$D = kT < M > \tag{3}$$

where *k* is the Boltzmann constant and *T* is the absolute temperature.

However, since *D* is dependent on the temperature (in contrast to the hydrodynamic mobility) and the solvent viscosity, it is often useful to introduce the hydrodynamic radius of a molecule R_H defined by the constitutive relationship

$$R_H = \frac{1}{6\pi\eta\langle M\rangle} = \frac{kT}{6\pi\eta D} \tag{4}$$

R_H is a quantity of primary importance because it solely depends on the shape and size of molecules being independent not only of temperature and the viscosity but also particle density and other parameters characterizing the solvent. Physically R_H corresponds to the radius of an equivalent sphere having the same hydrodynamic mobility as the molecule of an arbitrary shape.

For the fibrinogen molecule, R_H is rather insensitive to its conformations depending mostly on the contour length. In this respect, the intrinsic viscosity [η] is more sensitive to conformational changes of the molecules. It is defined as the second virial coefficient in the expansion of the suspension dynamic viscosity against the concentration of the solute (molecules) (*40*). This can be mathematically formulated as

$$\eta = \eta_s\left[1 + [\eta]_c\, c + 0\left(c^2\right)\right] \tag{5}$$

where η_s is the solvent dynamic viscosity and *c* is the concentration of the solute.

Using this definition, $[\eta]_c$ can be defined as (*41*)

$$[\eta]_c = \frac{\eta - \eta_s}{\eta_s c} \tag{6}$$

for $c \to 0$

It should be mentioned that confusion may arise because the solute concentration can be expressed using various concentrations.

In Ref. (*24*) the hydrodynamic radius and the intrinsic viscosity of fibrinogen were calculated as a function of the angle φ and the number of the beads in the side arms n_s keeping a fixed value of $n = 10$. The multipole expansion method was used to solve the linear Stokes equation with no-slip boundary conditions on the molecule surface. Values of R_H and [η] were calculated in a quasi-continuous form for various conformations of the fibrinogen molecule and n_s ranging between zero (Model A) and 12. In the latter case the length of each arm equals to 18 nm.

Results obtained in these calculations for some limiting conformations are collected in Table 2. As can be seen, the presence of side arms exerts only a limiting influence on R_H, which increases from 8.54 nm (no arms) through 10.8 nm ($n_s = 12$, $\varphi = 90°$) to 11 nm for the fully extended molecule conformation ($n_s = 12$, $\varphi = 180°$).

Note that the theoretical values of R_H predicted if the molecule shape is approximated by a spheroidal or cylindrical shape are much lower than those derived from Model B (see Table 2).

In contrast to hydrodynamic radius, variations in the intrinsic viscosity with fibrinogen conformations are much more significant. Thus, for model A (no arms), $[\eta] = 27.1$ (Table 2), for $n_s = 12$, $\varphi = 90°$, $[\eta] = 43.6$ and for the fully extended conformation $n_s = 12$, $\varphi = 180°$, $[\eta] = 62.3$.

Using these values, in Ref. (*24*) the average hydrodynamic radii and intrinsic viscosities of the fibrinogen molecule were calculated in the thermodynamic limit, i.e., assuming that the probability of a given conformation of side arms is governed by the Boltzmann statistics. In the case of zero interaction energy between the arms and the central nodule the following values of intrinsic viscosity, hydrodynamic radius and the orientation angle are predicted (for $n_s = 12$):

$$\begin{aligned} &<R_H> = 10.5 \text{ nm} \\ &[\eta] = 44.6 \qquad (7) \\ &<\varphi> = 94.7^{\circ} \end{aligned}$$

These parameters correspond, therefore, to the situation where electrostatic interactions within the fibrinogen molecule are absent.

It was also shown that in the presence of repulsive interaction these values increase monotonically with the magnitude and the effective range of the interaction energy ϕ_0.

On the other hand, in the presence of attractive interactions between the arms and the central nodule, the average angle decreases significantly, thus $<R_H>$ becomes closer to 10 nm and $[\eta]$ closer to 30. Hence, by comparing these theoretical predictions with experimental data one can estimate the interaction energy between arms and the central nodule of the molecule, which is mostly governed by electrostatic interactions (*24*).

Reliable values of the hydrodynamic radius of fibrinogen can be acquired by the dynamic light scattering (DLS) measurements. The primary parameter derived from these measurements is the autocorrelation function converted to the average translational diffusion coefficient. Knowing the diffusion coefficient the hydrodynamic radius can be calculated using Eq. (4). Such measurements done for various pH and ionic strength were reported in Ref. (*23*). For pH = 7.4, $I = 0.15$ M NaCl (physiological conditions) it was determined that $D = 2.15 \times 10^{-7}$ cm^2 s^{-1} ($R_H = 10$ nm). For pH = 3.5, $I = 10^{-3}$ M, $D = 2.01 \times 10^{-7}$ cm^2 s^{-1}, ($R_H = 10.7$ nm).

As seen, for pH = 7.4, the hydrodynamic radius of fibrinogen assumes lower values than the previous estimate for the neutral molecule (10.5 nm). This may confirm the existence of attractive interactions at this pH.

However, more unequivocal estimations of the interaction energy can be derived from the viscosity measurements done in Ref. (*24*) for the same set of physicochemical parameters. The intrinsic viscosity values are: $[\eta] = 35$ for pH = 7.4, $I = 0.15$ M, and $[\eta] = 50$ for pH = 3.5, $I = 10^{-3}$ M. Comparing these data with experimental predictions it was predicted that for pH = 7.4 and $I = 0.15$ M, the interaction energy $\phi_0 = -4$ kT.

On the other hand for pH = 3.5, $I = 10^{-3}$ M it was predicted that there appears electrostatic repulsion between the arms and the body characterized by the energy of $\phi_0 = 4$ kT.

Knowing ϕ_0 one can estimate the number of effective (uncompensated) charges on the arms and the central nodule of the fibrinogen molecule. It was determined in Ref. (*23*) that at pH = 7.4 and $I = 0.15$ M the overall number of elementary (positive) charges is 6 (3 per each arm) and the number of elementary charges (negative) on the central nodule is -6. Considering additionally that the net charge of the fibrinogen molecule under these conditions is -8 elementary charges (*23*), one can predict the charge distribution over the fibrinogen molecule as shown in Table 3.

Table 3. Predicted conformations of the fibrinogen molecule. Adapted with permission from Ref. (*24*). Copyright 2012 Elsevier

Conformation	**$\langle R_H \rangle$** **$\langle[\eta]\rangle$** **$\langle\varphi\rangle$**	**Remarks**
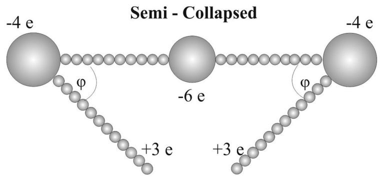 Semi - Collapsed -4 e -4 e φ φ -6 e +3 e +3 e	$\langle R_H \rangle = 10.0$ nm $\langle[\eta]\rangle = 35$ $\langle\varphi\rangle \sim 56^{\circ}$	Attractive energy $\phi_0 \sim -4$ kT, Occurs under physiological conditions pH =7.4, I =0.15 M
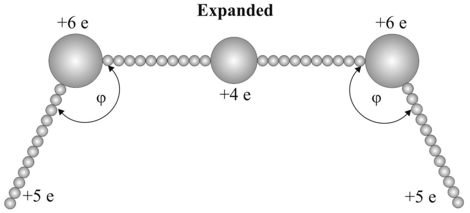	$\langle R_H \rangle = 10.7$ nm $\langle[\eta]\rangle = 50$ $\langle\varphi\rangle \sim 115^{\circ}$	Repulsive energy between arms and body $\phi_0 \sim 4$ kT, occurs for pH < 4, or pH >10 lower ionic strenght

These estimates are quite significant because the presence of positive charges at the ends of the flexible arms explains anomalous adsorption of fibrinogen at negatively charged surfaces such as mica (*42*) modified glass (*43*) or polystyrene latex particles (*44*) at pH = 7.4. These aspects are discussed in more detail later on.

On the other hand, for pH = 3.5, $I = 10^{-3}$ M, the following charge distribution over the fibrinogen molecule was predicted. There are 5 positive charges per each arm, 4 positive charges at the central nodule and 12 additional positive charges distributed over the rest of the molecule (see Table 3). Because the entire molecule is positively charged, one can deduce that fibrinogen adsorption on negatively charged surfaces should proceed irreversibly at this pH. Indeed, in Ref. (*27*) it was predicted that the for this charge distribution, the energy minimum for the fibrinogen/mica interactions in the side-on configuration equals to -34.8 kT. Accordingly, the characteristic relaxation time for the fibrinogen molecule desorption is 10^9 seconds (ca. 11.000 days), which is practically infinite from the experimental point of view.

It can also be concluded from this analysis that the fibrinogen model B, in which the presence of flexible arms is considered, properly reflects the available experimental data such as the diffusion coefficient (hydrodynamic radius) and the intrinsic viscosity. By exploiting these findings two main conformational states of the fibrinogen molecule can be distinguished. For a physiological conditions, pH = 7.4, $I = 0.15$ M NaCl, a semi-collapsed conformation dominates, characterized by the angle $<\varphi> = 56°$, intrinsic viscosity of 35 and the hydrodynamic radius of 10.0 nm. On the other hand, for pH 3.5 and $I < 10^{-3}$ M, an expanded conformation exists, characterized by a high intrinsic viscosity of 50, a hydrodynamic radius of 10.7 nm and the angle $< \varphi> = 115°$ (see Table 3).

Fibrinogen Adsorption Kinetics

Knowing the hydrodynamic radius and diffusion coefficient of the fibrinogen molecule one can predict adsorption kinetics at initial stages where the surface blocking effects, stemming from particles accumulated at interfaces, remain negligible.

On the other hand, to describe adsorption kinetics for higher coverages, information is required about the maximum amount of adsorbed particles (called the jamming coverage) and the blocking function, referred to as the available surface function (ASF) (*45–48*). This kind of information can be derived using the above models of fibrinogen and performing the Brownian-dynamics (BD) or Monte-Carlo (RSA) simulations, which are more universal and efficient (*26*, *27*, *45–51*).

The general rules of the Monte-Carlo simulation scheme, based on the random sequential adsorption concept, are (*45–51*):

(i) a particle is created, whose position and orientation is selected at random within prescribed limits defining the adsorption domain,

- (ii) if the particle fulfills prescribed criteria it becomes deposited and its position remains unchanged during the entire simulation process (postulate of an irreversible adsorption),
- (iii) if the deposition criteria are violated, a new attempt is made uncorrelated with previous attempts.

There are usually two major deposition criteria (i) no overlapping of any previously adsorbed particles and (ii) a contact with the bare interface.

Despite the simplicity of the governing rules, the RSA method is a powerful tool for generating adsorbed molecule populations of the number N_p exceeding 10^6 particles. The primary parameter characterizing such particle populations is the dimensionless coverage defined as

$$\Theta = S_g N_p / \Delta S \tag{8}$$

where S_g is the characteristic cross-section area of a molecule and ΔS is the surface area of the simulation plane.

Once a monolayer configuration or an ensemble of configurations at fixed Θ are generated, they can be statistically analyzed to determine, for example, the surface blocking function $B\Theta$ defined as the probability of adsorbing an additional particle on the interface already covered by N_p particles (*45–50*). In simulations $B\Theta$ is calculated as the average number of attempts to deposit the particle, from the formula

$$B(\Theta) = <1 / N_{att}> \tag{9}$$

where N_{att} is the number of attempts at depositing the particle and < > means the ensemble average.

Using the blocking function concept one can define the jamming coverage Θ_∞, which is a quantity of vital significance

$$B\left(\Theta_\infty\right) = 0 \tag{10}$$

Thus, by definition, at the jamming state, there is no space available for adsorption of particles of a given size and shape.

In the case of hard sphere adsorption on planar surfaces $\Theta_\infty = 0.547$ as determined by (*49*). It is interesting to note that this value is markedly smaller than the maximum hexagonal packing of hard spheres in 2D, equal to $\pi / 2\sqrt{3} = 0.9069$ or the regular packing, equal to $\pi / 4 = 0.7854$.

Jamming coverages were also determined for non-spherical particles of elongated shape such as spheroids, cylinders and spherocylinders (*46*). For spherocylinder characterized by the axis ratio 2:1, $\Theta_\infty = 0.583$ and for the axis ratio 15:1, $\Theta_\infty = 0.445$ (*47*). However, these results were obtained for convex particles of regular geometrical shapes. Therefore, they cannot be directly applied for predicting the jamming coverage of molecules approximated by the bead model. Calculations for such a case were recently performed for the fibrinogen Model A adsorbing side - on at a planar interface of infinite extension (*26*). The equivalent aspect ratio for this shape is 14.6, i.e., very similar to the spherocylinder. It was determined that the jamming coverage for the side-on adsorption of such a model fibrinogen molecule was 0.291, which is a lower value than the above obtained for the spherocylinder having a convex shape (0.445). It is interesting to mention that the jamming coverages are universal quantities, independent of the size of molecules.

However, for practical applications one is more interested in experimentally accessible parameters such as the surface concentration N_∞, defined as the number of particles or molecules per unit surface area of the interface. It can be calculated from Eq. (8) rearranged as

$$N_\infty = \Theta_\infty \,/\, S_g \qquad (11)$$

In practice N_∞ is often expressed as the number of molecules (particles) per a square µm. Thus, the above value of $\Theta_\infty = 0.291$ for fibrinogen corresponds to $N_\infty = 2.27\text{x}10^3$ µm^{-2} considering that S_g for the Model A molecule in the side-on orientation equals to 128 nm^2 (*26*). However, N_∞ is a specific parameter depending not only on the particle shape but also its size.

The interesting case of the end-on adsorption of fibrinogen on surfaces pre-covered by the jammed side-on monolayer was considered in Ref. (*27*). The jamming coverage for the end–on configuration, $\Theta_{\perp\infty}$ was 0.216, which corresponds to the surface concentration $N_{\perp\infty}$ of 6.13x10^3 µm^{-2}. This is higher than before because the cross-section area of Model A fibrinogen molecule in the end-on orientation is only 35 nm^2 (*27*).

The RSA calculations performed according to the above scheme can also be used in determining surface blocking functions, which have essential significance for analyzing adsorption kinetics of fibrinogen. From calculations performed in Ref. (*26*), the following expression for the blocking function was derived for the side-on adsorption of fibrinogen,

$$B(\Theta) = (1 + a_1\,\overline{\Theta} + a_2\,\overline{\Theta}^{\,2} + a_3\,\overline{\Theta}^{\,3})\,(1- \overline{\Theta}\,)^4 \qquad (12)$$

where $\overline{\Theta} = \dfrac{\Theta}{\Theta_\infty}$ is the normalized coverage for the side-on orientation $a_1 = -\,0.727$, $a_2 = -2.01$ and $a_3 = 1.882$.

For not too high coverage range, Eq. (12) can be approximated by the second order series expansion

$$B(\Theta\,) = 1 - C_1\Theta + C_2\Theta^2 + 0\left(\Theta^3\right) \qquad (13)$$

where $C_1 = 16.3$ and $C_2 = 82$ (side-on adsorption).

In Proteins at Interfaces III State of the Art 2012; Horbett, T., et al.;
ACS Symposium Series; American Chemical Society: Washington, DC, 2012.

On the other hand, for Θ approaching the jamming coverage, the blocking function assumes the form (*46*)

$$B(\Theta) = C_{\infty}\left(1 - \frac{\Theta}{\Theta_{\infty}}\right)^{4} \tag{14}$$

where $C_{\infty} = 0.0653$.

For the end-on adsorption of fibrinogen on surfaces pre-covered by the side-on monolayer, the blocking functions is given by (*27*).

$$B(\Theta) = B_0(1 + a_1\overline{\Theta} + a_2\overline{\Theta}^2 + a_3\overline{\Theta}^2)(1 - \overline{\Theta})^2 \tag{15}$$

where $B_0 = 0.130$, $\overline{\Theta} = \Theta_{\perp} / \Theta_{\perp\infty}$ is the normalized coverage for the end-on orientation and $a_1 = -0.851$, $a_2 = -0.566$, $a_3 = 0.609$.

It is worthwhile mentioning that these results were obtained within the framework of the standard RSA model, whose application requires no adjustable parameters.

Knowing the jamming coverage and the blocking functions one can quantitatively analyze the kinetics of fibrinogen adsorption and desorption using the phenomenological approach based on the continuity (mass-balance) equations (*35*, *45*). The advantage of this approach is the possibility of studying long-lasting adsorption processes (10^3 - 10^6 seconds) for broad range of bulk protein concentration. This makes such calculations useful for interpreting a variety of experimental data concerning fibrinogen adsorption. Such phenomenological descriptions involve the formulation of the constitutive equation describing the flux of protein molecules at the edge of the adsorption layer, which is as follows (*26*, *27*, *45*)

$$j_a = \frac{1}{S_g}\frac{d\Theta}{dt} = k_a\, n(\delta_a)\, \widetilde{B}(\Theta) - \frac{k_d}{S_g}\Theta \tag{16}$$

where j_a is the net adsorption/desorption flux, t is the adsorption time, $\widetilde{B}(\Theta)$ is the generalized blocking function, k_a, k_d are the adsorption and desorption constants, and $n(\delta_a)$ is the concentration of particles at the adsorption boundary layer of the thickness δ_a.

To describe the net adsorption kinetics, Eq. (16) is used as the boundary condition for the bulk mass transfer equations formulated for various transport mechanisms. For most applications, the general blocking function $\widetilde{B}(\Theta)$ can be approximated by the above discussed RSA blocking functions $B(\Theta)$. Moreover, the kinetic adsorption and desorption constant occurring in Eq. (16) can be expressed in terms of physical parameters characterizing the transport conditions, such as the protein diffusion coefficient, the specific energy distribution governed by the depth of the primary minimum ϕ_m, the energy barrier height ϕ_b, etc. (*26*,

In Proteins at Interfaces III State of the Art 2012; Horbett, T., et al.;
ACS Symposium Series; American Chemical Society: Washington, DC, 2012.

27, *45*). This allows one to determine the depth of the energy minimum (binding energy) by comparing theoretical predictions derived from the phenomenological models with experimental results.

Eq. (16) is nonlinear and it is coupled with the bulk transport equation. Therefore, it cannot be analytically solved in the general case. However, limiting analytical solutions of vital significance can be derived (*26*). For example, under equilibrium conditions, where the adsorption flux vanishes, Eq. (16) reduces to the isotherm equation

$$\frac{\Theta_e}{B(\Theta_e)} = S_g K_a n_e \tag{17}$$

where Θ_e is the equilibrium coverage of the protein, $K_a = k_a / k_d$ is the equilibrium adsorption constant and n_e is the equilibrium concentration of particles in the bulk.

The adsorption isotherm, i.e., the dependence of Θ_e on n_b, can be derived by a numerical inversion of this equation.

Another limiting analytical solution can be derived from Eq. (16) in the case of a quasi-stationary transport, where the particle concentration $n(\delta_a)$ is in a local equilibrium with the surface coverage. This stems from the fact that the relaxation time of the bulk transport is usually much longer than the characteristic time of the surface coverage variations. Under such conditions the constitutive expression for the adsorption flux, Eq. (16) becomes (*27*)

$$j_a = \frac{K\,B(\Theta) - K_d\Theta}{(K-1)B(\Theta)+1} k_c n_b \tag{18}$$

where $K = k_a / k_c$ are the dimensionless coupling constants, $K_d = k_d / S_g k_c n_b$ is the dimensionless desorption constant, and k_c is the bulk transfer rate constant, known in analytical form for many types of flows and interface configurations (*45*, *46*).

In order to obtain an explicit dependence of the coverage on time, Eq. (18) can be integrated, which yields

$$\int_{\Theta_0}^{\Theta} \frac{(K-1)B\left(\Theta'\right)+1}{K\,B\left(\Theta'\right)-K_d\Theta'}\, d\Theta' = t / t_{ch} = \tau \tag{19}$$

where Θ_0 is the initial coverage of particles, $t_{ch} = 1 / S_g\, k_c\, n_b$ is the characteristic time of particle monolayer formation under convection transport conditions and $\tau = t / t_{ch}$ is the dimensionless time.

Eq. (19), with the blocking functions given by Eq. (12) or Eq. (15), represents a general solution for particle adsorption/desorption kinetics under convection driven transport. However, it can only be evaluated by numerical integration methods as done in Ref. (*26*) for the irreversible ($K_d = 0$), side-on adsorption of fibrinogen.

A more complicated situation arises in the case of diffusion-controlled adsorption of the protein. In this case the constitutive expression for the flux, Eq. (16), cannot be integrated directly because the flux from the bulk to the interface and the concentration $n(\delta_a)$ remain non-stationary for all times. In this case, to explicitly evaluate particle adsorption kinetics, one has to solve the non-stationary bulk diffusion equation with Eq. (16) serving as the boundary condition (*26*, *27*, *45*). For sake of convenience it is transformed to a dimensionless form involving the adsorption and desorption constants given by

$$\begin{aligned} \overline{k}_a &= k_a t_{ch} / L = \frac{1}{DS_g n_b} k_a \\ \overline{k}_d &= k_d t_{ch} = \frac{1}{D(S_g n_b)^2} k_d \end{aligned} \qquad (20)$$

where t_{ch}, L are the characteristic time and the length scale, respectively, defined as

$$\begin{aligned} t_{ch} &= L^2 / D = 1 / D(S_g n_b)^2 \\ L &= 1 / S_g n_b \end{aligned} \qquad (21)$$

As can be noticed, the characteristic monolayer formation time increases rapidly for diluted suspensions, proportionally to n_b^{-2} analogously as the dimensionless desorption constant $\overline{k}_d$. On the other hand, the dimensionless adsorption constant $\overline{k}_a$ increases proportionally to n_b^{-1}. As a result, these two parameters become very large for diluted protein solutions, often met under experimental conditions. Hence, for the above discussed case of fibrinogen (*26*), the characteristic adsorption time for the bulk protein concentration of 1 ppm ($n_b = 1.78 \times 10^{12}$ cm^{-3}) is 9.27×10^5 seconds and the adsorption constant $\overline{k}_a = 3 \times 10^5$. For n_b = 100 ppm ($n_b = 1.78 \times 10^{14}$ cm^{-3}), t_{ch} is reduced to 93 seconds and $\overline{k}_a = 3 \times 10^3$.

Using these data calculation were performed in Ref. (*26*) for the irreversible, side-on adsorption of fibrinogen controlled by diffusion.

It was shown that for such high values of $\overline{k}_a$ typical for fibrinogen adsorption for low concentration rages (1 to 10 ppm), adsorption kinetics remains linear in respect to $(t/t_{ch})^{1/2}$ until the coverage approaches 0.9 of the jamming coverage. In this case the surface concentration of adsorbed fibrinogen molecules is governed by the formula

$$N = 2\left(\frac{D}{\pi}\right)^{\frac{1}{2}} t^{\frac{1}{2}} n_b \qquad (22)$$

where n_b is the number concentration of fibrinogen molecules in the bulk.

Experimental Evidences

Fibrinogen Adsorption

In Ref. (*32*), measurements for the fibrinogen/mica system were performed with the aim of unequivocally elucidating adsorption mechanisms for such a model hydrophilic substrate.

In order to properly interpret these experimental data, thorough characteristics of fibrinogen solutions and mica were done. The electrophoretic mobility of fibrinogen as a function of pH and the ionic strength was determined using the micro-electrophoretic method. It was calculated from these measurements that the zeta potential of fibrinogen ζ_f for pH < 5.8 was positive, equal to 24 and 28 mV for pH = 3.5 and the ionic strength of 10^{-2} and 10^{-3} M, respectively. On the other hand, for pH = 7.4, ζ_f became negative, equal to - 19 and – 21 mV for the ionic strength of 10^{-2} and 10^{-3} M, respectively. Accordingly from the electrophoretic mobility measurements, the isoelectric point of fibrinogen (pH value where its electrophoretic mobility and zeta potential vanished) was pH = 5.8. The corresponding charge distribution over fibrinogen derived from these measurements and the above theoretical calculations is shown in Table 3.

Zeta potential of the mica substrate was determined via the streaming potential measurements according to the procedure described in Refs. (*35*, *53*, *54*). For the ionic strength of 10^{-3} M, zeta potential of mica was – 63 mV for pH = 3.5 and – 112 mV at pH = 7.4. For the ionic strength of 10^{-2} M, zeta potential of mica was less negative, equal to – 52 mV for pH = 3.5 and – 80 mV for pH = 7.4.

Fibrinogen adsorption experiments were conducted in Ref. (*32*) under diffusion-controlled transport and the number of adsorbed molecules was determined by AFM imaging (semi-contact mode, air) of the monolayers. The topology of fibrinogen monolayers on mica acquired in these experiments (pH = 3.5, $I = 10^{-2}$ M NaCl) is shown in Figure 1. For comparison, a monolayer of the same coverage derived from numerical simulations using Model A, is also shown. As can be seen, fibrinogen molecules appear as isolated entities, which facilitates their enumeration by AFM. Therefore, using this counting procedure the kinetics of fibrinogen adsorption on mica can be quantitatively evaluated.

In Figure 1 (Part b), the kinetics is shown as the dependence of the reduced surface concentration of fibrinogen N/c_b on the square root of the adsorption time $t^{1/2}$ (c_b is the fibrinogen bulk concentration in ppm connected with the number concentration n_b via the dependence $c_b = n_b 10^6 M_w/A_v$).

As can be seen, the experimental data in Figure 1b are in agreement with theoretical results (depicted by the solid line) stemming from Eq. (22), pertinent to an irreversible, diffusion-controlled adsorption mechanism (*26*, *27*).

It is worthwhile observing that results shown in Figure 1b have interesting practical implications because one can conveniently determine the unknown bulk concentration of fibrinogen by plotting N vs. the square root of adsorption time, $t^{1/2}$. As discussed in Ref. (*32*) one can accurately determine fibrinogen concentration of 0.1 ppm and less.

part „a"

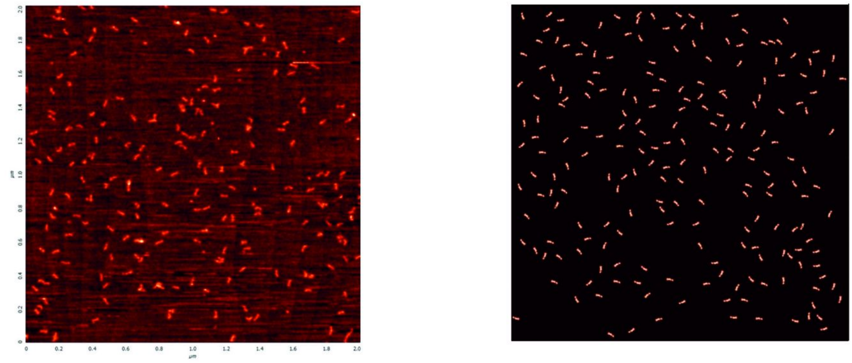

Experimental, AFM

Simulations

part „b"

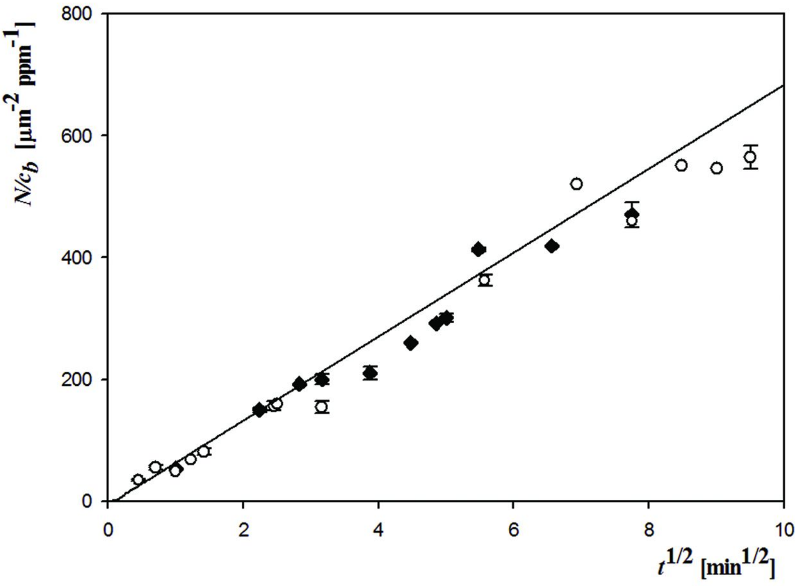

Figure 1. Part "a". Experimental (l.h.s. of the picture) and simulated (MC-RSA method, r.h.s. of the picture) monolayers of fibrinogen on mica at the coverage of 0.67%. Part "b". The dependence of the reduced surface concentration of fibrinogen N/c_b [µm^{-2} ppm^{-1}] on the square of adsorption time $t^{1/2}$, $I = 10^{-3}$ M. The full points denote experimental results obtained by a direct AFM enumeration for pH = 3.5 (various bulk concentration of fibrinogen) and the hollow points denote results obtained for pH = 7.4. The solid line shows exact theoretical results obtained using the RSA model. Adapted with permission from Ref. (39). Copyright 2011 Elsevier.

Table 4. Mechanisms of fibrinogen adsorption on hydrophilic surfaces and immobilization of colloid particle on its monolayers

Adsorption mechanism	Physicochemical conditions	Remarks
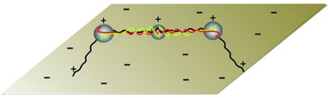	pH <5, $I = 10^{-2} – 0.15$ M	Side-on mechanisms
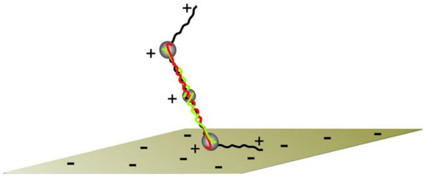	pH <5, $I = 10^{-2} – 0.15$ M	End-on, transient mechanism
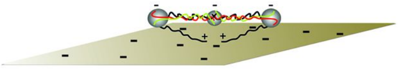	pH > 6, $I <10^{-3}$ M	Side-on, “levitation”
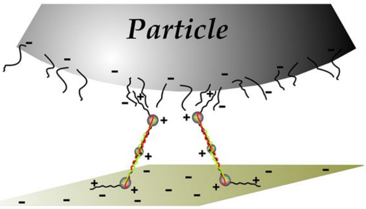	pH <5, $I = 8x10^{-4}$ M	‘hopping’ mechanism of colloid immobilization (two Fb molecules forming the site)
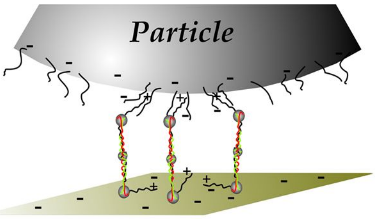	pH > 6, $I = 10^{-2} – 0.15$ M	‘hopping’ mechanism of colloid immobilization (three Fb molecules forming the site)

The results shown in Figure 1b suggest that fibrinogen adsorption on mica for pH = 3.5 was irreversible and bulk transport controlled with negligible surface transport resistance. This seems quite natural considering the strong attraction between fibrinogen molecules and the oppositely charged mica substrate. Under these circumstances the fibrinogen molecules could adsorb side-on as schematically shown in Table 4.

However, identical adsorption kinetics of fibrinogen was also observed in the case of pH = 7.4 (see Figure 1b), where the average (mean-field) zeta potential of fibrinogen and mica were both negative. It should be mentioned that such anomalous fibrinogen adsorption at pH = 7.4 was previously observed by Zembala and Dejardin (*31*), Malmsten (*25*), Ortega-Vinuesa et al. (*14*, *15*), Toscano and Santore (*19*) and Kalasin and Santore (*43*).

This anomalous adsorption can be explained in terms of a heterogeneous charge distribution over the fibrinogen molecule above predicted (see Table 3). Thus, the molecules could efficiently adsorb in the side-on orientation with the arms touching the interface and the main body levitating above the surface. The distance between the molecule and the interface can be changed by regulating the ionic strength. Thus, it can exceed 10 nm for ionic strength of 10^{-3} M and below. Such an adsorption mechanism is shown schematically in Table 4.

However, the AFM measurements alone cannot furnish a decisive proof of this hypothesis. This can be achieved via the *in situ* measurements done under wet conditions using the streaming-potential and colloid deposition methods.

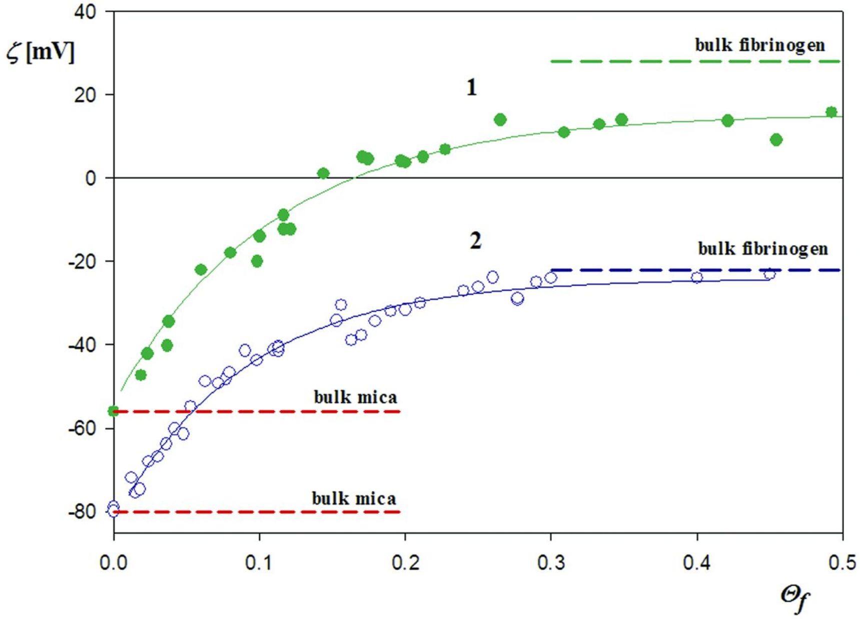

Figure 2. The dependence of the zeta potential of mica ζ on the coverage of fibrinogen Θ_f. The points denote experimental results obtained from the streaming potential measurements for 1. pH = 3.5, 2. pH = 7.4, I = 10^{-2} M NaCl. The solid lines represent exact theoretical results calculated according to the electrokinetic model developed in Refs. (33, 35).

Streaming Potential Measurements

Streaming potential measurements were carried out using a home-made apparatus exploiting the parallel-plate channel flow, according to the procedure previously described (*32*, *35*, *52–54*). Two series of experiments were carried out for pH = 3.5 and 7.4. The dependence of the streaming potential on the coverage of fibrinogen adsorbed in situ under diffusion transport was systematically studied. From these measurements the zeta potential of fibrinogen covered mica ζ was calculated using the Smoluchowski equation.

The dependencies of ζ on the fibrinogen coverage for pH = 3.5 and 7.4 are shown in Figure 2. As seen, pH = 3.5, where Fb is positively charged, a steep, quasi-linear increase in the zeta potential of mica is observed for $\Theta_f < 0.1$. Then, for $\Theta_f > 0.16$ (inversion point), the zeta potential of mica becomes positive and it approached the saturation value, which is markedly lower than the bulk zeta potential of fibrinogen (equal to 24 mV for this pH).

At pH = 7.4 (lower curve, Figure 2) the mica zeta potential also increased monotonically with the fibrinogen coverage but it remained negative, attaining the value of -20 mV for higher coverage. This is close to being bulk value of fibrinogen at this pH (-19 mV).

It was additionally confirmed in separate desorption experiments (*32*) that no changes in the fibrinogen covered mica zeta potential were observed upon flushing the cell with pure electrolyte over a prolonged time period. These experiments proved, therefore, that fibrinogen adsorbed irreversibly on mica surface both at pH = 3.5 and 7.4, which agrees with previous observations shown in Figure 1b.

More refined analysis of this behavior was carried out in terms of the electrokinetic model developed in Refs. (*33–35*), which considers a uniform 3D distribution of charge over adsorbed protein molecules. This model was successfully applied for interpreting the zeta potential of surfaces covered by colloid particles (*55*) and polyelectrolytes (*37*). As seen in Figure 2, for pH = 3.5, theoretical results derived from this model, where a side-on adsorption of fibrinogen was assumed, quantitatively agree with experimental data for the entire range of coverage. This is a quite interesting because such a unique, functional dependence enables a precise determination, via the streaming potential measurements, of the coverage of fibrinogen under wet, in situ conditions. This also implies that the bulk concentration of fibrinogen can be precisely measured by this method. Given the large slope of the zeta vs. fibrinogen coverage dependence one can expect that this method is more robust, than others, chemical type, methods.

As observed in Figure 2, the theoretical model also works for pH = 7.4 (lower curve). However, in this case, agreement with experiments is attained using the effective zeta potential of adsorbed fibrinogen molecules of – 30 mV, which is considerably more negative than in the bulk (-19 mV). This observation supports the side-on adsorption mechanism of fibrinogen shown in Table 4, where the positively charged arms form bonds with the substrate and the more negative body of the molecule is exposed to the flow.

Colloid Deposition on Fibrinogen Layers

Additional information about the dynamic behavior of fibrinogen monolayers on mica can be acquired via the colloid deposition method. In Ref. (*39*) systematic experiments of this kind involving negative and positive polystyrene latex particles (referred to as the L800 sample) were performed. In the first step of these experiments fibrinogen monolayers of desired coverages were produced and fully characterized by the streaming potential measurements. Afterwards, latex deposition was carried out in a thermostated cell under diffusion over time period of 24 hours. The number of latex particle adsorbed as a function of deposition time was determined by optical microscope imaging under wet conditions and independently by AFM imaging in air. An advantage of the optical microscopy is that it enables measurements to be carried out under wet conditions, where particle positions over the substrate surface remain undisturbed. This allows one to reliably determine the coverage of particles and their distributions over bare and fibrinogen covered substrates.

These measurements enabled one to determine unique functional dependencies between the fibrinogen coverage Θ_f and the maximum coverage of latex particles deposited after long period of time Θ_L. Such dependency obtained for a negative polystyrene latex, having the zeta potential of -105 mV at pH = 3.5, $I = 10^{-2}$ M is plotted in Figure 3. The inset shows the latex particle monolayer at the maximum coverage $\Theta_{max} = 0.48$, which was used as a normalization variable in Figs. 3 - 5. As can be seen, Θ_L/Θ_{max} increases abruptly with the fibrinogen coverage, attaining 0.9 for $\Theta_f = 0.1$ and almost 1 (a saturated latex monolayer coverage) for $\Theta_f = 0.16$. These results are rather unexpected given the negative zeta potential both of the latex and mica covered by fibrinogen (see Figure 2). Indeed, the classical DLVO theory, based on the concept of mean-field zeta potential, predicts a negligible latex deposition for this range of fibrinogen coverage (dashed line in Figure 3a). As discussed in Ref. (*39*) this deviation of experimental results from the DLVO theory is direct proof of a heterogeneous charge distribution over mica induced by fibrinogen coverage fluctuations. Because fibrinogen molecules exhibited a net positive zeta potential at pH = 3.5, a local increase in their concentration at mica could lead to formation of favorable adsorption sites, capable of immobilizing latex particles. This effect was analyzed in terms of the fluctuation theory developed to interpret particle deposition on surfaces covered by polyelectrolytes (*35–37*) and fibrinogen molecules (*39*).

The basic assumption of the charge fluctuation approach is that particle adsorption occurs at sites formed by n_f fibrinogen molecules adsorbed close to each other. Depending on the number of molecules forming a site population, they differ in the binding strength of colloid particles. The sites are assumed to be randomly distributed over the substrate surface (*39*) Accordingly, the coverage of sites formed by n_f fibrinogen molecules is governed by the Poisson statistics, i.e.,

$$\Theta_s\left(n_f\right) = \frac{\left(\Theta_f\right)^{nf}}{n_f!} \qquad (23)$$

With this assumption, using the RSA theory of site covered surfaces (*56*), one can calculate the latex coverage on fibrinogen monolayers from the analytical expression

$$\Theta_L / \Theta_{max} = 1 - \frac{1 + 0.314\alpha^2 + 0.45\alpha^3}{1 + \frac{1}{\Theta_{max}}\alpha + 0.66\alpha^3 + \alpha^{7/2}} \qquad (24)$$

where $\alpha(n_f) = \pi a^2 N_s(n_f) = \lambda^2 \Theta_s(n_f)$ and λ^2 is the ratio of the latex to fibrinogen cross-section area, equal to 3.93×10^3 in this case.

As can be seen in Figure 3, theoretical results predicted from Eq. (24) properly reflect experimental data if $n_f = 2$ is assumed (see curve 2). On the other hand, theoretical results calculated for $n_f = 1$ (curve 1 in Figure 3a) considerably overestimate the experimental data. This means that an efficient latex particle immobilization is only possible on sites formed by two fibrinogen molecules adsorbed close to each other. This is an essential finding which provides valuable hints concerning mechanisms of colloid particle deposition on fibrinogen monolayers. Therefore, in Refs. (*39*, *57*) extensive measurements were performed, where the role of pH and ionic strength in latex particle deposition on fibrinogen monolayers was systematically studied.

In Figure 3b such dependencies of Θ_L/Θ_{max} on Θ_f acquired for various pH (equal to 3.5, 7.4, 9.7 and 11) at a fixed ionic strength of 10^{-2} M are presented. As observed, in contrast to previously shown dependence for pH = 3.5 (Figure 3a), the results obtained for pH = 7.4 and 9.7 can be well accounted for by the theoretical model, given by Eq. (24), if $n_f = 3$ is assumed. This means that an efficient latex particle immobilization at this pH occurred on sites formed by three fibrinogen molecules. On the other hand, for pH = 11 there was practically no deposition of latex on fibrinogen covered mica.

Additional series of experiments were also performed in Ref. (*57*) to elucidate the role of the ionic strength at a fixed pH = 4. The results of these experiments are shown in Figure 4. As shown, all results obtained for ionic strength within the range 0.15 to 10^{-3} M are practically the same (within experimental error bounds) and can be well described by the theoretical model assuming $n_f = 2$. However, for lower ionic strength, the latex deposition efficiency (expressed as the Θ_L/Θ_{max} on Θ_f dependencies) abruptly decreases, and vanishes for $I = 3 \times 10^{-4}$ M.

It is interesting to mention that analogous results were previously reported in Ref. (*36*) where kinetics of deposition of negatively charged polystyrene latex particles on a cationic polyelectrolyte monolayers (poly allylamine hydrochloride, PAH) pre-adsorbed on mica was studied. Ionic strength in these experiments was either 10^{-2} or 10^{-3} M, NaCl. It was demonstrated that the increase in the maximum coverage of latex with the PAH coverage could be properly reflected by Eq. (24) assuming that the efficient adsorption site is formed by four closely spaced PAH molecules.

part „a”

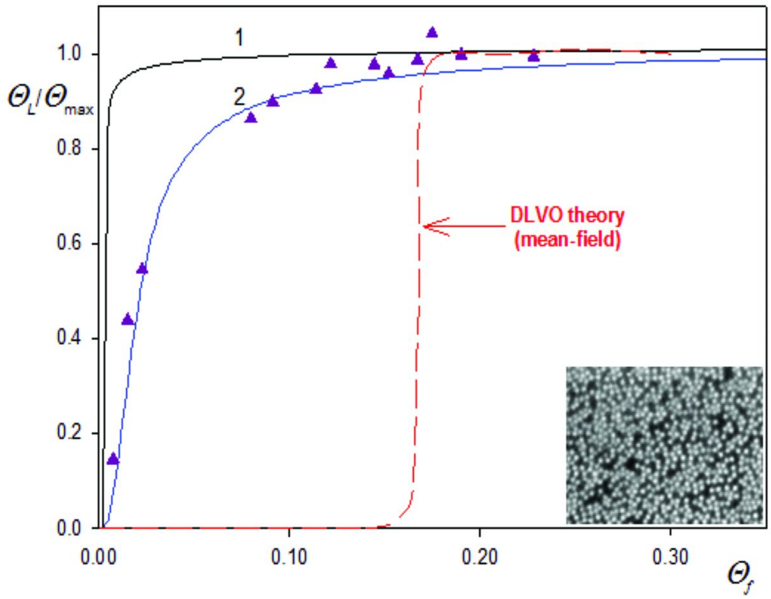

part „b”

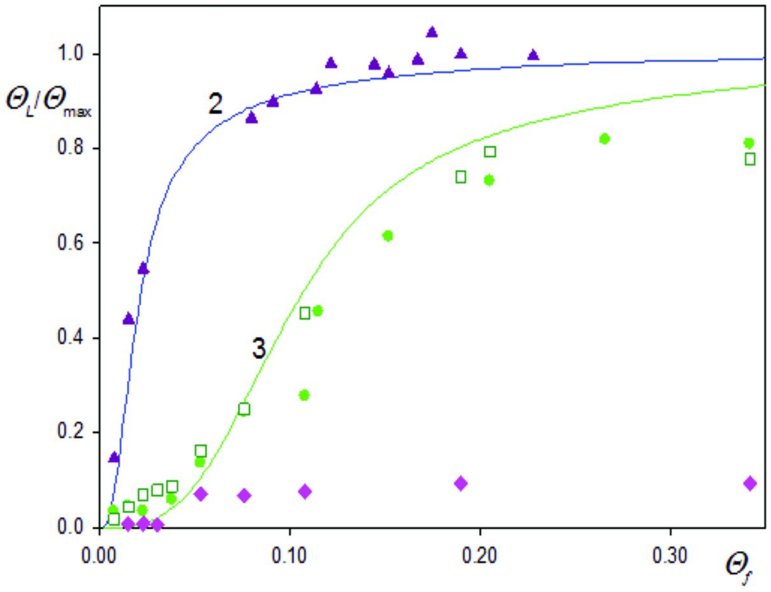

Figure 3. Part "a". The dependence of the normalized coverage of latex particles, Θ_L/Θ_{max} on the fibrinogen coverage Θ_f The points (▲) denote the averaged experimental results obtained by optical microscopy and AFM, for ionic strength 10^{-2} M, pH = 3.5, T = 293 K. The solid lines 1-2 denote theoretical

prediction derived from the fluctuation theory, Eqs. (23, 24) for the adsorption site composed of one and two fibrinogen molecules, respectively (23, 24). The dashed line denotes the theoretical results derived from the mean-field DLVO theory. The inset shows the latex monolayer deposited on fibrinogen monolayer for $\Theta_L = \Theta_{max} = 0.48$ Part "b", The dependence of the normalized coverage of latex particles, Θ_L/Θ_{max} on the fibrinogen coverage Θ_f. The points denote the averaged experimental results obtained for ionic strength of 10^{-2} M and various pH: (▲), pH = 3.5, (●), pH = 7.4, (□), pH = 9.7, ((), pH = 11. The solid line denotes theoretical prediction derived from the fluctuation theory, Eqs. (23, 24) for the adsorption site composed of two (curve 2) and three (curve 3) fibrinogen molecules.

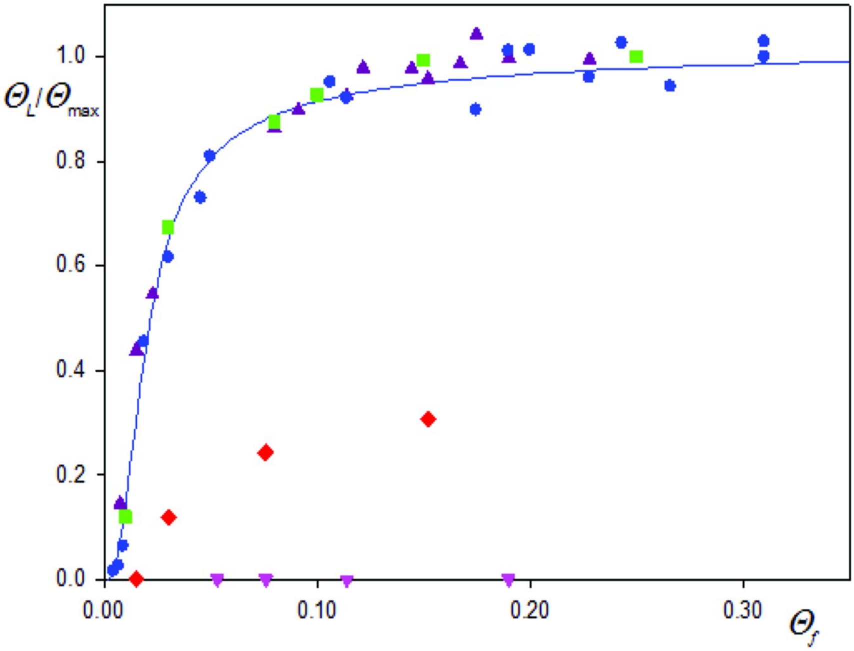

Figure 4. The dependence of the normalized coverage of latex particles, Θ_L/Θ_{max} on the fibrinogen coverage Θ_f The points denote the averaged experimental results obtained by optical microscopy and AFM for pH = 3.5 – 4, (■), ionic strength 0.15 M; (▲), ionic strength 10^{-2} M; (●), ionic strength 10^{-3} M; (♦), ionic strength $8x10^{-4}$ M; (▼), ionic strength $3x10^{-4}$ M. The solid line denotes theoretical prediction derived from the fluctuation theory, Eqs. (23, 24) for the adsorption site composed of two fibrinogen molecules.

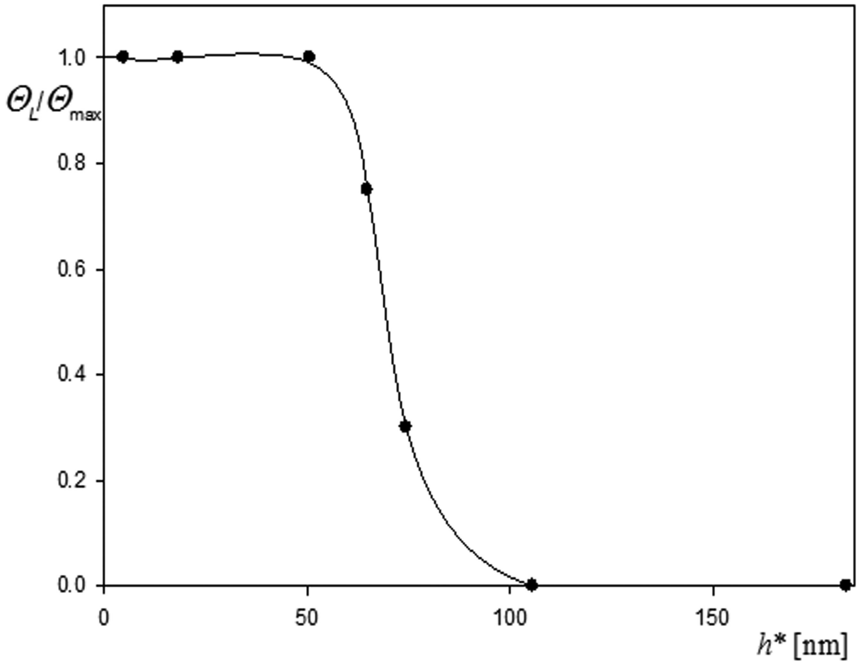

Figure 5. The dependence of the normalized coverage of L800 latex particles, Θ_L/Θ_{max} on the minimum approach distance h.The points denote the averaged experimental results obtained by optical microscopy and AFM for pH = 3.5 - 4 and the solid line is the non-linear fit of experimental data.*

A quantitative interpretation of these results requires a thorough analysis of the interaction energy profile of the latex particle with the mica substrate covered by the protein for various ionic strength and pH (*57*). Briefly speaking, because of the highly negative zeta potential of latex and mica under these experimental conditions, there appears a considerable repulsion extending over distances many times larger than the electrical double-layer thickness $\kappa^{-1} = (\varepsilon kT / 2e^2 I)^{1/2}$ (ε is the dielectric permittivity of the liquid, e is the elementary charge). It was estimated in Ref. (*57*) that the minimum approach distance of latex particles to the mica interface h^* equals to 6 κ^{-1}. This means that for $I = 10^{-2}$ M, $h^* = 18.3$ nm, for $I = 10^{-3}$ M, $h^* = 54.3$ nm and for $I = 6\text{x}10^{-4}$ M (pH = 4), $h^* = 74.4$ nm. Thus, latex particles practically cannot approach the mica substrate at distances closer than h^*. This excludes the possibility that they can deposit directly on fibrinogen molecules, because their diameter is 6.7 nm (see Table 1). Therefore, latex deposition becomes only possible if they contact the arms protruding from the fibrinogen molecule. However, as stated above, the length of these arms is 18 nm, thus latex deposition for ionic strength below 10^{-3} M would not be possible. This contradicts experimental observations which are presented in Figure 5 as the dependence of the normalized latex coverage Θ_L/Θ_{max} (for $\Theta_f = 0.1$) on the minimum approach distance h^*. As can be seen in Figure 5, the threshold value (which is defined as the value where Θ_L/Θ_{max} falls to 0.5) is 75 nm. This considerably exceeds not only the diameter of the fibrinogen molecule but also its length of 49 nm (see Table 1). However, this threshold distance is quite close to the length of the molecule with fully extended arms, equal to 67 nm.

Hence, the most probable mechanism which accounts for these experimental findings is the 'hopping' mechanism shown schematically in Figure 6 (*57*). Accordingly, latex deposition on fibrinogen monolayers is a multistage process consisting of following steps:

(i) One of a few closely separated fibrinogen molecules adsorbed in the side-on configuration is activated due to natural fluctuations and transferred into the transient end-on configuration.
(ii) Latex particle is immobilized on the end of the arm and a transient fibrinogen/latex complex is formed.
(iii) The immobilized latex particle forms additional contact with the next fibrinogen molecule activated into the end-on configuration. The binding energy is increased twice.

Obviously step (iii) can be repeated since additional bonds between the interface and the latex particle can be formed via fibrinogen molecules, with the binding energy increasing in a quantum-like fashion (i.e., two-, three-, etc. times). This ensures irreversible immobilization of latex.

It was shown in Ref. (*57*) by performing calculations of the probability of the appearance of the transient state of fibrinogen and the fibrinogen/latex complex that it is sufficiently high to irreversibly immobilize latex particles over the time of 24 hours. It was also shown that the for low pH, where the fibrinogen molecule is strongly charged, two bonds formed between the arm and the latex particles are sufficient to irreversibly capture a single latex particle. On the other hand, for pH = 7.4 and above, because of the decreased charge of the arms, three bonds are needed. For pH > 9.7, the charge of the amidine groups stemming from lysine and arginine amino acids vanishes, which prohibits latex deposition.

Although these results were obtained for the model system mica/fibrinogen/latex, it is expected that a similar mechanism can explain bioparticle immobilization on fibrinogen monolayers leading to clotting and thrombus formation.

It is also interesting to mention that the proposed hopping mechanism can be used to explain above mentioned results concerning latex deposition on PAH monolayers (*36*).

A decisive argument to support this conclusion is that the hydrated diameter of the PAH molecule is only 1.13 nm (*36*), whereas the minimum approach distance of latex particles varies between 18.3 and 54.3 nm for $I = 10^{-2}$ and 10^{-3}

M, respectively, as above discussed. Thus, the only possibility to form an efficient contact between a latex particle and adsorbed PAH molecules is if the latter are activated into the end-on conformations forming tails or loops.

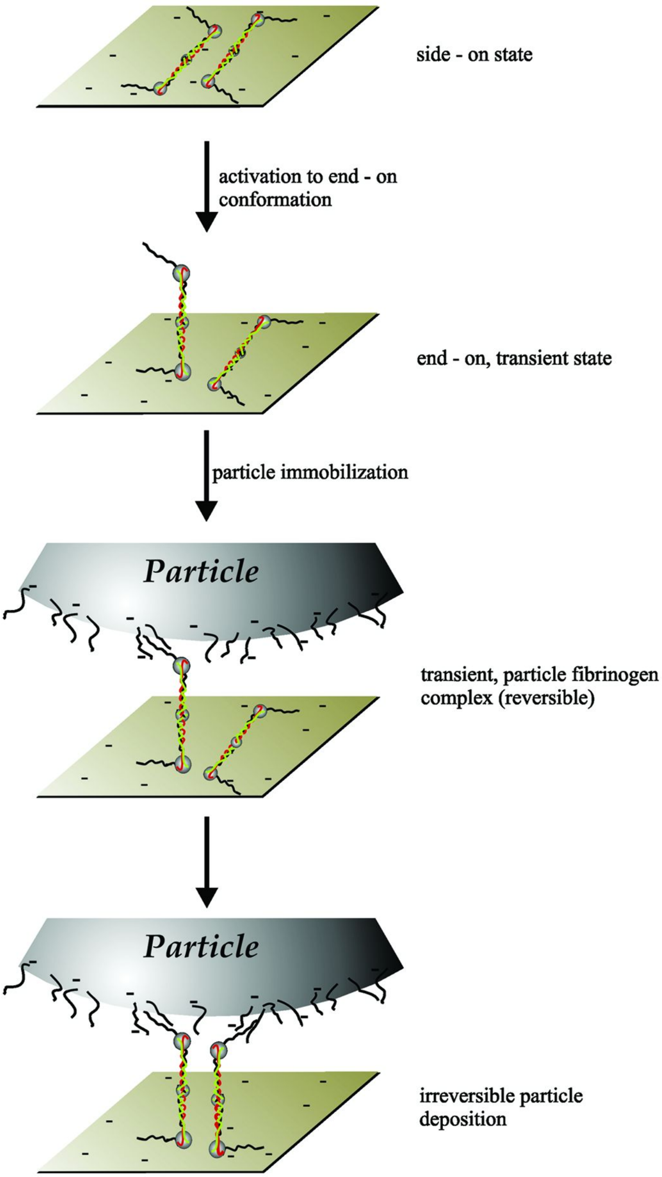
side - on state
activation to end - on conformation
end - on, transient state
particle immobilization
Particle
transient, particle fibrinogen complex (reversible)
Particle
irreversible particle deposition

Figure 6. A schematic view of the colloid deposition mechanism of fibrinogen monolayers.

Conclusions

Analysis of experimental data obtained by DLS, microelectrophoretic and dynamic viscosity measurements, in terms of theoretical approaches based on bead modeling, revealed a highly heterogeneous charge distribution over the fibrinogen molecule. The positive charge, (up to pH = 9.7), is located at ends of the Aα chains, and the negative charge is mainly located at the main body of the molecule. However, for pH close to 4, the entire molecule is positively charged.

The highly anisotropic charge distribution predicted for pH 7.4 - 9.7 explains anomalous adsorption of fibrinogen at negatively charged surfaces such as mica at this pH range determined by AFM enumeration of isolated fibrinogen molecules and *in situ* streaming potential measurements. It was also confirmed that fibrinogen adsorption for a coverage range below 0.3 proceeds irreversibly according to the side-on mechanism.

Colloid deposition experiments confirmed, however, the existence of dynamic transient state of fibrinogen molecules in the end-on orientations. Based on this hypothesis a multistage ‘hopping’ mechanism of colloid particle deposition on fibrinogen monolayers was proposed. The essential point is that particles are immobilized on the end part of the arms forming a transient fibrinogen/latex complex. An irreversible immobilization of colloid particles is finally achieved if two or more additional bonds are formed with closely separated fibrinogen molecules. This also explains ‘quantum’ effects experimentally observed in latex deposition on fibrinogen monolayers.

Although these results were obtained for the model system mica/fibrinogen/latex, it is expected that the above mechanism is quite universal explain also deposition of colloid or bioparticles on polyelectrolyte monolayers formed on solid substrates.

Acknowledgments

This work was partially supported by the MNiSZW Grant No.: N N204 026438.

References

1. Doolittle, R. F. *Annu Rev. Biochem.* **1984**, *53*, 195–229.
2. Herrick, S.; Blanc – Brude, O.; Gray, A.; Laurent, G. *J. Biochem. Cell Biol.* **1999**, *31*, 741–746.
3. Lim, B.; Lee, E. H.; Sotomayor, M.; Schulten, K. *Structure* **2008**, *16*, 449–459.
4. Blombäck, B. *Thromb. Res.* **1996**, *83*, 1–75.
5. Mosesson, M. W. *J. Thromb. Haemostasis* **2005**, *3*, 1894–1904.
6. Ehrlich, P.; Shulman, S.; Ferry, J. D. *J. Am. Chem. Soc.* **1952**, *74*, 2258–2265.
7. Katz, S.; Gutfreund, K.; Shulman, S.; Ferry, J. D. *J. Am. Chem. Soc.* **1952**, *74*, 5706.
8. Shulman, S. *J. Am. Chem. Soc.* **1953**, *75*, 5846.

9. Hall, C. E.; Slayter, H. S. *J. Biophys. Biochem. Cytol.* **1959**, *5*, 11–16.
10. Fowler, W. E.; Erickson, H. P. *J. Mol. Biol.* **1979**, *134*, 241–249.
11. Weisel, J. W.; Stauffacher, C. V.; Bullitt, E.; Cohen, C. *Science* **1985**, *230*, 1388–1391.
12. Verklich, Y. I.; Gorkum, O. V.; Medved, L. V.; Nieuwenhuizen, W.; Weisel, J. W. *J. Biol. Chem.* **1993**, *268*, 13577–13585.
13. RCSB Protein Data Bank, http://www.pdb.mde-berlin.de
14. Ortega - Vinuesa, J. L.; Tengvall, P.; Lundström, I. *Thin Solid Films* **1998**, *324*, 257–273.
15. Ortega - Vinuesa, J. L.; Tengvall, P.; Lundström, I. *J. Colloid Interface Sci.* **1998**, *207*, 228–239.
16. Sit, P. S.; Marchant, R. E. *J. Thromb. Haemostasis* **1999**, *82*, 1053–1060.
17. Marchin, K. L.; Berrie, C. L. *Langmuir* **2003**, *19*, 9883–9888.
18. Jung, S. Y.; Lim, S. M.; Albertorio, F.; Kim, G.; Gurau, M. C.; Yang, R. D.; Holden, M. A.; Cremer, P. S. *J. Am. Chem. Soc.* **2003**, *125*, 12782–12786.
19. Toscano, A.; Santore, M. M. *Langmuir* **2006**, *22*, 2588–2597.
20. Averett, L. E.; Schoenfisch, M. H. *Analyst* **2010**, *135*, 1201–1209.
21. Watt, K. W. K.; Takagi, T.; Doolittle, R. F. *Proc. Natl. Acad. Sci. U.S.A.* **1978**, *75*, 4731.
22. Henschen, A.; Lottspeich, F.; Kehl, M.; Southan, C. *Ann N. Y. Acad. Sci.* **1983**, *408*, 28.
23. Wasilewska, M.; Adamczyk, Z.; Jachimska, B. *Langmuir* **2009**, *25*, 3698–3704.
24. Adamczyk, Z.; Cichocki, B.; Ekiel – Jeżewska, M. L.; Słowicka, A.; Wajnryb, E.; Wasilewska, M. *J. Colloid Interface Sci.*, in press.
25. Malmsten, M. *J. Colloid Interface Sci.* **1994**, *166*, 333–342.
26. Adamczyk, Z.; Barbasz, J.; Cieśla, M. *Langmuir* **2010**, *26*, 11934–11945.
27. Adamczyk, Z.; Barbasz, J.; Cieśla, M. *Langmuir* **2011**, *27*, 6868–6878.
28. Norde, W.; Rouwendal, E. *J. Colloid Interface Sci.* **1990**, *139*, 169–176.
29. Elgersma, A. V.; Zsom, R. L. J.; Lyklema, J.; Norde, W. *J. Colloid Interface Sci.* **1990**, *138*, 145–156.
30. Norde, W.; Arai, T.; Shirahama, H. *Biofouling* **1991**, *4*, 37–51.
31. Zembala, M.; Dejardin, P. *Colloids Surf., B* **1994**, *3*, 119–129.
32. Wasilewska, M.; Adamczyk, Z. *Langmuir* **2011**, *27*, 686–696.
33. Adamczyk, Z.; Warszyński, P.; Zembala, M. *Bull. Pol. Acad. Sci. Chem.* **1999**, *47*, 239–258.
34. Sadlej, K.; Wajnryb, E.; Bławzdziewicz, J.; Ekiel – Jeżewska, M. L.; Adamczyk, Z. *J. Chem. Phys.* **2009**, *30*, 144706–144711.
35. Adamczyk, Z.; Nattich, M.; Wasilewska, M.; Zaucha, M. *Adv. Colloid Interface Sci.* **2011**, *168*, 3–28.
36. Adamczyk, Z.; Zembala, M.; Michna, A. *J. Colloid Interface Sci.* **2006**, *303*, 353–364.
37. Adamczyk, Z.; Michna, A.; Szaraniec, M.; Bratek, A.; Barbasz, J. *J. Colloid Interface Sci.* **2007**, *313*, 86–96.
38. Adamczyk, Z.; Nattich, M.; Wasilewska, M. *Adsorption* **2010**, *16*, 259–269.
39. Adamczyk, Z.; Nattich, M.; Wasilewska, M.; Sadowska, M. *J. Colloid Interface Sci.* **2011**, *356*, 454–464.

40. Brenner, H. *Int. J. Multiphase Flow* **1974**, *1*, 195–341.
41. Harding, S. E. *Biophys. Chem.* **1995**, *55*, 69–93.
42. Tsapikouni, T. S.; Missirlis, Y. F. *Colloids Surf., B* **2007**, *57*, 89–96.
43. Kalasin, S.; Santore, M. M. *Colloids Surf., B* **2009**, *73*, 229–236.
44. Adamczyk, Z.; Bratek-Skicki, A.; Dąbrowska, P.; Nattich-Rak, M. *Langmuir* **2012**, *28*, 474–485.
45. Adamczyk Z. *Particles at Interfaces*; Hubbard, A., Ed.; Elsevier Academic Press: Amsterdam, 2006
46. Viot, P.; Tarjus, G.; Ricci, S. M.; Talbot, J. *J. Chem. Phys.* **1992**, *97*, 5212–5218.
47. Ricci, S.; Talbot, J.; Tarjus, G.; Viot, P. *J. Chem. Phys.* **1992**, 5219–5228.
48. Talbot, J.; Tarjus, G.; van Tassel, P.; Viot, P. *Colloid Surf., A* **2000**, *165*, 287–324.
49. Hinrichsen, E.; Feder, J.; Jossang, T. *J. Stat. Phys.* **1986**, *44*, 793–827.
50. Weroński, P. *Adv. Colloid Interface. Sci.* **2006**, *118*, 1–24.
51. Adamczyk, Z. *Curr. Opin. Colloid Interface Sci.* **2012**, *17*, 173–186.
52. Scales, P. J.; Grieser, F.; Healy, T. W. *Langmuir* **1990**, *6*, 582–589.
53. Scales, P. J.; Grieser, F.; Healy, T. W; White, L. R.; Chan, D. Y. C. *Langmuir* **1992**, *8*, 965–974.
54. Zembala, M. *Adv. Colloid Interface Sci.* **2004**, *112*, 59–92.
55. Adamczyk, Z.; Zaucha, M.; Zembala, M. *Langmuir* **2010**, *26*, 9368–4377.
56. Jin, X.; Wang, N. H. L.; Tarjus, G.; Talbot, J. *J. Phys. Chem.* **1993**, *97*, 4256–4258.
57. Nattich – Rak, M.; Adamczyk, Z.; Sadowska, M. *Colloids Surf., B*, in preparation.

Chapter 6

AFM-Based Friction Force Spectroscopy: A Novel Methodology for the Study of the Strength and Lateral Diffusion of Proteinaceous Films

Javier Sotres,[1] Liselott Lindh,[2] Olof Svensson,[1] Alejandro Barrantes,[1] and Thomas Arnebrant*,[1]

[1]Biomedical Science, Faculty of Health and Society, Malmoe University, 20506 Malmoe, Sweden
[2]Prosthetic Dentistry, Faculty of Odontology, Malmoe University, 20506 Malmoe, Sweden
***E-mail: thomas.arnebrant@mah.se**

We present a novel methodology for the study of proteinaceous films based on the friction force spectroscopy operation mode of the atomic force microscope. It provides information both on the strength at the nanoscale level and on the lateral diffusion properties of these systems. The usefulness of the data generated by this methodology are shown through its application to the study of different types of monolayers of model proteins, as well as to the study of the more complex and heterogeneous salivary films.

Introduction

Proteinaceous films can confer diverse properties to surfaces such as specific sensing (*1*, *2*), stabilization of emulsions/dispersions (*3*), biocompatibility (*4*, *5*), or simply act as protective/lubricant barriers (*6*, *7*). Here we present a novel method for their study based on the friction force spectroscopy (FFS) operation mode of the atomic force microscope (AFM) (*8*, *9*). Basically, in this mode the

In Proteins at Interfaces III State of the Art 2012; Horbett, T., et al.;
ACS Symposium Series; American Chemical Society: Washington, DC, 2012.

AFM tip is raster scanned across the sample surface while varying the applied load force. In other words, an AFM tip is used to scratch the samples. It is then not surprising that operating in this mode allows probing the resistance of the films to externally applied mechanical damage (*10–13*). This information is itself of great value due to the vast number of natural and artificial systems where proteinaceous films are present and exposed to mechanical damage (*14–18*). Moreover, we have showed that AFM-based FFS is capable of providing information on lateral diffusion processes within the probed films (*10–13*). For a comprehensive understanding of the methodology and of the results it provides, we present here a general overview of the methodology itself followed by its application to the study i) of model layers of soft globular proteins (bovine serum albumin, BSA), ii) of model layers of amphiphilic disordered proteins (β-casein), and iii) of the more complex and heterogeneous salivary films.

AFM-Based Friction Force Spectroscopy

The methodology presented employs an AFM operated in the FFS mode for probing the proteinaceous films. An AFM uses a sharp (nm-sized) tip attached at the free end of a cantilever to probe the samples. The normal deflection and lateral torsion of the cantilever can be detected with high precision so that the applied load force (directly related to the normal deflection) and the friction force between tip and sample (directly related to the lateral torsion) can be measured with sub-nanoNewton resolution (Figure 1a). Because of these characteristics and its ability to operate in a liquid environment, AFM is an ideal technique for probing the mechanical properties of nm-sized biological coatings. The most common way of operating an AFM consists in scanning the surface of the samples while simultaneously varying the vertical position of the sample in order to keep constant the load applied by the tip. In this way, the inverse of the sample vertical position is registered and associated to the topography. The capability of recording simultaneously topography and friction constitutes the basis for AFM-based FFS. Specifically, the methodology is based on performing two-dimensional constant-load scans of the surface of the films. For each of these scans the topography (height image) of the sample is registered, as well as the average value of the friction force registered during the two-dimensional scan. Then the applied load is modified between the scans. Thus, the response of the films to the scratch is characterized by the dependence with the applied load of the topography of the sample (Figure 1b) and of the tip-sample friction (Figure 1d). Along with the two-dimensional height images, the evolution of the topography is also represented by plotting the average roughness (here the height standard deviation) of each of the scans against the load applied during their acquisition (Figure 1c). The interested reader is referred to (*10*) for a more detailed technical description of AFM-based FFS.

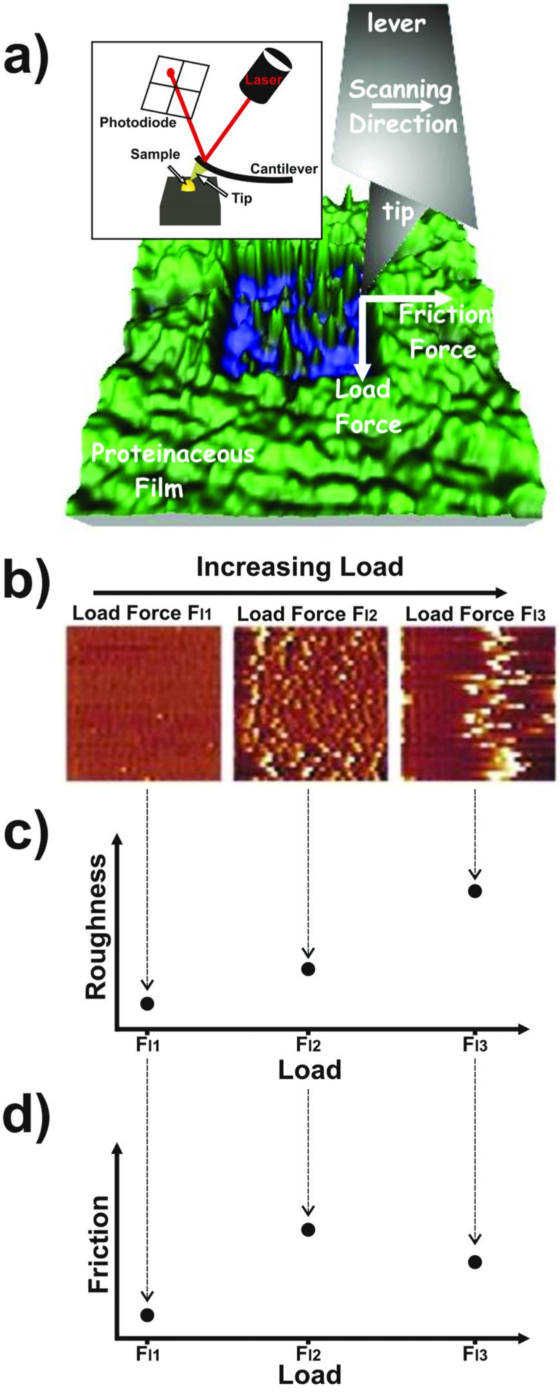
a)
lever
Scanning
Direction
Laser
Photodiode
Sample
Cantilever
Tip
tip
Friction
Force
Load
Force
Proteinaceous
Film
b)
Increasing Load
Load Force F_{l1}
Load Force F_{l2}
Load Force F_{l3}
c)
Roughness
F_{l1}
F_{l2}
F_{l3}
Load
d)
Friction
F_{l1}
F_{l2}
F_{l3}
Load

Figure 1. ***a)*** *Illustration of an AFM tip scratching a proteinaceous film. While scanning the sample, both load and friction forces are exerted. These forces induce vertical and torsional deflections of the cantilever. A position sensitive photodiode is used to monitor these deflections, or more specifically, the deviations of a laser beam reflected on the back of the free end of the cantilever (see figure inset).* ***b)*** *Examples of topography images recorded during the scratch of a proteinaceous film (specifically a β-casein monolayer). Scan area: 2µm x 2µm. Color scale goes from 0nm (black) to 6nm (white).* ***c)*** *Corresponding schematic illustration of data points for roughness and* ***d)*** *for friction. (see color insert)*

AFM-based FFS allows studying the strength of the films by scanning their surfaces at gradually increasing loads until the films are broken, and, eventually, completely removed. In turn, as it is shown in the sections below, scanning the films at gradually decreasing loads after their complete removal allows studying the lateral diffusion of components of these films.

Studies on Monolayers of Model Proteins

For presenting the basics of AFM-based FFS, we show in this section results obtained for monolayers of model proteins adsorbed on solid surfaces. Specifically, results are presented for monolayers formed by bovine serum albumin (BSA) molecules, and for monolayers formed by β-casein molecules, both of them adsorbed on hydrophobic surfaces (silica hydrophobized by silanization, water contact angle θ_C~100°). The choice of these systems is not casual. BSA, a serum protein with numerous biochemical applications (*19*), is considered a representative example of soft globular proteins (*20*). In contrast, β-casein, a milk protein with valuable emulsifying properties (*21*, *22*), is considered a representative example of disordered amphiphilic proteins. Both molecules form monolayers when adsorbed in aqueous media on hydrophobic substrates (*10*). Different mechanical properties, and therefore resistance to wear, are expected for these systems.

Scratch of BSA Monolayers – Determination of the Strength of the Films

A representative example of a FFS measurement on a BSA monolayer formed on hydrophobized silica in PBS buffer pH 7.4 is shown in Figure 2. As commented in the previous section, the applied load was gradually increased until the monolayer was completely removed, and then gradually decreased down to values similar to those applied at the beginning of the experiment. Figure 2a shows the topography of scans which are selected from, and representative of, those acquired during the complete FFS measurement. The evolution of the topography is also illustrated by plotting the roughness of the complete set of scans (roughness plot, Figure 2b). The average friction force between the film and the AFM tip is also shown for all the performed scans (friction plot, Figure 2c).

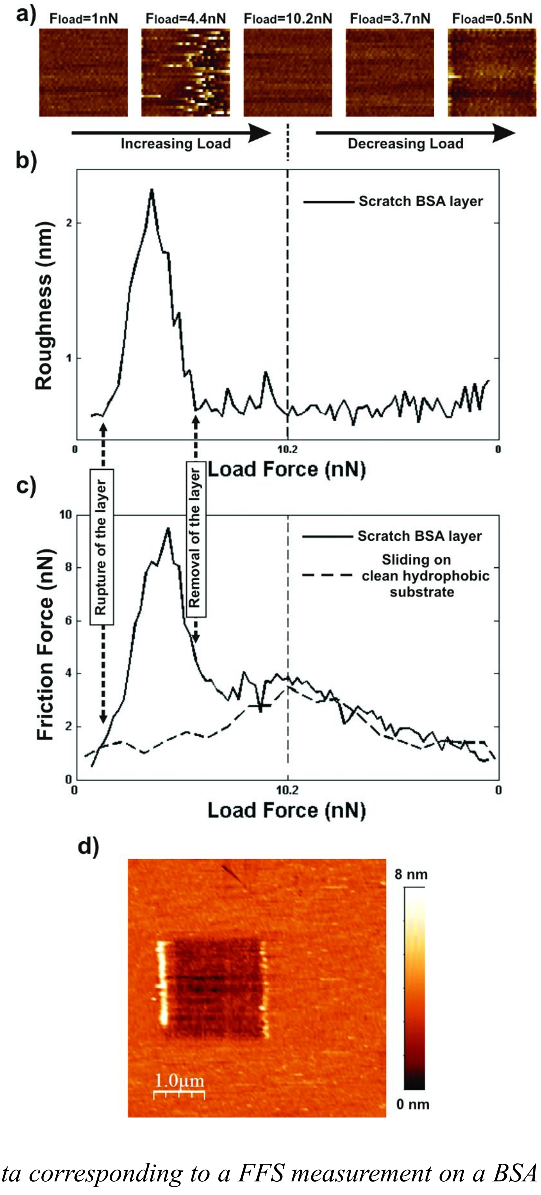

Figure 2. Data corresponding to a FFS measurement on a BSA monolayer on a hydrophobized silica surface in PBS buffer. ***a)*** *Representative images of the evolution of the topography of the sample surface during the scratch. Scan area: 2μm x 2μm. Color scale goes from 0nm (black) to 5nm (white).* ***b)*** *&* ***c)*** *Corresponding roughness and friction plots. In c) the frictional response obtained with the same tip on a clean substrate is also shown.* ***d)*** *Topography of a wider area obtained after the scratch. Reprinted with permission from (10). Copyright 2011 American Chemical Society. (see color insert)*

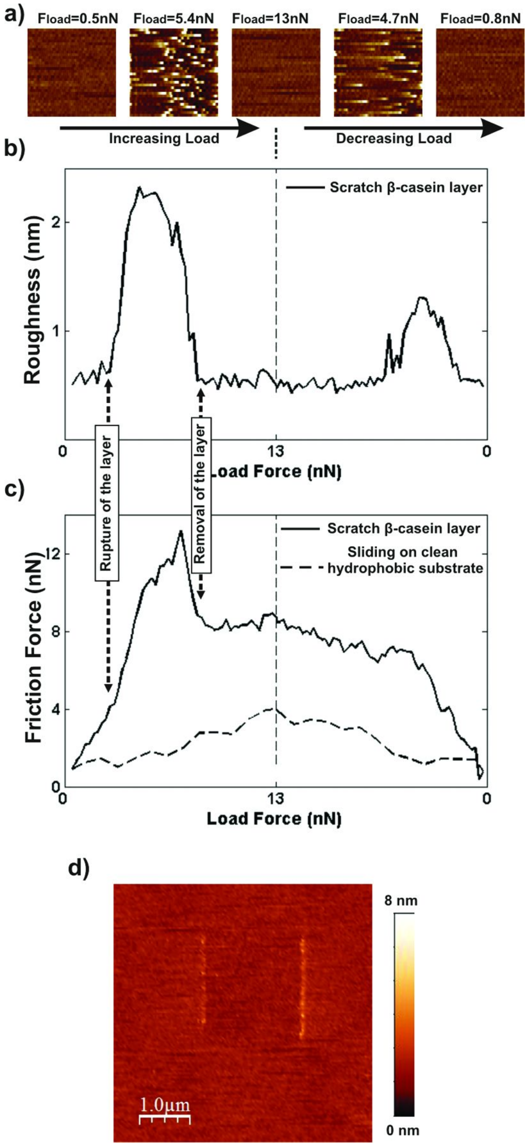

Figure 3. Data corresponding to a FFS measurement on a β-casein monolayer on a hydrophobized silica surface in PBS buffer. ***a)*** *Representative images of the evolution of the topography of the sample surface during the scratch. Scan area: 2μm x 2μm. Color scale goes from 0nm (black) to 5nm (white).* ***b)*** *&* ***c)*** *Corresponding roughness and friction plots. In c) the frictional response obtained with the same tip on a clean substrate is also shown.* ***d)*** *Topography of a wider area obtained after the scratch. Reprinted with permission from (10). Copyright 2011 American Chemical Society. (see color insert)*

In the beginning of the experiment the topography shows a planar surface characterized by a low and homogeneous roughness. This is indicative of a non-destructive sliding of the tip on top of the BSA layer. When the load is further increased the layer eventually breaks as shown by a sudden increase in roughness. The scan for which this occurs is referred to as "Rupture Scan". A planar topography is again visualized if the load is further increased. The scan from where this is observed is referred to as "Sweeping Scan". For higher loads, friction overlaps with that measured when probing a clean hydrophobized silica surface with the same tip (dotted line in Figure 2c). This is an indicator of the tip interacting directly with the hydrophobic substrate as a consequence of the removal of the layer. Overlap in friction continues if the load is then decreased, suggesting that the tip keeps sliding on top of the exposed underlying substrate. This is also supported by i) the lack of changes in the topography when decreasing the load, and by ii) the topography visualized by very soft imaging of the sample after the scratch (Figure 2d) which shows that the protein layer is not recovered. Thus, once they are removed, no diffusion of the BSA molecules onto the scratched area is observed.

The data presented exemplifies how the simultaneous monitoring of topography and friction during the scratching process allows characterizing the strength of the films. Specifically, this strength is characterized in terms of the load and friction forces needed both to break, i.e. forces applied during the Rupture Scan, and to completely remove them, i.e. forces applied during the Sweeping Scan.

Scratch of β-Casein Monolayers – The Study of Lateral Diffusion Processes

Figure 3 shows data from a FFS measurement on a β-casein monolayer on a hydrophobized silica surface in PBS buffer pH 7.4. The corresponding selected representative scans (Figure 3a), roughness plot (Figure 3b) and friction plot (Figure 3c) are shown for a ramp of increasing loads followed by a ramp of decreasing loads.

At the beginning of the experiment, the data resemble those presented for BSA monolayers. Rupture and Sweeping Scans can be clearly identified as those corresponding to the kinks observed in the roughness plot. As in the case of the films composed of BSA molecules, it is straightforward to determine the forces needed for the rupture and for the complete removal of the monolayer. After removal of the monolayer, friction increases at the same rate as measured for the clean substrate (dotted line in Figure 3c) but with absolute values several nN higher. This difference in friction remains in the first part of the decreasing load ramp. When the load is further decreased, the topography reveals one more difference with respect to the scratch of BSA layers: the β-casein coverage is recovered. This recovery is also confirmed i) by a decrease in friction down to values similar to those measured in the beginning of the scratch (when the layer was intact), and ii) by the topography of the sample visualized after the scratch (Figure 3d) showing no differences in height between the scratched and the non-scratched areas. Considering the small size of the tip compared to that of the probed area, and that the experiments are performed in protein-free solution, neither proteins taken up by the tip nor proteins in the bulk solution could act as a reservoir with sufficient amount of molecules for coverage of the scratched area. Only the surrounding protein layer can constitute such a reservoir. Therefore, the recovery of the protein layer constitutes an indicator of the lateral diffusion of the proteins on the substrate.

The recovery of the β-casein coverage is observed on the topography only when the load goes beyond a certain threshold value. This can be explained by the molecules diffusing on the hydrophobic substrates with a velocity higher, or at least similar, to that of the tip (16 $\mu m \cdot s^{-1}$ for the experiments presented). If this is the case, the molecules constantly oppose the sliding of the tip. Thus, only when the load is above a certain threshold value will the friction force be enough to sweep diffusing molecules away. For lower forces the tip is no longer able to sweep the proteins away, and starts to slide over them. As a consequence, the molecules are again observed in the topography images. This mechanism is also the origin of the friction force difference observed between the regime of the scratch of the β-casein layer where the underlying substrate is visualized, and the scratch of the clean substrate itself. While a constant difference in friction between two systems is usually attributed to a difference between their adhesiveness, we believe this does not hold in our case. The fact is that, as shown by the topography, the molecules do diffuse and they eventually manage to separate tip and substrate when the applied forces are low enough. Thus, the force needed to sweep the diffusing molecules can be considered to be, at least, the major component of the higher friction measured in the scratch of the β-casein monolayer.

The results presented show how AFM-based FFS joins the group of techniques which, along with others such a fluorescence recovery after photobleaching or single particle tracking (*23*), are capable of performing studies of lateral diffusion of biomolecules.

Comparison of the Strengths Measured for BSA and for β-Casein Monolayers

We have shown that AFM-based FFS provides the forces needed for the rupture of different systems (BSA and β-casein monolayers), a quantity that can be used to characterize the strength of the systems themselves. But, for validating the applicability of the methodology, it is needed to demonstrate that it is sensitive to differences between the strengths measured for different systems, and also if this difference can shed light on the structure and/or organization at the molecular level of the compared systems. This is indeed shown for AFM-based FFS by the experiments on BSA and β-casein monolayers previously presented. Figure 4 shows the same roughness and friction data as Figures 2 and 3, but zoomed in the region where the rupture and removal of the layers are observed. Both experiments were performed with the same tip in order to minimize tip-induced differences. The plots show that, at the experimental conditions, higher forces are needed both to break and to remove β-casein layers than BSA layers. More specifically, our experiments provide ratios between the rupture forces measured on both systems, $(F_{\beta\text{-casein}}/F_{BSA})_{\text{Rupture Scan}}$, of *(1.4 ± 0.3) nN* for the load and of *(1.7 ± 0.3) nN* for the friction forces. The ratios of the forces needed for the complete removal of the layers, $(F_{\beta\text{-casein}}/F_{BSA})_{\text{Sweeping Scan}}$, are *(1.5 ± 0.2) nN* for the load and of *(2.0 ± 0.2) nN* for the friction forces.

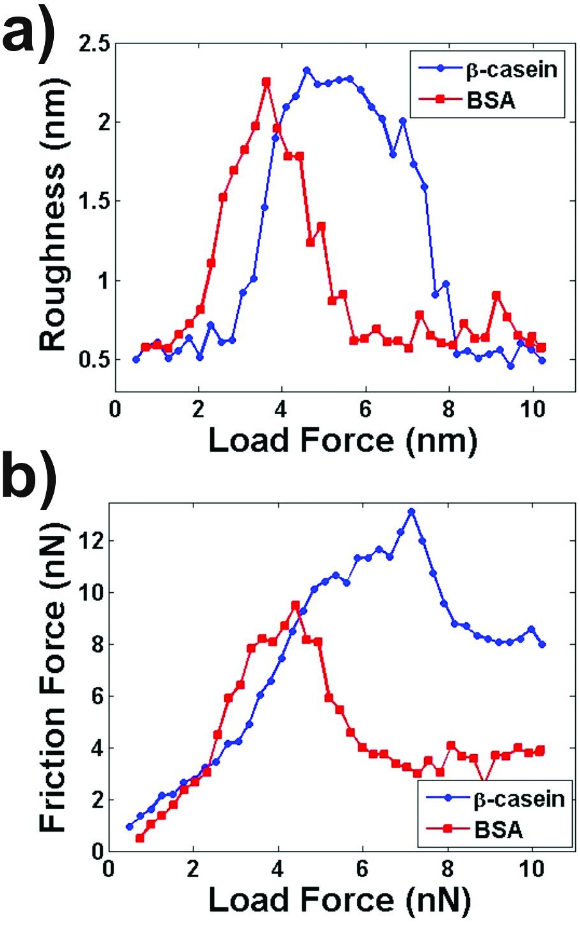

Figure 4. Superposition of the ***a)*** *roughness and* ***b)*** *friction plots from Figures 2 and 3, zoomed on the region showing the rupture and the complete removal of the respective β-casein and BSA layers. (see color insert)*

The studied systems are representative examples of layers composed by amphiphilic disordered proteins (β-casein) and of layers composed by soft globular proteins (BSA). Our results can most probably be explained in terms of these characteristics. When adsorbed on hydrophobic substrates, most globular proteins undergo partial denaturation, exposing their hydrophobic core to the substrate. Therefore, an attractive hydrophobic interaction develops between the molecule and the substrate, this being also the case for BSA (*24*). In contrast, repulsive electrostatic interactions are expected to dominate lateral interactions between similar adjacent molecules with isoelectric point, pI, far from the experimental pH (the pI of BSA is ~4.6 (*25*) while the pH of the ambient PBS buffer is 7.4). β-casein is considered a highly amphiphilic protein for pHs above its isoelectric point (pI 4.5 (*26*)). In these conditions a high negative charge concentrates at its N-terminal domain, whereas the C terminus is barely charged but rich in hydrophobic groups. Thus, β-casein self-organizes with its hydrophobic moiety anchored at the hydrophobic substrate (*27*). Therefore, molecule and substrate interact through attractive hydrophobic forces. As in the case of BSA layers, repulsive electrostatic forces develop between adjacent β-casein molecules, or more specifically, between their negatively charged hydrophilic parts. But in contrast to the case of BSA layers, the lateral interaction between β-casein molecules also has an attractive component: the force developed between the hydrophobic moieties of adjacent molecules. The existence of this attractive lateral force suggests that β-casein forms more compact layers than BSA. In fact, this is supported by ellipsometry experiments (*10*), which for the present experimental conditions provide areas per molecule of ca. 17.8 nm^2 and 70.2 nm^2 for β-casein and BSA respectively. It is not difficult to hypothesize about the mechanisms by which a more compact layer will result in higher yield strengths. An AFM tip sliding on the protein layer transfers friction energy to the underlying molecules. The rupture of the layer corresponds to the point where sufficient energy is received by the molecules, allowing them to jump out of the path of the tip. However, the transferred friction energy is not permanently stored by the molecules. It can be dissipated in different ways. One possibility is to dissipate energy through the layers themselves, this being more probable for more compact layers. In this case, a higher amount of energy has to be transferred to the underlying molecules in order to reach the critical amount needed to break the layers before this transferred energy dissipates. This explains the higher strengths measured for the more densely packed β-casein layers.

Quantification of the Strength of the Films

We have shown that AFM-based FFS allows a precise determination of the forces needed to break protein films. However, because of being a quantity dependent on the size and shape of the tip, force is not an optimal quantity for characterizing the rupture of the films. For this reason, we have developed a scheme for the characterization of the rupture of the films in terms of a tip-independent parameter. For this, we make use of the maximum distortion energy criterion (also known as the von Mises yield criterion), which can be used to relate forces measured during the scratching of thin films with their yield strength (*28*). This criterion states that a ductile material will start to yield when the applied von Mises stress, σ_{VM}, reaches the value of the yield strength of the material, S_y. For a three-dimensional system, σ_{VM} is given by (*29*):

$$\sigma_{VM} = \frac{1}{\sqrt{2}}\left[\left(\sigma_x - \sigma_y\right)^2 + \left(\sigma_y - \sigma_z\right)^2 + \left(\sigma_z - \sigma_x\right)^2 + 6\left(\tau_{xy}^2 + \tau_{yz}^2 + \tau_{zx}^2\right)\right]^{1/2}$$

where σ_x, σ_y, and σ_z are the normal stresses and τ_{xy}, τ_{yz}, and τ_{zx} the shear stresses. The tip-sample normal direction is denoted as the z-axis, and the tip sliding direction as the x-axis. In this case, only σ_z and τ_{xz} will have non-zero values in an AFM-based FFS experiment. For determining these quantities, assumptions have to be made on the characteristics of the contact between tip and sample.

We have described the deformation of the protein films prior to their rupture with the Hertz contact model (*30*). This model is considered valid for elastic non-adhesive contacts. We have not observed irreversible changes in the mechanical properties of the studied systems after being exposed to normal force or FFS measurements in which the maximum applied forces where below those needed to break them. Thus, we can consider the compression of the films to be approximately elastic before the rupture event. Regarding adhesion, even though it was sporadically observed when performing normal force curves, it can be neglected as it was always much smaller than the forces needed to break the films. Moreover, previous work also has proved that the Hertz model provides with a good description of the elastic behavior of adsorbed protein layers probed by AFM (*31*).

Assumptions need to be made also on the geometry and size of the tip. For this, we have considered, as a first approximation, that its final apex has a spherical shape. Despite of its simplicity, this geometrical approximation has shown to provide a reasonable good modeling for the variation of the contact area with the applied load in AFM experiments (*32*). The size of a sphere is characterized by its radius, R_{tip}. This parameter is commonly obtained by imaging a sample containing features of known size and shape. From these images, the tip and the sample surfaces can be deconvoluted (*33*). Features of similar size to that of the part of the tip involved in the friction measurement should be used. In our case this size will be similar to the thickness of the protein films, which is in the order of a few nanometers. For this reason we have used Highly Oriented Pyrolytic Graphite (HOPG) surfaces to characterize the AFM tips. These surfaces consist on atomically flat terraces separated by steps of heights that commonly go from one up to several dozens of atomic layers. When imaged, these steps show a width which is geometrically related to R_{tip}, allowing its determination (Figures 5a-c).

Within the previous scheme, the maximum normal and shear stresses exerted by the sliding tip are given by:

$$\left(\sigma_z\right)_{\max} = \frac{3F_L}{2\pi r_c^2}$$

$$\left(\tau_{xz}\right)_{\max} = \frac{3F_F}{2\pi r_c^2}$$

where r_c is the radius of the contact area between the interacting surfaces:

$$r_c = \sqrt{R_{tip}\delta}$$

where δ is the film indentation depth. Thus, the von Mises stress can be expressed as:

$$\sigma_{VM} = \frac{1}{\sqrt{2}}\left[2\sigma_z^2 + 6\tau_{yz}^2\right]^{1/2} = \frac{1}{\sqrt{2}}\left[2\left(\frac{3F_L}{2\pi R_{tip}\delta}\right)^2 + 6\left(\frac{3F_F}{2\pi R_{tip}\delta}\right)^2\right]^{1/2}$$

The yield strength of protein layers can then be determined by calculating σ_{VM} for the moment of the rupture of the layer, i.e. $S_y=\sigma_{VM}(F_L=F_{LR}, F_F=F_{FR})$. The load and friction forces at the moment of rupture, F_{LR} and F_{FR}, are obtained directly from the FFS measurements. The Hertz model states that δ and F_L are related by:

$$F_L(\delta) = \frac{4ER_{tip}^{1/2}}{3(1-\upsilon^2)}\delta^{3/2}$$

where E is the Young modulus of the sample and υ is the Poisson ratio (assumed to be 1/3 (*34*)). The relationship between F_L and δ (and therefore the indentation corresponding to the rupture force $\delta(F_{LR})$) can be obtained by fitting to the previous equation normal force curves performed on the proteinaceous films (Figure 5d).

We have applied this approach to determine S_y for both BSA and β-casein layers. Results for the experiments shown in Figures 2 and 3 are $S_y \approx (62 \pm 18)\ MPa$ for BSA, and $Sy \approx (67 \pm 15)\ MPa$ for β-casein layers.

We are aware that the Hertz model for a spherical tip and a planar sample constitutes just an approximation for modeling the contact between the tip and the proteinaceous films. Therefore, the scheme presented for quantifying the strength of the adsorbed films may be subject to improvement. This constitutes an open research line for the future.

Sensitivity of AFM-Based FFS to Environmentally-Induced Changes of the Proteinaceous Films

A crucial test for AFM-based FFS consists in determining its sensitivity to variations in the strength of the proteinaceous films induced by changes in the surrounding medium. In this section we present experiments where this sensitivity was tested for β-casein monolayers, specifically by varying the pH of the ambient solution and the wettability of the underlying substrate.

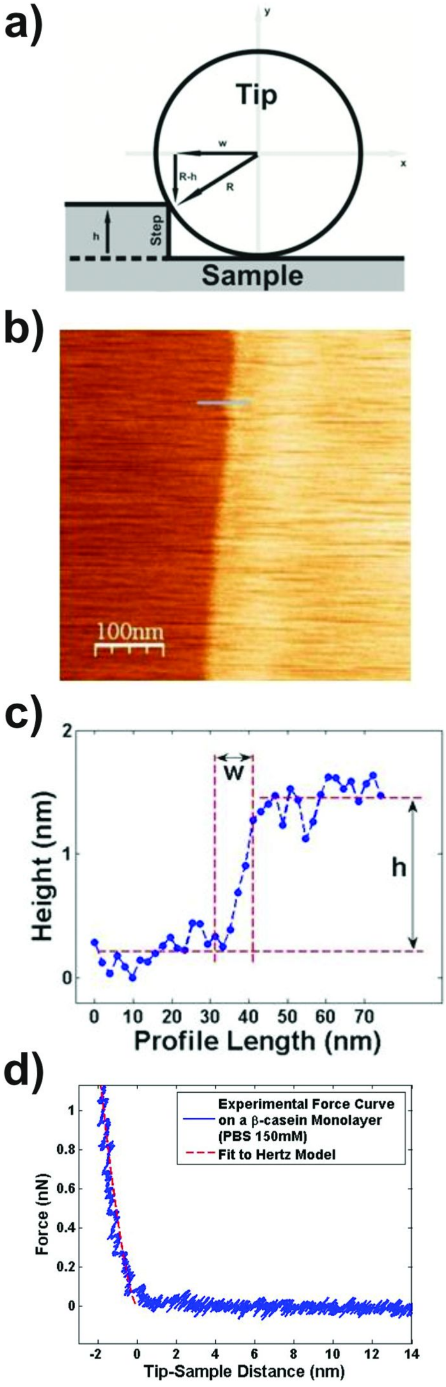
a)
y
Tip
w
x
R-h
R
h
Step
Sample
b)
100nm
c)
W
h
Height (nm)
2
1
0
0
10
20
30
40
50
60
70
Profile Length (nm)
d)
Experimental Force Curve on a β-casein Monolayer (PBS 150mM)
Fit to Hertz Model
Force (nN)
1
0.8
0.6
0.4
0.2
0
-2
0
2
4
6
8
10
12
14
Tip-Sample Distance (nm)

*Figure 5. **a)** Schematic drawing of a spherical tip probing a HOPG step. Once that h and w are obtained experimentally, the tip radius can be determined through the relationship $R_{tip} = (h^2+w^2)/2h$. **b)** AFM scan of the topography of an HOPG step. **c)** Height profile perpendicular to the imaged HOPG step (profile positions are highlighted in blue in b)) from where the height, h, and width, w, of the step can be inferred. **d)** Force curve performed on a β-casein monolayer in PBS buffer (solid blue line), and the corresponding fit to the Hertz model (dashed red line). (see color insert)*

Dependence of the Strength of β-Casein Monolayers with the pH of the Ambient Solution

Data are shown in Figure 6 from a representative experiment where a β-casein layer was scratched with the same tip at three different pH values: 7, 5 and 3.3. The data clearly show that AFM-based FFS is sensitive to pH-induced differences in the strength of the β-casein layer, and therefore validate its applicability.

Specifically, from Figure 6 it can be observed that the forces needed both to break and to remove the layers are strongest at pH 5 and lowest at pH 3.3. These results are not unexpected. The higher strength attained when the pH of the surrounding liquid is closer to the isoelectric point of the protein (~4.5 for β-casein) can be explained by the minimization of the electrostatic repulsion between adjacent molecules. It is also clear from the data that changing the pH from 5 to 3.3 causes a bigger effect that going from 5 to 7. One reason can be found in the pH dependence of the interactions between adjacent molecules, and between molecules and substrate. At low pHs the substrate-facing C-terminal region of the β-casein molecules develops a net positive charge, in this way reducing its hydrophobic character (*35*). Therefore, at low pHs, the hydrophobic attraction both between molecules and substrate, and between adjacent molecules, is lowered. This leads to the measured reduced strength.

Dependence of the Strength of β-Casein Monolayers with the Wettability of the Underlying Substrate

The dependence of the adhesiveness between biological material and synthetic substrates with the water wettability of the latter is a thoroughly studied topic. The main aim of these studies has been to gain knowledge that can be used in the fabrication of "easy-release" coatings for exposure to any kind of media containing biological molecules (*36*). This wettability dependence has also been studied for the adsorption of milk proteins on solid surfaces (*37*). In fact, this is believed to be the first step in fouling of heat exchangers, one of the great challenges in the dairy industry (*38*).

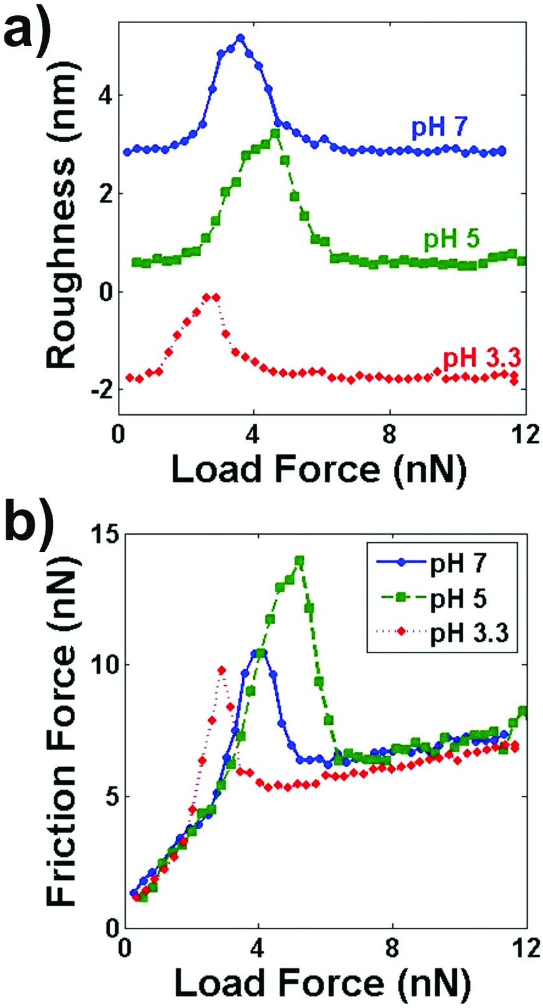

Figure 6. ***a)*** *Roughness and* ***b)*** *friction plots corresponding to three different FFS measurements on the same β-casein monolayer, formed on a hydrophobized silica surface, and probed with the same tip, in water with its pH adjusted to three different values: 7, 5 and 3.3. In a), an arbitrary offset has been applied to each of the curves for a better visualization. Reprinted with permission from (10). Copyright 2011 American Chemical Society. (see color insert)*

Regarding the strength of binding/retention of biological molecules to surfaces in contact with aqueous solutions of biological material, the property which is relevant to study is the resistance to shear-induce re-entrainment of this material into the biological stream (*36*). It is obvious that AFM-based FFS offers the possibility to study this property directly. Here, we present data showing that the methodology is sensitive to variations in the strength of β-casein layers induced by small changes in the wettability of their substrates. Figure 7 shows two AFM-based FFS measurements performed on β-casein layers formed on silica surfaces silanized to different surface coverage so that they give raise to different water contact angles, θ_c. Specifically, results are presented for layers formed on surfaces with values θ_c of 99.2° and 84.6°. It is clear from the plots that lower forces are needed both to break and to remove layers formed on more hydrophobic surfaces. While further experimental work would be needed for elucidating the molecular mechanisms leading to this observation, data clearly shows that AFM-based FFS is sensitive to changes in the strength of the layers induced by small variations in the wettability of their substrates.

Studies on Adsorbed Salivary Films

The mouth is an entry for a huge variety of substances, both harmful and beneficial, into the human body. As a consequence, oral surfaces are constantly confronted to different chemical and mechanical challenges due to extrinsic factors which can lead to dental erosion, a growing problem worldwide affecting both adults and children (*39*). Salivary protein films constitute a major issue in the study of dental erosion as they cover all surfaces within the oral cavity (*40–42*). The protection offered by salivary films against erosion is experimentally well-established, both in the cases of acidic corrosion (*43*) and of mechanical abrasion (*44*). However, this is usually proved indirectly by investigating the effect of the presence of an adsorbed film on different properties of a sample (such as hardness, roughness or worn volume) when subjected to an erosion process. In contrast, FFS can be used to directly study the protective properties of adsorbed salivary films, an strategy that has also shed light on the lateral diffusion properties of some of their components (*11*).

Even though AFM-based FFS results have been reported for salivary films formed on substrates with a wide range of water wettability properties (*11*, *12*), for the sake of simplicity we only present experiments performed on salivary films formed on hydrophobic substrates (as in the previous cases, silica hydrophobized by silanization $\theta_C \sim 100°$). Figure 8 shows data from a FFS measurement on a film formed by incubation of such a substrate in fresh unstimulated human whole saliva for 1h, followed by removal of loosely bound material by rinsing with water pH 7. As in the previous cases, selected representative scans (Figure 8a), the roughness plot (Figures 8b and 8c) and the friction plot (Figures 8d and 8e) are shown for a ramp of increasing loads followed by a ramp of decreasing loads. It can be noticed how two different types of representations are used for the roughness and friction plots. As in the previous cases, data for the increasing and decreasing load ramps are plotted in sequence (Figures 8b and 8d), but also superimposed (Figures 8c and 8e).

For adsorbed salivary films, as in the case of proteins monolayers, AFM-based FFS measurements provide a precise determination of the Rupture and Sweeping Scans, and therefore of the load and friction forces needed for the rupture and complete removal of the films. It can also be observed that these forces are similar to those reported for the case of BSA and β-casein monolayers. Moreover, determination of the yield strength provides a value of $S_y \approx (121 \pm 38)$

MPa. Pressures measured in the oral cavity using force transducers are in the order of kPa when mucosal surfaces are involved (e.g. pressure on the tongue while swallowing (*45*), or lingual contact against the teeth (*46*)). Comparison of these data with our estimation of S_y leads to think that salivary films would resist these types of contacts. A different situation is found for contact between teeth. Bite pressures reported from force transducers-based experiments are in the order of MPa (*47*). This is in the same order of magnitude as S_y for salivary films. Therefore, it would be plausible that these films would be damaged upon biting.

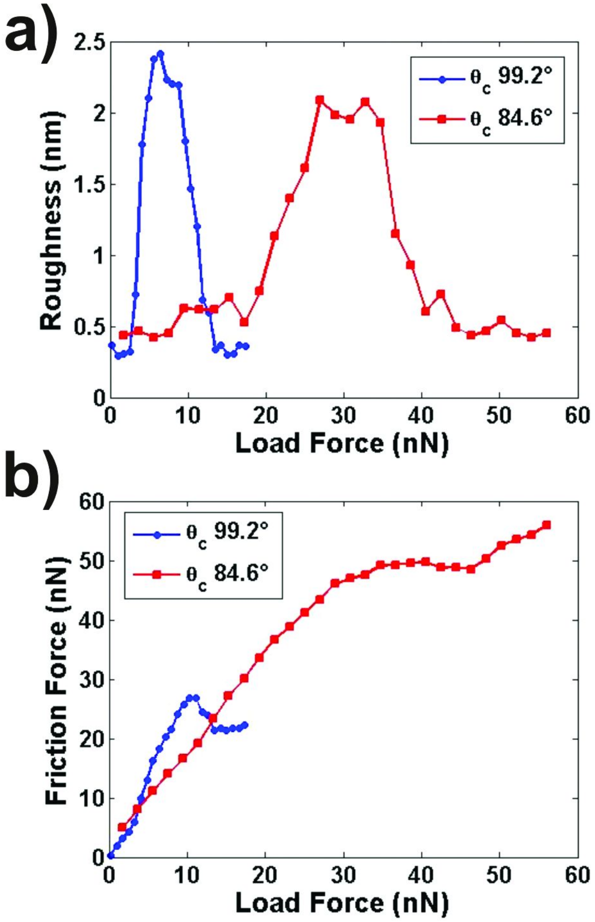

*Figure 7. **a)** Roughness and **b)** friction plots corresponding to two different FFS measurements performed on β-casein layers, formed on silica surfaces silanized up to different coverage, so that different hydrophobicities are achieved (specifically those characterized by water contact angles, θ_c, of ca. 99.2° and 84.6°). (see color insert)*

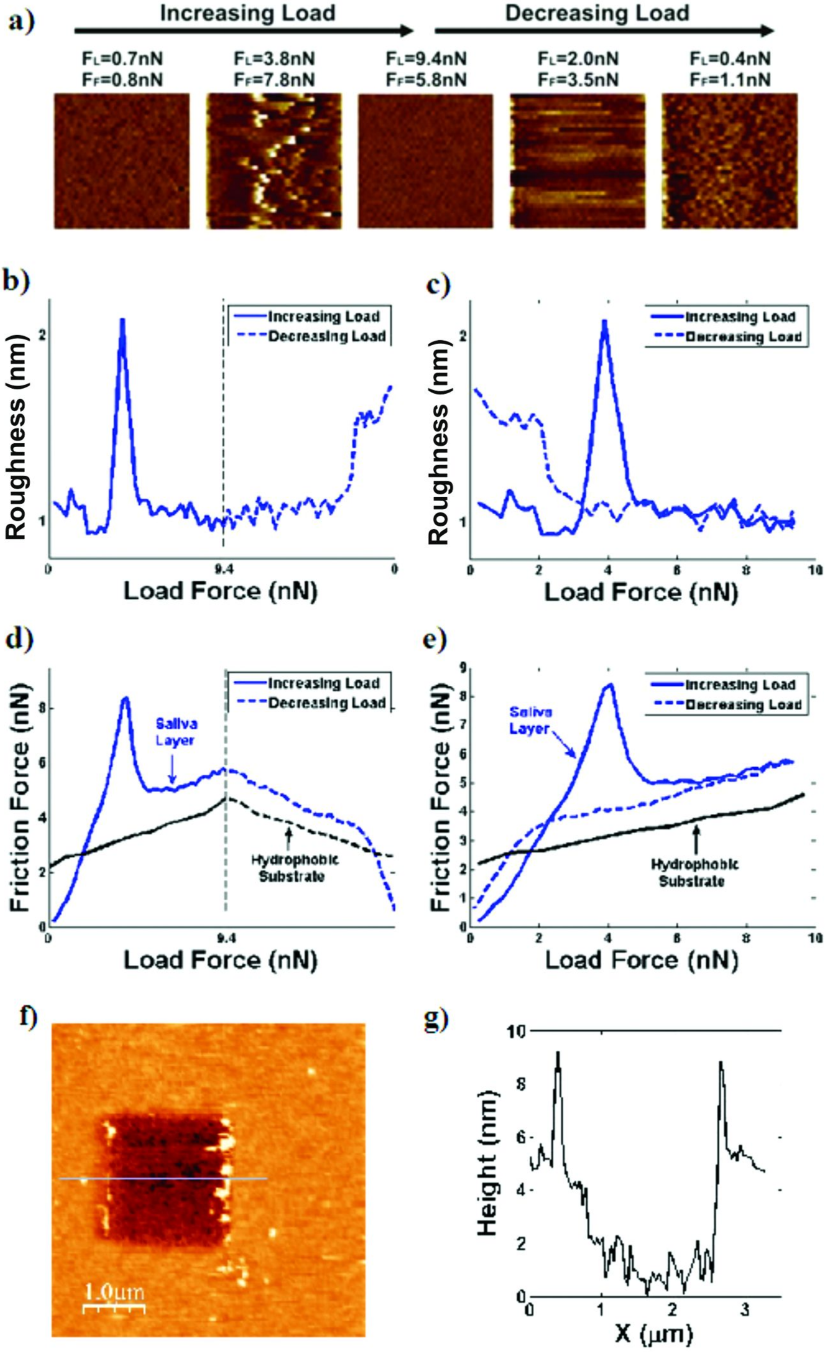
a)
Increasing Load
Decreasing Load
FL=0.7nN FF=0.8nN
FL=3.8nN FF=7.8nN
FL=9.4nN FF=5.8nN
FL=2.0nN FF=3.5nN
FL=0.4nN FF=1.1nN
b)
Roughness (nm)
Load Force (nN)
0
9.4
0
1
2
Increasing Load
Decreasing Load
c)
Roughness (nm)
Load Force (nN)
0 2 4 6 8 10
1
2
Increasing Load
Decreasing Load
d)
Friction Force (nN)
Load Force (nN)
0
9.4
0 2 4 6 8
Increasing Load
Decreasing Load
Saliva Layer
Hydrophobic Substrate
e)
Friction Force (nN)
Load Force (nN)
0 2 4 6 8 10
0 1 2 3 4 5 6 7 8 9
Increasing Load
Decreasing Load
Saliva Layer
Hydrophobic Substrate
f)
1.0μm
g)
Height (nm)
X (μm)
0 1 2 3
0 2 4 6 8 10

Figure 8. Data corresponding to a FFS measurement on a salivary film on methylated silica in water pH5. ***a)*** *Representative images of the evolution of the topography during the scratch. Scan area 2 µm x 2 µm. Color scale from 0 nm (black) to 10 nm (white).* ***b)*** *and* ***c)*** *Corresponding SD vs. F_L curves, where the roughness data for the increasing and decreasing load ramps are plotted consecutively (b) and superposed (c).* ***d)*** *and* ***e)*** *Corresponding F_F vs. F_L curves, where the roughness data for the increasing and decreasing load ramps are plotted consecutively (d) and superposed (e). For reference, friction measured on a clean methylated silica surface is included in (d) and (e).* ***f)*** *Topography of a wider area obtained after the scratch of the sample. Color scale from 0 nm (black) to 10 nm (white).* ***g)*** *Cross-sectional profile of the scratched area. Location is indicated by the blue line in (f). Reprinted with permission from (11). Copyright 2011 American Chemical Society. (see color insert)*

The data presented in Figure 8 suggest that some of the components of the salivary film have the ability to laterally diffuse on top of the underlying hydrophobic substrate. First, the recovery of the coverage is observed in the topography images, as well as an increase in roughness in the end of the decreasing load ramp. This recovery is accompanied by a pronounced decrease in friction down to values just slightly higher than those measured in the beginning of the scratch. As in the case of β-casein monolayers, in the regime preceding this recovery friction varies at the same rate as that measured on clean hydrophobized silica (also shown if Figures 8d and 8e), but with higher absolute values. However, data also suggest that the original structure and/or composition of the film are not completely recovered after the FFS measurement. It is clear that neither the sample roughness not the friction signals coincide at the beginning and at the end of the scratch. Moreover, soft imaging of the scratched area (Figures 8f and 8g) indicates both that some fraction of the original film has been irreversibly removed (there is a difference in height between the scratched and the non-scratched areas), and that some fraction has diffused back (the height of the scratched area is lower than that reported for the thickness of the rinsed pellicle (*40*)).

A deeper understanding of the response of the film to the experiment is achieved by repeatedly scratching the same area of the sample. Figures 9a and 9b respectively contain the roughness and friction plots for the same scratch as in Figure 8, and for a second scratch performed immediately afterwards on the same zone of the sample. Friction measured with the same tip on the clean substrate is also included in Figure 9b. Both roughness and friction in the beginning of the second scratch match those measured in the end of the first scratch, and also those measured in the beginning and at the end of subsequent ones. Similar results were obtained when probing, with the same tip, different zones of the sample. Thus, some components only contribute to the measured roughness and friction when scratching a film for the first time, suggesting that they do not laterally diffuse afterwards.

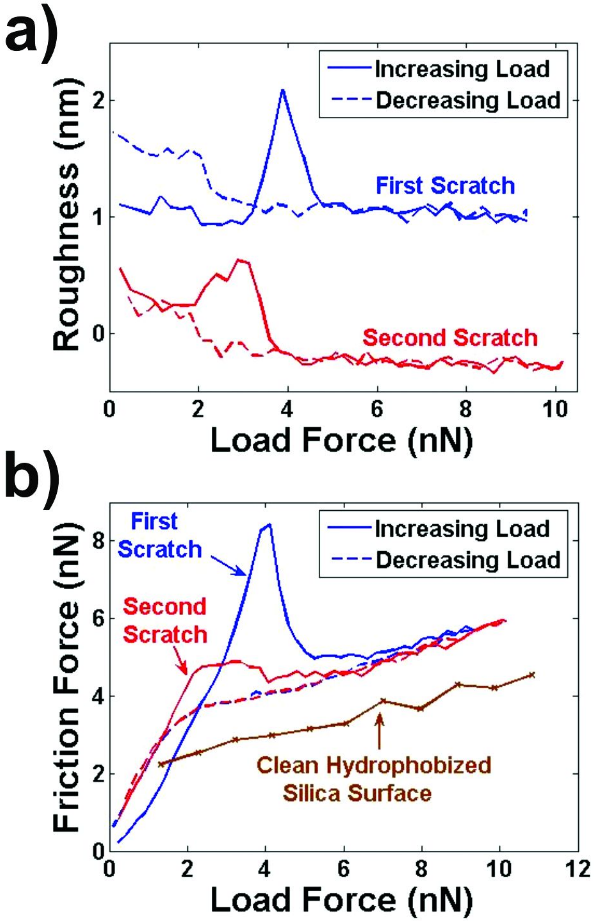

*Figure 9. **a)** Roughness and **b)** friction plots of two consecutive scratches on a salivary film on a hydrophobized silica surface in water pH 5. An arbitrary offset has been applied to the roughness plots so that they can be clearly differentiated. In b) the frictional response obtained on a clean substrate is also shown. Reprinted with permission from (11). Copyright 2011 American Chemical Society. (see color insert)*

Thus, our results indicate that salivary films formed on hydrophobic surfaces are composed of two different fractions, only one of them with the ability to diffuse over the underlying substrates.

Conclusions

This work presents a novel and powerful methodology, i.e. AFM-based FFS, for the study of the strength of proteinaceous films at the nanoscale level, and the diffusion of proteins within such films. Different experiments are presented for validating the applicability of the methodology to a wide variety of systems. First, we show how the methodology is sensitive enough to measure and resolve the strength of layers formed by soft globular proteins (BSA) and by amphiphilic disordered proteins (β-casein). It is also shown how the methodology is sensitive to variations in the strength of the layers induced by changes in their environmental conditions such as the pH of the ambient liquid or the wettability of the underlying substrate. Moreover, the sensitivity of AFM-based FFS to lateral diffusion processes is proved through the reported diffusion of β-casein molecules on hydrophobic surfaces.

As we show, AFM-based FFS can be successfully applied not only to the study of simple systems such as monolayers of model proteins, but also to the study of more complex ones such as those formed on solid surfaces exposed to saliva. Effectively, AFM-based FFS provides with the strength of salivary films, and also shows sensitivity to the lateral diffusion of some of their fractions, i.e. it provides structural information of these systems. The successful application of AFM-based FFS to the study of this system opens the possibility for its application as a tool for diagnosis of the resistance of salivary films against erosion. Moreover, these results consolidate AFM-based FFS as a promising methodology for the study of many other types of films formed upon adsorption of biological fluids onto solid surfaces.

Acknowledgments

This work was supported by research grants from Knowledge Foundation (KK stiftelsen, Biofilms-research centre for biointerfaces), Swedish Laryng Foundation and Malmö University. Thomas Arnebrant acknowledges the Gustaf Th Ohlsson foundation for financial support.

References

1. Gupta, S.; Elias, M.; Wen, X.; Shapiro, J.; Brillson, L.; Lu, W.; Lee, S. C. *Biosens. Bioelectron.* **2008**, *24*, 505–511.
2. Lang, H. P.; Hegner, M.; Gerber, C. *Mater. Today* **2005**, *8*, 30–36.
3. Dickinson, E. In *Emulsions-A Fundamental and Practical Approach*; Sjoblom, J., Ed.; Kluwer Academic Publishers: Dordrecht, 1992.
4. Alves, C. M.; Yang, Y.; Carnes, D. L.; Ong, J. L.; Sylvia, V. L.; Dean, D. D.; Agrawal, C. M.; Reis, R. L. *Biomaterials* **2007**, *28*, 307–315.
5. Jones, M. I.; McColl, I. R.; Grant, D. M.; Parker, K. G.; Parker, T. L. *J. Biomed. Mater. Res.* **2000**, *52*, 413–421.
6. Hahn-Berg, I. C.; Rutland, M. W.; Arnebrant, T. *Biofouling* **2003**, *19*, 365–369.
7. Sharma, A. *J. Dispersion Sci. Technol.* **1998**, *19*, 1031–1068.
8. Bhushan, B.; Gupta, B. K.; Azarian, M. H. *Wear* **1995**, *181-183*, 743–758.
9. Meyer, E.; Luthi, R.; Howald, L.; Bammerlin, M.; Guggisberg, M.; Guntherodt, H. J. *J. Vac. Sci. Technol., B* **1996**, *14*, 1285–1288.
10. Sotres, J.; Barrantes, A.; Arnebrant, T. *Langmuir* **2011**, *27*, 9439–9448.

11. Sotres, J.; Lindh, L.; Arnebrant, T. *Langmuir* **2011**, *27*, 13692–13700.
12. Sotres, J.; Pettersson, T.; Lindh, L.; Arnebrant, T. *J. Dent. Res.* **2012** Accepted.
13. Sotres, J.; Svensson, O.; Arnebrant, T. *Langmuir* **2011**, *27*, 981–992.
14. Michalski, M.-C.; Michel, F.; Sainmont, D.; Briard, V. *Colloids Surf., B* **2002**, *23*, 23–30.
15. Nassar, A.-E. F.; Bobbitt, J. M.; Stuart, J. D.; Rusling, J. F. *J. Am. Chem. Soc.* **1995**, *117*, 10986–10993.
16. Reach, G.; Feijen, J.; Alcock, S. *Biosens. Bioelectron.* **1994**, *9*, R21–R28.
17. Sun, D.; Wharton, J. A.; Wood, R. J. K. In *Advanced Tribology*; Luo, J. B., Meng, Y. G., Shao, T. M., Zhao, Q., Eds.; Springer: Heidelberg, 2009; pp 825−826.
18. Zu, X.; Lu, Z.; Zhang, Z.; Schenkman, J. B.; Rusling, J. F. *Langmuir* **1999**, *15*, 7372–7377.
19. Francis, G. L. *Cytotechnology* **2010**, *62*, 1–16.
20. Norde, W. *Adv. Colloid Interface Sci.* **1986**, *25*, 267–340.
21. Ai, Y.; Wei, D. Q. *J. Macromol. Sci., Pure Appl. Chem.* **2008**, *45*, 456–461.
22. Dickinson, E. *Colloids Surf., B* **2001**, *20*, 197–210.
23. Chen, Y.; Lagerholm, B. C.; Yang, B.; Jacobson, K. *Methods* **2006**, *39*, 147–153.
24. Browne, M. M.; Lubarsky, G. V.; Davidson, M. R.; Bradley, R. H. *Surf. Sci.* **2004**, *553*, 155–167.
25. Ghosh, S.; Basu, M. K.; Schweppe, J. S. *Anal. Biochem.* **1972**, *50*, 592–601.
26. Cordeschi, M.; Di Paola, L.; Marrelli, L.; Maschietti, M. *Biophys. Chem.* **2003**, *103*, 77–88.
27. Kull, T.; Nylander, T.; Tiberg, F.; Wahlgren, N. M. *Langmuir* **1997**, *13*, 5141–5147.
28. Wang, L. Y.; Yin, Z. F.; Zhang, J.; Chen, C. I.; Hsu, S. *Wear* **2000**, *237*, 155–162.
29. Leckie, F. A.; Bello, D. J. *Strength and Stiffness of Engineering Systems*; Springer: New York, 2009.
30. Popov, V. L. *Contact Mechanics and Friction*; Springer, New York, 2010.
31. Parra, A.; Casero, E.; Lorenzo, E.; Pariente, F.; Vazquez, L. *Langmuir* **2007**, *23*, 2747–2754.
32. Carpick, R. W.; Ogletree, D. F.; Salmeron, M. *J. Colloid Interface Sci.* **1999**, *211*, 395–400.
33. Zeng, Z.-g.; Zhu, G.-d.; Guo, Z.; Zhang, L.; Yan, X.-j.; Du, Q.-g.; Liu, R. *Ultramicroscopy* **2008**, *108*, 975–980.
34. Radmacher, M.; Fritz, M.; Cleveland, J. P.; Walters, D. A.; Hansma, P. K. *Langmuir* **1994**, *10*, 3809–3814.
35. Portnaya, I.; Ben-Shoshan, E.; Cogan, U.; Khalfin, R.; Fass, D.; Ramon, O.; Danino, D. *J. Agric. Food Chem.* **2008**, *56*, 2192–2198.
36. Baier, R. *J. Mater. Sci.: Mater. Med.* **2006**, *17*, 1057–1062.
37. Santos, O.; Nylander, T.; Schillén, K.; Paulsson, M.; Trägårdh, C. *J. Food Eng.* **2006**, *73*, 174–189.
38. Belmar-Beinya, M. T.; Fryera, P. *J. Dairy Res.* **1993**, *60*, 467–483.
39. Jaeggi, T.; Lussi, A. *Monogr. Oral Sci.* **2006**, *20*, 44–65.

40. Arnebrant, T. In *Biopolymers at Interfaces*, 2nd ed.; Malmsten, M., Ed.; Marcel Dekker: New York, 2003.
41. Lendenmann, U.; Grogan, J.; Oppenheim, F. G. *Adv. Dent. Res.* **2000**, *14*, 22–28.
42. Svendsen, I. E.; Lindh, L. *Biofouling* **2009**, *25*, 255–261.
43. Nekrashevych, Y.; Stösser, L. *Caries Res.* **2003**, *37*, 225–231.
44. Joiner, A.; Schwarz, A.; Philpotts, C. J.; Cox, T. F.; Huber, K.; Hannig, M. *J. Dent.* **2008**, *36*, 360–368.
45. Yoshikawa, M.; Yoshida, M.; Tsuga, K.; Akagawa, Y.; Groher, M. E. *Dysphagia* **2011**, *26*, 232–237.
46. Kieser, J.; Singh, B.; Swain, M.; Ichim, I.; Waddell, J.; Kennedy, D.; Foster, K.; Livingstone, V. *Dysphagia* **2008**, *23*, 237–243.
47. Hidaka, O.; Iwasaki, M.; Saito, M.; Morimoto, T. *J. Dent. Res.* **1999**, *78*, 1336–1344.

Chapter 7

Simultaneous versus Sequential Adsorption of β-Casein/SDS Mixtures. Comparison of Water/Air and Water/Hexane Interfaces

A. Dan,[1] G. Gochev,[1] Cs. Kotsmar,[2] J. K. Ferri,[3] A. Javadi,[1]
M. Karbaschi,[1,4] J. Krägel,[1] R. Wüstneck,[1] and R. Miller*,[1]

[1]Max-Planck Institute of Colloids & Interfaces, Potsdam/Golm, Germany
[2]University of California at Berkeley,
Berkeley, California 94720-1462, U.S.A.
[3]Department of Chemical Engineering, Lafayette College,
Easton, Pennsylvania 18042, U.S.A.
[4]Sharif University of Technology, Teheran, Iran
*E-mail: Reinhard.Miller@mpikg.mpg.de

This chapter is dedicated to the surface properties of mixed protein/surfactant adsorption layers, formed by two different experimental approaches, i.e. by sequential and simultaneous adsorption, respectively. A special modification of a drop profile analysis tensiometer, consisting of a coaxial double capillary, provides a unique protocol for studies of mixed surface layers formed by sequential adsorption of the individual components in addition to the traditional simultaneous adsorption from their mixed solution. A CFD simulation allowed to optimize the drop exchange process performed with the special double capillary arrangement.

The experiments show that properties of sequentially formed layers differ significantly from those formed simultaneously, which can be explained by the different nature and structure of the complexes formed at the two different locations. The nature of the interface, water/air or water/oil, influences strongly the adsorption behavior of the protein molecules and consequently the mixed layers due to their different degree of polarity and hydrophobicity. Washing out experiments are performed in order to support the proposed

In Proteins at Interfaces III State of the Art 2012; Horbett, T., et al.;
ACS Symposium Series; American Chemical Society: Washington, DC, 2012.

mechanism of the protein displacement process from mixed surface layers, i.e., to check how many protein molecules are left in the adsorption layer. Based on the experimental studies of the milk protein β-casein (βCS) mixed with the anionic surfactant sodium dodecyl sulfate (SDS) at water/air and water/hexane interfaces, the results are discussed according to different mechanisms describing the different location of interaction.

1. Introduction

The stability of many products in the field of food, cosmetic, pharmaceuticals is controlled by mixed adsorption layers of proteins and low molecular weight surfactants (*1*). While neither single protein nor the surfactants are suitable, their mixtures at optimum mixing ratios are able to provide the right properties to the products, which is essentially true for foams and emulsions.

It is generally accepted that in mixed protein/surfactant solutions complexes are formed. According to Kotsmar et al. (*2*) the main interaction forces between protein and surfactant molecules are of electrostatic and hydrophobic nature. Depending on the pH and the mixing ratio, the resulting complexes are more or less surface active as compared to the protein alone. By adding a non-ionic surfactant to a protein solution, the surface activity of the resulting complex is gradually decreased. Consequently, the protein would be step by step displaced from the interface by free surfactant molecules (*3*). For ionic surfactants, the situation is much more complicated. At small amounts the ionic surfactant binds to the protein molecules via electrostatic interactions (*4*) and they proceed until the available charges in the protein molecules are compensated by the surfactant ions. The resulting complexes show an increase in surface activity as compared to the original protein. With decreasing protein/surfactant mixing ratios, the hydrophobic interaction becomes more important, thus making the complex more hydrophilic and hence less surface active. A competitive adsorption between the hydrophilized protein/surfactant complexes and free surfactant molecules sets in. Depending on the total concentration and the pH in some systems even a precipitation is observed, caused by an aggregation of the most hydrophobic complexes.

The described phenomena are observed for different proteins, such as β-casein, β-lactoglobulin, lysozyme, at different pH and ionic strength and also at the water/air and water/oil interfaces. The possibility for the protein to interact directly with the molecules of the oil phase is also changing the conformation of the adsorbed complexes. It is observed that the proteins are much stronger adsorbed at a water/oil interface, the adsorbed amount is larger and also the resulting adsorption layers are thicker (*5*).

As it was shown recently, the structure and properties of the complexes are different when formed in the bulk of the solution or at the interface, respectively, which can be probed by performing experiments with different adsorption routes. In processes of a simultaneous adsorption, the proteins und surfactants are mixed in the solution bulk and the complexes are formed in the bulk before they adsorb at the interface. These complexes may eventually change their conformation there. In a sequential adsorption protocol, the components are allowed to adsorb one after another (*3*). Thus, proteins can be adsorbed first from a protein solution of a given concentration. Then, the protein is removed from the bulk phase and surfactant is added. The surfactant molecules also diffuse to the interface and adsorb there. They can either penetrate into the existing protein adsorption layer, or interact with the proteins and form surface complexes. At higher surfactant concentration, the proteins are displaced into the bulk phase by the surfactant molecules and the adsorption layer is mainly covered by the free surfactant molecules. The structures of these complexes are different at the water/air or water/hexane interface, and depend on the place where they are formed.

The target of this manuscript is to present the experiment protocols essentially for the sequential adsorption route, and to demonstrate the extent of proteins replaced from the interface due to the addition of surfactant. Due to the interaction with the oil phase the conformation of protein molecules at the water/oil interface is different. Adsorption experiments with the two types of protocols, simultaneous and sequential adsorption, show clearly that the properties of the complexes formed in the solution bulk differ from those formed at the interface.

The present state of the art is that the community of interfacial dynamics and 2D rheology assumes that the adsorption dynamics is closely linked to the process of foam or emulsion formation. Regarding the stability of foams and emulsions, there is not yet a clear view due to the complexity of stabilizing mechanism. Obviously, the 2D rheology has impact on this however we cannot give velar relationships now. Until recently, there were no reliable experiments available and we are now in the stage of accumulating knowledge in order to sooner or later provide clear mechanisms, i.e. relationships between dilations and shear rheology of interfacial layers and the stabilizing mechanisms of foams and emulsions.

2. Theoretical Background

There is a well established thermodynamic theory for describing the formation of adsorption layers from protein or mixed protein/surfactant solutions. However, these models do not allow appreciating yet the peculiarities arising from different adsorption routes. Therefore, we give only a very brief summary of the adsorption models here, in order to present the state of the art.

For the adsorption of proteins alone at a liquid interface, the following basic equation of state was derived in (*6*):

$$-\frac{\Pi\omega_0}{RT} = \ln(1-\theta_P) + \theta_P(1-\omega_0/\omega_P) + \alpha_P\theta_P^2, \qquad (1)$$

where Π is the surface pressure, R the gas law constant, T the absolute temperature, α_P is the intermolecular interaction parameter, ω_0 is the molar area of the solvent, which is taken equal to the area occupied by an adsorbed segment of the protein molecule. The total adsorption of proteins in all n possible states $\Gamma_P = \sum_{i=1}^{n} \Gamma_{Pi}$ allows to determine the total surface coverage by proteins $\theta_P = \omega_P \Gamma_P = \sum_{i=1}^{n} \omega_i \Gamma_{Pi}$. The index P stands for protein. For each state j of the adsorbed protein we obtain a respective adsorption isotherm,

$$b_{Pj} c_P = \frac{\omega_P \Gamma_{Pj}}{(1-\theta_P)^{\omega_j/\omega_P}} \exp\left[-2\alpha_P (\omega_j/\omega_P)\theta_P\right]. \tag{2}$$

Here c_P is the protein bulk concentration and b_{Pj} is the equilibrium adsorption constant for the protein in the jth state. The model given by Eqs. (1) and (2) describes the evolution of states of protein molecules with increasing adsorption or surface pressure. This model agrees in many details very well with experimental results (*2–5*).

The first thermodynamic model for adsorption layers formed from mixed solutions was presented in 2004 (*7*). This model was further refined and allows a semi-quantitative description of the adsorption of proteins mixed with ionic as well as non-ionic surfactants. The main equation of this model reads

$$-\frac{\Pi \omega_0^*}{RT} = \ln(1-\theta_P-\theta_S) + \theta_P(1-\omega_0/\omega_P) + \alpha_P \theta_P^2 + \alpha_S \theta_S^2 + 2\alpha_{PS}\theta_P\theta_S, \tag{3}$$

The parameter α_{PS} is the only one additional to those characterizing the single components (subscripts S and P refer to parameters characteristic for the individual surfactant and protein) and describes the interaction between protein and surfactant molecules. Small differences between ω_0 and ω_S can be accounted for by introducing

$$\omega_0^* = \frac{\omega_0 \theta_P + \omega_{S0}\theta_S}{\theta_P + \theta_S}. \tag{4}$$

For a protein molecule adsorbed in the state of minimum molar area $\omega_1 = \omega_{min}$, and the surfactant, respectively, the adsorption isotherms have the following form:

$$b_{P1} c_P = \frac{\omega_P \Gamma_{P1}}{(1-\theta_P-\theta_S)^{\omega_1/\omega_P}} \exp\left[-2\alpha_P(\omega_1/\omega_P)\theta_P - 2\alpha_{PS}\theta_S\right], \tag{5}$$

$$b_S c_S = \frac{\theta_S}{(1-\theta_P-\theta_S)} \exp\left[-2\alpha_S\theta_S - 2\alpha_{PS}\theta_P\right]. \tag{6}$$

This set of equations was used in (*2*) to describe different mixed protein/surfactant adsorption layers. We will, however, not use it here, as the model cannot distinguish between the specific properties between layers built up on a sequential or simultaneous adsorption route.

3. Experimental Protocol for Sequential and Simultaneous Adsorption Routes

The basis of the experimental setup used in the present studies is a classical drop profile analysis tensiometer (PAT1, SINTERFACE Technologies, Berlin, Germany). The image of a droplet formed at a capillary tip is acquired via a video camera and the extracted profile fitted by the Gauss-Laplace equation in order to determine the surface tension value (*8*). A special equipment of the PAT1, a coaxial double capillary, is used for the bulk exchange experiments, as it was first described by Wege et al. (*9*). The details of the setup were explained recently in (*10*, *11*). In brief, a drop of a solution of concentration C_1 is formed using syringe 1. The drop bulk is then exchanged by injecting a second solution of concentration C_2, via syringe 2 (cf. Figure 1). Regarding the experimental protocols and technical data for monitoring and control of the droplet size, a pulse-like flow with different injection volume dV and waiting time dt between two pulses are applied via syringe 2 into the drop. The software of PAT1 allows to keep the drop volume V_D or area A_D constant via a feedback control algorithm using syringe 1. During the exchange process, the concentration of the compound in the drop, i.e. $C_1(t)$ evolves continuously from the initial C_1 to the final concentration C_2 within several seconds, minutes or even hour, depending on the liquid exchange rate (*12*). The surface tension values are measured simultaneously from the drop profile via the PAT standard software.

The great advantage of the double capillary technique for the investigation of interfacial properties is based on the assumption that the material exchange between the bulk and interface is governed by an adsorption/desorption mechanism. Clearly the diffusion and convection transport mechanisms support the adsorption process via exchanging the bulk. However, during the exchange process the sub-layer should not be disturbed by forced convection or turbulences, otherwise the adsorbed layer cannot be formed correctly.

For high liquid flow rates and a position of the inner capillary tip deeper inside the drop, the probability of this problem is higher. On the other hand, for low injection rates far from the drop apex, a very weak convective flow can correspond to a slow exchange process that could never lead to a complete bulk exchange during a reasonable experimental time. Therefore, optimized operational conditions for the liquid exchange should be applied in order to establish a complete bulk exchange.

Mixed adsorption layers composed of protein and surfactant molecules can be formed via two different experimental strategies. As noted by several authors, the mixing protocol and equilibration time also for classic mixing can largely affect the adsorption. The classical way is when the protein and surfactant molecules adsorb simultaneously from a mixed solution. Alternatively, the individual components are adsorbed one after another, i.e., in a sequential way (*13*). The interfacial properties of the mixed layers formed in these two different ways can differ significantly, depending on the location where the protein/surfactant complexes are formed. The complex formation in the simultaneous adsorption route happens in the solution bulk, while in the process of sequential adsorption the surfactants form complexes with the pre-adsorbed proteins at the interface only. The formation of both types of mixed adsorption layers was studied earlier by the drop profile analysis tensiometer PAT-1, specially equipped with a coaxial double capillary (*3*, *9*, *13–15*). The general setup and measuring principle were described in detail in (*8*) while Ferri at al. (*12*) described all up to date known fields of application of the double capillary/double dosing arrangement first proposed by Wege et al. (*9*) for drop bulk exchange processes. Using this arrangement we can easily perform an *'in-situ'* subphase exchange in a single pendent drop without disturbing the surface layer, providing the required experimental protocol for performing a sequential adsorption of two individual components besides the traditional simultaneous adsorption route.

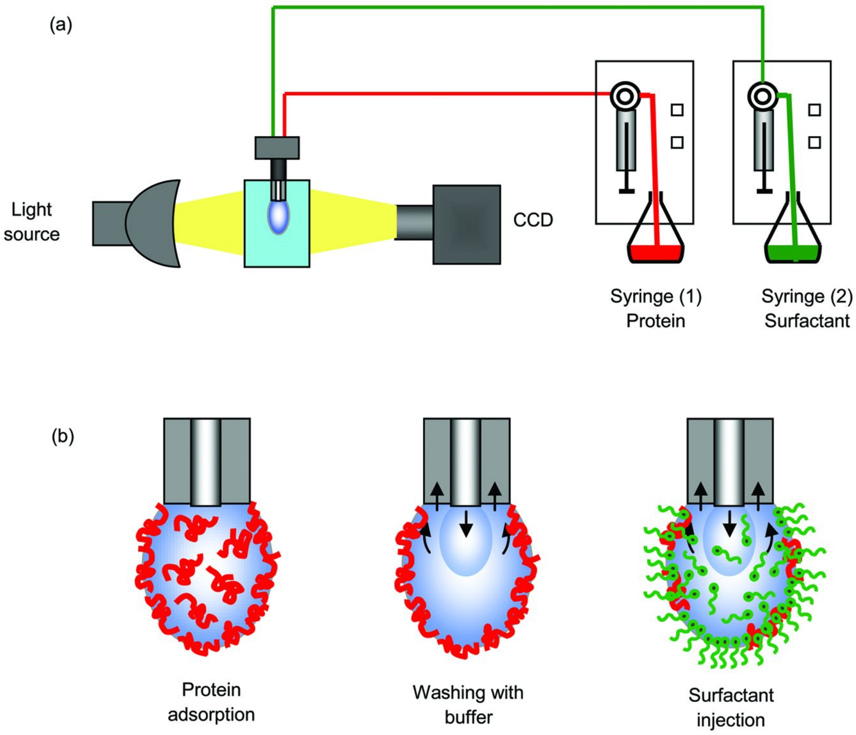

Figure 1. Schematic of the PAT1 tensiometer with a double dosing system and a coaxial double capillary (a); schematic of a bulk exchange with a protein drop, subsequent washing off the bulk with pure buffer and then injection of a surfactant solution (b).

In Scheme 1 we show the timeline of mixed protein/surfactant adsorption layers formed in a sequential adsorption experiment. First, a droplet is formed via the outer capillary with a pure protein solution (in buffer at a fixed pH), which documents the adsorption kinetics up to the equilibrium reached in the plateau region (stage-I).

At a sufficiently high protein concentration the interface is completely covered by adsorbed protein molecules. Once the proteins reach the interface, the hydrophobic parts are directed towards the air or oil phase, while hydrophilic parts remain in the aqueous bulk phase. Depending on the available time and space, this can lead to an unfolding of the molecular structure and consequently, increases the free energy of adsorption due to the larger attachment of proteins at the interface (*18*). During the subsequent first bulk exchange experiment with the pure buffer solution the protein molecules are washed off from the drop bulk, while keeping the drop volume and hence the drop surface area constant (stage-II). As we can see, there is no remarkable desorption of protein molecules from the interface during this exchange, which is confirmed by an almost negligible increase in surface tension.

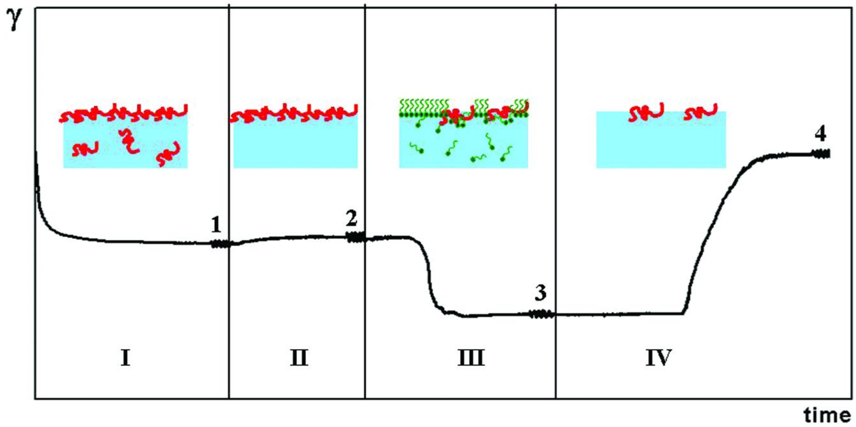

Scheme 1. Experimental protocol for mixed βCS/SDS layers formed via sequential adsorption made with a coaxial double capillary to measure dynamic surface tensions: I – pre-adsorption of βCS until equilibrium, II – bulk exchange against a pure buffer solution, i.e. replacement of proteins from the drop bulk, III – bulk exchange with SDS solution, i.e. modification of the surface structure by forming protein/surfactant complexes at the interfaces, IV – final bulk exchange against a buffer solution (washing out). 1,2,3,4 – Drop oscillations as a possible additional test of the surface layer composition (not discussed here)

The result of this exchange is a drop with a protein covered surface but containing no protein molecule in the drop bulk. In the second bulk exchange process, now we inject the surfactant solution into the drop through the inner capillary, replacing the buffer solution (stage-III). The protein/surfactant complexes are formed at the interface, which leads to modification of the pre-adsorbed protein layer. A decrease in surface tension is observed during this bulk exchange process; the absolute values of the new surface tension plateaus depend on the surfactant concentration of the injected solution. The final bulk exchange (washing out experiment) is performed again with a pure buffer solution (stage-IV). This washing-off removes any molecules from the drop bulk. We can also assume that all the surfactant molecules, freely adsorbed and bound to the protein molecules at the interface, are removed provided sufficient time is available to reach the respective local equilibrium for the surfactants. However, the protein molecules still in the adsorbed state after the sequential adsorption stay in the interfacial layer even after this washing off experiments and hence, it provides a qualitative estimation of the remaining amount of proteins. This experimental approach cannot be applied to systems where the complexes precipitate. This will affect the drop stability and hence the results.

For the case of simultaneous adsorption, the experimental protocol is shown in Scheme 2. The mixed solution of protein and surfactant forms a droplet at the outer capillary and the protein/surfactant complexes formed already in the bulk adsorb with free surfactant molecules in a competitive manner at the drop surface (stage-I). After this competitive adsorption, when the adsorption kinetics reached equilibrium, a washing off experiment is performed against a pure buffer solution (stage-II) to understand the replacement of adsorbed complexes. Note, the low frequency harmonic oscillations of the drop surface area are performed after each stage of the experiments to obtain the dilational viscoelastic properties of the adsorption layers as a qualitative measure of the surface composition.

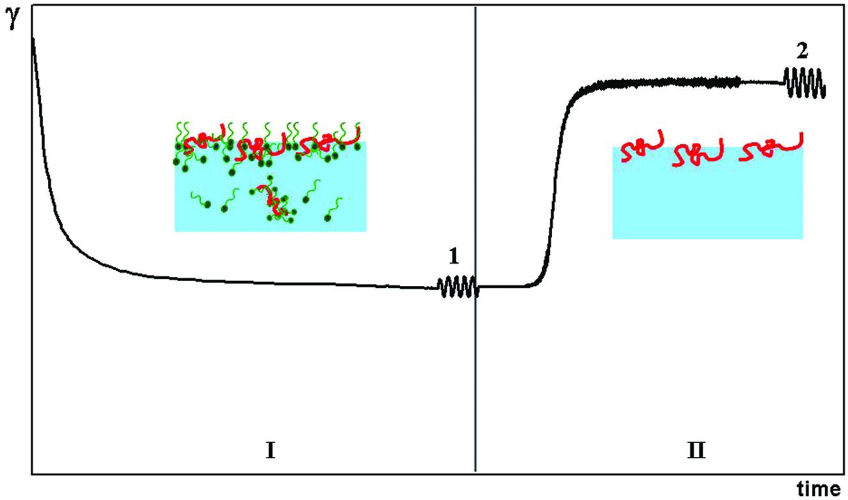

Scheme 2. Experimental protocol for simultaneously formed mixed βCS/SDS adsorption layers performed with a coaxial double capillary to measure dynamic surface tensions: I – adsorption from a mixed solution of βCS and SDS until equilibrium, II – bulk exchange with a pure buffer solution (washing off). 1,2 – periodic drop oscillations (not further analyzed here)

4. Fluid Dynamics of the Drop Exchange

As discussed above, the bulk exchange via the double capillary is a new experimental tool. However, a verification of its efficiency is required in order to know if the drop bulk is really perfectly mixed. Then, the simplest description of the evolution of the bulk concentration is given by (*10*):

$$C_1(t) = C_{\infty,1}\exp(-t/\tau)\,. \tag{7}$$

Here $\tau = V_D/R_E$ is the residence time of the liquid in the drop, $C_{1,\infty}$ is the concentration of bulk at the beginning and $C_{2,\infty}$ is the concentration of the species at the final stage (i.e. $C_{1,\infty} = 0$).

$$C_2(t) = C_{\infty,2}(1-\exp(-t/\tau)) \tag{8}$$

Experimental studies via the injection of a suitable dye solution and the related computational fluid dynamic (CFD) simulation results show that the mentioned assumptions are not a priori true (*11*). For a high injection flow rate of a liquid with a density higher than the droplet bulk this assumption is acceptable after a certain exchange time, e.g. t= 4 s, see Figure 2. However, for low injection rate conditions the inhomogeneous exchange process shown in Figure 3 is very far from a complete mixing. Another important issue is that during the exchange process the quality of drop profile has to be very high as it is used for determining the surface tension.

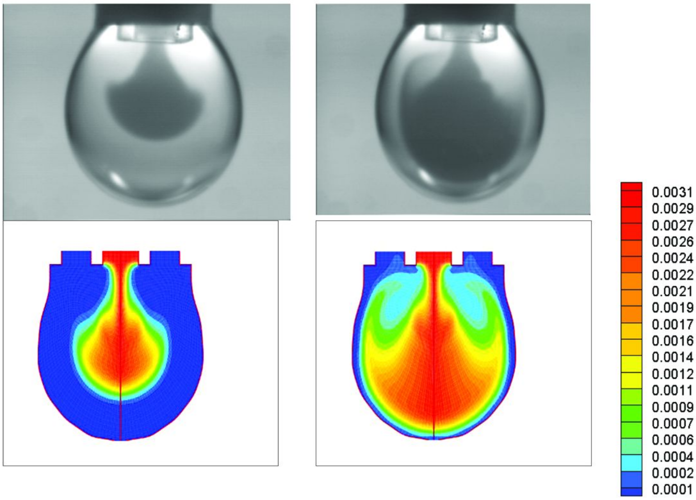

t=1.2 s t=4.0 s

Figure 2. Dye exchange experimental snapshots (top) and CFD simulation of dye concentration contours (bottom) for high injection rate conditions dt=0.1 s and dV=0.1 mm³ (11).

Figure 2 shows that for high injection rates, after starting the exchange process, a significant drop shaking and instability due to hydrodynamic and vibration effects appear. Hence, there are difficulties for the online surface tension monitoring. These observed instabilities can also cause strong disturbances of the adsorbed layer and must therefore be avoided. For any inhomogeneous exchange conditions a surfactant-rich region could come close to the drop surface and then creates a Marangoni convection (see for example Figure 4, at about t=25 s and 30 s). Marangoni convection can enhance the distribution of surface active components in the drop and also boosts mixing in the bulk (*11*, *16*).

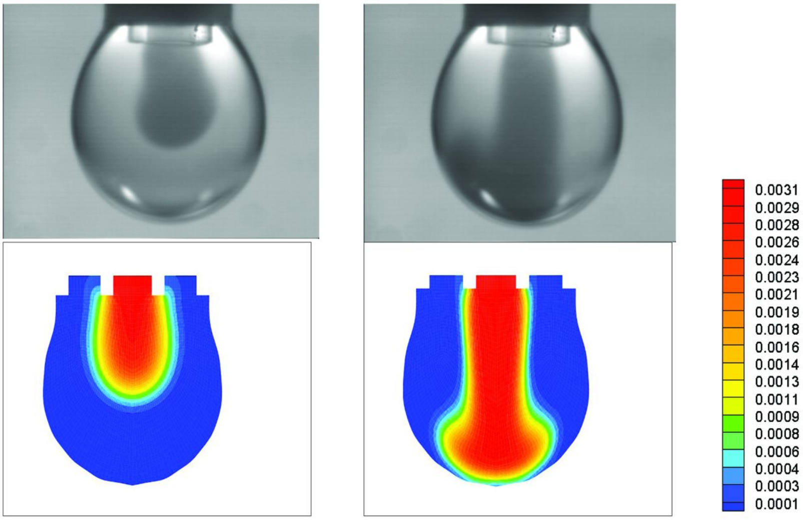

t=8 s

t=22 s

Figure 3. Dye exchange experimental snapshots (top) and CFD simulation of dye concentration contours (bottom) for low injection rate conditions dt=0.33 s and dV=0.033 mm^3 (10).

For the injected solution with a density lower than that in the drop bulk, for example just due to a difference in concentration of the solute or temperature, the exchange process can be influenced significantly (Figure 5). The injected flow may return back to the outer capillary without reaching drop center. The easiest ways to overcome this problem is to increase the injection rate within the suitable limits, or protrusion of the inner capillary tip deeper into the droplet center. In Figure 5 we see these two options for improving the drop bulk exchange.

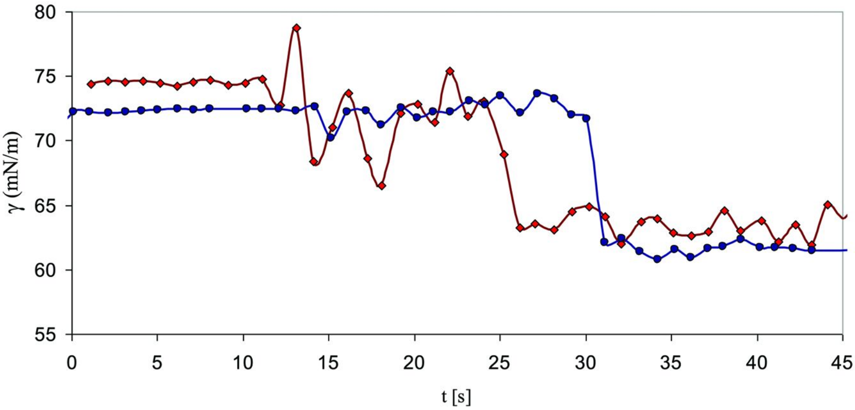

Figure 4. Surface tension measurements during drop exchange (starting around t=10 s) for high (♦ dt=0.1 s, dV=0.1 mm³) and low (● dt=0.33 s, dV=0.033 mm³) injection rates, Marangoni onset appears at about 25 and 30 s, respectively.

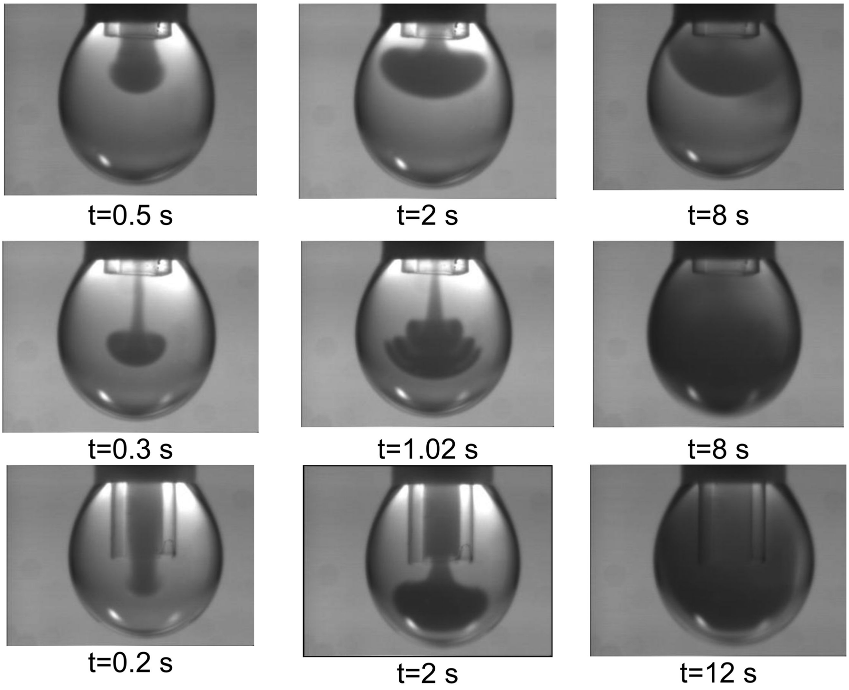

Figure 5. Dye exchange experimental snapshots (top) for dye solution 0.3 mg/ml + 1.5% Ethanol (density slightly lower than water), for dt=0.1s and dV=0.1 mm³ (top row) and for dt=0.1 s, dV=0.2 mm³ (central row), and for dt=0.1 s, dV=0.1 mm³ with deep immersed inner capillary (bottom row).

For the current setup in absence of surface activity effects and thus no Marangoni convection, the evolution of drop surface concentration (C_s) respect to the inlet dye concentration (C_{inlet}) are predicted via CFD simulation of the corresponding Navier Stokes equations presented in Figure 6. This figure shows the effect of increasing injection rate (dV) on the normalized drop surface concentration (C_s/C_{inlet}) at constant injection interval time dt. For the studied case and conditions (dt=0.1 s), the medium injection rate 0.067 mm^3 looks optimal, as the lower injection rate needs a very long time for getting close to the complete exchange and the higher injection rates cause drop shaking problem.

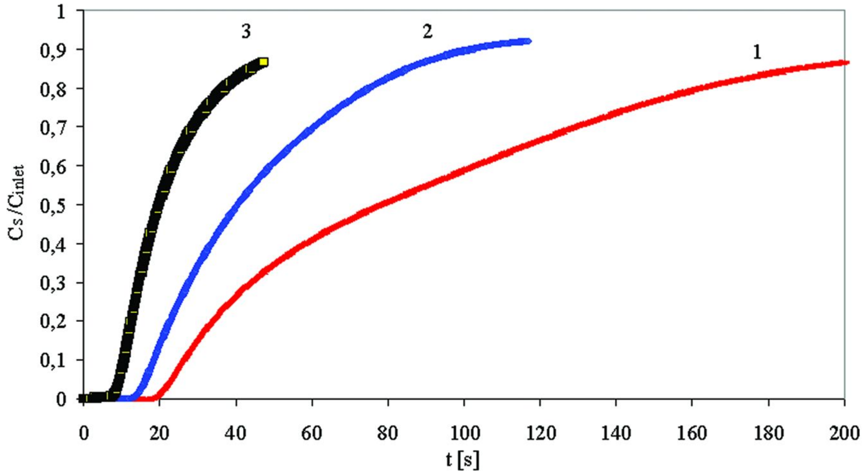

Figure 6. Normalized drop surface concentration (C_s) respect to the inlet concentration (C_{inlet}) during drop water exchange by a dye solution 0.3 mg/ml for dt=0.1 s and different injection rates dV=0.033 (1), 0.067 (2) and 0.1 mm^3/pulse (3), respectively.

5. Adsorption Isotherm of Frequently Studied Proteins

The surface behaviour of an aqueous protein solution depends on the native characteristics of the protein macromolecule such as chemical and spatial structure, molecular weight and net charge. Figure 7 shows experimental surface pressure isotherms, obtained by drop/bubble profile analysis tensiometry, for the globular proteins β-lactoglobulin (BLG), lysozyme, bovin serum albumin (BSA) and human serum albumin (HSA) and the random coil protein β-casein (BCS). For the different proteins, the onset of measurable π-values varies within a wide concentration region and the shapes of the π-c curves are quite different. The runs for BSA, HSA and BCS virtually follow the same trend of an initial steep increase and subsequent formation of a plateau region, while those for BLG and lysozyme show continuous increase of the surface pressure with increasing concentration in the studied region. It is evident from Figure 7 that BSA and HSA behave rather similarly since the molecular structure of these albumins is analogous, i.e. their amino acids sequences coincide by about 80%.

Comparison between the adsorption kinetics data for BSA, BCS, HSA and BLG obtained with and without forced convection in the solution sub-phase leads to the conclusion that the adsorption of proteins at the water/air interface is thermodynamically reversible, in contrast to the kinetic irreversibility of the process as discussed in (*17*, *18*). In contrast to the pure protein system, the addition of a low molecular weight surfactant to the solution provokes replacement of the protein from the surface (*19*, *20*). The mechanism of this process comprises both modification of the surface activity of the protein due to formation of less adsorbing complexes and competitive adsorption by the surfactant molecules, and is discussed in details below.

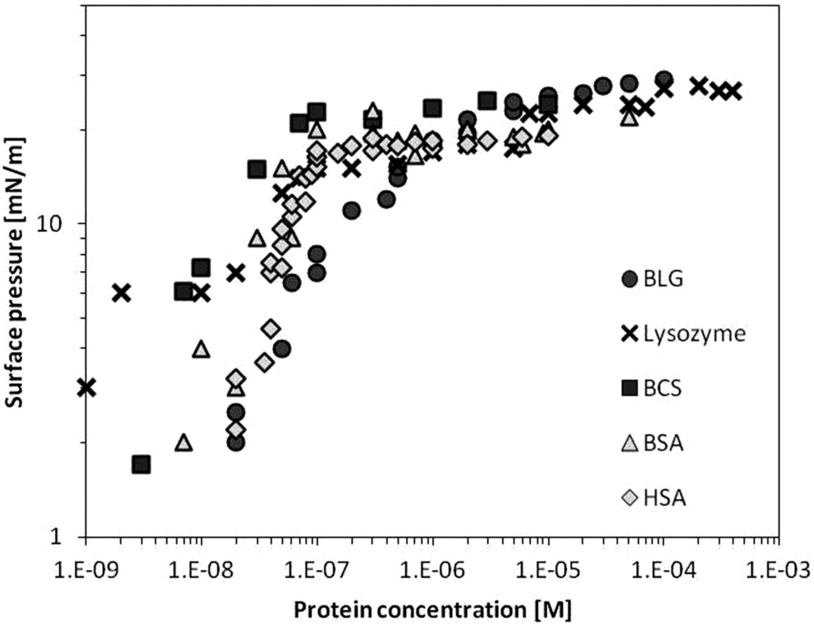

Figure 7. Surface pressure vs. protein bulk concentration plots for BLG, redrawn from (16), Lysozyme, redrawn from (22), BCS, new data, BSA, redrawn from (23), HSA, redrawn from (24).

The interfacial properties of proteins are strongly affected by the type of the hydrophobic fluid (gas or oil) which is in contact with the solution. Figure 8 shows experimental surface pressure isotherms, again obtained by the most reliable drop/bubble profile analysis tensiometry, for BLG and BCS at water/air (w/a) and water/hexane (w/h) interface. One clearly distinguishes between the curves for the different interfaces as those for w/h interface are shifted to lower protein concentrations. As discussed in the literature, e.g. in (*16*, *21*), such shift of the adsorption isotherm is related to the stronger affinity of the hydrophobic residues of the protein for the oil phase. Theoretical processing of the experimental data for BLG by the model mentioned above shows smaller ω-values at the water/hexane interface, which indicates a more compact layer of the protein that has a different conformation in contact with the oil phase (*16*, *18*). As discussed below, the elucidation of the interfacial properties of protein/surfactant solutions are based on these findings.

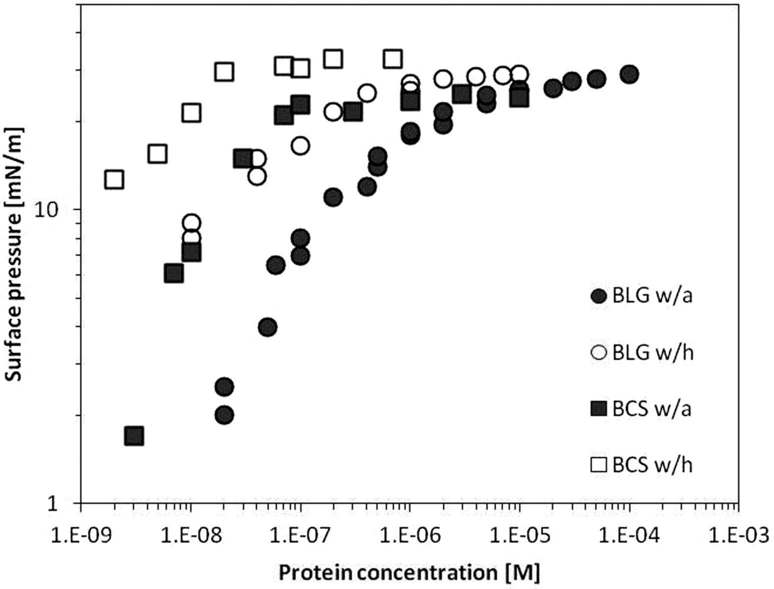

Figure 8. Surface pressure vs. protein bulk concentration plots for BLG, redrawn from (16, 18) and BCS, new data, at water/air and water/hexane interface.

6. Exchange Dynamics at Water/Air and Water/Hexane Interfaces

In order to analyze under which condition a pre-adsorbed protein can be more or less displaced from a liquid interface by competing surfactant molecules, we followed the two strategies detailed above, i.e. injected surfactant solutions of various concentration and then replaced this solution with a pure buffer solution in order to probe how much protein is left at the surface after the final washing.

Figure 9 shows the adsorption dynamics curves for mixed βCS/SDS layers formed after the second bulk exchange with different SDS concentration at W/A and W/H interfaces.

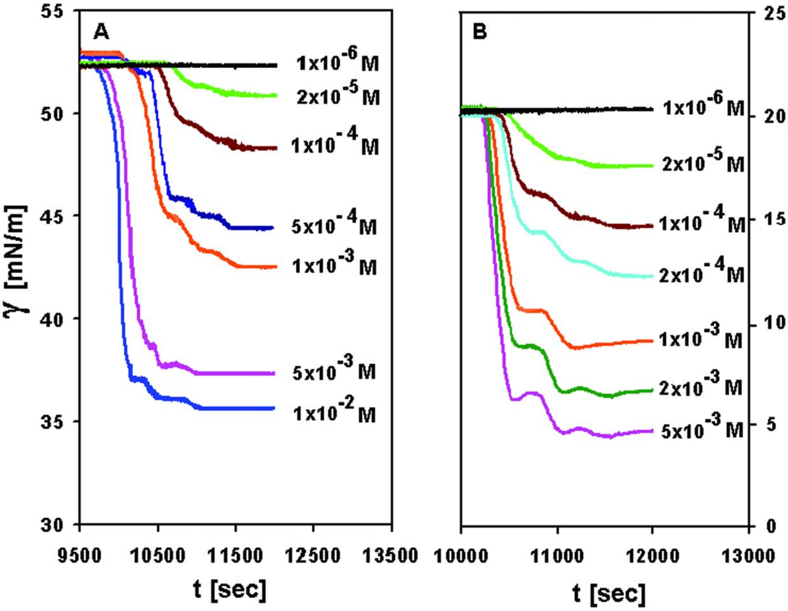

Figure 9. Surface tension dynamics during the drop exchange against different [SDS] obtained for sequential adsorption experiments at W/A (A) and W/H (B) interfaces; the concentration of βCS is kept constant to 10^{-6} mol/dm^3.

One can see in both cases, the higher the SDS concentration, the faster is the surface tension decrease and the lower is the final surface tension plateau. It suggests that mixed layers are formed by the interaction between protein and surfactant only at the interface and at higher surfactant concentration an increasing amount of protein molecules is displaced from the surface layer by the surfactant molecules due to stronger competition, i.e., the surface layer is dominated by the adsorbed surfactant molecules. In this case the situation is that a protein/surfactant complex in the bulk of the droplet and the interface has free adsorbed surfactant molecules in addition to protein/surfactant complexes combined to different extents. Note, the dynamic curves for both interfaces W/A (Figure 9A) and W/H (Figure 9B) certainly show two humps before the tension values reach a plateau, which become more pronounced at higher SDS concentration. This is probably due to the convection pattern inside the drop, i.e. the flow field of the inflowing liquid does not involve all the liquid inside the drop immediately, as we can understand from the discussion of the hydrodynamics above. A quantitative understanding still requires further investigations.

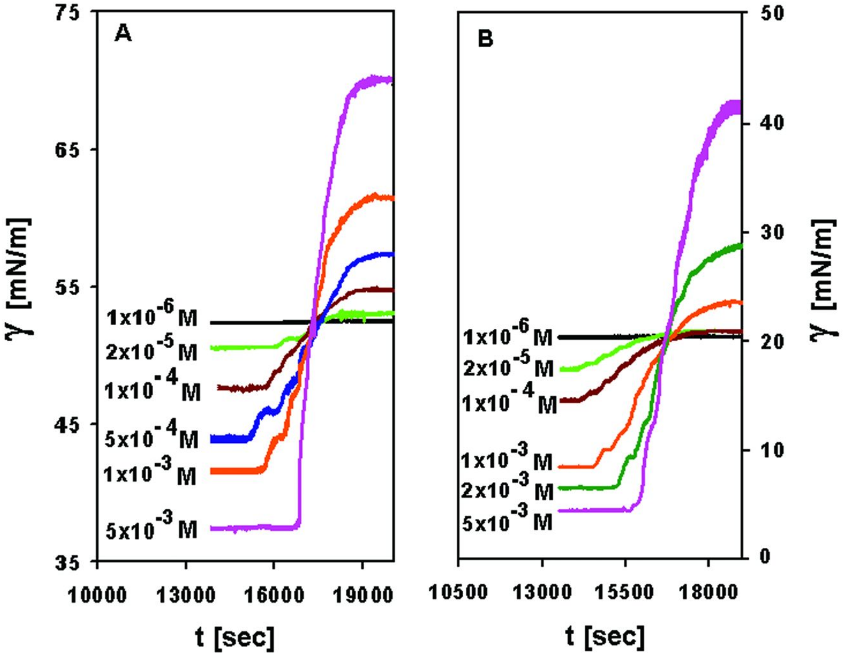

Figure 10. Surface tension dynamics during final drop exchange (washing out) experiments measured after sequential adsorption from an initial βCS solution and subsequently from SDS solutions of different concentrations at W/A (A) and W/H (B) interfaces; the concentration of βCS is kept constant to 10^{-6} mol/dm^3.

The curves shown in Figure 10 represent the corresponding final bulk exchange (washing out experiments) of the previously injected SDS of different concentrations against a pure buffer solution. In contrast to protein, only surfactants molecules are reversibly adsorbed and thus desorb completely as described in a recent report (*9*). This means that within the experimental time all protein molecules which had not been displaced from the drop surface by the surfactants further stay in the surface layer after this washing out experiment due to their high free energy of adsorption (*18*). One can see for both W/A (Figure 10A) and W/H (Figure 10B) interfaces, at lower SDS concentrations there are no significant changes in the final surface tension plateaus with increasing surfactant concentrations and the absolute values are close to that of pure βCS solution. The addition of the anionic surfactant SDS to the pre-adsorbed proteins leads to a complex formation first via strong electrostatic interaction resulting in an increased surface activity of the complexes and hence, they cannot be displaced from the surface layer by any co-adsorbing free surfactant molecules. Any hydrophobic interaction is of secondary importance in the complex formation at these low surfactant concentrations. Consequently, almost all the adsorbed protein molecules are left in the surface layer after washing off. At higher surfactant concentrations, however, the hydrophobic binding of SDS becomes increasingly significant. As a consequence the complexes become hydrophilized once all the charge sites of the proteins have been compensated by the electrostatically bound SDS. The resulting complexes become less surface active and can easily desorb into the solution bulk, leading to a decreasing presence of remaining proteins after washing off. This results in a higher surface tension plateau after the washing out experiment.

The results presented in Figure 11 show the desorption dynamics of mixed surface layers formed after simultaneous adsorption (the dynamic adsorption curves are not shown here) at different SDS concentrations. Similar to the sequential adsorption experiments, the desorption of SDS molecules from the mixed surface layer results in an almost negligible change in the surface tension plateaus at low surfactant concentrations for both W/A (Figure 11A) and W/H (Figure 11B) interfaces and the absolute values increase with increasing SDS concentration at higher concentrations. At low surfactant concentration, the surface structure does not depend on the location where the proteins and surfactant interact and neither the conformation of the protein.

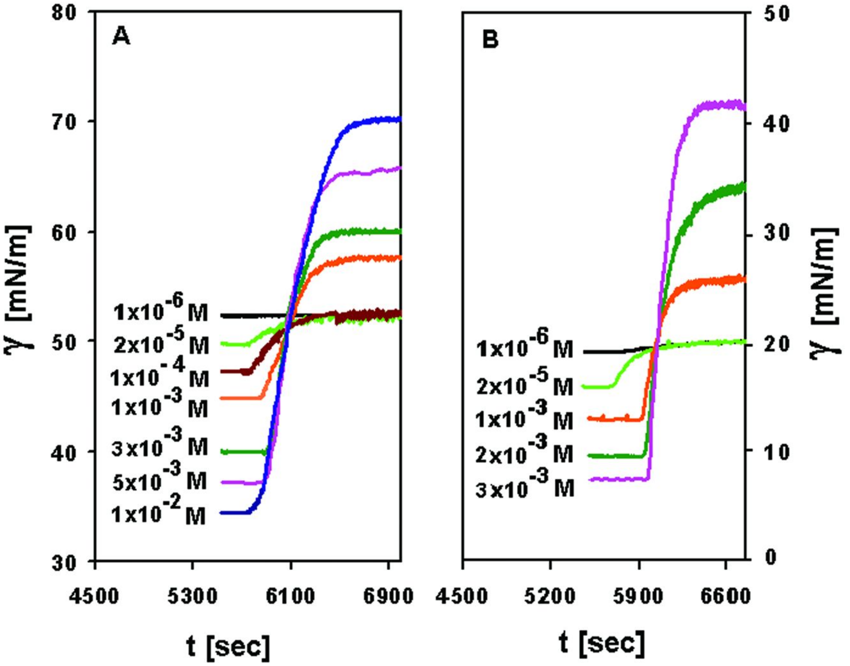

Figure 11. Surface tension dynamics during drop-bulk exchange experiments against pure buffer solution measured after simultaneous adsorption from a mixed solution of βCS/SDS for different used [SDS] at W/A (A) and W/H (B) interfaces; the concentration of βCS is kept constant to 10^{-6} mol/dm^3.

Once the complexes formed in the bulk reach the interface, they adopt a conformation that the surface activity of the adsorbed complexes are almost identical to the complexes only formed in the surface layer. However, at higher SDS concentration, the dynamics of desorption from the surface layers formed from mixed solutions deviate significantly, which can be explained only by the different composition and structure of the adsorbed complexes. This can be better understood in the isotherms shown in Figure 12, representing the state of remaining proteins after the final washing off.

For both W/A and W/H interfaces, the exchange dynamics obtained from sequential and simultaneous adsorption experiments follow the similar trend. However, there are some definite differences between the behaviors of such mixed adsorption layers formed at the W/A interface and those at the W/H interface, i.e., dependency on used surfactant concentrations and the composition of the mixed adsorption layers must be different. Indeed, the complexes formed at the W/H interface are more stable obviously due to different conformation and consequently, deep penetration of the hydrophobic segments of the protein molecules into the organic subphase (*24*, *25*). It suggests that the amount of hydrophobically bound SDS complexes should be lower at the W/H interface. Compared to the W/A interface, the behavior of the mixed layers at the W/H interface is governed by the properties of the complexation rather than by the amount adsorbed competing with the free surfactants.

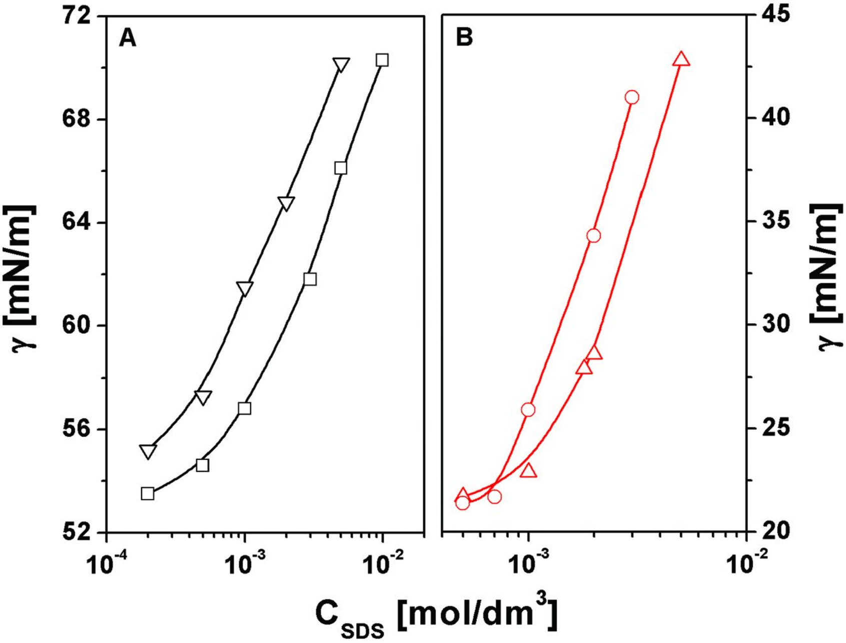

Figure 12. Isotherms for washing off experiments after sequential (▽,△) and simultaneous (□,○) adsorption at W/A (A) and W/H (B) interfaces.

]

7. Comparison of the Two Routes at Water/Air and Water/Hexane Interfaces

The mixed protein/surfactant layers formed via two different routes show different equilibrium surface properties, which can be caused obviously only by the location where the proteins and surfactants meet each other – in the bulk as it occurs in the simultaneous adsorption or in the surface layer during sequential adsorption. In order to compare the results, the isotherms shown in Figure 13 have been constructed from the equilibrium surface tension values for the mixed βCS/SDS layers formed via sequential and simultaneous adsorption experiments after stage-III and stage-I, respectively, and illustrated along with the isotherms of pure SDS. The patterns of the isotherms for the two different interfaces are similar.

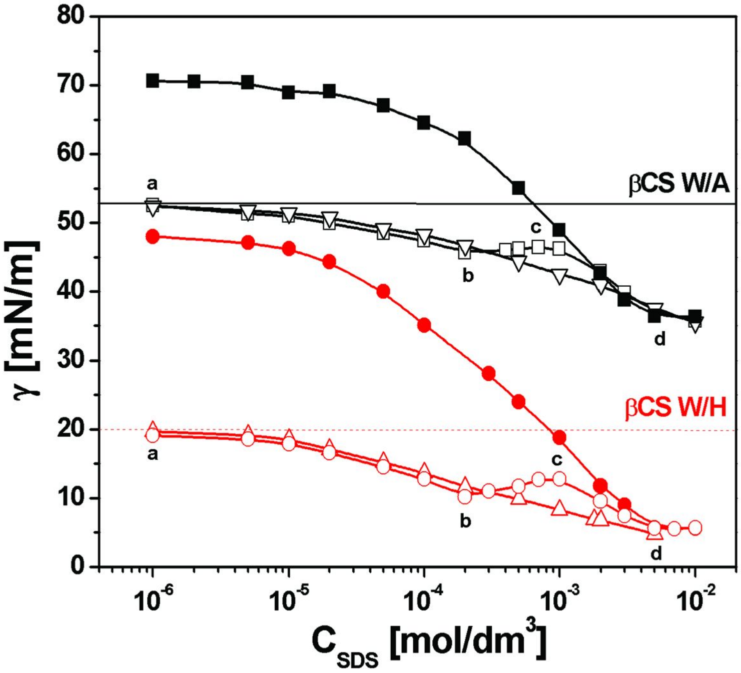

Figure 13. Adsorption isotherms of pure SDS at W/A (black ■) and W/H (red ●) interfaces, and its mixed layers with βCS built-up via sequential (▽,△) and simultaneous (□,○) adsorption at W/A (▽,□) and W/H (△,○) interfaces. The symbol a, b, c and d are used to show the region-wise comparison of two different isotherms; the horizontal lines indicate the equilibrium surface tension values of 10^{-6} mol/dm^3 βCS solution at W/A (black solid) and W/H (red dash) interfaces.

The tensiometric profiles evidence formation of a mixed layer (Figure 13, open symbols). All start from a lower surface tension value, corresponding to the value of the βCS solutions in absence of SDS (horizontal lines). It has been found that there are surface tension maxima in the simultaneous adsorption isotherms in the region 'bcd' in Figure 13. In contrast, the adsorption isotherms obtained for the sequential adsorption route do not show such maxima. At this stage of interaction the complexes formed in the bulk aggregate and form larger structures and precipitate. This corresponds to a partial depletion of adsorbing species and hence to an increase in the measured tensions. In contrast, in sequential adsorption, an aggregation of the complexes formed only at the interface is not feasible obviously due to different conformation of the pre-adsorbed protein molecules. There is actually no excess of more and more hydrophobic complexes available to form such superstructured aggregates. This remarkable difference is clear evidence that the way how mixed protein/surfactant layers are formed has a decisive role on their equilibrium surface properties. A quantitative analysis is not possible here as the respective theoretical models do not exist. Therefore, modification of the available theoretical models (*18*, *24*, *26*, *27*) is needed in order to quantify the characteristic features of the mixed layer owing to phenomenological differences in the two different ways of their formation.

Despite this remarkable difference, the simultaneously and sequentially formed mixed layers of βCS and the non-ionic surfactant C_{12}DMPO (dodecyl dimethyl phosphine oxide) showed similar equilibrium surface properties, as it was observed by Kotsmar et al. in a recent study (*3*). The similarity in the behavior is attributed to the type of surfactant used (non-ionic surfactant in pH 7), i.e. the interaction is only of hydrophobic nature and happens between the hydrophobic groups in the protein and surfactant molecules. In contrast, for the anionic surfactant SDS and βCS, the complex formation is considered to be driven first by electrostatic and only then mainly by hydrophobic interactions. Thus, one can suggest that the behavior of the resulting protein/surfactant complexes differ in their structure and composition.

In Figure 12, the isotherms for washing off after sequential and simultaneous adsorption at the two interfaces are illustrated. The results shown here are corresponding only to higher SDS concentration, as there is no significant difference in the isotherms for the two different adsorption routes. A steep increase of the surface tension values suggests an increasing amount of displaced proteins from the surface layer by surfactant molecules. At the W/A interface, after washing off in the sequential adsorption experiment, the surface tension reaches much higher values in comparison to those obtained in the simultaneous adsorption case (Figure 5A). The accessibility of the hydrophobic parts of the pre-adsorbed proteins is more favorable by the surfactants to form less surface active complexes, which can be easily displaced from the surface layer by the surfactant molecules. This leads to a decreasing presence of the protein/surfactant complexes at the interface after sequential adsorption. In the other case, an increased number of surfactants are consumed in the formation of associated complexes in the bulk solution that restricts the adsorption of free surfactant molecules at the interface. The amount of freely adsorbed surfactants is essentially less and, consequently, the surface is covered by an increased amount of adsorbed complexes after simultaneous adsorption.

At the W/H interface, the picture is totally opposite, i.e., in simultaneous adsorption after washing off, the surface tension increases much earlier than in a sequential adsorption (Figure 12B). As discussed before, the complexes formed at the W/H interface are more stable and cannot desorb easily into the bulk. This suggests an increasing presence of the adsorbed complexes at the interface after sequential adsorption. In contrast, in simultaneous adsorption, the surfactants adsorb strongly with high adsorption energy at the W/H interface and consequently, an increasing amount of complexes desorb from the surface layer after simultaneous adsorption.

8. Conclusions and Outlook

As was shown above, there are significant differences in the interfacial behavior of mixed protein/surfactant complexes adsorbed at the water/air and water/hexane interfaces. Moreover, the location at which these complexes are formed is essential for their properties in the interfacial layer.

For mixtures of β-CS with different surfactants we have demonstrated that there are two main types of interaction, a hydrophobic and for ionic surfactants also an electrostatic interaction. The cartoon (cf. Scheme 3) shows schematically that the surface activity of the formed complexes decreases gradually with the amount of added surfactant. This leads to a progressive replacement of protein molecules from the interface.

This mechanism was confirmed by the experimental findings shown in Figs. 9 to 13. For mixtures of β-CS and ionic surfactants we postulated a primary electrostatic interaction, resulting in an increased surface activity of the complex. Further addition of surfactant molecules leads to a subsequent hydrophobic interaction with the complexes. As a consequence, the charge of the complexes is reversed and the surface activity decreases step by step until their complete replacement from the interface by free surfactants. This is schematically shown in Scheme 4.

Note, the mentioned mechanisms are valid for both discussed interfaces. When we compare the amount of protein replaced from the interface by surfactants, we can see that due to the interaction with the molecules of the oil phase, the proteins are stronger adsorbed at the water/oil interface and, therefore, a larger amount remains there. Hence, the conformational changes of the proteins, caused by a direct interaction between surfactants and proteins in the solution bulk, as it is the case for simultaneous adsorption processes are such, that the complexes cannot be anchored at the water/oil interface as strongly as it is possible for the protein alone.

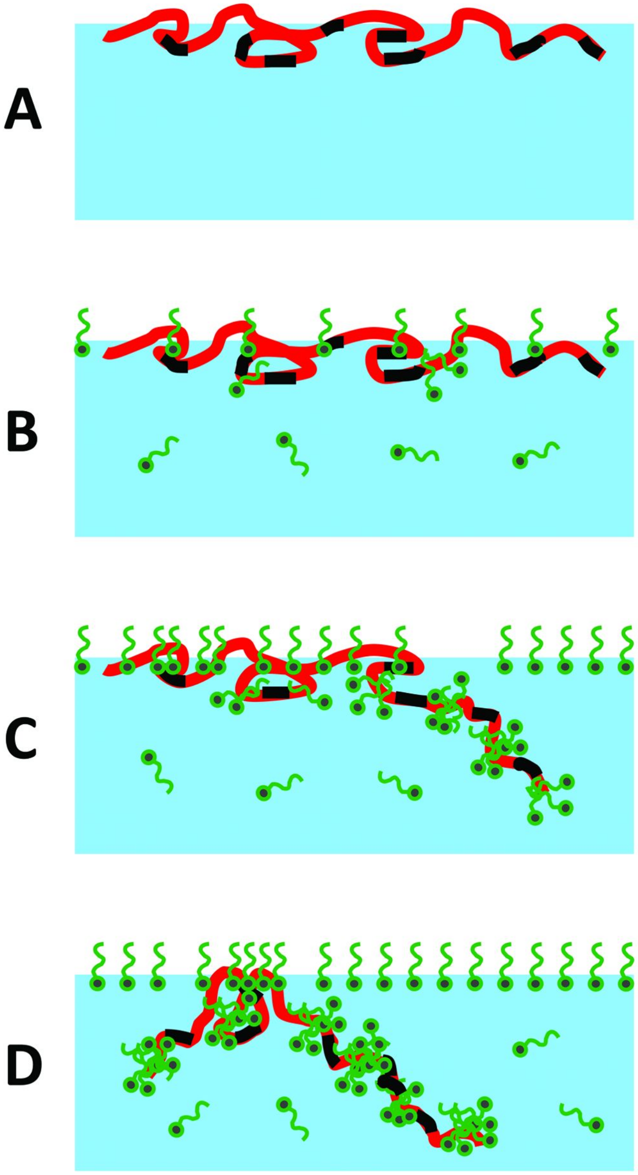

Scheme 3. Illustration of protein displacement from the surface layer by the surfactant molecules in sequential adsorption: A – adsorption of pure protein, B – penetration of surfactant molecules into the preformed protein layer, C – more and more surfactants binding to the protein backbone, D – denaturation of protein from the interface; redrawn from (13)

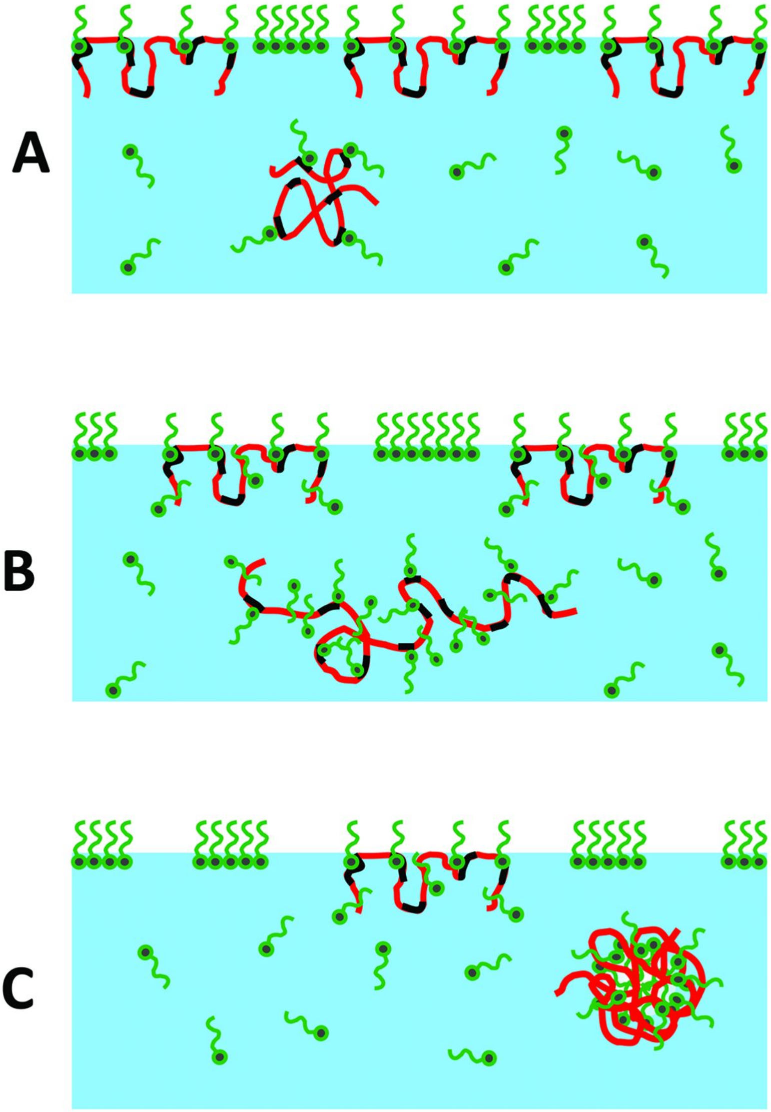

Scheme 4. Protein/surfactant complex formation in the solution bulk and their competitive adsorption with the free surfactant molecules at the interface: A – binding of SDS by initial electrostatic and subsequent hydrophobic interaction, B – change in conformation of βCS to accommodate more surfactant molecules, C – self-association of the complexes; redrawn from (13)

In sequential adsorption, one of the possible mechanisms for the displacement of protein from the surface layer was proposed in the light of 'orogenic displacement' (*28–32*) and it occurs in several steps as depicted in Scheme 3A-D. The proteins first adsorb at the interface by changing its conformation and tightly attach to the surface (Scheme 3A). Then, surfactant molecules gradually penetrate into the pre-adsorbed protein layer, adsorb and modify the surface structure by forming protein/surfactant complexes at the interface (Scheme 3B-C). The denaturation of the protein molecules continues until the protein network loses its rigidity and is able to desorb into the droplet bulk (Scheme 3D). However, again the surfactant would first have to hydrophilize the patches formed after a break-off of a preformed protein layer network to make them wetted by the aqueous solution. Thus, the protein/surfactant mixed layer formation must be at least driven by the interplay between an orogenic mechanism and hydrophilization of the protein layer (patches) with the surfactants. In contrast, for simultaneous adsorption, this mechanism cannot be applied, as the adsorbing species are the protein/surfactant complexes and available free surfactant molecules, which simply adsorb in a competitive manner.

Future work will have to focus on a quantitative understanding of the described differences in the adsorption behavior for different interfaces. We can expect that also the polarity of the oil will have a significant influence, however, there are only results for pure protein solutions available in literature so far. Moreover, the pH of the solution influences strongly the number of net charges in the protein, hence, the surface activity and also the amount of ionic molecules bound to each protein molecules. These peculiarities will have to be reflected by future theoretical models as well.

As it was addressed recently (*33*), a single set of model parameters should be able to describe all interfacial properties in an acceptable quality, including the adsorption kinetics, the equilibrium state and the dilational visco-elasticity. Although the shear visco-elasticity cannot be linked quantitatively to the adsorption layer properties, it has at least to be in a qualitative agreement with the picture obtained by the other experimental techniques. A throughout understanding of mixed protein/surfactant adsorption layers at liquid interfaces is yet pending.

Acknowledgments

The work was financially supported by projects of the DFG (Mi418/20-1) and the European Space Agency (PASTA).

References

1. *Food Colloids - Fundamentals of Formulation*, Special Publication No. 258; Dickinson, E., Miller, R., Eds.; Royal Society of Chemistry: London, 2001
2. Kotsmar, Cs.; V. Pradines, V.; Alahverdjieva, V. S.; Aksenenko, E. V.; Fainerman, V. B.; Kovalchuk, V. I.; Krägel, J.; Leser, M. E.; Noskov, B. A.; Miller, R. *Adv. Colloid Interface Sci.* **2009**, *150*, 41.

3. Kotsmar, Cs.; Grigoriev, D. O.; Makievski, A. V.; Ferri, J. K.; Krägel, J.; Miller, R.; Möhwald, H. *Colloid Polym. Sci.* **2008**, *286*, 1071.
4. Alahverdjieva, V. S.; Fainerman, V. B.; Aksenenko, E. V.; Leser, M. E.; Miller, R. *Colloids Surf., A* **2008**, *317*, 610.
5. Pradines, V.; Fainerman, V. B.; Aksenenko, E. V.; Krägel, J.; Wüstneck, R.; Miller, R. *Langmuir* **2001**, *27*, 965.
6. Fainerman, V. B.; Lucassen -Reinders, E. H.; Miller, R. *Adv. Colloid Interface Sci.* **2003**, *106*, 237.
7. Fainerman, V. B.; Zholob, S. A.; Leser, M. E.; Michel, M.; Miller, R. *J. Colloid Interface Sci.* **2004**, *274*, 496.
8. Loglio, G.; Pandolfini, P.; Miller, R.; Makievski, A. V.; Ravera, F.; Ferrari, M.; Liggieri, L. In *Studies in Interface Science*; Möbius, D., Miller, R., Eds.; Elsevier: Amsterdam, 2001; Vol. 11, p 439.
9. Wege, H. A.; Holgado-Terriza, J. A.; Neumann, A. W.; Cabrerizo-Vilchez, M. A. *Colloids Surf., A* **1999**, *156*, 509.
10. Ferri, J. K.; Gorevski, N.; Kotsmar, Cs.; Leser, M. E.; Miller, R. *Colloids Surf., A* **2008**, *319*, 13.
11. Javadi, A.; Ferri, J. K.; Karapantsios, Th. D.; Miller, R. *Colloids Surf., A* **2010**, *365*, 145.
12. Ferri, J. K.; Kotsmar, Cs.; Miller, R. *Adv. Colloid Interface Sci.* **2010**, *161*, 29.
13. Dan, A.; Kotsmar, Cs.; Ferri, J. K.; Javadi, A.; Karbaschi, M.; Krägel, J.; Wüstneck, R.; Miller, R. *Soft Matter* **2012**, *8*, 6057.
14. Cabrerizo Vilchez, M.; AWege, H. A.; Holgado Terriza, J. A. *Rev. Sci. Instrum* **1999**, *70*, 2438.
15. Ferri, J. K.; Dong, W. F.; Miller, R. *J. Phys. Chem. B* **2005**, *109*, 14764.
16. Javadi, A.; Karbaschi, M.; Bastani, D.; Ferri, J. K.; Kovalchuk, V. I.; Kovalchuk, N.; Javadi, K.; Miller, R. *Colloids Surf., A* **2012** submitted.
17. Svitova, T. F.; Wetherbee, M. J.; Radke, C. J. *J. Colloid Interface Sci.* **2003**, *261*, 170.
18. Fainerman, V. B.; Miller, R.; Ferri, J. K.; Watzke, H.; Leser, M. E.; Michel, M. *AdV. Colloid Interface Sci.* **2006**, *163*, 123.
19. Kotsmar, Cs.; Pradines, V.; Alahverdjieva, V. S.; Aksenenko, E. V.; Fainerman, V. B.; Kovalchuk, V. I.; Krägel, J.; Leser, M. E.; Noskov, B. A.; Miller, R. *Adv. Colloid Interface Sci.* **2009**, *150*, 41.
20. Yampolskaya, G.; Platikanov, D. *Adv. Colloid Interface Sci.* **2006**, *128*, 159.
21. Pradines, V.; Krägel, J.; Fainerman, V. B.; Miller, R. *J. Phys. Chem. B* **2009**, *113*, 745.
22. Alahverdjieva, V. S.; Grigoriev, D. O.; Ferri, J. K.; Fainerman, V. B.; Aksenenko, E. V.; Leser, M. E.; Michel, M.; Miller, R. *Colloids Surf., A* **2008**, *323*, 167.
23. Berthold, A.; Schubert, H.; Brandes, N.; Kroh, L.; Miller, R. *Colloids Surf., A* **2007**, *301*, 16.
24. Makievski, A. V.; Fainerman, V. B.; Bree, M.; Wüstneck, R.; Krägel, J.; Miller, R. *J. Phys. Chem. B* **1998**, *102*, 417.
25. Chipot, C.; Pohorille, A. *J. Am. Chem. Soc.* **1998**, *120*, 11912.

26. Miller, R.; Fainerman, V. B.; Leser, M. E.; Michel, M. *Colloids Surf., A* **2004**, *233*, 39.
27. Miller, R.; Fainerman, R.; Leser, M. E.; Michel, M. *Curr. Opin. Colloid Interface Sci.* **2004**, *9*, 350.
28. Mackie, A. R.; Gunning, A. P.; Ridout, M. J.; Wilde, P. J.; Morris, V. J. *Langmuir* **2001**, *17*, 6593.
29. Gunning, P. A.; Mackie, A. R.; Gunning, A. P.; Wilde, P. J.; Woodward, N. C.; Morris, V. J. *Food Hydrocolloids* **2004**, *18*, 509.
30. Mackie, A. R.; Gunning, A. P.; Wilde, P. J.; Morris, V. J. *J. Colloid Interface Sci.* **1999**, *210*, 157.
31. Rereira, L. G. C.; Theodoly, O.; Blanch, H. W.; Radke, C. J. *Langmuir* **2003**, *19*, 2349.
32. Freer, F. M.; Yim, K. S.; Fuller, G. C.; Radke, C. J. *J. Phys. Chem. B* **2004**, *108*, 3835.
33. Wüstneck, R.; Fainerman, V. B.; Aksenenko, E. V.; Kotsmar, Cs.; Pradines, V.; Krägel, J.; Miller, R. *Colloids Surf., A* **2012**, *404*, 17.

Chapter 8

Control of Protein Adsorption and Cell Adhesion by Mixed Polymer Brushes Made by the "Grafting-To" Approach

**Eva Bittrich,[1] Sina Burkert,[1] Klaus-Jochen Eichhorn,[1]
Manfred Stamm,[1,2] and Petra Uhlmann*,[1]**

**[1]Leibniz Institute of Polymer Research Dresden, Hohe Strasse 6,
D-01069 Dresden, Germany
[2]Technische Universität Dresden, Physical Chemistry of Polymer Materials,
01062 Dresden, Germany
*E-mail: uhlmannp@ipfdd.de**

The capability of mixed polymer brush systems to modify and switch physico-chemical properties of biointerfaces is demonstrated in this paper. Mixed brushes were composed of the temperature sensitive polymer poly(N-isopropyl acrylamide) (PNIPAAM) and two polyelectrolytes, poly(2-vinylpyridine) (P2VP) and poly(acrylic acid) (PAA). Using these polymers binary brushes were prepared, the first one consisting of PNIPAAM – P2VP representing a system sensitive for temperature and pH changes, and the second one consisting of two polyelectrolytes (P2VP-PAA) showing sensitivity to pH changes of the surrounding fluid. Selected aspects concerning the environmental sensitivity as well as the protein adsorption affinity of these brushes are discussed. The stimuli-response towards temperature (PNIPAAm-P2VP) and pH (P2VP-PAA) of these binary polymer brushes was utilized to switch the adsorbed amount of protein and finally to regulate cell adhesion at brush coated surfaces.

In Proteins at Interfaces III State of the Art 2012; Horbett, T., et al.;
ACS Symposium Series; American Chemical Society: Washington, DC, 2012.

1. Introduction

Thin polymer layers have been proven to be able to modify physico-chemical interface properties to control the adsorption behaviour of proteins at artificial surfaces.

Here two approaches are interesting for application. One strategy is to create biocompatible surfaces by modifying the interface of artificial material with protein resistant surface layers (*1*, *2*), since the exposure of such foreign materials to blood without protein resistance may lead e.g. to the unwanted adsorption of plasma proteins and platelets resulting in surface-induced thrombosis (*3*). On the other hand the creation of functional interfaces that can be loaded/unloaded with proteins for drug delivery or sensor applications in a controllable way is promising (*4*). Such biocompatible or functional interfaces can be provided by thin polymer brush films that are grafted chemically to a substrate. Brush films and have been investigated theoretically and increasingly experimentally in recent years (*5–7*).

1.1. Polymer Brushes

The term “brush” is often used as synonym for a dense layer of chain-like polymers with one end attached to a substrate. Such layers may appear in different conformations (Figure 1) depending on the grafting density as well as on interaction with the substrate and the surrounding medium (*8*).

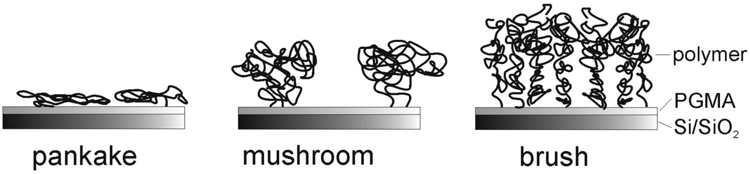

Figure 1. Different conformations of tethered polymer chains at a surface.

Several grafting techniques (*9*), such as the “grafting to” method, enable to covalently bind polymer chains with only one reactive end-group towards a surface. Here, a very thin film of poly(glycidylmethacrylate) (PGMA) is used to enable the formation of chemical bonds with the oxidic substrate as well as with the in this case carboxy terminated polymer chains (Figure 2) (*10*, *11*). Owing to better characterization possibilities silicon wafers are used as substrates but also other substrates like glass, metals or artificial tissues are possible (*12–14*).

The covalent linkage of the polymer to the surface has several advantages, as easy and controllable introduction of polymer chains with high surface density, precise localization of the chain at the surface, and the possibility to graft different types of polymers onto the same substrate.

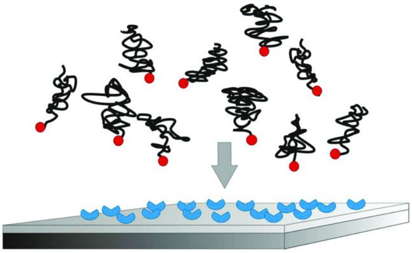

Figure 2. Schematic "grafting-to" mechanism of COOH-functionalized polymer chains.

By using these polymer brushes it is possible to generate versatile surfaces with reproducible interface functionalization as well as stable homogeneous (with a certain order in z-direction) and adaptive smooth thin polymer films with a roughness of less than 1 nm (*15–17*). By grafting of two (or more) incompatible polymers mixed brushes can be formed that are characterized by switchable physico-chemical surface properties (*18–20*). These brushes represent polymer systems with remarkable responsive properties, i.e. they are able to adapt and respond to external fields and environmental conditions like temperature, pH or solvent (Figure 3) (*21*, *22*). Mixed brushes are characterized by a collaborative response of the grafted chains of one brush component to environmental changes.

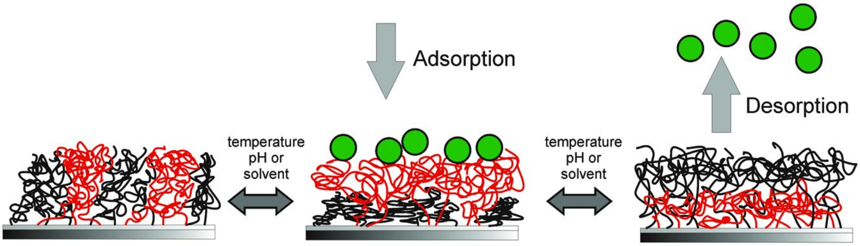

Figure 3. Mixed polymer brushes and their possible switching behaviour including the adsorption and desorption process.

We used binary brushes of weak polyelectrolytes consisting of poly(2-vinylpyridine) (P2VP) and poly(acrylic acid) (PAA). Generally, the degree of dissociation of weak polyelectrolytes (annealed brush) depends on the pH value, and the thickness results from a balance of the osmotic pressure of the counterions inside the brush and the configurational elasticity of the chains (*23*). In the osmotic regime, with a low concentration of additional ions in the surrounding solution, the ion concentration inside the brush is higher than outside and most of the counterions condense inside the brush. One of the used polylelectrolytes (P2VP) was combined with poly(N-isopropyl acrylamide) (PNIPAAM), a polymer well known to be water soluble at room temperature. Besides it shows a phase transition to a water insoluble state when crossing its lower critical solution temperature (LCST) of 32°C. It was recently shown that even in the brush conformation (at relatively low grafting density and in very homogeneous brushes made by the grafting-to approach) this polymer is showing the expected phase transition (*30*), however, also above the LCST those PNIPAAm brushes keep their protein resistance, apparently because the structure of the interfacial water layer remains intact in the sense to prevent the adsorption of proteins yet (*24*). Polymer brushes, as very thin homogeneous coatings turn out to be accordingly due to their molecular conformation (chain conformation), surface mobility, steric effects induces by the brush conformation, and their variability very promising for the design of tailored biointerfaces.

1.2. Protein Adsorption

The adsorption of proteins to surfaces, as the initial event when a material comes into contact with a biosystem, is driven by various forces, including hydrophobic and electrostatic interaction, entropic driving forces as well as hydrogen bonding (*25*). For charged polymers, e.g. polyelectrolytes, electrostatic interaction with proteins and changes in the entropy of the system during adsorption can be identified as major driving forces for adsorption.

Dependent on the pH of the environmental solution and on the isoelectric points (IEP) of the involved polyelectrolytes and proteins, equal or opposite surface charges of the grafted polymers and proteins can be adjusted respectively, leading to controlled adsorption and desorption processes (*26*). The influence of the amount of counter ions inside a mono brush on the entropic driving forces of the adsorption process was recently shown by investigating the adsorption of model proteins on spherical polyelectrolyte brushes (*27*). Here sodium or potassium ions in aqueous solution often act as counter ions which are responsible for local charge neutrality in polyelectrolyte brushes. The influence of buffer molecules on adsorption and desorption of a model protein at a PAA brush was recently shown by using in-situ a combination of a quartz microbalance (QMC-D) with spectroscopic ellipsometry (*28*).

Non-charged water soluble polymers like the well investigated poly(ethylene glycol) (PEG) or the already mentioned poly(N-isopropyl acrylamide) are especially in a brush conformation very promising (*29*), because brush parameters as grafting density and molecular weight can be well adjusted to prevent primary and ternary protein adsorption by steric repulsion, additionally these polymers are likely to undergo stable interactions with water molecules making the formation of stable water layers at the surface likely, which also contributes to resistance to non-specific protein adsorption (*30*). Those protein resistant surfaces are important for applications in the field of bioprocessing, sensors, blood contacting devices, contact lenses etc. An interesting option to create advanced biomaterials are surfaces showing a controlled and/ or changing bioresponse triggered by stimuli as changing environmental conditions or signalling molecules. A first step in this direction is the creation of surfaces that induce protein adsorption/ desorption in a controlled manner, and are able to switch between activity and inertness in this sense. To achieve this it is essential to understand the mechanism of protein adsorption to be able to control the driving forces of adsorption which are mainly enthalpic / entropic, van der Waals, electrical double layer and hydrophobic forces (*29*, *30*).

We discuss some selected aspects of how the environmental sensitivity of mixed brushes can be used to regulate protein adsorption affinity and cell adhesion.

2. Experimental

2.1. Materials

All polymers (see Table 1) were purchased from Polymer Source, Inc. (Canada). Highly polished single-crystal silicon wafers of {100} orientation with a native SiO_2 layer thickness of about 2 nm were used as substrates (Si-Mat Germany). An elaborate basic cleaning procedure of the silicon wafers enables the formation of homogeneous dense and adhering brush layers. Poly(glycidyl methacrylate) (PGMA) acted as adhesion promoter between substrate and the polymer layer. All dry layer thicknesses were determined by ellipsometry at λ=632.8 nm (SE-402 from Sentech Instruments GmbH) (see table 1) with fixed refractive indices (*22*).

Table 1. Used polymers with their corresponding dry layer thickness (d) and refractive index (n) in a homopolymer brush conformation

polymer	*notation*	*Mn [g/mol]*	*PDI*	*d [nm]*	*n (λ=632.8 nm)*
poly(glycidyl methacrylate)	PGMA	17,500	1.7	2.3 ± 0.1	1.525
poly(2-vinylpyridine)[a]	P2VP	40,600	1.08	6 ± 0.2	1.595
poly-*N*-isopropylacrylamide[a]	PNIPAAM	66,000	1.35	14.5± 0.2	1.490
poly(tert-butyl acrylate)[a]	PtBA	42,000	1.12	7.4 ± 0.2	1.466

[a] Those polymers are end-functionalized with one COOH group, which reacts with PGMA.

0.01M phosphate buffered saline solution (Aldrich, Germany) as high salt solutions and 0.01M acetate buffer (acid pH) as well as 0.01M trishydroxymethylaminomethane (TRIZMA) buffer (basic pH) as low salt solutions were used for adsorption measurements, simulating biological conditions. For the adsorption measurements human serum albumin (HSA), a plasma protein from human blood, and α-chymotrypsin, an enzyme of the bovine pancreas, were used (Sigma-Aldrich). The isoelectric points of these proteins are pH 4.7 and pH 8.1, respectively (*22*, *31*).

2.2. Preparation of the Polymer Brushes

The cleaned substrates were spin-coated with 0.02 wt% solution of PGMA in tetrahydrofuran (THF) and put in a vacuum oven for 20 min at 100 °C. To obtain *mono polymer brush* layers, 1 wt% for all polymers in THF was spin-coated on the PGMA layer. The adhesion was performed by annealing the coated substrate in a vacuum oven at 150 °C over night for all homopolymer brush layers. Non-covalently bound polymer was removed by extraction in the respective solvent.

The *mixed polymer brush* system consisting of P2VP-PNIPAAM was prepared in a similar way. After deposition of PGMA on the substrate primarily 1 wt% of P2VP in THF solution was spin-coated. The grafting was performed at 150 °C for 5 minutes in vacuum. Secondly, after THF extraction, 1 wt% solution of PNIPAAM in THF was spin-coated and annealed in the similar way (170 °C, 3 h, extraction in THF).

The PAA-P2VP brushes were prepared in a slightly different way. Firstly 1 wt% of PtBA in THF solution was spin-coated, grafted at 150°C for 12 min and non-covalently bound polymer removed by extraction. Secondly P2VP was spin-coated, annealed over night at 150°C in an vacuum oven and the wafers extracted again afterwards. In a last step the PtBA was hydrolized to PAA in a benzene solution saturated with p-toluene sulfonic acid under reflux at 55°C for 1h.

2.3. Surface Analysis Methods

Comprehensive analysis methods were used to carefully characterize the polymer brush layers and their behaviour towards bio-molecule adsorption. In Table 2 all techniques with their relevant parameters are mentioned.

In-situ protein adsorption experiments were performed with null-ellipsometry using the experimental setup shown in Figure 4.

The adsorbed amount of protein Γ was calculated from the ellipsometrically measured protein layer thickness by using an equation that was originally proposed by de Fejter:

$$\Gamma = d_p\left(\frac{n_p - n_l}{d_n / d_c}\right)$$

In which d_p is the layer thickness of the adsorbed protein layer, n_p is the refractive index of the protein layer, n_l is the refractive index of the ambient solution, and d_n/d_c is the refractive index increment of the protein (*33*). This method is based on experiments showing that the refractive index of a protein in aqueous solution is a linear function of the protein concentration (*34*). It was desired to model the brush and the protein layer individually in a two layer model with n_{protein}=1.375 of an aqueous protein top layer (*35*). However if this model was not applicable a combined "composite" layer of swollen polymer brush and "dry" protein was assumed and both effective n and d values fitted for the combined layer leading to a total adsorbed amount of the combined layer of protein and polymer brush.

To evaluate the adsorbed amount of protein the amount of polymer was finally subtracted from the total amount, whereas the amount of polymer was calculated from the dry layer thickness. This model was mainly used for charged brushes, since proteins are most likely to penetrate into these brushes during the adsorption process (*26*).

Table 2. Characteristic parameters of used techniques

Method	*Company*	*Measuring principle*	*relevant information*
In-situ spectroscopic ellipsometry (λ= 428 … 763 nm)	M44, J. A. Woollam Co., Inc., Lincoln, NE, USA	Changes of the polarized light upon specular reflection	Swollen layer thick-ness and refractive index of the brush
In-situ single-wavelength-null-ellipsometry (Figure 4, λ=632.8 nm)	Multiscope, Optrel, Berlin, Germany		Ellipsometric angles after protein adsorption
Streaming(Zeta)-Potential	ElectroKinetic Analyser Anton Paar KG, Austria (*32*)	Electro kinetic surface properties	Zeta-potential, isoelectric point (IEP)
Contact Angle	OCA20, Dataphysics, Germany	Surface free energy and wettability	contact angles

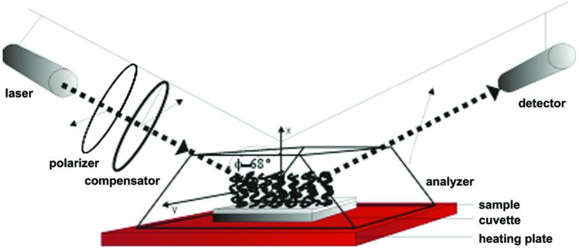

Figure 4. Null-ellipsometry setup: Brush coated silica wafers were inserted into a cuvette, fixed and immersed in buffer solution. Concentrated protein solution was added after the swelling process.

3. Results and Discussion

3.1. Physico-Chemical Surface Properties

We are presenting two mixed brush systems: P2VP-PNIPAAM and PAA-P2VP where changes in the physico-chemical surface properties could be achieved by the stimuli temperature or pH, respectively.

For the first system we additionally investigated the wetting behaviour and the surface charge properties of the mono brushes PNIPAAM, and P2VP and compared them with **PNIPAAM-P2VP mixed brushes**. PNIPAAM containing brushes are interesting, because these brushes undergo a phase transition from a more hydrophilic to a more hydrophobic state at their lower critical solution temperature (LCST) at 32°C (*36*, *37*). Since this switching temperature can be modified, for example by copolymerisation (*38*), these mixed brushes could be suitable for biomedical applications.

In Figure 5 the temperature dependence of the respective contact angles is presented. For P2VP no changes in the advancing contact angle in the range of 20°C to 40°C could be measured whereas PNIPAAM mono brushes showed the expected temperature dependent increase of the advancing contact angle towards a more hydrophobic surface (Figure 5a).

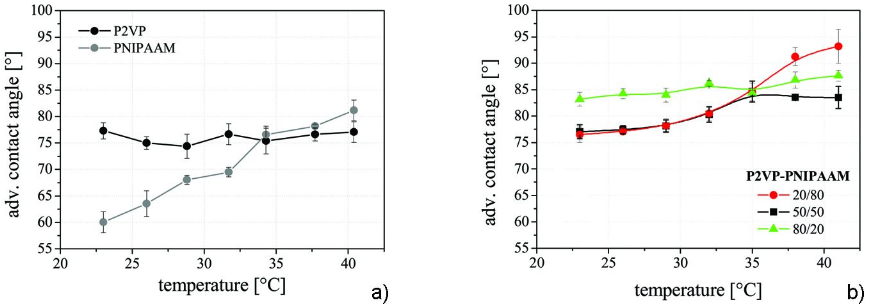

Figure 5. (a) Temperature dependent advancing contact angles of PNIPAAM and P2VP mono brushes. (b) Temperature dependent advancing contact angles of P2VP-PNIPAAM mixed brushes with different compositions.

This change in hydrophilicity was also observed for P2VP-PNIPAAM mixed brushes where the contact angle differences between 20°C and 40°C increased with the amount of PNIPAAM in the binary brush (Figure 5b). Surprisingly, the mixed brush surface was found to be more hydrophobic at higher temperatures than the PNIPAAm mono brushes, which could indicate an interaction between PNIPAAm and P2VP chains.

Information about surface charge states of these P2VP-PNIPAAm brushes was gained by zeta (ζ) potential measurements (*39*), as from zeta potential curves the isoelectric point (IEP) of the brush coated surface at $\zeta = 0$ was determined. In Figure 6 the pH at the IEP (pH_{IEP}) is plotted for different compositions of P2VP-PNIPAAM. It was observed that PNIPAAM strongly influenced the surface properties even at low concentrations.

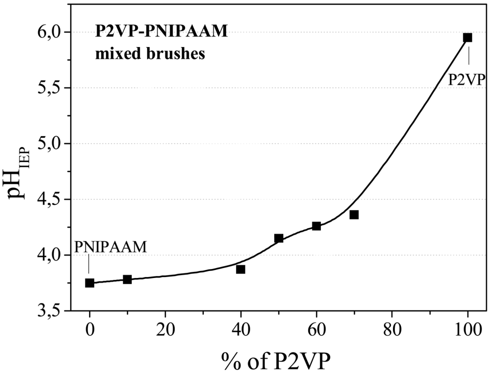

Figure 6. Isoelectrical point (IEP)for different compositions of P2VP-PNIPAAM mixed brushes.

The second system we are presenting is a **PAA-P2VP mixed brush** consisting of two different polyelectrolytes. For the pH sensitive switching behaviour of this mixed brush and its corresponding mono brushes the dependency of the surface potential and the contact angle on the pH was reported in literature (*40*). Here swelling measurements are presented for PAA and P2VP mono brushes as well as a 50:50 mixed brush in Figure 7.

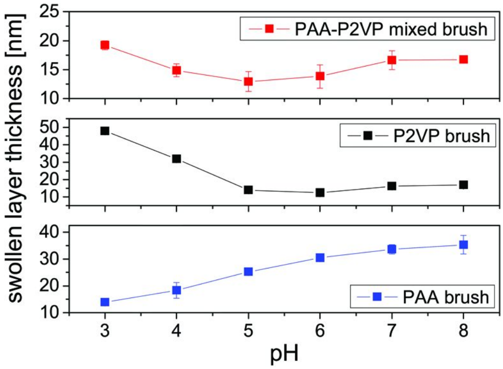

Figure 7. Swollen layer thicknesses of PAA and P2VP mono brushes as well as PAA-P2VP mixed brushes measured with spectroscopic ellipsometry.

Since PAA is a weak acid and P2VP a weak base both polymers have dissociable groups and the degree of dissociation depends on the pH (*25*, *26*). The amount of COO^- groups in the PAA brush increases above its IEP of pH 2.1 whereas the amount of NH^+ groups in the P2VP brush decreases until this polymer is neutral at its IEP at pH 6.0. Furthermore counterions from solution (e.g. Na^+, Cl^-) diffuse into these charged brushes to preserve local charge neutrality. Hence for a fixed ionic strength of the surrounding solution the thickness and the refractive index of the swollen polymer layers vary with pH because of different degrees of stretching of the chains due to the repulsion of equally charged monomers as well as the gain of entropic energy by the separation of counterions (*41*).This leads to an increase of layer thickness with increasing pH for PAA and a decrease with increasing pH for P2VP mono brushes. For the mixed brush a qualitative combination of the swelling behaviour of the individual components is visible but the total swollen layer thickness is considerably lower than the one for the mono brushes. In the pH range from 3.2 to 6.7 the negatively charged PAA and positively P2VP chains interact leading to an uncharged surface at pH 4.9 (*39*).

3.2. Stimuli Responsive Adsorption of Proteins

Having studied the surface properties of the two mixed brushes, aspects of their influence on protein adsorption will now be presented. We firstly present temperature sensitive adsorption experiments at P2VP-PNIPAAM brushes for two different pH in Figure 8 and will show the pH-dependent reversibility of adsorption at P2VP-PAA brushes (Figure 9), giving two examples of tunable adsorption processes at mixed brushes.

For the **P2VP-PNIPAAM mixed brush** the adsorbed amount of human serum albumin (HSA) dependent on brush composition and two different temperatures (22 °C, 40 °C) is displayed in Figure 8a for measurements at pH 4 and in Figure 8b at pH 7.4. For both pH values a higher adsorbed amount of protein was observed at 40 °C, above the LCST of PNIPAAm, as compared to the adsorption at room temperature. Additionally the protein amount increased with increasing P2VP content. Comparing the measurements at pH 4 and pH 7.4 a higher adsorbed amount was found at pH 4 for both temperatures and all brush compositions, most pronounced for high P2VP content. For a comprehensive explanation of these findings more information on the brush-solution interface in-situ would be needed. However a deswelling with temperature of the P2VP-PNIPAAm brushes with the ratios 20:80 and 50:50 could be shown by in situ spectroscopic ellipsometry at pH 7.4 (*42*). Thus, the collapse of PNIPAAm chains could be hold responsible for the increase of adsorbed amount with temperature. This is highly interesting since comparable PNIPAAm mono brushes proved to be protein resistant below and above the LCST (*24*). In general the resistance of PNIPAAm brushes above the LCST was found to depend on molecular weight and grafting density (*43*). Thus the low density of PNIPAAm chains in the mixed brushes could be the reason for the observed effect.

Also an effect of the P2VP is probable. At pH 4 both P2VP and HSA are positively charged and adsorption takes place under repulsive conditions, whereas at pH 7.4 P2VP is neutral and hydrophobic forces are most likely to drive the adsorption process. Additionally, the IEP of the mixed brush shifts with the ratio of components (see Figure 6), indicating a change in the charge conditions inside the brush with composition. Thus electrostatically driven protein adsorption should be affected. An interaction of PNIPAAm and P2VP chains is possible as well and was indicated by a higher hydrophobicity of the surfaces as measured by the contact angle (Figure 5).

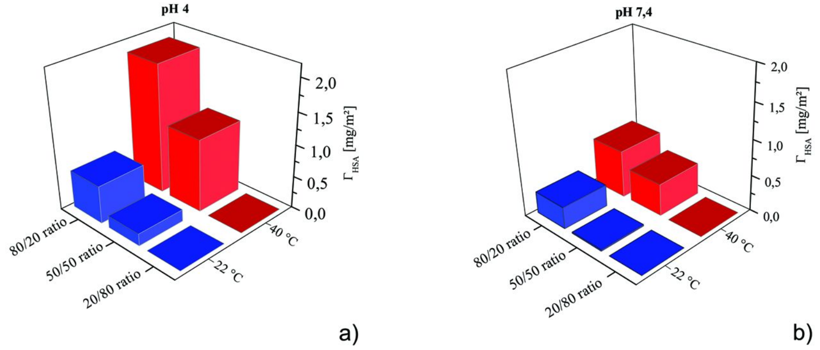

Figure 8. a,b: Adsorbed amount of HSA on various P2VP-PNIPAAM mixed brushes at two pH values, different surface composition and temperature.

In summary tuning of the adsorbed amount of 1 mg/ml HSA in 0.01 M PBS solution on P2VP-PNIPAAM mixed brushes by brush composition, pH and temperature could be shown, and possible mechanisms for the observed adsorption behavior were discussed. A detailed explanation of the effects leading to the observed protein amounts is desired, but needs more characterization of this rather complex behaving soft matter film.

The reversibility of switching the adsorbed amount of protein sensitive to pH changes is presented for a **PAA-P2VP mixed brush** (Figure 9). Adsorption of α-chymotrypsin (IEP: 8.1) was carried out at pH 7.8 in 0.01M TRIZMA buffer and very high amounts of protein could be adsorbed. The counter ion release mechanism is discussed in literature to explain this high adsorption affinity (*25*, *26*). In the presented experiments adsorption takes place at electrostatic attractive conditions between the positively charged protein and the negatively charged surface due to COO^- groups at the swollen PAA chains. Upon adsorption protein molecules replace counter- and co-ions in the brush layer and at the brush solution interface. Thus, this mixed brush system serves as a support for ion exchange, in the presented case due to the charged PAA chains. After adsorption at pH 7.8 the buffer was exchanged to pH 4 (0.01M acetate buffer). At this pH positively charged P2VP is dominating the surface of the PAA-P2VP mixed brush and the electrostatic conditions become repulsive, thus leading to desorption of the protein.

With this approach the adsorbed amount could be switched between 26 mg/m^2 and 0.5 mg/m^2 which is equivalent to a release of 98% of the adsorbed amount of protein into the surrounding solution. Also the reversibility of this adsorption-desorption process was tested and after three cycles the adsorbed amount was still 95% of that of the initial adsorption. Nevertheless long-time reversibility measurements were not done so far but will be considered in the future.

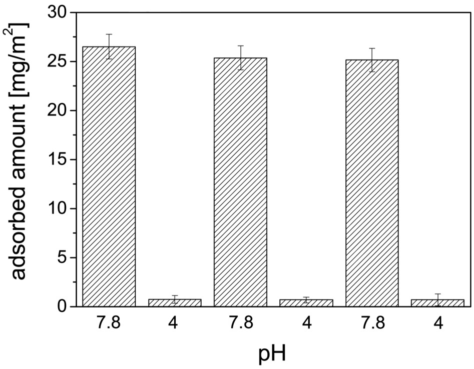

Figure 9. Reversible switching of the adsorbed amount of a-Chymotrypsin at PAA-P2VP brushes shown for three switching cycles.

3.3. Cell Adhesion onto P2VP-PNIPAAM Brushes

L929 mouse fibroblasts were obtained from DSMZ, Braunschweig, Germany and cultivated in RPMI medium (RPMI 1640; Pan Biotech GmbH, Aidenbach, Germany) containing 10% fetal calf serum and antibiotics. Further details of cell cultivation are described herein (*44*). Thin glass slides were used as substrates. Polymer brushes were grafted on those slides as described in section 2.2. The brushes were subsequently conditioned at 37°C in PBS solution. In the next step PBS was exchanged with the tempered cell culture medium. After a period of 30 min L929 mouse fibroblasts with a density of $7.7 \cdot 10^4$ cells/cm^2 were seeded while keeping the temperature at 37°C. The cultivation of the cells at 37°C was proceeded until confluence of the cells was reached. Images at room temperature were made after a cooling time of six hours. L929 mouse fibroblasts were found to become adherent on P2VP mono brushes (see Figure 10). A confluent monolayer was reached after 24h. By contrast no proliferation and adherence was seen for PNIPAAM mono brushes. The cells seem to agglomerate in small groups. Regardless, all three polymer systems showed no cell toxicity during the measuring time of three days. The following images were made using a common light microscope; brightness and contrast depend on manual adjustment.

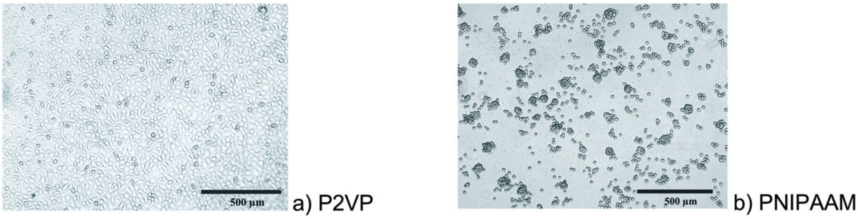

Figure 10. L929 mouse fibroblasts cell growth images at 37 °C on a) P2VP and b) PNIPAAM mono brushes, similar images were made at 22°C.

Taking a mixed brush system we wanted to combine cell adhesion and no adhesion by temperature sensitive switching. P2VP-PNIPAAM showed very promising results (Figure 11).

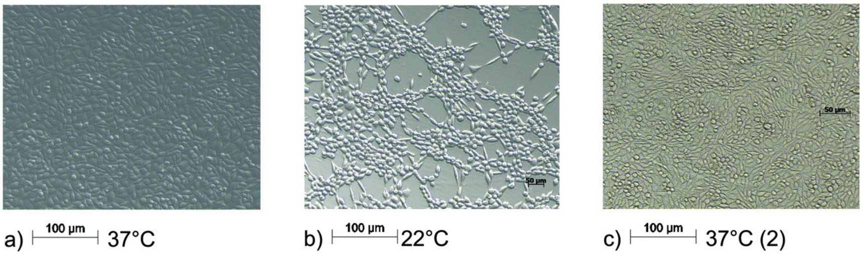

Figure 11. L929 mouse fibroblasts cell growth images on a-c) P2VP-PNIPAAM (80:20) mixed brushes at different temperatures.

We were able to induce a reversible switching of the cell sheet by changing the surrounding conditions. In Figure 11a typical spindle-shaped cell morphology is seen for P2VP-PNIPAAM at 37°C. The good proliferation enables the formation of a confluent monolayer. When switching to 22°C PNIPAAM is dominating the surface and the cells start to roll together and agglomerate. The reverse switching to 37°C is clearly shown in Figure 11c, where a confluent monolayer of cells is formed again. This resembles the results we obtained for the protein adsorption measurements. A switching was also seen for mixed brushes with a composition of 50:50 and 20:80. However in the case of 80:20 brushes the switching effect is the greatest.

4. Conclusions

We demonstrated the tuning and switching of the physico-chemical surface properties and hence the affinity to adsorb biological components, i.e. proteins and cells, for selected combinations of polymers into binary mixed brushes.

In the first system, we presented a temperature sensitive mixed brush, P2VP-PNIPAAM, with its surface properties tunable from hydrophilic to more hydrophobic. This dewetting behaviour was accompanied with an increased affinity for protein adsorption and cell adhesion for higher temperatures, in for example switching the adsorbed amount of HSA from 0.5 mg/m^2 to 2 mg/m^2 for a (80:20) P2VP-PNIPAAM mixed brush. The surface potential and adsorption measurements show, that PNIPAAM strongly influenced the physico-chemical surface properties of the mixed brush, which could be used to design a switchable surface in the desired manner.

Furthermore the reversibility of the pH sensitive swelling due to changes in the electrostatic charges along the polymer chains for a fixed ionic strength of the buffer solution was demonstrated for P2VP-PAA mixed brushes. Very high adsorbed amounts of α-chymotrypsin of 26 mg/m^2 could be detected around the IEP of the protein at pH 7.8. This adsorption behaviour was used to release high amounts of protein (25 mg/m^2) into the buffer solution when switching the PAA-P2VP brush in changing the pH to electrostatic repulsive conditions at pH 4. The reversibility of the adsorption and desorption was proven for three cycles with only marginal decreases in the adsorption affinity and a remaining adsorbed amount of 95% of the initial adsorption before the third release process.

Acknowledgments

The work was kindly supported by the Deutsche Forschungsgemeinschaft (DFG) in the frame of the Sonderforschungsbereich 287 *"Reaktive Polymere in nichthomogenen Systemen, in Schmelzen und an Grenzflächen"* within the particular project B10 and in the DFG-NFS cooperation project *"Design of new responsive materials based on functional polymer brushes for smart tuning and sensoring of proteins and particles adsorption"* in the frame of "Materials World Network".

For performing the cell adhesion experiments we thank T. Götze and C. Werner, Max-Bergmann Center, Leibniz IPF Dresden.

References

1. Horbett, T. A. *Cardiovasc. Pathol.* **1993**, *2*, 137.
2. Norde, W. *Adv. Colloid Interface Sci.* **1986**, *25*, 267.
3. Andrade, J. D.; Hlady, V. *Adv. Polym. Sci.* **1986**, *79*, 1.
4. Roos, A.; Klee, D.; Schuermann, K.; Höcker, H. *Biomaterials* **2003**, *24*, 4417.
5. Filippova, N. L. *Langmuir* **1998**, *14*, 1162.
6. Sun, T.; Wang, G.; Feng, L.; Liu, B.; Ma, Y.; Jiang, L.; Zhu, D. *Angew. Chem., Int. Ed.* **2004**, *43*, 357.
7. Reichelt, S.; Eichhorn, K.-J.; Aulich, D.; Hinrichs, K.; Jain, N.; Appelhans, D.; Voit, B. *Colloids Surf., B* **2009**, *69*, 169.
8. Milner, S. T. *Science* **1991**, *251*, 905.
9. Bialk, M.; Prucker, O.; Rühe, J. *Colloids Surf., A* **2002**, *198-200*, 543.
10. Luzinov, I.; Julthongpiput, D.; Liebmann-Vinson, A.; Cregger, T.; Foster, M. D.; Tsukruk, V. V. *Langmuir* **2000**, *16*, 504.
11. Zdyrko, B.; Iyer, K. S.; Luzinov, I. *Polymer* **2006**, *47*, 272.
12. Kaper, H. J.; Busscher, H. J.; Norde, W. *J. Biomat. Sci., Polym. Ed.* **2003**, *14*, 313.
13. Zhou, F.; Huck, W. T. S. *Chem. Commun.* **2005**, 5999.
14. Motornov, M.; Minko, S.; Nitschke, M.; Grundke, K.; Stamm, M. *Polym. Mater: Sci. Eng.* **2003**, *88*, 264.
15. Alexander, S. J. *J. Phys. (Paris)* **1977**, *38*, 983.
16. Ionov, L.; Stamm, M.; Minko, S.; Hoffmann, F.; Wolff, T. *Macromol. Symp.* **2004**, *210*, 229.
17. Biesalski, M.; Rühe, J. *Macromolecules* **1999**, *32*, 2309.
18. Minko, S.; Usov, D.; Goreshnik, E.; Stamm, M. *Macromol. Rapid Commun.* **2001**, *22*, 206.

19. Sydorenko, A.; Minko, S.; Schenk–Meuser, K.; Duschner, H.; Stamm, M. *Langmuir* **1999**, *15*, 8349.
20. Minko, S.; Patil, S.; Datsyuk, V.; Simon, F.; Eichhorn, K.-J.; Motornov, M.; Usov, D.; Tokarev, I.; Stamm, M. *Langmuir* **2002**, *18*, 289.
21. Luzinov, I.; Minko, S.; Tsukruk, V. V. *Prog. Polym. Sci.* **2004**, *29*, 635.
22. Uhlmann, P.; Ionov, L.; Houbenov, N.; Nitschke, M.; Grundke, K.; Motornov, M.; Minko, S.; Stamm, M. *Prog. Org. Coat.* **2006**, *55*, 168.
23. Biesalski, M.; Johannsmann, D.; Ruehe, J. *J. Chem. Phys.* **2002**, *117*, 4988.
24. Burkert, S.; Bittrich, E.; Kuntzsch, M.; Müller, M.; Eichhorn, K.-J.; Uhlmann, P.; Stamm, M. *Langmuir* **2010**, *26*, 1786–1795.
25. Norde, W. In *Biopolymers at Interfaces*; Malmsten, M., Ed.; Surfactant Science Series; Marcel Dekker: New York, 1998; Vol. 75.
26. Uhlmann, P.; Houbenov, N.; Brenner, N.; Grundke, K.; Stamm, M. *Langmuir* **2007**, *23*, 57.
27. Wittemann, A.; Ballauff, M. *Phys. Chem. Chem. Phys.* **2006**, *8*, 5269.
28. Bittrich, E.; Rodenhausen, K. B.; Eichhorn, K.-J.; Hofmann, T.; Schubert, M.; Stamm, M.; Uhlmann, P. *Biointerphases* **2010**, *5*, 159.
29. Halperin, A. *Langmuir* **1999**, *15*, 2525.
30. Bittrich, E.; Burkert, S.; Müller, M.; Eichhorn, K.-J.; Stamm, M.; Uhlmann, P. *Langmuir* **2012**, *28*, 3439–3448.
31. Oliva, F. Y.; Avalle, L. B.; Camara, O. R.; De Pauli, C. P. *J. Colloid Interface Sci.* **2003**, *261*, 299.
32. Grundke, K.; Jacobasch, H. J.; Simon, F.; Schneider, S. *J. Adhes. Sci. Technol.* **1995**, *9*, 327.
33. de Fejter, J. A.; Benjamins, J.; Veer, F. A. *Biopolymers* **1978**, *17*, 1759.
34. Malmsten, M. *J. Colloid Interface Sci.* **1994**, *166*, 333.
35. Werner, C.; Eichhorn, K.-J.; Grundke, K.; Simon, F.; Grählert, W.; Jacobasch, H.-J. *Colloids Surf., A* **1999**, *156*, 3.
36. Tanaka, T.; Fillmore, D. J. *J. Chem. Phys.* **1979**, *70*, 1214.
37. Kraft, S.; Müller, M.; Uhlmann, P.; Stamm, M. *Polym. Mater.: Sci. Eng.* **2006**, *51*, 723.
38. Lee, K. K.; Jung, J. C.; Jhon, M. S. *Polym. Bull,* **1998**, *40*, 455.
39. Jacobasch, H. J. *Prog. Org. Coat.* **1989**, *17*, 115.
40. Houbenov, N.; Minko, S.; Stamm, M. *Macromolecules* **2003**, *36*, 5897.
41. Pincus, P. *Macromolecules* **1991**, *24*, 2912.
42. Burkert, S. Sensitive Polymeroberflächen zur Steuerung der Adsorption von Biomolekülen. Ph.D. Thesis, TU Dresden, December 2009; p 73. http://www.qucosa.de/fileadmin/data/qucosa/documents/2610/Promotion%20Sina%20%20Burkert%20_SLUB_final.pdf.
43. Xue, C; Yonet-Tanyeri, N; Brouette, N; Sferrazza, M; Braun, P. V; Leckband, D. E. *Langmuir* **2011**, *27*, 8810.
44. Nitschke, M.; Gramm, S.; Götze, T.; Valtink, M.; Drichel, J.; Voit, B.; Engelmann, K.; Werner, C. *J. Biomed. Mater. Res., Part A* **2007**, *80A*, 1003.

Chapter 9

Understanding Protein-Surface Interactions at the Atomistic Level through the Synergistic Development of Experimental and Molecular Simulation Methods

T. Abramyan,[1] G. Collier,[1] T. G. Kucukkal,[2] X. Li,[1] J. A. Snyder,[1] A. A. Thyparambil,[1] N. A. Vellore,[1] Y. Wei,[1] J. A. Yancey,[1] S. J. Stuart,[2] and R. A. Latour*,[1]

[1]Bioengineering Department, Clemson University,
Clemson, South Carolina 29631
[2]Chemistry Department, Clemson University,
Clemson, South Carolina 29631
***E-mail: LatourR@clemson.edu**

Despite decades of study, relatively little is yet understood regarding the molecular-level events that mediate protein-surface interactions. Experimental methods alone are generally too limited to provide the atomistic level of detail that is needed to characterize the molecular interactions that are involved. Molecular modeling methods, on the other hand, are inherently able to provide this capability. However, these computational methods require experimental data for tuning and validation before they can be confidently applied. In order to address this 'chicken-or-the-egg' type of problem, we are working on the synergistic development of experimental methods to provide the kinds of data that are needed to both tune and validate molecular simulation methods along with simulation methods that are needed for proper comparison with experimental results. The combination of these methods paves the way towards accurate prediction of protein adsorption behavior. Once developed, these methods have the potential to provide a valuable tool to help understand, predict, and control protein-surface interactions.

In Proteins at Interfaces III State of the Art 2012; Horbett, T., et al.;
ACS Symposium Series; American Chemical Society: Washington, DC, 2012.

Introduction

The interaction of proteins with material surfaces is of fundamental importance in a broad range of applications in biotechnology and biomolecular engineering. Applications include the understanding and control of biomineralization processes, the design of medical implant surfaces for improved biocompatibility, substrates for tissue engineering and regenerative medicine for the control of cellular response, systems for targeted drug delivery, the design of surfaces for biosensors, bioassays, bioseparation, and biocatalysis, and the design of decontamination strategies for biodefense, to mention just a few (*1–10*). The key element in all of these applications is the bioactive state of the protein, which is primarily determined by its orientation and conformation on a surface.

Because of its importance, the issue of protein-surface interactions has been widely studied experimentally over the past several decades. However, because of the inherent limitations of most experimental methods to probe events at the atomistic level, protein adsorption behavior on surfaces is still not well understood or able to be well controlled. Due to this situation, the design of most systems that are dependent on protein-surface interactions can still only be approached by trial-and-error methods. New techniques are therefore needed to provide a better understanding of protein-surface interactions at the atomistic level to enable system design to transition from trial-and-error to a knowledge-based approach.

Molecular simulation is one of the most promising areas of technology with great potential to help overcome these present limitations (*11*). But, before this potential can be realized, molecular simulation methods must first be specifically developed for this type of application. This need, however, presents a ‘chicken-or-the-egg’ type of problem. Experimental methods are generally limited in terms of their ability to provide quantitative detail of molecular behavior at the atomistic level and molecular simulation methods can provide this level of detail that is lacking. However, before molecular simulation can accurately represent molecular behavior, the methods must first be developed, which require comparison with quantitative experimental data at the atomistic level for validation. The solution to this dilemma lies in the development of experimental and molecular simulation methods in a synergistic manner. Experimental methods must be designed to provide data that characterizes atomistic behavior that can be used for direct comparison and validation of the methods developed for molecular simulation and, likewise, molecular simulation methods must be designed to provide the kinds of data that can be directly compared with results generated from the developed experimental methods.

In order to understand the kinds of experimental data that are needed, one must first understand some of the basic principles behind these types of simulations. Due to the large size of the molecular systems involved (i.e., tens to hundreds of thousands of atoms), the simulation of protein adsorption behavior requires the use of classical, or empirical force field-based, simulation methods (*11*) rather than quantum mechanical techniques. These classical methods use what is called a force field equation along with empirically set parameters to represent the interactions between the atoms contained in a given molecular system. A force field equation calculates the total potential energy of a molecular system by summing up contributions to the potential energy from the various types of atom-atom interactions in the system. This is called a force field equation because when differentiated with respect to atomic position, it yields the force vectors acting on the atoms. These forces can subsequently be used to perform molecular dynamics simulations to predict how the conformational state of the system evolves over time. The form of the force field equation that is used for many types of empirical force field simulations, which is similar to the CHARMM force field (*12*), is shown in the following equation:

$$E = \sum_{bonds} k_b(b-b_o)^2 + \sum_{angle} k_\theta(\theta-\theta_o)^2 + \sum_{dihedrals} k_\varphi[1+\cos(n\varphi-\delta)] + \sum_{vdW} \varepsilon_{ij}\left[\left(\frac{R_{ij}}{r_{ij}}\right)^{12} - 2\left(\frac{R_{ij}}{r_{ij}}\right)^{6}\right] + \sum_{Coulomb} \frac{q_i q_j}{4\pi\varepsilon_o r_{ij}} \quad (1)$$

where the first three terms on the right-hand side of this equation represent the potential energy contributions from the covalently bonded atoms in the system. These terms represent covalent bond stretching ($b - b_o$), bond angle bending ($\theta - \theta_o$), and dihedral angle rotation (φ). For these terms, the variables b, θ, and φ, represent the various bond lengths, bond angles, and dihedral angles, respectively, of the conformational state at a given time. The k parameters represent empirical force field parameters that reflect the relative stiffnesses of the system as it deviates from reference positions designated by additional force field parameters b_o, θ_o, and φ_o, with $\varphi_o = 0$. The last two terms of the force field equation represent the contributions of the nonbonded interactions to the potential energy of the system. The first of these two calculates the van der Waals (vdW) interactions, represented with a Lennard-Jones (L-J) 12-6 model. These are considered to be pairwise interactions acting between all nonbonded atoms (i.e., atoms separated by more than two covalent bonds along a covalently bonded chain or between two atoms in different molecules in the system), where ε_{ij} and R_{ij} represent the L-J well depth and the atomic separation distance between the designated pairs of atoms when they are in their minimum energy position, respectively, for atoms i and j. The second nonbonded term calculates the energy contributions from the electrostatic interactions between pairs of atoms, which are represented by Coulomb's law, where q_i and q_j represent the partial charges centered on atoms i and j, and ε_o is the relative permittivity of free space.

Figure 1 illustrates a protein over a surface with the protein color coded by amino acid residue type. E_{system} represents the potential energy of the entire system of atoms (i.e., the force field equation), which is determined as the sum of the individual potential energy contributions from the interactions between all of the atoms in the system with one another—i.e., from covalent bond stretching, bending, and dihedral rotation (bonded terms) and electrostatic and van der Waals (vdW) interactions, with the *ks* representing empirical parameters that are ideally set to accurately represent the potential energy provided by each type of interaction as a function of the relative position of the atoms (see eqn. 1). For the simulation of this type of system, force field parameters are thus necessary to describe how the atom types in the amino acid residues of the protein interact with each other, with the surrounding water and ions of the aqueous solution, and with the atom types of the material surface, and how the atom types contained within the material surface interact with one another, with the protein, and with the water and ions in the aqueous solution. Fortunately, force field parameters have already been fairly well developed by the biophysics community to represent the interactions between amino acids residues in aqueous solution and by the materials science community to represent the behavior of many types of synthetic materials. However, interactions between the atom types of material surfaces with the atom types of amino acid residues of a protein and the aqueous solution represent unique situations that previously developed force fields have not been designed to represent (*14*, *15*). Rather, these types of interactions must be addressed by those interested in the development of force field parameters and methods for the simulation of protein adsorption behavior (*14*, *16–25*). The development of these parameters, which fortunately only involves the nonbonded terms of the force field, thus requires experimental data from which these parameters can be adjusted, tuned and validated. Secondly, once these parameters have been developed and validated, experimental data are further required to characterize adsorbed protein orientation, conformation, and bioactivity so that simulations of protein adsorption behavior using a validated interfacial force field parameter set can be further assessed and validated as well.

In addition to the development of experimental methods to support computational models of protein adsorption behavior, synergistically developed molecular modeling methods are needed to provide simulation results that can be directly compared to experimental data. The problem faced here is that experimental measurements of protein adsorption behavior provide values that represent the averaged behavior of billions of protein molecules over time frames ranging from seconds to hours, while a conventional molecular dynamics simulation can typically provide the averaged behavior of a single protein molecule over tens of nanoseconds of time. To overcome this seemingly insurmountable obstacle, advanced sampling methods are required that enable molecular simulations to represent thermodynamically equilibrated ensembles of states, which can then be directly compared with experimental data.

In light of these issues, the overall objectives of our research group at Clemson University over the past decade have been to develop a suite of synergistically designed experimental and simulation methods for the purpose of accurately simulating, predict, understand, and control protein-surface interactions. As an approach to achieve this goal, our experimental group has focused on the development of methods to determine the free energy of adsorption using a simple host−guest peptide model to generate experimental data that can be used for the parameterization of an interfacial force field that can be used to accurately represent protein-surface interactions, and the development of experimental methods to characterize the orientation, conformation, and bioactivity of adsorbed proteins. Our simulation group, in turn, has focused on the development of methods to calculate adsorption free energy using the same host−guest peptide model and surfaces used by our experimental group, along with methods that enable us to tune and validate interfacial force field parameters for use for the simulation of protein adsorption behavior. We have also been developing advanced sampling methods that are needed to generate equilibrated ensembles of states when simulating protein adsorption behavior for direct comparison with experimental results on adsorbed protein orientation, conformation, and bioactivity. The subsequent sections of this chapter provide an overview of the development of each of these methods along with examples of results provided by their application. More complete details on each of our methods are provided in our referenced publications that have resulted from these efforts.

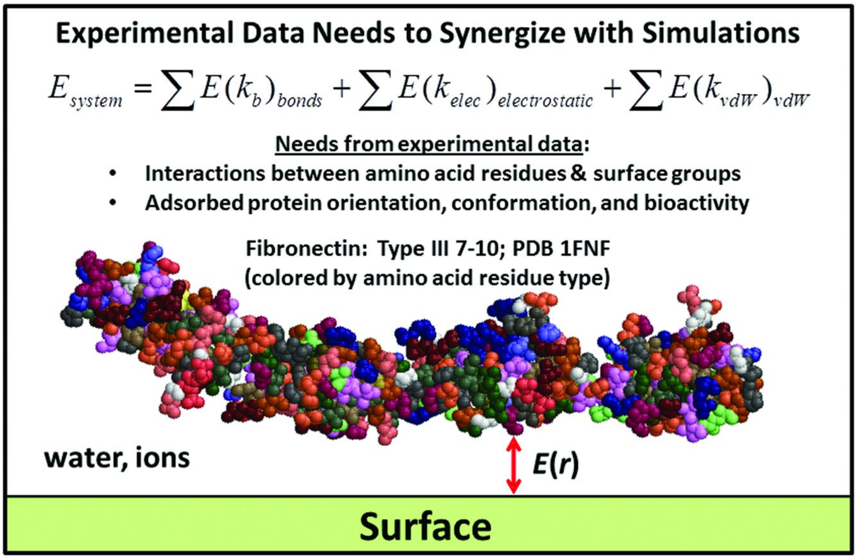
Experimental Data Needs to Synergize with Simulations
$E_{system} = \sum E(k_b)_{bonds} + \sum E(k_{elec})_{electrostatic} + \sum E(k_{vdW})_{vdW}$
Needs from experimental data:
• Interactions between amino acid residues & surface groups
• Adsorbed protein orientation, conformation, and bioactivity
Fibronectin: Type III 7-10; PDB 1FNF
(colored by amino acid residue type)
water, ions
E(r)
Surface

Figure 1. Experimental methods need to be synergized with molecular simulations. Illustration of a fibronectin protein fragment (Protein Data Bank (www.rcsb.org) ID 1FNF (13), color coded by amino acid residue type) interacting with a material surface. Experimental data are needed to quantitatively characterize the interactions of amino acid residues of a protein in aqueous solution with functional groups presented by a surface (e.g,. E(r)) and the orientation, conformation, and bioactivity of adsorbed proteins to provide a basis for the evaluation and validation of the protein adsorption behavior that is predicted from the simulations.

Experimental Methods To Determine the Free Energy of Peptide-Surface Interactions

The measurement of the standard-state free energy of peptide-surface interactions ($\Delta G°_{ads}$) is often conducted using methods such as surface plasmon resonance spectroscopy (SPR) (*26*, *27*) and the quartz crystal microbalance (QCM) technique (*28*, *29*). Despite their wide application, these methods are largely restricted to the characterization of peptide adsorption behavior for a relatively small set of materials that can readily form nanoscale–thick films over the respective SPR or QCM sensor surfaces. Many materials including most polymers, ceramics, and inorganic glasses, however, are not readily suitable for use with these methods. To address these limitations, we have shown that desorption forces (F_{des}) obtained using a standardized atomic force microscopy (AFM) method correlate linearly with $\Delta G°_{ads}$ values measured from SPR for peptide-surface interactions under a range of different solvent conditions, including both phosphate buffered water (PBW) and phosphate buffered saline (PBS) at pH 7.4 (*30*, *31*). These combined approaches thus provide a means to determine $\Delta G°_{ads}$ for peptide adsorption to surfaces that can be used with SPR or QCM as well as for any macroscopically flat material surface not conducive to SPR or QCM using the correlated AFM technique. In this section, we introduce the SPR and AFM methods we have developed to characterize peptide adsorption behavior and show how they can be used to experimentally provide $\Delta G°_{ads}$ for a wide variety of peptide-surface combinations using a relatively simple adsorption system.

Adsorbent Surfaces: Self-Assembled Monolayers (SAMs) on Gold and Material Surfaces Not Conducive to SPR

As model experimental surfaces for both SPR and AFM studies, we have used alkanethiol SAM surfaces on gold with the structure of $Au\text{-}S(CH_2)_{11}\text{-}Y$, with Y representing functional groups contained in a wide range of organic polymers, such as: Y = OH, CH_3, OC_6H_5, NH_2, $COOH$, $NHCOCH_3$, $COOCH_3$, and EG_3OH (EG: ethylene glycol segment, ($\text{-}O\text{-}CH_2\text{-}CH_2\text{-}$) (*26*, *32*). We have also investigated material surfaces that are not conducive for SPR, including fused silica glass (Chemglass Life Sciences, Vineland, NJ), high density polyethylene (HDPE) (MW=125,000 Da, Sigma Chemical Co., St. Louis, MO), and poly(methyl-methacrylate) (PMMA) (MW=350,000 Da, Sigma Chemical Co., St. Louis, MO). HDPE and PMMA surfaces are spin-coated from dodecalin (0.5% (w/w) at 1500 rpm for 60s) and chloroform solutions (1.5% (w/w) at 1000 rpm for 60s), respectively, onto fused silica glass slides, although bulk material surfaces can also be used. We typically then characterize our surfaces for quality assurance by x-ray photoelectron spectroscopy (XPS), static water contact angle, ellipsometry for thickness, and AFM for surface roughness.

Host−Guest Peptide Model

The host−guest model peptides that we designed for our studies (synthesized by Biomatik, Wilmington, DE; characterized by analytical HPLC and mass spectral analysis with 98% purity) have the amino acid sequence of TGTG-X-GTGT (for SPR studies) and TGTG-X-GTCT (for AFM studies) with zwitterionic end groups, where G, T, and C are glycine (-H side-chain), threonine (-CH(CH$_3$)OH side-chain), and cysteine (-CH$_2$SH side chain), respectively. X represents a "guest" amino acid residue, which can be any of the 20 naturally occurring amino acid types, which is placed in the middle of the peptide to represent the characteristics of a mid-chain amino acid in a protein by positioning it relatively far from the zwitterionic end groups of the peptide. The threonine (T) residues and the zwitterionic end groups were selected to enhance aqueous solubility and to provide additional molecular weight for SPR detection while the nonchiral glycine residues were selected to inhibit the formation of secondary structure, thus simplifying its adsorption behavior. The cysteine (C) residue was required for the AFM studies as the linker to connect our host−guest peptide sequences to the AFM probe tip. Preliminary SPR studies that we have conducted using both of these peptide models have shown that the TGTG-X-GTCT peptide can be used in AFM studies as an equivalent system for comparison with the TGTG-X-GTGT peptide model used by SPR (*30*).

Determination of $\Delta G°_{ads}$ by SPR Spectroscopy

We conduct peptide adsorption experiments with SPR using a Biacore X SPR spectrometer (Biacore, Inc., Piscataway, NJ) in either PBW or PBS, pH 7.4, using the following methods. Briefly, SPR sensorgrams for peptide adsorption are recorded in the form of resonance units (RU; 1 RU = 1.0 pg/mm^2 (*33*)) as a function of time for six independent runs of peptide concentrations over each SAM surface at 25°C. The data obtained are then used to generate isotherm curves by plotting the raw SPR signal (i.e., the signal from both surface adsorption and solution bulk-shift effects) as a function of peptide solution concentration.

The equation that we use for the determination of $\Delta G°_{ads}$ from the adsorption isotherms was derived based on the chemical potential of the peptide in its adsorbed versus bulk-solution state (*34*). During an SPR experiment to measure the adsorption of a peptide to a surface, the overall change in the SPR signal (i.e., the raw SPR signal) reflects both of the excess amount of adsorbed peptide per unit area, q (measured in RU), and the bulk–shift response, which is linearly proportional to the concentration of the peptide in solution. This relationship can be expressed as:

$$SPR = q + mC_b = \frac{QC_b}{C_b + C^o K^{-1}} + mC_b \qquad (2)$$

where C_b (mol/L, M) is the concentration of the peptide in bulk solution, $C°$ is the peptide solution concentration under standard-state conditions (taken as 1.0 M), m (RU/M) is the proportionality constant between the bulk shift in the SPR response and the peptide concentration in the bulk solution, K (unitless) is the effective equilibrium constant for the peptide adsorption reaction, and Q (RU) is amount of peptide adsorbed at surface saturation. Each isotherm plot of the raw SPR response vs. C_b is fit with equation (2) by non-linear regression to solve for the parameters Q, K, and m using a nonlinear statistical analysis software program (e.g., SAS Institute, Cary, NC). In order to measure peptide adsorption behavior with minimal influence from peptide-peptide interactions, we use the premise that peptide-peptide interactions are minimized at very low solution concentrations, but then influence the isotherm shape (and thus Q) as the surface becomes crowded at higher values of C_b. The initial slope of the isotherm should thus not be influenced by peptide-peptide interactions. Based on this principle, we have derived the relationship shown in equation (3), which enables $\Delta G°_{ads}$ to be determined from an adsorption isotherm that is generated by SPR with minimal influence of peptide-peptide interactions. Readers are referred to our initial publication of this method for details on this derivation (*35–37*). Accordingly, $\Delta G°_{ads}$ (kcal/mol) is calculated from the parameters obtained from our raw SPR sensorgrams as:

$$\Delta G^{o}_{ads} = -RT\ln[(\mathrm{C_s}/\mathrm{C_b})_{C_b\to 0}] = -RT\ln\left(\frac{QK}{\delta C^{o}}+1\right) \qquad (3)$$

where the theoretically defined parameter δ is the thickness of the adsorbed layer of the peptide, R (kcal/mol·K) is the ideal gas constant, and T (K) is the absolute temperature.

We have applied these methods to characterize the adsorption response of a large range of peptides-surface systems for the determination of $\Delta G°_{ads}$. Figure 2 shows an example of sensorgrams from a set of SPR experiments for TGTG-V-GTGT peptides on a SAM surface (Figure 2.A) and the resulting adsorption isotherms from the raw sensorgram data (Figure 2.B). $\Delta G°_{ads}$ values for a set of peptides with 12 different X residues over a set of nine different functionalized SAM surfaces are presented in Table I.

Determination of Effective $\Delta G°_{ads}$ Using a Standardized AFM Method.

As noted above, the use of experimental techniques such as SPR for the determination of $\Delta G°_{ads}$ is limited to use for materials that can readily form nano-scale thick surfaces over sensor surfaces, thus limiting these techniques to a relatively small set of materials. In order to provide a means of obtaining values of $\Delta G°_{ads}$ for a much broader set of materials (i.e., surfaces that are not conducive for use with techniques such as SPR), we have developed a standardized AFM method that could be applied to any macroscopically smooth surface for the determination of effective $\Delta G°_{ads}$ values by correlating the force of desorption measured by AFM with $\Delta G°_{ads}$ values measured by SPR.

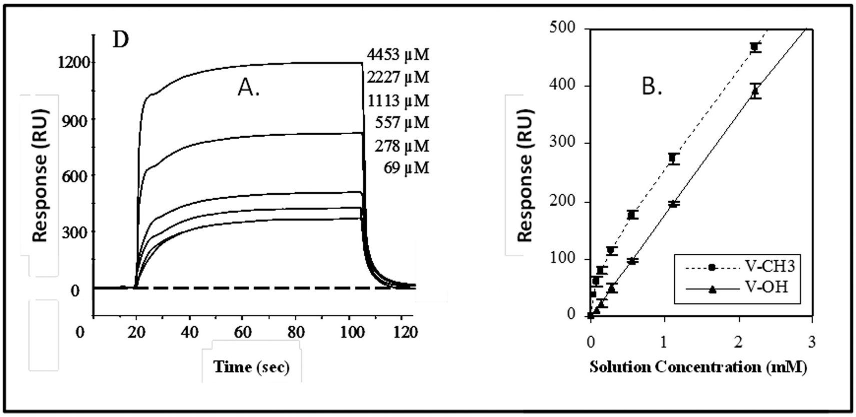

Figure 2. Example data plots for a TGTG-V-GTGT peptide on SAM surfaces. (A) SPR response curves (SPR signal, RU) vs. time for a range of peptide solution concentrations on a CH_3-SAM surface. (B) Resulting adsorption isotherms using the raw SPR data from which $\Delta G°_{ads}$ is determined using equation (3) (error bars represent 95% confidence intervals). Reproduced with permission from ref. (35). Copyright 2008 American Chemical Society.

The desorption force for peptide-surface interactions (F_{des}) is measured from force curves using an AFM instrument (MFP-3D instrument, Asylum Research, Santa Barbara, CA) with DNP-10 silicon nitride cantilevers (Veeco Nanofabrication Center, Camarillo, CA) at room temperature in a fluid cell filled with droplets of either PBW or PBS, pH 7.4. For this technique, our TGTG-X-GTGT host−guest peptides are modified to TGTG-X-GTCT to provide a cysteine amino acid that is used to link the peptides to the AFM tips. The modified host−guest peptide sequences are tethered to AFM tips via a heterobifunctional PEG tether (3.4-kDA pyridyldithio poly(ethyl-glycol) succinimidylpropionate (PD-PEG-NHS), Creative PEGWorks, Winston Salem, NC), the specific details of which have been published (*30*). Tips with PEG-OH (i.e., without the peptide) are then also used as controls. Although there is uncertainty in the density of tethered peptides on the probe tip, as long as the AFM force measurements for peptide-surface interactions are obtained using a standardized methodology, similar probe tip densities (although unknown) can be expected. The functionalized tip with the peptide is then brought in contact with a selected substrate surface for one second of surface delay and then retracted at a constant vertical scanning speed of 0.1 µm/s. The peptide-surface interaction force is then recorded as a function of the tip-to-sample separation distance on approach and retraction. From this data for each peptide-surface combination, the unbinding force that is measured during the plateau region ending right at the separation distance (max sep), which corresponds to the contour length of the PEG spacer and the peptide sequence, is taken as the F_{des}, as illustrated in Figure 3 (*39*, *40*).

Table I. Values of $\Delta G^{\circ}_{\text{ads}}$ (kcal/mol) for peptide-SAM combinations. An asterisk (*) indicates a condition in which peptide adsorption was so strong that it was determined to be irreversible within the experimental time frame, in which case $\Delta G^{\circ}_{\text{ads}}$ could not be determined. The guest amino acids (X) are ranked by a standard hydrophobicity scale (*38*) from the most-to-least degree of hydrophobicity (mean (± 95% confidence interval), *N* = 6)

-X-	SAM-OH	SAM-COOH	SAM-EG$_3$OH	SAM-NH$_2$	SAM-NHCOCH$_3$	SAM-COOCH$_3$	SAM-OC$_6$H$_5$	SAM-OCH$_2$CF$_3$	SAM-CH$_3$
Non-Polar Guest Residues									
-L-	0.003 (0.001)	-1.30 (0.43)	-0.40 (0.28)	-2.34 (0.80)	-1.04 (0.30)	-2.06 (0.31)	-2.68 (0.72)	-.3.09 (0.31)	3.87 (0.69)
-F-	*	*	-0.30 (0.13)	*	-2.44 (0.40)	*	*	-3.97 (0.24)	-4.16 (0.16)
-V-	-0.002 (0.001)	-1.11 (0.31)	-0.26 (0.06)	-3.90 (0.12)	-0.16 (0.10)	*	*	-3.99 (0.22)	-4.40 (0.31)
-A-	*	*	-0.97 (0.36)	*	*	*	*	*	*
-W-	-0.001 (0.001)	-1.14 (0.52)	-1.72 (0.33)	-2.71 (0.32)	-1.94 (0.45)	-0.92 (0.36)	-1.65 (0.60)	-3.42 (0.27)	-3.89 (0.34)
Polar Guest Residues									
-T-	-0.001 (0.001)	-0.87 (0.46)	-0.28 (0.15)	-3.15 (0.50)	-0.16 (0.09)	-0.40 (0.14)	-2.89 (0.75)	-2.81 (0.40)	-2.76 (0.28)
-G-	-0.001 (0.001)	-0.68 (0.36)	-0.30 (0.20)	-2.56 (0.32)	-1.86 (0.20)	-1.18 (0.30)	-3.51 (0.22)	-3.30 (0.37)	-3.40 (0.39)
-S-	-0.002 (0.001)	-1.10 (0.10)	-0.34 (0.11)	-2.09 (0.98)	-1.49 (0.47)	-1.55 (0.26)	-3.20 (0.28)	-3.22 (0.24)	-2.75 (0.23)
-N-	-0.004 (0.003)	-0.86 (0.38)	-0.59 (0.11)	-3.22 (0.41)	-1.64 (0.23)	-1.37 (0.68)	-3.02 (0.16)	-3.41 (0.32)	-4.33 (0.62)
Charged Guest Residues									
-R-	-0.002 (0.001)	-1.53 (0.19)	-0.20 (0.10)	-3.03 (0.31)	-1.60 (0.80)	-1.17 (0.35)	-2.26 (0.82)	-3.45 (0.31)	-4.15 (0.55)
-K-	-0.001 (0.001)	-1.71 (0.19)	-0.19 (0.07)	-3.14 (0.20)	-0.12 (0.07)	-1.77 (0.07)	-3.35 (0.25)	-3.54 (0.45)	-3.34 (0.39)
-D-	-0.003 (0.001)	-1.06 (0.09)	-0.44 (0.14)	-3.75 (0.20)	-1.93 (0.52)	-1.34 (0.50)	-3.89 (0.23)	-3.59 (0.37)	-3.54 (0.60)

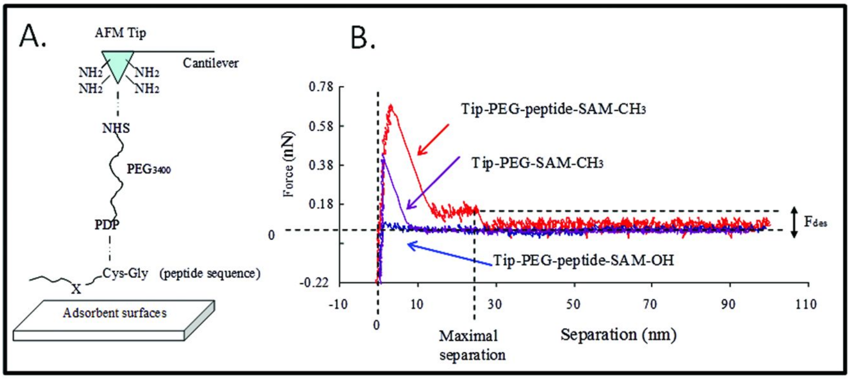

Figure 3. (A) AFM Tip linkage. Peptide sequences are coupled to AFM tips via a 3.4 kDa polyethylene glycol (PEG) crosslinker. (B) AFM force-separation curves recorded during adsorption-desorption of TGTG-V-GTCT peptide on a CH_3-SAM (upper red curve) and an OH-SAM (bottom blue curve). The middle (purple) curve represents a control group with the AFM tip without the peptide (only covered with PEG) on a SAM-CH_3 surface. Reproduced with permission from ref. (30). Copyright 2010 American Chemical Society.

In order to apply this method for the determination of effective values of ΔG°_{ads}, AFM studies were first conducted to measure F_{des} for a set of eight different types of peptides on a set of eight different types of SAM surfaces that were also evaluated by SPR. As presented in Figure 4, these comparisons show that a strong correlation exists between F_{des} from AFM and ΔG°_{ads} from SPR, with this correlation then subsequently used to determine effective ΔG°_{ads} values from F_{des} measurements for surfaces not conducive for use with SPR (e.g., silica glass, HDPE, and PMMA).

As shown in Figure 4, the averaged F_{des} values from AFM are linearly related to the ΔG°_{ads} results obtained by SPR, with a correlation coefficient of $R^2 = 0.89$. This result indicates that the standardized AFM method is able to be extended to estimate ΔG°_{ads} for peptide-surface systems that are not amenable for evaluation by SPR using the generated correlation between these two parameters.

These synergistically combined methods thus provide the ability to make thermodynamic measurements of peptide-surface interactions for any macroscopically flat surface, including surfaces that are not amenable for use with SPR or QCM methods. Importantly for our specific needs, these methods also provide a means to obtain experimental data that is useful for the evaluation, modification, and validation of interfacial force field parameters that are required to enable peptide and protein adsorption behavior to be accurately represented by molecular simulation.

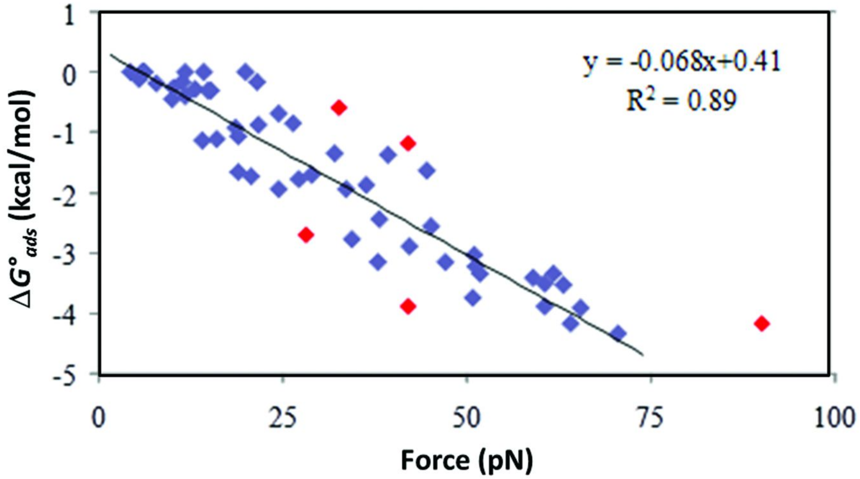

Figure 4. Correlation between $\Delta G°_{ads}$ by SPR and desorption force by AFM for an equivalent set of 64 different types of peptide-SAM systems in PBS; pH=7.4. Reproduced with permission from ref. (31). Copyright 2012 American Chemical Society.

Computational Methods To Calculate the Free Energy of Peptide-Surface Interactions from Molecular Simulation

To complement our experimental values of $\Delta G°_{ads}$ for the interaction of TGTG-X-GTGT peptides on surfaces as addressed in the previous section, synergistically designed computational methods are needed for the calculation of $\Delta G°_{ads}$ for comparison with the experimental results. For our studies, we have selected the CHARMM force field and molecular simulation program (*12*) and used existing CHARMM force field parameters in order to evaluate the ability of this force field to accurately represent the strength of peptide adsorption for this type of molecular system. Similar methods can be applied for any selected force field.

Molecular models were first constructed for each of the nine different types of alkanethiol SAM surfaces and silica glass, and the TGTG-X-GTGT peptides used in our SPR studies. Models of HDPE and PMMA are also currently under development. Eight different guest amino acid residues (X) were used in the simulations, with X = V, F, T, W, G, N, D, and K (thus representing each class of amino acid: nonpolar aliphatic, aromatic, polar, negatively charged, and positively charged).

Each system was constructed by placing a water layer on top of the surface layer using CHARMM's TIP3P water model. An additional 15 Å water layer with waters kept fixed was placed between the top water layer and adjacent (bottom) surface layer to prevent interaction of the peptide with the bottom of the surface layer when periodic boundary conditions are applied. The host−guest peptide was introduced into the top water layer and overlapping waters were deleted. The dimensions of surface and water layers in the x and y directions (parallel to the surface) were approximately 45-55 Å. Where necessary, to correctly generate the periodic boundary conditions for systems with bonds extending across the periodic boundaries between the primary and image cells, CHARMM PATCH commands were used for creating bonds, angles, and dihedrals between the primitive and adjacent image cells. A representative illustration of the model system for a TGTG-V-GTGT peptide over a CH_3 SAM surface is shown in Figure 5.

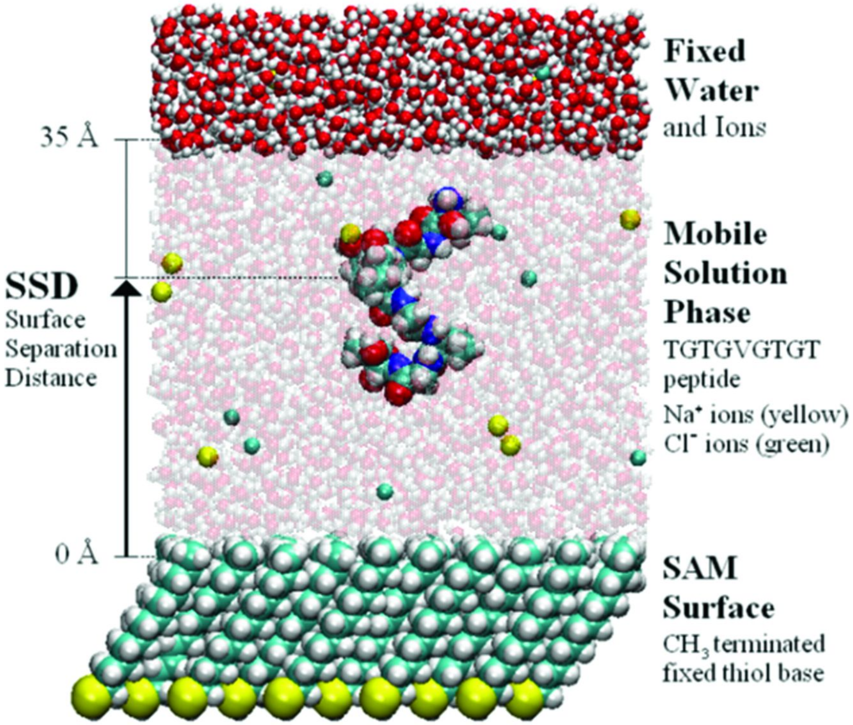
Fixed
Water
and Ions
35 Å
SSD
Surface
Separation
Distance
Mobile
Solution
Phase
TGTGVGTGT
peptide
Na⁺ ions (yellow)
Cl⁻ ions (green)
0 Å
SAM
Surface
CH3 terminated
fixed thiol base

Figure 5. Molecular model of a TGTG-V-GTGT peptide over a hydrophobic CH_3-SAM surface in TIP3P water. Reproduced with permission from ref. (20). Copyright 2010 American Chemical Society.

In preparation for our simulations, each solvated host−guest peptide/surface system was subject to 100 ps of heating from 0 to 298 K, followed by 10 ns of dynamics in the *NVT* ensemble (i.e., the canonical ensemble; constant number of atoms (*N*), constant volume (*V*), and constant temperature (*T*)) with the peptide unrestrained using the modified velocity-verlet integrator (VV2) with a Nosé-Hoover thermostat to control temperature and a time-step set to 2 fs. The length of the simulation cell along the *z*-axis direction (i.e., long axis, or height of the cell) was determined so as to establish 1 atm pressure for all simulations (*41*). The SAM surfaces were simulated using the parameters from the CHARMM general force-field (CGenFF) (*42*). The initial model of amorphous silica surface was generated using the Large-scale Atomic/Molecular Massively Parallel Simulator (LAMMPS) software package with surface terminated by silanol (≡Si-OH) groups (complements of Dr. Chris Lorenz of King's College, London, UK). The remainder of each system was simulated using standard CHARMM22 protein force field parameters.

In order to track the position of the peptide as it interacts with each surface in a simulation, we define a reaction coordinate which we call the surface separation distance (SSD). The SSD represents the z-coordinate distance between the center of mass of all peptide atoms and the center of mass of all atoms comprising a selected set of surface atoms, chosen to represent the surface plane. To accurately calculate adsorption free energy from a molecular simulation of peptide adsorption, it is necessary to (*i*) adequately sample the peptide's position over the entire range of SSD and (*ii*) adequately sample the conformational state of the peptide at each SSD position. Simulations can then be performed to determine the probability of the peptide to be positioned in an adsorbed state on the surface relative to its probability to be in a nonadsorbed state in bulk solution above the surface. This ratio thus provides a measure similar to that used in our experimental methods where ΔG°_{ads} is determined at equilibrium from the concentration of the peptide when adsorbed to a surface compared to its concentration in bulk solution, as shown in equation (3).

In order to represent a properly equilibrated system in our simulations, we use a biased-energy replica-exchange molecular dynamics (REMD (*43*)) advanced sampling method, which our group has previously developed for this purpose (*20*, *36*, *44*). This method combines two advanced sampling strategies in a single simulation: a biased energy function added to the REMD simulation enables the peptide to escape from a strongly adsorbing surface, thus addressing the SSD sampling problem, combined with an REMD simulation, which uses elevated temperatures combined with statistical mechanics algorithms to enhance conformational sampling of the peptide. While the use of either of these advanced sampling methods alone does not provide adequate sampling for the accurate calculation of adsorption free energy, their combined use enables both sampling problems to be efficiently overcome in a single simulation, thus enabling adsorption free energy to be properly determined. We also must note that under the canonical ensemble (i.e., constant *NVT* conditions), adsorption free energy is more appropriately represented by the standard-state Helmholz free energy of adsorption, $\Delta A^{\circ}_{\mathrm{ads}}$, while the experimental conditions (represented by the isothermal-isobaric ensemble; i.e., constant *NPT* conditions; with P = pressure) provide a measure of the standard-state Gibbs free energy of adsorption, ΔG°_{ads}. However, under condensed-phase aqueous conditions, there is negligible difference between these two values, given the very small compressibility of water. Thus for our simulations, we will subsequently refer to the calculated free energy values as being representative of $\Delta G^{\circ}_{ads},$ with direct comparison then being made to our experimentally measured values of adsorption free energy.

In order to calculate $\Delta G°_{ads}$ from our simulations, the biasing function is first derived using windowed umbrella sampling (*45*, *46*) along the SSD reaction coordinate. For this method, a harmonic restraining potentials is applied to force the peptide to sample the full SSD-coordinate space between 3 and 25 Å with overlapping windows of the SSD coordinate. The resulting sampled SSD trajectories from the umbrella sampling simulations are then analyzed using the weighted histogram analysis method (WHAM) (*47*) to calculate a potential of mean force (PMF) profile as a function of SSD, from which a free energy vs. SSD profile can be obtained. The resulting PMF profile is then fit to a modified Derjaguin, Landau, Verwey, and Overbeek (DLVO) potential (*48*) and the negative of this fitted function is added to the force field equation as a biasing potential in subsequent biased-REMD simulations. This rather complex procedure is necessary to enable the peptide to escape from a strongly adsorbing surface during the REMD simulation, in order to adequately sample the position of the peptide over the full SSD-coordinate space for the proper calculation of $\Delta G°_{ads}$. After conducting a biased-REMD simulation, the resulting biased SSD-position probability density profile is corrected using statistical mechanics principles to remove the effects of the applied biasing function to give an unbiased probability distribution. Readers are referred to our previous publications for more complete details of these methods (*20*, *36*, *44*).

Using the resulting unbiased probability distribution, a value for the adsorption free energy is calculated using the expression:

$$\Delta G^{\circ}_{ads} = -RT\ln\left\{\frac{W}{\delta}\sum_{i=1}^{N}\left(P_i / P_b\right)\right\} \tag{4}$$

where the subscripts '*i*' and '*b*' represent the interfacial and bulk solution regions of the system, P_i and P_b are the probabilities of the peptide being at positions SSD_i, and SSD_b, respectively, with SSD_b defined to be the distance from the surface for which peptide-surface interactions become negligibly small, which for our systems is typically beyond 15 Å from the surface plane. N is the number of incremental segments spanning the SSD-coordinate space for which $P_i \neq P_b$, δ is the theoretical thickness of the adsorbed layer similar to the value used in equation (3), and W is the bin width used to produce the probability distribution. $\Delta G°_{ads}$ values for the interaction of each host−guest peptide on each of the surfaces can thus be determined from simulations for comparison with the experimental results obtained from our SPR and AFM studies for these same systems as a direct means of assessing the accuracy of the force field that is used in the simulations. Differences between the calculated and experimental $\Delta G°_{ads}$ values are then used to identify situations where interfacial force field parameters need to be adjusted to properly represent peptide adsorption behavior, which is the topic of the following section. An example of these comparisons is shown in Figure 6.

Figure 6 compares the calculated adsorption free energy values from simulation with the experimental values presented in Table I for each of the SAM surface systems corresponding to the nine different surface functional groups. From Figure 6, it is apparent that for several of the SAM systems the agreement between the experiment and simulation exceeds our defined target of 1.0 kcal/mol in magnitude, implying that inaccurate peptide adsorption behavior is predicted from the simulations with the CHARMM force field parameters. Such results suggest that the current set of CHARMM parameters require refinement before protein adsorption behavior can be accurately predicted by simulation. It is also evident from Figure 6 that the best agreement between simulation and experiment occurs for those SAM surfaces having the most hydrophilic surface functional groups, such as OH and EG_3OH. As indicated, the magnitude of the $\Delta G°_{ads}$ values are substantially underestimated (i.e., indicating overly weak adsorption) relative to the experimental values for the more hydrophobic CH_3, OC_6H_5, and OCH_2CF_3 functionalized surfaces, and also for the positively charged NH_2 functionalized SAM surfaces, thus revealing systems in need of parameter adjustment.

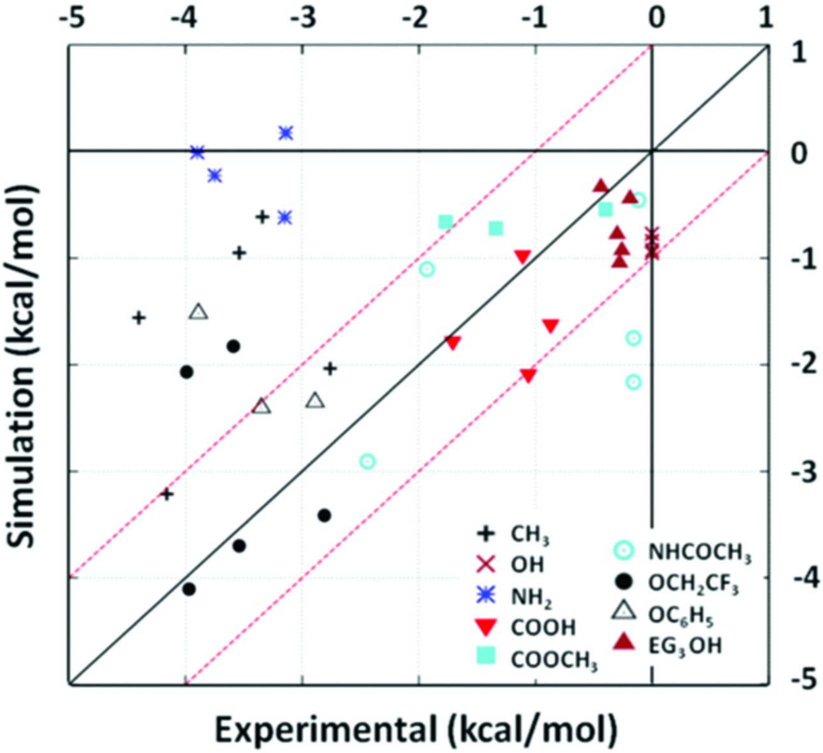

Figure 6. Comparison of the free energy of adsorption ($\Delta G°_{ads}$) estimated from the biased REMD simulation with that from the experimental results for peptide adsorption on SAM surfaces. Reproduced with permission from ref. (20). Copyright 2010 American Chemical Society.

Force Field Parameter Adjustment To Correct Identified Errors in the Free Energy of Peptide-Surface Interactions

The discrepancies identified in the previous section from comparisons between experimentally obtained ΔG°_{ads} values and those obtained by simulation indicate a need for parameter adjustment of the CHARMM force field in order to accurately represent interactions of the peptides with the surface. However, these adjustments must be made in a way that influences the peptide-surface interaction without altering the conformational behavior of the peptide in solution, for which the CHARMM force field parameters have been previously and accurately tuned. To provide this capability, we modified the CHARMM program code to provide the capability to use an interfacial force field, independently from the conventional CHARMM force field used for both the solution phase and solid phase of our molecular system. We refer to this modified program as dual-force field (Dual-FF) CHARMM (*21*). When applied to the simulation of peptide adsorption to a material surface, the Dual-FF approach, which is diagrammed in Figure 7, thus enables one to model the surface, solution, and interfacial phases separately and accurately using force fields that were parameterized for each of their respective molecular environments. And, because adsorption behavior is primarily influenced by the nonbonded parameters of the force field (i.e., electrostatic and vdW interactions; see equation 1), adjustment of the interfacial force field to correct identified errors in ΔG°_{ads}, only requires the tuning of these respective nonbonded parameters.

To implement the Dual-FF capability into a simulation package like CHARMM, it was necessary to make relatively minor modifications to the program's code. The approach our group has used to modify the CHARMM program was to add a phase-type identifier for each atom in the simulated system that is set to a user-defined value for each phase present in the system. The topology and parameter files and storage arrays were then updated to include an interfacial set of partial charges and L-J parameters, as described in equation (1). The calculation of potential energies from the pairwise nonbonded interactions was then modified to depend on the atom phase-types for each specific interaction: if the two atoms being compared belong to the same phase (i.e., solution phase or solid phase), the standard intra-phase parameters of the CHARMM force field are used, and if the two atoms compared belong to different phases, the interfacial parameters are used. The implementation of such a nonbonded scheme is relatively simple for cutoff-based nonbonded interactions; however, implementing Ewald summation (*49*) for the rigorous treatment of long-range electrostatic interactions is more involved and is still under development. Despite this current limitation, preliminary studies have shown that using simple cutoffs versus Ewald summation affects the peptide adsorption free energies less than about 0.5 kcal/mol, which are within the 95% confidence intervals of our calculated adsorption free energy values.

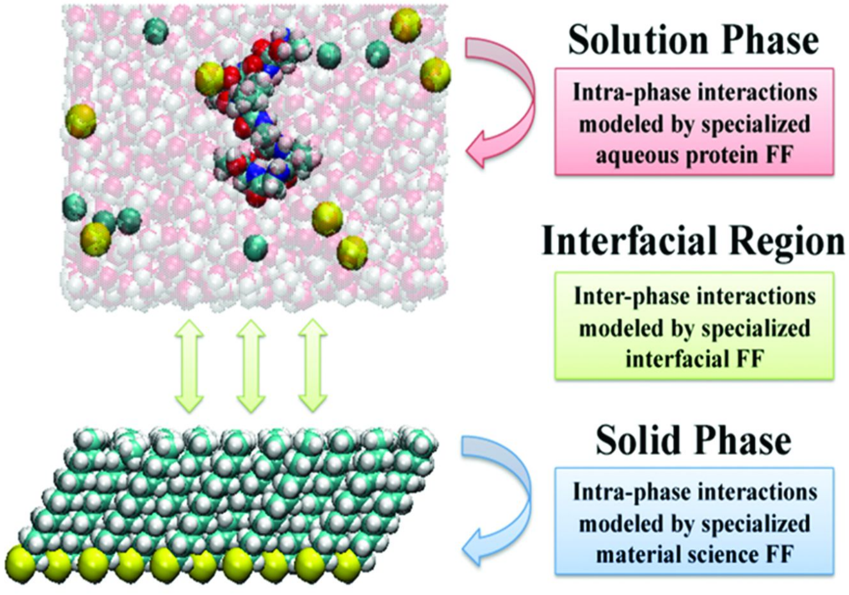
Solution Phase
Intra-phase interactions modeled by specialized aqueous protein FF
Interfacial Region
Inter-phase interactions modeled by specialized interfacial FF
Solid Phase
Intra-phase interactions modeled by specialized material science FF

Figure 7. Schematic representation of the dual force field (Dual FF) model applied to a peptide adsorption simulation. The solution and solid surface phases are modeled by specialized force fields that accurately represent intra-phase interactions while all interactions between atoms of the solution phase with the solid phase are handed by a specialized interfacial force field that is tuned to accurately represent peptide adsorption free energy.

Following these methods, simulations are first conducted using the conventional CHARMM force field parameters to calculate ΔG°_{ads} for comparison with experimental ΔG°_{ads} values. Figure 8 presents an example data set for silica glass and CH_3-SAM surfaces, which reveal that the strength of peptide adsorption is generally underestimated for the CH_3-SAM surface and greatly overestimated for silica glass, thus indicating that interfacial force field parameter adjustment is required for these systems if the strength of adsorption is to be accurately represented in a simulation of protein adsorption behavior.

Once errors in adsorption free energy are found, the next challenge is to develop a reasonable approach for the adjustment of interfacial force field parameters to correct the adsorption behavior, which is mediated by electrostatic and vdW interactions and the way in which they control the competition between the peptide and water/ions for the functional groups of the surface. Our current approach, which is still undergoing refinement, is to use the Dual-FF program to separate the contributions of electrostatic and vdW interactions to determine which of these two factors have the greatest influence on peptide adsorption behavior. Electrostatic interactions can be eliminated by setting partial charges controlling the interactions between the solution-phase atoms (i.e., peptide, water, and ions) and surface-phase atoms to zero, while vdW interactions can be effectively eliminated by setting the well-depth parameter of the Lennard-Jones 12-6 potential (ε_{ij}) to a very low value (e.g., 10^{-4} kcal/mol), which then makes vdW attraction negligibly small while maintaining atomic repulsion, thus preventing atom-atom overlap. It is worth emphasizing that these changes apply only to the interfacial interactions, thus leaving the solution and surface structure mostly unchanged. By comparing the PMF vs. SSD profiles obtained from umbrella sampling simulations using these conditions in comparison to the behavior provided by the regular set of CHARMM force field parameters, it can be determined which set of parameters most strongly influences the adsorption behavior, thus indicating which parameters should be adjusted to most effectively correct the identified errors in the ΔG°_{ads} values. The order of the adjustments made to the interfacial parameters is also important for the convergence of calculated free energies to the experimental values. Given the common presence of G and T amino acid residues for each of our host−guest peptides, interfacial parameters are first adjusted for the TGTG-X-GTGT host−guest peptides with X = G and T by adjusting the partial charges and L-J well depth (ε) parameters of the TIP3P water and surface functional groups until their calculated free energies match their respective experimental values within 0.5 kcal/mol. Adjustments are then made to the amino acid parameters of the other guest amino acid residues, with a focus on the adjustment of atom types that may be unique to each particular amino acid type. Figure 8 shows the results of this procedure to correct the errors in ΔG°_{ads} for peptide adsorption on silica glass and a CH_3-SAM surface, with ΔG°_{ads} values from simulations using the tuned interfacial force field parameters being brought into close agreement with the experimentally determined values.

Once established, the interfacial force field parameter set can then be applied for the simulation of actual protein adsorption behavior to assess whether the tuning of interfacial parameters to adjust the relative strength of each type of amino acid residue with functional groups of a given surface will in turn enable the orientational and conformational behavior of the protein on the surface to also be correctly predicted by the simulation. Before simulations of protein adsorption behavior can be attempted, however, two further developments are also required. First, because of the increased complexity of simulating protein adsorption behavior, additional computational methods are needed to support this type of molecular simulation. In particular, the simulation of protein adsorption behavior involves sampling of the much larger conformational phase space of a protein over an adsorbing surface; this requires the implementation of more advanced sampling methods for system equilibration within a reasonable amount of computational time. Secondly, in order to validate the accuracy of protein adsorption behavior predicted by simulation, experimental data is required that can be quantitatively compared with simulation results for validation. These two issues are addressed in the following two sections.

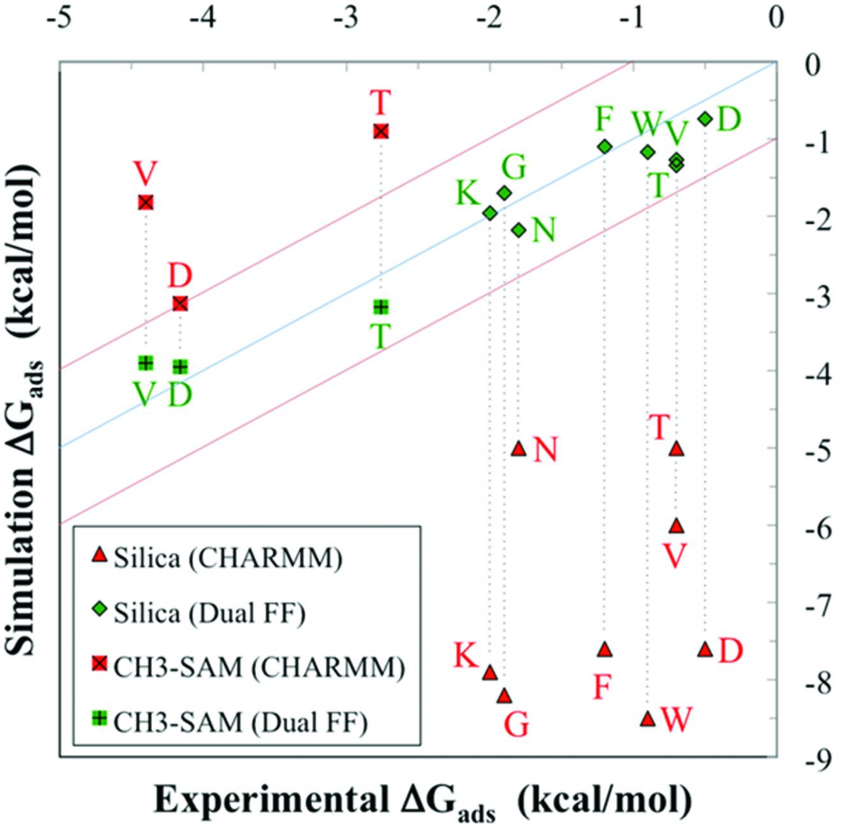

Figure 8. Comparison of the mean ΔG°_{ads} values calculated in simulation with matched experimental values. The values shown in red are those obtained from a simulation with regular CHARMM parameters (i.e., using conventional CHARMM22 and CGenFF parameters to describe every interaction) and the values shown in green are obtained from a Dual-FF simulation using optimized interfacial force field parameters. 95% confidence intervals for both the experimental and simulation mean values are on the order of about 0.5 kcal/mol.

Advanced Sampling Methods for the Simulation of Protein-Surface Interactions

Molecular dynamics simulations have been widely applied to provide insight into the structure, dynamics, and thermodynamics of biological macromolecules in solution. However, the use of conventional all-atom molecular dynamics (MD) methods to simulate the complex conformational behavior of large molecular systems is computationally very inefficient; both because of the extremely large number of degrees of freedom that must be represented in a simulation

In Proteins at Interfaces III State of the Art 2012; Horbett, T., et al.;
ACS Symposium Series; American Chemical Society: Washington, DC, 2012.

and because of the inherent problem of very slow phase-space sampling that arises due to the presence of relatively high energy barriers separating the extremely numerous local energy minima separating the conformational states contained within these types of systems. More efficient methods of searching the conformational phase space of a complex molecular system have been developed to address these issues. The most promising types of methods to surmount these problems include (*i*) the use of coarse-graining (CG) combined with the implicit representation of solvation effects, which involves combining groups of atoms into single 'bead' elements and incorporating solvation energy effects directly within the force field, and (*ii*) the combination of statistical mechanics algorithms along with elevated temperature to accelerate the crossing of energy barriers in the system. In this section, we provide an overview of our efforts to develop and implement both of these types of advanced sampling techniques for the efficient simulation of protein adsorption behavior.

Among these types of methods, REMD has proven to be one of the most successful and extensively used for the simulation of biological molecules (*43*). As introduced above, REMD conducts a number of parallel simulations at sequentially increasing temperature levels and periodic attempts to exchange configurations between adjacent levels following a Boltzmann-weighted process. By sampling and exchanging over the temperature space, the molecular system is able to overcome the kinetic trapping problem experienced in conventional MD simulations. Still, practical difficulties remain in the application of REMD for large molecular systems (*50*). In REMD, the number of processors required is essentially dictated by the REMD algorithm, with large molecular systems requiring the use a large number of closely spaced temperature levels (i.e., large number of replicas). This ensures sufficient overlap between the potential energy distributions of adjacent replicas as necessary to obtain an acceptable probability of successful exchanges. The implementation of REMD thus becomes increasingly computationally expensive as the size of the molecular system being simulated increases. Furthermore, the use of a large number of replicas also results in the slow diffusion of replicas over the numerous temperature levels, thus resulting in poor sampling efficiency.

To overcome the above problems of the REMD method, we have developed a new empirical sampling method, which we call "temperature intervals with global exchange of replicas" (TIGER2) (*50*, *51*). This advanced sampling method was specifically designed for systems that are deemed to be too large for REMD. Similar to REMD, a TIGER2 simulation involves the use of a number of replicas (N_r) running in parallel at different temperature levels; however, the number of replicas used in the simulation can be determined by the user instead of the algorithm itself, thus letting the user set the computational cost of the simulation to match the available computational resources. In a TIGER2 simulation, the sampling is composed of a series of cycles with each cycle containing four stages: (1) rapid heating from a baseline temperature (T_B) to the replica temperature (T_m) by rescaling the momenta of the atoms within the replica by a factor of $\sqrt{T_m/T_B}$ and thermally equilibrating, (2) molecular dynamics sampling at constant temperature (T_m), (3) rapid quenching of replicas back down to T_B by rescaling the momenta by a factor of $\sqrt{T_B/T_m}$ followed by thermal equilibration, and (4) global replica reassignment. Stage (4) consists of two substeps: (*i*) one state from among the set of (N_r−1) quenched states is randomly selected using a uniform probability distribution, and the potential energy of this state is then compared with the potential energy from the production run of the baseline replica and possibly exchanged using the Metropolis criterion (*52*), and (*ii*) all replicas except the baseline replica are then reassigned to higher temperature levels according to their potential energies; i.e., a higher potential energy state is assigned to a higher temperature level. This algorithm thus enables temperature to be used to accelerate the crossing of energy barriers in the system with much less computational cost than REMD. The validity of this new advanced sampling method has been demonstrated by comparison with REMD simulation results for the folding behavior of relatively small peptides and proteins that could be handled by both methods, including alanine dipeptide, $(AAQAA)_3$ [$(Ala\text{-}Ala\text{-}Gln\text{-}Ala\text{-}Ala)_3$], chignolin (Gly-Tyr-Asp-Pro-Glu-Thr-Gly-Thr-Trp-Gly) peptides , and protein G (*50*, *51*). The TIGER2 results closely matched the REMD results for each of these model systems, thus demonstrating that the TIGER2 algorithm is able to closely approximate Boltzmann statistics, as required for the accurate simulation of a molecular system. Interested readers are referred to our published papers on the use of TIGER2, especially a recent paper that provides guidance regarding parameter set up for its proper implementation (*51*).

As mentioned above, coarse graining combined with implicit solvation methods provide another approach to greatly improve the efficiency of a molecular simulation, especially for large molecular systems. We are presently developing methods to simulate protein adsorption onto polymeric surfaces, such as PMMA, using a modified version of the CHARMM molecular simulation program. We use a ‘Go-like’ CG model for the protein (*53*, *54*), in which each amino acid residue is treated as a single bead, with the groups of polymer surface atoms also then combined into CG bead elements. A surface adsorption energy term described by a Lennard-Jones-type potential (see equation 1) is then used to guide the adsorption behavior of amino acid residues when they come into close proximity to the surface. For each type of surface, the parameters in the surface adsorption term are tuned by mapping calculated adsorption free energies to our experimental data set as presented above, which also enables solvation effects to be directly incorporated into the CG parameters.

Using the tuned residue-surface interaction parameters and the CG model for each system, the adsorbed orientation and conformation of the protein with respect to the surface can be explored to obtain a molecular-level understanding of the factors influencing protein-surface interactions. Following system equilibration using an advanced sampling method such as TIGER2, the CG models are reverse-mapped back to all-atom models with explicit solvation added to the system and then further equilibrated using TIGER2 to provide the final predicted ensemble of adsorbed protein states. The resulting equilibrated distribution of adsorbed protein states can then be analyzed to characterize the adsorbed orientation and conformational structure of the protein on the surface. Bioactivity assessment can also be conducted by evaluating the solvent accessibility and conformational state of designated bioactive sites within the protein. These results can then be compared with data from synergistically matched experimental studies for validation, which is the subject of the following section.

Experimental Studies of Protein-Surface Interactions To Measure Adsorbed Protein Orientation, Conformation, and Bioactivity

In order to provide experimental data that can be used to validate our developed capabilities to accurately simulate protein adsorption behavior, synergistically designed experimental methods are required to provide quantitative results that describe a protein's adsorbed orientation, conformation, and bioactivity. Of particular importance, because our initial protein adsorption simulations necessarily represent protein adsorption without the complicating influence of protein-protein interactions on a surface, it is essential that our experimental methods provide data that also represent this condition.

We have focused on the development of three different experimental methods to provide this level of characterization: adsorbed-state circular dichroism spectropolarimetry (CD) (*55*, *56*), amino acid side-chain modification with mass spectrometry (*57*), and adsorbed-state bioactivity assays (*55*, *57*); with the experimental conditions set to provide minimal lateral interactions (MLI) between the adsorbed proteins. To obtain MLI conditions, experimental methods are applied that allow adsorbed proteins to unfold on a surface with minimal interference of neighboring adsorbed proteins. We have addressed this problem by controlling three parameters that influence the relative kinetics of protein adsorption to a material surface and unfolding of the adsorbed proteins on the surface. These three experimental parameters are: (*i*) protein solution concentration, (*ii*) adsorption time in which the surface is exposed to the protein solution, and (*iii*) equilibration time beneath a protein-free buffer solution following adsorption .

CD Spectroscopy To Measure Changes in Adsorbed Protein Secondary Structure and the Establishment of MLI Conditions

CD is an extremely powerful and sensitive method to characterize the secondary structure of proteins (i.e., percent α-helix, β-sheet, and random loop content) both in solution and when adsorbed to surfaces. Our CD studies are conducted using a Jasco J-810 spectropolarimeter over the wavelength range of 190-300 nm, by strictly complying with the quality standards recommended by Kelly et al. (*58*).

The secondary structure of the native state of proteins in solution is determined using 1.0 mg/mL protein solutions in a 0.01 cm path-length quartz cuvette. Traditionally, CD has been applied only to proteins in solution or to proteins adsorbed to colloidal particles, and therefore, its common application with adsorbed protein on flat transparent solid substrates is relatively recent, although McMillin and Walton reported the use of CD to probe the structure of adsorbed proteins on a flat surface as early as 1974 (*59*). We have been developing CD methods over the past decade to study the effect of adsorption on the secondary structure of protein (*56*, *60*) and have recently further refined our methods to substantially enhance our signal-to-noise ratio, providing a very high level of accuracy and reproducibility. Figure 9 shows an example data set from a recent study on the adsorption behavior of human fibrinogen (Fg), which shows that Fg undergoes substantially different changes in its secondary structure following adsorption to different surface chemistries (*56*).

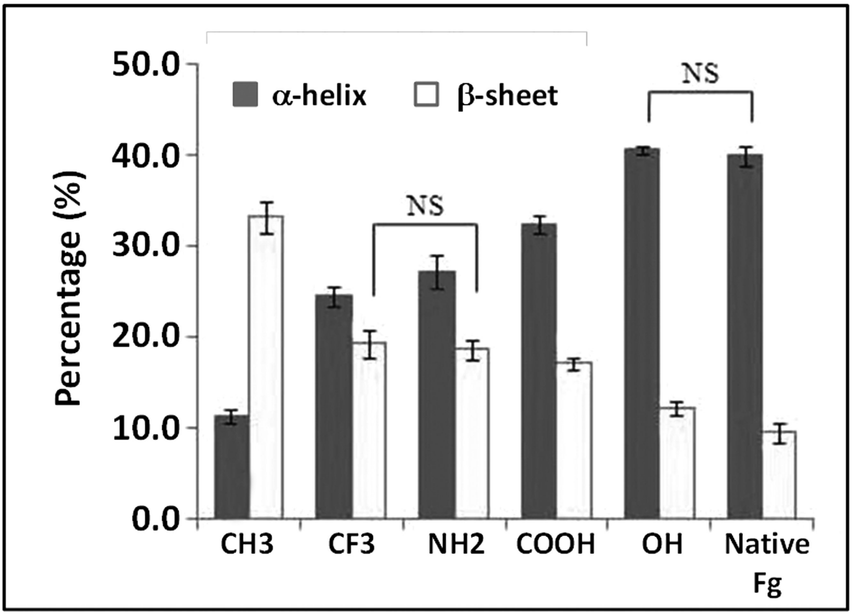

Figure 9. Changes in secondary structure of adsorbed human fibrinogen (Fg) adsorbed from 0.1 mg/mL Fg in PBS solution on functionalized SAM surfaces determined by CD compared to its native conformation. (N = 6, mean ± 95% CI). (NS denotes not significant, all other values are significantly different from one another; p < 0.05). Reproduced with permission from ref. (56). Copyright 2009 American Chemical Society.

For the determination of the secondary structure of proteins in their adsorbed state, we use a custom designed cuvette that is capable of supporting four individual slides to increase the signal-to-noise ratio so as to obtain an accurate measurement of the structure of the adsorbed protein layers (*56*). Background spectra are first collected for four sets of slides immersed in plain buffer solution for each material surface prior to protein adsorption. The protein is then adsorbed onto the same set of slides, which are remounted in the cuvette and analyzed to determine the effective CD spectra with the corresponding background spectra subtracted to isolate the spectra from the adsorbed proteins alone. The surface density of proteins on the slides is determined by measuring the effective absorbance at 195 nm. The spectra are converted to units of molar ellipticity and then deconvoluted using CDPro software to obtain a quantitative assessment of the secondary structural content of the adsorbed protein.

Using the techniques that have been described above, the changes in surface density and secondary structure of adsorbed protein are monitored as a function of varying bulk protein solution concentration from which the protein is adsorbed. Results show that the degree of protein unfolding on the surface tends to increase as the protein is adsorbed from increasingly dilute solutions, which reflects a reduction in protein-protein interactions on the surface as the kinetics of protein adsorption are slowed, thus providing increased time for adsorbed proteins to unfold and spread out on the surface before neighboring proteins adsorb and prevent their further spreading. Protein adsorption studies from increasingly dilute solutions are performed until a point where the degree of protein unfolding on the surface no longer changes with further dilution, thus indicating that MLI conditions have been attained. Subsequent characterizations of the adsorbed protein layer are then performed using these conditions to determine adsorbed protein orientation, conformation, and bioactivity under MLI conditions.

Characterization of Adsorbed Protein Orientation and Changes in Tertiary Structure by Amino Acid Labeling/Mass Spectrometry Under MLI Conditions

While CD provides an excellent means of measuring protein secondary structure, it does not provide useful information regarding the orientation and tertiary conformation of adsorbed proteins. We have therefore developed amino acid side-chain labeled methods combined with mass spectrometry to provide this type of molecular-level information (*57*). In this method, we first adsorb a protein to a surface under MLI conditions and then treat the adsorbed protein layer to irreversibly label solvent-accessible side chains of targeted amino acids. Control studies are also performed to label solvent accessible amino acid residues of the protein in solution. The protein is then digested from the surface, or digested in solution (control), and the positions of the labeled amino acids within the protein structure are identified by mass spectrometry. Because side-chain modification will only take place for amino acid residues that are solvent accessible, any change in the number and position of the labeled amino acid residues upon adsorption provides quantitative information regarding both the orientation and changes in the tertiary structure of the adsorbed protein. Accordingly, amino acid residues that are found to be labeled in solution but unlabeled following adsorption provide an indication that those residues are adsorbed down on the surface and are no longer solvent accessible, thus providing an indication of adsorbed protein orientation. Alternatively, residues that are found to be labeled following adsorption that are not labeled in solution provide indication of tertiary unfolding of the protein, with these normally buried (i.e., solvent inaccessible) residues becoming solvent exposed after adsorption.

An example of the results of amino-acid labeling of tryptophan (Trp) residues combined with mass spectrometry results for hen egg white lysozyme (HEWL) is shown in Figure 10. In solution, nearly all Trp residues of HEWL were found to be labeled, and are thus indicated to be solvent accessible. In comparison, when HEWL was adsorbed on a hydrophobic CH_3-SAM surface (Figure 10.A), the Trp residues located in the bioactive site of this enzyme were found to be unlabeled, while these same residues were all labeled when the enzyme was adsorbed on a hydrophilic OH-SAM surface (Figure 10.B). These results thus suggest that, under the conditions applied, HEWL is primarily adsorbed to the hydrophobic surface in an orientation with its bioactive site down against the surface in a non-solvent-accessible manner, while the protein orientation on the OH-SAM surface is such that the bioactive site remains solvent accessible.

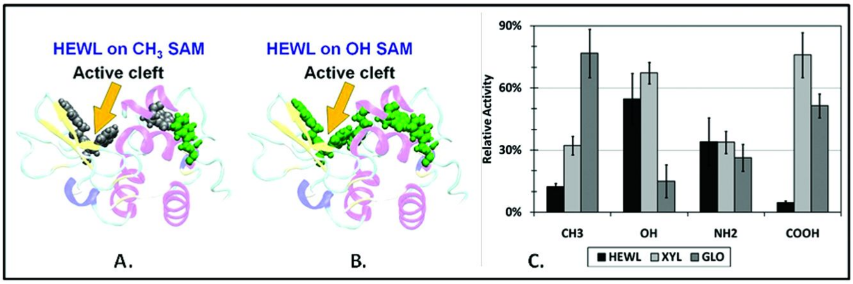

Figure 10. Changes in solvent accessibility of tryptophan residues (Trp) in HEWL adsorbed on (A) CH_3-SAM and (B) OH-SAM followed by Trp labelling and tryptic digestion. Trp residues colored gray indicate Trp residues that were not modified, and those colored green represents Trp residues that were modified during the modification process. PDB images of HEWL (PDB# 1GXV). (C) Graph of the relative activities of the adsorbed enzyme layers on the various SAMs. The surfaces were incubated in 1.0 mg/mL enzyme solutions for 24 h, after which activity assays were carried out for 2 min. (N = 4, mean ± 95% CI). Reproduced with permission from ref. (57). Copyright 2009 American Chemical Society.

Characterization of Adsorbed Protein Bioactivity Under MLI Conditions

To complement the results from our CD and amino acid labeling/ mass spectrometry techniques, we have adapted and applied solution-state bioacitivity assays (turbidometric & colorimetric) that are specific to a given protein to assess the effects of adsorption on its bioactivity (*55*). For this purpose, an initial calibration plot of solution-state bioactivity is obtained. Subsequently, proteins are adsorbed onto the slides of the same custom-designed cuvette that are used for our CD studies under MLI conditions, followed by rinsing to remove loosely bound protein, and the protein solution is then replaced by bulk buffer solution, with the surface density of protein then quantified by monitoring the absorbance at 195 nm. Absorbance values at 195 nm are then followed over time to ensure that the protein is irreversibly adsorbed to the surface, confirming that the measured bioactivity is not influenced by soluble protein in buffer solution that may have desorbed from the surface after the slides are mounted in the cuvette holder. The rates of change in absorbance with respect to the concentration of the substrates are then used to estimate the specific activity per mg of the enzyme, which, when normalized to its activity in solution, characterizes the effect of adsorption on the bioactivity of the adsorbed enzymes.

Figure 10.C shows results from recent studies by our group investigating the effect of adsorption of three enzymes (HEWL, xylanase (XYL) and glucose oxidase (GLO)) on various SAM surface chemistries. These data show that the bioactive states of these enzymes are substantially influenced by both the type of enzyme and the type of surface to which it is adsorbed. When considered along with the results from the Trp-labeling studies that have been conducted with HEWL, these combined results indicate that the difference in HEWL activity on the CH_3-SAM (Figure 10.A) vs. the OH-SAM (Figure 10.B) surfaces is primarily due to the adsorbed orientation of this protein.

Concluding Remarks

Empirical force field molecular simulation methods provide a relatively new and exciting area for development for the investigation of peptide and protein interactions with material surfaces. However, as addressed in this chapter, these methods must first be carefully developed, which requires the synergistic design of experimental and simulation methods. Experimental methods are required that can provide the kinds of experimental data that can be used to quantitatively evaluate, tune, and validate interfacial force field parameters that will enable atoms in a protein, aqueous solution, and material surfaces to interact with one another in a realistic manner. Experimental methods are also required to characterize the orientation, conformation, and bioactivity of adsorbed proteins with minimal influence from protein-protein interactions on the surface so that the results from protein adsorption simulations using a validated interfacial force field can themselves be evaluated and validated. Similarly, synergistic simulation methods are needed to closely match experimental conditions and enable large molecular systems to be equilibrated in an efficient manner so that simulation results can be directly and properly compared with the generated experimental data.

While each of these areas of development represent a very challenging task in its own right, if molecular simulation methods can be developed to the point of accurately representing protein interactions with material surfaces, these methods will then have the potential to provide the long-sought-after capability to understand, predict, and control protein adsorption behavior at the atomistic level. Once achieved, these methods will provide an extremely valuable tool to guide the design and optimization of biointerfaces with a wide range of applications in the broad fields of biotechnology and biomolecular engineering.

Acknowledgments

We gratefully acknowledge the many previous members of Dr. Latour's research group who have contributed to this overall effort, the names and contributions of which are provided in our publications. We also greatly thank the agencies that have supported this research program including NIH (grant nos. R01 EB00616, P41 EB001046 (RESBIO Biomaterials Center), and R01 GM074511) and the Defense Threat Reduction Agency-Joint Science and Technology Office for Chemical and Biological Defense (grant no. HDTRA1-10-1-0028). We also would like to thank Dr. Lara Gamble and Dr. David Castner of NESAC/BIO at the University of Washington for assistance with surface characterization with XPS under the funding support by NIH NIBIB (grant no. EB002027).

References

1. Latour, R. A. Biomaterials: Protein-surface interactions. In *The Encyclopedia of Biomaterials and Bioengineering*, 2nd ed.; Wnek, G. E., Bowlin, G. L., Eds.; Informa Healthcare: New York, 2008; Vol. 1, pp 270−284.
2. Castner, D. G.; Ratner, B. D. Biomedical surface science: Foundations to frontiers. *Surf. Sci.* **2002**, *500*, 28–60.
3. Hlady, V.; Buijs, J. Protein adsorption on solid surfaces. *Curr. Opin. Biotechnol.* **1996**, *7*, 72–77.
4. Tsai, W. B.; Grunkemeier, J. M.; McFarland, C. D.; Horbett, T. A. Platelet adhesion to polystyrene-based surfaces preadsorbed with plasmas selectively depleted in fibrinogen, fibronectin, vitronectin, or von Willebrand's factor. *J Biomed Mater Res* **2002**, *60*, 348–359.
5. Geelhood, S. J.; Horbett, T. A.; Ward, W. K.; Wood, M. D.; Quinn, M. J. Passivating protein coatings for implantable glucose sensors: Evaluation of protein retention. *J. Biomed. Mater. Res., Part B* **2007**, *81B* (1), 251–260.
6. Kusnezow, W.; Hoheisel, J. D. Antibody microarrays: promises and problems. *Biotechniques* **2002** (Suppl), 14–23.
7. Wu, Z. Q.; Chen, H.; Liu, X. L.; Brash, J. L. Protein-resistant and fibrinolytic polyurethane surfaces. *Macromol. Biosci.* **2012**, *12* (1), 126–131.
8. Norde, W. My voyage of discovery to proteins in flatland ... and beyond. *Colloids Surf., B* **2008**, *61* (1), 1–9.
9. Herr, A. E. *Protein Microarrays for the Detection of Biothreats*; Dill, K., Liu, R. H., Grodzinski, P., Eds.; Springer: New York, 2009; pp 169−190.
10. Zhang, Z.; Zhang, M.; Chen, S. F.; Horbetta, T. A.; Ratner, B. D.; Jiang, S. Y. Blood compatibility of surfaces with superlow protein adsorption. *Biomaterials* **2008**, *29* (32), 4285–4291.
11. Leach, A. R. *Molecular Modelling. Principles and Applications*; Pearson Education Ltd.: Harlow, U.K., 1996.
12. Brooks, B. R.; Brooks, C. L.; Mackerell, A. D.; Nilsson, L.; Petrella, R. J.; Roux, B.; Won, Y.; Archontis, G.; Bartels, C.; Boresch, S.; Caflisch, A.; Caves, L.; Cui, Q.; Dinner, A. R.; Feig, M.; Fischer, S.; Gao, J.; Hodoscek, M.; Im, W.; Kuczera, K.; Lazaridis, T.; Ma, J.; Ovchinnikov, V.;

Paci, E.; Pastor, R. W.; Post, C. B.; Pu, J. Z.; Schaefer, M.; Tidor, B.; Venable, R. M.; Woodcock, H. L.; Wu, X.; Yang, W.; York, D. M.; Karplus, M. CHARMM: The biomolecular simulation program. *J. Comput. Chem.* **2009**, *30* (10), 1545–1614.

13. Leahy, D. J.; Aukhil, I.; Erickson, H. P. 2.0 A crystal structure of a four-domain segment of human fibronectin encompassing the RGD loop and synergy region. *Cell* **1996**, *84*, 155–164.
14. Latour, R. A. Molecular simulation of protein-surface interactions: benefits, problems, solutions, and future directions. *Biointerphases* **2008**, *3* (3), FC2–12.
15. Collier, G.; Vellore, N. A.; Yancey, J. A.; Stuart, S. J.; Latour, R. A. Comparison between empirical protein force fields for the simulation of the adsorption behavior of structured LK peptides on functionalized surfaces. *Biointerphases* **2012**, *7* (1), 1–19 article 24.
16. Tomasio, S. D.; Walsh, T. R. Atomistic modelling of the interaction between peptides and carbon nanotubes. *Mol. Phys.* **2007**, *105* (2-3), 221–229.
17. Tomasio, S. M.; Walsh, T. R. Modeling the binding affinity of peptides for graphitic surfaces. Influences of aromatic content and interfacial shape. *J. Phys. Chem. C* **2009**, *113* (20), 8778–8785.
18. Iori, F.; Di Felice, R.; Molinari, E.; Corni, S. GoIP: An atomistic force-field to describe the interaction of proteins with Au(111) surfaces in water. *J. Comput. Chem.* **2009**, *30* (9), 1465–1476.
19. Kokh, D. B.; Corni, S.; Winn, P. J.; Hoefling, M.; Gottschalk, K. E.; Wade, R. C. ProMetCS: An atomistic force field for modeling protein-metal surface interactions in a continuum aqueous solvent. *J. Chem. Theory Comput.* **2010**, *6* (5), 1753–1768.
20. Vellore, N. A.; Yancey, J. A.; Collier, G.; Latour, R. A.; Stuart, S. J. Assessment of the transferability of a protein force field for the simulation of peptide-surface interactions. *Langmuir* **2010**, *26* (10), 7396–7404.
21. Biswas, P. K.; Vellore, N. A.; Yancey, J. A.; Kucukkal, T. G.; Collier, G.; Brooks, B. R.; Stuart, S. J.; Latour, R. A. Simulation of multiphase systems utilizing independent force fields to control intra-phase and inter-phase behavior. *J. Comput. Chem.* **2012**, *33*, 1458–1466.
22. Hower, J. C.; He, Y.; Jiang, S. Y. A molecular simulation study of methylated and hydroxyl sugar-based self-assembled monolayers: Surface hydration and resistance to protein adsorption. *J. Chem. Phys.* **2008**, *129* (21).
23. Xie, Y.; Zhou, J.; Jiang, S. Y. Parallel tempering Monte Carlo simulations of lysozyme orientation on charged surfaces. *J. Chem. Phys.* **2010**, *132* (6).
24. Gray, J. J. The interaction of proteins with solid surfaces. *Curr. Opin. Struct. Biol.* **2004**, *14* (1), 110–115.
25. Masica, D. L.; Gray, J. J. Solution- and adsorbed-state structural ensembles predicted for the statherin-hydroxyapatite system. *Biophys. J.* **2009**, *96* (8), 3082–3091.
26. Tamerler, C.; Oren, E. E.; Duman, M.; Venkatasubramanian, E.; Sarikaya, M. Adsorption kinetics of an engineered gold binding Peptide by surface plasmon resonance spectroscopy and a quartz crystal microbalance. *Langmuir* **2006**, *22* (18), 7712–8.

27. Green, R. J.; Frazier, R. A.; Shakesheff, K. M.; Davies, M. C.; Roberts, C. J.; Tendler, S. J. Surface plasmon resonance analysis of dynamic biological interactions with biomaterials. *Biomaterials* **2000**, *21* (18), 1823–35.
28. Ansorena, P.; Zuzuarregui, A.; Perez-Lorenzo, E.; Mujika, M.; Arana, S. Comparative analysis of QCM and SPR techniques for the optimization of immobilization sequences. *Sens. Actuators, B* **2011**, *155* (2), 667–672.
29. Janshoff, A.; Steinem, C. Label-free detection of protein-ligand interactions by the quartz crystal microbalance. *Methods Mol. Biol.* **2005**, *305*, 47–64.
30. Wei, Y.; Latour, R. A. Correlation between desorption force measured by atomic force microscopy and adsorption free energy measured by surface plasmon resonance spectroscopy for peptide-surface interactions. *Langmuir* **2010**, *26* (24), 18852–61.
31. Thyparambil, A. A.; Wei, Y.; Latour, R. A. Determination of peptide-surface adsorption free energy for material surfaces not conducive to SPR or QCM using AFM. *Langmuir* **2012**, *28* (13), 5687–5694.
32. Silin, V. V.; Weetall, H.; Vanderah, D. J. SPR studies of the nonspecific adsorption kinetics of human IgG and BSA on gold surfaces modified by self-assembled monolayers (SAMs). *J. Colloid Interface Sci.* **1997**, *185* (1), 94–103.
33. *BIAtechnology Handbook*; Biacore AB: Uppsala, Sweden, 1998; 4-1.
34. Wei, Y.; Latour, R. A. Benchmark experimental data set and assessment of adsorption free energy for peptide−surface interactions. *Langmuir* **2009**, *25* (10), 5637–5646.
35. Wei, Y.; Latour, R. A. Determination of the adsorption free energy for peptide-surface interactions by SPR spectroscopy. *Langmuir* **2008**, *24* (13), 6721–9.
36. O'Brien, C. P.; Stuart, S. J.; Bruce, D. A.; Latour, R. A. Modeling of peptide adsorption interactions with a poly(lactic acid) surface. *Langmuir* **2008**, *24* (24), 14115–14124.
37. Raut, V. P.; Agashe, M. A.; Stuart, S. J.; Latour, R. A. Molecular dynamics simulations of peptide-surface interactions. *Langmuir* **2005**, *21* (4), 1629–39.
38. Hessa, T.; Kim, H.; Bihlmaier, K.; Lundin, C.; Boekel, J.; Andersson, H.; Nilsson, I.; White, S. H.; von Heijne, G. Recognition of transmembrane helices by the endoplasmic reticulum translocon. *Nature* **2005**, *433* (7024), 377–81.
39. Horinek, D.; Serr, A.; Geisler, M.; Pirzer, T.; Slotta, U.; Lud, S. Q.; Garrido, J. A.; Scheibel, T.; Hugel, T.; Netz, R. R. Peptide adsorption on a hydrophobic surface results from an interplay of solvation, surface, and intrapeptide forces. *Proc. Natl. Acad. Sci. U.S.A.* **2008**, *105* (8), 2842–7.
40. Pirzer, T.; Geisler, M.; Scheibel, T.; Hugel, T. Single molecule force measurements delineate salt, pH and surface effects on biopolymer adhesion. *Phys. Biol.* **2009**, *6* (2), 25004.
41. Yancey, J. A.; Vellore, N. A.; Collier, G.; Stuart, S. J.; Latour, R. A. Development of molecular simulation methods to accurately represent protein-surface interactions: The effect of pressure and its determination for a system with constrained atoms. *Biointerphases* **2010**, *5* (3), 85–95.

42. Vanommeslaeghe, K.; Hatcher, E.; Acharya, C.; Kundu, S.; Zhong, S.; Shim, J.; Darian, E.; Guvench, O.; Lopes, P.; Vorobyov, I.; MacKerell, A. D. CHARMM General Force Field: A force field for drug-like molecules compatible with the CHARMM all-atom additive biological force fields. *J. Comput. Chem.* **2010**, *31* (4), 671–690.

43. Sugita, Y.; Okamoto, Y. Replica-exchange molecular dynamics method for protein folding. *Chem. Phys. Lett.* **1999**, *314*, 141–151.

44. Wang, F.; Stuart, S. J.; Latour, R. A. Calculation of adsorption free energy for solute-surface interactions using biased replica-exchange molecular dynamics. *Biointerphases* **2008**, *3*, 9–18.

45. Beutler, T. C.; Vangunsteren, W. F. Umbrella sampling along linear-combinations of generalized coordinates - Theory and application to a glycine dipeptide. *Chem. Phys. Lett.* **1995**, *237* (3-4), 308–316.

46. Mezei, M. Adaptive umbrella sampling - self-consistent determination of the non-Boltzmann bias. *J. Comput. Phys.* **1987**, *68* (1), 237–248.

47. Kumar, S.; Bouzida, D.; Swendsen, R. H.; Kollman, P. A.; Rosenberg, J. M. The weighted histogram analysis method for free-energy calculations of biomolecules. 1. The Method. *J. Comput. Chem.* **1992**, *13*, 1011–1021.

48. Overbeek, J. T. G. Recent developments in understanding of colloid stability. *J. Colloid Interface Sci.* **1977**, *58* (2), 408–422.

49. Darden, T.; York, D.; Pedersen, L. Particle mesh Ewald: an N-log(N) method for Ewald sums in large systems. *J. Chem. Phys.* **1993**, *98*, 10089–10092.

50. Li, X.; Stuart, S. J.; Latour, R. A. TIGER2: An improved algorithm for temperature intervals with global exchange of replicas. *J. Chem. Phys.* **2009**, *130*, 1–9 article 174106.

51. Li, X.; Latour, R. A. The TIGER2 empirical accelerated sampling method: Parameter sensitivity and extension to a complex molecular system. *J. Comput. Chem.* **2011**, *32*, 1091–1100.

52. Metropolis, N.; Rosenbluth, A. W.; Rosenbluth, M. N.; Teller, A. H.; Teller, E. Equation of state calculations by fast computing machines. *J. Chem. Phys.* **1953**, *21* (6), 1087–1092.

53. Go, N. Theoretical studies of protein folding. *Annu. Rev. Biophys. Bioeng.* **1983**, *12*, 183–210.

54. Karanicolas, J.; Brooks, C. L. I. Improved Go-like models demonstrate the robustness of protein folding mechanisms towards non-native interactions. *J. Mol. Biol.* **2003**, *334*, 309–325.

55. Fears, K. P.; Latour, R. A. Assessing the influence of adsorbed-state conformation on the bioactivity of adsorbed enzyme layers. *Langmuir* **2009**, *25* (24), 13926–13933.

56. Sivaraman, B.; Fears, K. P.; Latour, R. A. Investigation of the effects of surface chemistry and solution concentration on the conformation of adsorbed proteins using an improved circular dichroism method. *Langmuir* **2009**, *25*, 3050–3056.

57. Fears, K. P.; Sivaraman, B.; Powell, G. L.; Wu, Y.; Latour, R. A. Probing the conformation and orientation of adsorbed enzymes using side-chain modification. *Langmuir* **2009**, *25* (16), 9319–9327.

58. Kelly, S. M.; Jess, T. J.; Price, N. C. How to study proteins by circular dichroism. *Biochim. Biophys. Acta, Proteins Proteomics* **2005**, *1751* (2), 119–139.

59. McMillin, C. R.; Walton, A. G. A circular dichroism technique for the study of adsorbed protein structure. *J. Colloid Interface Sci.* **1974**, *48* (2), 345–349.

60. Hylton, D. M.; Shalaby, S. W.; Latour, R. A. Direct correlation between adsorption-induced changes in protein structure and platelet adhesion. *J. Biomed. Mater. Research, Part A* **2005**, *73A* (3), 349–358.

Chapter 10

Proteins and Peptides at Gold Surfaces: Insights from Atomistic Simulations

L. Bellucci, G. Brancolini, A. Calzolari, O. Carrillo Parramon, S. Corni,* and R. Di Felice*

**Centro S3 Istituto Nanoscienze - CNR, via Campi 213/A,
41125 Modena, Italy
*E-mails: stefano.corni@nano.cnr.it; rosa.difelice@nano.cnr.it**

Computer simulations at the atomistic level, jointly with experiments, can provide the microscopic picture behind protein-surface interactions. The complexity of the inherent phenomena, that span several time and length scales, call for a hierarchical strategy, from electronic structure approaches (limited in the accessible sizes and times) to classical methods, able to treat larger systems and longer time scales, but involving more assumptions and providing less details. Here we introduce the atomistic simulation methods that we have developed and applied to treat the interaction of peptides and proteins with the Au(111) surface in water. We succinctly describe principles, assumptions and limitations of *ab initio*, classical atomistic molecular dynamics and Brownian dynamics docking methods as applied to the protein-surface problem, with specific focus on the work of our group. The possible extension to coarse-grained method is also discussed.

Introduction

There is a wide consensus in considering the interaction between proteins and inorganic surfaces as the key to understand the biological response to inorganic materials. In fact, any inorganic materials that come into contact with a biosystem (being an extended surface or a nanoparticle) is readily covered with the proteins expressed by the biosystem. The subsequent biological fate of the inorganic materials (e.g., being recognized as an extraneous body or activate specific

In Proteins at Interfaces III State of the Art 2012; Horbett, T., et al.;
ACS Symposium Series; American Chemical Society: Washington, DC, 2012.

biological pathways) is determined by which proteins adsorb on the surface, their orientation, their possible conformational changes and the associated disclosure of cryptic epitopes (*1–4*). This has been verified in biological and biomedical applications such as cell-adhesion and proliferation on artificial scaffolds, study of the biocompatibility of surgical implants, prevention of bacteria adhesion to surface. Moreover, understanding adsorption processes of bio-molecules to the inorganic surfaces constitute the first step to rationalize the behavior of the new generation of nanoscale-based systems, which are of great importance in many emerging disciplines spanning from nanotechnology to nanomedicine (*5–9*).

The importance of unraveling the microscopic determinants of protein-surface interaction is thus clear, but this task is still a challenge. From an experimental point of view, in fact, interrogating the interface requires to get rid of the preponderant signal from the bulk. Moreover, proteins are intrinsically complicate systems, and measurements are often challenging already in bulk solution, even more so at interfaces. While various experimental methods have been used to explore protein-surface interfaces (*10–14*) these are by no means routine experiments (*15*, *16*). In this context, computational simulations can provide an important contribution to the understanding of protein surface interaction.

In particular, simulations that take into account the chemical nature of the system, possibly at the atomistic level of detail, can provide the most intimate level of knowledge. Unfortunately, simulations of protein-surface interactions are also very challenging. Firstly, protein-surface systems are large from an atomistic point of view, as they easily comprise (including solvent water molecules) tens or hundreds of thousands of atoms. In addition, biomolecular adsorption on solid surfaces is a complex process that involves many dynamical steps, from the initial recognition of the molecule by the surface to the equilibrium conformational rearrangement of the adsorbed molecule. Therefore, to analyze the adsorption phenomenon, it is necessary to investigate the dynamical behavior of the system, that, in many cases is hard to be directly sorted out (*16*, *17*). The rationalization of such aspects represents one of the major challenges for both experimental and theoretical investigation methodologies .

Finally, computational approaches that have been developed during the years to treat proteins and to treat inorganic surfaces separately are not always straightforward to integrate, since the underlying approximations may be different; often these approaches are implemented in different codes.

In the last few years, together with our coworkers, we have developed and applied various levels of computational description for investigating protein-surface interactions. In particular, we have identified the surface(s) of gold as an important system, and our activity has been mainly focused on this material. In fact, gold is important in practical applications (it enables optical and electrochemical detection (*18*), has been used in nanobioelectronics (*19*, *20*), and is relevant for plasmonics (*21*). Gold easily exposes a clean and relatively defectiveless surface in the experiments, which limits the uncertainties in the comparison with theoretical, defect-free, models. Moreover, adsorption of simple molecules on Au in controlled conditions (e.g. ultra-high vacuum) has been studied extensively (*22–24*). While these studies do not have an immediate relevance for protein-surface interaction (where the role of the aqueous solution cannot be neglected), they are important as an intermediate step to compare with calculations.

Our development has followed a sequential multiscale strategy (*25*, *26*), improved by including information from experiments whenever possible. *Multiscale* refers to the use of different levels of computational description, apt to the investigation of the system properties at different length and time scales. *Sequential* indicates that the different levels of computational description are not applied to different portions of the system within a given calculation (as in a *parallel* or *concurrent* multiscale approach), but that they are applied one after the other to the entire system (e.g., the output of one calculation is the starting point of another at a different level).

For example, *ab initio* simulations provide a picture of the system detailed up to the electronic structure, but they are currently limited to few hundreds or mostly thousand of atoms, and to phenomena taking place in the hundreds of ps domain (*27*). Classical atomistic molecular dynamics (MD), in the bio-oriented flavor encoded in force fields such as AMBER (*28*), CHARMM (*29*) and OPLS (*30*) and software packages such as GROMACS (*31*) and NAMD (*32*), are neglecting electronic structure details as well as a faithful description of the fastest vibrational motions in the systems, but can explore hundreds of thousands of atoms over a time span up to the μs (ms with specialized supercomputers (*33*)). Clearly, each technique can address only a subset of the open issues on protein-surface interactions; therefore, building a comprehensive microscopic picture of protein-surface interaction requires more than a single technique.

Our group has tackled the problem of investigating protein-gold interactions using (i) first-principle simulations at the density functional theory (DFT) level (*34–37*), (ii) classical atomistic MD with a force field derived by DFT calculations and experimental data (GolP) (*38*), (iii) Brownian dynamics (BD) simulations of the protein-surface docking, guided by an implicit water force field (ProMetCS) developed from GolP (*39*). In this chapter we introduce all these techniques, focusing on the specific flavors used by us. Moreover, we discuss some selected examples of the applications of these techniques to show their potentialities and the current limitations. Finally, we also dedicate the last section to discuss coarse-grained models for proteins (*40*). In such models the atomistic structural and/or dynamical details are partially lost (several atoms are grouped in single interaction sites, some motions are projected out) in favor of faster simulations (routinely μs) of larger systems (e.g., entire virus capsides). In perspective, the extension of these simplified methods to protein-gold systems may help unraveling large protein rearrangements (or even unfolding) of proteins interacting with surfaces.

Ab Initio Studies

The power of *ab initio* computational methods lies in their high theoretical level and their practical accuracy in reproducing and interpreting experimental data, without the inclusion of *ad-hoc* empirical parameters. *Ab initio* methods allow access to the electronic structure of the system, which is ultimately responsible for the interaction mechanisms of matter in any phase. (e.g.

polarization effects, bond formation/breaking, screening, etc). All the *ab initio* results we present in the following are based on density functional theory (DFT), which provides the ground-state energy of an interacting system of electrons in an external potential in terms of a functional of the ground-state electronic density. This kind of calculations have the significant advantage of being able to predict in an unbiased manner the electronic structure, the equilibrium geometry and the time evolution of complex systems that are *a priori* unknown, but the disadvantage of requiring large computational efforts. The current trend away from wavefunction-based methods toward the use of DFT is justified by the profitable compromise for the latter between the resulting accuracy and the scale of the systems that can be tackled. It is to be remarked that the most commonly used DFT approaches (i.e., those based on Generalized Gradient Approximation, GGA, exchange-correlation functionals such as PBE and PW91 mentioned below) do not catch the effects of dispersion interactions, which is dominant for most of the amino acids on gold (*38*). Recently, various approaches have been proposed to overcome this limitation (we refer to a recent review addressing specifically dispersion for molecules on surfaces (*41*)).

In the context of protein/inorganic interfaces, the huge size of the system prevents the application of *ab initio* approaches to the whole target system. Yet, they are doable and they have an important role to understand protein/surface interactions in model systems: (i) Structural and electronic DFT (*42*) ground state characterizations of entire or partial amino acids adsorbed at inorganic substrates, which unravel a degree of adsorbate/substrate coupling beyond the level of pure physisorption and are a basis for the development of classical force fields (*34–37*, *43*); (ii) Car-Parrinello (CP) molecular dynamics (MD) simulations (*44*), which reveal electronic coupling also for a peptide on Au(111) in water (*37*). CP is one of the most popular examples of *ab initio* molecular dynamics (AIMD). CP implements - in a unified Lagrangian framework - the classical Newton's dynamics of the nuclei under the effect of the forces due to the corresponding electronic structure, evaluated *ab initio* at the DFT level. Thus, CP conjugates the statistical time evolution, typical of molecular dynamics, with the description of the electronic structure of the interface, typical of the *ab initio* techniques.

Cysteine/Au(111) by DFT

Cysteine is an example of molecules with a reactive group that functions as anchor for attaching to metal surfaces. It has, in fact, a thiol functionality and behaves similarly to methanethiols on gold (*34*, *35*, *45*). The adsorption of cysteine on Au(111) involves S(thiolate)-Au bonds, with the S headgroups sitting preferentially at bridge sites. DFT-PW91 calculations were carried out for both atomic optimization and single-point electronic structure calculations (hydration effects were not investigated): details of the methodology are reported in the original works (*34*, *35*). The computed dissociative adsorption energy gain of ~20 kcal/mol indicates the formation of a covalent bond, which is reinforced by the analysis of the electronic structure. The investigation of the electronic density of states (DOS) for the most stable adsorption configuration shows peaks due to the hybridization between the S *p* orbitals and the Au *d* band: in particular, a bonding peak is located at 5 eV below the Fermi level and an antibonding peak is located at 1 eV below the Fermi level. Figure 1 illustrates the DOS and representative bonding and antibonding orbitals formed by the cysteine highest occupied molecular orbital (HOMO) with the Au *d* orbitals. It was also shown that the amino functional group of cysteine can participate in the molecule/surface bonding, by increasing the interaction energy and forming other hybrid orbitals (*34*, *35*). The adsorption mechanism of cysteine on Au(111) complies with the Newns-Anderson model of atomic and molecular chemisorption (*46*): this essentially states that interaction of a localized orbital on the adsorbate with the narrow *d* band of the metal produces hybrid orbitals of both bonding and antibonding type, below and above the edges of the metal *d* band.

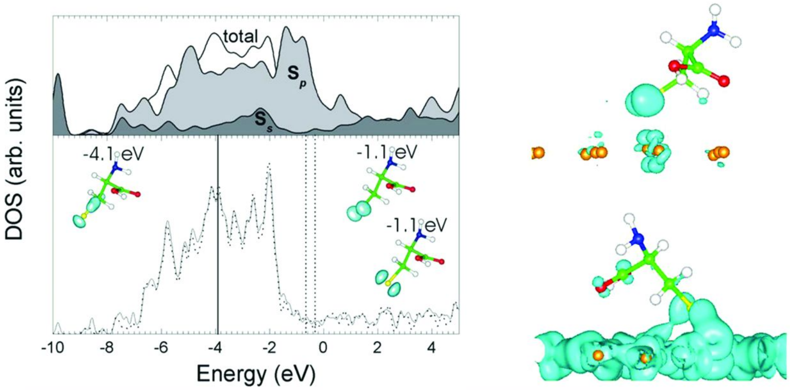

Figure 1. Left bottom: Density of states (DOS) of the cysteine/Au(111) system (solid line) and of the clean unreconstructed Au(111) surface (dotted line). The solid (dotted) vertical lines identify the energy positions of the selected hybrid bonding (antibonding) S-Au orbitals on the right side. The Fermi level has been set as the origin of the energy scale. The insets show charge density plots of the S-localized orbitals of the isolated cysteine radical and the corresponding energy levels are indicated (on the same energy scale used for the DOS). Left top: s and p S-projected DOS of cysteine adsorbed in the thiolate geometry on Au(111) with the S at the bridge lattice site (gray areas) and total DOS of the interface. Right: bonding (bottom) and antibonding (top) representative orbitals formed by the cysteine HOMO with the Au d bands. Adapted from ref. (35) with permission. Copyright 2003 American Chemical Society.

Histidine/Au(111) and GolP by DFT

Within the working hypothesis that the interaction of proteins with inorganic surfaces occurs mainly through the amino acid side chains, the investigation of the coupling of the histidine side chain with a gold surface may yield significant insights on the interaction mechanisms in more complex situations. This system is inherently different from the case of cysteine: in fact, imidazole does not have an obvious functional group that protrudes from the molecule but the reactive N atoms are part of the hetero-ring (we can broadly speak of an aromatic as opposed to alkylic adsorbate). DFT-PBE calculations (excluding hydration effects) reveal that, irrespectively of the initial condition for atomic relaxation (molecular orientation and registry with the substrate lattice), the optimal adsorption geometry is with the imidazole plane almost perpendicular to the surface plane and the unprotonated N1 atom on top of a Au atom of the (111) lattice (Figure 2) (*36*).

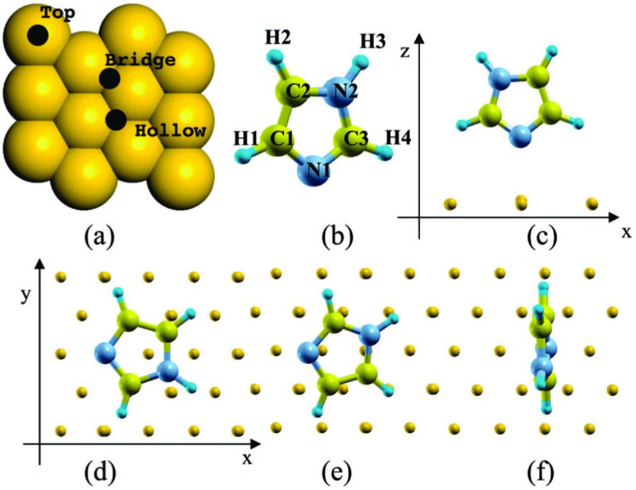

Figure 2. (a) Top view of the Au surface top (111) plane with highlights of the three typical low-energy adsorption sites in the hexagonal lattice. (b) Structure of imidazole with atomic labeling. (c) Side view of the most energetically favorable optimized geometry (d) Top view of a starting configuration in which the N1 atom is located above a top Au site (N1 is one-fold coordinated with Au) and the imidazole plane lays parallel to the (111) substrate planes. (e-f) Top views of other starting configurations that were taken into account, with also N2 towards the surface. Adapted from ref. (36) with permission. Copyright 2008 Americal Chemical Society.

The adsorption energy gain of ~10 kcal/mol is half of that for cysteine on Au(111). This value is definitely larger than the typical values for physisorption of the order of a few kcal/mol (*47*), yet smaller than those indicative of strong chemical bonds (such as those formed by thiols with gold). Despite the fact that imidazole does not have an obvious functional group for anchoring to surfaces and correspondingly adsorbs less strongly than thiols on Au(111), actually the N1 lone pair behaves as such. Consequently, the Newns-Anderson adsorption picture is found also in this case: examples of bonding and antibonding orbitals are illustrated in Figure 3. A thorough inspection of the hybrid orbitals, presented in the original work (*36*), shows the formations of both π and σ N1-Au "bonds".

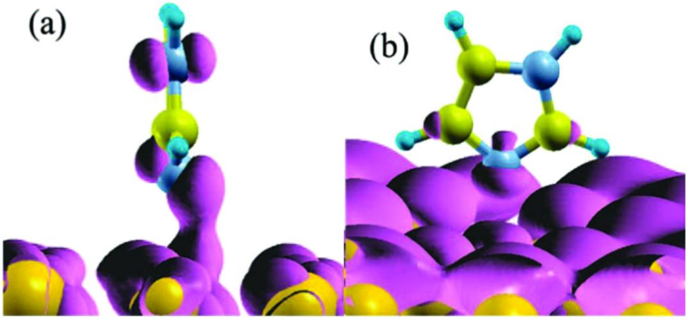

Figure 3. Isosurfaces plots of relevant hybrid orbitals formed at the imidazole/Au(111) interface. (a) Bonding orbital with π-like shape with energy 5.18 eV below the Fermi level. (b) Antibonding orbital with σ-like shape with energy 0.75 eV above the Fermi level. Adapted from ref. (36) with permission. Copyright 2008 American Chemical Society.

Similar DFT calculations were performed for several amino acid side chains on Au(111) *in vacuo* and the results were used to parameterize novel interaction terms for the classical force fields to simulate protein interaction with the Au(111) surface. The OPLS force field was originally chosen (*38*), but the procedure is also compatible with other force fields such as AMBER and GROMACS. The OPLS GolP force field was employed to simulate β-sheet folds on Au(111) (*48*).

Polyserine/Au(111) by Car-Parrinello MD

To our knowledge, only one *ab initio* MD simulation of a whole peptide on an inorganic surface (including liquid water, Figure 4) has been reported so far (*37*), which was feasible thanks to a huge international supercomputing effort, namely the DEISA consortium (www.deisa.eu). The results of the simulation indicate that weak chemical interactions of dative-bond character confer to a prototype secondary structure (an antiparallel β-sheet made of hydroxyl amino acids) and its hydration layer the capability of discriminating among gold surface sites in a cooperative manner.

The first-principle character of the simulation allows direct access to the electronic structure of the system (composed of approx. 600 atoms) at every instant along the trajectory of 20 ps. Although no covalent bond between the β-sheet (or water) and the surface is detected, a weak but not negligible electronic interaction exists, beyond the simple physisorption picture. This weak-interaction regime can be described as an incipient oxygen-to-gold dative bond, and it is not related to nonbonding interactions (e.g., van der Waals forces). Figure 4(b-d) shows the distribution of Löwdin net atomic charges during the simulation for the gold atoms, as well as for the oxygen atoms of water (O_{wat}) and of Ser side chains (O_{ser}). The Löwdin population analysis reveals a small, but evident, electron donation from the Ser hydroxyl groups and water molecules to the gold surface. Gold atoms of the inner zone (Figure 4b) maintain an average neutral behavior (i.e., $q \sim 0e$-), whereas those of the two external layers present a net electron accumulation. The opposite is true for water molecules close to the surface (Figure 4c) and for the O_{ser} belonging to interface **1** (Figure 4d), which roughly donate an average charge amount of ~0.05*e*- per oxygen atom. Water molecules that are distant >3-4 Å from the surface and the O_{ser} of the interface **2** are instead hardly affected by the presence of the metal. Concisely, a weak surface/side-chain interaction is active, but no strong chemisorption exists for the polyserine on Au(111). This notable interaction is due to the collective action of many adsorption sites: although each of them contributes quite weakly, the concerted process makes adhesion effective.

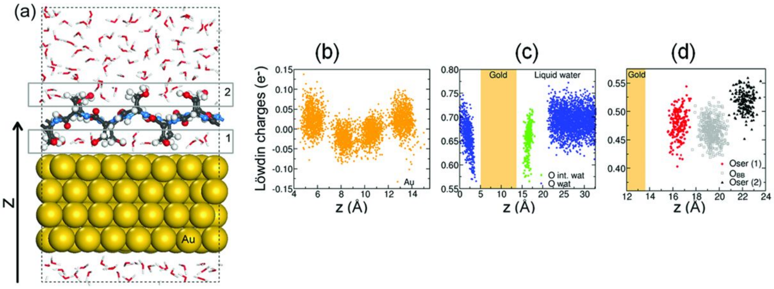

*Figure 4. (a) Side view of the system in the simulated unit cell (dashed line), with definition of interfaces **1** and **2**. (b-d) Distribution of the atomic Löwdin charges over the entire simulation span for: the 4 Au layers in panel (b); interstitial (green) and liquid (blue) water oxygens in panel (c); the oxygens of Ser side chains (O_{ser}) at interface **1** (red dots) and **2** (black triangles) and the backbone oxygens (O_{BB}, gray). Adapted from ref. (37) with permission. Copyright 2010 American Chemical Society.*

By an analysis of correlation maps (*37*), it is also shown that the hydration layer plays an active role in surface-site discrimination by the peptide, via its own adsorption site preferences. This evidence supports the concept of the hydrated protein as a single entity, where both the protein and the hydration layer contribute to the recognition process, competing with the rest of the solvent for the gold surface. Similar recognition water capability has been further detected in H_2O/Au interface at room temperature (*49*).

Ab initio molecular dynamics simulations are powerful tools to investigate the structure and interaction mechanisms of small peptides on metal surfaces. However, they are not doable in any desirable case. The feasibility conditions are: (i) the preparation of a model system of contained size, which plays a role in larger realistic systems (such as serine side chains in gold-binding peptides); (ii) the availability of huge supercomputing resources. The backdrop is the short simulation length, in the range of tens of picoseconds, during which complex plastic motions are not accessible. The advantage is that, for all the motions that are indeed accessible, one gets automatically the electronic structure of the system, which is the basic ingredient that allows for a deep insight into the mechanisms for coupling, recognition and selectivity.

Classical Atomistic MD

On a general ground, MD simulations (*50–52*) propagate an initial molecular conformation forward in time, providing a detailed information on the atomic motions of the system. Therefore, MD is the "natural" tool of choice to study the dynamical evolution of the adsorption processes. Hence, it is not surprising that most of the atomistic simulations of protein-surface interactions are currently performed at this level.

The heart of MD simulation method is the availability of a suitable potential-energy function to solve the equation of motion for the nuclei. In the already introduced *ab-initio* CP method (*44*, *51*), the energy function is obtained resolving the electronic structure of the molecular system "on the fly" during the simulation. As noted above, the CP method requires considerable computational resources (because of the cost of propagating DFT quantities at each step) that limit the possible system size and the time length of the simulation. The description of the time evolution of the nuclei of the system (i.e. nuclear motion) is penalized by the necessity to integrate the equation of motion of the fast fluctuations of the electronic degrees of freedom (adiabatic condition). The latter requires the use of time steps smaller than those needed to integrate the motion of the nuclei alone, thus limiting the exploration of the phase space at the atomic scale. The drawback of this approach is, therefore, the huge computational load and, consequently, the short accessible simulation times that do not currently allow the description of processes of a large-atomic-scale object that occur on long time scales as the adsorption processes or conformational rearrangements of biomolecules at metal surface in solution.

On the contrary, classical MD relies on the possibility to parameterize predefined potential energy-functions for either the intramolecular and intermolecular interactions of the system by using empirical/experimental data and/or independent electronic structure calculations. In this way, the explicit description of the electronic structure is abandoned, the system is modeled fully at the classical level and the time evolution of the system is obtained by numerically integrating the Newton's equations of motion at the atomic time scale. The classical MD simulation method introduces further approximations with respect to *ab initio* MD. However, since it requires less computational resources and operates at the atomic time scale, it can be efficiently used to investigate dynamical atomistic conformational processes that occur in the time regime of hundred of nanoseconds/ a few microseconds (*53*) or even, with special programs and dedicated machines, in the regime of milliseconds (*33*).

Classical MD simulations have been widely adopted in the study of biological systems (*54*, *55*), however, its applicability is subordinated to the availability of a suitable potential-energy function and the related parameters. The potential-energy functions and the parameter set define the so called classical force fields (FFs): AMBER (*28*), CHARMM (*29*) and OPLS (*30*) are, for example, biomolecular FFs routinely used to perform MD simulations by using specific bio-oriented MD codes such as GROMACS (*31*) and NAMD (*32*). The functional form of these biomolecular FFs is essentially the same and consist of several discrete terms that describe the different interactions (the so called "bonding" and "non-bonding" interactions) among the atoms of the system: harmonic terms are used to describe atom bond lengths and angles, Fourier series terms are used to describe torsions, whereas Lennard-Jones and Coulomb functions are used to describe intermolecular interactions (*52*). The set of parameters are typically determined by quantum chemical calculations possibly corrected to reproduce desired experimental data. The mentioned biomolecular FFs share very similar potential-energy functions, however, the protocols used in the FF parameterization differ from each other and, therefore, the parameters are not interchangeable among different FFs.

Although the FFs to describe protein in water have been developed for a long time and are still being improved, FFs purposely designed to treat biomolecules-surfaces interaction are still elusive (*56*, *57*). For protein-gold interfaces a new FF was produced and described by our group (*38*). It is an extension of the OPLS/AA FF where specific parameters to describe the interaction of biomolecules with the Au(111) surface are added. This classical gold-protein FF, termed GolP, is based on an atomistic (although rigid) description of the gold substrate. It is defined with the same potential-energy functions of the OPLS FF, therefore it is compatible with bio-oriented MD codes mentioned above. Last but not least, it includes gold polarization effects (image charges induced by the adsorbed charge density (*58*)). The FF parameters are based on a careful mixing of quantum mechanical calculations (DFT and MP2 level of theory) and experimental data of adsorption energies of various organic molecules from the gas phase to Au(111) (see the original paper for details (*38*)).

GolP FF has been applied to determine the adsorption free energy of amino acids on the gold surface (*59*, *60*). Using MD simulations and thermodynamic integration techniques (*61*, *62*) Hoefling *et al* (*63*) computed the potential of mean force for all proteogenic amino acids as a function of the distance between the center of mass of each amino acid and the gold layer. From the adsorption free energy profile the authors were able to describe the adsorption of the amino acids with the gold surface has a triphasic behavior. In an initial diffusive phase, the potential of the gold is hardly influencing the amino acid. At a distance of 5 Å from the bound state, the slope of the energy potential increases significantly, and the amino acid associates with the gold. In the final binding phase, the potential becomes even steeper. They observed that the adsorption free energies of the amino acids are dependent on their chemical character, and they determined an order of affinity based on the nature of the amino acids. In particular, aromatic amino acids have the highest affinity followed, in the order, by sulfur-containing, positive, polar and, sharing the lowest affinity aliphatic and negative amino acids. An important finding of this computational study was a correlation of the β-sheet propensity of amino acids with the adsorption to gold, highlighting the tendency of the gold surface to induce amino acid internal conformations suitable for β-sheet formation.

In a more recent work, Hoefling *et al* (*48*) studied the interaction between the gold surface and polypeptides with β-sheet folding by using standard MD simulation and GolP FF. The authors observed that the substrate adsorption occurred quickly, but the adsorption of the substrate to the gold surface is not specific. Furthermore, extending the length of the simulation to 100 ns, no desorption or major rearrangements of the protein have been observed, once the substrate adsorption occurred. The mentioned studies answered some important basic questions about the protein/gold interaction; however, increasing the biomolecule complexity, other issues related to the sampling of large-scale conformational changes appear. To exemplify these kinds of phenomena a preliminary MD simulation was performed on a complex system composed by the Amyloid β (Aβ) peptide (*63*) (PDB code 1IYT), gold surface and water (see Figure 5). Aβ is the building block of the amyloid plaques characteristic of Alzheimer's disease. The system was modeled with GolP FF in explicit SPC water using periodic boundary condition (*50*, *64*). The simulation was performed at constant temperature (300 K) with the GROMACS software package. In Figure 5 three sets of initial conformations of the hybrid system are reported. Gold surface spans the XY plane of a rectangular box of size 90×90×75 Å. The first system (S1) is depicted in the top left of Figure 5. It was obtained by positioning the center of mass of the Aβ peptide at center of the rectangular box, and aligning the molecule so that the major principal axes of inertia corresponds to the X axis. The second and the third systems (S2 and S3) were obtained by consecutive rotation of the S1 structure around the X axis, and are depicted respectively in the top center, and in the top right of Figure 5. In all the systems the protein heavy atoms were initially held at a distance greater than 16 Å from gold surface, ensuring that the protein was not interacting with the surface at the beginning of the simulations. Following the scheme shown in Figure 5, the system S1 and S2 system were used as starting point of a MD simulation each, whereas the S3 system was used as the starting point for two independent simulations. In the bottom of Figure 5 are shown the final conformations (i.e. E1, E2, E3_A and E3_B) for all the systems after 16 ns of classical MD simulation.

From the analysis of the MD trajectories, we observed that Aβ quickly approached the gold surface in the first few nanoseconds of the MD simulations. In all cases the adsorbed peptides remained trapped to the gold surface and during the rest of the simulation, large conformational rearrangements of the peptide were not observed. Comparing the final structures reported in the bottom of Figure 5, it was not possible to identify a preferential "binding mode" or "adsorption mode" of the (Aβ) peptide to the gold surface. In particular, the large difference between the conformation E3_A and E3_B shows that the adsorption conformation is not merely determined by the starting conformation. The description of the adsorption process, however, is restricted to the observation of an unique adsorption event for each simulation. Moreover, the adsorption process is unspecific and it depends on how the substrate (randomly) approaches the surface. The observation of these few events are not enough to describe the complex dynamical behavior of the peptide on gold, and enhanced sampling techniques are necessary to explore the possible adsorption modes and conformations of the biomolecules at the gold/water interface.

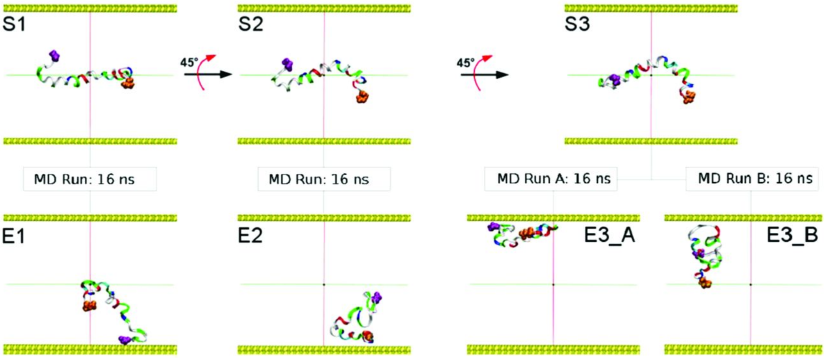

Figure 5. The Aβ peptide is shown in cartoon representation. C-terminus and N-terminus are depicted in purple and orange respectively. The other residues are encoded by color: red for negative residues, blue for the positive residues, green for the polar residues, and white for the hydrophobic residues. Gold slab is in yellow. Water molecules, which fill the whole box of simulation, are not shown. In the top, the initial structures used as starting point for the MD simulations are shown (i.e S1, S2 and S3). In the bottom, we depict the final structures from the MD simulations (i.e. E1, E2, E3_A and E3B).

Among the various methods used to enhance the sampling of MD simulations (*52*), we mention the temperature-replica exchange MD (*65*) (T-REMD), the temperature intervals with global exchange of replicas (TIGER & TIGER2) (*66*) and non-Markovian metadynamics (*67*), which have been applied to protein-surface systems. Ensuring an adequate sampling of the conformation of the adsorbed substrate, these techniques begin to be widely used in the study of the heterogeneous systems, where the interactions differ in type and in the intensity and the sampling can be particularly difficult (*54*, *55*). In the very recent work of Schneider and Colombi Ciacchi (*68*), for example, the adhesion force between a small peptide and oxide surfaces has been studied by using metadynamics and steered molecular dynamics (*69*) techniques.

With the aid of these advanced techniques to improve the sampling, the Classical MD simulations provide one of the most powerful methods of investigation for the study of the adsorption process and biomolecules/inorganic interface in solution, which however require large amounts of high performance computing (HPC) resources. A major challenge remains the extension and the parameterization of the new force fields designed to describe the protein/inorganic-surface interactions.

Rigid-Body Docking: Predicting Protein-Surface Encounter Complexes

Brownian Dynamics (BD) and Langevin Dynamics (LD) computational methods are usually employed for the study of the motion and the interactions of biological macromolecules in solvent. These methods offer the possibility of accessing phenomena whose time- and length-scale is much greater than that normally achievable in atomistic MD simulations.

BD strategies are based on physical approximations to reduce the complexity of the system simulated. In rigid-body docking the macromolecules are treated as rigid bodies, neglecting their internal degrees of freedom which are not always fundamental for the description of the processes under investigation. This approximation which greatly reduces the complexity, allow the atomic details of the macromolecules to be conserved. A range of methodological developments have been implemented in a number of software packages. Atomically detailed rigid-body BD simulations have been implemented for example in UHBD (*70*), SDA (*71*) and Macrodox (*72*), which are routinely used to evaluate electrostatic properties of biomolecular systems as well as to perform Brownian Dynamics simulations for a wide range of length scales enabling the investigation of molecules with tens to millions of atoms.

In order to describe the diffusion and association of proteins to metal surfaces, a BD methodology developed for the computation of protein-protein encounter complexes (*73*) has been recently adapted to the protein-surface problem and implemented in SDA6.00 (*74*). In protein-surface docking with SDA, the protein is modeled as a particle diffusing in a solvent that is treated as a continuum exercising frictional and random, stochastic forces on the protein; while the metal surface is described as a large multi-layers cluster placed in the XY-plane (Figure 6).

For the description of the protein-surface association processes with BD methods, the implicit solvent model must be designed specifically for the surface considered. It has been shown that existing implicit solvent models can be successfully used for hydrophobic surfaces, where there is no water between the surface and the protein (*75*, *76*). On the contrary, some MD simulations with explicit water have shown that for strong polar surfaces, protein binding is not occurring to the surface but rather to a structured water layer (*77*, *78*). Even when the protein binds directly to the surface, the structuring of water close to hydrophilic surface modifies water properties w.r.t the bulk, and standard continuum model cannot be applied (*79*).

To properly describe the adsorption of proteins to metal surfaces with a continuum solvent in BD, specific properties of the hydration shell on metal surfaces should be accounted for by including additional, semi-empirically parameterized terms in the protein-surface forces (*17*, *39*).

In protein-surface docking with BD, the starting position and orientation of the protein is generated randomly at a given distance from the surface, which defines the limit where the protein-surface interaction energy becomes negligible. At each BD step a protein-surface interaction energy and the force acting on the protein are computed using the implicit-solvent ProMetCS force field, developed and parameterized for protein-gold surface interaction (*39*). The ProMetCS energy includes the following terms: (i) a sum of pair-wise interatomic Lennard-Jones terms that describes van der Waals and weak chemical interactions between the biomolecule and the gold surface (based on the fully atomistic force field GolP, see above (*38*)); (ii) the electrostatic interaction free energy in the water environment, which includes an “image-charge” interaction energy of the protein effective charges with a flat infinite, overall uncharged, metal surface along with the direct Coulomb interaction of protein effective charges with the charges placed at each Au atom, mimicking a gold surface non-zero potential. Electrostatic energy also includes a desolvation correction term (*80*, *81*) which takes into account the change of the electrostatic interaction energy due to polarization and distortion of the hydration shell at small protein – Au surface distance; (iii) a protein hydrophobic desolvation and (iv) a surface desolvation free energy term arising from the partial replacement of the metal hydration shell by the protein.

Millions of putative protein-docking complexes can be generated in a few hours on a commodity cluster by this BD. The low-energy protein-surface complexes resulting from the docking must therefore be clustered according to their conformational similarity to reduce this overwhelming number of structures. Data-mining techniques, like clustering of structures by similarity, are efficient tools to sort out representative information from either most stable or populated docking poses (*82*). Various applications of this method are presently on-going in our group. As an example, we report in Figure 6 one of the structure obtained by docking ubiquitine, a small protein, on Au(111) (*83*). This system has been chosen since there are experimental NMR data that identify the ubiquitine patch interacting with Au nanoparticles (*13*), making a comparison with docking results possible.

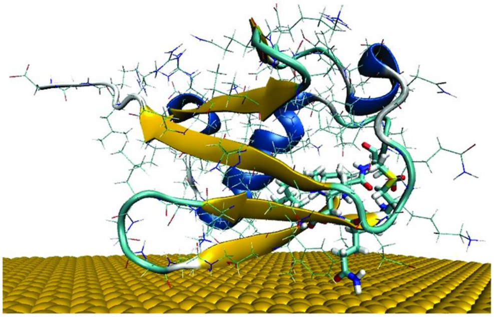

Figure 6. Example of a protein-surface association complex obtained by BD rigid docking. The protein is ubiquitin, docked on a neutral Au(111) surface in water.

Finally, we remark that rigid body docking, when used alone, is useful only if the protein conformation is not drastically altered by adsorption. Alternatively, it can be combined with classical MD simulations, which are in principle able to describe conformational changes: rigid body docking provides initial structures for the protein-surface encounter complex, then MD simulations can be started to investigate conformational rearrangements due to the interaction with the surface. In practice, the time-scales accessible to MD are currently too short, in general, to study extensive changes of secondary and tertiary structural elements, such as partial or complete unfolding. Expensive enhanced sampling techniques could be used in selected cases to investigate the problem. Alternatively, models describing the protein to a coarser level than atomistic MD may reach the required time scales. These models are introduced in the next section.

Extending Coarse-Grained Protein Models to Protein-Surface Systems

When we simplify the structure of a protein by considering only those atoms or sets of atoms that are supposed to be fundamental in the behavior of the system, we say that we are dealing with a coarse-grained model. Different coarse-grained models of proteins could be set depending on the properties and the phenomena under study (*40*). Figure 7 shows different examples and their applications.

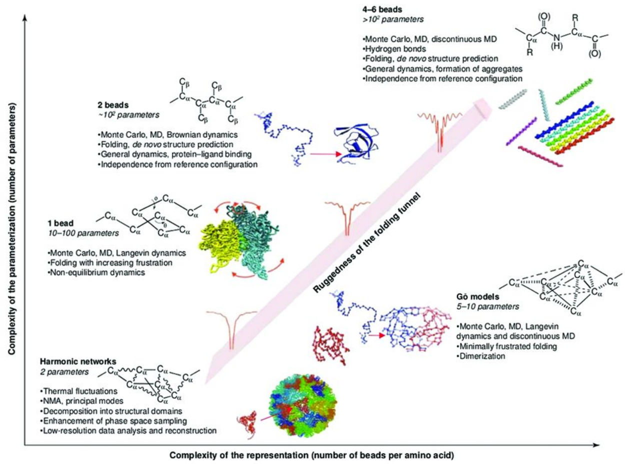
4–6 beads
>10² parameters
•Monte Carlo, MD, discontinuous MD
•Hydrogen bonds
•Folding, de novo structure prediction
•General dynamics, formation of aggregates
•Independence from reference configuration
2 beads
~10² parameters
•Monte Carlo, MD, Brownian dynamics
•Folding, de novo structure prediction
•General dynamics, protein–ligand binding
•Independence from reference configuration
1 bead
10–100 parameters
•Monte Carlo, MD, Langevin dynamics
•Folding with increasing frustration
•Non-equilibrium dynamics
Ruggedness of the folding funnel
Gō models
5–10 parameters
•Monte Carlo, MD, Langevin dynamics and discontinuous MD
•Minimally frustrated folding
•Dimerization
Harmonic networks
2 parameters
•Thermal fluctuations
•NMA, principal modes
•Decomposition into structural domains
•Enhancement of phase space sampling
•Low-resolution data analysis and reconstruction
Complexity of the parameterization (number of parameters)
Complexity of the representation (number of beads per amino acid)

Figure 7. Different coarse-grained models, with a description of the cases in which they are normally used depending on the level of accuracy needed and on the complexity of the problem under study. This is illustrated in a two axes graph indicating the complexity of the representation (that is the number of beads per aminoacid) and the complexity of the parametrization (number of parameters used to analize the problem). Reprinted with permission from ref. (40). Copyright 2005 Elsevier.

The reduced number of atoms is not the only feature of a coarse-grained model: in addition to the simplification of the structure the corresponding potentials and nonbonded interactions have to be modified accordingly. This can be seen as follows: suppose that the atomistic structure of the protein can be described by a set of N variables $\{Q_1,...,Q_N\}$ and their momenta. These variables can be for example the usual Cartesian coordinates or, more likely, proper internal coordinates (e.g., bond lengths, angles and dihedrals). Coarse graining a protein means to reduce this set of variables to a smaller one, $\{Q_1,...,Q_R\}$ with $R < N$. The basic function from which we can get a proper theoretical description of the physical system is the probability density of finding the system in a given state, $P\{Q_1,...,Q_N\}$. In our coarse-grained model, we have a new probability density which comes from integrating out $N - R$ variables. In terms of the potential energy of the protein $V\{Q_1,...,Q_N\}$ and after integrating out momenta, the new probability density reads

$$P(Q_1,\ldots,Q_R) = N \int dQ_{R+1} \ldots dQ_N \exp(-\beta V) \quad (1)$$

Therefore, if we reduce the number of degrees of freedom of a protein, we have to use a new potential energy $V_{CG}(Q_1,....Q_R)$ that reproduces the probability density in eq. 1. How to find this new potential energy is not an easy task, and some assumptions and approximations have to be considered. Some authors use the so-called Boltzmann Inversion method (BI (*84*)), where the potential energy is written as:

$$V(Q_1,\ldots,Q_N) = \sum_{i=1}^{N} V_i(Q_i) \quad (2)$$

This is a strong assumption but it generally leads to coherent results. The probability density $P_i(Q_i)$ of each reduced variable Q_i becomes independent from the others and it is straightforward to show that

$$V_i(Q_i) = -k_B T \ln P_i(Q_i) \quad (3)$$

The probability $P_i(Q_i)$ can be extracted from a standard atomistic MD, which makes the use of this potential for coarse-grained simulations possible.

Alternative approaches can be used in order to find a theoretical potential for the coarse grained model. If the model consists only of the Cα, one of them is the so-called Kovacs potential (*85*). It is a harmonic potential between each pairs of Cα and reads

$$V(r_{ij}) = K(r_{ij})(r_{ij} - r_{ij}^0)^2 \quad (4)$$

with

$$K(r_{ij}) = a\left(\frac{d}{r_{ij}}\right)^6 \quad (5)$$

The general form eq. 4 is often used to retain the topology of the protein unchanged. $K(r_{ij})$ is called Kirchhoff function and has to do with the type of interaction between the atoms. r_{ij} is the distance between Cα atoms (or *beads*) i and j and r_{ij}^0 is the initial equilibrium position of the bead pair. The distance dependence of the Kirchhoff function in eq. 5 comes from the study of the mean forces that Cα atoms feel in atomistic molecular dynamics. The fitted values a and d are respectively 40 kcal mol^{-1}Å^{-2} and 3.8 Å. This potential leads to good coarse-grained dynamics, which accurately conserves the main dynamical properties of the protein (*86*).

Another approach is to build a potential from the principal component analysis (PCA) of a fully atomistic MD. This is done with the set of eigenvectors and eigenvalues $\{\vec{e}_i, \lambda_i\}$ found with essential dynamics (*87*) as:

$$V(\vec{r}) = \frac{1}{2}\sum_{i=1}^{M} \frac{k_B T}{\lambda_i}\left(\Delta\vec{r}\cdot\vec{e}_i\right)^2 \qquad (6)$$

where M is the number of essential modes retained in the model, $\Delta\vec{r} = \vec{r} - \vec{r}^{\,0}$ and $\vec{r}^{\,0}$ is the equilibrium position vector ($\vec{r}$ and $\vec{r}^{\,0}$ are 3N vectors collecting the Cartesian coordinates of all the N atoms in the system). The potential V in eq. 6 is a second order approximation to the total potential that depends on the results of essential dynamics. V replaces the entire force field considered in a standard molecular dynamics, i.e., it accounts for bound, unbound and solvation interactions. Using this potential in a Langevin or Brownian dynamics for the coarse-grained protein, one gets an equivalent trajectory of the protein with the same flexibility (B-factors, RMSD, correlation patterns, Lindemann coefficients, etc) of the original MD.

One can take advantage of this second order potential energy to study systems with higher complexity. That could be the case, for example, of a protein on a metallic surface where the interaction with the metal can be added to V in eq. 6 giving rise to a hybrid potential. We are currently testing this method by including in such hybrid potential a term accounting for the direct interaction with gold based on GolP, and another term taking into account protein and metal desolvation, as in ProMetCS (*39*).

We are also testing an even simpler coarse-grained model for protein-surface interactions, based only on the backbone atoms, which uses only a Lennard-Jones 12-6 potential. We use effective interaction parameters obtained by assuming that all the atoms of an aminoacid side chain are concentrated on its corresponding Cα. This is a really simplistic assumption that will be improved in the future. The interaction with gold is again introduced by protein-Au Lennard-Jones terms obtained from GolP.

Preliminary results are encouraging. As an example, in Figure 8 we show a comparison of the B-factors obtained by an atomistic GolP MD (10 ns long) and the corresponding LD using the simple coarse-grained potential for ubiquitine on an Au(111) surface in water. As it can be seen, both lines describe qualitatively the same behavior, which means that even such simple potential and backbone based coarse-grained model is providing reasonable results.

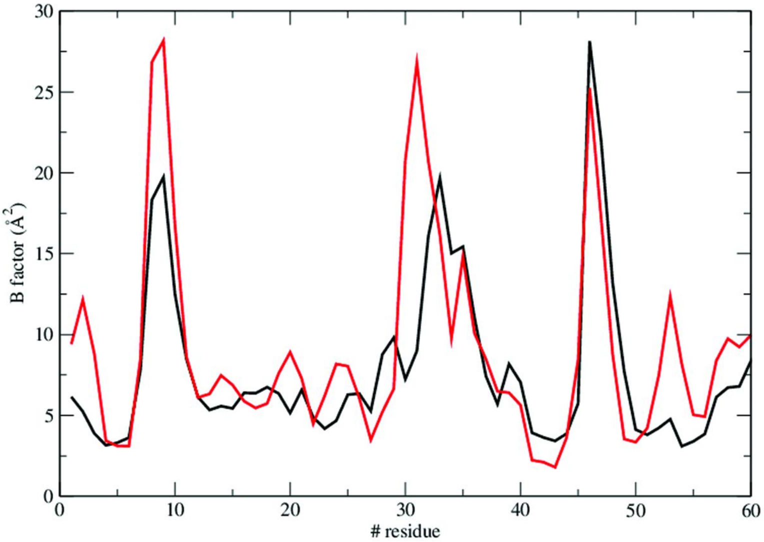

Figure 8. B factors describing the mean dispersion of backbone atoms for ubiquitine docked on a gold surface. Black line refers to the atomistic MD results. Red line refers to the results of the LD with the hybrid potential described in the text. MD and LD simulations are both 10ns long. As it can be seen, both qualitatively represent the same overall behavior, although minor deviations are present.

Conclusions

In this chapter we have succinctly introduced the various computational approaches that our group has been developing and applying to the study of the interaction between proteins and inorganic (gold) surfaces. Our approach comprises a sequential multiscale strategy that can be applied to materials other than gold and that can provide an answer to many of the open questions in the field. The development and use of these tools evolve in parallel with experiments, as the picture provided by combining experiments and computations is broader and more solid than that coming from one of the two sources alone. We have also put particular care in making our development freely and openly available to the scientific community (http://web.fisica.unimo.it/prosurf/toolbox.html), with the hope of triggering further improvements and allowing applications by other groups. Finally, we have also sketched some of the lines of ongoing developments, which include the testing of enhanced sampling methods and the use of coarse-grained models. We note that a similar approach can be extended to DNA interaction with inorganic solid surfaces and nanoparticles.

Acknowledgments

We are grateful to Elisa Molinari for continuous stimulating discussions. The work presented here is mostly the result of a joint effort of our group at the Center S3 CNR-NANO and the groups of Rebecca Wade, Gideon Schreiber, Israel Rubinstein, Alexander Vaskevic and Kay Gottschalk, who are most gratefully acknowledge here. Our work is funded by the European Commission through projects PROSURF (contract FP6-028331) and DNA-NANODEVICES (contract FP6-029192), by the Italian Institute of Technology, Platform Computational, through Seed project MOPROSURF (2010-2013) and by MIUR under the FIRB project ITALNANONET. The computational facilities and staff at CINECA (Bologna, Italy) are acknowledged. The EU FP6 DEISA infrastructure network (DECI project Psi-Wat) provided the supercomputing time for the CP simulation, carried out at BSC in Spain, while the EU FP7 PRACE infrastructure network (Preparatory project 2010PA0412) provide the time for preliminary simulations of Amyloid β peptide on gold, carried out at TGCC in France.

References

1. Norde, W.; Lyklema, J. *J. Biomater. Sci., Polym. Ed.* **1991**, *2*, 183–202.
2. Brash, J. L.; Horbett, T. A. In *Proteins at interfaces. II. Fundamentals and applications*; Horbett, T. A., Brash, J. L., Eds.; American Chemical Society: Washington, DC, 1995; pp 1–23.
3. Lynch, I.; Dawson, K. A.; Linse, S. *Science's STKE* **2006**, *2006*, pe14.
4. Lundqvist, M.; Stigler, J.; Elia, G.; Lynch, I.; Cedervall, T.; Dawson, K. A. *Proc. Natl. Acad. Sci. U.S.A.* **2008**, *105*, 14265–14270.
5. Wagner, V.; Dullaart, A.; Bock, A. K.; Zweck, A. *Nat. Biotechnol.* **2006**, *24*, 1211–1218.
6. Farokhzad, O. C.; Langer, R. *ACS Nano* **2009**, *3*, 16–20.
7. Xia, Y.; Lim, B. *Nature* **2010**, *467*, 923–924.
8. Sarikaya, M.; Tamerler, C.; Alex, K. Y. J.; Schulten, K.; Baneyx, F. *Nat. Mater.* **2003**, *2*, 577–585.
9. Mahmoudi, M.; Lynch, I.; Ejtehadi, M.; Monopoli, M. P.; Baldelli Bombelli, F.; Laurent, S. *Chem. Rev.* **2011**, *111*, 5610–5637.
10. Goobes, G.; Goobes, R.; Schueler-Furman, O.; Baker, D.; Stayton, P. S.; Drobny, G. P. *Proc. Natl. Acad. Sci. U.S.A.* **2006**, *103*, 16083–16088.
11. Wei, Y.; Latour, R. A. *Langmuir* **2009**, *25*, 5637–5646.
12. Baugh, L.; Weidner, T.; Baio, J. E.; Nguyen, P.-C. T.; Gamble, L. J.; Stayton, P. S.; Castner, D. G. *Langmuir* **2010**, *26*, 16434–16441.
13. Calzolai, L.; Franchini, F.; Gilliland, D.; Rossi, F. *Nano Lett.* **2010**, *10*, 3101–3105.
14. Liu, Y.; Jasensky, J.; Chen, Z. *Langmuir* **2012**, *28*, 2113–2121.
15. Gray, J. *Curr. Opin. Struct. Biol.* **2004**, *14*, 110–115.
16. Cohavi, O.; Corni, S.; De Rienzo, F.; Di Felice, R.; Gottschalk, K. E.; Hoefling, M.; Kokh, D.; Molinari, E.; Schreiber, G.; Vaskevich, A.; Wade, R. C. *J. Mol. Recognit.* **2009**, *23*, 259–262.

17. Cohavi, O.; Reichmann, D.; Abramovich, R.; Tesler, A. B.; Bellapadrona, G.; Kokh, D. B.; Wade, R. C.; Vaskevich, A.; Rubinstein, I.; Schreiber, G. *Chem. Eur. J.* **2011**, *17*, 1327–1336.
18. Bortolotti, C. A.; Battistuzzi, G.; Borsari, M.; Facci, P.; Ranieri, A.; Sola, M. *J. Am. Chem. Soc.* **2006**, *128*, 5444–5451.
19. Alessandrini, A.; Salerno, M.; Frabboni, S.; Facci, P. *Appl. Phys. Lett.* **2005**, *86*, 133902–133903.
20. Chen, Y.-S.; Hong, M.-Y.; Huang, G. S. *Nat. Nanotech.* **2012**, *7*, 197–203.
21. Zeng, S.; Yong, K.-T.; Roy, I.; Dinh, X.-Q.; Yu, X.; Luan, F. *Plasmonics* **2011**, 491–506.
22. Wetterer, S.; Lavrich, D.; Cummings, T.; Bernasek, S.; Scoles, G. *J. Phys. Chem. B* **1998**, *102*, 9266–9275.
23. Syomin, D.; Koel, B. E. *Surf. Sci.* **2002**, *498*, 61–73.
24. Corradini, V.; Menozzi, C.; Cavallini, M.; Biscarini, F.; Betti, M. G. *Surf. Sci.* **2003**, *532*, 249–254.
25. Ayton, G. S.; Noid, W. G.; Voth, G. A. *Curr. Opin. Struct. Biol.* **2007**, *17*, 192–198.
26. Tozzini, V. *Acc. Chem. Res.* **2010**, *43*, 220–230.
27. Enhanced sampling can effectively extend the time frame for both *ab initio* and classical simulations. The interpretation of results, however, rely on statistical mechanics theories of chemical kinetics. Here we limit ourselves to the time-span accessible to straight simulations.
28. Cornell, W. D.; Cieplak, P.; Bayly, C. I.; Gould, I. R.; Merz, K. M.; Ferguson, D. M.; Spellmeyer, D. C.; Fox, T.; Caldwell, J.; Kollman, P. A. *J. Am. Chem. Soc.* **1995**, *117*, 5179–5197.
29. MacKerell, A. D., Jr.; et al. *J. Phys. Chem. B* **1998**, *102*, 3586–3616.
30. Jorgensen, W. L.; Maxwell, D. S.; Tirado-Rives, J. *J. Am. Chem. Soc.* **1996**, *118*, 11225–11236.
31. Hess, B.; Kutzner, C.; Van Der Spoel, D.; Lindahl, E. *J. Chem. Theory Comput.* **2008**, *4*, 435–447.
32. Phillips, J. C.; Braun, R.; Wang, W.; Gumbart, J.; Tajkhorshid, E.; Villa, E.; Chipot, C.; Skeel, R. D.; Kale, L.; Schulten, K. *J. Comput. Chem.* **2005**, *26*, 1781–1802.
33. Shaw, D. E.; Maragakis, P.; Lindorff-Larsen, K.; Piana, S.; Dror, R. O.; Eastwood, M. P.; Bank, J. A.; Jumper, J. M.; Salmon, J. K.; Shan, Y.; Wriggers, W. *Science* **2010**, *330*, 341–346.
34. Di Felice, R.; Selloni, A. *J. Chem. Phys.* **2004**, *120*, 4906–4914.
35. Di Felice, R.; Selloni, A.; Molinari, E. *J. Phys. Chem. B* **2003**, *107*, 1151–1156.
36. Iori, F.; Corni, S.; Di Felice, R. *J. Phys. Chem. C* **2008**, *112*, 13540–13545.
37. Calzolari, A.; Cicero, G.; Cavazzoni, C.; Di Felice, R.; Catellani, A.; Corni, S. *J. Am. Chem. Soc.* **2010**, *132*, 4790–4795.
38. Iori, F.; Di Felice, R.; Molinari, E.; Corni, S. *J. Comput. Chem.* **2009**, *30*, 1465–1476.
39. Kokh, D. B.; Corni, S.; Winn, P. J.; Hoefling, M.; Gottschalk, K. E.; Wade, R. C. *J. Chem. Theory Comput.* **2010**, *6*, 1753–1768.
40. Tozzini, V. *Curr. Opin. Struct. Biol.* **2005**, *15*, 144–150.

41. Tkatchenko, A.; Romaner, L.; Hofmann, O.; Zojer, E.; Ambrosch-Draxl, C.; Scheffler, M. *MRS Bull.* **2010**, *35*, 435–442.
42. Gross, E. K. U.; Dreizler, R. M. *Density Functional Theory*; Springer-Verlag, 1995.
43. De Renzi, V.; Di Felice, R.; Marchetto, D.; Biagi, R.; Del Pennino, U.; Selloni, A. *J. Phys. Chem. B* **2004**, *108*, 16–20.
44. Car, R.; Parrinello, M. *Phys. Rev. Lett.* **1985**, *55*, 2471–2474.
45. Vargas, M. C.; Giannozzi, P.; Selloni, A.; Scoles, G. *J. Phys. Chem. B* **2001**, *105*, 9509–9513.
46. Hammer, B.; Nørskov, J. K. Theory of Adorption and Surface Reactions. In *Chemisorption and Reactivity of Supported Clusters and Thin Films*; Lambert, R. M., Pacchioni, G., Eds.; Kluwer Academic Publishers: The Netherlands, 1997.
47. Kleiman, G. G.; Landman, U. *Phys. Rev. Lett.* **1973**, *31*, 707–710.
48. Hoefling, M.; Monti, S.; Corni, S.; Gottschalk, K. E. *PLoS One* **2011**, *6*, e20925.
49. Cicero, G.; Calzolari, A.; Corni, S.; Catellani, A. *J. Phys. Chem. Lett.* **2011**, 2582–2586.
50. Frenkel, D.; Smit, B. *Understanding molecular simulation: from algorithms to applications*; Academic Press Inc.: 1996.
51. Marx, D.; Hutter, J. *Ab initio molecular dynamics: basic theory and advanced methods*; Cambridge University Press: 2009.
52. Schlick, T. *Molecular modeling and simulation: an interdisciplinary guide*; Springer Verlag: 2010; Vol. 21.
53. Klepeis, J. L.; Lindorff-Larsen, K.; Dror, R. O.; Shaw, D. E. *Curr. Opin. Struct. Biol.* **2009**, *19*, 120–127.
54. Van Der Kamp, M. W.; Shaw, K. E.; Woods, C. J.; Mulholland, A. J. *J. R. Soc., Interface* **2008**, *5*, 173–190.
55. Adcock, S. A.; McCammon, J. A. *Chem. Rev.* **2006**, *106*, 1589–1615.
56. Vellore, N. A.; Yancey, J. A.; Collier, G.; Latour, R. A.; Stuart, S. J. *Langmuir* **2010**, *26*, 7396–7404.
57. Puleo, D. A.; Bizios, R. *Biological Interactions on Materials Surfaces: Understanding and Controlling Protein, Cell, and Tissue Responses*; Springer Verlag: 2009.
58. Iori, F.; Corni, S. *J. Comput. Chem.* **2008**, *29*, 1656–1666.
59. Hoefling, M.; Iori, F.; Corni, S.; Gottschalk, K.-E. *Langmuir* **2010**, *26*, 8347–8351.
60. Hoefling, M.; Iori, F.; Corni, S.; Gottschalk, K. E. *ChemPhysChem* **2010**, *11*, 1763–1767.
61. Trzesniak, D.; Kunz, A. P. E.; van Gunsteren, W. F. *ChemPhysChem* **2007**, *8*, 162–169.
62. Kästner, J. *Wiley Interdiscip. Rev.: Comput. Mol. Sci.* **2011**, *1*, 932–942.
63. Crescenzi, O.; Tomaselli, S.; Guerrini, R.; Salvadori, S.; D'Ursi, A. M.; Temussi, P. A.; Picone, D. *Eur. J. Biochem.* **2002**, *269*, 5642–5648.
64. Schlick, T. F *Biol. Rep.* **2009**, *1*, 1–9.
65. Sugita, Y.; Okamoto, Y. *Chem. Phys. Lett.* **1999**, *314*, 141–151.
66. Li, X.; Latour, R. A.; Stuart, S. J. *J. Chem. Phys.* **2009**, *130*, 174106–174109.

67. Laio, A.; Gervasio, F. L. *Rep. Prog. Phys.* **2008**, *71*, 126601–126622.
68. Schneider, J.; Colombi Ciacchi, L. *J. Am. Chem. Soc.* **2012**, *134*, 2407–2413.
69. Isralewitz, B.; Gao, M.; Schulten, K. *Curr. Opin. Struct. Biol.* **2001**, *11*, 224–230.
70. Madura, J. D.; Briggs, J. M.; Wade, R. C.; et al. *Comput. Phys. Commun.* **1995**, *91*, 57–95.
71. Gabdoulline, R. R.; Wade, R. C. *Biophys. J.* **1997**, *72*, 1917–1929.
72. Northrup, S. H. *Macrodox v.2.0.2: Software for Prediction of Macromolecular Interaction*; Tennesse Technological University: Cookeville, TN, 1995.
73. Gabdoulline, R. R.; Wade, R. C. *Methods* **1998**, *14*, 329–341.
74. http://projects.villa-bosch.de/mcmsoft/sda/6.00/.
75. Tomasio, S. M.; Walsh, T. R. *J. Phys. Chem. C* **2009**, *113*, 8778–8785.
76. Mitternacht, S.; Schnabel, S.; Bachmann, M.; Janke, W.; Irback, A. *J. Phys. Chem. B* **2007**, *111*, 4355–4360.
77. Skelton, A. A.; Liang, T.; Walsh, T. R. *ACS Appl. Mater. Interfaces* **2009**, *1*, 1482–1491.
78. Horinek, D.; Mamatkulov, S. I.; Netz, R. R. *J. Chem. Phys.* **2009**, *130*, 124507.
79. Latour, R. A. *Biointerphases* **2008**, *3*, FC2–FC9.
80. Gabdoulline, R. R.; Wade, R. C. *J. Phys. Chem.* **1996**, *100*, 3868–3878.
81. Elcock, A. H.; Gabdoulline, R. R.; Wade, R. C.; McCammon, J. A. *J. Mol. Biol.* **1999**, *291*, 149–162.
82. Shao, J.; Tanner, S. W.; Thompson, N.; Cheatham, T. E., III. *J. Chem. Theory Comput.* **2007**, *3*, 2312–2334.
83. Brancolini, G.; Kokh, D. B.; Calzolai, L.; Wade, R. C.; Corni, S. Docking of ubiquitin on gold nanoparticles. Unpublished
84. Reith, D.; Pütz, M.; Müller-Plathe, F. *J. Comput. Chem.* **2003**, *24*, 1624–1636.
85. Rueda, M.; Chacón, P.; Orozco, M. *Structure* **2007**, *15*, 565–575.
86. Emperador, A.; Carrillo, O.; Rueda, M.; Orozco, M. *Biophys. J.* **2008**, *95*, 2127–2138.
87. Carrillo, O.; Laughton, C. A.; Orozco, M. *J. Chem. Theory Comput.* **2012**, *8*, 792–799.

Chapter 11

Protein−Carbohydrate Interactions on the Surfaces of Glycosylated Membranes

Jia Luo and Zhi-Kang Xu*

**MOE Key Laboratory of Macromolecular Synthesis and Functionalization,
Department of Polymer Science and Engineering, Zhejiang University,
Hangzhou 310027, P. R. China
*E-mail: xuzk@zju.edu.cn. Fax: + 86 571 8795 1773**

The study of the protein−carbohydrate interactions is not only vital to gain an understanding of how information-rich carbohydrates participate in recognition events in vivo but also because it is a great source of inspiration for the design of advanced materials including saccharide-based microstructures. Hence, it is an emerging topic on fabrication of glycosylated surfaces for both fundamental and application purposes, especially for membrane surfaces. In this chapter, we summarize some crucial achievements of glycosylation on the membrane surfaces and give an insight reviewing in the protein−carbohydrate interactions on the surfaces of glycosylated membranes.

1. Introduction

Carbohydrates and their derivatives serve numerous functions in biological processes. The most vital and interesting function is performed as recognition elements, which specifically recognized by other biomolecules (*1*). This kind of recognition phenomena play crucial role in living organisms. It is based on protein−carbohydrate interactions that mainly occurred on the out surface of cell membrane, on which exist a dense layer named glycocalyx (*2*). Glycocalyx dominates the intercellular specific interaction, and contributes to the steric repulsion that prevents nonspecific adhesion (*3*). Therefore, there is a growing interesting to mimic the glycocalyx layer and to construct carbohydrate-rich structures for both fundamental and application purposes (*4*–*6*).

In Proteins at Interfaces III State of the Art 2012; Horbett, T., et al.;
ACS Symposium Series; American Chemical Society: Washington, DC, 2012.

Separation membranes with carbohydrate-rich surfaces are platforms to mimic both the specific recognition properties and the anti-nonspecific adsorption of the glycocalyx on cell surface. The platforms are named glycosylated membrane surfaces and have normally been fabricated by grafting glycopolymer brushes on the membrane surfaces to prepare glycosylated membranes (*7–11*). This chapter focuses on the protein−carbohydrate interactions on the glycosylated membrane surfaces. Firstly, we will present some fundamental knowledge according to glycobiology and the widely accepted mechanisms of protein−carbohydrate recognition. Then we summarize some important theoretical achievements based on glycosylated membranes, mainly referring to the interactions between lectins and saccharide ligands immobilized on the membrane surfaces.

2. Basis of Protein−Carbohydrate Interactions

2.1. Carbohydrates and Glycobiology

Carbohydrates, also known as saccharides, are a class of organic compounds with the empirical formula $C_m(H_2O)_n$, and composed of polyhydroxy aldehyde or ketone (*12*). The study of carbohydrates, which has been lasting for over a hundred years, began in the late nineteenth century with the work of Emil Fischer (*13*). In living organisms, carbohydrates have an extremely widespread distribution, occurring as monosaccharides, disaccharides, oligosaccharides, polysaccharides or glycoconjugates. Glycoconjugates are general terms of glycoproteins, glycopeptides and glycolipids, usually found at cell surfaces as a part of cell membranes (*14*).

Carbohydrates and their derivatives serve numerous functions in biological processes (*15*). The most well-known and fully studied roles of carbohydrates are energy source (e.g. glucose and starch) and structural components (e.g. cellulose and chitosan) (*16*). Often, carbohydrates perform a function as a recognition element in biological events (*17*). That is, they are specifically recognized by other biomolecules. Recognition between carbohydrates and other biomolecules play a pivotal role in a variety of biological phenomena based on cell−cell interactions, such as apoptosis, immune response, fertilization, embryogenesis, cell migration, organ formation, microbial and viral infection, blood clotting, inflammation and cancer metastasis (*18–23*). Actually, carbohydrates used to be considered as less information-rich molecules and were once called “molecules in search of a function” (*24*). With the development of research techniques, the role of carbohydrates in recognition has started to be thoroughly understood in the past three decades.

Carbohydrates can be highly branched molecules, and their monomeric units may be connected to each other by abundant linkage types, which differ from other two classes of biological polymers protein and DNA, both of them are almost linear in structure (*25*). Additional variety caused by ring size, anomeric configuration, and modification (e.g., acylation, sulfation, and phosphorylation) also gives carbohydrates strong potential for diversity. Such complexity allows carbohydrates to provide almost unlimited variations in their chemical structures, and have the capacity to encode information for specific molecular recognition and to convey information at a molecular level (*14*).

It is suggested that carbohydrates have been coupled with biomolecules via glycosylation. This process can be found in biological phenomena ubiquitously as one of co-translational and post-translational modification events to form glycosylated biomolecules for recognition (*25*). Under biosynthetic way, glycosylation refers to the enzymatic process that attaches saccharides to proteins, lipids, peptides, or other biomolecules to form glycoconjugates including glycoproteins, glycolipids and glycopeptides. In addition, alterations in glycosylation patterns have been observed for all types of malignant cells and cells found from numerous types of diseased tissues (*14*).

2.2. Protein–Carbohydrate Interactions in Biology

Compared to protein–protein and protein−DNA interactions, protein−carbohydrate interactions have intrigued scientists in recent decades for their vital role in specific recognition. In addition, it is now clear that protein–carbohydrate interactions are also at the key point of many other important biological processes including intracellular and intercellular routing, such as endocytosis, signalling and catalysis. These phenomena are essential processes by which living organisms control over complex biological functions (*12*, *14*, *25*).

Generally, there are three types of carbohydrate-binding protein prominent in biological processes: carbohydrate-specific enzymes, antibodies and lectins. Other than antibodies and enzymes, lectins are neither the products of the immune system nor biological catalysts. Lectins, which are highly specific for their saccharide moieties, can be found in most organisms, ranging from viruses and bacteria to plants and animals. Each lectin molecule contains typically two or more carbohydrate-combining sites. Namely, they are di- or polyvalent (*26*, *27*).

There are three classical lectin families: legume lectins, C-type lectins, and galectins (*28*). Moreover, according to the monosaccharide for which they exhibit the highest affinity, lectins can also be divided into five classes: mannose, galactose/*N*-acetylgalactosamine, N-acetylglucosamine, N-acetylneuraminic acid and fucose (*29*). Legumes is the largest and most thoroughly studied family of lectins (*30*).

In the legume family of lectins, almost all members are isolated from seeds of the plants. Among them, Concanavalin A (Con A) and Peanut agglutinin (PNA) are two of the well-characterized lectins (*28*). Con A, from Jack bean, was first isolated in 1919 by James Sumner. It was the first lectin to be commercially available, and has been widely utilized by biologists to characterize glycoproteins and glycoconjugates on the surface of various cells. Con A mainly binds internal and non-reducing terminal α-D-mannosyl and α-D-glucosyl groups, and was shown to be specific for mannose and glucose. Con A is a homotetramer, with each sub-unit (26.5 kDa, 235 amino-acids, heavily glycated) binding a metallic atom (usually Mn^{2+} and Ca^{2+}) (*31*). Its tertiary structure has been clarified, and its affinity for the mannose and glucose are well known. PNA is plant legume lectin derived from Arachis hypogaea. The name "Peanut agglutinin" originates from its ability to agglutinate neuramidase-treated erythrocytes. As for affinity to carbohydrates, PNA specifically binds the sequence Gal-β(1-3)-GalNAc.

The classification of lectins according to their monosaccharide specificity can not cover the exquisite specificity for di-, tri-, and oligosaccharides. Actually, lectins with same specific groups may obviously differ in their affinities for different oligosaccharides. On the other hand, different lectins specific for the same oligosaccharide, may recognize different regions of its surface (*28*).

Although it has been technically possible for computer simulation of the structures of carbohydrate-protein complexes for more than a decade, it remains elusive for the accurate prediction of binding affinity. Peoples commonly believe that carbohydrates interact with lectins through subtle balance of hydrogen bonds, metal coordination, van der Waals and hydrophobic interactions (*32*). Lectin specificity is often explained in terms of orientation of the polar residues in the binding site, which allow the formation of hydrogen bonds with specific saccharides. It is the availability of large numbers of hydroxyl groups on carbohydrates and sufficient hydroxyl, amine, and carboxyl groups of lectins enables the formation of the complex networks based on hydrogen bonds (H-bonds) (*33*). In these H-bonds networks, hydroxyl groups serve both as donors and acceptors to form cooperative H-bonds between the binding sites of Lectins and the corresponding saccharides. Moreover, carbohydrates are amphipathic molecules, and they contain significant hydrophobic patches. Therefore, besides the aliphatic hydrogen, which can be exploited in binding to proteins via H-bonds, a key part in recognition is played by the aromatic residues in the active sites of many carbohydrate-binding proteins (*25*). In addition, divalent cations are involved in protein−carbohydrate recognition either indirectly or directly (*32*). By shaping the binding site, $Ca^{2+}$and Mn^{2+} can assist the formation of binding sites, and Ca^{2+} in C-type lectins can directly bind to carbohydrate. For example, Con A is a tetramer in solution above pH 6.9, whereas it is a dimer below pH 5.9. Each subunit typically have a transition metal ion binding site S1 (typically Mn^{2+}), a Ca^{2+} binding site S2, and a saccharide binding site. The divalent cations play roles in stabilizing the conformation of saccharide binding site (*16*).

Unlike to monosaccharides, the affinities of lectins to oligosaccharides may also be influenced by the shape of the flexible molecules of oligosaccharides. By molecular modeling and high-resolution nuclear magnetic resonance (NMR) studies, it is shown that oligosaccharides have considerable freedom of rotation around the glycosidic bonds, in another word, flexibility. The flexibility around glycosidic linkages leads to conformational heterogeneity, so that oligo-saccharides may have numerous topographic features, which make the binding mechanism more complex (*28*).

2.3. Cluster Glycoside Effect

A considerable challenge, coming from protein−carbohydrate interactions, is that the binding between lectin and monovalent carbohydrate is often weak. The typical association constants are seldom reported to be beyond 10^6 M^{-1}, whereas dissociation constants for most lectin−monosaccharide interactions are in the mM range (*34*). It is usually explained to the fact that lectins generally possess shallow, solvent-exposed binding pockets, and the protein−carbohydrate interactions are intrinsically more dynamic than many other protein−ligand interactions. However, association constants of lectin−oligosaccharide interactions can be up to 1000-fold higher than that of lectin−monosaccharide interactions. The binding affinity generally increases with increasing oligosaccharide size (*35*). Moreover, as mentioned above, carbohydrate-binding lectins are typically aggregated into oligomeric structures in nature. Learning from nature, it is reasonable to consider that lectin−carbohydrate recognitions, which arise from several relatively weak interactions, is not simple monomeric binding events, but an oligo- or polymeric binding mechanisms. Hence, the monovalent binding limitations can be circumvented through multivalency.

Some works reported the phenomena that when several saccharides clustered together in the right type and orientation, there is a rapid increase in both affinity and specificity (*34*). This increase should be expected not only due to the increase of local concentration but also as the effects of “cluster” or “multivalent effect”. In a classic work in 1988, Lee and co-workers highlighted the importance of the “cluster effect” through the study of the affnity of the hepatic asialoglycoprotein lectin for a range of mono- and multi-antennary β-D-galactosyl terminated structures (*36*). They demonstrated the affinity of multivalent ligands for binding was 1×10^6 -fold greater than that of an equivalent monovalent trisaccharide. Furthermore, internal branch structure of the multivalent ligands had some effect on binding process as a comparatively minor role. This phenomenon was defined by Lee and co-workers in 1995 as the “cluster glycoside effect” (*37*).

Myriad reports of the binding of multivalent saccharides to lectins have appeared by synthesis of multimeric carbohydrates as ligands for carbohydrate-binding proteins during the past decade (*38–49*). Most of them show some enhancement in activity compared to the corresponding monovalent ligand on a valence-corrected basis. Nevertheless, there exists horrendous variation in the magnitude of the cluster glycoside effect. In another words, the enhancements on per mole of saccharide range from zero to 10^6. Although there are not an accurate relationship between valence and affinity, a general trend can be summarized. That is, enhancements observed for linear polymers are near 10^5 fold, for dendrimers approximate 10^3, and for glycoclusters about 10^2.

The physiological advantages conferred by multivalent binding have been studied through synthetic arrays. Besides the highly specificity and versatility, kinetics effects of such binding events are likely critical for biological processes (*34*, *35*, *37*). For instance, compare to monovalent interaction, multivalent bindings exhibit greater reversibility in the presence of competing ligands, so that glycoside clusters are less likely to entrap cells in unproductive binding events. In addition, multiple weak interactions are expected to be more resistant to shear stress on surfaces of cells interact in the bloodstream environment. Furthermore, this weakly affinity can facilitate targeting the protein to its destination via the formation of transient states.

2.4. Molecular Mechanisms of Cluster Glycoside Effect

To begin with, the mechanisms of the cluster glycoside effect are yet to be rigorously studied, but their implications are ambiguous, mainly owning to the absence of detailed thermodynamic data on the binding processes and the structural information regarding the bound complex. Nonetheless, some valuable conclusions have been reached. Considering the mechanisms through which cluster glycoside effects arise, there are several relevant interpretations, include the intramolecular chelate effect, intermolecular aggregative process, and steric stabilization (*34*).

2.4.1. Intramolecular Chelate Effect

The name of “chelate effect” comes mostly from the metal chelates, which are myriad in inorganic chemistry. Usually a bivalent ligand binding to a bivalent receptor with an affinity greater than that of the monovalent ligand is well-accepted. Any thermodynamic parameter characterizing a bivalent association is related to a monovalent association and the interaction energy. To clarify the intramolecular mechanism, a term should be represented in the following:

$$\Delta J_{bi} = \Delta J_{mono} + \Delta J_{\mathrm{int}} \qquad (1)$$

where ΔJ represents the change in any thermodynamic property during binding, “bi” refers to that parameter for the bivalent ligand, “mono” refers to that parameter for the monovalent ligand, and “int” refers to the interaction parameter, or the energetic consequence of physical linkage (*50*). For evaluation of interactions, the interaction free energies can be ΔJ_{int}, which is often divided to the entropic and enthalpic contributions.

Entropic Contributions

As a particle, the overall interaction entropy can be considered as the algebraic sum of four parts: the translational, rotational, conformational, and solvation-associated entropies.

The translational entropy of a particle in the gas phase is described by the Sakur-Tetrode equation as follows (*34*),

$$S = k_B N_i \left[\left(\ln\left(\left(\frac{2\pi i m_1 k_B T}{h^2} \right)^{3/2} V \right) + \frac{3}{2} \right) - \ln(N_i - 1) \right] \qquad (2)$$

where k_B is the Boltzman constant, T is the temperature, h is Planck's constant, m_1 is the mass of the monomeric molecule, and N_i is the number of monomers in the aggregate particle.

Similarly, the rotational entropy of a particle is given by the function as follows,

$$\frac{S}{R} = \log \frac{e^{3/2}\sqrt{\pi}}{\sigma}\left(\frac{T^3}{\theta_a\theta_b\theta_c}\right)^{1/2} \tag{3}$$

where θ_a, θ_b, and θ_c represent the rotational degrees of freedom about the three principal axes and σ is the symmetry number of the molecule. A symmetrical molecule ($\sigma > 1$) will have a rotational entropy diminished by an amount equal to Rlog(σ).

Based on these theories, translational entropies vary as the natural logarithm of the molecular weight, as well as the rotational entropy has a logarithmic relationship to the rotational degrees of freedom, which is indirectly related to the molecular weight of the ligand. That is, the favorable contributions of the translational and rotational entropy to interaction free energy of tethering two or more ligands to a multivalent ligand are roughly equivalent to that of the monovalent ligand.

The restriction of conformational degrees of freedom during ligand binding process reduces conformational entropy of the molecule. The conformational entropy associated with a rotational mode is related to the internal partition function as follows,

$$Q = \frac{1}{n}\left(\frac{8\pi I_r kT}{h^2}\right)^{1/2} \tag{4}$$

where I_r is the reduced moment of inertia about the rotational axis, n is the symmetry number for the internal rotation.

The entropy associated with this partition function is then given by the expression as follows,

$$S(Q) = R(0.5 + \ln Q) \tag{5}$$

Jencks gave a value approximately 4.3 eu for the rotational entropy of a completely unrestrained rotor, providing a maximum loss of entropy for localization of 1.4 kcal mol^{-1} around room temperature (*51*), whereas other researchers suggested different values (*52*, *53*). Actually, unfavorable conformational entropy losses during ligand binding are proved to be smaller than previously appreciated by the above theories, at least in some cases. This evaluation is again fraught with uncertainty.

Perhaps the mainly reason of uncertainty in multivalent binding is the solvation-associated contributions to ΔS_{int}, due to the ambiguious molecular basis of the change in entropy associated with the solvation of various solutes.

Enthalpic Contributions

In principle, there are two effects contribute to the interaction enthalpy (*34*). The first effect, which would give unfavorable contribution, is that the linker domain might alter the position of the ligand within the binding site. In the second place, the linker itself could provide a favorable contribution to the interaction enthalpy by interacting with the surface of the lectins around the binding site. To avoid the first effect, linkers simply need to incorporate sufficient length and flexibility to facilitate interaction with the carbohydrate recognition domain within the binding site. The linker domain should be sufficient length to span two sites on a single protein. Otherwise, there will be an infinite unfavorable contribution to ΔH_{int}. As an example, Kiessling and co-workers found that the attainment of maximal activity seems to coincide with an average length sufficient to span two sites on a single lectin. We have mention that polymeric saccharides exhibited a highest enhancement in activity compared to the corresponding monovalent ligand which could reach to 10^6 fold. Here we would like to give an explanation that it may be due to polymeric glycosides are of sufficient length to span two binding sites.

2.4.2. Intermolecular Aggregative

Multivalent saccharides can also bind multivalent proteins in an intermolecular assay, which is the basis for the familiar precipitin reaction (*54*). After the intermolecular interactions, large aggregates potentially precipitate from solution. Actually, this intermolecular aggregative mechanism of cluster glycoside effect seems by far the most reasonable model, since the phenomena of multivalent saccharide ligands aggregate multivalent lectins has been recognized for a long period (*55–57*). In addition, this well-studied, ubiquitous aggregative behavior for protein-carbohydrate interactions plays a vital role *in vivo*. It implies that such multivalent lectin-carbohydrate recognition may lead to clustering.

2.4.3. Steric Stabilization

Proteins have also been stabilized through surface incorporation of hydrophilic polymers as methoxy polypropylene glycol (*58*, *59*). Whitesides and co-workers have proposed a third mechanism: the steric stabilization. In this motif, interactions between a large ligand and the surface of a protein would prevent the approaching of other macromolecules. However, the experimental evidence supported the relevance of the mechanism to the cluster glycoside effect is still ineffective and indirect (*34*).

2.5. Evaluation of Protein−Carbohydrate Interactions

Here we would like to give a brief introduction rather than detailed summary for all of the evaluation methods. A wide range of assays has been utilized for the measurement of protein−carbohydrate binding constants. Generally, there have been several approaches for evaluation of dynamic processes of protein−carbohydrate binding events, such as the inhibition of hemagglutination (HIA) (*60*), the enzyme-linked lectin assay (*61*), surface plasmon resonance (SPR) (*62*, *63*), nuclear magnetic resonance (NMR), etc. On the other hand, isothermal titration calorimetry (ITC) is the most vital method in providing direct thermodynamic binding data of lectin-carbohydrate interactions in past decades (*64*, *65*). Furthermore, thanks to the development of computer technology, molecular simulation methods also provide data for independently predicting conformational and dynamic processes of protein−carbohydrate interactions (*66*).

3. Protein−Carbonhydrate Interactions on the Surfaces of Glycosylated Membranes

3.1. Why Do Glycosylation of Membranes?

In living entities, carbohydrates are found on the surface of external cell membrane in the form of polysaccharides, glycoproteins, glycolipids or/and other glycoconjugates, which are known as the glycocalyx. The glycocalyx interact with corresponding proteins mainly in two opposite ways, one is contributing to steric repulsion that prevents undesirable non-specific adhesion of other proteins and cells, the other is serving as sites for the specific recognition of other cells, biomolecules and pathogen (*1*, *67*). Definitely, protein−carbohydrate interactions play a pivotal role in a variety of biological processes based on cell−cell recognitions, such as apoptosis, immune response, fertilization, embryogenesis, cell migration, organ formation, microbial and viral infection, blood clotting, inflammation and cancer metastasis. The two mostly vital characters of protein−carbohydrate interactions are the specificity and the so-called cluster glycoside effects.

In 1992, Stanley proposed a concept named “glycosylation engineering”, which mainly focused on the relationship between the structures and functions of saccharides. After that, material scientists introduced this concept and methods of glycosylation to the field of material science and engineering (*68*). A variety of glycosylated materials were fabricated and found broad application prospects in drug delivery, macromolecular therapy, tissue culture, antibacterial, virus recognition, saccharide biochips, and saccharide biosensors (*69–71*). As for the polymeric materials, there just a few works for surface glycosylation have been reported. For example, Roger et al. functionalized poly(ethylene terephthalate) (PET) fibers via aminolysis followed by the tethering of maltose, maltotriose, and maltohexose, respectively (*72*, *73*). Similarly, diazirine-based photo-reagents binding with galactose and lactose were successfully tethered on the polystyrene

(PS) surface (*74*). Ying et al. bound galactose ligands on an acrylic acid graft-copolymerized PET film which allowed a good control of hepatocyte attachment (*75*).

Affinity chromatography (*76*) is a unique separation method as it is the only technique that permits the purification of proteins on the basis of biological functions rather than individual physical or chemical properties. The high specificity of affinity chromatography is due to the strong interaction between the ligands and the proteins of interest. Membrane separation, which allows the processing of a large amount of sample in a relatively short time and provides a system with rapid reaction kinetics, have very important impacts in separation industry. The integration of membrane separation and affinity chromatography surely provides numerous advantages over traditional affinity chromatography. Affinity membrane, which combines the advantage of convection mass transfer of membrane separation with the high specific recognition of affinity chromatography, is a new developed technology for isolation and purification of biomolecules. For the high specificity of protein−carbohydrate interactions we discussed above, it is of great interesting to immobilize saccharides onto the surfaces of membranes, to develop a novel glycosylated affinity membrane, which can be utilized for selective separation and purification of proteins. Moreover, the glycosylated layer on the membrane surface is expected to mimic both the anti-nonspecific adsorption and specific recognition properties of the glycocalyx on cell surface.

Our group has made great progress on both fundamentals and applications in the area of glycosylation of membranes (*7–11*, *77–94*). In this section, we will give an insight reviewing in the protein−carbohydrate interactions on the glycosylated membranes, which will be mostly focused on fundamental principles rather than practical applications.

3.2. Construction of Glycosylated Membranes

Glycosylation of membrane can be obtained via a variety of methods. Early works of membrane glycosylation in our laboratory referred to glycosylation of bulk material. In 2003, we synthesized a carbohydrate containing acrylonitrile-based copolymer poly[acrylonitrile-co-(α-allyl glucoside)] (PANCAG) for the first time via copolymerization of acrylonitrile (AN) and α-allyl glucoside (AG) by water-phase precipitation copolymerization (WPPCP) method using $K_2S_2O_8$-Na_2SO_3 as initiator system and water as reaction medium (*87*). Then, glycosylated polyacrylonitrile-based copolymer membrane was obtained via non-solvent induced phase separation (*10*). At the same time, AG was grafted on the surfaces of microporous polypropylene membrane (MPPM) via a plasma irradiation process to improve the hydrophilicity and antifouling property of this membrane (*8*). In 2006, we reported a facile way to fabricate nanoscale fibers from two glycopolymers by electrospinning, one is PANCAG containing cyclic glucose residues and another is poly[acrylonitrile-co-(D-gluconamidoethyl meth-acrylate)] (PANCGAMA) having linear glucose residues (*94*). Chemical structures of AG, PANCAG and PANCGAMA are showed in Figure 1. As an example of glycosylation of honeycomb-patterned surfaces, poly(styrene-co-2-(2-,3-,4-,6-tetra-O-acetyl-β-D-glucosyloxy) ethyl methacrylate) (PS-co-AcGEMA) with well-defined linear and/or comb-like structures were synthesized by atom transfer radical polymerization (ATRP), and then utilized as precursors for the fabrication of pattern films by the breath figure method (*89*).

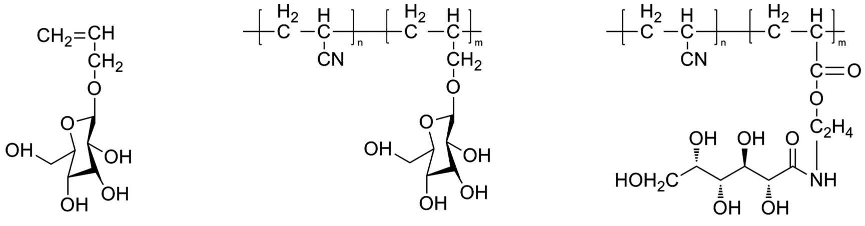
AG PANCAG PANCGAMA

Figure 1. Chemical structures of AG, PANCAG and PANCGAMA.

Glycosylation of membrane surfaces can be divided into three aspects: surface-initiated polymerization of the saccharide monomers (“graft from”); coupling saccharide pendants onto a functional group-contained, polymer brushes modified surface (“graft to”); and immobilization of carbohydrate macromolecules.

3.2.1. “Graft From”

This method is based on the synthesis of saccharide derivatives with a vinyl group and the subsequent formation of grafting glycopolymers on the membrane surfaces. The advantage of this strategy is convenient to obtain the glycosylated membrane surfaces. But the disadvantage is also obvious. Synthesis and purification of saccharide vinyl monomers, which are not straightforward, limit the diversities of glycosylated membrane surfaces.

In 2003, the N_2-plasma-induced graft polymerization of saccharide-containing monomer AG was carried out on microporous polypropylene hollow fiber membranes. Then, a ring-opening glycomonomer D-gluconamidoethyl methacrylate (GAMA) was grafted onto the surface of PAN ultrafiltration membrane by ultraviolet (UV)-initiated grafting polymerization (*8*). In 2006, AG was grafted onto MPPM by UV-induced graft polymerization to generate a glycosylated porous surface for the first time (*82*).

A controllable approach with the combination of the breath figure method and ATRP was developed to fabricate carbohydrate microarrays (*88*). Amphiphilic block copolymers were adopted to generate breath figures with hydrophilic functional groups aggregated mainly inside the pores, which affords a chance of site-directed surface grafting. Then, through surface-initiated ATRP, 2-(2,3,4,6-tetra-O-acetyl-β-D-glucosyloxy)ethyl methacrylate (AcGAMA) were selectively grafted inside the pores rather than on the top surface of the films.

3.2.2. "Graft To"

This strategy is based on the direct formation of polymer brushes and subsequent linkage of saccharide pendants by selected chemical reactions. In this method, the backbone of polymer brushes is clear and controllable, and the diversities of glycosylated membrane surfaces are simple to obtain. However, chemical reactions are not always effective and efficient between the functional group of polymer brushes and the saccharide chemicals.

For example (*91*), poly(acrylonitrile-co-hydroxyethyl methacrylate) was electrospun into nanofibrous mat with an average fiber diameter of 200 nm and glucose ligands were bound on the nanofiber surface through a reaction between glucose pentaacetate and the hydroxyl groups of poly(acrylonitrile-co-hydroxyethyl methacrylate).

Turning to microporous membrane, a UV-induced graft polymerization of 2-aminoethyl methacrylate hydrochloride (AEMA) was carried out on the MPPM to generate an amino-functionalized surface, and then saccharide pendants were bound with the grafted functional layer to form glycopolymer by the reaction between the functionalized amino groups on the membrane surface and carbohydrate lactones (*11*).

Acrylamide was grafted onto the MPPM surface by photoinduced graft polymerization in the presence of benzophenone. The amide groups of grafted poly(acrylamide) were then transformed to primary amine groups by the Hofmann rearrangement reaction. Then saccharide chemicals were coupled with the grafted functional layer to form glycopolymer by the reaction between primary amine groups and carbohydrate lactones (*83*).

Comb-like glycopolymer brushes on the MPPM surface were obtained by a combination of UV-induced graft polymerization and surface-initiated ATRP. 2-Hydroxyethylmethacrylate (HEMA) was firstly grafted to the MPPM surface under UV irradiation in the presence of benzophenone and ferric chloride (*84*). ATRP initiator was then coupled to the hydroxyl groups of poly(HEMA) brushes. Surface-initiated ATRP of D-gluconamidoethyl methacrylate was followed at ambient temperature in aqueous solvent. Furthermore, the poly(HEMA)-grafted MPPM can be simply modified by the immobilization of saccharide ligands through the reaction between hydroxyl groups and acetylated saccharides (*78*).

Click chemistry, with its high yield and specificity, makes "graft to" strategy one of the most reliable glycosylation methods for fabricating the desirable glycosylated membranes. In this method, carboxyl groups were covalently bound on the MPPM surfaces by UV-induced grafting of acrylic acid (AA). The AA-grafted membrane surfaces were then reacted with propargylamine to give terminal alkyne-modified MPPMs (*9*). Subsequently, azide-containing glucose pendants were linked to the membrane surfaces by click chemistry. In another work, carbohydrate derivative was easily bound onto the alkyne-modified membrane surface via thiol-yne click chemistry (*81*).

3.2.3. Immobilization of Carbohydrate Macromolecules

Asymmetric membranes fabricated from poly(acrylonitrile-co-maleic acid) (PANCMA) were immobilized with chitosan and/or gelatin by the reaction between carboxyl groups of polysaccharides and the PANCMA membrane surface in the presence of 1-ethyl-3-(3-dimethylaminopropyl) carbodiimide (*85*). Chitosan-modified poly(acrylonitrile-co-acrylic acid) (PANCAA) nanofibrous membranes were firstly prepared by a coupling reaction between the primary amino groups of chitosan and the carboxyl groups of PANCAA electrospun membranes (*90*).

3.3. Protein−Carbonhydrate Interactions on the Surfaces of Glycosylated Membranes

As discussed above, several approaches for glycosylation of membranes have been developed. Based on the diversities of the glycosylated membrane surfaces, we also made efforts to study the relationship between the microstructure and recognition behavior of the glycopolymers on the membrane surfaces. It is no doubt interactions between proteins and glycosylated polymer brushes on the membrane surfaces are complex processes, which differ from that in solution and on flat substrates owing to the complexity of the membrane surface. Comparing to the great steric hindrance of flat substrate, microporous membrane offer more flexibility to polymer chains since its high specific surface area. Previous studies confirmed that cyclic saccharides provided specific recognition sites for corresponding proteins, while ring-opening saccharides offered better hydrophilicity and anti-adsorption ability to proteins. Here we will present detailed discussion of the protein−carbohydrate interactions on the surfaces of glycosylated membrane.

3.3.1. Linear Chain Saccharides for Anti-Nonspecific Adsorption

Usually, a hydrophilic surface will suppress the adsorption of biomolecules or cells on the membrane and reduce biofouling. Glycopolymer with linear chains grafted on the membrane surfaces are highly hydrophilic due to the multiple hydroxyl groups in saccharide moieties. BSA was utilized as a model protein to evaluate the protein fouling characteristics of the nascent and grafted membranes. It was found that the amount of BSA adsorbed on the membrane surface decreased obviously with the increase of the saccharide grafting degree in a certain range, and the relative flux reductions of the glycosylated membranes after protein fouling were lower than that of unmodified membrane, as well as the flux recovery ratio of the glycosylated membranes remained a relative high value. The BSA adsorption experiment proved that a ring-open glycopolymer tethered surface could reduce non-specific protein adsorption obviously (*11*, *83*).

In nature, cells solve the problem of nonspecific adsorption and adhesion very well. We can assume that the so-called glycocalyx plays an important role in this process. Actually, it has been proved in our work that highly aggregated surface-tethered carbohydrate ligands, mimicking the glycocalyx on the cell surface, result in not only the enhancement of binding strength in specific recognition against proteins, but also the minimization of nonspecific protein adsorption. The mechanism of this anti-fouling phenomenon could be stated as follows: The linear glycosylated polymer brushes could form a hydration layer on the membrane surfaces. Proteins are amphipathic molecules, so the hydrophobic patches could be certainly excluded from the hydration layer formed by hydroxyl-rich glycopolymer brushes. At the same time, the glycosylated polymer exhibit a steric repulsion that prevents protein approaching. Moreover, the as-adsorbed proteins on the hydrophilic modified membrane surfaces could easily be washed away, which offered the glycosylated membranes relative high flux recovery ratios (*95*).

3.3.2. Cyclic Saccharides for Specific Interactions

The two mostly vital characters of protein−carbohydrate interactions are the specificity and the so-called cluster glycoside effects, which have been discussed in the previous section. However, binding events occurred on the membrane surfaces may be more complex than that in solution and on the flat substrates. Following is an in-depth summary of the achievements recent years.

Specificity

The specificity between saccharide ligands and corresponding proteins is often explained in terms of orientation of the polar residues in the binding site, which allow the formation of hydrogen bonds with specific saccharides. In another words, conformation of saccharide is a vital role for the recognition event. Herein, cyclic saccharide pendants, which could present in different three-dimensional conformations, are necessary for recognition.

For example, specific interactions of Con A with α-D-mannose and α-D-glucose residues with free 3-, 4-, and 6-hydroxyl groups are favored. In our previous work, Con A was used as the model protein to evaluate the recognition property of the tethered polyAG chains. When AG density on the surface exceeded a critical value, Con A adsorbed to the membrane surface dramatically by formation of complexes with the glucose residues of tethered glycopolymer chains. On the other hand, almost no interactions were detected without $MnCl_2$, $CaCl_2$, and NaCl in PBS. Mn^{2+} and Ca^{2+} are two ions necessary for shaping the binding sites of Con A, which was mentioned in Section 2, while NaCl stabilizes Con A in solution (*82*).

In another work, protein adsorption experiments were carried out to study the nonspecific and specific interactions between lectins and glycosylated surfaces. Two kinds of lectins, Con A and PNA were used for this purpose. PNA is plant legume lectin specifically binds the sequence β-galactose and Gal-β(1-3)-GalNAc. For the fluorescence images of polystyrene (PS) surface after recognized with FITC-labeled lectins, distinctly, the fluorescent intensity of glucose-functionalized PS surface interacted with Con A is much brighter than that of the analogous specimen interacted with PNA. On the other hand, the galactose- and lactose-functionalized PS surfaces are bright after recognition with FITC-labeled PNA, and the fluorescent intensity is correspondingly weak after interaction with Con A. These results proved the specificity of protein−carbohydrate interactions on the membrane surfaces (*80*).

Cluster Glycoside Effect on the Membrane Surfaces

The interaction between lectin and monovalent carbohydrate is normally weak. For increasing of both affinity and specificity of binding, multivalent interactions, also named “cluster glycoside effect” by Lee and coworkers (*37*), are required by designing multivalent glycoside ligands. Generally, glycosylated polymer chains exhibit the highest enhancement of association constant. This phenomenon may due to the flexibility and relatively long linker between saccharide ligands, which could reduce the unfavorable contribution of the interaction free energy (see 2.4.1). Glycosylated polymer chains were grafted on the membrane surfaces via a variety of methods. The cluster glycoside effect through the lectin-binding events were observed when increase saccharide density. On the other hand, more efficient strategies for high density glycosylation are designed for more effective recognition (see 3.2.2).

Interactions between FL-Con A and the glycosylated membrane surface were studied by CLSM. Comparing with the original and poly(HEMA)-grafted membranes, the fluorescent intensity of glucose-tethered MPPM-HEMA-Glu with low binding degree (BD) (about 0.39 μmol/cm^2) increases but is also relatively weak, which can be ascribed to the low affinity between Con A and small amount of glucose on the membrane surface (*7*). When the density of glucose ligands bound to the membrane surface is high enough, multiple interactions are then formed and the affinity is obviously enhanced between the glucose ligands and Con A. This phenomenon is a typical example to the “cluster glycoside effect” on the glycosylated membrane surfaces. As intuitively shown in Figure 2, fluorescence intensity of the sample with a BD of 0.92 μmol/cm^2 is much stronger than that of the sample with a BD of 0.42 μmol/cm^2. In addition, desorption of FL-Con A adsorbed on the membrane surfaces was also evaluated. It was found that Con A adsorbed on the membrane surface can be effectively desorbed with 1 M glucose solution for all glycosylated samples. These results suggest that the glycosylated MPPMs are promising candidates for the isolation of proteins.

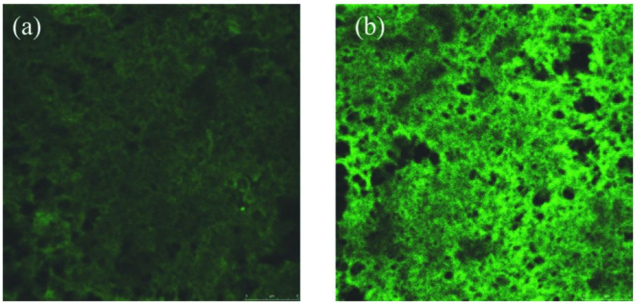

Figure 2. CLSM pictures of the glycosylated membrane surfaces after interaction with FL-Con A: (a) GD = 3.73 μmol/cm^2, BD = 0.42 μmol/cm^2; (b) GD = 3.73 μmol/cm^2, BD = 0.92 μmol/cm^2. The side length in each image is 5 μm. (Reproduced with the permission from ref. (7) Copyright 2008 The Royal Society of Chemistry.)

Overall, with the incorporation of high densities of carbohydrate on the membrane surface, the multivalent contact points between the carbohydrates and the proteins can result in the so-called cluster glycoside effect, which led to almost a significant enhancement of the binding potencies.

Mutilayer Adsorption and the "Transference" Mechanism

The tentacle-like poly(HEMA) chains on the membrane with pendent saccharide ligands not only increase the specific area of membrane but also are benefit to adsorb multilayer proteins, which can enhance the binding capacity of protein on the affinity membrane (*79*). In adsorption breakthrough curves, Con A is adsorbed by monolayer on the glycosylated membrane at first. After the monolayer adsorption of Con A saturates, the adsorption rate gets slow and the effluent concentration increases rapidly. Then the effluent concentration reaches a constant value which is lower than the feed concentration. Therefore, Con A keeps adsorbing on the glycosylated MPPM even if the adsorption rate is very slow. The driving force for it comes from the unsaturation of the affinity membrane. As schematically shown in Figure 3, Con A molecules adsorbed on the outer layer of flexible polymer brushes can be transferred into the inner layer through the reversible binding between Con A and glucose residues. Therefore, multilayers of Con A are adsorbed on the affinity membranes. This transference can be affected by the saccharide density, flow rate of protein solution, and degree of saturation.

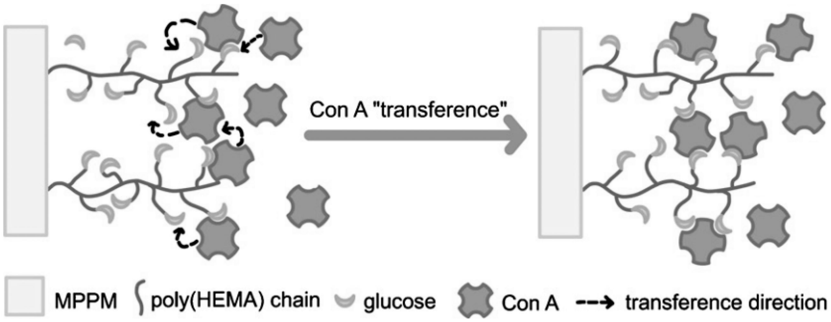

Figure 3. Scheme for the Con A "transference" mechanism. (Reproduced with permission from ref. (79). Copyright 2009 Elsevier.)

Oligosaccharides Recognition on the Membrane Surfaces

To mimic cellular events such as protein recognition and binding, we described the carbohydrate decoration of poly(2-hydroxyethyl methacrylate)-grafted microporous polypropylene membranes (poly(HEMA)-g-MPPMs) with mono- and disaccharides (*77*). Galactose, lactose, glucose, and maltose were covalently attached on the surfaces of poly(HEMA)-g-MPPMs (denoted as MPPM-Gal, MPPM-Lac, MPPM-Glc and MPPM-Mal, respectively). MPPM-Lac has enhanced affinity to PNA as compared with MPPM-Gal having similar BD of saccharide. Meanwhile, MPPM-Mal shows no enhanced affinity to Con A in comparison with MPPM-Glc as the BD of saccharide is above 0.9 μmol/cm^2, where the "glycoside cluster effect" occurs. It has been demonstrated that when lectin binds disaccharide, the non-reducing residue of disaccharide occupies the monosaccharide binding site with the additional contacts to the lectin. Nevertheless, in the complex of PNA and lactose, Ser211 OG forms hydrogen bonds with O3 Glc, O4 Gal, and O5 Gal in the primary site, and a strong hydrogen bond to the O3 Glc is provided by N Gly213, which is not involved in binding Gal in the primary site. In this complex, further hydrogen bonding is provided via O6 Glc and occasionally, through O2 Glc. Since O6 and O2 of Glc are usually more exposed to the solvent than O3, the hydrogen bonds with them are usually water-mediated. The association constant for lactose-PNA binding (1.99×10^3 M^{-1}) is usually larger than that for galactose-PNA binding (0.69×10^3 M^{-1}). Therefore, with the same BD of saccharide, MPPM-Lac adsorbed more PNA than MPPM-Gal did. However, not all of the oligosaccharides show enhanced affinity to lectins in comparison with monosaccharides. Goldstein has concluded that Con A showed binding specificity toward saccharides with glucose or mannose residues that possessed free 3-, 4-, and 6-hydroxyl groups. That is to say, if oligosaccharides with α(1→3)-, α(1→4)-, α(1→6)-glycosidic linkages contained modified hydroxyl groups at these critical binding positions, only the non-reducing terminal saccharide of these oligomers exhibited specific binding ability. So maltose with α(1→4)-glycosidic linkages shows no enhanced affinity towards Con A compared with glucose.

Effects of Length and Density of the Glycopolymer Chains: Necessity of Spacers

Linear polymeric brushes have unique advantages owing to their flexible property which can contact proteins with suitable space distribution. The possible molecular mechanisms have been discussed in Section 2.

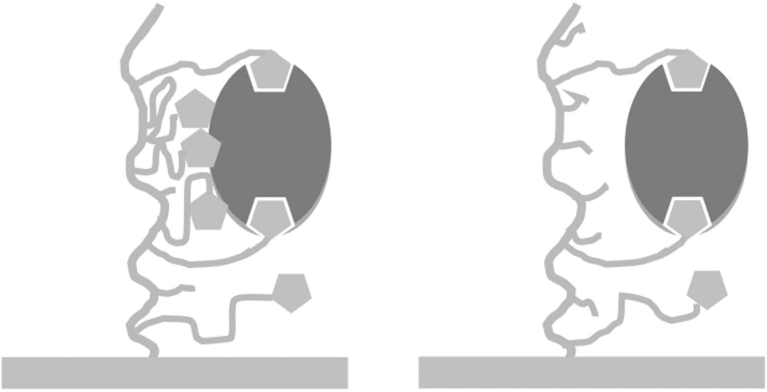

Figure 4. Schematic representation of RCA 120 adsorption of glycopolymer brushes with different saccharide epitope density.

The relationship between structures of glycopolymer brushes and lectin adsorption were investigated via surface-initiated atom transfer radical polymerization (SI-ATRP) and surface plasmon resonance (SPR). A vinyl monomer with galactose pendant, 2-lactobionamidoethyl methacrylate (LAMA), was synthesized. Initiators of ATRP were fixed on gold surface by self-assembly of mercaptoundecanol (MUD). Glycopolymer brushes with different thicknesses were fabricated through SI-ATRP in a living fashion. The grafting density was controlled by changing the density of the initiator via mixing of MUD and undecanethiol. SPR was used to study the effects of brush thickness, grafting density and epitope density on the adsorption of lectin RCA120, which binds galactose specifically (unpublished data). Results indicate that mass transport effect is the key point. The total amount of adsorbed RCA120 increased only when the brush thickness was less than 10 nm because lectin molecules can only reach limited depth. Moreover, as the grafting density was raised, the amount of adsorbed lectin increased and then leveled off. In addition, the mass transport coefficient was reduced by increasing grafting density due to the increasing steric hindrance. Similarly, the highest binding capacity was achieved with a LAMA proportion of 30%. Additional saccharide pendant will lower the binding strength and the transport velocity (As shown in Figure 4). In conclusion, the brush thickness, grafting density and saccharide epitope density were studied. The achievement of an optimal steric arrangement for lectin binding is crucial to keep the balance between the cluster glycoside effect and the mass transport effect.

It is known that the presence of a molecular spacer between the ligand and the support matrix can improve the binding capacity of a glycosylated membrane. The longer spacer gives rises to a better exposure to the ligand and benefit for protein adsorption. Herein, if the flexible spacer has sufficient length, the mobility of ligand may also allow the multilayer adsorption.

4. Summary and Outlook

In summary, the protein−carbohydrate interactions on the glycosylated membrane surfaces are complex processes. The relationship between the microstructure and recognition behavior of the glycopolymers differ from that in solution and on flat substrates owing to the complexity of the membrane surface. Comparing to the great steric hindrance of flat substrate, microporous membrane offer more flexibility to polymer chains since its high specific surface area. In brief, our previous studies showed that cyclic saccharides provide specific recognition sites for corresponding proteins, while ring-opening saccharides offere better hydrophilicity and anti-adsorption ability against non-specific biofouling.

Meanwhile, we constructed several surface-glycosylated membranes by different methods. The preparation methods of glycosylation can also be extended to other polymer materials such as nanoparticles and nanofibers. And, these surface-glycosylated membranes will find a great application in protein separation systems as affinity membranes due to the specific interactions between saccharide ligands and lectins.

However, there are still some challenges. For the purpose of mimicking glycocalyx layer of cell surface, oligosaccharide monomers with more information should be introduced into the glycosylation of membranes. Moreover, precisely tunable polymer linker and spacer are required for more effective recognition process. Last but not least, chemical approach, which is not bio-friendly, may not be the most appropriate way for bio-mimicking glycosylation. So, enzymatic glycosylation should be introduced onto the membrane surface, since the biocompatible process, for diversity of saccharide-based functionalized affinity membranes.

Acknowledgments

We thank financial support from the National Natural Science Foundation of China (Grant No. 50933006). Contribution from Dr. Zheng-Wei Dai, Dr. Meng-Xin Hu and Mr. Xiang-Ling Meng are also acknowledged.

References

1. Holland, N. B.; Qiu, Y.; Ruegsegger, M.; Marchant, R. E. *Nature* **1998**, *392*, 799–801.
2. Frey, A.; Giannasca, K. T.; Weltzin, R.; Giannasca, P. J.; Reggio, H.; Lencer, W. I.; M.R., N. *J. Exp. Med.* **1996**, *184*, 1045–1059.
3. Gupta, A. S.; Wang, S.; Linka, E.; Andersone, E. H.; Hofmann, C.; Lewandowski, J.; Kottke-Marchant, K.; Marchant, R. E. *Biomaterials* **2006**, *27*, 3084–3095.
4. Sharon, N. *Biochim. Biophys. Acta* **2006**, *1760*, 527–537.
5. Fukui, S.; Feizi, T.; Galustian, C.; Lawson, A. M.; Chai, W. *Nature* **2002**, *20*, 1011–1017.
6. Serizawa, T.; Yasunaga, S.; Akashi, M. *Biomacromolecules* **2001**, *2*, 469–475.
7. Hu, M.-X.; Wan, L.-S.; Liu, Z.-M.; Dai, Z.-W.; Xu, Z.-K. *J. Mater. Chem.* **2008**, *18*, 4663–4669.
8. Kou, R.-Q.; Xu, Z.-K.; Deng, H.-T.; Liu, Z.-M.; Seta, P.; Xu, Y.-Y. *Langmuir* **2003**, *19*, 6869–6875.
9. Wang, C.; Wu, J.; Xu, Z.-K. *Macromol. Rapid Commun.* **2010**, *31*, 1078–1082.
10. Xu, Z.-K.; Yang, Q.; Kou, R.-Q.; Wu, J.; Wang, J.-Q. *J. Membr. Sci.* **2004**, *243*, 195–202.
11. Yang, Q.; Xu, Z.-K.; Hu, M.-X.; Li, J.-J.; Wu, J. *Langmuir* **2005**, *21*, 10717–10723.
12. Flitsch, S. L.; Ulijn, R. V. *Nature* **2003**, *421*, 219–220.
13. Ladmiral, V.; Melia, E.; Haddleton, D. M. *Eur. Polym. J.* **2004**, *40*, 431–449.
14. Dwek, R. A. *Chem. Rev.* **1996**, *96*, 683–720.
15. Varkie, A. *Glycobiology* **1997**, *97*, 97–130.
16. Zeng, X.; Andrade, C. a. S.; Oliveira, M. D. L.; Sun, X.-L. *Anal. Bioanal. Chem.* **2012**, *402*, 3161–3176.
17. Sears, P.; Wong, C. H. *Science* **2001**, *291*, 2344–2350.
18. Engering, A.; Geijtenbeek, T. B.; Van Kooyk, Y. *Trends Immunol.* **2002**, *23*, 480–485.
19. Karlsson, K. A. *Biochem. Soc. Trans.* **1999**, *27*, 471–474.
20. Rudd, P. M.; Elliott, T.; Cresswell, P.; Wilson, I. A.; Dwek, R. A. *Science* **2001**, *291*, 2370–2376.
21. Geijtenbeek, T.; Torensma, R.; Van Vliet, S.; Van Duijnhoven, G.; Adema, G.; Van Kooyk, Y.; Figdor, C. *Cell* **2000**, *100*, 575–585.
22. Sacchettini, J. C.; Baum, L. G.; Brewer, C. F. *Biochemistry* **2001**, *40*, 3009–3015.
23. Kansas, G. S. *Blood* **1996**, *88*, 3259–3287.
24. Cook, G. M. *J. Cell Sci. Suppl.* **1986**, *4*, 45.
25. Bertozzi, C. R.; Kiessling, L. L. *Science* **2001**, *291*, 2357–2364.
26. Gilbert, H. J.; Bolam, D. N.; Szabo, L.; Xie, H.; Williamson, M. P.; Simpson, P. J.; Jamal, S.; Boraston, A. B.; Kilburn, D. G.; Warren, R. a. J. *R. Soc. Chem.* **2002**, *275*, 89–98.
27. Sharon, N.; Lis, H. *Adv. Exp. Med. Biol.* **2001**, *491*, 1–16.

28. Lis, H.; Sharon, N. *Chem. Rev.* **1998**, *98*, 637–674.
29. Bundle, D. R.; Young, N. M. *Curr. Opin. Struct. Biol.* **1992**, *2*, 666–673.
30. Sharon, N.; Lis, H. *FASEB J.* **1990**, *4*, 3198.
31. Emmerich, C.; Helliwell, J. R.; Redshaw, M.; Naismith, J. H.; Harrop, S. J.; Raftery, J.; Kalb (Gilboa), J. A.; Yariv, J.; Dauter, Z.; Wilson, K. S. *Acta. Crystallogr.* **1994**, *D50*, 749.
32. Spillmann, D.; Burger, M. M. *J. Cell Biochem.* **1996**, *61*, 562–568.
33. Lemieux, R. U. *Acc. Chem. Res.* **1996**, *29*, 373–380.
34. Lundquist, J. J.; Toone, E. J. *Chem. Rev.* **2002**, *102*, 555–578.
35. Dimick, S. M.; Powell, S. C.; Mcmahon, S. A.; Moothoo, D. N.; Naismith, J. H.; Toone, E. J. *J. Am. Chem. Soc.* **1999**, *121*, 10286–10296.
36. Lee, R. T.; Lee, Y. C. *Biochem. Biophys. Res. Commun.* **1988**, *155*, 1444.
37. Lee, Y. C.; Lee, R. T. *Acc. Chem. Res.* **1995**, *28*, 321–327.
38. Baussanne, I.; Law, H.; Defaye, J.; Benito, J. M.; Mellet, C. O.; Gtcia Fernandez, J. M. *Chem. Commun.* **2000**, *16*, 1489–1490.
39. Burke, S. D.; Zhao, Q.; Schuster, M. C.; Kiessling, L. L. *J. Am. Chem. Soc.* **2000**, *122*, 4518–4519.
40. Fan, E.; Zhang, Z.; Minke, W. E.; Hou, Z.; Verlinde, C. L. M. J.; Hol, W. G. J. *J. Am. Chem. Soc.* **2000**, *122*, 2663–2664.
41. Tsutsumiuchi, K. A. K.; Okada, M. *Polym. J.* **1999**, *31*, 935–941.
42. Kanai, M.; Mortell, K. H.; Kiessling, L. L. *J. Am. Chem. Soc.* **1997**, *119*, 9931–9932.
43. Sanders, W. J.; Gordon, E. J.; Dwir, O.; Beck, P. J.; Alon, R.; Kiessling, L. L. *J. Biol. Chem.* **1999**, *274*, 5271–5278.
44. Mann, D. A.; Kanai, M.; Maly, D. J.; Kiessling, L. L. *J. Am. Chem. Soc.* **1998**, *120*, 10575–10582.
45. Choi, S.-K.; Mammen, M.; Whitesides, G. M. *J. Am. Chem. Soc.* **1997**, *119*, 4103–4111.
46. Hasegawa, T.; Kondoh, S.; Matsuura, K.; Kobayashi, K. *Macromolecules* **1999**, *32*, 6595–6603.
47. Tsuchida, A.; Akimoto, S.; Usui, T.; Kobayashi, K. *J. Biochem.* **1998**, *123*, 715–721.
48. Kamitakahara, H.; Suzuki, T.; Nishigori, N.; Suzuki, Y.; Kanie, O.; Wong, C.-H. *Angew. Chem., Int. Ed.* **1998**, *37*, 1524–1528.
49. Defrees, S. A.; Phillips, L.; Zalipsky, S.; Guo, L. *J. Am. Chem. Soc.* **1996**, *118*, 6101–6104.
50. Jencks, W. P. *Proc. Natl. Acad. Sci. U.S.A.* **1981**, *78*, 4046.
51. Page, M. I.; Jencks, W. P. *Proc. Natl. Acad. Sci. U.S.A.* **1971**, *68*, 1678.
52. Carver, J. P. *Pure Appl. Chem.* **1993**, *65*, 763.
53. Searle, M. S.; Williams, D. H. *J. Am. Chem. Soc.* **1992**, *114*, 10690.
54. Bhattacharyya, L.; Brewer, C. F. *Eur. J. Biochem.* **1989**, *178*, 721–726.
55. Bhattacharyya, L.; Brewer, C. F. *Eur. J. Biochem.* **1992**, *208*, 179–185.
56. Perillo, N. L.; Pace, K. E.; Seilhamer, J. J.; Baum, L. G. *Nature* **1995**, *378*, 736–739.
57. Pace, K. E.; Lee, C.; Stewart, P. L.; Baum, L. G. *J. Immunol.* **1999**, *163*, 3801.

58. Inada, Y.; Matsushima, A.; Hiroto, M.; Nishimura, H.; Kodera, Y. *Adv. Biochem. Eng. Biotechnol.* **1995**, *52*, 129.
59. Inada, Y.; Furakawa, M.; Sasaki, H.; Kodera, Y.; Hiroto, M.; Nishimura, H.; Matsushima, A. *Trends Biotechnol.* **1995**, *13*, 25.
60. Landsteiner, K.; , *The Specificity of Serological Reactions*; Dover Press: New York, 1962.
61. Mccoy, J. P.; Varani, J.; Goldstein, I. *J. Cell Res.* **1983**, *151*, 96–103.
62. Myszka, D. G. J. *J. Mol. Recognit.* **1999**, *12*, 279.
63. Zhang, Y.; Luo, S.; Tang, Y.; Yu, L.; Hou, K.-Y.; Cheng, J.-P.; Zeng, X.; Wang, P. G. *Anal. Chem.* **2006**, *78*, 2001–2008.
64. Friere, E.; Mayorga, O. L.; Straume, M. *Anal. Chem.* **1990**, *61*, 950–959.
65. Dam, T. K.; Brewer, C. F. *Chem. Rev.* **2002**, *102*, 387–430.
66. Fadda, E.; Woods, R. J. *Drug Discovery Today* **2010**, *15*.
67. Yang, Q.; Kaul, C.; Ulbricht, M. *Langmuir* **2010**, *26*, 5746–5752.
68. Ejaz, M.; Ohno, K.; Tsujii, Y.; Fukuda, T. *Macromolecules* **2000**, *33*, 2870–2874.
69. Sun, X. L.; Faucher, K. M.; M., H.; D., G.; E.L., C. *J. Am. Chem. Soc.* **2002**, *124*, 7258–7259.
70. Bundy, J. L.; Fenselau, C. *Anal. Chem.* **2001**, *73*, 751–757.
71. Renaudie, L.; Le Narvor, C.; Lepleux, E.; Roger, P. *Biomacromolecules* **2007**, *8*, 679–685.
72. Bech, L.; Meylheuc, T.; Lepoittevin, B.; Roger, P. *J. Polym. Sci., Part A: Polym. Chem.* **2007**, *45*, 2172.
73. Renaudie, L.; Narvor, C. L.; Lepleux, E.; Roger, P. *Biomacromolecules* **2007**, *8*, 679.
74. Chevolot, Y.; Martins, J.; Milosevic, N.; Leonard, D.; Zeng, S.; Malissard, M.; Berger, E. G.; Maier, P.; Mathieu, H. J.; Crout, D. H. G.; Sigrist, H. *Bioorg. Med. Chem.* **2001**, *9*, 2943.
75. Ying, L.; Yin, C.; Zhuo, R. X.; Leong, K. W.; Mao, H. Q.; Kang, E. T.; Neoh, K. G. *Biomacromolecules* **2003**, *4*, 157–165.
76. Zou, H.; Luo, Q.; Zhou, D. *J. Biochem. Biophys. Methods* **2001**, *49*, 199–240.
77. Hu, M.-X.; Xu, Z.-K. *Colloids Surf., B* **2011**, *85*, 19–25.
78. Hu, M.-X.; Yang, Q.; Xu, Z.-K. *J. Membr. Sci.* **2006**, *285*, 196–205.
79. Hu, M.-X.; Wan, L.-S.; Xu, Z.-K. *J. Membr. Sci.* **2009**, *335*, 111–117.
80. Hu, M.-X.; Wan, L.-S.; Fu, Z.-S.; Fan, Z.-Q.; Xu, Z.-K. *Macromol. Rapid Commun.* **2007**, *28*, 2325–2331.
81. Wang, C.; Ren, P.-F.; Huang, X.-J.; Wu, J.; Xu, Z.-K. *Chem. Commun.* **2011**, *47*, 3930–3932.
82. Yang, Q.; Hu, M.-X.; Dai, Z.-W.; Tian, J.; Xu, Z.-K. *Langmuir* **2006**, *22*, 9345–9349.
83. Yang, Q.; Tian, J.; Dai, Z.-W.; Hu, M.-X.; Xu, Z.-K. *Langmuir* **2006**, *22*, 10097–10102.
84. Yang, Q.; Tian, J.; Hu, M.-X.; Xu, Z.-K. *Langmuir* **2007**, *23*, 6684–6690.
85. Dai, Z.-W.; Nie, F.-Q.; Xu, Z.-K. *J. Membr. Sci.* **2005**, *264*, 20–26.
86. Dai, Z.-W.; Wan, L.-S.; Xu, Z.-K. *J. Membr. Sci.* **2008**, *325*, 479–485.

87. Xu, Z.-K.; Kou, R.-Q.; Liu, Z.-M.; Nie, F.-Q.; Xu, Y.-Y. *Macromolecules* **2003**, *36*, 2441–2447.
88. Ke, B.-B.; Wan, L.-S.; Xu, Z.-K. *Langmuir* **2010**, *26*, 8946–8952.
89. Ke, B.-B.; Wan, L.-S.; Zhang, W.-X.; Xu, Z.-K. *Polymer* **2010**, *51*, 2168–2176.
90. Che, A.-F.; Liu, Z.-M.; Huang, X.-J.; Wang, Z.-G.; Xu, Z.-K. *Biomacromolecules* **2008**, *9*, 3397–3403.
91. Che, A.-F.; Huang, X.-J.; Xu, Z.-K. *J. Membr. Sci.* **2011**, *366*, 272–277.
92. Che, A.-F.; Huang, X.-J.; Xu, Z.-K. *Macromol. Biosci.* **2010**, *10*, 955–962.
93. Che, A.-F.; Nie, F.-Q.; Huang, X.-D.; Xu, Z.-K.; Yao, K. *Polymer* **2005**, *46*, 11060–11065.
94. Yang, Q.; Wu, J.; Li, J.-J.; Hu, M.-X.; Xu, Z.-K. *Macromol. Rapid Commun.* **2006**, *27*, 1942–1948.
95. Rana, D.; Matsuura, T. *Chem. Rev.* **2010**, *110*, 2448–2471.

Chapter 12

Protein Surface Interactions and Biocompatibility: A Forty Year Perspective

John L. Brash[*]

McMaster University, School of Biomedical Engineering,
Dept. of Chemical Engineering Hamilton, Ontario, Canada L8S 4L7
[*]E-mail: brashjl@mcmaster.ca

Research in the author's laboratory on proteins at interfaces over the past four decades, with biocompatibility as the underlying theme, is reviewed. A principal focus in fundamental studies has been the dynamics of adsorbed protein layers in both simple systems and real biofluids. Investigations on protein resistant surfaces based on surface modification with poly(ethylene oxide) and poly(2-methacryloyloxyethyl phosphorylcholine) (polyMPC) have also been a major theme. Most of our work has been done in the context of biomaterials for use in blood contact and the hypothesis that blood compatibility, and biocompatibility in general, depends on control of protein adsorption has guided much of our more recent efforts. Specifically we have hypothesized that surfaces which prevent non-specific protein adsorption and promote specific adsorption of target proteins, should have improved biocompatibility. Blood contacting surfaces that promote fibrinolysis by specific adsorption of plasminogen and tissue plasminogen activator, or that prevent coagulation by adsorption of antithrombin have been investigated on this basis.

In Proteins at Interfaces III State of the Art 2012; Horbett, T., et al.;
ACS Symposium Series; American Chemical Society: Washington, DC, 2012.

Introduction

Over the past four decades our lab has carried out research aimed at understanding how proteins behave at interfaces. Such understanding is crucial for many applications in biomedicine and biotechnology, or indeed for any situation in which a surface is in contact with a protein-containing fluid. The list of such applications is long and continues to grow. It includes: medical devices (blood contacting, ophthalmic, soft tissue, orthopedic, dental), biosensors, protein purification (chromatography, filtration), therapeutic apheresis, hemodialysis, biomicrofluidic systems, drug delivery, solid phase immunoassays, biofouling (biomedical & non-biomedical (marine fouling bio/food processing)), and liposomes. Clearly motivation for studying proteins at interfaces is strong and research continues at a brisk pace. Very little was published on this topic prior to 1970. Early on I wrote a review on the subject; published in 1971 it has the title "Adsorption of Proteins and Lipids to Nonbiological Surfaces" (*1*). There are 127 references in total and of these, only 67 are papers reporting original research on protein adsorption. A search of Pubmed under "protein adsorption" returns a total of more than 20,000 papers, ranging from 3 to 8 per year in the 1950s to over 1100 in 2011. The field "took off" in the 1960s and has continued to grow over the ensuing 40 plus years.

In this chapter our work on proteins at interfaces is reviewed briefly under several headings that represent the broad themes of the research. Most of the work has been done in the context of understanding tissue-material interactions, with particular emphasis on blood-material interactions. Accordingly blood proteins and the solid-solution interface are emphasized.

Fundamental Aspects: Single Proteins and Simple Mixtures

The main "fact" or axiom of proteins at interfaces is that proteins are highly surface active: they adsorb. Alternatively it may be stated that "any protein will adsorb to any surface". This behavior is attributable to the macromolecular and amphipathic character of these molecules. Besides adsorption itself, interactions include desorption (at some interfaces), re-orientation with respect to the interface, exchange of adsorbed and dissolved proteins, diffusion of adsorbed proteins over the interface, aggregation, conformational change, and denaturation.

Some of our early work addressed the question of reversibility of adsorption (*2*). This has been an issue of considerable interest (*3*). It is not clear that it is entirely settled, but the consensus appears to be that desorption is slow, perhaps infinitely so, to the point where adsorption can be considered irreversible. One must be careful in these discussions to distinguish between protein leaving the surface in response to a decrease in solution concentration (true desorption) and protein being displaced by adding a surfactant such as sodium dodecyl sulfate (SDS). Besides its fundamental importance, reversibility is of interest for two main reasons: (1) It is of interest to know whether protein that adsorbs and then desorbs conserves its conformational and biological properties: knowledge in this regard is lacking; (2) The application of equilibrium thermodynamics requires reversibility. Estimates of affinity constants from adsorption "isotherms" have frequently been reported (*4*, *5*), but generally speaking these are "apparent", not true affinities. The finding by many groups that adsorption versus concentration data fit well to the Langmuir equation is in general fortuitous and does not mean that the Langmuir model with its assumptions of reversibility, no protein-protein interactions etc describes the interactions. The "isotherm" or adsorption-concentration behavior of proteins can be summarized as showing that adsorption increases (usually rapidly) with concentration, and reaches a plateau or quasi plateau indicating a limiting surface coverage. This limit has been interpreted in terms of the number of molecules per unit area and the molecular dimensions of the protein, often suggesting the formation of more or less tight protein monolayers (*6–9*).

Notwithstanding the fact that adsorbed proteins tend not to desorb, they nonetheless can exchange with other proteins in solution either of the same or different species. Using double radiolabeling methods we showed in early work that in the albumin-polyethylene system a dynamic equilibrium existed with equal rates of adsorption and desorption, and that the rate and extent of exchange increased with increasing shear rate and concentration (*10*). Self exchange was also demonstrated for fibrinogen interactions with polyelectrolyte complexes (*11*). In this work it was also shown that several populations of adsorbed fibrinogen molecules existed: rapidly exchanging, slowly exchanging and non-exchanging. Extrapolating from this work it is likely that there is in general a range of behavior with exchange occurring rapidly in some systems and in some not at all.

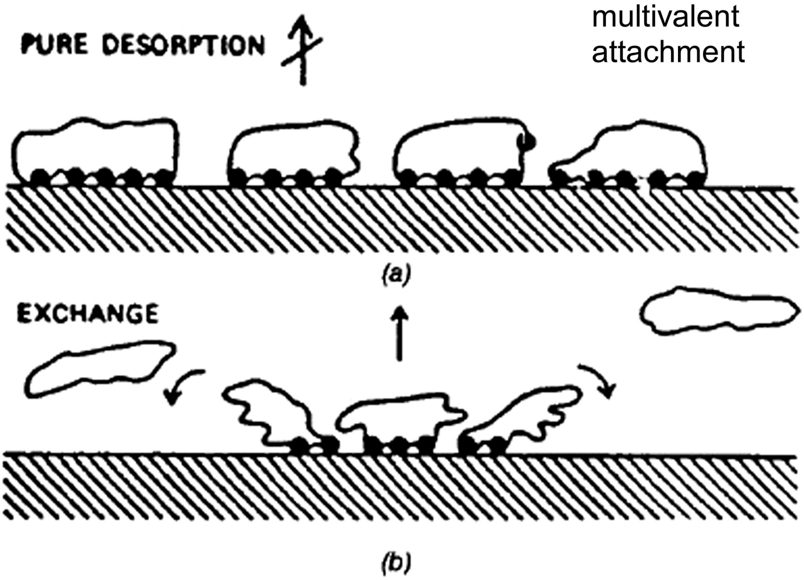

Figure 1. Explanation for non-occurrence of desorption and possible mechanism of self exchange. Reproduced with permission from reference (12). Copyright 1985 Plenum.

It seems paradoxical that proteins can exchange but not desorb, since in order to exchange, the protein has to leave the surface, i.e. desorb. A reasonable explanation is shown in Figure 1 due to Andrade (*12*).

The key idea is that proteins are attached multivalently to the surface, i.e. these very large molecules are bound to the surface not just by one interaction but several. So for desorption to occur all of the bonds must be broken simultaneously or in rapid succession, an event of very low probability. However if protein molecules are present in solution, as in the exchange scenario, one can imagine a single adsorbed protein-surface bond breaking and simultaneously a single bond forming with an adjacent solution molecule. Repetition of this process for the same adsorbed protein would result in whole molecule exchange, i.e. one molecule would leave and another arrive to take its place. This constitutes a concerted, synergistic process involving interactions between the dissolved and adsorbed molecules.

Our interests in real, as opposed to model biological systems led us to focus our attention on adsorption from systems of more than one protein and ultimately plasma and blood. We showed that in binary solutions of albumin and fibrinogen where the ratio of the protein concentrations was similar to that in blood, fibrinogen was adsorbed preferentially on both glass and polyethylene surfaces with glass showing the stronger preference (*13*). Surface enrichment of fibrinogen was also observed by Lee *et al* (*14*) for several hydrophobic surfaces in solutions of fibrinogen, gamma globulin and albumin. From these and other early observations it was tempting to conclude that fibrinogen would always be a major component of the protein layers adsorbed from blood. And indeed this is often assumed to the present day. However, this is much too simplified a view as is elaborated below in the discussion on plasma and blood.

Adsorption from Plasma and Blood

Since we were interested mainly in unraveling the complexities of blood-material interactions we turned our attention to the adsorption of proteins from plasma and blood. Our experimental technique of choice was (and is) trace labeling of proteins with radioiodine, of which there are two convenient isotopes, I-125 and I-131, allowing measurement of the adsorbed quantities of two proteins simultaneously with excellent precision. This remains, in our view, probably the best available method for the measurement of one protein in a complex system of many.

In work on adsorption from plasma (*15*), we investigated the kinetics of albumin, IgG and fibrinogen interactions with several surfaces, some hydrophilic, some hydrophobic. We discovered, contrary to predictions from single protein studies, that fibrinogen was not always a major component of the adsorbed layer. It was not detected on any of the hydrophilic surfaces, and, of the hydrophobic surfaces, it was adsorbed substantially to polystyrene but only transiently to polyethylene and siliconized glass. Albumin and IgG also showed lower adsorption than expected based on their concentrations in plasma. These results suggested that the plasma itself interacts with initially adsorbed proteins and that since the major plasma proteins were adsorbed in relatively small quantities, proteins of lower concentration, and perhaps even trace proteins, might be important.

The concept of displacement of one protein by another during plasma-surface interactions was also hinted at by these data. Beginning in the 1960s Vroman had been working on the adsorption of fibrinogen from plasma, noting in particular that fibrinogen, detectable on the surface at short exposure time by immunological methods, could not be detected at longer times (*16*). This process was referred to as "conversion" of the protein to a form no longer able to bind antibody. Using radiolabeling methods it was shown by us and by Horbett that "conversion" was in fact material loss of fibrinogen from the surface (*17*, *18*). From data on fibrinogen adsorption versus plasma concentration or time (Figure 2) we concluded that fibrinogen was adsorbed substantially at short time or from highly diluted plasma. At longer time or in more concentrated plasma the adsorbed fibrinogen was displaced by other plasma components (presumably proteins). These components would, perforce, be of higher binding affinity and lower concentration than fibrinogen. These phenomena constitute the basis of the Vroman effect which in essence describes competitive adsorption in multi-protein systems.

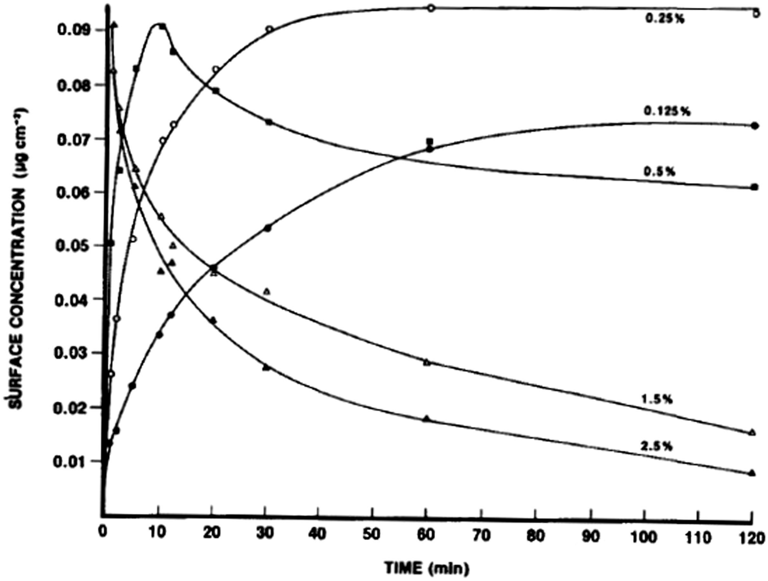

Figure 2. Fibrinogen adsorption from plasma to glass versus time at varying plasma concentration (plasma diluted with buffer). The higher the plasma concentration, the more rapidly the fibrinogen is displaced. Reproduced from reference (17). Copyright 1984 Schattauer.

We subsequently developed a more extensive data base (*19*) and found that most surfaces, except for some hydrophilic ones, showed a Vroman effect, but with quantitative differences from surface to surface, i.e. the position and height of the adsorption maxima with respect to time and plasma concentration were variable.

Identification of the displacing protein or proteins became a topic of considerable interest. Vroman *et al* suggested that proteins of the intrinsic coagulation pathway, particularly high molecular weight kininogen (HMWK), were responsible (*20*, *21*). This was supported by work in our lab using plasma deficient in, or deficient in and then reconstituted with, HMWK (*22*) which showed that the effect was greatly diminished in HMWK-deficient plasma and then was restored when purified HMWK was added back. This work also showed that fibrinogen was not removed from surfaces by plasmin digestion as might have been suspected. Further support for HMWK in this role came from experiments with binary solutions of fibrinogen and HMWK which showed that HMWK displaced initially adsorbed fibrinogen from a glass surface (*23*). Indeed, fibrinogen adsorption in this system as a function of concentration was exactly analogous to that in plasma. Bantjes *et al* proposed that, in addition to HMWK, high density lipoprotein (HDL) might be an important fibrinogen displacing species (*24*). Recent work in our lab has shown that HDL is highly surface active and that apolipoprotein AI (and therefore HDL itself) is extensively adsorbed from plasma to a wide range of materials (*25*, *26*).

Despite this and other work, including on the Vroman effect (*27*), it cannot be said that competitive adsorption is understood in any rigorous sense. Noh and Vogler (*27*) have argued that, due to the finite capacity of the surface, smaller proteins are adsorbed in preference (number basis) to larger ones and smaller proteins are exchanged for bigger ones. Vroman has suggested that in plasma, adsorption is sequential and that over time more abundant proteins are replaced by less abundant ones (*28*). This is supported by observations indicating the sequence albumin > IgG > fibrinogen > fibronectin > HMWK. That there is a sequence seems beyond dispute, but it seems likely that binding affinity as well as concentration should be a factor. Indeed there may well be several other factors that combine to determine the composition of the protein layer on any surface at any time. There is also little doubt that the layer is complex and contains many proteins as opposed to one or even a few regardless of the time of contact.

Related to competitive adsorption our lab has expended much effort in attempts to determine the composition of protein layers adsorbed from plasma. It is of course important to understand how surface properties affect the competition so that ultimately adsorption can be controlled. In these experiments surfaces are exposed to plasma under defined conditions and the adsorbed proteins are eluted with sodium dodecyl sulfate (SDS). The eluates are then subjected to SDS polyacrylamide gel electrophoresis (SDS-PAGE) for separation and to immunoblotting for identification. We have used panels selected from among 25 antibodies directed against some of the more abundant proteins, coagulation factors, complement proteins, cell adhesive proteins and others. Of course this approach is limited in the sense that only proteins probed for can be identified, leaving many others (on the order of several hundred) as “not tested”. A second limitation is that proteins must be SDS-elutable to be identified. Given the surfactant power of SDS this is less of a concern.

In general we have shown that any protein probed for on any surface is found to be present, although quantitatively there is variation from protein to protein and surface to surface (*29–40*). Figure 3 shows SDS-PAGE data for several surfaces including hydrophobic and hydrophilic polymers, liposomes, a heparinized surface (CBAS), and a polysulfone hemodialyzer membrane (*25*). The gel patterns appear similar with a concentration of bands in the 50-70 kDa region and a prominent band at ~27 kDa which has been identified as apolipoprotein AI. However there are important differences as revealed by immunoblotting.

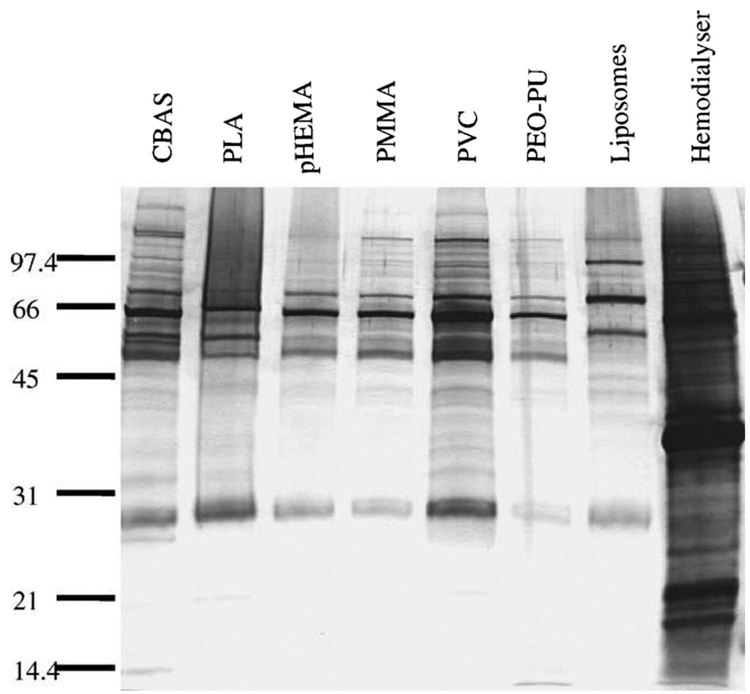

Figure 3. SDS-PAGE (12%, gold stained, reduced) of proteins eluted from surfaces after plasma contact. Reproduced from reference (25). Copyright 2002 Elsevier.

Figure 4 shows immunoblots of proteins eluted from plasma-exposed PVC. It is seen that virtually all of the proteins tested for were detected. Strong responses were seen in particular for fibrinogen, plasminogen, C3, transferrin, albumin, IgG, vitronectin, and apolipoprotein A-I. Other surfaces showed different patterns but responses were almost always strong for fibrinogen, albumin, vitronectin and apolipoprotein AI.

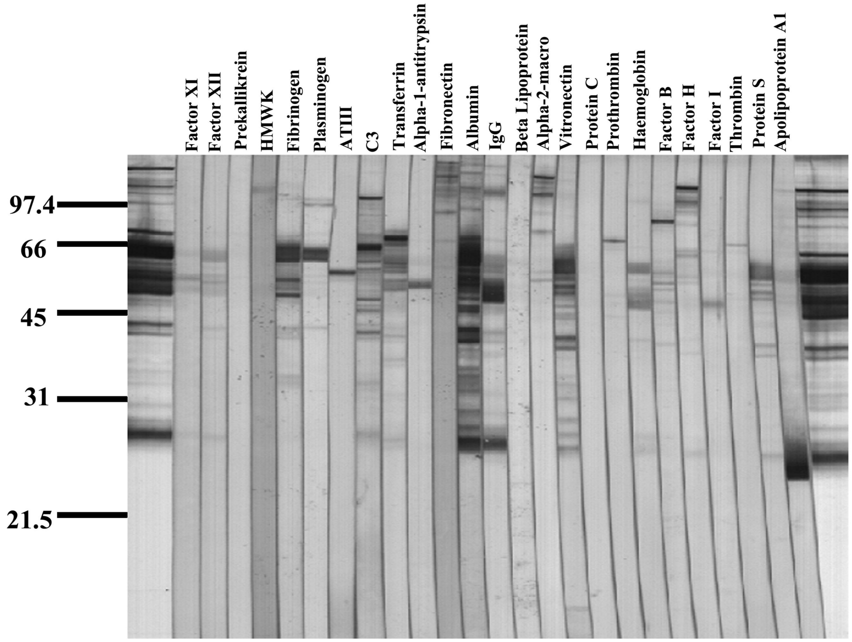
Factor XI
Factor XII
Prekallikrein
HMWK
Fibrinogen
Plasminogen
ATIII
C3
Transferrin
Alpha-1-antitrypsin
Fibronectin
Albumin
IgG
Beta Lipoprotein
Alpha-2-macro
Vitronectin
Protein C
Prothrombin
Haemoglobin
Factor B
Factor H
Factor I
Thrombin
Protein S
Apolipoprotein A1
97.4
66
45
31
21.5

Figure 4. Immunoblots of proteins associated with PVC following incubation in human plasma. Reproduced from reference (33). Copyright 2002 Wiley.

A more recent approach to the analysis of protein layer composition is the use of proteomics based methods. These often involve elution of adsorbed proteins, separation by 2-D gel electrophoresis, excision of individual spots (proteins) from the gel, proteolytic digestion to give smaller peptide fragments and identification by mass spectrometry. The latter requires the use of large data bases and informatics analysis (*41*). These methods have been widely applied to biofluids such as plasma, serum, tear fluid etc. Application to adsorbed proteins is less developed although a few reports have appeared (*42–45*). These studies emphasize the huge complexity of the adsorbed layers. Zhang *et al* identified 88 different proteins adsorbed from plasma to polystyrene nanoparticles (*45*), and Capriotti *et al* identified about 130 different plasma proteins adsorbed to cationic liposomes (*43*). Interestingly it was found in the latter work that differences among different cationic liposome compositions were minimal.

It is clear that much work remains to be done to unravel competitive protein adsorption and to determine the "proteome" of adsorbed proteins. Given the huge range of surfaces of interest, the variables such as contact time and concentration, the different bio-environments such as blood, tissue, tear fluid etc, this is a formidable and forbidding task. However, given the widely held belief that biocompatibility is strongly influenced by adsorbed proteins it remains true that detailed knowledge of the protein layers and their dependence on surface properties may be the key to solving this problem.

Resistance to Adsorption

Beginning in the 1980s a new impetus for research on proteins at interfaces came from interest in so-called "protein resistant" surfaces, and the discovery that certain hydrophilic polymers (notably polyethylene oxide) incorporated at the interface could inhibit adsorption. This has since become a major focus of research.

Non-fouling surfaces are of interest for a number of applications including marine structures, bioprocessing equipment, biosensors, and biocompatible materials. Prevention of nonspecific or indiscriminate protein adsorption is the primary requirement for such surfaces. Indeed nonspecific protein adsorption may be regarded as the "enemy" of biocompatibility since in general, tissue-material interactions begin with the rapid formation of an adsorbed protein layer, followed by cell interactions which are strongly dependent on the layer composition. For example platelets in blood adhere specifically to adsorbed fibrinogen. A key objective in biocompatibility research is to gain control over protein adsorption (*46*) and one element of such control is to minimize nonspecific adsorption.

The creation of a protein resistant surface is problematic since proteins, being amphiphilic and macromolecular, are highly surface active. Thus any interface in a protein containing system will tend to accumulate protein, and as of now there is no known surface which can prevent protein adsorption completely. As mentioned, the most successful strategy is to modify the material by the incorporation of various polymers (generally hydrophilic polymers) at the surface. Examples are polyethylene oxide (PEO), also referred to as polyethylene glycol (PEG), and its derivatives, polysaccharides (*47*), polyacrylamide (*48*), polyvinylpyrrolidone (PVP) (*49*), polyzwitterionic materials such as polybetaines (*50–52*), and mixed charge SAMs with exactly balanced positive and negative charges (*53*). A number of methods have been used to incorporate these modifiers including simple coating, blending and surface grafting by photochemical, radiation, plasma and chemical techniques.

Work in our lab has used several of these approaches and has focused on PEO/PEG and poly(2-methacryloyloxyethyl phosphorylcholine) (polyMPC) as modifiers. In early work PEO was grafted to a polyurethane-urea by introducing isocyanate groups into the surface followed by reaction with hydroxy- or amino-terminated PEO (*35*, *54*). On these surfaces adsorption from single protein solutions was reduced by up to 95%; adsorption of fibrinogen from plasma was also greatly reduced.

Making use of gold-thiol chemistry, we prepared PEO-modified surfaces by grafting thiol-terminated PEO to gold. An interesting result from this work was that for 750 and 2000 MW PEO layers, resistance to fibrinogen increased with chain density, but at densities greater than ~0.5/nm^2 adsorption increased again (*55*). It was suggested that at higher chain density, beyond the maximum in protein resistance, the PEO layer lost water giving a surface having reduced protein resistance. Using the same gold-PEO system, we also showed that the "distal" chain end group of PEO had an effect on protein resistance. For hydrophobic, methoxy, chain ends the maximum in resistance at a "critical" PEO density was again observed, whereas for hydrophilic, hydroxyl, chain ends, resistance increased up to the same "critical" density and then remained constant (*56*). Thus the distal chain end chemistry, most likely reflecting hydration state in this case, affected protein resistance but only at chain density greater than the critical value. This behavior is reminiscent of the leveling off of resistance as PEO chain length increases (*57*), which may also reflect a maximum or limiting hydration state.

In work on grafting by atom transfer radical polymerization (ATRP) we used MPC and oligoethylene glycol methacrylate (OEGMA) as monomers and silicon as substrate (*58–63*). ATRP gives grafts of uniform and controlled ("dial in") chain length. Graft density can be controlled by the initiator density. For poly(MPC) surfaces in the brush regime (~0.4 chains/nm^2), we found that the adsorption of fibrinogen and lysozyme decreased with increasing chain length of the grafts (*59*). Grafts of chain length 200 (MW 59,000 Da) gave very low adsorption levels corresponding to reductions of greater than 98% compared to unmodified silicon. Experiments using mixtures of the two proteins showed that suppression of adsorption on the poly(MPC)-grafted surfaces was similar for both, i.e. it was not dependent on protein size or charge. We also prepared surfaces with a range of chain density and molecular weight of poly(MPC) (*61*), and showed that fibrinogen adsorption was affected by both graft density and chain length, but more strongly by graft density.

OEGMA has PEO side chains and grafting gives a surface with a high density of these short PEOs. Surfaces prepared by graft ATRP of OEGMA on silicon (*60*) were found to be strongly protein resistant. In experiments to compare PEO and MPC moieties, OEGMA (MW 300, PEO side chains of average length 4.5) and MPC (MW 295, phosphoryl choline side chains) were grafted to silicon with varying density and chain length. Adsorption of fibrinogen and lysozyme to both surface types were found to decrease with increasing graft density and chain length (*62*). Moreover adsorption on the MPC and OEGMA surfaces for a given chain length and density was essentially the same; surfaces were equally resistant to fibrinogen and lysozyme whether of low or high graft density. The data from experiments with these surfaces suggested that the main determinant of the protein resistance of these surfaces is the "water barrier layer" resulting from their hydrophilic character (*63*).

Analogous poly(OEGMA) surfaces were prepared on a polyurethane-urea rather than the model silicon substrate discussed above (*64*, *65*). OEGMAs of varying MW (i.e. varying side chain length) were investigated. Trends in protein resistance similar to those for the silicon based surfaces were observed. The adsorption of both fibrinogen and lysozyme decreased with increasing poly(OEGMA) main chain length for a given side chain length (number of EO units). For a given main chain length, the fibrinogen adsorption level did not change significantly with increasing side chain length. Surprisingly, lysozyme adsorption increased with increasing side chain length, possibly due to decreasing graft density as monomer size and footprint on the surface increased.

Perhaps the most promising materials we have worked with in terms of protein resistance are blends of PEO with polyurethane (*7*, *66–68*). A great advantage of such materials is the simplicity of the preparation method. Solutions of the two components are mixed, a film is cast or a part is coated and the solvent evaporated.

In Proteins at Interfaces III State of the Art 2012; Horbett, T., et al.;
ACS Symposium Series; American Chemical Society: Washington, DC, 2012.

In an aqueous environment the PEO migrates to the interface producing a surface that is rich in PEO as indicated by water contact angles and surface elemental composition. The PEO component in these materials is a triblock copolymer with a polyurethane-like middle block which interacts with the PU matrix to prevent leaching in aqueous contact.

Materials with a range of copolymer loading (PEO content) in the matrix and varying PEO block molecular weight were prepared. On blends containing 20 wt % copolymer, fibrinogen adsorption was found to be reduced by greater than 95% for all PEO block molecular weights from 550 to 50007. At lower copolymer content (<10 wt %), fibrinogen adsorption decreased with decreasing PEO block length, i.e. there was an apparent “inverse” dependence of resistance on PEO molecular weight. In contrast to PEO-grafted surfaces, the PEO on these blend surfaces is not chain-end tethered. The copolymer is present in the form of microdomains such that in contact with aqueous fluids the density of the domains increases from bulk to surface (*67*). At the highest loading the material at the aqueous-polymer interface was essentially 100% copolymer (Figure 5). It is not clear what, if any, dependence of adsorption on PEO MW should be expected for such a structure. A possible explanation for the inverse dependence of resistance on PEO MW at low copolymer content may be increasing surface coverage of the copolymers (and therefore of the PEO) with decreasing block length. Lysozyme, a much smaller protein, showed adsorption trends similar to fibrinogen, but in competitive experiments with fibrinogen, lysozyme was preferentially adsorbed.

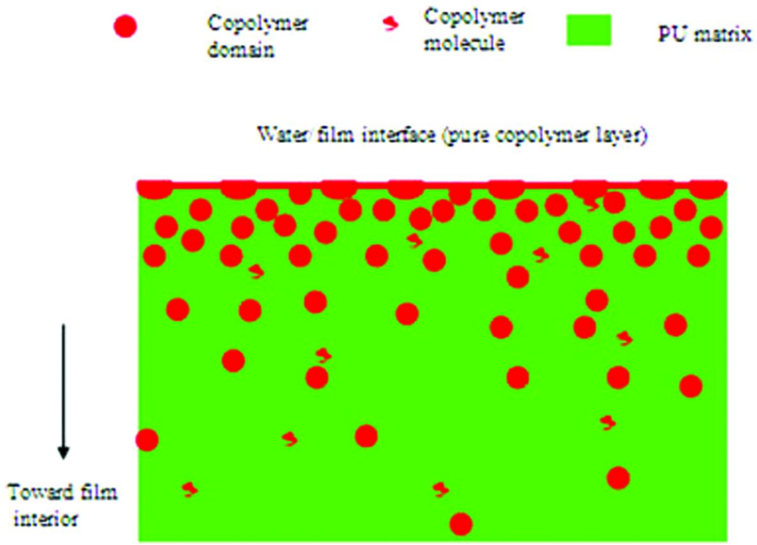

Figure 5. Suggested microstructure of 20% PEO-PU-PEO/polyurethane blends. Cross section (thickness dimension). Reproduced from reference (67). Copyright 2008 Wiley.

Adsorption from plasma to these blends showed similar trends with respect to copolymer content and PEO block length: for blends of low copolymer content, resistance to adsorption was greatest on the blend materials with the shortest PEO blocks, and increased with increasing copolymer content for all PEO block lengths (*37*). As seen in Figure 6 fibrinogen adsorption showed the Vroman effect for the matrix and the blends of higher PEO block length but not for the blend of low block length (MW 550). On materials of high copolymer content (20 wt %), fibrinogen, albumin, complement C3, and apolipoprotein AI were undetectable by immunoblotting after exposure to plasma for 3 h. This result indicates very strong protein resistance under quasi "real life" conditions.

These materials were also shown to be resistant to fibrinogen adsorption and platelet adhesion in whole blood (*68*). Both platelet adhesion and fibrinogen adsorption decreased with increasing copolymer content and with decreasing PEO block size for a given copolymer content. Fibrinogen adsorption and platelet adhesion were linearly and strongly correlated as has been reported by others (*69*, *70*).

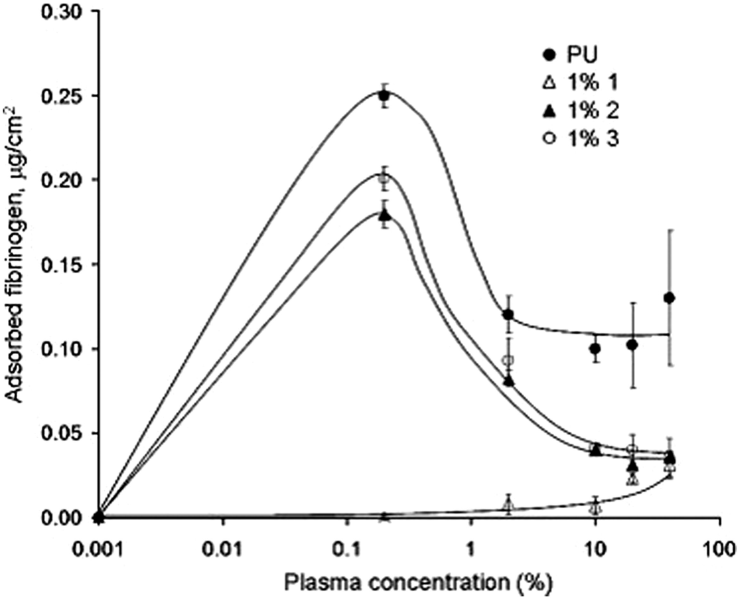

Figure 6. Fibrinogen adsorption from plasma to blends containing 1 wt % of copolymers. "1,2,3" in the legend indicate PEO block lengths of 550, 2000, and 5000 respectively. Reproduced from reference (37). Copyright 2009 Wiley.

The copolymers used in this work are analogous to poloxamers (Pluronics®) which have a center block of polypropylene oxide (PPO) flanked by end blocks of PEO. Pluronics have also been used to modify surfaces for protein resistance, for example by simple adsorption where the center segment is expected to interact strongly with a hydrophobic substrate such as polyethylene. Lee *et al* showed that protein adsorption was significantly reduced on such surfaces (*71*).

To conclude this section on protein resistance it is appropriate to comment on the mechanism whereby polymers such as PEO inhibit adsorption. Two general mechanisms have been proposed which may be referred to as "steric exclusion" and "water barrier", respectively. Steric exclusion holds that chain flexibility of the grafts (e.g. PEO) allows compression of the grafted layer by approaching proteins. This implies a loss of entropy and generates a repulsive interaction. Several lines of evidence suggest that this mechanism is not important. Prime and Whitesides showed that PEO of very short length (DP=2) is protein resistant (*72*). Also several carbon chain polymers such as PVP (*49*, *73*), with relatively stiff chains, and non-flexible mixed charge SAMs (*53*) have been shown to be protein resistant.

The water barrier mechanism holds, simply, that water associated with and strongly bound to the polymer layers "protects" the surface against adsorption. We believe that the bulk of the evidence, including our own work reviewed above, points to the "water barrier" as the more important mechanism. Rosenhahn *et al* (*74*) have reviewed this area with particular reference to PEO and have argued in favor of a mechanism based on a stable hydration layer.

Control of Protein Adsorption for Biocompatibility

According to the generally accepted paradigm of tissue-material interactions, protein adsorption is the first significant event and subsequent interactions are determined by the properties of the protein layer (*46*), i.e., the identities of the proteins in the layer and their conformational state. We have postulated, accordingly, that controlling protein adsorption is the key to biocompatibility and have proposed a design principle based on such control. The principle has two elements: (1) prevention of nonspecific or indiscriminate protein adsorption since the nonspecifically adsorbed proteins will support undesirable interactions such as platelet adhesion to adsorbed fibrinogen in blood contact; (2) promotion of the selective/exclusive adsorption of proteins that will give a desired biological activity such as anticoagulant, antibacterial, or anti-inflammatory. For this purpose ligands that will bind the target protein(s) must be built into the surface .

These ideas have formed the basis for materials development work in our lab over a number of years. The previous section on protein resistant surfaces describes our efforts on prevention or minimization of nonspecific adsorption. In this section our work on protein-selective surfaces and on surfaces that combine protein resistance with protein selectivity is summarized. The focus is exclusively on surfaces for blood contacting applications and includes:

- Surfaces that lyse fibrin by capture of endogenous plasminogen and tissue plasminogen activator (t-PA) to generate plasmin. These may be referred to as fibrinolytic surfaces.
- Surfaces that specifically adsorb or scavenge thrombin.
- Surfaces that specifically adsorb antithrombin to neutralize thrombin.
- Surfaces that capture and inhibit factor XIIa to inhibit the intrinsic coagulation pathway.

Fibrinolytic Surfaces

The idea in this work is, effectively, to mimic the physiologic process of fibrinolysis by which fibrin formed in response to vascular injury is lysed by proteolytic degradation once the injury is repaired so that vascular patency is maintained. Lysis occurs via the formation of a complex of plasminogen and t-PA on the surface of fibrin which generates plasmin, the clot-lysing enzyme (*75*). Plasminogen and t-PA bind to fibrin by interacting with carboxy-terminal lysine residues. Lysine in which the ε-amino and carboxyl groups are free has specific binding affinity for plasminogen and has been used as an affinity chromatography ligand for the isolation of plasminogen from plasma (*76*).

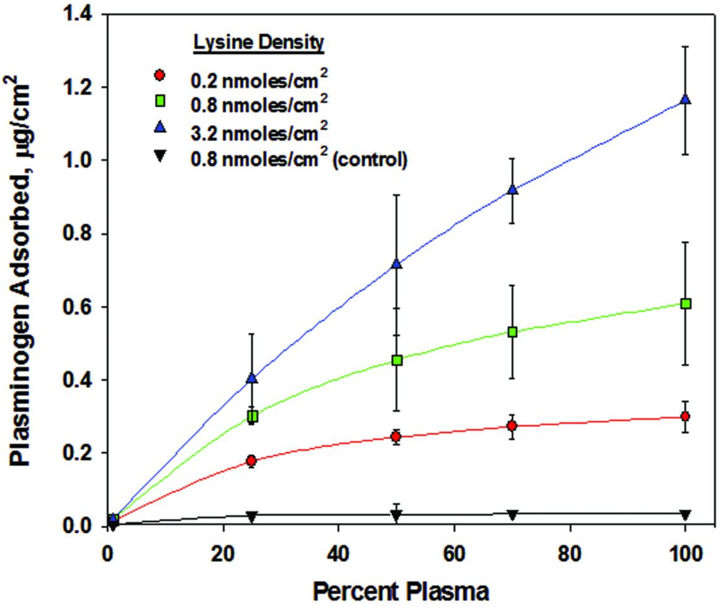

Figure 7. Plasminogen adsorption from plasma to lysine-containing polyurethane surfaces of varying lysine density. Reproduced from reference (83). Copyright 2000 Wiley.

We have adapted this approach to prepare surfaces on which lysine with its ε-amino and carboxyl groups free is immobilized. Our work in this area is extensive and only highlights are discussed here; details are provided in a recent review (*77*). In initial work, a sulfonated polyurethane (PU) was used as substrate (*78*, *79*) and lysine was attached through the sulfonate groups. Analogous silica glass materials were also investigated (*80–82*). Although these surfaces showed indications of specific interactions with plasminogen, the lysine density achievable was limited. We later developed lysinized polyurethane surfaces by photochemical attachment of a coating reagent containing covalently bound lysine (*83*). The density of lysine on these surfaces ranged from 0.2 to 3.2 nmol/cm^2, compared to typical values of ~0.003 nmol/cm^2 on the sulfonated PU and glass. Plasminogen adsorption from plasma to these surfaces increased with increasing lysine density and reached a value of 1.2 μg/cm^2 for the surface with the highest lysine density suggesting a monolayer of plasminogen and virtual exclusion of other proteins (*83*) (Figure 7). Immunoblot data showed that the high density lysine surface adsorbed only plasminogen and excluded the other plasma proteins tested for.

Since t-PA is known to bind specifically to lysine it might be expected that it would also adsorb from blood to lysinized surfaces. Investigation of the interactions of t-PA with our "plasminogen-exclusive" surfaces showed them to have a high capacity for t-PA by adsorption from buffer. However t-PA was not detected on exposure to plasma even by immunoblotting (*84*). It was also shown that t-PA pre-adsorbed from buffer was ~90% displaced upon contact with plasma. Thus neither adsorption of endogenous t-PA nor preadsorption of exogenous t-PA could be expected to generate significant plasmin for clot lysis. Nonetheless when lysinized surfaces exposed to plasma and then to t-PA were placed in fresh plasma, clots that began to form were rapidly lysed, thus demonstrating the potential of these surfaces for fibrinolysis given an appropriate source of t-PA. Experiments to assess fibrinolysis were also conducted in flowing whole blood (*85*). The blood contacting surface was pretreated with t-PA prior to blood exposure. Thrombus formation was initiated rapidly on all surfaces. On the lysine surface, but not on controls, the thrombus was lysed within minutes, providing further validation of the lysine-derivatized surface for clot lysis.

More recently in collaboration with professor Hong Chen at Soochow University we have worked on clot lysing surfaces that address both aspects of the strategy for controlling protein adsorption, i.e. inhibition of nonspecific adsorption and promotion of specific adsorption. Initial designs were based on PEO for protein resistance. Lysine was attached to the "distal" end of PEO grafts on either poly(dimethyl siloxane) (PDMS) or PU. The PEO then acts as a spacer as well as a protein resistant element, making the lysine more accessible for interactions with blood. These surfaces were shown to reduce nonspecific protein adsorption significantly and to bind plasminogen from plasma with a high degree of selectivity (*86*, *87*). They were also able to lyse clots when treated with t-PA. It was found, however, that the PEO spacer, due to its protein resistant properties, inhibited the specific binding of plasminogen, resulting in relatively slow rates of plasminogen uptake and clot lysis compared to analogous surfaces without PEO.

Investigation of the effect of PEO chain length showed that lysinized surfaces with PEO spacers of relatively short length adsorbed plasminogen and lysed fibrin more rapidly than those with longer PEO (*88*). The optimum PEO molecular weight was less than the values of a few thousand Da that have been shown to maximize protein resistance in general (*57*).

Surfaces combining poly(2-hydroxyethyl methacrylate) (poly(HEMA)) and lysine were also developed (*89*). The objective was to achieve higher densities of the protein resistant component by using “grafting from” as opposed to “grafting to” that is required with PEO. Poly(HEMA) was chosen as the spacer for its excellent biocompatibility and for its abundant side chains with active hydroxyl ends permitting the generation of a high density of lysine. HEMA was graft polymerized from a vinyl-functionalized PU surface and lysine was then coupled to the hydroxyl groups of the HEMA. The lysine density on this surface was ~4-fold greater than on a PU-PEO-Lys surface of similar structure. With increased plasminogen binding capacity, these surfaces also showed more rapid clot lysis than the PEO-lysine surfaces.

Thrombin Scavenging Surfaces

Thrombin may be regarded as the key player in coagulation and thrombosis given its direct role in the conversion of fibrinogen to fibrin and its potent platelet activating properties (*90*). Therefore if coagulation is to be avoided the formation of thrombin must be prevented or, if formed, it must be rapidly inhibited, i.e. it must be scavenged. Surfaces that bind and inhibit thrombin may be designated thrombin scavengers.

To prepare such surfaces we have used peptidic thrombin inhibitors based on the phenylalanine-proline-arginine (FPR) sequence that is known to bind and inhibit thrombin (*91*). Gold layers deposited on polyurethane were used as the substrate, and the peptides, Cys-Pro-Arg, Cys-(L)Phe-Pro-Arg, and Cys-(D)Phe-Pro-Arg, included terminal cysteine residues to allow surface attachment via the gold-thiol reaction (*92*). These peptides are related to the well-known thrombin inhibitor Phe-Pro-Arg chloromethyl ketone (PPACK) and were shown to have significant thrombin inhibitory activity in solution. We showed that the peptide-modified surfaces were able to adsorb thrombin with high affinity from buffer and that thrombin was taken up selectively from plasma. The Cys-(D)Phe-Pro-Arg modified surfaces showed particularly high affinity for thrombin. It was also shown that the activity of thrombin adsorbed on the peptide surfaces was inhibited, and inhibition was greatest on the Cys-(D)Phe-Pro-Arg surface.

Hirudin, a peptide of molecular weight 6,900 Da found in leeches, is a direct and powerful thrombin inhibitor and has also been used for surface modification (*93–96*). The N-terminal of hirudin binds to the apolar binding site of thrombin and the C-terminal interacts with the anion-binding exosite. The Pro46-Lys47-Pro48 sequence of hirudin may occupy the basic specificity pocket near the active site of thrombin. Hirudin is thus able to inhibit both free and fibrin-bound thrombin (*97*). We have developed surfaces modified with both PEO and hirudin. Two different methods of attaching the PEO and hirudin were explored, viz., “sequential” (PEO, then hirudin) and “direct” (formation of a PEO-hirudin complex, then attachment of the complex). Thrombin was found to be adsorbed more extensively to the PEO–hirudin than to the PEO-alone surfaces and adsorption was similar on the direct and sequential hirudin surfaces. When the PEO–hirudin surfaces were incubated with thrombin, the enzymatic activity decreased indicating retention of thrombin inhibitory activity in the immobilized hirudin. The sequential surface showed greater thrombin inhibitory activity than the direct, probably due to masking of binding sites by PEO in the ATH-PEO conjugate.

It should be acknowledged that surfaces modified with direct thrombin inhibitors may have limited utility in blood contacting applications since the thrombin-inhibitor interactions are irreversible, so that when the inhibitor sites are “exhausted”, no further inhibition can occur. The classical thrombin inhibitor heparin is not subject to this limitation since it acts as a recycling catalyst for the thrombin-antithrombin reaction and is regenerated after each interaction (*98*, *99*). Heparinization may thus be seen as a more promising anticoagulant strategy than modification with direct thrombin inhibitors.

Surfaces Specific for Antithrombin (AT): Heparinized Surfaces

Heparinized surfaces have been investigated extensively for blood contacting applications, but have produced mixed results, due, at least in part, to limitations inherent in heparin itself. For example, only about one-third of the molecules in “standard” heparin preparations contain the specific pentasaccharide sequence that activates AT, leading to low and variable anticoagulant activity (*100*) in a given heparin preparation. Also, heparin binds several other plasma proteins as well as AT (*101*, *102*), and this can lead to much reduced efficacy of surface-bound heparin.

As an alternative to heparin, a covalently linked complex of antithrombin and heparin (ATH) has been developed by Chan *et al* (*103*). ATH has shown increased anticoagulant activity compared to heparin (*103*), probably because, unlike heparin, all ATH molecules have at least one pentasaccharide sequence (*100*). The potential of ATH for both indirect anticoagulant activity through the catalytic effect of heparin and direct activity through permanently activated antithrombin (*100*) gives the possibility of a biomaterial surface with improved antithrombogenic properties. In addition, ATH offers more alternatives for surface attachment and, because heparin is permanently bound to AT, restricted access to other proteins (*104*).

We have prepared ATH-modified surfaces based on both gold (*105*, *106*) and polyurethane (*107*, *108*) as substrates. The surfaces were designed both to inhibit thrombin via ATH and to suppress nonspecific protein adsorption via PEO attachment. For the gold based surfaces thiol-terminated PEO was first chemisorbed then ATH was attached covalently to the distal terminus of the PEO. It was shown that ATH-immobilized surfaces bound significantly greater amounts of AT from buffer and plasma than analogous surfaces modified with heparin, indicating the enhanced anticoagulant potential of ATH (*105*). Immunoblot analysis of proteins adsorbed from plasma demonstrated that surfaces chemisorbed with PEO, whether or not also modified with ATH, inhibited non-specific adsorption. Assessment of heparin activity (anti-factor Xa assay) showed that the ratio of active heparin density to total heparin density, taken as a measure of heparin bioactivity, was greater on the ATH- than on the heparin-modified surfaces. Platelet adhesion from flowing whole blood was found to be reduced on PEO- and ATH-modified surfaces compared to bare gold, and the PEO–ATH modified surfaces, but not the heparinized surfaces, were shown to prolong the clotting time of recalcified plasma (*106*).

Similar behavior was seen for polyurethane-PEO-ATH surfaces. These were prepared by covalent attachment of PEO to the polyurethane substrate and coupling of ATH to PEO via lysine amino groups of ATH (*107*, *108*). The PEO and PEO-ATH surfaces were equally protein resistant, suggesting that the presence of ATH at the PEO chain ends did not affect nonspecific protein interactions. Surfaces were prepared with varying PEO molecular weight and it was found that PEO in the lower MW range showed greater protein resistance. Also AT binding from plasma was greatest for the PEO of lower MW (300 and 600 Da). It was concluded that for the PEO−ATH surfaces, PEO in the low MW range may be optimal for achieving an appropriate balance between resistance to nonspecific protein adsorption and the ability to take up ATH and bind antithrombin in blood contact. The need for such a balance is general for these dual-functioning surfaces.

Surfaces Specific for Factor XIIa: Inhibition of the Intrinsic Coagulation Pathway

Approaches to surface modification for the prevention of clot formation, including those discussed above, generally target the later stages of the coagulation cascade (*39*, *92*, *109*, *110*). Surface designs to interrupt the cascade in the initial stages are rare. In recent work, we have prepared surfaces modified with corn trypsin inhibitor (CTI) to bind and inhibit factor XIIa, formed in the initial step of the intrinsic system (*111–113*). Corn trypsin inhibitor is a 12,500 Da protein derived from corn kernels; it is a potent inhibitor of factor XIIa (*114*, *115*).

Surfaces were modified with both PEO and CTI. With gold as substrate, two methods of attaching the PEO and the bioactive component, “sequential” and “direct”, were again used. Both types of surface showed reduced protein adsorption, increased factor XIIa inhibition and longer clotting times compared to controls. Although the CTI density was lower on the sequential surfaces they exhibited greater CTI activity than the direct surfaces, suggesting a more favorable deployment of CTI on the surface.

The question arises for these dual functioning surfaces (protein resistant/protein specific) as to the effect of the ratio of PEO to bioactive component on biologic function: i.e., is there an optimal ratio that maximizes both protein resistance and bioactivity? We addressed this question for the gold PEO/CTI system by preparing surfaces with varying ratios of PEO to CTI. From measurements of protein resistance, factor XIIa inhibition and coagulation times, it was found that as the ratio of CTI-conjugated PEO to free PEO increased, bioactivity increased but protein resistance was relatively unaffected. It was concluded that the highest possible ratio of CTI-conjugated to free PEO, i.e. all PEOs conjugated, was optimal for factor XIIa inhibition and prolongation of plasma coagulation. The data in this study indicated that tethered PEO retains its protein resistance when the distal chain ends are conjugated. This behavior appears to be general for such “dual” functioning surfaces (*107*, *108*).

PEO-CTI surfaces were also prepared based on polyurethane as substrate using a sequential method of attachment (*113*). Both PU-PEO (control) surfaces and the PU-PEO-CTI surfaces showed low fibrinogen adsorption from buffer and plasma, indicating again that PEO retained its protein resistance when conjugated to CTI. Although the CTI density was lower on PU-PEO-CTI than on PU modified only with CTI, PU-PEO-CTI exhibited greater factor XIIa inhibition and a longer plasma clotting time, suggesting that PEO facilitates the interaction of CTI with factor XIIa.

Work on catheters coated with CTI showed, using an accelerated catheter thrombosis model in rabbits, that the time to catheter occlusion was longer with CTI-coated catheters than with unmodified catheters (*116*). From the evidence of all these studies, therefore, it appears that modification with CTI may be a useful approach to coagulation-resistant surfaces.

Conclusion

It seems appropriate to conclude this auto-review by posing the question: “What have we learned from our work of more than four decades investigating protein-surface interactions?” This question might be addressed to the entire body of literature on this subject. The present discussion is limited, however, to our own work as reviewed above. The following indicates our current perspective.

From our work on single protein systems it may be concluded that protein layers are inherently dynamic. There appears to be continuous exchange between adsorbed and dissolved proteins, albeit with varying extents and rates of exchange for different protein-surface combinations. In general hydrophilic surfaces are more dynamic than hydrophobic. As a corollary, the results of this work also indicate that there are multiple “populations” of adsorbed proteins with different exchange characteristics and therefore different binding energies.

The notion of the dynamic layer extends to multi protein systems including real biologic fluids, with strong supporting evidence from our work on fibrinogen and plasminogen adsorption from plasma. The Vroman effect, observed in several laboratories, is a manifestation of protein layer dynamics in blood-material contact. Again the parameters of these phenomena depend on the particular system being considered.

The complexity of protein layers adsorbed from blood and other biofluids is enormous. At the present time no theoretical or empirical model exists that can predict protein adsorption from real biofluids; only experiments can provide this information. However it seems unlikely that detailed layer compositions and the biologic status of the adsorbed proteins will become known in detail with present experimental techniques. Nonetheless knowledge of these layer properties and their dependence on surface properties will be important if logical approaches to biocompatible materials are to be developed. This poses an enormous challenge to the biomaterials research community.

Considerable progress has been made in the development of protein resistant surfaces. The main approach, involving incorporation of hydrophilic polymers by grafting or other means, has succeeded up to a point. Phospholipid-like surfaces, and zwitterionic surfaces in general, also show great promise. Nevertheless, the goal of total resistance, i.e. surfaces showing zero (undetectable) protein adsorption, remains elusive. It appears that water binding and structuring may be mainly responsible for protein resistance. Also in the case of polymer-modified surfaces, the evidence supports the viewpoint that polymer density on the surface is more important than polymer chain length. In total, the evidence thus far suggests that surfaces having high densities of modifier leading to maximum hydrophilicity should be pursued. However it may be that from a practical point of view a limit has been reached with this approach implying that fresh approaches are needed.

The concept of surface design for biocompatibility based on control of protein adsorption, and specifically prevention of non-specific adsorption combined with promotion of specific adsorption, appears valid but requires much more exploration and refinement. From our work thus far on fibrinolytic surfaces and anticoagulant surfaces, practical implementation of the concept appears feasible, subject to the limitations on complete prevention of non-specific adsorption referred to. Other challenges are achieving sufficiently high surface densities of the protein capture ligand, and ensuring continuity of function over time, probably requiring that the specific interactions be reversible. Balancing protein resistance and specificity, which may be in mutual opposition, is also an issue.

Acknowledgments

I am most grateful to all my students, co-workers and colleagues who have contributed to the work described in this chapter. The achievements of our lab owe as much to their input as to mine. Their names can be found in the reference list. Financial support over the years by the Natural Sciences and Engineering Research Council of Canada, the Canadian Institutes of Health Research (previously the Medical Research Council of Canada), and the Heart and Stroke Foundation of Ontario is also gratefully acknowledged.

References

1. Brash, J. L.; Lyman, D. J. In *Biosurfaces*; Hair, M. L., Ed.; Marcel Dekker: New York, 1971; Vol 1, pp 177−232.
2. Chan, B. M. C.; Brash, J. L. *J. Colloid Interface Sci.* **1981**, *82*, 217–225.
3. Norde, W. *Adv. Colloid Interface Sci.* **1986**, *25*, 267–340.
4. Boisson, C.; Jozefonvicz, J.; Brash, J. L. *Biomaterials* **1988**, *9*, 47–52.
5. Valero Vidal, C.; Olmo Juan, A.; Igual Muñoz, A. *Colloids Surf., B* **2010**, *80*, 1–11.
6. Brash, J. L.; Lyman, D. J. *J. Biomed. Mater. Res.* **1969**, *3*, 175–189.
7. Tan, J.; McClung, W. G.; Brash, J. L. *J. Biomed. Mater. Res.* **2008**, *85A*, 873–880.
8. Norde, W. *Adv. Colloid Interface Sci.* **1986**, *25*, 267–340.
9. Vermeer, A. W.; Giacomelli, C. E.; Norde, W. *Biochim. Biophys. Acta* **2001**, *1526*, 61–9.

10. Brash, J. L.; Samak, Q. *J. Colloid Interface Sci.* **1978**, *65*, 494–504.
11. Brash, J. L.; Uniyal, S.; Pusineri, C.; Schmitt, A. *J. Colloid Interface Sci.* **1983**, *95*, 28–37.
12. Andrade, J. D. In *Surface and Interfacial Aspects of Biomedical Polymers*; Andrade, J. D., Ed.; Plenum: New York, 1985. Vol 2, pp 1−80.
13. Brash, J. L.; Davidson, V. J. *Thrombos. Res.* **1976**, *9*, 249–259.
14. Lee, R. G.; Adamson, C.; Kim, S. W. *Thrombos. Res.* **1974**, *4*, 485–490.
15. Uniyal, S.; Brash, J. L. *Thrombos. Haemostasisis* **1982**, *47*, 285–290.
16. Vroman, L.; Adams, A. L. *J. Biomed. Mater. Res.* **1969**, *3*, 43–67.
17. Brash, J. L.; ten Hove, P. *Thrombos. Haemostasisis* **1984**, *51*, 326–330.
18. Horbett, T. A. *Thrombos. Haemostasis* **1984**, *51*, 174–81.
19. Wojciechowski, P.; ten Hove, P.; Brash, J. L. *J. Colloid Interface Sci.* **1986**, *111*, 455–465.
20. Vroman, L.; Adams, A. L.; Fischer, G. C.; Munoz, P. C. *Blood* **1980**, *55*, 156–59.
21. Schmaier, A. H.; Silver, L.; Adams, A. L.; Fischer, G. C.; Munoz, P. C.; Vroman, L.; Colman, R,W. *Thrombos. Res.* **1984**, *33*, 51–67.
22. Brash, J. L.; Scott, C. F.; ten Hove, P.; Wojciechowski, P.; Colman, R. W. *Blood* **1988**, *71*, 932–939.
23. Déjardin, P.; ten Hove, P.; Yu, X. J.; Brash, J. L. *Langmuir* **1995**, *11*, 4001–4007.
24. Breemhaar, W.; Brinkman, E.; Ellens, D. J.; Beugeling, T; Bantjes, A. *Biomaterials* **1984**, *5*, 269–74.
25. Cornelius, R. M.; Archambault, J.; Brash, J. L. *Biomaterials* **2002**, *23*, 3583–3587.
26. Cornelius, R. M.; Macri, J.; Brash, J. L. *J. Biomed. Mater. Res.* **2011**, *99A*, 109–1152011.
27. Noh, H.; Vogler, E. A. *Biomaterials* **2007**, *28*, 405–422.
28. Vroman, L. *Sem. Thrombos. Hemostasis* **1987**, *13*, 79–85.
29. Mulzer, S. R.; Brash, J. L. *J. Biomed. Mater. Res.* **1989**, *23*, 1483–1504.
30. Babensee, J. E.; Cornelius, R. M.; Brash, J. L.; Sefton, M. V. *Biomaterials* **1998**, *19*, 839–849.
31. Yamazaki, A.; Winnik, F. M.; Cornelius, R. M.; Brash, J. L. *Biochim. Biophys. Acta* **1999**, *1421*, 103–115.
32. McClung, W. G.; Clapper, D. L.; Hu, S. P.; Brash, J. L *J. Biomed. Mater. Res.* **2000**, *49*, 409–414.
33. Cornelius, R. M.; Archambault, J. G.; Berry, L.; Chan, A.; Brash, J. L. *J. Biomed. Mater. Res.* **2002**, *60*, 622–632.
34. Cornelius, R. M.; Sanchez, J.; Olsson, P.; Brash, J. L. *J. Biomed. Mater. Res.* **2003**, *67A*, 475–83.
35. Archambault, J. G.; Brash, J. L. *Colloids Surf., B* **2004**, *39*, 9–16.
36. Unsworth, L. D.; Sheardown, H.; Brash, J. L. *Biomaterials* **2005**, *26*, 5927–33.
37. Tan, J.; Brash, J. L. *J. Biomed. Mater. Res.* **2009**, *90A*, 196–204.
38. Sask, K. N.; Zhitomirsky, I.; Berry, L. R.; Chan, A. K. C.; Brash, J. L. *Acta Biomater.* **2010**, *6*, 2911–19.
39. Alibeik, S.; Zhu, S.; Brash, J. L. *Colloids Surf., B* **2010**, *81*, 389–396.

40. Cornelius, R. M.; McClung, W. G.; Richardson, R. M. A.; Estridge, C.; Plaskos, N.; Yip, C. M.; Brash, J. L. *ASAIO J.* **2002**, *48*, 45–56.
41. Cristea, I. M.; Gaskell, S. J.; Whetton, A. J. *Blood* **2004**, *103*, 3624–3634.
42. Oughlis, S.; Lessim, S.; Changotade, S.; Bollotte, F.; Poirier, F.; Helary, G.; Lataillade, J. J.; Migonney, V.; Lutomski, D. *J. Chromatogr., B* **2011**, *879*, 3681–3687.
43. Capriotti, A. L.; Caracciolo, G.; Cavaliere, C.; Crescenzi, C.; Pozzi, D.; Laganà, A. *Anal. Bioanal. Chem.* **2011**, *40*, 195–202.
44. Sund, J.; Alenius, H.; Vippola, M.; Savolainen, K.; Puustinen, A. *ACS Nano* **2011**, *5*, 4300–4309.
45. Zhang, H.; Burnum, K. E.; Lun, M. L.; Petritis, B. O.; Kim, J. S.; Qian, W. J.; Moore, R. J.; Heredia-Langner, A.; Webb-Robertson, B. L. M.; Thrall, B. D.; Camp, D. G., II; Smith, R. D.; Pounds, J. G.; Liu, T. *Proteomics* **2011**, *11*, 4569–4577.
46. Brash, J. L. *J. Biomat. Sci., Polym. Ed.* **2000**, *11*, 1135–1146.
47. McArthur, S. L.; McLean, K. M.; Kingshott, P.; St John, H. A. W.; Chatelier, R. C.; Griesser, H. J. *Colloids Surf., B* **2000**, *17*, 37–48.
48. D. Xiao, D.; Zhang, H.; Wirth, M. *Langmuir* **2002**, *18*, 9971–9976.
49. Telford, A. M.; James, M.; Meagher, L.; Neto, C. *ACS Appl. Mater. Interfaces* **2010**, *2*, 2399–2408.
50. Zhang, Z.; Chen, S.; Jiang, S. *Biomacromolecules* **2006**, *7*, 3311–3315.
51. Vaisocherová, H.; Yang, W.; Zhang, Z.; Cao, Z.; Cheng, G.; Piliarik, M.; Homola, J.; Jiang, S. *Anal. Chem.* **2008**, *80*, 7894–7901.
52. Z. Jin, Z.; W. Feng, W.; S. Zhu, S.; H. Sheardown, H.; Brash, J. L. *J. Biomater. Sci., Polym, Ed.* **2010**, *21*, 1331–1344.
53. Chen, S.; Yu, F.; Yu, Q.; He, Y.; Jiang, S. *Langmuir* **2006**, *22*, 8186–8191.
54. Archambault, J. G.; Brash, J. L. *Colloids Surf., B* **2004**, *33*, 111–120.
55. Unsworth, L. D.; Sheardown, H.; Brash, J. L. *Langmuir* **2005**, *21*, 1036–1041.
56. Unsworth, L. D.; Sheardown, H.; Brash, J. L. *Langmuir* **2008**, *24*, 1924–29.
57. Gombotz, W. R.; Guanghui, W.; Horbett, T. A.; Hoffman, A. S. *J. Biomed. Mater. Res.* **1991**, *25*, 1547–62.
58. Feng, W.; Brash, J. L.; Zhu, S. *J. Polym. Sci., Part A-1: Polym. Chem.* **2004**, *42*, 2931–2942.
59. Feng, W.; Zhu, S.; Ishihara, K.; Brash, J. L. *Langmuir* **2005**, *21*, 5980–87.
60. Feng, W.; Chen, R.; Brash, J. L.; Zhu, S. *Macromol Rapid Commun* **2005**, *26*, 1383–88.
61. Feng, W.; Brash, J. L.; Zhu, S. *Biomaterials* **2006**, *27*, 847–55.
62. Feng, W.; Zhu, S. P.; Ishihara, K.; Brash, J. L. *Biointerphases* **2006**, *1*, 50–60.
63. Feng, W.; Nieh, M-P.; Zhu, S.; Brash, J. L.; Harroun, T. A.; Katsaras, J. *Biointerphases* **2007**, *2*, 34–43.
64. Jin, Z.; Feng, W.; Beisser, K.; Zhu, S.; Sheardown, H.; Brash, J. L. *Colloids Surf., B* **2009**, *70*, 53–59.
65. Jin, Z.; Feng, W.; Zhu, S.; Sheardown, H.; Brash, J. L. *J. Biomed. Mater. Res.* **2009**, *91A*, 1189–1201.
66. Tan, J.; Brash, J. L. *J. Appl. Polym. Sci.* **2008**, *108*, 1617–28.
67. Tan, J.; Brash, J. L. *J. Biomed. Mater. Res.* **2008**, *85A*, 862–872.

68. Tan, J.; McClung, W. G,; Brash, J. L. *J. Biomater. Sci., Polym. Ed.*, accepted.
69. Tsai, W. B.; Grunkemeier, J. M.; McFarland, C. D.; Horbett, T. A. *J. Biomed. Mater. Res.* **2002**, *60*, 348–359.
70. Tsai, W. B.; Grunkemeier, J. M.; Horbett, T. A. *J. Biomed. Mater. Res.* **1999**, *44*, 130–139.
71. Lee, J. H.; Kopecek, J.; Andrade, J. D. *J. Biomed. Mater. Res.* **1989**, *23*, 351–68.
72. Prime, K.; Whitesides, G. *Science* **1991**, *252*, 1164–1167.
73. Robinson, S.; Williams, P. A. *Langmuir* **2002**, *18*, 8743–8748.
74. Rosenhahn, H.; Schilp, S.; Kreuzer, H. J.; Grunze, M. *Phys. Chem. Chem. Phys.* **2010**, *12*, 4275–4286.
75. Anglés-Cano, E. *Chem. Phys. Lipids* **1994**, *67-68*, 353–62.
76. Deutsch, D. G.; Mertz, E. T. *Science* **1970**, *170*, 1095–1096.
77. Li, D.; Chen, H.; Brash, J. L. *Colloids Surf., B* **2011**, *86*, 1–6.
78. K. Woodhouse, K. A.; Wojciechowski, P.; Santerre, J. P.; Brash, J. L. *J. Colloid Interface Sci.* **1992**, *152*, 60–69.
79. Woodhouse, K. A.; Brash, J. L. *Biomaterials* **1992**, *13*, 1103–1108.
80. Woodhouse, K. A.; Brash, J. L. *J. Colloid Interface Sci.* **1994**, *164*, 40–47.
81. Woodhouse, K. A.; Weitz, J. I.; Brash, J. L. *J. Biomed. Mater. Res.* **1994**, *28*, 407–415.
82. Woodhouse, K. A.; Weitz, J. I.; Brash, J. L. *Biomaterials* **1996**, *17*, 75–77.
83. McClung, W. G.; Clapper, D. L.; Hu, S. P.; Brash, J. L. *J. Biomed. Mater. Res.* **2000**, *49*, 409–414.
84. McClung, W. G.; Clapper, D. L.; Anderson, A. B.; Babcock, D. E.; Brash, J. L. *J. Biomed Mater Res***.** **2003**, *66A*, 795–801.
85. McClung, W. G.; Babcock, D. E.; Brash, J. L. *J. Biomed. Mater. Res.* **2007**, *81A*, 644–651.
86. Chen, H.; Wang, L.; Zhang, Y.; Li, D.; McClung, W. G.; Brook, M. A.; Sheardown, H.; Brash, J. L. *Macromol. Biosci.* **2008**, *8*, 863–870.
87. Chen, H.; Zhang, Y.; Li, D.; Hu, X.; Wang, L.; McClung, W. G.; Brash, J. L. *J. Biomed. Mater. Res.* **2009**, *90A*, 940–946.
88. Li, D.; Chen, H.; McClung, W. G; Brash, J. L. *Acta Biomater.* **2009**, *5*, 1864–1871.
89. Li, D.; Chen, H.; Wang, S.; Wu, Z.; Brash, J. L. *Acta Biomater.* **2011**, *7*, 954–958.
90. Davie, E. W.; Fujikawa, K.; Kisiel, W. *Biochemistry* **1991**, *30*, 10363–10370.
91. Claeson, G. *Blood Coagulation Fibrinolysis* **1994**, *5*, 411–436.
92. Sun, X. L.; Sheardown, H.; Tengvall, P.; Brash, J. L. *J. Biomed. Mater. Res.* **2000**, *49*, 66–78.
93. Phaneuf, M. D.; Szycher, M.; Berceli, S. A.; Dempsey, D. J.; Quist, W. C.; LoGerfo, F. W. *Artif. Organs* **1998**, *22*, 657–665.
94. Seifert, B.; Romaniuk, P.; Groth, T. *Biomaterials* **1997**, *18*, 1495–1502.
95. Lahann, J.; Klee, D.; Pluester, W.; Hoecker, H. *Biomaterials* **2001**, *22*, 817–826.
96. Horne, M. K.; Brokaw, K. J. *Thrombos. Res.* **2003**, *112*, 111–115.
97. Grutter, M. G.; Priestle, J. P; Rahuel, J.; Grossenbacher, H.; Bode, W.; Hofsteenge, J.; Stone, S. R. *EMBO J.* **1990**, *9*, 2361–2365.

98. Carrell, R.; Skinner, R.; Wardell, M.; Whisstock, J. *Mol. Med. Today* **1995**, *1*, 226–31.
99. Jin, L.; Abrahams, J. P.; Skinner, R.; Petitou, M.; Pike, R. N.; Carrell, R. W. *Proc. Natl. Acad. Sci. U.S.A.* **1997**, *94*, 14683–8.
100. Berry, L.; Stafford, A.; Fredenburgh, J.; O'Brodovich, H.; Mitchell, L.; Weitz, J.; et al. *J. Biol. Chem.* **1998**, *273*, 34730–6.
101. Young, E.; Prins, M.; Levine, M. N.; Hirsh, J. *Thrombos. Haemostasis* **1992**, *67*, 639–43.
102. Manson, L.; Weitz, J. I.; Podor, T. J.; Hirsh, J.; Young, E. *J. Lab Clin. Med.* **1997**, *130*, 649–55.
103. Chan, A.; Berry, L.; Obrodovich, H.; Klement, P.; Mitchell, L.; Baranowski, B.; et al. *J. Biol. Chem.* **1997**, *272*, 22111–22117.
104. Berry, L. R., Andrew, M., Chan, A. K. C. In *Polymeric biomaterials. Part II: Medical and Pharmaceutical Applications of Polymers,* 2nd ed.; Dumitriu, S., Ed.; Marcel Dekker: New York, 2001; pp 669−702.
105. Sask, K. N.; Zhitomirsky, I.; Berry, L. R.; Chan, A. K. C.; Brash, J. L. *Acta Biomater.* **2010**, *6*, 2911–19.
106. Sask, K. N.; McClung, W. G.; Berry, L. R.; Chan, A. K. C.; Brash, J. L. *Acta Biomater.* **2011**, *7*, 2029–34.
107. Sask, K. N.; Berry, L. R.; Chan, A. K. C.; Brash, J. L. *Langmuir* **2012**, *28*, 2099–2106.
108. Sask, K. N.; Berry, L. R.; Chan, A. K. C.; Brash, J. L. *J. Biomed. Mater. Res., Part A* **2012**, *100A*, 2821–2828.
109. Du, Y. J.; Brash, J. L.; McClung, G.; Berry, L. R.; Klement, P.; Chan, A. K. C. *J. Biomed. Mater. Res.* **2007**, *80A*, 216–225.
110. Chen, H.; Chen, Y.; Sheardown, H.; Brook, M. A. *Biomaterials* **2005**, *26*, 7418–7424.
111. Alibeik, S.; Zhu, S.; Yau, J.; Weitz, J. I.; Brash, J. L. *Acta Biomaterialia* **2011**, *7*, 4177–4186.
112. Alibeik, S.; Zhu, S.; Yau, J. W.; Weitz, J. I.; Brash, J. L. *J. Biomed. Mater. Res.* **2012**, *100A*, 856–862.
113. Alibeik, S.; Zhu, S.; Yau, J. W; Weitz, J. I.; Brash, J. L. *J. Biomat. Sci., Polym. Ed.* **2012**, *23*, 1981–1993.
114. Hojima, Y.; Pierce, J. V.; Pisano, J. J. *Thrombos. Res.* **1980**, *20*, 149–162.
115. Mahoney, W. C.; Hermodson, M. A.; Jones, B.; Powers, D. D.; Corfman, R. S.; Reeck, G. R. *J. Biol. Chem.* **1984**, *259*, 8412–8416.
116. Yau, J. W.; Stafford, A. R; Fredenburgh, J. C; Brash, J. L.; Roberts, R.; Weitz, J. I. *Acta Biomater.* **2012**, *8*, 4092–4100.

Chapter 13

Regulation of Protein/Surface Interactions by Surface Chemical Modification and Topographic Design

Dan Li and Hong Chen*

Jiangsu Key Laboratory of Advanced Functional Polymer Design and Application, Department of Polymer Science and Engineering, College of Chemistry, Chemical Engineering and Materials Science, Soochow University, Suzhou, 215123, P. R. China
***E-mail: chenh@suda.edu.cn**

Protein/surface interaction has long been an important topic in life sciences and materials engineering. Regulating these interactions is not only of great theoretical interest but is also key in meeting the requirements of many biomedical applications. The surface properties, including chemistry and topography, of a solid material are dominant factors influencing protein adsorption. In this chapter, we summarize our contributions to understanding protein/surface interactions and regulating these interactions by surface chemical modification and topographic design. It is hoped that this report may be of help for readers who wish to improve the biological performance of their materials by surface engineering.

Protein/surface interactions have been recognized as critical in a number of fields including blood-contact materials, biological separations and biosensors (*1–4*). Different applications require different interactions. For example, if used as the platform for a protein sensor (*5*, *6*), the surface should have high binding capacity for the target protein while resisting all nonspecific protein adsorption; if used as the substrate for protein purification or protein delivery (*7*), the surface should have the ability to regulate adsorption and desorption. Therefore, it is

In Proteins at Interfaces III State of the Art 2012; Horbett, T., et al.;
ACS Symposium Series; American Chemical Society: Washington, DC, 2012.

crucial to be able to control protein/surface interactions to meet the requirements of a specific application. In addition, protein adsorption is believed to be the first significant event when a material comes into contact with a biological environment, and the events which follow, including cell/surface interactions, are largely dependent on the properties of the adsorbed layer (*8*). If the initial protein adsorption can be controlled, then one may be able to prevent undesirable events and promote favorable ones.

Protein adsorption behavior may be affected by both surface chemistry and topography (*9–12*). The effect of surface chemistry is more obvious since proteins interact with materials through the chemical groups exposed on their respective surfaces. With the development of chemical modification techniques, surface chemical composition can be varied over a wide range, and the spatial distribution of the modifiers on the surface can be controlled. This allows extensive investigation of the correlations between surface chemistry and protein adsorption and the formulation of approaches for regulating surface/protein interactions by chemical modification. The effects of surface topography have recently received keen attention. Topographical properties such as roughness, curvature and geometry have been correlated to protein behavior. More importantly, the synergy of topography and chemical composition may endow a surface with unexpected properties which have not been considered in the context of regulating protein/surface interactions.

Our research is mainly focused on understanding and regulating protein/surface interactions. Chemical modification strategies such as incorporating bioinert polymers to resist nonspecific protein adsorption (bioinert surface) and conjugating special ligands for specific protein recognition (bioactive surface) have been successfully applied to prepare biofunctional surfaces including antifouling surfaces, antithrombogenic surfaces and fibrinolytic surfaces. Recent work also includes stimuli-responsive surfaces, chiral surfaces and amphiphilic diblock copolymer modified surfaces. With respect to topographical surfaces, we have paid particular attention to the synergy of topography and surface chemistry, especially for stimuli-responsive polymers. It is our hope that by providing details of these examples from the work of our lab, further progress in the regulation of protein/surface interactions may be realized.

Regulation of Protein/Surface Interactions by Chemical Modification

Proteins contain various chemical functions and may interact with surfaces by hydrogen bonding, hydrophobic interactions and electrostatic interactions. Therefore, surface chemistry is the main property influencing protein adsorption. Over the past several years we have made great efforts to develop methods for the regulation of protein/surface interactions by incorporating various molecules, including bioinert polymers, high affinity ligands, stimuli-responsive polymers, stereoisomeric molecules and amphiphilic diblock copolymers.

Bioinert Surfaces

Protein resistance or bioinertness is required in most biomedical applications of materials. Considerable effort has been made to find/develop bioinert surface modifiers. A number of hydrophilic polymers have been shown to be protein resistant such as poly(ethylene glycol) (PEG) (*13*), poly(N-vinylpyrrolidone) (PVP) (*14*), poly(2-methacryloyloxyethyl phosphorylcholine) (PMPC) (*15*), etc. The key consideration is how to incorporate these bioinert polymers into material surfaces. For commercialization purposes, simple methods such as blending the modifier with the bulk material are preferred. For example, we prepared a protein resistant poly(dimethylsiloxane) (PDMS) surface by incorporating mono- or bis-triethoxysilyl PEG (TES-PEG-Me or TES-PEG-TES) into PDMS during curing. As shown in Figure 1A, PEG was covalently bound to the PDMS backbone through TES groups and the PEG chains migrated to the surface when exposed to water (*16*, *17*). PEG incorporated by this method, namely chemical blending, is superior in durability to physically blended PEG, which is prone to leaching out in an aqueous environment.

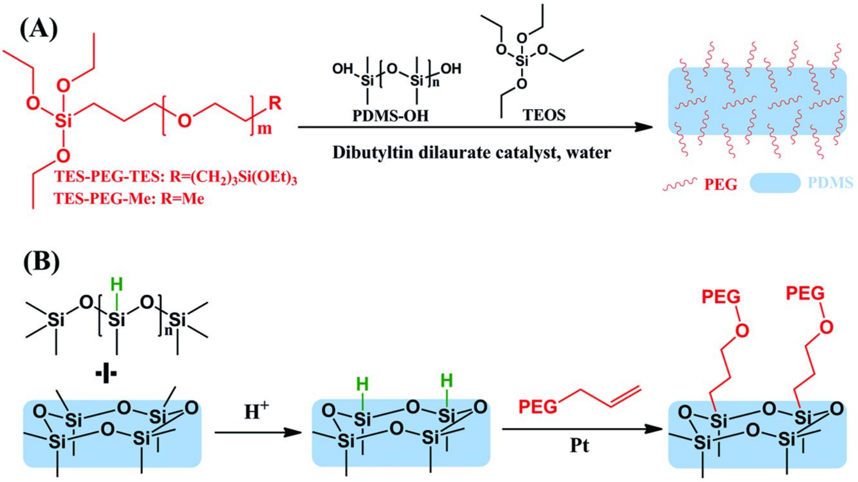

Figure 1. Surface modification of PDMS with PEG: (A) blending, (B) surface grafting.

Compared to bulk modification, covalent grafting of bioinert polymers to a substrate is an effective way to form a stable protein-resistant surface with minimal or no effect on the bulk mechanical properties. We have described an effective method to graft PEG chemically on PDMS surfaces in which abundant Si-H groups were created by acid-catalyzed equilibration in the presence of polymethylhydrosiloxane (MeHSiO)*n*. An allyl-terminated PEG was then grafted by platinum-catalyzed hydrosilylation (Figure 1B). Measurements using radiolabeling indicated that fibrinogen adsorption from buffer to the PEG-modified PDMS was reduced by more than 90% compared with controls (*18*). In follow on work, a chemically heterogeneous patterned surface was fabricated from the PEGylated PDMS surface by vacuum ultraviolet (VUV) lithography. On exposure to a solution of fluorescein labeled fibrinogen, the surface exhibited distinct localization of protein on the UV exposed areas (*19*).

Surface grafting of bioinert polymers, typically PEO, by the "grafting to" method may limit the grafting density due to steric restrictions and thus limit the protein resistance of the surface. Since surface initiated atom transfer radical polymerization (SI-ATRP) was first reported in 1997 (*20*), many researchers have turned to "grafting from" strategies, which can readily generate non-fouling surfaces by forming dense layers of bioinert polymer (*21–23*). Very recently, we prepared, for the first time, well controlled PVP-grafted silicon surfaces using SI-ATRP (Figure 2). Polymerization of the nonconjugated monomer NVP was achieved using CuCl/5,7,7,12,14,14-hexamethyl-1,4,8,11-tetraazacyclotetradecane (Me$_6$TATD) as catalyst. The surface with a PVP thickness of 15 nm reduced the level of adsorption of fibrinogen, human serum albumin (HSA), and lysozyme by 75, 93, and 81%, respectively (*24*). A similar ATRP system was also successfully used to prepare PVP-grafted PDMS surfaces (Figure 2). It was shown that the modified surfaces were strongly hydrophilic, and fibrinogen adsorption was reduced by 96% compared to unmodified PDMS (*25*). However, in spite of the extensive application of SI-ATRP, it is not suitable for the surface modification of some polymeric materials since the metal ions may penetrate into the bulk. Conventional radical polymerization therefore remains important. Recently, we introduced a facile method for radical polymerization on polyurethane (PU) surfaces. In this method, vinyl groups are incorporated into the PU surface; these groups are subsequently "copolymerized" with double-bond containing monomers. We showed that fibrinogen adsorption was reduced by 94% and 87% respectively on poly(N-isopropyl acrylamide) (PNIPAAm) and poly(2-hydroxyethyl methacrylate) (PHEMA) grafted PU surfaces prepared in this way (*26*). In addition, the molecular weight of the surface-grafted PNIPAAm could be controlled by adjusting the monomer concentration. Protein adsorption was found to decrease gradually with increasing molecular weight of PNIPAAm up to 7.9×10^4 where it reached a plateau (*27*).

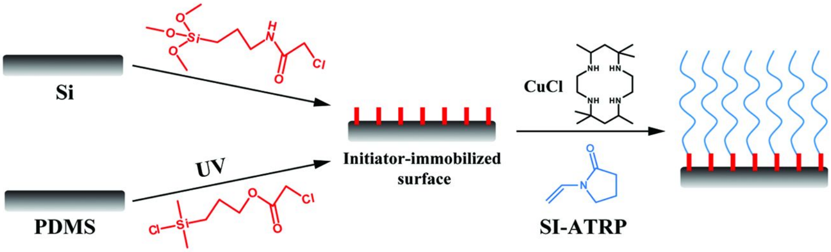

Figure 2. SI-ATRP of N-vinylpyrrolidone on silicon and PDMS surfaces.

To date, many surfaces have been reported to be protein resistant after chemical modification with different chemical compounds. Great efforts have been made to correlate the properties of single molecules or macromolecules with protein-resistance. However, in recent years, increasing attention is being paid to the distribution of the functional groups or polymer chains. For example, Jiang and coworkers demonstrated, using mixed-charge SAMs and polymer coatings, that when the positive charges and negative charges are uniformly distributed at the molecular level, the surface has ultra-low fouling properties due to strong hydration (*28*, *29*). In the case of polymer brush modified surfaces, structural parameters such as the length and surface density of the polymer chains should always be taken into account. For instance, on the PVP-grafted silicon surface mentioned above, fibrinogen adsorption decreased gradually with increasing PVP thickness and the critical thickness for maximum protein resistance was found to be ~13 nm (*24*). This behavior has been observed on most bioinert polymer grafted surfaces (*15*, *30*).

With respect to graft density, many studies have shown that protein adsorption decreases with increasing graft density of bioinert polymer (*30–33*), while other studies are more ambiguous. Brash et al. investigated protein adsorption on PEO grafted model surfaces with varying chain length and chain density. They found that protein resistance increased with chain density to a maximum at a critical density beyond which adsorption increased. It was suggested that, at high chain density, the surface-grafted PEO is dehydrated giving a surface that is no longer protein resistant (*34*). We also investigated the effect of PEG graft density and conformation on protein adsorption to a PEG-grafted surface. PU surfaces were modified using monobenzyloxy polyethylene glycol (BPEG), then PEG or monomethoxy poly(ethylene glycol) (MPEG) with various chain lengths were grafted as fillers. An increase of graft density after backfilling was demonstrated by chemical titration. However, fibrinogen and albumin adsorption increased on all surfaces after PEG or MPEG backfilling. It was suggested that BPEG was changed from a arched comformation to a extended one as a result of backfilling. This caused the hydrophobic benzyloxy end groups to be exposed to the exterior, which played a key role in the increase of protein adsorption (*35*). It should be noted in any case that protein-surface interactions are by no means determined by any single parameter; chemical composition, chain arrangement and nature of the adsorbed protein should be considered together.

The emergence of new bioinert polymers and the development of surface modification techniques has given more choices for preparing protein-resistant surfaces. Several surfaces have exhibited protein resistance superior to that of PEG modified surfaces; the terms "superlow protein adsorption" and "zero protein adsorption" have been used to describe such surfaces. However, caution should be used in describing quantitative data on protein adsorption especially when measured using only one method. The most widely used methods for the quantification of protein adsorption, such as surface plasmon resonance (SPR), quartz crystal microbalance (QCM) and radiolabeling, are all based on different principles. To obtain adsorbed amounts, the raw data from these methods (the physical signal) must be transformed using calibration or modeling, leading in some cases to unreliable results. For labeling-based methods, the free "labels" cannot be completely cleared from the labeled protein solution and may result in an erroneous estimate of adsorbed amount. In this regard, one should first test the possibility of interactions between the free labels and the surface (*36*).

Changes in the conformation of a protein on adsorption to a material surface, which may influence its biological activity, are always of concern, perhaps more so than the adsorbed amount. For example, Latour et al. concluded that platelet adhesion was strongly correlated with the degree of adsorption-induced unfolding of fibrinogen and not at all with the adsorbed amount (*37*). However, probing the conformation of an adsorbed protein remains a challenge due to the very low protein amounts that are below the detection limits of typical techniques, such as infrared spectroscopy, Raman spectroscopy and circular dichroism. Recently, conformational changes of lysozyme adsorbed on flat gold surfaces with different chemistries were measured in our laboratory using surface-enhanced Raman scattering (SERS). Instead of fabricating a metal substrate with special topographical features, colloidal silver nanoparticles were simply mixed with the protein adsorbed on gold surfaces to enhance the Raman signals. We found that the small amount of silver nanoparticles used (low laser power, short contact time 2-3 min) generated a measurable Raman signal for lysozyme while having negligible influence on the lysozyme structure. Data obtained by this technique revealed that the conformational change of lysozyme adsorbed on a hydrophilic PEG-modified surface was much smaller than that on a hydrophobic octadecane-modified surface, consistent with the high specific activity of lysozyme on the PEG surface (*38*).

Bioactive Surfaces

Promoting the binding of specific proteins on a surface is also important in many biomaterial applications such as protein purification, biosensing, anticoagulation etc. This requires the introduction of bioactive ligands with affinity for specific proteins to give so-called “bioactive” surfaces. An optimized bioactive surface should be able to bind the target protein selectively while preventing nonspecific protein adsorption. Although this may be achieved in some cases by surface grafting of bioactive ligands with high graft density, elimination of all nonspecific protein adsorption is not an easy task given that typical environments such as blood always contain surface-active components. The most commonly employed strategy is to use a bioinert polymer as a spacer to immobilize the bioactive ligand (*2*, *39*). The inert spacer can resist non-specific protein adsorption and thus minimize unwanted biological responses. In addition, it provides a favorable microenvironment that is useful in maintaining the activity of the ligand(s) on the surface (*40*).

Since PEG-grafted surfaces have been shown to be particularly effective for protein resistance, PEG has been extensively used as a spacer for preparing bioactive surfaces (*41–44*). We synthesized an asymmetric PEG with an allyl group and an N-succinimidyl carbonate (NSC) group at the respective chain termini and grafted it onto a Si-H functionalized PDMS surface by hydrosilylation. The NHS groups distal to the surface are available for covalent immobilization of amine-containing bioactive molecules (*45*). In the case of heparinized PDMS, high specificity for antithrombin with minimal fibrinogen adsorption was noted in plasma studies (*46*). Recently, PDMS and PU surfaces with fibrinolytic activity were prepared by immobilizing ε-lysine (ε-amino groups free) on the surface through a PEG spacer. It was shown that these lysinated surfaces reduce nonspecific protein adsorption while binding plasminogen from plasma with a high degree of selectivity (Figure 3). When activated by t-PA the plasmin generated at the surface was shown to dissolve fibrin clots in vitro (*47*, *48*). However, the PEG spacer, while effectively resisting nonspecific protein adsorption, is a deterrent to the specific binding of plasminogen due to the protein resistant properties of the PEG and the enhanced mobility of the chain-end conjugated lysines. Since the repellent effect of PEG is known to be dependent on chain length, we investigated the effect of PEG chain length on plasminogen binding to lysine at the PEG distal terminus. PEG-lysine surfaces were prepared using PEGs of different molecular weight (PEG300 and PEG1000) and their effects on the "balance" between nonspecific and specific protein binding were investigated (*49*). It was concluded that lysinated surfaces with PEG spacers of the relatively shorter length adsorbed plasminogen more rapidly than those with longer PEG, although the ultimate adsorbed quantities were the same. Correspondingly, the surface with the greater plasminogen binding capacity lysed fibrin clot more rapidly.

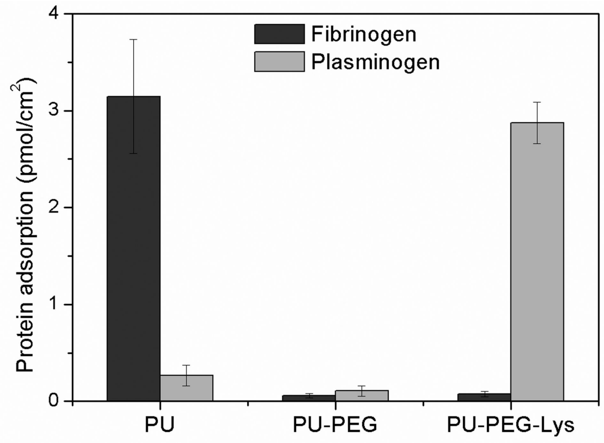

Figure 3. Fibrinogen adsorption from buffer and plasminogen adsorption from plasma on PU, PU-PEG and PU-PEG-Lys surfaces.

The surface density of spacer achievable by the "grafting to" strategy is limited due to steric hindrance, and the density of chain-end conjugated bioactive ligands is correspondingly limited. Therefore a "grafting from" strategy may be more effective. Moreover, if the surface-grafted polymers have abundant side chains with active chain ends, this permits the generation of a high concentration of chemically active sites on the surface for binding bioactive molecules. Of the various polymers available to form such grafts, PHEMA and POEGMA have found the most widespread use (*50–54*). The pendant hydroxyl groups of PHEMA and POEGMA brushes can be activated by thionyl chloride, p-nitrophenyl chloroformate (NPC), disuccinimidyl carbonate (DSC), 1,1′-carbonyldiimidazole (CDI), succinic anhydride (SA) etc. Amine-containing bioactive molecules can then be immobilized. Trmcic-Cvitas et al. recently compared the activation efficiency of 10 coupling agents when functionalizing a POEGMA surface with streptavidin and found that DSC activated surface afforded the highest streptavidin content (*55*). We have optimized our fibrinolytic PU surface using PHEMA as a spacer and DSC as a coupling agent for ε-lysine. The lysine density reached a value of 2.81 nmol cm^{-2} compared to 0.76 nmol cm^{-2} on a comparable PU-PEG-lysine surface. With increased plasminogen binding capacity, this surface showed more rapid clot lysis (20 min) in a standard in vitro assay than the corresponding PEG-lysine system (40 min) (*56*). To further improve the protein resistance of the spacer, a random copolymer of OEGMA and HEMA [poly(OEGMA-co-HEMA)] was grafted from PU surface as a spacer for ε-lysine immobilization. The quantity of fibrinogen adsorbed from buffer to the PU-poly(OEGMA-co-HEMA)-Lys surface was ~0.14 µg cm^{-2}, much lower than to the PU-PHEMA-Lys surface (~0.28 µg cm^{-2}) (*57*).

Surface-grown spacers could also be random or diblock copolymer brushes containing both a bioinert segment and a chemically active segment for the immobilization of bioactive molecules (*58–60*). The main advantage of this strategy lies in the simplicity of the process since the coupling agent is introduced simultaneously with the grafting of the spacer. In addition, the contributions of the bioinert and bioactive moieties can be well defined by varying the conditions or feed composition during the copolymerization. Liu et al. developed a highly sensitive microarray immunoassay device by grafting a random copolymer of glycidyl methacrylate (GMA) and PEGMA on a glass chip via SI-ATRP and printing the probe proteins on the copolymer brush (*61*). Our lab developed a novel bioactive surface grafted with a diblock copolymer of POEGMA and poly(N-hydroxysuccinimidyl methacrylate) (PNHSMA) by SI-ATRP: POEGMA was used as the protein-resistant component and PNHSMA for binding high densities of various bioactive molecules. This surface exhibited high binding capacity for three typical bioactive molecules, biotin, heparin and collagen, and high selectivity for their specific targets. For example, the biotinylated surface showed strong fluorescence intensity upon incubation with a solution of fluorescein labeled avidin, while there was essentially no detectable fluorescence signal to indicate the adsorption of fluorescein labeled HSA (Figure 4) (*62*).

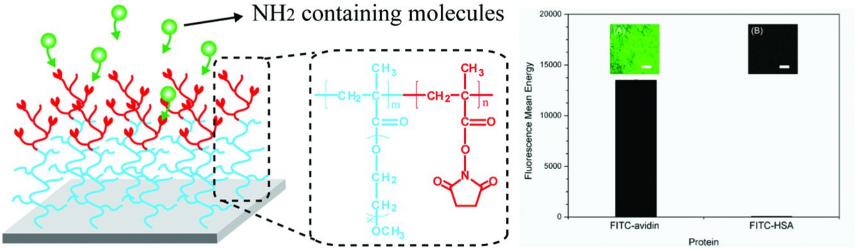

Figure 4. Schematic illustration of POEGMA-b-PNHSMA modified silicon surface and its performance in avidin binding and HSA repelling after biotinated. (Reproduced with permission from ref. (62). Copyright 2010 Royal Society of Chemistry)

Other Surfaces

Smart surfaces which can undergo dramatic changes in physicochemical properties in response to specific environmental stimuli have attracted increasing attention in applications that require the regulation of protein adsorption and desorption, such as drug delivery and protein purification (*63–66*). PNIPAAm modified surfaces, exhibiting lower critical solution temperature (LCST) behavior, have been well studied for the regulation of surface wettability (*67*) and cell attachment/detachment (*68*, *69*). It is expected that protein adsorption and desorption could also be regulated by temperature on PNIPAAm modified surfaces. In this regard, we investigated protein adsorption on PNIPAAm brushes of varying thickness prepared by SI-ATRP on silicon. As shown in Figure 5A, in the low thickness range (<15 nm), all the PNIPAAm-modified surfaces showed high resistance to HSA adsorption. The difference in adsorption above and below the LCST increased only slightly with thickness. The difference was much greater for a layer of greater thickness (~38.1 nm). Moreover the data for HSA, fibrinogen and lysozyme showed that adsorption was protein size dependent. Increasing the temperature from 23 °C to 37 °C resulted in increases of 300% and 184%, respectively, for HSA and fibrinogen adsorption, but only 32% for lysozyme (Figure 5B) (*70*).

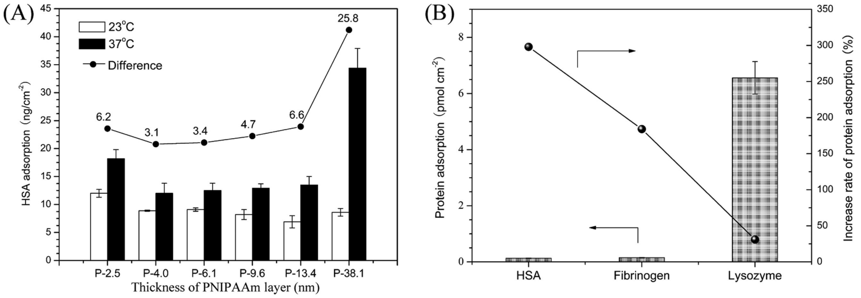

Figure 5. (A) Protein adsorption on PNIPAAm modified silicon surfaces at 23 °C and 37 °C as a function of PNIPAAm thickness. (B) HSA, fibrinogen and lysozyme adsorption at 23 °C and the increase rate of their adsorption (from 23°C to 37°C) on P-38.1 surface. Reproduced with permission from ref. (70). Copyright 2010 Elsevier.

Chirality is one of the basic features of biological molecules and many intriguing chiral events occur naturally at biointerfaces. It has been found that surfaces modified with chiral molecules have some stereoselectivity for biological materials including cells (*71*) and nucleic acids (*72*). However, few studies have attempted to investigate the interactions of such “chiral” surfaces with proteins (*73*). In this connection, we prepared SAMs of the natural amino acid L-cysteine and its enantiomer D-cysteine on gold surfaces and compared the adsorption of fibrinogen, fibronectin, HSA and lysozyme on the two surfaces. Protein adsorption was greater on the L-cysteine surface as was the subsequent adhesion of L929 cells (*74*). The protein and cell effects are clearly related, presumably through fibronectin adsorption.

Amphiphilic copolymer modified surfaces also have the potential to regulate protein adsorption since the hydrophilic and hydrophobic domains may interact with the corresponding domains of the copolymer. Varying the length of each block may change the protein/surface interactions, which holds promise for finding a modified surface that specifically interacts with a protein. To our knowledge no work has been reported directly aiming at this purpose, but some work has involved protein adsorption on amphiphilic copolymer modified surfaces. The most extensively studied systems are spin-coated polymer layers with microphase separated structures, on which proteins are localized exclusively to the hydrophobic regions, eg. PS (*75*, *76*). However, the dimensions of the micro-domains in these surfaces, ranging from tens to hundreds of nanometers, are large compared to the domains on the surface of proteins; therefore it is not expected that protein adsorption would be influenced by interactions between domains on the surface and those on the protein. Therefore, regulation of adsorption for these surfaces by varying copolymer composition does not seem likely. In comparison, various surface-grafted amphiphilic copolymer brushes have also been shown to form micro-domains on the surface (*77–79*) but the domain size in this case may be smaller since the phase separation is restricted to some extent by chain anchoring. For instance, Gao et al. prepared POEGMA-*b*-PMMA brushes on silicon surfaces via SI-ATRP. Various patterns including spherical aggregates, wormlike aggregates, strip patterns etc. were obtained and the feature size could be reduced to less than 10 nm (*79*). However, there are few studies on the interaction of proteins with amphiphilic block copolymer grafted surfaces. To this end, our lab recently carried out preliminary experiments on PVP-*b*-PS, PNIPAAm-*b*-PS and POEGMA-*b*-PS grafted surfaces (*80–82*). We showed that PVP- , PNIPAAm- and POEGMA-grafted surfaces are all protein-resistant; PVP-*b*-PS and POEGMA-*b*-PS surfaces exhibited increased protein uptake compared with their precursors, while PNIPAAm-*b*-PS did not. For POEGMA-b-PS surface, varying relative length of POEGMA and PS resulted in the change of the surface microstructure as well as the change of protein adsorption. These results indicate that copolymers with different blocks and different block lengths do affect on protein adsorption. It would be interesting to determine whether protein selectivity could be achieved by varying the length of each block.

Regulation of Protein/Surface Interactions by Topographical Design

In addition to chemical properties, surface topography also plays an important role in protein adsorption. Surface topography can be either regular or random and the properties that may influence protein/surface interactions include roughness, curvature and shape of the topographic features (*11*).

The most general and striking effect of topographical structure is the dramatic increase in the amounts of protein adsorption (on the basis of "apparent" as opposed to “true” area) resulting from the large surface area introduced by topographic modification. This can be helpful in biosensing applications that require large amounts of analyte. Recently we fabricated a stable gold nanoparticle layer (GNPL)-decorated ELISA plate via a chemical plating method. This surface presents three-dimensional micro- and nano-sized porous structures, consisting of gold nanoparticles with size range 100 to 150 nm. Surface roughness can be varied by adjusting the quantity of plating solution. It was shown that protein adsorption gradually increased with increasing surface roughness. The adsorption of lysozyme, HSA and fibrinogen was 2.76-, 2.34- and 3.26-fold higher, respectively, on the roughest surface than on unmodified high-binding ELISA plate. In addition, the activity of the adsorbed lysozyme was 3.86-fold higher than on ELISA plate (Figure 6(A)) (*83*). The increase in activity is possibly due to the altered conformation of lysozyme and less steric hindrance for approaching its substrate molecule on the three-dimensional micro- and nano-structured surface. With its high binding capacity and its ability to maintain the biological activity of adsorbed proteins, the GNPL decorated surface was found to amplify ELISA signals significantly and to decrease the limit of detection for carcinoembryonic antigen (CEA), an important biomarker related to many cancers (Figure 6(B)) (*83*, *84*). Moreover, we found that the surface wettability of the GNPL affected the ELISA performance. The freshly fabricated GNPL surfaces post-treated by “blow-dry” and “heat-dry” methods exhibited superhydrophilicity and superhydrophobicity respectively. The former showed a stronger ELISA signal than the latter presumably due to the larger contact area allowing efficient interaction of antibodies and GNPL surfaces (*84*).

It is generally considered that surface topography with feature dimensions comparable to those of proteins should have a strong influence on protein adsorption. Therefore, various nano-scale topographies have been fabricated, including variable nano-roughness (*85*, *86*), topographic elements of variable curvature (*87*), and various geometric features (*88*). For example, Rechendorff et al. investigated protein adsorption on evaporated tantalum films with varying RMS roughness (from 2.0 to 32.9 nm). They found that the saturation uptake of fibrinogen increased with increasing roughness beyond the accompanying increase in surface area, while the adsorption of a nearly globular protein BSA was less influenced by the roughness. The authors speculated that the strongly anisotropic fibrinogen may favor the orientation that perpendicular to the surface with increased roughness (*85*). Rockwell et al. further explained this phenomenon as the result of the increase in average surface curvature since side-on binding of fibrinogen on a surface with larger average curvature requires protein distortion which is energetically unfavorable (*86*). Compared with nano-scale topography, micro-scale topography seems not to influence protein adsorption greatly. We recently investigated fibrinogen adsorption on a patterned PDMS surface with micro-scale dot-like protrusions. The patterned surface showed a 46% increase in fibrinogen adsorption compared to the corresponding flat surface, while the surface area was only 8% greater. In addition, on exposing the patterned surface to fluorescein labeled fibrinogen, a clear fluorescent pattern was seen. As shown in Figure 7, fibrinogen was adsorbed preferentially on the spaces between protrusions. Platelets were found to adhere to the same locations (*89*).

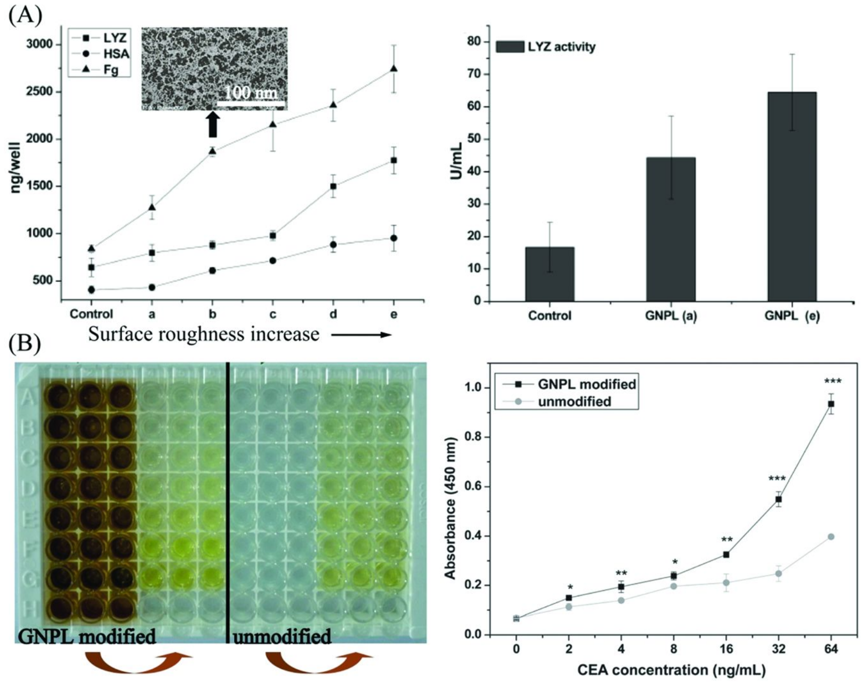

Figure 6. GNPL modified ELISA plates. (A) Adsorbed protein amounts and activity (Reproduced with permission from ref. (83). Copyright 2011 American Chemical Society). (B) Sandwich ELISA signals for the detection of CEA. (Reproduced with permission from ref. (84). Copyright 2012 Royal Society of Chemistry)

The introduction of nanostructure is believed to be an effective way to enhance surface properties. In fact, a great number of natural surfaces exhibit special properties due to the synergy between chemical composition and topography. For example, lotus leaf has a superhydrophobic surface resulting from the hydrophobic surface layer of waxes and the amplification effect of micro- and nano-topographical papillae. We carried out experiments to see whether surface/protein interactions would be influenced by this specialized topography. Lotus leaf-like polyurethane/Pluronic® surfaces were fabricated by blending and replica molding. Micro-papillae with diameters of 7-10 μm were distributed randomly and evenly on this surface. As expected, both the hydrophobicity of the unmodified PU surface and the hydrophilicity of the PU/Pluronic® surface were enhanced by the lotus leaf-like topography. It is noteworthy that, as shown in Figure 7, the introduction of lotus leaf-like structure further enhanced the protein-resistance of the PU/Pluronic® surface, even though the surface area was dramatically increased. Protein adsorption on the PU/ Pluronic® surface was reduced by 88.9% compared with the unmodified PU surface. When lotus leaf-like topography was constructed on the PU/ Pluronic® surface, adsorption was reduced further, namely by 97.1% compared to unmodified topographical PU

(*90*). The increase in protein-resistance on the lotus leaf-like PU/Pluronic surface should be attributed to the enhancement of surface hydrophilicity.

The combination of chemical composition and topography may give rise to various extraordinary effects (*91*, *92*) which have not as yet been exploited for the regulation of protein adsorption. It has been demonstrated in some cases that the combination of nanostructure and stimuli-responsive polymers can enhance the stimuli responsiveness of surface properties (*93*). For example, the property of reversible switching between superhydrophilicity and superhydrophobicity was achieved by grafting PNIPAAm on roughened silicon substrates (*94*). The changes in the amounts protein adsorption by applying external stimuli on a planar smart surface are only in the range from tens to hundreds of nanograms per square centimeter, which is far from the requirements of most of the related applications. It is expected, however, that the effects of external stimuli on protein adsorption will be enhanced by chemistry-topography synergy.

Recent efforts in this connection were made in our research group by combining the nanoeffects of 3D nanostructured silicon nanowire arrays (SiNWAs) with surface-grafting of various stimuli-responsive polymers. The pH switch for protein adsorption was greatly enhanced on poly(methacrylic acid) (PMAA)-grafted array. This material showed an extremely high capacity for lysozyme binding at pH 4 (~80-fold increase compared to planar Si-PMMA), while increasing the pH to 9 resulted in the release of ~90% of the adsorbed lysozyme without loss of protein activity (*95*).

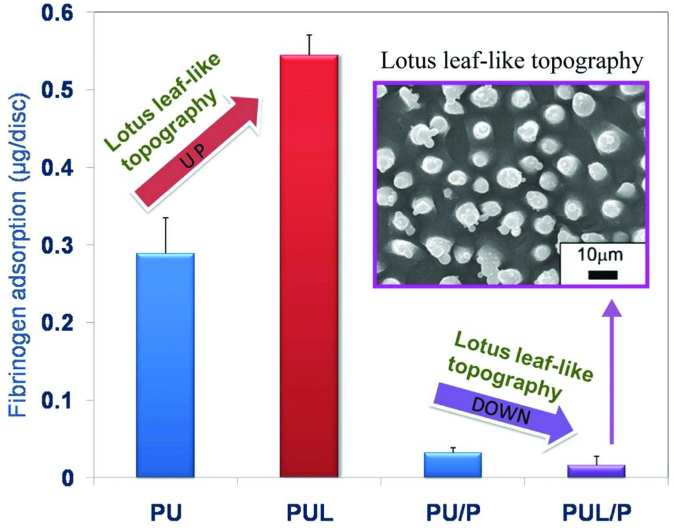

Figure 7. Effects of lotus leaf-like topography (L) on protein adsorption to PU and PU/Pluronic® (PU/P) surfaces. (Reproduced with permission from ref. (90). Copyright 2010 Elsevier)

The synergy between stimuli-responsiveness and nanoscale topography is, however, still unclear. It is possible that the great enhancement in stimuli-responsiveness of protein adsorption should be related to surface wettability as shown for the lotus leaf-like PU/Pluronic® surface, since protein adsorption is related to surface wettability. However, data from our studies do not support this hypothesis. We investigated stimuli-responsiveness of surface wettability and fibrinogen adsorption on both PMAA- and PNIPAAm-modified SiNWAs (Figure 8) (*96*). Compared with the corresponding modified flat silicon surfaces, the introduction of nanoscale roughness enhanced the thermo-responsive wettability of SiNWAs-PNIPAAm but weakened the pH-responsive wettability of SiNWAs-PMAA. Strikingly, the stimuli-responsiveness of fibrinogen adsorption on the polymer modified SiNWAs did not correspond to the surface wettability effects; the SiNWAs-PNIPAAm surface showed good resistance to non-specific protein regardless of temperature, while the SiNWAs-PMAA surface showed strongly pH-dependent protein adsorption. The stimuli-responsiveness of fibrinogen adsorption on these two polymer modified SiNWAs was related to that on the corresponding smooth surfaces. The introduction of the nano-structure further enhanced the effects of surface-grafted polymers on the protein adsorption.

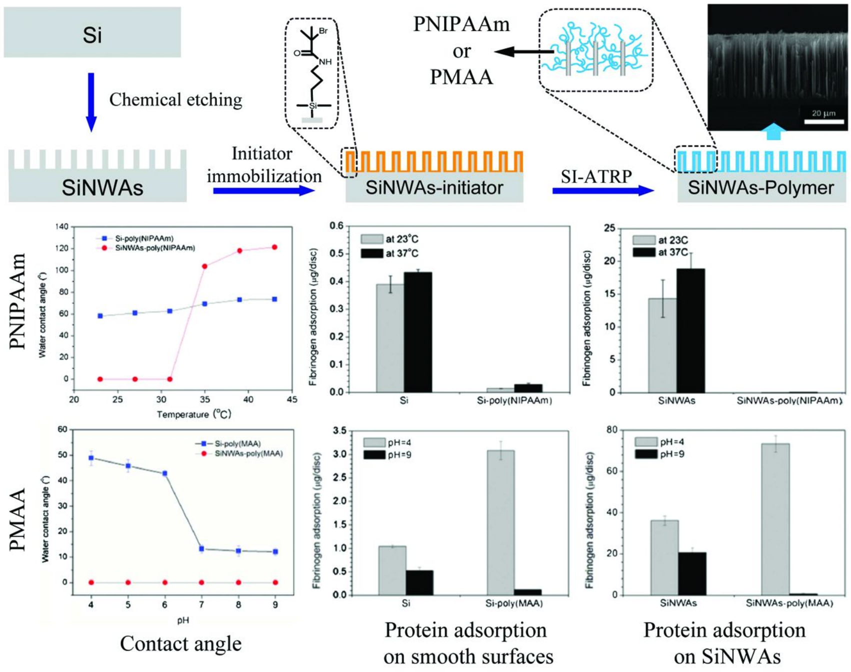

Figure 8. Schematic illustration of stimuli-responsive polymer modified SiNWAs and the responsiveness of surface wettability and protein adsorption. (Reproduced with permission from ref. (96). Copyright 2011 Royal Society of Chemistry)

Conclusions

With the development of surface modification technologies, our understanding of protein/surface interactions has made considerable progress. Studies using these surfaces have provided useful information with respect to the regulation of protein adsorption.

Work to date shows that surface chemical composition is well correlated with quantity of adsorbed protein. However, the effects of spatial distribution of surface chemistry (e.g. chemical domains) have not been well studied, in particular with respect to protein conformation which is, after all, closely associated with biological activity. Studies on this aspect have been limited due to the lack of methods for the investigation of protein conformation on a surface. Therefore, more efforts should be made to develop methods for the study of protein/surface interactions focusing on the protein conformation, and to regulate the conformation of a surface-associated protein by surface modification.

Although the effects of surface topography on protein adsorption have aroused growing interest in recent years, data from different studies are generally not comparable since the chemical properties of the surfaces are seldom taken into account. Surfaces with different chemical composition may have different effects on protein adsorption. That is, at least in part, why the correlations of topographical structure and protein adsorption obtained from different studies are not always consistent. So further studies on this aspect should take account of chemistry as well as topography. The synergy between these two factors may endow the surface with unexpected properties; however, this has not been fully exploited and utilized for the regulation of protein/surface interactions. Work in our lab suggests that this synergy has enormous potential in this regard.

It is our hope that the ideas and approaches for regulating protein/surface interactions enunciated here will be adopted more widely in biomaterials research, and that many new ideas based on these principles will emerge in the near future.

Acknowledgments

This work was financially supported by the National Science Fund for Distinguished Young Scholars (21125418), the National Natural Science Foundation of China (20920102035, 20974086) and the Priority Academic Program Development of Jiangsu Higher Education Institutions (PAPD).

References

1. Vogler, E. A. *Biomaterials* **2012**, *33*, 1201–1237.
2. Chen, H.; Yuan, L.; Song, W.; Wu, Z.; Li, D. *Prog. Polym. Sci.* **2008**, *33*, 1059–1087.
3. Zhang, L.; Sun, Y. *Biochem. Eng. J.* **2010**, *48*, 408–415.
4. Vogler, E. A.; Siedlecki, C. A. *Biomaterials* **2009**, *30*, 1857–1869.
5. Arruda, D. L.; Wilson, W. C.; Nguyen, C.; Yao, Q. W.; Caiazzo, R. J., Jr.; Talpasanu, I.; Dow, D. E.; Liu, B. C. S. *Expert Rev. Mol. Diagn.* **2009**, *9*, 749–755.

6. Merkoci, A. *Biosens. Bioelectron.* **2010**, *26*, 1164–1177.
7. Mano, J. F. *Adv. Eng. Mater.* **2008**, *10*, 515–527.
8. Anderson, J. M. *Annu. Rev. Mater. Res.* **2001**, *31*, 81–110.
9. Nel, A. E.; Maedler, L.; Velegol, D.; Xia, T.; Hoek, E. M. V.; Somasundaran, P.; Klaessig, F.; Castranova, V.; Thompson, M. *Nat. Mater.* **2009**, *8*, 543–557.
10. Lord, M. S.; Foss, M.; Besenbacher, F. *Nano Today* **2010**, *5*, 66–78.
11. Song, W.; Chen, H. *Chinese Sci. Bull.* **2007**, *52*, 3169–3173.
12. Yuan, L.; Yu, Q.; Li, D.; Chen, H. *Macromol. Biosci.* **2011**, *11*, 1031–1040.
13. Harris, J. M. *Poly(ethylene glycol) chemistry: biotechnical and biomedical applications*; Plenum Press: New York, USA, 1992.
14. Higuchi, A.; Shirano, K.; Harashima, M.; Yoon, B. O.; Hara, M.; Hattori, M.; Imamura, K. *Biomaterials* **2002**, *23*, 2659–2666.
15. Inoue, Y.; Ishihara, K. *Colloids Surf., B* **2010**, *81*, 350–357.
16. Chen, H.; Brook, M. A.; Sheardown, H. *Biomaterials* **2004**, *25*, 2273–2282.
17. Chen, H.; Brook, M. A.; Chen, Y.; Sheardown, H. *J. Biomater. Sci., Polym. Ed.* **2005**, *16*, 531–548.
18. Chen, H.; Zhang, Z.; Chen, Y.; Brook, M. A.; Sheardown, H. *Biomaterials* **2005**, *26*, 2391–2399.
19. Gan, J.; Chen, H.; Zhou, F.; Huang, H.; Zheng, J.; Song, W.; Yuan, L.; Wu, Z. *Colloids Surf., B* **2010**, *76*, 381–385.
20. Huang, X. Y.; Wirth, M. J. *Anal. Chem.* **1997**, *69*, 4577–4580.
21. Fristrup, C. J.; Jankova, K.; Hvilsted, S. *Soft Matter* **2009**, *5*, 4623–4634.
22. Ayres, N. *Polym. Chem.* **2010**, *1*, 769–777.
23. Xu, F. J.; Neoh, K. G.; Kang, E. T. *Prog. Polym. Sci.* **2009**, *34*, 719–761.
24. Wu, Z.; Chen, H.; Liu, X.; Zhang, Y.; Li, D.; Huang, H. *Langmuir* **2009**, *25*, 2900–2906.
25. Wu, Z.; Tong, W.; Jiang, W.; Liu, X.; Wang, Y.; Chen, H. *Colloids Surf., B* **2012**, *96*, 37–43.
26. Wu, Z.; Chen, H.; Huang, H.; Zhao, T.; Liu, X.; Li, D.; Yu, Q. *Macromol. Biosci.* **2009**, *9*, 1165–1168.
27. Zhao, T.; Chen, H.; Zheng, J.; Yu, Q.; Wu, Z.; Yuan, L. *Colloids Surf., B* **2011**, *85*, 26–31.
28. Chen, S.; Cao, Z.; Jiang, S. *Biomaterials* **2009**, *30*, 5892–5896.
29. Chen, S.; Jiang, S. *Adv. Mater.* **2008**, *20*, 335–338.
30. Feng, W.; Zhu, S.; Ishihara, K.; Brash, J. L. *Biointerphases* **2006**, *1*, 50–60.
31. Yoshikawa, C.; Goto, A.; Tsujii, Y.; Fukuda, T.; Kimura, T.; Yamamoto, K.; Kishida, A. *Macromolecules* **2006**, *39*, 2284–2290.
32. Nagase, K.; Watanabe, M.; Kikuchi, A.; Yamato, M.; Okano, T. *Macromol. Biosci.* **2011**, *11*, 400–409.
33. Perrino, C.; Lee, S.; Choi, S. W.; Maruyama, A.; Spencer, N. D. *Langmuir* **2008**, *24*, 8850–8856.
34. Unsworth, L. D.; Sheardown, H.; Brash, J. L. *Langmuir* **2005**, *21*, 1036–1041.
35. Chen, H.; Hu, X.; Zhang, Y.; Li, D.; Wu, Z.; Zhang, T. *Colloids Surf., B* **2008**, *61*, 237–243.
36. Du, Y. J.; Cornelius, R. M.; Brash, J. L. *Colloids Surf., B* **2000**, *17*, 59–67.

37. Sivaraman, B.; Latour, R. A. *Biomaterials* **2010**, *31*, 832–839.
38. Huang, H.; Xie, J.; Liu, X.; Yuan, L.; Wang, S.; Guo, S.; Yu, H.; Chen, H.; Zhang, Y.; Wu, X. *ChemPhysChem* **2011**, *12*, 3642–3646.
39. Yu, Q.; Zhang, Y.; Wang, H.; Brash, J.; Chen, H. *Acta Biomater.* **2011**, *7*, 1550–1557.
40. Wan, J.; Thomas, M. S.; Guthrie, S.; Vullev, V. I. *Ann. Biomed. Eng.* **2009**, *37*, 1190–1205.
41. Lata, S.; Piehler, J. *Anal. Chem.* **2005**, *77*, 1096–1105.
42. Gouzy, M. F.; Sperling, C.; Salchert, K.; Pompe, T.; Streller, U.; Uhlmann, P.; Rauwolf, C.; Simon, F.; Böhme, F.; Voit, B. *Biomaterials* **2004**, *25*, 3493–3501.
43. Zimmermann, J. L.; Nicolaus, T.; Neuert, G.; Blank, K. *Nat. Protoc.* **2010**, *5*, 975–985.
44. Sask, K. N.; Zhitomirsky, I.; Berry, L. R.; Chan, A. K. C.; Brash, J. L. *Acta Biomater.* **2010**, *6*, 2911–2919.
45. Chen, H.; Brook, M. A.; Sheardown, H.; Chen, Y.; Klenkler, B. *Bioconjugate Chem.* **2006**, *17*, 21–28.
46. Chen, H.; Chen, Y.; Sheardown, H.; Brook, M. A. *Biomaterials* **2005**, *26*, 7418–7424.
47. Chen, H.; Zhang, Y.; Li, D.; Hu, X.; Wang, L.; McClung, W. G.; Brash, J. L. *J. Biomed. Mater. Res.* **2009**, *90A*, 940–946.
48. Chen, H.; Wang, L.; Zhang, Y.; Li, D.; McClung, W. G.; Brook, M. A.; Sheardown, H.; Brash, J. L. *Macromol. Biosci.* **2008**, *8*, 863–870.
49. Li, D.; Chen, H.; McClung, W. G.; Brash, J. L. *Acta Biomater.* **2009**, *5*, 1864–1871.
50. Xu, F.; Li, Y.; Kang, E.; Neoh, K. *Biomacromolecules* **2005**, *6*, 1759–1768.
51. Xu, F.; Zhong, S.; Yung, L.; Tong, Y.; Kang, E.; Neoh, K. *Tissue Eng.* **2005**, *11*, 1736–1748.
52. Raynor, J. E.; Petrie, T. A.; García, A. J.; Collard, D. M. *Adv. Mater.* **2007**, *19*, 1724–1728.
53. Tugulu, S.; Silacci, P.; Stergiopulos, N.; Klok, H. A. *Biomaterials* **2007**, *28*, 2536–2546.
54. Lee, B. S.; Chi, Y. S.; Lee, K. B.; Kim, Y. G.; Choi, I. S. *Biomacromolecules* **2007**, *8*, 3922–3929.
55. Trmcic-Cvitas, J.; Hasan, E.; Ramstedt, M.; Li, X.; Cooper, M. A.; Abell, C.; Huck, W. T. S.; Gautrot, J. E. *Biomacromolecules* **2009**, *10*, 2885–2894.
56. Li, D.; Chen, H.; Wang, S.; Wu, Z.; Brash, J. L. *Acta Biomater.* **2011**, *7*, 954–958.
57. Wu, Z.; Chen, H.; Liu, X.; Brash, J. L. *Macromol. Biosci.* **2012**, *12*, 126–131.
58. Park, S.; Lee, K. B.; Choi, I. S.; Langer, R.; Jon, S. *Langmuir* **2007**, *23*, 10902–10905.
59. Iwasaki, Y.; Omichi, Y.; Iwata, R. *Langmuir* **2008**, *24*, 8427–8430.
60. Kitano, H.; Suzuki, H.; Matsuura, K.; Ohno, K. *Langmuir* **2010**, *26*, 6767–6774.
61. Liu, Y.; Wang, W.; Hu, W.; Lu, Z.; Zhou, X.; Li, C. M. *Biomed. Microdevices* **2011**, *13*, 769–777.

62. Zhang, Y.; Yu, Q.; Huang, H.; Zhou, F.; Wu, Z.; Yuan, L.; Li, D.; Chen, H. *Soft Matter* **2010**, *6*, 2616–2618.
63. Mendes, P. M. *Chem. Soc. Rev.* **2008**, *37*, 2512–2529.
64. de las Heras Alarcon, C.; Pennadam, S.; Alexander, C. *Chem. Soc. Rev.* **2005**, *34*, 276–285.
65. Nagase, K.; Kobayashi, J.; Okano, T. *J. R. Soc., Interface* **2009**, *6*, S293–S309.
66. Cole, M. A.; Voelcker, N. H.; Thissen, H.; Griesser, H. J. *Biomaterials* **2009**, *30*, 1827–1850.
67. Yakushiji, T.; Sakai, K.; Kikuchi, A.; Aoyagi, T.; Sakurai, Y.; Okano, T. *Langmuir* **1998**, *14*, 4657–4662.
68. Murakami, D.; Yamato, M.; Nishida, K.; Ohki, T.; Takagi, R.; Yang, J.; Namiki, H.; Okano, T. *Biomaterials* **2006**, *27*, 5518–5523.
69. Yamato, M.; Konno, C.; Utsumi, M.; Kikuchi, A.; Okano, T. *Biomaterials* **2002**, *23*, 561–567.
70. Yu, Q.; Zhang, Y.; Chen, H.; Wu, Z.; Huang, H.; Cheng, C. *Colloids Surf., B* **2010**, *76*, 468–474.
71. Bandyopadhyay, D.; Prashar, D.; Luk, Y.-Y. *Langmuir* **2011**, *27*, 6124–6131.
72. Gan, H.; Tang, K.; Sun, T.; Hirtz, M.; Li, Y.; Chi, L.; Butz, S.; Fuchs, H. *Angew. Chem., Int. Ed.* **2009**, *48*, 5282–5286.
73. Wang, X.; Gan, H.; Sun, T. *Adv. Funct. Mater.* **2011**.
74. Zhou, F.; Yuan, L.; Li, D.; Huang, H.; Sun, T.; Chen, H. *Colloids Surf., B* **2012**, *90*, 97–101.
75. Lau, K. H. A.; Bang, J.; Kim, D. H.; Knoll, W. *Adv. Funct. Mater.* **2008**, *18*, 3148–3157.
76. George, P. A.; Donose, B. C.; Cooper-White, J. J. *Biomaterials* **2009**, *30*, 2449–2456.
77. Zhao, B.; Brittain, W. J.; Zhou, W.; Cheng, S. Z. D. *J. Am. Chem. Soc.* **2000**, *122*, 2407–2408.
78. Kong, X.; Kawai, T.; Abe, J.; Iyoda, T. *Macromolecules* **2001**, *34*, 1837–1844.
79. Gao, X.; Feng, W.; Zhu, S.; Sheardown, H.; Brash, J. L. *Langmuir* **2008**, *24*, 8303–8308.
80. Liu, X.; Wu, Z.; Zhou, F.; Li, D.; Chen, H. *Colloids Surf., B* **2010**, *79*, 452–459.
81. Yu, Q.; Zhang, Y.; Chen, H.; Zhou, F.; Wu, Z.; Huang, H.; Brash, J. L. *Langmuir* **2010**, *26*, 8582–8588.
82. Zhang, Y.; Yu, Q.; Zhou, F.; Xu, Y.; Chen, H. *Chinese Sci. Bull.* **2010**, *55*, 2808–2814.
83. Zhou, F.; Yuan, L.; Wang, H.; Li, D.; Chen, H. *Langmuir* **2011**, *27*, 2155–2158.
84. Zhou, F.; Wang, M.; Yuan, L.; Cheng, Z.; Wu, Z.; Chen, H. *Analyst* **2012**, *137*, 1779–1784.
85. Rechendorff, K.; Hovgaard, M. B.; Foss, M.; Zhdanov, V.; Besenbacher, F. *Langmuir* **2006**, *22*, 10885–10888.
86. Rockwell, G. P.; Lohstreter, L. B.; Dahn, J. *Colloids Surf., B* **2011**, *91*, 90–96.
87. Roach, P.; Farrar, D.; Perry, C. C. *J. Am. Chem. Soc.* **2006**, *128*, 3939–3945.

88. Galli, C.; Collaud Coen, M.; Hauert, R.; Katanaev, V.; Gröning, P.; Schlapbach, L. *Colloids Surf., B* **2002**, *26*, 255–267.
89. Chen, H.; Song, W.; Zhou, F.; Wu, Z.; Huang, H.; Zhang, J.; Lin, Q.; Yang, B. *Colloids Surf., B* **2009**, *71*, 275–281.
90. Zheng, J.; Song, W.; Huang, H.; Chen, H. *Colloids Surf., B* **2010**, *77*, 234–239.
91. Wang, H.; Wang, L.; Zhang, P.; Yuan, L.; Yu, Q.; Chen, H. *Colloids Surf., B* **2011**, *83*, 355–359.
92. Yuan, L.; Wang, H.; Yu, Q.; Wu, Z.; Brash, J. L.; Chen, H. *J. Mater. Chem.* **2011**, *21*, 6148–6151.
93. Xin, B.; Hao, J. *Chem. Soc. Rev.* **2010**, *39*, 769–782.
94. Sun, T. L.; Wang, G. J.; Feng, L.; Liu, B. Q.; Ma, Y. M.; Jiang, L.; Zhu, D. B. *Angew. Chem., Int. Ed.* **2004**, *43*, 357–360.
95. Yu, Q.; Chen, H.; Zhang, Y.; Yuan, L.; Zhao, T.; Li, X.; Wang, H. *Langmuir* **2010**, *26*, 17812–17815.
96. Yu, Q.; Li, X.; Zhang, Y.; Yuan, L.; Zhao, T.; Chen, H. *RSC Adv.* **2011**, *1*, 262–269.

Chapter 14

Mechanisms of the Foreign Body Response to RFGD Plasma-Generated PEO-Like Films

Luisa M. Szott*,[1] and Thomas A. Horbett[2,3]

[1]PROFUSA, Inc., 1219 18th Street, San Francisco, California 94107
[2]Department of Bioengineering, 3720 15th Avenue NE, Box 355061,
University of Washington, Seattle, Washington 98195
[3]Department of Chemical Engineering, 3720 15th Avenue NE, Box 355061,
University of Washington, Seattle, Washington 98195
***E-mail: lizzy.szott@profusacorp.com**

Monocyte-derived macrophages play a central role in the foreign body response (FBR) to biomaterials through their interaction with adsorbed proteins on the material's surface. Fibrinogen (Fg) is a key adhesion protein in the FBR, and much effort has been spent on generating materials that reduce or eliminate its adsorption. However, although ultralow Fg adsorption (< 5 ng/cm^2) and almost complete monocyte adhesion resistance was achieved with poly(ethylene oxide) (PEO)-like tetraglyme coatings *in vitro*, no effect on macrophage adhesion or fibrous capsule formation in mouse *in vivo* studies was observed. In order to better understand the mechanisms of the FBR to tetraglyme, the role of complement proteins and adsorbed Fg state and their effect on monocyte adhesion *in vitro* were investigated.

The Foreign Body Response

The term "biomaterials" is used to refer to natural and synthetic materials that come in contact with biological systems in a variety of applications, most notably as medical devices (*1*). Each year, billions of dollars are spent in the U.S. on medical devices, such as intraocular lenses, joint prostheses, heart valves, vascular grafts, and glucose sensors. Materials used for these devices are varied, and are typically chosen because of desirable mechanical requirements, chemical stability, and lack of cytotoxicity. In general, existing medical devices have a limited lifetime, having to be replaced anywhere from one to fifteen years after implantation. With an increasingly large aging population in the United States, there is a need to develop devices with an improved lifetime, to minimize the need to replace surgically implanted devices.

The implantation of a medical device requires tissue trauma, which initiates the coagulation and wound healing mechanism (*2*). However, implantation of a medical device can sometimes lead to complications or device failure. For instance, the use of coronary stents to treat atherosclerosis can lead to intima hyperplasia as a result of vessel wall injury (*3*). Similarly, synthetic vascular grafts used to treat patients requiring bypass surgery can fail due to thrombosis or neointimal hyperplasia (*4*). Soft tissue implants, like glucose sensors (*5*), can be encapsulated by fibrous tissue that isolates it from the rest of the body. The mechanisms involved in mediating these adverse tissue responses to biomaterials, especially the foreign body response (FBR), are not fully understood. It is believed, however, that biomaterial surface properties greatly affect the FBR, though the characteristics most important in inducing a reduced host response have not yet been clearly identified (*6–10*).

Wound healing and inflammation are important processes in the maintenance of homeostasis, as they are critical in the clearing of invading pathogens and repair and replacement of injured tissue. Normal wound healing follows three phases: inflammation, proliferation, and maturation. During the inflammatory phase, damaged cells release tissue factor and exposed collagen fibers in the injured vasculature lead to the activation of the blood protein Hageman factor (coagulation factor XII) (*11*), which initiates the intrinsic coagulation pathway. Platelets are quickly recruited to the injury site, where they change shape, release activating growth factors like platelet-derived growth factor (PDGF), adenosine diphosphate (ADP), and transforming growth factor β (TFG-β), and take part in helping to form a fibrin plug for the wound (*12*). Once bleeding has been controlled, plasminogen is activated and the fibrin clot is broken down by plasmin. Soon after, circulating neutrophils are recruited by chemotactic factors to the injury site, where they phagocytose dead tissue and any present pathogens to clear the way for new tissue deposition. Neutrophils are replaced by activated macrophages a few hours later, and they continue clearing dead tissue, as well as releasing cytokines that help activate and recruit fibroblasts.

During the proliferation phase of wound healing, recruited fibroblasts deposit collagen, which will serve as the extra-cellular matrix for newly deposited tissue. The deposited collagen is called granulation tissue, as it is highly random and has a granular appearance due to extensive capillary formation (*12*). The wound contracts, and the granulation tissue fills in the lesion. The maturation phase begins with the reorganization and strengthening of the collagen fibers, and continues until the scar tissue has regained some of the original tissue's strength.

While normal wound healing results in the formation of new tissue at the injury site, implantation of a biomaterial into soft tissue often results in the formation of a fibrous capsule surrounding it. This is especially problematic when the device needs to be in contact with surrounding tissue in order to be functional, such as in the case of glucose sensors. Monocyte-derived macrophages have been identified as the key cell type involved in the mediation of the acute phase as well as the longer term FBR to biomaterials (*13*), via interaction with adsorbed proteins on the biomaterial's surface. A severe localized drop in pH (to 3.5) in the area under adherent macrophages has been reported (*14*). In addition, adherent macrophages have been shown to release cytokines, chemokines, and growth factors that affect the behavior of neighboring cells (*14*). In addition, adherent macrophages can fuse and form foreign body giant cells (FBGC) on the biomaterial's surface. The FBGCs attempt to degrade the biomaterial (*15*), and release lysosomal contents (*16*), oxygen radicals, and inflammatory cytokines (*17*), which can also lead to surrounding tissue injury.

Although the exact mechanisms of the FBR to biomaterials are not fully understood, especially the effects of chemical and mechanical properties of the biomaterial, adsorbed proteins on the biomaterials' surface are known to mediate subsequent cellular interactions, at least in the so called acute phase of the FBR (*18*, *19*). The reduction of non-specific protein adsorption to biomaterials has thus been the focus of a significant volume of research, as a way to reduce protein and blood interactions with the biomaterials, which are known to initiate the FBR. However, poly(ethylene oxide) (PEO)-like tetraglyme ($CH_3O(CH_2CH_2O)_4CH_3$) coatings generated in our lab using radiofrequency glow-discharge (RFGD) plasma have been shown to reduce protein adsorption and cell adhesion *in vitro*, but do not result in an altered FBR *in vivo* (*20*). These prior studies in our lab thus revealed a need for a more comprehensive investigation of the mechanisms of the FBR to tetraglyme coatings.

The Role of Adsorbed Fibrinogen

Almost instantly after coming in contact with blood upon implantation, proteins adsorb onto the biomaterial's surface. The surface chemistry of the implanted biomaterial greatly affects the type and amount of protein that adsorbs on its surface (*18*). It is believed that these adsorbed proteins mediate initial cell adhesion to the devices, which would otherwise not be recognized by the body. Several studies have established the importance of fibrinogen (Fg), a 340 kDa blood plasma adhesion protein, in the FBR (*21–23*), due to its role in monocyte/macrophage adhesion via the $\alpha_M\beta_2$ integrin (*2*).

In vivo leukocyte adhesion to intraperitoneally implanted PET disks was greatly reduced in hypofibrinogenemic mice as compared to normal mice, and adhesion was restored upon the addition of exogenous Fg to the peritoneal cavity of mice (*22*). The *in vivo* phagocyte adhesion to Fg pre-adsorbed surfaces was found to have a stronger correlation with the amount of SDS non-elutable Fg than with total adsorbed Fg (Γ_{Fg}), suggesting importance in changes in the conformation of the adsorbed Fg. The importance of the structure of adsorbed Fg has also been strongly shown in studies with platelets. Total Γ_{Fg} and platelet adhesion to several surfaces were poorly correlated, but the availability of platelet binding sites as measured with monoclonal antibodies was well correlated with platelet adhesion (*24*). In another recent study there was a strong correlation between platelet adhesion and loss of alpha helix in adsorbed Fg but not to total Γ_{Fg} on self-assembled monolayers terminated with different functional groups (*25*).

Fg is often described as an elongated dimeric protein with identical subunits, about 47.5 nm long (*26*), but each "monomer" in the dimer is actually a triplex made up of 3 non-identical peptide chains, known as Aα, Bβ, and γ (*27*). Each triplex set of chains extends out from a central nodule, known as the E domain, where disulfide bonds cross-link the N-terminal ends of the triplexes. The two peripheral nodules, known as the D domains, contain coiled-coils (*26*) in which the 3 individual chains wrap around each other. Multiple putative monocyte binding sites have been identified on Fg, primarily on the γC and the βC domains (*28*, *29*). However, two peptide sequences in Fg's γ chain, P1 (^{190}GWTWFQKRLDGSV^{202}) and P2 (^{377}YSMKKTTMKIIPFNRLTIG^{395}), have been shown to be required for monocyte/macrophage chemotaxis and binding via the $\alpha_M\beta_2$ integrin (*30*, *31*). The incubation of $\alpha_M\beta_2$-expressing cells with either peptide results in inhibition of adhesion to adsorbed Fg, though P2 was found to be 10 to 15 times more potent at inhibiting cell adhesion than P1 (*32*). Upon immobilization, the two peptides were found to support $\alpha_M\beta_2$-mediated cell adhesion (*22*) and promote cell migration in a transwell cell model (*33*). Subsequent studies have identified P2 as playing a more important role in $\alpha_M\beta_2$-mediated cell adhesion, as adhesion was shown to be impaired when P2 was deleted in mutant γC Fg chains, but not when P1 was deleted (*33*).

The $\alpha_M\beta_2$ receptor, also known as MAC-1, CD11b/CD18, and CR3, is a member of the integrin family (*34*), known to mediate cell adhesion to other cells, to extra-cellular matrix components, and to adsorbed proteins. The $\alpha_M\beta_2$ integrin is exclusively expressed on leukocytes, and plays an important role in various monocyte/macrophage functions, such as cytokine production, inflammation, immune response, complement activation, cell activation, and cell adhesion. The $\alpha_M\beta_2$ integrin has more than 30 ligands, including iC3b (*35*), Fg (*32*), Factor X (*36*), and vitronectin (*37*). Interestingly, the various ligands to this integrin do not appear to be structurally related, and the characteristics of all these ligands responsible for mediating the binding to the receptor have not yet been fully identified (*33*).

Our lab has generated poly(ethylene oxide) (PEO)-like tetraglyme ($CH_3O(CH_2CH_2O)_4CH_3$) coatings using radiofrequency glow discharge (RFGD) plasma on fluoroethylene propylene (FEP, $(CF(CF_3)\text{-}CF_2(CF_2\text{-}CF_2)_n)_m)$) substrates (*38*), whose protein adsorption resistance can be controlled by varying deposition parameters, namely the deposition power. Tetraglyme coatings generated using a 10W deposition power display a much lower Γ_{Fg} than uncoated FEP controls, and, in fact, have been shown to display an ultralow (< 10 ng/cm^2) Γ_{Fg} from low concentration protein solutions and to support low monocyte adhesion *in vitro* (*39*). Thus, a more detailed study of 10W tetraglyme's resistance to Fg adsorption, as well as its effect on the FBR, was necessary.

Previous studies of RFGD plasma deposited tetraglyme have shown that deposition power strongly affects ether carbon content and increased hydrocarbon content and resistance to Fg adsorption and monocyte adhesion. We used this knowledge to prepare surfaces that were very low-fouling ether carbon-rich (10W) and high fouling hydrocarbon-rich (80W) tetraglyme coatings, and also used uncoated FEP substrates, all of which were exposed to a wide range of Fg concentrations. We also measured primary human monocyte adhesion to surfaces after Fg pre-adsorption over a wide range of concentrations. Finally, as a measure of the biological activity of adsorbed Fg, we measured the binding of anti-P2 monoclonal antibody to estimate the degree of P2 epitope exposure on Fg adsorbed to these surfaces.

The binding of monoclonal antibodies to sites of interest on adsorbed proteins can be used to make conclusions about the exposure of binding epitopes and overall conformation of a protein. By correlating with cell adhesion and radiolabeled protein adsorption studies, the importance of different sites on a protein with regards to cell-protein interactions can be determined. We used a monoclonal antibody specific to the P2 epitope (^{377}YSMKKTTMKIIPFNRLTIG^{395}), which has been shown to be an important ligand to the monocyte **α**M**β**2 integrin (Mac-1, CD11b/CD18, CR3), mediating cell adhesion and migration (*22*, *33*), to study its exposure in Fg adsorbed on tetraglyme.

The surface chemistry of the tetraglyme films included in this study was confirmed using electron spectroscopy for chemical analysis (ESCA) (Table 1). Ether carbon (C-O, 286.8 eV) was the dominant species (80%) found on 10W tetraglyme coatings, which is why we refer to them as PEO-like. Hydrocarbon (C-C/C-H, 285 eV) and carbonyl species (C=O, 288 eV) were present in lower amounts on these surfaces, 15% and 5%, respectively. The predominant carbon species on 80W tetraglyme samples was hydrocarbon (C-H) (86%), with ether carbon and carbonyl groups present in smaller quantities, 11% and 3%, respectively. the integrity of the tetraglyme films was confirmed by the absence of large quantities of Fluorine. Trace amounts of Fluorine, within the limit of detection of F in ESCA (*40*), was detected in the 80W samples.

Table 1. Elemental and high resolution carbon functional group (C_{1s}) composition of 10W and 80W RFGD tetraglyme coatings and FEP films analyzed using ESCA. 10W tetraglyme samples have a C/O ratio of 2.3, consistent with the 2.0 value expected for PEO. Data are displayed as mean ± SEM; n = 4

Samples	*C%*	*O%*	*F%*	*C/O*	*C-C/C-H*	*C-O*	*C=O*
10W	69 ± 0.2	31 ± 0.2	0	2.3 ± 0.0	15 ± 3	80 ± 4	5 ± 1
80W	91 ± 0.5	9 ± 0.5	0.2 ± 0.1	10.6 ± 1.4	86 ± 2	11 ± 2	3 ± 0.2
FEP	38 ± 0.1	0.1 ± 0.0	62 ± 0.1	N/A	N/A	N/A	N/A

Γ_{Fg} to 10W and 80W tetraglyme coatings and FEP samples was measured from a series of increasingly concentrated Fg solutions in buffer using ^{125}Fg (*41*, *42*) (Figure 2). Γ_{Fg} to 10W tetraglyme was much lower than on FEP and 80W tetraglyme samples for all protein solutions and concentrations tested. Γ_{Fg} to 10W tetraglyme coatings from low concentration Fg solutions (less than 0.03 mg/ml Fg) is very similar to that reported by Shen et al (*21*, *39*), with Γ_{Fg}

found to be approximately 4 ng/cm^2. However, Γ_{Fg} to 10W tetraglymes from Fg concentrations greater than 0.03 mg/ml was significantly greater, reaching a high of 63 ng/cm^2 from 3 mg/ml Fg solutions. Γ_{Fg} to 10W tetraglyme coatings from plasma diluted to various degrees was, as expected, lower than from Fg in buffer, with 5 ng/cm^2 Γ_{Fg} from 1% plasma (equivalent to 0.03 mg/ml Fg concentration) and 55 ng/cm^2 Γ_{Fg} from 100% plasma (equivalent to 3 mg/ml Fg concentration) (data not shown).

The effect of Fg adsorption on monocyte adhesion was then evaluated using primary human monocytes isolated from peripheral whole blood. 10W and 80W tetraglyme and FEP samples were pre-adsorbed with Fg solutions in buffer of increasing concentrations, and monocyte adhesion was measured after two hours (Figure 2). The number of adherent monocytes to 10W tetraglyme samples was found to be much lower than to 80W and FEP samples for all solutions tested. Despite the marked increase in adsorbed Fg on 10W tetraglyme coatings as a result of incubating them with protein solutions of increasing concentrations (Figure 1), a corresponding marked increase in the number of adherent monocytes was not observed (Figure 2). Monocyte adhesion to 10W tetraglymes increased linearly with Fg concentration used for pre-adsorption from 0.003 mg/ml to 0.3 mg/ml Fg, but there was a significant drop in the adhesion on surfaces preadsorbed at higher Fg concentrations. A similar trend was observed in the 80W tetraglyme samples, though the differences in cell adhesion between the different samples were not statistically significant. Monocyte adhesion to FEP samples, however, did not follow this same trend. Instead, monocyte adhesion increased slightly and steadily with increasing Fg solution concentration.

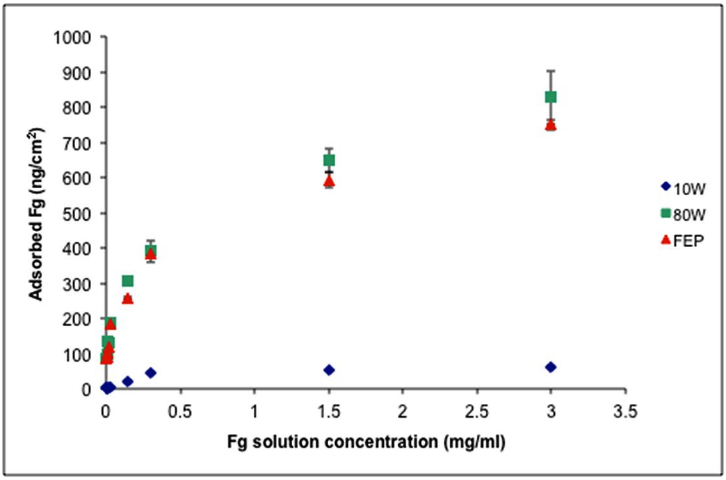

Figure 1. Two hour fibrinogen adsorption to 10W and 80W tetraglyme coatings and FEP from pure Fg solutions ranging from 0.003 to 3 mg/ml concentration Fg solutions. Data are displayed as mean +/- SEM; n = 3.

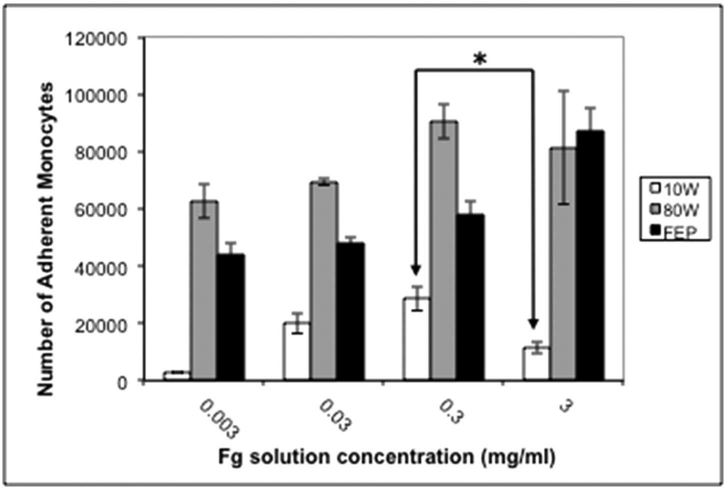

Figure 2. Two hour monocyte adhesion to Fg pre-adsorbed 10W and 80W tetraglyme and FEP samples. The asterisk denotes statistical significance. Data are displayed as mean +/- SEM; n = 3.

Because a linear correlation was not observed between monocyte adhesion and Γ_{Fg} to tetraglyme materials, we then investigated the P2 binding site, or epitope, exposure on 10W and 80W tetraglymes and FEP substrates (Figure 3). The P2 epitope was of interest as it has been previously shown by others to be involved in monocyte adhesion via interaction with the $\alpha_M\beta_2$ integrin (*32*, *33*). The measured epitope exposure (antibody binding) was corrected for differences in Γ_{Fg} by dividing the antibody binding by Γ_{Fg}. The degree of P2 epitope exposure per ng of adsorbed Fg was much greater on 10W tetraglyme samples over the entire range of Fg concentrations tested than on either 80W or FEP samples. No significant difference in degree of epitope exposure was seen between 80W and FEP samples. On all materials, the highest degree of epitope exposure was generally observed in those samples with the least Γ_{Fg}. The reduction of total Γ_{Fg} observed for 10W tetraglyme surfaces appears to be accompanied by an increase in its ability to adhere monocytes. Fg adsorbed to the highly hydrated PEO like surface is probably not as structurally altered nor as immobilized by many strong interactions with the surface as on more hydrophobic surfaces, and this may well account for the higher retention of macrophage binding sites detected with our P2 antibody probe.

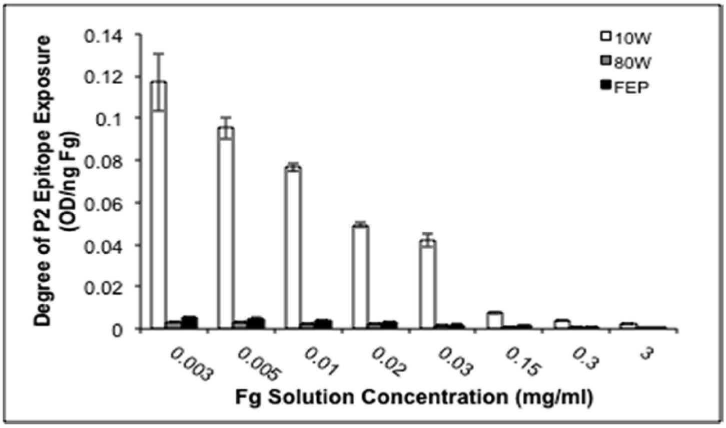

Figure 3. Degree of P2 epitope exposure on 10W and 80W tetraglyme and FEP samples pre-adsorbed with Fg from different concentration pure Fg solutions, measured by monoclonal antibody binding. Data are displayed as mean +/- SEM; n = 3.

Whereas no correlation between total Γ_{Fg} (measured with I-125 labeled Fg) and adhesion was observed for 10W tetraglyme, there was a linear correlation between degree of P2 epitope exposure and normalized monocyte adhesion to 10W tetraglyme surfaces pre-adsorbed with pure Fg solutions (cells/ng Fg). This trend was observed also on all the other two surfaces tested, with an R^2 value greater than 0.90 for all materials. These analyses thus confirm the importance of not only studying the amount of adsorbed Fg, but also the state in which it is present on the surfaces. In the case of tetraglyme coatings, even though Γ_{Fg} is greatly reduced as compared to uncoated controls, the small amount of Fg is present in a more biologically active state, with a greater degree of P2 epitope exposure taking place on these surfaces. Thus, although the focus in biomaterial design has been on lowering or eliminating non-specific protein adsorption, the state and biological activity of the adsorbed protein must be probed in order to design more biocompatible surfaces.

The Role of the Complement System

Recent studies of the mechanisms of the FBR to biomaterials have concentrated largely on the interaction of Fg with monocytes and monocyte-derived macrophages (*23*, *30*), despite the fact that many complement proteins and activation fragments are known to directly impact inflammatory cells. C3 cleavage and degradation products induce inflammation e.g. C3a is a very potent anaphylatoxin known to activate and recruit phagocytes, while iC3b, a degradation fragment of C3b, is an opsonin (*43*) known to be a ligand for a monocyte adhesion receptor **α**M**β**2 (CR3, Mac-1, or CD11b/CD18) (*34*, *35*). C3b is also involved in mediating monocyte and macrophage phagocytosis and cell adherence, as well as contributing to the formation of the C5 convertase, which results in the cleavage of C5 into the potent anaphylatoxin C5a and C5b. The presence of C5b initiates the formation of the Membrane Attack Complex (MAC, C5b-9), the common terminal complex for all pathways of complement activation (*44*).

The role of biomaterial suface chemistry in complement activation has been studied to some extent. Activation of the complement system as a result of blood-biomaterial interactions during hemodialysis (*45*) and cardiopulmonary bypass (*46*) has been well documented. Hydroxyl-rich biomaterials, such as cellulose dialysis membranes (*47*), hydroxyethlylmethacrylate-ethylmethacrylate (HEMA-EMA) copolymers (*48*), and poly(vinyl alcohol) (PVA) hydrogels (*49*), have been found to activate the complement system. Hydroxyl-rich surfaces activate to a greater degree than amine and carboxyl-rich surfaces (*50*). Hirata et al (*51*) showed OH-SAMs induced greater activation via the biomaterial-dependent alternative pathway (AP) than CH_3-SAMs, with the degree of complement activation increasing with increasing surface hydroxyl group density (*52*).

In addition, PEG-acrylate films have been found to be more complement activating than sulfonated PEG-acrylate films (*53*), due to the terminal hydroxyl group on the PEG-acrylate films. In addition, small amounts of intact and cleaved C3, a sign of complement activation, have been found to adsorb on PEO-thiols on gold surfaces with different terminal groups (*54*) after incubation with pooled normal human plasma. However, degree of complement activation by PEG cannot be solely attributed to the terminal groups present on these surfaces. Nanocapsules coated with PEG were found to be less complement activating than methoxy-terminated PEG (MePEG) coated nanocapsules, attributed to the conformation of the PEG chain on the nanocapsule and its ability to prevent protein adsorption from taking place (*55*). In addition, although OH-PEG coated surfaces were found to activate the complement system to a larger degree than CH3-PEG coated surfaces, the degree of complement activation by CH3-PEG coatings was found to increase with storage time, due to oxidation of the coatings over time (*56*).

Recently, several studies have shown the importance of complement protein 3 (C3) in mediating monocyte adhesion to a variety of polystyrene surfaces (*57*), as cell adhesion was found to decrease significantly when C3-depleted serum was used to pre-adsorb surfaces. Adhesion levels were restored upon the addition of exogenous C3 to the depleted serum used for the study. Monocytes have cell-surface receptors for many complement activation products, such as C3a and iC3b (*58*). C3a is believed to induce monocytes to generate cytokines (*59*), while iC3b is an opsonizing ligand for the **α**M**β**2 (CD11b/CD18, Mac-1) integrin that is powerful enough to induce phagocytosis (*58*). In addition, the quantitative upregulation of the **α**M**β**2 integrin on blood monocytes has been linked with the alternative complement pathway activation occurring as a result of blood contact with PVA hydrogel surfaces (*49*, *60*).

There is some evidence that C3 can adsorb on PEO surfaces (*54*, *61*). Thus, we became interested in investigating a possible relationship between complement proteins and the FBR to tetraglyme films. Our lab measured complement C3 adsorption to 10W tetraglyme-coated FEP and uncoated FEP surfaces was measured after exposure to 1 or 10% normal human serum or 1 or 10% normal human plasma, using ^{125}I labeled C3 (Figure 4) (*62*). Γ_{C3} on tetraglyme coatings was lower than that to FEP substrates from all protein solutions tested. Γ_{C3} was the highest on both materials from 1% serum, presumably due to reduced completion at this lower protein concentration and the absence of Fg, which readily adsorbs on to FEP and tetraglyme surfaces. The maximum amount of Γ_{C3} on tetraglyme coatings and FEP films, observed from 1% serum, was 11 and 37 ng/cm C3, respectively.

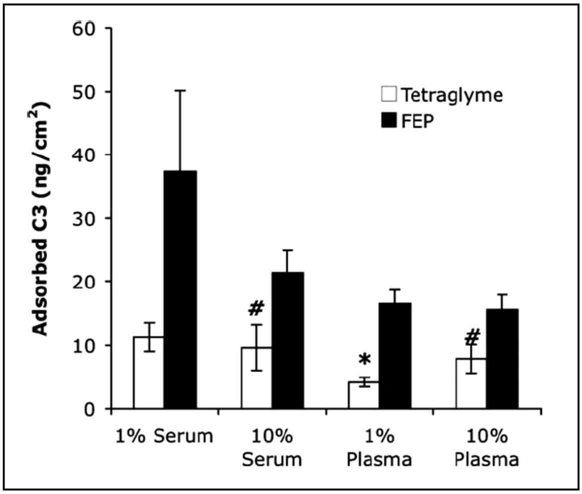

Figure 4. Complement C3 adsorption to tetraglyme and FEP from 1 or 10% normal human serum or normal heparinized human plasma. Data are displayed as mean +/- SEM; n = 3. The amount of adsorbed C3 from 1% plasma (, p = 0.05) and from 10% serum and 10% plasma (#, p = 0.10) on tetraglyme were found to be significantly lower than that on FEP. Reproduced with permission from reference (62). Copyright 2010 John Wiley and Sons.*

Although Γ_{C3} was low, even small amounts of adsorbed proteins are known to mediate cell responses, as previously demonstrated by Tsai et al (*63*). Thus, we directly investigated the role of adsorbed C3, as compared to Fg, in monocyte adhesion using the selective depletion and repletion method (Figure 5) (*62*). Tetraglyme and FEP samples were pre-adsorbed with either heparinized normal human plasma or serum or C3-depleted serum. In addition, C3-depleted serum restored with physiologically relevant amounts of pure C3 (125 μg/ml) and C3-depleted serum and normal serum with 0.3 mg/ml Fg added to it were also included to gain a better understanding of the role each of the proteins play in monocyte adhesion. Pre-adsorption with complement C3-depleted serum resulted in a large reduction in the number of adherent monocytes on both tetraglyme and FEP as compared to normal human serum. Using C3-depleted serum replenished with pure C3 resulted in partial restoration of monocyte adhesion to tetraglyme, but had only a minimal effect on FEP. Paired with the drop in monocyte adhesion upon absence of C3, these results support our hypothesis that that presence of C3 is important in monocyte adhesion to tetraglyme.

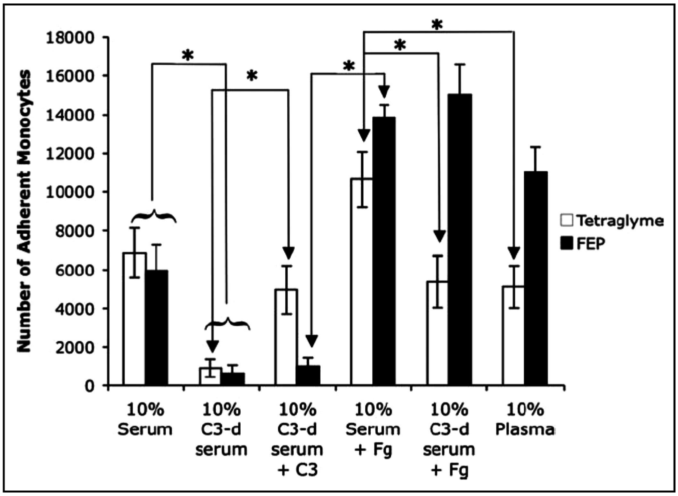

Figure 5. Two hour monocyte adhesion to protein pre-adsorbed tetraglyme and FEP. Data are displayed as mean +/- SEM; n = 4. Asterisks denote statistical significant differences in numbers of adherent monocytes in the pairs connected by arrows (p = 0.05). Reproduced with permission from reference (62). Copyright 2010 John Wiley and Sons.

The addition of 0.3 mg/ml Fg to C3-depleted serum restored monocyte adhesion to levels seen with 10% plasma on tetraglyme, and resulted in greater monocyte adhesion on FEP than with normal plasma or 10% normal serum with the same amount of Fg added to it. Surprisingly, monocyte adhesion was found to be slightly greater on tetraglyme surfaces pre-adsorbed with 10% normal serum than 10% normal plasma. The addition of 0.3 mg/ml Fg to 10% normal serum to the pre-adsorption protein solution resulted in a sharp increase in the number of adherent monocytes for both tetraglyme and FEP as compared to samples pre-adsorbed with 10% normal serum and 10% C3-depleted serum restored with C3. In fact, the greatest number of adherent monocytes to tetraglyme were observed when normal serum with 0.3 mg/ml Fg added to it was used to pre-adsorb the samples, presumably due to a synergistic effect between Fg and C3 (present in normal human serum).

To gain a better understanding of the nature of the observed monocyte-C3 interaction, we measured complement activation by tetraglyme films (Figure 6) (*64*). Tetraglyme, which has a very low surface hydroxyl group concentration, would not expected to be a complement activating material, but we tested it anyway, and were surprised.

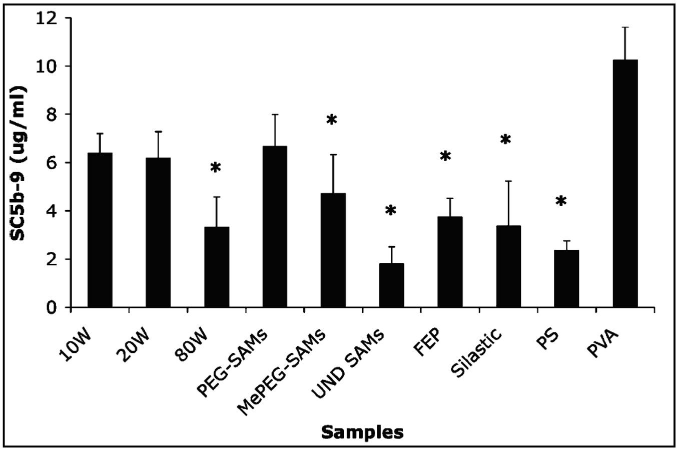

Figure 6. The amount of soluble SC5b-9 (in **μ***g/mL) present in 100% serum after incubating for 90 min at 37C with different biomaterials was measured to determine the degree of biomaterial-induced complement activation. Data are displayed as mean +/- SEM; n = 9 per material (n = 3 per donor). Asterisks denote statistically significant differences in the amount of SC5b-9 generated in serum by various biomaterials compared with PVA (positive control;* **α** *= 0.05). Reproduced with permission from reference (64). Copyright 2010 John Wiley and Sons.*

Tetraglyme films generated using three different deposition powers (10W, 20W, and 80W) with varying ether carbon contents as well as the FEP substrate were included in this study. In addition, hydroxyl-terminated PEG, methoxy-terminated MePEG, and methoxy-terminated $(CH_2)_{11}$ undecanethiol SAMs on gold were included as PEG controls. Hydroxyl-rich poly(vinyl alcohol) (PVA) was included as a positive control, while Silastic was included as a negative control. The surface chemistry of the various materials included in the study was verified using ESCA. The absence of hydroxyl groups on the tetraglyme surfaces was confirmed using tri-fluoroacetic acid (TFAA) derivatization of the surfaces (data not shown). Samples were incubated in pooled normal human serum for 90 minutes at 37° C. The amount of SC5b-9, the inactive Membrane Attack Complex, as a result of incubation with serum was measured using ELISA, as an indicator of degree of complement activation.

Despite having no surface hydroxyl groups, 10W and 20W tetraglyme surfaces were found to be as complement activating as hydroxyl-terminated SAMs, and slightly less complement activating than PVA gels, the positive control included in the study. The specific surface functionality responsible for this complement activation phenomenon is unclear at this time. One potential explanation for the observed results can be explained by recent results (*65*) suggesting that adsorbed proteins on a biomaterial's surface initiate complement activation via the classical pathway. This classical pathway activation results in

C3b generation, which then adsorbs onto the biomaterial's surface, initiating the alternative pathway amplification of the complement system.

Our C3 protein adsorption and complement activation studies with tetraglyme indicate an important but unexpected interaction between complement proteins and PEO-containing surfaces that may have implications in the FBR to these materials. Although well-controlled *in vitro* models were used for our studies, it is important to note that they were conducted using a simplified environment using static conditions. Thus, care must be taken when extrapolating our results to explain *in vivo* results. Nevertheless, these results indicate complement may be a contributor to the FBR to tetraglyme films.

Conclusions

The FBR to implanted biomaterials is complex and involves many kinds of proteins and cells. Despite recent progress, a complete understanding of the mechanisms by which the body interacts with implanted materials has not yet been achieved. In particular, the complex role of macrophages in orchestrating the FBR has not been fully elucidated. This is partly due to the lack of a realistic *in vitro* model, where the interaction of various molecules and cells can be evaluated together, which more closely resembles that which may occur in the body. In addition, the specific requirements for a biocompatible material have not yet been established. Finally, it is important to note that although the inflammatory response and the complement system have been discussed here as independent mechanisms, in the body they interact a great deal. The implantation of a device requires tissue injury, which can initiate a number of tissue responses to the implant, such as coagulation, complement activation, fibrinolysis, or inflammation. These mechanisms are not mutually exclusive, but rather inter-related, and it is likely that they are all involved, to some extent, in the FBR to biomaterials. The understanding of the mechanisms by which the body interacts with implanted devices is a daunting task, yet it's necessary in order to gain the understanding needed in order to engineer biomaterials that will have an improved compatibility *in vivo*.

References

1. Ratner, B. D. *Biomaterials science : an introduction to materials in medicine*; Academic Press: San Diego, 1996.
2. Anderson, J. M.; Rodriguez, A.; Chang, D. T. Foreign body reaction to biomaterials. *Semin. Immunol.* **2008**, *20* (2), 86–100.
3. Farb, A.; et al. Pathology of acute and chronic coronary stenting in humans. *Circulation* **1999**, *99* (1), 44–52.
4. Didisheim, P.; Watson, J. T. Cardiovascular Applications. In *Biomaterials Science: An Introduction to Mateirals in Medicine*; Ratner, B. D., et al., Eds; Academic Press: San Diego, 1996; pp 133−141.
5. Gerritsen, M. Problems associated with subcutaneously implanted glucose sensors. *Diabetes Care* **2000**, *23* (2), 143–145.

6. Kamath, S.; et al. Surface chemistry influences implant-mediated host tissue responses. *J. Biomed. Mater. Res., Part A* **2008**, *86* (3), 617–626.
7. Nair, A.; et al. Species and density of implant surface chemistry affect the extent of foreign body reactions. *Langmuir* **2008**, *24* (5), 2015–2024.
8. Su, J.; et al. A mathematical model for foreign body reactions in 2D. *Int. J. Comput. Math.* **2011**, *88* (3), 610–633.
9. Su, J.; et al. A Predictive Tool for Foreign Body Fibrotic Reactions Using 2-Dimensional Computational Model. *Open Access Bioinformatics* **2011**, *2011* (3), 19–35.
10. Thevenot, P.; Hu, W.; Tang, L. Surface chemistry influences implant biocompatibility. *Curr. Top. Med. Chem.* **2008**, *8* (4), 270–280.
11. Silver, F. H.; Christiansen, D. L. *Biomaterials science and biocompatability*; Springer: New York, 1999.
12. Martin, P.; Leibovich, S. J. Inflammatory cells during wound repair: the good, the bad and the ugly. *Trends Cell Biol.* **2005**, *15* (11), 599–607.
13. Anderson, J. M.; et al. Monocyte, macrophage and foreign body giant cell interactions with molecularly engineered surfaces. *J. Mater. Sci.: Mater. Med.* **1999**, *10* (10/11), 579–588.
14. Reichert, W. M.; et al. 2010 Panel on the biomaterials grand challenges. *J. Biomed. Mater. Res., Part A* **2011**, *96* (2), 275–287.
15. Jenney, C. R.; Anderson, J. M. Effects of surface-coupled polyethylene oxide on human macrophage adhesion and foreign body giant cell formation in vitro. *J. Biomed. Mater. Res.* **1999**, *44* (2), 206–216.
16. Kuby, J. *Immunology*, 3rd ed; W.H. Freeman: New York, 1997.
17. Hernandez-Pando, R.; et al. Inflammatory cytokine production by immunological and foreign body multinucleated giant cells. *Immunology* **2000**, *100* (3), 352–358.
18. Horbett, T. A. Principles underlying the role of adsorbed plasma proteins in blood interactions with foreign materials. *Cardiovasc. Pathol.* **1993**, *2* (3), 137S–148S.
19. Horbett, T. A. The role of adsorbed adhesion proteins in cellular recognition of biomaterials. *BMES Bull.* **1999**, *23* (2), 5–9.
20. Shen, M.; et al. PEO-like plasma polymerized tetraglyme surface interactions with leukocytes and proteins: in vitro and in vivo studies. *J. Biomater. Sci., Polym. Ed.* **2002**, *13* (4), 367–390.
21. Shen, M.; Horbett, T. A. The effects of surface chemistry and adsorbed proteins on monocyte/macrophage adhesion to chemically modified polystyrene surfaces. *J. Biomed. Mater. Res.* **2001**, *57* (3), 336–345.
22. Tang, L.; Eaton, J. W. Fibrin(ogen) mediates acute inflammatory responses to biomaterials. *J. Exp. Med.* **1993**, *178* (6), 2147–2156.
23. Tang, L.; Wu, Y.; Timmons, R. B. Fibrinogen adsorption and host tissue responses to plasma functionalized surfaces. *J. Biomed. Mater. Res.* **1998**, *42* (1), 156–163.
24. Tsai, W. B.; Grunkemeier, J. M.; Horbett, T. A. Variations in the ability of adsorbed fibrinogen to mediate platelet adhesion to polystyrene-based materials: a multivariate statistical analysis of antibody binding to the

platelet binding sites of fibrinogen. *J. Biomed. Mater. Res., Part A* **2003**, *67* (4), 1255–1268.

25. Sivaraman, B.; Latour, R. A. The relationship between platelet adhesion on surfaces and the structure versus the amount of adsorbed fibrinogen. *Biomaterials* **2010**, *31* (5), 832–839.
26. Fuss, C.; Palmaz, J. C.; Sprague, E. A. Fibrinogen: structure, function, and surface interactions. *J. Vascular Interventional Radiol.: JVIR* **2001**, *12* (6), 677–682.
27. Pechik, I.; et al. Structural basis for sequential cleavage of fibrinopeptides upon fibrin assembly. *Biochemistry* **2006**, *45* (11), 3588–3597.
28. Lishko, V. K.; et al. Multiple binding sites in fibrinogen for integrin alphaMbeta2 (Mac-1). *J. Biol. Chem.* **2004**, *279* (43), 44897–44906.
29. Yakovlev, S.; et al. Interaction of fibrin(ogen) with leukocyte receptor alpha M beta 2 (Mac-1): further characterization and identification of a novel binding region within the central domain of the fibrinogen gamma-module. *Biochemistry* **2005**, *44* (2), 617–626.
30. Hu, W. J.; et al. Molecular basis of biomaterial-mediated foreign body reactions. *Blood* **2001**, *98* (4), 1231–1238.
31. Forsyth, C. B.; et al. Integrin alpha(M)beta(2)-mediated cell migration to fibrinogen and its recognition peptides. *J. Exp. Med.* **2001**, *193* (10), 1123–1133.
32. Ugarova, T. P.; Yakubenko, V. P. Recognition of fibrinogen by leukocyte integrins. *Ann. N. Y. Acad. Sci.* **2001**, *936*, 368–385.
33. Ugarova, T. P.; et al. Sequence gamma 377-395(P2), but not gamma 190-202(P1), is the binding site for the alpha MI-domain of integrin alpha M beta 2 in the gamma C-domain of fibrinogen. *Biochemistry* **2003**, *42* (31), 9365–9373.
34. Arnaout, M. A. Structure and function of the leukocyte adhesion molecules CD11/CD18. *Blood* **1990**, *75* (5), 1037–1050.
35. Zhang, L.; Plow, E. F. Amino acid sequences within the alpha subunit of integrin alpha M beta 2 (Mac-1) critical for specific recognition of C3bi. *Biochemistry* **1999**, *38* (25), 8064–8071.
36. Mazzone, A.; Ricevuti, G. Leukocyte CD11/CD18 integrins: biological and clinical relevance. *Haematologica* **1995**, *80* (2), 161–175.
37. Kanse, S. M.; et al. Promotion of leukocyte adhesion by a novel interaction between vitronectin and the beta2 integrin Mac-1 (alphaMbeta2, CD11b/CD18). *Arterioscler., Thromb., Vasc. Biol.* **2004**, *24* (12), 2251–2256.
38. Lopez, G. P.; et al. Glow discharge plasma deposition of tetraethylene glycol dimethyl ether for fouling-resistant biomaterial surfaces. *J. Biomed. Mater. Res.* **1992**, *26* (4), 415–439.
39. Shen, M.; et al. Inhibition of monocyte adhesion and fibrinogen adsorption on glow discharge plasma deposited tetraethylene glycol dimethyl ether. *J. Biomater. Sci., Polym. Ed.* **2001**, *12* (9), 961–978.
40. Ratner, B. D.; Castner, D. G. Electron spectroscopy for chemical analysis. In *Surface Analysis - Techniques and Applications*; Vickerman, J. C., Reed, N. M., Eds.; John Wiley and Sons, Ltd.: Chichester, UK, 1996.

41. Helmkamp, R. W.; et al. High specific activity iodination of gamma-globulin with iodine-131 monochloride. *Cancer Res.* **1960**, *20*, 1495–1500.

42. Horbett, T. A. Adsorption of proteins from plasma to a series of hydrophilic-hydrophobic copolymers. II. Compositional analysis with the prelabeled protein technique. *J. Biomed. Mater. Res.* **1981**, *15* (5), 673–695.

43. Baron, S. *Medical microbiology*; 4th ed.; University of Texas Medical Branch at Galveston:Galveston, TX, 1996.

44. Markiewski, M. M.; et al. Complement and coagulation: strangers or partners in crime? *Trends Immunol.* **2007**, *28* (4), 184–192.

45. Varela, M. P.; et al. Biocompatibility of hemodialysis membranes: interrelations between plasma complement and cytokine levels. *Blood Purif.* **2001**, *19* (4), 370–379.

46. Moore, F. D., Jr.; et al. The effects of complement activation during cardiopulmonary bypass. Attenuation by hypothermia, heparin, and hemodilution. *Ann. Surg.* **1988**, *208* (1), 95–103.

47. Rabb, H.; et al. Use of a bovine model to study the role of adhesion molecule CD11/CD18 in hemodialysis-induced neutropenia. *Am. J. Kidney Dis.* **2002**, *39* (3), 587–593.

48. Payne, M. S.; Horbett, T. A. Complement activation by hydroxyethylmethacrylate-ethylmethacrylate copolymers. *J. Biomed. Mater. Res.* **1987**, *21* (7), 843–859.

49. Gemmell, C. H.; et al. Material-induced up-regulation of leukocyte CD11b during whole blood contact: material differences and a role for complement. *J. Biomed. Mater. Res.* **1996**, *32* (1), 29–35.

50. Tang, L.; Liu, L.; Elwing, H. B. Complement activation and inflammation triggered by model biomaterial surfaces. *J. Biomed. Mater. Res.* **1998**, *41* (2), 333–340.

51. Hirata, I. I.; et al. Study of complement activation on well-defined surfaces using surface plasmon resonance. *Colloids Surf., B* **2000**, *18* (3−4), 285–292.

52. Hirata, I.; et al. Deposition of complement protein C3b on mixed self-assembled monolayers carrying surface hydroxyl and methyl groups studied by surface plasmon resonance. *J. Biomed. Mater. Res., Part A* **2003**, *66* (3), 669–676.

53. Jang, H. S.; et al. Complement activation by sulfonated poly(ethylene glycol)-acrylate copolymers through alternative pathway. *Colloids Surf., B* **2006**, *50* (2), 141–146.

54. Unsworth, L. D.; Sheardown, H.; Brash, J. L. Polyethylene oxide surfaces of variable chain density by chemisorption of PEO-thiol on gold: adsorption of proteins from plasma studied by radiolabelling and immunoblotting. *Biomaterials* **2005**, *26* (30), 5927–5933.

55. Peracchia, M. T.; et al. Complement consumption by poly(ethylene glycol) in different conformations chemically coupled to poly(isobutyl 2-cyanoacrylate) nanoparticles. *Life Sci.* **1997**, *61* (7), 749–761.

56. Arima, Y.; Toda, M.; Iwata, H. Complement activation on surfaces modified with ethylene glycol units. *Biomaterials* **2008**, *29* (5), 551–560.

57. McNally, A. K.; Anderson, J. M. Complement C3 participation in monocyte adhesion to different surfaces. *Proc. Natl. Acad. Sci. U.S.A.* **1994**, *91* (21), 10119–23.
58. Janeway, C. A.; et al.; *Immunobiology*; Garland Science: New York, 2001.
59. Janatova, J. Activation and control of complement, inflammation, and infection associated with the use of biomedical polymers. *ASAIO J.* **2000**, *46* (6), S53–62.
60. Gorbet, M. B.; Sefton, M. V. Complement inhibition reduces material-induced leukocyte activation with PEG modified polystyrene beads (Tentagel) but not polystyrene beads. *J. Biomed. Mater. Res., Part A* **2005**, *74* (4), 511–522.
61. Jenney, C. R.; Anderson, J. M. Adsorbed serum proteins responsible for surface dependent human macrophage behavior. *J. Biomed. Mater. Res.* **2000**, *49* (4), 435–447.
62. Szott, L. M.; Horbett, T. A. The role of complement C3 and fibrinogen in monocyte adhesion to PEO-like plasma deposited tetraglyme. *J. Biomed. Mater. Res., Part A* **2010**, *95* (4), 1252–1260.
63. Tsai, W. B.; Grunkemeier, J. M.; Horbett, T. A. Human plasma fibrinogen adsorption and platelet adhesion to polystyrene. *J. Biomed. Mater. Res.* **1999**, *44* (2), 130–139.
64. Szott, L. M.; et al. Complement activation on poly(ethylene oxide)-like radiofrequency glow discharge-deposited surfaces. *J. Biomed. Mater. Res., Part A* **2011**, *96* (1), 150–161.
65. Nilsson, B.; et al. The role of complement in biomaterial-induced inflammation. *Mol. Immunol.* **2007**, *44* (1−3), 82–94.

Chapter 15

Effect of Microtopography on Fibrocyte Responses and Fibrotic Tissue Reactions at the Interface

David W. Baker and Liping Tang*

**Bioengineering Department, University of Texas at Arlington,
Arlington, Texas 76019-0138
*E-mail: ltang@uta.edu**

Governing the biomaterial mediated tissue response is critically importance for the future design and improvement of many medical implants. As such, an enormous amount of research effort has been placed on seeking a means to alter or control implant associated tissue reactions. Ultimately, the numerous strategies attempted boil down to a single notion of manipulating proteins and cells at the material interface. While the mechanisms and processes governing such reactions are not entirely understood, surface modification techniques have become the primary strategy, encompassing a wide variety of methods to improve the biomaterial interaction. While methods such as surface chemistry, functionality, and hydophobicity have all lead to various degrees of improvement, surface topography may be the largest contributor to combat adverse tissue and cellular reactions. We focus our discussion on the recent advances of surface topography manipulation and its effect on specific cellular responses both *in vitro* and *in vivo*. In particular we and others have found that micropillar topography has a profound effect on cellular morphology, migration, differentiation, and expression *in vitro*. The resultant influence of micropillar arrays on tissue responses *in vivo* however have only just begun to be investigated. Surprisingly, our own research has revealed that fibrocytes, circulating fibroblasts, but not macrophages are mostly responsible

In Proteins at Interfaces III State of the Art 2012; Horbett, T., et al.;
ACS Symposium Series; American Chemical Society: Washington, DC, 2012.

for micropillar-mediated tissue responses *in vivo*. A better understanding of the interactions between fibrocytes and micropillar topography may provide critical information for improving implant safety and function.

With continued advances in biomedical devices including novel polymers and intricate fabrication methods for advanced material implants there is a demand, now more than ever, to control the foreign body response and the biocompatibility of implants. Unfortunately, almost all biomedical implants are plagued with significant adverse reactions with localized tissue contact. Implant associated inflammation and tissue fibrosis lead to implant encapsulation and infection often resulting in the rejection of many medical devices (*1*, *2*). Poor tissue integration and the formation of thick fibrotic capsules surrounding implants contribute to the failure of many medical devices including, breast implants (*3*), drug delivery vehicles (*4*), and biosensors (*5*), as well as spine/joint (*6*, *7*), and eye implants (*8*). To improve the safety and efficacy of medical implants, substantial research efforts have been placed on the development of novel strategies for altering implant-associated tissue reactions.

An account of the foreign body reaction has been well established, while specific relationships between the various processes are not entirely understood. Most medical implants are covered with a layer of plasma proteins, seconds to minutes, following exposure to bodily fluids or blood (*9*). A few hours and days later, implants are surrounded by a large number of immune cells and a small number of fibroblast-like cells. Subsequently, collagen-rich fibrotic capsules are formed isolating the medical devices from the surrounding host tissue. After biomaterial implants are enclosed by adsorbed plasma proteins, a dense population of macrophages/monocytes forms prior to fibrotic tissue formation. It is therefore generally believed that biomaterial:protein interactions dictate biomaterial tissue compatibility and that biomaterial-mediated phagocyte interactions are responsible for the subsequent fibrotic tissue formation.

Surface Modifications on Cellular Responses

Intensive research efforts have lead to a deeper understanding of protein:biomaterial and protein:cellular interactions. The results of these works have also lead to a plethora of surface modification techniques. These studies have uncovered that surface chemistry, roughness, charge, hydrophobicity, or even simple micro and nano topographical cues alter protein and cellular reactions *in vitro*. The question remains however as to how these surface modifications will hold up to the foreign body response *in vivo*.

Adding surface functionality to a material has become an important modification technique to control protein and cellular interactions. By increasing surface functionality, it is possible to control the hydrophilicity, the interfacial free energy, and/or the ionic nature of the surface properties while leaving the bulk material properties unaffected (*10*). Some of the more common functional groups imparted to biomaterials are carboxyl (-COOH), hydroxyl (-OH), methyl ($-CH_3$), and amine ($-NH_2$). While these functionalities have shown significant influences on protein interactions and alteration of cellular function *in vitro*, the influence of surface functionality on implant-mediated fibrotic tissue responses *in vivo* was insignificant (*11*, *12*). The disappointing results may be influenced by the fact that the functional groups can only interact with cells at the interface. The effect of the surface functional groups may be substantially enhanced by increasing functionalized surface areas. To test this hypothesis, surface fuctionalization of polypropylene microspheres with varying species and densities of functional groups were tested for their ability to prompt fibrotic tissue responses (*11*, *13*). Indeed, our results have revealed that microparticles carrying various functional groups prompt an altered extent of fibrotic tissue responses, including capsule thickness, collagen deposition, and cell infiltration around the implant (*11*, *13*). Despite of these exciting observations, the effect of surface functional groups on tissue responses may be, in part, surface topography dependent. For example, it has been shown that substrates bearing different surface chemistry but similar topography prompt similar inflammatory responses, indicating topography as a major contributor to tissue repair (*14*). Therefore, several studies were carried out to investigate the influence of implant topography on tissue responses.

Implant Topography on Cellular and Tissue Responses

The geometrical configuration of the topographical features has become a significant target in the design of biomaterials. Subjects such as porosity, pore size, patterning, alignment, interconnectivity, surface roughness and curvature have all become increasingly hot topics with the design of scaffolds and novel biomaterials utilizing pores, pits, channels, grooves, pegs, and pillars. These architectural changes, even on substrates of the same chemical makeup, have revealed significant differences in cell responses and protein adhesion *in vitro*. One example is that the notion of cell contact guidance, a cells ability to respond to surface features, has been proven critical in manipulating cellular behavior (*15*). Cells respond to environmental cues by adjusting their morphology, orientation, expression, and even characteristics through differentiation. As such, a wide range of topographical signals have been investigated in an attempt to control cellular functions. A simple modification is to enhance the surface roughness characteristics. Although random, not organized or confined, surface roughness has shown improvements in cellular attachment and expression over smooth surfaces (*16*, *17*). Furthermore, surface porosity has been found to affect tissue vascularity. By analyzing tissue vascularization at the tissue interface, an early study found that larger pore polytetrafluoroethylene (PTFE) membranes (0.8-8 micrometer pore size) prompted 80-100 fold more vascular structure than small pore membranes (0.02 micrometer pore size) (*18*). Furthermore, for 3D scaffold constructs, vascularization has been shown to be significantly faster for pores with a size greater than 250 μm (*19*). It has been documented by many studies that interconnected pores and high porosity of scaffolds maximizes cell penetration during seeding as well as nutrient supply and waste transport (*20*). Interconnected pores however are most often random. In the design of specific constructs, such as blood vessels, it may be beneficial to have higher degree of structural orientation (*21*). In a study on porosity characteristics of β-tricalcium phosphate it was found that the size of the interconnections between pores was more important for the degree of vascularization than the actual pore size (*22*). Interestingly, with similar scaffolds, it was found that the degree of fibrous tissue in-growth increased with decreasing pore size from 700 to 300 μm (*23*). The degree of organization and pore shape has also been studied for collagen formation. In vitro, large scale (200 μm) rectangular pores or diamond shaped pores were found to guide cell and collagen orientation more effectively than square shaped pores (*24*). While it is clear that the characteristics of porosity influence cell infiltration and vascularity, it has also been shown that protein adsorption, cell migration and cell differentiation are influenced not only by pore size but also by the pore curvature, suggesting an intimate mechanosensing cellular mechanism (*25*).

Despite of these exciting observations, the mechanism(s) governing such topography-mediated tissue responses are mostly undetermined due to the fact that the substrates and characteristics vary significantly, and in earlier works parameters such as interconnectivity were not controlled. To identify the physical factors critical for differential cellular responses, surfaces with more sophisticated and controlled geometrical patterning are needed. Substrates with different sizes (from nanometers to micrometers) of channels, grooves and pillars have become available in recent years with the development of lithography and nanotechnology. The effect of these man-made structures on protein and cellular behavior has been widely studied. Surface features as small as 10 nm have generally been recognized to affect both protein adsorption and cellular responses (*17*). Similar to native cues of the extracellular matrix (ECM), nanotopography is theorized to provide biomimetic cell–modulating signals altering cell attachment, migration, and proliferation for cells such as osteoblasts, fibroblasts, endothelial, epithelial and macrophages (*17*). Along these lines micro-surface roughness has been shown to substantially enhance the mechanosensing of osteoblasts and increase bone formation (*26*). A study without osteoinductive media similarly found that osteogenic capacity can be tuned by controlling the diameter of mixed micro/nanoscale pits on polycaprolacton (*27*). This study found that topography alone was sufficient to promote *in vitro* bone formation by human osteoblasts. Alternatively, macrophage behavior may be modulated by nanogrooves *in vivo* altering cytokine secretion and ultimately affecting the foreign body response (*14*). Channels or grooves have also shown a remarkable ability to organize alignment and migration of cells *in vitro*. Endothelial cells for instance have been shown to preferentially align in the direction of the channels when coated with fibronectin (*28*). Tenocytes are similarly affected by microgrooves in the 50μm range impacting shape, alignment, and matrix organization (*29*). It has been further discussed by McNamara et al. that mechano-transduction from topography alignment cues (microgrooved silica glass 12.5μm wide 2μm deep) leads to chromosomal repositioning and gene regulation (*30*). This is thought to be a result of tensile and compressive forces acting on the nuclear lamina (*30*). These studies and others clearly demonstrate that geometrical constraints such as patterning, space, height, and curvature, may dictate cellular attachment proliferation and even gene expression of many cell types.

Surface Topography on Implant Tissue Compatibility

Channels and grooves have mostly been limited to *in vitro* studies with few deviations toward the *in vivo* setting. A murine study utilizing poly(e-caprolactone), poly(lactic acid) and poly(dimethyl siloxane) gratings from 250nm to 2µm found that macrophage behavior was affected *in vivo* primarily with cell adhesion on the larger sized gratings (*14*). In contrast however a study utilizing polystyrene disks with microgrooves from 1-10µm found no discernible differences in the tissue reaction between smooth and microgrooved implants in a goat model (*31*). Despite these and other differences, microgrooved substrates have made a significant impact on our understanding of cellular attachment and alignment cues *in vitro*, although alignment is primarily limited to a unilateral direction. Another disadvantage to microgrooves is the ability to alter the substrate rigidity, which more closely resembles the bulk properties of the material and is less precisely controlled with long unidirectional channels. To further investigate cellular attachment and alignment but also improve on the rigid flexible nature of the surface we turn to micropillars.

Micropillars or pegs have several unique features that provide a good model implant for cellular studies. First the geometrical configuration of micro pillars including diameter, spacing and height are easily controlled by lithography or mold inversion process techniques. The pattern, typically square, hexagonal (Figure 1), or semiordered may also be specifically designed, and has been shown to either hamper (square orientation with small spacing) or favor (hexagonal orientation with larger spacing) cellular migratory responses. The shape of the pillar, curvature, or edge constraints, can also be concisely constructed (*32*). Micropillars additionally offer a unique flexibility or elasticity to surfaces that otherwise would be highly rigid. In conjunction, the surface area may be greatly increased and the hydrophilicity/ hydrophobicity may be altered on an intrinsically nonadhesive surface by the addition of micropillars (*33*). This unique characteristic is controlled by the density and stiffness of the pillars, which are ultimately effected by their spacing, height, and diameter. The stiffness of the pillars and the ability of the cells to exert contractile forces may have a significant influence on the cellular biology. Studies have shown that culturing cells on micropillars tends to promote cell attachment while reducing proliferation (*34*). By providing contact guidance, micropillars are observed to support cell adhesion and elongation as well as cytoskeleton orientation. In addition several studies have recently reported mechanical regulation of cell function or differentiation due to elastomeric changes based on pillar height (*35*).

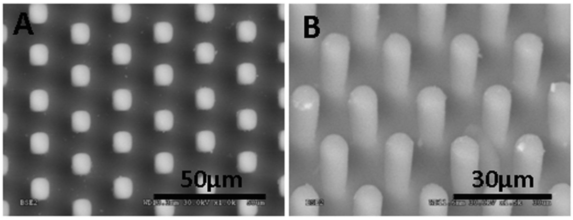

Figure 1. Hexagonal arrangement of micropillars from (A) the top or (B) the side view. In both A and B the pillars are spaced 20 µm apart on center, are 25 µm in height, and have a diameter of 10 µm. (Adapted with permission from reference (36). Copyright 2011 American Chemical Society.)

Concise topographical changes by the alteration of pillar geometry and size characteristics can also result in a significant shift in inflammation and fibrosis around an implant. We have recently observed a drastic change in cellular responses to varying pillar geometries. Surprisingly we have found that different types of cells prompt varying responses to the same micropillar substrates (*36*). We focused our study on macrophages and fibroblasts as they are thought to be the main cells responsible for inflammatory and fibrotic responses. What we found is that differences in the height of the micropillars (14-25 µm) altered the attachment and growth of fibroblasts, increasing with height, however differences in the spacing of the pillars (20-70 µm) hampered growth of macrophages *in vitro*. The difference in fibroblast growth was in agreement with several previous studies which attribute the increased spatial surface area to greater extracellular matrix production and cell activation (*33*, *37*). Interestingly the macrophage response was unexpected and contradictory to the general assumption that macrophages are solely responsible for triggering fibrotic tissue reactions. This indicated that the pillar topography may have had a greater impact on the fibroblast activation/ adhesion *in vivo*. Our *in vivo* results uncover significant differences in the tissue response at the biomaterial interface in cell density, capsule thickness, collagen percentage, granulation tissue thickness and angiogenesis (*36*). It is not clear however what the source of the fibrotic cells is, how surface topography affected the fibroblast response, and if this change alone can account for the differences in the tissue response at the interface.

Coincidentally, recent studies have uncovered novel circulating fibroblast-like cells termed fibrocytes (*38*, *39*). Fibrocytes, often denoted by either $CD45^+$ or $CD34^+$ in conjunction with either collagen I^+ or $vimentin^+$, have been shown in many recent works to play a pivotal role in the pathogenesis of pulmonary, renal, hepatic and dermal fibrosis (*40–42*). In wound healing these fibroblast-like precursor cells differentiate into myofibroblasts and secrete collagen, vimentin, actin, and other proteins which influence the developing fibrotic matrix. Our studies have revealed the presence of fibrocyte cells at the implant interface (*36*, *43*). Interestingly it has been demonstrated in pulmonary fibrosis that fibrocyte recruitment corresponds directly with collagen production in the lung (*44*). In our investigation we similarly demonstrate that the fibrocyte response to the implant correlates with the collagen production at the interface and the progression of the fibrotic reaction out to 14 days. We observe a maximal accumulation of fibrocytes around 10 days post implantation, followed by a decrease in numbers as the fibrocytes down-regulate expression of leukocyte CD34 and CD45 markers and up-regulate α-SMA during the transition to myofibroblasts (*43*). Myofibroblasts are found at the site of tissue injury and are believed to be critically involved in the healing process by secreting ECM proteins and promoting contraction (*45*). Several environmental factors such as the presence of transforming growth factor beta (TGF-β) have been shown to transition fibrocytes into myofibroblasts *in vitro* (*46*). Interestingly it has also been shown that other factors such as interleukin 1-beta (IL-1β) may function to maintain fibrocytes in a pro-inflammatory state leading to an increase in the inflammatory cell population during wound healing (*47*). We hypothesize that the microenvironment cues are altered by the various pillar geometries and cellular interactions, allowing fibrocytes and fibroblasts to have a more dominant influence on the tissue response. The question remains however as to how a difference in pillar geometry alters the micro-environmental cues.

Effect of Surface Topography on Protein Adsorption and Cellular Behavior at the Interface

Several studies have suggested that micropillar features provide more surface area for cells to form focal connections (*33*, *37*). Alternatively, it has been shown that patterning of polydimethylsiloxane (PDMS) surfaces with dot-like protrusions increased fibrinogen adsorption by 46% compared with the flat surface, while surface area was only increased by 8% (*48*). This alteration in fibrinogen adsorption was shown to influence fibroblast adhesion and morphology. Additionally it was found that human fibroblasts attempt to endocytose or internalize polymethylmethacrylate nanocolumns (160nm in height, 230nm spacing, and 100nm in diameter), showing a more macrophage-like morphology (*49*, *50*). These differences show the vast potential of micropillars and controlled topographical features to alter cellular behavior.

Altering the features of the micropillars such as height, spacing, diameter, and configuration also changes material substrate properties such as elasticity. It has been shown in several studies that cells are highly responsive to substrate stiffness or rigidity (*35*, *51*). As an example, micropost rigidity has been found to impact stem cell morphology, focal adhesions, and cytoskeleton contractility leading to alterations in stem cell fate, or differentiation (*35*). We hypothesize that these mechanisms may similarly impact precursor fibrocytes in the foreign body response. Enhancing the predisposition of fibrocytes to differentiate into myofibroblasts leads to further collagen production and may also have a significant impact on the orientation and alignment of the collagen within the fibrotic capsule. As previously mentioned we have observed differences with macrophage and fibroblast cells in contact with smooth or pillared surfaces. These potential differences are demonstrated in the schematic shown in Figure 2 representing a hypothetical in vitro response. Shown here as fibroblastic or phagocytic cells, we have observed significant differences from the initial interaction to the preferential interaction and accumulation of cells on the smooth and pillared substrates. While phagocytic cells preferentially adhere and spread on the smooth surface, fibroblastic cells become more prominent on the micropillar substrate. Fibrocytes may behave similarly with an enhanced response to the cues provided by micropillars. We hypothesize that this cell: surface interaction would increase fibrocyte signaling while decreasing phagocytic cell reactions. The difference in the resultant response may be more inflammatory on the smooth surface with an increase in factors such as IL-1β and TNF-α, or more wound healing with increased TGF-β and myofibroblast production.

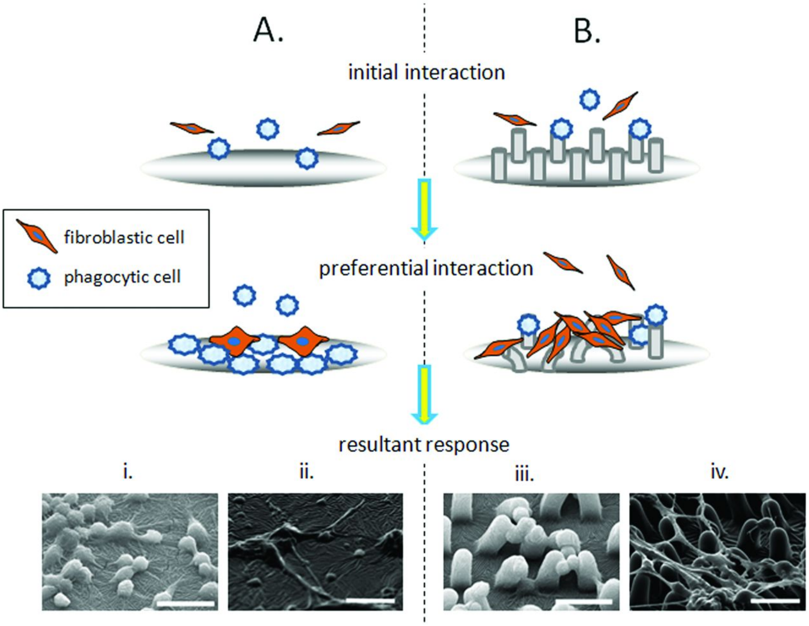

Figure 2. Schematic of cellular response to smooth (A) and micropillar (B) substrates. After the initial cellular-substrate interaction, there is a preferential interaction of fibroblastic cells on the pillared substrate, and phagocytic cells on the smooth substrate. The resultant response shows a spreading cell morphology for both phagocytic (i) and fibroblastic (ii) cells on the smooth substrate. Alternatively the resultant response on the pillared substrate shows small low proliferative phagocytic cells (iii), and spindle shaped highly proliferative fibroblastic cells (iv). (All scale bars = 25 μm.)

There are at least three main modes of cell mediation to the biomaterial surface, focal adhesions, close contacts, and extracellular contacts. Cells are guided by focal adhesions, which in turn are mostly altered by the initial protein adsorption to the implant. Interestingly the amount, composition and degree of host protein adsorption may be altered by specific topographical cues. This simple shift in initial protein interaction with the surface has shown great propensity to influence the final cellular interactions and shift the inflammatory/fibrotic response. This could either enhance or diminish the encapsulation effect which may result in enhanced functionality of the medical device. Micropillars have been shown to alter the protein attachment at the interface based on topography. An intrinsically hydrophilic material may lose its resistance to protein binding based on geometry (*52*). Alternatively, a hydrophobic material may lose its resistance to cell adhesion. This interaction may be primarily due to spatial changes in topography, however there are also intrinsic changes in the surface area and free energy. In addition it has been observed that there are significant differences in the micro and nano scale interactions. A recent study suggests that the adhesion and mechanical cues provided by the pillars alters the microenvironment, enhancing adhesive interactions with cells and the production of proteins that form mechano-chemical feedback (*34*). The alteration of these cues can have a profound influence on cellular behavior.

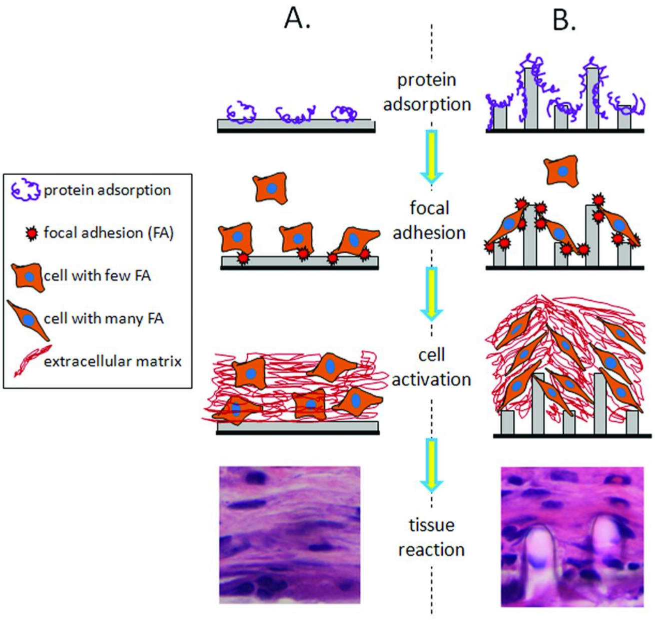

Figure 3. Schematic depicting theoretical protein adsorption, focal adhesion, and cell activation on smooth (A) and pillared (B) substrates, leading to the observed tissue reaction. Micropillar surfaces may provide increased protein adsorption, followed by greater focal connections, and altered cellular activation. A shifting orientation of cellular attachment and activation may lead to production differences and directional changes in matrix accumulation. Histology images are presented (hematoxylin and eosin staining) for subcutaneous PDMS film (smooth substrate) and pillar [20 µm spacing 25 µm height] implants at two weeks in a murine model.

Shifting focal adhesions and directional organization of the cells on channels and grooves is found to have an additional impact on the later organization of the extracellular matrix. It is well known that channels or grooves alter the cellular morphology often in the direction of the grooves dependent upon geometrical constraints. In addition, it has been found that the primary organization of cells results in alignment of produced ECM and further orientation of subsequent cell layers *in vitro,* more closely resembling the native tissue (*53*). The ECM is made up of polysaccharides and proteins (*54*) and works to regulate cell function as both a positive and negative regulator of differentiation and gene expression (*54*). It has been observed that shifting cellular patterns show a resultant change in the ECM. This dramatic effect of ECM on cellular behavior has been described in several culture models such as hepatocytes, mammary epithelial cells, and keratinocytes (*54*). Based on the above analysis performed on channels we hypothesize that a similar mechanism would exist for the *in vivo* formation of the ECM in response to micropillars. Figure 3 outlines the theoretical difference in protein adsorption, cellular adhesion, and cell activation leading to the observed tissue reaction. Increased surface area and protein adsorption may lead to increased cellular adhesion on micropillar substrates over smooth surfaces (Figure 3). It is also possible that the increased focal contacts, as a result of changing pillar dimensions, would enhance the mechano-chemical feedback to the cell. Based on the geometrical constraints, or lack of constraints, the ECM formation would be laid down in a manner resembling the initial cellular attachment. Indeed, our histological analysis confirms similar trends for the smooth and micropillar surfaces (*36*). Therefore, with precise control of the micropillar parameters, such as stiffness or rigidity, it may be possible to engineer the orientation of the extracellular matrix.

Changing Collagen Alignment with Micropillar Topography

The idea of contact guidance, cells orientation due to physiological topography is not new. The trends in research however are suggesting that there may be a greater impact on the protein arrangement due to topography which in turn alters the cellular response. With a shift in the cellular response the produced extracellular matrix may orient in a similar fashion as dictated by topography. It has been shown that cell expression, morphology, and even nucleus deformation are all responsive to the topography *in vitro* (*55*). On the other hand, matrix production and collagen alignment, while distinctly arranged by micro- and nano-grooves *in vitro*, may be responsive to micropillar substrates *in vivo*.

As a model for topographical features, we investigated three spatial arrangements of micropillars (*36*). All pillars were 10µm in diameter in a hexagonal arrangement. To investigate the tissue response to various geometries, the interspaces and heights of the pillars were altered. Three spatial dimensions were investigated distancing the pillars from center to center at 20, 35, and 70 µm. Two pillar heights were investigated at 14, and 25 µm. We found that different cell types, specifically macrophages and fibroblasts, respond differently to the same microtopographical cues (*36*). *In vivo* we observe that higher micropillar substrates gather more granulocytes and fibroblasts. In fact cellular density at the interface of taller pillar substrates increased more than 50% over the control. Additionally the capsule thickness was found to increase with pillar height but only becoming statistically significant when pillars were placed further apart. While the increase in cellular density may be closely related to a change in the tensile modulus or stiffness of the pillars, there is also a clear augmentation in the response resulting from the spacing or distance between pillars. Our results suggest that the greater distance and increased height had a substantial effect on the cellular activation and production of ECM. Taking a closer look at the tissue responses we similarly noticed that the granulation tissue (accumulation of phagocytic cells), neoangiogenesis, and collagen production where all enhanced by the increasing pillar dimensions.

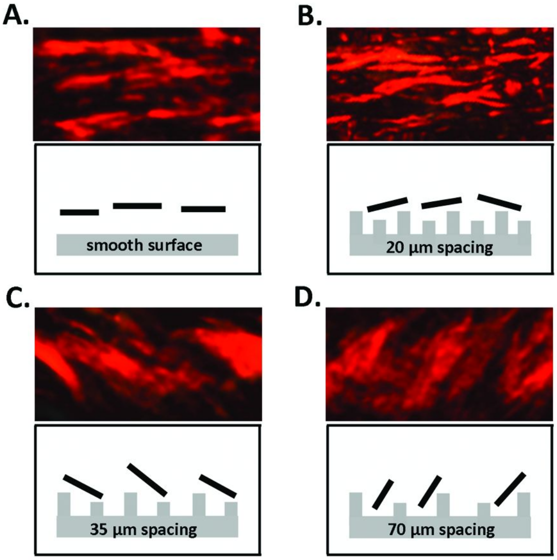

Figure 4. Representative histological images and schematics of observed in vivo collagen alignment with PDMS micropillar samples. Collagen alignment is observed at the biomaterial interface with picro-sirius red staining taken with polarized microscopy. The birefringent images show collagen 1 fibril orientation for smooth (A), 20 (B), 35 (C), and 70 (D), µm spaced micropillars at a height of 25 µm. Schematics outline general orientation of collagen fibrils (black vectors) observed in the samples.

Animal implantation study supports that the micropillar topography may shift the inflammatory fibrotic response dependent upon pillar height and spacing. The resultant change *in vivo* is a drastic difference in the amount of granulation tissue, which is important for wound healing, as well as the level of collagen production by resident and recruited fibroblasts. Interestingly investigation into specific collagen fiber alignment with polarized light microscopy demonstrates that the specific pillar orientation alters the layout of the collagen fibrils. Such differential collagen fiber alignment can be observed in the birefringent images from picro-sirius red staining for collagen as well as representative vectors for the collagen fibril orientation (Figure 4). The smooth surface control and each pillar substrate, three pillar spacings and two pillar heights, were studied after two weeks *in vivo*. In the control sample (without pillar), implants are surrounded with dense collagen fibrils which are mostly oriented in parallel with the substrate or flow like a wave through the implant interface (Figure 4a). This response is also observed to be translated though the fibrotic capsule mimicking the same fiber directions when the capsule reaches the normal tissue of the epidermis. As the pillars become further spaced apart the fiber orientation begins to lose this intrinsic wave and become more segregated adapting to an un-parallel formation. In the 35 µm spacing arrangement (Figure 4c), there is clear organization at the interface of cells with the implant. In the 70 µm spacing (Figure 4d), the fibers seem disconnected with a greater percent at almost perpendicular angles to the pillar implant. This difference in organization may potentially have a profound influence on the fibrotic capsule contraction around the implant. It should be noted that similar trends were also observed for the 14 µm pillar height (not shown), but were less significant. It is clear that the micropillar configurations not only had a profound effect on the fibrotic outcome but also influenced the direction and orientation of the resultant ECM produced throughout the fibrotic capsule. This result may have further implications into the potential use for micropillar implants where it may be possible to orient the collagen fibers in applications such as anisotropic tissues for which collagen alignment is of utmost importance to the function of the tissue.

Implications/Applications

Micro- and nano- topography has a high potential to alter cellular and protein interactions at the material interface. Our results suggest that surface topography affects fibrocyte responses and subsequent collagen production/orientation. By creating an un-parallel collagen matrix, the presence of surface micropillars at the interface may indirectly reduce fibrotic capsule contraction. Despite of many exciting findings, numerous gaps remain in our understanding on the influence of surface topography on cellular responses. For example; how surface topography affects cellular responses such as activation? How the microenvironment cues are altered by the various pillar geometries? What role increased protein adsorption and focal adhesions play? How pillar height and spacing affect fibrocyte responses? And why various cell types respond differently to the same topographical cues?

The results of these works may have significant impact on the design of medical implants with improved safety and/or tissue reactivity. For example, many load-bearing soft tissues are subject to a high degree of mechanical anisotropy, including heart valves, blood vessels, tendons, skin, cartilage, myocardium and pericardium (*24*, *56*). To develop physiologically equivalent replacements, the aim of tissue engineering is to mimic the native structure. It is believed that the basis for the anisotropy is the collagen fiber structure. While there are several models that exist to study the nature of the collagen formation and alignment, the development of a substrate to direct cell function and matrix production in a physiologically equivalent manner remains a difficult challenge. For example, hydrogels are typically used to study collagen formation, however load constraints must constantly be applied to control the structural organization of the collagen fibers (*56*). Micropillars may offer an alternative approach in the design of anisotropic collagen fibril formation with concise design parameters to control the cells, matrix production, and alignment.

Acknowledgments

This work was supported by NIH Grant EB007271 and AHA-South Central Affiliate Grant-in-Aid Award.

References

1. Tang, L.; Eaton, J. W. *Am. J. Clin. Pathol.* **1995**, *103*, 466–471.
2. Tang, L.; Eaton, J. W. *Mol. Med.* **1999**, *5*, 351–358.
3. Prantl, L.; Schreml, S.; Fichtner-Feigl, S.; Poppl, N.; Eisenmann-Klein, M.; Schwarze, H.; Fuchtmeier, B. *Plast. Reconstr. Surg.* **2007**, *120*, 275–284.
4. Patil, S. D.; Papadimitrakopoulos, F.; Burgess, D. J. *Diabetes Technol. Ther.* **2004**, *6*, 887–897.
5. Clark, H. R.; Barbari, T. A.; Rao, G. *Biotechnol. Prog.* **1999**, *15*, 259–266.
6. Seymour, J. P.; Kipke, D. R. *Biomaterials* **2007**, *28*, 3594–3607.
7. Sargeant, A.; Goswami, T. *J. Surg. Orthop. Adv.* **2006**, *15*, 111–112.
8. Steedman, M. R.; Tao, S. L.; Klassen, H.; Desai, T. A. *Biomed. Microdevices* **2010**, *12*, 363–369.
9. Tang, L.; Ugarova, T. P.; Plow, E. F.; Eaton, J. W. *J. Clin. Invest.* **1996**, *97*, 1329–1334.
10. Thevenot, P.; Hu, W.; Tang, L. *Curr. Top. Med. Chem.* **2008**, *8*, 270–280.
11. Nair, A.; Zou, L.; Bhattacharyya, D.; Timmons, R. B.; Tang, L. *Langmuir* **2008**, *24*, 2015–2024.
12. Tang, L.; Wu, Y.; Timmons, R. B. *J. Biomed. Mater. Res.* **1998**, *42*, 156–163.
13. Kamath, S.; Bhattacharyya, D.; Padukudru, C.; Timmons, R. B.; Tang, L. *J. Biomed. Mater. Res., Part A* **2008**, *86*, 617–626.
14. Chen, S.; Jones, J. A.; Xu, Y.; Low, H. Y.; Anderson, J. M.; Leong, K. W. *Biomaterials* **2010**, *31*, 3479–3491.
15. Sutherland, J.; Denyer, M.; Britland, S. *J. Anat.* **2005**, *206*, 581–587.
16. von Recum, A. F.; van Kooten, T. G. *J. Biomater. Sci., Polym. Ed.* **1995**, *7*, 181–198.
17. Lord, M. S.; Foss, M.; Besenbacher, F. *Nano Today* **2010**, *5*, 66–78.
18. Brauker, J. H.; Carr-Brendel, V. E.; Martinson, L. A.; Crudele, J.; Johnston, W. D.; Johnson, R. C. *J. Biomed. Mater. Res.* **1995**, *29*, 1517–1524.
19. Laschke, M. W.; Harder, Y.; Amon, M.; Martin, I.; Farhadi, J.; Ring, A.; Torio-Padron, N.; Schramm, R.; Rucker, M.; Junker, D.; Haufel, J. M.;

Carvalho, C.; Heberer, M.; Germann, G.; Vollmar, B.; Menger, M. D. *Tissue Eng.* **2006**, *12*, 2093–2104.

20. Ikada, Y. *J. R. Soc., Interface* **2006**, *3*, 589–601.
21. Hu, X.; Shen, H.; Yang, F.; Bei, J.; Wang, S. *Biomaterials* **2008**, *29*, 3128–3136.
22. Bai, F.; Wang, Z.; Lu, J. X.; Liu, J. A.; Chen, G. Y.; Lv, R.; Wang, J.; Lin, K. L.; Zhang, J. K.; Huang, X. *Tissue Eng. Part A* **2010**, *16*, 3791–3803.
23. Bai, F.; Zhang, J. K.; Wang, Z.; Lu, J. X.; Chang, J. A.; Liu, J. A.; Meng, G. L.; Dong, X. *Biomed. Mater.* **2011**, *6*, 015007.
24. Engelmayr, G. C., Jr.; Papworth, G. D.; Watkins, S. C.; Mayer, J. E., Jr.; Sacks, M. S. *J. Biomech.* **2006**, *39*, 1819–1831.
25. Berry, C. C.; Campbell, G.; Spadiccino, A.; Robertson, M.; Curtis, A. S. *Biomaterials* **2004**, *25*, 5781–5788.
26. Boyan, B. D.; Lossdorfer, S.; Wang, L.; Zhao, G.; Lohmann, C. H.; Cochran, D. L.; Schwartz, Z. *Eur. Cell Mater.* **2003**, *6*, 22–27.
27. Wilkinson, A.; Hewitt, R. N.; McNamara, L. E.; McCloy, D.; Dominic, M. R. M.; Dalby, M. J. *Acta Biomater.* **2011**, *7*, 2919–2925.
28. Feinberg, A. W.; Wilkerson, W. R.; Seegert, C. A.; Gibson, A. L.; Hoipkemeier-Wilson, L.; Brennan, A. B. *J. Biomed. Mater. Res., Part A* **2008**, *86*, 522–534.
29. Kapoor, A.; Caporali, E. H.; Kenis, P. J.; Stewart, M. C. *Acta Biomater.* **2010**, *6*, 2580–2589.
30. McNamara, L. E.; Burchmore, R.; Riehle, M. O.; Herzyk, P.; Biggs, M. J.; Wilkinson, C. D.; Curtis, A. S. G.; Dalby, M. J. *Biomaterials* **2012**, *33*, 2835–2847.
31. Walboomers, X. F.; Croes, H. J.; Ginsel, L. A.; Jansen, J. A. *J. Biomed. Mater. Res.* **1998**, *42*, 634–641.
32. Ng, C. K. M.; Yu, K. N. *Biointerphases* **2012**, *7*, 21.
33. Schulte, V. A.; Diez, M.; Moller, M.; Lensen, M. C. *Biomacromolecules* **2009**, *10*, 2795–2801.
34. Patel, A. A.; Thakar, R. G.; Chown, M.; Ayala, P.; Desai, T. A.; Kumar, S. *Biomed. Microdevices* **2010**, *12*, 287–296.
35. Fu, J.; Wang, Y. K.; Yang, M. T.; Desai, R. A.; Yu, X.; Liu, Z.; Chen, C. S. *Nat. Methods* **2010**, *7*, 733–736.
36. Baker, D. W.; Liu, X.; Weng, H.; Luo, C.; Tang, L. *Biomacromolecules* **2011**, *12*, 997–1005.
37. Frey, M. T.; Tsai, I. Y.; Russell, T. P.; Hanks, S. K.; Wang, Y. L. *Biophys. J.* **2006**, *90*, 3774–3782.
38. Bucala, R.; Spiegel, L. A.; Chesney, J.; Hogan, M.; Cerami, A. *Mol. Med.* **1994**, *1*, 71–81.
39. Quan, T. E.; Cowper, S.; Wu, S. P.; Bockenstedt, L. K.; Bucala, R. *Int. J. Biochem. Cell Biol.* **2004**, *36*, 598–606.
40. Quan, T. E.; Cowper, S. E.; Bucala, R. *Curr. Rheumatol. Rep.* **2006**, *8*, 145–150.
41. Strieter, R. M.; Keeley, E. C.; Hughes, M. A.; Burdick, M. D.; Mehrad, B. *J. Leukoc. Biol.* **2009**, *86*, 1111–1118.

42. Mori, L.; Bellini, A.; Stacey, M. A.; Schmidt, M.; Mattoli, S. *Exp. Cell Res.* **2005**, *304*, 81–90.
43. Thevenot, P. T.; Baker, D. W.; Weng, H.; Sun, M. W.; Tang, L. *Biomaterials* **2011**, *32*, 8394–8403.
44. Phillips, R. J.; Burdick, M. D.; Hong, K.; Lutz, M. A.; Murray, L. A.; Xue, Y. Y.; Belperio, J. A.; Keane, M. P.; Strieter, R. M. *J. Clin. Invest.* **2004**, *114*, 438–446.
45. Gabbiani, G. *J. Pathol.* **2003**, *200*, 500–503.
46. Schmidt, M.; Sun, G.; Stacey, M. A.; Mori, L.; Mattoli, S. *J. Immunol.* **2003**, *171*, 380–389.
47. Chesney, J.; Metz, C.; Stavitsky, A. B.; Bacher, M.; Bucala, R. *J. Immunol.* **1998**, *160*, 419–425.
48. Chen, H.; Song, W.; Zhou, F.; Wu, Z.; Huang, H.; Zhang, J.; Lin, Q.; Yang, B. *Colloids Surf., B* **2009**, *71*, 275–281.
49. Dalby, M. J.; Riehle, M. O.; Sutherland, D. S.; Agheli, H.; Curtis, A. S. *J. Biomed. Mater. Res., Part A* **2004**, *69*, 314–322.
50. Dalby, M. J.; Berry, C. C.; Riehle, M. O.; Sutherland, D. S.; Agheli, H.; Curtis, A. S. *Exp. Cell Res.* **2004**, *295*, 387–394.
51. Dickinson, L. E.; Rand, D. R.; Tsao, J.; Eberle, W.; Gerecht, S. *J. Biomed. Mater. Res., Part A* **2012**, *100*, 1457–1466.
52. Lensen, M. C.; Schulte, V. A.; Salber, J.; Diez, M.; Menges, F.; Moller, M. *Pure Appl. Chem.* **2008**, *80*, 2479–2487.
53. Guillemette, M. D.; Cui, B.; Roy, E.; Gauvin, R.; Giasson, C. J.; Esch, M. B.; Carrier, P.; Deschambeault, A.; Dumoulin, M.; Toner, M.; Germain, L.; Veres, T.; Auger, F. A. *Integr. Biol.* **2009**, *1*, 196–204.
54. Lin, C. Q.; Bissell, M. J. *FASEB J.* **1993**, *7*, 737–743.
55. Pan, Z.; Yan, C.; Peng, R.; Zhao, Y. C.; He, Y.; Ding, J. D. *Biomaterials* **2012**, *33*, 1730–1735.
56. Thomopoulos, S.; Fomovsky, G. M.; Chandran, P. L.; Holmes, J. W. *J. Biomech. Eng.* **2007**, *129*, 642–650.

Chapter 16

Specific and Nonspecific Interactions between Salivary Proteins and *Streptococcus mutans*

**Chun-Ping Xu,[1] Henk J. Busscher,[1] Henny C. van der Mei,[1]
and Willem Norde*,[1,2]**

**[1]Department of Biomedical Engineering, University Medical Center
Groningen, and University of Groningen, Antonius Deusinglaan 1, 9713 AV,
Groningen, The Netherlands
[2]Laboratory of Physical Chemistry and Colloid Science,
Wageningen University and Research Center, Dreijenplein 6, 6703 HB,
Wageningen, The Netherlands
*E-mail: Willem.Norde@wur.nl**

Adhesion of proteins to natural surfaces, such as the bacterial cell wall, may be controlled by non-specific and/or specific interactions. The latter ones are mediated by adhesins on the (bacterial) surface. This paper reports on the interaction between saliva proteins and *Streptococcus mutans*, an oral bacterium that is involved in tooth decay, by comparing two strains of *S. mutans*, one with and one without the adhesin antigen I/II on its surface. Bacterium-saliva interaction is characterized in terms of enthalpy (calorimetry), strength of adhesive bond (AFM), affinity (adsorption isotherms), and kinetics of adhesion of the bacterial strains to a saliva-coated surface (parallel plate flow chamber). The study shows that the presence of antigen I/II at the streptococcal surface adds favorable binding sites that are biologically recognized by (a number of) salivary proteins. Thus, superimposed on generic interactions, specific pH-dependent short-range interactions contribute dominantly to the adhesion of antigen I/II containing *S. mutans* to salivary coatings, such as salivary conditioning films on tooth surfaces.

In Proteins at Interfaces III State of the Art 2012; Horbett, T., et al.;
ACS Symposium Series; American Chemical Society: Washington, DC, 2012.

Introduction

Adhesion of bacteria is occurring widely spread in nature as well as in technological applications. In nature bacterial mass predominantly exists in biofilms at surfaces (*1*), as, *e.g.*, in soil and surface waters, in the marine environment, and in organisms.

Several biological fluids contain bacteria and proteins. Both are surface active, that is they prefer to be accommodated at a surface. Usually, the proteins are present in a much higher number than the bacteria and they are much smaller, and, therefore diffuse faster. They easily win the race for the surface and form a film at the surface before the bacteria arrive. The bacteria, that subsequently adhere to the pre-adsorbed protein layer, may proliferate and form a “biofilm” (*2*). Biofilms are micro-ecosystems in which different strains and species of microorganisms efficiently cooperate in order to protect themselves against environmental stress and to facilitate nutrient uptake (*3*). In the human body many different biofilms exist. Some of them are essential for the maintenance of health, and offer, for instance, protection against invasion of pathogens (*4*), whereas other biofilms are detrimental to the body. An example of adverse biofilms is oral biofilm on tooth surfaces. Bacteria in the oral cavity feed on food remnants, notably sugars and other carbohydrates, thereby producing acids that cause dental caries, *i.e.,* the decay of tooth enamel and dentine. Streptococci play a major role in the initiation of dental caries.

The interaction between adhering bacteria and the pre-adsorbed salivary conditioning film includes generic, non-specific forces, such as electrostatic, hydrophobic and steric forces. Superimposed on these, specific interactions may play a major role. Specific interactions are usually between a ligand and a receptor and may be referred to as “biological recognition”. Both the non-specific and specific interactions originate from the same fundamental forces, but in specific interactions there is a synergy of different types of forces operating highly directionally in a confined space, yielding strong attraction between the interacting species.

Several bacteria have proteinaceous structures on their surface, so-called “adhesins”, that promote their adhesion through biological recognition of saccharides or protein receptors. Bacterial adhesins usually appear in close association with surface appendages.

Many proteins have been investigated for their role in adhesion of bacteria to a substratum surface (*5*–*9*). The proteins may influence bacterial adhesion because of their adsorption to the substratum surface as well as because of their interaction with the surface of the bacteria. Adhesion of bacteria onto a layer of adsorbed proteins is believed to be important in the pathogenesis of (prosthetic) infections (*10*, *11*). For instance, the Antigen I/II (Ag I/II) family proteins at streptococcal surfaces are involved in specific interactions with salivary proteins (*12*, *13*). The Ag I/II proteins are extended fibrillar structures having a length of about 50 nm (*14*). They are covalently attached to the bacterial cell wall via their C-terminal end, see Figure 1.

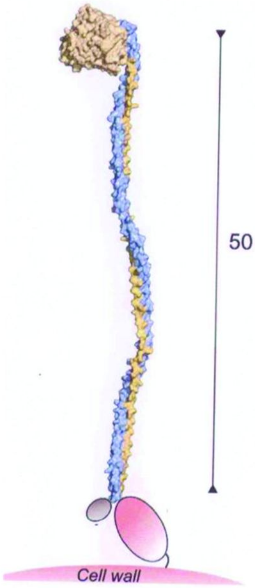

Figure 1. Model of the structure of the Antigen I/II family of proteins, an adhesin at the surface of Streptococcus mutans, that interacts with salivary proteins. Adapted from reference (14).

When extending normally to the cell surface, the projected surface area of AgI/II is estimated to be about 100 nm^2. More specifically, *Streptococcus mutans* is a commensal organism in the human oral cavity and, as a virulent cariogenic species, is often associated with dental caries. It is therefore relevant to investigate the mechanism by which *S. mutans* adheres to dental surfaces. In vivo, teeth are coated with an organic layer largely composed of adsorbed salivary proteins (*15*, *16*), referred to as “acquired pellicle” or, more generally, the adsorbed salivary conditioning film. Hence, adhesion of oral bacteria to these surfaces is governed by the interaction between the bacteria and constituents of the salivary conditioning film (*17*). Since Ag I/II proteins at the surface of *S. mutans* interact specifically with different salivary proteins, it is interesting to investigate the role of Ag I/II in the adhesion of *S. mutans* to salivary conditioning films.

We selected strains of *S. mutans* with and without Ag I/II at its surface, respectively, that were exposed to salivary proteins. The interaction of the two strains with these proteins were compared using different experimental approaches (*18*, *19*), that is, strength of adhesion by determining the adhesive force using atomic force microscopy (AFM) (*20*–*22*), bacterial adhesion to a salivary conditioning film monitored in a parallel plate flow chamber (PPFC), amount of salivary proteins adsorbing to bacterial cell surfaces by determining adsorption isotherms, and enthalpy of saliva-bacterium interaction by isothermal titration calorimetry (ITC) (*19*, *23*). Thus, a better understanding of the interaction between *S. mutans* and salivary proteins has been obtained. It appears to be the outcome of a complex interplay of physical-chemical forces, involving specific and non-specific interactions.

Materials and Methods

Culturing and Harvesting Conditions

S. mutans LT11 (having Ag I/II at its surface) and the isogenic mutant *S. mutans* IB03987 (without Ag I/II) were used in this study. The bacterial cells were maintained at −80 °C in brain-heart infusion broth (BHI; OXOID, Basingstoke, UK) containing 7% dimethyl sulfoxide (Merck, Darmstadt, Germany). For culturing, *S. mutans* LT11 was plated onto BHI agar and *S. mutans* IB03987 onto BHI agar supplemented with 5 µg ml^{-1} kanamycine monosulfate (Sigma-Aldrich, Steinheim, Germany) and incubated overnight at 37 °C in 5% CO_2. Next, bacterial colonies were precultured in 10 ml BHI batch culture overnight. This preculture was used to inoculate a main culture of 200 ml BHI broth, which was allowed to grow overnight. Bacteria were harvested by centrifugation at 6500 g for 5 min at 10 °C and washed twice with demineralized water. Bacterial aggregates were dissociated by mild sonication on ice for 3 x 10 s at 30 W (Vibra Cell model 375, Sonics and Materials Inc., Danbury, Ct, USA). Sonication was done intermittently while cooling on ice. This procedure was found to prevent cell lysis of both strains. Finally, the bacteria, having a radius of about 500 nm, were resuspended in phosphate buffer (composition, see below) pH 6.8 or pH 5.8 to concentrations of 5 x 10^9, 5 x 10^8, and 5 x 10^7 cells per ml, as determined in a Bürker-Türk counting chamber. Bacteria were used directly after harvesting.

Saliva

Human whole saliva from 20 healthy volunteers was collected into ice-chilled beakers after stimulation by chewing Parafilm. Volunteers gave their consent to saliva donation, in agreement with the Ethics Committee at UMCG (approval no. M09.069104). After pooling and two times centrifugation at 10,000 g for 5 min at 10 °C, phenylmethylsulfonyl fluoride was added to a final concentration of 1 mM to inhibit protease activity. Then the solution was centrifuged again at 10,000 g for 5 min at 10 °C, dialyzed overnight against demineralized water at 4 °C and freeze-dried for storage. Prior to experiments the lyophilized saliva was dissolved in phosphate buffer (composition, see below) pH 6.8 or pH 5.8 to a concentration of 6 mg ml^{-1}. This solution was centrifuged at 10,000 g for 5 min at 10 °C and the supernatant was used in the experiments. The protein content in the supernatant was 1.4 mg ml^{-1}, according to the Bio-Rad protein assay (Bio-Rad Laboratories, San Francisco, CA, USA), which is comparable to the protein concentration in human whole saliva.

Buffer Solution

Phosphate buffer containing 2 mM potassium phosphate (K_3PO_4), 50 mM potassium chloride (KCl) and 1 mM calcium chloride ($CaCl_2$) was used throughout this study. The pH was adjusted to 6.8 or 5.8 by adding hydrochloric acid (HCl).

Strength of Adhesion As Determined by AFM

Bacteria were immobilized in a dense layer on an isopore polycarbonate membrane (*24*). AFM cantilever tips (DNP from Veeco, Woodbury, USA) were mounted in a micromanipulator under microscopic observation to allow only the tip of the cantilever to be coated. A droplet of saliva was placed on a glass slide and the tip of the cantilever was submersed in the droplet for 30 min. The bacterial layer and the protein-coated tip were prepared shortly before measurements. AFM was performed at room temperature in buffer using a Dimension 3100 system (Nanoscope III Digital Instruments, Woodbury, USA). An array of 32 x 32 force-distance curves (approach and retract) at scan rates of 2 Hz were collected over the entire field of view (2 μm x 2 μm). For the conversion of cantilever deflection into force a spring constant of 0.06 N m^{-1} for the saliva-coated tips was used, determined by the Cleveland method (*21*). A typical force-distance curve for a probe adhering to a surface is shown in Figure 2. Approach curves were fitted to an exponential function, where the interaction force F is described as

$$F = F_0 \exp\,(-\,d/\Lambda) \qquad (1)$$

in which F_0 is the repulsive force at zero separation between the interacting species, d the separation distance and Λ the decay length of $F(d)$.

The strength of adhesion is probed when the saliva-coated tip is retracted from the bacterial surface. The force of adhesion, F_{adh}, is defined as the minimum in the force-distance curve. To ensure that saliva-coated tips were not damaged during the measurements the force distance curve at 0 s of clean glass were determined before and after scanning the bacterial cell surface. Whenever the 0 s force on the clean glass surface before and after scanning had a difference of ≥ 0.2 nN a new tip was made.

Between 200-300 force-distance curves, using bacteria from 5 different cultures, were determined and the distributions of F_0, Λ, and F_{adh} were plotted in histograms from which median values are derived.

Bacterial Adhesion Monitored in a PPFC

The PPFC and image analysis system have been described in detail in reference (*25*). Briefly, glass slides (76 mm x 26 mm) were sonicated for 3 min in a surfactant solution (2% RBS 35 detergent in water; Omniclean), rinsed thoroughly with tap water, methanol, tap water, and demineralized water. The bottom plate was coated with a salivary film by immersing the plate overnight at room temperature in the saliva preparation of the desired pH. XPS analysis indicated proteinaceous composition of the coating. Prior to each experiment the flow chamber and all tubings were filled with buffer solution, taking care of removing all air bubbles from the system. Next, a bacterial suspension of 5 x 10^8 cells ml^{-1} was allowed to flow through the system. Bacterial adhesion to the bottom plate of the flow chamber was monitored in real time, using a phase-contrast microscope (Olympus BH-2) coupled to a CCD-MXR camera (High Technology, Eindhoven, The Netherlands) equipped with 40x ultra-long-working-distance lens (Olympus ULWD-CD plan 40PL). The camera was coupled to an image analyzer (TEA, Difa, Breda, The Netherlands). The flow rate of the bacterial suspension was set at 1.4 ml per min by adjusting the hydrostatic pressure yielding a shear rate of 15 s^{-1}, which for a bacterium with radius 500 nm implies a shear force of about 2.5 x 10^{-5} nN. Images were taken every 1-2 min during the first 30 min, and thereafter with 10 to 30 min intervals over a period of up to 4 h, where after the flow was stopped. Then, an air bubble was passed through the flow chamber, exerting a shear force of about 10 nN, and the percentage of removed bacteria recorded, giving a semi-quantitative indication of the strength by which the bacteria adhere to the salivary protein layer.

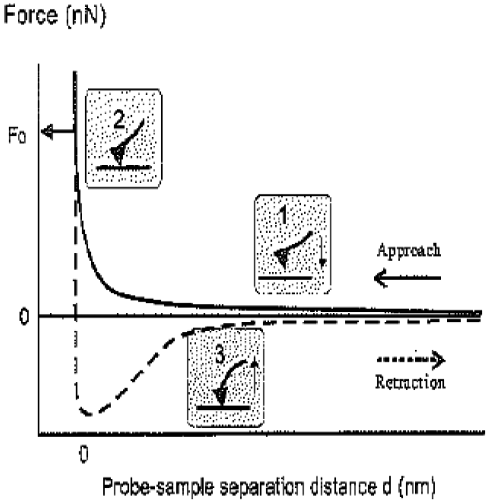

Figure 2. Scheme of a force-distance curve in Atomic Force Microscopy. (1) no interaction force is detected at large separation between the cantilever tip (or probe) and the surface; (2) a repulsive force (——) is detected on approaching the surface and (3) an attractive force (- - -) as the cantilever is retracted from the surface.

Each image (512 x 512 pixels, with 8-bit resolution) was obtained after summation of 15 consecutive images, taken with 1 s time intervals, to improve the signal-to-noise ratio and to eliminate moving bacteria from the analysis. The surface area grabbed by an image was 0.017 mm^2. All experiments were performed in 5-fold using separate bacterial cultures. In a parallel experiment, using the buffer solution without bacteria, it was confirmed that the flow of 1.4 ml per min did not remove the protein from the saliva-coated glass, as probed by XPS.

Enthalpy of Saliva-Bacterium Interaction Measured by Isothermal Titration Calorimetry

The interaction between salivary components and the bacterial cell surface was probed in a twin-type isothermal microcalorimeter TAM 2277 (Thermometric, Jarfalla, Sweden). In a twin-type calorimeter the heat flowing into or from a reaction ampoule relative to a reference ampoule is channeled through thermocouples (Peltier elements) to a heat sink. The Peltier elements convert the heat into an electrical power, P, signal and, hence, integration of the output signal $P(t)$ equals the heat exchange (*26*). At constant pressure, p, the heat exchange q equals the enthalpy H effect of the process in the reaction ampoule relative to that in the reference ampoule

$$q_p = \Delta H \qquad (2)$$

The calorimeter contains four identical ampoules (2.2 ml), three of which were filled with 1.5 ml bacterial suspension (5×10^7, 5×10^8, or 5×10^9 bacteria ml^{-1}, respectively) and one, the reference cell, with adhesion buffer. All solutions were stirred with a special home-made two-blades stirrer causing minimum heat effects. The ampoules were lowered gradually in the calorimeter, which was set at 25 °C and left in the measuring position to reach thermal equilibrium. The calorimeter was placed in a room of constant temperature (20 ± 0.1 °C) allowing a baseline stability of ±0.1 μW over 24 h. After reaching a stable baseline, saliva was injected in the ampoules in four consecutive steps of 60 μl with time intervals of 40 minutes, at a controlled rate of 2 μl s^{-1}. All experiments were performed in five-fold.

Adsorption Isotherms for Salivary Proteins at the Bacterial Cell Wall

In parallel experiments, outside the calorimeter, but under otherwise identical conditions, protein adsorption to the bacterial cell surface was determined. After each injection of salivary proteins solution to the bacterial suspension and allowing for 40 min incubation time the suspension was centrifuged at 10,000 g for 5 min and the protein content in the supernatant was determined by spectrophotometry at 280 nm. The amount of protein adsorbed was derived from mass balance, *i.e.,* the difference between the amounts of protein injected and in the supernatant after adsorption. Titration of buffer solution into bacterial suspension was taken as reference.

Statistical Analysis

Initial deposition rates and adhesion numbers after 4 h, as determined in PPFC experiments, were subjected to a Student's t-test to determine significant differences. The AFM data were analyzed using the Statistical Package for the Social Sciences (Version 11.0, SPSS, Chicago, Ill, USA).

Results and Discussion

The median values of the repulsive force at contact F_0, the decay length Λ of the repulsive force upon approach, and the adhesion force F_{adh}, all derived from the AFM measurements, are summarized in Table 1. The repulsive force to allow contact between the streptococcal surface and the saliva coated tip is not significantly different between LT11 and IB03987. It suggests that Ag I/II does not play a role in the deposition stage of the bacterium-surface interaction. At pH 5.8 and pH 6.8 the bacteria are negatively charged. In the same buffer as used in our study the zeta-potential of LT11 is −15 mV at pH 6.8 and −20 mV at pH 5.8 and for IB03987 it is −29 mV at pH 6.8 and −27 mV at pH 5.8 (*27*). The salivary conditioning film is negatively charged as well (*28*, *29*). Values for the zeta-potential of a salivary film at enamel and dentin surfaces were reported to be -17 mV and -13 mV, respectively, in the buffer of pH 6.8 (*30*). At pH 5.8 the charge (and potential) is expected to be somewhat less negative. Hence, the bacterial strain and the salivary coating repel each other electrostatically, the more so the more negative the zeta-potentials of the interacting species are. In line with this, F_0 should be much larger for IB03987 than for LT11 at pH 6.8 as well as, but to a lesser extent, at pH 5.8. However, since at both pHs F_0 values are more or less the same for the two strains, it is concluded that F_0 is not dominated by electrostatic interaction. The same conclusion is reached when comparing F_0 values for IB03987 at pH 5.8 and 6.8. Furthermore, according to the Gouy-Chapman model (*31*), the decay length of the repulsive force between charged species that interact in a buffer of about 0.05 M ionic strength (as in our experiments) is in the range of a few nm, that is, much shorter than the decay lengths derived from the AFM data. Most likely, the repulsive force manifested in the approach curve involves a long-range steric component (*32*).

Upon retraction, attractive adhesion forces may be detected. Figure 3 shows histograms of F_{adh} for each strain at pH 6.8 and pH 5.8. The fluctuations in the distributions of F_{adh} is assigned to variations in contact between the salivary protein-coated cantilever tip and heterogeneously distributed surface characteristics of a single bacterial cell. The median adhesion forces are stronger for LT11 than for IB03987, especially at pH 6.8; see Table 1. The median adhesion force for the Ag I/II lacking IB03987 strain is below the detectable limit, both at pH 6.8 and pH 5.8. For the Ag I/II containing LT11 strain F_{adh} depends strongly on pH, *i.e.,* 0.4 nN at pH 6.8 and 0.1 nN at pH 5.8. The difference in adhesion strength between the two strains points to the involvement of Ag I/II in the interaction with the saliva coating and the influence of pH on F_{adh} for LT11 suggests participation of ionizable groups (having pK value(s) between 5.8 and 6.8). Furthermore, the observation of an attractive adhesion force only after the bacterium has made contact with the salivary coating implies that the adhesive bond is established at close separation in a confined space, which is typical for specific interaction. This, together with the pH-dependence, suggests pairing between oppositely charged groups (in a non-polar environment). In ref. (*33*) a collection of several single-bond recognition forces is presented revealing that the strength of such a specific bond typically ranges between 0.05 and 0.25 nN. Assuming that the strength of specific bonding between Ag I/II and salivary proteins is in the same range, a force of 0.4 nN (as measured for LT11 at pH 6.8) involves 2-8 Ag I/II molecules. Taking a surface area of 100 nm^2 per Ag I/II molecule (see Figure 1) and a contact area of 2000 nm^2 between the saliva-coated AFM tip and the bacterial surface the degree of coverage of a LT11 cell by Ag I/II is calculated to be between 10% and 40 %.

Table 1. Median values for the repulsive force at contact F_0, the decay length of the repulsive force upon approach Λ, and the adhesive force upon retraction F_{adh}, for the interaction between a saliva-coated AFM tip and the surface of *S. mutans* LT11 and IB03987*

	pH 6.8		*pH 5.8*	
	LT11	*1B03987*	*LT11*	*1B03987*
F_0 (nN)	3.1	3.0	4.6	4.7
Λ (nm)	21	19	23	37
F_{adh} (nN)	-0.4	-0.1	-0.0	-0.0

* Data taken from reference (*18*).

The adhesion kinetics of *S. mutans* LT11 and IB03987 to salivary protein coating at pH 6.8 and pH 5.8, as monitored in a PPFC, are presented in Figure 4. For the different systems the rate of deposition was more or less constant for the first 90 min, except in the case of IB03987 at pH 6.8 where the rate levels off already after about 30 min, reaching a stationary value that is much lower than for the other cases. The observed characteristic features*, i.e.*, the initial deposition rates and the adhesion saturation values, are summarized in Table 2. The deposition rate of bacterial cells in a PPFC, where the flow of the suspension is laminar, is determined by convective diffusion and gravitational sedimentation (*34*, *35*). In systems where specific interactions were not active, deposition rates were found to increase with decreasing repulsive force at contact F_0 (*36*). In the present study this trend is observed as well, not only for IB03987, but also for LT11. It is another indication that specific interaction between Ag I/II and salivary proteins occurs after the bacterium and the saliva-coated surface have been in physical contact. This conclusion is further corroborated by the finding that, for both pH values, the initial rates of deposition do not differ between the two strains. It is further interesting to note that for a given pH (in particular pH 6.8) the ζ-potentials of LT11 and IB03987 are markedly different which is not reflected in the initial deposition rate. Hence, the kinetics of deposition on the negatively charged salivary protein film are not governed by electrostatic interactions, as was also concluded from comparison of F_0-values (obtained by AFM) between the two strains and at both pHs.

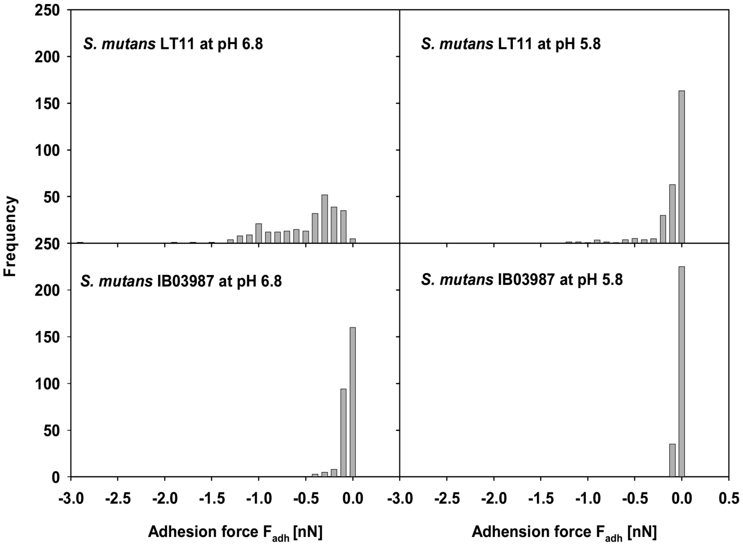

Figure 3. Distribution of the adhesion force F_{adh} between a saliva-coated AFM tip and surfaces of S. mutans LT11 and IB03987. Each histogram is based on 200-300 force-distance curves, equally divided over five different bacteria. Redrawn from reference (18).

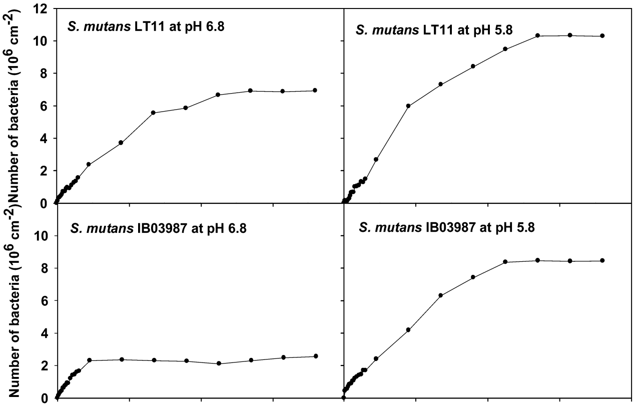

Figure 4. Kinetics of adhesion of S. mutans LT11 and IB03987 to salivary coatings, determined in a parallel plate flow chamber. Redrawn from reference (18).

In Proteins at Interfaces III State of the Art 2012; Horbett, T., et al.;
ACS Symposium Series; American Chemical Society: Washington, DC, 2012.

In all cases the number of bacteria adhering after 4 h represent adhesion saturation (under the prevailing conditions). In the absence of specific interaction with the salivary proteins, that is for IB03987, adhesion saturation is much higher at pH 5.8 than at pH 6.8. Although the initial deposition rate was found not to be significantly influenced by electrostatic interactions, adhesion saturation, that is the steady-state density of adhering cells per unit area of the substrate surface, may well be affected by electrostatic interaction. The ζ-potential of IB03987 is reported to be about the same at pH 5.8 and pH 6.8 (− 27 mV and − 29 mV, respectively) (*27*), and assuming that the charge density of the salivary protein coating is more negative at higher pH, adhesion is electrostatically less favorable at higher pH. However, it seems unlikely that electrostatic effects are primarily responsible for the large difference in adhesion saturation of IB03987 at the two pH values. For LT11 the influence of pH on adhesion saturation has largely disappeared or, otherwise stated, at pH 6.8 adhesion saturation is much higher for LT11 than for IB03987. This may be a manifestation of favorable specific bonds formed between Ag I/II moieties at the LT11 cell surface and the salivary proteins. The slightly higher adhesion saturation for LT11 as compared to IB03987, at pH 5.8, then suggests that, at this pH value, AgI/II is much less involved in specific interaction.

Table 2. Interaction between *S. mutans* LT11 and IB03987 and a salivary coating in a parallel plate flow chamber. Initial deposition rate, number of adhering bacteria per unit surface area after 4 h, and percentage of bacteria detached by a passing air bubble. Experiments were done in five-fold with separately prepared saliva-coated glass plates and different bacterial cultures*

	pH 6.8		*pH 5.8*	
	LT11	*1B03987*	*LT11*	*1B03987*
initial deposition rate ($cm^2\ s^{-1}$)	1679 ± 165	1441 ± 119	1315 ± 28	1258 ± 169
adhesion after 4 h ($10^6\ cm^{-2}$)	9.6 ± 2.3	2.5 ± 0.7	12.7 ± 1.1	10.5 ± 2.1
detachment by passing air bubble (%)	55 ± 9	76 ± 2	73 ± 3	76 ± 5

* Data taken from reference (*18*).

Finally, the percentages of bacterial cells that are detached by a passing air bubble, given in Table 2, indicate strong adhesion of LT11 at pH 6.8, in line with the values of F_{adh}, derived from AFM.

In Figure 5 adsorption isotherms are presented, where the amounts of salivary proteins adsorbed per unit area bacterial surface are plotted as a function of the protein concentration in solution after adsorption. In all cases adsorption appeared to be irreversible towards variation of dissolved protein concentration. This is a common feature of protein adsorption (*37*). However, exchange of protein between the adsorbed and the dissolved state may well be possible (*38*). Since the adsorption isotherms reflect partitioning of the proteins between the surface (mg m^{-2}) and the solution (mg ml^{-1}) they are insensitive to the total surface area, *i.e.,* the number of bacteria, in the system.

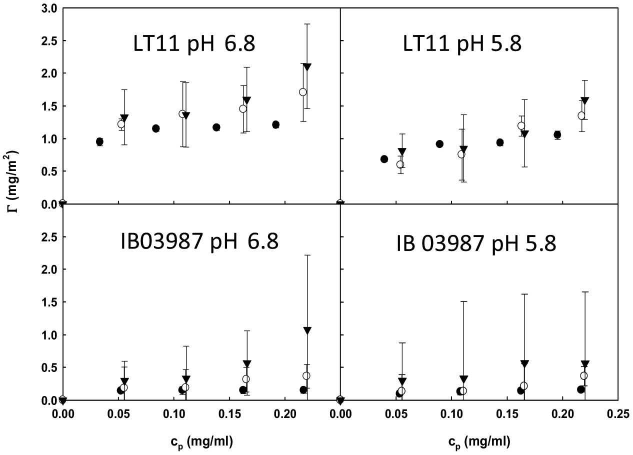

Figure 5. Adsorption isotherms for salivary proteins on the surfaces of S. mutans LT11 and IB03987, obtained after consecutive injections of 60 µl salivary protein solution (1.4 mg ml^{-1}) into 1.5 ml bacterial suspension containing (●) 5 x 10^{-9}, (○) 5 x 10^{-8}, (▼) 5 x 10^{-7} bacteria per ml. Redrawn from reference (19).

Clearly, because the adsorbed amount is derived from the difference in solution concentration before and after adsorption, the experimental error is larger when that difference is smaller, that is when a smaller number of bacterial cells is supplied. The adsorption isotherms show that the affinity of salivary proteins to adsorb at the *S. mutans* surface is much higher for the LT11 strain, demonstrating the role of Ag I/II in the binding process. The lower protein adsorption at the LT11 surface at pH 5.8 as compared to pH 6.8 points to decreased specific binding via Ag I/II, in line with the AFM and PPFC results. Protein adsorption at full coverage of the substrate surface typically is in the range of a few mg m^{-2} (the exact value depends on the size, shape and orientation of the protein molecule) (*37*, *39*); hence, it appears that adsorption of salivary proteins at the *S. mutans* surface is compatible with (sub-)monolayer coverage.

At constant pressure and temperature the affinity of the protein-bacterium interaction is given by the change in Gibbs energy, ΔG, of the system resulting from that interaction. The more negative ΔG , the higher the affinity is, or, in other words, the stronger the adhesive bond. Because the adsorption isotherms do not represent reversibility with respect to protein concentration in solution, they do not allow for deduction of ΔG (*40*). The value of ΔG is composed of a change in enthalpy, ΔH, and in entropy ΔS, according to

$$\Delta G = \Delta H - T\Delta S \qquad (3)$$

where T is the temperature in Kelvin. For irreversible processes ΔS is not experimentally accessible either, but ΔH may be determined calorimetrically as the heat exchange between the system and its environment, as given by equation (2). At constant volume, which is practically the case when no gaseous components are involved in the interaction, the enthalpy change equals the change in energy.

Enthalpy changes due to the adsorption of salivary proteins to the surface of *S. mutans* cells are, for each injection step, presented in Figure 6. Enthalpy effects arising from metabolic activity is minimal because all experiments are carried out in the absence of nutrients. Note that the adsorbed amount after each injection step can be read off from the adsorption isotherms in Figure 5.

AFM data and adsorption isotherms indicated that the non-specific interaction of salivary proteins with the Ag I/II-lacking surface of the IB03987 is relatively weak. The calorimetric data in the lower panels of Figure 6 reveal that this interaction is essentially a-thermal, *i.e.,* $\Delta H \approx 0$. It implies that the driving force for this non-specific interaction is entropy gain, $\Delta S > 0$. Entropy-driven adsorption has often been reported for proteins. Adsorption of salivary proteins to the Ag I/II-containing LT11 cells is strongly exothermic, *i.e.,* $\Delta H < 0$ (Figure 6, upper panels). Apparently, the specific interaction between Ag I/II and salivary proteins is energetically favorable. The difference in ΔH between pH 6.8 and pH 5.8 indicates suppression of Ag I/II involvement at the lower pH, just as is concluded from adsorption isotherms, AFM and PPFC experiments. It is further worth mentioning that a 100-fold increase in bacterial concentration (= 100-fold increase in available surface area) yields only a 4-5 fold increase in adsorption enthalpy. It means that at higher supply of sorbent surface area the enthalpy change per bacterial cell decreases drastically. In this context, it is instructive to plot ΔH per bacterium as a function of the amount of protein adsorbed per bacterial cell (taken from the isotherms in Figure 5). The result is presented in Figure 7, showing that only for LT11 at pH 6.8, and only in case of not too high bacterial concentration, a significant enthalpy effect per bacterium can be detected. Thus, for LT11, pH 6.8, it is established that the enthalpy per bacterium increases, *i.e.,* becomes more negative, with increasing surface coverage up to a value beyond which further adsorption proceeds a-thermally. That value may mark full occupation of Ag I/II binding sites at the bacterial surface. This occurs at about 4×10^{-12} mg protein per bacterium, which, for a spherical bacterium having a radius of 500 nm, corresponds to 1.25 mg m^{-2}. Comparison with the semi-plateau value of the adsorption isotherm of LT11 at pH 6.8 (Figure 5), it is inferred that saturation of the bacterial surface with salivary proteins is dominated by Ag I/II mediated specific interaction, but leaving some space on the surface for non-specific adsorption.

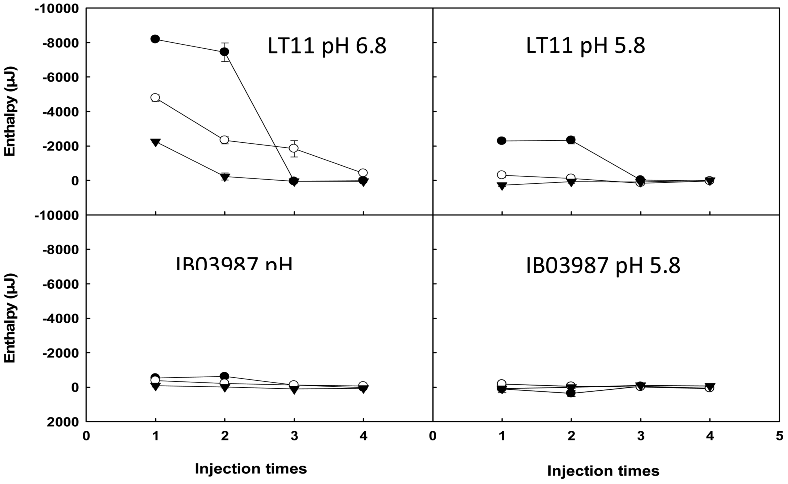

Figure 6. Enthalpy of adsorption of salivary proteins to the surface of S. mutans LT11 and IB03987 upon consecutive injections into bacterial suspensions. Conditions and symbols as in Figure 5. Redrawn from reference (19).

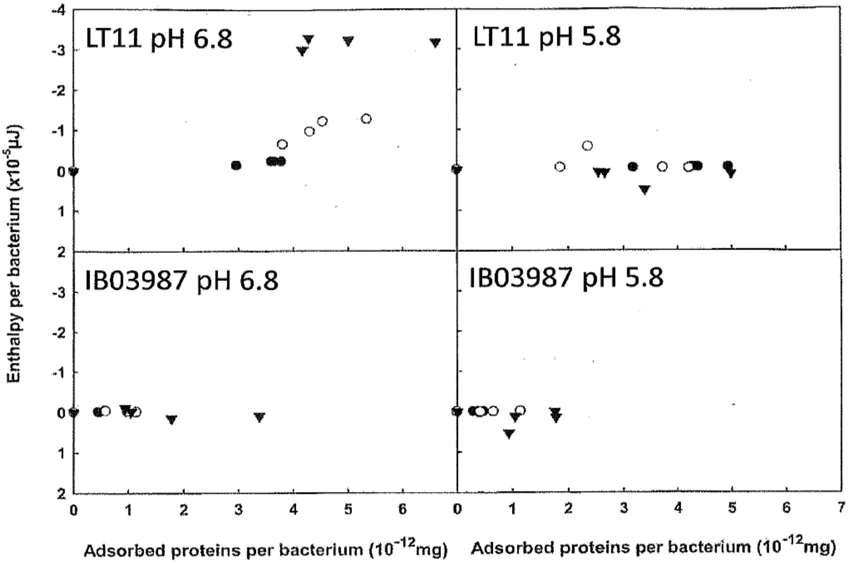

Figure 7. Enthalpy of adsorption of salivary proteins to the surface of S. mutans LT11 and IB03987 as a function of the amount of protein adsorbed at the bacterial surface. Symbols as in Figure 5.

The smaller enthalpy change per bacterium at higher bacterial concentration in a suspension containing a given amount of saliva may be due to the presence of a larger number of Ag I/II binding sites. Douglas and Russell (*41*) have identified various salivary proteins that have a preference to bind to the surface of *S. mutans*. They probably bind with different enthalpy effects. In case of the lowest bacterial concentration (5 x 10^7 cells ml^{-1}) the number of Ag I/II moieties is limited and, therefore, they all become saturated with the enthalpically most favorably binding proteins. The highest bacterial concentration (5 x 10^9 cells ml^{-1}) offers 100x more binding sites to the same amount of salivary proteins. Then, a much smaller fraction of the Ag I/II binding sites interacts with the strongest binding protein, another fraction with the second strongest binding protein, *etcetera*. The result is a much lower enthalpy effect per bacterium.

Conclusions

Using two *Streptococcus mutans* strains, one with the adhesin Antigen I/II at its surface and its isogenic mutant that does not contain the adhesin, we were able to distinguish between generic and specific contributions to their interaction with salivary proteins. Results obtained from a variety of experiments, *i.e.*, kinetics of deposition of the bacteria on a saliva-coated surface, binding isotherms and enthalpy of adsorption of salivary proteins at the bacterial cell walls, reveal a major contribution of specific interaction between the Antigen I/II containing *S. mutans* strain and salivary proteins. This conclusion is corroborated by a dominant contribution from specific interaction to the adhesive bond strength, as measured by retracting a saliva-coated AFM tip from the surface of the bacterial cells. It was deduced that the generic interaction between the bacterium and the surface is long-ranged, whereas the specific interaction, involving Antigen I/II, is short-ranged, which is typical for biological recognition. This short-range interaction appears to be strongly pH-dependent suggesting the involvement of ion pairing, which, in a confined space that is more or less shielded from the aqueous environment, leads to the observed strong attractive force causing a highly exothermic effect. This study demonstrates how a multi-sided experimental approach provides insight in the mechanism of *S. mutans*-salivary proteins interaction. Following a similar approach may as well be successful in investigating other biological recognition processes.

Acknowledgments

We acknowledge ZON-MW for financial support (Grant 9110)

References

1. Aguilar, C.; Vlamakis, H.; Losick, R.; Kolter, R. *Curr. Opin. Microbiol.* **2007**, *10*, 638–643.
2. Escher, A.; Characklis, W. G. In *Biofilms*; Characklis, W. G., Marshall, K. C., Eds.; Wiley & Sons: New York, 1990; pp 445−486.

3. Gottenbos, B.; Van der Mei, H. C.; Busscher, H. J. *Methods Enzymol.* **1999**, *310*, 523–534.
4. Chan, R. C. Y.; Irvin, R. T.; Bruce, A. W.; Costerton, J. W. *Infect. Immunol.* **1985**, *47*, 84–89.
5. Fletcher, M. *Microbiol. Sci.* **1987**, *4*, 133–136.
6. Kuusela, P.; Vartio, T.; Vuento, M.; Myhre, E. B. *Infect. Immunol.* **1985**, *50*, 77–85.
7. Pratt-Terpstra, I.; Weerkamp, A. H.; Busscher, H. J. *J. Gen. Microbiol.* **1987**, *133*, 3199–3260.
8. Muller, E.; Takeda, S.; Goldmann, D.; Pier, G. B. *Infect. Immunol.* **1991**, *59*, 3323–3326.
9. McDowell, S. G.; An, Y. H.; Draughn, R. A.; Friedman, R. J. *Lett. Appl. Microbiol.* **1995**, *21*, 1–4.
10. Tojo, M.; Yamashita, N.; Goldmann, D. A.; Pier, G. B. *J. Infect. Dis.* **1988**, *157*, 713–722.
11. Timmerman, C. P.; Pleer, A.; Besnier, J. M.; De Graaf, L.; Cremers, F.; Verhoef, J. *Infect. Immunol.* **1991**, *59*, 4187–4192.
12. Hajishengallis, G.; Koga, T.; Russell, M. W. *J. Dental Res.* **1994**, *73*, 1493–1502.
13. Jakubovics, N. S.; Van Dolleweerd, C. J.; Kelly, C. G.; Jenkinson, H. F. *Mol. Microbiol.* **2005**, *55*, 1591–1605.
14. Larson, M. R.; Rajashankar, K. R.; Patel, M. H.; Robinette, R. A.; Crowley, P. J.; Michalek, S.; Brady, L. J.; Deivanayagan, C. *Proc. Natl. Acad. Sci. U.S.A.* **2010**, *107*, 5983–5988.
15. Mayhall, C. W. *Archs. Oral Biol.* **1970**, *15*, 1327–1341.
16. Ørstavik, D.; Kraus, F. W. *J. Oral Path.* **1973**, *2*, 60–76.
17. Ørstavik, D. *Arch. Oral Biol.* **1978**, *23*, 167–174.
18. Xu, C-P.; Van de Belt-Gritter, B.; Dijkstra, R. J. B.; Norde, W.; Vander Mei, H. C.; Busscher, H. J. *Langmuir* **2007**, *23*, 9423–9428.
19. Xu, C-P.; Van de Belt-Gritter, B.; Busscher, H. J.; Van der Mei, H. C.; Norde, W. *Colloids Surf., B* **2007**, *54*, 193–199.
20. Dufrene, Y. F. *J. Bacteriol.* **2002**, *184*, 5205–5213.
21. Dufrene, Y. F. *Current Opin. Microbiol.* **2003**, *6*, 317–323.
22. Bakker, D. P.; Huijs, F. M.; De Vries, J.; Klijnstra, J. W.; Busscher, H. J.; Van der Mei, H. C. *Colloids Surf., B* **2003**, *32*, 179–190.
23. Norde, W.; Lyklema, J. *J. Colloid Interf. Sci.* **1978**, *66*, 295–302.
24. Kasas, S.; Ikai, A. *J. Biophys.* **1995**, *68*, 1678–1680.
25. Busscher, H. J.; Van der Mei, H. C. *Clin. Microbiol. Rev.* **2006**, *19*, 127–141.
26. Briggner, L. E.; Wadsö, I. *J. Biochem. Biophys. Methods* **1991**, *22*, 101–118.
27. Petersen, F. C.; Assev, S.; Van Der Mei, H. C.; Busscher, H. J.; Scheie, A. A. *Infect. Immunol.* **2002**, *70*, 249–256.
28. Göcke, R.; Gerath, F.; Von Schwanewede, H. *Clin. Oral. Invest.* **2002**, *6*, 227–235.
29. Johnson, M.; Levine, M. J.; Nancollas, G. H. *Crit. Rev. Oral Biol. Med.* **1993**, *4*, 371–378.
30. Weerkamp, A. H.; Uyen, H. M.; Busscher, H. J. *J. Dental Res.* **1988**, *67*, 1483–1487.

31. Norde, W. *Colloids and Interfaces in Life Sciences and Bionanotechnology*; CRC Press: Boca Raton, FL, 2011; Chapters 9 and 16.
32. Rijnaarts, H.; Norde, W.; Lyklema, J.; Zehnder, A. J. B. *Colloids Surf., B* **1999**, *14*, 179–195.
33. Busscher, H. J.; Norde, W.; Van der Mei, H. C. *Appl. Environm. Microbiol.* **2008**, *74*, 2559–2564.
34. Li, J.; Busscher, H. J.; Norde, W.; Sjollema, J. *Colloids Surf., B* **2011**, *84*, 76–81.
35. Li, J.; Busscher, H. J.; Van der Mei, H. C.; Norde, W.; Krom, B. P.; Sjollema, J. *Colloids Surf., B* **2011**, *87*, 427–432.
36. Vadillo-Rodriguez, V.; Busscher, H. J.; Norde, W.; De Vries, J.; Van der Mei, H. C. *Microbiology* **2004**, *150*, 1015–1022.
37. Haynes, C. A.; Norde, W. *Colloids Surf., B* **1994**, *2*, 517–566.
38. Norde, W.; Anusiem, A. C. I. *Colloids Surf.* **1992**, *66*, 299–306.
39. Norde, W. *Colloids Surf., B* **2008**, *61*, 1–9.
40. Norde, W.; Lyklema, J. *J. Colloid Interface Sci.* **1979**, *71*, 350–366.
41. Douglas, C. W. I.; Russell, R. R. B. *Arch. Oral Biol.* **1984**, *29*, 751–757.

Chapter 17

Measurement of Time-Dependent Functional Activity of Adsorbed Fibrinogen and Platelet Adhesion on Material Surfaces

Li-Chong Xu,[1] Pranav Soman, Bryan M. Scheetz,
and Christopher A. Siedlecki*,[1,2]

[1]Department of Surgery and Biomedical Engineering Institute,
The Pennsylvania State University, College of Medicine,
Hershey, Pennsylvania 17033
[2]Department of Bioengineering Biomedical Engineering Institute,
The Pennsylvania State University, College of Medicine,
Hershey, Pennsylvania 17033
***E-mail: csiedlecki@psu.edu. Phone: (717) 531-5716. Fax: (717) 531-4464**

Fibrinogen adsorbed on material surfaces undergoes conformational changes and subsequently mediates platelet adhesion. Recent evidence has shown that the platelet binding epitope located in the γ-chain dodecapeptide plays an important role in platelet adhesion to biomaterials. In this chapter, we describe a series of studies using an immuno-AFM technique employing an antibody-modified probe for measuring the probability of this γ-chain dodecapeptide epitope (γ392-411) being available (a measure of protein functional activity) following fibrinogen adsorption to model material surfaces. AFM measurements show that the functional activity of fibrinogen appears to be both time and substrate dependent, with the surface characteristics and compositions of protein solution affecting the time dependence. The probability of antibody binding correlates well with temporal changes in platelet adhesion to these material surfaces, suggesting that the availability of the γ-chain in fibrinogen is a useful predictor of platelet adhesion. Results demonstrated that the utility of

In Proteins at Interfaces III State of the Art 2012; Horbett, T., et al.;
ACS Symposium Series; American Chemical Society: Washington, DC, 2012.

this approach for measuring protein function at or near the molecular scale and offers new opportunities for improved insights into the molecular basis for the biological response to biomaterials.

1. Introduction

With the widespread and remarkable successes of medical devices, biomaterials have had an enormous impact on health care (*1*). Much of this success has been achieved through judicious selection of existing materials, with little understanding of the fundamental molecular scale structure-function relationships in these materials. In the case of blood-contacting devices, blood–material interactions trigger a wide range of adverse biological responses including complement activation, blood coagulation, and thrombosis (*2*). Surface-induced thrombosis has particularly remained a main problem for the biocompatibility and eventual success of both implanted and peripheral medical devices.

One important mechanism of surface-induced thrombosis involves the interaction of circulating blood platelets with plasma proteins adsorbed on a biomaterial surface, as protein adsorption is viewed as the initial event occurring when a biomaterial comes into contact with blood. While blood contains a multitude of proteins having a variety of biological functions and activities, fibrinogen has been identified as one of the most important proteins involved in platelet adhesion/activation and thrombus formation, particularly in areas of low shear stress (*3*). An improved understanding of adsorption and functional activity of fibrinogen on biomaterial surfaces is critically important for the development and application of new blood contacting biomaterials.

Fibrinogen is the third most abundant blood plasma protein, and plays the dual roles of serving as a ligand for platelet adhesion to a surface and/or as a linker for platelet aggregation (*4*), in addition to its roles in coagulation. Circulating inactive platelets do not bind soluble fibrinogen in its native conformation, but readily adhere to adsorbed/activated fibrinogen through the platelet integrin receptor $\alpha_{IIb}\beta_3$ (GPIIb/IIIa) (*5*). There is increasing evidence that the conformational state and the availability of platelet-binding sites in adsorbed fibrinogen may actually be a more important indicator of platelet adhesion than simply the amount of adsorbed fibrinogen present at the surface (*6–9*). Fibrinogen is a symmetric molecule with a 2-fold axis of symmetry and each side of the molecule is composed of three pairs of intertwined polypeptide chains designated as Aα, Bβ, and γ. Each fibrinogen molecule possesses three pairs of potential platelet binding peptide sequences, two RGD-containing sequences in each of the Aα chains (RGDF and RGDS) and an epitope (HHLGGAKQAGDV) located at the C-terminus in each of the γ chains. The γ-chain dodecapeptide sequence, the structure of which has already been reported elsewhere (*10*, *11*), is generally viewed as the primary ligand for platelet adhesion to adsorbed fibrinogen as mutations in this region have dramatic effects on platelet adhesion to surfaces (*12*, *13*). Thus, the availability of dodecapeptide in γ-chain of fibrinogen molecule is defined as the functional activity of fibrinogen in platelet adhesion within this chapter. Many investigators have reported that the functional activity is related to the conformation and/or the orientation of adsorbed fibrinogen (*6*, *14–16*).

Fibrinogen undergoes conformational changes upon adsorption to material surfaces and the transient exposure of functional epitopes appears to be both time and surface dependent (*15*, *17–19*). Agnihotri and Siedlecki (*19*) measured the time-dependent changes in the structure of individual fibrinogen molecules under aqueous conditions following adsorption on hydrophobic graphite and hydrophilic mica surfaces, respectively. On the basis of differences in the relative height of the D and E domains, four orientation states were observed for fibrinogen adsorbed on these surfaces, and the conformational changes could be explained by a two-step spreading model where in the first step the protein spreads very rapidly after adsorption, and in the second step the spreading can be modeled as exponential decay of height resulting from interactions with the substrate. Material surface properties, including surface charge, roughness, wettability, and the specific chemical groups on the surface all appear to affect the conformational changes of fibrinogen upon adsorption on surfaces (*20–24*). However, these studies were often carried out on model substrates such as mica and gold, and the conformational change of fibrinogen response to biomedical related polymeric surfaces is less well understood, in part due to complicated surface chemistry and topography.

The development of immunological atomic force microscopy (AFM) techniques makes it possible to measure the availability of functional epitopes in proteins adsorbed on surfaces regardless of material surface property. For example, we measured the adsorption and functional activity of fibrinogen adsorbed on segmented polyurethane biomaterial surfaces and found that fibrinogen activity was dependent on soft and hard segments chemistries, and hard segment content (*25*). These polyurethane biomaterials undergo reorientation and rearrangement during hydration, resulting in net hard segment enrichment at the surface. This dynamic phase restructuring of hard domains leads to a decrease in fibrinogen adsorption and functional activity, as well as subsequent platelet adhesion (*26*). The success in application of immuno-AFM technique makes it practical to measure the functional activity of proteins adsorbed on surface by looking at the molecular scale, and is helpful for understanding the biological responses at material surface.

2. Measurement of Functional Acticity of Fibrinogen by Immuno-Atomic Force Microscopy

2.1. Immuno-Atomic Force Microscopy

AFM has been used extensively for studying biological molecules including proteins, lipid membranes, DNA and cells under physiologically relevant aqueous conditions with nanometer scale resolution, although generally on ultrasmooth model surfaces such as mica, high oriented pyrolytic graphite or self-assembled monolayers (*23*, *27–29*). The low surface roughness of these model surfaces is ideal to characterize protein features including specific domain and conformational changes in the proteins upon adsorption. However, it is very difficult to distinguish the proteins of interest from the complicated multi-proteins adsorption based on topography alone. More importantly, clinically used biomaterials have rough topographies and make detection/identification of specific proteins on these surfaces even more difficult. Although it has been reported that the fibrinogen on two clinically relevant biomaterials, poly(dimethylsiloxane) PDMS and low density polyethylene (LDPE) can be detected by phase imaging (*30*), the surface is often too rough to clearly distinguish the adsorbed proteins (*31*). There remains a need to develop new techniques that do not rely on topography to recognize specific proteins.

An alternative non-conventional AFM technique, force spectroscopy, provides a unique method for detection of specific proteins without dependence on topography. Hinterdorfer et al. (*32*) used the methodology for the study of molecular recognition of single binding events and for the localization of sites on biosurfaces by combining force microscopy with molecular recognition by specific ligands. This method indicated the potential application for characterizing rate constants and kinetics of molecular recognition complexes and for molecular mapping of biosurfaces such as membranes. We previously (*33*) used an AFM probe functionalized by covalently linking polyclonal antibodies against fibrinogen to detect fibrinogen in a dual-protein film. The patterned dual component protein films were formed by microcontact printing bovine serum albumin on a mica surface and then backfilling with fibrinogen. The adhesion mode was used to generate binary recognition images where the specific and non-specific interactions were differentiated based on a statistically derived cut-off value with a recognition efficiency >80%.

On the basis of our experience with AFM protein recognition by polyclonal antibodies, we extended the force spectroscopy technique to study the protein activity and indirectly the putative conformational changes in protein upon adsorption. This approach was also similar to measurements of functional activity and conformational changes in proteins that were previously detected by monoclonal antibodies (mAb) against specific peptides of the protein after adsorption by enzyme-linked immunosorption assay or radiolabeling (*34*, *35*). Balasubramanian *et al.* (*15*) investigated the time-dependent functional changes in fibrinogen adsorbed to polytetrafluoroethylene, polyethylene, and silicone surfaces using a mAb against the C-terminal dodecapeptide sequence 400-411 of the γ chain and confirmed that fibrinogen undergoes biologically significant conformational changes upon adsorption to polymeric biomaterials. Alternatively, the force measurement mode of AFM provides another approach to study the functional activity of protein at molecular scale by measuring antigen-antibody debonding forces with a mAb functionalized probe. Furthermore, probability of recognition of a specific epitope can be recorded as a function of time so that the time-dependent functional activity of adsorbed protein is revealed (*16*).

2.2. Functionalization of AFM Probe and Operation of AFM

To recognize the specific epitopes in proteins adsorbed on surfaces, the AFM probe is functionalized with the appropriate monoclonal antibodies. The following protocol decribed is one of the methods for attachment of antibodies. Although it uses a chemical fixation technique, the method provides sufficient mobility and flexibility for proteins to rotate and orient themselves for binding (*36*). Briefly, pyramidal Si_3N_4 AFM probes are cleaned in 10ml of acetone for 15 minutes and then glow-discharge plasma treated for 30 minutes at 100W power. The tips are modified by placing into 10 ml of 1% (v/v) aminopropyltriethoxysilane (APTES) in ethanol for 1 hr to provide a reactive amine group, and then rinsed 3 times using DI water. Tips are then reacted in 15 ml of 10% glutaraldehyde for 1 hr and washed 3 times using DI water to remove the glutaraldehyde. The reaction of glutaraldehyde with the amino silane on the nitride surface provides a bridging agent between the solid support and the antibodies. The activated probes are incubated for 1 hr with mAb (NYB4-2xl-f, Accurate Chemical, Westbury, NY) (25 μg/ml) that recognize fibrinogen γ392-411, a region that includes the platelet binding dodecapeptide sequence γ400-411. Modified tips are stored in PBS at 4°C and used within 2 days.

2.3. Measurement of Functional Activity of Proteins by Immuno-AFM and Platelet Adhesion

Human platelet poor plasma (PPP) and purified proteins in PBS were used for studies. Proteins were adsorbed onto the material surface for 5 min in an external fluid cell, and remaining free protein was washed away 3 times using a syringe pump for 5 min each, while the residence time was recorded. AFM Si_3N_4 probes modified with mAb were used to detect the fibrinogen activity on surfaces. The techniques for fibrinogen activity measurements by AFM have been described in a previous publication (*16*). Briefly, the force volume mode of AFM was used to measure interaction forces between fibrinogen and the probes modified with mAbs across the area. Force curves were continuously acquired as 32×32 array of individual force curves cross the each scanning area at a certain scan rate. Thus, the amount of time required for completion of one recognition map could be determined. As controls for these measurements, material samples were incubated with bovine serum albumin (BSA) (1 mg/ml) for 5 min and used for measuring the nonspecific interactions of the antibody with proteins.

To correlate the molecular scale protein functional activity to macroscale platelet adhesion, platelet adhesion was carried on material surfaces which were pre-adsorbed with proteins or PPP and then allowed to reside in PBS for the desired time periods. Human platelet rich plasma (PRP) was collected from either human blood donated by healthy volunteers in accordance with institutional policies or from the blood bank at the Hershey Medical Center. Fresh blood was collected in Vacutainer® blood collection tubes with EDTA, and no other agents were added to the blood. The blood was centrifuged at 180g and 25°C for 20 min to collect PRP and to remove the blood cells, followed by careful removal of the upper platelet-rich layer with a polyethylene pipette. PRP was centrifuged at 1500g for 10 min to separate platelets into pellet. The supernatant was collected as PPP. The platelet pellet was washed with PBS and gently re-suspended in PBS, and then diluted with PBS or PPP, recalcified with $CaCl_2$ to yield a final platelet concentration of 2.0×10^8 platelets/ml and Ca^{2+} concentration of 2.5mM. Platelet adhesion was performed by incubation of materials in platelet solution for 10 min under static condition. The platelet solution was aspirated and then the samples were rinsed with PBS for 5 times. Platelets adhered on surfaces were analyzed by fluorescence microscopy (*37*) or lactate dehydrogenase (LDH) assay (*16*), which have been described in previous publications.

2.4. AFM Data Analysis

The individual retraction force curves were extracted and analyzed off-line with tools developed in Matlab software. The rupture force and rupture length were calculated from each retraction force curve. The rupture force was calculated from the distance between the zero deflection value to the point of maximum deflection during probe separation from the surface for each force curve using Hook's law, $F_{rupture} = -k \times d_{max,}$, where k is the cantilever spring constant. The rupture length was calculated from the distance that the tip moves from the zero interaction force during separation to the position where the probe has separated and returned to zero deflection (Figure 1). Both rupture force and rupture length can be used to distinguish the specific and non-specific interactions.

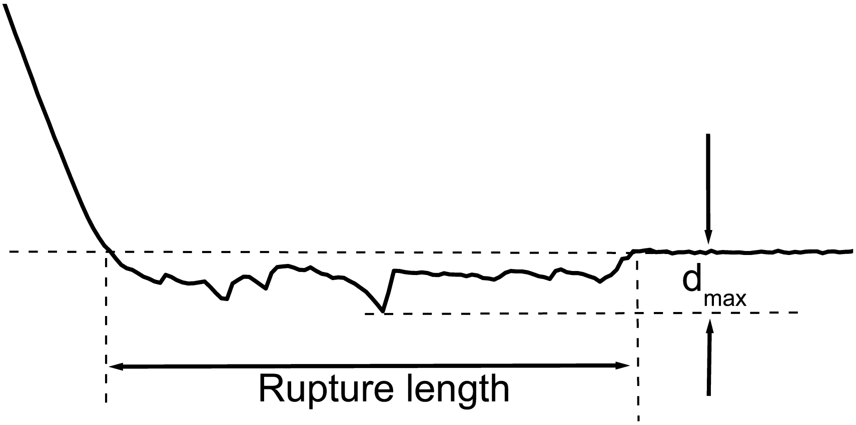

Figure 1. A representative force curve of specific interactions showing the calculation of rupture force and rupture length.

The nonspecific forces were collected from the interactions of albumin and antibodies and pooled to produce a histogram of rupture force (or rupture length). Mean value (μ) and standard deviation (σ) were thus established. A 95% confidence interval limit determined as μ+1.96σ is used as a cut-off value for differentiating the specific and nonspecific interactions of mAb and proteins. Interactions above this limit were considered as specific interactions. Thus, the rupture force (length) map is converted into binary recognition map, where the warm colors indicate the recognition of a specific interaction and cool colors represent the nonspecific interactions (Figure 2).

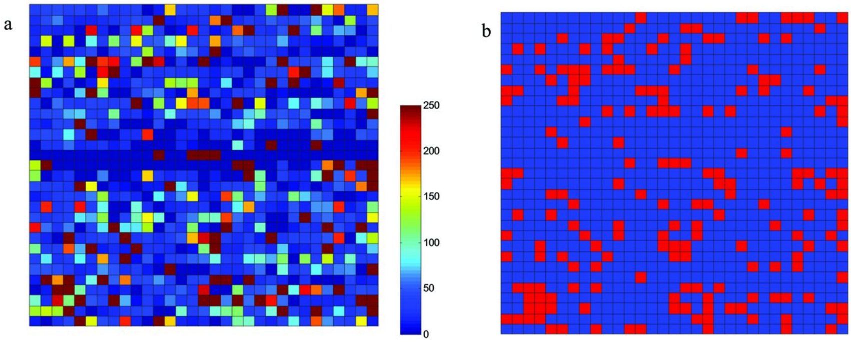

Figure 2. (a) A representative rupture length map of interactions of mAb probe and fibrinogen adsorbed surface, and (b) binary recognition map after data were filtered through a cut-off value with 95% confidence.

Interactions between protein and the mAb probe were acquired at varied scan rates as a 32×32 array of individual force curves. The time corresponding to each individual force measurement was determined from the scan rate for the particular image. The force data was bundled into groups of 32, corresponding to one scan line across the rupture force or length map. The probability of detecting a positive binding event was calculated as follows:

Probability of recognition = number of specific binding events in each scan line /32.

The time-dependent probability recognition data from multiple experiments ($n \geq 3$) were pooled together and presented as the mean of 5 time points.

3. Fibrinogen Adsorption and Platelet Adhesion on Model Mica Surfaces

3.1. Time-Dependent Functional Activity of Fibrinogen Adsorbed on Mica Surfaces

Freshly cleaved muscovite mica was incubated with protein solutions of fibrinogen (100 μg/ml) or bovine serum albumin (BSA, 100μg/ml) for 5 min, and rupture forces were collected by a functionalized AFM probe having a mAb and as a function of residence time (*16*). Figure 3a shows the distribution of rupture forces between a mAb-modified AFM probe and bare mica substrates for one particular probe. Most of the rupture forces are found in the range of 400 to 700 pN with a maximum occurring at ~520 pN. Figure 3b shows force distributions between adsorbed BSA and the same mAb probe. There is a substantial shift in the force distribution, with most of the rupture forces in the range of 0 – 150 pN. The lack of overlap between force values in Figures 3a and 3b suggests that the probe encounters little bare mica during the measurements. The mean and standard deviation of this distribution were used to establish a cut - off value for specific/nonspecific interactions (150 pN for this particular probe) based on a 95 % confidence interval. Histograms of these rupture forces were in the range of

0 – 400 pN. Figure 3b and 3c show that there are sufficient differences between the distributions to be confident that the coupled antibody specifically recognizes its antigen. Data obtained spatially was converted to the appropriate time of measurement and probability of antigen recognition at that time was determined as described in section 2.4.

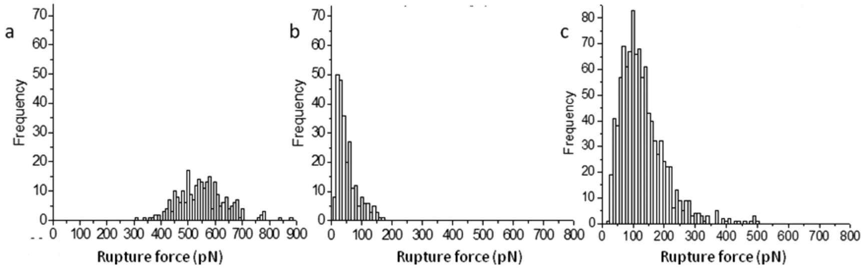

Figure 3. Representative distributions of maximum rupture forces between monoclonal anti-fibrinogen (mAb) modified probe and (a) bare mica (b) BSA adsorbed on mica (100μg/ml) (c) fibrinogen adsorbed on mica (100μg/ml). Scan Rate = 1 Hz. (Reproduced with permission from reference (16). Copyright 2008 American Chemical Society.)

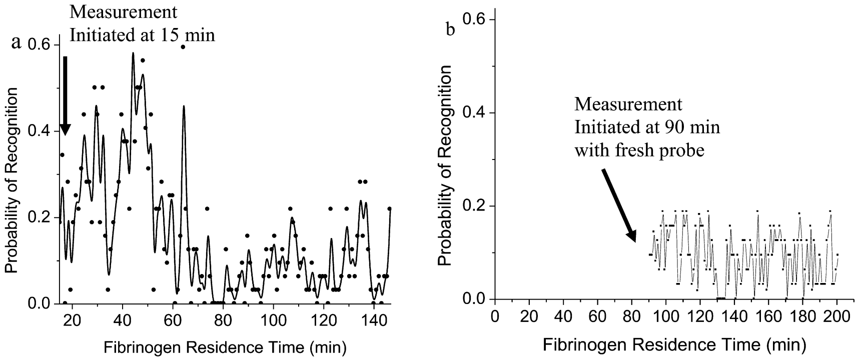

Figure 4. Time-dependent changes in the probability of recognition between an AFM probe coupled with mAb and adsorbed fibrinogen (100μg/ml). (a) Measurement was initialed at 15 min and (b) measurement was initiated at 90 minutes fibrinogen residence time. The black line shows a running 5 point average to guide the eye. (Reproduced with permission from reference (16). Copyright 2008 American Chemical Society.)

Figure 4(a) shows an example of a typical probability plot for antigen recognition measured against fibrinogen-adsorbed surfaces. Individual time points are shown by the data points and clearly demonstrate that the activity of fibrinogen is time dependent, with the maximum likelihood of recognition occurring in the time range around 45 minutes and then decreasing at longer adsorption times. Due to the time required for setup of AFM experiments, the measurement of AFM is generally initialed at 10-15 min after protein adsorption on mica surface. One concern was that the long scanning time could affect the activity of the mAb on probe. Therefore, measurements were initialed at residence time of 90 min with a fresh mAb probe. The probabilities of recognition were still in the range of 0-0.18, similar to those in Figure 4(a) after 90 minutes. A comprehensive series of control experiments confirmed that the long time scanning of mAb probe has no significant effect on its activity and that changes are due to temporal effects.

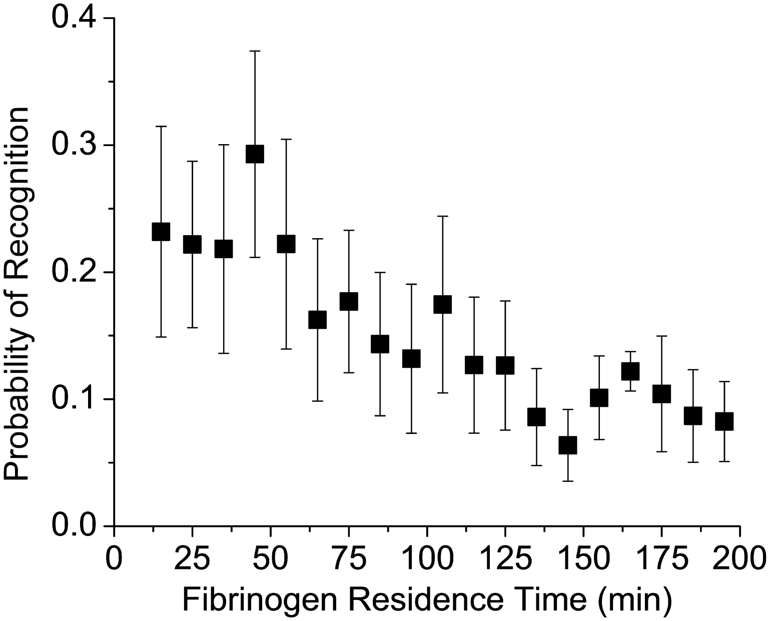

Figure 5. The pooled probability data of antigen recognition showing the functional activity of fibrinogen adsorbed on mica surface. (Reproduced with permission from reference (16). Copyright 2008 American Chemical Society.)

Figure 5 shows pooled probability data from multiple experiments (n ≥ 6 for each time point) as a function of fibrinogen residence time on mica substrate. The probability of antibody-antigen recognition, indicating the functional activity of adsorbed fibrinogen, peaks at ~45 minutes post-adsorption and thereafter decreases with increasing adsorption time. Although fibrinogen activity at 15, 25 and 35 minutes residence time is not statistically significant when compared to activity at 45 minutes, the recognition probability peak at ~45 minutes was consistently seen in all the experiments. Moreover, statistical analysis indicates that functional activity of adsorbed fibrinogen as measured by AFM force spectroscopy at the 45 minute time point is significantly greater than all time points ≥65 minutes ($P<0.001$).

3.2. Platelet Adhesion to Mica Surfaces Measured by LDH Assay

Macro-scale platelet adhesion measurements on mica substrates were carried out using a standard LDH assay to assess time dependence. Multiple experiments ($n \geq 6$) for each time point were carried out and the data was pooled according to the fibrinogen residence time on the substrate. Results in Figure 6 show that platelet adhesion reaches a peak at ~ 45 minutes fibrinogen residence time, which correlates well with the molecular scale AFM results. Statistical analysis indicate that platelet adhesion at 45 minutes fibrinogen residence time is significantly greater than platelet adhesion at 15 minutes ($p<0.001$) and at all times greater than or equal to 90 minutes ($p<0.01$).

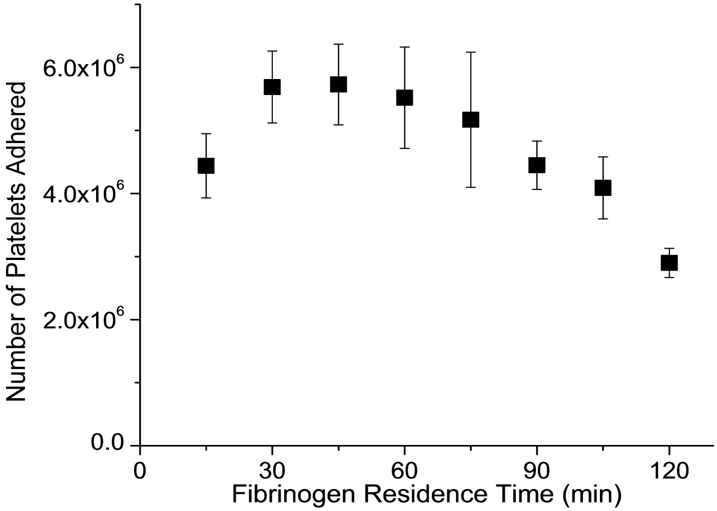

Figure 6. Platelet adhesion data from multiple experiments ($n \geq 6$ for each time point) showing changes in platelet adhesion as a function of fibrinogen residence times on mica substrates. (Reproduced with permission from reference (16). Copyright 2008 American Chemical Society.)

4. Effects of Protein Solution Composition on Functional Activity of Fibrinogen on Mica Surfaces (*37*)

Competitive adsorption of proteins from protein mixtures is important in a variety of applications such as tissue compatibility of biomaterials, cell culture on solid supports, and bacterial adhesion to implanted materials. Within the context of blood-biomaterial interactions, the Vroman effect is recognized as a general phenomenon of protein adsorption in competition between two or more proteins for the same adsorbent surface. The generalized Vroman effect has proteins adsorbing from mixtures through a series of adsorption-displacement steps in which low molecular weight (MW) proteins arriving first at a surface are displaced by relatively higher MW proteins arriving later (*38*). Adsorption of fibrinogen from blood plasma to many materials exhibits the Vroman effect with respect to plasma dilution and exposure time (*39*, *40*). However, the literature in biomaterials science does not always consistently support the Vroman effect. There is evidence that the competitive adsorption and displacement of fibrinogen with small plasma proteins such as albumin is related to protein concentrations and surface properties including hydrophobicity, surface charge and surface capacity (*38*, *41–43*) . Moreover, many studies on competitive protein adsorption look only at the amounts of individual protein, while there is less information available on the functional activity of protein, which is much more important in mediating platelet adhesion and activation.

In this section, the immuno-AFM recognition technique is extended to investigate the effects of protein solution concentration, residence time and co-incubation with BSA on the molecular potency of fibrinogen on mica substrates. The subsequent platelet adhesion on mica surfaces was measured to correlate the functional activity of protein at material surface.

4.1. Functional Activity of Fibrinogen in Mixed Protein Layers Adsorbed on Mica Surface

Fibrinogen or BSA solutions in PBS having two different concentrations (total protein concentration = 0.1 mg/ml or 1 mg/ml) were incubated with mica substrates at three different ratios (w/w) of fibrinogen:BSA (100:0, 50:50, and 10:90) for 5 min in an external fluid cell. The functional activity of fibrinogen adsorbed was measured by a mAb modified probe, as in the procedures described previously. The functional activity of fibrinogen as recognized by the mAb is illustrated in Figure 7. In protein solutions with a low concentration of 0.1 mg/ml protein, a 100% fibrinogen solution shows that the biological activity of fibrinogen increases with residence time, reaches a peak at 45 min postincubation, and then decreases with increasing residence time, as in the previous observation. With 50% fibrinogen, there is a shift in the time to peak activity of fibrinogen. The maximum activity is detected at 15 min residence time and steadily decreases with residence time. With 10% fibrinogen, no distinct peaks in fibrinogen activity were measured and the activity remains steady in the low probability range 0-0.1 (Figure 7a).

When the protein solution was 1 mg/ml, the functional activity of fibrinogen on mica surface shifts slightly towards earlier residence times as the ratio of BSA in the binary protein solution increases. Co-incubation with 50% BSA does not alter the biological activity of fibrinogen, but merely shifts the activity peak to an earlier time point of 40 min instead of 45 min. With 10% fibrinogen, there is a drastic shift in the activity of fibrinogen (Figure 7b), and the activity of fibrinogen is highest at 20 min residence time, and decreases with increasing residence time.

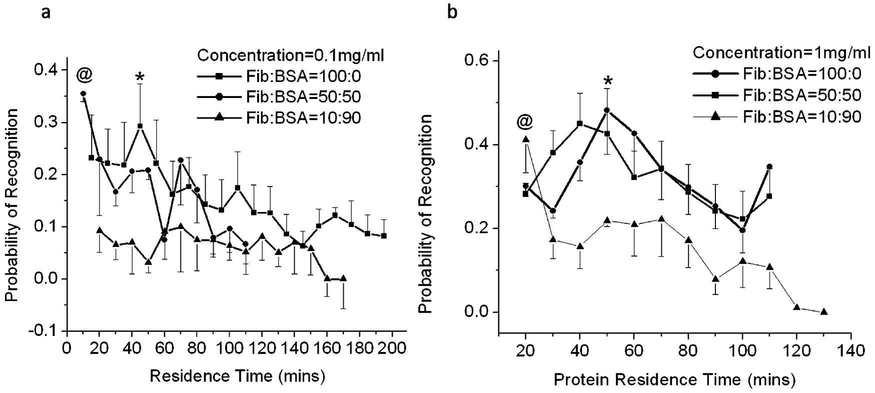

Figure 7. Pooled data from multiple measurements (n≥3 for each time point) showing the functional activity of fibrinogen on mica surfaces incubated in binary mixture with total protein concentration of (a) 0.1 mg/ml, and (b) 1 mg/ml. (Reproduced with permission from reference (37). Copyright 2011 American Chemical Society.)

4.2. Platelet Adhesion on Mica Surface Incubated in Fibrinogen and BSA Solution

Human platelet adhesion was carried out on mica surfaces that were incubated in fibrinogen and BSA mixture solution and then allowed to reside in PBS for different time periods. The adherent platelets were observed by fluorescence microscopy. Results show that the number of adherent platelets generally increases with an increase in the ratio of fibrinogen in the binary mixture. At 90% fibrinogen, some of the platelets were activated, whereas for 10% fibrinogen, minimal platelet activation was observed.

In the mixtures having total concentration of 0.1 mg/ml, platelet adhesion for pure fibrinogen correlated well with functional activity of fibrinogen at a molecule scale, i.e., a platelet adhesion peak is observed at 45 min residence time and platelet adhesion decreased with residence time. The introduction of BSA into solution changes peak platelet adhesion towards earlier time points (Figure 8a), again consistent with AFM results. For example, in the case of 50% fibrinogen, platelet adhesion peaks at 15 min, and decreases with residence time, similar to the functional activity of fibrinogen on surfaces (Figure 7a). Results suggest that the presence of BSA influences the conformational changes in fibrinogen, and the activity of fibrinogen is highest around 15 min and decreased at later time.

The high concentration protein solution (1 mg/ml) produces similar trends in platelet adhesion (Figure 8b). A small amount of BSA appears to have no effect on platelet adhesion as the platelet adhesion trend remains the same for 100% fibrinogen and 90% fibrinogen, with maximal adhesion occurring at 45 min residence time. However, a shift in the platelet adhesion peak is seen with increasing amount of BSA (50% and 90% BSA). At 90% BSA, the maximum platelet adhesion occurs at 15 min, again correlating well with molecular data (Figure 7b). For the pure BSA solution, there is no change in platelet adhesion with residence time and platelet adhesion lies in the low range, as expected.

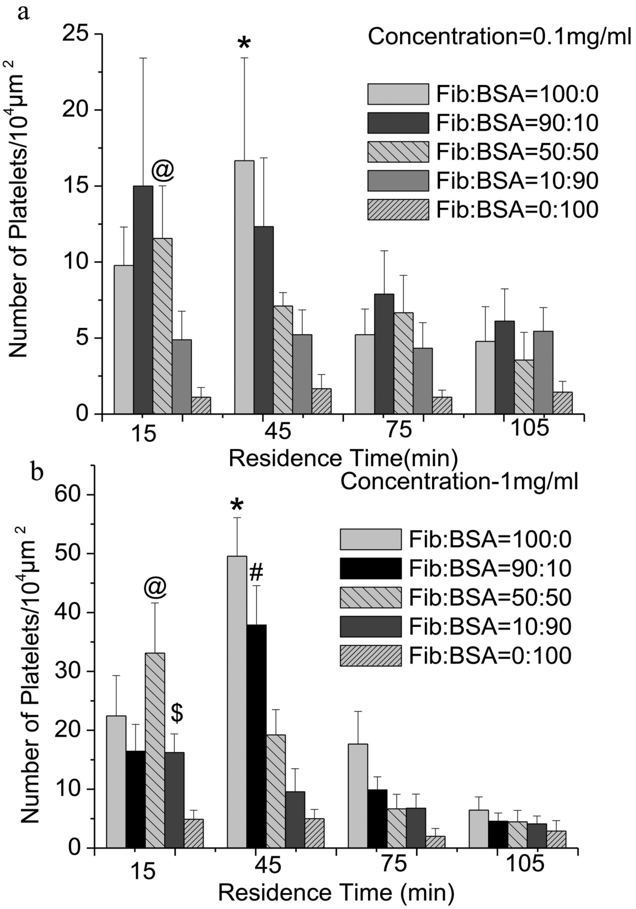

Figure 8. Pooled data from multiple measurements (n≥3 for each time point) showing the platelet adhesion on mica surfaces which were incubated in binary mixture with total protein concentration of (a) 0.1 mg/ml, and (b) 1 mg/ml. (Reproduced with permission from reference (37). Copyright 2011 American Chemical Society.)

5. Functional Activity of Fibrinogen and Platelet Adhesion on Polymeric Biomaterial Surfaces

The conformational change of proteins upon adsorption is seen to be time-dependent, but is also believed to be surface dependent. The previous conformational changes in fibrinogen described in this paper were all studied on a model hydrophilic mica surfaces from simple protein systems (pure fibrinogen and/or BSA). It is interesting to investigate the functional activity of fibrinogen adsorbed from complex plasma protein solutions on clinically relevant polymeric biomaterial surfaces. In this section, the functional activity of fibrinogen adsorbed from platelet poor plasma protein solutions on five different synthetic materials is discussed. Polydimethylsiloxane (PDMS), polystyrene (PS), low density polyethylene (LDPE), segmented polyether urethane urea (SPEUU) Biospan-P and SPEUU Biospan MS/0.4 were used as test materials. The first three of these materials have homogeneous surface chemistry and are primary reference materials for *in vitro* and *in vivo* tests of hemocompatibility and biocompatibility in the evaluation of biomaterials (*44*, *45*). Polyurethanes are important polymers for blood-contacting applications such as cardiovascular devices (*46*, *47*). Polyurethane biomaterials contain hard and soft segments forming a microphase separation structure with a heterogeneous surface structure and chemistry. This heterogeneous structure is believed to contribute to the improved success of the polymer in blood-contacting applications (*48*).

5.1. Functional Activity of Fibrinogen Adsorbed from Plasma Proteins on Polymeric Biomaterial Surfaces

Figure 9 shows the probability of recognition of fibrinogen activity as a function of residence time in PBS for a variety of biomaterial surfaces following incubation with platelet poor plasma (PPP) for 5 min. Results show the activity of fibrinogen varies with time on all these polymeric surfaces. In general, lower activity is observed early (<30 min) and late (>90 min) for all the material surfaces. A significant peak in activity ($p<0.001$) appears around 60-65 min post-incubation on PDMS and polystyrene surfaces, respectively (Figures 9a and 9b). While the fibrinogen activity at 60-65 min on the LDPE surface is significantly higher than the activity at times less than 30 min, similar to the PDMS and polystyrene. A further peak in activity was observed around 80-90 min post-incubation, after which the fibrinogen activity decreased, although still showing activity levels comparable to those at 60 to 65 minutes (Figure 9c). In stark contrast to the results seen with the three homopolymers, the chemically-heterogeneous phase separated polyurethanes show only small variances in fibrinogen activity across the time range (Figures 9d and 9e), although the activity at ~65 min on SPEUU Biospan MS/0.4 surface is significantly higher than that at time less than 30 min or at 90 and 120 min ($p<0.01$). Similarly, a higher fibrinogen activity was also observed around 60-65 min on another SPEUU Biospan-P surface.

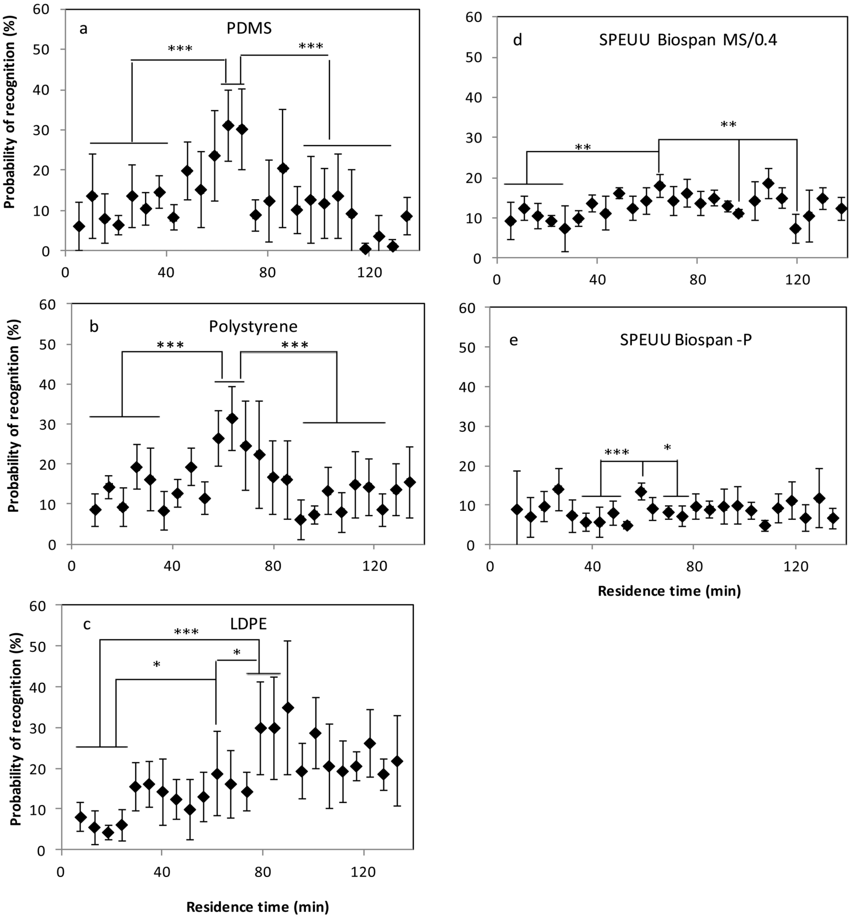

Figure 9. Time-dependent fibrinogen activity on a variety of biomaterial surfaces (a) PDMS, (b) polystyrene, (c) LDPE, (d) SPEUU MS/0.4, and (e) SPEUU Biospan-P after adsorbed with human PPP for 5 min.

5.2. Platelet Adhesion on Polymeric Biomaterial Surfaces

Macro-scale platelet adhesion measurements on polymeric biomaterial surfaces were carried out using a standard LDH assay to assess the time dependence of fibrinogen activity after adsorption. The numbers of platelets adherent to biomaterial surfaces that were incubatd with PPP and allowed to reside in PBS for 15, 30, 45, 60, 90 and 120 min are illustrated in Figure 10. The fibrinogen activity at the same time points as measured by the immuno-AFM probe is also shown in the same figure. Overall, the results show that the trends in platelet adhesion with residence time are quite consistent with the functional activity of fibrinogen, particularly for the three homopolymer materials. The phase separated polyurethane biomaterials show lower adhesion of platelets, consistent with the low probability of fibrinogen activity recognition, however, a peak in platelet adhesion still appears around 60 min residence time, corresponding to the small peak in fibrinogen activity at this time point (Figures 10d and 10e). Combined, these results suggest that the availability of γ chain in fibrinogen adsorbed on biomaterial surface is an important determinant of platelet adhesion.

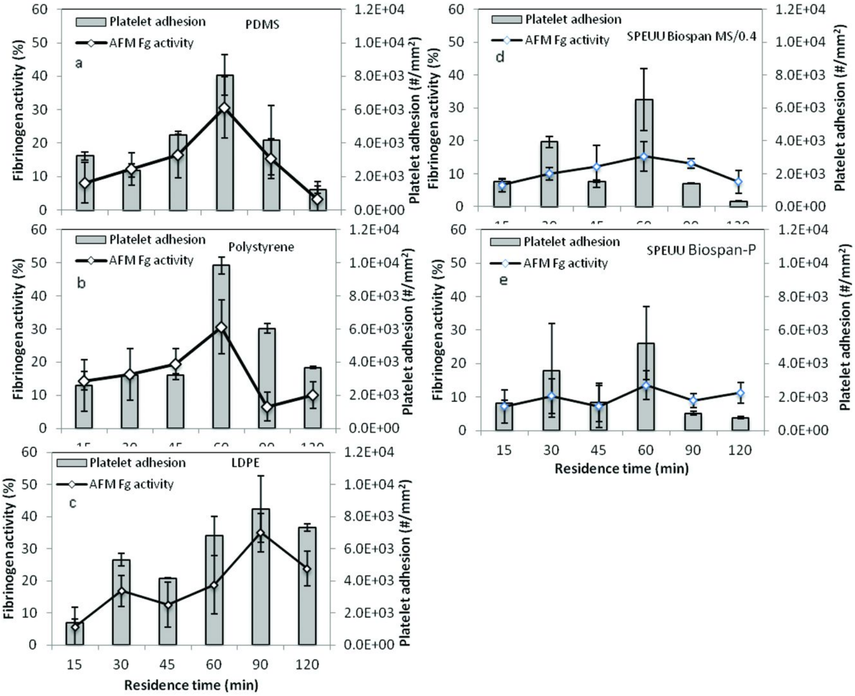

Figure 10. Platelet adhesion on a variety of biomaterial surfaces after 15, 30, 45, 60, 75, 90, 120 min residence time following adsorption from PPP. (a) PDMS, (b) polystyrene, (c) LDPE, (d) SPEUU MS/0.4, and (e) SPEUU Biospan-P.

5.3. Relationship between Platelet Adhesion and Fibrinogen Functional Activity

The macro-scale platelet adhesion data correlated well with the molecular scale fibrinogen activity on each of the biomaterial surfaces. To further probe this information, all data points were pooled together and graphed to show the platelet adhesion as a function of the probability of epitope recognition regardless of material type. When all five polymers were analyzed together, and using the Boltzmann equation to quantify the dose-response relationship, the relationship was poor with an R^2 value of 0.784 (data not shown). However, when the data were separated as being either on a homopolymer or on a phase separated copolymer, much better correlations were seen on homogeneous polymers. Figure 11 illustrates these relationships between platelet adhesion and fibrinogen activity on the three homogeneous polymers (PDMS, PS, and LDPE, Figure 11a) and heterogeneous copolymers (SPEUU Biospan MS/0.4 and P, Figure 11b). A strong relationship between the activity of fibrinogen and measured platelet adhesion was obtained from three different homopolymer materials (Figure 11a). However, the two different phase-separated polyurethane materials possessing heterogeneous surface chemistries appear to deviate from this activity/adhesion relationship and show a weaker relationship (R^2=0.628). The fitting parameters for the equation are tabulated in Table 1.

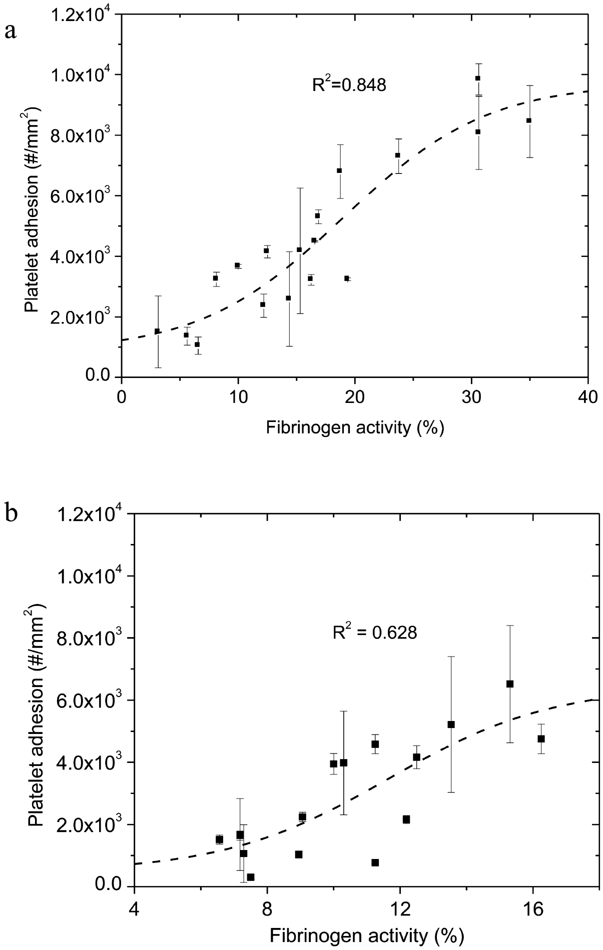

Figure 11. Relationship between platelet adhesion and probability of recognition for fibrinogen activity on surfaces of (a) homopolymers and (b) heterogeneous copolymers (broken line = Boltzman sigmoidal fit to data).

Results in Table 1 show that the response of platelet adhesion to fibrinogen activity on heterogeneous copolymer surfaces is lower than that on the homogeneous polymers, regardless of whether one looks at the initial or final values. It should be noted that the SPEUU materials never reached the same level of protein activity as the homopolymers, so that the final value of platelet adhesion shown here may not be the value that would be reached if somehow the activity levels were increased. However, there is still a 50% increase in the final platelet adhesion level for the homopolymers compared to the phase-separated polymers. These phase-separated polyurethane biomaterials consist of both hard and soft segments having a microphase separated structure (*49*). It has been suggested that the ~50 to 100 nm sized phases in SPEUU materials and heterogeneous surface chemistry may be responsible for the increased levels of blood compatibility seen in these materials, an observation that is supported the results is seen in this current study (Figure 11b).

Table 1. Fitting parameters of Boltzmann equation,

$$y = \frac{A_1 - A_2}{1 + e^{(x - x_0)dx}} + A_2$$

Polymer	*Initial (A_1)*	*Final (A_2)*	*Center (x_0)*	*Width (dx)*	*R^2*
Homogeneous	832.5	9734.9	19.0	6.2	0.848
Heterogeneous	463.5	6474.5	11.6	2.5	0.628

6. Conclusions

The immuno-AFM technique extends the scope of traditional AFM imaging studies to epitope recognition in adsorbed proteins, and provides a unique opportunity to begin to assess the biological activity of single adsorbed protein molecules. The molecular scale measurements revealed that the functional activity of fibrinogen varies with residence time on all material surfaces studied. Although the exact mechanisms behind the changes in activity with time are not clear from these studies, the changes in conformational structure of proteins following adsorption are believed to contribute to the changes in availability of the platelet binding epitope located in γ chain. The transient exposure of this functional domain appears to be both time and substrate dependent. On a mica surface, the probability of epitope recognition peaked at ~45 min post adsorption of fibrinogen and the inclusion of albumin into the fibrinogen solution moves the peak in biological activity to earlier time points. On the synthetic polymeric material surfaces, the peak in bioactivity occurred at residence times ranging from 60 to 90 min depending on material. No matter how the activity of protein varied with residence time and substrate, trends between platelet adhesion and probability of epitope recognition by AFM are largely consistent, indicating that the γ chain in fibrinogen is a useful predictor of platelet adhesion.

References

1. Langer, R.; Tirrell, D. A. Designing materials for biology and medicine. *Nature* **2004**, *428*, 487–92.
2. Gorbet, M. B.; Sefton, M. V. M. V. Biomaterial-associated thrombosis: roles of coagulation factors, complement, platelets and leukocytes. *Biomaterials* **2004**, *25*, 5681–703.
3. Hantgan R. R., Lord S. T. Fibrinogen structure and physiology. In *Hemostasis and Thrombosis: Basic Priciples and Clinical Practice*, 5th ed.; Colman, R. W., Marder, V. J., Clowes, A. W., George, J. N., Goldhaber, S. Z., Eds.; J.B. Lippincott Company: Philadelphia, 2006.
4. Savage, B.; Shattil, S. J.; Ruggeri, Z. M. Modulation of Platelet-Function through Adhesion Receptors - A Dual Role for Glycoprotein-IIB-IIIA (Integrin-Alpha(Iib)Beta(3) Mediated by Fibrinogen and Glycoprotein-IB-von-Willebrand Factor. *J. Biol. Chem.* **1992**, *267*, 11300–6.
5. Mosesson, M. W. Fibrinogen and fibrin structure and functions. *J. Thromb. Haemostasis* **2005**, *3*, 1894–904.
6. Sivaraman, B.; Latour, R. A. The relationship between platelet adhesion on surfaces and the structure versus the amount of adsorbed fibrinogen. *Biomaterials* **2010**, *31*, 832–9.
7. Hylton, D. M.; Shalaby, S. W.; Latour, R. A. Direct correlation between adsorption-induced changes in protein structure and platelet adhesion. *J. Biomed. Mater. Res., Part A* **2005**, *73A*, 349–58.
8. Tsai, W. B.; Grunkemeier, J. M.; Horbett, T. A. Human plasma fibrinogen adsorption and platelet adhesion to polystyrene. *J. Biomed. Mater. Res.* **1999**, *44*, 130–9.
9. Tsai, W. B.; Grunkemeier, J. M.; Horbett, T. A. Variations in the ability of adsorbed fibrinogen to mediate platelet adhesion to polystyrene-based materials: A multivariate statistical analysis of antibody binding to the platelet binding sites of fibrinogen. *J. Biomed. Mater. Res., Part A* **2003**, *67A*, 1255–68.
10. Kloczewiak, M.; Timmons, S.; Lukas, T. J.; Hawiger, J Platelet receptor recognition site on human fibrinogen - synthesis and structure function relationship of peptides corresponding to the carboxy-terminal segmental of the gamma-chain. *Biochemistry* **1984**, *23*, 1767–74.
11. Mayo, K. H.; Burke, C.; Lindon, J. N.; Kloczewiak, M. H-1-NMR sequential assignments and secondary structure- analysis of human fibrinigen gamma-chain C-terminal residues 385-411. *Biochemistry* **1990**, *29*, 3277–86.
12. Farrell, D. H.; Thiagarajan, P.; Chung, D. W.; Davie, E. W. Role of fibrinogen alpha-chain and gamma-chain sites in platelet aggregation. *Proc. Natl. Acad. Sci. U.S.A.* **1992**, *89*, 10729–32.

13. Wu, Y. G.; Simonovsky, F. I.; Ratner, B. D.; Horbett, T. A. The role of adsorbed fibrinogen in platelet adhesion to polyurethane surfaces: A comparison of surface hydrophobicity, protein adsorption, monoclonal antibody binding, and platelet adhesion. *J. Biomed. Mater. Res., Part A* **2005**, *74A*, 722–38.
14. Chiumiento, A.; Lamponi, S.; Barbucci, R. Role of fibrinogen conformation in platelet activation. *Biomacromolecules* **2007**, *8*, 523–31.
15. Balasubramanian, V.; Grusin, N. K.; Bucher, R. W.; Turitto, V. T.; Slack, S. M. Residence-time dependent changes in fibrinogen adsorbed to polymeric biomaterials. *J. Biomed. Mater. Res.* **1999**, *44*, 253–60.
16. Soman, P.; Rice, Z.; Siedlecki, CA Measuring the Time-Dependent Functional Activity of Adsorbed Fibrinogen by Atomic Force Microscopy. *Langmuir* **2008**, *24*, 8801–6.
17. Balasubramanian, V.; Slack, S. M. Effects of fibrinogen residence time and shear rate on the morphology and procoagulant activity of human platelets adherent to polymeric biomaterials. *ASAIO J.* **2001**, *47*, 354–60.
18. Steiner, G. Conformational changes during protein adsorption. FT-IR spectroscopic imaging of adsorbed fibrinogen layers. *Anal. Chem.* **2007**, *79*, 1311–6.
19. Agnihotri, A.; Siedlecki, C. A. Time-dependent conformational changes in fibrinogen measured by atomic force microscopy. *Langmuir* **2004**, *20*, 8846–52.
20. Lu, D. R.; Park, K. Effect of Surface Hydrophobicity on the Conformational-Changes of Adsorbed Fibrinogen. *J. Colloid Interface Sci.* **1991**, *144*, 271–81.
21. Sit, P. S.; Marchant, R. E. Surface-dependent conformations of human fibrinogen observed by atomic force microscopy under aqueous conditions. *Thromb. Haemostasis* **1999**, *82*, 1053–60.
22. Marchin, K. L.; Berrie, C. L. Conformational changes in the plasma protein fibrinogen upon adsorption to graphite and mica investigated by atomic force microscopy. *Langmuir* **2003**, *19*, 9883–8.
23. Toscano, A.; Santore, M. M. Fibrinogen adsorption on three silica-based surfaces: Conformation and kinetics. *Langmuir* **2006**, *22*, 2588–97.
24. Sivaraman, B.; Fears, K. P.; Latour, RA Investigation of the Effects of Surface Chemistry and Solution Concentration on the Conformation of Adsorbed Proteins Using an Improved Circular Dichroism Method. *Langmuir* **2009**, *25*, 3050–6.
25. Xu L. C., Soman P., Agnihotri A., Siedlecki CA. Atomic force microacopy methods for characterizing protein interactions with microphase-separated polyurethane biomaterials. In *Biological Interactions on Materials Surfaces Understandig and Controlling Protein, Cell, and Tissue Responses*; Puleo D. A., Bizios R., Eds.; Springer: Dordrecht, 2009; pp 44−69.
26. Xu, L.-C.; Runt, J; Siedlecki, C. A. Dynamics of hydrated polyurethane biomaterials: Surface microphase restructuring, protein activity and platelet adhesion. *Acta Biomater.* **2010**, *6* (6), 1938–1947.
27. Cohen, S. R.; Bitler, A. Use of AFM in bio-related systems. *Curr. Opin. Colloid Interface Sci* **2008**, *13*, 316–25.

28. Gaczynska, M.; Osmulski, P. A. AFM of biological complexes: What can we learn? *Curr. Opin. Colloid Interface Sci.* **2008**, *13*, 351–67.
29. Hussain, M. A.; Agnihotri, A.; Siedlecki, C. A. AFM imaging of ligand binding to platelet integrin alpha(IIb)beta(3) receptors reconstituted into planar lipid bilayers. *Langmuir* **2005**, *21*, 6979–86.
30. Holland, N. B.; Marchant, R. E. Individual plasma proteins detected on rough biomaterials by phase imaging AFM. *J. Biomed. Mater. Res.* **2000**, *51*, 307–15.
31. Soman, P.; Rice, Z.; Siedlecki, C. A. Immunological identification of fibrinogen in dual-component protein films by AFM imaging. *Micron* **2008**, *39*, 832–42.
32. Hinterdorfer, P.; Baumgartner, W.; Gruber, H. J.; Schilcher, K.; Schindler, H. Detection and localization of individual antibody-antigen recognition events by atomic force microscopy. *Proc. Natl. Acad. Sci. U.S.A.* **1996**, *93*, 3477–81.
33. Agnihotri, A.; Siedlecki, C. A. Adhesion mode atomic force microscopy study of dual component protein films. *Ultramicroscopy* **2005**, *102*, 257–68.
34. Shiba, E.; Lindon, J. N.; Kushner, L.; Kudryk, B.; Salzman, E. W. Detection by monoclonal antibodies of conformational change in fibrinogen adsorption on artificial surfaces. *Thromb. Haemostasis* **1987**, *58*, 33.
35. Shiba, E.; Lindon, J. N.; Kushner, L.; Matsueda, G. R.; Hawiger, J.; Kloczewiak, M.; et al. Antibody-detectable changes in fibrinogen adsorption affecting platelet activation onpolymer surfaces. *Am. J. Physiol.* **1991**, *260*, C965–C74.
36. Chowdhury, P. B.; Luckham, P. F. Probing recognition process between an antibody and an antigen using atomic force microscopy. *Colloids Surf., A* **1998**, *143*, 53–7.
37. Soman, P.; Siedlecki, C. A. Effects of Protein Solution Composition on the Time-Dependent Functional Activity of Fibrinogen on Surfaces. *Langmuir* **2011**, *27*, 10814–9.
38. Noh, H.; Vogler, E. A. Volumetric interpretation of protein adsorption: Competition from mixtures and the Vroman effect. *Biomaterials* **2007**, *28*, 405–22.
39. Le, M. T.; Mulvihill, J. N.; Cazenave, J. P.; Dejardin, P. Transient adsorption of fibrinogen from plasma solutions flowing in silica capillaries. In *Proteins at Interfaces II*; Horbett, T. A., Brash, J. L., Eds.; ACS Symposium Series 602; American Chemical Society: Washington, DC, 1995; pp 129−137.
40. Slack, S. M.; Horbett, T. A. Changes in Fibrinogen Adsorbed to Segmented Polyurethanes and Hydroxyethylmethacrylate-Ethylmethacrylate Copolymers. *J. Biomed. Mater. Res* **1992**, *26*, 1633–49.
41. Lassen, B.; Malmsten, M. Competitive Protein Adsorption at Plasma Polymer Surfaces. *J. Colloid. Interface Sci.* **1997**, *186*, 9–16.
42. Nonckreman, C. J.; Rouxhet, P. G.; Dupont-Gillain, C. C. Dual radiolabeling to study protein adsorption competition in relation with hemocompatibility. *J. Biomed. Mater. Res., Part A* **2007**, *81A*, 791–802.

43. Huang, Y.; Lü, X.; Qian, W.; Tang, Z.; Zhong, Y. Competitive protein adsorption on biomaterial surface studied with reflectometric interference spectroscopy. *Acta Biomater.* **2010**, *6* (6), 2083–90.
44. van Kooten, T. G.; Spijker, H. T.; Busscher, H. J. Plasma-treated polystyrene surfaces: model surfaces for studying cell-biomaterial interactions. *Biomaterials* **2004**, *25*, 1735–47.
45. Bélanger, M. C.; Marois, Y. Hemocompatibility, biocompatibility, inflammatory and in vivo studies of primary reference materials low-density polyethylene and polydimethylsiloxane: A review. *J. Biomed. Mater. Res.* **2001**, *58*, 467–77.
46. Ghanbari, H.; Viatge, H.; Kidane, A. G.; Burriesci, G.; Tavakoli, M.; Seifalian, A. M. Polymeric heart valves: new materials, emerging hopes. *Trends Biotechnol.* **2009**, *27*, 359–67.
47. Macocinschi, D.; Filip, D.; Vlad, S.; Cristea, M.; Butnaru, M. Segmented biopolyurethanes for medical applications. *J. Mater. Sci.: -Mater. Med.* **2009**, *20*, 1659–68.
48. Lamba, N. M. K.; Woodhouse, K. A.; Cooper, S. L. *Polyurethanes in Biomedical Applications*; CRC Press: Boca Raton, FL, 1998.
49. Xu, L. C.; Siedlecki, C. A. Microphase separation structure influences protein interactions with poly(urethane urea) surfaces. *J. Biomed. Mater. Res.: Part A* **2010**, *92A*, 126–36.

Chapter 18

Understanding the Role of Exogenous and Endogenous Surfactants in Gas Embolism

**Joshua W. Lampe,[1] Portonovo S. Ayyaswamy,[2]
and David M. Eckmann*[,3,4]**

**[1]Center for Resuscitation Science, Department of Emergency Medicine,
Hospital of the University of Pennsylvania, Philadelphia, Pennsylvania 19104
[2]Mechanical Engineering and Applied Mechanics,
University of Pennsylvania, Philadelphia, Pennsylvania 19104
[3]Department of Anesthesiology and Critical Care, Hospital of the University
of Pennsylvania, Philadelphia, Pennsylvania 19104
[4]Department of Bioengineering, University of Pennsylvania,
Philadelphia, Pennsylvania 19104
*Email: Eckmanndm@uphs.upenn.edu**

Important pathological and biophysical processes occur at the gas-liquid interface created when a bubble is introduced into the bloodstream. The bubble-cell adhesion force and bubble surface tension play an important role in the cellular response to bubble contact, and research suggests that the use of exogenous surfactants, which reduce both the adhesion force and surface tension, confer significant protection against gas embolism. To better understand the role of the gas-liquid interface in the pathology of gas embolism, the motion of a freely convected bubble in a surfactant laden fluid was studied numerically and the adsorption of proteins and surfactants to the gas-liquid interface were studied experimentally. The numerical studies have elucidated complex relationships between the shear stress experienced by the endothelial cell layer in the blood vessel and the surface tension of the freely convected bubble. The experimental studies indicate that it is possible to prevent protein adsorption to the gas-liquid interface using exogenous surfactants. The gas-liquid interface is a unique and viable target for pharmacological intervention during gas embolism.

In Proteins at Interfaces III State of the Art 2012; Horbett, T., et al.;
ACS Symposium Series; American Chemical Society: Washington, DC, 2012.

Introduction

Over 300,000 cardiopulmonary bypass (CPB) surgeries are performed annually in the United States. It is estimated that as much as 70% of the patient population report some neurological deficit after the procedure (*1*) and that 6-8% of the patient population suffers from a serious neurological morbid event, including stroke or death (*2*, *3*). While a cause for these neurological complications has not been identified, cerebrovascular gas embolism is consistent with this morbidity and has been frequently implicated (*4*, *5*). While it may be possible to reduce the amount of foreign matter (gas and particulate) introduced into the blood stream during CPB surgeries, it seems impossible to eliminate the problem entirely. Therefore, it is relevant to ask what kind of prevention and treatment methods can be developed.

A gas bubble in a blood vessel can exist in three distinct scenarios. The the bubble can be convected through the vessel freely, the bubble can adhere to the vessel wall but not occlude the vessel (partially dewetted bubble), or the bubble can occlude the blood vessel. The force balance that describes these situations can be derived from Newton's second law as:

$$\rho\left(\frac{\partial \mathbf{u}}{\partial t}+\mathbf{u}\cdot\nabla\mathbf{u}\right)=-\nabla p+\nabla\cdot\mu\left(\nabla\mathbf{u}+\nabla^{T}\mathbf{u}\right)+\rho\mathbf{g}+IFB \tag{1}$$

where ρ is the fluid density, μ is the fluid viscosity, u is velocity, t is time, p is pressure, g is the acceleration due to gravity and *IFB* is an interfacial force balance that describes the interfacial forces that apply to the specific scenario. Three prototypical scenarios are discussed below.

In the scenario where the bubble is freely convected, all terms are nonzero and the interfacial force balance takes the form

$$IFB=\int_{S(t)}\sigma\kappa\mathbf{n}_f\delta\left(\mathbf{x}-\mathbf{x}_f\right)ds \tag{2}$$

where σ is the surface tension, κ is the curvature of the interface, $\boldsymbol{n}_f$ is the unit normal pointing into the bulk fluid, $\boldsymbol{x}_f$ is the position vector on the interface, $S(t)$ is the instantaneous surface area of the bubble, and $\delta(\boldsymbol{x}-\boldsymbol{x}_f)$ is the Dirac delta function that is nonzero only when $\boldsymbol{x}=\boldsymbol{x}_f$. The interface of a freely convected bubble is free to deform, and the shear stress will be a function of interfacial position. Interfacial curvature will be a function of the local surface tension - pressure balance as well as the local velocity.

In the scenario where the bubble is partially dewetted or has occluded the blood vessel additional terms are needed to describe the forces that arise from bubble-wall contact. In this scenario the interfacial force balance takes the form

$$IFB=\int_{S(t)}\sigma\kappa\mathbf{n}_f\delta\left(\mathbf{x}-\mathbf{x}_f\right)ds+\int_{l}\sigma\cos(\phi)\mathrm{d}l+\iint_{A}\beta\mathrm{dA} \tag{3}$$

where φ is the contact angle along the dewetted perimeter, l is the length along the dewetted perimeter, β is an adhesion force, and A is the dewetted area. The bubble surface area exposed to the fluid stream, *S(t)*, is subject to the same conditions as the freely convected bubble, however, the bubble surface area exposed to the vessel wall, *A*, is constrained by the shape of the vessel wall.

Interpretation of the adhesion force, *β*, is complicated by molecular constituents in blood. Dispersive adhesion is expected in these situations, but there may also be chemical adhesion which will arise from specific receptor-ligand interactions, hydrogen bonds, and electrostatic bonds that arise between biosurfactants absorbed onto the bubble interface and the endothelial glycocalyx. One critical example of chemical adhesion is bubble induced thrombogenesis.

Examining Eq. 1, it becomes clear that the interfacial force balance is the best therapeutic target. Blood velocity, density, and viscosity can be manipulated within physiological limits, but it is challenging to dictate these properties at the capillary level, which is required to aid bubble clearance from tissue beds. However, the interfacial force balance is highly dependent on the molecular composition of the interface, and it may be possible to control molecular composition of the interface through the addition of exogenous surfactants.

In Eq. 2, surface tension is related to the molecular composition of the interface through the Gibbs adsorption equation

$$\Gamma = -\frac{1}{RT}\frac{\partial \sigma}{\partial \ln C_{bulk}} \qquad (4)$$

where Γ is the surface excess concentration, R is the Universal Gas Constant, T is the temperature, and C_{bulk} is the bulk concentration of the surfactant. The addition of exogenous surfactants would affect the surface excess concentrations impacting the surface tension, the contact line, and the dispersive adhesion components of the interfacial force balance. Exogenous surfactants will also effect the chemical adhesion component of the force balance by displacing thrombogenic proteins from the interface.

In the recent past, we have experimentally studied the potential protective effect of exogenous surfactants against bubble induced thrombogenesis, a physiological process, and endothelial cell damage, a biophysical process. To better understand the impact that surfactants have on thrombogenesis, we examined platelet-platelet and platelet-bubble interactions as well as shear induced thrombin generation in the presence and absence of an exogenous surfactant. The surfactants Pluronic F-127, Perftoran (an emulsified perfluorocarbon), and Dow Corning Antifoam 1519US were used in these studies. The presence of exogenous surfactants at the time of bubble introduction was found to reduce platelet-platelet and platelet-bubble binding (*6*). Thrombin generation, a shear rate and time dependent process, was also attenuated by the presence of exogenous surfactants (*7*).

The effects of endogenous and exogenous surfactants on bubble-endothelial cell interactions were also studied in in-vivo and ex-vivo experiments. In-vivo experiments were conducted using intravital microscopy to observe and record (video) bubble shape, motion, and adhesion in the rat cremaster muscle. In these studies it was found that the presence of exogenous surfactants did not impact early bubble dynamics, but did increase the rate of bubble breakup and gas readsorbtion by the blood (*8*). Ex-vivo experiments were performed using a vessel perfusion chamber and rat arterioles excised from the jejunum. The ex-vivo setting enabled the perfusion of the vessel with a variety of solutions to study the impact of exogenous and endogenous surfactants separately. Bubble-endothelial cell layer adhesion force was greatest when the perfusing solution contained only bovine serum albumin (BSA). When the perfusing solution was rat serum, the adhesion force was lower than for the BSA perfusion solution, suggesting that protein heterogeneity interferes in the development of the adhesion force seen in the BSA experiment (*9*). The presence of Perftoran or Pluronic PF-127 in the perfusate before the introduction of air led to the lowest measured adhesion force. Pharmacological studies of vasoconstriction and vasodilation after the clearance of the air bubble suggested that the reduction in measured adhesion force correlated with a protection of endothelial vasodilatory function (*10*).

Having demonstrated the impact of exogenous surfactants on the physiological processes of thrombogenesis and platelet interactions, as well as the physical processes of bubble adhesion, bubble readsorption, and bubble clearance, we sought to precisely understand the role of surfactant adsorption in bubble dynamics in blood flow as well as the competition of blood borne proteins and exogenous surfactants for space as the gas-blood interface.

Numerical Modeling of Gas Embolism: Interface Fluid Mechanics and Mass Transport

Introduction

Interfacial adsorption problems relevant to gas embolism may be investigated using *in silico* computational modeling to examine chemical reaction dynamics including membrane dynamics of endothelial cell contact with embolism bubbles. We have developed a numerical model to compute the motion and deformation of bubbles and cells in surfactant-laden blood flow, evaluate local cellular deformation during bubble transit through the microvasculature, and determine dose-dependent effects of pharmacological agents to minimize shear stress exposure, cell membrane deformation and limit vessel occlusion (*11–18*).

We consider the axisymmetric motion of a nearly occluding gas bubble in a surfactant laden Casson fluid in a cylindrical tube. The shape and location of the bubble interface are determined using a modified front- tracking method. The properties of the bulk fluid include both the shear-thinning effects of blood as well as the Fahraeus and Fahraeus-Lindqvist effects (see (*19*)). The surfactant properties, in general, are similar to those of ethoxylated surfactants and follow either the Langmuir or Frumkin isotherm. Three different vessel sizes, corresponding to a small artery, large arteriole, and a small arteriole in normal humans (*20*), are considered. The corresponding representative flow Reynolds numbers are 200, 2, and 0.2, respectively. The degree of bubble occlusion is characterized by the ratio of the equivalent-volume bubble radius to vessel radius (aspect ratio), λ, in the range $0.9 \leq \lambda \leq 1.05$. For non-spherical bubbles, the applicable radius of the bubble is taken to be that of a spherically shaped bubble which has the same volume as the non-spherical one (equivalent-volume spherical radius). The initial bulk flow corresponds to a fully established Casson flow in a cylindrical vessel.

Problem Formulation

We consider the axisymmetric motion of a nearly occluding gas bubble of density ρ_g and viscosity μ_g in a cylindrical vessel of radius R (diameter d) as shown in Figure 1. Gravity acts in the direction from top to bottom. Both the gas and the liquid phases are modeled as incompressible fluids governed by the continuity and the Navier-Stokes equations (*18*):

$$\nabla \cdot \boldsymbol{u} = 0 \qquad (5)$$

$$\rho\left(\frac{\partial \boldsymbol{u}}{\partial t} + \boldsymbol{u}\cdot\nabla\boldsymbol{u}\right) = -\nabla p + \nabla\cdot\mu(\nabla\boldsymbol{u} + \nabla^T\boldsymbol{u}) + \int_{S(t)}\left[\sigma(\Gamma(s))C\boldsymbol{n}_f + \frac{\partial\sigma(\Gamma(s))}{\partial s}\boldsymbol{t}_f\right]\hat{\delta}(\boldsymbol{x}-\boldsymbol{x}_f)dS + \rho\boldsymbol{g} \qquad (6)$$

Here, $\boldsymbol{u} \equiv (v_r, v_z)$, is the fluid velocity with v_r, v_z as the velocity components along the radial and axial directions, p is the pressure, ρ and μ are the density and the viscosity of the medium, $\boldsymbol{g}$ is the gravitational acceleration, s is an arc length measure on the interface, C is the curvature of the interface, σ is the surface tension coefficient which is a function of the surfactant concentration Γ, $S(t)$ denotes the instantaneous location of the interface, $\boldsymbol{n_f}$ denotes the unit normal vector on the interface (pointing into the bulk fluid), $\boldsymbol{t_f}$ is the unit tangential vector at the interface, x_f denotes the position vector on the interface, and $\hat{\delta}(\boldsymbol{x} - \boldsymbol{x_f})$ stands for the 2D axisymmetric Dirac delta function that is non-zero only when $\boldsymbol{x} = \boldsymbol{x_f}$. The density and viscosity of the medium are:

$$[\rho,\mu](r,z,t) = [\rho_l,\mu_l]H(r,z,t) + [\rho_g,\mu_g](1 - H(r,z,t)) \qquad (7)$$

Here, t is time, and $H(r,z,t)$ is a Heaviside function such that,

$$H(r,z,t) = \begin{cases} 1 & (r,z,t)\text{ in the bulk,} \\ 0 & (r,z,t)\text{ in the bubble} \end{cases} \qquad (8)$$

The bulk liquid is modeled as a two-layer fluid of density ρ_l consisting of a cylindrical core of concentrated red blood cell (RBC) suspension, surrounded by a cell-free layer. The cell-free layer is modeled as a Newtonian fluid of constant viscosity μ_{layer} (*21*) while the RBC suspension is modeled as a shear-thinning Casson fluid of viscosity μ_c (*19*, *20*). The viscosity of the liquid μ_l as a function of the radial position in a bubble-free tube is thus,

$$\mu_l = \begin{cases} \mu_c, & 0 \le r \le (1-\delta)R \\ \mu_{layer}, & (1-\delta)R < r \le R \end{cases} \qquad (9)$$

where δ is the non-dimensional thickness of the cell-free layer normalized with R and

$$\mu_c = \left[\sqrt{\mu_\infty} + \sqrt{\frac{\tau_y}{|\gamma|}}\left(1 - e^{-\sqrt{m|\gamma|}}\right)\right]^2 \tag{10}$$

in which μ_∞ is the asymptotic Newtonian viscosity, τ_y is the yield stress, γ is the prevalent local shear rate and m is the Casson viscosity regularization exponent. The expressions for μ_∞ and τ_y as functions of core hematocrit H_C are given by (*22*) as:

$$\mu_\infty = \frac{\mu_p}{(1 - H_C)^{C_1}} \;;\tau_y^{1/2} = C_2\left[\left(\frac{1}{1 - H_C}\right)^{C_1/2} - 1\right] \tag{11}$$

C_1 and C_2 are constants whose values for human blood are given as 2.0 and 0.3315, respectively. We have previously solved these equations for $d = 40\ \mu m$ (small arteriole) and 100 μm (large arteriole) for $H_D = 0.45$ (*13*), and have documented values for H_C, δ, and β. In (*13*), we have also examined a vessel size $d = 2\ mm$ (small artery). At such a large radius, $\delta \rightarrow 0$ and $H_C \sim H_D$. The surface tension of the interface, separating the continuous and dispersed phases, varies with the surfactant concentration, Γ, on the interface, according to the equation of state given by the Langmuir isotherm (*23*):

$$\sigma = \sigma_s + \Re T \Gamma_\infty \ln\left(1 - \frac{\Gamma}{\Gamma_\infty}\right) \tag{12}$$

where σ_s is the surface tension of a surfactant-free clean interface, $\mathcal{R}$ is the ideal gas constant, T is the absolute temperature and Γ_∞ is the maximum monolayer interface surfactant concentration. Alternately, the equation of state can also be given by the Frumkin isotherm:

$$\sigma = \sigma_s + \Re T \Gamma_\infty\left(\ln\left(1 - \frac{\Gamma}{\Gamma_\infty}\right) + \frac{\xi}{2}\left(\frac{\Gamma}{\Gamma_\infty}\right)^2\right) \tag{13}$$

where ξ is the Frumkin interaction parameter. The evolution of the surfactant concentration at the interface is given by (*24*) as:

$$\frac{\partial \Gamma}{\partial t} + \nabla_s \cdot (\boldsymbol{u}_s \Gamma) + \Gamma(\nabla_s \cdot \boldsymbol{n}_f)(\boldsymbol{u} \cdot \boldsymbol{n}_f) = D_s \nabla_s^2 \Gamma + j_n \tag{14}$$

with j_n being the diffusional flux at the interface given by Fick's law: $j_n = D_l(n_f \cdot \nabla)C$. Also, u_s and $u \cdot n_f$ are the tangential and normal components of the velocity on the interface, respectively, D_s is the surface diffusion coefficient, D_l is the bulk diffusion coefficient, C is the bulk concentration, and, $\nabla_s = \nabla - n_f(n_f \cdot \nabla)$ is the gradient operator along the interface. The diffusional flux on the interface, $D_l(n_f \cdot \nabla)C$, is balanced by the adsorption and desorption terms as:

$$D_l(\boldsymbol{n}_f \cdot \nabla)C = k_a C_s\left(1 - \frac{\Gamma}{\Gamma_\infty}\right) - k_d \Gamma, \tag{15}$$

in which k_a and k_d are the adsorption and desorption coefficients, respectively, and C_s is concentration in the sublayer adjacent to the interface. The governing equation for the bulk concentration C then becomes:

$$\frac{\partial C}{\partial t} + (\mathbf{u} \cdot \nabla)C = \nabla \cdot (D\nabla C) - \int_{S(t)} \left[k_a C_s\left(1 - \frac{\Gamma}{\Gamma_\infty}\right) - k_d \Gamma\right] \hat{\delta}(\boldsymbol{x} - \boldsymbol{x}_f)\, dS \tag{16}$$

where the diffusion coefficient D may be written as:

$$D = D_l H. \tag{17}$$

These governing equations are coupled with suitable initial and boundary conditions (see (*13*) for details). Scaling the equations to yield their non-dimensional form provides the following relevant non-dimensional parameters: Reynolds number $\mathrm{Re} = \rho U_{max} d/\mu$, Weber number $\mathrm{We} = \rho_l U_{max}{}^2 d/\sigma$, Froude number $\mathrm{Fr} = U_{max}/\sqrt{(gd)}$, surface Péclet number $\mathrm{Pe}_s = U_{max} d/D_s$, desorption Stanton number $\mathrm{St}_d = k_d d/U_{max}$, dimensionless adsorption depth $\alpha = \Gamma_\infty/C_0 d$, bulk Péclet number $\mathrm{Pe} = U_{max} d/D_l$, and adsorption Stanton number $\mathrm{St}_a = k_a/U_{max}$. The capillary number $\mathrm{Ca} = \mu U_{max}/\sigma$ is the ratio of *Re* and *We*. Here, C_0 (mol/cm^3) is the far field bulk concentration and Γ_∞ (mol/cm^2) is the maximum monolayer interface surfactant concentration. U_s is a representative surface velocity, with $U_s \sim U_{max}$. Important time scales in this problem are: convection time scale d/U_{max}, momentum diffusion time scale $\rho d^2/\mu$, and mass diffusion time scales d^2/D_l and d^2/D_s.

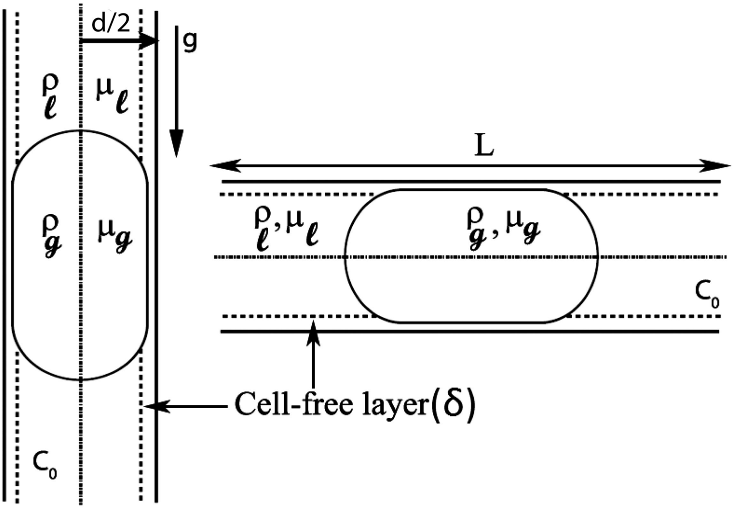

Figure 1. Schematic of a nearly occluding bubble in vertical and horizontal vessel configurations.

Numerical Method

The governing equations are solved using a front-tracking method coupled with a level contour reconstruction procedure. This procedure and the validation of the numerical model is described in detail in (*13*, *17*, *18*), and is only be briefly discussed here:

- Given a particular interface position, and bulk and interface concentration distributions, calculate the surface tension forces and distribute them as body forces to the fixed Eulerian grid.
- Solve the fluid flow equations with the given conditions to obtain the velocity and pressure fields.
- Use the computed velocity field to update the interface and bulk surfactant values.
- Update the position of the interface using the velocity field in a Lagrangian fashion.
- Reconstruct the interface using the level contour reconstruction procedure if the bubble volume changes by more than 0.5% or periodically after every few time steps.
- If the interface is reconstructed, project the surface concentration profile to the new interface in such a way as to conserve the amount of surfactant on the interface.
- Repeat these steps until either steady state is reached or the bubble reaches the outlet of the computational domain.

Results

Upon the introduction of the bubble, diffusive and convective mechanisms in the bulk phase bring the surfactant from the bulk medium to the gas-liquid interface. Adsorption and desorption mechanisms are initiated. Vortical motions inside the bubble are similar to, but considerably weaker than those within a clean bubble. Diffusion and advection of the adsorbed surfactant occur at the interface, the latter due to surface mobility. Consistent with the bulk concentration and interfacial capacity for adsorption and desorption of the surfactant, a steady state mass transfer profile is eventually established displaying a non-uniform distribution of the surfactant at the interface.

The distribution of the surfactant at the interface is complex. In Figure 2, we display the steady state interface concentrations of the surfactant as a function of arc length for various Reynolds numbers. The arc length along the interface is measured starting from the trailing edge of the bubble, and it is normalized with respect to the total arc length from the trailing edge to the leading edge.

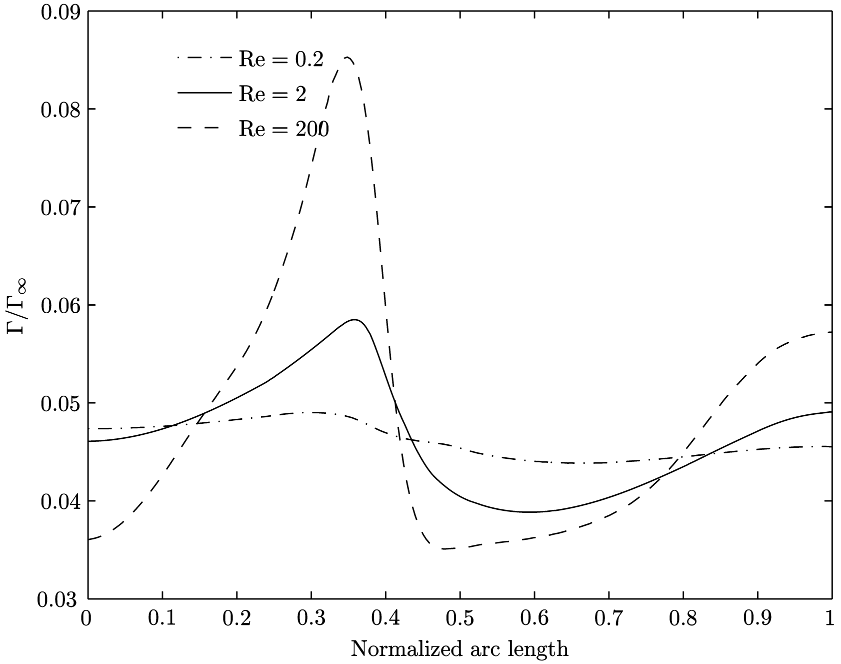

Figure 2. Interface concentration for the three cases of Reynolds numbers with identical far-field concentration. The aspect ratio (λ) is 1.0. The normalized arc length along the surface of the bubble is measured from the rear stagnation point.

At every Reynolds number, the highest and the lowest surfactant concentrations on the interface occur in the vicinity of the convergent and divergent stagnation rings, respectively, accompanied by a complicated distribution elsewhere along the interface. An important quantity of interest is the time variation of the shear stress τ at any given point on the vessel wall as the moving bubble approaches, moves over this point and departs. As the bubble moves, the entrained fluid surrounding it causes rapid changes in the magnitude and the sign of the shear stresses experienced by the wall. For a given point on the wall, the changes in shear stress manifest as a solitary wave. This solitary wave has major potential physiological implications including induction of a complex pattern of endothelial cell membrane stretch and compression, activation of mechanotransduction pathways, loss of plasma membrane integrity and plasma membrane stress failure. A comparison of the shear stresses experienced by a point on the vessel wall for clean and surfactant-coated bubble motions, is shown in Figure 3. The shear stress is normalized with the corresponding base value, τ_{ref}. In this figure, only the duration of time where there is significant deviation in the stress from its basal value is displayed, and this period corresponds to the motion of the bubble over the point.

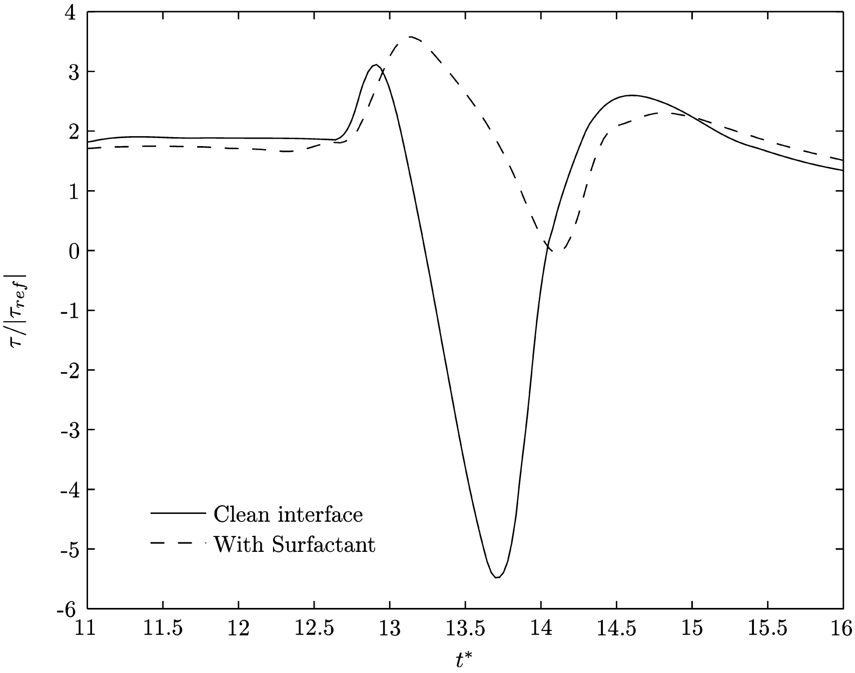

Figure 3. Variation of shear stress at a point on the vessel wall as the bubble passes over it. Normalization of the shear stress is done with the corresponding basal value. λ is 1.0, Re = 0.2, τ_{ref} = 56 dyn cm^{-2}.

The effect of the surfactant is more pronounced at lower values of the Reynolds numbers (e.g., 0.2 and 2). This is because a decrease in Reynolds number corresponds to a decrease in the surface mobility of the bubble. In turn, the recirculating vortex that is primarily responsible for causing the stress reversals is also weaker. Furthermore, for $\lambda \geq 1.0$, the presence of the surfactant increases the minimum gap size between the bubble interface and the vessel wall, which is more pronounced at lower Reynolds numbers and results in reduced stress variations. The physiologically relevant range of Reynolds numbers spans six orders of magnitude from O(10^{-3}) to O(10^3). The presence of the surfactant therefore has its predominant effects at lower Reynolds numbers, encountered in arteriols and capillaries.

The jump in the value of the shear stress from its maximum to its minimum (see Figure 3), $\Delta\tau = \tau_{max} - \tau_{min}$, is an index of the magnitude of the shear stress change to which the luminal endothelial cell surface is subjected. The time rate of change of $\Delta\tau$ is a measure of the impulse character of the solitary wave as it traverses the cell surface. Together they provide a mechanism for cell injury by rapid bidirectional stretching of the cell surface. The effect of the presence of a surfactant is to minimize both the magnitude and impulse character of the solitary wave and thereby reduce the passing bubble's effect on the wall. The protective surfactant effects to reduce cellular injury or death have occurred in vessels of a size corresponding to lower Reynolds numbers (*6*, *8*, *10*, *25–27*) as we have predicted.

Protein Adsorption to the Gas Liquid Interface

Background

The numerical simulations demonstrated that surface tension is critical to the biophysics of gas embolism, regardless of bubble-vessel contact. Therefore, control of the surface tension at the gas-liquid (GL) interface during gas embolism provides a unique pharmacologic pathway to modulate the resulting pathology. In order to better understand interactions between endogenous and exogenous surfactants and the GL interface it is necessary to accurately quantify the surface concentration. Customarily, equilibrium surface concentration at the GL interface is estimated by fitting measurements of equilibrium surface tension to a surface equation of state (SEOS). A SEOS is derived through the combination of the Gibbs adsorption equation, Eqn. 4, with an appropriate isotherm,

$$\Gamma = Kf(C) \tag{18}$$

which relates the surface excess to a function of concentration, $f(C)$, using the constant K. It is readily apparent from Eq. 4 and Eq. 2 that the system of equations can be solved without explicitly calculating Γ. Instead, a theoretical maximal surface excess value, $\Gamma_{\max}$, is calculated using the so-called maximal slope method or through a least squares fit of experimental data to the desired SEOS.

Despite the widespread use of this technique, there are reasons to doubt assumptions required to implement the method (*28*). Protein structure complexity (*29*), the relatively weak surface activity of protein molecules (*30*), and variability in protein tertiary structure stability (*31*, *32*) complicate the application of the Gibbs adsorption equation to protein adsorption. The Gibbs adsorption equation requires that the interfacial layer is homogenous and reversibly adsorbed, while there is experimental and theoretical evidence that this is not always the case for proteins (*33–36*). Attempts to use a SEOS to estimate surface concentrations for multi-species solutions comprised of multiple surfactants and/or proteins are even more questionable. The resulting surface concentration estimates are highly model-dependent and mathematically non-unique (*37*).

There are few accepted methods for measuring surface excess concentration, interfacial homogeneity, or interfacial mobility. The adsorbed concentration on the GL interface has been measured using neutron reflectivity (*32*, *38*, *39*), ellipsometry (*40–43*), and radiolabeling (*44*). Neutron reflectivity and ellipsometry are model dependent and can only be applied to single species solutions. Radiolabeling provides model-independent surface excess concentration data for a single protein species. It is not currently possible to measure the surface excess concentrations in solutions that contain more than one protein species.

To improve our understanding of endogenous and exogenous surfactant adsorption during gas embolism, we undertook a comprehensive experimental study of protein/PF-127 adsorption to the GL interface. Surface tension measurements were made for single and multispecies solutions as a function of time and bulk concentration. In addition, we developed confocal laser scanning microscopy (CLSM) methods to measure interfacial layer mobility, homogeneity, and gain insight into surface excess concentration.

Materials, Methods, and Image Analysis

Protein and Surfactant Solution Materials

A PBS buffer solution was created from stock salts and MilliQ de-ionized water. The PBS buffer solution is 136 mM NaCl, 8.1 mM Na_2HPO_4, 2 mM KCl, 1.5 mM KH_2PO_4, and 31 mM NaN_3. These salts were used as purchased from Sigma without further purification. The PBS buffer was maintained at pH 7.4 and stored at room temperature.

For increased repeatability, small volumes (< 50 mL) of 1 % mass concentration BSA (Fraction V A 9647) and 0.1% mass concentration BF (Fraction 1 type I-S F 8630) were made and refrigerated for future dilution in PBS. These solutions were used to create all solutions with mass concentrations less than 1% for BSA or 0.1% for BF. Fresh large volume solutions were created for any experiment requiring 1% BSA or 0.1% BF solutions. The proteins were used without concentration verification or further purification.

Bovine serum albumin (BSA, Cat. No. A9647) and human fibrinogen (HF, Cat. No. F4129) were obtained from Sigma and used without further purification. BSA labeled with the fluorophore Texas Red (BSA-TR, Cat. No. A23017) and Human Fibrinogen (HF) labeled with Oregon Green (HF-OG, Cat. No. F7496) were purchased from Molecular Probes, a division of Invitrogen. The BSA conjugate has approximately 3 Texas Red fluorophores attached to the protein molecule. The HF conjugate has approximately 13 Oregon Green fluorophores attached to the protein molecule. A test drop of Texas Red in PBS buffer was imaged to ensure that Texas Red is not a surface active molecule.

Pluronic F-127 (Molecular Probes P-6866) was obtained as a 10% solution in DI water that had been 0.2 μm filtered, and was used as purchased without further purification. More dilute solutions were created by mixing aliquots of the stock 10% PF-127 with the PBS buffer detailed above. This was done to provide uniformity in the buffer used in all experiments.

Surface Tension Measurements

Surface pressure (Π) was measured using a tensiometer purchased from Ramé Hart (model 100-00, Ramé Hart, inc, Mountain Lakes, NJ, USA). A pendant air bubble was formed within the test solution using an automated dispensing system and a ‘j’ shaped syringe. Proprietary software controlled bubble size for the duration of the experiment and recorded surface tension data. Experiments were conducted at room temperature.

Surface pressure (Π) for fluorescently labeled proteins was measured using a KSV Minimicro System 2 with a Wilhelmy plate microbalance. Data were recorded by computer using proprietary software. The minitrough was housed in a Plexiglas box, with openings appropriate for setup, cleaning, and data cables. The box contained several extra beakers of water to aid in humidity control. After an experiment was started, the box was sealed to allow for humidity stabilization to minimize evaporation. Experiments were run at room temperature.

Confocal Laser Scanning Microscopy

The inverted CLSM used in these experiments was manufactured by Olympus, model IX81 with Fluoview FV1000 controller. Fluoview version 1.6 was used to control the microscope, and a 40X water immersion objective (1.15 NA) was used to visualize the droplet interface. The HF-OG samples were excited by argon laser (488 nm, 30 mW), and BSA-TR samples were excited by HeNe laser (543 nm, 1 mW). Fluorescence was detected by photomultiplier detector. Scan speed ranged from 2.0 μs/pixel to 10.0 μs/pixel in measurements with different purposes with image sizes of 512×512 pixels under one way scan mode. The time consumed to take a single image was 0.5 s the shortest and 2.7 s the longest, which are small enough for us to detect the adsorption kinetics of protein adsorption.

The droplet holder, fabricated for this experiment, was comprised of a small (1.5 inch diameter) plastic Petri dish with a hole bored in the bottom. This hole was covered by a glass coverslip (standard thickness No. 1). The droplet of interest was deposited on the coverslip at the bottom of the Petri dish. The inverted microscope objective imaged the droplet from below the coverslip. The Petri dish lid was used to create a closed volume, and additional water droplets were placed in the Petri dish out of view to minimize evaporation. The Petri dish was cleaned with HPLC grade ethanol and deionized water between each use.

Results

Surface tension was measured as a function of surfactant concentration and time for BSA, BF, and PF-127. Figure 4 shows the surface tension values at 20 hours for all the singles species adsorption experiments. The four point logistic equation

$$\gamma = (\gamma_{\mathrm{max}} - \gamma_{\mathrm{min}})/[1 + \ln C_{\mathrm{half}}/\ln C_{\mathrm{bulk}})^{M}) + \gamma_{\mathrm{min}} \qquad (19)$$

has been fitted to the data to determine the values of γ_{max}, γ_{min}, M, and C_{half} to enable the surface concentration calculation. The value for Γ is determined using the maximum slope method. The results of the curve fit and the surface excess calculations are included in Table I.

Table I. Adsorption parameters calculated using the logistic equation. SOURCE: Reproduced with permission from reference (*45*). Copyright 2011 Old City Publishing

surfactant	σ_{max} *[mN/m]*	σ_{min} *[mN/m]*	C_{half} *[ln(pmoles)]*	*M* *unitless*	$C_{max}{}^{a}$ *[ln(pmoles)]*	$\Gamma_{apparent}{}^{a}$ *[pmoles/cm²]*	*n/V* *[#/nm³]*
BSA	72.4±0.8	42.9±2.1	9.44±0.71	-2.4±0.3	17.21	77.31	4/322
BF	72.0±2.0	47.4±1.5	5.46±0.44	-3.1±0.7	9.14	135.93	9/12150
PF-127	72.0±0.8	40.9±1.1	9.67±0.24	-6.6±1.0	NA	191.5	NA

[a] These parameters are calculated and the error is expected to be large

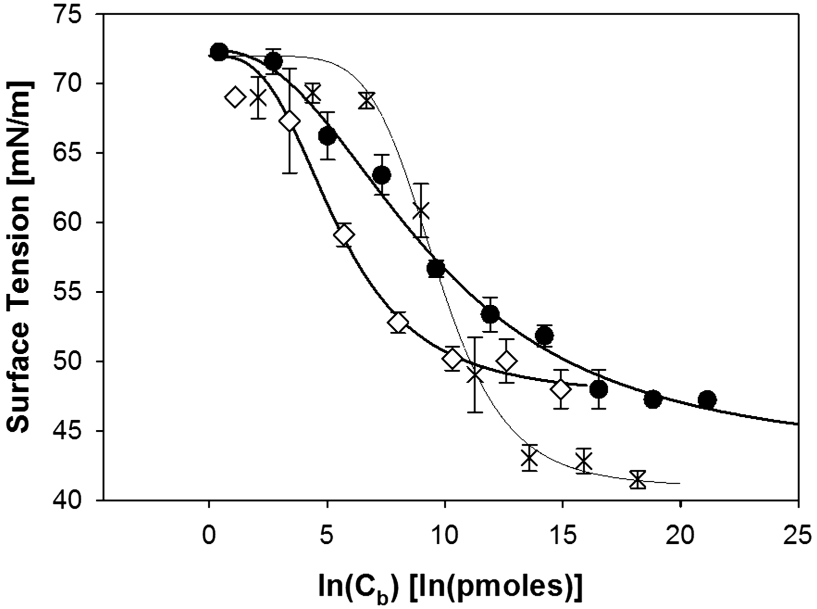

Figure 4. Equilibrium surface tension data for BSA (●), BF (◇) and PF-127 (x). Lines show the fit of the four point logistic equation to the data. (Adapted with permission from reference (45). Copyright 2011 Old City Publishing.)

Competitive adsorption experiments were also completed across a wide spectrum of concentrations. Figure 5 shows select equilibrium surface tension data for competitive adsorption between BSA or BF and PF-127. In both cases, the PF-127 concentration was 800 nM. The BSA concentrations were: 15 nM, 1.5 µM, and 150 µM. The BF concentrations were: 2.9 nM, 294 nM, and 2.94 µM. The maximum concentrations used in these experiments is the same order of magnitude as the physiological concentrations for the two proteins. The spectrum of protein concentrations used here create surface excess concentrations that modeling suggest might exist on a freely convected gas bubble in blood. Surface excess concentrations The data in panel A suggest that the interface is composed of a combination of BSA and PF-127, while the data in panel B suggest that the interface is primarily composed of PF-127.

It is not currently possible to use competitive surface tension values, as shown in Figure 5, to calculate the surface excess concentrations of the surfactants. To gain a better understanding of the nature of the GL interface, we used CLSM to image the adsorption of labeled proteins. Figure 6 is a CLSM image showing heterogeneous protein adsorption to the GL interface for a droplet containing HF-OG at a concentration of 29 pM. This interface was highly mobile.

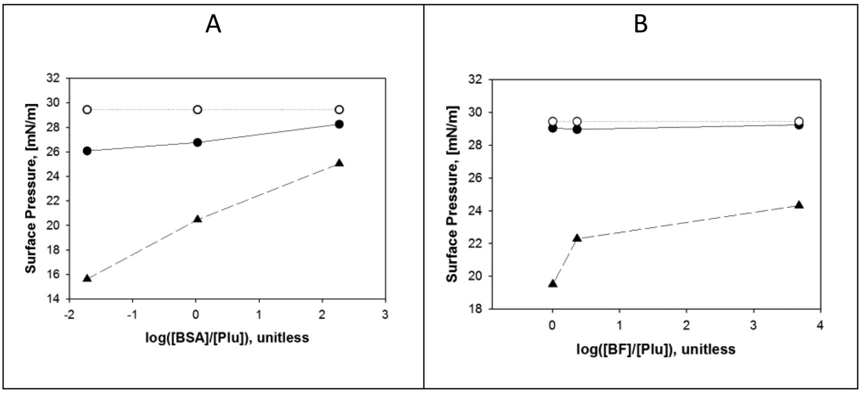

Figure 5. Comparison of single species and multispecies adsorption. The PF-127 concentration is 800 nM in both panels, and PF-127 surface pressure is represented by the open circles (○). The equilibrium surface tension data for the multi-species experiments is represented by filled circles (●). Panel A shows BSA-PF-127 competition and Panel B shows BF-PF-127 competition. In both panels the single species protein surface tension data is represented by filled triangles (▲).

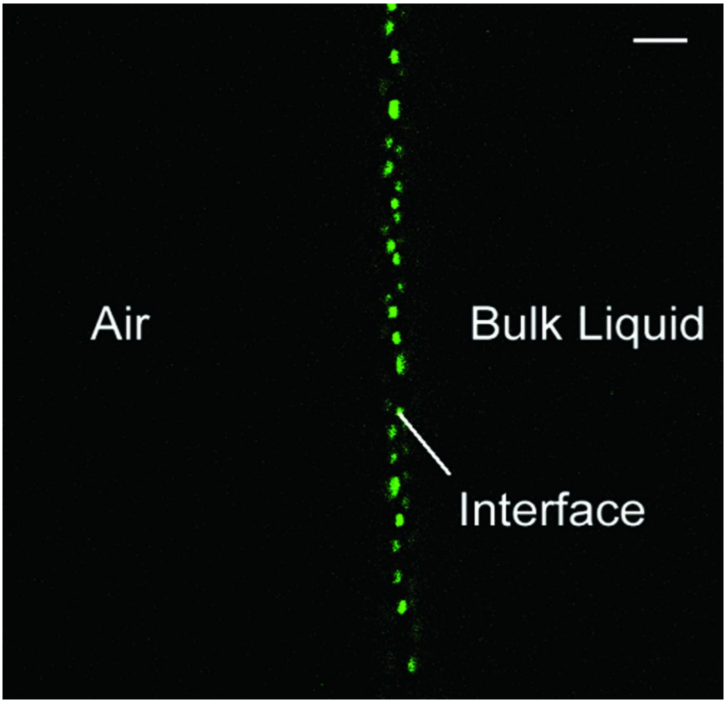

Figure 6. HF-OG creates a highly mobile, inhomogeneous interfacial layer. Confocal image of the GL interface for a HF-OG droplet with a bulk protein concentration of 29 pM in a PBS buffer. Scale bar is 10 um. (Reproduced with permission from reference (47). Copyright 2010 American Chemical Society.)

Fluorescence recovery after photobleaching (FRAP) is a technique wherein a small segment of a CLSM image is photobleached using high power laser illumination. In these experiments, fluorescence recovery indicates that new unbleached molecules have occupied the space where photobleaching occurred. Figure 7 shows FRAP measurements for a droplet that contained HF-OG at a concentration of 753 pM and Texas Red labeled BSA (BSA-TR) at a concentration of 7.5 μM. In this droplet, photobleaching was observed for both proteins, indicating that the interface was relatively immobile.

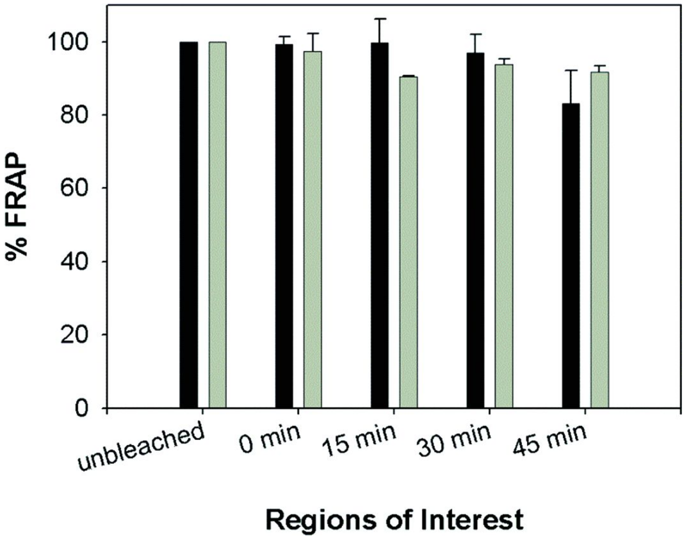

Figure 7. FRAP data for a two species droplet containing 7.5 μM BSA-TR and 753 pM HF-OG. Fluorescence recovery for BSA-TR is represented by the black bars and fluorescence recovery for HF-OG is represented by the gray bars. Unbleached-area-interfacial intensity increases as a function of time during the experiments. Error bars represent the 90% confidence interval on the mean. (Reproduced with permission from reference (47). Copyright 2010 American Chemical Society)

CLSM can also be used to gain qualitative measures of surface excess concentration. As shown in Figure 6, the greater concentration of HF-OG at the interface manifests as greater fluorescence in the CLSM image.

Figure 8 compares the radial HF-OG fluorescence intensity of 4 droplets containing either HF-OG or a combination of HF-OG and PF-127. The GL interface is located approximately at the 8 μm mark on the abscissa. The fluorescence intensity of droplets containing HF-OG are shown in thin lines, and the fluorescence intensity of droplets containing HF-OG and PF-127 are shown in bold lines. The 80 μM concentration of PF-127 concentration in these droplets is sufficient to prevent HF-OG adsorption.

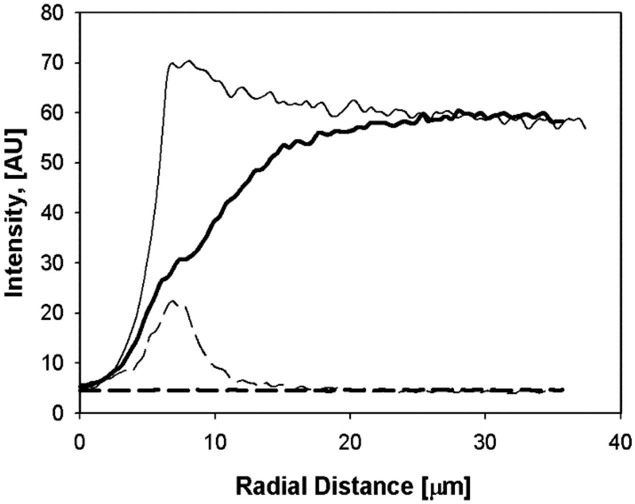

Figure 8. Pluronic F-127 blocks protein adsorption. Plot shows four average intensity profiles measured at 1 h near the droplet edge. The ImageJ ROI, referred to in the abscissa, is shown in Figure 1(a). The thick solid line is the intensity profile for a droplet containing 2.9 μM HF-OG and 80 μM PF-127. The thick dashed line is the intensity profile for a droplet containing 29 pM HF-OG and 80 μM PF-127. The thin solid line is the intensity profile for a droplet containing only 2.9 μM HF-OG, and the thin dashed line is the intensity profile for a droplet containing only 29 pM HF-OG. (Reproduced with permission from reference (47). Copyright 2010 American Chemical Society)

Discussion

Given the problems associated with using standard SEOS approaches to model protein adsorption, we compared our experimental results with the predictions of the molecular weight dependent model developed by Krishnan et al (*30*). This model did not fit the equilibrium surface tension data shown in Figure 4 particularly well. Upon closer examination, it was discovered that the spherical approximations used in the model (*30*) underestimate the volume of the BSA molecule by ~30%. As a result, we reformulated the model to include dependence on molecular volume, as shown below:

$$\sigma = \sigma_{\min} + RT\Gamma\left[28.14 + \ln(\varepsilon / P) - \ln C_{bulk} - \ln(V / n)\right] \qquad (20)$$

In which σ is the concentration dependent surface tension, $\sigma_{\min}$ is the minimum surface tension that can be created for a given protein, R is the universal gas constant, T is the absolute temperature, Γ is the surface excess concentration, ε is a packing efficiency parameter, P is the partition coefficient describing protein adsorption, C_{bulk} is the bulk protein concentration, and *n* is the number of molecules in the unit cell volume, *V*, which is no longer constrained to sphere packing. This model is described more fully in (*30*) and (*45*). Comparisons of the molecular weight dependent and molecular volume dependent models with the experimental data from Figure 4 are shown in Figure 9 below.

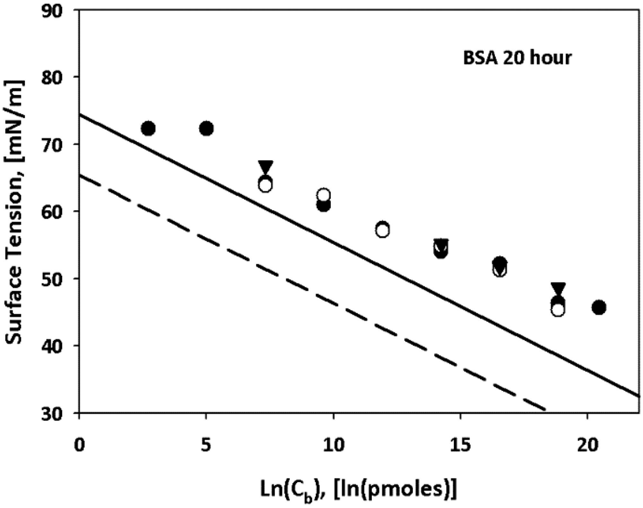

Figure 9. Comparison of 20 surface tension data for BSA solutions at a variety of concentrations. The dashed line is the predictions of the model in [TRAUBE] and the solid line is the prediction of Eq. [5]. Different symbols represent different repetitions of the same experiment. (Reproduced with permission from reference (45). Copyright 2011 Old City Publishing.)

The thickness of the adsorbed layer for the volume dependent model can be calculated from the equation:

$$\Omega_{\max} = \frac{\Gamma_{GL}}{C_{int}^{\max}} = \frac{\Gamma_{GL} V}{\varepsilon n \left(1.66 \times 10^{12}\right)} \tag{21}$$

In which the value of V/n is the volume of the interface allocated per adsorbed protein molecule. Using the data from (*30*) (Γ_{GL} = 3.2 pmoles/cm^2, ε = 0.45) and the values for V/n for BSA and HSA, we find that the interface thickness for HSA is 4.1 nm and the interface thickness for BSA is 6.8 nm. This estimate for the thickness of the BSA layer is in remarkably good numeric agreement with the estimate obtained using Neutron Reflectivity which predicts a difference of 130% (*38*).

Experiments where BSA and BF competed with PF-127 for interfacial area demonstrated that the surface tension was similar to the surface tension for droplets containing only PF-127 when the Pluronic concentration was higher than 800 nM as shown in Figure 5. This is suggestive that the interface contains primarily PF-127 despite physiological levels of BSA and BF, but it is not conclusive. This concentration range is in good agreement with our prior in-vivo data that showed that PF-127 was protective against gas embolism. Additional surface concentration data is required to determine if PF-127 can prevent protein adsorption.

Rao and Damadoran suggested that the time lag between surface excess formation and surface tension change in protein solutions could be explained by protein molecule aggregation at the interface. Figure 6 shows the existence of two adsorbed phases of HF-OG at the interface of a 29 pM HF-OG droplet. This image implies that HF aggregates at the interface, and results in a series of islands of aggregated HF surrounded by areas of non-aggregated HF. This interface was much more mobile than the more homogeneous layers formed by HF-OG at higher concentrations. The expected surface tension for this HF solution at the time of this image is ~60 mN/m (*46*). This image highlights the difficulties associated with using the Gibbs adsorption equation to model protein adsorption.

FRAP experiments demonstrated that HF-OG forms an immobile interfacial layer, and that BSA-TR does not (*47*). Photobleached regions of interest (ROI) on BSA-TR droplets recovered full fluorescence in less time than was required to complete a single image while the ROIs formed on HF-OG droplets could be observed for the duration of the experiment. The very rapid fluorescence recovery of the BSA-TR interface demonstrates that the adsorbed BSA layer is unstructured and *highly* mobile for a minimum of 1 h, even at physiological concentrations O(100 μM). In contrast, droplets of HF-OG, at varying concentrations, establish immobile and irreversibly adsorbed protein layers. The time required to establish an immobile and irreversibly adsorbed layer is concentration dependent. The photobleached ROIs were roughly 10 μm long x 3 μm wide x 1 μm deep, corresponding to the confocal plane. Because the ROI photobleached at time 0 min on the 2.9 μM HF-OG drop did not leave the 1-μm thick focal plane, or translate in the focal plane, we can conclude that the ROI did not move more than 1 μm in 60 min, suggesting that the HF-OG interfacial layer is immobile.

FRAP experiments were also conducted to investigate interfacial mobility during competitive adsorption. The results are shown in Figure 7. In this experiment a droplet containing 7.5 μM BSA-TR and 145 pM HF-OG was used. Several characteristics of the interface could be observed. First, adsorbed BSA-TR and HF-OG were homogeneously distributed along the GL interface, indicating that BSA-TR is trapped in, or a member of, an HF-OG interfacial layer. Second, photobleached BSA-TR was evident in this experiment, although it was never observed in single species BSA-TR droplets, confirming that the single species BSA-TR interface is extremely mobile. Finally, the ROI bleached at time zero in the droplet containing both BSA-TR and HF-OG did not exhibit total fluorescence recovery at 1 h, while the ROI bleached at time zero in the single species HF-OG droplet containing a higher HF-OG concentration (290 pM) did exhibit full recovery. This suggests that the HF-OG is able to form a stable interfacial network that contains a significant amount of non-HF (BSA) proteins, even at low concentrations. These results convincingly prove that adsorbed layers of multiple proteins cannot be described by linear combinations of the adsorbed single protein layers.

To determine if PF-127 is able to prevent protein adsorption, fluorescence intensity data were collected as a function of HF-OG concentration with a PF-127 concentration of 80 μM. As shown in Figure 8, no HF-OG intensity peaks were detected at the interface. Clearly, PF-127 is dominating the interface, effectively inhibiting fibrinogen absorption. This finding has profound implications for the mechanism through which PF-127 is able to preserve endothelial function during gas embolism (*10*). In addition to reducing the contact line tension of an occluding micro-bubble, PF-127 prevents significant protein adsorption, which explains the observed attenuation of the physiological reaction to the bubble interface (*6*, *26*, *48*).

Toward Surface Excess Measurements of Competitive Adsorption

The work of Guggenheim (*49*) demonstrated that the adsorbed surface excess mass can be measured from an arbitrarily large interfacial volume, provided the concentration difference between the interfacial and bulk volumes can be measured. Confocal images of the GL interface show a significant difference in interfacial and bulk fluorescence. Provided that there is a linear relationship between measured fluorescence and protein concentration it is possible to make a ratiometric measurement of protein concentration using

$$P = \frac{I_{\mathrm{int}}}{I_{avgbulk}} = \frac{C_{\mathrm{int}}}{C_{bulk}} = \frac{M_{\mathrm{int}}/V_{voxel}}{M_{bulk}/V_{voxel}} = \frac{M_{\mathrm{int}}}{M_{bulk}} \qquad (22)$$

where P is the partition coefficient, C is the concentration in standard units of both the interface and the bulk, I represents the measured intensity in arbitrary units from both the interface and the bulk, M represents the mass in one voxel at the interface or the bulk, and V represents the volume imaged in a single voxel. The surface excess mass calculation is straightforward.

Using previously reported modeling (*30*), the bulk concentrations required to ‘fill’ the interface are estimated to be 10.5 μM for BSA-TR. The partition coefficient for BSA-TR at or below a concentration of 0.07% was found to be 17.9 ± 7. Using the voxel volume, the partition coefficient estimate, the bulk concentration and the interfacial area the surface excess, Γ in units of mass/area, can be calculated and compared with published NR results. The CLSM surface excess estimate is highly dependent on the bulk concentration value, so the method was benchmarked against NR data for a 5 mg/L BSA solution, a concentration that guarantees incomplete monolayer adsorption. Using the mean calculated partition coefficient of 17.9, a pixel volume of 0.81 μm^3 and an interfacial area of 0.9 μm^2, the estimated surface excess concentration is 0.81 ± 0.32 mg/m^2 with an estimated molecular footprint of 13,612 ± 8663 $Å^2$ These values compare remarkably well with published NR data (*38*) which estimate the surface excess concentration to be 1.0 mg/m^2 with an interfacial area of 11,000 $Å^2$ for the same bulk BSA concentration. Similar benchmarking is not available for HF-OG.

CLSM based surface concentration measurements are predicated on a linear relationship between measured fluorescence intensity and local concentration. In our original manuscript, we showed that the partition coefficient was not dependent on microscope PMT voltage or laser power settings, that there was a linear relationship between concentration and measured intensity in the bulk, and that the labeled proteins exhibited similar surface activity to the unlabeled proteins. There are other ways in which the quantum yield could be different at the interface than in the bulk. We continue to work to improve this method in the hopes that it will allow rigorous surface excess concentration measurements for multi-species adsorption.

Conclusions

We have developed a numerical method to evaluate motion of a finite gas bubble in a blood vessel in the presence of a soluble surfactant in the bulk medium. Our model considers both convective and diffusive transport mechanisms in the bulk and on the interface. The surfactant adsorbs onto and desorbs from the interface as governed by interfacial thermodynamics. The main observations include: (a) the presence of a surfactant dramatically and beneficially alters the shear stress, yielding an important cellular mechanoprotective influence that may have substantial clinical role in the prevention of gas embolism-related tissue injury; (b) the surfactant is shown to adsorb opportunistically onto the gas-liquid interface, which modifies the interfacial tension and results in a change of the bubble shape as well as its residence time adjacent to the cell surface (residence time of the bubble adjacent to an endothelial cell is a critical quantity in gas embolism; experimental studies have shown that this time determines cell response); and (c) the effect of the surfactant is most prominent in the arteriolar vessels, where gas embolism exerts its most significant pathology.

Surface tension measurements have been completed for single and multi-species solutions as a function of surfactant, concentration, and time. CLSM images of fluorescently labeled proteins were acquired to provide direct insight into the nature of the interfacial layers created by BSA-TR and HF-OG. Protein adsorption is still poorly understood. Our main findings are: (a) proper accounting for interfacial volume allows for the prediction of experimentally observed differences in HSA and BSA adsorption; (b) surface tension and surface concentration data indicate that PF-127 at a concentration of 800 nM or higher prevents protein adsorption, suggesting a dosage for pharmacological alteration of the physiological response to gas embolism; (c) protein adsorption can create heterogeneous interfaces, further complicating modeling efforts; (d) surface layers formed by BSA-TR are fundamentally different than surface layers formed by BSA-TR in combination with HF-OG, suggesting that multiple proteins cannot be accurately modeled as linear combinations of single protein solutions.

Acknowledgments

The authors gratefully acknowledge the support of this work through NIH Grants R01 HL67986 (DME) and R01 HL60230 (DME), and ONR Grants N00014-08-1-0436 (DME) and N00014-10-1-0074 (DME).

References

1. Smith, P. L.; Newman, S. P.; Ell, P. J.; Treasure, T.; Joseph, P.; Schneidau, A.; Harrison, M. J. *Lancet* **1986**, *327*, 823–825.
2. Clark, R. E.; Brillman, J.; Davis, D. A.; Lovell, M. R.; Price, T. R. P.; Magovern, G. J. *J. Thorac. Cardiovasc. Surg.* **1995**, *109*, 249–258.
3. Roach, G. W.; Kanchuger, M.; Mangano, C. M.; Newman, M.; Nussmeier, N.; Wolman, R.; Aggarwal, A.; Marschall, K.; Graham, S. H.; Ley, C.; Ozanne, G; Mangano, D. T. *N. Engl. J. Med.* **1996**, *335*, 1857–1864.
4. Herren, J. I.; Kunzelman, K. S.; Vocelka, C.; Cochran, R. P.; Spiess, B. D.; Faraci, F. M. *Stroke* **1998**, *29*, 2396–2403.
5. Padayachee, T. S.; Parsons, S.; Theobold, R.; Linley, J.; Gosling, R. G.; Deverall, P. B. *Ann. Thorac. Surg.* **1987**, *44*, 298–302.
6. Eckmann, D. M.; Armstead, S. C.; Mardini, F. *Anesthesiology* **2005**, *103*, 1204–1210.
7. Eckmann, D. M.; Diamond, S. L. *Anesthesiology* **2004**, *100*, 77–84.
8. Branger, A. B.; Eckmann, D. M. *Anesthesiology* **2002**, *96*, 971–979.
9. Suzuki, A.; Eckmann, D. M. *Anesthesiology* **2003**, *99*, 400–408.
10. Suzuki, A.; Armstead, S. C.; Eckmann, D. M. *Anesthesiology* **2004**, *101*, 97–103.
11. Eckmann, D. M.; Zhang, J.; Lampe, J.; Ayyaswamy, P. S. *Ann. N. Y. Acad. Sci.* **2006**, *1077*, 256–269.
12. Mukundakrishnan, K.; Quan, S.; Eckmann, D. M.; Ayyaswamy, P. S. *Phys. Rev. E* **2007**, *76*, 036308–15.
13. Mukundakrishnan, K.; Ayyaswamy, P. S.; Eckmann, D. M. *Phys. Rev. E* **2008**, *78*, 36303.
14. Mukundakrishnan, K.; Eckmann, D. M.; Ayyaswamy, P. *Ann. N. Y. Acad. Sci.* **2009**, *1161*, 256–267.
15. Mukundakrishnan, K.; Ayyaswamy, P.; Eckmann, D. *J. Biomech. Eng.* **2009**, *131*, 074516.
16. Swaminathan, T.; Ayyaswamy, P.; Eckmann, D. *Ann. Biomed. Eng.* **2010**, *38*, 3649–3663.
17. Swaminathan, T. N.; Mukundakrishnan, K.; Ayyaswamy, P. S.; Eckmann, D. M. *J. Fluid Mech.* **2010**, *642*, 509.
18. Zhang, J.; Eckmann, D. M.; Ayyaswamy, P. S. *J. Comput. Phys.* **2006**, *214*, 366–396.
19. Ayyaswamy, P. S. Introduction to Biofluid Mechanics. In *Fluid Mechanics*; Kundu, P. K., Cohen, I. M., Eds.; Academic Press: MA, 2007.
20. Fung, Y. *Biomechanics: circulation*; Springer Verlag: 1997.
21. Sharan, M.; Popel, A. S. *Biorheology* **2001**, *38*, 415–428.
22. Das, B.; Johnson, P. C.; Popel, A. S. *Biorheology* **2000**, *37*, 239–258.
23. Levich, V. G.; Spalding, D. B. *Physicochemical hydrodynamics*; Prentice-Hall: Englewood Cliffs, NJ, 1962.
24. Stone, H. *Phys. Fluids A* **1990**, *2*, 111–112.
25. Branger, A. B.; Eckmann, D. M. *J. Appl. Physiol.* **1999**, *87*, 1287–1295.
26. Eckmann, D. M.; Lomivorotov, V. N. *J. Appl. Physiol.* **2003**, *94*, 860–868.
27. Eckmann, D. M.; Armstead, S. C. *Anesthesiology* **2006**, *105*, 1220.

28. Menger, F. M.; Shi, L.; Rizvi, S. A. A. *J. Am. Chem. Soc.* **2009**, *131*, 10380–10381.
29. Miller, R.; Fainerman, V. B.; Makievski, A. V.; Kragel, J.; Grigoriev, D. O.; Kazakov, V. N.; Sinyachenko, O. V. *Adv. Colloid Interface Sci.* **2000**, *86*, 39–82.
30. Krishnan, A.; Siedlecki, C. A.; Vogler, E. A. *Langmuir* **2003**, *19*, 10342–10352.
31. Hambardzumyan, A.; Aguie-Beghin, V.; Daoud, M.; Douillard, R. *Langmuir* **2004**, *20*, 756–763.
32. Lu, J. R.; Su, T. J.; Penfold, J. *Langmuir* **1999**, *15*, 6975–6983.
33. Erickson, J. S.; Sundaram, S.; Stebe, K. J. *Langmuir* **2000**, *16*, 5072–5078.
34. Vessely, C. R.; Carpenter, J. F.; Schwartz, D. K. *Biomacromolecules* **2005**, *6*, 3334–3344.
35. Sundaram, S.; Ferri, J. K.; Vollhardt, D.; Stebe, K. J. *Langmuir* **1998**, *14*, 1208–1218.
36. Rao, C. S.; Damodaran, S. *Langmuir* **2000**, *16*, 9468–9477.
37. Fainerman, V. B.; Miller, R. *Langmuir* **1999**, *15*, 1812–1816.
38. Lu, J. R.; Su, T. J.; Thomas, R. K. *J. Colloid Interface Sci.* **1999**, *213*, 426–437.
39. Lu, J. R.; Su, T. J.; Howlin, B. J. *J. Phys. Chem. B* **1999**, *103*, 5903–5909.
40. Wierenga, P. A.; Egmond, M. R.; Voragen, A. G. J.; de Jongh, H. H. *J. Colloid Interface Sci.* **2006**, *299*, 850–857.
41. Feijter, J. A. D.; Benjamins, J.; Veer, F. A. *Biopolymers* **1978**, *17*, 1759–1772.
42. Russev, S. C.; Arguirov, T. V.; Gurkov, T. D. *Colloids Surf., B* **2000**, *19*, 89–100.
43. Grigoriev, D. O.; Fainerman, V. B.; Makievski, A. V.; Krägel, J.; Wüstneck, R.; Miller, R. *J. Colloid Interface Sci.* **2002**, *253*, 257–264.
44. Graham, D. E.; Phillips, M. C. *J. Colloid Interface Sci.* **1979**, *70*, 415–426.
45. Lampe, J. W.; Ayyaswamy, P. S.; Eckmann, D. M. *Int. J. Transp. Phenom.* **2011**, *3−4*, 283–300.
46. Hernandez, E. M.; Franses, E. I. *Colloids Surf., A* **2003**, *214*, 249–262.
47. Lampe, J. W.; Liao, Z.; Dmochowski, I. J.; Ayyaswamy, P. S.; Eckmann, D. M. *Langmuir* **2010**, *26*, 2452–2459.
48. Eisen, L. A.; Narasimhan, M.; Berger, J. S.; Mayo, P. H.; Rosen, M. J.; Schneider, R. F. *J. Intensive Care Med.* **2006**, *21*, 40–46.
49. Aveyard, R. H. *An introduction to the principles of surface chemistry*; Ebsworth, E. A. V., Ed.; Cambridge University Press: 1973.

Chapter 19

Annexin A5 Binding and Rebinding to Mixed Phospholipid Monolayers Studied by SPR and AFM

Xuezhong Du,[1,3] David W. Britt,[2] and Vladimir Hlady[*,1]

**[1]Department of Bioengineering, University of Utah,
Salt Lake City, Utah 84112, U.S.A.
[2]Department of Biological Engineering, Utah State University,
Logan, Utah 84112, U.S.A.
[3]Present address: School of Chemistry and Chemical Engineering,
Nanjing University, Nanjing, P.R. China
[*]E-mail: vladimir.hlady@utah.edu**

Annexin A5 binding to the fluid and immobilized mixed monolayers of dipalmitoylphosphatidylcholine (DPPC) and dipalmitoylphosphatidylserine (DPPS) in the presence of Ca^{2+} ions was investigated using surface plasmon resonance (SPR) spectroscopy and atomic force microscopy (AFM). The amount of adsorbed annexin A5 found on the fluid DPPC-DPPS monolayer was almost twice as high as that found on the immobilized monolayer. The larger amount of protein bound to the fluid monolayer was likely due to the protein induced recruitment of negatively charged lipids and formation of specific binding patterns in the fluid monolayer. Bound annexin A5 could be completely desorbed in the presence of ethylenediaminetetraacetic acid (EDTA) from immobilized monolayer, but only partially removed from the fluid monolayer. AFM imaging suggested that adsorbed annexin A5 was confined to the polar lipid heads – subphase interface in surface patches of protein whose size correlated well with the size of paired annexin A5 trimers.

In Proteins at Interfaces III State of the Art 2012; Horbett, T., et al.;
ACS Symposium Series; American Chemical Society: Washington, DC, 2012.

Introduction

Annexin A5 belongs to a family of structurally homologous proteins that bind to phospholipid membranes in a calcium-dependent manner. Annexins are thought to participate in a variety of membrane-related processes, including exocytosis, endocytosis, vesicle trafficking, ion channel regulation and inflammation (*1*). Although the biochemical properties of annexins have been extensively investigated and their molecular structure in crystalline and membrane-bound forms has been elucidated in detail, their *in vivo* function still remains unclear (*2*). Annexin A5 is one of the most broadly distributed and abundant members of its family and has been implicated in blood coagulation where it competes for blood platelet phosphatidylserine binding sites with prothrombin and also inhibits the activity of phospholipase A1 in vitro (*3*).

The crystal structure of annexin A5 reveals a tetrad of calcium binding site domains each containing a four-helix bundle with a fifth helix capping the binding site (*4*). The protein face which coordinates calcium ions is the feature which binds to phospholipid membranes via calcium bridges (*5*). Distinct binding sites for phospholipid head groups are known, including a novel, double-Ca^{2+} recognition site for phosphoserine that may serve as a phosphatidylserine receptor site *in vivo* (*6*).

The annexin A5 molecular surface exhibits an overall flat topology with one convex and one concave side (Figure 1ab). The convex face of the molecule, opposite to the N terminus, is the area responsible for anchoring to phospholipid membranes. It contains two amino acid side chains (Trp 185 and Ala 101) that are found inserted into the phospholipid bilayer thus facilitating the formation of Ca^{2+}-bridges (*6*). Annexin A5 in solution exists as a monomer, but in the presence of Ca^{2+} it can form trimers and 2-D crystals upon binding to phospholipid assemblies containing negatively charged phospholipids (*7*). A variety of techniques, such as fluorescence spectroscopy (*8*), electron paramagnetic resonance (EPR) (*9*), fourier transform infrared (FTIR) (*10*, *11*), nuclear magnetic resonance (NMR) (*12*), electron microscopy (*13*), ellipsometry (*14*, *15*), and atomic force microscopy (AFM) (*16*, *17*) have been used to study annexin A5 binding to membranes containing negatively charged phospholipids. Adsorption of annexin A5 to phospholipid mono- and bilayers has also been studied using IR reflection adsorption spectroscopy and Brewster angle microscopy (*18*, *19*), and with quartz crystal microbalance (*20*).

Here we compare annexin A5 adsorption to fluid and to immobilized mixed dipalmitoylphosphatidylcholine (DPPC) and dipalmitoylphosphatidylserine (DPPS) monolayers. The objective of the study, illustrated in Figure 1cd, was to find whether the annexin A5 binding to the fluid DPPC-DPPS monolayer at the air/water interface leads to the recruitment of lipid molecules and rearrangement of the monolayer which subsequently improves the affinity for re-binding of the same protein. Binding kinetics of annexin A5 were measured with an *in situ* surface plasmon resonance (SPR) spectroscopy. This SPR technique enables label-less, real-time recording of protein adsorption kinetics to monolayers at the air/water interface (*21*). SPR measures the changes in the refractive index in the interfacial region and with the appropriate model these changes can provide information about the surface concentration of proteins (*22*, *23*). The SPR experiments were complemented with AFM imaging to obtain information about the annexin A5 adsorption-desorption behavior and its spatial distribution at the phospholipid monolayer interface.

Experimental Section

Materials

Dipalmitoylphosphatidylcholine (DPPC) and dipalmitoylphosphatidylserine (DPPS) (both from Avanti Polar Lipids) were prepared as 0.5 mM stock solutions in chloroform (Spectrograde, Merck) and stored at 4°C prior to use. The DPPC−DPPS mixture (DPPC/DPPS molar ratio 4:1) was prepared volumetrically from the stock solutions. Annexin A5 (human, 33 kDa, 2.2 mg/ml, Sigma) was stored at −70 °C prior to use. Double-distilled deionized water (pH 5.5) was used for buffer preparation. *N*-(2-hydroxyethyl)piperazine-*N′*-2-ethanesulfonic acid hemisodium salt (HEPES, >99.5%, Sigma), NaCl (99.5%, Sigma), $CaCl_2 \cdot 2H_2O$ (99%, Sigma), and ethylenediaminetetraacetic acid (EDTA, disodium salt dihydrate, (99%, Sigma) were used to prepare Ca^{2+} and EDTA-containing buffers: Ca^{2+} buffer contained 10 mM HEPES, 150 mM NaCl, 3 mM $CaCl_2$, pH 7.4, and EDTA buffer contained 10 mM HEPES, 150 mM NaCl, 4 mM EDTA, pH 7.4.

Langmuir Trough and Monolayer Preparation

A small KSV−5000 Langmuir trough (36.5 cm × 7.5 cm, KSV Instruments) with symmetric compression barriers was used to construct surface pressure – molecular area ($\pi - A$) isotherms for the mixed lipid monolayers on water, HEPES, and HEPES + Ca^{2+} subphases. The trough was enclosed in a dust free cabinet on an anti-vibration table and maintained at ~20°C. A flame-cleaned Pt Wilhelmy plate, attached to a force transducer, was positioned in the middle of the trough. After aspirating the air/water interface during a blank compression cycle to remove any contaminants the DPPS-DPPC solution was spread dropwise at the air/water or air/buffer interface followed by 15 min for solvent evaporation, then compressed at a rate of 150 mm^2/min until film collapse.

For monolayer transfers compression was stopped at 20 mN/m. After holding the film at 20 mN/m for 1 h it was transferred onto an octadecyltrichlorosilane (OTS)-modified silicon wafer (*24*) by the Langmuir-Schaefer method: the hydrophobically modified Si wafer was horizontally pushed into the subphase through the interface and placed into a small beaker immersed in the subphase. The remaining lipids were aspirated from the interface, and the beaker containing the monolayer coated wafer was removed and maintained hydrated for subsequent AFM imaging.

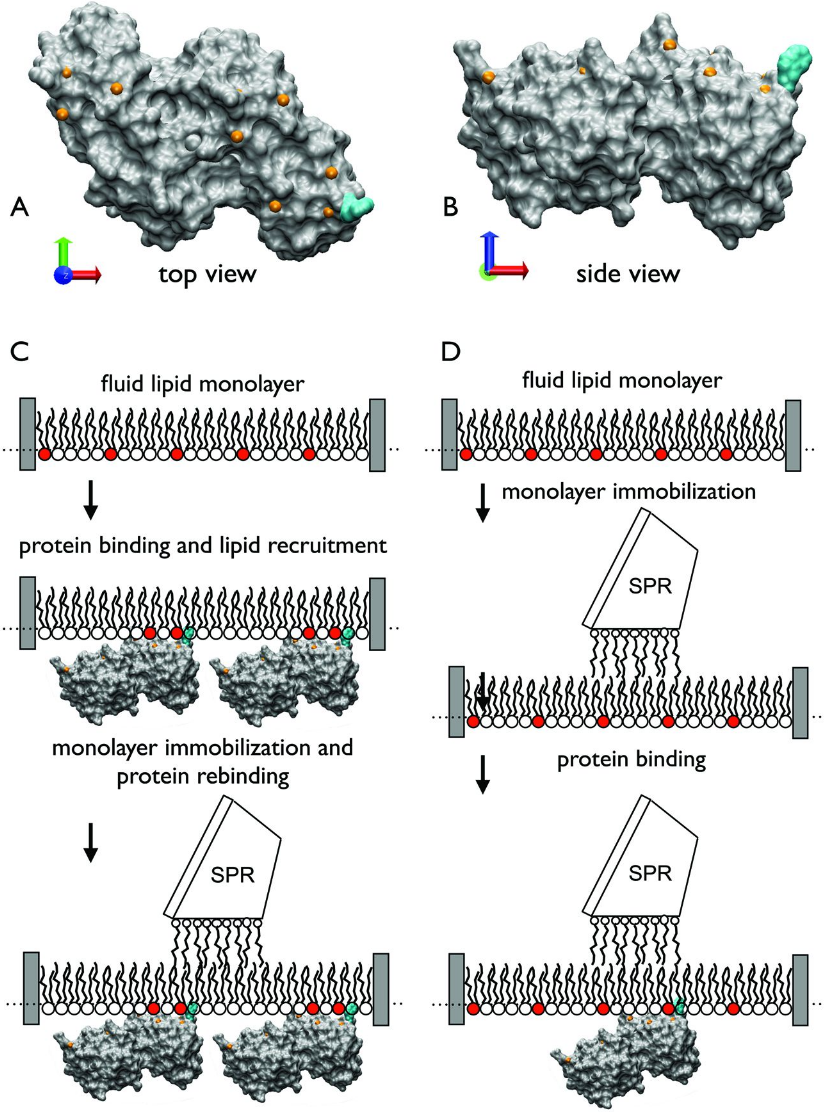
A
top view
B
side view
C
fluid lipid monolayer
protein binding and lipid recruitment
monolayer immobilization and protein rebinding
SPR
D
fluid lipid monolayer
monolayer immobilization
SPR
protein binding
SPR

Figure 1. (A-B) Top and side views of annexin A5. Cation binding sites and Trp 185 are outlined in lighter color. (C-D) Schematic illustration of annexin binding experiments to fluid and immobilized (D) monolayers. (C) The initial adsorption on fluid monolayer is carried out without the presence of SPR sensor. Adsorbed annexin recruits the DPPS (filled circles) into the binding site, thus improving the affinity for re-binding of the same protein. (D) Annexin binding to the monolayer immobilized by the contact with hydrophobically modified SPR sensor prior to the protein adsorption.

SPR Measurement

Compact SPR sensors (Spreeta, Texas Instruments) (*25*) were used for all SPR measurements. These devices combine the sensing Au surface with all the optic and electronic components required for SPR experiments in a compact and lightweight assembly with *p*-polarized near-infrared light (840 nm) as the light source. The Au surfaces of the SPR sensors were first cleaned with O_2 plasma for 1 min (Plasmod, Tegal Corp.), and then rendered hydrophobic with 2 mM octadecanethiol (ODT, >95% GC, Fluka) in absolute ethanol for 10 min followed by rinsing with absolute ethanol and double-distilled water, respectively. A dual microtrough-SPR set-up, schematically shown in Figure 2, was used to measure annexin A5 adsorption/desorption cycles from the mixed lipid monolayers. Each PTFE microtrough had an undercut perimeter in order to eliminate meniscus and obtain a flat air/water interface. One microtrough contained the KSV-surface pressure transducer and was used to measure the volume of DPPC-DPPS chloroform solution required to obtain the surface pressure of ~25 mN/m during film spreading as no compression barriers were used. The same volume of DPPC-DPPS solution was then spread at the interface of the second microtrough for protein adsorption/desorption experiments. A slow dropwise spreading technique with additional time for chloroform evaporation was used to reach the target surface pressure. The annexin A5 solution (5 µL) was injected into the subphase by microsyringe (Hamilton, Gastight 10 µL) to achieve a final concentration of 1 µg/ml; in the desorption cycle protein-free solution was pumped into one end of the microtrough while the equivalent volume was pumped out of the opposite end to exchange the subphase several times (~5) over. The SPR sensor was brought into contact with the DPPC−DPPS monolayer, which immobilized the monolayer onto the ODT-modified surface of the SPR sensor. As depicted in Figure 1, when the hydrophobically modified SPR sensor contacted the mixed lipid monolayer *after* the first cycle of annexin A5 adsorption took place, the experiment is referred to as "binding to fluid monolayer" (i.e., annexin A5 adsorption took place before the SPR sensor immobilized the DPPC-DPPS monolayer). When the SPR sensor contacted the DPPC-DPPS monolayer *before* annexin A5 was injected into subphase to initiate the first adsorption-desorption cycle the experiment is referred to as "binding to an immobilized monolayer" (i.e., the monolayer was immobilized by the ODT-modified surface of the SPR sensor before any protein adsorption took place). In each case after the first adsorption-desorption cycle, a re-binding of annexin A5 was measured using SPR by repeating the adsorption-desoprtion cycle one more time.

AFM Measurement

AFM imaging was performed in a contact mode under buffer solution using a Nanoscope II SPM (Digital Instruments Inc.) equipped with a "D" scanner (10 μm × 10 μm). A low force constant cantilever (0.01 N/m, Park Scientific Instruments) was used to minimize manipulation of the monolayer by the tip. The AFM tip was first cleaned under a high-intensity UV lamp for ~15 min just prior to imaging to remove organic contaminants from the tip surface. An O-ring was used to seal the flow cell of the AFM to keep the sample in buffer solution during the transfer and imaging. After the mixed phospholipid monolayer was imaged under solution, 1 μg/ml annexin A5 solution in the Ca^{2+}-containing buffer was slowly injected into the AFM flow cell. The annexin-bound monolayer was imaged after 30 min incubation.

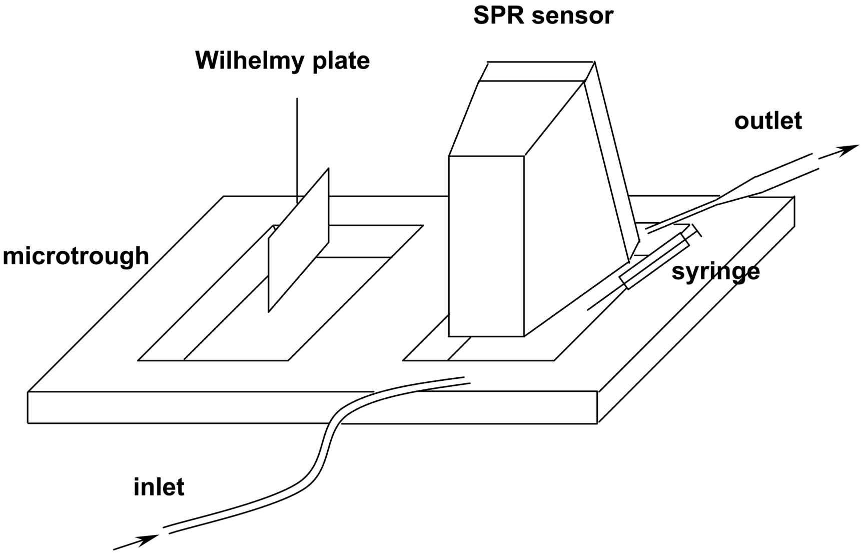

Figure 2. Schematic representation of dual Langmuir microtrough−SPR setup for protein adsorption to and desorption from the lipid monolayer. Left trough was used to find the amount of spread lipids to achieve surface pressure, π = 20 mN/m. Right trough was used for protein binding experiments. Protein was injected into the subphase using microsyringe and adsorption took place from unstirred solution. In the desorption step, aqueous subphase was exchanged several times with protein-free solutions.

Results and Discussion

Figure 3 shows the $\pi - A$ isotherms measured for the 4:1 DPPC-DPPS monolayers on several different subphases. The monolayer on pure water showed a transition from liquid-expanded to liquid-condensed phase without any obvious plateau. In the absence of Ca^{2+} in the buffer, the monolayer displayed an isotherm similar to that on pure water but with increased molecular areas, attributed to the influence of HEPES and NaCl in the buffer subphase. In the presence of Ca^{2+} in the buffer, the monolayer was more expanded at low surface pressures (i.e. larger molecular areas) but was more compact (i.e. smaller molecular areas) at high surface pressures with a cross-over point at ~15 mN/m. It has been shown that Ca^{2+} ions mediate binding of proteins to lipid membranes by direct interaction with the phosphoryl moiety of the phospholipid headgroup (*26*), which gives rise to a change in headgroup orientation at the low and high surface pressures. The effects Ca^{2+} ions exerted on dioleoylphosphatidylserine (DOPS) included the change in the surface area per molecule from 0.675 to 0.625 nm^2 upon Ca^{2+} binding (*27*, *28*), possibly a partial or complete neutralization of negative charges on the phosphatidylserine (PS) headgroups, as well as its dehydration and consequent conformational changes (*29*).

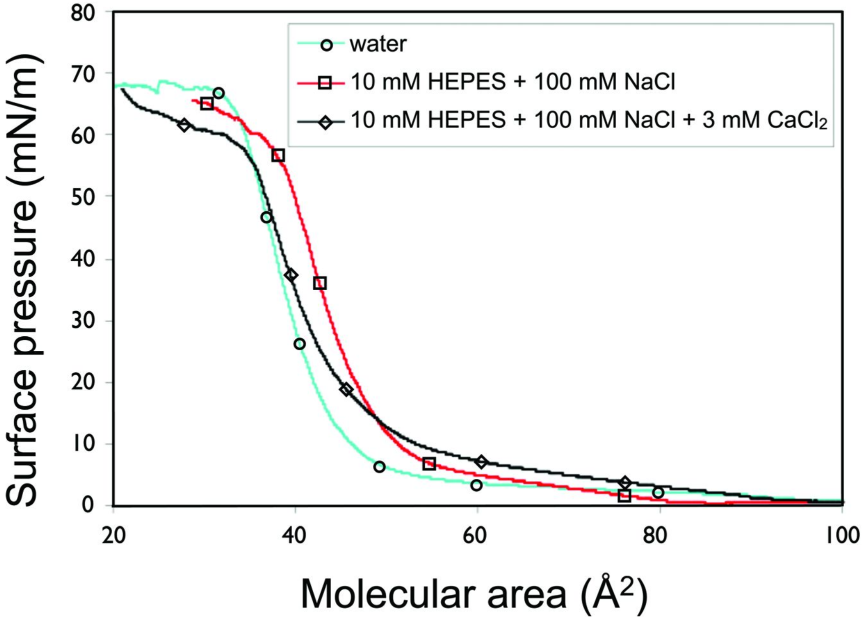

Figure 3. Surface pressure − area isotherms of DPPC−DPPS monolayers (DPPC/DPPS, molar ratio 4:1) on various subphases measured with the compression rate of 150 mm^2/min.

Figure 4a shows the typical SPR sensorgrams of annexin A5 binding to the DPPC−DPPS monolayers on Ca^{2+}-containing buffer subphases. In the case of binding to the fluid monolayer the SPR sensor was brought in contact with the monolayer just prior to the onset of the first desorption cycle with EDTA-containing buffer. After the desorption cycle was over and the Ca^{2+}-containing buffer was restored, the adsorption/desorption cycle was repeated and monitored with SPR. The results showed that the re-binding of annexin A5 to a previously fluid monolayer resulted in almost twice as high adsorbed amount as that found on the immobilized monolayer. Namely, the refractive indices of the two types of DPPC−DPPS monolayers at the initial conditions (i.e. fluid vs. immobilized) and the initial SPR baselines should have been, in principle, identical before first adsorption because the same volumes of mixed lipids solution were spread onto the identical trough areas. Increased annexin A5 adsorption to the *fluid* phospholipid monolayer was likely due to the increased number of interactions between protein and DPPS head groups via Ca^{2+} bridges generated by recruitment and lateral diffusion of DPPS within the fluid monolayer. The recruitment of DPPS into the protein binding site is equivalent to a template-induced affinity increase and explains the higher amount of bound annexin A5. The templating effect was confirmed by measuring annexin A5 re-binding in the second adsorption/desorption cycle which resulted in an even higher adsorbed amount. Such a build-up of annexin A5 was probably the results of more efficient final 2-D packing of the protein molecules at the interface. Upon desorption with the EDTA-containing buffer, followed by Ca^{2+}-containing buffer, the adsorbed annexin A5 was only partially removed from the previously fluid monolayer indicating that a favorable matching of lipids to protein combined with the lateral protein-protein interactions have strengthened the adsorbed layer. The occurrence of EDTA desorption resistant forms of blood platelet membrane bound annexin has been described in the literature (*30*, *31*).

In the case of annexin A5 adsorption to *immobilized* DPPC−DPPS monolayer the amount of the protein adsorbed in the initial adsorption cycle was typically ~ 45% lower than that found for the fluid monolayer: the baseline refractive index (RI) of 1.33745 increased to RI ~ 1.33773 during for adsorption on *immobilized* DPPC−DPPS monolayer vs. the final RI of ~ 1.33807 on the *fluid* monolayer. The lower protein affinity to the *immobilized* monolayer was futher indicated in the desorption step during which bound annexin A5 was completely desorbed from the surface in the presence of EDTA. In the second adsorption/desorption cycle annexin A5 re-binding to *immobilized* monolayer was almost identical to that found in the initial adsorption/desorption cycle. In contrast, EDTA desorbed only ~1/3 of the bound protein from the *fluid* monolayer, and the second adsorption/desorption cycle resulted in another ~30% increase of bound annexin A5 amount above what was found prior to the first desorption step.

Figure 4b shows the change of the refractive index unit (RIU) with time, d(RIU)/dt, (i.e. therefore proportional to the binding rate) as a function of the refractive index. In the second adsorption step, the binding rate was significantly faster in the case of (previously) *fluid* monolayer when compared with those found for immobilized monolayer. From the differences in protein re-binding to *fluid* and *immobilized* monolayers we infer that the effect was due to the protein-induced templating of the DPPC-DPPS monolayer during which DPPS molecules were recruited into spatial patterns that facilitated stronger binding of annexin A5. Similar monolayer templating effects have been already observed in our lab with ferritin (*21*, *32*). It is known that Ca^{2+} concentration during binding determines the manner in which annexin A5 binds to membranes (*2*, *31*). The present study suggests that the fluidity of the lipid layer might have also caused differences between the forms of bound annexin (*31*, *33*, *34*).

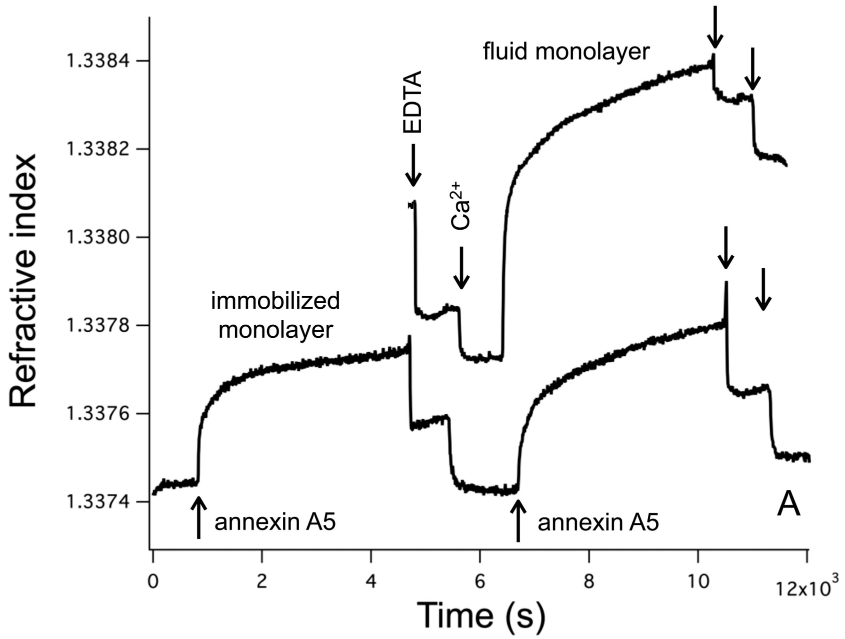

Refractive index
1.3384
1.3382
1.3380
1.3378
1.3376
1.3374
EDTA
Ca2+
fluid monolayer
immobilized monolayer
annexin A5
annexin A5
A
0
2
4
6
8
10
12x10^3
Time (s)

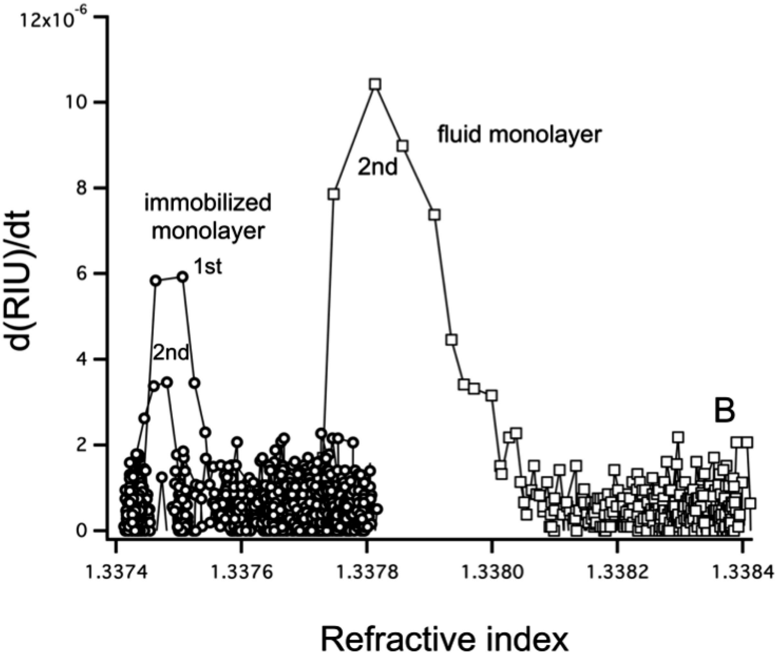

12x10^-6
10
8
6
4
2
0
d(RIU)/dt
fluid monolayer
2nd
immobilized monolayer
1st
2nd
B
1.3374
1.3376
1.3378
1.3380
1.3382
1.3384
Refractive index

Figure 4. (A) SPR sensorgrams of annexin A5 binding to fluid and immobilized DPPC−DPPS monolayers (DPPC/DPPS, molar ratio 4:1) using solution annexin A5 concentration of 1 μg/ml; (B) change of the refractive index unit (RIU) with time (proportional to the protein binding rate) as a function of the refractive index (proportional to the protein adsorbed amount).

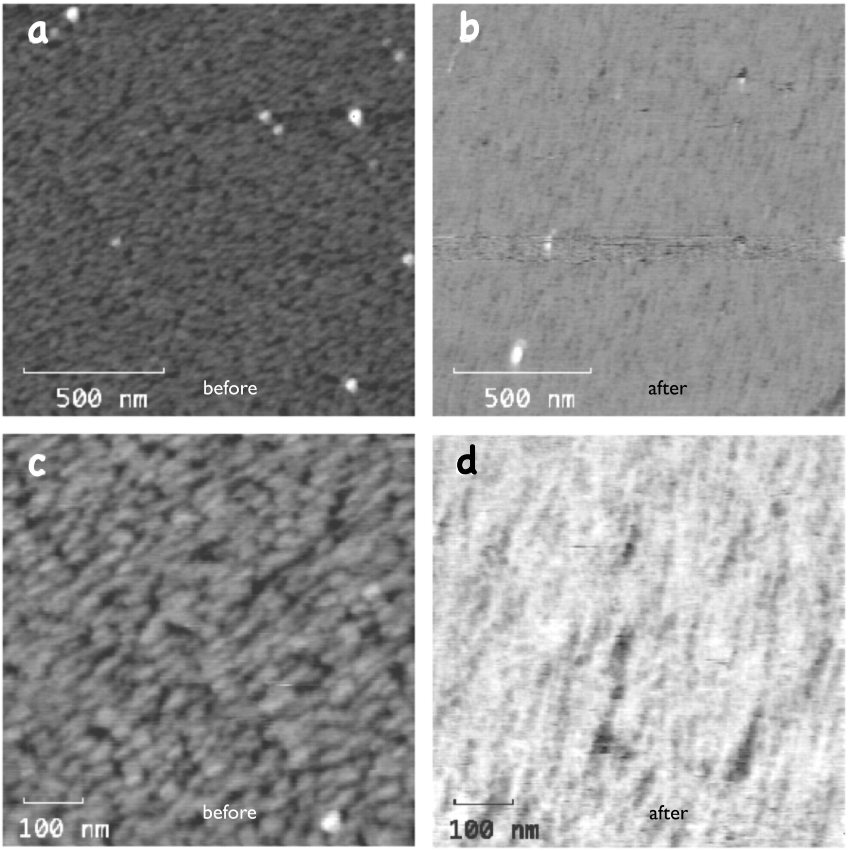

Figure 5. Lower resolution AFM topography of DPPC−DPPS monolayer (DPPC/DPPS, molar ratio 4:1) transferred at the surface pressure 20 mN/m prior to (a, c) and after annexin A5 binding from 1 μg/ml solution (b,d). Scale bars: 500 nm (a,b) and 100 nm (c,d).

Figure 5 shows AFM topographical images of DPPC−DPPS monolayer before (Figure 5a,c) and after (Figure 5b,d) annexin A5 adsorption in the presence of Ca^{2+}-containing buffer solution. The DPPC-DPPS monolayer was transferred at the surface pressure 20 mN/m, and the corresponding AFM images show the transferred monolayer as composed of small and isolated domains with with heights ~ 2.0 nm with respect to the underlying OTS-silicon. The theoretical length of a DPPC molecule was reported to be at about 2.8 nm (*35*). Taking into the account the phase of the monolayer with tilted chains at 20 mN/m, it is reasonable to expect that the transferred phospholipid monolayer to have the roughness near 2.0 nm. This roughness is the result of sub-100 nm sized domains formed through calcium condensed lipid aggregates. Unlike pure DPPC monolayers that exhibit micron-sized domains, none are observed for the mixed DPPC-DPPS system at 20 mN/m on the calcium containing HEPES buffer subphase.

After annexin A5 binding to the monolayer for 30 min, the lower resolution AFM images revealed a surface topography consistent with a nearly uniform, featureless monolayer with only a few defect sites (Figure 5b,d). It has been shown that annexin A5 does not interact or penetrate into the mixed DPPC−DPPS monolayer in the absence of Ca^{2+} even at the low surface pressure of 10 mN/m (*36*). Previous studies by ellipsometry (*14*), low-angle neutron scattering (*37*), and NMR (*38*) also confirmed a peripheral binding of annexin A5 without substantial penetration into the phospholipids monolayers (*39*).

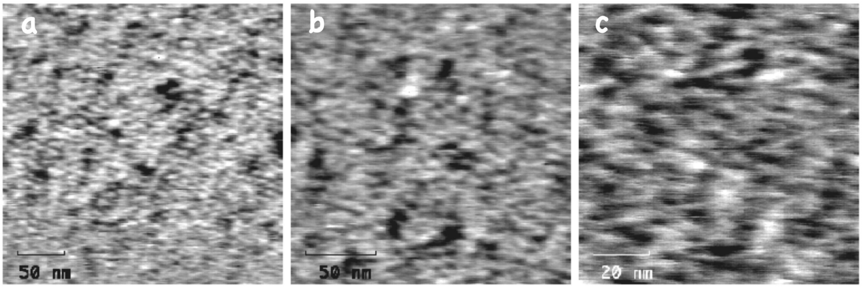

Figure 6. Higher resolution AFM topography of different DPPC−DPPS monolayer areas with adsorbed annexin A5 layer. The DPPC−DPPS monolayer (DPPC/DPPS, molar ratio 4:1) was transferred at the surface pressure 20 mN/m. The adsorption of protein took place from 1 μg/ml annexin A5 solution in the Ca^{2+}-containing buffer for 30 minutes before the AFM imaging. Scale bars: 50 nm (a,b) and 20 nm (c).

Higher resolution AFM images revealed features with lateral dimensions near 10 nm, which might correspond to protein assemblies (Figure 6). The trimers of annexin A5 are the basic building blocks of protein 2-D crystals (*16*, *41*), and are observed to be 10 nm in diameter by electron microscopy (*41*) and 14 nm by AFM (increase due to tip-sample convolution) (*42*). Based on the size, the ellipsoidal-shaped objects in Figure 6 (size ~10 nm, height ~3.0 nm) correlate well with the size and height of paired annexin A5 trimers (*26*). Overall, the AFM images supported the 2-D nucleation model proposed by Brisson et al (*40*). First annexin A5 molecules bind to several DPPS molecules in a Ca^{2+}-dependent manner, then these bound molecules serve as a 2-D nucleus for binding of other

In Proteins at Interfaces III State of the Art 2012; Horbett, T., et al.;
ACS Symposium Series; American Chemical Society: Washington, DC, 2012.

annexins (*38*). The protein−protein interactions then propagate and ultimately result in the formation of 2-D crystals of annexin A5 with the protein−lipid interactions acting as anchoring points of the 2-D arrays with the membrane (*40*). However, Fourier analysis of the present AFM images did not reveal long range order. Given the difference between annexin A5 adsorption on *fluid* vs. *immobilized* lipid monolayers (Figure 4), the absence of the long range order might not be unexpected since AFM was used to image protein adsorbed to the *immobilized* mixed lipids monolayer.

Summary

In this study we investigated the effect of DPPC-DPPS monolayer fluidity on annexin A5 binding and re-binding. The difference between the amount of protein adsorbed to *fluid* vs. *immobilized* monolayers could be explained by protein-induced monolayer templating during which the local recruitment of DPPS molecules improves the protein binding affinity. The increased annexin A5 affinity to previously fluid and templated monolayer was confirmed by improved protein re-binding to the templated film. Bound annexin A5 could be completely desorbed in the presence of ethylenediaminetetraacetic acid (EDTA) from immobilized monolayers, but only partially removed from the monolayer that was fluid during the initial protein adsorption step. AFM imaging revealed features that could be attributed to unordered 2-D protein-patches built up of dimers of the annexin A5 trimers.

Acknowledgments

This study was supported by NIH grant RO1 HL84586.

References

1. Raynal, P.; Pollard, H. B. *Biochim. Biophys. Acta* **1994**, *1197*, 63–93.
2. *Annexins: Molecular Structure to Cellular Function*; Seaton, B. A., Ed.; Chapman and Hall: New York, 1996.
3. Andree, H. A. M.; Stuart, M. C. A.; Hermens, W. T.; Reutelingsperger, C. P. M.; Hemker, H. C.; Frederik, P. M.; Willems, G. M. *J. Biol. Chem.* **1992**, *267*, 17907–17912.
4. Concha, N. O.; Head, J. F.; Kaetzel, M. A.; Dedman, J. R.; Seaton, B. A. *Science* **1993**, *261*, 1321–1324.
5. Brisson, A.; Mosser, G.; Huber, R. *J. Mol. Biol.* **1991**, *220*, 199–203.
6. Swairjo, M. A.; Concha, N. O.; Kaetzel, M. A.; Dedman, J. R.; Seaton, B. A. *Nat. Struct. Biol.* **1995**, *2*, 968–974.
7. Pigault, C.; Follenius-Wund, A.; Schmutz, M.; Freyssinet, J.-M.; Brisson, A. *J. Mol. Biol.* **1994**, *236*, 199–208.
8. Kohler, G.; Hering, U.; Zschornig, O; Arnold, K. *Biochemistry* **1997**, *36*, 8189–8194.

9. Megli, F. M.; Selvaggi, M.; Liemann, S.; Quagliariello, E.; Huber, R. *Biochemistry* **1998**, *37*, 10540–10546.
10. Silvestro, L.; Axelsen, P. H. *Biochemistry* **1999**, *38*, 113–121.
11. Wu, F.; Flach, C. R.; Seaton, B. A.; Mealy, T. R.; Mendelsohn, R. *Biochemistry* **1999**, *38*, 792–799.
12. Saurel, O.; Cezanne, L.; Milon, A.; Tocanne, J.-F.; Demange, P. *Biochemistry* **1998**, *37*, 1403–1410.
13. Brisson, A.; Bergsma-Schutter, W.; Oling, F.; Lambert, O.; Reviakine, I. *J. Cryst. Growth* **1999**, *196*, 456–470.
14. Andree, H. A. M.; Reutelingsperger, C. P. M.; Hauptmann, R.; Hemker, H. C.; Hermens, W. T; Willems, G. M. *J. Biol. Chem.* **1990**, *265*, 4923–4928.
15. Willems, G. M.; Janssen, M. P.; Comfurius, P.; Galli, M.; Zwaal, R. F. A.; Bevers, E. M. *Biochemistry* **2000**, *39*, 1982–1989.
16. Reviakine, I.; Bergsma-Schutter, W.; Brisson, A. *J. Struct. Biol.* **1998**, *121*, 356–362.
17. Reviakine, I.; Bergsma-Schutter, W.; Morozov, A. N.; Brisson, A. *Langmuir* **2001**, *17*, 1680–1686.
18. Wu, F.; Gericke, A.; Flach, C. R.; Mealy, T. R.; Seaton, B. A.; Mendelsohn, R. *Biophys. J.* **1988**, *74*, 3273–3281.
19. Fezoua-Boubegtiten, Z.; Desbat, B.; Brisson, A. R.; Lecomte, S. *Biochim. Biophys. Acta* **2010**, *1798*, 1204–1211.
20. Carton, I.; Brisson, A. R; Richter, R. P. *Anal. Chem.* **2010**, *82*, 9275–9281.
21. Du, X.-Z.; Hlady, V.; Britt, D. W. *Biosens. Bioelectron.* **2005**, *20*, 2053–2060.
22. Stenberg, E.; Persson, B.; Roos, H.; Urbaniczky, C. *J. Colloid Interface Sci.* **1991**, *143*, 513–526.
23. Jung, L. S.; Campbell, C. T.; Chinowsky, T. M.; Mar, M. N.; Yee, S. S. *Langmuir* **1998**, *14*, 5636–5648.
24. Buijs, J.; Britt, D. W.; Hlady, V. *Langmuir* **1998**, *14*, 335–341.
25. Weimar, T. *Angew. Chem., Int. Ed.* **2000**, *39*, 1219–1221.
26. Brisson, A.; Mosser, G.; Huber, R. *J. Mol. Biol.* **1991**, *220*, 199–203.
27. Mattai, J.; Hauser, H.; Demel, R. A.; Shipley, G. C. *Biochemistry* **1989**, *28*, 2322–2330.
28. Demel, R. A.; Paltauf, F.; Hauser, H. *Biochemistry* **1987**, *26*, 8659–8665.
29. Reviakine, I.; Simon, A.; Brisson, A. *Langmuir* **2000**, *16*, 1473–1477.
30. Boustead, C. M.; Brown, R.; Walker, J. H. *Biochem. J.* **1993**, *291*, 601–608.
31. Trotter, P. J.; Orchard, M. A.; Walker, J. H. *Biochem. J.* **1995**, *308*, 591–598.
32. Turner, N. W.; Wright, B. E.; Hlady, V.; Britt, D. W. *J. Colloid Interface Sci.* **2007**, *308*, 71–80.
33. Trotter, P. J.; Orchard, M. A.; Walker, J. H. *Biochim. Biophys. Acta* **1994**, *1222*, 135–140.
34. Liemann, S.; Huber, R. *Cell Mol. Life Sci.* **1997**, *53*, 516–521.
35. Yang, X. M.; Xiao, S. J.; Lu, Z.; Wei, Y. *Surf. Sci.* **1994**, *316*, L1110–L1114.
36. Rosengarth, A.; Wintergalen, A.; Galla, H. J.; Hinz, H. J.; Gerke, V. *FEBS Lett.* **1998**, *438*, 279–284.
37. Swairjo, M. A.; Roberts, M. F.; Campos, M. B.; Dedman, J. R.; Seaton, B. A. *Biochemistry* **1994**, *33*, 10944–10950.

38. Ravanat, C.; Torbet, J.; Freyssinet, J. M. *J. Mol. Biol.* **1992**, *226*, 1271.
39. Hofmann, A.; Benz, J.; Liemann, S.; Huber, R. *Biochim. Biophys. Acta* **1997**, *1330*, 254–256.
40. Pigault, C.; Follenius-Wund, A.; Schmutz, M.; Freyssinet, J.-M.; Brisson, A. *J. Mol. Biol.* **1994**, *236*, 199–208.
41. Oling, F.; Bergsma-Schutter, W.; Brisson, A. *J. Struct. Biol.* **2001**, *133*, 55–63.
42. Richter, R. P.; Brisson, A. *Langmuir* **2003**, *19*, 1632–1640.

Chapter 20

Soil Binds Prions and Influences Their Biologic Properties

S. L. Bartelt-Hunt,*,[1] S. E. Saunders,[2] and J. C. Bartz[3]

[1]Department of Civil Engineering, University of Nebraska-Lincoln,
203B Peter Kiewit Institute, Omaha, Nebraska 68182-0178
[2]Stanford University Law School, 559 Nathan Abbott Way,
Stanford, California 94305-8610
[3]Department of Medical Microbiology and Immunology,
Creighton University, 2500 California Plaza, Omaha, Nebraska 68178
***E-mail: sbartelt2@unl.edu**

The prion protein is believed to be the causative agent of a host of fatal neurodegenerative diseases, including chronic wasting disease and scrapie. The prion protein is shed into the environment and is strongly bound to soil. Evidence suggests that binding to soil can influence the biologic properties of the prion protein, including prion replication and infectivity. The physicochemical properties of soil influence this behavior, and some evidence suggests that local soil type may play a role in prion disease transmission in the environment.

The Prion Protein

Prion Diseases

Prion diseases, also called transmissible spongiform encephalopathies (TSEs), are a group of inevitably fatal neurodegenerative diseases that impact a number of mammalian species and include bovine spongiform encephalopathy (‘mad cow’ disease), scrapie, chronic wasting disease, transmissible mink encephalopathy, and Creutzfeldt-Jakob disease (*1*). Clinical symptoms of prion diseases include dementia, impaired motor control, and irregular behavior (*2*, *3*). Prion diseases are distinguished pathologically by spongiform degeneration of the brain and accumulation of the abnormal prion protein in the central nervous system (*1*).

In Proteins at Interfaces III State of the Art 2012; Horbett, T., et al.;
ACS Symposium Series; American Chemical Society: Washington, DC, 2012.

Strong evidence indicates that the infectious agent of TSEs (i.e. the prion, PrP^{Sc}) is an abnormally-folded conformer of a normal cellular protein, PrP^{c} (*4–6*). The folded conformation of PrP^{Sc} conveys distinct biological and physicochemical properties to PrP^{Sc}, including resistance to proteolysis, increased hydrophobicity (and thus, decreased solubility in aqueous solvents), and a propensity for aggregation (*1*). The normal prion protein is a cell surface glycoprotein that has been identified in numerous mammalian species and is expressed most abundantly in the central nervous system but also in lymphoid cells, lung, heart, gastrointestinal tract, muscle, and other locations throughout the body (*7*). The function of the normal form of the prion protein has not been determined, but experiments suggest that it is involved in protection of the cell from oxidative damage (*8*). It is known that PrP^{c} binds strongly with copper and other trace metals, and its function may therefore involve interactions with these metals in vivo (*9*). The conversion of PrP^{c} to the PrP^{Sc} conformation is the central event in prion agent replication. The amino acid sequence of PrP^{c} and PrP^{Sc} is the same, and thus the only identified difference is protein conformation (*10*). PrP^{Sc} has a higher β-sheet content and a decreased α-helix content compared to PrP^{c} (*11*).

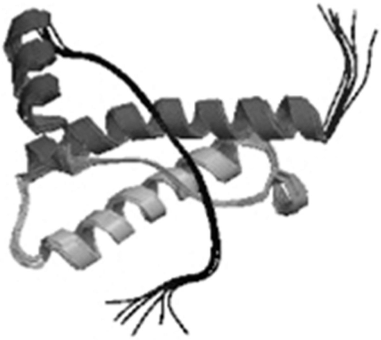

Figure 1. Elk PrPc nuclear magnetic resonance-derived structure. Image from The Worldwide Protein Bank (www.wwpdb.org). Adapted from ref. (12).

The tertiary structure of PrP^{c} has been determined by nuclear magnetic resonance (NMR) and other methods (*12*), but that of PrP^{Sc} is still unknown due to the insolubility of its aggregates. Figure 1 shows an NMR-derived image of the structure of elk PrP^{c}. PrP^{c} consists of a flexibly disordered N-terminal tail, a well structured globular domain, and a flexibly disordered C-terminal (*12*). A disulfide bond joins two cysteines in the C-terminal region (*9*). PrP^{c} is thought to exist mostly as a soluble monomer. A trimeric model has been proposed for PrP^{Sc}, where trimers of PrP^{Sc} combine to form the characteristic fibrils that accumulate in the central nervous system of diseased animals (*9*). PrP^{Sc} is very resistant to protease degradation; however, the N-terminal domain of PrP^{Sc} is vulnerable to degradation possibly because it is on the exterior of the structure. PrP^{Sc} resistance to proteases is often used to distinguish PrP^{Sc} from PrP^{c}. For example, proteinase K (PK) completely degrades PrP^{c} with incubation at 37°C for short periods (<1 hr), but only cleaves the N-terminal of PrP^{Sc}, leaving the infectious C-terminal core intact (*13*).

Environmental Transmission of Prion Diseases

Scrapie and chronic wasting disease (CWD) are two prion diseases of particular environmental concern as they are horizontally transmissible and remain infectious after years in the environment (*14–18*). In one study, the scrapie agent remained infectious after burial in garden soil for 3 years (*19*). In another report, a previously scrapie-infected sheephouse and pasture were 'decontaminated' and left uninhabited; sheep introduced 16 years later subsequently contracted scrapie suggesting that scrapie remained infectious after 16 years (*20*). A controlled study indicated that the CWD agent remained infectious for at least 2 years in a pasture (*17*). Epidemiological modeling suggests that indirect, environmental routes of transmission were responsible for two CWD outbreaks in captive mule deer (*21*).

Prions can enter the environment through shedding from infected animals and also after decomposition of infected carcasses. Prions are shed from diseased host animals in a diverse set of biologic matrices, including feces, urine, saliva, blood, skin, milk, placenta, antler velvet, and nasal mucus and a comprehensive review of prion shedding was recently performed by Gough and Maddison (*22*). Prion shedding can occur many months prior to clinical manifestation of the disease (*22*, *23*). Prions also enter the environment after decomposition of diseased animal carcasses (*17*), as prions are present near-ubiquitously throughout a diseased host. Uptake of prions to naïve hosts can occur via ingestion or inhalation of contaminated material (*24–27*), although the significant routes of natural exposure remain uncertain.

Recent experimental and epidemiological work suggests that soil may play a role in natural prion transmission. Indirect, environmental transmission has been implicated in multiple CWD and scrapie outbreaks (*20*, *21*). Prions are known to sorb (i.e. bind) to a wide range of soils and soil minerals and remain infectious (*28–30*). The potential for CWD or scrapie transmission by exposure to contaminated soil exists since cervids and other ruminants are known to ingest and inhale soil (*31*, *32*). For instance, mule deer in north central Colorado ingested between 8-30 g of soil per day in one study, depending on the season (*32*). Thus, soil and soil minerals may act as significant environmental reservoirs and vectors of prion diseases.

Prion Interactions with Soil

Kinetics of Prion Sorption to Soil

Prion adsorption to soil could play an important role in prion mobility, proteolysis, and infectivity. Prion adsorption has generally been observed to be strong and fast for a wide range of surfaces, and it has been demonstrated that PrP^{Sc} has a higher affinity for clays and clay soils compared with sand and sandy soils (*33–37*). Prion sorption appears to be strongly irreversible and resistant to desorption by detergent and chaotropic treatments (*27*, *38*). Previous studies of prion sorption to soil using recombinant PrP (recPrP) and purified PrP^{Sc} have observed maximal adsorption in less than 2 hours (*34*, *38*, *39*). However, these studies do not take into account the competitive matrix (animal tissue, blood, saliva, or excreta) in which prions will enter the environment. In a previous study, we evaluated the kinetics of PrP adsorption using a complex and relevant prion model, infected HY TME (hyper strain of transmissible mink encephalopathy) brain homogenate, and compared these data to previous studies using recPrP or purified PrP^{Sc}.

Table 1. Properties of Soil Used in Sorption Experiments. Reproduced with permission from reference (*40*). Copyright 2009 American Chemical Society

Soil/ Mineral	*Sand*	*Silt*	*Clay*	*Specific Surface Area*	*Organic Carbon Content*	*Soil pH*	*Cation Exchange Capacity*
	% of Total			*m^2/g*	*%*		*meq/100g*
Rinda Silty Clay Loam	5.1	60.4	34.5	23.0	1.2	5.5	36.2
Dickinson Sandy Loam	76.9	12.9	10.3	1.7	1.1	7.5	13.8
Fine Quartz Sand	≈100	0	0	0.16	≈0.0		1.4
Bentonite	0	0	≈100	15.5	≈0.0		85.2

Sorption assays were conducted using fine white sand (particle size <0.25mm), sodium bentonite, and two whole soils, a sandy loam and a silty clay loam. Properties of the soils and minerals used are presented in Table 1. Soils (10 mg fine sand, 3 mg sandy loam, 1 mg silty clay loam or 0.5 mg bentonite) were combined with brain homogenate for a total volume of 200 µl of DPBS in 0.2 ml PCR tubes at pH 7. Both non-sterile and gamma-irradiated soils were evaluated. Soil-homogenate mixes were rotated at 24 rpm at 22°C. Samples were removed at specified time points and allowed to settle or centrifuged at 100 g for 5 sec. The supernatant was removed and the pellets were washed 2-3 times with DPBS. Supernatants and washes were stored at -80°C until analysis.

In these experiments, the amount of adsorbed PrP was monitored for up to 63 d using two initial brain homogenate doses, 0.5% and 2.5% (Figure 2). Total PrP in the aqueous fraction was also monitored over time for all experiments (Figure 3). PrP in aqueous controls and samples was evaluated using a 96-well immunoblot assay (*41*). Soil pellets were evaluated using the same 96-well assay method with some modifications. First, pellets were saturated with 5% bovine serum albumin in DPBS for 30 min at 22°C. followed by 10 min of incubation with 3M guanidinium thiocyanate and were washed 2 times with DPBS. Soil pellets were then incubated for 30 min at 37°C with blotto and primary antibody. Samples were immunoblotted with anti-PrP mAb 3F4 (1:10,000 dilution). Pellets were washed 2 times with DPBS, incubated with secondary antibody (horseradish-preoxidase conjugated anti-mouse IgG, 1:2000), and washed 2 times with DPBS. Pellets were loaded into the 96 well-plate and developed with the aqueous controls and samples. Aqueous samples and pellets were not treated with proteinase K prior to quantification.

As seen in Figure 2, we observed that PrP adsorption to sand, bentonite and soil reached a maximal solid phase concentration (C_S) at times ranging from 24 hr (silty clay loam soil) to 30 days (sand). Previous studies conducted using recombinant PrP or purified PrP^{Sc} have observed maximum prion sorption to soils or minerals in less than 2 hours (*34*, *38*, *39*). Kinetics of prion sorption from brain homogenate was also investigated by Maddison et al. (*42*), which found that PrP^{Sc} from brain homogenate sorbed within 24 hours to sily clay loam soils.

The influence of brain homogenate (BH) dose (0.5% vs. 2.5%) was investigated. For sand, PrP sorption behavior was similar, with the 2.5% having a 30% higher $C_{s,max}$. Similarly, the brain homogenate dose did not strongly affect the sorption behavior of PrP to bentonite. For the sandy loam soil, sorption behavior was similar between the BH doses, but increases in C_s were observed after 22 d for both doses and represent a 40- and 520-fold increase, respectively, over the initial $C_{s,max}$. A similar increase was observed at the 2.5% dose only for the silty clay loam soil where C_s increased 3-fold after 22 d to 8000 μg BE/mg. At the time points when these increases in C_s were observed, there was a consistently low aqueous PrP concentration (Figure 3) and therefore, these observed increases cannot be due to additional binding of PrP. This observed results may be due to changes in PrP or other bound constituents increasing antibody affinity. As the 0.5% dose did not exhibit such large increases in C_s at longer time points, it is possible at that this lower dose, the majority of PrP was more strongly adsorbed and was resistant to conformational changes or changes in protein aggregation.

The influence of soil microbial populations on prion adsorption and degradation was investigated by evaluating PrP sorption to both non-sterilzed and gamma-irradiated soils. Observed PrP sorption (Figure 2) and aqueous PrP concentration (Figure 3) were similar over the experiment, indicating that PrP was not affected by soil bacteria. Degradation of recPrP by soluble soil enzymes has been demonstrated (*43*), and thus, it is possible that some of the observed PrP degradation could be due to native soil proteases. Since PrP degradation was observed for sand samples, which has negligible soil organic matter, it is more likely that PrP degradation is attributable to proteases present in the brain homogenate.

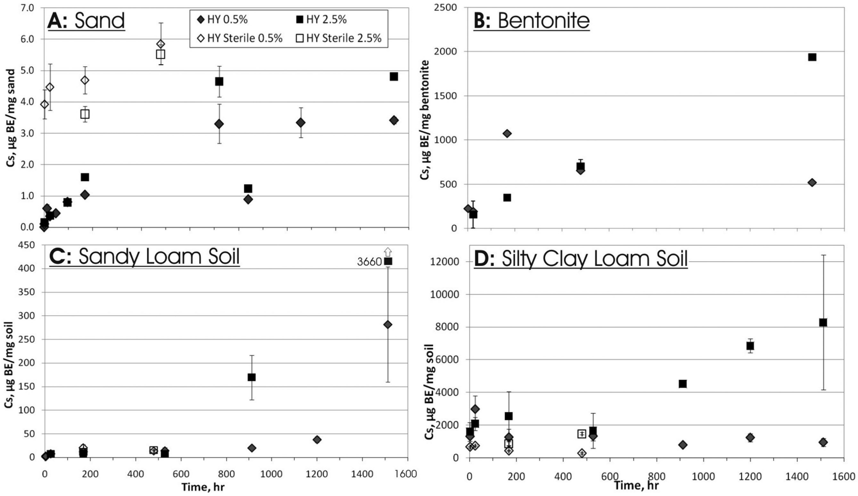

Figure 2. PrP adsorbed to soils over time. ***A:*** *Fine quartz sand* ***B:*** *Bentonite* ***C:*** *Sandy loam soil. Note the 1512 hr 2.5% data point is 3660 µg BE/mg soil (±155 µg BE SE).* ***D:*** *Silty clay loam soil. Error bars show ± the standard error. Reproduced with permission from reference (40). Copyright 2009 American Chemical Society.*

As seen in Figure 3, we observed decreases of PrP in the aqueous fraction over time, which could be due to PrP degradation by active proteases in brain homogenate, sorption to soil, sorption to the tube, or inactivation of the 3F4 epitope. Inactivation of the antibody epitope would imply a conformational change in PrP, which is unlikely considering the conformational stability of PrP^{Sc}. Adsorption of PrP to the polypropylene PCR tube is possible; however, in a previous experiment utilizing polypropylene tubes and CWD-infected brain homogenate, no decrease in PrP signal was observed through 30 d (*44*), suggesting that the effect of this is minimal. PrP adsorption to sand was inconsequential compared to the remaining aqueous fraction (a 1:200 ratio). Thus, the decreases in aqueous PrP indicates degradation of PrP. We demonstrated previously that HY TME (hyper strain of transmissible mink encephalopathy) can be degraded by active proteases in brain homogenate at 22°C and pH 7. The relatively constant PrP in the aqueous fraction between 30 and 60 d could be due to near-complete adsorption of the proteases responsible for PrP degradation. Constant aqueous and solid phase PrP from 30 d to 60 d suggests the system reached equilibrium after 30 d.

PrP Sorption to Soil

Prion sorption (physical or chemical binding) to soil could play an important role in prion transport or immobilization, provide protection from or enhance *in situ* proteolysis, and induce conformational changes that enhance or decrease infectivity, all of which could affect the transmissibility of CWD, scrapie, and BSE in the environment. Various studies, summarized in Table 2, have quantified prion binding to various soils and soil components.

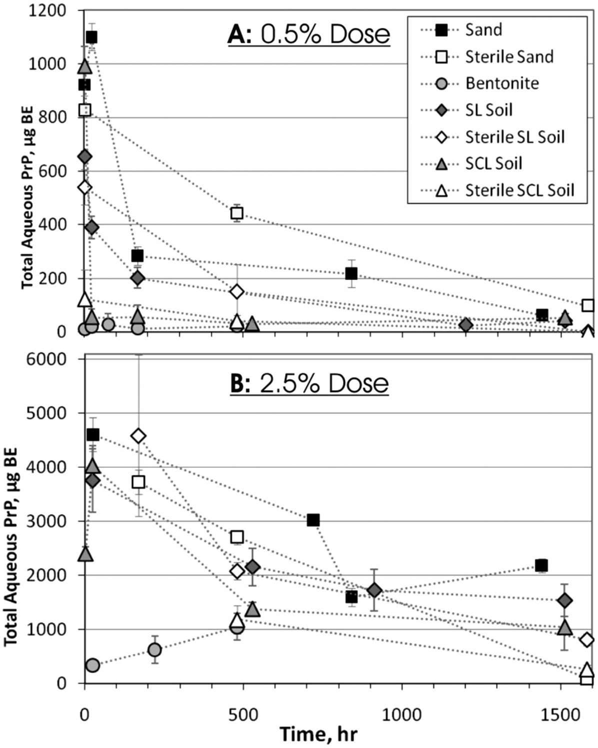

Figure 3. Total aqueous PrP quantified over time. ***A:*** *Initial BH dose of 0.5% (an initial aqueous fraction of 1000 µg BE).* ***B:*** *Initial 2.5% BH dose (an initial aqueous fraction of 5000 µg BE). Data points are connected by straight lines for clarity. Error bars show ± the standard error. Reproduced with permission from reference (40). Copyright 2009 American Chemical Society.*

As with other proteins, prion sorption is most likely a function of electrostatic attractions and repulsions and hydrophobic interactions. RecPrP studies have identified electrostatic attraction between positively-charged peptides and negatively-charged mineral surfaces as the most significant adsorption mechanism (286, 359). However, since the three-dimensional structure of PrP^{Sc} remains unknown, it is a challenge to model the specific mechanisms that are significant in PrP^{Sc} adsorption. It is known that PrP^{Sc} is highly insoluble and aggregated, and hydrophobic interactions could therefore play a larger role in PrP^{Sc} sorption to amorphous clay minerals. PrP^{Sc} adsorption to quartz sand was shown to be maximal around the isoelectric point (IEP, at pH ≈ 4 for prions), corresponding to maximal PrP^{Sc} aggregation (*34*). Maximum adsorption near the IEP has been shown for many other proteins and surfaces (*45*).

Because the N-terminal domain is known to be flexibly-disordered and contains a high number of positively-charged amino acids, it may play a significant role in electrostatic attraction to negatively-charged mineral surfaces (*46*). The N-terminal domain is lost upon desorption of PrP^{Sc} from clay (*33*, *42*), and PK-digestion is required to desorb PrP^{Sc} from clay and sandy soils (*33*). More full-length recPrP adsorbs to montmorillonite than N-terminal truncated recPrP (*37*). However, the N-domain is not needed for prion adsorption (*33*, *34*, *47*).

Prions enter the environment concurrently with organic matter from the host. In addition, the soil environment contains native organic matter. Thus, it is important to consider the role organic matter plays in prion sorption. RecPrP has been shown to have a high affinity for organic matter, equal to or greater than that calculated for mineral surfaces (*36*, *39*, *47*). In addition, humic acid was found to increase the recPrP sorption capacity of kaolinite about 10-fold (*36*). It is also important to note that solution ionic strength and the homoionic salt species (e.g. Na^+, Ca^{2+}) can significantly affect the measured sorption capacities for organic matter and clay minerals, including PrP capacity (*35*, *36*). While other proteins have been shown to enter the interlayer areas of expandable clays (e.g. smectites) (*48*), potentially decreasing their bioavailability, Johnson et al. (*34*) found that purified PrP^{Sc} did not enter the interlayer area of Na^+-montmorillonite. However, choice of homoionic species can affect the height of the interlayer area.

Conformational changes in protein structure upon interaction with soil minerals have been well documented and can range from slight unfolding to significant changes in secondary structure and can also include aggregation or disaggregation. Proteins can also reorient over time between side-on and end-on orientations. PrP^{Sc} is aggregated, and changes in aggregation could occur, potentially affecting infectivity (*49*). One study did find that recPrP does not form β-sheets or self-aggregate, as seen *in vitro*, when adsorbed to clay (*46*). More must be done to determine what conformational changes (if any) occur to PrP^{Sc} when it binds to minerals and how these changes affect agent survival and infectivity.

Experimental methods for prion sorption have initially focused on using detergents and boiling to desorb prions into solution where they are detected by immunoblotting techniques. Bound PrP is usually first separated from unsorbed prions by low-speed centrifugation (in some cases by using a sucrose cushion) (*27*, *34*, *41*). Unsorbed PrP can be detected by normal immunoblotting, but bound PrP must be desorbed before detection. Unfortunately, detergent and boiling extraction methods typically have very low PrP recoveries, presumably due to the strong and near-irreversible binding of PrP to soil particles. Recoveries reported are 61-67% (wastewater sludge) (*50*) and 5-40% for sandy and clay soils (*33*, *51*). An electroelution method developed by Rigou et al. reported similar recoveries (5-40%) (*37*). It is likely that desorption selects for a certain PrP population, such as loosely-bound aggregates.

Table 2. Review of prion sorption literature

Soil/Mineral	***Sorption Capacity (μgPrP/mg)***	***Equilibration Time***	***Prion Material Used***	***Refer-ence***
Whole soils	ND	24 h, 7 d, 21 d	ME7 (mouse) BH	(*33*)
		2 h – 90 d	ovine recPrP	(*33*)
		1–60 d	ovine recPrP	(*37*)
		1 h	263K (hamster) BH	(*28*)
		2 h	purified HY (hamster) PrP^{Sc}	(*34*)
		1, 3, & 6 months	ovine recPrP	(*51*)
		1 h	RML (mouse) BH	(*41*)
		1–26 months	263K (hamster) BH	(*18*)
Sandy Loam (1% OM)	0.07	1 h – 60 days	HY (hamster) BH	(*39*)
Silty Clay Loam (1% OM)	0.2	1h – 60 days	HY (hamster) BH	(*40*)
Loamy soil (w/ high OM)	30.5	24 h (max at ~1 h)	ovine recPrP	(*39*)
Sandy soil (w/ high OM)	15.5	24 h (max at ~1 h)	ovine recPrP	(*39*)
Organic matter	333 or 1000	24 h (max at ~1 h)	ovine recPrP	(*39*)
Catechol (synthetic OM)	ND	1 h-72 h	ovine recPrP, C-term recPrP	(*47*)
Fine quartz sand	>110 pH 4, >50 pH 7	4 h	purified HY (hamster) PrP^{Sc}	(*35*)
Fine quartz sand	0.0001	1h-60 days	HY (hamster) BH	(*40*)
Quartz microparticles	13.6-27.1	2 h	purified HY (hamster) PrP^{Sc}	(*34*)
Mica	ND	1 h	ovine recPrP	(*38*)
Kaolinite	1.7-2.6	2 h	purified HY (hamster) PrP^{Sc}	(*34*)
	≈50	10 min	murine recPrP	(*36*)

Continued on next page.

Table 2. (Continued). Review of prion sorption literature

Soil/Mineral	*Sorption Capacity (µgPrP/mg)*	*Equilibration Time*	*Prion Material Used*	*Reference*
Montmorillonite- Na^+	ND	10 h	ovine recPrP	(*46*)
	87-174	2 h	purified HY (hamster) PrP^{Sc}	(*34*)
	1000	2 h	ovine recPrP, C-term recPrP	(*34*)
	>1200	10 min	murine recPrP	(*36*)
Montmorillonite- Ca^{2+}	>400	10 min	murine recPrP	(*36*)
Bentonite- Na^+	0.04	1h-20 d	HY (hamster) BH	(*40*)

Abbreviations - ND: not determined, OM: organic matter, BH: brain homogenate.

Influence of Prion Strain, Species, and N-terminal Truncation on Prion Adsorption to Soil

The environmental fate of PrP^{Sc} may vary with strain and species. Prion strains are operationally defined by distinct neuropathological characteristics (*52*). The amino acid sequence of PrP is species specific, and PrP^{Sc} conformation is strain dependent (*53–57*). A quantitative comparison of prion adsorption to soil as a function of prion strain and species was conducted by Saunders et al. (*58*). It was determined that the competitive matrix in which prions enter the environment can significantly affect prion interactions with soil, and that these interactions will vary with prion strain and species.

In these experiments, brain tissue from hamsters infected with the HY TME and DY TME (drowsy strain of TME) agents at terminal disease as well as brain tissue from uninfected hamsters and an elk infected with CWD were used. Sorbents investigated included fine sand, sandy loam soil, and silty clay loam soil (Table 1).

For batch isotherm studies, brain homogenate was combined with each sorbent for a total volume of 200 µl in DPBS in 0.2ml PCR tubes at pH 7. Mass ratios of total brain equivalents (BE) to soil ranged from 1:0.05 to 1:20. The soil-brain homogenate mixtures were incubated at 22°C and rotated at 24 rpm. Samples were removed at specified time points and allowed to settle or centrifuged at 100 g for 5 sec. For isotherm experiments, samples were equilibrated for 1 week (168 hr) unless otherwise noted. The supernatant was removed and the pellets were washed 2 times with DPBS. The original supernatant, first wash, and final pellet were collected and stored at -80°C. PrP in aqueous controls and samples was evaluated using a 96-well immunoblot assay (*41*) as described above in the section on prion kinetics. Prior to analysis, some samples were treated with proteinase K (PK) to quantify PrP^{Sc} sorption to soils.

Maximum adsorption of HY TME PrP occurred at an intermediate aqueous concentration for sand and both whole soils (Figure 4A, C, and D). DY TME PrP adsorption was consistently lower than HY PrP for all sorbents, with similar isotherm shapes for DY and HY PrP. DY PrP adsorption was on average 60%, 65%, and 90% lower than HY for sand, sandy loam, and silty clay loam soils, respectively. In contrast to HY and DY PrP, CWD-elk PrP adsorption was maximal at the lowest concentration tested and decreased gradually as the aqueous concentration (C_W) increased (Figure 4B). Since the conformational differences between HY and DY PrP^{Sc} are not fully defined, it is difficult to explain the stronger adsorption affinity of HY PrP. Differences in PrP^{Sc} aggregation may be responsible. DY PrP^{Sc} is known to be more soluble than HY PrP^{Sc} in the presence of detergents (*53*), which may indicate it is less hydrophobic. Fundamental information on PrP^{Sc} structure and strain variance is needed before differences in adsorption can be explained.

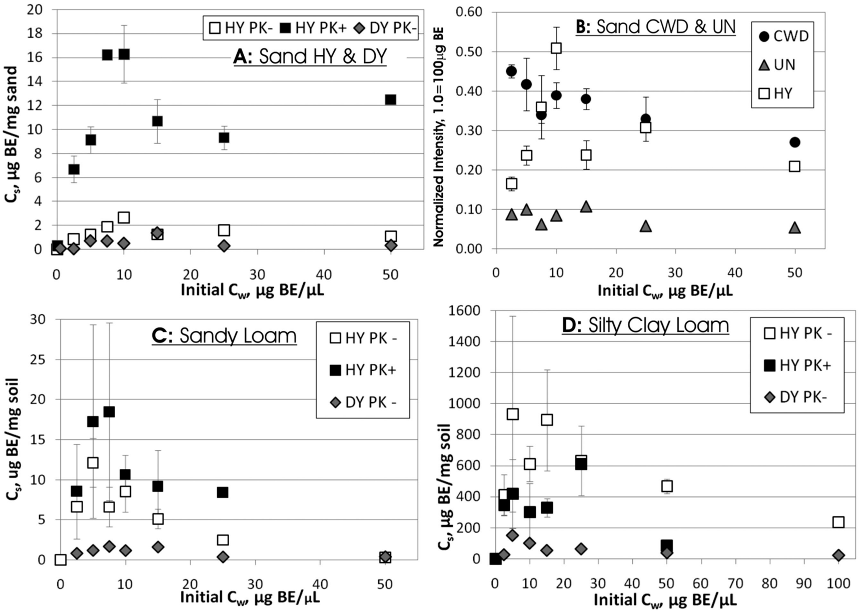

Figure 4. Quantified isothermal studies of PrP adsorption. Panel A: HY TME PK-digested (HY PK+) or undigested (HY PK-), and DY TME undigested (DY PK-) PrP adsorption to fine quartz sand. Panel B: CWD-elk and uninfected (hamster) PrP adsorption to sand reported as normalized intensities. HY results are from Panel A. Panel C: Adsorption of HY PK+, HY PK-, and DY PK- PrP to sandy loam soil. Panel D: Adsorption of HY PK+, HY PK-, and DY PK- PrP to silty clay loam. Error bars show ± the standard error. N ≥ 3 for all points except 50 µg BE/µL points in A, B, & C and 100 µg BE/µL in D, where n = 1. Reproduced with permission from reference (58). Copyright 2009 American Chemical Society.

Additional isotherms were generated using PK-digested HY TME brain homogenate. The N-domain of PrP^{Sc} is removed by proteinase K digestion, which also completely degrades PrP^{c} (*44*). Isotherm shapes for PK-digested samples were similar to that observed for undigested samples (Figure 4). We have demonstrated previously that a large population of PrP will enter and exist in the environment without the N-terminal domain (*44*). Because the N-terminal domain is known to be flexibly-disordered and contains a high number of positively-charged amino acids, it may play a significant role in electrostatic attraction to negatively-charged mineral surfaces (*46*). Evidence suggests the N-domain might play a role in sorption to clays (*29*). However, the present results confirm previous reports that the N-domain is not needed for prion adsorption (*29*, *34*). PK-digested PrP^{Sc} adsorption to sand and sandy loam soil was on average 8-fold and 2-fold greater, respectively, than PrP in undigested homogenate (Figure 4A and 4C). In contrast, PrP^{Sc} adsorption (PK+) to silty clay loam soil was on average 50% less than undigested PrP (Figure 4D). This result is in agreement with a previous observation that more full-length recPrP adsorbs to montmorillonite clay than N-terminally truncated recPrP (*27*).

The underlying reasons for the increased adsorption of PK-treated PrP^{Sc} to sand and sandy soils is not clear. The N-domain of PrP^{Sc} is susceptible to proteases and therefore is likely on the exterior of the molecule (*44*). Removal of the N-domain may eliminate steric hindrances, allowing PrP^{Sc} to adsorb more readily to quartz surfaces. PK-digestion may modify PrP^{Sc} aggregation, yielding a conformation that promotes interaction with quartz surfaces but is less preferential for clay surfaces.

PrP^{Sc} aggregation may be an important factor in adsorption. In contrast to infectious tissue isotherms, PrP^{c} (not aggregated) in uninfected hamster brain homogenate did not exhibit a distinct intermediate maximum (Figure 4B). Furthermore, accelerated fibrillation of a prion peptide on a silicon surface has been reported compared with peptide fibrillation in solution (*59*), and aggregation of other proteins upon adsorption has also been shown (*60*, *61*).

The results presented here provide further evidence that rodent models may not recapitulate the behavior of natural prion diseases, such as CWD,in the environment. In kinetic studies conducted with sand and sandy loam soil, HY PrP adsorption plateaued after 30 d, while CWD PrP adsorption continued to increase through at least 60 d (*58*). Furthermore, unlike HY and DY PrP, adsorption of CWD PrP did not exhibit an intermediate maximum after a 1 week equilibration time in isothermal experiments (Figure 4B).

Strain differences in PrP adsorption were also observed as HY TME PrP consistently exhibited greater sorbed phase concentrations than DY TME PrP. HY and DY are both hamster strains and therefore exist in similar brain homogenate matrices but differ in the three-dimensional structure of PrP^{Sc} (*53–55*, *57*). It is possible that equal amounts of DY and HY PrP adsorb, but that the resulting conformation or orientation of bound DY PrP yields a decreased affinity for the primary antibody (mAb 3F4) compared with bound HY PrP. This would imply different adsorption mechanisms between the two strains.

Changes in the brain homogenate matrix due to PK-digestion may be partially responsible for differences in truncated and full-length PrP^{Sc} adsorption. A coomassie blue stain comparing the total protein before and after PK-digestion indicated a 60% decrease in protein content upon digestion, with a majority of the remaining peptides less than 14kDa (Figure 5). Thus, PK-digested homogenate has fewer large polypeptides than undigested homogenate to compete for adsorption sites, possibly allowing more PrP^{Sc} to adsorb. In addition, PK-digestion may reduce constituents which favorably or unfavorably coat or modify soil surfaces.

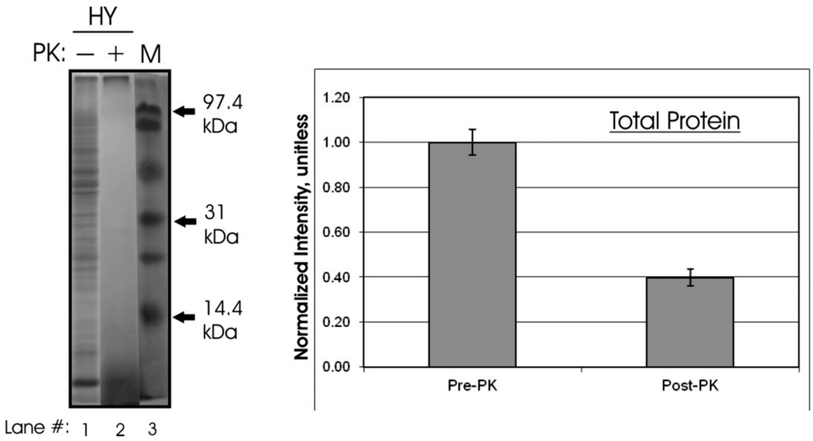

Figure 5. Total protein degradation due to PK digestion. On the left: representative Coomassie Blue stain of 2.5 µl of 10% HY TME- infected BH treated or untreated with proteinase K. M: molecular weight marker. On the right: signal intensities of digested samples (n = 4) were normalized against un-digested samples (n = 5). Error bars show ± 1 standard error of the mean. Reproduced with permission from reference (58). Copyright 2009 American Chemical Society.

Influence of Soil Binding on the Biologic Properties of the Prion Protein

Information regarding the ability of soil-bound prions to replicate (i.e. convert PrP^{c} to PrP^{Sc}) and initiate infection in a host animal is important for understanding environmental CWD and scrapie transmission. It has been demonstrated that HY TME (hamster) PrP^{Sc} bound to montmorillonite clay and three whole soils remains infectious via oral inoculation (*62*). In a previous study, we utilized protein misfolding serial amplification (PMCA) and animal bioassay to quantitatively compare unbound and soil-bound prion replication and infectivity to further investigate the influence of soil binding on the biologic properties of the prion protein.

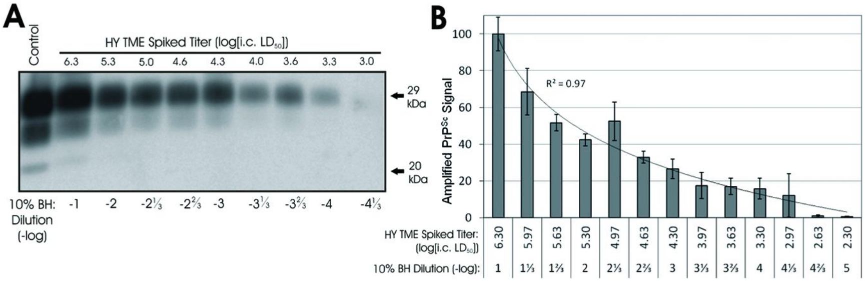

Figure 6. Single-round semi-quantitative PMCA. ***(A):*** *Representative blots of serial dilutions of a HY TME brain homogenate subjected to one round of PMCA, shown with a 200 µg BH control. All samples PK-digested and blotted with mAb 3F4. For reference, the frozen (PMCA–) signal of the 10^{-2} dilution (not shown) is at the limit of western blot detection.* ***(B):*** *Quantification of blots shown in (A). Amplified signal was calculated by normalizing blot intensities ($n \geq 3$) to 200 µg HY TME controls ($n = 4$) run on the same gel and then normalized to 10^{-1} HY controls subjected to PMCA concurrently. Error bars show ±1 standard error of the mean. Reproduced with permission from reference (30). Copyright 2011 American Society for Microbiology.*

Protein misfolding cyclic amplification (PMCA) is a method developed by Claudio Soto and colleagues (*63*, *64*) for studying prion replication (i.e. conversion of PrP^c to PrP^{Sc}). It has been used to study the basic components of the infectious prion agent (*65*, *66*), for detection of low levels of prions (*67–69*), and to investigate prion strain propagation (*70–73*). The PMCA method is somewhat analogous to polymerase chain reaction (PCR). It consists of cycles of sonication followed by incubation at 37°C. In this manner very small amounts of PrP^{Sc} can be amplified and detected by normal western blotting. An infectious seed (whether brain homogenate, soil, or other material) is added to uninfectious brain homogenized in a 'conversion buffer'. The sample is then subjected to repeated cycles of sonication followed by incubation at 37°C. An unsonicated/unincubated control is kept frozen for comparison. After a specified number of cycles (designated as one PMCA round), the samples are diluted in fresh uninfected brain homogenate and then subjected to more cycles of sonication and incubation. PrP^{Sc} is then assayed for in samples and controls using western blot. It is hypothesized that the PMCA method works by breaking PrP^{Sc} aggregates with sonication, then allowing these smaller fragments to recruit and convert PrP^c in the uninfectious brain homogenate substrate, generating more PrP^{Sc}. Newly generated PrP^{Sc} from PMCA has been shown to be infectious (*73*). A relationship exists between the input titer of prions and the number of serial PMCA rounds required for PrP^{Sc} detection (*73*, *74*). A serial dilution of HY TME brain homogenate (with initial titer of $10^{9.3}$ intracerebral (i.c.) 50% Lethal Dose (LD_{50}) per gram) was performed in triplicate, and the amplified signal of each sample after a single round of PMCA was evaluated (Figure 6). PMCA generated PrP^{Sc} was detected in all samples down to an input dilution of $10^{-4.3}$ µg equivalents ($10^{3.0}$ i.c. LD_{50}) of brain homogenate (Figure 6A). A logarithmic relationship (R^2 =0.97) best approximated the association between the input titer of HY TME agent and the abundance of PMCA generated PrP^{Sc} (Figure 6B).

Adsorption of PrP^{Sc} to Soil Reduces Prion Replication in Vitro

Saunders et al. (*30*) determined that adsorption of HY TME and CWD PrP^{Sc} to soil reduces prion replication via PMCA. Both unbound and soil-bound HY TME was subjected to PMCA (Figure 7A), and compared to the unbound sample, sorption of HY TME to a silty clay loam soil (Table 1) resulted in a 92% reduction in the abundance of amplified PrP^{Sc} (Figure 7A, lanes 5 and 9). An unbound HY control co-spiked with SCL soil (Figure 7A, lanes 6 and 7) was less amplified than the unbound HY control but significantly ($p<0.01$) greater than the soil-bound sample. PK-resistant PrP was not detected in any of the negative controls after PMCA for any experiment (Figures 7A). A similar reduction in replication via PMCA was observed with HY TME prions bound to a bentonite clay and humic acid coated silica particles (*30*). A reduction in amplification was not observed for HY TME to silica partices or a sandy loam soil (*30*). Similar behavior was also observed for CWD prions (data not shown).

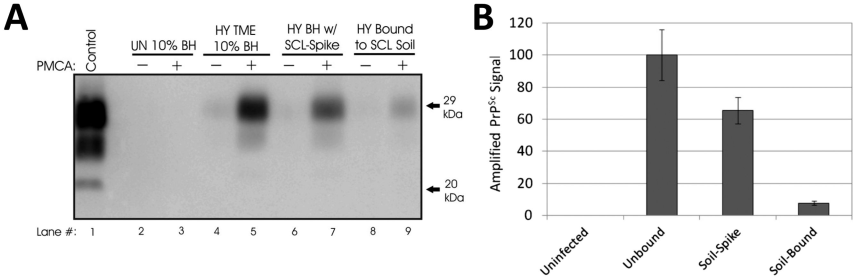

Figure 7. PMCA of HY TME bound to silty clay loam soil. ***(A):*** *Representative immunoblots of unbound and SCL soil-bound HY TME samples (24 hr) subjected or not subjected to PMCA.* ***(B):*** *Quantification of blots shown in (A). All amplified PrP^{Sc} signals were normalized to unbound HY TME controls subjected to PMCA concurrently Error bars show ±1 standard error of the mean. Reproduced with permission from reference (30). Copyright 2011 American Society for Microbiology.*

The observed decrease in the ability of prions to replicate upon binding to certain soils could be due to a number of factors. Conformational changes in PrP^{Sc} structure, including changes in aggregation state, may occur upon binding to soil (*29*, *58*). Differences in aggregate size and PrP^{Sc} structure observed beween different prion strains are known to influence infectious titer (*13*, *49*), and changes in these properties due to soil adsorption could decrease titer. This hypothesis is supported by previously documented variance in PrP adsorption with respect to soil type (*34*, *58*). It has been shown that the N-terminus of PrP plays an important role in PrP adsorption to clay surfaces but may hinder adsorption to sand surfaces, implying different PrP adsorption paradigms for clay and sand surfaces. Thus, different prion adsorption paradigms may have led to the observed variance in PMCA efficiency through differential changes in PrP^{Sc} conformation and/or aggregation state.

Alternatively, PrP^{Sc} binding to soil may also 'inactivate' a portion of the total PrP^{Sc}, through direct PrP^{Sc}-soil surface interactions or through interactions between PrP^{Sc} and other bound brain constituents. Evidence for this mechanism is found in the inefficient desorption of PrP from clay and organic surfaces even under harsh denaturing conditions (*28*, *33*, *34*, *75*).We have previously observed desorption from clay surfaces between 15-50%, and desorption from humic acid coated surfaces was approximately 25% (or near 0% without PK digestion), while desorption from SiO_2 and sand was near 100%.

Given that the ability to desorb PrP^{Sc} and the ability of soil-bound PrP^{Sc} to amplify PrP^{res} correlate with respect to soil type, it is plausible that the fraction of PrP^{Sc} that is irreversibly bound to the soil surface is unable to convert PrP^{c} and thereby initiate pathogenesis. This would imply two populations of PrP^{Sc} bound to soil: one that is both desorbable and infectious and one that is neither. Furthermore, based on this evidence, it could be hypothesized that desorption of PrP^{Sc} must occur for PrP^{c} conversion to take place.

Soil-Bound PrP^{Sc} Is Less Infectious

The ability of soil-bound PrP^{Sc} to remain infectious was also investigated by Saunders et al. (*30*). In this study, intracerebral inoculation of groups of 5 hamsters with either HY TME, or SCL-bound HY TME resulted in all animals succumbing to disease with an incubation period of 62±3 and 74±3 days respectively. To investigate the possibility that the 14 day extension of incubation period in the SCL-bound HY TME group was due to a reduction in titer, ten-fold serial dilutions of HY TME or SCL-bound HY TME inoculum were intracerebrally inoculated into groups of 5 Syrian hamsters. The titers for the unbound and SCL-bound aged HY TME inoculum were $10^{7.5}$ and $10^{6.2}$ i.c. $LD_{50}/25\mu l$, respectively, representing a 1.3-log decrease in HY TME titer upon binding to SCL soil (Table 3). Brain material from an animal infected with the 10^{-2} SCL-bound HY agent was intracerebrally inoculated into 5 Syrian hamsters and resulted in all animals succumbing to disease in 61±3 days which is not statistically different than HY TME ($p>0.05$) suggesting that SCL binding to HY PrP^{Sc} does not permanently alter the agent. All diseased animals exhibited clinical signs of hyperexcitability and ataxia and PrP^{Sc} migration properties that were consistent with HY TME agent infected animals.

Table 3. Reduced titer of soil-bound HY TME agent. Reproduced with permission from reference (*30*). Copyright 2011 American Society for Microbiology

Agent dilution	*Inoculum*	
	HY TME	*HY TME sorbed to SCL*
10^{-2}	62±3 (5/5)[a]	74±3 (5/5)
10^{-3}	n.d.	78±3 (5/5)
10^{-4}	74±4 (5/5)	84±3 (5/5)
10^{-5}	n.d.	96±3 (5/5)
10^{-6}	98±3 (5/5)	120±25 (3/5)
10^{-7}	127±18 (5/5)	>275 (0/5)
10^{-8}	>275 (0/5)	>275 (0/5)
10^{-9}	>275 (0/5)	>275 (0/5)
Mock	>275 (0/5)	>275 (0/5)
Titer:	**$10^{7.5}$ i.c. LD_{50}/25µl**	**$10^{6.2}$ i.c. LD_{50}/25µl**

[a] Mean incubation period in days±SEM (number affected/number inoculated).

Do Soil Properties Influence Prion Disease Incidence?

As CWD in particular continues to spread geographically and disease residence times in cervid populations and habitats increases, environmental factors may play an increasingly important role in sustaining or heightening disease prevalence (*76*). It is possible that the residence time of prions in the environment as well as the efficiency of prion transmission could vary significantly with local soil properties. Experimental data on the influence of prion-soil interactions on the biologic properties of the protein outlined above clearly provide the basis for potential variance in prion incidence due to soil factors, most especially soil type. The influence of soil factors on disease incidence is certainly not without precedent, however, the epidemiological data on prion soil risk factors are as yet limited (*77*, *78*).

Acknowledgments

This work was supported by National Science Foundation (CBET-1149242) and the Nation Center for Research Resources (P20 RR0115635-6, C06 RR17417-01 and G200RR024001).

References

1. Prusiner, S. B. *Brain Pathol.* **1998**, *8*, 499–513.
2. Chesebro, B. *Br. Med. Bull.* **2003**, *66*, 1–20.
3. Williams, E. S.; Miller, M. W.; Kreeger, T. J.; Kahn, R. H.; Thorne, E. T. *J. Wildlife Manage.* **2002**, *66*, 551–563.
4. Deleault, N. R.; Harris, B. T.; Rees, J. R.; Supattapone, S. *Proc. Natl. Acad. Sci. U.S.A.* **2007**, *104*, 9741–9746.
5. Prusiner, S. B. In *Prion Biology and Diseases*, 2nd ed.; Pruisner, S. B., Ed.; Cold Spring Harbor Laboratory Press: Cold Spring Harbor, NY, 2004; pp 1−89.
6. Wang, F.; Wang, X.; Yuan, C. G.; Ma, J. *Science* **2010**, *327*, 1132–1135.
7. Zomosa-Signoret, V.; Arnaud, J. D.; Fontes, P.; Alvarez-Martinez, M. T.; Liautard, J. P. *Vet. Res.* **2008**, *39*, 9.
8. Haigh, C. L.; Brown, D. R. *J. Neurochem.* **2006**, *98*, 677–89.
9. Govaerts, C.; Wille, H.; Prusiner, S. B.; Cohen, F. E. In *Prion Biology and Diseases*, 2nd ed.; Pruisner, S. B., Ed.; Cold Spring Harbor Laboratory Press: Cold Spring Harbor, NY, 2004.
10. Caughey, W.; Raymond, L.; Horiuchi, M.; Caughey, B. *Proc. Natl. Acad. Sci. U.S.A.* **1998**, *95*, 12117–22.
11. Pan, K. H.; Baldwin, M.; Nguyen, J.; Gasset, M.; Serban, A.; Groth, D.; Mehlhorn, I.; Huang, Z.; Fletterick, R. J.; Cohen, F. E.; Prusiner, S. B. *Proc. Natl. Acad. Sci. U.S.A.* **1993**, *90*, 10962–10966.
12. Gossert, A. D.; Bonjour, S.; Lysek, D. A.; Fiorito, F.; Wüthrich, K. *Proc. Natl. Acad. Sci. U.S.A.* **2005**, *102*, 646–650.
13. Bessen, R. A.; Marsh, R. F. *J. Virol.* **1992**, *66*, 2096–2101.
14. Greig, J. R. *Vet. J.* **1940**, *96*, 203–206.
15. Hadlow, W. J.; Kennedy, R. C.; Race, R. E. *J. Infect. Dis.* **1982**, *146*, 657–664.
16. Miller, M. W.; Williams, E. S. *Nature* **2003**, *425*, 35–36.
17. Miller, M. W.; Williams, E. S.; Hobbs, N. T.; Wolfe, L. L. *Emerg. Infect. Dis.* **2004**, *10*, 1003–1006.
18. Seidel, B; Thomzig, A.; Buschmann, A.; Groschup, M. H.; Peters, R.; Beekes, M.; Tertze, K. *PLoS One* **2007**, *5*, e435.
19. Brown, P.; Gajdusek, D. C. *Lancet* **1991**, *337*, 269–70.
20. Georgsson, G.; Sigurdarson, S.; Brown, P. *J. Gen. Virol.* **2006**, *87*, 3737–3740.
21. Miller, M. W.; Hobbs, N. T.; Tavener, S. J. *Ecol. Appl.* **2006**, *16*, 2208–2214.
22. Gough, K. C.; Maddison, B. C. *Prion* **2010**, *4*, 275–282.
23. Tamgüney, G.; Miller, M. W.; Wolfe, L. L.; Sirochman, T. M.; Glidden, D. V.; Palmer, C. P.; Lemus, A.; DeArmond, S. J.; Pruisner, S. B. *Nature* **2009**, *461*, 529–532.
24. Hamir, A. N.; Kunkle, R. A.; Richt, J. A.; Miller, J. M.; Cutlip, R. C.; Jenny, A. L. *J. Vet. Diagn. Invest.* **2005**, *17*, 3–19.
25. Hamir, A. N.; Kunkle, R. A.; Richt, J. A.; Miller, J. M.; Greenlee, J. J. *Vet. Pathol.* **2008**, *45*, 7–11.
26. Kincaid, A. E.; Bartz, J. C. *J. Virol.* **2007**, *81*, 4482–4491.
27. Sigurdson, C. J.; Williams, E. S.; Miller, M. W.; Spraker, T. R.; O'Rourke, K. I.; Hoover, E. A. *J. Gen. Virol.* **1999**, *80*, 2757–2764.

28. Leita, L.; Fornasier, F.; Nobili, M. D; Bertoli, A.; Genovesi, S.; Sequi, P. *Soil Biol. Biochem.* **2006**, *38*, 1638–1644.
29. Saunders, S. E.; Bartelt-Hunt, S. L.; Bartz, J. C. *Prion* **2008**, *2*, 162–169.
30. Saunders, S. E.; Shikiya, R. A.; Langenfeld, K. A.; Bartelt-Hunt, S. L.; Bartz, J. C. *J. Virol.* **2011**, *85*, 5476–5482.
31. Arthur, W. J.; Alldredge, A. W. *Rangeland Ecol. Manage.* **1979**, *32*, 67–71.
32. Beyer, W. N.; Connor, E. E.; Gerould, S. Estimates of soil ingestion by wildlife. *J. Wildlife Manage.* **1994**, *58*, 375–382.
33. Cooke, C. M.; Rodger, J.; Smith, A.; Fernie, K.; Shaw, G.; Somerville, R. A. *Environ. Sci. Technol.* **2007**, *41*, 811–817.
34. Johnson, C. J.; Phillips, K. E.; Schramm, P. T.; McKenzie, D.; Aiken, J. M.; Pedersen, J. A. *PLoS Pathog.* **2006**, *2*, 296–302.
35. Ma, X.; Benson, C. H.; McKenzie, D.; Aiken, J. M.; Pedersen, J. A. *Environ. Sci. Technol.* **2007**, *41*, 2324–2330.
36. Polano, M.; Anselmi, C.; Leita, L.; Negro, A.; Nobili, M. D. *Biochem. Biophys. Res. Comm.* **2008**, *367*, 323–329.
37. Rigou, P.; Rezaei, H.; Grosclaude, J.; Staunton, S.; Quiquampoix, H. *Environ. Sci. Technol.* **2006**, *40*, 1497–1503.
38. Vasina, E. N.; Dejardin, P.; Rezaei, H.; Grosclaude, J.; Quiquampoix, H. *Biomacromolecules* **2005**, *6*, 3425–3432.
39. Pucci, A.; D'Acqui, L. P.; Calamai, L. *Environ. Sci. Technol.* **2008**, *42*, 728–733.
40. Saunders, S. E.; Bartz, J. C.; Bartelt-Hunt, S. L. *Envion Sci Technol* **2009**, *43*, 7728–7733.
41. Genovesi, S.; Leita, L.; Sequi, P.; Andrighetto, I.; Sorgato, M. C.; Bertoli, A. *PLos One* **2007**, *2*, e1069.
42. Maddison, B. C.; Owen, J. P.; Bishop, K.; Shaw, G.; Rees, H. C.; Gough, K. C. *Environ. Sci. Technol.* **2010**, *44*, 8503–8508.
43. Rapp, D.; Potier, P.; Jocteur-Monrozier, L.; Richaume, A. *Environ. Sci. Technol.* **2006**, *44*, 6324–6329.
44. Saunders, S. E.; Bartz, J. C.; Telling, G. C.; Bartelt-Hunt, S. L. *Environ. Sci. Technol.* **2008**, *42*, 6573–6579.
45. Quiquampoix, H.; Abadie, L.; Baron, M. H.; Leprince, F.; Matumoto-Pintro, P. T.; Ratcliffe, R. G.; Staunton, S. In *Proteins at Interfaces II: Fundamentals and Applications*; Horbett, T. A., Brash, J. L., Eds.; American Chemical Society: Washington, DC, 1995.
46. Revault, M.; Quiquampoix, H.; Baron, H. M.; Noinville, S. *Biochim. Biophys. Acta* **2005**, *1724*, 367–374.
47. Rao, M. A.; Russo, F.; Granata, V.; Berisio, R.; Zagari, A.; Gianfreda, L. *Soil Biol. Biochem.* **2007**, *39*, 493–504.
48. Harter, R. D.; Stotzky, G. *Soil Sci Soc Amer Proc* **1973**, *37*, 116–123.
49. Silveira, J. R.; Raymond, G. J.; Hughson, A. G.; Race, R. E.; Sim, V. L.; Hayes, S. F.; Caughey, B. *Nature* **2005**, *437*, 257–261.
50. Hinckley, G. T.; Johnson, C. J.; Jacobson, K. T.; Bartholomay, C.; McMahon, K. D.; McKenzie, D.; Aiken, J. M.; Pedersen, J. A. *Environ. Sci. Technol.* **2008**, *42*, 5254–5259.
51. Cooke, C. M.; Shaw, G. *Soil Biol. Biochem.* **2007**, *39*, 1181–1191.

52. Fraser, H.; Dickinson, A. G. *Nature* **1967**, *216*, 1310–1311.
53. Bessen, R. A.; Marsh, R. F. *J. Virol.* **1992**, *66*, 2096–2101.
54. Bessen, R. A.; Marsh, R. F. *J. Virol.* **1994**, *68*, 7859–7868.
55. Caughey, B.; Raymond, G. J.; Bessen, R. A. *J. Biol. Chem.* **1998**, *273*, 32230–32235.
56. Kascsak, R.; Rubenstein, R.; Merz, P. A.; Carp, R. I.; Wisniewski, H. M.; Diringer, H. *J. Gen. Virol.* **1985**, *66*, 1715–1722.
57. Safar, J.; Willie, H.; Itri, V.; Groth, D.; Serban, H.; Torchia, M.; Cohen, F. E.; Prusiner, S. B. *Nat. Med.* **1998**, *4*, 1157–1165.
58. Saunders, S. E.; Bartz, J. C.; Bartelt-Hunt, S. L. *Environ. Sci. Technol.* **2009**, *43*, 7728–7733.
59. Ku, S. H.; Park, C. B. *Langmuir* **2008**, *24*, 13822–13827.
60. Brynda, E.; Houska, M.; Lednicky, F. *J. Colloid Interface Sci.* **1986**, *113*, 164–171.
61. Marchin, K. L.; Berrie, C. L. *Langmuir* **2003**, *19*, 9883–9888.
62. Johnson, C. J.; Pedersen, J. A.; Chappell, R. J.; McKenzie, D.; Aiken, J. M. *PLoS Pathog.* **2007**, *3*, e93.
63. Castilla, J.; Saa, P.; Hetz, C.; Soto, C. *Cell* **2005**, *121*, 195–206.
64. Saa, P.; Castilla, J.; Soto, C. *J. Biol. Chem.* **2006**, *281*, 35245–35252.
65. Deleault, N. R.; Harris, B. T.; Rees, J. R.; Supattapone, S. *Proc. Natl. Acad. Sci. U.S.A.* **2007**, *104*, 9741–9746.
66. Wang, F.; Wang, X.; Yuan, C. G.; Ma, J. *Science* **2010**, *327*, 1132–1135.
67. Angers, R. C.; Seward, T. S.; Napier, D.; Green, M.; Hoover, E.; Spraker, T.; O'Rourke, K.; Balachandran, A.; Telling, G. C. *Emerg. Infect. Dis.* **2009**, *15*, 696–703.
68. Gonzalez-Romero, D.; Barria, M. A.; Leon, P.; Morales, R.; Soto, C. *FEBS Lett.* **2008**, *582*, 3161–3166.
69. Haley, N. J.; Mathiason, C. K.; Zabel, M. D.; Telling, G. C.; Hoover, E. A. *PLoS One* **2009**, *4*, e7990.
70. Ayers, J. I.; Schutt, C. R.; Shikiya, R. A.; Aguzzi, A.; Kincaid, A. E.; Bartz, J. C. *PLoS Pathog.* **2010**, *7*, e1001317.
71. Castilla, J.; Morales, R.; Saa, P.; Barria, M.; Gambetti, P.; Soto, C. *EMBO J.* **2008**, *27*, 2557–2566.
72. Deleault, A. M.; Deleault, N. R.; Harris, B. T.; Rees, J. R.; Supattapone, S. *J. Gen. Virol.* **2008**, *89*, 2646–2650.
73. Shikiya, R. A.; Ayers, J. I.; Schutt, C. R.; Kincaid, A. E.; Bartz, J. C. *J. Virol.* **2010**, *84*, 5706–5714.
74. Chen, B.; Morales, R.; Barria, M.; Soto, C. *Nat. Methods* **2010**, *7*, 519–20.
75. Saunders, S. E.; Bartz, J. C.; VerCauteren, K. C.; Bartelt-Hunt, S. L. *Environ. Sci. Technol.* **2010**, *44*, 4129–4135.
76. Almberg, E. S.; Cross, P. C.; Johnson, C. J.; Heisey, D. M.; Richards, B. J. *PLoS One* **2011**, *6*, e19896.
77. Saunders, S. E.; Bartz, J. C.; Bartelt-Hunt, S. L. *Chemosphere* **2012**, *87*, 661–667.
78. Saunders, S. E.; Bartelt-Hunt, S. L; Bartz, J. C. *Emerg. Infect. Dis.* **2012**, *18*, 369–376.

Chapter 21

Orientation of Adsorbed Antibodies: *In Situ* Monitoring by QCM and Random Sequential Adsorption Modeling

Christine Dupont-Gillain*

Université catholique de Louvain, Institute of Condensed Matter and Nanosciences – « Bio- and soft matter » division, Croix du Sud 1/L7.04.01, 1348 Louvain-la-Neuve, Belgium
***E-mail: christine.dupont@uclouvain.be**

Antibodies (IgGs) are widely used for diagnostic assays, for which they are in certain cases immobilized by adsorption on hydrophobic substrates. Antigen recognition efficiency will depend on the orientation of the adsorbed IgG molecules. The aim of the present study was to investigate the binding-ability of a range of IgG isotypes from rat and mouse, all directed against the same antigen, using quartz crystal microbalance. The results allow identifying some isotypes which adsorb in higher amount and which provide a better bound antigen to adsorbed IgG ratio. This ratio was found to remain rather constant with the adsorbed IgG amount. Random sequential adsorption (RSA) modeling was used to simulate IgG adsorption. In the chosen modeling conditions, it is shown that even if adsorption in flat orientation is more favorable, a high proportion of IgG molecules adsorb in end-on orientation when surface coverage increases, owing to the low surface area spaces left between IgG molecules already adsorbed in flat orientation. The apparent discrepancy between experimental data collected by QCM and the output of RSA modeling may be attributed to variations in the water content of the adsorbed layer, to steric hindrance and multivalency effects upon antigen binding, or to the role of albumin molecules used to prevent non specific adsorption of the antigen.

In Proteins at Interfaces III State of the Art 2012; Horbett, T., et al.;
ACS Symposium Series; American Chemical Society: Washington, DC, 2012.

Introduction

Antibodies, which are proteins made of two identical light chains and two identical heavy chains, recognize specific antigens through interaction with their variable parts, located at two extremities of their three-lobular structure (*1*). Owing to this property, they are essential for the design of many diagnostic tools. In particular, the very widespread enzyme-linked immunosorbent assays (ELISA) rest on the adsorption of antibodies at the surface of hydrophobic polystyrene plates. The ability of antibodies to bind antigens after adsorption is related to the accessibility of their variable parts. Therefore, a better response is expected if the antibodies are adsorbed through their constant part, in an end-on orientation, rather than in side-on or, even worse, flat orientation (*2*).

The forces governing antibodies adsorption have been investigated, and hydrophobic as well as electrostatic interactions have been identified as playing a major role (*3*). On hydrophobic surfaces, it was actually shown that the affinity of antibodies for the surface was not much affected by pH and ionic strength, pointing to the weak contribution of electrostatic interactions, which were however shown to affect the maximum adsorbed amount. On hydrophilic surfaces, adsorption was strongly reduced in conditions of electrostatic repulsion (*4*).

Studying the orientation of adsorbed antibodies is highly challenging. In a first approach, if it is considered that adsorbed proteins tend to form a monolayer at the interface, the adsorbed amount may give an indication on orientation, since less molecules will fit in the monolayer in flat compared to end-on orientation. Based on close-packed monolayers, an adsorbed mass of 2.0 and 3.7 mg/m^2 was indeed estimated for flat and end-on adsorbed antibodies, respectively (*4*). Using neutron reflectivity, Petrash and colleagues showed that a human γ-globulin adsorbed on a hydrophobic self-assembled monolayer formed a dense layer at close contact with the substrate, on top of which a second, less dense layer was found. This was attributed to the combination of molecules lying down on the substrate and of end-on adsorbed antibodies (*5*).

To probe the orientation of adsorbed antibodies in relation with their use for diagnostic assays, it is actually more convenient (although more indirect) to measure their antigen binding ability. From theoretical considerations, it may be expected that antibodies adsorb mainly in flat orientation on hydrophobic substrates to maximize hydrophobic interactions with the surface. However, experimental evidences clearly show that antigen recognition occurs, thus that part of the adsorbed antibodies have their variable parts pointing towards the solution, but in an extent that is higly variable from one antibody to another and that is difficult to predict (*3*). When a low bound antigen to adsorbed antibody ratio is observed, it is actually difficult to know whether this is due to a low amount of antibodies adsorbed in end-on orientation, with the variable parts pointing towards the solution, or to steric hindrance between adjacent recognition sites which may occur at high surface coverage, as suggested in some studies (*6*). Using quartz crystal microbalance (QCM) to measure the adsorption from different concentrations of an anti-streptavidin antibody, followed by streptavidin binding, Wiseman and colleagues suggested that antibodies adsorb in flat orientation at low surface coverage, when enough space is available at the interface to do so, while they tend to adsorb in end-on orientation at high surface coverage *ie* when adsorption occurs from a more concentrated solution (*2*).

Given the difficulty to predict the behavior, and in particular the orientation, of antibodies upon adsorption, attempts to maximize the sensitivity of ELISA assays are usually empirical. Factors known to affect the antigen binding efficiency include concentration of antibody solution, nature of blocking agent used (albumin, casein, surfactants or combination thereof), order and duration of adsorption and washing steps. Strategies can be used to immobilize antibodies in end-on orientation, through coupling of the constant part to the substrate (*3*, *7*). For example, protein A or protein G are known receptors for the Fc fragment of antibodies, and can be preadsorbed or linked to the substrate to further direct the orientation of antibodies. Owing to the perspectives opened by the possibility to produce chimeric antibodies, an alternative approach could consist in selecting an antibody with a constant part that would be particularly suitable for adsorption in end-on position, then coupling the desired variable part to this constant part. For this reason, it is interesting to evaluate the antigen-binding efficiency of antibodies with different constant parts, ie from different species or different isotypes (*1*).

The aim of this work is to study the orientation of adsorbed γ-immunoglobulins (IgGs). A range of IgG isotypes from rat and mouse directed against the same antigen, 2,4-dinitrophenol (DNP), was selected. Their adsorption as well as their antigen-binding ability were probed using quartz crystal microbalance (QCM). The results are then interpreted in the light of random sequential adsorption modeling.

Materials and Methods

Materials

IgGs used in this study originate from either rat or mouse, and are from different isotypes as detailed in Table I. These monoclonal antibodies are all directed against 2,4-dinitrophenol (DNP). They were purchased from IMEX (Brussels, Belgium) under the reference listed in Table I, and received as 1 mg/ml solutions in phosphate buffer supplemented with 0.1 % sodium azide.

DNP coupled to albumin (DNP-alb; 30 to 40 DNP groups per albumin molecule; Sigma-Aldrich) was used as the antigen in QCM experiments. The molar mass of DNP alone is indeed too small to allow its detection using QCM. Bovine serum albumin (BSA; fraction V, ≥96 %; Sigma-Aldrich) was used as the blocking agent.

All solutions (IgG, DNP-alb and BSA) were prepared in phosphate buffer saline (PBS). The composition of PBS, prepared using ultrapure water (PurelabUltra, Elga), was as follows: 0.2 g/l KCl (Sigma-Aldrich), 8 g/l NaCl (Sigma-Aldrich), 0.88 g/l KH_2PO_4 (Merck), 1.28 g/L $Na_2HPO_4.12\ H_2O$ (VEL).

NaN_3 (Sigma-Aldrich) at 2 g/l was added to prevent biological contamination and pH was adjusted to 7.4 using 1 M NaOH. PBS was filtered before use (0.2 µm sterile syringe filter, VWR). The concentration of the IgG solutions was 4, 10 and 20 µg/ml, BSA blocking solution was prepared at a concentration of 10 mg/ml, and DNP-alb solution had a concentration of 20 µg/ml.

Table I. IgGs used in the present work

Species	*Isotype*	*IMEX reference*
Mouse	IgG 1κ	MA-DNP-1
	IgG 2aκ	MA-DNP-2
	IgG 2bκ	MA-DNP-3
	IgG 3κ	MA-DNP-4
Rat	IgG 1κ	LO-DNP-1
	IgG 1κ	LO-DNP-2
	IgG 2aκ	LO-DNP-16
	IgG 2bκ	LO-DNP-57

For QCM experiments, standard gold-coated crystals (QSX 301 from Q-Sense) were used. Their surface was modified by deposition of a thin polystyrene layer. This was done by spin-coating of a 0.5 % (w:w) polystyrene (M_w = 230,000 g/mol; Aldrich) solution in toluene (VWR). Spin-coating was performed under a nitrogen atmosphere on a WS-400B-6NPP-Lite spin-coater from Laurell, using the following parameters: volume of solution = 100 µl, speed = 2,000 rpm, acceleration = 20,000 rpm/s, time = 20 s. The obtained polystyrene-coated sensors were then heated for 1 h in an oven at 80°C to remove traces of solvent.

QCM Experiments

IgG adsorption, followed by blocking step with BSA then DNP-alb recognition were monitored *in situ* using quartz crystal microbalance (QCM). The system used was a Q-Sense E4 (Biolin Scientific, Sweden), equipped with four QFM 401 flow modules. The flow was ensured by a peristaltic pump (Ismatec, Germany); it was set at 10 µl/min throughout the whole experiment. The temperature was fixed at 20°C. Experiments were performed using the successive steps described in Table II. To reduce the amount of IgG solution needed, a closed-loop circuit was used after 1 h of IgG adsorption, until the end of that step.

Table II. Steps used in QCM experiments

Step	*Solution used*	*Typical duration*
Establishment of a baseline	PBS	2 h
IgG adsorption	IgG (4, 10 or 20 µg/ml)	14 h
Rinsing	PBS	90 min
Blocking	BSA (10 mg/ml)	90 min
Rinsing	PBS	90 min
Antigen binding	DNP-alb (20 µg/ml)	90 min
Rinsing	PBS	90 min

The mass deposited on the crystal surface after each deposition step (IgG, BSA, DNP-alb) was calculated on the basis of the shift of frequency (Δf) recorded between the baseline established before that step in PBS, and the one established during the subsequent rinsing step in PBS. Although this means that the adsorbed mass is then the one of the molecules remaining at the interface after rinsing (and not the one accumulated at the interface in equilibrium with the protein solution), this is necessary to avoid effects related to the density and viscosity of the solutions interfering with the results. Δf was then converted into an increment of adsorbed mass Δm using Sauerbrey equation:

$$\Delta m = - C.\ \Delta f/n$$

in which C is the mass sensitivity constant, related to the quartz crystal (here, $C = 17.7\ \text{ng.cm}^{-2}.\text{Hz}^{-1}$) and n is the overtone used for the measurement. Note that Sauerbrey equation only holds if the characteristics of the adsorbed layer can be assimilated to the one of the quartz crystal, *ie* if the layer is rigid and homogeneous. In the present case, the dissipation shifts recorded upon IgG adsorption were always lower than 2.10^{-6}, and the $\Delta D/\Delta f$ ratio was in the range of 5.10^{-8} or lower, where ΔD is the recorded shift of energy dissipation. In such conditions, it is considered that the Sauerbrey equation gives a good estimation of the adsorbed mass (*8*). Dissipation values will therefore not be further exploited. The obtained Δm (in ng/cm^2) were further converted into molar surface concentrations (in pmol/cm^2), using a molar mass of 146 kDa and 71.4 kDa for IgGs and DNP-alb, respectively. The calculated values must however be interpreted with caution given the fact that not only the adsorbed molecules but also water coupled to the adsorbed layer are probed by QCM (*9*).

Random Sequential Adsorption Modeling

Random sequential adsorption (RSA) modeling was developed by Schaaf, Talbot and colleagues (*10–12*). It consists in considering the filling of an interface by objects using the following hypotheses: (i) objects arrive sequentially at the interface, in a randomly chosen position; (ii) once deposited, an object cannot move from its initial position, (iii) objects cannot overlap. This approach can be used to simulate protein adsorption, if one considers that proteins are not deformable, that they only adsorb in the form of a monolayer (three-dimensional aggregates are not formed), that they cannot diffuse in the lateral plane and that their adsorption is irreversible. This latter assumption is not too far from reality on hydrophobic substrates (*13*).

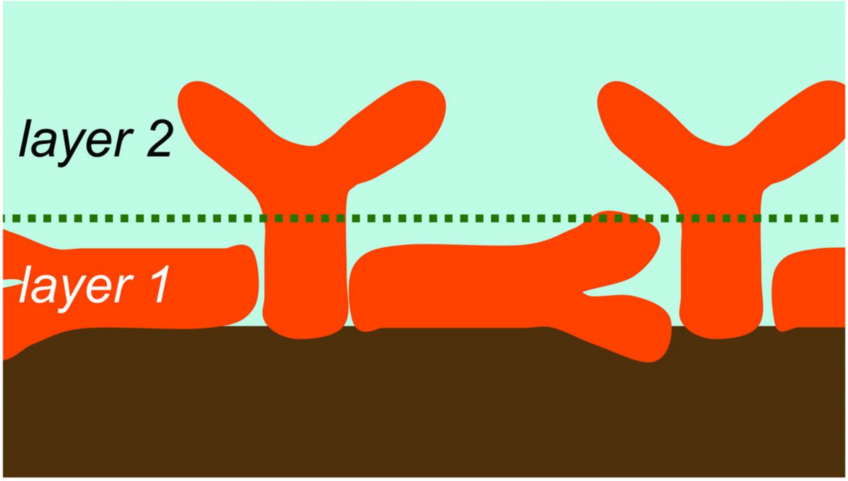

Figure 1. Schematic representation of the two-layer system chosen for RSA modeling.

RSA modeling was performed using the Matlab environment (The Mathworks Inc.). The approach was first validated for the deposition of hard spheres (not shown here), by comparing the obtained results with the ones reported in the literature (*10*). The approach was then extended to the case of IgGs. Given the anisotropy of the adsorbed object in that case, new hypotheses were made. The shape of IgGs was simplified to a Y-shaped object, with arms of a width of 4 nm and a length of 7 nm, in agreement with the known dimensions of IgG molecules (*1*). An angle of 90° was imposed between the two arms bearing the variable parts. Only two possible orientations were considered for adsorption: end-on with the constant part in contact with the substrate or flat, which correspond respectively to the minimum (10 nm^2) and maximum (84 nm^2) occupied surface area at the interface. The orientation was randomly chosen (end-on or flat with equal probability) at each deposition of a particle in a randomly chosen location. The interfacial area was divided in two layers, as depicted in Figure 1. Layer 1, at close vicinity of the substrate surface, can accommodate IgG molecules in flat orientation, as well as the stalk of IgGs standing in end-on position. As in the original RSA model, no overlap of molecules is allowed within this layer. A second layer (layer 2 on Figure 1) was designed to accommodate the upper part of end-on-oriented IgGs (area considered for the projection of this upper part = 40 nm^2). While no overlapping is allowed within layer 2, it is however allowed to overlap molecules between layer 1 and 2. This means that the adsorption of end-on IgGs is allowed in small spaces left between flat IgGs. Finally, given the fact that adsorption in flat orientation is *a priori* energetically more favorable on hydrophobic substrates, after being assigned to a given location, IgGs adsorbed in end-on orientation were allowed to lie down if enough surface area was available at this location.

Results and Discussion

Monitoring the Typical Steps of an ELISA Assay Using QCM

The Δf measured within the course of typical QCM experiments are presented in Figure 2, for an IgG 2aκ from rat (LO-DNP-16) adsorbed from solutions at three different concentrations (4, 10 and 20 µg/ml). For each experimental curve, the three main steps of the experiment are clearly visible, *ie* a significant negative Δf, corresponding to an increase of mass coupled to the sensor, is recorded after IgG adsorption (t ~ 15h), BSA blocking (t ~18 h), and DNP-alb binding (t ~ 20 h). The increase in adsorbed IgG amount with the concentration of IgG in solution is also evident, Δf being of the order of 15, 30 and 45 Hz for IgG solutions at 4, 10 and 20 µg/ml, respectively. Further decrease of the measured frequency upon blocking of the free surface sites using BSA is inversely related to the adsorbed IgG amount. Finally, the amount of bound DNP-alb seems to be directly related to the IgG adsorbed amount.

The results obtained by QCM for the 8 different IgGs tested, adsorbed from solutions at three different concentrations, are summarized in Figure 3. For most IgGs, the trend observed in Figure 2 is found again, *ie* the adsorbed amount increases with the concentration in solution (Figure 3a). For the IgG 2aκ from mouse, however, saturation seems to be already reached at a concentration of 10 µg/ml. This antibody is also the one that adsorbs with the highest amount (~8 pmol/cm^2) in the concentration range tested. On the contrary, IgG 2bκ from rat adsorbs only in very small amounts, and the amount of adsorbed IgG 3κ from mouse is only slightly higher. To give an point of comparison, an adsorbed amount of 6 pmol/cm^2 corresponds to 8.76 mg/m^2. This is roughly twice the value expected for a closely-packed layer of end-on oriented IgGs (*4*). It should however be kept in mind that water coupled to the adsorbed layer contributes to the frequency shift recorded by QCM (*9*).

The absolute amount of antigen bound to the preadsorbed IgGs (Figure 3b) is the highest for IgG 1κ and 2aκ from rat. As a general trend, this absolute amount increases with the concentration of the solutions used for IgG adsorption. The relation between the adsorbed IgG amount and the corresponding recognized antigen amount is better visualized in Figure 3c, which shows detected DNP-alb/adsorbed IgG molar ratios. This ratio shows values in the range of 0.5 to 1, the highest ratios being recorded for IgG 3κ from mouse and IgG 1κ and 2aκ from rat. Note that the high value reported for IgG2bκ from rat must be ignored since it results from the very low and uncertain amounts of adsorbed IgGs for this isotype. At this stage, it seems thus clear that a significant fraction of the adsorbed IgGs have their variable parts available for binding. In principle, each IgG molecule could bind with two DNP molecules. The maximum value achievable for the antigen/IgG ratio is thus two. It should be recalled here that DNP is coupled to albumin, with 30-40 DNP molecules per albumin molecule. It is thus possible for a single detected DNP-alb molecule to bind to several binding sites of IgGs. A antigen/IgG ratio of 0.5 is compatible with a layer in which half of the IgGs would be in flat orientation (no binding), and the other half in end-on orientation, with one binding site occupied (or two binding sites occupied by the same DNP-alb molecule). Of course, many other combinations of orientations can be invoked to explain this ratio, including mixtures of flat, side-on, and end-on orientation, with zero, one or two sites occupied per IgG molecule, possibly by the same DNP-alb molecule.

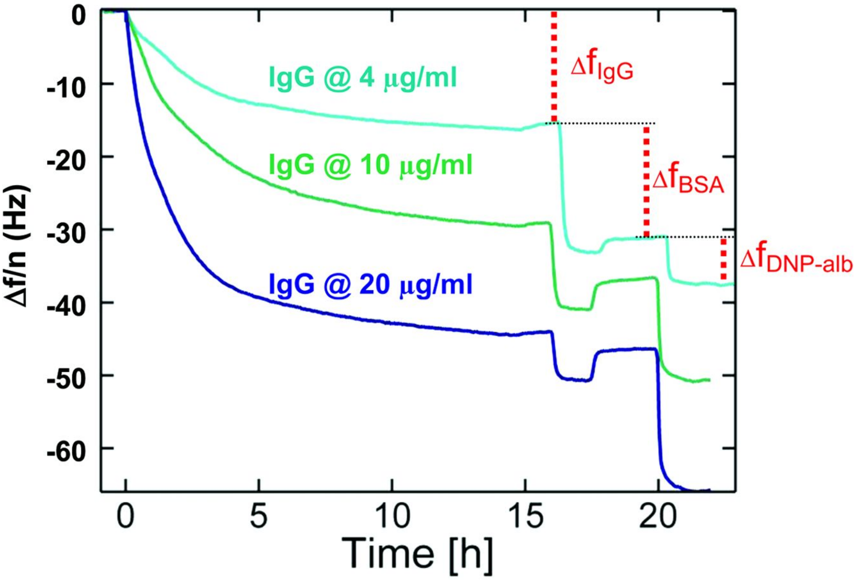

Figure 2. Results of QCM experiments performed with an IgG 2aκ from rat. The IgG concentration in solution is indicated above each recorded curve. The results are shown for the 11th overtone. Δf_{IgG}, Δf_{BSA} and $\Delta f_{DNP\text{-}alb}$ refer to the shift of frequency measured for IgG adsorption, BSA blocking and DNP-alb binding steps, respectively.

In Proteins at Interfaces III State of the Art 2012; Horbett, T., et al.;
ACS Symposium Series; American Chemical Society: Washington, DC, 2012.

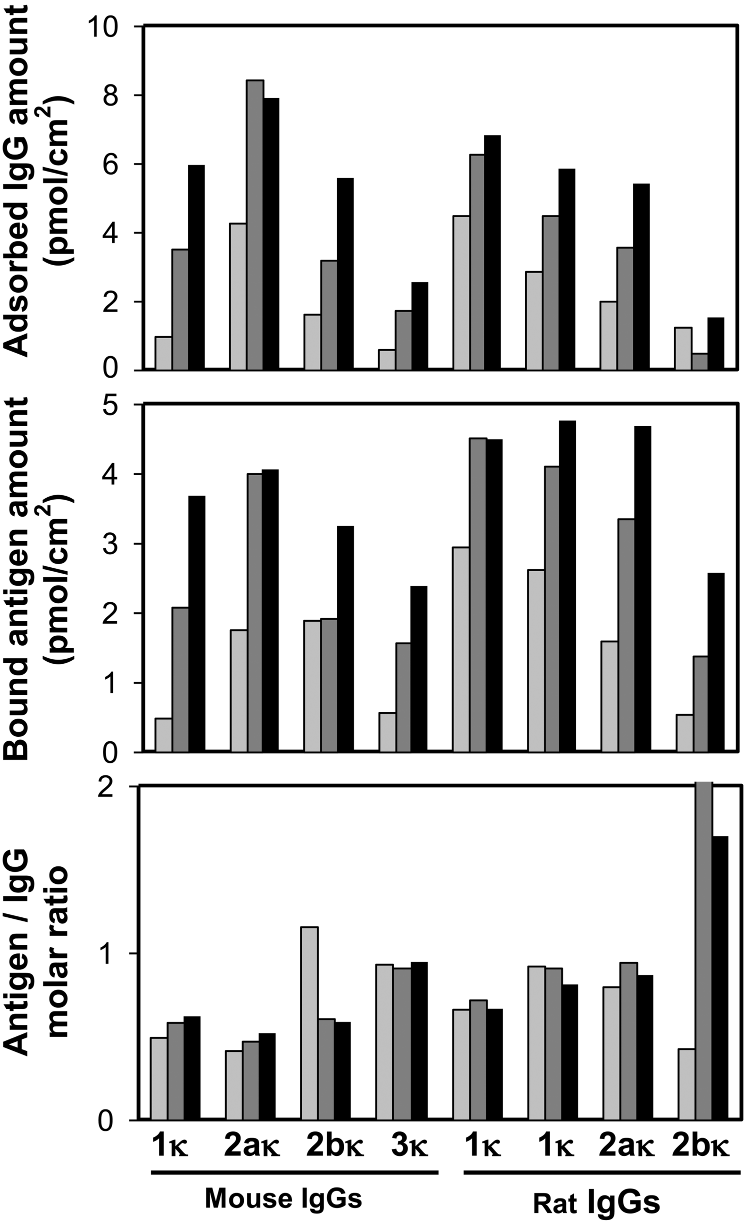

Figure 3. Summary of QCM results obtained with the 8 different IgGs used in this study: (a) adsorbed IgG amount, (b) detected antigen binding, (c) bound antigen to adsorbed IgG ratio. Three different concentrations of IgGs in solution were used: light grey = 4 μg/ml, grey = 10 μg/ml, black = 20 μg/ml.

Figure 4 shows the evolution of Δf recorded after bringing the antigen in contact with the adsorbed IgG layer, as a function of the Δf recorded upon IgG adsorption. Two main trends are observed. On the one hand, there is a roughly linear behaviour for IgGs of a given species. This implies that, whatever the adsorbed amount, the proportion of available sites remains approximately constant. This can also be observed in Figure 3c, where the antigen / IgG ratio remains rather constant with the concentration of the IgG solution. This is in contradiction with the results of Wiseman and colleagues (*2*), which indicated that antibodies shifted from flat to end-on orientation when surface coverage increased. On the other hand, the overall orientation of antibodies within the adsorbed layer seems to be related to the species from which the IgGs originate. The constant part of rat IgGs would thus be the more suitable for binding in an appropriate orientation for further recognition by the antigen.

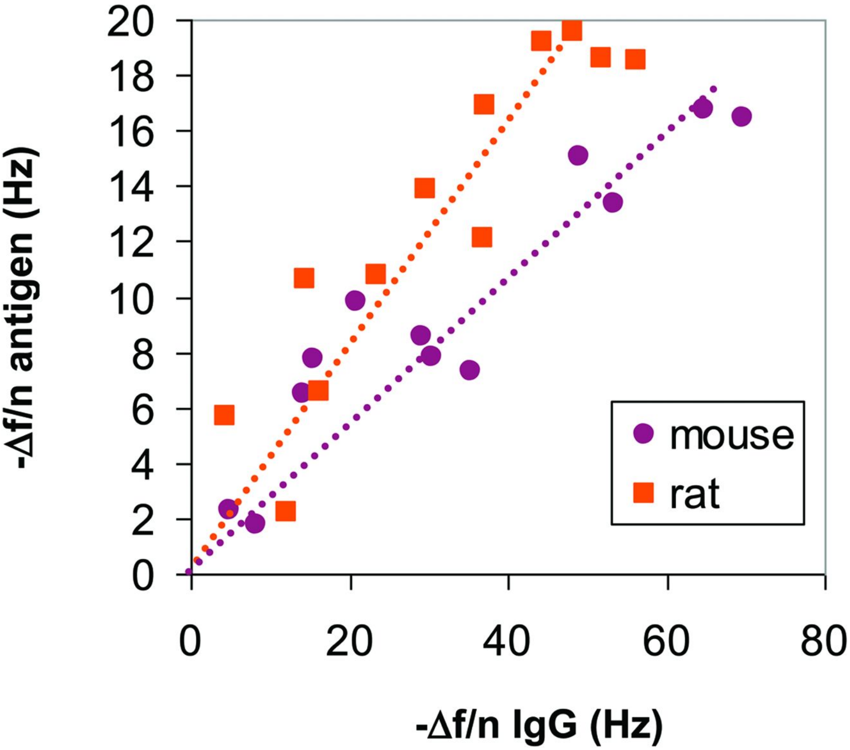

Figure 4. Evolution of Δf recorded by QCM upon antigen binding as a function of Δf recorded for IgG adsorption in the same experiment. The results are reported for the 8 different IgGs tested, adsorbed from three different concentrations each (closed circles for mouse IgGs and closed squares for rat IgGs). The broken lines are visual guides highlighting correlations.

BSA is commonly used to block surface sites remaining available after IgG adsorption, in order to prevent unspecific binding of the antigen to the surface. This is illustrated in Figure 5, in which the Δf recorded upon BSA adsorption is plotted as a function of Δf recorded upon the previously performed IgG adsorption step. A clear inverse correlation is observed, showing that when the adsorbed IgG amount increases, less BSA molecules can be further added to the adsorbed layer. At the highest IgG adsorbed amounts (Δf ~70 Hz), a Δf close to zero is actually observed for the BSA adsorption step. It should be kept in mind that exchanges between the adsorbed IgG layer and BSA molecules brought in solution may occur, resulting in no net increase (or even a decrease since the molar mass of albumin is lower than the one of IgGs) of mass detected by QCM. On polystyrene, protein adsorption is however generally found to be rather irreversible, and such exchanges are not favored (*13*). More particularly, Elgersma et al. (*14*) studied the effect of BSA addition in the solution on a layer of IgGs previously adsorbed on polystyrene. At pH 7, the adsorbed amount, as estimated from reflectometry results, was shown not to be affected, suggesting the absence of exchange between these proteins.

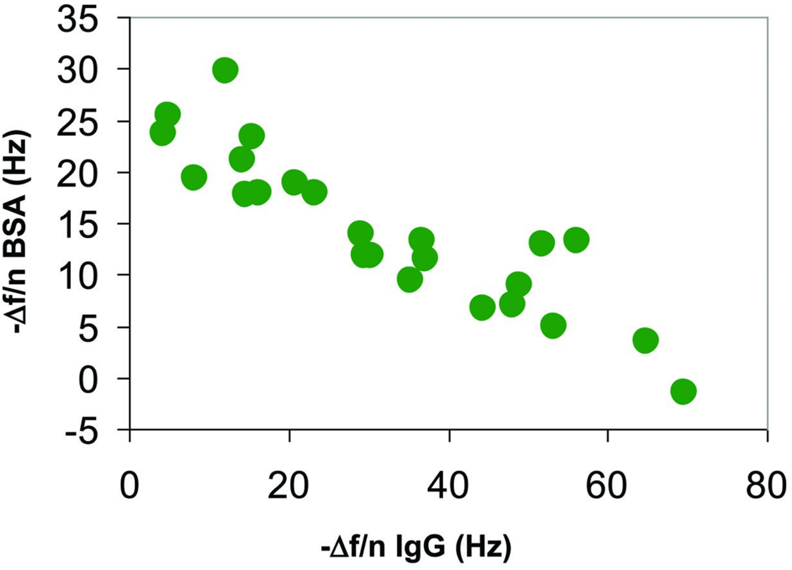

Figure 5. Evolution of Δf recorded after the BSA blocking step as a function of Δf recorded upon IgG adsorption in the same experiment. The results are reported for the 8 different IgGs tested, adsorbed from three different concentrations each.

IgGs Orientation Simulated Using RSA Modeling

RSA modeling was performed to tentatively clarify the evolution of IgGs orientation within adsorbed layers upon increasing the surface coverage. Figure 6 shows snapshots of the progressively filled surface, together with the computed end-on / flat orientation ratio at each depicted stage of the process.

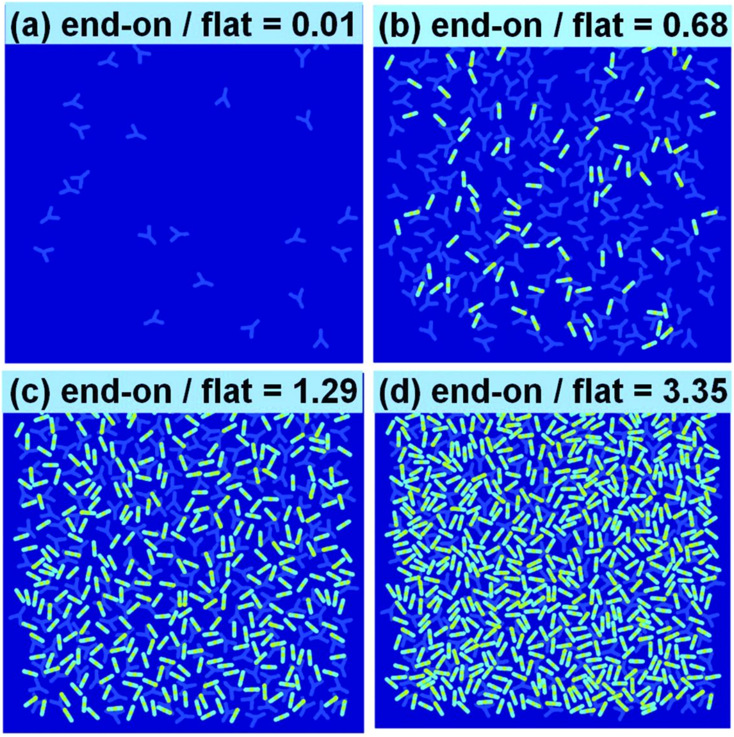

Figure 6. Snapshots (from a to d) illustrating the progressive coverage of the surface with IgG molecules adsorbed in flat orientation (medium blue) or in end-on orientation (light blue). The yellow areas refer to overlapping between molecular parts present in the first and the second layers defined for RSA modeling (see text for details).The end-on / flat orientation ratio corresponding to each depicted stage of the process is given in inset. (see color insert)

At the beginning of the filling process, since the probability is high that enough surface area is available for end-on adsorbed IgGs to shift to flat orientation, IgG molecules are mostly adsorbed in flat orientation. When the surface is progressively filled, this probability is reduced, and IgGs adsorbed in end-on orientation start to stay in this orientation, which increases the end-on / flat orientation ratio. Finally, in the last stages of the surface filling procedure, the only spaces available at the interface become too small to accommodate IgGs in flat orientation, and only end-on oriented IgGs continue filling the surface, which causes a high increase of the end-on / flat orientation ratio.

This is further illustrated in Figure 7, which summarizes the whole virtual adsorption process. Up to a total adsorbed amount of 1.4 pmol/cm^2, the amount of IgGs adsorbed in flat orientation is higher than the one of end-on adsorbed IgGs. At higher adsorbed amounts, the amount of IgG molecules in flat orientation does not increase anymore, while there is a sharp increase of adsorption in end-on orientation. The maximum achievable adsorbed amount is of about 3.3 pmol/cm², which corresponds to 4.8 mg/m². At this surface concentration, the end-on / flat ratio reaches a value of 3.38. A surface concentration of 2 mg/cm² is expected for a closed-packed layer of flat IgGs, while values between 2.6 and 5.5 are expected for end-on adsorbed IgGs, depending on the contraction of their Fab fragments (*4*). The value obtained here by RSA simulation seems thus reasonable, since close-packing cannot be achieved when random adsorption is considered, but on the other hand, the combination of flat and end-on adsorbed molecules increases the adsorbed amount.

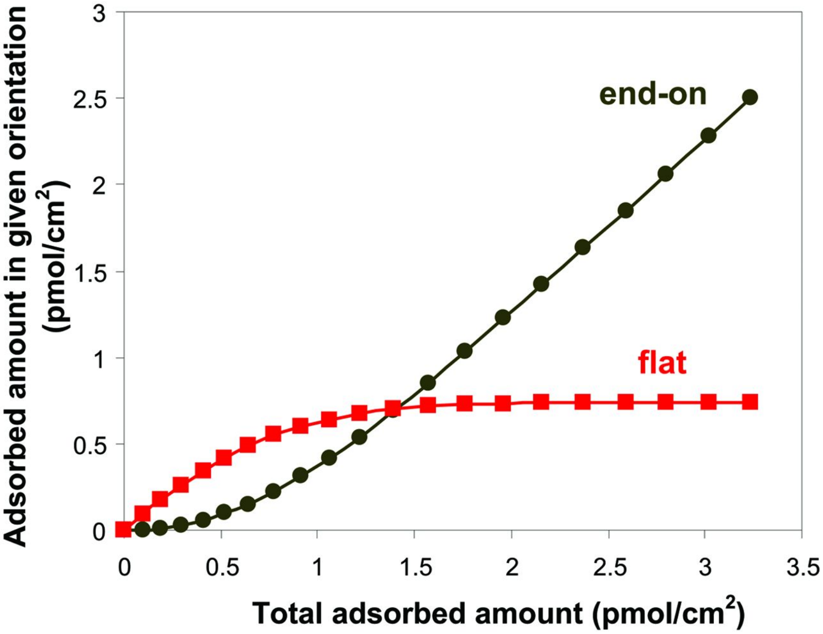

Figure 7. Results of RSA modeling : evolution of the adsorbed amount of IgG molecules in a given orientation (closed circles: end-on, closed squares: flat) as a function of the total adsorbed amount.

Experimental Observations versus Modeling Outputs

Besides allowing differences in behavior related to IgGs origin and isotype to be observed, our QCM results show that the bound antigen to adsorbed IgG ratio is in the range of 0.5 to 1. We observed however that this ratio does not vary much with the adsorbed amount, *ie* it remains quite constant when the adsorbed IgG amount increases.

RSA modeling was used to highlight the fact that although IgG adsorption in flat orientation is *a priori* energetically more favorable on hydrophobic substrates, a significant amount of end-on adsorbed IgG can be found in the adsorbed layer. This is due to the much lower surface area occupied by the latter compared to the former. After the surface is filled to a certain level by IgG molecules adsorbed in flat orientation, the low surface area of the left interfacial spaces does not allow much more adsorption in that orientation, but many more IgG molecules can accommodate in these left spaces in end-on position. At high level of surface coverage, a majority of the adsorbed IgG molecules are thus in end-on position.

In the present modeling approach, we only considered two orientations *ie* flat and end-on. This constitutes of course a very simplified view. Moreover, we only considered end-on adsorption with the two variable parts of IgG molecules standing upwards. Actually, if one of the variable parts is used for adsorption, very similar results would be obtained, but only one binding site would then be available for antigens instead of two. It would still lead to the conclusion that the amount of binding sites pointing outwards is increasing with surface coverage.

We can first compare the adsorbed amount predicted by RSA modeling to the values computed from QCM experiments with the range of antibodies studied here. The values extracted from QCM data for the highest IgG concentration in solution are for most of the IgGs studied roughly two times higher than the value of 3.3 pmol/cm^2 predicted by RSA modeling. The value obtained from modeling depends of course on the shape and dimensions chosen to simulate IgG molecules. However, the most important difference certainly arises from the presence of coupled water in the adsorbed layer, which is probed by QCM together with the adsorbed IgGs (*9*). Water could thus account for about half of the detected mass.

In the work of Wiseman et al. (*2*), for the adsorption of a monoclonal anti-streptavidin human IgG1 on a model hydrophobic substrate, the dissipation shift recorded by QCM increased exponentially when the IgG adsorbed amount increased. This may suggest a higher water content in the adsorbed layer at high surface occupancy, which could result from the more important presence of end-on-oriented molecules. The progressive increase of IgG molecules adsorbed in end-on position with surface coverage predicted here by RSA modeling fits thus well with the conclusions of the study of Wiseman et al. (*2*). On the contrary, our QCM data show a quite constant bound antigen to adsorbed IgG ratio with increasing adsorbed amount. There might be different tentative explanations to this discrepancy.

First, the increased presence of coupled water in the adsorbed layer with surface coverage may lead to an overestimation of the IgG adsorbed amount. Consequently, the antigen to antibody ratio measured when higher IgG concentrations are used for adsorption would be decreased. In the present study, however, ΔD values were always very low, and were roughly linearly correlated to Δf values (results not shown), indicating that the water content of the adsorbed layer remains quite constant whatever the surface coverage.

Second, the antigen used in the present study (DNP) is coupled to albumin to allow its detection by QCM. This may lead, on the one hand, to steric hindrance in reason of the size of albumin. Albumin shape can be assimilated to an equilateral triangle with sides of ~8 nm and a thickness of ~3 nm (*15*). On the other hand, 30 to

40 DNP molecules are coupled to each albumin molecule, allowing multivalency effects. The detection of one albumin molecule may actually account for multiple binding events. These two effects will be amplified at high IgG surface coverage, due to the proximity of variable parts of different IgG molecules in that case. This would cause the bound antigen to adsorbed IgG ratio to remain relatively constant with the IgG adsorbed amount, despite the higher proportion of IgGs adsorbed in end-on orientation at higher surface coverage.

A third explanation to the relatively constant antigen binding level with IgG adsorbed amount could reside in the role played by albumin used for the blocking step applied between IgG adsorption and antigen binding. Our results indicate that the lower the IgG adsorbed amount, the higher the albumin adsorbed amount upon blocking. The adsorbed albumin molecules may actually modify the orientation of previously adsorbed antibodies. Albumin is a soft protein (*16*), and tends to denature in contact with hydrophobic surfaces. Upon relaxation at the interface, it may provoke a change of orientation of adsorbed IgGs, which would cause a better availability of the variable parts. Similarly, it was shown that the availability of cell-binding domains of adhesion proteins was increased by adsorbing them together with albumin (*17*, *18*). In these latter studies, albumin was however brought in solution simultaneously to the investigated proteins. It is difficult to predict if albumin may play a similar role when it is brought at the interface after IgG adsorption has already taken place. If this was the case, even though RSA modeling predicts adsorption in flat orientation at low surface coverage, orientation could change to end-on after albumin adsorption, thereby increasing recognition by the antigen.

Conclusion

The adsorption of 8 different IgG isotypes from rat and mouse, all directed against DNP, and their antigen binding efficiency was monitored using QCM. The results show that the adsorbed IgG amount increases with the IgG concentration in solution, and that the maximum adsorbed amount differs from one isotype to another, the highest adsorbed amount being recorded for IgG 2aκ from mouse. A blocking step, consisting of BSA adsorption, was applied before antigen binding. The QCM data show an inverse correlation between the IgG and BSA adsorbed amounts, in line with the fact that albumin molecules are expected to fill the empty spaces remaining between IgG adsorbed molecules at low IgG adsorbed amount. Antigen binding was then shown to be the most efficient for rat antibodies, which points to their better orientation upon adsorption. For a given IgG, the ratio of bound antigen to adsorbed IgG was relatively constant for different IgG adsorbed amounts, which could mean that the fraction of IgG molecules oriented with their variable parts pointing upwards remains quite constant whathever the adsorbed amount.

RSA modeling was performed to tentatively clarify the evolution of IgG molecule orientation upon increasing the surface coverage. The results of modeling show that the fraction of IgG molecules adsorbed in end-on orientation increases with the surface coverage, owing to the fact that, when the surface coverage becomes higher, the only spaces available at the interface are too small to accommodate IgGs in flat orientation, and only end-on oriented IgGs continue filling the interface. The apparent discrepancy between the experimental results collected using QCM and the theoretical results obtained through RSA modeling could be explained by a variable content in coupled water in the adsorbed layers depending on surface coverage, by steric hindrance and multivalency effects upon antigen binding, or by the role of albumin molecules used to prevent non specific adsorption of the antigen.

Acknowledgments

The author wishes to thank Pierre de Thier for his strong involvement in the present work, and Kevin Mc Evoy and Paul Rouxhet for useful discussions. This work was funded by Région Wallonne (Belgium), under the frame of the AMOVIM project. Colleagues involved in the project are gratefully acknowledged for their stimulating ideas.

References

1. Roitt, I. M.; Brostoff, J.; Male, D. K. *Immunology*, 3rd ed.; Mosby Year Book Europe: London, 1993; 416 pp.
2. Wiseman, M. E.; Franck, C. W. *Langmuir* **2012**, *28*, 1765–1774.
3. Giacomelli, C. E. In *Encyclopedia of Surface and Colloid Science*, 2nd ed.; Somasundaran, P., Ed.; Taylor and Francis: Oxford, U.K., 2006; Vol. 1, pp 510−530.
4. Buijs, J.; Lichtenbelt, J. W. T.; Norde, W.; Lyklema, J. *Colloids Surf., B* **1995**, *5*, 11–23.
5. Petrash, S.; Cregger, T.; Zhao, B.; Pokidysheva, E.; Foster, M. D.; Brittain, W. J.; Sevastianov, V.; Majkrzak, C. F. *Langmuir* **2001**, *17*, 7645–7651.
6. Xu, H.; Lu, J. R.; Williams, D. E. J. *Phys. Chem. B* **2006**, *110*, 1907–1914.
7. Lu, B.; Smyth, M. R.; O'Kennedy, R. *Analyst* **1996**, *121*, 29R–32R.
8. Reviakine, I.; Johannsmann, D.; Richter, R. P. *Anal. Chem.* **2011**, *83*, 8838–8848.
9. Reimhult, E.; Larsson, C.; Kasemo, B.; Höök, F. *Anal. Chem.* **2004**, *76*, 7211–7220.
10. Schaaf, P.; Talbot, J. *J. Chem. Phys.* **1989**, *91*, 4401–4409.
11. Schaaf, P.; Talbot, J. *Phys. Rev. Lett.* **1989**, *62*, 175–178.
12. Tarjus, G.; Schaaf, P.; Talbot, J. *J. Chem. Phys.* **1990**, *93*, 8352–8360.
13. Nonckreman, C. J.; Rouxhet, P. G.; Dupont-Gillain, C. C. *J. Biomed. Mater. Res., Part A* **2007**, *81*, 791–802.
14. Elgersma, A. V.; Zsom, R. L. J.; Lyklema, J.; Norde, W. *Colloids Surf.* **1992**, *65*, 14–28.
15. Carter, D. C.; Ho, J. X. *Adv. Protein Chem.* **1994**, *45*, 153–203.
16. Norde, W. *Colloids Surf. B* **2008**, *61*, 1–9.

17. McClary, K. B.; Ugarova, T.; Grainger, D. W. *J. Biomed. Mater. Res.* **2000**, *50*, 428–439.
18. Lewandowska, K.; Balachander, N.; Sukenik, C. N.; Culp, L. A. *J. Cell Physiol.* **1989**, *141*, 334–345.

Chapter 22

Material-Driven Fibronectin Fibrillogenesis

Marco Cantini,[1] Cristina González-García,[1]
Virginia Llopis-Hernández,[1] and Manuel Salmerón-Sánchez*,[1,2]

[1]Center for Biomaterials and Tissue Engineering,
Universitat Politècnica de València, Valencia, Spain
[2]CIBER de Bioingeniería, Biomateriales y Nanomedicina, Valencia, Spain
***E-mail: masalsan@fis.upv.es. Tel : + 34 96 387 72 75. Fax: +34 96 387 72 76**

Publication Date (Web): December 12, 2012 | doi: 10.1021/bk-2012-1120.ch022

Material-driven fibronectin fibrillogenesis is a novel route to engineer the network structure and biological activity of fibronectin fibrillar matrices in analogy with their physiological cell-mediated assembly. We identify specific surface chemistries that promote the cell-free formation of physiological-like fibronectin fibrils in a time- and concentration-dependent process. Our most recent and relevant results, reviewed in the chapter, demonstrate the role of this material-induced fibrillogenesis in cell adhesion, extracellular matrix organization and degradation, and cell differentiation.

Introduction

The need for new synthetic materials able to serve as bio-inspired scaffolds for tissue engineering has driven multidisciplinary efforts for the identification of cell-free routes able to recapitulate the properties of the extracellular matrices (ECMs). Cells within tissues are in fact surrounded by fibrillar matrices that support and regulate cell adhesion, migration, proliferation and differentiation. Fibronectin (FN) is a core ECM component, whose organization into fibrillar networks is driven by cells through an integrin-mediated process involving contractile forces. In the first part of the chapter we describe this so-called cell-mediated FN fibrillogenesis, while the second part reviews the methods that have been proposed up to now seeking to reproduce FN fibrils in the absence of cells. These methods range from the use of denaturant agents to the use of

In Proteins at Interfaces III State of the Art 2012; Horbett, T., et al.;
ACS Symposium Series; American Chemical Society: Washington, DC, 2012.

mechanical force to stretch and assemble the molecules into fibrils. Finally, the organization of FN into a physiological fibrillar network upon adsorption onto a specific surface chemistry has been recently proposed by us: the last part of the chapter demonstrates cell-free, material-induced FN fibrillogenesis into a matrix with enhanced biological activity.

Cell-Driven Fibronectin Fibrillogenesis

The extracellular matrix (ECM) is a dynamic and heterogeneous meshwork of fibrillar and non-fibrillar components that provide an active microenvironment for cell adhesion, differentiation, migration and proliferation. It acts as a reservoir for growth factors and fluids and can be assembled into elaborated structures participating in basement membranes and providing a scaffold for tissue organization; moreover, it regulates numerous cell functions by activating multiple signaling pathways at adhesion sites. ECM is composed of collagens, laminins and other glycoproteins such as fibronectin (FN). These structural ECM components are secreted by cells as soluble protein units, which are assembled into functional supramolecular structures in a highly regulated manner (*1–3*). The ECM also plays an important role in disease: defects in assembly stop embryogenesis, deranged assembly promotes scarring, tumorigenesis and fibrotic disease; delayed assembly provokes birth defects, chronic wounds and skeletal malformations (*4*).

Fibronectin is a ubiquitous glycoprotein and the core component of the ECM. It is synthesized by adherent cells which then assemble it into a fibrillar network in an integrin binding-dependent mechanism (*5*). The assembly of FN matrix is the initial step which orchestrates the assembly of other ECM proteins and promotes cell adhesion, migration and signaling. The FN matrix is formed by fibrils that form linear and interconnected networks; thin fibrils predominate in early stages of matrix assembly (5 nm diameter) and, as the matrix matures, these fibrils cluster together into thicker ones (25 nm diameter) (*4*).

The functional properties of the FN matrix are diverse. FN fibrils possess binding sites for multiple ECM components needed for the assembly of several other ECM proteins. Moreover, they provide support for cell adhesion receptors (most notably integrins) that transduce signals triggering cell fate (*1*, *2*). FN matrix also controls the availability of growth factors, for example regulating the activation of TGF-β (*6*). Therefore, FN matrix has an important role for normal cell adhesion and growth, and plays a critical role in early development (*7*).

Fibronectin Structure

FN is a single gene-encoded protein. Its 8 kb mRNA can be alternatively spliced allowing the expression of 20 monomeric isoforms in humans and up to 12 in mice (*8*), which may result in an even larger variety of FN isoforms if we consider the possible combinations between monomers to form FN dimers. The most common mechanism of splicing generates the two major different forms of

FN: plasma (pFN) and cellular FN (cFN). pFN is produced by hepatocytes and secreted into the blood, where it remains in a soluble form until the activation of haematopoietic cells' integrins by a platelet-mediated mechanism allows pFN to bind and assemble into fibrils, which are required for thrombus growth and stability (*9*, *10*). On the other hand, cFN is secreted by cells as a dimer in a compact globular structure and then is assembled into fibrils (insoluble form) in a cell-dependent process.

FN is a multidomain protein as illustrated in Figure 1. It contains domains to interact with other ECM proteins, glycosaminoglicans (GAGs), integrins, other FN molecules and also pathogens such as bacteria (*11*). Each subunit of the FN molecule ranges in size from 230 to 270 kDa, depending on alternative splicing of the mRNA, and binds into dimers via two disulfide bonds at the C-terminus of the protein. FN contains three types of repeating modules, types I, II and III (Figure 1). The type I and II units contain two intramolecular disulfide bonds to stabilize the folded structure, while type III units lack this kind of bridges. Both type I and II protein modules are structured in β-sheets enclosing a hydrophobic core that contains highly conserved aromatic amino acids (*4*, *11*).

Extra type III repeats (A and B) are produced by alternative splicing and included in cFN molecules, but they are not present in pFN; it seems that the alternative exons are not necessary for matrix assembly, but lacking them may affect matrix levels (*4*, *11*). A variable region V is present in the vast majority of cFN subunits, but only in one subunit of the pFN dimer. Results concerning this region suggest that it is essential for FN dimer secretion (*13*) and that it provides the binding site for $\alpha_4\beta_1$ integrin (*14*).

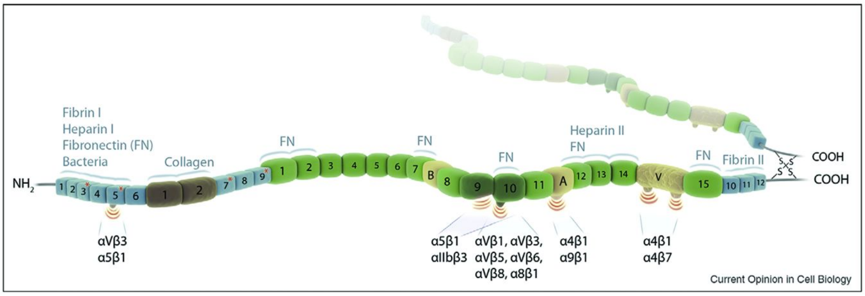

Figure 1. Molecular structure of FN that consists of three different modules (type I, blue; type II, brown; type III, green). The alternatively spliced extradomains B, A and variable region (V) are also indicated. The FN dimer forms via two disulfide bonds at the C-terminus. Integrin binding sites are indicated, as well as other binding domains for FN, collagen, fibrin, heparin and bacteria. Reproduced with permission from ref. (12). Copyright 2008 Elsevier.

Essential Domains for FN Assembly

FN matrix assembly is a cell-dependent process mediated by the binding of FN dimers to integrin receptors. The essential domains for FN assembly include:

- FN dimerization, which depends on the covalent association of the subunits mediated by a pair of disulfide bonds at the C-terminus of the FN molecule (Figure 1).
- The 70-kDa fragment, which extends from type I_1 to I_9, including the N-terminal assembly and the collagen/gelatin binding domains. This fragment binds to cells in monolayer culture and, when added in excess, it blocks FN matrix assembly. Similarly, the assembly is blocked when antibodies to this region are used (*15*, *16*). Within the 70-kDa fragment, the 40-kDa collagen/gelatin binding modules do not appear to play a direct role in the assembly. It seems that the binding activity resides only in the type $I_{1\text{-}5}$ portion of the molecule (the N-terminal assembly domain): it is the nexus point that binds FN molecules to each other by noncovalent interactions (*17*).
- The Arg-Gly-Asp (RGD) sequence located in repeat III_{10} and the synergy sequence PHSRN located in repeat III_9, whose binding to $\alpha_5\beta_1$ integrin is required for the cell-mediated FN assembly to occur (*18*). Although both sites are required for fibril formation, the synergy site is not essential because matrix levels are drastically reduced but not ablated with FN lacking this sequence (*19*). Not only $\alpha_5\beta_1$ integrin binds to RGD (Figure 1), but also several additional integrins, including all members of the α_v subfamily, $\alpha_8\beta_1$, $\alpha_9\beta_1$ and the platelet-specific $\alpha_{IIb}\beta_3$. Interestingly, in absence of $\alpha_5\beta_1$ integrin expression in cells or ablation of α_5 integrin gene in mice, FN can still be assembled by the operation of other integrins, most notably the α_v integrin subfamily (*20*, *21*). However, the α_v-class-produced fibrils are shorter and thicker than the α_5-produced (*12*).

As mentioned above, the N-terminal assembly domain $I_{1\text{-}5}$ is essential for FN fibrillogenesis; although, other FN binding domains are implicated in matrix assembly: $III_{1\text{-}2}$ and $III_{12\text{-}14}$ can bind FN; in addition, III_1 can bind to III_7, and $III_{2\text{-}3}$ can interact with $III_{12\text{-}14}$ (*11*). All these domains can promote FN fibrillogenesis due to the property of binding FN, but they can also participate in intramolecular interactions that keep soluble FN in a compact form (*22*).

FN Fibrillogenesis and Regulation of Matrix Assembly

FN in solution has a compact conformation and does not form fibrils even at extremely high concentrations. This compact form is maintained by intramolecular interactions between $III_{2\text{-}3}$ and $III_{12\text{-}14}$ modules (*22*). FN-integrin binding induces integrin clustering, which groups together cytoplasmic molecules such as FAK, Src Kinase, paxillin and others, promoting the formation of focal complexes. These complexes activate the polymerization of the actin cytoskeleton and kinase cascades-mediated intracellular signaling pathways (*23*).

Receptor clustering by dimeric FN helps to organize FN into short fibrils. After that, the contractility of the cytoskeleton contributes to FN fibril formation (*24*, *25*). The stretching due to cell contractility provokes a progressive extension of the FN molecule and the exposure of binding sites that mediate lateral interactions between FN molecules. Indeed, FN has intrinsic protein-disulfide isomerase activity in the C-terminal module I_{12}, and this activity may introduce intermolecular disulfide bonds within fibrils (*26*). Initial thin fibrils then grow in length and thickness as the matrix matures and FN fibrils are converted in an insoluble form (*4*). Proper integration of extracellular signals with active intracellular pathways plays a crucial role in the initiation, progression and regulation of FN matrix assembly (*27*).

Cell-Free Assembly of Fibronectin Fibrils

The need for controllable and reproducible *in vitro* models of fibronectin (FN) fibrils and for new synthetic materials able to serve as bio-inspired scaffolds for tissue engineering has driven the efforts in biology and regenerative medicine for the identification of cell-free routes able to induce FN fibrillogenesis. These routes are based on the assumption that unfolding of soluble FN dimers from their globular conformation is needed for FN-FN interactions to occur, leading eventually to FN polymerization and fibril formation. The methods that have been used in literature include:

- addition of reducing (*28*, *29*) or oxidizing (*30*) agents to the protein solution;
- use of denaturing (*31–34*), cationic (*35*, *36*) or anionic (*37*, *38*) compounds;
- use of peptidic FN fragments (*39–41*);
- force-based assembly, via application of mechanical tension (*42–46*) or shear forces (*47–57*);
- surface-initiated assembly (*58–62*).

Williams and co-workers firstly found that reduction of FN by dithiothreitol (DTT) induced the self-assembly of plasma FN via unfolding of disulfide-stabilized globular domains and subsequent promotion of non-covalent binding interactions among FN molecules (*28*). Sakai et al. demonstrated that a disulfide exchange mechanism from intramolecular to intermolecular bonds is involved in FN multimers formation at low DTT concentration and suggested also the involvement of the terminal region of the FN chains, as well as of type I and type II repeats (*29*). Vartio also reported disulfide-bonded polymerization of FN, induced by low concentrations of strong oxidants, such as $FeCl_3$ and $CuSO_4$ (*30*).

Another cell-free method to induce FN fibrillogenesis *in vitro* involves the addition of denaturants to a protein solution. Mosher and co-workers first used guanidine as denaturing agent (*31*, *32*); denatured FN dimers partially expose their free sulfhydryl groups, allowing multimeric FN to form. Peters and collaborators studied the macromolecular structure of this kind of multimeric FN and observed fibrillar structures similar to the ones formed in culture by human skin fibroblasts using high-resolution cryo-scanning electron microscopy (cryo-HRSEM) (*33*, *34*). These fibrils had at least two distinct structural arrangements: the majority had a rope-like structure that appeared to consist of nodules (10-13 nm in diameter), while few ones adopted a straight conformation with a smooth surface. The former fibrils had one free end, whilst the latter had both ends attached to the substrate, suggesting that a factor favoring one conformational state over the other might have been the tension applied to the fibrils (*33*). The nodules were proposed to represent discrete domains of 3 to 4 type III repeats, as they could be labeled with the monoclonal antibody IST-2 to the III_{13-14} repeats in FN and they were observed in FN fragments that only contain type III repeats (*34*).

Also anionic molecules, specifically heparin, were found to induce FN fibrillogenesis in the absence of cells (*37*, *38*). Jilek and Hörmann found that FN was partially precipitated by heparin, and electron micrographs showed the presence of filamentous structures (*37*); the authors suggested that heparin induces the transition of FN from a globular to an elongated form, exposing masked binding sites responsible for self-association and therefore leading to the formation of fibrillar precipitates. Afterwards, Richter et al. observed the formation of fibrils, visible by phase-contrast microscopy, when heparin-induced FN precipitation was performed onto hydrophobized glass cover slides (*38*). Precipitation was considerably dependent on the ionic strength, indicating that electrostatic forces played a major role in the aggregation of FN. Electrostatic interactions were also involved in FN polymerization induced by polyamines (cationic molecules) (*35*, *36*).

Interaction of FN dimers with purified recombinant fragments of FN was shown to induce fibrillogenesis in the absence of cells (*39–41*). Morla and collaborators showed that anastellin, a C-terminal recombinant fragment from the first type-III repeat of FN (III_1-C) bound to FN and induced spontaneous disulfide crosslinking of the molecule (probably through disulphide exchange) into multimers of high relative molecular mass, which resembled matrix fibrils (*39*). Treatment of FN with this aggregation-inducing fragment also converted FN into a form with greatly enhanced adhesive properties (termed “superfibronectin”), which suppressed cell migration. Briknarová et al. later proved that the main structural features of anastellin resemble those of amyloid fibril precursors, implying some similarity between fibronectin and amyloid fibril formation (*41*). Hocking and co-workers obtained the formation of high molecular mass FN multimers using a recombinant III_{10} FN module (*40*). Authors suggested a mechanism where the interaction of the III_{10} fragment with the III_1 domain in intact FN promoted a conformational change within the III_1 module, which unmasked the amino-terminal binding site and triggered the self-polymerization of FN, leading to the formation of disulfide-stabilized multimers in the absence of cells.

Zhong et al. confirmed the importance of molecular unfolding for FN fibrillogenesis by applying mechanical tension to expose the self-assembly sites within FN, thereby enhancing the binding of soluble FN in the absence of cells (*42*). The role of mechanical tension for the formation of FN fibrils was further investigated by Baneyx and Vogel, who observed FN assembly into extended fibrillar networks after adsorption to a dipalmitoyl phosphatidylcholine (DPPC) monolayer in contact with physiological buffer (*43*). The authors suggested that mechanical tension caused by domain separation of the lipid monolayer pulled the proteins into an extended conformation, exposing cryptic self-assembly sites and allowing the formation of networks stabilized by disulfide crosslinking.

Spatz et al. also induced fibrillogenesis by applying mechanical tension to FN (*44–46*). This group developed a system where cell-free FN fibrillogenesis could be achieved through a two-stage process initiated by the shear-stress independent partitioning of globular FN molecules to the air/liquid interface, where they formed an insoluble two-dimensional sheet, followed by force-dependent fibrillogenesis along a superhydrophobic surface made of elastic micropillars. Specifically, globular FN molecules were found to assemble into an insoluble sheet at the air/water interface; the partitioning of FN to the interface apparently induced a mechanical deformation of the globular FN, allowing it to pre-assemble into a stable network. This is in agreement with the expectations that FN fiber formation requires proper alignment of the outer type I domains, enabling specific intermolecular interactions between the type I domains of different chains (*63*, *64*). Subsequent application of force to this FN sheet attached to a micropillar array resulted in the formation of rough fibers with globular subdomains, whose sizes were affected by the tension applied to the FN layer. The average force applied to the FN particles by micropillar bending was approximately 8 pN per molecule, which is within the range necessary for FN unfolding (*65–67*). HRSEM images of immunogold-labeled FN showed that force-induced fibrils displayed much more intense labeling than the relaxed FN particles, suggesting that mechanical stretching of FN fibers exposes cryptic antigenic sites that are not available in its globular conformation (*44*). Finally, Kaiser and Spatz adapted this force-induced FN fibrillogenesis to obtain a method for the production of highly regular arrays of nanofibrils from other extracellular matrix proteins besides FN, including collagen I (COL I) and laminin (*46*). These results were congruent with the model proposed by Guan et al. for the fabrication of DNA nanowires, indicating a common mechanism of polymer fibrillogenesis induced by de-wetting (*68*). The necessity for self-association sites was suggested by the observation that bovine serum albumin (BSA), even at high concentrations, did not yield nanofibrils, despite its ability to concentrate at the air/buffer interface (*44*, *46*). Moreover, the engineered ECM could be transferred from the micropillar array onto polyethylene glycol (PEG) hydrogels, reconstituting the nanofibrils in buffer and simultaneously eliminating the substrate microtopography.

Other cell-free routes for the force-induced assembly of FN were based on the application of shear forces to a FN solution in different setups, that included manual pulling of single fibrils out of a concentrated drop of FN (*47*, *49*, *51*, *53*, *56*, *57*), stirring of a FN solution in a ultrafiltration cell (*47*, *48*, *50*, *55*), and wet extrusion of a concentrated FN solution (*52*, *54*, *55*). The first method produced thin microscale FN fibrils by simply drawing them out from a small pool of a concentrated FN solution with a thin glass rod or a pipette tip and depositing them onto a substrate (*47*, *49*, *51*, *53*, *56*); FN was allowed to self-associate under the influence of a directional shear force (*47*). Manually deposited fibers pulled from concentrated solutions of soluble FN resembled *in vivo* FN fibers in diameter and composition (*49*). Fluorescence images of manually deposited fibers showed that submicron fibrils emerged from the surface of the FN solution and bundled together to form larger cables of fibrils (*56*). Mechanical characterization of these fibers revealed that they show signs of breakage only when stretched over 5-6 times their resting length, that high extensions involve unfolding of type III modules, and that the mechanically strained fibers clearly bind more N-terminal 70 kD FN fragment than the relaxed ones, suggesting that mechanical tension exposes cryptic binding sites for this fragment (*56*).

Instead of fibers, concentration of a FN solution under a continuous unidirectional stirring motion was used to produce oriented FN mats (*47*, *48*, *50*, *55*). The yield of FN mat was drastically improved in the presence of urea, which denatures FN by unfolding it into an elongated conformation (*69*) that favors lateral association and fibril growth (*48*). Finally, shear-dependent fibrillogenesis was achieved via wet extrusion of urea-denatured concentrated protein solutions (*52*, *54*, *55*). This method led to the production of large FN cables (up to 1.5 cm in diameter), which, once hydrated, had a parallel fibril alignment and a porous cross-sectional structure, with pore sizes between 10 and 100 μm in diameter (*55*).

The last cell-free route of FN fibrillogenesis is based on the unfolding of soluble FN as a result of its adsorption onto a material surface (*58*–*62*). For example, Nelea and Kaartinen described FN filament formation on a surface with negative potential (polysulfonated substrate) in the absence of cells (*60*). The height and width of FN filaments were close to those characteristic of the extended FN dimer, indicating that these filaments were being formed from alignment of extended FN, and as such, they could represent an initial alignment process during FN assembly. From the height profile analysis of AFM scans, the filaments were revealed to be formed of a chain with periodic arrangement of connected beads giving a "bead-on-a-string" appearance (*60*). The adsorption of FN onto a surface with high negative charge density was suggested by Pernodet et al. to open and extend the molecule via interaction with the $III_{12–14}$ modules (*58*). Interactions between $I_{1–5}$ and $III_{12–14}$ modules of two FN molecules would then create a staggered alignment (*70*–*72*), and position two type $III_{1–7}$ modules interacting with each other; the region spanning type $III_{1–7}$ modules has been reported to drive FN fibrillogenesis (*73*). Since type III modules are larger than other modules, two type $III_{1–7}$ regions could create a thicker stretch in the filament with the appearance of a bead. This would justify the "bead-on-a-string" appearance observed by Nelea and Kaartinen (*60*).

Finally, Feinberg and Parker demonstrated that surface-initiated assembly could be used to engineer multiscale, free-standing nanofabrics using a variety of ECM proteins (FN, LAM, FNG, COL_{I}, COL_{IV}) (*61*). The authors used protein-surface interactions to unfold ECM proteins and trigger their assembly. Specifically, the process involved adsorbing nanometer-thick layers of ECM proteins from a solution onto a hydrophobic surface at high density to partially unfold them and expose cryptic binding domains (*74*, *75*), transferring the ECM proteins in the unfolded state to a relatively hydrophilic, dissolvable surface, and thermally triggering surface dissolution to synchronize matrix assembly and its non-destructive release.

Finally, the formation of a physiological-like fibronectin network after adsorption on a particular surface chemistry was reported by us (*62*). Details of this process are provided in the next section.

Material-Driven Fibronectin Fibrillogenesis

The challenge of controlling and directing cellular responses has demanded significant efforts in regenerative medicine research to engineer materials that recapitulate the characteristics of the ECM, such as materials presenting cell-adhesive motifs or protease-degradable cross-links (*76*, *77*). However, material-based approaches to reconstitute the network structure and bioactivity of FN fibrillar matrices have not been established yet. As previously commented, the use of denaturing or unfolding agents and the application of forces to promote FN fibril assembly indicate that changes in the structure of FN are required to drive its assembly into fibers (*31*, *39*, *43*, *44*). In our group, we hypothesized that adsorption of individual FN molecules onto particular surface chemistries would induce exposure of self-assembly sites, driving FN fibril assembly, and we identified poly(ethyl acrylate) (PEA) as a potential surface chemistry suitable for this purpose (*78*, *79*). We investigated the organization of FN molecules at the material (PEA) interface and studied its analogy with the physiological cell-induced FN fibrillogenesis (*62*).

Physiological Organization of Fibronectin at the Material Interface

We analyzed the organization of FN at the material interface on two similar chemistries: poly(ethyl acrylate) (PEA) and poly(methyl acrylate) (PMA), which differ in one single carbon in the side chain (Figure 2a) (*62*). Both surface chemistries show similar wettability and total amount of adsorbed FN (Figure 2b). However, the conformation and distribution of the protein following passive adsorption onto these surfaces are completely different (Figure 2c). Interconnected FN fibrils are organized upon adsorption from a solution of concentration 20 μg/mL on PEA (Figure 2c), in a process that we refer to as material-driven fibrillogenesis, whereas only dispersed molecules are present on PMA (Figure 2c). FN fibril formation on PEA is dependent on the FN solution concentration, as lower concentrations result in dispersed adsorbed molecules (*62*). We next examined the role of the 70 kDa amino-terminal domain of FN in this material-driven fibrillogenesis process. As previously stated, the 70 kDa amino-terminal regions are known to be essential for cell-mediated FN assembly, and within this region, the $I_{1\text{-}5}$ repeats confer FN binding activity (*80*). This domain is not accessible in the folded, compact structure of FN in solution and a conformational change of the molecule is mandatory for physiological matrix assembly to occur (*11*). Strikingly, material-driven fibrillogenesis absolutely requires the 70 kDa amino-terminal region of FN. Indeed, addition of the 70 kDa fragment completely blocks the organization of FN at the material interface and only discrete molecular aggregates can be observed (Figure 2c), without any trace of the assembled FN network; the resulting adsorbed FN resembles the protein adsorbed onto the control PMA polymer. These results demonstrate that a particular polymer chemistry (PEA) drives assembly of adsorbed FN molecules into FN fibrils; this material-driven fibrillogenesis requires the 70 kDa amino-terminal domain of FN.

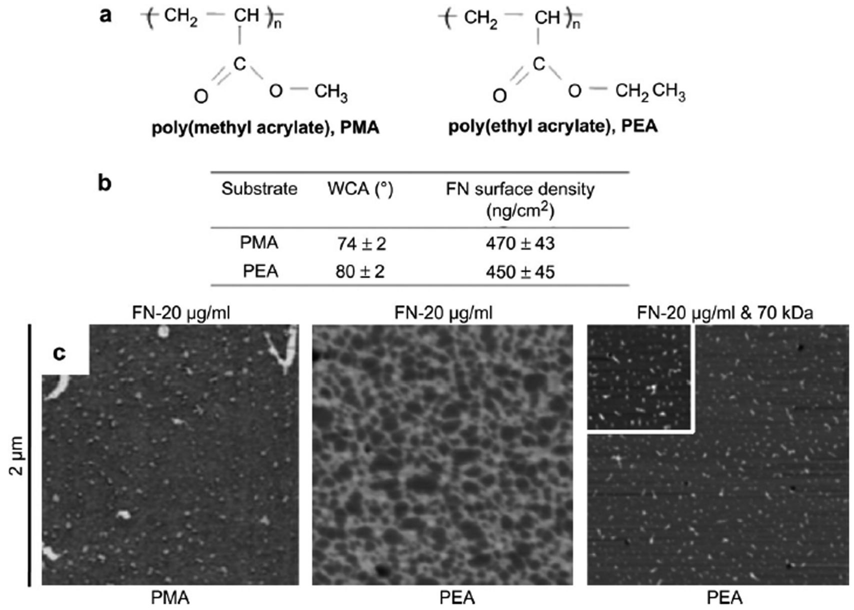

Substrate	WCA (°)	FN surface density (ng/cm^2)
PMA	74 ± 2	470 ± 43
PEA	80 ± 2	450 ± 45

Figure 2. FN adsorption on material substrates. a) Chemical structure of the polymers PEA and PMA. b) Water contact angle on the different substrates and equilibrium surface density of adsorbed FN from a solution of concentration 20 μg/mL. c) FN distribution on material substrates as obtained by AFM: globular aggregates on PMA and FN network on PEA after adsorption from a solution of concentration 20 μg/mL. FN fibrillogenesis is blocked on PEA in the presence of the amino-terminal 70 kDa FN fragment, leading to dispersed molecular aggregates. Reproduced with permission from ref. (62). Copyright 2011 Elsevier.

The dynamics of the formation of the FN network on PEA were followed via AFM at different adsorption times (*81*). At the very beginning of the adsorption process (10 s), isolated FN molecules are homogeneously distributed on the material. After 30 s of adsorption, the molecules tend to align suggesting the initial formation of intermolecular connections, which result in protein-protein contacts through the surface. After 60 s, AFM images reveal the formation of a protein network on the material surface. Increasing the adsorption time results in thickening the fibrils which make up the protein network (*81*). These results allow one to conclude that FN organization on the material interface occurs in a timescale that is adequate to be followed via AFM, whose acquisition time is in the minute range.

Seeking to follow the adsorption process in a more detailed way, a different experiment was planned. Instead of fixing the concentration of the solution from which the protein was adsorbed and varying the adsorption time, we fixed the adsorption time from solutions of increasing concentration of FN (*79*). Figure 3 shows AFM images for FN adsorbed onto PEA substrates after immersion for 10 min in protein solutions of different concentrations: 2, 2.5, 3.3, 5, 20, and 50 μg/mL. The lowest concentration (Figure 3a) results in isolated extended FN molecules homogeneously distributed on the material. For a concentration of 2.5 μg/mL (Figure 3b), a higher density of FN molecules is observed; extended FN molecules tend to align, suggesting the initial formation of intermolecular connections. FN conformation in Figure 3c suggests the incipient formation of a protein network on the material when FN is adsorbed from a solution with a concentration of 3.3 μg/mL. Protein adsorption from higher solution concentrations gives rise to the formation of FN networks on the material with higher cross-link density, i.e., a higher number of cross-link points and lower distance between them (*79*).

The development of a FN network in the absence of cells gains a distinct bioengineering interest because it is a way to improve the biocompatibility of materials. It is well documented that cells recognize faster and with higher affinity already assembled FN fibrils versus adsorbed protein (*11*, *23*). The existence of cell-free routes able to induce the formation of FN fibrils from isolated molecules has been described previously in this chapter and they include biochemical routes or the application of mechanical tension. In our case, the formation of FN networks on PEA (Figure 3) must be a consequence of the following sequence of events:

(1) Conformational change of FN upon adsorption on PEA. FN has a compact folded structure in physiological buffer, stabilized through ionic interactions between its arms (*22*). Its interaction with chemical groups of the substrate (a vinyl backbone with -$COOCH_2CH_3$ side chain) provokes conformational changes in the molecule that lead to the extension of the protein arms (Figure 3a). Adsorption onto slightly charged surfaces (net negative charge in the -COO^- group) gives rise to elongated structures of the molecule, as obtained for SiO_2 and glass (*74*, *75*). FN likely orients at the surface, so that its hydrophobic segments interact with the methyl groups of PEA, maybe throughout the heparin-binding fragment, as proposed for the FN-DPPC interaction (*43*), but with more efficient arm extension because of the net negative charge of the surface.

(2) Enhanced FN-FN interaction on the PEA substrate. As the adsorption process continues, the conformation of individual FN molecules favors FN-FN interactions involving the amino-terminal 70 kDa fragment (*74*), probably throughout the interaction between $I_{1\text{-}5}$ and $III_{1\text{-}2}$ domains located near the amino side (*8*). Figure 3b shows the relative orientation of two FN molecules compatible with this hypothesis.

(3) Formation of the FN network. New FN molecules are preferentially adsorbed in close contact to the proteins already present on the substrate (Figure 3c), probably as a consequence of the presence of polar-oriented FN molecules; this enhances the collision rate of FN self-assembly sites (*8*), giving rise to the initial formation of a protein network on the substrate. This process leads to a well-interconnected network of FN on the surface of the substrate (Figure 3) (*79*). Adsorption from solutions of higher concentrations leads to the formation of a protein network with thicker arms (panels d-f in Figure 3). The formation of a FN network on PEA is not a universal property of this protein. For example, a similar network was found for fibrinogen (*82*) and collagen IV (*83*), but only globular-isolated molecules were observed after laminin (*84*) and vitronectin adsorption (*85*).

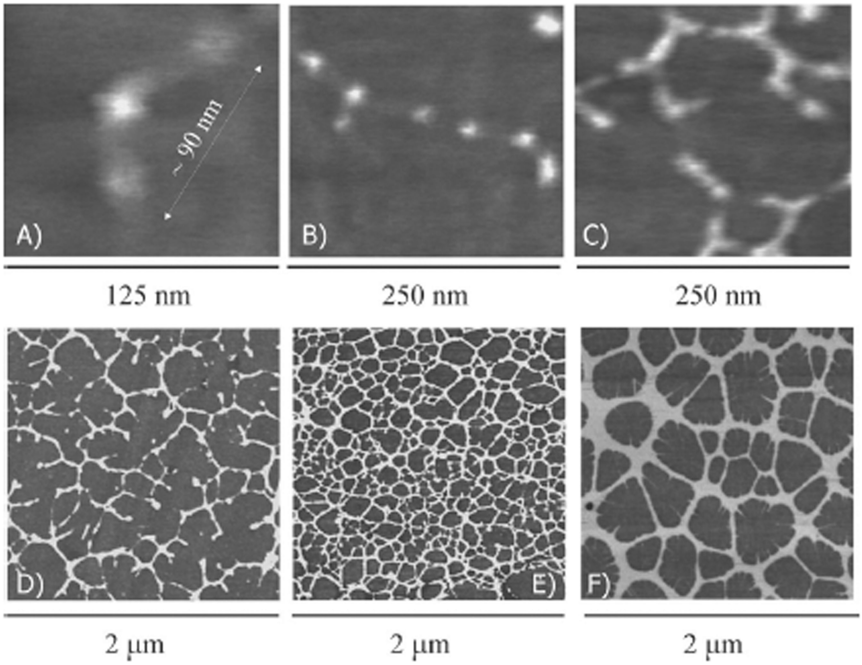

Figure 3. AFM phase imaging of FN molecules on PEA: (A) isolated molecule, (B) two FN molecules interacting through the amino-terminal ($I_{1\text{-}5}$ and $III_{1\text{-}2}$) domains, (C) assembly of FN molecules into an incipient network, (D) assembly of FN into a non-completely interconnected network, (E) interconnected FN network, and (F) thickening of protein network arms at higher concentrations. FN was adsorbed for 10 min from solutions with a concentration of 2, 2.5, 3.3, 5, 20, and 50 µg/mL, respectively. Reproduced with permission from ref. (79). Copyright 2009 American Chemical Society.

Biological Activity of the Material-Driven Fibronectin Fibrillogenesis

Given its similarities with the physiological assembly of FN, the material-driven FN fibrillogenesis is expected to yield a protein network with enhanced biological activity; indeed, the conformation adopted by the protein should promote the exposure of domains that favor the interaction with cells and other proteins (Figure 4).

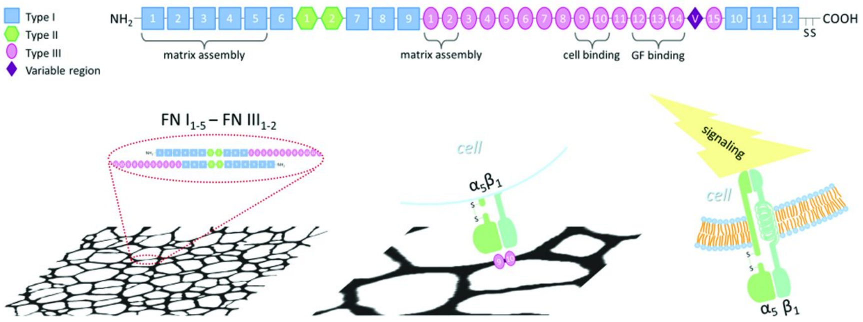

Figure 4. Molecular structure of a monomer of FN with indication of the main domains involved in matrix assembly, cell binding, or growth factor binding. The material-driven fibrillogenesis leads to the formation of a biologically active network through interactions between $I_{1\text{-}5}$ and $III_{1\text{-}2}$ domains.

A first evidence of the biological activity of this FN network was obtained by investigating cell adhesion on electrospun fibers of PEA. Random and aligned fibers of the polymer were obtained seeking to mimic the spatial organization of the extracellular matrix; the existence of a FN network assembled on the electrospun PEA fibers was assessed by AFM (*79*). Fibroblast adhesion studies demonstrated that this FN network is biologically active, more than the FN adsorbed on the underlying glass (Figure 5); this is supporting the hypothesis that the material-driven FN network shares some similarities with the physiological one (both of them are assembled via the 70 kDa-domain as explained previously). It is evident that cells tend to interact with PEA fibers rather than glass and start to orient, modifying their characteristic spread morphology, following the fibers' direction (Figure 5e,f). Complementary material in reference (*79*) shows a movie of living cells, which migrate throughout the surface, in a real tactile exploration, until a PEA fiber is found. Then, the cell morphology is modified to adapt the cell-substrate contact along the electrospun PEA fiber; also, the cells may "jump" from the supporting glass to the PEA fibers, preferring to move on the FN network.

In Proteins at Interfaces III State of the Art 2012; Horbett, T., et al.;
ACS Symposium Series; American Chemical Society: Washington, DC, 2012.

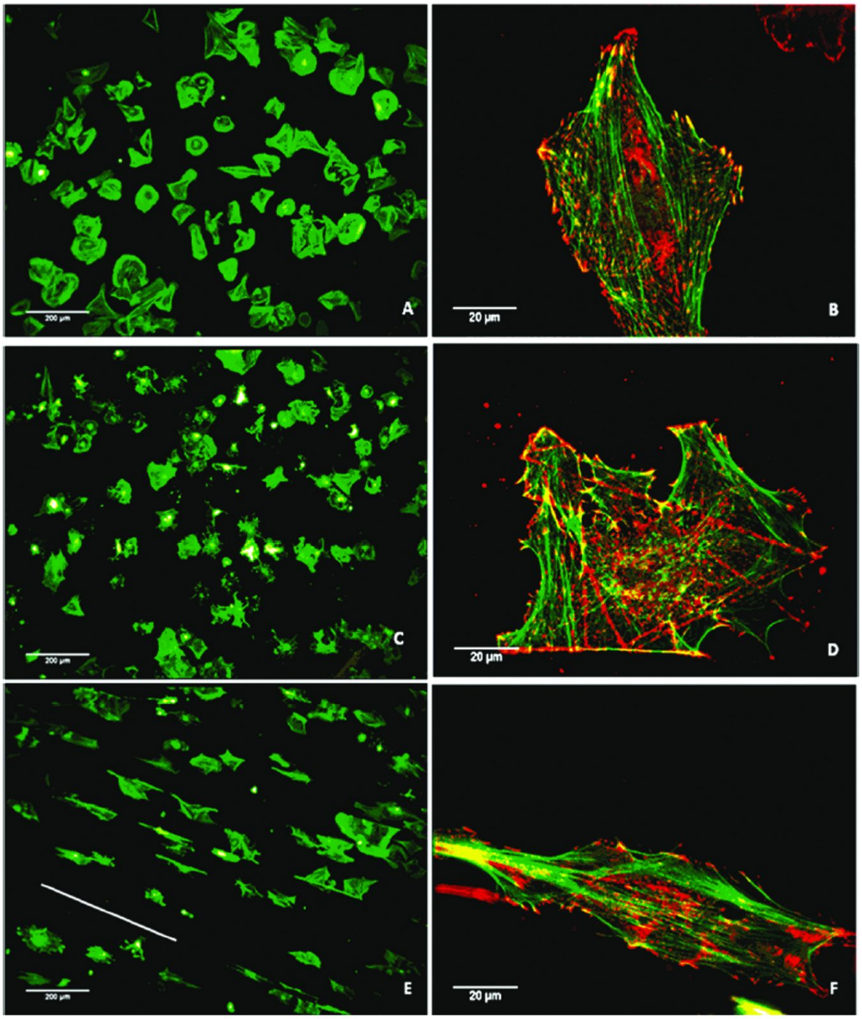

Figure 5. Overall morphology of fibroblasts adhering on (C and D) random and (E and F) aligned FN-coated PEA fibers compared to the (A and B) control of FN-coated glass visualized by actin (A, C, and E) or double stained for vinculin (red) and actin (green) (B, D, and F). The line in e represents the main direction of PEA fiber alignment. Magnification for A, C, and E, 10x: bar, 200 µm. Magnification for B, D, and E: 100x; bar, 20 µm. Reproduced with permission from ref. (79). Copyright 2009 American Chemical Society.

Cells adhering to the material-driven FN network show well-developed focal adhesion complexes and actin stress fibers. Interestingly, when adhering on random PEA fibers, cells tend to develop a rounded morphology with multiple projections, which resemble stellate morphology characteristic of cells in a 3D environment (Figure 5c,d). On the other hand, on the oriented fibers fibroblasts immediately acquire an extended morphology with asymmetrical organization of the adhesive complexes (Figure 5f), suggesting activation of their motility.

Late FN matrix formation, after 3 days of culture, is again influenced by the formation of the FN network on the PEA fibers, reflecting the high biological activity of the pre-organized protein. Matrix formation is excellent on both the PEA fibers and the control glass; however, in agreement with the initial cell adhesion, newly synthesized FN is preferentially deposited on PEA fibers (*79*). Thus, one can assume that, by tailoring the fiber orientation, we can control the organization of the provisional FN matrix secreted by the cells.

Besides organization, the ECM undergoes proteolytic degradation, which is a mechanism for the removal of the excess matrix usually associated with remodeling and mainly operated by a family of proteases known as matrix metalloproteinases (MMPs). The proteolytic remodeling of matrix proteins at the biomaterials interface has only recently received attention (*86–89*): in our group we have shown that the activation of proteolytic routes in MC3T3-E1 cells is a MMP-dependent phenomenon sensitive to surface chemistry by making use of FN-coated self-assembled monolayers (SAMs) with a controlled ratio of methyl/hydroxyl groups (*90*). Recently, we have demonstrated that the material-driven fibrillogenesis also affects the proteolytic degradation process: the activity of MMP2 and MMP9 is higher on the substrate (PEA) where a FN network is formed compared to PMA (Figure 6) (*91*).

We have also compared cell differentiation on the substrate-assembled FN network versus those substrates that do not promote FN fibrillogenesis. Particularly, we evaluated the biological activity of the material-driven FN networks by examining the myogenic differentiation process (*62*). The material-induced FN network supported significantly higher sarcomeric myosin expression and cell bipolar alignment and fusion into myotubes, markers of myogenesis (Figure 7a, PEA-20), as compared to the same substrate coated with a lower density of FN that does not lead to the fibrillar organization of the protein at the material interface, and to PMA polymer coated with the same density of FN but lacking any fibrillar organization (Figure 7a) (*62*). Surprisingly, myogenic differentiation was considerably more robust on the PEA-assembled FN matrix than on collagen type I, which represents the standard substrate for myogenic differentiation (*62*, *92*). It is important to emphasize that these differences in myogenic differentiation are not due to differences in the number of cells on the substrates (*62*).

In order to gain a deeper comprehension of the phenomena undelying the biological activity of the substrate-induced FN fibrils, we employed different blocking antibodies and FN fragments to assess the role of different parts of the FN molecule in the myogenic differentiation process (Figure 7b). Addition of the adhesion-blocking HFN7.1 antibody inhibited differentiation on PEA to levels found for the substrates on which FN is not organized into a network (Figure 7b, PEA-HFN7.1) (*62*). The HFN7.1 antibody binds to the flexible linker between the 9th and 10th type III repeats of FN where the integrin-binding domain is located, demonstrating that this domain is essential for myogenic differentiation on FN fibrils. Moreover, HFN7.1 is specific for human FN (adsorbed on the substrate) and does not cross-react with mouse FN (cell-secreted), indicating that the human FN adsorbed onto the substrate prior to cell seeding provided the dominant signal for differentiation. Then, we examined whether a recombinant fragment of FN spanning the 7th - 10th type III repeats ($FNIII_{7-10}$) would recapitulate the material-dependent differences in myogenic differentiation (*92*). $FNIII_{7-10}$ encompasses the integrin-binding domain of FN, but does not contain the domains involved in FN-FN interactions (I_{1-5} and III_{1-2} or III_{12-14} domains). Adsorption of this fragment onto PEA was found to yield minimal levels of myogenic differentiation (Figure 7b, PEA-$FNIII_{7-10}$), demonstrating that both integrin-binding domains and domains involved in FN-FN interactions are required for enhanced myogenic differentiation on PEA-driven FN matrices (*62*). Consistent with our observations for the FN network formation (Figure 2c), addition of the 70 kDa amino-terminal fragment during the adsorption process of FN blocked the differentiation of myoblasts on PEA (Figure 7b, PEA-70 kDa). This result demonstrates the importance of FN-FN interactions and of the fibrillar structure of the protein in the cell differentiation process. FN assembly via interactions involving the 70 kDa amino-terminal fragment is mandatory for the differentiation process to occur (*62*). As a control, when albumin (a protein with molecular weight similar to the 70 kDa fragment) is added during the network assembly process of FN, the formation of the network is not disturbed and myoblast differentiation levels are not affected (Figure 7b, PEA-BSA). Importantly, the addition of the 70 kDa FN fragment once the FN network is already assembled has no effect on the subsequent myoblast differentiation (*62*).

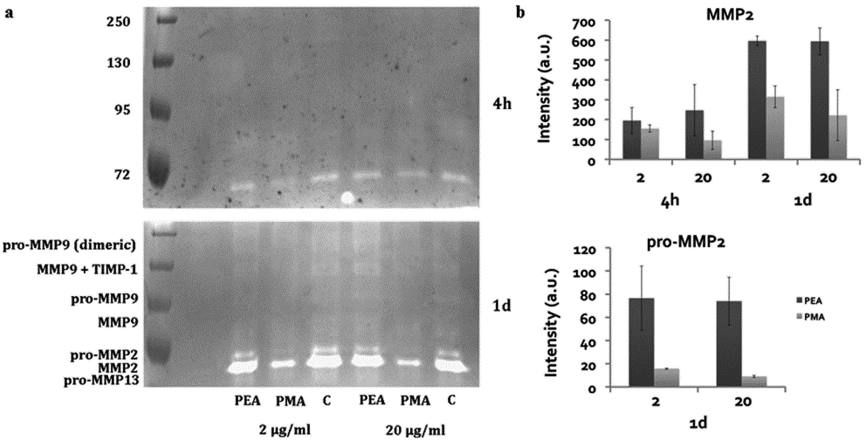

Figure 6. Effect of material-driven fibrillogenesis on matrix proteolytic degradation. a) Gelatin zymography showing the activity of MMP2, 9 and 13, and of their various forms (pro-MMP13, MMP2, pro-MMP2, MMP9, pro-MMP9, MMP9+TIMP1, dimeric pro-MMP9). b) Quantification of the gel bands for MMP2 and pro-MMP2.

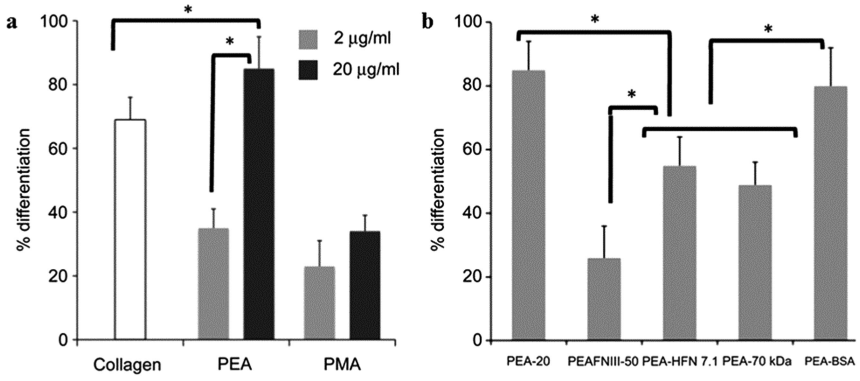

Figure 7. a) Myogenic differentiation as determined by the percentage of sarcomeric myosin-positive cells on the different substrates after adsorbing FN from solutions of concentrations 2 and 20 μg/mL. b) Both the central FN domain (FNIII$_{7-10}$) and the amino-terminal fragment (70-kDa) involved in FN fibrillogenesis enhance myogenic differentiation on the material-driven FN network on PEA. b) Myogenic differentiation as determined by the percentage of sarcomeric myosin-positive cells on the substrate-induced FN network (PEA-20), after coating PEA with a recombinant fragment of FN (FNIII7-10), blocking the central FN domain with HFN7.1 antibody (PEA-HFN7.1), after adsorbing FN altogether with the 70 kDa fragment, which blocked the formation of the FN network (PEA-70 kDa), and control experiment for the 70 kDa fragment using BSA instead (PEA-BSA). Statistically significant differences ($p<0.05$) are indicated with ∗. Reproduced with permission from ref. (62). Copyright 2011 Elsevier.

The effect of material-driven FN fibrillogenesis on myoblast differentiation was further studied by making use of gradients of adsorbed FN onto flat substrates of PEA (gPEA) and PMA (gPMA) (Figure 8) (*93*). FN gradients were obtained by pulling out the samples from a FN solution of concentration 10 μg/ml at a controlled velocity. The progressive formation of interconnected FN fibrils on PEA as the adsorption time increased was revealed by AFM. The independent FN clusters observed at one end of the substrate interconnected with each other as we moved to the center of the sample, finally establishing a fully developed network of FN fibrils. No fibril formation was detected for PMA, and, as the adsorption time increased, only a higher amount of globular FN molecules was found along the sample. The FN surface density gradient on PMA sustained homogeneous differentiation, while the assembly of FN fibrils on PEA led to a monotonic increase in the differentiation degree along the gradient. A statistically significant enhancement in myogenic differentiation was observed at the end of the gradient, where the FN network was fully developed. Both in gPEA and gPMA cell density increased monotonically alongside the FN gradient, with the differences more significant for PEA than PMA. Cells initially adhered uniformly along the FN gradient and then migrated in response to the biochemical gradient of signals provided by the formation of the FN gradient. Indeed, migration was more prominent along PEA, where FN adopts a more biologically active, physiological-like, distribution compared to PMA. This phenomenon is consistent with the diminished levels of differentiation on PEA with respect to PMA: cell migration is in fact inversely correlated with differentiation of myoblasts (*94*, *95*).

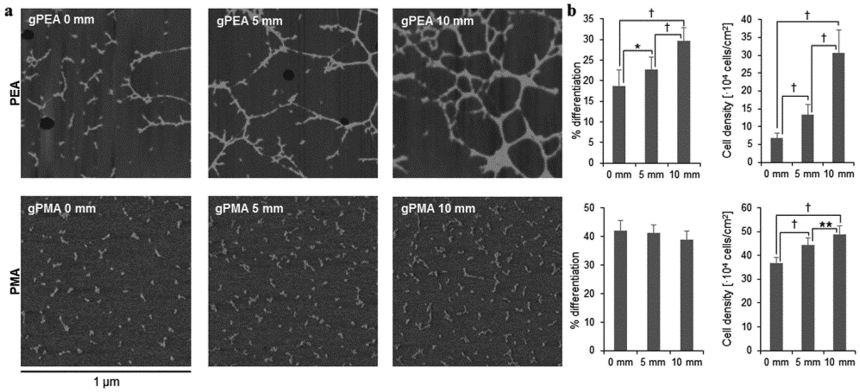

*Figure 8. Gradients of adsorbed FN. a) FN conformation along the gradient, as observed by the phase magnitude in AFM: on PEA FN gradually forms an interconnected network of fibrils, whilst on PMA no fibrillogenesis is observed, as FN maintains a globular conformation while the amount of adsorbed protein increases. b) Myogenic differentiation (as determined by the percentage of sarcomeric myosin-positive cells) and cell density at different positions along the gradients. Statistically significant differences (as determined by ANOVA) are indicated with *P<0.1, **P<0.05, †P<0.005). Reproduced with permission from ref. (93). Copyright 2012 Springer Science and Business Media.*

Taken together, these data further demonstrate the role of material-driven fibrillogenesis in myogenic differentiation. A gradient wherein the sole amount of FN was varied, but where the globular-like conformation of the protein was maintained (i.e., gPMA), did not yield any differential effect on myoblast differentiation and, still, supported cell migration. On the other hand, a gradient characterized by a gradual formation of FN fibrils (i.e., gPEA) led to cell migration and to a gradient of myogenic differentiation. We attributed the increases in cell differentiation along this gradient to the gradual formation of a network of FN fibrils (*62*) and a progressively higher cell density (*96*).

Besides myogenic differentiation, we investigated the role of FN fibrillogenesis in skeletal mesenchymal stem cells differentiation on PMA and PEA (*97*): in this case, we found that the differentiation towards the osteoblastic lineage, determined by quantifying protein levels for osteocalcin, osteopontin and Runx2, is enhanced on the substrate that does not induce the formation of a FN network (Figure 9). Moreover, by extending this study to another member of the family of the poly(alkyl acrylates), the poly(butyl acrylate), PBA, we identified a novel mechanism able to regulate the differentiation of skeletal stem cells, i.e., surface mobility.

PMA, PEA and PBA differ only in the number of carbons in their side chain, respectively 1, 2, and 4. PBA exhibits similar surface wettability as the other two acrylates, and adsorbs approximately the same amount of FN (*97*). Moreover, the adsorbed FN layer adopts comparable supramolecular organization on both PEA and PBA (*97*), irrespective of the small differences in material chemistry and, consequently, independently of physical properties such as stiffness or surface mobility (*98*). As a result, one can investigate the effect of the physical properties of the substrate on cell differentiation after discarding effects purely related to the organization of FN at the cell-material interface (*99*). The effect of matrix elasticity on mesenchymal stem cell differentiation has been reported to occur on synthetic substrates with stiffness mimicking the physiological tissue microenvironment, which, for osteoblastic lineages, should be in the range of osteoid precursors of bone (25-40 kPa) (*100*). The elastic modulus measured for PEA and PBA is one order of magnitude higher (500 kPa) than the stiffness of the natural microenvironment (*97*). Thus, since cells must deform the substrate to sense it, taking into account the range of force that cells can exert (1-5 nN mm^{-2}) (*101*, *102*) as well as the distribution of focal adhesions on these surfaces (*97*), it would appear that cells are not able to deform the underlying substrates and, consequently, both PEA and PBA must be sensed simply as rigid substrates by cells; this would indicate that changes in skeletal stem cells differentiation are not linked to stiffness (*103*).

There is some evidence that the mobility of the adhesion ligands at the cell-material interface improves cell behavior. Increasing the tether length of a synthetic peptide containing the RGD and the synergy sequence PHSRN to the underlying substrate enhanced cell spreading and reduced the time to form focal adhesions (*104*). Similarly, disorder can be interpreted as one form of mobility, and it was found that disordered nanopatterns of RGD on a bioinert background provided a much greater variety of ligand density for positive cell adhesion (*105*). On a more physical ground, disorder and mobility are related to the same thermodynamic magnitude: entropy; this would suggest that surfaces of higher entropy would favor cell adhesion. Furthermore, osteoblast differentiation of skeletal stem cells has been found to be enhanced on disordered nanoscale topographies (*106*), which can be equally described as surfaces of increased entropy as compared to the ordered system with qualitatively the same nanotopography. In this study, we demonstrate that even if FN is adsorbed with the same density and supramolecular distribution on PEA and PBA, cell differentiation along the osteoblastic lineages is enhanced on PBA (Figure 9), on which more focal adhesions are found (*97*). The glass transition temperature of PBA is 30 °C below that of PEA (Figure 9a), which means that surface mobility is enhanced on PBA. This property can also be related to the fact that the organization of FN takes place with faster dynamics on PBA than PEA, i.e., from lower concentrations of the adsorbing FN solution (*98*). Strikingly, surface mobility not only enhances cell adhesion, as previously shown for other systems (*107*), as seen by the higher number of focal adhesion plaques found in PBA than PEA (*97*), but it targets skeletal stem cell differentiation along the osteoblastic lineage with greater efficiency, as shown by the upregulation of characteristic osteoblastic markers osteocalcin, osteopontin and Runx2 (Figure 9). In addition, it has been recently shown that subtle differences in –CH_3 chain lengths are able to induce changes in MSC phenotype (*108*), supporting a direct effect of surface mobility on cell differentiation.

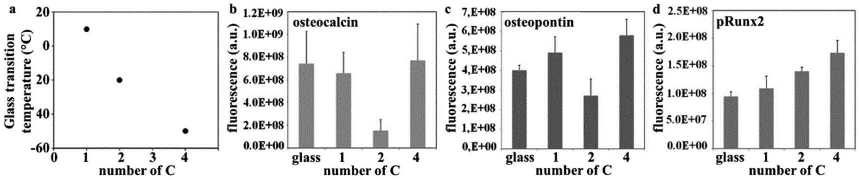

Figure 9. a) Glass transition temperature of different substrates as a function of the length of the side group (number of C); b,c) Quantification of osteocalcin (b) and osteopontin (c) levels from images of immunostaining after 21 days of culture; d) Quantification of the phosphorylation of Runx2 from immunostaining images after 1 day of culture. Reproduced with permission from ref. (97). Copyright 2012 The Royal Society of Chemistry.

Using a family of coatings obtained via plasma polymerization of ethyl acrylate (EA), we have been able to further investigate the effect of surface mobility on the interaction between material surface, proteins and cells (*109*). We have observed that surface mobility not only enhances cell adhesion, but is also able to modulate protein adsorption and cell-mediated fibronectin reorganization. The substrates are produced by glow discharge of a mixture of EA vapor with the non-reactive carrier gas argon; the characterization via X-ray photoelectron spectroscopy proves that the plasma polymerization of EA under the conditions employed in this study gives rise to nanometer coatings, whose chemical composition, albeit different than that obtained by conventional polymerization of the same monomer (PEA) due to monomer fragmentation (*110*), maintains some of its characteristic functionalities and is not appreciably affected by the duration of the plasma discharge (*109*). On the other hand, these coatings exhibit a marked increase of wettability at decreasing treatment times (Figure 10a), which derives from an increase of surface mobility (confirmed by dynamic contact angle measurements (*111*)) due to a decrease of film thickness (*112*) (measured via AFM) and of its cross-linking degree (estimated via adsorption kinetics of the vapor of a solvent of PEA) (*109*). We proposed a model for these polymer films that foresees that at shorter treatment times the polymeric chains of the growing plasma deposit are being grafted to the activated surface of the underlying substrate, giving rise to an only slightly cross-linked thin polymer film with high chain mobility; longer treatment time lead to thicker films, with higher cross-linking degree and lower chain mobility, as a result of both covalent cross-linking and physical entanglement between the polymer chains (Figure 10b). So, this process gives rise to a novel family of coatings with controlled wettability and surface mobility that do not induce fibrillogenesis of the adsorbed FN as PEA, but are able to modulate the activity of adsorbed FN and cell response, in terms of initial adhesion and cell-mediated matrix reorganization. Specifically, the higher the surface mobility of the coating, the more active is the conformation of the protein, as shown by monoclonal antibody binding of cell-adhesive epitopes within the central integrin binding domain of FN (Figure 10c). Moreover, MC3T3-E1 cells respond accordingly to the FN-coated substrates: the more mobile coatings support optimal cell adhesion, even at low FN surface density, as shown by the early formation of focal contacts that result in a higher number and bigger size of the focal adhesions compared to less mobile coatings (Figure 10d). Similarly, a stronger cell-mediated FN reorganization is found on the polymer films with higher surface mobility, where lower interaction strength between the adsorbed protein and the substrate enables higher reorganization (Figure 10d).

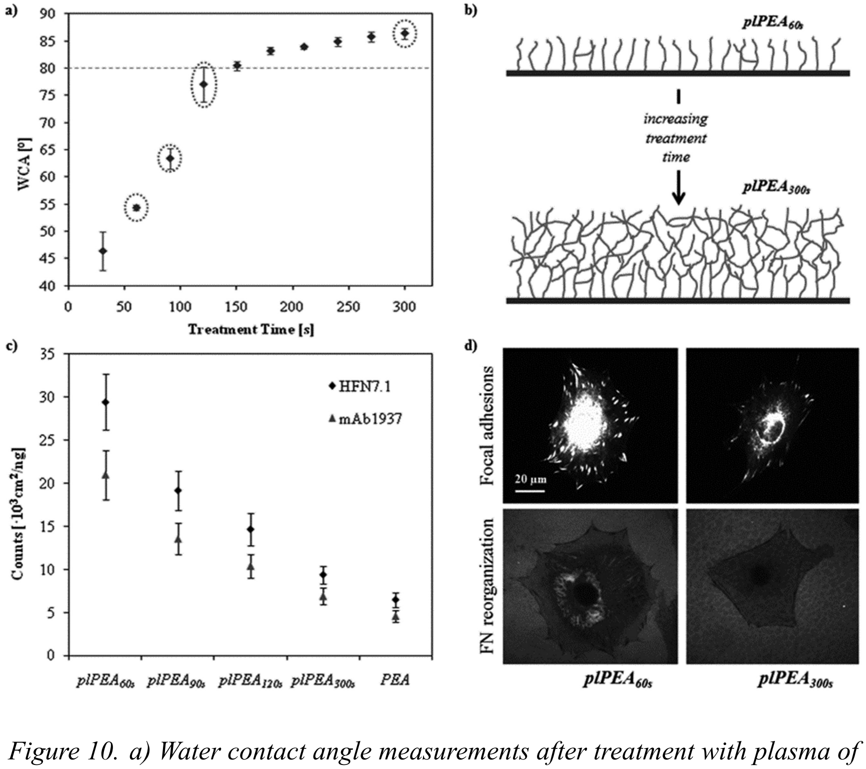

Figure 10. a) Water contact angle measurements after treatment with plasma of ethyl acrylate (EA) at different times; the circles indicate the treatment times chosen for the subsequent studies: 60s (WCA = 54.3±0.5°, plPEA$_{60s}$), 90s (63.4±1.8°, plPEA$_{90s}$), 120s (77.0±3.3°, plPEA$_{120s}$), 300s (86.4±1.0°, plPEA$_{300s}$); the WCA of spin-coated polyethylacrylate (indicated by the dotted line) is 80.0±1.4°. b) Model of the plasma-polymerized coatings at increasing treatment times. c) Monoclonal antibody binding for HFN7.1 and mAb1937 (monoclonal antibodies directed against sites within the central integrin binding domain of FN) measured through ELISA (values are normalized by the surface density of fibronectin). d) Focal adhesion protein vinculin and FN reorganization of MC3T3-E1 osteoblast-like cells on samples coated with a surface density of FN of ~100 ng cm^{-2}. Reproduced with permission from ref. (109). Copyright 2012 The Royal Society of Chemistry.

In conclusion, the FN network formed upon passive adsorption on surface chemistries such as PEA is endowed with a distinctive biological activity, since it was shown to support enhanced cell adhesion, matrix secretion and degradation, and to affect also higher order cellular functions such as cell differentiation. The improved biological properties of this artificial FN network confirm the similarity of this cell-free fibrillogenesis process and of the resulting network structure with the physiological FN fibrils, paving the way for its explotation to control and direct cell behavior in more complex systems that would include other ECM components mimicking natural tissue and cell microenvironments.

The model surfaces employed in our studies have also permitted to identify a novel mechanism able to modulate protein and cell interaction with synthetic surfaces: surface mobility, a surface property whose effect on protein adsorption and cell adhesion has until now received very poor attention. In our work, we observed that surfaces with higher mobility supported stronger cell adhesion, cell-mediated FN reorganization and could even target cell differentiation. Within this perspective, further studies are needed to corroborate this new concept and gain a more comprehensive understanding of the mechanisms underlying these phenomena: extending the range of surface mobilities explored, one could evaluate which ranges of molecular mobility allow to direct or control cell response, permitting to fully exploit the potential of this surface property for tissue engineering applications.

References

1. Larsen, M.; Artym, V. V.; Green, J. A.; Yamada, K. M. *Curr. Opin. Cell Biol.* **2006**, *18*, 463–71.
2. Vakonakis, I.; Campbell, I. D. *Curr. Opin. Cell Biol.* **2007**, *19*, 578–83.
3. Zhou, X.; Rowe, R. G.; Hiraoka, N.; George, J. P.; Wirtz, D.; Mosher, D. F.; Virtanen, I.; Chernousov, M. A.; Weiss, S. J. *Genes Dev.* **2008**, *22*, 1231–1243.
4. Singh, P.; Carraher, C.; Schwarzbauer, J. E. *Annu. Rev. Cell Dev. Biol.* **2010**, *26*, 397–419.
5. Hynes, R. O. *Fibronectins. Springer Series in Molecular Biology*; Rich, A., Ed.; Springer: New York, 1990; pp 1−538.
6. Fontana, L.; Chen, Y.; Prijatelj, P.; Sakai, T.; Fässler, R.; Sakai, L. Y.; Rifkin, D. B. *FASEB J.* **2005**, *19*, 1798–808.
7. George, E. L.; Georges-Labouesse, E. N.; Patel-King, R. S.; Rayburn, H.; Hynes, R. O. *Development* **1993**, *119*, 1079–91.
8. Pankov, R.; Yamada, K. M. *J. Cell Sci.* **2002**, *115*, 3861–3863.
9. Cho, J.; Mosher, D. F. *J. Thromb. Haemostasis* **2006**, *4*, 1461–9.
10. Ni, H.; Yuen, P. S. T.; Papalia, J. M.; Trevithick, J. E.; Sakai, T.; Fässler, R.; Hynes, R. O.; Wagner, D. D. *Proc. Natl. Acad. Sci. U.S.A.* **2003**, *100*, 2415–9.
11. Mao, Y.; Schwarzbauer, J. E. *Matrix Biol.* **2005**, *24*, 389–99.
12. Leiss, M.; Beckmann, K.; Girós, A.; Costell, M.; Fässler, R. *Curr. Opin. Cell Biol.* **2008**, *20*, 502–7.

13. Schwarzbauer, J. E. *Curr. Opin. Cell Biol.* **1991**, *3*, 786–791.
14. Guan, J.-L.; Hynes, R. O. *Cell* **1990**, *60*, 53–61.
15. Mcdonald, J. A.; Quade, B. J.; Broekelmann, T. J.; LaChance, R.; Forsman, K.; Hasegawa, E.; Akiyama, S. *J. Biol. Chem.* **1987**, *262*, 2957–67.
16. Sechler, J. L.; Corbett, S. A.; Wenk, M. B.; Schwarzbauer, J. E. *Ann. N.Y. Acad. Sci.* **1998**, *857*, 143–154.
17. Sottile, J.; Schwarzbauer, J.; Selegue, J.; Mosher, D. F. *J. Biol. Chem.* **1991**, *266*, 12840–3.
18. Ruoslahti, E.; Obrink, B. *Exp. Cell Res.* **1996**, *227*, 1–11.
19. Sechler, J. L.; Corbett, S. A.; Schwarzbauer, J. E. *Mol. Biol. Cell* **1997**, *8*, 2563–73.
20. Wennerberg, K.; Lohikangas, L.; Gullberg, D.; Pfaff, M.; Johansson, S.; Fässler, R. *J. Cell Biol.* **1996**, *132*, 227–238.
21. Wu, C.; Keivens, V. M.; Otoole, T. E.; Mcdonald, J. A.; Ginsberg, M. H. *Cell* **1995**, *83*, 715–724.
22. Johnson, K. J.; Sage, H.; Briscoe, G.; Erickson, H. P. *J. Biol. Chem.* **1999**, *274*, 15473–9.
23. Geiger, B.; Bershadsky, A.; Pankov, R.; Yamada, K. M. *Nat. Rev. Mol. Cell Biol.* **2001**, *2*, 793–805.
24. Hall, A. *Biochem. Soc. Trans.* **2005**, *33*, 891–895.
25. Yoneda, A.; Ushakov, D.; Multhaupt, H. A. B.; Couchman, J. R. *Mol. Biol. Cell* **2007**, *18*, 66–75.
26. Langenbach, K. J.; Sottile, J. *J. Biol. Chem.* **1999**, *274*, 7032–8.
27. Shi, F.; Sottile, J. *J. Cell Sci.* **2008**, *121*, 2360–71.
28. Williams, E. C.; Janmeyn, P. A.; Johnson, R. B.; Mosher, F. *J. Biol. Chem.* **1983**, *258*, 5911–5914.
29. Sakai, K.; Fujii, T.; Hayashi, T. *J. Biochem.* **1994**, *115*, 415–21.
30. Vartio, T. *J. Biol. Chem.* **1986**, *261*, 9433–7.
31. Mosher, D. F.; Johnson, R. B. *J. Biol. Chem.* **1983**, *258*, 6595–601.
32. Mosher, D. F. U.S. Patent 4,705,751, 1987.
33. Chen, Y.; Zardi, L.; Peters, D. M. P. *Scanning* **1997**, *19*, 349–355.
34. Peters, D. M. P.; Chen, Y.; Zardi, L.; Brummel, S. *Microsc. Microanal.* **1998**, *4*, 385–396.
35. Vuento, M.; Salonen, E.; Riepponen, P. *Biochimie* **1980**, *62*, 99–104.
36. Vuento, M.; Vartio, T.; Saraste, M.; von Bonsdorff, C. H.; Vaheri, A. *Eur. J. Biochem.* **1980**, *105*, 33–42.
37. Jilek, F.; Hörmann, H. *Hoppe-Seyler's Z. Physiol. Chem.* **1979**, *360*, 597–604.
38. Richter, H.; Wendt, C.; Hörmann, H. *Biol. Chem. Hoppe-Seyler* **1985**, *366*, 509–514.
39. Morla, A.; Zhang, Z.; Ruoslahti, E. *Nature* **1994**, *367*, 193–196.
40. Hocking, D. C.; Smith, R. K.; McKeown-Longo, P. J. *J. Cell Biol.* **1996**, *133*, 431–44.
41. Briknarová, K.; Åkerman, M. E.; Hoyt, D. W.; Ruoslahti, E.; Ely, K. R. *J. Mol. Biol.* **2003**, *332*, 205–215.

42. Zhong, C.; Chrzanowska-Wodnicka, M.; Brown, J.; Shaub, A.; Belkin, A. M.; Burridge, K. *J. Cell Biol.* **1998**, *141*, 539–51.
43. Baneyx, G.; Vogel, V. *Proc. Natl. Acad. Sci. U.S.A.* **1999**, *96*, 12518–23.
44. Ulmer, J.; Geiger, B.; Spatz, J. P. *Soft Matter* **2008**, *4*, 1998–2007.
45. Volberg, T.; Ulmer, J.; Spatz, J.; Geiger, B. In *IUTAM Symposium on Cellular, Molecular and Tissue Mechanics*; Garikipati, K., Arruda, E. M., Eds.; Springer: Netherlands, 2010; Vol. 16, pp 69−79.
46. Kaiser, P.; Spatz, J. P. *Soft Matter* **2010**, *6*, 113–119.
47. Ejim, O. S.; Blunn, G. W.; Brown, R. A. *Biomaterials* **1993**, *14*, 743–748.
48. Brown, R. A.; Blunn, G. W.; Ejim, O. S. *Biomaterials* **1994**, *15*, 457–464.
49. Wòjciak-Stothard, B.; Denyer, M.; Mishra, M.; Brown, R. A. *In Vitro Cell. Dev. Biol.: Anim.* **1997**, *33*, 110–7.
50. Ahmed, Z.; Idowu, B. D.; Brown, R. A. *Biomaterials* **1999**, *20*, 201–9.
51. Ahmed, Z.; Brown, R. A. *Cell Motil. Cytoskeleton* **1999**, *42*, 331–43.
52. Underwood, S.; Afoke, A.; Brown, R. A.; MacLeod, A. J.; Dunnill, P. *Bioprocess Eng.* **1999**, *20*, 239–248.
53. Harding, S. I.; Underwood, S.; Brown, R. A.; Dunnill, P. *Bioprocess Eng.* **2000**, *22*, 159–164.
54. Underwood, S.; Afoke, A.; Brown, R. A.; MacLeod, A. J.; Shamlou, P. A.; Dunnill, P. *Biotechnol. Bioeng.* **2001**, *73*, 295–305.
55. Ahmed, Z.; Underwood, S.; Brown, R. A. *Tissue Eng.* **2003**, *9*, 219–31.
56. Little, W. C.; Smith, M. L.; Ebneter, U.; Vogel, V. *Matrix Biol.* **2008**, *27*, 451–61.
57. Klotzsch, E.; Smith, M. L.; Kubow, K. E.; Muntwyler, S.; Little, W. C.; Beyeler, F.; Gourdon, D.; Nelson, B. J.; Vogel, V. *Proc. Natl. Acad. Sci. U.S.A.* **2009**, *106*, 18267–72.
58. Pernodet, N.; Rafailovich, M.; Sokolov, J.; Xu, D.; Yang, N.-L.; McLeod, K. *J. Biomed. Mater. Res., Part A* **2003**, *64*, 684–92.
59. Pellenc, D.; Berry, H.; Gallet, O. *J. Colloid Interface Sci.* **2006**, *298*, 132–44.
60. Nelea, V.; Kaartinen, M. T. *J. Struct. Biol.* **2010**, *170*, 50–9.
61. Feinberg, A. W.; Parker, K. K. *Nano Lett.* **2010**, *10*, 2184–2191.
62. Salmerón-Sánchez, M.; Rico, P.; Moratal, D.; Lee, T. T.; Schwarzbauer, J. E.; García, A. J. *Biomaterials* **2011**, *32*, 2099–105.
63. Erickson, H. P. *J. Muscle Res. Cell Motil.* **2002**, *23*, 575–80.
64. de Jongh, H. H. J.; Kosters, H. A.; Kudryashova, E.; Meinders, M. B. J.; Trofimova, D.; Wierenga, P. A. *Biopolymers* **2004**, *74*, 131–5.
65. Oberhauser, A. F.; Badilla-Fernandez, C.; Carrion-Vazquez, M.; Fernandez, J. M. *J. Mol. Biol.* **2002**, *319*, 433–47.
66. Rief, M.; Gautel, M.; Gaub, H. E. In *Advances in Experimental Medicine and Biology: Elastic Filaments Of The Cell*; Granzier, H. L., Pollack, G. H., Eds.; Springer: New York, 2000; Vol. 481, pp 129−141.
67. Krammer, A.; Lu, H.; Isralewitz, B.; Schulten, K.; Vogel, V. *Proc. Natl. Acad. Sci. U.S.A.* **1999**, *96*, 1351–6.
68. Guan, J.; Ferrell, N.; Yu, B.; Hansford, D. J.; Lee, L. J. *Soft Matter* **2007**, *3*, 1369–1371.
69. Nelea, V.; Nakano, Y.; Kaartinen, M. T. *Protein J.* **2008**, *27*, 223–33.

70. Peters, D. M. P.; Mosher, D. F. In *Extracellular Matrix Assembly and Structure*; Yurchenco, P. D., Birk, D. E., Mecham, R. P., Eds.; Academic Press: San Diego, CA, 1989; pp 315–350.
71. Mosher, D. F.; Fogerty, F. J.; Chernousov, M. A.; Barry, E. L. R. *Ann. N. Y. Acad. Sci.* **1991**, *614*, 167–180.
72. Mosher, D. F. *Curr. Opin. Struct. Biol.* **1993**, *3*, 214–222.
73. Sechler, J. L.; Rao, H.; Cumiskey, A. M.; Vega-Colón, I.; Smith, M. S.; Murata, T.; Schwarzbauer, J. E. *J. Cell Biol.* **2001**, *154*, 1081–8.
74. Bergkvist, M.; Carlsson, J.; Oscarsson, S. *J. Biomed. Mat. Res., Part A* **2003**, *64*, 349–56.
75. Baugh, L.; Vogel, V. *J. Biomed. Mat. Res., Part A* **2004**, *69*, 525–34.
76. Lutolf, M. P.; Gilbert, P. M.; Blau, H. M. *Nature* **2009**, *462*, 433–41.
77. Petrie, T. A.; Raynor, J. E.; Dumbauld, D. W.; Lee, T. T.; Jagtap, S.; Templeman, K. L.; Collard, D. M.; García, A. J. *Sci. Transl. Med.* **2010**, *2*, 45ra60.
78. Rico, P.; Rodríguez Hernández, J. C.; Moratal, D.; Altankov, G.; Monleón Pradas, M.; Salmerón-Sánchez, M. *Tissue Eng., Part A* **2009**, *15*, 3271–81.
79. Gugutkov, D.; González-García, C.; Rodríguez Hernández, J. C.; Altankov, G.; Salmerón-Sánchez, M. *Langmuir* **2009**, *25*, 10893–900.
80. Schwarzbauer, J. E. *J. Cell Biol.* **1991**, *113*, 1463–73.
81. Gugutkov, D.; Altankov, G.; Rodríguez Hernández, J. C.; Monleón Pradas, M.; Salmerón Sánchez, M. *J. Biomed. Mat. Res., Part A* **2010**, *92*, 322–31.
82. Rodríguez Hernández, J. C.; Rico, P.; Moratal, D.; Monleón Pradas, M.; Salmerón-Sánchez, M. *Macromol. Biosci.* **2009**, *9*, 766–75.
83. Coelho, N. M.; González-García, C.; Planell, J. A.; Salmerón-Sánchez, M.; Altankov, G. *Eur. Cells Mater.* **2010**, *19*, 262–72.
84. Rodríguez Hernández, J. C.; Salmerón Sánchez, M.; Soria, J. M.; Gómez Ribelles, J. L.; Monleón Pradas, M. *Biophys. J.* **2007**, *93*, 202–7.
85. Toromanov, G.; González-García, C.; Altankov, G.; Salmerón-Sánchez, M. *Polymer* **2010**, *51*, 2329–2336.
86. Page-McCaw, A.; Ewald, A. J.; Werb, Z. *Nat. Rev. Mol. Cell Biol.* **2007**, *8*, 221–233.
87. Kenny, H. A.; Kaur, S.; Coussens, L. M.; Lengyel, E. *J. Clin. Invest.* **2008**, *118*, 1367–1379.
88. Yang, C.-M.; Chien, C.-S.; Yao, C.-C.; Hsiao, L.-D.; Huang, Y.-C.; Wu, C. B. *J. Biol. Chem.* **2004**, *279*, 22158–22165.
89. Wan, R.; Mo, Y.; Zhang, X.; Chien, S.; Tollerud, D. J.; Zhang, Q. *Toxicol. Appl. Pharmacol.* **2008**, *233*, 276–285.
90. Llopis-Hernández, V.; Rico, P.; Ballester-Beltrán, J.; Moratal, D.; Salmerón-Sánchez, M. *PloS One* **2011**, *6*, e19610.
91. Llopis-Hernández, V.; Rico, P.; Moratal, D.; Salmerón-Sánchez, M. *Matrix Biol.* Unpublished.
92. García, A. J.; Vega, M. D.; Boettiger, D. *Mol. Biol. Cell* **1999**, *10*, 785–98.
93. Ballester-Beltrán, J.; Cantini, M.; Lebourg, M.; Rico, P.; Moratal, D.; García, A. J.; Salmerón-Sánchez, M. *J. Mater. Sci. Mater. Med.* **2012**, *23*, 195–204.

94. Bondesen, B. a; Jones, K. a; Glasgow, W. C.; Pavlath, G. K. *FASEB J.* **2007**, *21*, 3338–45.
95. Olguin, H. C.; Santander, C.; Brandan, E. *Dev. Biol.* **2003**, *259*, 209–224.
96. Konigsberg, I. R. *Dev. Biol.* **1971**, *26*, 133–152.
97. González-García, C.; Moratal, D.; Oreffo, R. O. C.; Dalby, M. J.; Salmerón-Sánchez, M. *Integr. Biol.* **2012**, *4*, 531–9.
98. Brizuela Guerra, N.; González-García, C.; Llopis, V.; Rodríguez-Hernández, J. C.; Moratal, D.; Rico, P.; Salmerón-Sánchez, M. *Soft Matter* **2010**, *6*, 4748–4755.
99. Rowlands, A. S.; George, P. a; Cooper-White, J. J. *Am. J. Physiol.: Cell Physiol.* **2008**, *295*, C1037–44.
100. Engler, A. J.; Sen, S.; Sweeney, H. L.; Discher, D. E. *Cell* **2006**, *126*, 677–89.
101. Balaban, N. Q.; Schwarz, U. S.; Riveline, D.; Goichberg, P.; Tzur, G.; Sabanay, I.; Mahalu, D.; Safran, S.; Bershadsky, A.; Addadi, L.; Geiger, B. *Nat. Cell Biol.* **2001**, *3*, 466–472.
102. Galbraith, C. G.; Yamada, K. M.; Sheetz, M. P. *J. Cell Biol.* **2002**, *159*, 695–705.
103. Reilly, G. C.; Engler, A. J. *J. Biomech.* **2010**, *43*, 55–62.
104. Kuhlman, W.; Taniguchi, I.; Griffith, L. G.; Mayes, A. M. *Biomacromolecules* **2007**, *8*, 3206–13.
105. Huang, J.; Gra, S. V.; Corbellini, F.; Rinck, S.; Bock, E.; Kemkemer, R.; Kessler, H.; Ding, J.; Spatz, J. P. *Nano Lett.* **2009**, *9*, 1111–1116.
106. Dalby, M. J.; Gadegaard, N.; Tare, R.; Andar, A.; Riehle, M. O.; Herzyk, P.; Wilkinson, C. D. W.; Oreffo, R. O. C. *Nat. Mater.* **2007**, *6*, 997–1003.
107. Kong, H. J.; Polte, T. R.; Alsberg, E.; Mooney, D. J. *Proc. Natl. Acad. Sci. U.S.A.* **2005**, *12*, 4300–4305.
108. Curran, J. M.; Pu, F.; Chen, R.; Hunt, J. a *Biomaterials* **2011**, *32*, 4753–60.
109. Cantini, M.; Rico, P.; Moratal, D.; Salmerón-Sánchez, M. *Soft Matter* **2012**, *8*, 5575–5584.
110. Yasuda, H. *J. Polym. Sci., Macromol. Rev.* **1981**, *16*, 199–293.
111. Yasuda, H.; Sharma, A. K.; Yasuda, T. *J. Polym. Sci., Polym. Phys. Ed.* **1981**, *19*, 1285–1291.
112. Reiter, G. *Europhys. Lett.* **1993**, *23*, 579–584.

Chapter 23

Effect of Albumin Adsorption on Biotribological Properties of Artificial Joint Materials

A. P. Serro,[1,2] R. Colaço,[1] and B. Saramago[*,1]

[1]Centro de Química Estrutural, Instituto Superior Técnico,
Universidade Técnica de Lisboa, Av. Rovisco Pais,
1049-001 Lisboa, Portugal
[2]Centro de Investigação Interdisciplinar Egas Moniz,
Instituto Superior de Ciências da Saúde Egas Moniz,
Campus Universitário, Quinta da Granja, Monte de Caparica,
2829-511 Caparica, Portugal
[*]E-mail: b.saramago@ist.utl.pt

The interaction of total joint replacement materials with the periprosthetic fluid, which substitutes the lubricant existent in natural joints, is responsible for the lubrication mechanisms that minimize friction and wear in prosthesis. The adsorption behavior of albumin, the most abundant protein in the periprosthetic fluid, has been recognized as critical for the lubrication mechanism, but the role played by this protein is not still totally understood. This chapter describes the main contributions to this topic of the work carried out in our laboratory during the last years. Tribological tests were done on different prosthetic pairs, using Hanks' balanced salt solution, with and without albumin, to model the lubricant. The role of hyaluronic acid in the lubricant was also assessed. Parallel determinations of albumin adsorption on the surfaces involved, by QCM and other methods, as well as characterization of the tribo-surfaces at a submicrometer level, by AFM and SEM, were performed. We confirmed that, in general, albumin has a protective role of the sliding surfaces. However, in certain experimental conditions, adhesion forces between eventually denaturated protein molecules adsorbed on the sliding surfaces may hamper the lubrication process.

In Proteins at Interfaces III State of the Art 2012; Horbett, T., et al.;
ACS Symposium Series; American Chemical Society: Washington, DC, 2012.

Introduction

Total joint replacements (TJRs) became a successful and relatively common way to restore normal motion to damaged human joints, like hip and knee. The most commonly used artificial joints combine a metallic or ceramic head articulating against a ultra high molecular weight polyethylene (UHMWPE) cup, and are lubricated by the periprosthetic fluid which substitutes the lubricant existent in natural joints. The tribological behavior of the articulating surfaces in TJRs is considered the main critical factor affecting their lifetime and reliability. In particular, wear of the UHMWPE bearing surface when sliding against the hard ball which substitutes the femoral head leads to the generation of polymeric wear debris. These debris may cause the inflammation of surrounding tissues resulting in bone resorption (osteolyse), which often results in the loosening of fixation of the acetabular and/or femoral parts (*1*, *2*). Moreover, corrosion and leaching of metal ions from metallic counterfaces into body fluids are also significant problems during long term use. For example, stainless steel has been extensively used in many biomedical applications, but the products of its corrosion and released Cr, Ni, Mn, and Mo ions (*3*), can trigger several adverse reactions, from simple allergies and hypersensitivity to the metals to tumor formation (*4*). Several approaches to overcome these problems have been attempted over the years, usually on a trial and error basis, such as the research of new formulations and processing methods for the polymer (*5*) or surface treatments and coatings both on polymer and counterbody (*6*–*9*).

The interaction of the TJR materials with the periprosthetic fluid determines the lubrication mechanisms that minimize friction and wear in prosthesis. The composition of the periprosthetic fluid produced after implantation has been reported to be similar to that found before the surgery (*10*). This fluid contains biological macromolecules with potential lubrication properties. Proteins are some of those macromolecules whose role is not yet completely understood. Hyaluronic acid is another component which is responsible for the viscoelastic properties of synovial fluid (*11*). The decline of the concentration of this compound after arthroplasty leads to a reduction in the liquid viscosity which may affect the tribological behavior of the artificial joint.

Among the proteins present in the periprosthetic fluid, albumin is the most abundant. The conformation and adsorption behavior of this protein has been recognized as critical for the lubrication ability of the periprosthetic fluid (*12*). Under high load and low sliding speed, albumin is believed to form a protective layer on articular surfaces, thus enhancing the boundary lubrication regime. However, in other conditions, the presence of albumin may have the opposite effect (*13*). Several authors reached different conclusions probably because a diversity of factors, such as the concentration of the macromolecules in the lubricant, their binding state and the eventual interaction with other macromolecules, may affect the complex tribological mechanisms. Furthermore, the methods and the experimental conditions (load, velocity, geometry, etc.) used in the friction tests also influence the results of the in vitro tribological experiments.

The objective of this chapter is to contribute for the clarification of the role played by albumin in the lubrication process of orthopedic prosthesis through systematic studies performed in the same experimental conditions, with different TJR materials. We will present mainly the results of our own research, although references to contributions from other authors will be given whenever appropriate.

The chapter is organized in three sections. First, a description of the experimental techniques used in our studies for adsorption measurements, tribological tests and surface characterization is provided. The main section describes our work starting by the study of friction of the most commonly used prosthetic joint materials (UHMWPE against metallic and ceramic counterfaces) in the presence of different lubricants. The choice of the lubricants was made in order to identify the effects of the main components of the periprosthetic fluid: hyaluronic acid and albumin. The results of this work revealed the major role of albumin in the performance of these tribological pairs and led to the development of a parallel investigation on the adsorption of albumin upon the various surfaces involved in the tribological tests. On the other hand, the minimization of friction and wear of UHMWPE components through adequate surface treatments and coatings on the metallic parts was also a goal of our research. A series of tribological and adsorption studies were developed along this line with the collaboration with other research groups that prepared several types of coatings, namely titanium nitrides and diamond like carbons (DLCs), and modified the surface through ion implantation. Finally, general conclusions are presented in a closing section.

Experimental

Tribological Tests

Rotating pin-on-disk friction tests have been carried out in a Wazau TRM1000 tribometer, at room temperature. Pins were cut from UHMWPE (CHIRULEN®, Poly Hi Solidur, Germany) sheet. Disks of AISI 316L austenitic stainless steel (MediMet, Germany), Co–28Cr–6Mo alloy (MediMet, Germany) and alumina (Maret SA, Switzerland) were used. In some studies the stainless steel (SS) disks were coated with titanium nitrides and DLCs. The coatings were deposited by physical vapor deposition (PVD). Titanium nitrides were prepared in Ceramed (Portugal) and DLC's in the Argonne National Laboratory (USA). Some TiN samples were ion implanted with chlorine and argon in Instituto Tecnológico Nuclear (Portugal). The average roughness, (Ra), of the counterface materials measured by AFM did not exceed 20 nm, while that of standard UHMWPE was 126 nm.

Normal loads employed varied between 21.6 and 117.7 N, in order to have values for the mean pressure at the interface between 0.39 and 1.53 MPa. The tangential sliding velocity was 46 mm/s. These values of pressure and velocity lie in the range typically found in hip joints (0–50 mm/s) (*11*). The sliding distances were typically 1000 m.

The wear rate of UHMWPE, whose density is 935 kg m^{-3}, was calculated following a weight loss measurement technique.

To compare the tribological behavior of DLC coatings and SS against UHMWPE, a microtribometer from CSM Instruments with a pin-on-plate reciprocating movement configuration was used. The upper UHMWPE semispheres were fixed on a cantilever, while the SS and DLC coated samples were mounted on a flat-bottom teflon liquid cell. In the case of these microtribological tests, the sliding distance was 100 m and the normal forces of 1 to 25 mN were applied in order to achieve average contact pressures between 1 and 10 MPa, respectively, and velocities of 25 mm/s and 5 mm/s were adopted to simulate the conditions typically found in joint prosthesis.

In all experiments bovine serum albumin (BSA, Serva Ref. 11930) and hyaluronic acid sodium salt from streptococcus (HA, Fluka Ref. 53747) were used to prepare solutions in Hanks' balanced salt solution (HBSS, pH=7.3, Sigma Ref. H8264).

Adsorption Studies

Quantification of adsorbed protein onto plates (metallic and ceramic disks) was performed by radiolabeling using ^{125}I-BSA. The protein was labeled with ^{125}I according to the iodogen method (*14*). The solution used in the substrate incubations was obtained by the addition of the labeled protein to an unlabeled albumin solution with a concentration of 4 mg/ml, in order to obtain a final activity of approximately 7.6×10^6 cpm/mg. Incubations were carried out for 2 h at room temperature, using a ratio of 0.9 ml of solution per square centimeter of the surface area of the samples. After rinsing the samples with HBSS, γ -activity of the samples was counted, and BSA surface concentration was calculated (*15*).

X-ray photoelectron spectroscopy (XPS) was used to estimate the BSA adsorption on plates, based on the analysis of nitrogen content. It was performed using a VG Scanning Auger Microprobe (Microlab 310F). The spectra were obtained at a pressure of $\approx 5\times10^{-9}$ mbar using X-ray from a Mg Kα source (15 kV/20 mA).

The QCM-D (KSV Instruments Ltd, Finland, model QCM-Z500) was used to determine BSA adsorption on the surface of AT-cut 5-MHz piezoelectric quartz crystals coated with UHMWPE, SS, alumina, titanium nitrides and DLCs. The polymeric coatings were deposited by spin coating, while all the others were by PVD (see above). Alumina coatings were prepared at INESC (Portugal). The fundamental frequency along with the third, fifth, seventh, ninth, and eleventh harmonics were monitored as a function of time to determine the changes in frequency upon the sequential addition of HBSS, BSA solution, and HBSS to the quartz crystal. The dissipation change was also recorded throughout the process. The experiments were performed at 25 °C. Considering the baseline for the first addition of HBSS, the subsequent changes correspond to the formation of a protein layer on the surface of the crystal followed by a weak removal of loosely adsorbed BSA during rinsing with the solvent. If the viscoelastic properties of the adsorbed film cannot be neglected, there are four unknown parameters when modeling the properties of the adsorbed layer, namely thickness, density, elasticity and viscosity. The QCM-D software (QCM-Z500 Data analyser, version 1.62) based on the surface mechanical impedance model allows to model thickness, viscosity and elasticity for a viscoelastic layer whose density is known. Assuming the value of 1.15 g/cm^3 for the density of the adsorbed BSA film (*16*), the remaining parameters were calculated. The BSA adsorption, Γ, was determined using the modified Sauerbrey equation which includes the viscoelastic properties of the adsorbed material (*17*).

Ellipsometric data were used to calculate the adsorbed amount of BSA on DLC coated silicon wafers from the equation of de Feijter et al. (*18*). The measurements were performed using an Imaging Ellipsometer (EP3, Nanofilm Surface Analysis) operated in the polarizer-compensator-sample-analyzer (PCSA) mode (null ellipsometry). The light source was a solid-state laser with a wavelength of 532 nm. Experiments were carried out at 25 °C in a liquid cell connected to a peristaltic pump, following the same sequence of solutions introduction as referred for QCM-D.

The depletion method was used to assess adsorption on nanopowders of α-alumina (Al_2O_3, Alfa Aesar, ref. 39814) and of 316L SS (QinetiQ, Tesimorph ES-25). An amount of powder correspondent to a surface area of 3 m^2 was equilibrated with 10 ml of protein solution. Tubes were incubated at 37 °C for 12 h with rotation end-over-end, after which they were centrifuged at 12239 × *g* until a clear supernatant was obtained. Protein concentration in the supernatant was measured using UV spectroscopy (Hitachi U-2000 spectrophotometer) at 279 nm. The amounts of adsorbed protein were calculated from the differences between initial and equilibrated concentrations.

SEM and AFM Imaging

Surfaces were observed by scanning electron microscopy (SEM) with an Hitashi S2400 equipment. For these analyses, the non-metallic surfaces were previously submitted to Au thin layer sputtering in order to make surfaces conductive.

A Veeco DI CP-II atomic force microscope was used for the surface characterization at a submicrometer lever. Silicon-etched probes, with a nominal radius of 10 nm and a nominal constant of 40 N/m, were used. The imaging was performed in noncontact atomic force microscopy (NC-AFM) tapping mode, at room humidity (~ 50%) and temperature (20 to 22°C) conditions.

For the measurement of the film thickness, the samples were tested under water, using a liquid MicroCell. First, the protein film was removed by performing two scans in contact mode atomic force microscopy (C-AFM) on areas typically of 3 × 3 μm^2. These scans were made at a scan rate of 1 Hz, a resolution 512 lines, and a load of 0.9 μN. Immediately after, 6 × 6 μm^2 scans were performed with the same probe over the cleaned area, in NC mode, in order to visualize the surface.

The adhesion forces between AFM tips and sample surfaces were obtained directly from force–distance curves performed in liquid medium (HBSS), considering the maximum deflection on the probe–surface separation. For these measurements, silicon nitride triangular cantilevers (MLCT-AUNM, VeecoTM) with average spring constants of 0.16 N/m were used. The tips functionalized with BSA were prepared according to the method described in reference (*19*).

Results and Discussion

Comparison of Most Used Joint Materials Behavior in Several Lubricants

Several studies (*11*, *20*, *21*) have been reported on the effect of the various components of synovial fluid on friction and wear in artificial joints, but different authors reached different conclusions. Nevertheless, there is general agreement that hyaluronic acid (HA) and albumin are the most important components for the tribological behavior of these systems: HA is responsible for the high viscosity and albumin adsorbs on the joint material surfaces.

We compared the tribological behavior of the most used pairs of joint materials: UHMWPE against alumina (Al_2O_3), AISI 316L austenitic stainless steel and Co–28Cr–6Mo alloy (CoCrMo) in various lubrication conditions (*22*). The biological model fluid Hanks' balanced salt solution (HBSS) and solutions of bovine serum albumin (BSA, 4 mg/mL), of hyaluronic acid (HA, 3 mg/mL) and of both components (BSA, 4 mg/mL + HA, 3 mg/mL) in HBSS were used as lubricants. The friction coefficient was measured as a function of time using a pin-on-disk apparatus and the wear mechanisms were investigated through SEM observations of both disks and pins.

Figure 1 shows the values of the dynamical friction coefficient, μ, retrieved between 8 and 16 m of running distance, in the tests carried out using HBSS and HBSS +HA as lubricants, for the three tribological pairs (UHMWPE/Al_2O_3, UHMWPE/steel, UHMWPE/CoCrMo) under three different loading conditions, versus the Sommerfeld parameter, z, defined as $\eta vr/F$, where η is the viscosity of the lubricant, v the sliding speed, r the radius of the pin, and F the normal load in the contact region. This plot, the so-called Stribeck plot, shows that, despite the scattering of the points, all experiments were carried out under mixed lubrication conditions ($0.02 < \mu < 0.09$) (*20*). However, when the lower viscosity lubricant (HBSS) was used, the regime was closer to boundary lubrication, while the addition of hyaluronic acid increased the liquid viscosity which resulted in the decrease of the friction coefficient due to the enhancement of the lubrication hydrodynamic component.

When the friction coefficient was monitorized along larger distances further information could be obtained. In the tests carried out with HBSS or HBSS+HA, the friction coefficient increased rapidly during the first stages of sliding and then slowly, but continuously, independently of the pair and of the loading conditions. A different behavior was observed when protein was added to the lubricant. Comparison of the friction coefficients measured in HBSS and HBSS+BSA (see Figure 2) shows that they increase at a much slower rate in the presence of BSA, especially in the case of the metallic counterfaces. For alumina the stabilizing effect of protein is less apparent. The decrease of the friction coefficient when BSA is added to the lubricant is difficult to explain on the basis of the lubrication regime, since the addition of protein does not affect greatly the rheological properties of the lubricant, in particular its viscosity. However, if the lubrication regime may be considered as mixed, the presence of an adsorbed layer of protein at the liquid/solid interfaces reduces the interaction between the solid surfaces, which enhances the boundary component of the lubrication, as previously mentioned by Spencer and coworkers (*10*).

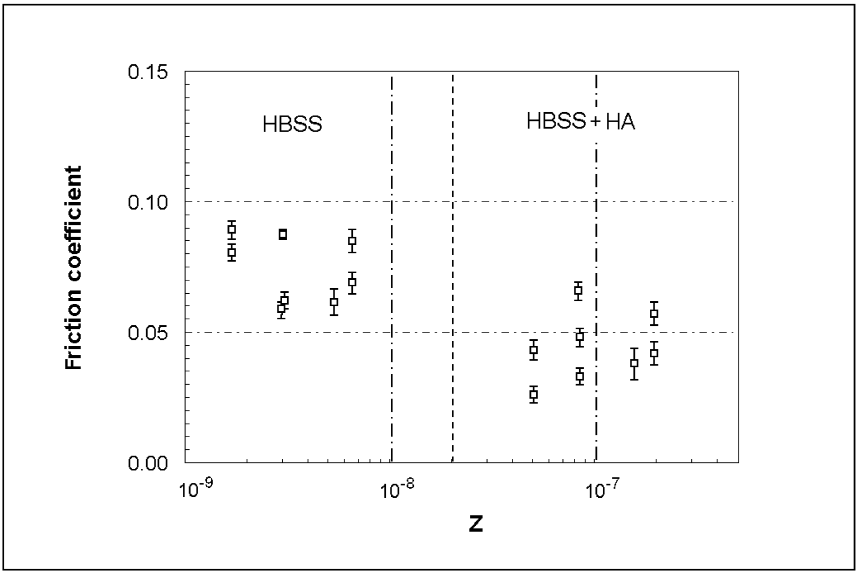

Figure 1. Dynamical friction coefficients measured for the three tribological pairs (UHMWPE/Al_2O_3, UHMWPE/steel, UHMWPE/CoCrMo) under three different loading conditions, using HBSS and HBSS +HA as lubricants, as a function of the Sommerfeld parameter, z, (Stribeck plot). (Reproduced with permission from reference (22). Copyright 2006 Elsevier).

SEM observations of the surfaces of the steel, of CoCrMo alloy and of alumina before and after the friction experiments should contribute to the understanding of the underlying phenomena that can explain the above described behavior. The observation of the worn surfaces of steel and of CoCrMo alloy (Figures 3a and 3c) shows that when the lubricant did not contain BSA, the wear mechanisms were essentially abrasion, identified by the parallel grooves on the surface, and film transfer of UHMWPE. In both metallic substrates, when BSA was added to the lubricant the active wear mechanisms remained the same, but the transfer of polymeric film no longer occurred (Figures 3b and 3d).

Conversely, the polymeric film transfer to the alumina counterbody still occurs when the lubricant contains protein (Figure 3f), while in the absence of protein, only a few long, filamentary, polymeric debris, could be detected (Figure 3e). A possible explanation for this situation may be given in terms of the stability of the adsorbed albumin layer that protects the counterbody surface against the transfer of the polymer. In comparison with the metallic surfaces, the albumin layer adsorbed on alumina should be less effective in the protection of the underlying surface.

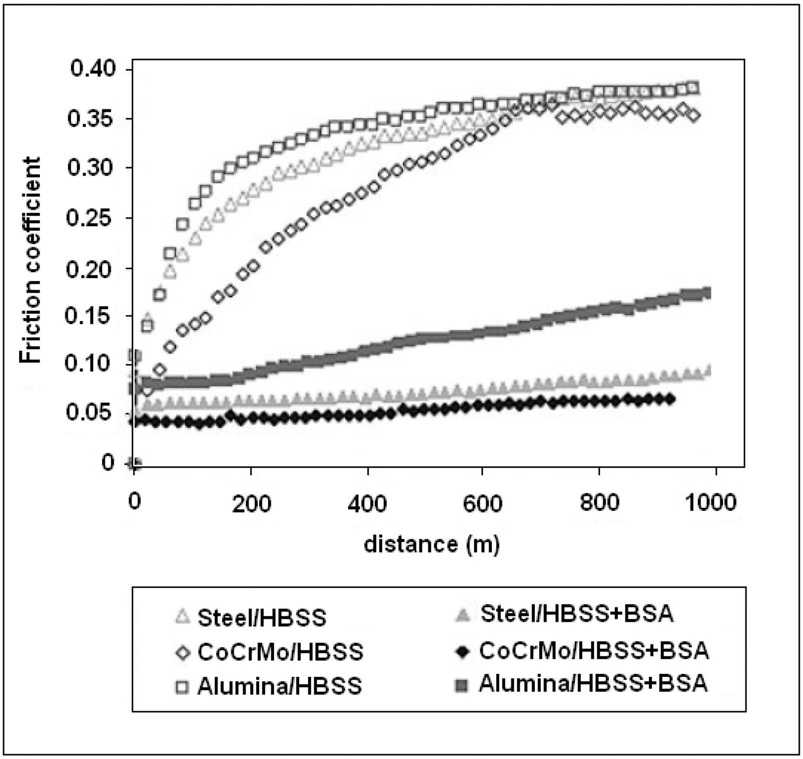

Figure 2. Friction coefficient vs. distance for the three tribological pairs in HBSS and in HBSS + BSA. (Reproduced with permission from reference (24). Copyright 2006 John Wiley and Sons).

The SEM observations are consistent with the results of the tribological tests (Figure 2): the friction coefficient increased during the tests with alumina independently of the lubricant composition, although it kept a lower value in the presence of albumin. This behavior is not in agreement with the results of other authors (*10*, *23*), who found that the transfer of polymeric film to alumina counterfaces did not occur when the lubricant was either protein or Ringer's solution.

In order to further understand the important role played by albumin on friction and wear of prosthetic components, studies of albumin adsorption/desorption processes on the prosthetic materials, under the conditions of the friction tests, were planned.

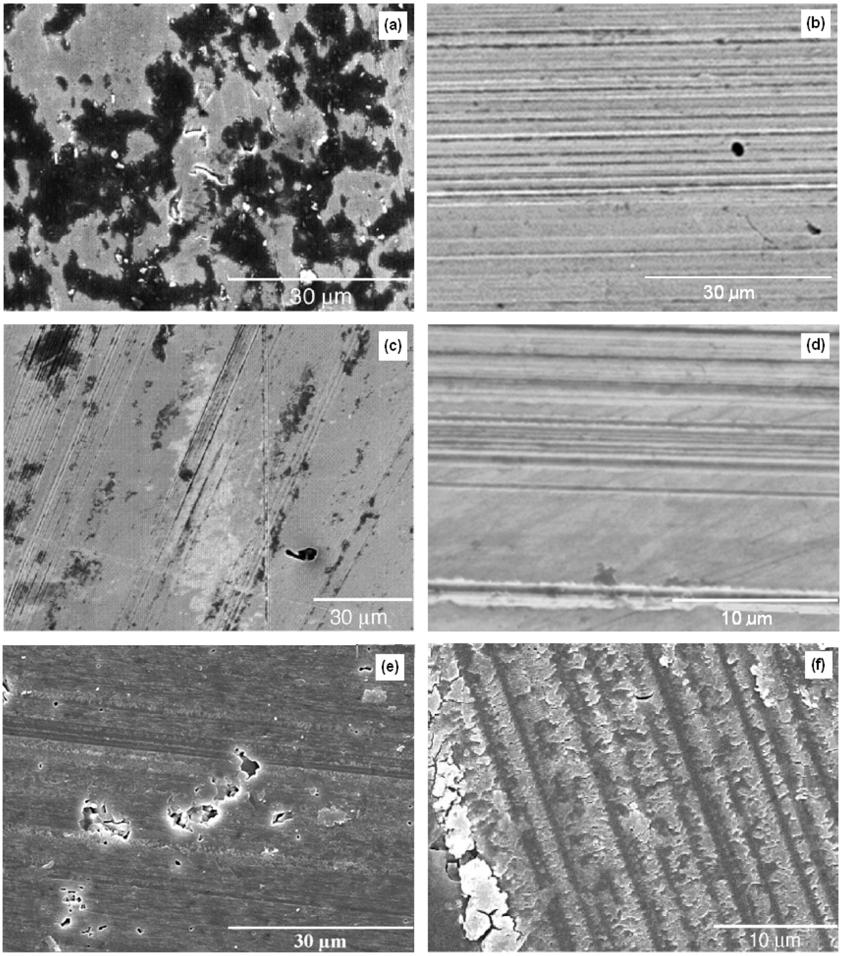

Figure 3. SEM images of the worn surfaces of steel 316L (a,b), CoCrMo (c,d), and alumina (e,f) in the absence of BSA (left) and in the presence of BSA (right). (Adapted with permission from reference (22). Copyright 2006 Elsevier).

Adsorption of Albumin on Prosthetic Materials

Adsorption on Steel, CoCrMo Alloy, and Alumina

Although most authors agree that albumin enhances boundary lubrication through adsorption on the joint material surfaces, there is still some controversy about this subject (*10*, *11*, *20*, *21*, *23*). Our previous study on UHMWPE sliding against counterfaces of alumina, CoCrMo alloy, and stainless steel indicated that the presence of albumin in the lubricant fluid reduces the friction coefficient. However, the extent of the reduction depends on the counterface: it is more important for the metals than in the case of alumina.

The objective of this study (*24*) was to assess albumin adsorption on the surfaces of alumina, CoCrMo alloy, and stainless steel, from HBSS+BSA solutions with a protein concentration of 4mg/mL, in order to confirm our assumption about the preferential adsorption of albumin on the metals than on alumina. Although several studies on albumin adsorption on the surface of prosthetic materials have been reported in the literature, a comparative study under the same conditions is required because adsorption is known to depend strongly on pH, ionic strength, and temperature, among other factors (*25*).

The adsorption studies carried out using radiolabeled albumin (^{125}I-BSA) led to the amounts of BSA adsorbed onto the counterface materials indicated in Figure 4a. X-ray photoelectron spectroscopy (XPS) measurements of the N 1s peak were used to assess qualitatively the protein adsorption under the assumption that the presence of nitrogen derives only from the protein molecules. Then, a comparison of the adsorbed amounts on the three materials may be based on the analysis of the intensities of N 1s peaks (Figure 4b). These data suggest that the amount of adsorbed albumin is maximal for steel and minimal for alumina but the difference in the peak intensities is much smaller than the difference in the adsorbed radiolabeled albumin activity. A comparison of our radiolabeling adsorption data with values from the literature was attempted: a reasonable agreement was observed for alumina (*26*), while for stainless steel, our values were much higher than those reported by other authors (*27–29*). No reports could be found relative to BSA adsorption on CoCrMo at the date of this work.

AFM observation of the surfaces after the friction tests with HBSS+BSA (images not shown) led to the conclusion that the morphology of the adsorbed protein layer depends on the substrate. Alumina revealed the substrate signature together with small albumin aggregates compatible with a ruptured thin layer. In contrast, the substrate features were not visible on the metallic surfaces that showed the presence of large albumin aggregates.

The results of all experimental techniques point out in the same direction: albumin adsorbs at a greater extent on the metallic surfaces than on alumina. We now try to correlate these results with the surface properties of the different materials.

The main components of the intermolecular forces responsible for protein adsorption are hydrophobic and electrostatic interactions (*30–32*). At neutral pH, the metallic surfaces are negatively charged (the zeta potential (ZP) is approximately -1.6 mV for CoCrMo and - 2.8 mV for stainless steel (*33*)), while the surface of alumina has a positive charge (*26*). Considering that the albumin molecules have negative surface charges at neutral pH (*22*), they may bind directly to the alumina surface and, through ion bridging to the metallic surfaces (the presence of Mg^{2+} cations was found to increase by one order of magnitude the adsorbed amount of BSA (*33*)). Furthermore, alumina has a much higher surface polarity than do the metals (see Table I in (*24*)). This means that the driving force for albumin adsorption should be higher on steel and on CoCrMo, the most hydrophobic surfaces, than on alumina.

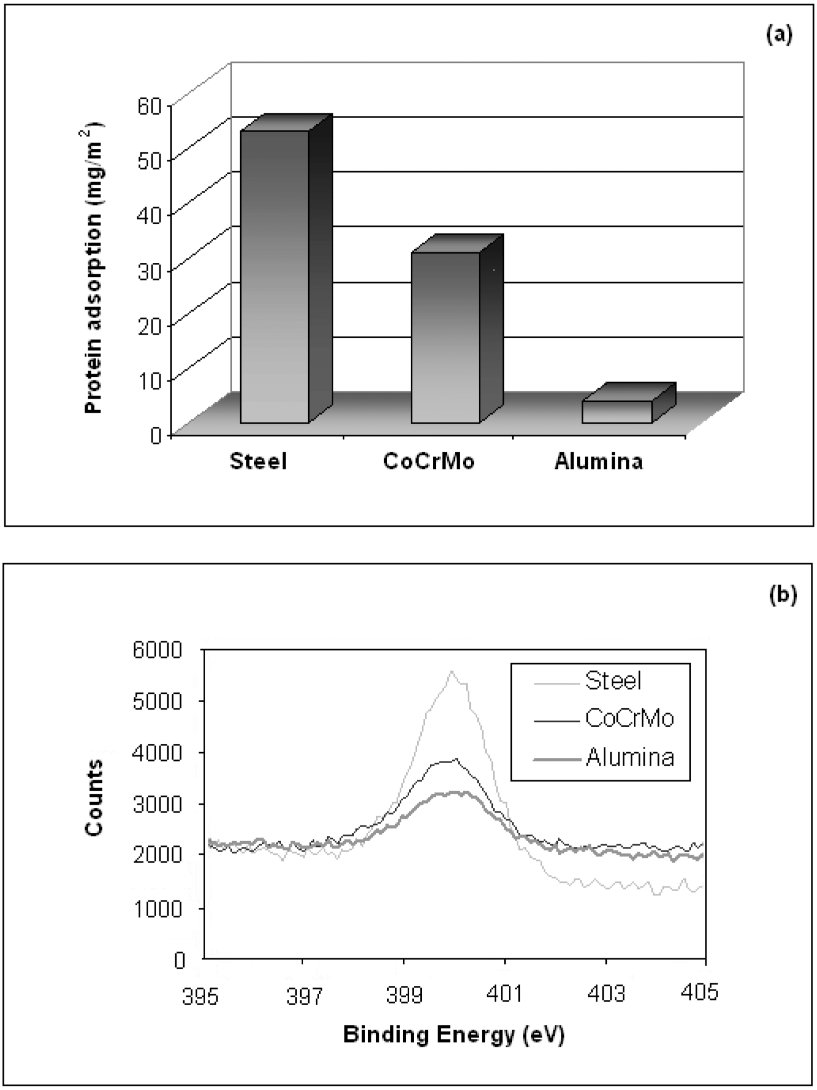

Figure 4. Saturation adsorption values obtained using ^{125}I-BSA (a) and N1s peak heights in XPS spectra recorded after BSA adsorption: stainless steel> CoCrMo> alumina (b). (Reproduced with permission from reference (24). Copyright 2010 John Wiley and Sons).

In conclusion, the adsorption results confirmed our predictions about the role played by albumin on friction and wear of prosthetic components. These results explain why the presence of albumin in the lubricant protects more efficiently the metallic surfaces than the surface of alumina, against polymeric transfer, leading to a better tribological performance of the prosthetic pairs involving metallic counterfaces against UHMWPE.

Adsorption on UHMWPE

Among the macromolecules present in the periprosthetic fluid, albumin and hyaluronic acid (HA) are known to play an important role in the biolubrication process. However, until the date of this work, information about the binding of albumin or HA to UHMWPE, the most used polymeric component of prosthetic pairs, was, to our knowledge, practically inexistent.

We decided then to investigate the adsorption of bovine serum albumin (BSA) and of HA onto UHMWPE using a quartz crystal microbalance with dissipation (QCM-D), and atomic force microscopy (AFM) (*19*). BSA adsorption on the UHMWPE coated quartz crystals was measured in the concentration range 0.05–20 mg/mL. These concentrations enclose the values found in the synovial liquids of patients with osteoarthritis which were reported to lie between 8 and 13 mg/mL (*34*). Furthermore, according to Kitano et al. (*11*), a concentration of 12 mg/mL for albumin should simulate that found in periprosthetic fluid under chronic inflammatory conditions after total joint arthroplasty.

In Figure 5 the QCM-D experimental results are compared with the isotherms calculated with Langmuir, Freundlich and Temkin models, the most used approaches to fit protein adsorption data (see, e.g. (*35*, *36*)). Freundlich and Temkin models seem to describe better the observed increase in protein adsorption as the concentration increases. Using the linear form of the Langmuir equation (Scatchard plot) led to a non-linear plot which indicated that the Langmuir model should not be applied in this situation due to the heterogeneous nature of adsorption and the positive cooperativity in protein binding. Comparison of the plateau values with the theoretical values of BSA adsorption correspondent to monolayers (maximum value of 3.65 mg/m^2, calculated for an end-on configuration of a "heart" shaped protein molecule (*37*)) shows that our value of Γ_{max} =7.4 mg/m^2 is far above. This value may result from the formation of a protein multilayer and/or the increase in the amount of water coupled to the protein film (*38*). The Gibbs free energy of adsorption estimated by the Temkin model (-37.4 kJmol^{-1}) is highly negative, indicating a strong adsorption of the protein.

The adsorption of HA onto UHMWPE was also investigated by QCM-D, but, only the concentration of 0.5 mg/mL was tested, in order to keep a low viscosity which is a requirement of this technique. Comparison with the amount of BSA adsorbed from solutions with similar concentration, led to the conclusion that adsorption of HA is approximately one order of magnitude lower (*19*).

The simultaneous adsorption of HA and BSA to the polymer was studied using a solution containing [BSA] = 4 mg/mL + [HA] = 0.5 mg/mL. The average adsorbed amount was similar to that obtained with the single BSA solution. The scatter of the results does not allow identification of any difference due to the presence of HA.

Figure 6 compares AFM images of the bare surface of UHMWPE with the images of the samples after incubation in solutions containing [BSA] = 4 mg/mL, [HA] = 0.5 mg/mL and [BSA] = 4mg/mL + [HA] = 0.5 mg/mL. The incubation in these solutions originated films with different morphology. While the film obtained by incubation in the BSA solution (Figure 6b) presents a globular structure typical of albumin molecules (*39*) with large agglomerates, the incubation in HA solution (Figure 6c) led to a film with a needle-like structure. The adsorption from the solution containing both components gave rise to globular structures similar to those observed on BSA incubated surfaces, but of smaller size (Figure 6d).

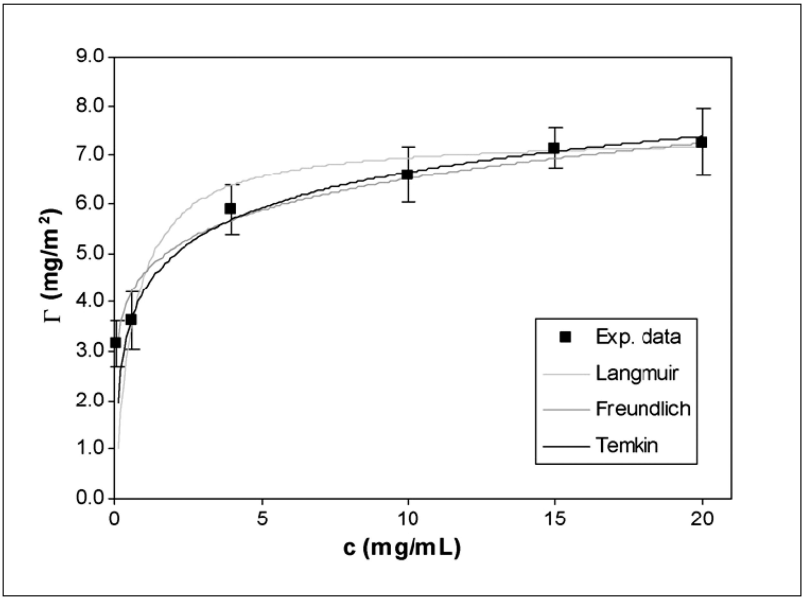

Figure 5. Adsorption of BSA onto UHMWPE determined by QCM-D. The lines represent theoretical adsorption isotherms calculated according to the Langmuir, Freundlich and Temkin models. (Reproduced with permission from reference (19). Copyright 2010 Elsevier).

The adhesion forces measured between AFM tips functionalized with BSA and the bare or protein coated polymer were almost equal and very low (F_{ad}=0.4-0.5 nN) suggesting that the protein molecules adsorbed to the UHMWPE substrates have high conformational stability. In fact, negligible values of self-adhesion forces indicate a small tendency of a surface-bound protein to destabilize when interacting with other bound proteins (*40*).

Similar results were obtained with the bare tip against UHMWPE incubated in the BSA solution, with and without HA, (F_{ad}= 0.8 nN in both cases) which also point to a high binding affinity of the protein to the polymer adsorbent, in agreement with Gibbs free energy of adsorption estimated by the Temkin model.

To our knowledge, this was the first report where adsorption of both albumin and hyaluronic acid on the surface of UHMWPE was quantitatively characterized. The main conclusion was that while BSA adsorbs strongly and extensively on UHMWPE, the adsorption of HA is very low. Furthermore, the stable nature of the protein layer adsorbed on UHMWPE may be considered as a favorable condition for the boundary lubrication of the polymer.

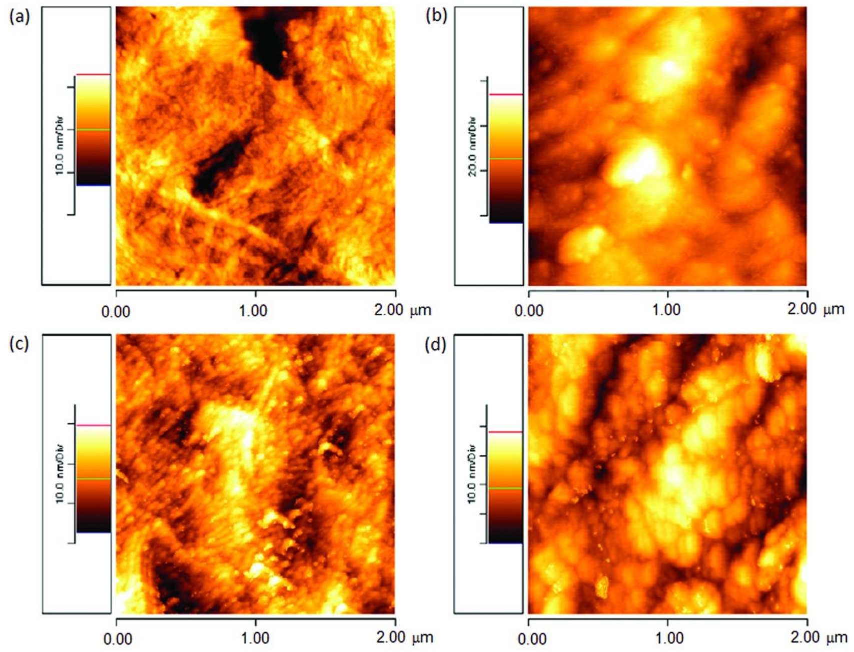

Figure 6. Topographic AFM images of the surface of UHMWPE bare (a) and after incubation in solutions containing [BSA] = 4mg/mL (b), [HA] = 0.5mg/mL (c) and [BSA] = 4mg/mL+ [HA] = 0.5mg/mL (d). (Reproduced with permission from reference (19). Copyright 2010 Elsevier).

Comparison of Adsorption Data Obtained Using Several Techniques under Similar Experimental Conditions

As previously mentioned, when investigating the adsorption of BSA on the surface of three prosthetic materials, we found that albumin adsorbs more extensively on metallic surfaces (stainless steel and CoCrMo) than on alumina. However, the values obtained for protein adsorption on the metallic plates using the protein radiolabeling technique were unexpectedly high, in disagreement with the XPS estimations, as well as with the values reported by other authors using different techniques but similar experimental conditions (*26*, *27*, *41*).

These findings raised the question of the purpose in comparing adsorption values obtained on sorbents in various states of aggregation and using different methods. A thorough investigation in the literature revealed only a few comparative studies of protein adsorption on the same material obtained with different experimental techniques (*38*, *42*). The main purpose of this work, described in reference (*43*), was to contribute to the analysis and eventual clarification of the above question through adsorption studies of the target systems constituted by protein (BSA) and two widely used prosthetic materials

(316L stainless steel and alumina), using various techniques: depletion, protein radiolabeling, QCM-D and AFM.

The results of the depletion measurements carried out with 316L stainless steel (SS) nanopowders (Figure 7a) agreed very well with those reported by Hansen et al. (*44*) for the adsorption of BSA onto powder of 304L SS. The adsorption isotherm of BSA on SS powder indicated that the adsorption process is continuous and leads to a saturation value which should be close to that of one end-on monolayer. In the case of Al_2O_3, our values are slightly smaller than those of Rezwan et al. (*37*) but the isotherms have the same shape. The adsorption isotherm on alumina powder suggested a two-step process (Figure 7a). The first step should correspond to the formation of a side-on adsorption on the positively charged alumina surface. According to those authors, after adsorption of the first layer of BSA, the surface charge of the alumina is completely masked and, during the second stage, the arriving protein molecules interact with the molecules that are already adsorbed to form dimers.

The BSA adsorption values measured on alumina and SS plates with QCM-D are shown in Figure 7b. These values were obtained with the modified Sauerbrey equation because the viscoelastic effects are not negligible for films adsorbed from high albumin concentration (> 4mg/ml). Assuming a density of 1.15 g/cm^3 for the adsorbed BSA, thicknesses of 2.5±0.8 nm and 3.8±0.9 nm were estimated for the protein layers formed on Al_2O_3 and SS, respectively. The mass uptakes measured with the QCM-D are higher than the values obtained by the depletion method. Usually, this difference is attributed to the fact that the mass obtained from the frequency shift includes water in the protein film, coupled via direct hydration or entrapped in cavities (*38*).

However, the main point here is the abnormality in the previously determined radiolabeling values measured on SS plates (see Figure 4a) when compared not only with the QCM-D results but also with the values measured on the SS powder. The values obtained by radiolabeling are always higher: a double for alumina, and one order of magnitude larger for SS. The discrepancy between the adsorption values measured on metallic surfaces by radiolabeling and other techniques was reported by other authors. Brash et al. (*45*) claimed that erroneously high values obtained for adsorption of BSA on metal surfaces could be attributed to the interactions of residual free ^{125}I-iodide in the protein solution with the surface. However, according to these authors, the effect depends on the metal. While radiolabeled BSA leads to reasonable values for adsorption on titanium, the values obtained for copper are very high. In the absence of a thorough explanation for the strange results obtained with radiolabeled proteins, we decided to neglect the adsorption values measured using this technique not only for the metallic alloy but for the ceramic, as well.

The AFM images of the films adsorbed from solutions with [BSA] = 4 mg/ml on SS and alumina surfaces (images not shown) confirmed the different morphology of both albumin layers. On the SS surface, a dense film of adsorbed protein with holes was observed, which may correspond to the end-on monolayer with packing faults. In contrast, the film adsorbed on the alumina surface was more homogeneous with no holes and showed the globular structure typical of albumin molecules (*39*). It seemed consistent with a side-on monolayer.

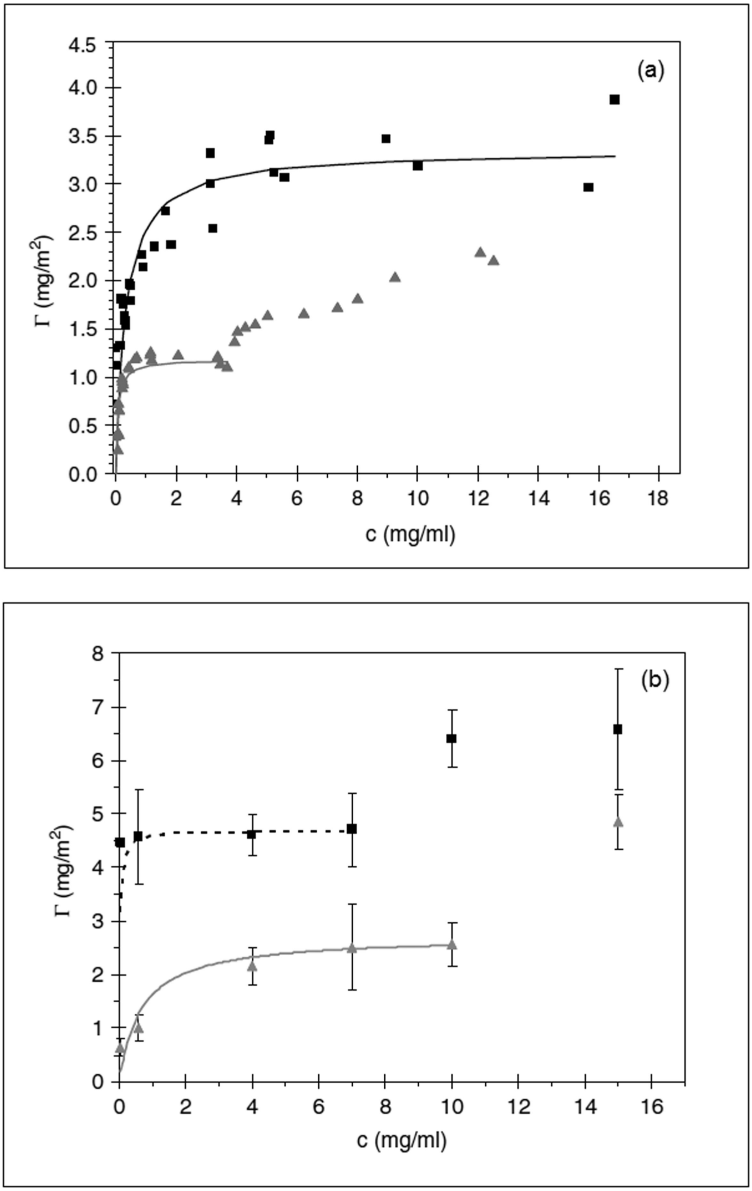

Figure 7. BSA adsorption, Γ, on powders (a) and on coated quartz crystals (b), as a function of the protein concentration. The curves are theoretical adsorption isotherms calculated using the Langmuir model and the symbols are: SS (■) and alumina (▲). The error bars were calculated from the standard deviations corrected with the Student parameter for a 97.5% confidence. (Reproduced with permission from reference (43). Copyright 2008 John Wiley and Sons).

Furthermore, AFM investigation of the albumin films thickness, by scratching in liquid medium (water), yielded an average value of 4 nm for the layer adsorbed on SS, in excellent agreement with the thickness estimated with the QCM-D. In case of alumina, the poor quality of the AFM images did not allow quantification of the thickness but the albumin films appeared to be thinner (*43*).

Summarizing, protein adsorption on both metallic and ceramic materials is independent of the aggregation state (powder or plate) of the materials. However, care should be taken when comparing the results of several techniques used to measure adsorption. Depletion may be considered one of the most reliable techniques because the mass uptakes are directly measured without recourse to any assumptions. In contrast, protein radiolabeling can be quite misleading. QCM-D coupled with AFM has the advantage of yielding information on the physical characteristics of the adsorbed film, besides the adsorbed amounts.

Effect of Albumin on Tribology of Coated Joint Materials

Titanium Nitride Coatings: TiN, TiNbN, and TiCN

In order to improve the tribological performance of the prosthetic pairs, several solutions have been proposed. A promising choice involves the protection of the metallic surfaces with ceramic coatings which appeared to be a good solution because both polymer wear and ion release are reduced while a high mechanical resistance and a low cost are kept (*8*, *9*).Titanium nitrides have been successfully applied as coating materials due to their tribological properties, biocompatibility and affordable price. Titanium nitride (TiN) is one of the most studied ceramic coatings due to its known biocompatibility (*46*). It leads to a significant increase in the metallic surface hardness, helps in the protection against corrosion (*8*) and reduces the bacterial colonization (*47*). Other nitrides such as TiNbN and TiCN may be interesting alternatives.

We present here a comparative study of TiN, TiNbN, and TiCN deposited on stainless steel substrates (*48*). The dynamical friction coefficients measured with the pairs involving titanium nitrides against UHMWPE, in HBSS and in HBSS+BSA, are presented in Figure 8a. In the absence of protein, the evolution of the friction coefficient exhibits a running in period where the friction coefficient increased rapidly and then tended asymptotically to a constant value which is similar for TiN and TiNbN and slightly lower than that of TiCN. Addition of BSA to the lubricant lowers significantly the friction coefficients for the three materials, with special relevance for TiNbN. The polymeric wear against all counterfaces in the presence of protein was much smaller than the corresponding wear in HBSS ($7.8\text{-}9.5\times10^{-12}$ in HBSS and $0.5\text{-}1\times10^{-12}$ in HBSS+BSA). In spite of the dispersion, the results pointed out to a minimum wear rate for the TiN coating in pure HBSS, and for the TiNbN, in the protein solution.

The main conclusion which can be drawn from the above results is that TiN exhibits the best tribological performance in HBSS, probably due to the lowest value of its hardness, while TiNbN seems to be the better choice when albumin was added to the lubricant.

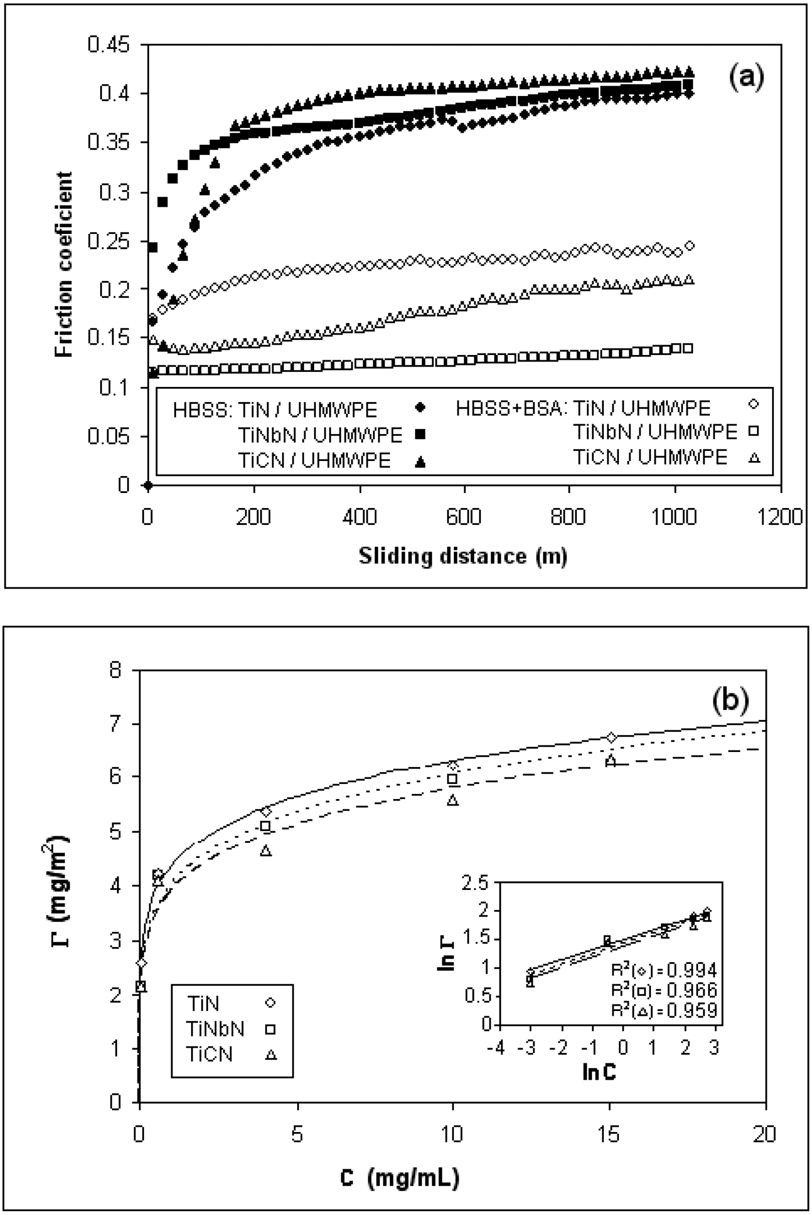

Figure 8. Friction coefficient versus distance for the tribological pairs involving titanium nitrides against UHMWPE in HBSS and in HBSS+BSA (a); BSA adsorption on the titanium nitrides: the lines represent theoretical adsorption isotherms calculated according to the Freundlich model (b). (Reproduced with permission from reference (48). Copyright 2009 Elsevier).

BSA adsorption on the quartz crystals coated with the titanium nitrides was investigated in the concentration range 0.05-15 mg/mL using the QCM-D technique. The experimental results were better described by the isotherms calculated with the Freundlich model (Figure 8b), although Langmuir model could also be applied. The albumin adsorption behavior on the three coatings is quite similar, even though TiN presents slightly higher adsorption. Differences in the affinity of albumin to the three coatings (inferred from the Langmuir model application) were not very significant.

Determination of the thickness of the adsorbed protein layer was made by scratching the adsorbed protein films with the AFM tip. From the topographic profiles, average values between 3 and 8 nm were obtained for the thickness of the protein film, in qualitative agreement with those estimated with QCM-D. It is interesting to notice that, although TiNbN does not adsorb more albumin than the other coatings, the conformation of the adsorbed protein on its surface seems to be different (AFM images not shown) which may be somehow related with the best tribological performance of the TiNbN coating in the presence of protein.

The adsorption measurements reported above did not allow a direct correlation between the adsorbed amount and/or the affinity of BSA to a particular coating with the improvement of its tribological behavior when BSA is added to the lubricant. Other factors such as the conformation of the adsorbed protein molecules and the viscoelastic properties of the protein layer may be important.

Cl-Implanted TiN Coatings

Ion implantation has been used to modify a large variety of surface properties, such as the surface hardness, the resistance to friction, wear, fatigue, corrosion and oxidation. The mechanical properties of the underlying material are preserved, since the depth of penetration of the ions is generally lower than 1 μm. There are several studies about the effect of the implantation of hydrogen, helium, nitrogen, argon, oxygen or carbon ions in biomaterials used in joint prostheses (*49–51*). The role of chlorine ion in this type of applications was never investigated.

We undertook an investigation to assess if ion implanted TiN coatings deposited on the metallic components were a good solution to improve the tribological performance of prosthetic pairs (*52*). The behavior of TiN and TiN implanted with Cl and Ar ions was compared.

The dynamical friction coefficients for the tribological pairs TiN/UHMWPE, TiN(Cl)/UHMWPE and TiN(Ar)/UHMWPE measured in the tests carried out using HBSS and HBSS + BSA are shown in Figure 9a.

In the absence of albumin, the friction coefficient reached similar values for the non-implanted and the chlorine-implanted TiN, lower than those obtained with the Ar-implanted TiN, although the running-in period is much longer for the Cl-implanted TiN. Since argon and chlorine atoms have approximately the same size, the difference in the friction coefficients suggests that the effect of chlorine-implantation must elapse from chemical transformations rather than from physical changes due to the implantation process. XPS analysis of TiN coatings revealed that, after Cl-implantation, part of TiN was oxidized mainly to

TiO_2. Wear reduction observed with TiN(Cl) (Figure 9b) may be attributed to the substitution of the hard TiN counterface by the titanium oxide layer with lower hardness which is less wear-aggressive for the polymer surface.

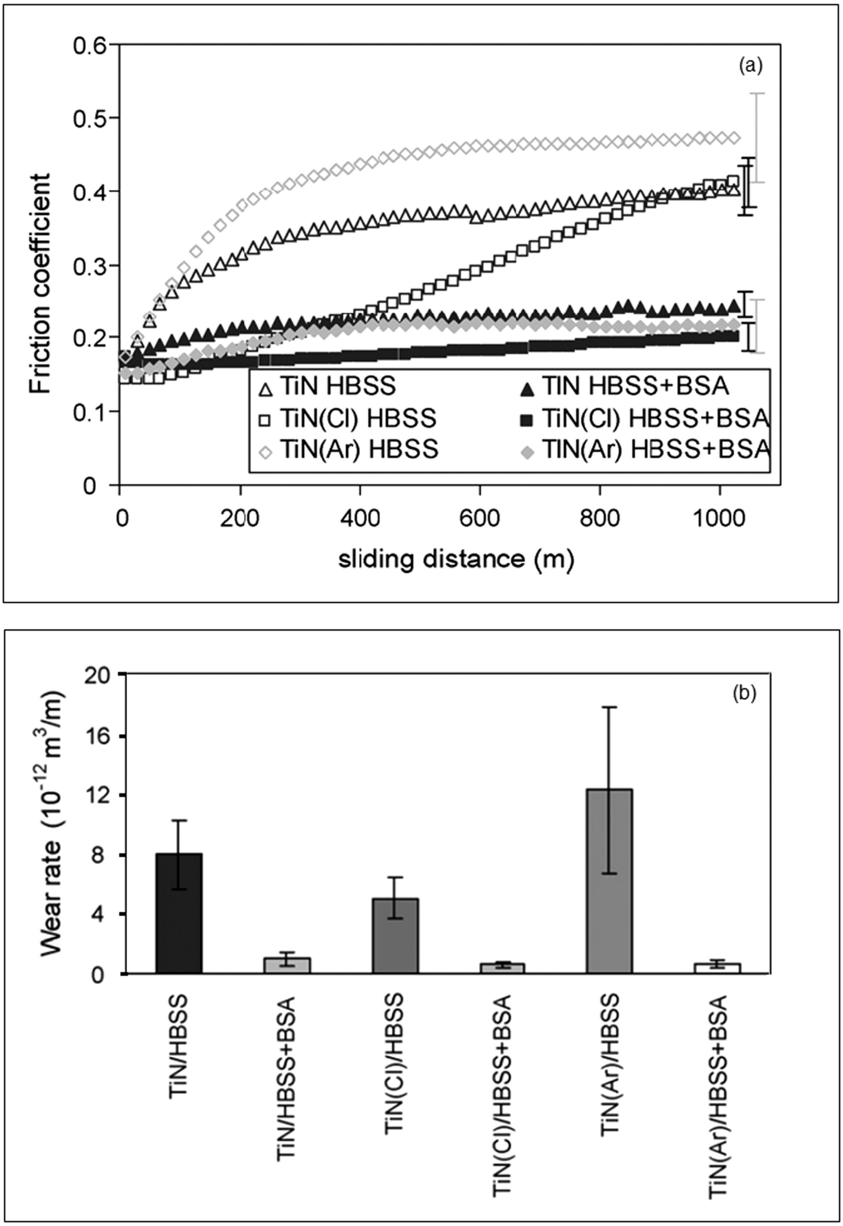

Figure 9. Friction coefficient vs. distance (a) and wear rate (b) for the tribological pairs TiN/UHMWPE, TiN(Cl)/UHMWPE and TiN(Ar)/UHMWPE in HBSS and HBSS + BSA. (Reproduced with permission from reference (52). Copyright 2007 Elsevier).

The decrease of the friction coefficient when BSA is added to the lubricant is evident in Figure 9a while the decrease in wear is shown in Figure 9b. Although the effect of the protein is so important that it attenuates the differences between non-implanted and ion implanted TiN coatings, the Cl-implanted TiN coating still leads to the lowest friction and wear.

Radiolabeling measurements of albumin adsorption on TiN and TiN(Cl) from HBSS+BSA solutions (unpublished results) confirmed the presence of an albumin layer on these surfaces which enhances the boundary component of the lubrication, reducing friction and wear. The change of the wear mechanism from abrasive, when the lubricant is HBSS, to adhesive when BSA is added to HBSS is evident from SEM images of the worn surfaces of UHMWPE tested against TiN and TiN(Cl) (images not shown).

In conclusion, the tribological behavior of the prosthetic pair TiN coated SS/UHMWPE may be improved through implantation of chlorine atoms in the TiN coating. When albumin was added to HBSS, friction and wear decreased significantly due to protein adsorption but, still, the Cl-implanted TiN coating led to the best tribological results.

Diamond-Like Carbon Coatings

Diamond-like carbon coatings (DLCs) have emerged as promising materials, because these coatings, already used in other biomedical applications, such as heart valves, blood pumps and stents, exhibit a unique combination of chemical inertness, mechanical and tribological properties (*53–56*). In the present work (*57*) we investigated the role of albumin on the tribological behavior of two DLCs, with different degrees of hydrogenation, against UHMWPE.

The novelty of this study, with respect to the widespread investigation of tribological performance of DLCs carried out at macroscales, is the use of a microtribometer that gives the possibility of obtaining information about the microscale mechanisms.

Two types of DLC films, designated by a-C and N3FC, were deposited on the SS substrates: the a-C coating is hydrogen-free (at.% hydrogen $< 5\%$) while N3FC is a new hydrogenated Argonne-DLC (*58*).

Adsorption of BSA (with 1, 4 and 10 mg/mL concentrations) on the DLCs was investigated by QCM-D technique, using quartz crystals coated with the N3FC type film. Due to technical reasons it was not possible to obtain a-C coated quartz crystals for these experiments. Ellipsometric measurements of the amount of BSA adsorbed on N3FC, a-C and SS were carried out using protein solution with a concentration of 4 mg/mL. Both techniques indicate that the DLCs adsorb more albumin than SS. The ellipsometric results show that a-C adsorbs a significantly larger amount of BSA than N3FC.

The tribological performance of the DLC coatings against UHMWPE was investigated using HBSS and HBSS+BSA solutions as lubricants, and two values for the applied normal stress. Figure 10 presents the initial stages of the evolution of the friction coefficient values for the tribological pairs N3FC/UHMWPE, a-C/UHMWPE and SS/UHMWPE. Two concentrations of the protein were tested, 4 and 10 mg/mL, but the results were similar and only the results for the latter are shown here. The average values of the friction coefficient are higher for the DLCs than for SS, when HBSS was the lubricant. Addition of albumin led to slightly higher friction coefficient values with all counterfaces, indicating that a less efficient lubricant action was obtained with the albumin solution than with pure HBSS. The fact that albumin has a greater affinity to the surface of the DLCs than to that of SS does not seem to influence the tribological behavior.

SEM analysis of the counterfaces was also carried out. Wear tracks and traces of polymeric transfer were observed only on the samples used in the experiments with HBSS+BSA which suggested a slight enhancement of the polymeric wear in the presence of the protein.

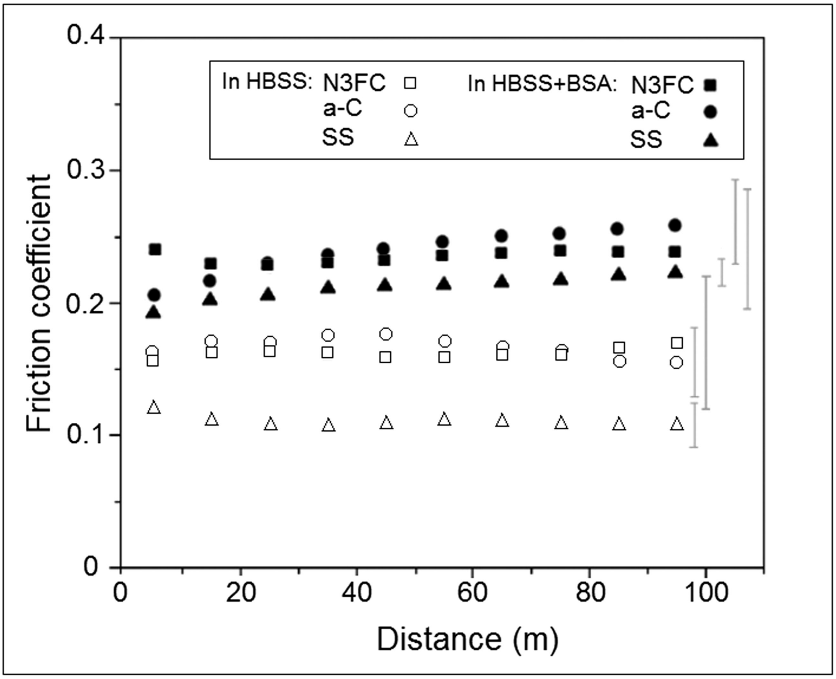

Figure 10. Friction coefficient vs. distance for N3FC, a-C and SS in HBSS and HBSS+BSA, with protein concentration of 10 mg/mL (contact stress 10 MPa). Data are from reference (57).

In order to understand better the lubrication mechanisms of the systems studied in this work, we investigated the effect of the normal stress applied in the tribological experiments. Two distinct stresses (1 MPa and 10 MPa) were tested using the pair N3FC/UHMWPE. From the results obtained for the variation of the friction coefficient with the sliding distance (not shown), it was clear that the friction coefficient increased with the decrease of the stress, independently of the lubricant. This finding can be explained by the influence of the adhesion forces which became important for low loads. In the presence of protein, the friction coefficient at the lower stress (1 MPa) increased significantly with the sliding distance. Such behavior should then be attributed to an increase of the adhesion forces, resulting from conformational changes of the protein during the experiment which eventually led to the protein denaturation. The formation of bridges between the two sliding surfaces may originate a high-shear-strength, thus impairing the system lubrication.

DLC coatings present a graphitic nature that is usually recognized as being responsible for its lubricating character. Several authors observed the formation of a thin transfer layer onto the partner surface upon sliding against many types of counterfaces (*59*, *60*). However, the buildup of this transfer layer on the counterfaces may or may not occur, depending on the tribological conditions and on the lubricant nature. When the lubricant is distilled water or NaCl solution, a reduction of friction and wear has been generally observed (*61*). However, in the presence of the physiologically relevant biomolecules, the formation of DLC transfer layer may be prevented, and consequently the UHMWPE wear will not decrease.

In our experimental conditions the studied DLC coatings did not improve the tribological behavior of the uncoated SS, regardless of the employed lubricant. These unexpected results refer to microtribometer tests where the initial stages of the tribological process were investigated, in contrast with most values previously reported, that were obtained with pin-on-disk or ball-on disk tribometers and simulators. We can therefore conclude that the eventual buildup of the lubricating DLC transfer layer did not occur, at least in the first one hundred meters of sliding. This means that, if the lubricant contains proteins or other biomolecules that adsorb immediately after contacting the biomaterial surfaces, the eventual benefit of the DLC coating for the tribological behavior may be lost.

Conclusions

In this investigation we studied the effect of the presence of albumin in the lubricant composition upon friction and wear of several pairs of joint materials. These pairs included always one UHMWPE component while the other varied from metal or metallic alloy to ceramics and ceramic coatings.

In all cases, with the exception of DLC coatings, the tribological tests were performed using a pin-on-disk tribometer where the sliding distances were typically of the order of 1000 m. The results revealed the major role of albumin in the tribological performance of the systems: under these experimental conditions, the friction coefficients decreased significantly when BSA was added to the lubricant.

Following the usual reasoning that attributed to BSA a protective role of the sliding surfaces though the formation of adsorbed layers, we tried to correlate the friction coefficient decrease with the extent of albumin adsorption. Indeed, in comparison with stainless steel and CoCrMo alloy, alumina was the surface where addition of albumin to the lubricant had the smallest tribological effect and simultaneously presented the lowest adsorption. However, the same explanation did not hold when applied to the titanium nitride coated materials. This means that the tribological performance seems to depend, not only on the extent of adsorption, but also on the conformation of the adsorbed protein which, in turn, determines the stability of the adsorbed layer.

The importance of the conformation of the adsorbed protein is also apparent when discussing the results obtained with DLC coatings using a microtribometer. In this case, albumin did not protect the surfaces during the initial meters of sliding distance. In fact, the reverse situation happened, with adhesion forces between eventually denaturated protein molecules adsorbed both on UHMWPE and DLC-coated surfaces being responsible for an increase in friction and wear.

Acknowledgments

This work was financially supported by the projects POCI/SAU-BMA/55493/2004 and PEst-OE/QUI/UI0100/2011.

Poly Hi Solidur, Ticona and MediMet who kindly offered the UHMWPE sheets and powder, and the metal disks, respectively, are acknowledged.

The authors are grateful to Dra. Virginia Chu (INESC MN) for the thickness measurements, to Prof. M. Barbosa (INEB) for making possible the protein radiolabeling and the ZP determinations of plates, to Eng. R. Azevedo who carried out these ZP measurements, and to Eng. J. Corker (group of Prof. J.M. Ferreira) from the University of Aveiro who provided the ZPs of powders.

Dr. F. Silva (INESC MN) is acknowledged for having done the alumina coating of the quartz crystals, Dr. Ali Erdemir and Dr. Osman Eryilmaz from Argonne National Laboratory (USA) for the DLC coatings, Dr Luis Ferreira for performing the irradiations in Nuclear Technological Institute of Portugal and to Dr. Luis Santos (IST) for his assistance in the ellipsometric analyses.

The collaboration of all the students and colleagues involved in this work whose names are given in the corresponding references is deeply appreciated.

References

1. Bosetti, M.; Zanardi, L.; Bracco, P.; Costa, L.; Cannas, M. *Biomaterials* **2003**, *24*, 1419–1426.
2. Ingham, E.; Fisher, J. *Biomaterials* **2005**, *26*, 1271–1286.
3. Cadosch, D.; Chan, E.; Gautschi, O. P.; Simmen, H.- P.; Filgueira, L. *J. Orthop. Res.* **2009**, *27* (7), 841–846.
4. Gillespie, W. L.; Frampton, C. M. A.; Henderson, R. J.; Ryan, P. M. *J. Bone Jt. Surg., Br. Vol.* **1988**, *70* (4), 539–542.
5. Muratoglu, O. K.; Bragdon, C. R.; O'Connor, D. O.; Jasty, M.; Harris, W. H. *J. Arthoplasty* **2001**, *16* (2), 149–160.
6. Alonso, F.; Ugarte, J. J.; Sansom, D.; Viviente, J. L.; Oñate, J. I. *Surf. Coat. Technol.* **1996**, *83*, 301–306.
7. Tamura, Y.; Yokoyama, A.; Watari, F.; Kawasaki, T. *Dent. Mater. J.* **2002**, *21* (4), 355–372.
8. Raimondi, M. T.; Pietrabissa, R. *Biomaterials* **2000**, *21*, 907–913.
9. Gutmanas, E. Y.; Gotman, I. *J. Mater. Sci.: Mater. Med.* **2004**, *15* (4), 327–330.

10. Widmer, M. R.; Heuberger, M.; Vörös, J.; Spencer, N. D. *Tribol. Lett.* **2001**, *10*, 111–116.
11. Kitano, T.; Ateshian, G. A.; Mow, V. C.; Kadoya, Y.; Yamano, Y. *J. Biomech.* **2001**, *34*, 1031–1037.
12. Fang, H.; Hsieh, M.; Huang, H.; Tsai, C.; Chang, M. *Colloids Surf., B* **2009**, *68*, 171–177.
13. Roba, M.; Naka, M.; Gautier, E.; Spencer, N. D.; Crockett, R. *Biomaterials* **2009**, *30*, 2072–2078.
14. Iodine-125: *Guide to Radioiodination Techniques*, Amersham Life Science; Little Chalfont: Buckinghamshire, UK, 1993; p 64.
15. Lima, J.; Sousa, S. R.; Ferreira, A.; Barbosa, M. A. *J. Biomed. Mater. Res.* **2001**, *55*, 45–53.
16. Welle, A. *J. Biomater. Sci., Polym. Ed.* **2004**, *15*, 357–370.
17. Lukkari, J.; Salomäki, M.; Ääritalo, T.; Loikas, K.; Laiho, T.; Kankare, J. *Langmuir* **2002**, *18*, 8496–8502.
18. de Feijter, J. A.; Benjamins, J.; Veer, F. A. *Biopolymers* **1978**, *17*, 1759–1772.
19. Serro, A. P.; Degiampietro, K.; Colaço, R.; Saramago, B. *Colloids Surf., B* **2010**, *78*, 1–7.
20. Sawae, Y.; Murakami, T.; Chen, J. *Wear* **1998**, *216*, 213–219.
21. Saikko, V. *Trans ASME* **2003**, *125*, 638–642.
22. Gispert, M. P.; Serro, A. P.; Colaço, R.; Saramago, B. *Wear* **2006**, *260*, 149–158.
23. Kumar, P.; Oka, M.; Ikeuchi, K.; Shimizu, K.; Yamamuro, T.; Okumura, H.; Kotoura, Y. *J. Biomed. Mater. Res.* **1991**, *25*, 813–828.
24. Serro, A. P.; Gispert, M. P.; Martins, C.; Brogueira, P.; Colaço, R.; Saramago, B. *J. Biomed. Mater. Res., Part A* **2006**, *78A* (3), 581–589.
25. Haynes, C. A.; Norde, W. *Colloids Surf., B* **1994**, *2*, 517–566.
26. Fukuzaki, S.; Urano, H.; Yamaguchi, T. *J. Ferment. Bioeng.* **1997**, *84*, 407–413.
27. Fukuzaki, S.; Urano, H; Nagata, K. *J. Ferment. Bioeng.* **1995**, *80*, 6–11.
28. Rubio, C.; Costa, D.; Bellon-Fontaine, M. N.; Relkin, P.; Pradier, C. M.; Marcus, P. *Colloids Surf., B* **2002**, *24*, 193–205.
29. Sakiyama, T.; Tomura, J.; Imamura, K.; Nakanishi, K. *Colloids Surf., B* **2004**, *33*, 77–84.
30. Dulm, P. V.; Norde, W. *J. Colloid Interface. Sci.* **1983**, *91*, 248–255.
31. Malmsten, M. *J. Colloid Interface. Sci.* **1998**, *207*, 186–199.
32. Smith, I. O.; Baumann, M. J.; McCabe, L. R. *J. Biomed. Mater. Res., Part A* **2004**, *70*, 436–441.
33. Pradier, C. M.; Costa, D.; Rubio, C.; Compère, C.; Marcus, P. *Surf. Interface Anal.* **2002**, *34*, 50–54.
34. Gerwin, N.; Hops, C.; Lucke, A. *Adv. Drug Delivery Rev.* **2006**, *58* (2), 226–242.
35. Adamson, A. W. In *Physical Chemistry of Surfaces*, 5th ed.; John Wiley & Sons: New York, 1990.
36. Andrade, J. D. In *Surface and Interfacial Aspects of Biomedical Polymers*; Andrade, J. D., Ed.; Plenum Press: New York, 1985; Vol. 2, Chapter 1.

37. Rezwan, K.; Meier, L. P.; Rezwan, M.; Vörös, J.; Textor, M.; Gaukler, L. J. *Langmuir* **2004**, *20*, 10055–10061.

38. Höök, F.; Vörös, J.; Rodahl, M.; Kurrat, R.; Boni, P.; Ramsden, J. J.; Textor, M.; Spencer, N. D.; Tengvall, P.; Gold, J.; Kasemo, B *Colloids Surf., B* **2002**, *24*, 155–170.

39. Sheller, N. B.; Petrash, S.; Foster, M. D.; Tsukruk, V. V. *Langmuir* **1998**, *14*, 4535–4544.

40. Sethuraman, A.; Han, M.; Kane, R. S.; Belfort, G. *Langmuir* **2004**, *20*, 7779–7788.

41. Gun'ko, V. M.; Vlasova, N. N.; Golovkova, L. P.; Stukalina, N. G.; Gerashchenko, I. I.; Zarko, V. I.; Tischenko, V. A.; Goncharuk, E. V.; Chuiko, A. A. *Colloids Surf., A* **2000**, *167*, 229–243.

42. Zhou, C.; Friedt, J.-M.; Angelova, A.; Choi, K.-H.; Laureyn, W.; Frederix, F.; Francis, L. A.; Campitelli, A.; Engelborghs, Y.; Borghs, G. *Langmuir* **2004**, *20*, 5870–5878.

43. Gispert, M. P.; Serro, A. P.; Colaço, R; Saramago, B. *Surf. Interface Anal.* **2008**, *40* (12), 1529–1537.

44. Hansen, D. C.; Luther, G. W.; Waite, J. H. *J. Colloid Interface Sci.* **1994**, *168*, 206–216.

45. Sheardown, H.; Cornelius, R. M.; Brash, J. L. *Colloids Surf., B* **1997**, *10*, 29–33.

46. Vanraay, J.; Rozing, P. M; Vanblitterswijk, C. A.; Vanhaastert, R. M.; Koerten, H. K. *J. Mater. Sci.: Mater. Med.* **1995**, *6*, 80–84.

47. Groessner-Schreiber, B.; Neubert, A.; Muller, W. D.; Hopp, M.; Griepentrog, M.; Lange, K. P. *J. Biomed. Mater. Res., Part A* **2003**, *64*, 591–599.

48. Serro, A. P.; Completo, C.; Colaço, R.; dos Santos, F.; Lobato da Silva, C.; Cabral, J. M. S.; Araújo, H.; Pires, E.; Saramago, B. *Surf. Coat. Technol.* **2009**, *203*, 3701–3707.

49. Xiong, D. S.; Jin, Z. M. *Surf. Coat. Technol.* **2004**, *182* (2-3), 149–155.

50. Torrisi, L.; Visco, A. M.; Valenza, A. *Radiat. Eff. Defects Solids* **2003**, *158* (9), 621–623.

51. Pichat, A.; Rabbe, L. M.; Rieu, J.; Rambert, A.; Chabrol, C.; Robelet, M. *Surf. Coat. Technol.* **1991**, *45* (1-3), 15–22–..

52. Gispert, M. P.; Serro, A. P.; Colaço, R.; Botelho do Rego, A. M.; Alves, E.; da Silva, R. C.; Brogueira, P.; Pires, E.; Saramago, B. *Wear* **2007**, *262*, 1337–1345.

53. Xu, T.; Pruitt, L. *J. Mater. Sci :. Mater. Med.* **1999**, *10*, 83–90.

54. Lappalainen, R.; Anttila, A.; Heinonen, H. *Clin. Orthop. Relat. Res.* **1998**, *352*, 118–127.

55. Tiainen, V.-M. *Diamond Relat. Mater.* **2001**, *10* (2), 153–160.

56. Oñate, J. I.; Comin, M.; Braceras, I.; Garcia, A.; Viviente, J. L.; Brizuela, M.; Garagorri, N.; Peris, J. L.; Alava, J. I. *Surf. Coat. Technol.* **2001**, *142–144*, 1056–1062.

57. Carapeto, A. P.; Serro, A. P.; Nunes, B. M. F.; Martins, M. C. L.; Todorovic, S.; Duarte, M. T.; André, V.; Colaço, R.; Saramago, B. *Surf. Coat. Technol.* **2010**, *204*, 3451–3458.

58. Fenske, G. R. *Presented to Chicago Section STLE Meeting*, March 2009.
59. Fontaine, J.; Belin, M.; Le Mogne, T.; Grill, A. *Tribol. Int.* **2004**, *37*, 869–877.
60. Sanchez-Lopez, J. C.; Erdemir, A.; Donnet, C.; Rojas, T. C. *Surf. Coat. Technol.* **2003**, *163-164*, 444–450.
61. Roy, R. K.; Lee, K.-R. *J. Biomed. Mater. Res., Part B* **2007**, *83* (1), 72–84.

Chapter 24

Sustainable Growth Factor Delivery through Affinity-Based Adsorption to starPEG-Heparin Hydrogels

A. Zieris, S. Prokoph, K. R. Levental, P. B. Welzel, K. Chwalek, K. Schneider, U. Freudenberg, and C. Werner*

Leibniz Institute of Polymer Research Dresden (IPF), Max Bergmann Center of Biomaterials Dresden (MBC) and Technische Universität Dresden (TUD), Center for Regenerative Therapies Dresden (CRTD), Hohe Strasse 6, 01069 Dresden, Germany
***E-mail: werner@ipfdd.de**

Controlled delivery of growth factors is critically important in directing tissue regeneration, which motivates the development of customized biomaterials for growth factor provision. Following the lead of the natural extracellular matrix, reversible adsorption of growth factors to material building blocks possessing cytokine affinity is considered an advantageous design principle for that purpose. Based on this concept, a biohybrid hydrogel composed of star-shaped poly(ethylene-glycol) (starPEG) and heparin was developed. The presence of starPEG determines the structural and mechanical network characteristics, while heparin enables the reversible immobilization of growth factors and the covalent binding of cell adhesive peptides. By varying the molar ratio of starPEG to heparin during gel formation, different hydrogel types with gradated physical properties but constantly high heparin content were obtained. We show that the matrices bind and release various heparin-affine cytokines, including vascular endothelial growth factor (VEGF), fibroblast growth factor 2 (FGF-2), bone morphogenetic protein 2 (BMP-2) and stromal-cell derived factor-1α (SDF-1α), independently of the network characteristics. Moreover, the material could be used for the parallel provision of different growth factor combinations over a broad range of concentrations. The cytokine delivery by modular starPEG-heparin hydrogels was proven to be effective in different *in vitro* and *in vivo* experiments, suggesting that the hydrogel platform will be an important tool in advancing regenerative therapies.

The interaction between proteins and biomaterials is often considered an undesired side effect in the application of various medical devices, causing activation of blood coagulation, biofouling, inflammation and infection. However, regenerative therapies now use biomaterials to locally deliver functional proteins, such as growth factors (often interchangeably used with the term “cytokines”), to stimulate growth, migration and differentiation of cells according to the requirements of therapeutical processes.

Sustained release of growth factors from biomaterials can address problems such as ineffective or undefined dosing and unresponsiveness to cytokines, occurring with simple bolus injections. With the latter approach, growth factors often show a short half-life and poor bioactivity due to rapid diffusion, denaturation or degradation. Furthermore, as many of the applied proteins act on several tissues, severe adverse effects can occur if the signaling molecules are transported to adjacent sites. These issues highlight the need to control the spatio-temporal availability of bioactive growth factors in the context of specific therapies.

Consequently, the presentation of cytokines from three-dimensional polymeric matrices has recently received increasing attention (*1*, *2*). A simple and widely used approach is the conjugation of growth factors with polymers. This increases protein solubility and stability, reduces immunogenicity and prolongs the plasma half-life of the growth factor. For the synthesis of such conjugates, the polymer has to be stable and biocompatible as well as equipped with only one single reactive group at one terminal end to avoid protein crosslinking. Moreover, it should be attached by an approach that will lead to reproducible site-specific protein modification (*3*). Starting from the pioneering work of Davis *et al.* (*4*), a protein conjugation with poly(ethylene-glycol) (PEG), now called PEGylation, has emerged as an important growth factor delivery concept. PEGylated proteins are already on the market and in clinical development (*5*). In more advanced strategies, the conjugates can additionally be linked by bioresponsive elements or the proteins can be entrapped in polymeric micelles (*3*).

However, regenerative approaches can additionally benefit from growth factor provision by biofunctional scaffolds, which can simultaneously mediate cell adhesion and direct a desired cellular localization and assembly. Physiologically, cells are closely associated with their highly hydrated environment, the extracellular matrix (ECM). Viscoelastic hydrogels, pioneered by Wichterle (*6*), are hydrophilic, highly water absorbent networks of synthetic and/or natural polymers that can mimic the structural character of the natural ECM (*7*). With these systems, growth factors can be either physically entrapped in the delivery matrix or chemically conjugated to the molecular scaffold, while their release is determined by diffusion out of the network and/or matrix cleavage/degradation. In the context of these different strategies, physical growth factor adsorption to biomaterials, based on secondary chemical interactions, combines the advantages of a non-specific entrapment within the matrix and covalent conjugation to the scaffold. This approach can be used to provide cytokines which are either directly accessible when attached to the polymeric scaffold or which display their activity after release from the material (*2*). The concept of physical growth factor adsorption closely resembles the strategy within the natural ECM, where cytokines are reversibly immobilized to sulfated glycosaminoglycans (GAGs). This binding mainly occurs via spatially matching electrostatic interactions between negatively charged N- and O-sulfated groups of the GAGs and the basic lysine and arginine residues of the growth factors (*8*). This protects the cytokines from proteolytic cleavage and denaturation. Moreover, the dynamic protein binding and release by the GAGs also controls the cytokine diffusional distribution and presentation to cellular receptors (*9*). Consequently, by designing biomaterials with a certain growth factor affinity, such systems might allow for a prolonged delivery of highly bioactive proteins in the desired concentration regime.

If biomaterials are to successfully support regenerative therapies, beyond effectively binding and releasing growth factors, they have to meet several additional requirements depending on the specific therapeutic approach. As with the natural ECM, key characteristics to control cell behavior are the physicochemical and mechanical properties of the scaffold combined with the provision of insoluble cues mediating cell adhesion and susceptibility to cellular matrix remodeling (*10*). Growth factor delivery systems designed for therapeutic approaches should ideally address all of these demands. Among the first materials developed according to this requirement, a PEG-based synthetic analogue of collageneous ECM for the delivery of bone morphogenetic protein 2 (BMP-2) has been produced (*11*). This scaffold was successfully applied to repair bone defects, and was constructed with a combination of RGDSP-peptides (in single-letter amino acid code) controlling cell adhesion and matrix metalloproteinase (MMP)-sensitive linkers for cell responsive degradation. However, developing successful matrix systems for therapeutic applications requires the dissection of both the viscoelastic properties and molecular signals that influence cellular behavior. So far, very few biomaterials allow for systematic and independent variation of mechanical and biomolecular characteristics (*12*). To address this, we now employ a mean field approach to analyze the force balance within biohybrid polymer networks to identify conditions that allow for decoupling biophysical and biochemical cues (see section "Design and key characteristics of starPEG-heparin hydrogels").

In addition, regenerative processes involving cell migration, proliferation and differentiation are governed by the temporal, spatial and concentration-dependent interplay of multiple growth factors. Functional biomaterials should therefore simultaneously or sequentially provide several different cytokines. The first single matrix system that was used to deliver multiple growth factors with distinct kinetics was based on alginate and could be successfully applied to promote vascularization by releasing vascular endothelial growth factor (VEGF) and

In Proteins at Interfaces III State of the Art 2012; Horbett, T., et al.;
ACS Symposium Series; American Chemical Society: Washington, DC, 2012.

platelet-derived growth factor (PDGF) (*13*). Nevertheless, the integration of tunable mechanical and biofunctional material properties into one system that can be applied for the delivery of multiple cytokines remains a challenging but indispensable prerequisite to further enhance therapeutic effectiveness.

We have developed a biohybrid hydrogel that addresses these key issues and offers a versatile platform of engineered biomaterials for regenerative therapies. It is formed by crosslinking amine functionalized star-shaped PEG (starPEG) and carbodiimide/N-hydroxysulfosuccinimide (EDC/s-NHS)-activated heparin (*14*). We report the design and main features of this system, specifically describing its potential for the defined and sustainable delivery of heparin-binding growth factors. An analytical strategy adapted to guide the matrix development is explained in detail. The applicability of the novel materials is demonstrated by examples highlighting the capability of the system to stimulate angiogenesis.

Design and Key Characteristics of starPEG-Heparin Hydrogels

StarPEG-heparin hydrogels are formed using the synthetic polymer starPEG and the naturally occurring glycosaminoglycan heparin as building blocks (Figure 1). Such biohybrid materials combine the advantages of a structurally well-defined synthetic polymeric system, offering suitable mechanical properties, and the benefits of a naturally derived matrix, providing enhanced biofunctionality.

PEG represents one of the most common synthetic polymers used for the design of biomaterials. Beside its excellent biocompatibility, the hydrophilic and uncharged character of PEG effectively prevents unspecific protein adsorption. Moreover, as PEG is a hydrolytically stable polymer with a good solubility in water and many different organic solvents, the possibility to easily modify its terminal functional groups opens up perspectives for a versatile PEG macromer chemistry (*15*).

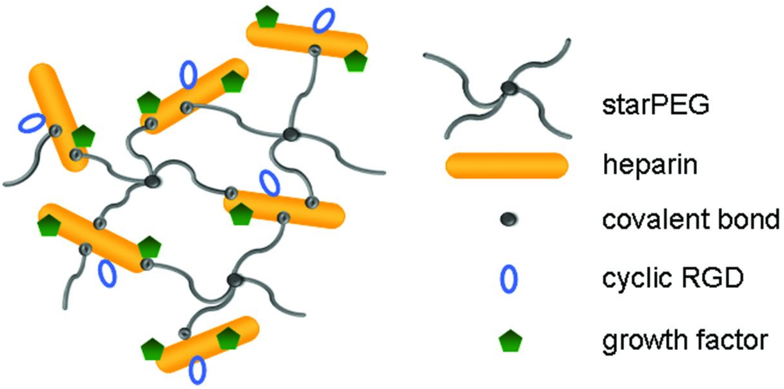

Figure 1. Design of the biohybrid starPEG-heparin hydrogel functionalized with adhesion ligands and growth factors. (see color insert)

Heparin is a glycosaminoglycan structurally related to the growth factor-binding ECM component heparan sulfate (*8*). While heparin can be mass-produced at low costs, it offers similar cytokine binding-properties as heparan sulfate at a smaller structural variance of its shorter chains (*16*). In the system presented here, heparin was used as a building block to equip the hydrogels with its intrinsic biofunctionality. Heparin-binding growth factors, such as VEGF (*17*), BMP-2 (*18*), fibroblast growth factor 2 (FGF-2) (*19*) and stromal-cell derived factor-1α (SDF-1α) (*20*), can be reversibly bound to the GAG. The binding is mainly driven by electrostatic interactions of their basic residues with the sulfate groups of heparin. Moreover, by applying EDC/s-NHS chemistry, integrin-binding cell adhesion peptides, such as cyclic RGDYK peptides (RGD-peptide, in single-letter amino acid code), can be covalently coupled to the carboxylic acid groups of heparin.

Conceptually, the network composition of starPEG-heparin matrices goes beyond classical strategies. Polymer-based hydrogels are often formed by interconnecting a polymeric building block with a short crosslinker. In contrast, starPEG-heparin gels follow a rational concept where starPEG functions as a flexible, structural building block, while heparin acts as a stiff, multifunctional crosslinker. The 14 kDa heparin used in these experiments carries up to ~ 24 carboxylic acid moieties (*8*). Consequently, by varying the molar ratio of starPEG to heparin (γ) from ~ 1.5 to 6, up to six four-arm starPEG molecules could be attached to form a dense meshwork. Applying a mean field approach, conditions could be identified, where the underlying expansion and retraction forces in the swollen hydrogels compensate each other in such a way that in a physiological situation, the concentration of the highly charged multifunctional crosslinker (i.e. heparin) stays nearly constant (Figure 2A). This key property of the starPEG-heparin matrices was theoretically predicted and experimentally verified (*21*, *22*). As a consequence, when the molar ratio of starPEG to heparin (γ) was increased from 1.5 to 6, gel types with an enhanced starPEG content but a constant heparin concentration of 0.8 % (w/w) were obtained, while the molar ratio of the components defines the degree of crosslinking.

The synthetic building block represents the component which critically determines the viscoelastic properties of the hydrogel matrices. Therefore, by increasing the content of starPEG, less hydrated (as indicated by a lower swelling degree, data not shown) and stiffer scaffolds (storage modulus varying from 1 to 14.8 kPa for γ = 1.5 to 6) could be produced (Figure 2B). This finding is related to a higher number of covalent crosslinks, thereby leading to the formation of a denser network with larger retraction forces, which is more rigid (higher storage modulus) and exhibits restricted water uptake (lower swelling).

However, independent of the different viscoelastic characteristics of the networks, all different hydrogel types contain large and constant quantities of heparin (~ 8 mg/ml). This rationally designed characteristic of the hydrogels is crucial for a subsequent biomolecular functionalization, as it should principally allow for a decoupling of the structural parameters and the biofunctionality. Consequently, based on the constant heparin concentration in hydrogels with varying mechanical characteristics, similar amounts of RGD-peptides (~ 0.6 mol RGD/mol heparin) were attached to the different gel types (*22*) (Figure 2C). As heparin also represents the basis for subsequent growth factor functionalization of the scaffold, the matrices might represent a system, where the cytokine delivery could be adapted independently of structural and mechanical material properties of the scaffold. Moreover, an advantage of the high heparin content within the gels is that the structural integrity of heparin can be preserved up to higher degrees of crosslinking, which might permit a rather unaffected interaction with several heparin-binding growth factors. Therefore, the developed starPEG-heparin hydrogels could represent a promising material for the independent and parallel delivery of multiple cytokines required to aid complex regenerative processes.

Methods for Characterizing the Interaction of Growth Factors with starPEG-Heparin Hydrogels

StarPEG-heparin hydrogels closely mimic the characteristics of the ECM by containing large quantities of heparin, which electrostatically binds and stabilizes numerous cytokines. To thoroughly characterize the interaction of growth factors with the hydrogels, several analytical methods have to be applied and compared (*1*). For this, fluorescently- or radioisotope (^{125}I)-labeled proteins were observed by confocal laser scanning microscopy (CLSM) or detected by gamma counting respectively. Additionally, growth factors were quantified by amino acid analysis via high performance liquid chromatography (HPLC) and immunological detection by an enzyme-linked immunosorbent assay (ELISA). All of these approaches are based on distinct detection mechanisms and therefore, experimental parameters had to be adjusted to the requirements of the particular method (Table I). This included the potential presence of a protein label and the setting used to present the protein solution to the hydrogels. However, despite these experimental differences, the combination of all four analytical approaches allowed the characterization of the binding and release of the growth factors over a wide range of concentrations.

The different methods were compared based on their ability to accurately and reliably quantify cytokine immobilization after adsorption and the diffusion-based release by starPEG-heparin hydrogels. Depending on the analytical approach, the protein could be directly detected in the gel network and/or in the supernatant of the surrounding medium. While all of the methods delivered the same qualitative results, the different experimental conditions showed quantitative differences (*23*). These discrepancies may arise from two effects. Firstly, an altered heparin-affinity was observed when a label had to be attached to the growth factors. Secondly, CLSM and HPLC were not compatible with the special immobilization chambers used to restrict non-specific protein binding to non-hydrogel surfaces. Only ELISA experiments could be performed using non-labeled protein and under conditions that minimized the contact area for non-specific protein interactions with ‘foreign’ glass or plastic surfaces. Due to these facts, in addition to its high sensitivity, ELISA was found to be the best performing assay for analyzing growth factor binding and release. For a more detailed discussion of the methodological optimization the reader is referred to (*23*).

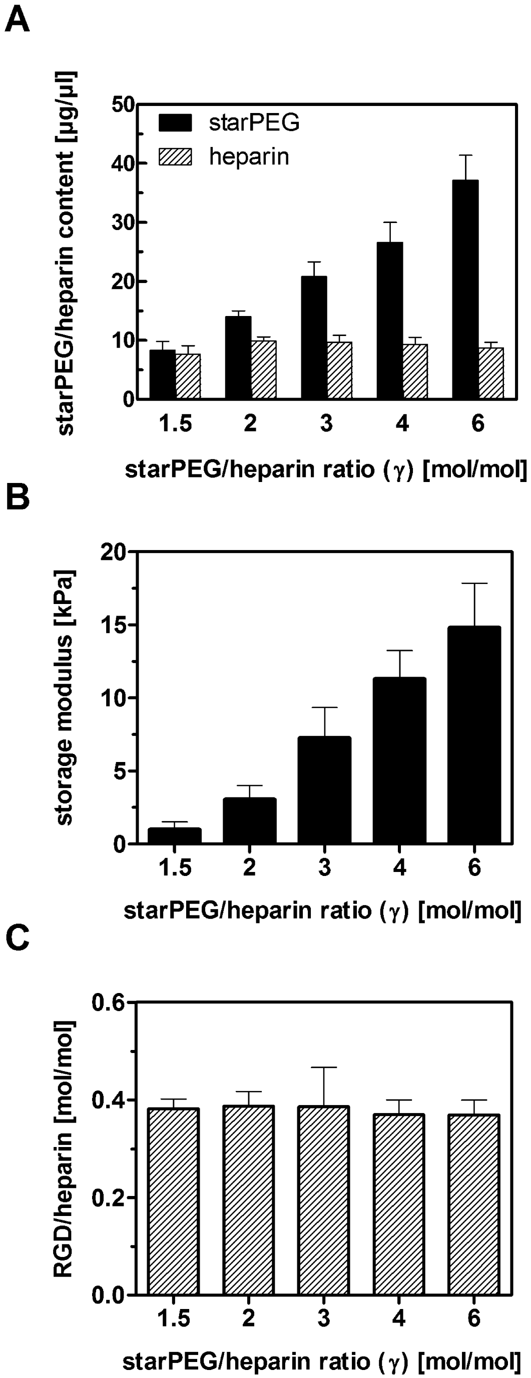
A
starPEG/heparin content [µg/µl]
0
10
20
30
40
50
starPEG
heparin
1.5
2
3
4
6
starPEG/heparin ratio (γ) [mol/mol]
B
storage modulus [kPa]
0
5
10
15
20
1.5
2
3
4
6
starPEG/heparin ratio (γ) [mol/mol]
C
RGD/heparin [mol/mol]
0.0
0.2
0.4
0.6
1.5
2
3
4
6
starPEG/heparin ratio (γ) [mol/mol]

Figure 2. Composition and key properties of different starPEG-heparin hydrogels. (A) Varying starPEG and constant heparin concentration in swollen gels matrices prepared with different molar starPEG/heparin ratios. (B) Gradual volumetric swelling characteristics of different hydrogel types depending on the starPEG content. (C) Constant RGD functionalization of different hydrogel types depending on the heparin content. All data are presented as mean ± root mean square deviation from n = 4. Adapted with kind permission from reference (22) (original Figure 2). Copyright 2012 John Wiley and Sons.

Table I. Experimental parameters used for growth factor binding and release studies with starPEG-heparin hydrogels. Due to higher sensitivity of these assays, cytokine release experiments were only performed via radiolabeling studies and ELISA. Adapted with kind permission from reference (*23*) (original Table 2). Copyright 2010 Springer Science and Business Media

	CLSM	*radiolabeling (^{125}I-) studies*	*HPLC*	*ELISA*
performance	well plate	immobilization chamber	well plate	immobilization chamber
analysis of protein	in gel and supernatant	in gel	in gel	in supernatant
protein labeled	yes	yes	no	no
sensitivity with particular setting	nanogram	picogram-nanogram	nanogram-microgram	picogram

Growth Factor Presentation by starPEG-Heparin Hydrogels

Uptake and Release of Growth Factors Depending on the Physicochemical Network Properties

To successfully support regenerative processes, it is important to realize that cellular behavior is critically influenced by interactions with the natural ECM. The physicochemical and structural properties of this network have been shown to have a major impact on cell fate (*10*). Therefore, in order to effectively advance therapeutic approaches for different tissues, biomaterials with distinct mechanical characteristics should be equally applicable for the delivery of functional signaling proteins.

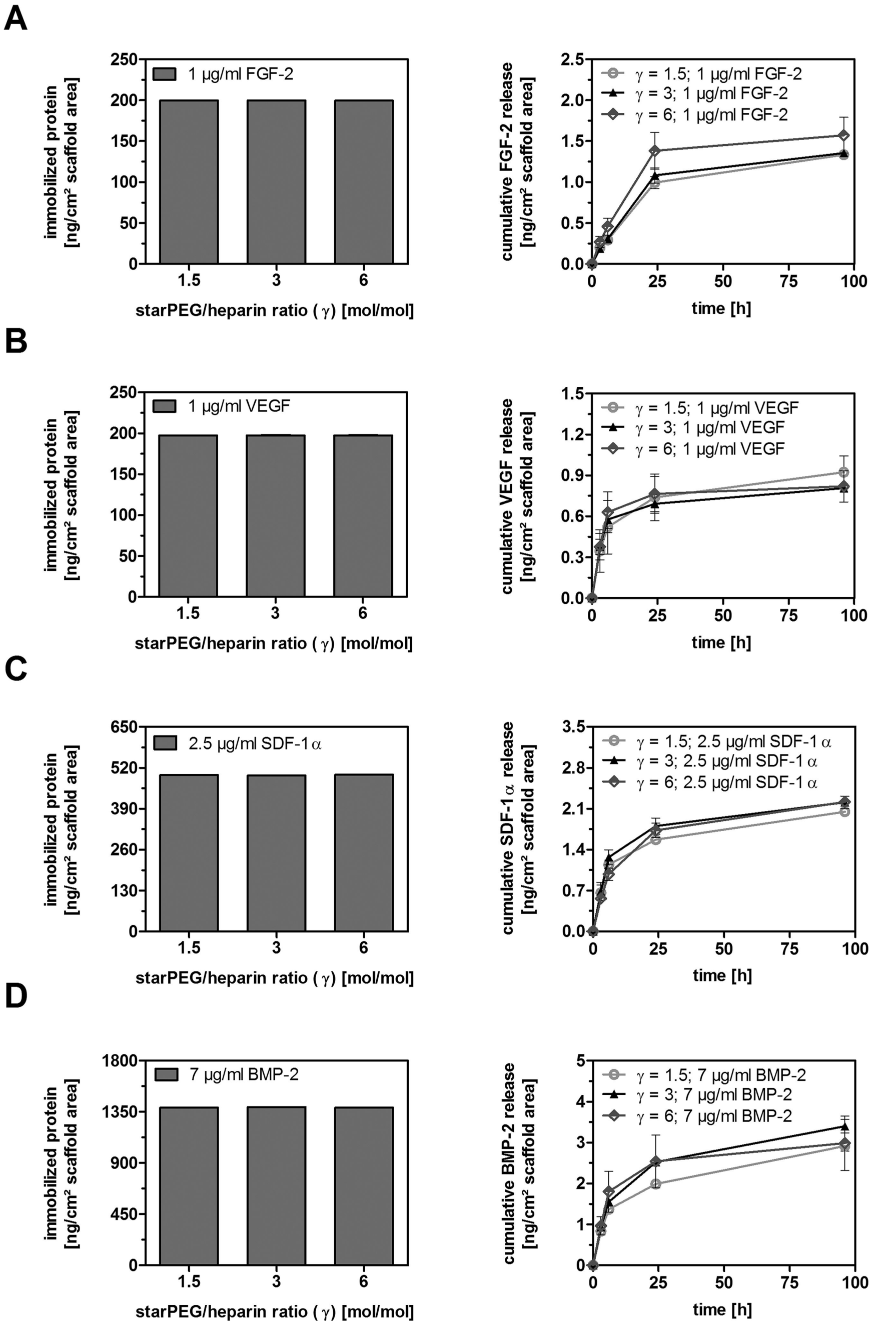

Figure 3. Amount of hydrogel-immobilized or -released growth factor determined for gel types differing in their crosslinking degree. Left: amount of electrostatically bound (A) FGF-2, (B) VEGF, (C) SDF-1α or (D) BMP-2 per cm² scaffold area for the different gel types γ = 1.5; 3 or 6 (low, intermediate and high crosslinking degree). Proteins were adsorbed from 200 µl immobilization

solution per cm² scaffold area. Right: cumulative amount of electrostatically bound (A) FGF-2, (B) VEGF, (C) SDF-1α or (D) BMP-2 released by the different gel matrices γ = 1.5; 3 or 6 (low, intermediate and high crosslinking degree). Proteins were released into 250 µl release medium per cm² scaffold area. All data are presented as mean ± root mean square deviation from n = 3. Adapted with kind permission from reference (24) (A and B, original Figure 2) and reference (22) (D, original Supporting Figure 2). Copyright 2010 Elsevier (24) and 2012 John Wiley and Sons (22).

To address this need, the influence of the starPEG-heparin network structure on the binding and release of various growth factors was investigated for hydrogel types differing in their crosslinking degree (γ = 1.5, 3 and 6) and therefore in their mechanical properties (soft, intermediate and stiff networks, see Figure 2B) (*22*, *24*). Figure 3 shows the results of these experiments for FGF-2 (A), VEGF (B), SDF-1α (C) and BMP-2 (D). For each of these proteins, it was demonstrated that similar quantities were bound by every scaffold independently of the gel type (Figure 3, left). Following growth factor immobilization by adsorption, the proteins were allowed to be released by diffusion from the hydrogels into the surrounding medium. Regarding the growth factor release kinetics (Figure 3, right), all proteins showed an initial burst release within the first hours. Such burst characteristics are often attributed to surface effects (*25*) and could have been caused by a protein fraction being entrapped in the meshwork but not bound specifically to heparin. However, after that, the protein continued to be released slowly over the course of the time period investigated. This suggests that the material has the potential to be used for applications that need long-term delivery profiles of growth factors. Moreover, comparable sequestered protein quantities were found for each scaffold independent of the gel type.

The results demonstrate that the binding and release of the different growth factors is independent of the mechanical hydrogel properties. Considering the mesh sizes of the matrices, with large pores in the range of ~ 16 nm for γ = 1.5 and ~ 7 nm for γ = 6 (*14*), it becomes clear that cytokine diffusion is not affected by differences in the network structure, but that the protein immobilization and delivery correlates with the constant heparin concentration of the different scaffolds. Consequently, starPEG-heparin hydrogels could be used as growth factor storage systems, presenting these proteins independently of the particular structural and mechanical properties of the scaffolds.

Uptake and Release of Growth Factors Depending on the Cytokine Concentration

Besides the influence of the viscoelastic cell environment, tissue regeneration is controlled by the concentration-dependent interplay of various signaling proteins. Therefore, biomaterials should be able to deliver large quantities of growth factors as well as provide several cytokines in parallel. StarPEG-heparin hydrogels might be promising candidates for such an application, based on their high heparin content.

Thus, as shown for the example of FGF-2 and/or VEGF, after evaluating the binding potential of starPEG-heparin hydrogels for high concentrations of single cytokines (Figure 4A), the possibility to deliver growth factor combinations was investigated (Figure 4B). For that, the immobilization and subsequent release of both proteins, introduced to the scaffolds either as single components or as combinations in different ratios, were analyzed for the gel with the intermediate crosslinking degree, $\gamma = 3$ (Figure 4B).

When evaluating the capacity of the matrices to take up various amounts of FGF-2 or VEGF separately (Figure 4A) (*24*), it was shown that the immobilized quantities at a defined concentration were similar for both proteins. Moreover, there was a linear correlation between the concentration of the incubation solution and the amount of immobilized FGF-2 or VEGF within the gel. This indicates that saturation of binding was not reached within the concentration range monitored. This result correlates with estimates of the maximal storage capacity of the applied hydrogel system, based on the calculated heparin concentration within the swollen network, and HPLC-based analysis of immobilization experiments with high concentrations of growth factors. Even after incubation with 50 µg/ml protein, the molar ratio of heparin to growth factor was still 26:1 for FGF-2 and 62:1 for VEGF. Moreover, as reported for FGF-2 (*26*), each heparin molecule is able to interact with several cytokine molecules, so that a saturation of binding will occur only at concentrations much higher than those used in this study.

In addition, it could be demonstrated that different combinations of FGF-2 and VEGF (Figure 4B) (*27*) can be bound to the matrices with the same efficiency as determined for the individual factors. Furthermore, the immobilized quantities of combinations of FGF-2 and VEGF at a defined concentration were found to be similar for both proteins.

Besides an evaluation of the starPEG-heparin hydrogel binding ability for FGF-2 and VEGF, experiments on the release of each single protein and of different combinations were performed. Figure 4C illustrates the cumulative release of either FGF-2 (left) or VEGF (right) alone and of different combinations of both proteins. Irrespective of the immobilized concentration or the particular factor considered, the release curves show once again the typical burst within the first hours followed by a continuous release over time. Similar to the trends observed for FGF-2 and/or VEGF immobilization, a linear correlation between the amount of gel-bound growth factors and the quantities being released was found. Additionally, different combinations of FGF-2 and VEGF could be released by the matrices with the same efficiency as for the individual factors. The large excess of heparin appears to prevent any interference between the growth factors during their combined application. Moreover, an additional advantage of these starPEG-heparin hydrogels is the comparable release of both cytokines at a particular loading quantity. Given this finding, the FGF-2 and/or VEGF release characteristics can be adjusted by the initial amount of protein loaded, which in turn can be tuned over a wide range of concentrations.

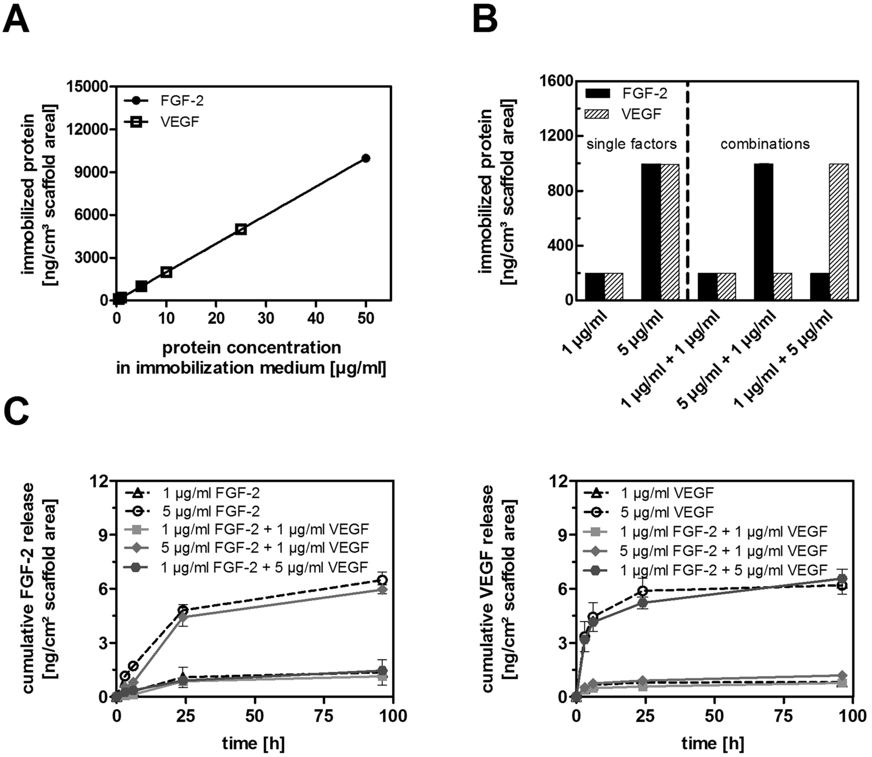

Figure 4. Amount of hydrogel-immobilized (top) and/or -released (bottom) FGF-2 and VEGF determined for different protein concentrations. (A) Uptake of single FGF-2 or VEGF in dependence on the protein concentration (0.5-50 µg/ml) in the immobilization medium; linear regression, R^2 (FGF-2) = 0.99999; R^2 (VEGF) = 0.99999. (B) Amount of electrostatically bound FGF-2 and/or VEGF per cm^2 scaffold area for different protein concentrations. Proteins were adsorbed from 200 µl immobilization solution per cm^2 scaffold area. (C) Cumulative amount of electrostatically bound FGF-2 (left) or VEGF (right) released by gels which were loaded with either single cytokines (dashed lines) or different combinations of FGF-2 and VEGF (continuous lines). Proteins were released into 250 µl release medium per cm^2 scaffold area. All data are presented as mean ± root mean square deviation from n = 3. Adapted with kind permission from reference (24) (A, original Figure 2) and reference (27) (B and C, original Figure 1). Copyright 2010 Elsevier (24) and 2011 Elsevier (27).

Growth Factor Delivery by starPEG-Heparin Hydrogels To Modulate a Specific Cell Behavior

In the context of regenerative medicine, the aim of growth factor delivery by biofunctional materials is to trigger a therapeutically relevant cell behavior. To illustrate the potential of cytokine administration by starPEG-heparin hydrogels for controlling cell fate decisions, cell culture experiments with an array of customized materials varying in their elastic characteristics and cell adhesive properties were performed.

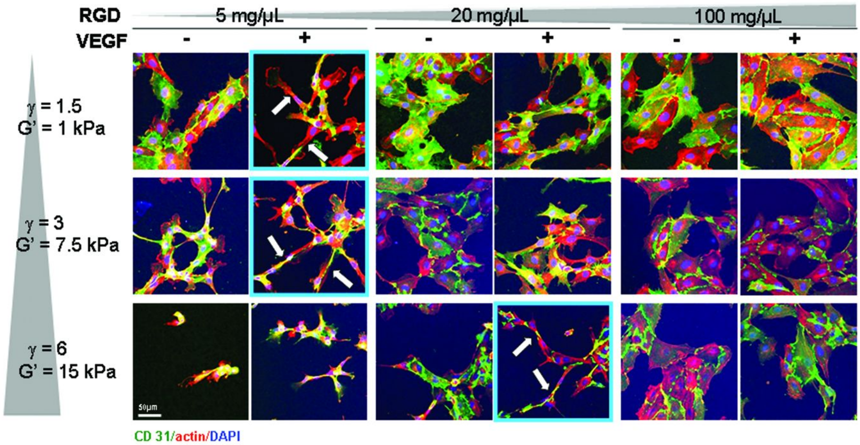

Figure 5. In vitro identification of pro-angiogenic conditions offered by VEGF delivery from starPEG-heparin hydrogels of different physical and biomolecuar characteristics. Endothelial cells elongate to form a network of cord-like structures on starPEG-heparin hydrogels with independently varying VEGF and RGD incorporation and storage modulus (turquoise frames, arrows indicate elongated cells). Representative confocal immunofluorescence images of CD31 (green, endothelial cell marker), actin (red), and DAPI (blue) staining of HUVECs plated for 20-24 hours on different scaffolds. Adapted with kind permission from reference (22) (original Figure 3). Copyright 2012 John Wiley and Sons. (see color insert)

As angiogenesis, the formation of new blood vessels from pre-existing capillaries, represents a key process for the regeneration of almost any tissue, it has to be inducible under a variety of different biophysical and biochemical properties of the cellular environment (*28*). StarPEG-heparin hydrogels were used to identify various pro-angiogenic conditions that were able to support morphological changes of endothelial cells indicative of *in vitro* capillary-like network formation (Figure 5, highlighted in turquoise, for exact quantification see reference (*22*)). In this example, a VEGF delivery from soft and intermediately elastic hydrogels (γ = 1.5 and 3) that were less adhesive (functionalized with low RGD concentrations) preferentially led to the development of an elongated phenotype. On more adhesive gels, cell spreading and the formation of a monolayer were observed. With VEGF released by stiffer hydrogels (γ = 6), endothelial cells required a higher RGD concentration to induce adequate cell adhesion and the formation of cord-like structures. In summary, with the gradual and independent variation of synergistically acting matrix characteristics, it could be shown that multiple sets of effective combinations of VEGF release, together with an appropriate network stiffness and adhesion ligand density can support the development of cord-like structures as it is required for blood vessel formation in distinct cellular environments within different tissues (*22*).

StarPEG-heparin hydrogels have also been applied as a culture carrier system to direct human mesenchymal stem cell (MSC) differentiation in the context of tissue engineering for bone regeneration. Similar to the natural situation being advantageous to the development of an osteogenic phenotype (*29*), the delivery of BMP-2 from cell adhesive, rather stiff hydrogels was found to preferentially promote MSC differentiation into this lineage (*22*).

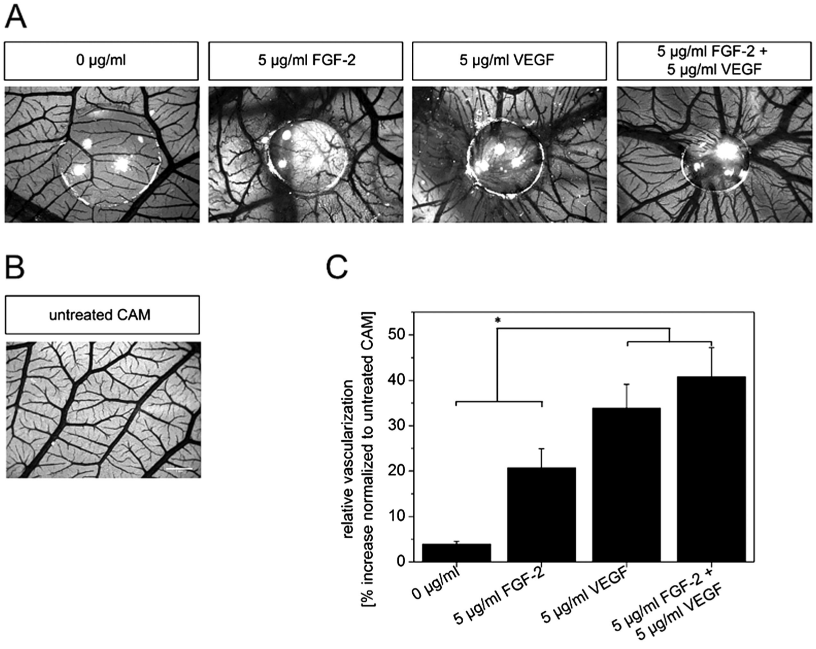

Figure 6. Effects of growth factor provision by starPEG-heparin scaffolds on vascularization in the chicken embryo CAM assay. (A and B) Representative images of the CAM vascularization in response to starPEG-heparin hydrogels with single FGF-2 or VEGF and a combination FGF-2 and VEGF (A) and the untreated CAM which served as a control (B) (scale bar 1 mm). (C) Quantification of the relative CAM vascularization in relation to starPEG-heparin hydrogels with single FGF-2 or VEGF and a combination of FGF-2 and VEGF. Data are presented as mean ± root mean square deviation from n = 5-16 (indicates p < 0.05; analysis of variance). Reproduced with kind permission from reference (27). Copyright 2011 Elsevier.*

After analyzing the effect of a growth factor administration by materials with tunable mechanical and biofunctional properties, the influence of concentration-dependent cytokine release and the provision of multiple growth factors was investigated. Both in *in vitro* migration assays and during subcutaneous implantation in mice, SDF-1α release from starPEG-heparin hydrogels could generate a growth factor gradient to induce site-directed attaction of early endothelial progenitor cells (eEPCs) towards SDF-1α (*30*). eEPC migration to ischemic tissues, with the incorporation of the cells into new capillaries and their release of intrinsic factors that promote angiogenesis, is a promising strategy for cardiac regeneration (*31*).

Moreover, we applied starPEG-heparin hydrogels for a combined delivery of FGF-2 and VEGF with the intention to support blood vessel formation (*27*). A parallel cytokine provision resulted in superior pro-angiogenic effects *in vitro* (enhanced endothelial cell survival/proliferation, morphology and migration) compared to the administration of single factors. We studied these effects further using *in vivo* experiments. Growth factor-functionalized hydrogels ($\gamma = 3$) were transferred to the developing chorioallantoic membrane (CAM) of fertilized chicken eggs (Figure 6). These onplants were surrounded by an increased number of allantoic vessels that looped towards the gel with the delivery of any angiogenic cytokine (A and C), compared to an untreated site (B). However, once again the combined provision of FGF-2 and VEGF enhanced the CAM vascularization most effectively (Figure 6 and reference (*27*)).

As a conclusion, starPEG-heparin hydrogels providing controlled release of various heparin-affine cytokines can be successfully applied in different tissue engineering approaches. The possibility to decouple the mechanical properties from the biofunctionalization is advantageous to adjust multiple different material parameters, with the option to deliver high quantities or several growth factors in parallel being of particular benefit for regenerative concepts.

Summary and Conclusion

For a successful strategy in regenerative medicine, therapeutically relevant growth factors need to be actively administered to the tissue of interest by biomaterials. The reversible adsorption of growth factors to materials that are composed of a building block with an intrinsic cytokine affinity, such as starPEG-heparin hydrogels, are ideal for this purpose. Different hydrogel types with distinct mechanical characteristics but a constant heparin content could be produced by varying the molar ratio of starPEG to heparin upon network formation. As heparin represents the basis for the growth factor interaction with the scaffolds, the matrices were found to bind and release various heparin-affine cytokines independently of the network stiffness and structural properties of the different gel types. Moreover, based on the high heparin content of the hydrogels, the material could be utilized for a modular delivery of growth factor combinations over a broad range of concentrations. Using this system, different *in vitro* and *in vivo* cell experiments demonstrated the suitability of cytokine delivery by distinct starPEG-heparin hydrogels to support tissue engineering approaches. In future, useful extensions of the introduced cytokine release system could be achieved by the inclusion of peptide units to control gel degradation (by incorporation of matrix metalloproteinase-sensitive peptide sequences) (*32*), and by selective heparin desulfation to modulate the affinity of the hydrogel to different growth factors.

In conclusion, starPEG-heparin hydrogels with independently adaptable physical and biomolecular composition demonstrated to be able to provide time-resolved multi-factor delivery of various growth factors. These results provide valuable new options for therapeutic tissue engineering concepts.

Acknowledgments

We would like to thank Tina Lenk (Leibniz Institute of Polymer Research Dresden) for radiolabeling of growth factors and Milauscha Grimmer (Leibniz Institute of Polymer Research Dresden) for performing HPLC analysis. U.F. and C.W. were supported by the Deutsche Forschungsgemeinschaft through grants WE 2539-7/1 and FOR/EXC999, and by the Leibniz Association. S.P., K.R.L., K.C. and C.W. were supported by the Seventh Framework Programme of the European Union through the Integrated Project ANGIOSCAFF. A.Z. was supported by the Dresden International Graduate School for Biomedicine and Bioengineering.

References

1. Tessmar, J. K.; Göpferich, A. M. *Adv. Drug Delivery Rev.* **2007**, *59*, 274–291.
2. Lee, K.; Silva, E. A.; Mooney, D. J. *J. R. Soc. Interface* **2011**, *8*, 153–170.
3. Duncan, R. *Nat. Rev. Drug Discovery* **2003**, *2*, 347–360.
4. Davis, F. F. *Adv. Drug Delivery Rev.* **2002**, *54*, 457–458.
5. Harris, J. M.; Chess, R. B. *Nat. Rev. Drug Discovery* **2003**, *2*, 214–221.
6. Wichterle, O.; Lim, D. *Nature* **1960**, *185*, 117–118.
7. Hoffman, A. S. *Adv. Drug Delivery Rev.* **2002**, *54*, 3–12.
8. Capila, I.; Linhardt, R. J. *Angew. Chem., Int. Ed.* **2002**, *41*, 391–412.
9. Flaumenhaft, R.; Rifkin, D. B. *Mol. Biol. Cell* **1992**, *3*, 1057–1065.
10. Hubbell, J. A. *Curr. Opin. Biotechnol.* **2003**, *14*, 551–558.
11. Lutolf, M. P.; Weber, F. E.; Schmoekel, H. G.; Schense, J. C; Kohler, T.; Müller, R.; Hubbell, J. A. *Nat. Biotechnol.* **2003**, *21*, 513–518.
12. Liu, W. F.; Chen, C. S. *Mater. Today* **2005**, *8*, 28–35.
13. Richardson, T. P.; Peters, M. C.; Ennett, A. B.; Mooney, D. J. *Nat. Biotechnol.* **2001**, *19*, 1029–1034.
14. Freudenberg, U.; Hermann, A.; Welzel, P. B.; Stirl, K.; Schwarz, S. C.; Grimmer, M.; Zieris, A.; Panyanuwat, W.; Zschoche, S.; Meinhold, D.; Storch, A.; Werner, C. *Biomaterials* **2009**, *30*, 5049–5060.
15. Tessmar, J. K.; Göpferich, A. M. *Macromol. Biosci.* **2007**, *7*, 23–39.
16. Uebersax, L.; Merkle, H. P.; Meinel, L. *Tissue Eng., Part B* **2009**, *15*, 263–289.

In Proteins at Interfaces III State of the Art 2012; Horbett, T., et al.;
ACS Symposium Series; American Chemical Society: Washington, DC, 2012.

17. Fairbrother, W. J.; Champe, M. A.; Christinger, H. W.; Keyt, B. A.; Starovasnik, M. *Structure* **1998**, *6*, 637–648.
18. Ruppert, R.; Hoffmann, E.; Sebald, W. *Eur. J. Biochem.* **1996**, *237*, 295–302.
19. Faham, S.; Hileman, R. E.; Fromm, J. R.; Linhardt, R. J.; Rees, D. C. *Science* **1996**, *271*, 1116–1120.
20. Sadir, R.; Baleux, F.; Grosdidier, A.; Imberty, A.; Lortat-Jacob, H. *J. Biol. Chem.* **2001**, *276*, 8288–8296.
21. Sommer, J.-U.; Dockhorn, R.; Welzel, P. B.; Freudenberg, U.; Werner, C. *Macromolecules* **2011**, *44*, 981–986.
22. Freudenberg, U.; Sommer, J.-U.; Levental, K. R.; Welzel, P. B.; Zieris, A.; Chwalek, K.; Schneider, K.; Prokoph, S.; Prewitz, M.; Dockhorn, R.; Werner, C. *Adv. Funct. Mater.* **2012**, *22*, 1391–1398.
23. Zieris, A.; Prokoph, S.; Welzel, P. B.; Grimmer, M.; Levental, K. R.; Panyanuwat, W.; Freudenberg, U.; Werner, C. *J. Mater. Sci.: Mater. Med.* **2010**, *21*, 914–923.
24. Zieris, A.; Prokoph, S.; Levental, K. R.; Welzel, P. B.; Grimmer, M.; Freudenberg, U.; Werner, C. *Biomaterials* **2010**, *31*, 7985–7994.
25. Huang, X.; Brazel, C. S. *J. Controlled Release* **2001**, *73*, 121–136.
26. Arakawa, T.; Wen, J.; Philo, J. S. *Arch. Biochem. Biophys.* **1994**, *308*, 267–273.
27. Zieris, A.; Chwalek, K.; Prokoph, S.; Levental, K. R.; Welzel, P. B.; Freudenberg, U.; Werner, C. *J. Controlled Release* **2011**, *156*, 28–36.
28. Patel, Z. S.; Mikos, A. G. *J. Biomater. Sci., Polym. Ed.* **2004**, *15*, 701–726.
29. Dellatore, S. M.; Garcia, A. S.; Miller, W. M. *Curr. Opin. Biotechnol.* **2008**, *19*, 534–540.
30. Prokoph, S.; Chavakis, E.; Levental, K. R.; Zieris, A.; Freudenberg, U.; Dimmeler, S.; Werner, C. *Biomaterials* **2012**, *33*, 4792–4800.
31. Dimmeler, S.; Burchfield, J.; Zeiher, A. M. *Arterioscler. Thromb. Vasc. Biol.* **2008**, *28*, 208–216.
32. Chwalek, K.; Levental, K. R.; Tsurkan, M. V.; Zieris, A.; Freudenberg, U.; Werner, C. *Biomaterials* **2011**, *32*, 9649–9657.

Chapter 25

Structural Insight of Antibody Adsorption for Improved Bioactivity and Detection

Xiubo Zhao,[1] Mohammed Yaseen,[2] Fang Pan,[2] and Jian R. Lu*,[2]

**[1]Department of Chemical and Biological Engineering,
University of Sheffield, Mappin Street, Sheffield S1 3JD, U.K.
[2]Biological Physics Group, School of Physics and Astronomy,
University of Manchester, Oxford Road, Manchester, M13 9PL, U.K.
*E-mail: J.lu@Manchester.ac.uk. Tel: +44 (0) 161 306 3926**

Antibody adsorption is a complex interfacial molecular process that is highly relevant to many technological developments such as biosensors, medical applications (e.g. pregnancy test and cancer diagnostics) and chromatography processes. However, the lack of basic understanding and effective control of the dynamic adsorption process and interfacial molecular conformation has limited its widespread applications. Therefore, it is of both fundamental and practical interests to understand how to manipulate antibody interfacial adsorption. This chapter reviews our recent biophysical studies of antibody adsorption at the silica/water interface using a number of interfacial techniques including Spectroscopic Ellipsometry (SE), Neutron Reflection (NR), Dual Polarisation Interferometry (DPI) and Atomic Force Microscopy (AFM). These measurements together help determine interfacial conformations of adsorbed proteins and illustrate the structural implications to their biological functions or activities, thereby providing direct information for better antibody immobilization and antigen detection.

In Proteins at Interfaces III State of the Art 2012; Horbett, T., et al.;
ACS Symposium Series; American Chemical Society: Washington, DC, 2012.

1. Introduction

Antibodies are glycoproteins produced by B-cells and are used for recognising foreign objects (antigens). They are typically made of two heavy chains and two light chains connected by disulfide bonds. Unlike other globular proteins such as albumin and lysozyme, an antibody is a Y shaped molecule with its molecular weight around 150 kDa and dimensions at approximately $142 \times 85 \times 38$ Å^3 (Figure 1a) (*1*). It has two antigen binding fragments (Fab) and one crystallisable fragment (Fc). The antigen binding sites (epitopes) are located at the N-terminal domains at the far ends of the Fab fragments. This region is extremely variable and allows them to bind to different antigens through a structure analogous to a lock.

One of the major applications of antibody adsorption is for biosensing and molecular probing. Protein based biosensors heavily rely on the performance of the proteins (e.g. enzymes, antibodies) immobilized on the active area or electrodes of the sensors. Unfortunately, protein adsorption onto surfaces or interfaces often induces certain conformational changes. In the meantime, the adsorbed proteins may adopt undesired orientations. Although both of these interfacial events cause the reduction of their biological functions or activities, the origins of these structural changes are different. Changes in conformation lead to the inability of the active sites in the recognition of the ligands, substrates or antigens whilst inappropriate orientations block the access to the binding sites. Various methods have been developed to immobilize proteins on solid substrate. These include interfacial chemical cross-linking, self-assembly, layer-by-layer deposition, and Langmuir–Blodgett (LB) technique (*2–4*). Although these elaborate protein immobilization approaches can improve the activities of the surface immobilized proteins, most of them need complicated molecular engineering skills and dedicated facilities, making them limited for widespread, fast and cost effective applications (*5*). The current industry prefers to use either direct printing or solution adsorption as efficient means for protein immobilization. Therefore, it is of both fundamental and practical significance to study how to control protein structural deformation and unfolding arising from unfavorable surface chemical nature and how to manipulate interfacial molecular orientations of physically adsorbed proteins to optimize their bioactivities.

In the past two decades, we have devoted extensive effort to the study of protein adsorption using albumin and lysozyme as models and their interaction with surfactants at air/water and solid/water interfaces (*6–21*). These studies focussed on unravelling protein interfacial conformation and structural unfolding (*22–25*). Several reviews have discussed interfacial structural changes upon adsorption of proteins to different model surfaces and interfaces (*6*, *7*, *16*, *25*). In the past few years, much of our effort has been devoted to the insight of implications of interfacial molecular orientations and structural deformations to their biological functions or activities (*25–33*). This chapter will start with the introduction of general background of protein adsorption and the techniques that have been widely used for the study of protein adsorption, followed by reviewing the adsorption of antibodies at different solid/liquid interfaces either for improving antigen detection or for probing interfacial protein conformation. Our discussion will focus on the detection of orientation of surface immobilized antibodies and their activities in antigen binding under different surface and solution conditions. The influence of surface chemistry on the structural deterioration of proteins and their biological consequences will not be the main theme of this review.

2. General Background of Protein Adsorption

Proteins are functional biomolecules that contain one or more polypeptide chains and that are folded into unique 3-dimensional globular (e.g. albumin, lysozyme) or fibrous (e.g. collagen) structures through a combination of intramolecular interactions (*34*) (e.g. hydrogen bonding, hydrophobic interactions, electrostatic attraction or repulsion, disulfide bonds). Some of them may also have non-peptide groups (e.g. polysaccharides, lipids) attached. The polypeptide chains within the protein are linear polymers comprised of 20 natural amino acids that are covalently linked together through amide bonds between neighbouring residues. As all native amino acids have the similar generic structure ($H_2NCHRCOOH$), it is the side-chain (R) of each amino acid that makes it specific and versatile. According to the diversity of the side-chains, amino acids can be divided into different categories such as polar, non-polar, aliphatic, positively or negatively charged, aromatic (*35–38*). The variation of the structure and property of the side-chain makes it possible to form an enormous number of proteins with a variety of biological functions. The structural complementarity and local intramolecular interactions not only enable the polypeptides to fold into favourable and stable 3D conformations but also, as a result of constraints, create some features on the outside surface of the proteins (e.g. charged areas either positive or negative, hydrophobic areas) that facilitate the adsorption of proteins to favourable surfaces and interfaces (*39*).

Protein adsorption is the adhesion and accumulation of protein molecules to surfaces or interfaces, and can be utilized with control, inducement or manipulation for different purposes. The adsorption of proteins to surfaces or interfaces is a complex process which normally is a consequence of intermolecular interactions. These may include different driving forces such as electrostatic interaction, hydrophobic interaction, surface energy, and also affected by environmental conditions such as solution pH, salt concentration and temperature. Generally, adsorption occurs when more energy is released or in other words when Gibbs free energy of the system is negative. Meanwhile, the surface and interfacial properties (e.g. roughness, texture) also have significant effects on protein adsorption.

Protein adsorption could cause many unfavourable issues. For examples, the residual protein adsorbed onto medical devices may result in cross-contamination between patients and the transmission of prions (*16*). Protein adsorption can stimulate the adhesion of clotting factors and fibrinogen onto implants and may induce thrombosis or restenosis (*40*). Non-specific adsorption of proteins can lead to the interference of specific recognition of epitopes, thereby reducing the effectiveness of *in situ* performance of sensor diagnostics. Protein adsorption in industry often causes protein fouling and sanitation issues. For example, excessive protein adsorption can block the filtration membranes and can serve as harbours for bacteria growth and reduce separation efficiency due to blockage. On the other hand, protein adsorption can also directly benefit many applications. For example, the adsorption of certain proteins can accelerate implant integration with local tissue environment by promoting cell adhesion and endothelialization. Hence, coating of a protein layer (such as collagen) onto cell culture scaffolds has been widely used in tissue engineering to facilitate cell adhesion and growth. Proteins such as enzymes and antibodies have been immobilized onto the sensor surfaces for a variety of biotechnological and diagnostic applications such as biocatalyst reactions, antigen detection and molecular probing. Here, we review our previous studies on antibody adsorption for the purpose of improving antigen detection and molecular conformation probing using a combination of leading biophysical techniques.

3. Common Experimental Techniques for Protein Adsorption Characterization

Many advanced techniques have been employed for the characterization of protein adsorption at surfaces and interfaces to understand the protein adsorption dynamics, determine the adsorbed amounts and interfacial layer structures (*15*). The most common techniques include spectroscopic ellipsometry (SE), Dual polarization interferometry (DPI), neutron reflection (NR), quartz crystal microbalance (QCM), Surface plasmon resonance (SPR), Atomic force microscopy (AFM) etc. Each of them has their advantages and disadvantages. AFM is a high-resolution (in the range of nanometers) technology to investigate the in-plane morphology of the proteins adsorbed on surfaces. It provides a three-dimensional surface profile in ambient condition and even a liquid environment. However, AFM can not provide the information of surface adsorbed amount of the proteins at the interfaces. It can also cause the deformation of soft proteins at the interfaces. Both SPR and QCM can provide the information of mass change in real time, but they lack the sensitivity of detecting structural information of the adsorbed layers. SE, however, is a convenient technology that can monitor the protein adsorption dynamics in real time and detect precise amount of the protein adsorbed, although it is less capable in determining the thickness and structure of the adsorbed layer. Both NR and DPI can determine the layer thickness of the adsorbed proteins. NR can even give detailed information on sublayer conformation at Angstrom level that most of the other technologies can not achieve. Over the last decade, NR has been extensively used by the authors for studying the protein adsorption at interfaces. Considering the advantages and disadvantages of these technologies, a combination of these techniques (NR, SE AFM, and DPI) has been used for the characterization of antibody adsorption in our previous studies and will be introduced in the following sections.

4. Antibody Immobilization for Antigen Detection

4.1. Antibody Orientation at Interface upon Adsorption

The adsorption of antibodies at the interface can result in four different molecular orientations (Figure 1): end-on (Fc attached to the support), sideways-on (one Fc and one Fab attached to the support), head-on (Fabs attached to the support) and flat-on (all three fragments attached to the support). Therefore, the molecular orientation of the antibody at the support surface has direct relevance to the antigen binding efficiency. Although end-on conformation is most preferred with the Fv fragments being orientated towards the solution side such that the binding sites are available, the actual situation in most cases on a given surface is a combination of different orientations with the flat-on being dominant (*16*, *25*, *26*). Furthermore, the molecular packing density of the antibodies at the support surface also has a significant effect to the accessibility of the binding sites. Hence, optimization of antibody orientation and packing density during interfacial immobilization will hugely improve the detection sensitivity.

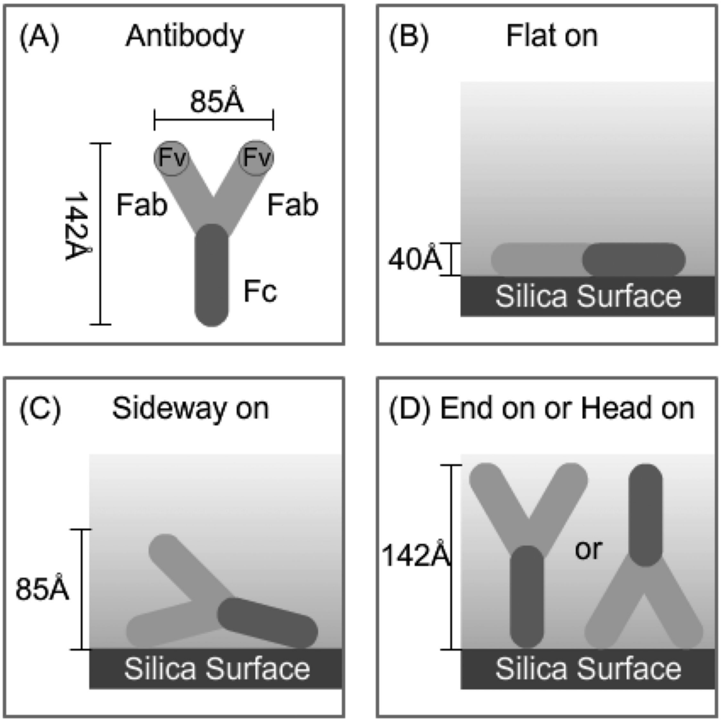

Figure 1. Schematic representations of the four representative interfacial orientations of the antibody adsorbed on the silica/water interface. (Reproduced with permission from ref. (25). Copyright (2009). The Royal Society.)

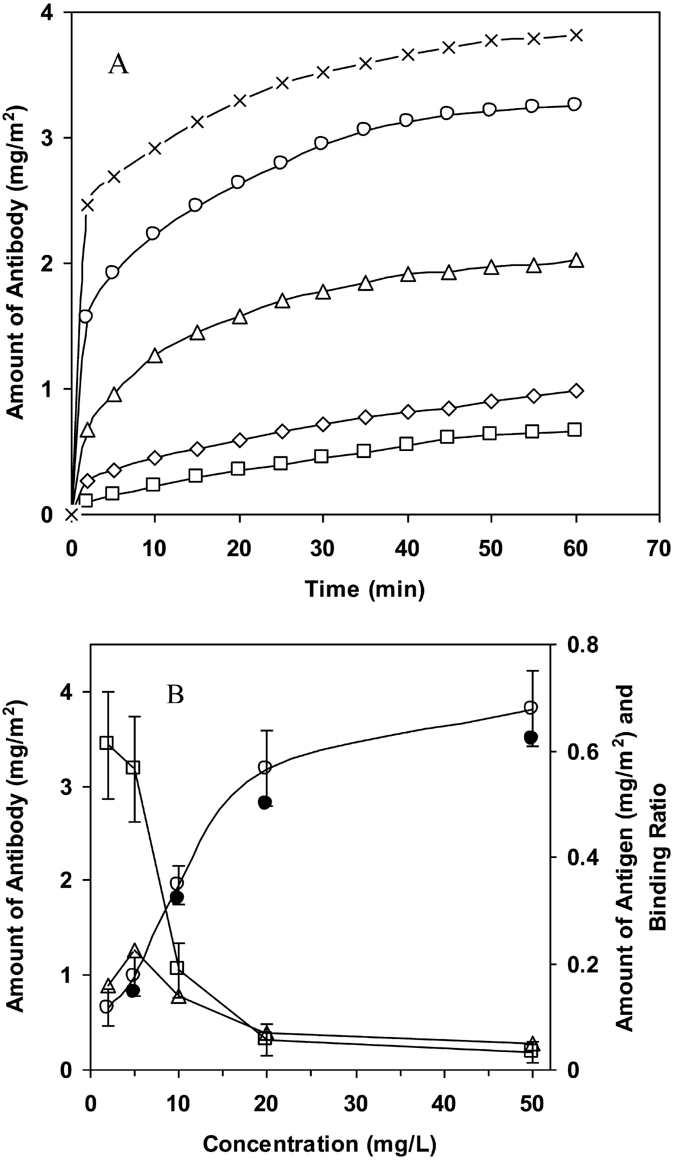

Figure 2. A. Dynamic adsorption of antibody at the silica/water interface studied by ellipsometry. B. Plots of antibody surface adsorbed amount obtained from ellipsometry (○, left axis) and neutron reflection (●, left axis), antigen binding amount (△, right axis) and binding ratio (□, right axis) at different antibody concentrations. The surface adsorbed amounts of antibody are all at 60 min. (Adapted with permission from ref. (30). Copyright (2011) American Chemical Society.)

4.2. Adsorption Dynamics and Concentration Effect

We here illustrate the dynamic process of antibody adsorption onto support surface using the adsorption of mouse monoclonal anti-human prostate specific antigen antibody (anti-hPSA) at the silica/water interface as an example. Similar to other globular proteins, the adsorption of anti-hPSA is time and concentration dependent (Figure 2A). The surface adsorbed amount of antibody steadily increases with time and then tends to plateau. This process becomes faster with increasing concentration. When looking at the surface adsorbed amount at the same adsorption duration (e.g. 1 hr), the amount of antibody adsorbed elevated dramatically at low concentration range (less than 20 mg/L) and then became slowed down over the high concentration range (Figure 2B). It was also found that desorption was negligible when washed by buffer, indicating the strong interaction between the anionic silicon oxide surface and the cationic parts of the antibody through electrostatic interaction. Ellipsometric measurements revealed that adsorption at low concentrations (<10 mg/L) resulted in less that 2 mg/m^2 of antibodies on the surface (Figure 2B). This amount of antibody adsorption could not fully cover the surface area as exposure of the surface to BSA could lead to more adsorption (*30*). When higher concentration was used, increased antibody adsorption was detected with no further BSA adsorption, indicating the full coverage of the surface. These findings are broadly consistent with the dynamic adsorption of anti-β-hCG (Human Chorionic Gonadotrophin) (*26*). It was found that faster saturation adsorption was reached when using higher concentration antibody solution with a greater saturated amount of adsorption. When the concentration is above 25 mg/ml, it only took 10 min to achieve the saturation adsorption.

4.3. Interfacial Orientation of Antibodies at the Silica/Water Interface

Apart from the amount of antibody adsorbed on the surface, the molecular orientation at the surface is also very important to the biological activity. Neutron reflection (NR) is capable of detecting the thickness and composition of nanofilms with sensitivity down to submolecular level (*13*, *25*, *41*). It has been widely used for studying biomolecular adsorption (*6*, *7*, *16*, *23*, *25*, *42–44*), particularly for probing the orientations of antibody at the interface taking into the account of molecular dimensions. Attempts have been tried to fit the data obtained from the adsorption of 5 mg/L solution (Figure 3) using a monolayer model but assumed that the molecules adopted “flat-on” (solid line), “side-on” (middle dotted line), and “head-on” or “end-on” (lower dotted line) orientations (*30*). Only a monolayer with a thickness of 42 Å could fit the measured profile. This thickness corresponds to the short axial length of the antibody molecule, showing that the molecules adsorbed at the interface adopted the “flat-on” orientation under the low concentrations. Other models using the thicknesses of 85 Å or 142 Å corresponding to the other two axial lengths with varying volume fractions (matching different scattering length densities) failed to fit the measured data.

The area per molecule was found to be 30900 Å^2, much bigger than the area occupied by a single antibody (12100 Å^2), indicating that the surface was not fully covered by the antibody molecules. These findings are highly consistent with the ellipsometric results outlined above and the previous work on hCG (Human Chorionic Gonadotrophin) antibody system (*26*, *28*, *45*). Xu et al. (*26*) have studied the adsorption of Anti-β-hCG at the silica/water interface. They reported that the antibody formed a uniform layer with a thickness of 41 Å under similar solution conditions, highly consistent with the result of the anti-hPSA. Meanwhile, AFM has been employed to investigate the morphology of the antibodies upon surface adsorption (*45*) (Figure 4). Many particle-like features were found to distribute on the silica surface. The height was found to be around 3 nm with lateral dimensions of 10 × 20 nm. These results also suggest the monomer adsorption with flat-on orientation on the surface.

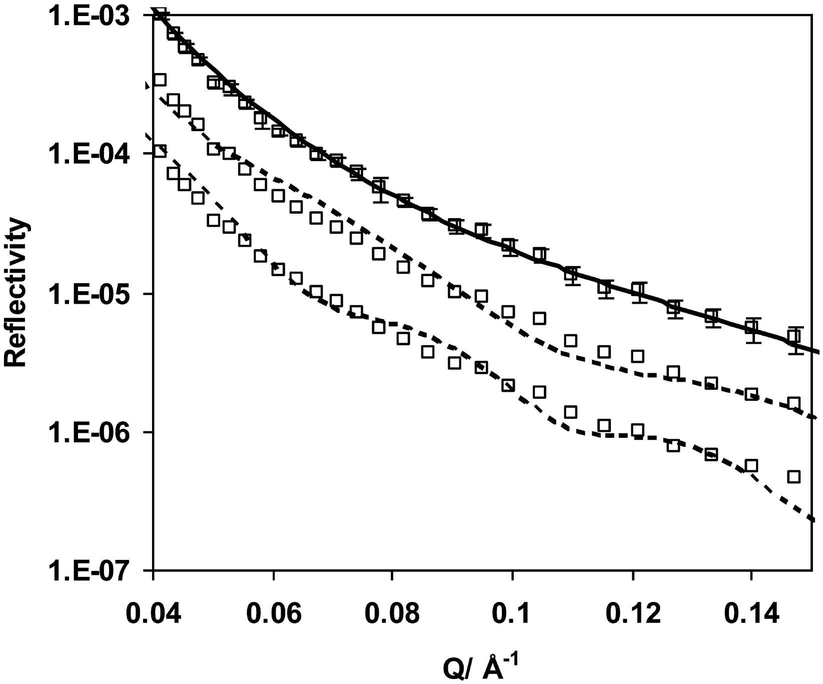

Figure 3. Plots of neutron reflectivity profiles at the SiO_2/D_2O buffer interface with antibody concentration of 5 mg/L (△) in phosphate buffer (I=20mM, pH 7 in D_2O). The solid line is the best fit assuming the antibodies adopted "flat-on" orientations at the interface (τ = 42 Å) while the middle and lower dotted lines (shift down 0.3 and 1 magnitudes for clarity) are the best fits assuming the antibodies adopted "side-on" (τ = 85 Å) and "head-on" or "end-on" (τ = 142 Å) orientations at the interface. (Adapted with permission from ref. (30). Copyright (2011) American Chemical Society.)

Increase in solution concentration resulted in more antibody adsorption and layer thickening. The layer can be described into three sublayers according to the different antibody volume fractions (Table 1). The inner sublayer has a thickness of 12 Å and low volume of antibody (22% - 29%). Middle sublayer has a thickness of 25-33 Å with relative higher volume fraction (29% - 46%) and the outer sublayer also has a thickness of 25-35 Å but with a very low volume fraction (9% - 22%). The thickness of inner sublayer does not change with concentration. However, the thickness of middle sublayer increases (from 25 to 33 Å) while the outer sublayer thickness decreases (from 35 to 25 Å) with increasing concentration from 10 to 50 mg/L. All the volume fractions of the three sublayers gradually increase with solution concentration (*30*). The total thickness of the three layers was around 70 Å with inhomogeneous molecular distributaries, indicating the tilting and overlapping of the molecules at the interface. Although the total thickness of the three layers is almost the same, the surface adsorbed amount of the antibody increased from 1.8 mg/m^2 to 3.5 mg/m^2 when the antibody concentration increased from 10 to 50 mg/L. This indicates that solution concentration has a significant effect to the molecular packing at the interface.

4.4. Effect of pH on Antibody Adsorption

Solution pH also has a significant effect on the adsorption of proteins. It not only changes the surface charge properties but also hugely affects the surface charge and hydrophilicity of the proteins. Silicon dioxide surface has been widely used as model surface for protein adsorption. The surface is slightly negatively charged above pH 2 and the charge density gradually increases with pH. Proteins are weakly charged and each has an isoelectric point. When pH is shifted away from the isoelectric point the net charge starts to increase and protein structural changes can occur resulting protein hydrophilicity changes. The increased charge density will change its affinity to the surface and also result in the electrostatic repulsion between molecules within the adsorbed layer. It is therefore of interest to examine how antibody adsorption is affected by solution pH and its implication to layer thickness, molecular orientation and their biological activity.

Table 1. Structural parameters of the anti-hPSA antibody layers adsorbed at the SiO_2/buffer interface (ionic strength at 20 mM, pH 7). (Reprinted with permission from ref. (*30*). Copyright (2011) American Chemical Society.)

Conc *(mg L^{-1})*	*τ* *(Å)*	*(ρ± 0.05) e^{-6}* *(Å^{-2})*	*φ*	*A* *(Å^2)*	*Γ* *(ng mm^{-2})*
5	42	5.95	0.14	30900	0.81
10	12	5.7	0.22	13736	1.8
	25	5.5	0.288		
	35	6.1	0.085		
20	12	5.7	0.22	9263	2.8
	30	5.2	0.39		
	28	5.8	0.186		
50	12	5.5	0.288	7117	3.5
	33	5	0.458		
	25	5.7	0.22		

Note: τ is the thickness of the layer, ρ is the scattering length density, φ is the volume fraction, A is the area per molecule and the Γ is the interfacially adsorbed amount.

A systematic study of the adsorption of anti-hPSA at the silica/water interface at a pH range from 4 to 8 is shown in Figure 5 with fixed antibody concentration (10 mg/L) and ionic strength (20 mM) (*31*). The adsorbed amount after 1 hr adsorption was found to increase with solution pH from 1.8 mg/m^2 at pH 4 to a maximum of 2.9 mg/m^2 at its isoelectric point (around pH 5.5), followed by the smooth decline with further increasing solution pH. This phenomenon is highly consistent with the adsorption of other antibodies and proteins at the silica/water interface. For example, Buijs *et al.* (*46*) have studied the adsorption of two monoclonal IgGs (IgG 1B, pI = 5.8 and IgG 2A, pI = 6.9) on silica surface at different pH. It was found that adsorption maxima occurred around the isoelectric points of the antibodies. The same trend was observed from our previous study on anti-β-hCG under similar solution conditions. The surface adsorbed amount of anti-β-hCG was found to increase from 2.2 mg/m^2 (at pH 4) to a maximum of 2.8 mg/m^2 (pH 6) and then drop to 1.3 mg/m^2 (*29*). This finding is also consistent with the adsorption of other proteins such as lysozyme and BSA at the same interface. For lysozyme, the maximum adsorption occurred at pH 11 while for BSA this occurred around pH 5, both near their isoelectric points (*6*).

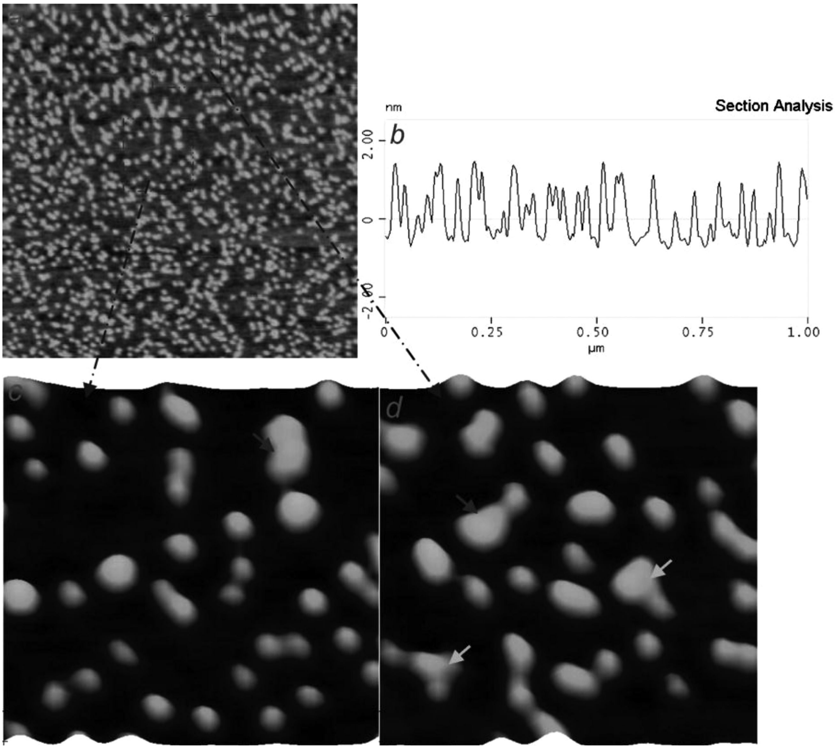

Figure 4. Anti-β-hCG adsorbed on silica from 5 mg/L solution at pH 8.0 and ionic strength of 20 mM for 1 min. (a) 1 µm ×1 µm image; (b) typical cross-sectional profile of image (a); (c and d) higher magnification images (0.2 µm ×0.2 µm) corresponding to square areas shown in image (a). The two enlarged images are presented at a pitch angle of 71° for clearer presentation. The z-scale for images (a), (c), and (d) is 5 nm. (Reproduced with permission from ref. (45). Copyright (2008) Elsevier Inc.)

Parallel neutron reflection studies under the same conditions supported the findings from ellipsometry. Furthermore, neutron reflection revealed the detailed information of layer thickness changes and molecular conformations (Table 2). Within the 5 different pHs (3.9 to 7.9) studied at the silica/water interface, the antibody was found to form uniform monolayer only at pH 7.9 with a thickness of 55±2 Å and the scattering length density (SLD, ρ) of 5.8×10^{-6} Å^{-2}, indicating an antibody volume fraction of 18.6%. The area per molecule was about 17000 Å^2 and was bigger than the footprint of the flat-on antibody (~12000 Å^2). All these structural details together suggest that whilst the antibodies stayed predominantly flat-on the entire layer was loose, consistent with the relatively large repulsive interactions within the layer and between antibody molecules and the substrate surface. At all other pHs, a three layer model had to be used to describe changes in the volume fraction along the surface normal. The thickness for the inner layer on the oxide surface was from 8 to 12 Å. The volume fractions of the inner layers were all around 25%. The thickness and volume fraction of the middle layers varied a lot and were also pH dependent. At pH 3.9 and 4.8, the middle layers were all at 25 Å but its volume fraction increased from 39% to 56%, indicating increased adsorption. At pH 5.3 and 6.1, the thicknesses of the middle layers were both around 30 Å, but the volume fraction dropped from 53% and 46%. At pH 7, the thickness and the volume fraction of the middle layer reduced to 25 Å and 29%, respectively. Although the outer layer thickness increased from 20 Å (at pH 4) to 35 Å (at pH 7.9), their volume fractions were significantly low (around 8%, except 15% at pH 6.1). Therefore, the middle layer was dominant and contained the main part of the antibody. The total surface adsorbed amount increased from 1.9 mg/m^2 (at pH 3.9), reached a maximum of 2.9 mg/m^2 when the pH was close to the pI of the antibody of around 5.5 (*28*), then resulted in the drastic decline at pH 6.1 (reflected in the large shrinkage of both thickness and volume fraction of the middle layer), consistent with the decline of surface adsorbed amount beyond the pI. Apart from pH 7.9, antibody adsorption formed three layer structures, suggesting the rather strong overlapping of the antibody fragments. The ellipsometry and neutron reflection work as described above provided detailed insights of the layer structure for the adsorption of anti-hPSA antibody at different pH values and are highly relevant for explaining the binding efficiency of the antigen.

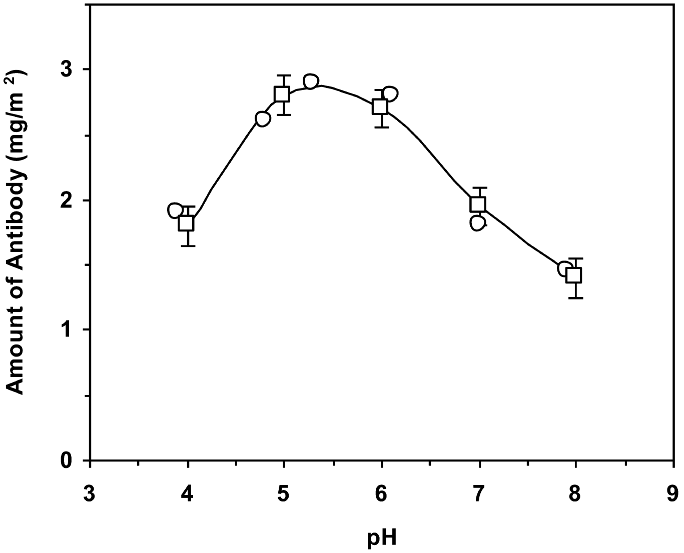

Figure 5. Surface adsorbed amount of antibody (left axis) obtained from ellipsometry (□) and NR (○) at different pH (ionic strength fixed at 20 mM). In each case the amount of antibody adsorbed was taken at 60 min after the adsorption started. Lines are drawn for eye guide. (Adapted with permission from ref. (31). Copyright (2009). The Royal Society.)

Table 2. Structural parameters of the anti-hPSA antibody layer at the SiO_2/buffer interface at different pH (ionic strength at 20 mM). (Reproduced with permission from ref. (*31*). Copyright (2009). The Royal Society.)

pH	$\tau \pm 2$ (Å)	$(\rho \pm 0.05) \times 10^{-6}$ (Å^{-2})	φ (±2%)	$A \pm 300$ (Å^2)	$\Gamma \pm 0.2$ (mg m^{-2})
3.9	8	5.6	25.4	13060	1.91
	25	5.2	39.0		
	20	6.1	8.5		
4.8	9	5.6	25.4	9570	2.6
	25	4.7	55.9		
	25	6.1	8.5		
5.3	10	5.6	25.4	8620	2.9
	30	4.8	52.5		
	25	6.1	8.5		
6.1	12	5.6	25.4	8940	2.8
	28	5.0	45.8		
	25	5.9	15.3		
7.0	12	5.7	22.0	13740	1.81
	25	5.5	28.8		
	35	6.1	8.5		
7.9	55	5.8	18.6	17160	1.45

Note: τ is the thickness of the layer, ρ is the scattering length density, φ is the volume fraction, A is the area per molecule and the Γ is the interfacially adsorbed amount.

4.5. Effect of Salt on Antibody Adsorption

The presence of counterions causes a screening effect, reducing protein adsorption (*6*). Addition of NaCl not only reduced the adsorbed amount of the antibody on silica surface but also shortened the time needed for reaching equilibrium adsorption. For example, the adsorption of anti-hPSA antibody in the presence of 5 mM NaCl resulted in an adsorbed amount of 2.8 mg/m^2 at the silica surface within 1 hr. This value reduced to 1.8, 1.5, 1.1 and finally 0.3 mg/m^2 when the NaCl concentration increased to 20, 50, 100 and 150 mM, respectively (Figure 6). Results from neutron reflection agreed with the data from ellipsometry. At the ionic strength of 5 mM, antibodies formed thick and dense layers. The inner layer near the oxide surface had a thickness of 10 Å and contained 32 % of antibody while the middle layer was much thicker (35 Å) and contained more antibodies (39 %). The outer layer near the water phase had a thickness of 25 Å but only contained 12 % antibody. Increase in the ionic strength to 20 mM resulted in the reduced thickness of the middle sublayer and the reduction of its volume fraction. Further increase of the NaCl concentration to 50 and 100 mM resulted in a uniform single layer adsorption with thicknesses of 58 and 42 Å, respectively. The antibody volume fractions at both NaCl concentrations were reduced to some 18%.

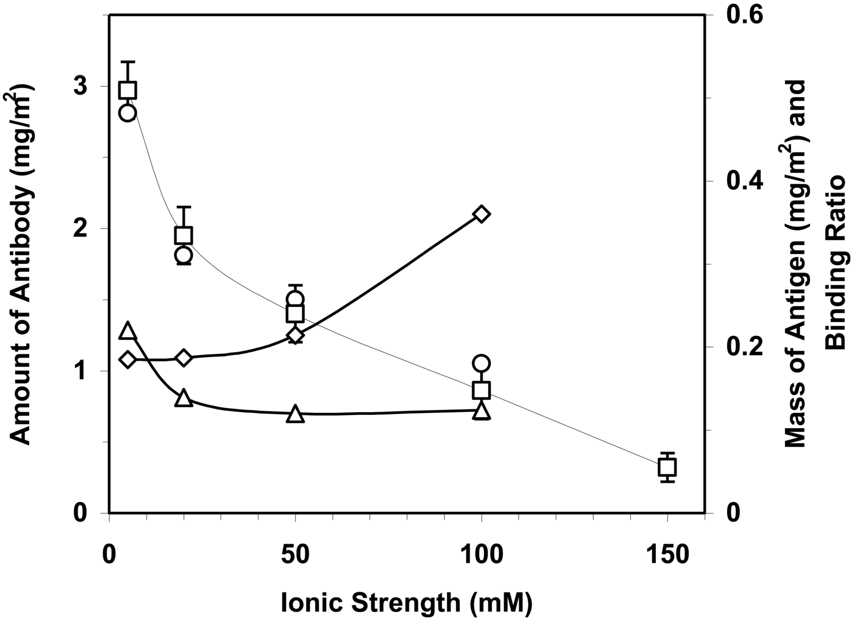

Figure 6. Surface adsorbed amount (left axis) of the Anti-hPSA antibody at 10 mg/L and pH 7 obtained by ellipsometry (□) and neutron reflection (○) under different ionic strengths with their corresponding antigen binding amount (△, right axis) and binding ratio (◇, right axis). Lines are for eye guide. (Reproduced with permission from ref. (31). Copyright (2009). The Royal Society.)

4.6. Effect of Surface Chemistry

Surface properties can influence approaching proteins and result in different adsorbed amount, different extent of unfolding and different conformations. For examples, lysozyme retained its globular protein structure upon adsorption onto the silica/water interface through electrostatic interaction. However, the adsorption of lysozyme onto the self-assembled hydrophobic octadecyltrichlorosilane (OTS)/water interface resulted in a densely packed thin sublayer next to the OTS surface and a diffuse thicker sublayer extending into the bulk solution, suggesting that the protein has denatured with its hydrophobic polypeptides adsorbed on OTS and hydrophilic polypeptides extended to the water solution (*14*). In contrast, it was found that coating of phosphorylcholine (PC) copolymer onto silica surface can effectively inhibit a range of protein adsorption due to the extreme outer surface hydrophilicity (*47*). Similarly, Su et al. (*17*) found that coating of a self-assembled monolayer of pentadecyltrichlorosilane with terminal hydroxyl groups ($C_{15}OH$) could also significantly reduce lysozyme adsorption. Due to the week interaction between the protein and the hydroxyl surface, adsorption was found to be completely reversible at the low concentration.

The adsorption of antibody onto the hydrophobic surface/water interface has been examined to explore the conformational changes arising from different adsorption driving forces and the subsequent effect on antigen binding. Compared to the changes at the silica/water interface, the adsorption of anti-hPSA antibody onto the self-assembled hydrophobic trimethoxyoctylsilane (C8) resulted in stronger adsorption due to the stronger interaction between the surface and the hydrophobic parts of the antibody. However, neutron reflection experiment revealed that adsorption of 10 mg/L of antibody at the C8/buffer interface for 1 hr resulted in a uniform layer of antibody with a thickness of 56 Å and volume fraction of 15.3%, suggesting that the antibody molecule still retained its 3D structure and was predominately flat on the surface, but might have some hydrophilic parts tilted due to the dislike to the surface.

4.7. Antigen Binding to the Surface Immobilized Antibody

The experimental study of antigen binding to surface immobilized antibody normally involves three steps: antibody adsorption onto support interface; blocking the non-specific surface adsorption and antigen binding. This experimental design takes into account of the main steps involved in the manufacturing of immunoassays and biosensors and their features involved in their applications. A typical example of antibody adsorption and antigen detection is shown in Figure 7 using the DPI technique having the capability of simultaneous monitoring of layer thickness, layer density, mass and reflective index in real time. The first step is the adsorption of antibody onto the solid/water interface. This is an important step as antibody packing density at the interface has direct implication to antigen binding amount and efficiency. However, antigen binding amount is not simply proportional to the amount of antibody adsorbed at the silica/water interface. As is shown in Figure 7, the lower amount of antibody at the interface has the better binding efficiency. Increasing antibody amount at surface reduces its antigen binding efficiency. This was due to the fact that a lower amount of antibody molecules at the interface was more loosely packed and thus had lower steric hindrance. There were plenty of spaces available for the antigen molecules to interact with the binding sites on the adsorbed antibody molecules. However, due to the very low amount of antibody molecules at the interface, the amount of antigens that could be bound was low as well. Increase in the amount of antibody at the interface resulted in a greater amount of antigen bound. Meanwhile, the steric hindrance also increased with the increasing amount of antibody. This process explained the drop of the binding ratio. Further increase of the antibody amount led to the decline of both antigen amount and binding ratio, indicating the crowding situation at the interface. Eventually, antigen binding amount and binding ratio tended to a low plateau due to the fact that only the antibodies on the top layer were accessible and that most of them were buried due to the crowding and overlapping. Thus steric hindrance is clearly significant for interfacial antibody-antigen recognition. Similar features were confirmed by the studies of anti-hCG antibody systems (*26*). Based on Figure 2, it was found that a good amount of antibody at the interface for antigen detection is around 1.5±0.5 mg/m^2, covering 50-70% of the surface. The antibody adsorption in Figure 7 resulted in an amount of 1.1 mg/m^2 at the interface. Buffer rinse washed off a small amount of loosely adsorbed antibody.

The second step is to block the non-specific adsorption using BSA. When the surface was not fully covered by antibodies, there are empty spaces that can result in non-specific antigen adsorption onto the substrate surface. BSA has been widely used as a non-specific blocking agent. After BSA blocking, the surface was washed again by buffer to wash off excess BSA. Finally, antigen was introduced to the surface to bind to the epitopes. The thickness of the adsorbed antibody layer fluctuated and then suffered from a small but steady decline with time, indicating molecular re-orientation at the interface after the fast initial adsorption. The thickness finally stayed at 4 nm, indicating that the molecules remained flat on surface. These findings agreed well with those obtained from ellipsometry and neutron reflection studies. BSA blocking did not result in any noticeable adsorption. However, mass increase was clearly detected after antigen binding. The layer thickness was still kept the same with an increase of layer density, suggesting that the antigen was inserted into the layer instead of staying on top of it.

Solution pH also affected antigen binding to surface immobilized antibody. Although antibody adsorption peaked around its pI of pH 5.5, the amount of antigen binding to the antibody did not follow the same trend. The amount of antigen binding peaked around pH 6 (Figure 7B). The best binding ratio was at pH 7, but the amount of antigen bound was not as high as that at pH 6. The reduction in antibody adsorption improved the accessibility of the binding sites, thereby improving the binding ratio over this pH region. But the amount of antigen bound was limited by the amount of antibody at the interface. Therefore, there is a balance between antigen binding amount and binding ratio. When the pH was above 7, the amount of antibody further declined. Antigen binding also dropped due to the reduction of surface immobilised antibody.

In contrast to solution pH, the addition of salt did not cause any significant effect to the antigen binding (Figure 6). The binding amount was found slightly high at very low ionic strength and then kept constant when the ionic strength was above 20mM. The binding ratio, however, increased smoothly due to the smooth reduction of surface immobilized antibody. Although antibody had stronger adsorption on hydrophobic/water interface, no obvious improvement of antigen binding was observed. The antigen binding amount at the optimal condition was equivalent to that observed at the silica/water interface but with a lower binding ratio.

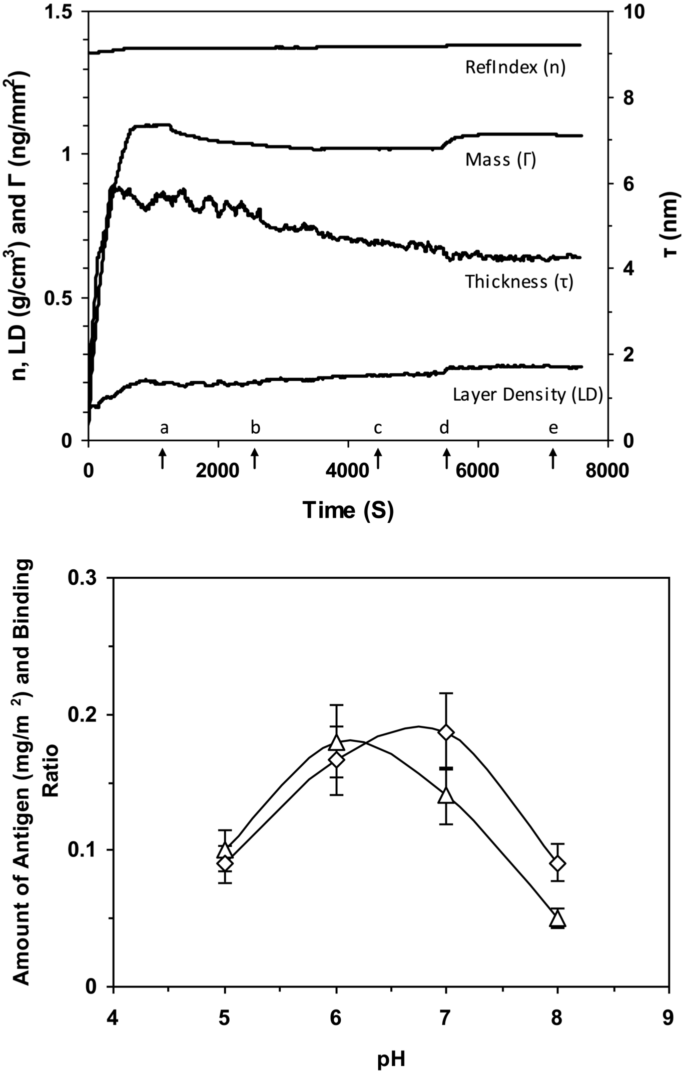

Figure 7. A, PSA Antibody adsorption, BSA blocking and antigen binding examined by DPI. Arrow indications: buffer wash after antibody adsorption (a); BSA blocking (b); buffer wash (c); antigen binding (d) and buffer wash thereafter (e). (Adapted with permission from ref. 30. Copyright (2011) American Chemical Society.) B, PSA Antigen binding amount (△) and binding ratio (◇) at different pH (ionic strength fixed at 20 mM). Lines are drawn for eye guide. (Adapted with permission from ref. (31). Copyright (2009). The Royal Society.)

4.8. Stability of the Immobilized Antibody

Antibodies adsorbed on the clean silica wafer surface were found to be highly stable. We examined the silicon wafers with surface adsorbed anti-hCG antibodies stored in sealed clean containers and left at room temperature for a period up to 4 months (*30*). Antigen detection experiments were then conducted every 2-3 weeks. The results clearly demonstrated that the surface adsorbed antibody molecules still retain stable bioactivity under the dry condition and ambient temperature over the period studied.

5. Surface Conformations of Proteins under Immunochemical Probing

As proteins are ubiquitous to bodily fluids, exposure of a medical device or implant into the body incurs a spontaneous molecular process of protein adsorption. The surface characteristics of a biomaterial can greatly influence its protein adsorption, cell attachment and hence its biocompatibility (*48*). Conversely, the surface properties of the adsorbing protein will also have an impact on adsorption dynamics and adsorbed protein conformation. As already indicated, interfacial adsorption of proteins often leads to changes in conformations, with the extent of variations dependent on protein stability and protein-surface interaction (*49*, *50*). The conformation of the adsorbed protein is crucial in influencing cell adhesion, migration and growth (*51*, *52*).

Incoming cells often "perceive" the dynamic surface protein amino acid signatures, as the biomaterial surface is largely covered up. When the protein is irreversibly adsorbed, the permanent exposure of certain peptide segments or epitopes into the bulk solution results in the surface acquiring different chemical and biological properties compared to the original biomaterial surface before protein adsorption. This would also explain why free fibrinogen in blood has no interaction with platelets, yet after its adsorption onto certain surfaces the attachment of platelets occurs as a result of changed protein conformation and exposure of active peptide sequences (*53*). Hence, quantifying the characteristic properties of such protruding surface peptides is paramount for the future development of biocompatible surfaces.

The surface adsorption of proteins can be investigated by various techniques as indicated previously. However, the surface conformation of adsorbed proteins at the nanoscale is much more difficult to quantify or observe directly. Here we present the use of specific protein monoclonal and polyclonal antibodies to probe the surface structure of adsorbed proteins such as fibrinogen and fibronectin through coadsorption with human serum albumin on different materials.

Fibrinogen is one of the most abundant soluble extracellular matrix (ECM) adhesion proteins present in blood and plays an important role in the maintenance of heamostasis. It is involved in thrombosis on surfaces and serves as a ligand to a variety of vascular cells, including platelets, monocytes and endothelial cells (*54*). Hence, out of the various proteins available for investigation, fibrinogen has been studied with great interest. The structure of fibrinogen is composed of two sets of three non-identical polypeptide chains: Aα, Bβ and γ chains held together by 29-disulfide bonds. The N-termini of each of the two sets of chains meet at the central E domain of the molecule. The C-termini of the Bβ and γ chains make up the two D domains with the Aα chains (positive net charge) extending out from the D domains (negative net charge). It has structural dimensions of 470 x 50 x 50 $Å^3$, a molecular weight of 340 000, an isoelectric point of 4.3 and a plasma concentration of about 2-3 mg/ml. Fibrinogen facilitates adhesion and aggregation of platelets and has a number of adhesion binding sites for vascular cell receptors such as those interacting with the β_3 integrins, the platelet-specific $\alpha_{IIb}\beta_3$ fibrinogen receptor and the $\alpha_v\beta_3$ vitronectin receptor (*55*, *56*). Within fibrinogen there are two RGD motifs within the Aα chain, Aα 95–98 (RGDF) and Aα 572–575 (RGDS), and a non-RGD dodecapeptide sequence in the γ chain (C-terminal γ 400–411) (*57*). Fibrinogen binding to $\alpha_v\beta_3$ relies essentially on the Aα 572–575 RGDS sequence, but binding to $\alpha_{IIb}\beta_3$ involves both the RGDS site and the non-RGD dodecapeptide γ 400–411 sequence (*58*), implying that their availability and geometrical location are important to facilitating the binding upon fibrinogen adsorption to a given material surface.

Fibronectin (Fn) is another important ECM protein that plays a key role in several fundamental cell functions including cell attachment and tissue repair (*59*). Fn is a multifunctional high-molecular-weight (450 KDa) dimeric glycoprotein that is present in the extracellular matrices of all connective tissues. The structures and functions of Fn have been reported and extensively discussed in the literature (*60–62*). The two nearly homologous subunits of Fn are composed almost entirely of three different types of repeating motifs or modular tertiary structural units, in general indicated as type I, II, and III repeats. Fn has been shown to be able to mediate specific cell-surface interaction via either simple peptide sequences such as RGD and its synergistic site PHSRN through integrin receptors in the cell membrane or the interaction of the $^4F_I{\cdot}^5F_I$ segments, which are part of the heparin I (Hep I) and fibrin (Fbn) binding domains. RGD, located at the apex of the loop connecting the sixth and seventh β strands within the type III 10th unit ($^{10}F_{III}$), is about 3.5 nm from the PHSRN synergy site located on the type III ninth unit. For such a protein, the crucial spatial distance of the correct peptide sequence and the appropriate conformation for its epitope “exposure” are basic requirements for maximizing the interaction with cells.

a) PUA

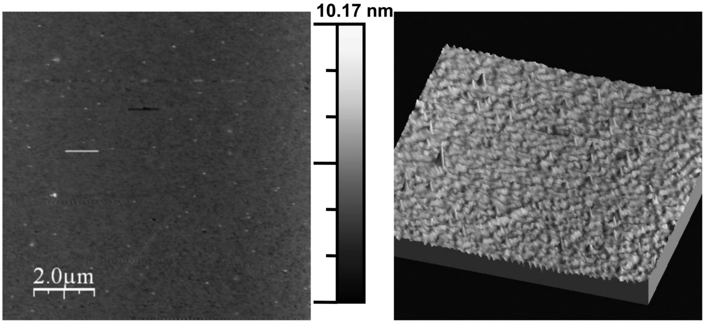

(b) PU4

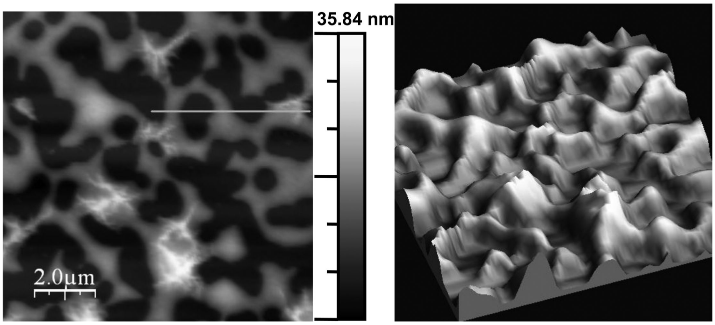

(c)

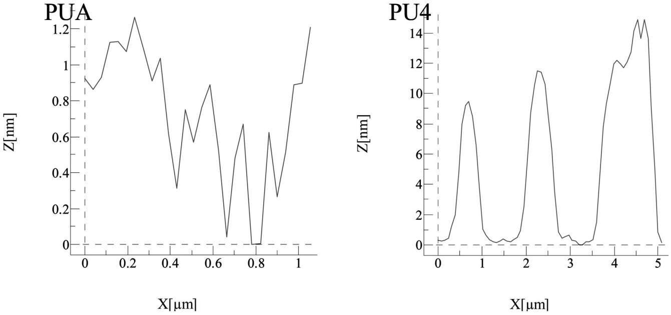

Figure 8. AFM surface topographic features (contact mode) with height images shown in air (left) and in 3D representation (right) (10μm x 10μm) of (a) PUA and (b) PU4. Both surfaces show micro-domain separation but in PU4 the features are much larger than in PUA. In (c) a graphical cross-sectional profile (z, x) is shown for the topographies represented by the lines on the 2D images for PUA and PU4. (Reproduced with permission from ref. (50). Copyright (2008) IOP Publishing Ltd.)

5.1. Fibrinogen Polypeptide Surface Conformations

Apart from a number of other attributes, biomaterial development has been marked by low non-specific protein adsorption. However, many biomaterials that are in current medical applications have also incorporated functional groups in addition to the base components such as poly (ethylene oxide) (PEO) and phosphorylcholine groups (PC) for reduced protein adsorption (*63*, *64*). Other biomaterials such as polyurethanes (PU) and their copolymers induce high protein adsorption, yet they are also used successfully as biocompatible biomaterials. The high protein adsorption was also observed with a nanocomposite (PU4) composed of poly(urethane) copolymer with silica nanocages. PU4 has also been found to be a highly useful biomaterial (*50*, *65*). From our investigations the explanation for this particular dilemma was related to the surface conformation of the adsorbed protein. Specifically, the incorporation of silica nanocages into poly(urethane) copolymers (PU) was shown to affect its surface topography and conformational orientations of adsorbed fibrinogen. Figure 8 shows the influence on the surface topography of these polyurethanes with and without silica nanocages from AFM imaging. Incorporation of silica nanocages causes clear micro-domain segregation, the coexistence of soft polyurethane domains together with the hard silica domains.

The two PU surfaces showed intermediate contact angles of around 50°, with little apparent effect of incorporation of the nanocages, however the PU surfaces had much higher adsorption of fibrinogen when compared to silicon oxide (weakly negatively charged with contact angle < 5°) and hydrophobic OTS (contact angle of ca 105°) on the basis of ellipsometric measurements. In brief, the equilibrated surface excesses showed no obvious correlation with surface hydrophobicity. The SE results also indicated two stage dynamic adsorption of fibrinogen, an initial fast adsorption followed by a slow fibrinogen surface reorientation and attainment of equilibrium absorption.

The surface conformations of adsorbed fibrinogen on various surfaces were probed by antibodies specific to certain sections of fibrinogen. Polyurethane copolymer biomaterial surfaces with (PU4) and without (PUA) silica nanocages were investigated. Three model surfaces including bare silicon oxide, and the two self-assembled monolayers bearing terminal cationic amine groups and hydrophobic C18 chains were also studied for comparison. Different conformations at the surface of different materials led to the different exposure of α and γ chains of fibrinogen and these were further elucidated through selective antibody binding and differential cell attachment. The different surface conformations were investigated using two anti-fibrinogen antibodies, monoclonal *Anti-Gamma* specific to the γ chain amino acids 434-453 (VRPEHPAETEYDSLYPEDDL) of human-fibrinogen and monoclonal *Anti-Alpha* specific to α chain of fibrinogen.

The real time SE results showed low anti-α but high anti-γ binding to the pre-adsorbed fibrinogen at the silicon oxide and PU4 surfaces. In contrast, at the PUA, C18 and amine surfaces high anti-α and low anti-γ binding interactions were observed. In Figure 9 the results are shown in a plot of molar fractions of anti-α or anti-γ against the amount of fibrinogen after the first 60 min adsorption.

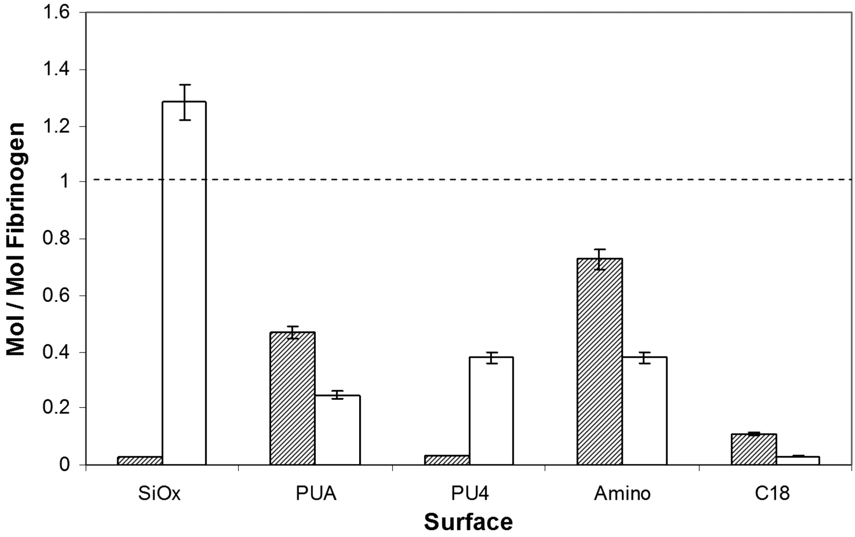

Figure 9. Binding of anti-α (shaded lines) and anti-γ (filled yellow) binding to fibrinogen preadsorbed on the five surfaces at 0.01 mg/ml and pH 7. The results are presented in molar ratios against the preadsorbed fibrinogen. Note that each fibrinogen has a pair of α and γ chains, thus the theoretical binding ratio is 2. The data errors are mean standard deviation from experiments performed in triplet. (Reproduced with permission from ref. (32). Copyright (2010) Elsevier Ltd.)

Minimal binding of anti-α antibody at the silicon oxide surface implied low availability of the α chains. The binding of anti-γ antibody to this surface resulted in a molar ratio of 1.3, suggesting that the γ chains were favourably aligned into the bulk solution for binding interaction. The high level of anti-γ binding also indicated that majority of the adsorbed fibrinogen molecules had both γ chains highly accessible. To avoid possible steric hindrance, the γ-chains would have to be bent into the bulk solution whilst the fibrinogen molecules lay slightly twisted but flat (Figure 10). The results were consistent with AFM imaging and the fact that weakly negatively charged silicon oxide may result in electrostatic repulsion from the alike negative charge domains of fibrinogen.

At the PU4 film surface, the relative trend of binding between the two antibodies was similar to the silicon oxide surface, that is, there was very little binding of anti-α antibody but there was clear binding from anti-γ antibody. In contrast, at the PUA surface, the hydrophilic OTS (C18) surface and the positively charged amine surface the trend was reversed in that higher anti-α binding than the anti-γ binding was observed.

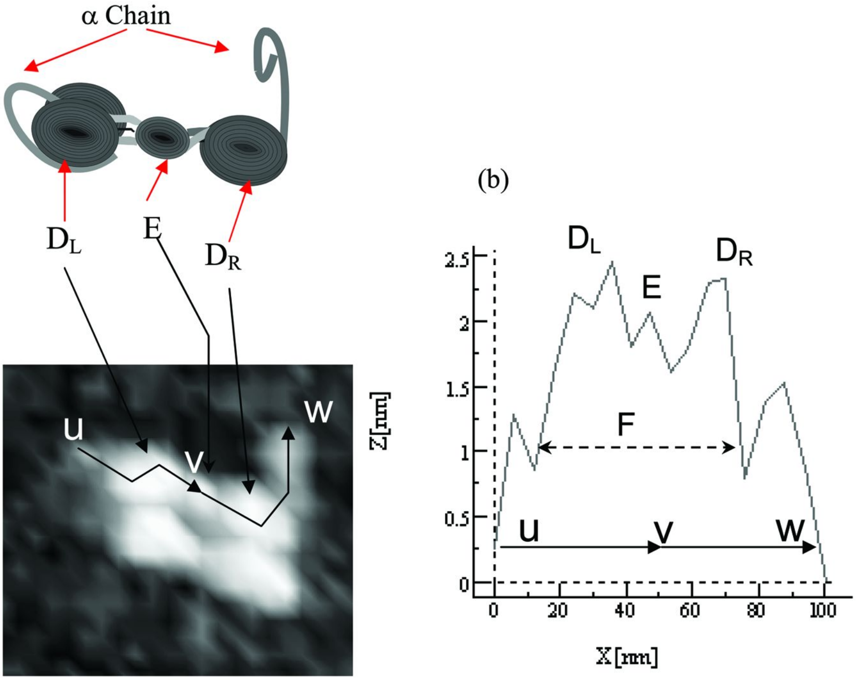

Figure 10. AFM surface tapping mode image in air at the SiO$_2$ surface after fibrinogen adsorption. (a) Height image magnification of a fibrinogen dimer. (b) A cross-sectional profile across a fibrinogen molecule along the path indicated in (a) by the black arrow; U, V to W. The left and right D domains in (a) and (b) are marked as D$_L$ and D$_R$, respectively, with the central E domain also indicated. The length of the fibrinogen molecule across the two D domains is about 60 nm. In (a), a schematic representation of a fibrinogen molecule is also shown to indicate the domains and the α chains. (Adapted with permission from ref. (32). Copyright (2010) Elsevier Ltd.)

5.1.1. Cell Attachment

The significance of the relative availability of α and γ chains from surface adsorbed fibrinogen was further illustrated by cell surface attachment. The surface chemistry as well as sub-micron morphological structures can influence cell attachment and growth on a substrate surface. Cells are also capable of detecting and selective binding to the regions of primary protein structures such as RGD and other amino acid sequences through integrin receptors. Their time dependent responses to different surfaces with pre-adsorbed proteins can work as a useful assessment of protein conformation and surface biocompatibility.

Cell surface attachment and growth was assessed using HeLa cells on the glass coverslips half coated with PUA and PU4, initially without fibrinogen adsorption. Cell attachment on the PUA surface was much lower than on the neighbouring bare glass surface, suggesting that the cells did not like to attach onto the polymer surface. A similar trend was observed on the PU4 surface, but the differences in cell number were much smaller, showing the improvement due to the silica nanocages present on the outer PU4 surface (Figure 11). The sensitivity of cell surface recognition to pre-adsorbed fibrinogen was then shown on the same surface, with the half coated coverslips being preadsorbed with 0.01 mg/ml fibrinogen. Again cells attachment to the PUA surface was much lower than on glass surface. On the other hand, cell numbers and shape on the PU4 surface became indistinguishable from the glass surface. The cells spread and grew better across the glass-PU4 polymer film boundaries. The results thus showed that after fibrinogen preadsorption, the PU4 polymer surface behaved like the glass coverslip surface; both surfaces induced similar cell attachment, healthy growth and promoted similar fibrinogen surface conformation.

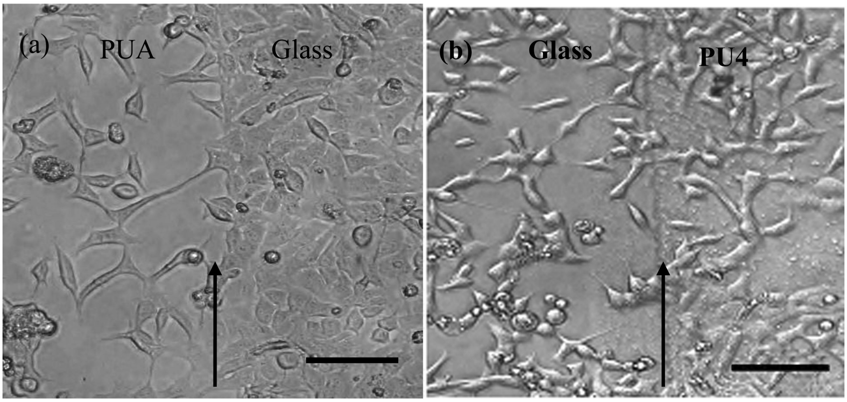

Figure 11. HeLa cell attachment and growth on glass coverslips half coated with (a) PUA after 3 days and (b) PU4 after 2 days of incubation with 0.01 mg/ml fibrinogen pre-adsorption. The boundary between the PU polymer film and bare glass is in the middle as indicated by vertical arrows. After 3 days of incubation the glass and PU4 coverslip was fully covered and indistinguishable. In each image the scale bar is 100 μm. (Adapted with permission from ref. (32). Copyright (2010) Elsevier Ltd.)

5.2. Fibronectin Surface Conformations with Coadsorption of HSA

The appropriate exposure of Fn binding motifs, as for other proteins, is critically conditioned by the simultaneous presence of other proteins in the biological medium and, in particular, in the ECM system. The complexity of interactions inherently is expected to increase as the interfering proteins become abundant. This is in particular the case when human serum albumin (HSA) is coadsorbed. HSA is the most abundant soluble blood protein whose lower molecular weight and much higher serum concentration favour transport to synthetic surfaces with respect to larger proteins such as Fn (*66*, *67*). Accordingly, the competitive coadsorption of HSA with Fn has been studied in view of its possible effect on the adsorption and bioactivity of Fn. The biological availability (i.e. the proper exposure of the epitopes for Fn in solution or onto surfaces) is a major issue in tuning the cell adhesive function of Fn (*68*). Thus, the cell adhesive function of Fn can only be tuned if an optimal exposure of the relevant cell-binding motifs in Fn is achieved.

The conformational state and the change induced in the Fn bioactivity by coadsorption and sequential adsorption with HSA onto poly-(hydroxymethylsiloxane) (PHMS), which is representative of the large class of polysiloxane biomaterials, was investigated (*33*). The surface conformation of Fn and its bioactivity were examined to determine the availability of a specific Fn cell-binding domain (i.e. the $^4F_1{\cdot}^5F_1$ segments within heparin I (Hep I) and fibrin (Fbn) binding domains). Initially the $^4F_1{\cdot}^5F_1$ segments were targeted using a polyclonal anti-fibronectin antibody as a probe, and the amount of adsorbed antibody was directly measured in situ for Fn, HSA, Fn coadsorbed with HSA (HSA + Fn), and various sequential adsorption processes using spectroscopic ellipsometry (SE) and quartz crystal microbalance with dissipation monitoring (QCM-D). AFM was employed to obtain information on the nanometric structure of the adsorbed protein layers. Furthermore, fibroblast adhesion and proliferation onto the surfaces preconditioned either with pure Fn or with Fn coadsorbed or sequentially adsorbed with HSA were determined to compare the relative efficiency of Fn adsorbed under different conditions in determining the cell-binding activity.

The amount of anti-Fn bound to 1 mol of Fn from each of the surfaces is shown in Figure 12, where the HSA surface clearly facilitated the least amount of antibody binding. The second smallest amount of anti-Fn binding occurred on the coadsorbed surface from the binary HSA + Fn solution (1:1 binary coadsorption mixture), and the highest amount of binding clearly occurred on the pure Fn adsorbed surface. However, it is interesting that whereas the SE and QCM-D data indicated that the adsorbed layers from HSA + Fn coadsorption were almost exclusively composed of Fn, the lower binding of anti-Fn suggested that the Fn molecules from the 1:1 binary mixture were somewhat less available for anti-Fn binding. Furthermore, the anti-Fn binding onto pure preadsorbed Fn and HSA + Fn coadsorption showed a steady increase over the period of the experiments, suggesting that the adsorbed Fn molecules continue to change their packing and conformation with time, an observation consistent with what was already reported in the literature (*69*).

As the Fn/anti-Fn binding is due to the proper exposure of $^4F_1{\cdot}^5F_1$ domains, the reduced anti-Fn binding to the surface layer of HSA + Fn coadsorption suggests that either a conformational change occurred for Fn, making the $^4F_1{\cdot}^5F_1$ domains unavailable, or coadsorbed HSA, however small the quantity, masked the binding domains.

To differentiate between these two possibilities, a sequential adsorption studies of HSA (0.1 mg/mL) on preadsorbed Fn (0.1 mg/mL) (i.e., Fn >>>HSA) and Fn (0.1 mg/mL) on preadsorbed HSA (0.1 mg/mL) (i.e., HSA >>>Fn) were performed. Here it was found that no significant Fn adsorption occurred on preadsorbed HSA under the studied conditions. Accordingly, the binding of anti-Fn with the adsorbed protein layer after sequential adsorption produced a mass increase almost identical to that found for pure HSA confirming that the exposed surface was predominantly HSA. Similarly, for the sequential adsorption of HSA onto preadsorbed Fn, no mass change was observed with respect to the initially adsorbed Fn, with this value being close to the one measured from pure Fn adsorption at equilibrium. Not surprisingly, a large amount of anti-Fn was adsorbed onto the protein layer after the sequential adsorption, confirming that the exposed surface in this case was predominantly composed of Fn with a very low quantity of HSA present in the layer. As already indicated, Fn has two subunits, each with $^4F_1{\cdot}^5F_1$ binding domains available for anti-Fn binding. Although the theoretical molar binding ratio is 2 it is unlikely that this ratio would ever be reached because of the steric constraints at the interface. For anti-Fn binding to pure Fn, the molar binding ratio was found to be almost about 1 and a little less than this for the sequential adsorption of HSA onto preadsorbed Fn.

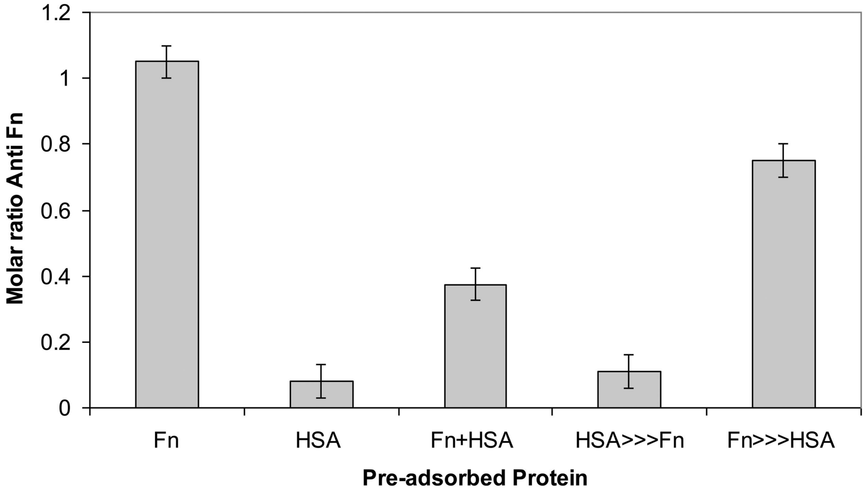

Figure 12. Anti-Fn antibody binding to differently adsorbed Fn calculated on the basis of moles of antibody bound per mole of Fn adsorbed on different surfaces where Fn+HSA is the 1:1 binary co-adsorption mixture, the sequential adsorption of HSA onto pre-adsorbed Fn is abbreviated as Fn>>>HSA, and sequential adsorption of Fn onto pre-adsorbed HSA represented as HSA>>>Fn. (Reproduced with permission from ref. (33). Copyright (2010) American Chemical Society.)

The mass adsorption results from the two sequential binding experiments suggest that no protein bilayers were formed, thus ruling out the possible HSA coadsorption masking the $^4F_1$·$^5F_1$ binding domains. The reduced anti-Fn binding for the protein layer formed from HSA + Fn coadsorption were thought to arise from the conformational effects promoted by HSA coadsorption. The time-dependent anti-Fn binding from all Fn-containing surfaces adds strong support to the proposition of the structural reorganization of Fn molecules from a closed to an open conformation, leading to further exposure of the $^4F_1$·$^5F_1$ binding domains. The results suggested that coadsorption of HSA may well influence the initial adsorption and conformation of Fn molecules and also their subsequent structural adjustment or relaxation.

6. Conclusions

Interfacial adsorption of monoclonal antibodies at the solid/water interface has direct relevance to many biotechnological applications. This review has described the development of interfacial measurements by a number of leading physical techniques to mimic the key steps of antibody immobilization during biosensor fabrication and dynamic processes of antigen binding during their practical uses. Systematic study of antibody adsorption under different solution conditions and surface properties provides a deep insight of antibody interfacial conformations and antigen binding behavior. Briefly, the antibody adsorption at the interface is both time and concentration dependant. Lower concentration resulted in monolayer adsorption with “flat-on” orientation while at higher concentrations overlapping of the molecules occurred, therefore reducing the accessibility of the binding sites. Both solution pH and salt concentration have significant effects to the antibody adsorption. The amount of antibody adsorbed reached a maximum near the isoelectric point and decreased when pH is moved away from it. The addition of salt reduces the antibody adsorption at the interface but did not seem have a significant effect to the antigen binding. However, solution pH was found to affect the antigen binding, better binding amount and ratio were found to occur around pH 6-7. Such detailed studies of interfacial structures and molecular binding processes offer a useful approach to optimize the conditions for antigen detection. The application of antibodies to probe the conformations of adsorbed proteins through specific antibody-antigen binding also provides a valuable tool for surface functionalization of biomaterials.

Acknowledgments

The authors wish to thank EPSRC, ISIS Neutron Facilities and Unilever Research Port Sunlight Laboratory for support.

References

1. Silverton, E. W.; Navia, M. A.; Davies, D. R. Three-dimensional structure of an intact human immunoglobulin. *Proc. Natl. Acad. Sci. U.S.A.* **1977**, *74*, 5140–5144.
2. Wang, K.-H.; Syu, M.-J.; Chang, C.-H.; Lee, Y.-L. Immobilization of glucose oxidase by Langmuir–Blodgett technique for fabrication of glucose biosensors: Headgroup effects of template monolayers. *Sens. Actuators, B* **2012**, *164*, 29–36.
3. Tajima, N.; Takai, M.; Ishihara, K. Significance of Antibody Orientation Unraveled: Well-Oriented Antibodies Recorded High Binding Affinity. *Anal. Chem.* **2011**, *83*, 1969–1976.
4. Kausaite-Minkstimiene, A.; Ramanaviciene, A.; Kirlyte, J.; Ramanavicius, A. Comparative Study of Random and Oriented Antibody Immobilization Techniques on the Binding Capacity of Immunosensor. *Anal. Chem.* **2010**, *82*, 6401–6408.
5. Choi, J. M.; An, J. Y.; Kim, B. W. Effect of Biolinker on the Detection of Prostate Specific Antigen in an Interferometry. *Biotechnol. Bioprocess Eng.* **2009**, *14*, 6–12.
6. Lu, J. R. Neutron reflection study of globular protein adsorption at planar interfaces. *Annu. Rep. Prog. Chem., Sect. C: Phys. Chem.* **1999**, *95*, 3–45.
7. Lu, J. R. Neutron reflection studies of interactions between surfactants and proteins at interfaces. *Annu. Rep. Prog. Chem., Sect. C: Phys. Chem.* **2002**, *98*, 3–32.
8. Lu, J. R.; Su, T. J.; Howlin, B. J. The effect of solution pH on the structural conformation of lysozyme layers adsorbed on the surface of water. *J. Phys. Chem. B* **1999**, *103* (28), 5903–5909.
9. Lu, J. R.; Su, T. J.; Penfold, J. Adsorption of Serum Albumins at the Air/Water Interface. *Langmuir* **1999**, *15*, 6975–6983.
10. Lu, J. R.; Su, T. J.; Thomas, R. K.; Penfold, J. Binding of Sodium Dodecyl Sulfate to Bovine Serum Albumin Layers Adsorbed at the Silica-Water Interface. *Langmuir* **1998**, *14*, 6261–6268.
11. Lu, J. R.; Su, T. J.; Thomas, R. K. Binding of Surfactants onto Preadsorbed Layers of Bovine Serum Albumin at the Silica-Water Interface. *J. Phys. Chem. B* **1998**, *102*, 10307–10315.
12. Lu, J. R.; Su, T. J.; Thomas, R. K. Structural Conformation of Bovine Serum Albumin Layers at the Air–Water Interface Studied by Neutron Reflection. *J. Colloid Interface Sci.* **1999**, *213*, 426–437.
13. Lu, J. R.; Su, T. J.; Thomas, R. K.; Penfold, J.; Webster, J. Structural conformation of lysozyme layers at the air/water interface studied by neutron reflection. *J. Chem. Soc., Faraday Trans.* **1998**, *94*, 3279–3287.
14. Lu, J. R.; Su, T. J.; Thomas, R. K.; Rennie, A. R.; Cubit, R. The denaturation of lysozyme layers adsorbed at the hydrophobic solid/liquid surface studied by neutron reflection. *J. Colloid Interface Sci.* **1998**, *206*, 212–223.
15. Lu, J. R.; Swann, M. J.; Peel, L. L.; Freeman, N. J. Lysozyme Adsorption Studies at the Silica/Water Interface Using Dual Polarization Interferometry. *Langmuir* **2004**, *20*, 1827–1832.

16. Lu, J. R.; Zhao, X.; Yaseen, M. Protein Adsorption Studied by Neutron Reflection. *Curr. Opin. Colloid Interface Sci.* **2007**, *12*, 9–16.
17. Su, T. J.; Green, R. J.; Wang, Y.; Murphy, E. F.; Lu, J. R. Adsorption of Lysozyme onto the Silicon Oxide Surface Chemically Grafted with a Monolayer of Pentadecyl-1-ol. *Langmuir* **2000**, *16*, 4999–5007.
18. Su, T. J.; Lu, J. R.; Thomas, R. K.; Cui, Z. F. Effect of pH on the Adsorption of Bovine Serum Albumin at the Silica/Water Interface Studied by Neutron Reflection. *J. Phys. Chem. B* **1999**, *103*, 3727–3736.
19. Su, T. J.; Lu, J. R.; Thomas, R. K.; Cui, Z. F.; Penfold, J. The Adsorption of Lysozyme at the Silica–Water Interface: A Neutron Reflection Study. *J. Colloid Interface Sci.* **1998**, *203*, 419–429.
20. Su, T. J.; Lu, J. R.; Thomas, R. K.; Cui, Z. F.; Penfold, J. The Conformational Structure of Bovine Serum Albumin Layers Adsorbed at the Silica-Water Interface. *J. Phys. Chem. B* **1998**, *102*, 8100–8108.
21. Su, T. J.; Lu, J. R.; Thomas, R. K.; Cui, Z. F.; Penfold, J. The Effect of Solution pH on the Structure of Lysozyme Layers Adsorbed at the Silica-Water Interface Studied by Neutron Reflection. *Langmuir* **1998**, *14*, 438–445.
22. Lu, J. R.; Perumal, S.; Zhao, X. B.; Miano, F.; Enea, V.; Heenan, R. R.; Penfold, J. Surface-induced unfolding of human lactoferrin. *Langmuir* **2005**, *21* (8), 3354–3361.
23. Lu, J. R.; Su, T. J.; Georganopoulou, D.; Williams, D. E. Interfacial dissociation and unfolding of glucose oxidase. *J. Phys. Chem. B* **2003**, *107* (16), 3954–3962.
24. Miano, F.; Zhao, X.; Lu, J. R.; Penfold, J. Coadsorption of Human Milk Lactoferrin into the Dipalmitoylglycerolphosphatidylcholine Phospholipid Monolayer Spread at the Air/Water Interface. *Biophys. J.* **2007**, *92*, 1254–1262.
25. Zhao, X.; Pan, F.; Lu, J. R. Interfacial assembly of proteins and peptides: recent examples studied by neutron reflection. *J. R. Soc. Interface* **2009**, *6*, S659–S670.
26. Xu, H.; Lu, J. R.; Williams, D. E. Effect of Surface Packing Density of Interfacially Adsorbed Monoclonal Antibody on the Binding of Hormonal Antigen Human Chorionic Gonadotrophin. *J. Phys. Chem. B* **2006**, *110*, 1907–1914.
27. Xu, H.; Perumal, S.; Zhao, X.; Du, N.; Liu, X.; Lu, J. R. Interfacial Adsorption of Antifreeze Proteins: a neutron reflection study. *Biophys. J.* **2008**, *94*, 4405–4413.
28. Xu, H.; Zhao, X.; Grant, C.; Lu, J. R.; Williams, D. E.; Penfold, J. Orientation of a Monoclonal Antibody Adsorbed at the Solid/Solution Interface: A Combined Study Using Atomic Force Microscopy and Neutron Reflectivity. *Langmuir* **2006**, *22*, 6313–6320.
29. Xu, H.; Zhao, X.; Lu, J. R.; Williams, D. E. Relationship between the Structural Conformation of Monoclonal Antibody Layers and Antigen Binding Capacity. *Biomacromolecules* **2007**, *8*, 2422–2428.
30. Zhao, X.; Pan, F.; Cowsill, B.; Lu, J. R.; Garcia-Gancedo, L.; Flewitt, A. J.; Ashley, G. M.; Luo, J. Interfacial Immobilization of Monoclonal Antibody

and Detection of Human Prostate-Specific Antigen. *Langmuir* **2011**, *27*, 7654–7662.

31. Zhao, X.; Pan, F.; Garcia-Gancedo, L.; Flewitt, A. J.; Ashley, G. M.; Luo, J.; Lu, J. R. Interfacial Recognition of Human Prostate-Specific Antigen by Immobilized Monoclonal Antibody: Effects of Solution Conditions and Surface Chemistry. *J. R. Soc. Interface* **2012**, *9*, 2457–2467.
32. Yaseen, M.; Zhao, X.; Freund, A.; Seifalian, A. M.; Lu, J. R. Surface structural conformations of fibrinogen polypeptides for improved biocompatibility. *Biomaterials* **2010**, *31*, 3781–3792.
33. Giamblanco, N.; Yaseen, M.; Zhavnerko, G.; Lu, J. R.; Marletta, G. Fibronectin Conformation Switch Induced by Coadsorption with Human Serum Albumin. *Langmuir* **2011**, *27*, 312–319.
34. McLain, S. E.; Soper, A. K.; Daidone, I.; Smith, J. C.; Watts, A. Charge-Based Interactions between Peptides Observed as the Dominant Force for Association in Aqueous Solution. *Angew. Chem., Int. Ed.* **2008**, *47*, 9059–9062.
35. Zhao, X.; Pan, F.; Xu, H.; Yaseen, M.; Shan, H.; Hauser, C. A. E.; Zhang, S.; Lu, J. R. Molecular Self-assembly and Applications of Designer Peptide Amphiphiles. *Chem. Soc. Rev.* **2010**, *39*, 3480–3498.
36. Ulijn, R. V.; Smith, A. M. Designing peptide based nanomaterials. *Chem. Soc. Rev.* **2008**, *37*, 664–675.
37. Zhao, X.; Pan, F.; Lu, J. R. Recent development of peptide self-assembly. *Prog. Nat. Sci.* **2008**, *18*, 653–660.
38. Stryer, L. *Biochemistry*, 3rd ed.; W.H. Freeman and Company: New York, 1988.
39. Salim, M.; McArthur, S. L.; Vaidyanathan, S.; Wright, P. C. Towards proteomics-on-chip: The role of the surface. *Mol. BioSyst.* **2010**, *7*, 101–115.
40. Yaseen, M.; Pan, F.; Zhao, X.; Lu, J., Surface Modification to Improve Biocompatibility. In *Comprehensive Biotechnology*, 2nd ed.; Moo-Young, M., Ed.; Elsevier: New York, 2011; Vol. 5, pp 65−81.
41. Lu, J. R.; Lee, E. M.; Thomas, R. K. The Analysis and Interpretation of Neutron and X-ray Specular Reflection. *Acta Cryst.* **1996**, *A52*, 11–41.
42. Zhao, X.; Pan, F.; Perumal, S.; Xu, H.; Lu, J. R.; Webster, J. R. P. Interfacial Assembly of Cationic Peptide Surfactants. *Soft Matter* **2009**, *5*, 1630–1638.
43. Lu, J. R.; Perumal, S.; Zhao, X.; Miano, F.; Enea, V.; Heenan, R. R.; Penfold, J. Surface-Induced Unfolding of Human Lactoferrin. *Langmuir* **2005**, *21*, 3354–3361.
44. Zhao, X.; Pan, F.; Coffey, P.; Lu, J. R. Cationic Copolymer-Mediated DNA Immobilization: Interfacial Structure and Composition As Determined by Ellipsometry, Dual Polarization Interferometry, and Neutron Reflection. *Langmuir* **2008**, *24* (23), 13556–13564.
45. Wang, X.; Wang, Y.; Xu, H.; Shan, H.; Lu, J. R. Dynamic adsorption of monoclonal antibody layers on hydrophilic silica surface: A combined study by spectroscopic ellipsometry and AFM. *J. Colloid Interface Sci.* **2008**, *323*, 18–25.

46. Buijs, J.; van-den-Berg, P. A. W.; Lichtenbelt, J. W. T.; Norde, W.; Lyklema, J. Adsorption Dynamics of IgG and Its F(ab′)2 and Fc Fragments Studied by Reflectometry. *J. Colloid Interface Sci.* **1996**, *178* (2), 594–605.
47. Lu, J. R.; Murphy, E. F.; Su, T. J.; Lewis, A. L.; Stratford, P. W.; Satija, S. K. Reduced Protein Adsorption on the Surface of a Chemically Grafted Phospholipid Monolayer. *Langmuir* **2001**, *17*, 3382–3389.
48. Mitragotri, S.; Lahann, J. Physical approaches to biomaterial design. *Nat. Mater.* **2009**, *8*, 15–23.
49. Roach, P.; Farrar, D.; Perry, C. C. Interpretation of Protein Adsorption: Surface-Induced Conformational Changes. *J. Am. Chem. Soc.* **2005**, *127*, 8168–8173.
50. Yaseen, M.; Salacinski, H. J.; Seifalian, A. M.; Lu, J. R. Dynamic protein adsorption at the polyurethane copolymer/water interface. *Biomed. Mater.* **2008**, *3*, 034123(12pp).
51. Keselowsky, B. G.; Collard, D. M.; García, A. J. Surface chemistry modulates fibronectin conformation and directs integrin binding and specificity to control cell adhesion. *J. Biomed. Mater. Res.* **2003**, *66A*, 247–259.
52. Barrias, C. C.; Martins, M. C.; Almeida-Porada, G.; Barbosa, M. A.; Granja, P. L. The correlation between the adsorption of adhesive proteins and cell behaviour on hydroxyl-methyl mixed self-assembled monolayers. *Biomaterials* **2009**, *30*, 306–316.
53. Massa, T. M.; Yang, M. L.; Ho, J. Y. C.; Brash, J. L.; Santerre, J. P. Fibrinogen surface distribution correlates to platelet adhesion pattern on fluorinated surface modified polyetherurethane. *Biomaterials* **2005**, *26*, 7367–7376.
54. Fuss, C.; Palmaz, J. C.; Sprague, E. A. Fibrinogen: Structure, function, and surface interactions. *J. Vascular and Interventional Radiology* **2001**, *12*, 677–682.
55. Farrell, D. H.; Thiagarajan, P.; Chung, D. W.; Davie, E. W. Role of fibrinogen α and β chain sites in platelet aggregation. *Proc. Natl. Acad. Sci. Biochem.* **1992**, *89*, 10729–10732.
56. Smith, J. W.; Ruggeri, Z. M.; Kunicki, T. J.; Cheresh, D. A. Interaction of integrins alpha v beta 3 and glycoprotein IIb-IIIa with fibrinogen. Differential peptide recognition accounts for distinct binding sites. *J. Biol. Chem.* **1990**, *265*, 12267–12271.
57. Doolittle, R. F.; Watt, K. W.; Cottrell, B. A.; Strong, D. D.; Riley, M. The amino acid sequence of the α-chain of human fibrinogen. *Nature* **1979**, *280*, 464–468.
58. Kloczewiak, M.; Timmons, S.; Lukas, T. J.; Hawiger, J. Platelet receptor recognition site on human fibrinogen. Synthesis and structure-function relationship of peptides corresponding to the carboxy-terminal segment of the gamma chain. *Biochemistry* **1984**, *23*, 1767–1774.
59. Pankov, R.; Yamada, K. M. J. Fibronectin at a glance. *Cell Sci.* **2002**, *115*, 3861–3863.

60. Baugh, L.; Vogel, V. J. Structural changes of fibronectin adsorbed to model surfaces probed by fluorescence resonance energy transfer. *Biomed. Mater. Res.* **2004**, *69*, 525–534.
61. Dolatshahi-Pirouz, A.; Jensen, T.; Kraft, D. C. F. M.; Kingshott, P.; Hansen, J. L.; Larsen, A. N.; Chevallier, J.; Besenbacher, F. Cell Adhesion, and Proliferation on Nanostructured Tantalum Surfaces. *ACS Nano* **2010**, *4*, 2874–2882.
62. Velzenberger, E.; Pezron, I.; Legeay, G.; Nagel, M. D.; Kirat, K. E. Probing Fibronectin-Surface Interactions: A Multitechnique Approach. *Langmuir* **2008**, *24*, 11734–11742.
63. Lewis, A. L.; Tolhurst, L. A.; Stratford, P. W. Analysis of a phosphorylcholine-based polymer coating on a coronary stent pre- and post-implantation. *Biomaterials* **2002**, *23*, 1697–1706.
64. Jin, H. J.; Park, J.; Valluzzi, R.; Cebe, P.; Kaplan, D. L. Biomaterial films of bombyx mori silk fibroin with poly(ethylene oxide). *Biomacromolecules* **2004**, *5*, 711–717.
65. Seifalian, A. M.; Salacinski, H. J.; Tiwari, A.; Edwards, A.; Bowald, S.; Hamilton, G. In vivo biostability of a poly(carbonate-urea)urethane graft. *Biomaterials* **2003**, *24*, 2549–2557.
66. Vogler, E. A.; Siedlecki, C. A. Contact activation of blood-plasma coagulation. *Biomaterials* **2009**, *30*, 1857–1869.
67. Putnam, F. W. *The Plasma Proteins*, 2nd ed.; Academic Press: New York, 1975; Vol. I.
68. Ugarova, P. T.; Zamarron, C.; Veklich, Y.; Bowditch, R. D.; Ginsberg, M. H.; Weisel, J. W.; Plow, E. F. Conformational Transitions in the Cell Binding Domain of Fibronectin. *Biochemistry* **1995**, *34*, 4457–4466.
69. Xia, N.; May, C. J.; McArthur, S. L.; Castner, D. G. Time-of-Flight Secondary Ion Mass Spectrometry Analysis of Conformational Changes in Adsorbed Protein Films. *Langmuir* **2002**, *18*, 4090.

Chapter 26

Synthesis of Glycocalyx-Mimetic Surfaces and Their Specific and Nonspecific Interactions with Proteins and Blood

Kai Yu[1] and Jayachandran N. Kizhakkedathu*[,1,2]

[1]Centre for Blood Research and Department of Pathology and Laboratory Medicine, University of British Columbia, Vancouver, British Columbia V6T 1Z3, Canada
[2]Department of Chemistry, University of British Columbia, Vancouver, British Columbia V6T 1Z3, Canada
***E-mail jay@pathology.ubc.ca. Phone (604) 822-7085**

Glycocalyx mimicking glycopolymer brushes presenting mannose, galactose and glucose residues in the pyranose form, were synthesized on planar substrates (Si wafer, gold chip) and monodispersed polystyrene (PS) particles to generate bioactive surfaces. We investigated the specific protein binding interactions of the surfaces with carbohydrate binding proteins as well as their non-specific protein interactions in blood plasma. Surface Plasmon Resonance (SPR) analysis showed that the glycopolymer brush presenting mannose residues showed specific multivalent interaction with lectin (Concanavalin A (Con A)). The grafting density has little influence on the binding mode, which indicated steric interference arising from the inter chain interaction has little influence on the binding. The glycopolymer brushes performed better against non-specific single protein adsorption than conventional polymer containing hydroxyl groups. There was some influence on the type of carbohydrates residues present as well the type of anticoagulant used for blood collection. SPR analysis showed that the total protein adsorption from plasma was greatly reduced, as low as 24.3 ng/cm^2 from undiluted plasma on the glucose carrying brush. All the glycopolymer brushes showed similar levels of

In Proteins at Interfaces III State of the Art 2012; Horbett, T., et al.;
ACS Symposium Series; American Chemical Society: Washington, DC, 2012.

platelet activation, however, the platelet adhesion on the surface was dependent on the type of carbohydrate residues present. Blood coagulation on the surfaces was not greatly influenced by the carbohydrate structure suggesting that surfaces may be non-thrombogenic. Our data demonstrate that the structure and presentation of carbohydrate residues are important factors in the design of carbohydrate arrays and synthetic blood contacting surfaces based on glycopolymers as these parameters are influencing the specific and non-specific interaction with proteins.

1. Introduction and Background

The glycocalyx is a carbohydrate-rich extracellular layer produced by the certain type of cells, for example, endothelial cells on the luminal side of the blood vessels. The interactions of glycocalyx with proteins present in the surrounding environments mediate a variety of critical biological processes involving highly specific events such as cell signalling, cell adhesion, fertilization and inflammatory responses (*1–3*). The specific interactions occur through the interaction of glycoproteins, glycolipids or polysaccharides displayed on the cell surfaces with lectins and other carbohydrate binding proteins. In addition, the glycocalyx also serves as a layer which prevents the undesirable non-specific adhesion of proteins and cells (*4–7*) to maintain the non-adhesive properties. In the case of endothelial lining of the blood vessels, the glycocoalyx helps to maintain the non-thrombotic properties of the native intravascular luminal wall (*8*). Thus, the development of artificial cell surface by mimicking of the glycocalyx may provide a promising route not only for the development of highly biocompatible surfaces but also for the comprehensive understanding of carbohydrate-receptor interactions.

The glycocalyx-mimetic surfaces can be either prepared by the physical adsorption or covalent grafting of monosaccharide or oligosaccharide by direct grafting (“grafting to” or “grafting from”) (*9–16*). However, most of these methods suffer from drawbacks such as stability in various conditions, limitation of the range of immobilized carbohydrate and the substrate-dependent nature of specific covalent attachment chemistry (*17*). Also, the surfaces prepared by the methods mentioned above have relatively low carbohydrate density. Thus new methods are required for development of glycocalyx mimicking surfaces.

Although the carbohydrate-protein interaction has shown high specificity, the affinity between single carbohydrate residue and protein is usually very weak (*18*, *19*). This limitation has been addressed by the nature using multivalent interactions, i.e. simultaneous contacts between carbohydrates that are clustered on cell surfaces and protein receptors that contain multiple binding sites (*20–22*). Thus to facilitate the carbohydrate-protein interactions on surfaces and to study their interactions, high carbohydrate density as well as the ability to fine tuning the carbohydrate density on the surfaces are required (*23–28*). Another important aspect is the carbohydrate structures assembled on the surface should preserve the stereo-chemistry of sugar residues in their natural pyranose form (*29*) on the cell surface to facilitate the specific protein interactions. The differences in sugar structures and stereo-chemistry may have influence in both specific and non-specific interaction with proteins (*29*, *30*). Thus it is critical to develop methods for the synthesis of glyco-polymer surfaces bearing carbohydrate units having similar stereo-chemistry to that present on cell surface glycocalyx to investigate their role in both specific interactions and non-specific interactions in biological environment.

Polymer brush based coatings have gained considerable attention recent years due to their robustness in the synthesis, substrate independent method of synthesis, mutifuctionality and stability (*31*, *32*). It has been shown that well-defined hydrophilic polymer brushes demonstrate excellent biocompatibility, protein and cell adhesion resistance (*33–39*). Thus polymer brushes carrying carbohydrate structures in their natural form are good model systems to study the carbohydrate-protein interactions and the development of blood contacting surfaces.

Ejaz and Fukuda were the first to report the preparation of glycopolymer brush using surface initiated atom transfer radical polymerization (SI-ATRP) of a methacrylate-based acetate protected glucose-containing monomer (*40*, *41*), Müller and co-workers adopted similar approaches for the preparation of glycopolymer brush on carbon nanotubes and Si wafer (*42*, *43*). Yang and Xu used a sugar-containing monomer D-gluconamidoethyl methacrylate (GAMA) (*44*), for the preparation of linear and comb-like grafted glycopolymer layers on polypropylene membranes (*45*, *46*). Using reversible addition–fragmentation chain transfer (RAFT) polymerization technique, Stenzel et al prepared stimuli-responsive glycopolymer brushes composed of N-acryloyl glucosamine and N-isopropylacrylamide (*47*). Although the glycopolymer surfaces produced by these methods showed good reduction in non-specific protein adsorption, their specific protein interaction was compromised due to the absence of sugar residues in their natural pyranose form found on cell surface (*29*, *41–46*). It is important that sugar residues should be in their natural form and the differences in sugar structures and stereo-chemistry have influence on both specific and non-specific interaction with proteins (*29*, *30*).

In this chapter, we report the synthesis of three novel hydrolytically stable, N-substituted acrylamide monomers carrying mannose, galactose and glucose in the pyranose form and the preparation of glycopolymer brush surfaces from these monomers. A comprehensive study on non-specific and specific interactions between glycopolymer brushes and proteins were carried out to illustrate the dependence of these interactions on sugar structures and stereo-chemistry. Specific protein interactions on glycopolymer brush structures were studied using Surface Plasmon Resonance spectroscopy (SPR) and Atomic Force Spectroscopy measurements. Blood protein and platelet interactions were studied to illustrate the hemocompatibility of the surfaces.

2. Results and Discussion

2.1. Synthesis of Glycopolymer Brush

2.1.1. Synthesis of N-Substituted Acrylamide Derivatives of Glycomonomers

Chemical structures of synthesized glycomonomers containing mannose, galactose and glucose residues are shown in Scheme 1A (*49*). The synthesis route for 2′-acrylamidoethyl-α-D-mannopyranoside is outlined in Scheme 1B. Similar routes were followed for the synthesis of 2′-acrylamidoethyl-β-D-glucopyranoside and 2′-acrylamidoethyl-β-D-galactopyranoside.

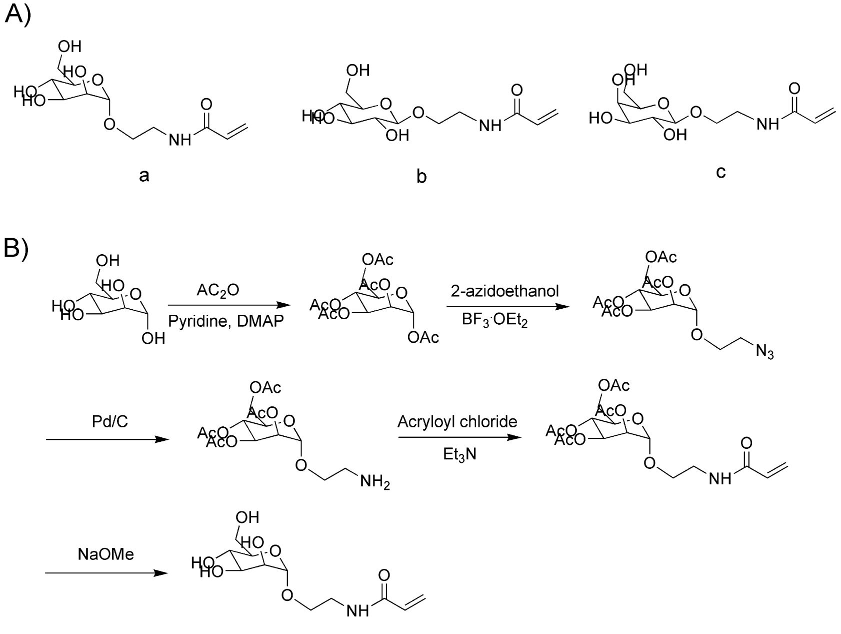

*Scheme 1. **A**: Chemical structures of 2'-acrylamidoethyl-α-D-mannopyranoside (compound **a**), 2'-acrylamidoethyl-β-D-glucopyranoside (compound **b**) and 2'-acrylamidoethyl-β-D-galactopyranoside (compound **c**). **B**: Synthesis of 2'-acrylamidoethyl-α-D-mannopyranoside.*

2.1.2. Synthesis and Characterization of Glycopolymer Brushes on Gold Chip and Silicon Wafer

Surface initiated atom transfer radical polymerization (SI-ATRP) was used to synthesize glycopolymer brushes carrying mannose, galactose and glucose in the natural pyranose form on SPR gold chip and silicon wafer (Scheme 2). A comparison of the characteristics of the glycopolymer layer formed on the substrates is given in Table 1. There were no dramatic differences in the grafting density of brush for different monomers at similar polymerization conditions suggesting that the carbohydrate structure was not influencing polymerization. Based on the radius of gyration (Rg) of free polymer and distance between grafted chains, all the grafted layers were found to be in the brush regime as per the definition of polymer brushes (*31*). For example, the calculated distance between the chains (3.3 nm) for the grafted layer with the lowest grafting density (glucose brush grown on Au chip with a grafting density 0.09 chains/nm^2) was less than twice the dimensions of the chain in solution (Rg = 7.8 nm) indicating that this polymer layer was in the brush regime.

The grafting of different glycopolymers on the Si wafer or Au chip resulted in a highly hydrophilic surface layer (water contact angles less than 10°) (Table 1) compared to relatively hydrophobic initiator modified surface (water contact angle on the initiator modified Au chip was 74.5 ± 1.1°). Furthermore, the water contact angles of newly synthesized brushes were considerably lower than the previously reported glycopolymer structures having similar thickness (*45*, *46*, *48*, *50*), which was attributed to the better hydration of the current glycopolymer structures owing to the monomer structure.

2.1.3. Kinetics of Polymerization of 2'-Acrylamidoethyl-α-D-mannopyranoside

The growth of mannose brushes by aqueous SI-ATRP was monitored by measuring grafted polymer layer thickness. Figure 1A shows the increase in polymer layer thickness measured by ellipsometry as a function of polymerization time. In the first 10 min, the thickness increased rapidly to 22.9 ± 1.4 nm, indicating a very fast initial polymerization. After extending the reaction time to 2 h, thickness was increased to 33.9 ± 1.7 nm. Further extending the reaction time to 24 h resulted in only a small change in the thickness.

The molecular weight of free polymer formed in solution along with the surface grafted polymers and total conversion of monomers were also monitored (Figure 1B, Figure 1C). The initial rate of the polymerization was very fast, the M_n rapidly increased to 100 000 g/mol, while the total monomer conversion (contributions from both solution polymerization and surface polymerization) reached 4.8% in 10 min. After extending the reaction time to 2h, the M_n increased to 135 000 g/mol, while the total conversion increased to 16%. After 24h, the M_n increased to 140 000 g/mol with the monomer conversion reaching 22.3%. The polysipersity of the chains decreased with monomer conversion and remained relatively constant above 10.7% conversion. Although the unusual non-linear nature of the first-order kinetic plot and the evolution of M_n with conversion were indicative of termination reactions in the early stage, symmetrical unimodal GPC traces were obtained for the glycopolymer formed. In aqueous ATRP, water acts both as an accelerator to increase the activity of the catalyst (*51*, *52*) and as a solvent. The high activity of Cu(I) complex generated high concentration of radicals resulting in high polymerization rate in the early stage (*53*).

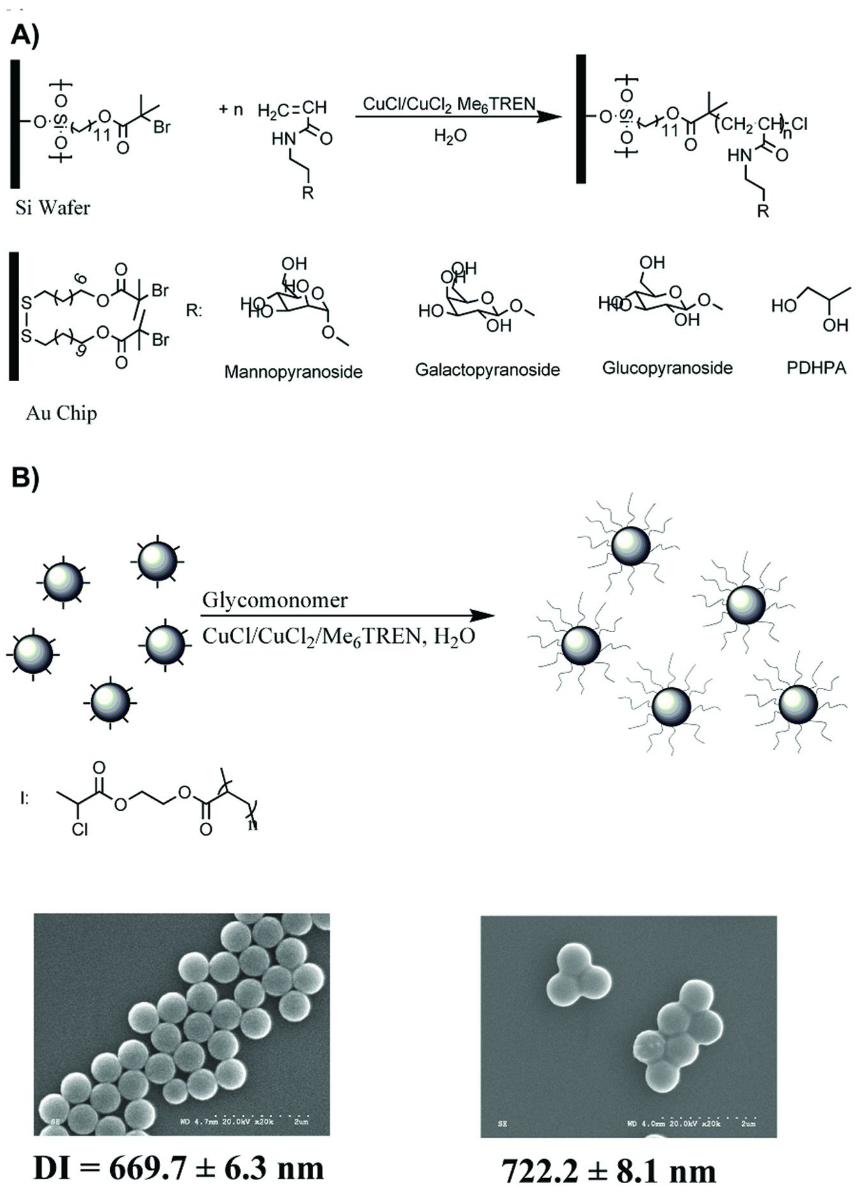
A)
Si Wafer
Br
+ n
CuCl/CuCl2 Me6TREN
H2O
Cl
R
Au Chip
R:
Mannopyranoside
Galactopyranoside
Glucopyranoside
PDHPA
B)
Glycomonomer
CuCl/CuCl2/Me6TREN, H2O
I:
DI = 669.7 ± 6.3 nm
722.2 ± 8.1 nm

Scheme 2. General synthesis scheme for PDHPA and glycopolymer brushes carrying different carbohydrate residues (mannose, galactose and glucose) on (A) planar substrates (Au chip and Si wafer) and on (B) initiator modified PS particles. Scanning electron micrographs of initiator modified PS particles and mannose brush grafted PS particles are also given. Adapted with permission from ref. (37). Copyright 2012 John Wiley and Sons.

Table 1. The characteristics of glycopolymer brushes grafted on different substrates[a]

	Substrates	*Molecular weight (M_n) and PDI of grafted polymer*	*Molecular weight (M_n) and PDI of free polymer in solution*	*Brush dry thickness (nm)*	*Water contact angle (°)[b]*	*Grafting density calculated from free polymer (chains/nm^2)*	*Grafting density calculated from grafted polymer (chains/nm^2)*
Mannose Brush	Si wafer	N/D	131000, 1.3	15.7 ±2.3[d]	8.8 ± 0.7	0.07	N/D
	Si wafer	N/D	131000, 1.3	27±1.2[d]	8.3 ± 0.2	0.12	N/D
	Si wafer	N/D	131000, 1.3	35.9 ±1.9[d]	5.1 ± 0.9	0.16	N/D
	Au Chip	N/D	130000, 1.3	1.3 ±0.5	14.7 ± 1.2	0.006	N/D
	Au Chip	N/D	130000, 1.3	4.6 ±1.1	9 ± 1.3	0.02	N/D
	Au Chip	N/D	123000, 1.3	19.6 ±2.8[d]	6.7 ± 2.6	0.1	N/D
	PS particle	75600, 1.3[c]	118000, 1.7	26.3±10.3[e]	N/D	0.13	0.21
Galactose Brush	Si wafer	N/D	183000, 1.3	35.6±1.7 [d]	6.9 ± 1.2	0.12	N/D
	Au Chip	N/D	158000, 1.4	24.4±1.6 [d]	7.8 ± 3.3	0.09	N/D
	PS particle	75000, 1.4[c]	116000, 1.4	25±12[e]	N/D	0.13	0.2
Glucose Brush	Si wafer	N/D	178000, 1.3	34.4±2[d]	5.6 ± 0.7	0.12	N/D
	Au Chip	N/D	134000, 1.2	22.2±1.7[d]	8.3 ± 1.9	0.09	N/D
	Au Chip[f]	N/D	248000, 1.3	58.6 ±4.6[d]	4.6 ± 3.2	0.24	N/D
	PS particle	69000, 1.4[c]	110000, 1.4	24±10.8[e]	N/D	0.13	0.21

[a] The values given are mean ± SD. M_n-Number average molecular weight. PDI- polydispersity. ND- not determined. [b] The water contact angle for the initiator modified Si wafer and Au chip were 76.7 ± 3.5°, 74.5 ± 1.1° respectively. [c] Cleaved from the surface; [d] determined by ellipsometry; [e] determined by SEM. [f] Glucose brush with higher grafting density on Au chip.

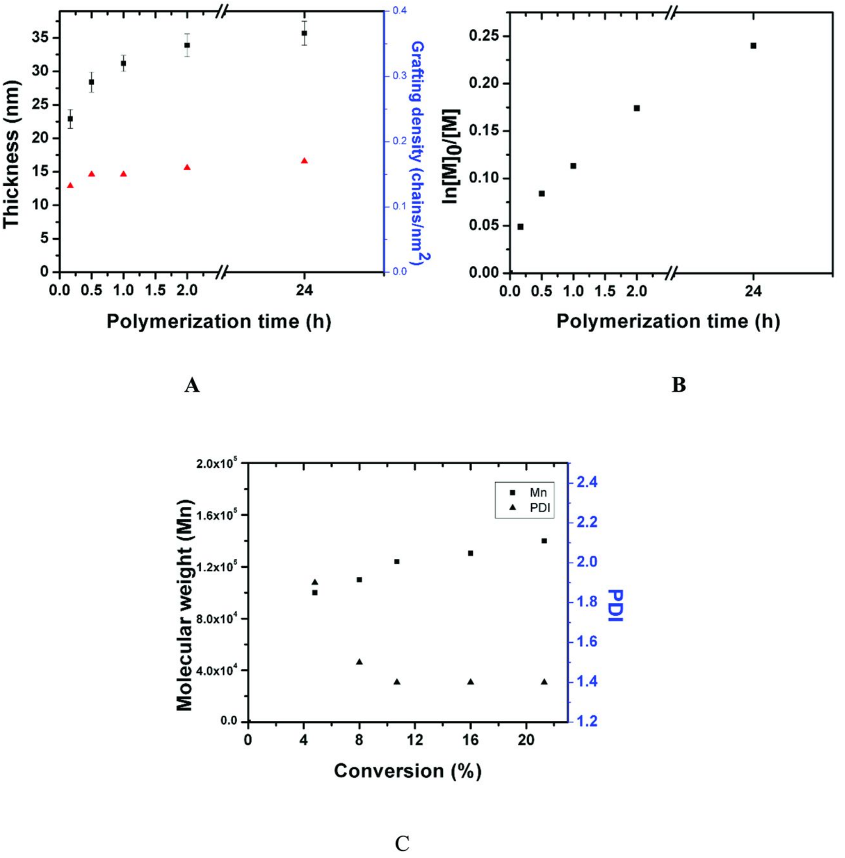

A

B

C

Figure 1. Thicknesses (■) and grafting densities (▲) of PAAEM brushes with polymerization time. Polymerization condition: [M]=5% W/V, Initiator: methyl 2 chloropropionate, [I]=0.75 mM, [CuCl]/[$CuCl_2$]/[Me_6TREN]=8mM/1mM/18mM, RT, ester based surface initiator was used (A). First order kinetic plot for surface initiated ATRP of 2'-acrylamidoethyl-α-D-mannopyranoside in H_2O (B). Dependence of molecular weight (Mn) and molecular weight distribution (Mw/Mn) on monomer conversion (C). Polymerization condition: [M]=5% W/V. Initiator: methyl 2-chloropropionate, [I]=0.75 mM, [CuCl]/[$CuCl_2$]/[Me_6TREN]=8mM/1mM/18mM, RT.

2.1.4. Synthesis and Characterization of Glycopolymer Brushes on Polystyrene (PS) Particles

Monodisperse PS particles were used for the preparation of the glycopolymer brushes as the particles have large specific surface area available (89,544 cm^2/g)

(*54*). The use of larger surface area in small volume will allow for a more accurate correlation of protein-surface interaction. Characteristics of the grafted layers on PS particle are given in Table 1. The grafted polymer chains were cleaved from PS particle in each case and the molecular weights were determined. It was found the molecular weight of the grafted glycopolymer was ~36% lower than that of glycopolymer formed solution (Table 1). Using the molecular weight of grafted polymer, a better estimate of the grafting density was obtained. The grafting density values calculated using the solution polymer data showed similar values to those of flat Si wafer and gold chip (Table 1). The grafted polymer layer properties did not show much dependence on the type of carbohydrate monomer under comparable polymerization conditions. The grafted glycopolymer layers on PS particle were in the brush regime as indicated by the measured Rg and calculated distance between the chains.

2.2. Specific Interaction with Carbohydrate-Recognizing Protein: Influence of Grafting Density

Carbohydrate arrays have been extensively used to facilitate the study of carbohydrate-protein recognition (*55–57*). The presentation of carbohydrates on the surface provides a means to simulate the oligosaccharides found on cell membrane. Furthermore, the structural features of carbohydrate array can be tuned for elucidating the molecular mechanisms of carbohydrate-protein recognition (*58–61*). Glycopolymer brush offers an opportunity to mimic the cell surface glycocalyx as sugar units are present as pendent structures along the polymer chain similar to proteoglycans present on the cell membrane (*27*, *28*). Also, different types of sugars can be introduced to the flexible chains on the surface to mimic oligosaccharide composed of different carbohydrate units. Hence, it offers rich opportunities to fine tune the binding interactions of multivalent lectins to carbohydrate on surfaces. Since glycopolymer chains are grafted closely on the surface (brush form), both enthalpic contribution due to multivalent binding and entropic penalties associated with the close packing of chains can be fine tuned by changing the molecular and structural features of brushes, including the composition, grafting density and length of grafted polymer.

To vary the grafting density of polymer chains, mannose brushes were grown from diluted SAM-Br carrying different ATRP initiator densities (*62*). Various compositions of SAMs are prepared by diluting the $BrC\text{-}(CH_3)_2COO(CH_2)_{11}S)_2$ (SAM-Br) and $(HO(CH_2)_{11}S)_2$ (SAM-OH) from 100:0 to 2:98 in the molar ratio. With decreasing SAM-Br concentration on the surface, the grafting density of the mannose brush decreased from 0.10 to 0.006 chains/nm^2, a ~16-fold difference without much influence on the molecular weight of the chains (Table 1). The distance between the polymer chains on the surface increased from 3.2 to 12.9 nm accordingly. It was proposed that brush at higher grafting density will experience a greater entropic penalty arising from the strong steric restrictions of extended chains (*63*). We investigated whether the steric factors are influencing the binding interactions of mulitivalent lectins. Such information is important in the design of highly sensitive sensor chips based on glycopolymer structures.

2.2.1. Surface Plasmon Resonance (SPR) Analysis of Lectin Binding to Glycopolymer Brush-Variation in Graft Density

A representative sensorgram of Con A interacting with mannose brushes with different grafting density is given in Figure 2A. We applied a non-regeneration protocol (*64*) to investigate the interaction between Con A and glycopolymer brushes with different graft densities. The current glycopolymer brushes show much stronger response and higher analyte concentration sensitivity (*23*, *65*). In addition, the glycopolymer brush modified chip can easily detect Con A with concentration as low as 10 nM (data not shown). The low detection limit indicated that the current glycopolymer chip has very high sensitivity, which is probably due to the high mannose density, very low non-specific protein binding and the flexibility of polymer chains. The sensorgram of Con A binding to galactose brush (inert carbohydrate residue) indicated that there was no association between Con A and galactose brush and was consistent with the reports that Con A has no affinity for galactose (*57*, *58*).

To further investigate the lectin binding behavior of various glycopolymer brushes, the equilibrium association constants were determined from the SPR sensorgram. We were interested in determining whether the decrease in SPR response brought by decreasing the density was also reflected in association constants. The association and dissociation taking place while Con A flowed through the glycopolymer brush modified chip. At equilibrium state, the equation 1 is valid where R_{eq}, SPR response to a solution of Con A of concentration C at equilibration, R_{max}, maximal SPR response when C is infinity, k_{on}, Association rate constant, k_{off}, disassociation rate constant (*64*).

$$\mathrm{d}R/\mathrm{d}t = \mathrm{k_{on}C(R_{max}\text{-}R_{eq})\text{-}k_{off}R_{eq}} = 0 \qquad (1)$$

Rearrangement and replacing the expression $k_{on}/k_{off} = K_A$ (association constant) yields the equation

$$\frac{1}{R_{\mathrm{eq}}} = \frac{1}{K_A R_{max}} \frac{1}{C} + \frac{1}{R_{max}} \qquad (2)$$

From the graphical representation $1/R_{\mathrm{eq}}$ against $1/C$, the association constant (K_A) was calculated for various glycopolymer brushes as a function of grafting density.

The plot of $1/R_{\mathrm{eq}}$ vs 1/C for mannose brush with grafting density 0.10 chains/nm^2 (Figure 2D) gave a linear relationship ($R^2 = 0.996$) except for two outliners at low concentrations. The calculated association constant was $(2.2 \pm 0.4) \times 10^6$ M^{-1}. This value is comparable to the values reported for the multivalent interaction between mannose and Con A measured by SPR, quartz crystal microbalance and other methods (*12*, *66*, *67*). The association constant agreed well with the literature data suggest the glycopolymer brush modified gold chips is a good model to study the binding interaction between carbohydrates and lectins.

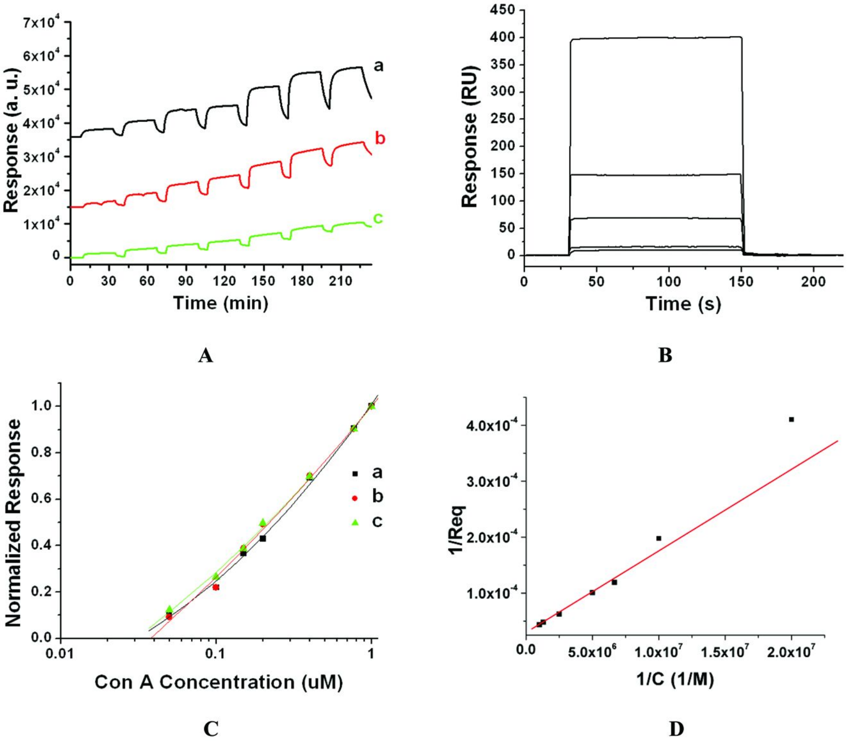

Figure 2. A: SPR sensorgram for the interaction of Con A with mannose brush with grafting density 0.1 (a), 0.02 (b) and 0.006 chains/nm² (c). Seven different concentration of Con A was injected and flowed through the channel. The concentration of Con A in the sequence of injection: 0.05, 0.10, 0.15, 0.2, 0.4, 0.8, 1 µM. B: SPR sensorgram for the interaction of Con A with galactose brush. The Con A concentration used, in descending order of response units (RU), were: 64, 32, 10, 1, 0.1 µM. C: Isotherms for Con A binding to glycopolymer brushes with different grafting density 0.1 (a), 0.02 (b) and 0.006 chains/nm² (c). D: Plot of 1/Req vs. 1/C obtained from the SPR data for Con A binding to surface grafted with mannose brush. The R² values for the linear fitting were 0.996. D: Plot of R_{eq} vs. C obtained from the SPR data for Con A binding to surface grafted with mannose brush. The R² values for the fitting were 0.998.

The SPR response decreased slightly with decreases in grafting density of the mannose brush. The adsorption isotherm is given in Figure 2C. The data showed that the grafting density did not have a strong influence on Con A binding to mannose residues in the brush. The association constants varied from (2.2 ± 0.4) × 10^6 to (2.7 ± 0.4) × 10^6 M^{-1} with decreasing grafting density from 0.1 to 0.006 chains/nm². The grafting density of the glycopolymer brush did not seem to have an influence on association constants in the Con A concentration range 0.05-1 µM. The large association constant is indicative of multivalent interaction irrespective of the change in grafting density. These results suggested that steric hindrance arising from inter-chain interactions was not influencing the binding characteristics of Con A to mannose residues within the glycopolymer brush.

2.3. Non-Specific Protein and Blood Interactions with Glycocalyx-Mimicking Polymer Brushes

2.3.1. Single Protein Interactions

An initial study was performed to understand the protein resistant properties of new glycopolymer brushes carrying different carbohydrate residues by fluorescence microscopy and ellipsometry. Glycopolymer brushes having similar dry thickness and grafting densities were used for these measurements. Fluorescently labelled bovine serum albumin (BSA) and fibrinogen were used in our experiments. In the initial studies, the performance of the different carbohydrate brushes were compared with a brush carrying two hydroxyl groups as the pendent group per monomer, poly-N-(2,3-dihydroxypropyl)acrylamide (PDHPA) (*68*), with similar properties.

2.3.1.1. Effect of Carbohydrate Structures

Results from the adsorption of single proteins from fluorescence microscopy measurements are shown in Figure 3A and B. The fluorescence intensities of the glycopolymer brushes after protein incubation were also compared with that of initiator modified silicon wafer and PDHPA brush. All the polymer brush structures considerably reduced the protein adsorption. The glycopolymer brushes performed better than PDHPA brush against protein adsorption. The glycopolymer brushes containing mannose, galactose and glucose, considerably reduced the BSA adsorption as evident from 149, 172 and 500-fold reduction in fluorescence intensity compared to the initiator modified surface, while the PDHPA brush showed 17-fold reduction in BSA adsorption. The fibrinogen adsorption was reduced by 21, 52, 115, 135-fold respectively for the PDHPA, mannose, galactose, glucose brushes (Figure 3B). The thicknesses of glycopolymer and PDHPA brushes didn't show any noticeable change after the incubation with BSA and fibrinogen solution for 1h (data not shown).

Glycopolymer brushes brought a larger reduction in protein adsorption than conventional polymer brush containing OH groups not presenting on carbohydrate derivatives. It may be due to i) highly hydrophilic nature of brushes originated from carbohydrate residues possessing hydrogen-donating abilities (*69–72*) ii) entropic repulsion brought by the highly stretched chains in brushes (*63*, *73*, *74*) iii) the chemical nature of carbohydrate units (*75*, *76*). Since protein-resistant properties of hydrated brush surface is originated from the repulsive forces between the hydration layer and protein, any differences in the structural properties and dynamic of water layer will bring a difference.

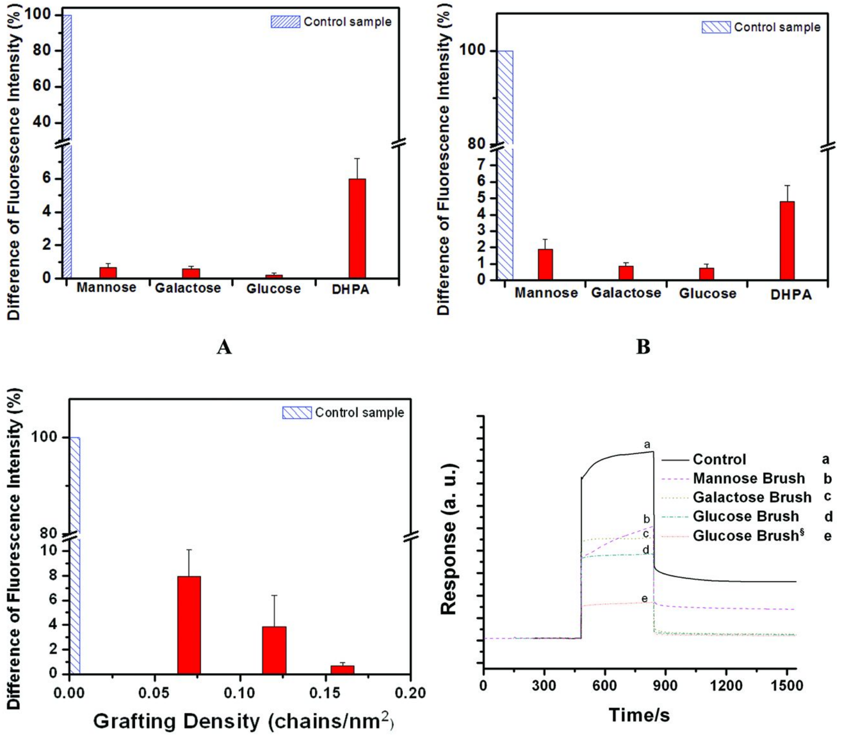

A B

C D

Figure 3. Fluorescence intensity reduction (values: mean ± standard deviation, n = 3) brought by glycopolymer brushes containing different carbohydrate units and PDHPA brush after incubating with fluorescently labeled BSA (A) and (B). C: Fluorescence intensity reduction (values: mean ± standard deviation, n = 3) brought by mannose brushes with different grafting density (0.07, 0.12, 0.16 chains/nm^2) after incubating the brushes with fluorescently labeled BSA. Initiator modified silicon wafer was set as the control sample. D: Effect of glycopolymer structure and anticoagulant on plasma protein adsorption studied by surface plasmon resonance (SPR) spectroscopy. ATRP-initiator modified Au chip was used as the control sample. The grafting densities of the mannose, galactose and glucose brushes were 0.1, 0.09 and 0.09 chains/nm^2, respectively. Glucose Brush§ refers to glucose brush with higher grafting density (0.24 chains/nm^2).

2.3.1.2. *Effect of Grafting Density of Brushes on Single Protein Adsorption*

The effect of brush properties against non-specific protein adsorption from single protein solution was investigated for arriving at a glycopolymer structure which shows minimal protein adsorption before moving to complex protein solutions like blood plasma. Mannose containing brushes with different grafting densities were used to study the adsorption of fluorescently labelled BSA for this purpose. As shown in Figure 3C, the BSA adsorption decreased dramatically with increasing grafting density from 0.07 to 0.16 chains/nm^2. The BSA adsorption decreased approximately 150-fold at high grafting density compared to 12-fold at low grafting density with respect to the control. Since the non-specific protein adsorption was suppressed considerably at higher grafting density, only these brushes were used for investigating the effect of different carbohydrate structures in blood plasma as given below.

2.3.2. Blood Interaction with Glycocalyx-Mimicking Surface

Sodium citrate and sodium heparin anticoagulated plasma were used for the current study. Since the presence of calcium ions is essential for the interaction of carbohydrate-binding protein and carbohydrate (*77*, *78*), we anticipated that specific interaction of calcium-dependent protein to carbohydrate residues in the glycopolymer brush would be compromised in the presence of sodium citrate as it chelate all the calcium ions. Thus, heparin was also used as anticoagulant for preparing blood plasma. In presence of heparin, the prevention of blood coagulation is achieved by the inhibition of thrombin activation. Since the extent of loss of calcium ions in heparin is much less compared to the citrate (*79*), we anticipated that the presence of heparin may not influence the calcium-dependent protein binding to carbohydrate residue present on the surface.

The interaction of the undiluted plasma with glycopolymer brushes (containing mannose, galactose and glucose units) grafted on gold chips at relatively high grafting density (0.1 chains/nm^2) was studied by SPR (Table 1). Figure 3D gives the SPR sensograms showing the binding of plasma protein from citrate anticoagulated plasma to glycopolymer surface containing mannose, galactose and glucose units at similar grafting density. The brushes carrying glucose and galactose units showed minimal protein adsorption from plasma compared to the control. The mannose brush adsorbed more proteins compared to glucose and galactose brushes. By assuming 1 a.u. was equal to 0.1 ng/cm^2 (*80*), the total amount of protein adsorbed onto mannose, galactose and glucose brushes were 258.4, 35.6 and 31.2 ng/cm^2 respectively. The total amount of protein adsorbed on the control hydrophobic surface was 504.4 ng/cm^2.

The grafting density also has effect on the adsorption of protein from plasma on carbohydrate containing brush. Protein adsorption on glucose brush with a high grafting density (0.24 chains/nm^2) prepared on Au-chip was compared with other brushes (Figure 3D). The total protein adsorption to this high density glucose brush (24.3 ng/cm^2) was slightly lower than the glucose brush with a grafting density of 0.09 chains/nm^2 (31.2 ng/cm^2).

The total protein adsorption from heparinized plasma on the mannose, galactose and glucose brushes were 249, 34.7 and 30 ng/cm^2, respectively at a grafting density of 0.09 chains/nm^2, which suggested that in presence of calcium, mannose brushes adsorbed more proteins compared to other glycopolymer structures. When the grafting density of the glucose brush was increased to 0.24 chains/nm^2, the total protein adsorption decreased slightly to 27.2 ng/cm^2, demonstrated the insignificant effect of grafting density. Importantly, in both anticoagulants, the glucose brush with high grafting density adsorbed the least amount of proteins from plasma.

SPR analysis showed that the high grafting density glucose brush performed equally or better compared to PEGylated surfaces, poly(β-peptoid), and hydroxyl carrying brushes reported in preventing non-specific protein adsorption from blood plasma. For example, the current standard for antifouling surface, poly[oligo(ethylene glycol) methyl ether methacrylate] (POEGMA) brushes (*81*), showed ~29 ng/cm^2 of adsorbed proteins from plasma. The protein adsorption on the poly(β-peptoid) brush was at level 100 ng/cm^2 (*82*), poly(2-hydroxyethyl methacrylate) (PHEMA) brushes (*83*) at the film thicknesses of 20–35 nm showed a very little protein adsorption (~3 ng/cm^2). In our recent study (*84*), we found hydroxyl-containing polymer including (PHEMA, poly(N-2-hydroxyethylacrylamide (PHEAA)) may be excellent in preventing non-specific protein interactions from single protein solution as well as from 100% EDTA anticoagulated blood plasma. However, polyhydroxyacrylamide brushes adsorbed considerable amount of proteins from citrated blood plasma as well from serum (unpublished results).

Zwitterionic polymer brush showed better performance than the glycopolymer brushes due to better hydration. Protein adsorption from plasma reported was ~6.1 ng/cm^2, 3 ng/cm^2, 0.3 ng/ ng/cm^2 respectively for on poly(sulfobetaine methacrylate) (PSBMA) (*85*), poly(carboxybetaine acrylamide) (PCBAA) (*86*) and carboxybetaine methacrylate (PCBMA) surfaces (*87*).

2.3.3. Platelet Activation Analysis

Figure 4A shows the platelet activation data in platelet poor plasma (PRP) prepared in sodium citrate upon incubation with glycopolymer brush structures grafted on PS particles by flow cytometry analysis. PS particles allowed us to use high surface to volume ratio for the analysis, for example, we used 100 cm^2 surface in 200 μL PRP. Bare PS particles gave the highest platelet activation compared to the buffer control ($p < 0.05$, number of donors: N = 5). In the case of glycopolymer brushes, the platelet activation levels were similar to that of buffer control ($p = 0.41$, 0.47, 0.35 respectively for the mannose, galactose and glucose brushes) after 1 h incubation indicated that the platelet activation is independent of the type of carbohydrate residues present. At the 3 h time point, similar data was obtained. Similar results were obtained in heparin anticoagulated PRP (Figure 4B) for different glycopolymer brushes.

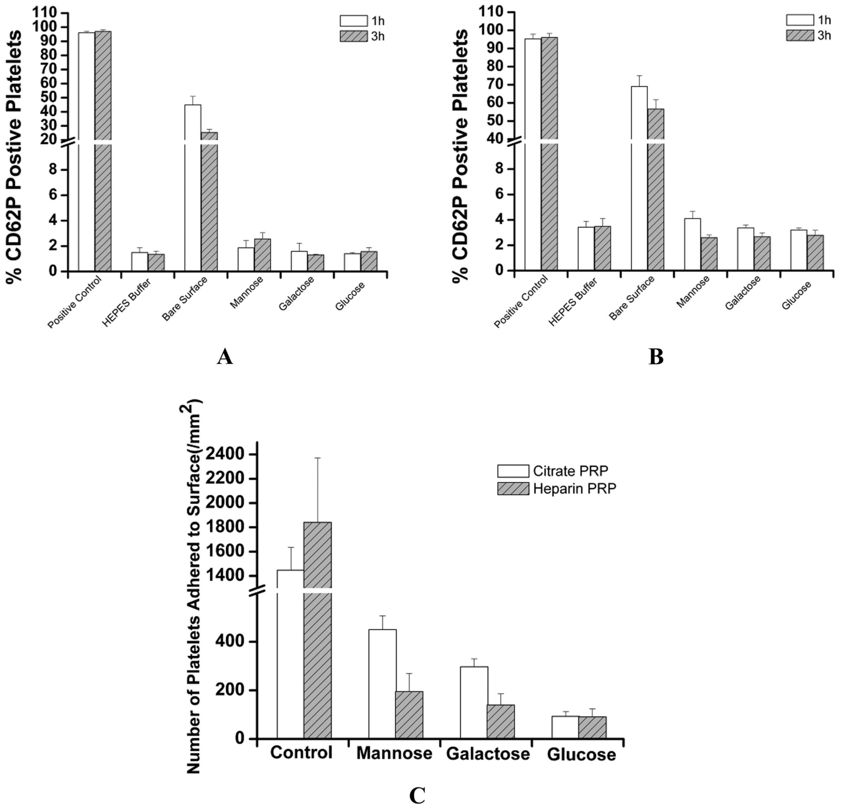

Figure 4. Effect of glycopolymer structure and anticoagulant on platelet activation. Platelet activation (values: mean ± standard deviation, n = 5) in presence of bare surface (PS particles) and glycopolymer brushes carrying different carbohydrate residues (100 cm^2 in 200 μL) in (A) citrate anticoagulated PRP and (B) heparin anticoagulated PRP at 37 °C. C: Effect of glycopolymer structures and anticoagulants on platelet adhesion studied by SEM analysis. Number of platelets adsorbed onto ATRP initiator modified bare silicon wafer (control sample) and glycopolymer brushes (mannose, galactose and glucose) modified Si wafer from citrate and heparin anticoagulated PRP. The grafting densities of the mannose, galactose and glucose brushes were 0.16, 0.12 and 0.12 chains/nm^2, respectively.

2.3.4. Platelet Adhesion Analysis

Platelet adhesion on glycopolymer brush structures was measured by scanning electron microscopy analysis. The number of adhered platelets onto the surface from citrate anticoagulated PRP was greatly reduced when glycopolymer brushes were grafted (Figure 4C). Unlike the case of platelet activation, clear differences were observed in the number of adhered platelets as well as the shape of adhered platelets on brushes carrying different carbohydrate residues. The number of platelets adhered to mannose, galactose and glucose brushes were 450 ± 57, 297 ± 33, 93 ± 20 per mm^2 respectively which constitute 3, 4.9 and 15.6-fold reduction compared to the bare surface control. The glucose brush showed the least platelet adhesion.

The morphology of the adhered platelets also showed dependence on the type of carbohydrate residues present (Figure 5). It is well established that activated platelets change their morphology on adsorption and can be characterized by the cytoskeletal rearrangements and ruffling of the surface membrane with the formation of multiple pseudopods (*88*). The platelets adhered on the hydrophobic control surface showed a spread-dendritic morphology. The morphology of the platelets on mannose and galactose brushes showed some signs of spreading. Whereas platelets present on the glucose brush showed the normal round morphology. The data suggest that platelets were less activated when presented with the glucose brush surface.

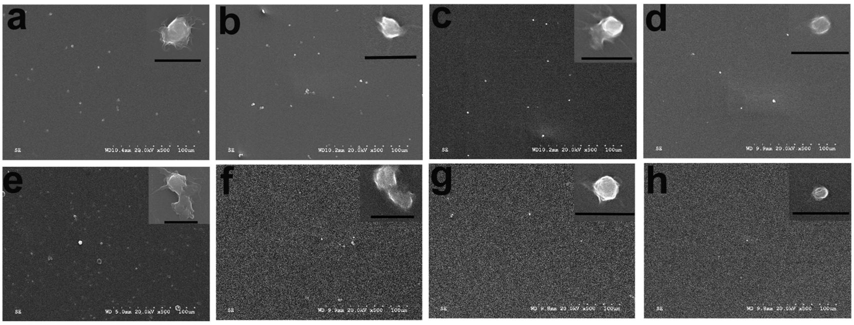

Figure 5. Effect of glycopolymer structure and anticoagulant on platelet adhesion studied by SEM analysis. Representative SEM micrographs at 500X and 5000X magnification (inset, scale bar 5 μm) of adhered platelets on (a) control (ATRP initiator modified Si wafer surface), (b) mannose brush, (c) galactose brush and (d) glucose brush from citrated PRP. Adhered platelets on (e) control, (f) mannose brush, (g) galactose brush and (h) glucose brush from heparinized PRP. The grafting densities of the mannose, galactose and glucose brushes were 0.16, 0.12 and 0.12 chains/nm^2, respectively. Reproduced with permission from ref. (37). Copyright 2012 John Wiley and Sons.

The numbers of platelets adhered onto mannose, galactose and glucose brushes from heparin anticoagulated PRP were 195 ± 75, 140 ± 45.6, 91 ± 33.4 per mm^2 respectively; this amounts to 9.4, 13.2 and 20.2-fold reduction compared to the control (Figure 4D). The influence of carbohydrate residues on the morphology of adhered platelets was found to be similar to that of citrate anticoagulated PRP (Figure 5).

2.3.5. Surface Induced Blood Coagulation: Thromboeleastography Analysis

Thromboelastography (TEG) is a technique that provides a continuous measurement of the blood coagulation from clot initiation, maturation and retraction to clot lysis (*89*). This analysis is much closer to *in vivo* as no additional agents are added to initiate blood coagulation and all the cell types and proteins present during the analysis. Standard parameters obtained from TEG blood clotting analysis are designated as R (the time from the start of the experiment to the initiation of the clot), K (kinetics of blood coagulation), MA (maximum amplitude or maximum strength of the clot). The interaction of the glycopolymer brushes with whole blood and PRP were measured. TEG parameters were correlated to the chemistry of the surfaces carrying different carbohydrates.

Figure 6A shows TEG traces for the incubation of bare surface (PS particles) and glycopolymer brushes with PRP in citrate anticoagulant. Similarity in the shape of TEG traces suggests that there was no significant difference in the clot structure formed in the presence of different surfaces and the buffer control. Figure 6B shows the effect of different surfaces on the initial coagulation time 'R' in PRP. The shorter 'R' value for bare surface compared to the buffer control indicate that the surface was more thrombogenic ($p < 0.1$, number of donors N = 5). The glycopolymer brushes showed similar 'R' values compared to the buffer control suggesting that these surfaces did not induce blood coagulation ($p = 0.48$, 0.33, 0.33 for mannose, galactose and glucose brushes respectively to the buffer control). The glucose brush showed a slightly longer 'R' value compared to other brushes.

In whole blood, similar observations were made (Figure 6B). The analyses in whole blood are closer to *in vivo* conditions as all the blood components were present during the measurement. The initial coagulation time, 'R' values, for glycopolymer brushes showed a similar trend as observed in the case of PRP. There were no significant differences between the buffer control and different glycopolymer brushes ($p = 0.23$, 0.20, 0.37 for mannose, galactose and glucose brushes respectively relative to the buffer control). Similar to the results obtained from PRP, the glucose brush showed a slightly longer 'R' value in whole blood.

3. Conclusions

Three novel monomers containing mannose, galactose and glucose in the pyranose form were synthesized. Glycopolymer brushes were prepared by SI-ATRP of the newly synthesized monomers. A comprehensive analyses on the specific and non-specific protein interaction with glycocalyx-mimcking surfaces were performed to illustrate the dependence on sugar structures and stereo-chemistry. Glycopolymer brushes presenting 100% mannose residues exhibited multivalent interaction with Con A and much higher sensitivity. The grafting density of the brushes has little influence on the binding model as evident from the small differences in association constants. Non-specific protein interaction to glycopolymer brushes was considerably reduced compared to the bare surface and brush structures carrying hydroxyl groups possibly due to the better hydration of carbohydrate structures. Carbohydrate structure dependent adsorption of proteins was observed in blood plasma with mannose brushes adsorbing most and glucose brushes adsorbing the least. Platelet adhesion on glycopolymer brushes was dependent on the type of carbohydrate residues present. Thormboelastography analysis revealed that the glycopolymer grafted surfaces did not significantly change the blood coagulation profile of platelet rich plasma or whole blood. The results presented here give insights into the use of carbohydrate structures in the design of polymer coatings for blood contacting applications.

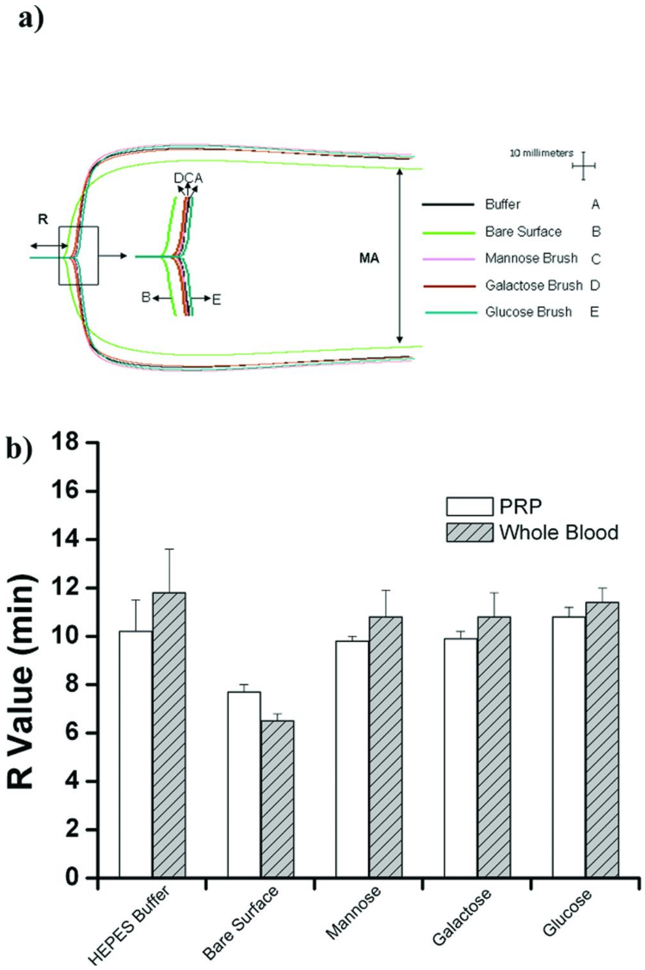

Figure 6. Surface induced blood coagulation analyzed by Thromboelastography (TEG). (a) A representative TEG trace of platelet rich plasma (PRP) incubated with bare surface (PS nanoparticles) and glycopolymer brushes on monodispersed PS particles at 37°C. (b) Initial coagulation times (R values, mean ± standard deviation, n = 5) for different surfaces in PRP (number of donors N = 5) and whole blood (number of donors N = 5). Standard error (SD, n = 5). Reproduced with permission from ref. (37). Copyright 2012 John Wiley and Sons.

4. Experimental Section

4.1. Synthesis of Carbohydrate-Containing Monomer

2′-Acrylamidoethyl-α-D-mannopyranoside, 2′-acrylamidoethyl-β-D-galactopyranoside and 2′-acrylamidoethyl-β-D-glucopyranoside were synthesized by a similar procedure reported in our recent paper (*49*). All the brush structures were characterized in terms of thickness, grafting density and molecular weight. Initiator modified polystyrene (PS) particles were synthesized by the procedure as we reported previously (*54*).

4.2. Synthesis of Poly(2′-acrylamidoethyl-α-D-mannopyranoside) (PAAEM) Brush (Mannose Brush) on SPR Chip

Copper (II) chloride ($CuCl_2$, 1.35 mg, 0.01 mmol), copper (I) chloride (CuCl, 8 mg, 0.08 mmol), Me_6TREN (52 μL, 0.18 mmol) were added successively into a glass tube followed by adding Milli Q water (12 mL). The solution was degassed with three freeze-pump-thaw cycles. The solution was then transferred into the glove box. The solution (1.5 mL) was drawn and added into the vial which containing 2′-acrylamidoethyl-α-D-mannopyranoside (75 mg). After the monomer was completely dissolved, initiator modified gold chip was fully immersed in the solution. Soluble methyl 2-chloropropionate (40 μL) in methanol (5 mL) was also added along with the substrate to the reaction solution. The surface-initiated ATRP was allowed to proceed at RT (22°C) for 24 h. The substrates were then rinsed with water thoroughly, followed by drying in an argon flow. The polymerization solution was dialyzed against deionized water, and then freeze dried to recover the soluble polymer formed along with the surface grafted polymer.

Poly(2′-acrylamidoethyl-β-D-galactopyranoside) (PAAEGal) brush (**Galactose brush**) and poly(2′-acrylamidoethyl-β-D-glucopyranoside) (PAAEGlc) brush (**Glucose brush**) were synthesized using similar procedures. Glucose brush with higher grafting density (0.24 chains/nm^2) was prepared by at a monomer concentration of 10 wt % while keeping all the other polymerization parameters constant. All the brush structures were characterized in terms of thickness, grafting density, molecular weight and polydispersity index (PDI).

The grafting density (σ) for glycopolymer brushes was estimated by using the equation (*49*), $\sigma=(h\rho N_A)/M_n$, where M_n is the molecular weight of free polymer in the solution, N_A is the Avogado's number, h is the dry polymer layer thickness measured by elliposometer, ρ is the density of glycopolymer (we assumed the density of glycopolymer brushes is equally to 1 g/cm^3).

4.3. Synthesis of Glycopolymer Brushes on Silicon Wafer

The initiator modification of Si wafer and preparation of glycopolymer brushes on initiator modified substrate were described in our earlier report (*49*). The mannose brushes with different grafting densities were grown on the mixed

SAMs with different molar ratio of ATRP surface initiator and an inert molecule octadecyltrichlorosilane.

4.4. Synthesis of Poly(2′-acrylamidoethyl-α-D-mannopyranoside) (PAAEM) Brush on Polystyrene (PS) Particles

The synthesis of monodisperse PS particles and surface initiator modification can be found in our earlier publication (*54*). Initiator modified PS particles (60 mg), non-ionic surfactant Brij 35 (3.3 mg), Milli Q water (2 mL) were added successively into a glass tube. The glass tube was degassed by three freeze-pump-thaw cycles. To help the PS particles disperse homogenously in water, the glass tube was subjected to ultrasonication for 15 min and transferred to the glovebox. In another glass tube, CuCl (6 mg), $CuCl_2$ (1.3 mg), Me6TREN (72 μL) were added successively followed by the addition of Milli Q water (6.5 mL). The glass tube was degassed by three freeze-pump-thaw cycles and transferred to the glovebox. 2′-Acrylamidoethyl-α-D-mannopyranoside (100 mg) was added to the prepared solution (1 mL). After the dissolution of monomer, the solution was mixed with 1 mL PS particles suspension. Sixteen microliters solution of methyl 2-chloropropionate in methanol ((40 μL in 5 mL) was also added along with the substrate to the reaction media. The suspension was stirred continuously and the polymerization was allowed to proceed at RT (22°C) for 24 h. The polymer grafted PS particles were cleaned by 3 repeated cycles of centrifugation and resuspension in $NaHSO_3$ solution (50 mM) and water to remove adsorbed copper complexes. Finally, the latex suspension was washed with 0.1 M EDTA solution three times and then with water three times to remove any copper complex remained within the grafted surface. Polymer brushes carrying galactose and glucose on PS particles were synthesized using similar procedures. All the grafted structures were characterized in terms of thickness, grafting density, molecular weight and PDI. The grafted polymer was cleaved from the surface by stirring a known amount of grafted latex (12 mg in 1 mL H_2O) with 1 mL of 0.7N NaOH until no change in the amount of polymer released was detected (2 weeks). The supernatant and washings were collected and analyzed by GPC for molecular weight determination.

4.5. Surface Plasmon Resonance (SPR) Analysis on Specific Interaction with Con A

SPR measurements were performed on a BIAcore 3000 (BIAcore, Uppsala, Sweden) operated using the BIAcore control software. The flow rate of analyte solution and PBS buffer (pH 4.8, containing 1 mM Ca^{2+}, 1 mM Mn^{2+}) through the flow cells was set as 30 μL/min. A series of 750 μL of Con A solutions was injected and flow through the channels. The concentration of each injection varied from 0.05 μM to 1 μM. There was no regeneration between consecutive injections. The galactose brush modified gold chip was set as the reference surface since there was no interaction between Con A and galactose brush. The response difference between mannose and galactose brushes modified surface was taken as the response due to the specific interaction between Con A and mannose brush.

4.6. Blood Collection

Blood from healthy consented donors was either collected into 3.8% sodium citrated tubes with a blood/anticoagulant ratio of 9:1 or sodium heparin (86 USP units) tubes at Centre for Blood Research, University of British Columbia. The protocol was approved by the University of British Columbia's clinical ethics board. Platelet rich plasma (PRP) was prepared by centrifuging citrated whole blood samples at 150 x g for 10 min in an Allegra X-22R Centrifuge (Beckman Coulter, Canada). Platelet-poor plasma (PPP) was prepared by centrifuging citrated whole blood samples at 1200 x g for 20 min.

4.7. Surface Plasmon Resonance (SPR) Analysis on Plasma Protein Adsorption

The flow rate of analyte solution and PBS buffer (pH 7.4) through the flow cells was set as 50 μL/min. Undiluted citrate anticoagulated or heparin anticoagulated human plasma (300 μL) was injected through the channels. PBS buffer was injected after 6 min to remove loosely adsorbed protein. The detector response was recorded.

4.8. Platelet Activation by Brush Grafted Surface

The platelet activation induced by the brush grafted surfaces was quantified by flow cytometric analysis. PS particles with and without grafted glycopolymer were used for the study. Citrate or heparin anticoagulated PRP (200 μL) was incubated at 37°C with 40 μL of polymer brush grafted PS particle suspension in HEPES buffer (final surface area ~ 100 cm^2) in a shaking platform (60 rpm). At different time intervals, aliquots of the incubation mixtures were removed for the assessment of platelet activation. Five microliters of post-incubation platelet/particle mixture was diluted in 45 μL of HEPES buffer, and was incubated for 20 min in the dark with 5 μL of monoclonal anti-CD62p-PE. After 20 min incubation, the reaction was stopped with the addition of 300 μL of PBS buffer (pH 7.4). The level of platelet activation was analyzed in a BD FACS Canto II flow cytometer (Becton Dickinson) by gating platelets specific events based on light scattering profile. Activation of platelets was expressed as the percentage of platelet activation marker CD62P-PE fluorescence detected in the 10,000 total events counted. Duplicate measurements were performed for each donor. For each sample PRP from 5 donors were used. Average values and standard deviations are reported. Platelets activated with 1 U/ml of bovine thrombin (Sigma-Aldrich, ON) was used as a positive control, and PE conjugated goat anti-mouse IgG polyclonal antibody was used as a non-specific binding control for the experiment.

4.9. Platelet Adhesion on Brush Grafted Surface

The level of platelet adhesion on glycopolymer brush grafted silicon wafer was quantified by SEM analysis. Glycopolymer brushes grafted (double sided) Si wafers (0.7 cm X 1cm) were incubated in PRP in an eppendroff tube placed in a shaking platform (60 rpm) at 37°C. After 3h, the substrates were taken out and carefully washed with PBS and fixed with 2.5% glycidaldehyde. After drying at ambient condition for overnight, the samples were sputter coated with a thin layer of Au and observed by scanning electron microscope. The SEM images were taken randomly at six different places on the substrate. The platelet adhesion was given as the average of the number of platelets adhered per unit area of the surface.

4.10. Blood Coagulation

Surface induced blood coagulation was measured using thromboelastography analysis. Freshly drawn whole blood in sodium citrate was mixed with brush grafted PS particles and the normal blood clotting cascade was then studied using Thromboelastograph Hemostasis System 5000 (TEG) from Haemoscope Corporation after recalcifying the suspension. Citrate anticoagulated blood samples (360 μL) were mixed with 40 μL of glycopolymer brushes grafted PS particle suspension in HEPES buffer (final surface area ~ 350 cm^2) and 340 μL of the suspension was transferred into the TEG cup. Blood coagulation was initiated by re-calcification with 20 μL of 0.2 M calcium chloride solution. HEPES buffer was used as the control. All TEG studies were performed at 37°C. Similar method was used for the analysis in PRP.

4.11. Characterization

NMR spectra were recorded on a Bruker Avance 300 MHz NMR spectrometer using deuterated solvents (Cambridge Isotope Laboratories, 99.8% D) with the solvent peak as a reference. Absolute molecular weights and polydispersities of glycopolymer samples were determined using gel permeation chromatography (GPC) on a Waters 2690 separation module fitted with a DAWN EOS multi-angle laser light scattering (MALLS) detector from Wyatt Technology Corp. with 18 detectors placed at different angles and a refractive index detector (Optilab DSP from Wyatt Technology Corp.). An ultrahydrogel linear column with bead size 6-13 μm (elution range 10^3 to 5×10^6 Da) and an ultrahydrogel 120 with bead size 6 μm (elution range 150 to 5×10^3 Da) from Waters were used. The dn/dc value of PAAEM in the mobile phase was determined at λ= 620 nm to be 0.154 mL/g and was used for determining molecular weight parameters. The *dn/dc* value is 0.158 for PAAEGal.

The variable-angle spectroscopic ellipsometry (VASE) spectra were collected on an M-2000V spectroscopic ellipsometer (J.A. Woollam Co. Inc., Lincoln, NE) at 70° at wavelengths from 480 to 700 nm with an M-2000 50W quartz tungsten halogen light source. The VASE spectra were then fitted with a multilayer model utilizing WVASE32 analysis software, based on the optical properties of a generalized Cauchy layer to obtain the “dry” thickness of the glycopolymer layers.

Acknowledgments

The authors acknowledge the funding provided by the Natural Sciences and Engineering Research Council (NSERC) of Canada and Canadian Institutes of Health Research (CIHR). The LMB Macromolecular and Biothermodynamics Hubs at the UBC were funded by Canada Foundation for Innovation and Michael Smith Foundation of Health Research (MSFHR). K.Y is a recipient of a CIHR/Canadian Blood Services (CBS) postdoctoral fellowship in Transfusion Science. J.N.K. is a recipient of a CIHR/CBS new investigator in Transfusion Science and MSFHR Career Investigator Award.

References

1. Sharon, N.; Lis, H. *Glycobiology* **2004**, *14*, 53R–62R.
2. Bertozzi, C. R.; Kiessling, L. L. *Science* **2001**, *291*, 2357–2364.
3. Dube, D. H.; Bertozzi, C. R. *Nat. Rev. Drug Discov.* **2005**, *4*, 477–488.
4. Foa, C.; Soler, M.; Benoliel, A. M.; Bongrand, P. *J. Mater. Sci.: Mater. Med.* **1996**, *7*, 141–148.
5. Dwek, R. A. *Chem. Rev.* **1996**, *96*, 683–720.
6. Alberts, B.; Bray, D.; Lewis, J.; Raff, M.; Roberts, K.; Watson, J. *Molecular Biology of the Cell*, 3rd ed.; Garland Science: New York, 1994; pp 477−506.
7. Sen, G. A.; Wang, S.; Link, E.; Anderson, E. H.; Hofmann, C.; Lewandowski, J.; Kottke-Marchant, K.; Marchant, R. E. *Biomaterials* **2006**, *27*, 3084–3095.
8. Weinbaum, S.; Tarbell, J. M.; Damiano, E. R. *Annu. Rev. Biomed. Eng.* **2007**, *9*, 121–167.
9. Holland, N. B.; Qiu, Y.; Ruegsegger, M.; Marchant, R. E. *Nature* **1998**, *392*, 799–801.
10. Sen Gupta, A.; Wang, S.; Link, E.; Anderson, E. H.; Hofmann, C.; Lewandowski, J.; Kottke-Marchant, K.; Marchant, R. E. *Biomaterials* **2006**, *27*, 3084–3095.
11. Zhu, J. M.; Marchant, R. E. *Biomacromolecules* **2006**, *7*, 1036–1041.
12. Smith, E. A.; Thomas, W. D.; Kiessling, L. L.; Corn, R. M. *J. Am. Chem. Soc.* **2003**, *125*, 6140–6148.
13. Hederos, M.; Konradsson, P.; Liedberg, B. *Langmuir* **2005**, *21*, 2971–2980.
14. Cao, X.; Pettit, M. E.; Conlan, S. L.; Wagner, W.; Ho, A. D.; Clare, A. S.; Callow, J. A.; Callow, M. E.; Grunze, M.; Rosenhahn, A. *Biomacromolecules* **2009**, *10*, 907–915.
15. Liang, P.-H.; Wang, S.-K.; Wong, C.-H. *J. Am. Chem. Soc.* **2007**, *129*, 11177–11184.
16. Huang, C. H.; Thayer, D. A.; Chang, A. Y.; Best, M. D.; Hoffmann, J.; Head, S.; Wong, C.-H. *Proc. Natl. Acad. Sci. U.S.A.* **2006**, *103*, 15–20.
17. Harris, L. G.; Schofield, W. C. E.; Doores, K. J.; Davis, B. G.; Badyal, J. P. S. *J. Am. Chem. Soc.* **2009**, *131*, 7755–7761.
18. Mandal, D. K.; Kishore, N.; Brewer, C. F. *Biochemistry* **1994**, *33*, 1149–1156.
19. Schwarz, F. P.; Puri, K. D.; Bhat, R. G.; Surolia, A. *J. Biol. Chem.* **1993**, *268*, 7668–7677.

20. Lundquist, J. J.; Toone, E. J. *Chem. Rev.* **2002**, *102*, 555–578.
21. Dam, T. K.; Brewer, C. F. *Biochemistry* **2008**, *47*, 8470–8476.
22. Mangold, S. L.; Cloninger, M. J. *Org. Biomol. Chem.* **2006**, *4*, 2458–2465.
23. Zhang, Y.; Luo, S. Z.; Tang, Y. J.; Yu, L.; Hou, K. Y.; Cheng, J. P.; Zeng, X. Q.; Wang, P. G. *Anal. Chem.* **2006**, *78*, 2001–2008.
24. Wang, D. N.; Liu, S. Y.; Trummer, B. J.; Deng, C.; Wang, A. L. *Nat. Biotechnol.* **2002**, *20*, 275–281.
25. Sun, X. L.; Faucher, K. M.; Houston, M.; Grande, D.; Chaikof, E. L. *J. Am. Chem. Soc.* **2002**, *124*, 7258–7259.
26. Gestwicki, J. E.; Cairo, C. W.; Mann, D. A.; Owen, R. M.; Kiessling, L. L. *Anal. Biochem.* **2002**, *305*, 149–155.
27. Liang, C. H.; Wang, S. K.; Lin, C. W.; Wang, C. C.; Wong, C. H.; Wu, C. Y. *Angew. Chem., Int. Ed.* **2011**, *50*, 1608–1612.
28. Gestwicki, J. E.; Cairo, C. W.; Strong, L. E.; Oetjen, K. A.; Kiessling, L. L. *J. Am. Chem. Soc.* **2002**, *124*, 14922–14933.
29. Varki, A. In *Essentials of Glycobiology*, 1st ed.; Varki, A., Cummings, R. D., Esko, J. D., Freeze, H. H., et al., Eds.; Cold Spring Harbor Laboratory Press; Plainview, NY, 1999; p 4.
30. Yang, Q.; Wu, J.; Li, J.-J.; Hu, M.-X.; Xu, Z.-K. *Macromol. Rapid Commun.* **2006**, *27*, 1942–1948.
31. Barbey, R.; Lavanant, L.; Paripovic, D.; Schuwer, N.; Sugnaux, C.; Tugulu, S.; Klok, H. A. *Chem. Rev.* **2009**, *109*, 5437–5527.
32. Zhao, B.; Brittain, W. J. *Prog. Polym. Sci.* **2000**, *25*, 677–710.
33. Zou, Y. Q.; Lai, B. F.; Kizhakkedathu, J. N.; Brooks, D. E. *Macromol. Biosci.* **2010**, *10*, 1432–1443.
34. Lai, B. F.; Creagh, A. L.; Janzen, J.; Haynes, C. A.; Brooks, D. E.; Kizhakkedathu, J. N. *Biomaterials* **2010**, *31*, 6710–6718.
35. Gao, G.; Lange, D.; Hilpert, K.; Kindrachuk, J.; Zou, Y.; Cheng, J. T.; Kazemzadeh-Narbat, M.; Yu, K.; Wang, R.; Straus, S. K.; Brooks, D. E.; Chew, B. H.; Hancock, R. E.; Kizhakkedathu, J. N. *Biomaterials* **2011**, *32*, 3899–3909.
36. Gao, G.; Yu, K.; Kindrachuk, J.; Brooks, D. E.; Hancock, R. E.; Kizhakkedathu, J. N. *Biomacromolecules* **2011**, *12*, 3715–3727.
37. Yu, K.; Lai, B. F.; Kizhakkedathu, J. N. *Adv. Healthcare Mater.* **2012**, *1*, 193–213.
38. Banerjee, I.; Pangule, R. C.; Kane, R. S. *Adv. Mater.* **2011**, *23*, 690–718.
39. Zhang, Z.; Zhang, M.; Chen, S. F.; Horbett, T. A.; Ratner, B. D.; Jiang, S. Y. *Biomaterials* **2008**, *29*, 4285–4291.
40. Ohno, K.; Tsujii, Y.; Fukuda, T. *J. Polym. Sci., Part A: Polym. Chem.* **1998**, *36*, 2473–2481.
41. Ejaz, M.; Ohno, K.; Tsujii, Y.; Fukuda, T. *Macromolecules* **2000**, *33*, 2870–2874.
42. Gao, C.; Muthukrishnan, S.; Li, W. W.; Yuan, J. Y.; Xu, Y. Y.; Müller, A. H. E. *Macromolecules* **2007**, *40*, 1803–1815.
43. Muthukrishnan, S.; Erhard, D. P.; Mori, H.; Müller, A. H. E. *Macromolecules* **2006**, *39*, 2743–2750.
44. Narain, R.; Armes, S. P. *Biomacromolecules* **2003**, *4*, 1746–1758.

45. Yang, Q.; Tian, J.; Hu, M. X.; Xu, Z. K. *Langmuir* **2007**, *23*, 6684–6690.
46. Yang, Q.; Xu, Z. K.; Dai, Z. W.; Wang, J. L.; Ulbricht, M. *Chem. Mater.* **2005**, *17*, 3050–3058.
47. Stenzel, M. H.; Zhang, L.; Huck, W. T. S. *Macromol. Rapid Commun.* **2006**, *27*, 1121–1126.
48. Yang, Q.; Kaul, C.; Ulbricht, M. *Langmuir* **2010**, *26*, 5746–5752.
49. Yu, K.; Kizhakkedathu, J. N. *Biomacromolecules* **2010**, *11*, 3073–3085.
50. Raynor, J. E.; Petrie, T. A.; Fears, K. P.; Latour, R. A.; García, A. J.; Collard, D. M. *Biomacromolecules* **2009**, *10*, 748–755.
51. Perrier, S.; Haddleton, D. M. *Macromol. Symp.* **2002**, *182*, 261–272.
52. Haddleton, D. M.; Perrier, S.; Bon, S. A. F. *Macromolecules* **2000**, *33*, 8246–8251.
53. Fan, X.; Lin, L.; Dalsin, J. L.; Messersmith, P. B. *J. Am. Chem. Soc.* **2005**, *127*, 15843–15847.
54. Kizhakkedathu, J. N.; Brooks, D. E. *Macromolecules* **2003**, *36*, 591–598.
55. Liang, P. H.; Wang, S. K.; Wong, C. H. *J. Am. Chem. Soc.* **2007**, *129*, 11177–11184.
56. Zhang, Y.; Luo, S. Z.; Tang, Y. J.; Yu, L.; Hou, K. Y.; Cheng, J. P.; Zeng, X. Q.; Wang, P. G. *Anal. Chem.* **2006**, *78*, 2001–2008.
57. Yonzon, C. R.; Jeoungf, E.; Zou, S. L.; Schatz, G. C.; Mrksich, M.; Van Duyne, R. P. *J. Am. Chem. Soc.* **2004**, *126*, 12669–12676.
58. Smith, E. A.; Thomas, W. D.; Kiessling, L. L.; Corn, R. M. *J. Am. Chem. Soc.* **2003**, *125*, 6140–6148.
59. Wang, X.; Ramstrom, O.; Yan, M. D. *Adv. Mater.* **2010**, *22*, 1946–1953.
60. Wang, X.; Ramstrom, O.; Yan, M. *Anal. Chem.* **2010**, *82*, 9082–9089.
61. Zhang, Y. L.; Li, Q. A.; Rodriguez, L. G.; Gildersleeve, J. C. *J. Am. Chem. Soc.* **2010**, *132*, 9653–9662.
62. Jones, D. M.; Brown, A. A.; Huck, W. T. S. *Langmuir* **2002**, *18*, 1265–1269.
63. Kizhakkedathu, J. N.; Janzen, J.; Le, Y.; Kainthan, R. K.; Brooks, D. E. *Langmuir* **2009**, *25*, 3794–3801.
64. Tang, Y. J.; Mernaugh, R.; Zeng, X. Q. *Anal. Chem.* **2006**, *78*, 1841–1848.
65. Schlick, K. H.; Cloninger, M. J. *Tetrahedron* **2010**, *66*, 5305–5310.
66. Kitano, H.; Takahashi, Y.; Mizukami, K.; Matsuura, K. *Colloids Surf., B* **2009**, *70*, 91–97.
67. Yu, L.; Huang, M.; Wang, P. G.; Zeng, X. *Anal. Chem.* **2007**, *79*, 8979–8986.
68. Zou, Y. Q.; Yeh, P. Y; Rossi, N. A. A.; Kizhakkedathu, J. N.; Brooks, D. E. *Biomacromolecules* **2010**, *11*, 284–293.
69. Herrwerth, S.; Eck, W.; Reinhardt, S.; Grunze, M. *J. Am. Chem. Soc.* **2003**, *125*, 9359–9366.
70. Schilp, S.; Rosenhahn, A.; Pettitt, M. E.; Bowen, J.; Callow, M. E.; Callow, J. A.; Grunze, M. *Langmuir* **2009**, *25*, 10077–10082.
71. Hucknall, A.; Rangarajan, S.; Chilkoti, A. *Adv. Mater.* **2009**, *21*, 2441–2446.
72. Senaratne, W.; Andruzzi, L.; Ober, C. K. *Biomacromolecules* **2005**, *6*, 2427–2448.
73. Singh, N.; Cui, X.; Boland, T.; Husson, S. M. *Biomaterials* **2007**, *28*, 763–771.
74. Feng, W.; Brash, J.; Zhu, S. *Biomaterials* **2006**, *27*, 847–855.

75. Luk, Y.-Y.; Kato, M.; Mrksich, M. *Langmuir* **2000**, *16*, 9604–9608.
76. Hower, J. C.; He, Y.; Bernards, M. T.; Jiang, S. *J. Chem. Phys.* **2006**, *125*, 214704.
77. Yamada, D.; Sekiya, F.; Morita, T. *J. Biol. Chem.* **1996**, *271*, 5200–5207.
78. Weis, W. I.; Drickamer, K.; Hendrickson, W. A. *Nature* **1992**, *360*, 127–134.
79. Brain, M.; Parkes, S.; Fowler, P.; Robertson, I.; Brown, A. *Crit. Care Resusc.* **2011**, *13*, 72–81.
80. Stenberg, E.; Persson, B. J.; Roos, H.; Urbaniczky, C. *J. Colloid Interface Sci.* **1991**, *143*, 513–526.
81. Gunkel, G.; Weinhart, M.; Becherer, T.; Haag, R.; Huck, W. T. S. *Biomacromolecules* **2011**, *12*, 4169–4172.
82. Lin, S. H.; Zhang, B.; Skoumal, M. J.; Ramunno, B.; Li, X. P.; Wesdemiotis, C.; Liu, L. Y.; Jia, L. *Biomacromolecules* **2011**, *12*, 2573–258.
83. Zhao, C.; Li, L.; Wang, Q.; Yu, Q.; Zheng, J. *Langmuir* **2011**, *27*, 4906–4913.
84. Bajgai, M.; Yu, K.; Kizhakkedathu, J. N. Submitted.
85. Yang, W.; Chen, S.; Cheng, G.; Vaisocherová, H.; Xue, H.; Li, W.; Zhang, J.; Jiang, S. *Langmuir* **2008**, *24*, 9211–9214.
86. Vaisocherová, H.; Yang, W.; Zhang, Z.; Cao, Z.; Cheng, G.; Piliarik, M.; Homola, J.; Jiang, S. *Anal. Chem.* **2008**, *80*, 7894–7901.
87. Cheng, G.; Li, G.; Xue, H.; Chen, S.; Bryers, J. D.; Jiang, S. *Biomaterials* **2009**, *30*, 5234–5240.
88. Koh, L. B.; Rodriguez, I.; Venkatraman, S. S. *Biomaterials* **2010**, *31*, 1533–1545.
89. Salooja, N.; Perry, D. J. *Blood Coagulation Fibrinolysis* **2001**, *12*, 327–337.

Chapter 27

Clarification of Protein Adsorption at Polymer Brush Surfaces Based on Water Structure Surrounding the Surface

Yuuki Inoue and Kazuhiko Ishihara*

**Department of Materials Engineering, School of Engineering,
The University of Tokyo, 7-3-1 Hongo, Bunkyo-ku, Tokyo 113-8656, Japan
*E-mail: ishihara@mpc.t.u-tokyo.ac.jp**

Protein adsorption behavior at the biocompatible polymer brush surfaces was quantitatively investigated based on the water structure surrounding the surface. The high repellency of protein adsorption at the polymer brush surface was analyzed using both quartz crystal microbalance with dissipation method and force-distance curve measurement in atomic force microscopy. The diffusion coefficients of water molecules among micro-silica beads with polymer brush layers were analyzed using nuclear magnetic resonance spectroscopy. These results clearly demonstrated that the dynamics of water molecules determine the protein adsorption behavior at the biocompatible polymer brush surfaces. Thus, polymer brush surface with water molecules with high diffusion coefficients, such as a zwitterionic group-bearing polymer brush surface, was effective in inhibiting protein adsorption.

Biological reactions, such as thrombus formation, immunoresponses, and inflammatory responses, are induced at a material surface when the surface comes into contact with blood or tissues. In many cases, these reactions are initiated by protein adsorption on the surface (*1*). Biomaterial surfaces therefore require quite strong inhibition of protein adsorption. Several concepts for fabricating biomaterial surfaces have been proposed in order to reduce protein adsorption, such as the introduction of higher polymer chain mobility by poly(ethylene

In Proteins at Interfaces III State of the Art 2012; Horbett, T., et al.;
ACS Symposium Series; American Chemical Society: Washington, DC, 2012.

oxide) (PEO) (*2–4*), the construction of artificial cell membrane structures by phospholipid polymers (*5–8*), and the fabrication of hydrophilic and highly dense polymer brush layers at the material surfaces (*9–17*). In particular, the hydrophilic polymer brush surfaces composed of zwitterionic monomer units have extremely higher resistance to protein adsorption than PEO-grafted surface. The underlying mechanism for the repellency of protein adsorption on the PEO-grafted surface has been theoretically and experimentally investigated (*18–22*). On the other hand, the comparable intermolecular interactions at the several kinds of hydrophilic polymer brush surfaces make it difficult to explain their high repellency of protein adsorption precisely. Water structure surrounding the hydrophilic polymer brush surfaces therefore should be considered in order to understand protein adsorption at a surface and obtain surfaces that do not adsorb proteins. Computer simulation (*23*, *24*) or a lot of experimental data (*6*, *25–28*) have indicated that protein adsorption would be strongly influenced by the hydration state around the surface. For example, Ishihara et al. clearly demonstrated that phospholipid polymer surfaces with a high fraction of free water reduced protein adsorption (*6*). Tanaka et al. reported that platelet adhesion was suppressed on the surface of poly(2-methoxyethyl acrylate) with bound freezing water, whose mobility is between that of nonfreezing water and that of free water (*27*). However, the role of water molecules at the protein–material interface is only assumed from information on static and bulk water molecules around the polymer chain. In addition, these studies involved the use of polymer-coated surfaces, which made it difficult to evaluate the water structure because of entanglement of the polymer chains or physical entrapment of water molecules in the polymer network. From these points of view, both surface-specific analysis of the water structure and a well-defined surface structure would be necessary to clarify the relationship between the protein adsorption behavior and water structure at the surface with extremely high biocompatibility.

The objective of this study is to quantitatively evaluate the relationship between protein adsorption behavior and water structure at biocompatible materials surfaces. Five kinds of polymer brush layers were prepared on several kinds of material surfaces using surface-initiated atom transfer radical polymerization (SI-ATRP). The surface structure and representative surface properties of the polymer brush layer were characterized well enough to regard the polymer brush structure as a model surface for polymeric biomaterials. The ultralow protein adsorption mass was analyzed using quartz crystal microbalance with dissipation (QCM-D) method to show the high protein adsorption repellency of the polymer brush surfaces. Furthermore, the interaction forces between proteins and polymer brush surfaces were quantitatively analyzed using force–distance curves obtained from atomic force microscopy (AFM) to more clarify the protein adsorption behavior at the polymer brush surfaces. The diffusion coefficients of water molecules among micro-silica beads with polymer brush layers were evaluated using proton nuclear magnetic resonance (^{1}H-NMR) measurements for the surface-specific analysis of the water structure (*29*, *30*). Our study indicated that a surface with water molecules of high mobility would reduce the direct interactions with proteins, leading to extremely high inhibition of protein adsorption.

Experiments

Materials

2-Methacryloyloxyethyl phosphorylcholine (MPC) was synthesized and purified using a previously reported method (*5*). [2-(Methacryloyloxy)ethyl]-dimethyl(3-sulfopropyl) ammonium hydroxide (SBMA) and 2-hydroxyethyl methacrylate (HEMA) were purchased from the Sigma-Aldrich Co. (St. Louis, MO, USA). *N*-Methacryloyloxyethyl-*N*,*N*-dimethylammonium α-*N*-methyl carboxylate (CBMA) was obtained from Osaka Organic Chemical Industry, Ltd. (Osaka, Japan). Trimethyl-2-methacroyloxyethylammonium chloride (TMAEMA) was purchased from the Tokyo Chemical Industry Co., Ltd. (Tokyo, Japan). Copper(I) bromide (CuBr), 2,2′-bipyridyl (bpy), and ethyl 2-bromoisobutyrate (EBIB) were purchased from the Sigma-Aldrich Co. and were used as received. Silicon wafers were purchased from the Furuuchi Chemical Co. (Tokyo, Japan). Gold sensor substrates for QCM-D measurement were purchased from Q-Sense (Gothenburg, Sweden). Micro-silica beads of diameter 10 μm were purchased from Fuji Silysia Chemicals, Ltd., Aichi, Japan.

Preparation of Initiator-Immobilized Substrates or Silica Beads

The SiO_2- and gold-attachable initiators for SI-ATRP, 11-(2-bromo-2-methylpropionyloxy)undecyltrichlorosilane (BrC10TCS) and 11-(2-bromo-2-methylpropionyloxy)undecylmercaptan (BUM), respectively, were synthesized using previously described methods (*31*, *32*). The initiators were immobilized at the surface in a 5.0 mmol/L solution of BrC10TCS in toluene in the case of the silicon wafers and silica beads, and in a 2.5 mmol/L solution of BUM in ethanol in the case of the gold sensor substrates, for 24 h (*15*). The initiator-immobilized substrates and silica beads were removed from the solution, rinsed with solvents, and dried in a dry box under reduced pressure.

Preparation of Polymer Brush Layers on Initiator-Immobilized Substrates or Silica Beads

MPC, SBMA, CBMA, HEMA, and TMAEMA were graft polymerized from the initiator-immobilized substrates or silica beads using SI-ATRP as follows (*15*). CuBr, bpy, and each monomer, in a specific molar ratio, were placed in a glass tube, and dehydrated and degassed solvents were added to the glass tube. Argon was bubbled into each monomer solution at room temperature for 10 min. The initiator-immobilized substrates or silica beads were then immersed in the solution, and EBIB was simultaneously added as the free-radical initiator at a [monomer]/[EBIB] ratio (which means the target polymerization degree (DP)) ranging from 10 to 200. After the glass tubes were sealed, polymerization was performed at 20 °C with stirring. After 24 h, the obtained substrates or silica beads were rinsed with solvents, and dried in a dry box under reduced pressure. The structure of the polymer brush surface is shown in Figure 1.

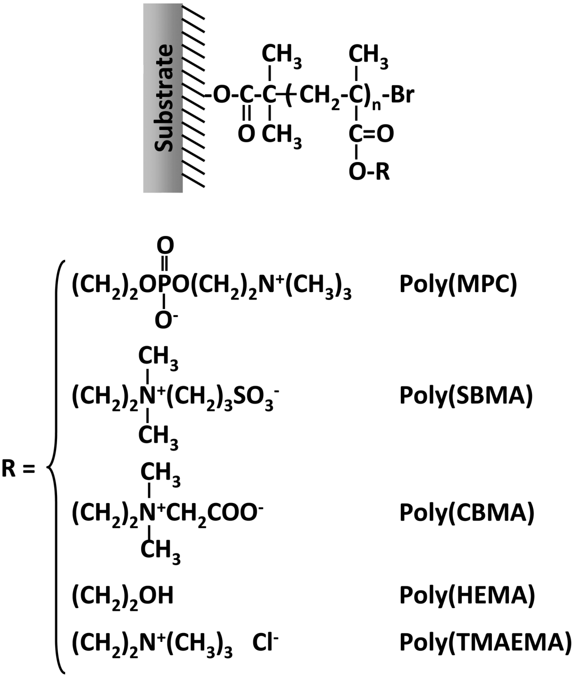

Figure 1. Chemical structures of the polymer brush surface fabricated in this study.

Physicochemical Surface Characterization

The elemental composition of the polymer brush surfaces was determined using X-ray photoelectron spectroscopy (XPS; AXIS-Hsi, Shimadzu/Kratos, Kyoto, Japan) with a magnesium anode nonmonochromatic source. The polymer brush layers were prepared on the BrC10TCS-immobilized silicon wafers. High-resolution scans for C_{1s}, N_{1s}, P_{2p}, S_{2p}, and Br_{3d} were acquired at a take-off angle of 90° for the photoelectrons. All the binding energies were referred to the C_{1s} peak at 285.0 eV.

The thickness of the grafted polymer layer under a dry condition was determined using a spectroscopic ellipsometer at an incident angle of 70° in the visible region (J. A. Woollam Co., Inc., Tokyo, Japan). The polymer brush layers were prepared on the BrC10TCS-immobilized silicon wafers. The thickness of the grafted polymer layer was estimated using the Cauchy layer model with an assumed refractive index of 1.49 at 632.8 nm. The graft density of the polymer chain in the polymer brush layer [σ (chains/nm^2)] was calculated from the equation $\sigma = h\rho N_A/M_n$. Here, h is the ellipsometric layer thickness (nm); ρ, the density of each dry polymer [1.30 g/cm^3 for poly(MPC) (*33*), poly(CBMA), and poly(SBMA); 1.15 g/cm^3 for poly(HEMA) (*9*) and poly(TMAEMA)]; N_A, Avogadro's number; and M_n, the absolute molecular weight of the polymer chains on the surface. It is reported that the molecular weight of the grafted polymer chains was equal to that of the polymer chains formed in each polymerization solution (*34*, *35*). In this study, the M_n was determined from the following equation, M_n = *"Target DP" × "Conversion (%) / 100" × "Molecular weight of each monomer"*, where, the conversion value was determined from ^{1}H-NMR of each polymerization solution. The surface coverage with each polymer chain was briefly estimated from the calculated graft density and cross-sectional area of each monomer unit. When we estimate the cross-sectional area, we consider a polymer chain as a cylinder and the contour length per monomer unit is set equal to the length of the C-C-C bond (0.25 nm) with the bulk density assumed to be unity (*36*).

The surface morphologies of the polymer brush surfaces were observed using AFM (Nanoscope IIIa, Bruker Japan Co., Ltd., Kanagawa, Japan) operated in the tapping mode. The polymer brush layers were prepared on the BrC10TCS-immobilized silicon wafers. The measurements were performed under a dry condition with a standard cantilever at a scan rate of 1.0 Hz. The root-mean-square (RMS) value of the surface roughness was calculated from the roughness profiles.

The Wilhelmy plate method was used to measure the dynamic contact angles in water for the polymer brush surfaces (DCA-100, Orientec Co., Ltd., Tokyo, Japan). Polymer brush layers at the approximate thickness of 5 nm were prepared on BrC10TCS-immobilized glass plates of dimensions 40 × 10 × 1.0 mm^3. A value of 72.8 dyn/cm was used as the surface tension of pure water and the moving rate of the crosshead was 3.0 mm/min. The measurement was repeated for 5 cycles for each sample.

The ζ-potential measurement was performed using an ELS-800 electrophoretic light-scattering spectrophotometer (Otsuka Electronics, Osaka, Japan) equipped with a plate sample cell to measure the surface potential in water containing 10 mmol/L sodium chloride. The polymer brush layers at the approximate thickness of 5 nm were prepared on the BrC10TCS-immobilized silicon wafer. The ζ-potential measurement for the polymer brush surfaces was performed at room temperature. The measurement was repeated at least three times.

Analysis of Water Structure Around Polymer Brush Surfaces

Silica beads with polymer brush layers at the approximate thickness of 5 nm (500 mg) were packed into NMR tubing (ϕ = 10 mm, JEOL, Tokyo, Japan), and distilled water (500 µL) was added. The interspaces among the silica beads are extremely small, therefore we could investigate the water structure in the vicinity of the polymer brush surface (Figure 2) (*29*, *30*). The diffusion coefficients of water molecules around the polymer brush layers were measured at 37 °C by ^{1}H-NMR spectroscopy (MU-25, JEOL, Tokyo, Japan) using the pulsed-field gradient method. The diffusion coefficient is assumed to be an indication of the mobility of the water molecules.

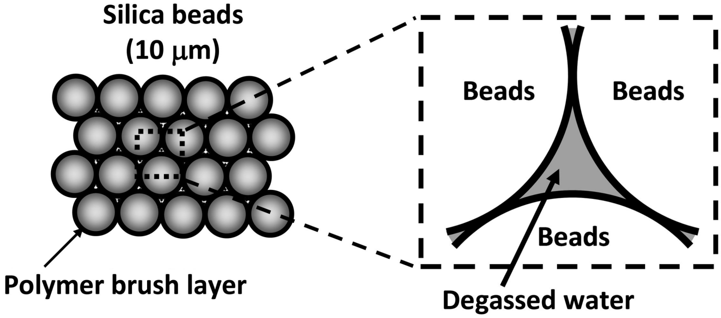

Figure 2. Schematic representation of water among the silica beads with polymer brush layers for the analysis of the water structure using ^{1}H-NMR.

Biological Analysis on Polymer Brush Surfaces

The adsorbed amounts of proteins from 100% fetal bovine serum (FBS) on the polymer brush surfaces were quantified using QCM-D (*15*, *37*). We prepared polymer brush layers on BUM-immobilized QCM gold sensors. The prepared QCM gold sensor was first exposed to phosphate-buffered saline (PBS, pH 7.4) at 37 °C until a stable baseline was established. Thereafter, the QCM sensors were exposed to FBS for 30 min, followed by PBS for an additional 10 min to replace FBS and to wash off the weakly adsorbed FBS from the surface. The change in the oscillator frequency was used to estimate the amount of adsorbed protein, using Sauerbrey's equation, as follows (*38*): Amount of adsorbed protein (ng/cm^2) = 17.7 × Frequency change at the seventh overtone (Hz).

The adsorption force of bovine serum albumin (BSA, Sigma-Aldrich) on the polymer brush layers was estimated using force–distance (*f–d*) curve measurements in an AFM apparatus. The polymer brush layers at the approximate thickness of 5 nm were prepared on BrC10TCS-immobilized silicon wafers. BSA was covalently immobilized on the cantilever (OTR8 with a spring constant of 0.15 N/m, Bruker Japan Co., Ltd.) through the condensation reaction between the amino groups in the protein and the carboxyl groups on gold-evaporated cantilever (*39*). The immobilization of BSA on the carboxyl group-terminated self-assembled monolayer on the gold-evaporated surface was confirmed from QCM-D and XPS measurements. The adsorption force of BSA on the polymer brush was evaluated in PBS at room temperature by the deflection shift value from the baseline at the retract trace of the *f–d* curve. At each measurement, more than 100 approaching/retracting *f–d* curves were collected, and the average value of the measured forces was defined as the adsorption force of BSA on the surfaces.

All measurements were repeated at least three times.

Results and Discussion

Physicochemical Surface Properties

In this study, five kinds of polymer brush layers, poly(MPC), poly(SBMA), poly(CBMA), poly(HEMA), and poly(TMAEMA), were prepared on several kinds of materials, such as silicon wafers, glass substrates, gold substrates, and micro-silica beads, using SI-ATRP with a free-radical initiator. The surface elements of the polymer brush surfaces were analyzed using XPS spectra. Specific peaks in the carbon (C_{1s}), nitrogen (N_{1s}), phosphorus (P_{2p}), and sulfur (S_{2p}) atom regions were detected at each polymer brush surface. Thus, XPS analysis confirmed the identities of each polymer chain at all the polymer brush surfaces.

The ellipsometric layer thickness obtained for the grafted polymer layers under a dry condition were plotted against the absolute molecular weights of the polymer chains (Figure 3). The thickness of the grafted polymer layer could be linearly controlled in the range 1–20 nm by the molecular weight of the grafted polymer chains. We calculated the graft density of each polymer chain in the polymer brush layers using the slope of the line shown in Figure 3 and the equation described in the Experiments section. The graft densities of the polymer chains in the poly(MPC), poly(SBMA), poly(CBMA), poly(HEMA), and poly(TMAEMA) layers were 0.26, 0.48, 0.67, 0.79, and 0.31 chains/nm^2, respectively. The well-defined structure of the polymer brush surface makes it possible to estimate the surface coverage with the grafted polymer chain at the surface using the method mentioned in the Experiments section. The calculated coverage with the grafted poly(MPC), poly(SBMA), poly(CBMA), poly(HEMA), and poly(TMAEMA) chains were 43%, 76%, 82%, 66%, and 37%, respectively. The graft density and coverage with the grafted polymer chains for all the polymer chains were greater than 0.1 chains/nm^2 and 30%, respectively, which indicated that highly dense polymer brush surfaces were formed using the SI-ATRP method (*40*).

The surface topology of the polymer brush surface and the RMS value as an indicator of the surface roughness were examined using AFM in a dry condition (*12*, *15*, *39*). Each polymer brush surface exhibited a slightly irregular structure, however the RMS value for the polymer brush surface was at most 1.0 nm. This RMS values were consistent with those reported in previous studies (*12*), indicating that the grafted polymer layers prepared by the SI-ATRP method would be considerably homogeneous. In particular, there was little difference among the RMS values of polymer brush surfaces with nearly equivalent thickness. This result indicated that the differences in surface properties among the polymer brush layers would mainly depend on the characteristics of the grafted polymer chains, not on the surface topology.

The wettability of the polymer brush surface were evaluated using dynamic contact angle measurement. The receding contact angle would be more important than the advancing contact angle since biological reactions occur under aqueous conditions. The advancing and receding contact angles for zwitterionic polymer brush surfaces were around and below 20°, respectively, which indicated a high wettability of these surfaces in dry and aqueous conditions (*41*). The cationic poly(TMAEMA) brush surface also had a high wettability in an aqueous condition (the receding contact angle was also below 20°), but the advancing contact angle for the surface was more than 60°. In contrast, the receding contact angle for the nonionic poly(HEMA) brush surface was more than 20°, which indicated that the poly(HEMA) brush surface had slightly low wettability in an aqueous condition. The hydrophilic hydroxyl group is smaller than the other hydrophilic functional groups and the poly(HEMA) synthesized in the polymerization solution was difficult to dissolve in water. This result suggested that the poly(HEMA) brush layer would contain very few water molecules. As a result, the wettability of the poly(HEMA) brush surface would be slightly lower than those of the other polymer brush surfaces in an aqueous condition.

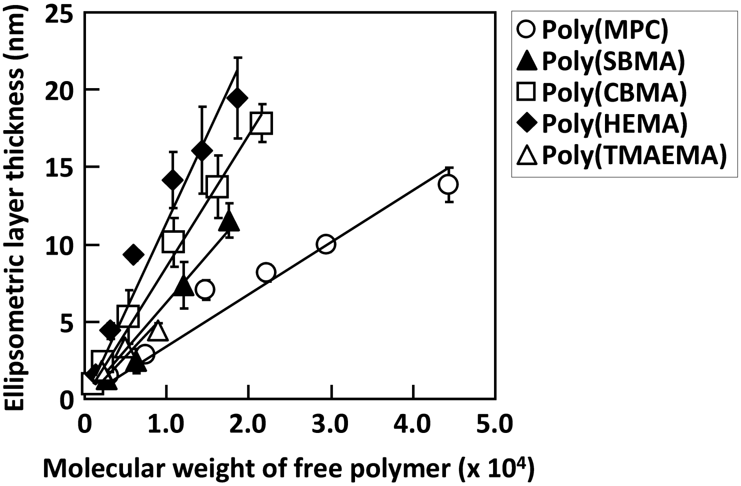

Figure 3. Relationship between the ellipsometric layer thickness at polymer brush surface and molecular weight of free polymer. Open circles; poly(MPC), filled triangles; poly(SBMA), open squares; poly(CBMA), filled diamonds; poly(HEMA), and open triangles; poly(TMAEMA) (Average ± standard error of the mean (SEM), n = 5).

The surface potential of the polymer brush surfaces was evaluated using the ζ-potential measurement in water containing 10 mmol/L sodium chloride at room temperature. The ζ-potentials of zwitterionic and nonionic polymer brush surfaces were slightly negative from -1.8 mV (poly(CBMA) brush surface) to -7.8 mV (poly(SBMA) brush surface). On the other hand, the ζ-potentials of cationic poly(TMAEMA) brush surfaces was 45.0 mV. The surface potentials of the polymer brush surfaces corresponded to the charge property of each grafted polymer chain and there was little difference among the zwitterionic or nonionic polymer brush surfaces.

Protein Adsorption Behavior on Polymer Brush Surfaces

The amounts of proteins adsorbed on the polymer brush surfaces from 100% FBS were quantified using QCM-D. It is known that the amount of adsorbed proteins on the polymer brush surface would decrease with the increasing layer thickness and graft density of polymer brush layer. That is, in the case that the polymer brush surface would have sufficient layer thickness and graft density, protein adsorption would be determined by the properties of grafted polymer chains, such as the charge condition or polymer chain-water interaction in a buffer solution. In this study, while five kinds of polymer brush surfaces have different graft densities according to the molecular size of each monomer unit, all the coverage with the grafted polymer chain was more than 40%. Therefore, it is considered that the there would be little influence of the different graft densities among the polymer brush surfaces on the protein adsorption behavior.

The relationship between the amount of adsorbed proteins and the ellipsometric layer thickness is shown in Figure 4. There were large differences in this relationship, depending on the chemical structure of the grafted polymer chain. The amounts of adsorbed proteins on the zwitterionic polymer brush surfaces drastically decreased at thicknesses up to 5 nm, and those on the surfaces with an approximate layer thickness of 10 nm were 17 ng/cm^2 for the poly(MPC) brush layer, 31 ng/cm^2 for the poly(SBMA) brush layer, and 79 ng/cm^2 for the poly(CBMA) brush layer. These results showed that the zwitterionic polymer brush surfaces would have excellent repellency of protein adsorption. In contrast, the amount of adsorbed proteins on the poly(HEMA) brush surface gradually decreased with increasing ellipsometric layer thickness, and that on the surface with an approximate layer thickness of 15 nm was 180 ng/cm^2. The amount of adsorbed proteins on the cationic poly(TMAEMA) brush surface increased with increasing ellipsometric layer thickness. These results demonstrated that protein adsorption would depend not only on the layer thickness, but also on the characteristics of the grafted polymer chains. It is considered that the main driving force for protein adsorption on the cationic poly(TMAEMA) brush surface would be the electrostatic interaction between the poly(TMAEMA) brush surface and negatively-charged proteins at a physiological condition existing in FBS. And the density of positive charge at the poly(TMAEMA) brush surface would increase with the increasing ellipsometric layer thickness. Therefore, more proteins adsorbed on the thicker poly(TMAEMA) brush surface.

To evaluate the direct interaction between negatively-charged proteins and polymer brush surfaces with different characteristics, the adsorption force of BSA was measured on the polymer brush layers with approximate thickness of 5 nm (Figure 5). The polymer brush layers with approximate thickness of 5 nm have the similar surface properties and the different amounts of adsorbed proteins, therefore, a clear relationship between the protein adsorption behaviors and water structure around the surfaces is expected. The maximum adsorption force of BSA was detected on the cationic poly(TMAEMA) brush surface, which means the adsorbed proteins via the strong electrostatic interaction hardly detach from the surface. This result also suggested that some negatively-charged proteins existing in FBS would be denatured at the cationic poly(TMAEMA) brush surface. Additionally, the adsorption force of BSA on the poly(TMAEMA) brush surface was not so large compared to the amount of adsorbed proteins, that is, more proteins adsorbed on the poly(TMAEMA) brush surface than that expected from the adsorption force. On the other hand, the order of the adsorption forces on the other polymer brush surfaces was similar to the adsorbed amount of proteins from 100% FBS. The amounts of proteins adsorbed on the surfaces (poly(TMAEMA): > 1000 ng/cm^2, other polymers: < 200 ng/cm^2, shown in Figure 4) indicated that multilayer adsorption would occur at the cationic poly(TMAEMA) brush surface, whereas the proteins adsorbed on the other polymer brush surfaces would be below monolayer adsorption (*42*). This result indicated that there would be a positive relationship between the amount and force of protein adsorption at the surface where proteins adsorb below a monolayer. In particular, this result also indicated that the high repellency of protein adsorption on the zwitterionic polymer brush layers would arise from the extremely low interaction of the surfaces with proteins.

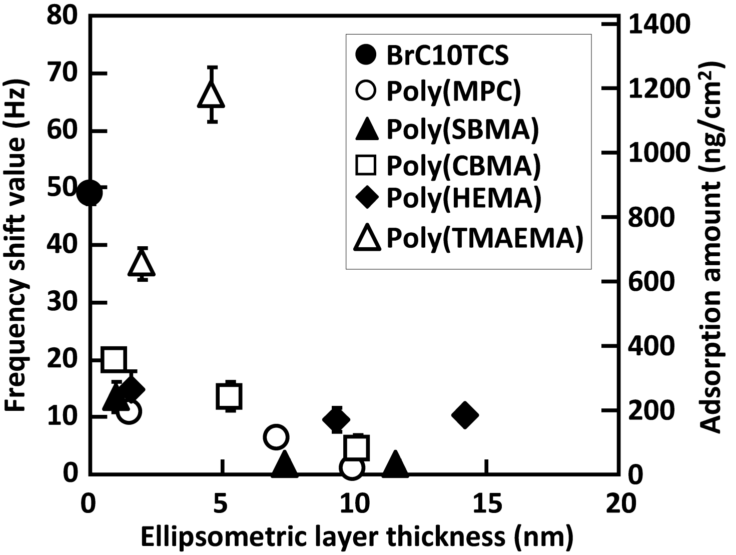

Figure 4. Relationship between frequency shift value (adsorbed amount of proteins) and the ellipsometric layer thickness at the different polymer brush surfaces. Filled circles; initiator-immobilized substrate, open circles; poly(MPC), filled triangles; poly(SBMA), open squares; poly(CBMA), filled diamonds; poly(HEMA), and open triangles; poly(TMAEMA). (Average ± SEM, n = 3).

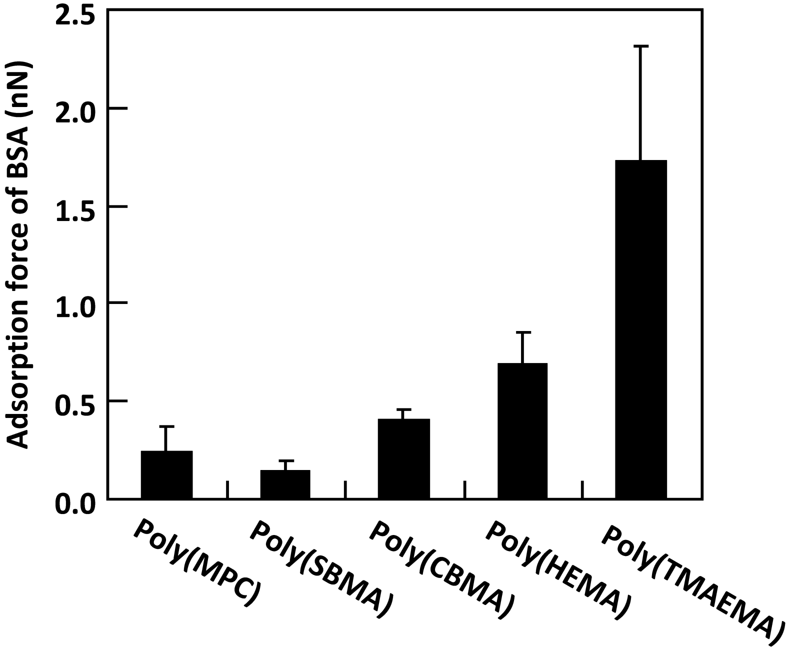

Figure 5. Adsorption force of bovine serum albumin (BSA) against the different polymer brush surfaces with 5-nm-thick (Average ± SEM, n = 3).

Water Structure Around the Polymer Brush Surface

Figure 6 shows the diffusion coefficients of water molecules among micro-silica beads with various polymer brush layers. The diffusion coefficient of pure water is known to be 3.0×10^{-5} cm^2/sec at 37 °C. On the other hand, the diffusion coefficient of water molecules among the bare micro-silica beads was measured to be 7.5×10^{-5} cm^2/sec. We could not apparently explain the reason why the diffusion coefficient of water molecules among bare or polymer brush layer-modified micro-silica beads increased compared to that of pure water, it might be related that water molecules in extremely small space have different characteristics from those in bulk state, such as a higher viscosity and a lower dielectric constant (*43*). Here, we discuss the diffusion coefficients separately, according to the solubility of the polymer chain in water, because the water structure around the polymer brush layer would differ depending on the polymer chain solubility. Among the polymer brush surfaces with water-soluble polymer chains, the water molecules at zwitterionic polymer brush surfaces had higher diffusion coefficients than those at the cationic polymer brush surface. The water molecules at the poly(MPC) brush surface had a particularly large diffusion coefficient. This result indicated that water molecules near the poly(MPC) brush surface would have high mobility. In contrast, the mobility of water molecules near the cationic poly(TMAEMA) brush surface was restrained. Recently, Takahara et al. reported the solubilizing states and dimensions of polymer chains in several polymer brush layers in aqueous media. In this report, the poly(MPC) chains expanded well in the aqueous media and the dimensions of the poly(MPC) chains were not changed by the high ionic strength of the aqueous medium (*44*). The relatively high diffusion coefficients of the water molecules and well-expanded structure of the poly(MPC) chains in ionic media indicated that water molecules may be bound quite weakly to the poly(MPC) chains. The water molecules at the poly(HEMA) brush surface, which had water-insoluble polymer chains and a relatively low wettability under aqueous conditions, showed higher diffusion coefficients than those at the other polymer brush layers. It is suggested that there would be a few water molecules having small diffusion coefficients as a result of interacting directly with the polymer chains. It was considered that the diffusion coefficients of the water molecules around the poly(HEMA) brush layer would mostly be high.

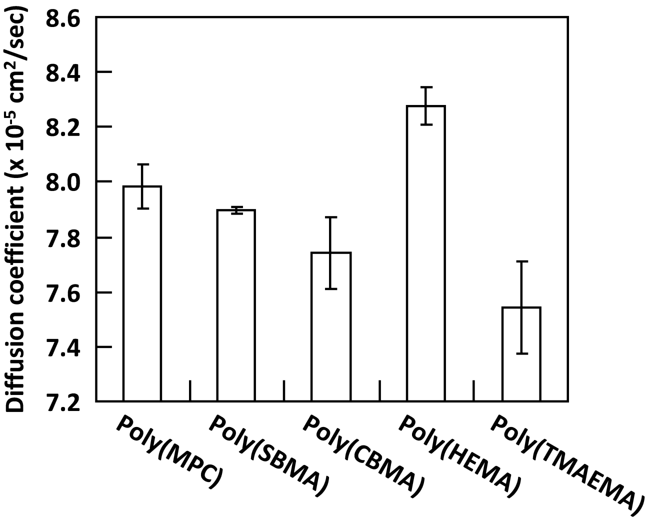

Figure 6. Diffusion coefficient of water molecules around the different polymer brush surfaces with 5-nm-thick (Average ± SEM, n = 3).

To quantitatively analyze the relationship between the protein adsorption behavior and water structure at the polymer brush surface, the adsorbed amounts of proteins and adsorption force of BSA were plotted as a function of the diffusion coefficients of the water molecules, as shown in Figure 7. The adsorption force of BSA (Figure 7b) gradually decreased with increasing diffusion coefficient of the water molecules around the polymer brush surfaces with water-soluble polymer chains, in contrast to the rapid decrease shown in the adsorbed amount of proteins (Figure 7a). Two kinds of molecular interactions, the electrostatic interaction and water structure, would influence on the large adsorption force of BSA at the poly(TMAEMA) brush surface. On the other hand, this result clearly indicated that the high mobility of water molecules around the zwitterionic polymer brush surfaces would result in small interaction with proteins. Proteins are surrounded by hydrating water molecules, and the conformations and activities of the proteins are maintained by molecular interactions through these hydrating water molecules. If the network structure of hydrating water molecules around the protein changes, the protein conformation is destroyed. In this regard, a surface with high-mobility water molecules would prevent proteins from detaching from the hydrating water molecules and changing the higher-order structure. As is also seen in Figure 7, a small difference in the diffusion coefficient resulted in a large difference in the protein adsorption mass. We hypothesize that this phenomenon is related to the diffusion range of the hydrating layer at the polymer brush surface, and studies of this are now progressing. The poly(HEMA) brush surface, which would have a different hydration state from that of the other polymer brush surfaces as mentioned above, was not in line with the other results. In the present study, we could not estimate the diffusion coefficient of the water molecules around the poly(HEMA) brush surface accurately. In addition, we could not explain the protein adsorption behavior at three kinds of zwitterionic polymer brush surfaces from the water structure surrounding the surfaces. Further analysis of the water structure around the polymer brush surface is needed to clarify the relationship between protein adsorption behavior and the water structure around the surface.

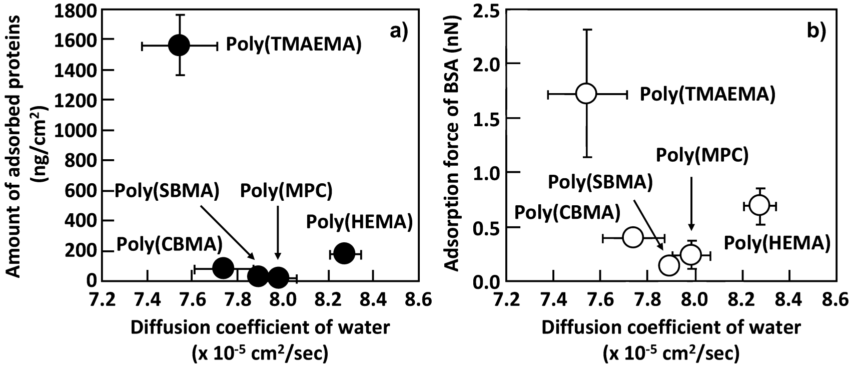

Figure 7. Relationship between (a) amount of adsorbed proteins and (b) adsorption force of bovine serum albumin (BSA) and diffusion coefficient of water at the different polymer brush surfaces (Average ± SEM, n = 3).

Conclusions

We intensively researched protein adsorption behavior, based on the water structures at well-defined and biocompatible polymer brush surfaces. First, we successfully fabricated polymer brush layers with varying chemical structures on several kinds of material surfaces. The well-characterized structures and properties of the polymer brush surfaces enabled us to regard them as model surfaces. The interactions between proteins and polymer brush surfaces were quantitatively analyzed using AFM; the amounts of proteins adsorbed on the surfaces were also determined. The surface-specific water structures were evaluated using the diffusion coefficients of water molecules enclosed among micro-silica beads with polymer brush layers. It was clarified that zwitterionic polymer brush surfaces, especially the polymer brush surface with phosphorylcholine groups, had little interaction with proteins, and the water molecules around these surfaces had higher mobility than those at the other water-soluble polymer brush surfaces. These results indicated that the active exchange of water molecules around the surface would reduce direct interactions with proteins, leading to extremely high repellence of protein adsorption. The control of surface polymer brush layers, focusing on the dynamics of water molecules, will lead to zero-protein-adsorption surfaces.

Acknowledgments

This study was partially supported by a Core Research for Evolutional Science and Technology (CREST) grant from the Science and Technology Agency, Japan.

References

1. Chen, H.; Yuan, L.; Song, W.; Wu, Z.; Li, D. *Prog. Polym. Sci.* **2008**, *33*, 1059–1087.
2. Ostuni, E.; Chapman, R. G.; Holmlin, R. E.; Takayama, S.; Whitesides, G. M. *Langmuir* **2001**, *17*, 5605–5620.
3. Norde, W.; Gage, D. *Langmuir* **2004**, *20*, 4162–4167.
4. Kenausis, G. L.; Voros, J.; Elbert, D. L.; Huang, N.; Hofer, R.; Ruiz-Taylor, L.; Textor, M.; Hubbell, J. A.; Spencer, N. D. *J. Phys. Chem. B* **2000**, *104*, 3298–3309.
5. Ishihara, K.; Ueda, T.; Nakabayashi, N. *Polym. J.* **1990**, *22*, 355–360.
6. Ishihara, K.; Nomura, H.; Mihara, T.; Kurita, K.; Iwasaki, Y.; Nakabayashi, N. *J. Biomed. Mater. Res.* **1998**, *39*, 323–330.
7. Inoue, Y.; Watanabe, J.; Ishihara, K. *J. Colloid Interface Sci.* **2004**, *274*, 465–471.
8. Goto, Y.; Matsuno, R.; Konno, T.; Takai, M.; Ishihara, K. *Biomacromolecules* **2008**, *9*, 828–833.
9. Yoshikawa, C.; Goto, A.; Tsujii, Y.; Fukuda, T.; Kimura, T.; Yamamoto, K.; Kishida, A. *Macromolecules* **2006**, *39*, 2284–2290.
10. Feng, W.; Brash, J.; Zhu, S. *J. Polym. Sci. A: Polym. Chem.* **2004**, *42*, 2931–2942.
11. Feng, W.; Zhu, S.; Ishihara, K.; Brash, J. L. *Langmuir* **2005**, *21*, 5980–5987.
12. Feng, W.; Brash, J. L.; Zhu, S. *Biomaterials* **2006**, *27*, 847–855.
13. Feng, W.; Zhu, S.; Ishihara, K.; Brash, J. L. *Biointerphases* **2006**, *1*, 50–60.
14. Feng, W.; Gao, X.; McClung, G.; Zhu, S.; Ishihara, K.; Brash, J. L. *Acta Biomater.* **2011**, *7*, 3692–3699.
15. Inoue, Y.; Ishihara, K. *Colloids Surf., B* **2004**, *274*, 465–471.
16. Yang, W.; Chen, S.; Cheng, G.; Vaisocherová, H.; Xue, H.; Li, W.; Zhang, J.; Jiang, S. *Langmuir* **2008**, *24*, 9211–9214.
17. Yang, W.; Xue, H.; Li, W.; Zhang, J.; Jiang, S. *Langmuir* **2009**, *25*, 11911–11916.

18. Jeon, S. I.; Lee, J. H.; Andrade, J. D.; De Gennes, P. G. *J. Colloid Interface Sci.* **1991**, *142*, 149–158.
19. McPherson, T.; Kidane, A.; Szleifer, I.; Park, K. *Langmuir* **1998**, *14*, 176–186.
20. Halperin, A. *Langmuir* **1999**, *15*, 2525–2533.
21. Efremova, N. V.; Sheth, S. R.; Leckband, D. E. *Langmuir* **2001**, *17*, 7628–7636.
22. Kane, R. S.; Deschatelets, P.; Whitesides, G. M. *Langmuir* **2003**, *19*, 2388–2391.
23. Lu, D. R.; Lee, S. J.; Park, K. *J. Biomater. Sci., Polym. Ed.* **1991**, *3*, 127–147.
24. He, Y.; Hower, J.; Chen, S.; Bernards, M. T.; Chang, Y.; Jiang, S. *Langmuir* **2008**, *24*, 10358–10364.
25. Kitano, H.; Imai, M.; Mori, T.; Gemmei-Ide, M.; Yokoyama, Y.; Ishihara, K. *Langmuir* **2003**, *19*, 10260–10266.
26. Kitano, H.; Tada, S.; Mori, T.; Takaha, K.; Gemmei-Ide, M.; Tanaka, M.; Fukuda, M.; Yokoyama, Y. *Langmuir* **2005**, *21*, 11932–11940.
27. Tanaka, M.; Mochizuki, A. *J. Biomed. Mater. Res. A* **2004**, *68*, 684–695.
28. Tanaka, M.; Mochizuki, A. *J. Biomater. Sci., Polym. Ed.* **2010**, *21*, 1849–1863.
29. Tsukahara, T.; Misutani, W.; Mawatari, K.; Kitamori, T. *J. Phys. Chem. B* **2009**, *113*, 10808–10816.
30. Tsukahara, T.; Hibara, A.; Ikeda, Y.; Kitamori, T. *Angew. Chem.* **2007**, *46*, 1180–1183.
31. Matyjaszewski, K.; Miller, P. J.; Shukla, N.; Immaraporn, B.; Gelman, A.; Luokala, B. B.; Siclovan, T. M.; Kickelbick, G.; Vallant, T.; Hoffmann, H.; Pakula, T. *Macromolecules* **1999**, *32*, 8716–8724.
32. Jones, D. M.; Brown, A. A.; Huck, W. T. S. *Langmuir* **2002**, *18*, 1265–1269.
33. Iwata, R.; Suk-In, P.; Hoven, V. P.; Takahara, A.; Akiyoshi, K.; Iwasaki, Y. *Biomacromolecules* **2004**, *5*, 2308–2314.
34. Husseman, M.; Malmstrom, E. E.; McNamara, M.; Mate, M.; Mecerreyes, D.; Benoit, D. G.; Hedrick, J. L.; Mansky, P.; Huang, E.; Russell, T. P.; Hawker, C. J. *Macromolecules* **1999**, *32*, 1424–1431.
35. Yamamoto, K.; Miwa, Y.; Tanaka, H.; Sakaguchi, M.; Shimada, S. *J. Polym. Sci. A: Polym. Chem.* **2002**, *40*, 3350–3359.
36. Ejaz, M.; Ohno, K.; Tsujii, Y.; Fukuda, T. *Macromolecules* **2000**, *33*, 2870–2874.
37. Dolatshahi-Pirouz, A.; Rechendorff, K.; Hovgaard, M. B.; Foss, M.; Chevallier, J.; Besenbacher, F. *Colloids Surf., B* **2008**, *66*, 53–59.
38. Sauerbrey, G. *Z. Phys.* **1964**, *155*, 206–222.
39. Inoue, Y.; Nakanishi, T.; Ishihara, K. *React. Funct. Polym.* **2011**, *71*, 350–355.
40. Tsujii, Y.; Ohno, K.; Yamamoto, S.; Goto, A.; Fukuda, T. *Adv. Polym. Sci.* **2006**, *197*, 1–45.
41. Kobayashi, M.; Terayama, Y; Yamaguchi, H.; Terada, M.; Murakami, D.; Ishihara, K.; Takahara, A. *Langmuir* **2012**, *28*, 7212–7222.
42. Baskin, A.; Lyman, D. J. *J. Biomed. Mater. Res.* **1980**, *14*, 393–403.

43. Hibara, A.; Saito, T.; Kim, H. B.; Tokeshi, M.; Ooi, T.; Nakao, M.; Kitamori, T. *Anal. Chem.* **2002**, *74*, 6170–6176.
44. Kikuchi, M.; Terayama, Y.; Ishikawa, T.; Hoshino, T.; Kobayashi, M.; Ogawa, H.; Masunaga, H.; Koike, J.-I.; Horigome, M.; Ishihara, K.; Takahara, A. *Polym. J.* **2012**, *44*, 121–130.

Chapter 28

Poly(ethylene glycol) and Poly(carboxy betaine) Based Nonfouling Architectures: Review and Current Efforts

Mojtaba Binazadeh,[1,#] Maryam Kabiri,[1,#] and Larry D. Unsworth[*,1,2]

[1]Department of Chemical and Materials Engineering, University of Alberta, Edmonton, Alberta, T6G 2V4, Canada
[2]National Institute for Nanotechnology, National Research Council (Canada), Edmonton, Alberta, T6G 2M9, Canada
[#]These authors have contributed equally to this work.
[*]E-mail: larry.unsworth@ualberta.ca

Non-specific adsorption of proteins at the tissue-material interface occurs shortly after implantation and is thought to initiate several host responses (thrombosis, inflammation, wound healing) as well as modify critical therapeutic properties like the drug release profile. Furthermore, it has been shown that substrate surface properties can dramatically affect the adsorbed amount of proteins, as well as their final adsorbed conformation. To further understand how surface properties can affect protein adsorption, two drastically different types of polymers that represent characteristics crucial for the inhibition of non-specific protein adsorption are of interest, viz., the 'gold-standard' poly(ethylene glycol) (PEG) and the zwitterionic polybetaines. Unlike PEG whose hydration is due to hydrogen bonding between water molecules and polar ether bonds of the polymer backbone, zwitterionic polybetaines are distinguished by forming a very stable hydration shell as a result of a positive and a negative charge on the same monomer segment within the polymer chain. Current proposed mechanisms of non-specific adsorption and antifouling behaviour of polymeric surfaces are largely lacking a detailed understanding of the interactions at the molecular level. Therefore, work is continuing to utilize these two polymer systems for understanding protein adsorption

In Proteins at Interfaces III State of the Art 2012; Horbett, T., et al.;
ACS Symposium Series; American Chemical Society: Washington, DC, 2012.

in differing ways. Through controlling secondary structures of peptides, it may be possible to systematically discuss how this affects adsorption to PEG modified surfaces, as well as the physicochemical properties. Moreover, through the use of poly (carboxybetaine methacrylamide) (PCBMA), it has been shown to be possible to control the hydration of the film, allowing for a systematic evaluation of the effect of hydration upon protein adsorption. It is thought that a clear study of molecular level events involved in the adsorption of proteins ultimately enables us to understand fundamental properties of proteins essential for further engineering of clinically relevant surfaces.

Non-specific adsorption of proteins at the tissue-material interface is known to influence a multiplicity of events related directly to the *in vivo* therapeutic efficacy of the tissue contacting biomaterial. Numerous studies have investigated the mechanisms of protein adsorption to surfaces in contact with physiological fluids, where the impetus for protein adsorption is thought to be a variety of forces present between surfaces and macromolecules within aqueous environments. Functional aspects of the therapeutic biomaterial reported to be influenced by non-specific protein adsorption, include the initiation of several host responses (thrombosis, inflammation, wound healing), the drug release profile, the biomaterial degradation, etc (*1*). It is well known that shortly after implantation, a layer of plasma proteins will cover the tissue contacting surface (*2–6*). Moreover, upon adsorption at the tissue-material interface these proteins may undergo a surface-induced conformational rearrangement. In addition to facilitating an increase in the protein-surface interaction, conformational changes in adsorbed proteins may lead to the exposure of occult domains that initiate adverse reactions such as the accumulation of inflammatory cells, foreign body response, and coagulation (*7–11*). It has been shown, for instance, that exposed protein domains may provide ligands that facilitate cell responses directly; for example, conformational changes in fibrinogen have been shown to expose several occult epitopes that interact with immune cells directly (*12–14*). Thus, significant effort has been expended in developing surfaces that either inhibit non-specific protein adsorption or minimize the conformational changes proteins undergo upon adsorption.

Surface engineering for the express purpose of inhibiting non-specific protein adsorption, or subsequent protein denaturing, has shown that substrate surface properties can dramatically affect the adsorbed amount of proteins, as well as their final adsorbed conformation (*15*). That said, issues surrounding protein adsorption to surfaces have not been resolved and require further attention for the express purpose of developing cost effective, convenient, and versatile strategies for rendering surfaces resistant to non-specific protein adsorption (*16*). In order to investigate protein adsorption mechanisms different researchers have conducted experiments with a single- or multi-component protein solution, on a vast variety of surface architectures (*17*, *18*). In fact too many surface architectures exist to be covered herein. Suffice it to say that despite these efforts, controlling protein adsorption has met with limited success. It is thought that there are two main reasons this has been the case: i. the inherent amphiphilic properties of proteins provide multiple pathways by which proteins may interact with surfaces (*19*); and ii. it is not just the presence of the protein that can initiate a bioresponse, but also its conformation. Thus, designing surfaces for the express purpose of inhibiting or controlling non-specific adsorption events has been the focus of decades of research, and continues to be both an industrially relevant and a scientifically interesting area of activity. As a means of further understanding how surface properties can affect protein adsorption, two drastically different types of polymers are of interest, *viz*., the ‘gold-standard’ poly(ethylene glycol) (PEG) and the zwitterionic polybetaines. Through the discussion of these different polymers, coupled with designed experiments using controlled protein and surface properties, it is thought that a better understanding of molecular events crucial to dictating protein adsorption events may be gained.

Fundamental Forces Leading to Nonspecific Protein Adsorption

There is a relatively low energy barrier between conformational states of various protein domains, which results in an overall native conformation that may be highly susceptible to structural changes induced by environmental disturbances: such as the introduction of a surface (e.g., air or bioimplant surface) (*20*). The interaction between a protein and a surface is thought to be the result of a balance between van der Waals, electrostatic, hydrophobic, and hydration forces (*21*). In aqueous solutions, London-van der Waals (dispersion) forces, which arise due to the interaction of two instantaneously induced dipoles, may constitute ~95% of all van der Waals types of interactions that exist between a protein and a surface found in aqueous media (*22*). Dispersion forces are considered long range and effective within distances <100 Å, decaying with the seventh power of distance (*23*). Introduction of a surface in an ion containing aqueous solution results in the disruption of the ion distribution throughout the aqueous media. To preserve charge neutrality, counter-ions from solution accumulate at the surface, resulting in the formation of the electrical double layer. The structure of this double layer is an area of active research, but a common representation is the Gouy-Chapman-Stern model. Wherein, the region closer to the surface, the Stern layer, is comprised of fixed counter-ions that interact with localized surface charges. The layer closer to bulk, the Gouy-Chapman layer, is characterized as having counter-ions (with respect to surface) which can exchange with those in the bulk fluid. This layer extends to the point where homogeneous distribution of ions in the bulk solution exists. The thickness of the double layer is a function of bulk ion concentration, ion valence, temperature, and medium permittivity. At a lower ionic strength, double layer thickness increases and is characterized as a more diffuse ion concentration (*22*). It is known that electrostatic forces influence the interaction of surface in contact with an electrolyte solution containing charged biomolecules, but may be either repulsive or attractive.

Caused mainly by hydrogen bonding, hydrophobic interactions (attractive) and hydration pressure (repulsive) represent energies that may be a hundred times greater than that of both electrostatic and dispersion forces (*22*). The release of highly ordered water molecules from the hydration shell imposed upon two hydrophobic domains is thought to be the driving force for the hydrophobic effect that leads to the spontaneous interaction of these moieties. Whereas, hydration pressure (hydrophilic repulsion) has been described as a result of resistance to the breakdown of the associated water molecules (due to hydrogen bonds) in the hydrated shell around hydrophilic entities (*22*). Characteristic decay lengths for hydrophobic interactions and hydration pressures have been reported to be ~13 and ~1 nm, respectively; the repulsive hydration pressure being a short range force compared to attractive hydrophobic interactions. The strength and range of the above-mentioned interactions depends on the protein (conformation, and isoelectric point), solution (pH, and ionic strength) and surface (roughness, and chemical) properties. Ultimately, the adsorption of proteins to surfaces is the result of a combination of these fundamental forces that may affect proteins up to 10 nm away from the surface in question (*24*).

Poly(ethylene glycol)

Obviously the literature surrounding protein adsorption to PEG modified surfaces is too vast to summarize within this chapter, especially given that one of the first references to the use of polyoxyethylene for blood contacting materials occurs as early as 1974 (*25*). Therefore attention is paid to the properties of PEG that may lend itself to providing a low biofouling platform, and important papers that have revealed these properties. In general, PEG is a linear polymer with the $–CH_2–CH_2–O–$ monomer that presents an uncharged but polar hydrogen bond accepting group (*20*). PEG has both hydrophilic segments (oxygen atoms) and hydrophobic segments (carbon atoms), which makes it soluble in both aqueous and organic solvents. In line with PEG properties, characteristics such as net neutral charge, hydrophilic nature, presence of hydrogen bond acceptors and no hydrogen bond donors are thought to be crucial for the inhibition of non-specific protein adsorption to PEGylated surfaces (*26*). In crystalline PEG, the chain adopts a helical structure with 3.5 monomer units per turn (*27*) and in water it forms a loose coil structure (*28*). In aqueous solutions, the ethylene glycol monomer can form up to two hydrogen bonds with water molecules. Finally, hydrogen bonds between PEG and water (*29*) gradually break upon increasing PEG concentration, solution temperature and/or solution salt concentration, which in turn results in the reduction of PEG solubility in water; resulting in the presence of the ‘cloud-point’ condition for PEG.

Although it is known that surface modification with PEG results in lower protein adsorption (*26*), the mechanisms responsible for such behaviour are not fully understood. In an aqueous solution, flexible ether bonds in a long chain of PEG confer rotational and conformational mobility to the polymer chain (*30*).

This molecular mobility is thought to persist even upon chemical tethering of one end to a surface (grafting), which yields a large volume in which a protein is thought to be hindered from entering (excluded volume). In fact, steric stabilization effects does not allow the approaching protein to permanently stay in the excluded volume (*31*) and reach the surface. In combination with this it has been shown that for shorter grafted PEG chains strongly associated water molecules (due to hydrogen bonds) in the hydrated shell around the PEG chain (*22*), may create a repulsive hydration force which repels proteins (*32*). Among the interesting studies of PEG properties is the surface force study by Claesson (*33*) where repulsive hydration forces between grafted PEG layers were measured directly. It was further confirmed by van Oss (*34*), *via* measurement of the free energy of repulsion, that soluble PEG molecules in aqueous solution repel each other. These findings are in line with the above mentioned dominant non-fouling mechanism observed for grafted shorter PEG chains (*32*) where hydration shell around a PEG chain exerts a repulsive force on the adsorbing protein. In addition to these attributes, the presence of a PEG layer either grafted or randomly immobilized chains on a surface forms a pseudo interface that may attenuate underlying hydrophobic and or electrostatic effects present on the unmodified surface (*35*).

Some papers of interest have been highlighted (Table 1) that have outlined some of the work discussed above. However, an important discussion for poly(ethylene glycols) involves the effect of chain density on how chemically grafting PEG *via* one end to the surface, inhibits protein-surface interactions. Prior to the work of Kingshott, et al. (2002), the discussion of protein adsorption to surfaces modified with grafted PEG revolved around understanding the effect of molecular weight, with numerous contradictory results being reported for very similar systems. Kingshott's work was influential in outlining the effect of 'pinning density', and was a work that inspired further study by Unsworth, et al. (2005, 2008). The primary contribution of which was showing that regardless of the grafted PEG molecular weight, when examined as a function of chain density, vastly different molecular weights yielded similar adsorbed amounts of protein from solution. Suggesting that an optimal chain density exists that modulates properties such as hydration and conformational freedom, which directly influences the ability of proteins to interact with the surface (*36*, *37*). Increasing chain density above this critical value may lead to a decrease in the number of water molecules associated with a grafted PEG chain (*38*), which may play a role in suppressing any associated hydration pressure as the hydration shell around the chain is disturbed and reduced in size. Increased chain density may also lead to a loss of grafted PEG conformational freedom, which may suppress any steric repulsion effects. In addition to this, it has been shown that protein adsorption becomes increasingly affected by distal chemistry effects as the grafted PEG chain density increases (*38*). In both cases, with hydroxyl end-group chemistries as well as optimal chain densities, it may be that the hydration state within the layer may play a dominant role in directing the interaction between proteins and surfaces (*38*). This was further confirmed by Chang et al. that higher hydration capacity of the polymer film provides a lower protein adsorption (*39*); furthermore, it was shown that the bounded water molecules, which form the

In Proteins at Interfaces III State of the Art 2012; Horbett, T., et al.;
ACS Symposium Series; American Chemical Society: Washington, DC, 2012.

hydration shell around a grafted PEG chain, contribute more in protein repellency of a PEG modified surface as compared to trapped water molecules which are confined in a network-like PEG layer (*40*).

Table 1. Important papers for PEG antifouling properties and their contribution (*41*)

Author, year	***Major contribution***
Gombotz et al., 1991 (*42*)	Grafted PEG antifouling mechanism 1: Excluded volume
van Oss, 1994 (*22*)	PEG antifouling mechanism 2: Repulsive hydration pressure from water shell around PEG chains in solution
Archambault et al., 1998 (*43*)	Effectiveness of grafted PEG coating on reducing plasma protein adsorption
McPherson et al., 1998 (*44*)	Identification of influential grafted PEG-surface parameters: Importance of chain density and weak effect of chain length
Sofia et al., 1998 (*45*)	Higher efficiency of grafted linear PEG compared to star form PEG
Kingshott et al., 2002 (*46*)	Effect of cloud point grafting on chain density
Unsworth et al., 2005 (*18*)	Grafting at critical chain density (~0.5 chain/nm^2): Maximum suppression of protein adsorption
Unsworth et al., 2008 (*38*)	Distal chemistry effect at grafted chain densities greater than critical value

Poly(carboxy betaine)

Although widely studied, the use of PEG as a non-fouling coating has some major disadvantages, namely, loss of function due to oxidation *in vivo* (*47*, *48*) and possible toxicity of its degradation by-products (*49*). It has also been shown that the anti-fouling properties of PEG is reduced upon exposure to complex media (blood serum or plasma) as compared to model media (single protein) (*50*). Recently, surfaces grafted with zwitterionic polymers have been shown to be a very promising alternative non-fouling architecture that exhibits a higher *in vivo* stability than PEG (*51*). A sub-category of these materials include polybetaines, which are distinguished by carrying a positive and a negative charge on the same monomer segment of the polymer chain. The family of polybetaines includes phosphobetaines (PB), sulfobetaines (SB), and carboxybetaines (CB) (*52*). There have been a number of studies examining how the physicochemical properties of polybetaines affect their non-fouling characteristics (Table 2). In general, it has been seen that grafting density was one of the most widely discussed factors, where increasing the grafting density of zwitterionic polymer was shown to increase the hydrophilicity of the surface as well as its resistance to protein adsorption (*53–55*). Conversely, increasing the thickness of the polymer film on the surface did not follow the same trend as grafting density (*56*). In fact, studies have shown that there is an optimum thickness for the grafted film (measured by either ellipsometry or atomic force microscopy), at which the protein adsorption onto surfaces grafted with polybetaines was undetectable using surface plasmon resonance techniques (*56–59*). It should be noted that for most of these works, no report of chain density had occurred (unless noted otherwise).

It is thought that optimal architectures for inhibiting protein adsorption should meet the following criteria: i) hydrophilicity, ii) surface charge neutrality, and iii) being an H-bond acceptor (not a donor) (*69*). Surface hydration has a long history for being considered as a major factor in dictating the non-fouling behaviour of materials (*70*, *71*). Along with this, it was proposed that the superior anti-fouling properties of polybetaines may be due to a very stable hydration shell created by strong electrostatic interactions with water (*72*). This is opposed to neutral and hydrohphilic PEG where the hydration layer formed on its surface occurs through hydrogen bonding, which is much weaker than the electrostatic interaction behind the zwitterion interaction with water molecules (*57*, *63*, *67*). Attesting to the differences in strength of interaction of water is the free energy changes for hydration of grafted zwitterionic polymer chains (-404 kJ/mol and -519 kJ/mol for carboxybetaine and sulfobetaine, respectively) that are significantly lower than that for grafted oligo(ethylene glycol) (-182 kJ/mol) (*73*). Although the total surface energies of different polybetaines was shown to be in the same range (~ 66 mJ/m^2) (*74*), considering the Hofmeister series for different salts (*75*) it can be concluded that the interaction of all different types of polybetaines (bearing phosphonate, sulfonate, or carboxylate moieties) with water would not necessarily be the same. Simulation studies performed on carboxybetaine and sulfobetaine proved that the positively charged group on the zwitterionic segment (i.e. quaternary amine group present on both of these polymers) is more hydrated than their negatively charged group (*73*). On the other hand, comparison between the negatively charged groups of these polymers led to the conclusion that a larger number of water molecules with higher mobility were bound to the chaotropic sulfonate moiety rather than kosmotropic carboxylate moiety. It was speculated that this is the main reason for lower friction on the surface of sulfobetaine compared to carboxybetaine (*76*, *77*). These are important indications which might be helpful in designing novel zwitterionic molecules in future.

Table 2. Important papers on polybetaines and studies published on the role of physicochemical properties in their antifouling behaviour

Author, year	*System*	*Major Conclusion*
Kadoma et.al., 1978 (*60*)	PB	First report on synthesis and blood compatibility
Lowe et.al. 2000 (*61*)	SB	First report on anti-fouling behaviour
West et.al., 2004 (*62*)	SB and PB	Superior anti-fouling properties of PB compared to SB, the major drawback of PB: very complex synthetic methods
Chen et.al., 2005 (*63*)	PB	Two important factors for anti-fouling properties: Charge balance and minimized dipole
Zhang et.al., 2006 (*64*)	CB	First report on synthesis, grafting and super-low fouling behaviour
Zhang et.al., 2006 (*65*)	SB	Optimum film thickness (5-12 nm): highly resistant to fibrinogen adsorption
Zhang et.al., 2008 (*66*)	CB	Longer spacer groups: more protein adsorption onto surface
Yang et.al., 2009 (*56*)	CB	Optimum film thickness (21 nm): ultra low protein adsorption (i.e. <5 ng/cm^2)
Shih et.al., 2010 (*67*)	SB	Optimum M_w for ultra low fouling properties: 135 kDa at physiologic temperature
Chang et.al., 2011 (*68*)	SB	Plasma treatment time of 90 seconds: the surface with highly balanced charge and lowest protein adsorption
Chang et.al., 2012 (*54*)	SB	Higher grafting density: lower protein adsorption and better capacity in stem cell preservation
Brault et.al., 2012 (*53*)	CB	Minimum of ~1.5 for refractive index: ultra low protein adsorption

Although different in structure, ion pairing between the protein and the surface (instead of surface hydration) was introduced as an influential factor that may also govern the non-fouling properties of these materials. More specifically, Estephan *et.al.* (*78*) attributed the anti-fouling behaviour of PEG and zwitterionic materials to a large extent to the neutrality of their surface charge, which results in lack of counter-ion release from the surface of these materials upon exposure to protein solutions. However, current proposed mechanisms are largely lacking a detailed understanding of the interactions at the molecular level. Therefore, work is continuing to utilize these two polymer systems for understanding protein adsorption in various ways; as discussed in the following current focus section.

Current Focus

Given these aspects of protein adsorption to surfaces modified with polymers, the current focus of work being conducted is twofold. Through utilizing well studied grafted PEG, it may be possible to further understand the effect that protein structure has upon adsorption and subsequent film properties. Herein the major question being asked is, how does protein secondary structure affect not only adsorption to PEG modified surfaces, but also the subsequent physicochemical properties of the formed film. The ubiquitous nature of both the components of proteins (ie. 22 natural amino acids) and the relatively limited types of secondary structures available, it may be possible to generate a better understanding regarding the role protein conformation has on adsorption and the adsorbed film properties. Moreover, through the use of poly (carboxybetaine methacrylamide) (PCBMA), it may be possible to control the hydration of the films formed primarily by holding chain density constant and merely altering the spacer groups within the zwitterion. Thus, providing an experimental platform that would allow for a better discussion of how hydration of the films affects protein-surface interactions.

Effect Protein of Structure on Adsorption and Adsorbed Film Properties

Protein folding occurs primarily due to the balance between the hydrophobic effect and hydrophilic domains (*79*). Depending on the internal coherency state (i.e. softness or hardness) that a protein acquire upon folding its adsorption trend might be influenced: soft proteins may even adsorb to hydrophilic electrostatically repelling surfaces since their structure gets rearranged upon coming in contact with the surface; in contrast, hard proteins with a strong internal coherence do not experience a structural rearrangement contribution to their adsorption (*80*). Although each protein has an unique structure that is overall determined by its amino acid sequence; several structural features are common. Proteins have a compact three dimensional structure with little internal space. Moreover, there are only a limited number of secondary structures that occurs throughout, where ~50% of the protein structure has a defined secondary structure (as opposed to a random coil) (*81*). While formation of secondary structure is a result of interactions such as hydrogen bonding between neighbouring amino acids in the protein's sequence. Secondary structure of a protein determines its physicochemical properties such as shape, size, hydrophobicity, and function in a physiological solution. However, near a surface the interactions between surface and protein might alter the balance of non-covalent interactions (hydrogen bonds, hydrophobic interactions, electrostatic interactions, and van der Waals) and consequently, lead to non-specific protein adsorption and denaturing.

Although the effect of many protein attributes (pI (*82*, *83*), size (*84*), and hydrophobicity (*85*)) on non-specific protein adsorption have been studied, there is a dearth in the literature surrounding the effect of secondary structure (*86*). Moreover, it is unknown how secondary structures will interact with the surface in general, important features include surface induced melting of the secondary structure and the resultant change in activity and functionality. Poly-L-Lysine

(PLL) was chosen as an appropriate model peptide for investigating the influence of secondary structure on both protein adsorption as well as the properties of the adsorbed film. The rationale behind this choice was that using the same molecule (ie. PLL) it is possible to adopt both α-helix and β-sheet structures depending on solution environmental conditions (*87*). In order to characterize both the protein adsorption, as well as the formed film properties, quartz crystal microbalance with dissipation and circular dichroism (CD) spectroscopy was used.

Preliminary Results: Circular Dichroism (CD)

Circular dichroism (CD) is an optical property of asymmetric molecules which can be used to rapidly determine folding properties and secondary structure of a protein. It occurs when a molecule absorbs left- and right-handed circularly polarized light in different extends (*88*). The difference between absorption of left- and right-handed circularly polarized light at different wavelengths can reveal secondary structure of protein. It has been shown that PLL maintains a random coil structure in solution at neutral pH, where other secondary structures can be induced through the manipulation of solution pH and temperature (*89*). Specifically, PLL α-helix conformations were induced by increasing the buffer pH from ~7 to 10.6 (37°C); the result of which has been shown to almost complete transformation of random coiled PLL to α-helices (*90*). This solution was then heated to 70°C for 50 min so as to transform α-helix PLL into β-sheet conformations. PLL secondary structures being confirmed using CD (Figure 1), where: α-helices have a maximum peak at ~190 nm and minimum peaks at ~205 and 222 nm; and β-sheets have a respective maximum and minimum peak at ~195 and ~215 nm (*91*, *92*). It has been found that α-helix and β-sheet secondary structures were stable in solution for up to 8 hrs (*93*), which is longer than the required time elapsed during QCM-D experiments.

PLL adsorption to Au coated quartz slides and 750 MW grafted PEG chemisorbed on Au surface were conducted so as to determine if the adsorption event ultimately influenced the secondary structure of these peptides (Figure 1). Given the minor differences in peak positions between the bulk and adsorbed PLL it is probable that no determinable denaturation of these peptides occurred upon adsorption and that any of these peak position differences could be attributed to slight differences in cuvette path-length and/or optical properties of the different cuvettes used in these studies. Especially as it has been previously reported that a 3 nm shift in CD peak position does not imply an overall difference in secondary structure (*88*, *91*). Moreover, the intensity of these peaks is proportional to relative concentration of these secondary structures within the electromagnetic (EM) beam path.That said, there is evidence that significantly higher peak intensities were obtained for PLL secondary structures upon adsorption to bare Au surfaces as compared to solution. These data might be due to using the bulk PLL concentration (0.1 mg/mL) for the molar ellipticity calculation, thus assuming that the bulk concentration was similar to that found in the adsorbed layer. It is well known that the surface concentration of adsorbed material can be much greater than the bulk concentration (i.e. surface excess). Consequently, it is probable that the concentration of PLL within the CD‘s electromagnetic beam may be much greater for the adsorbed layer than the bulk solution. The same argument is valid for PEG coated surfaces, where PLL secondary structure persists upon adsorption to 750 MW PEG modified gold surfaces and higher peak intensities were obtained for PLL adsorbed to PEG as compared to bulk solution. The apparent lack of secondary structure changes upon adsorption to PEG may not be unexpected as PEG has been shown to stabilize protein structures near a surface (*94*) and may be used as spacer to prevent surface induced denaturation (*95*).

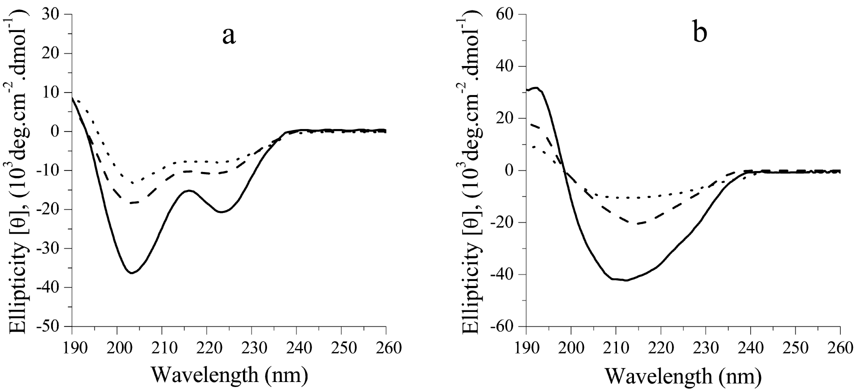

Figure 1. CD spectra of PLL in α-helix (a) and β-sheet conformation (b) in solution (........), adsorbed to Au coated quartz slides (________), adsorbed to 750 MW PEG layer chemisorbed on Au (— — — —) from 10 mM potassium phosphate buffer with 5 mM Na_2SO_4 at pH 10.6, T 37°C. Upon adsorption secondary structures seemed to be retained. Data represent the average of n=3 measurements, (41).

Quartz Crystal Microbalance with Dissipation Monitoring (QCM-D)

Another technique that has gained attention for monitoring protein adsorption to surfaces is QCM-D. QCM-D can be used to track formation and growth of a protein layer on the surface of quartz crystal as a function of time by monitoring changes in the frequency of the quartz oscillation (Δf) and dissipation (ΔD) (Figure 2) where dissipation factor ‘D’ is defined as (*96*):

$$D = \frac{E_{dissipated}}{2\pi E_{stored}} \qquad \text{eq (1)}$$

where '$E_{dissipated}$' and 'E_{stored}' are dissipated and stored energy during oscillation. Adsorption of mass to a quartz crystal will result in a shift in the oscillation frequency of the quartz crystal toward lower values (negative Δf). Moreover, if a rigid body adsorbs to the surface no change in the dissipation factor will be observed (ie. $\Delta D=0$), however, if the adsorbed layer has some viscoelastic properties then the dissipation factor will increase ($\Delta D>0$) due to energy loss caused by its oscillating. This technique, coupled with physical models, can be used to understand the kinetic physical properties of the adsorbed protein film including thickness or mass and shear viscosity (*97*).

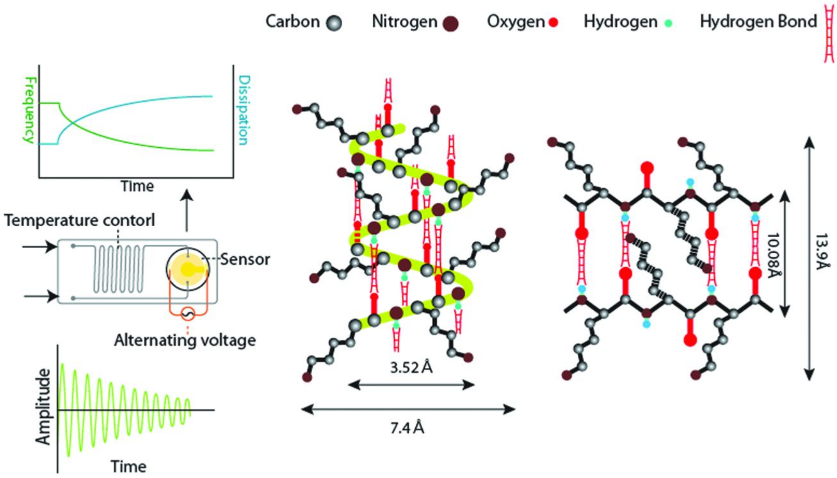

Figure 2. Schematic drawing of QCM-D and PLL in α-helix and β-sheet conformation (93).

By use of the Sauerbrey equation, adsorbed mass can be calculated as a linear function of frequency change. When dissipation changes observed during the adsorption process is greater than zero (non-rigid adsorbed layer) the Sauerbrey equation underestimates adsorbed mass (*98*). Thus, large changes in dissipation are often the case for viscoelastic adsorbed layers and a model that considers the viscoelastic properties of the adsorbed layer is needed. The Voight model is the simplest representation of a viscoelastic solid typically used. The model consists of a viscous dashpot and an elastic spring connected in parallel, which can represent the behaviour of a viscoelastic layer (*99*). For the viscoelastic layer (index "1") on quartz slide (index "0") immersed in a bulk Newtoniam fluid (index "2") the following equations hold (*99*):

$$\Delta f \approx \frac{1}{2\pi\rho_0 h_0}\left\{\frac{\eta_2}{\delta_2}+\left[h_1\rho_1\omega-2h_1\left(\frac{\eta_2}{\delta_2}\right)^2\frac{\eta_1\omega^2}{\mu_1^2+\omega^2\eta_1^2}\right]\right\} \qquad \text{eq (2)}$$

$$\Delta D \approx \frac{1}{2\pi f \rho_0 h_0}\left\{\frac{\eta_2}{\delta_2}+\left[2h_1\left(\frac{\eta_2}{\delta_2}\right)^2 \frac{\eta_1\omega^2}{\mu_1^2+\omega^2\eta_1^2}\right]\right\} \qquad \text{eq (3)}$$

$$\delta_2 = \sqrt{\frac{2\eta_2}{\rho_2\omega}} \qquad \text{eq (4)}$$

where ‘f’ stands for oscillation frequency, ‘D’ dissipation, ‘ρ’ density, ‘h’ thickness, ‘η’ viscosity, and ‘μ’ shear modulus. ‘ω’ is the ratio of the imaginary part of the Voight element complex shear modulus by its viscosity obtained from equation of the shear waves propagating in Voight element (*100*). For modeling purposes, as demanded by Voight viscoelastic model, flowing solution over the sensor has to be considered viscous and Newtonian. Uniform density and thickness for the adsorbed layer are assumed and the adsorbed hydrated layer was considered a viscoelastic solid element and quartz crystal was assumed purely elastic. It is also assumed that there is no slip between the adsorbed molecules and the Au coated crystal during the experiment. It is reported that the value of the layer density has only a minor influence on the modeling results (*101*). In fact, layer thickness and density are paired and changes in layer density result in a change of layer thickness. As a result, the adsorbed mass is relatively insensitive to minor differences in the assumed layer density (results not shown).

The fact that QCM-D can provide highly sensitive real time *in-situ* information about layers adsorbed on a surface makes it a powerful technique for probing protein adsorption on polymeric biomaterial surfaces. The advantage that tracking surface modification using QCM-D has is accurate determination of adsorbed mass. Dissipation factor monitoring also offers unique information about the viscoelastic properties of the surface including layer viscosity. QCM-D study by Weber et al. (*102*) showed that addition of up to 15% PEG segment to poly(DTE carbonate) decreased human fibrinogen adsorption. Their results suggest that the conformation of surface adsorbed fibrinogen is a function of PEG surface concentration. Yoshikawa et al. (*103*) also used QCM-D to measure protein adsorption on polymeric surfaces. Their results show that at high grafting density (0.7 chain/nm^2) poly (2-hydroxyethyl methacrylate), PHEMA, brushes shows the highest resistance to nonspecific adsorption of proteins with different sizes.

Preliminary Results: QCM-D

Solution conditions discussed previously (CD section) were used to alter the secondary structure of the PLL between α-helix and β-sheets for subsequent adsorption experiments. Preliminary results of PLL adsorption from 10 mM potassium phosphate buffer with 5mM sodium sulphate on bare Au measured using QCM-D (Figure 3) shows that the overall change in Δf was significantly larger for β-sheet adsorption compared to α-helix (-54.4 Hz frequency drop for β-sheet PLL as opposed to -10.1 Hz frequency drop for α-helix PLL). Moreover, the interaction of α-helix PLL with the Au sensor was initially faster than β-sheet PLL (ie. -52.8 Hz/min frequency drop for α-helix PLL as opposed to -6.4 Hz/min frequency drop for β-sheet PLL, respectively). Presence of 750 MW grafted PEG (Figure 3b) decreased the final frequency drop due to non-specific adsorption to 0.9 and 5.5 Hz for α-helix and β-sheet PLL, respectively. The initial frequency drop rate was -3.3 and -5.0 Hz/min for α-helix and β-sheet PLL adsorbed on 750 MW grafted PEG.

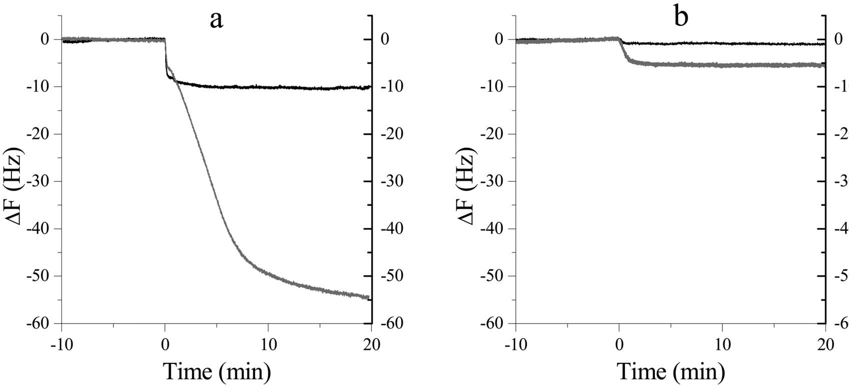

*Figure 3. Representative time course of α-helix (——) and β-sheet PLL (——) adsorption on a) bare QCM-D Au sensor, **b)** PEG 750 MW chemisorbed layer on Au sensor at 0.15 mL/min flow rate, 0.1 mg/mL PLL in 10 mM potassium phosphate buffer with 5 mM Na_2SO_4, (41).*

For modelling purpose (Voight viscoelastic model), 1 g/cm^3 and 0.7 cP where chosen for solution density and viscosity of 10 mM PB with 5 mM Na_2SO_4 at 37°C containing 0.1 mg/mL PLL respectively (*104*). 1 g/cm^3 was also chosen as PLL layer density. Initial rate of α-helix mass adsorption on bare gold surface, 322±30 ng/cm^{2}min, was higher than β-sheet, 120±1 ng/cm^{2}min. The final adsorbed amounts for α-helix and β-sheet adsorption on bare gold surface was determined to be 231±5 ng/cm^2 and 1087±14 ng/cm^2 respectively. One possible explanation for higher adsorbed amount/ thickness of the β-sheet PLL film can be the strong interaction of β-sheet PLL chains with each other. It was reported by Grigsby et al. (*105*) that interactions between PLL chains in aqueous solution are greater for β-sheet compared to α-helix conformation. They concluded the interaction to be hydrophobic in nature. By considering β-sheet and α-helix conformations as flat surface and a cylinder respectively, they attributed the interaction to be a function of surface to surface contact. Our preliminary QCM-D data suggest that secondary structures themselves may play an important role in facilitating peptide adsorption to a surface. PEG coating caused a significant drop in initial rate of α-helix mass adsorption from 322±30 ng/cm^{2}min on bare gold to 42±4 ng/cm^{2}min for 750 MW PEG layer. On bare gold, initial rate of β-sheet mass adsorption was

120±1 ng/cm^{2}min. Chemisorption of 750 MW PEG on Au surface reduced initial rate of β-sheet PLL mass adsorption to 93±4 ng/cm^2.min. By forming 750 MW PEG chemisorbed layer on Au surface, adsorption of α-helix PLL reduced to 11% of the α-helix PLL adsorption on bare gold and in case of β-sheet presence of 750 MW PEG layer on Au surface decreased the total adsorbed amount to 25% of the β-sheet PLL adsorption on bare gold.

Effect of Film Hydration on Protein Adsorption Events: A PCBMA Investigation

Previously, nonfouling characteristics of high molecular weight PEG were attributed to 'steric repulsion' mechanisms (*44*, *106–108*). However, work surrounding the use of self-assembled monolayers (SAM) of oligo(ethylene glycol) (OEG) exhibited excellent resistance to protein adsorption (*109*, *110*). Considering monodispersity and the confined boundaries of OEG-SAM, the idea of 'steric repulsion' being the only major mechanism for inhibiting surface-protein interactions was in serious question (*111*). Instead, polymer hydration (both internal and on the layers surface) began to be recognized as an important factor for imbuing antifouling behaviour to PEG coated surfaces (*112–114*).

The impact of hydration on protein-repellent properties of zwitterionic-based materials was firstly discussed by Ishihara *et.al.* (*115*). The results of their study suggested the significant role of free water surrounding 2-methacryloyloxyethyl phosphorylcholine (MPC) polymer in its resistance to protein adsorption. He *et.al* (*116*) also utilized molecular simulation to study phosphorylcholine-SAMs as a model system. It was shown that the residence time of water molecules near the zwitterionic surface was much longer compared to those in the vicinity of OEG surface. It was also speculated that this hydration layer above the zwitterionic surface may greatly impact the propensity for proteins to adsorb (*116*). The results of Nuclear Magnetic Resonance (NMR) studies on poly(sulfobetaine methacrylate) revealed that there are almost eight water molecules more tightly bound to sulfobetaine segments vs. only one water molecule bound to EG segment in PEG. Furthermore, the water molecules within the zwitterion-bound hydration layer showed higher mobility compared to those associated with PEG (*117*). Hence it was proposed that dynamic profile, quantity and state of the water molecules within the hydration layer are crucial factors that dictate the protein-surface interaction.

It is known that protein adsorption onto PCBMA-modified surfaces is largely influenced by the polymer chemistry (*118*). The number of spacer groups (-CH_2-) present between the two poles of the zwitterion within the monomer is thought to be the key factor affecting hydration of the polymer chain and, it was recently observed, conformation of the adsorbed protein (*118*). Modulated differential scanning calorimetery (MDSC) was employed for studying silica nanoparticles (SiNPs) functionalized with PCBMA differing in the number of spacer groups (1 or 5 –CH_2- group) and end-group chemistry (either phosphonate (Phospho) or 2,2,6,6-tetramethylpiperidine-N-oxyl (TEMPO)) in order to investigate surface hydration as well as the state of the water molecules inside the hydration layer

(Table 3). It was observed that systems bearing five spacer groups (PCBMA5) are more hydrated than the ones containing one spacer group (PCBMA1), regardless of the end-group chemistry (*118*). It is speculated that the charge separation caused by longer spacer groups increased the dipole moment of the zwitterions, which ultimately affected the overall hydrophilicity of the surface. In other words, variation of the length of spacer group can disturb the water environment due to changes in electric field at the interface of the polymer and water. Zeta potential studies also revealed that (at pH 7.0) the surface of the NPs modified with five spacer groups contain more positive charges (~14 mV more positive) than that of the NPs modified with one spacer group (*118*). This might also explain the observed higher water content (W_c) of these NPs (Table 3). On the other hand, the amount of bound water (i.e. sum of freezing and non-freezing water content, W_{fb} and W_{nf}, respectively) was greatly influenced by the end-group chemistry, explaining the higher affinity of Phospho end-group for water compared to TEMPO end-group (Table 3).

Table 3. MDSC-based characterization of hydrated SiNPs and calculated amount of different types of waters in the polymer matrix[a]. Adapted with permission from (*111*). Copyright 2011 American Chemical Society

Sample	W_c[b]	W_{fb}	W_{nf}	W_f
SiNP-PCBMA5 (Phospho)	34.2 ± 0.5	12.2 ± 0.4	7.1 ± 0.7	15 ± 1
SiNP-PCBMA1 (Phospho)	30.7 ± 0.7	8.5 ± 0.4	10.5 ± 0.5	11.6 ± 0.7
SiNP-PCBMA5 (TEMPO)	32.8 ± 0.7	9.1 ± 0.1	8 ± 1	15 ± 1
SiNP-PCBMA1 (TEMPO)	28.9 ± 0.4	6.8 ± 0.3	7 ± 2	14 ± 1

[a] The values represent an average water content (%) ± SD, n=3. [b] W_c: actual water content, W_{fb}: freezing bound water, W_{nf}: non-freezing bound water, W_f: unbounded free water.

The adsorption-induced unfolding of model proteins Human Serum Albumin (HSA) and α-Lactalbumin due to interaction with various PCBMA-functionalized NPs was also examined using circular dichroism (CD) techniques to understand not just how much protein adsorbed to these polymers but also how the chemistry of the surface affected their adsorbed conformation. These two model proteins were employed due to their difference in size and their similarity in charge: the two characteristics that can largely affect protein-surface interactions. α-Lactalbumin is a small (14.2 kDa) protein with a pI of ~4.5, whereas HSA is relatively large (66.4 kDa) with pI of ~4.7. It was seen that greater loosening/unfolding of α-lactalbumin occurred upon adsorption onto NPs modified with PCBMA5, as compared to other systems of study (Figure 4) (*118*). It is important to note that NPs of 70 - 120 nm begin to resemble flat surfaces for protein adsorption in that the curvature of the surface is no longer crucial to protein adsorption mechanisms (*119*). Therefore, as our NPs have diameters within this range (71-89 nm) NP size probably is not a determining factor in conformation of adsorbed protein.

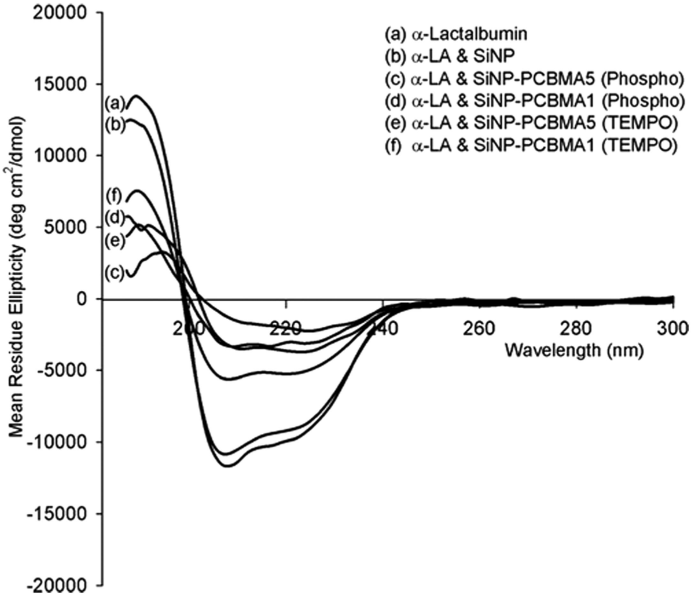

Figure 4. Representative circular dichroism spectra of native α-lactalbumin (a) and α-lactalbumin adsorbed to unmodified (b) and modified SiNPs (c−f). The measurements reflect the collection of 10 scans, repeated thrice, and the changes in the ellipticity while interacting with SiNPs were compared with the native state. Adapted with permission from (111). Copyright 2011 American Chemical Society.

Figure 4 also demonstrated the effect of end-group chemistry on the adsorption of α-lactalbumin. As illustrated, systems modified with Phospho end-groups showed larger conformational changes upon α-lactalbumin adsorption (*118*). The effect of end-group chemistry on HSA adsorption was evident from the CD studies (Figure 5), showing a stronger interaction between HSA and NPs modified with Phospho end-groups; resulting in a larger decrease in ellipticity of mixtures of HSA and NPs bearing Phospho end-group.

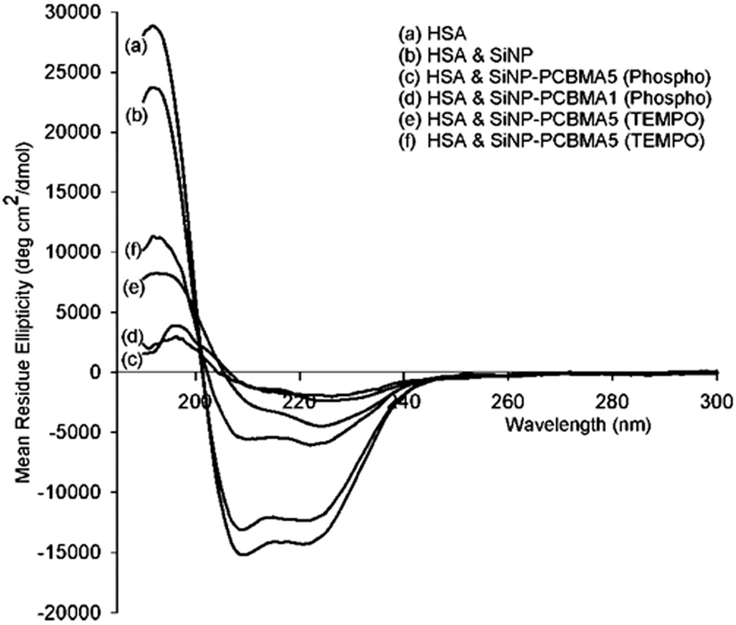

Figure 5. Representative circular dichroism spectra of native HSA (a) and HSA adsorbed to unmodified (b) and modified SiNPs (c−f). The measurements reflect the collection of 10 scans, repeated thrice, and the changes in the ellipticity while interacting with SiNPs were compared with the native state. Adapted with permission from (111). Copyright 2011 American Chemical Society.

The results presented above demonstrate the effect of polymer chemistry on the hydration of the system and ultimately on the non-fouling behaviour. Interestingly, it can be concluded that although systems modified with 5 spacer groups (PCBMA5) and/or Phospho end-group were shown to have higher water content, they caused greater unfolding of the adsorbed protein on their surface. This might invoke the idea that although presence of a water barrier on the surface can help diminishing nonspecific protein adsorption, the neutrality of the surface is playing a more crucial role in dictating surface induced unfolding events. However, more extensive experimental and simulation studies are required to fully identify the specific role of such different parameters in building the next generation of non-fouling architectures.

Summary

It is thought that through developing a clearer understanding of the molecular level events involved in the adsorption of proteins, through looking at surface properties as well as the fundamental properties of proteins, it may be possible to further engineer surfaces that are clinically relevant.

Acknowledgments

MB and LDU would like to acknowledge Hongbo Zeng for his support as MB's co-supervisor.

References

1. Vladkova, T. G. *Int. J. Polym. Sci.* **2010**, *2010*, 1–22.
2. Anderson, J. M.; Bonfield, T. L.; Ziats, N. P. *Int. J. Artif. Organs* **1990**, *13*, 375–382.
3. Andrade, J. D.; Hlady, V. *Ann. N.Y. Acad. Sci.* **1987**, *516*, 158–172.
4. Nath, N.; Hyun, J.; Ma, H.; Chilkoti, A. *Surf. Sci.* **2004**, *570*, 98–110.
5. Pankowsky, D. A.; Ziats, N. P.; Topham, N. S.; Ratnoff, O. D.; Anderson, J. M. *J. Vasc. Surg.* **1990**, *11*, 599–606.
6. Shen, M.; Garcia, I.; Maier, R. V.; Horbett, T. A. *J. Biomed. Mater. Res., Part A* **2004**, *70A*, 533–541.
7. Collier, T. O.; Anderson, J. M. *J. Biomed. Mater. Res.* **2002**, *60*, 487–496.
8. Evans-Nguyen, K. M.; Fuierer, R. R.; Fitchett, B. D.; Tolles, L. R.; Conboy, J. C.; Schoenfisch, M. H. *Langmuir* **2006**, *22*, 5115–5121.
9. Heuberger, M.; Drobek, T.; Spencer, N. D. *Biophys. J.* **2005**, *88*, 495–504.
10. Hu, W.-J.; Eaton, J. W.; Ugarova, T. P.; Tang, L. *Blood* **2001**, *98*, 1231–1238.
11. Lu, D. R.; Park, K. *J. Colloid Interface Sci.* **1991**, *144*, 271–281.
12. Shiba, E.; Lindon, N. J.; Kushner, L.; Matsueda, R. G.; Hawiger, J.; Kloczewiak, M.; Kudryk, B.; Salzman, W. E. *Am. J. Physiol.* **1991**, *260*, 965–974.
13. Smolarczyk, K.; Boncela, J.; Szymanski, J.; Gils, A.; Cierniewski, C. S. *Arterioscler., Thromb., Vasc. Biol.* **2005**, *25*, 2679–2684.
14. Ugarova, T. P.; Budzynski, A. Z.; Shattil, S. J.; Ruggeri, Z. M.; Ginsberg, M. H.; Plow, E. F. *J. Biol. Chem.* **1993**, *268*, 21080–21087.
15. Grinnell, F.; Feld, M. K. *J. Biomed. Mater. Res.* **1981**, *15*, 363–381.
16. Dalsin, J. L.; Messersmith, P. B. *Mater. Today* **2005**, *8*, 38–46.
17. Drotleff, S. Ph.D. thesis, University of Regensburg, Regensburg, Germany, 2006.
18. Unsworth, L. D.; Sheardown, H.; Brash, J. L. *Langmuir* **2005**, *21*, 1036–1041.
19. Hlady, V.; VanWagenen, R. A.; Andrade, J. D. In *Book Surface and Interfacial Aspects of Biomedical Polymers*; Plenum Press: New York, 1985; Vol. 2.
20. Gong, P.; Grainger, D. W. *Methods Mol. Biol* **2007**, *381*, 59–92.
21. Leckband, D.; Israelachvili, J. *Enzyme Microb. Technol.* **1993**, *15*.
22. van Oss, C. J. In *Interfacial forces in aqueous media*; CRC Press: Boca Raton, 1994.
23. Overbeek, J. T. G. In *Book Colloid science*; Elsevier: Amsterdam, 1952; Vol. 1.
24. Ramsden, J. J. In *Biopolymers at interfaces*, 2nd ed.; Malmsten, M., Ed.; Marcel Dekker, Inc.: New York, 2003.

25. Brash, J. L.; Uniyal, S.; Samak, Q. *Trans. - Am. Soc. Artif. Intern. Organs* **1974**, *A 20*, 69–76.
26. Ostuni, E.; Chapman, R. G.; Holmlin, R. E.; Takayama, S.; Whitesides, G. M. *Langmuir* **2001**, *17*, 5605–5620.
27. Alessi, M. L.; Norman, A. I.; Knowlton, S. E.; Ho, D. L.; Greer, S. C. *Macromolecules* **2005**, *38*, 9333–9340.
28. Vennemann, N.; Lechner, M. D.; Oberthür, R. C. *Polymer* **1987**, *28*, 1738–1748.
29. Dormidontova, E. E. *Macromolecules* **2002**, *35*, 987–1001.
30. Valentini, M.; Napoli, A.; Tirelli, N.; Hubbell, J. A. *Langmuir* **2003**, *19*, 4852–4855.
31. Lee, J. H.; Lee, H. B.; Andrade, J. D. *Prog. Polym. Sci.* **1995**, *20*, 1043–1079.
32. Li, L. Y.; Chen, S. F.; Zheng, J.; Ratner, B. D.; Jiang, S. Y. *J. Phys. Chem. B* **2005**, *109*, 2934–2941.
33. Claesson, P. M.; Blomberg, E.; Paulson, O.; Malmsten, M. *Colloids Surf., A* **1996**, *112*, 131–139.
34. Van Oss, C. J. In *Interfacial forces in aqueous media*; M. Dekker: New York, 1994.
35. Unsworth, L. D. Ph.D. thesis, McMaster University, Hamilton, Ontario, 2005.
36. Alexander, S. *J. Phys.* **1977**, *38*, 983–987.
37. Unsworth, L. D.; Tun, Z.; Sheardown, H.; Brash, J. L. *J. Colloid Interface Sci.* **2005**, *281*, 112–121.
38. Unsworth, L. D.; Sheardown, H.; Brash, J. L. *Langmuir* **2008**, *24*, 1924–1929.
39. Chang, Y.; Ko, C. Y.; Shih, Y. J.; Quemener, D.; Deratani, A.; Wei, T. C.; Wang, D. M.; Lai, J. Y. *J. Membr. Sci.* **2009**, *345*, 160–169.
40. Chang, Y.; Shih, Y. J.; Ko, C. Y.; Jhong, J. F.; Liu, Y. L.; Wei, T. C. *Langmuir* **2011**, *27*, 5445–5455.
41. Binazadeh, M.; Zeng, H.; Unsworth, L. D. 62nd Canadian Chemical Engineering Conference Vancouver, British Columbia; Canada. October 14-17, 2012.
42. Gombotz, W. R.; Guanghui, W.; Horbett, T. A.; Hoffman, A. S. *J. Biomed. Mater. Res.* **1991**, *25*, 1547–1562.
43. Archambault, J. G.; Brash, J. L. *Trans. Annu. Meet. Soc. Biomater.* **1998**, *21*, 251.
44. McPherson, T.; Kidane, A.; Szleifer, I.; Park, K. *Langmuir* **1998**, *14*, 176–186.
45. Sofia, S. J.; Premnath, V.; Merrill, E. W. *Macromolecules* **1998**, *31*, 5059–5070.
46. Kingshott, P.; Thissen, H.; Griesser, H. *J. Biomaterials* **2002**, *23*, 2043.
47. Li, L. Y.; Chen, S. F.; Jiang, S. Y. *J. Biomater. Sci., Polym. Ed.* **2007**, *18*, 1415–1427.
48. Shen, M. C.; Martinson, L.; Wagner, M. S.; Castner, D. G.; Ratner, B. D.; Horbett, T. A. *J. Biomater. Sci., Polym. Ed.* **2002**, *13*, 367–390.

49. Knop, K.; Hoogenboom, R.; Fischer, D.; Schubert, U. S. *Angew. Chem., Int. Ed.* **2010**, *49*, 6288–6308.
50. Hucknall, A.; Rangarajan, S.; Chilkoti, A. *Adv. Mater.* **2009**, *21*, 2441–2446.
51. Jiang, S.; Cao, Z. *Adv. Mater.* **2010**, *22*, 920–932.
52. Chen, S. F.; Li, L. Y.; Zhao, C.; Zheng, J. *Polymer* **2010**, *51*, 5283–5293.
53. Brault, N. D.; Sundaram, H. S.; Li, Y. T.; Huang, C. J.; Yu, Q. M.; Jiang, S. Y. *Biomacromolecules* **2012**, *13*, 589–593.
54. Chang, Y.; Higuchi, A.; Shih, Y. J.; Li, P. T.; Chen, W. Y.; Tsai, E. M.; Hsiue, G. H. *Langmuir* **2012**, *28*, 4309–4317.
55. Zhao, J.; Shi, Q.; Luan, S.; Song, L.; Yang, H.; Shi, H.; Jin, J.; Li, X.; Yin, J.; Stagnaro, P. *J. Membr. Sci.* **2011**, *369*, 5–12.
56. Yang, W.; Xue, H.; Li, W.; Zhang, J. L.; Jiang, S. Y. *Langmuir* **2009**, *25*, 11911–11916.
57. He, Y.; Hower, J.; Chen, S. F.; Bernards, M. T.; Chang, Y.; Jiang, S. Y. *Langmuir* **2008**, *24*, 10358–10364.
58. Huang, C. J.; Brault, N. D.; Li, Y. T.; Yu, Q. M.; Jiang, S. Y. *Adv. Mater.* **2012**, *24*, 1834–1837.
59. Yang, W.; Chen, S. F.; Cheng, G.; Vaisocherova, H.; Xue, H.; Li, W.; Zhang, J. L.; Jiang, S. Y. *Langmuir* **2008**, *24*, 9211–9214.
60. Kadoma, Y.; Nakabayashi, N.; Masuhara, E.; Yamauchi, J. *Kobunshi Ronbunshu* **1978**, *35*, 423–427.
61. Lowe, A. B.; Vamvakaki, M.; Wassall, M. A.; Wong, L.; Billingham, N. C.; Armes, S. P.; Lloyd, A. W. *J. Biomed. Mater. Res.* **2000**, *52*, 88–94.
62. West, S. L.; Salvage, J. P.; Lobb, E. J.; Armes, S. P.; Billingham, N. C.; Lewis, A. L.; Hanlon, G. W.; Lloyd, A. W. *Biomaterials* **2004**, *25*, 1195–1204.
63. Chen, S.; Zheng, J.; Li, L.; Jiang, S. *J. Am. Chem. Soc.* **2005**, *127*, 14473–14478.
64. Zhang, Z.; Chao, T.; Chen, S. F.; Jiang, S. Y. *Langmuir* **2006**, *22*, 10072–10077.
65. Zhang, Z.; Chen, S. F.; Chang, Y.; Jiang, S. Y. *J. Phys. Chem. B* **2006**, *110*, 10799–10804.
66. Zhang, Z.; Vaisocherova, H.; Cheng, G.; Yang, W.; Xue, H.; Jiang, S. Y. *Biomacromolecules* **2008**, *9*, 2686–2692.
67. Shih, Y. J.; Chang, Y. *Langmuir* **2010**, *26*, 17286–17294.
68. Chang, Y.; Chang, W. J.; Shih, Y. J.; Wei, T. C.; Hsiue, G. H. *ACS Appl. Mater. Interfaces* **2011**, *3*, 1228–1237.
69. Holmlin, R. E.; Chen, X. X.; Chapman, R. G.; Takayama, S.; Whitesides, G. M. *Langmuir* **2001**, *17*, 2841–2850.
70. Noh, H.; Vogler, E. A. *Biomaterials* **2007**, *28*, 405–422.
71. Parhi, P.; Golas, A.; Vogler, E. A. *J. Adhes. Sci. Technol.* **2010**, *24*, 853–888.
72. Chen, N.; Maeda, N.; Tirrell, M.; Israelachvili, J. *Macromolecules* **2005**, *38*, 3491–3503.
73. Shao, Q.; He, Y.; White, A. D.; Jiang, S. Y. *J. Phys. Chem. B* **2010**, *114*, 16625–16631.
74. Wu, L.; Jasinski, J.; Krishnan, S. *J. Appl. Polym. Sci.* **2012**, *124*, 2154–2170.

75. Cacace, M. G.; Landau, E. M.; Ramsden, J. J. *Q. Rev. Biophys.* **1997**, *30*, 241–277.
76. He, Y.; Shao, Q.; Chen, S. F.; Jiang, S. Y. *J. Chem. Phys.* **2011**, *135*.
77. Colak, S.; Tew, G. N. *Biomacromolecules* **2012**, *13*, 1233–1239.
78. Estephan, Z. G.; Schlenoff, P. S.; Schlenoff, J. B. *Langmuir* **2011**, *27*, 6794–6800.
79. Dill, K. A. *Biochemistry (Mosc)* **1990**, *29*, 7133–7155.
80. Norde, W.; Anusiem, A. C. I. *Colloids Surf.* **1992**, *66*, 73–80.
81. Kabsch, W.; Sander, C. *Biopolymers* **1983**, *22*, 2577–2637.
82. Chen, S.; Li, L.; Zheng, J. *Polymer* In Press, Accepted Manuscript.
83. Jordan, C. E.; Corn, R. M. *Anal. Chem.* **1997**, *69*, 1449–1456.
84. Yang, Q.; Kaul, C.; Ulbricht, M. *Langmuir* **2010**, *26*, 5746–5752.
85. Wang, D.; Douma, M.; Swift, B.; Oleschuk, R. D.; Horton, J. H. *J. Colloid Interface Sci.* **2009**, *331*, 90–97.
86. Müller, M.; Brissová, M.; Rieser, T.; Powers, A. C.; Lunkwitz, K. *Mater. Sci. Eng., C* **1999**, *8-9*, 163–169.
87. Shibata, A.; Yamamoto, M.; Yamashita, T.; Chiou, J. S.; Kamaya, H.; Ueda, I. *Biochemistry (Mosc)* **1992**, *31*, 5728–5733.
88. Greenfield, N. J. *Nat. Protoc.* **2006**, *1*, 2876–2890.
89. Chittchang, M.; Alur, H. H.; Mitra, A. K.; Johnston, T. P. *J. Pharm. Pharmacol.* **2002**, *54*, 315–323.
90. Chiou, J.-S.; Tatara, T.; Sawamura, S.; Kaminoh, Y.; Kamaya, H.; Shibata, A.; Ueda, I. *Biochim. Biophys. Acta* **1992**, *1119*, 211–217.
91. Parson, W. W. In *Modern Optical Spectroscopy: With Exercises and Examples from Biophysics and Biochemistry* Springer: New York, 2009.
92. Miles, A. J.; Whitmore, L.; Wallace, B. A. *Protein Sci.* **2005**, *14*, 368–374.
93. Binazadeh, M.; Zeng, H.; Unsworth, L. D. 149th International Symposium on Surfactants in Solution University of Alberta, Edmonton, Canada. June 24 - 28,2012.
94. van Oss, C. J. *J Mol Recognit* **2003**, *16*, 177–190.
95. Holmberg, K.; Bergstrom, K.; Stark, M. B., In *Polyethylene Glycol Chemistry: Biotechnical and Biomedical Application*, Harris, J. M., Ed. Plenum Press: New York, 1992; pp 303-324.
96. Notley, S. M.; Eriksson, M.; Wagberg, L. *J. Colloid Interface Sci.* **2005**, *292*, 29–37.
97. Weber, N.; Wendel, H. P.; Kohn, J. *J. Biomed. Mater. Res., Part A* **2005**, *72A*, 420–427.
98. Yan, M. Q.; Liu, C. X.; Wang, D. S.; Ni, J. R.; Cheng, J. X. *Langmuir* **2011**, *27*, 9860–9865.
99. Voinova, M. V.; Rodahl, M.; Jonson, M.; Kasemo, B. *Phys. Scr.* **1999**, *59*, 391–396.
100. Reed, C. E.; Kanazawa, K. K.; Kaufman, J. H. *J. Appl. Phys.* **1990**, *68*, 1993–2001.
101. de Kerchove, A. J.; Elimelech, M. *Macromolecules* **2006**, *39*, 6558–6564.
102. Weber, N.; Pesnell, A.; Bolikal, D.; Zeltinger, J.; Kohn, J. *Langmuir* **2007**, *23*, 3298–3304.

103. Yoshikawa, C.; Goto, A.; Tsujii, Y.; Fukuda, T.; Kimura, T.; Yamamoto, K.; Kishida, A. *Macromolecules* **2006**, *39*, 2284–2290.
104. Green, D. W.; Perry, R. H. In *Perry's Chemical Engineers' Handbook*, 8th ed.; McGraw-Hill: New York, 2008; pp 2−96, 92−449.
105. Grigsby, J. J.; Blanch, H. W.; Prausnitz, J. M. *Biophys. Chem.* **2002**, *99*, 107–116.
106. Jeon, S. I.; Lee, J. H.; Andrade, J. D.; de Gennes, P. G. *J. Colloid Interface Sci.* **1991**, *142*, 149.
107. Pertsin, A. J.; Grunze, M.; Garbuzova, I. A. *J. Phys. Chem. B* **1998**, *102*, 4918–4926.
108. Tasaki, K. *J. Am. Chem. Soc.* **1996**, *118*, 8459–8469.
109. Prime, K.; Whitesides, G. *Science* **1991**, *252*, 1164–1167.
110. Palegrosdemange, C.; Simon, E. S.; Prime, K. L.; Whitesides, G. M. *J. Am. Chem. Soc.* **1991**, *113*, 12–20.
111. Herrwerth, S.; Eck, W.; Reinhardt, S.; Grunze, M. *J. Am. Chem. Soc.* **2003**, *125*, 9359–9366.
112. Zheng, J.; Li, L.; Tsao, H.-K.; Sheng, Y.-J.; Chen, S.; Jiang, S. *Biophys. J.* **2005**, *89*, 158–166.
113. He, Y.; Chang, Y.; Hower, J. C.; Zheng, J.; Chen, S.; Jiang, S. *Phys. Chem. Chem. Phys.* **2008**, *10*, 5539–5544.
114. Hower, J. C.; He, Y.; Jiang, S. *J. Chem. Phys.* **2008**, *129*, 215101.
115. Ishihara, K.; Nomura, H.; Mihara, T.; Kurita, K.; Iwasaki, Y.; Nakabayashi, N. *J. Biomed. Mater. Res.* **1998**, *39*, 323–330.
116. He, Y.; Hower, J.; Chen, S.; Bernards, M. T.; Chang, Y.; Jiang, S. *Langmuir* **2008**, *24*, 10358–10364.
117. Wu, J.; Lin, W.; Wang, Z.; Chen, S.; Chang, Y. *Langmuir* **2012**, *28*, 7436–7441.
118. Abraham, S.; So, A.; Unsworth, L. D. *Biomacromolecules* **2011**, *12*, 3567–3580.
119. Lindman, S.; Lynch, I.; Thulin, E.; Nilsson, H.; Dawson, K. A.; Linse, S. *Nano Lett.* **2007**, *7*, 914–920.

Chapter 29

Peptide Adsorption and Function at Pendant PEO Brush Layers

Karl F. Schilke and Joseph McGuire*

**School of Chemical, Biological and Environmental Engineering,
Oregon State University, Corvallis, Oregon 97331
*E-mail: joseph.mcguire@oregonstate.edu**

Surfaces coated with pendant hydrophilic polymers such as polyethylene oxide (PEO) in a brush conformation are generally biocompatible and protein-repellent. However, theory predicts that small polypeptides can integrate into an otherwise non-fouling brush layer, if the peptide diameter is less than the brush chain spacing. In addition, such integrated peptides are protected from competitive elution by larger proteins. We describe experiments with nisin, a small (3.4 kDa) antimicrobial peptide, loaded into brush layers made with PEO-based triblocks on various substrates. Several techniques, including ellipsometry, circular dichroism (CD), TOF-SIMS, optical waveguide lightmode spectroscopy (OWLS), and antimicrobial assays indicate that nisin integrates into PEO brush layers without loss of antimicrobial activity. Fibrinogen does not elute entrapped nisin or adsorb at the nisin-loaded brush. A fundamental understanding of the mechanisms of peptide integration into PEO brush layers will enable novel approaches for drug delivery and bioactive, functional surface coatings for biomedical devices.

Introduction

An abundant literature describes the non-fouling properties of material surfaces presenting pendant PEO chains, and considerable effort continues to be made to improve our quantitative understanding of the protein repellent mechanisms of PEO coatings. On the other hand, there are relatively few reports

In Proteins at Interfaces III State of the Art 2012; Horbett, T., et al.;
ACS Symposium Series; American Chemical Society: Washington, DC, 2012.

in the literature that compare the adsorption of proteins of different sizes to a given PEO layer, and even fewer that describe the adsorption of peptides and small (< 5 kDa) proteins at pendant PEO layers. Despite the fact that the adsorption of sufficiently small proteins to pendant PEO brush layers is predicted theoretically, we have to date little experimentally-based, quantitative understanding of the adsorption and function of very small proteins at otherwise protein-repellent PEO layers. A better understanding of the mechanisms of peptide "entrapment" within PEO layers is very much needed, as it will provide direction for storage and controlled release of a variety of bioactive agents from a new array of biocompatible, functional surface coatings.

In this chapter we briefly summarize the expected effects of chain density and chain length on protein adsorption and repulsion by pendant PEO, and provide a short theoretical justification for peptide entrapment within PEO layers, as well as the retained capacity for large protein repulsion by peptide-containing PEO layers. We describe our past and current research on the behavior of nisin, a small antimicrobial peptide, at brush layers made with PEO-containing triblock polymers on various substrates. We summarize the most salient results in relation to adsorption, elution, structure and function of nisin at PEO-coated interfaces. Finally, we discuss the need to characterize the molecular origins of adsorption and entrapment of small peptides in surface-bound, pendant PEO layers.

Our early results with nisin were indicative of multilayer adsorption within the brush, suggesting that some nisin molecules were located adjacent to the surface itself ("primary adsorption"), while others were entrapped among the PEO chains. While the possibility of primary adsorption is predicted theoretically, it is also reasonable to expect that multi-layer adsorption will occur, to a degree largely determined by associations between peptides and the PEO chains and/or self-association of the peptides within the layer.

We are currently testing the hypothesis that, for a peptide of a size that allows adsorption at or integration into a PEO layer, the structure and amphiphilic character of the peptide will determine the adsorption affinity. Peptide structure and amphiphilicity are controllable, and adsorption affinity is quantifiable. This work holds promise for generating qualitative and quantitative information about the factors that influence peptide adsorption and integration, from which compelling strategies for drug loading, retention of function, and controlled release from blood contacting devices may be built.

Adsorption and Repulsion of Proteins at Pendant PEO Layers

The mechanisms commonly invoked to describe the protein-resistant nature of end-tethered PEO surfaces include steric barriers and hydration barriers (*1*, *2*). Steric repulsion is based on PEO chain compression and requires that the chains be of some minimum length. The water barrier mechanism is based on the thought that the binding of water to PEO is sufficiently tight that an approaching protein cannot interact with the surface. This is consistent with the observation that very short PEO chains (e.g., two or three monomers) can produce protein resistant surfaces.

To date the specific chemical and physical origins of the protein resistant character of end-tethered PEO remain a matter of debate, but consistent observations have been reported on the expected effects of PEO chain density and chain length on protein repulsion (*3–5*). At low chain density, where the distance (*D*) between polymer grafting sites is relatively large, the isolated chains form random coils with sufficient open area to allow protein adsorption (Figure 1, left).

At sufficiently high chain density, when $D < 2R_F$ (where R_F is the Flory radius of the polymer) the polymer chains can no longer form random coils, but must instead extend away from the surface in a "brush" configuration (Figure 1, right). Protein repulsion by brushes is generally very good, and largely independent of chain length (*1*, *4–7*).

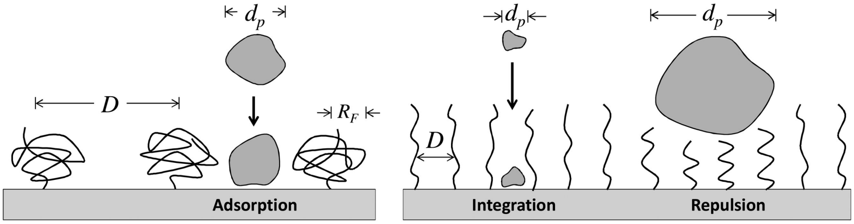

Figure 1. Schematic representation of protein adsorption and integration at pendant polymers at low ($D > 2R_F$, left) and high grafting density (right). At low density, individual polymer chains adopt a "mushroom" conformation, while at high density, a brush structure is formed. Proteins smaller than the polymer chain spacing may adsorb or integrate into the brush, while large proteins are repelled.

In contrast to protein *repulsion*, there are very few reports in the literature describing the *adsorption* of small proteins to a given PEO layer. It has been argued that once a sufficiently high chain density is achieved, the rejection capacity of the pendant polymer phase is determined by protein size, relative to the average distance between polymer chains (*8–10*). Halperin (*11*) formulated a model for protein adsorption in a PEO brush based on kinetic and thermodynamic considerations, and predicted two modes of protein adsorption: primary adsorption (at the surface itself) and secondary adsorption (at the periphery of the grafted PEO chains). Surface force experiments with compression of PEO brushes by protein-coated surfaces (*12*) suggested that a PEO brush may exhibit coexistence between an inner, dense hydrophobic phase and a dilute, mobile hydrophilic phase at the outer edge of the brush. Such coexistence would give rise to an inner region of the brush that is "attractive" for protein adsorption (*11*, *12*).

Fang *et al.* (*13*) formulated a model based on a generalized diffusion approach for protein interaction with PEO brushes. Their model showed that when the pendant chain layer thickness is greater than the size of the protein, both adsorption and desorption rates decrease with increasing chain length. Perhaps the most interesting outcome of their work is that the rate of desorption of adsorbed proteins is expected to decrease as the PEO chain length is increased. They explained that proteins will become "trapped" close to the surface by the barrier presented by the pendant chains, and suggested that such a trapping mechanism could be used in the design of strategies for the controlled release of proteins from surfaces.

Nisin Entrapment within Pendant PEO Layers

Nisin is a small (3.4 kDa) amphiphilic, cationic peptide that is an effective inhibitor of Gram-positive bacteria (*14*, *15*). It differs in mode of action from conventional antibiotics, which typically attack metabolic pathways. Nisin instead binds to a cell wall precursor within the bacterial membrane, where it self-associates to form pores and rapidly kills the cell. This physical kill mechanism minimizes the opportunity for the rise of resistant microorganisms, although nisin resistance is not unknown (*15*, *16*). The potential use of nisin in anti-infective coating strategies has motivated considerable interest in its adsorption and function at material interfaces.

In two earlier reports (*17*, *18*), we described the adsorption and elution of nisin at silanized silica surfaces coated with Pluronic® F108 (a PEO-based triblock surfactant), and examined the antimicrobial activity of nisin-loaded F108 layers after incubation in the presence of blood proteins. We also investigated the conformational rearrangement of nisin on bare hydrophobic and F108-coated surfaces.

The F108 triblocks used by Tai *et al.* were immobilized only by hydrophobic association. While physically adsorbed F108 has been shown to be resistant to elution in the presence of blood proteins, it is not resistant to elution when incubated with whole blood (*19*). In later articles, we described the individual and sequential adsorption of nisin and fibrinogen at surfaces coated with covalently-bound PEO-PPO-PEO triblocks (*20*), and at medical-grade polymer surfaces coated with covalently-bound PEO-polybutadiene-PEO triblocks (*21*). Salient results from those papers, along with some current results from our laboratory, are summarized below.

Nisin Behavior at Silanized Silica Surfaces Coated with Pluronic® F108 by Hydro-Phobic Association

Adsorption and Elution

We used automated, *in situ* ellipsometry to compare adsorption and elution kinetics of nisin at bare hydrophobic and F108-coated surfaces. Data recorded by Tai *et al.* (*17*) showed adsorbed amounts after four hours that were greater than values expected for monolayer adsorption in each case (Figure 2). Nisin adsorption to the F108-coated surface was generally observed to be slower than adsorption to the bare hydrophobic surface, likely owing to steric inhibition by the pendant PEO chains. Nisin elution in protein-free buffer was similar at each surface initially, but elution was observed to continue only at the bare hydrophobic surface. In the case of adsorption to the uncoated surface, this was attributed to greater solvent accessibility to nisin loosely held in the outer layers, while nisin integrated into the PEO brush would be expected to show greater resistance to elution.

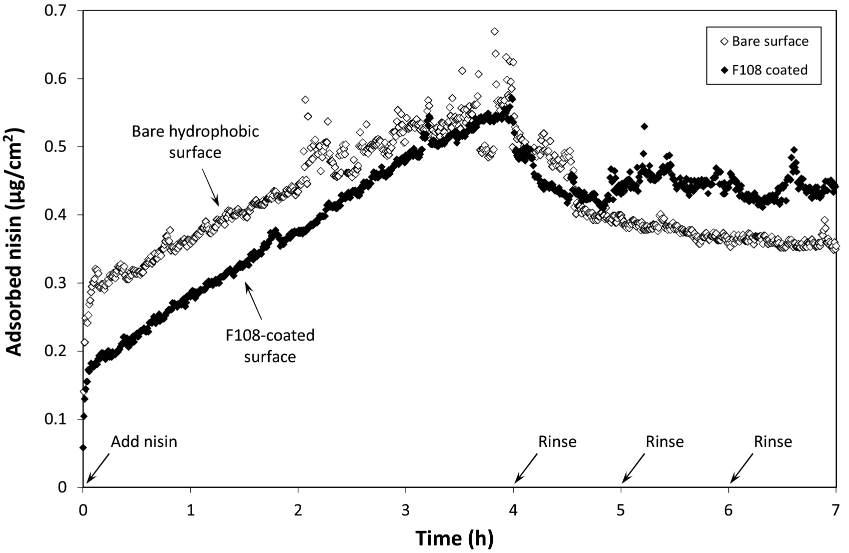

Figure 2. Comparison of adsorption and elution kinetics of nisin in buffer at bare hydrophobic (◇) and F108-coated (◆) surfaces. Reproduced from reference (17) with permission. Copyright © 2008 Elsevier, Inc.

The effect of the PEO chains on the adsorption and elution rates of nisin on these surfaces was revealed by further analysis of experimental data using a "history dependent" adsorption mechanism (*22–24*). Many macromolecular species, particularly proteins, exhibit history-dependent adsorption behavior due to slow relaxation of non-equilibrium structures at the interface. That is, for a given protein at a given surface loading, the rate of adsorption depends on the formation history of the adsorbed layer. This is particularly relevant near monolayer surface coverage, when protein-protein interactions strongly influence the availability of surface area that is suitable for adsorption.

Tie *et al.* (*24*) studied the adsorption of different proteins using optical waveguide lightmode spectroscopy (OWLS) in multi-step mode, in which a surface is alternately exposed to a protein solution and a protein-free solution (an "adsorb-rinse" cycle). In general, they observed that, at the same surface coverage, the initial adsorption rate during the second cycle was greater than that of the first step. They postulated that, for a given mass density at an interface, if the proteins were arranged in clusters or aggregates instead of being randomly distributed, then more "cleared" surface area would be available for subsequent adsorption. Conversely, if the adsorbed protein films were at equilibrium, we would expect to observe similar initial adsorption rates during each cycle, since the protein films would have identical packing and structural characteristics at each step.

A very simple illustration of this effect is shown in Figure 3. The total adsorbed mass is the same in each case (i.e., five "protein molecules" per unit area), but the adsorbed layer structure and packing is different, due to different formation histories. Assuming the intrinsic adsorption rate is high, one would expect a greater adsorption rate for the case illustrated on the right side of Figure 3, as there would be a higher probability of an incoming protein landing in a "cavity" on the surface free from other proteins. Such sequential-adsorption kinetic rate data can thus provide important information about the structure and mobility of the adsorbed layer.

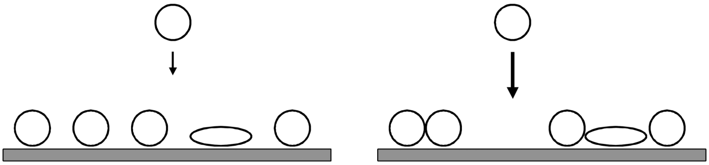

Figure 3. Protein adsorption to a surface, at which an identical number of proteins of the same type have already been adsorbed. Packing density differences between the layers (i.e. the cavity function) will affect the rate of adsorption of subsequent protein molecules at the surface. Flattened circles represent a conformationally-altered, immobile form of the protein. Adapted with permission from reference (25). Copyright © 2006 Elsevier, Inc.

Figure 4 shows the results of two sequential adsorption-elution cycles for nisin at a bare hydrophobic surface and at an F108-coated surface. For each surface, the initial slope of the second adsorption step was compared to the slope of the first adsorption cycle, at the same adsorbed mass density. At the bare hydrophobic surface (without F108), the initial adsorption rate during the second adsorption step greatly exceeded that observed, at the same surface coverage, during the first cycle.

In contrast, in the case of F108-coated silica, there was almost no increase in the rate of nisin adsorption for the second cycle. That is, the first and second step adsorption rates were similar on the F108-coated surface, indicating that there was much less post-adsorption rearrangement or "clustering" of nisin than on the bare surface (*24*). We proposed that the lateral mobility required for clustering, and the subsequent generation of unoccupied surface area, was sterically inhibited by the presence of the pendant PEO chains.

In summary, the sequential adsorption of nisin showed greater differences in adsorption rates between the first and second adsorption cycles, when evaluated at identical mass density, for uncoated surfaces compared to F108-coated surfaces. In addition, the rates of nisin adsorption and elution were generally slower at F108-coated surfaces. These results strongly suggested that nisin adsorption occurs via "entrapment" within the PEO brush layer at F108-coated surfaces, in this way slowing adsorption and spontaneous elution, and inhibiting post-adsorptive molecular rearrangements (clustering) by reducing the lateral mobility of nisin.

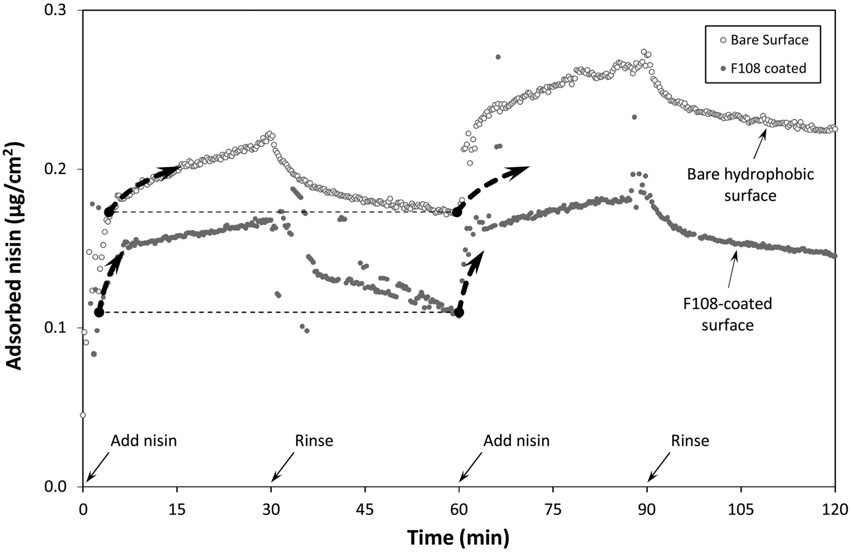

Figure 4. Sequential adsorption and elution kinetics exhibited by nisin at bare hydrophobic (○) and F108-coated (●) surfaces. The data recorded during the first adsorption cycle are shown overlaid on the second adsorption cycle (dashed arrows), in order to compare the initial adsorption rates at the same adsorbed mass density. Adapted with permission from reference (17). Copyright © 2008 Elsevier, Inc.

Structure and Antimicrobial Activity

We have evaluated the antimicrobial activity of nisin-loaded, F108-coated polystyrene microspheres and F108-coated polyurethane catheter segments against *Pediococcus pentosaceous*, a Gram-positive indicator strain (*18*). Retention of antimicrobial activity was evaluated after incubation of the catheter segments in the presence of blood proteins (equine serum), for contact periods up to seven days. While incubation with serum proteins reduced the level of retained activity on both bare hydrophobic and F108-coated materials, greater antimicrobial activity was recorded with F108-coated surfaces than with uncoated surfaces, and this difference was substantial after seven days.

With reference to the model for protein interactions with PEO brushes formulated by Fang *et al.* (*13*), any nisin remaining after elution from the outer region of the brush would be entrapped close to the surface by the pendant PEO chains. Desorption of these entrapped peptides would be expected to be substantially slower than the nisin adsorbed peripherally, due to the energetic and steric barrier presented by the PEO chains. We speculate that the release of active nisin after prolonged incubation with blood proteins may be due to a collision-mediated physical desorption mechanism between the microbial cells and the nisin-loaded, F108-coated surface.

Circular dichroism spectroscopy experiments with nisin adsorbed on F108-coated and uncoated, hydrophobic silica nanoparticles also suggested that nisin underwent conformational rearrangement at a greater rate and to a greater extent on the uncoated surfaces than on F108-coated surfaces (*18*). Collectively, these results suggest that entrapment in immobilized, pendant PEO chains confers some degree of conformational stability to nisin, and inhibits its elution from the brush by simple diffusion or competitive displacement by blood proteins.

Sequential Introduction of Nisin and Fibrinogen at Covalently Stabilized F108

Ryder *et al.* (*20*) treated silica microspheres with trichlorovinylsilane (TCVS) to introduce hydrophobic vinyl groups to their surfaces, followed by self-assembly of F108 to form a brush layer. The triblock-coated microspheres were γ-irradiated to covalently stabilize the PPO-surface association (*1*, *26*). Through absorption of radiation or interaction with water-derived radicals during γ-irradiation, surface-bound free radicals are formed. These radicals attack the adsorbed PPO centerblock, forming new covalent bonds between the surface and polymer.

The stability of the immobilized PEO layer was verified by triblock resistance to elution by SDS, and adequate layer uniformity was verified by fibrinogen repulsion. Incubation of uncoated or triblock-coated microspheres with nisin produced a significant positive change in zeta potential (surface charge), as a result of adsorption of the cationic peptide (Figure 5).

In sequential adsorption experiments, the introduction of anionic fibrinogen to nisin-loaded triblock layers caused the zeta potential to become more negative (Figure 5). This change is consistent with partial elution of nisin and/or location of fibrinogen at the interface. The magnitude of these changes was substantially greater at uncoated microspheres than with triblock-coated silica. These results confirmed that nisin integrates into the covalently-stabilized PEO layers, rather than competitively displacing the F108 triblocks from the surface. Entrapped nisin was also observed to be substantially more resistant to elution in the presence of fibrinogen than when adsorbed at an uncoated hydrophobic surface.

Retention of the capacity for blood protein repulsion by a nisin-loaded PEO brush layer is clearly shown in recent results from our lab, recorded with OWLS (Figure 6). Immobilized PEO layers were produced on OWLS sensor chips by first modifying the cleaned chip surface with TCVS vapor, and then coating with F108 as outlined above (*20*, *27*). A large change in adsorbed mass was observed upon introduction of fibrinogen to an uncoated hydrophobic OWLS sensor, consistent with formation of a monolayer. In contrast, sensors coated with an immobilized F108 layer or, notably, a nisin-loaded PEO layer, exhibit practically no adsorption of fibrinogen.

Closely related experiments were performed with pendant PEO layers formed on medical-grade polymer surfaces by adsorption and γ-irradiation of PEO-polybutadiene-PEO triblock surfactants (*7*, *21*, *28*), using a variation of the method described above to covalently stabilize the triblocks. The PEO-coated and uncoated polyurethane surfaces were challenged individually or sequentially with nisin and fibrinogen, as above, and then analyzed with time-of-flight secondary ion mass spectrometry (TOF-SIMS) and robust principal components analysis (PCA).

Fibrinogen-contacted polyurethane surfaces, with or without nisin, were statistically indistinguishable on both uncoated polymer surfaces. This result is consistent with nearly complete displacement or coverage of the previously adsorbed nisin by fibrinogen. In contrast, however, the nisin-loaded PEO layers remained essentially unchanged upon challenge with fibrinogen.

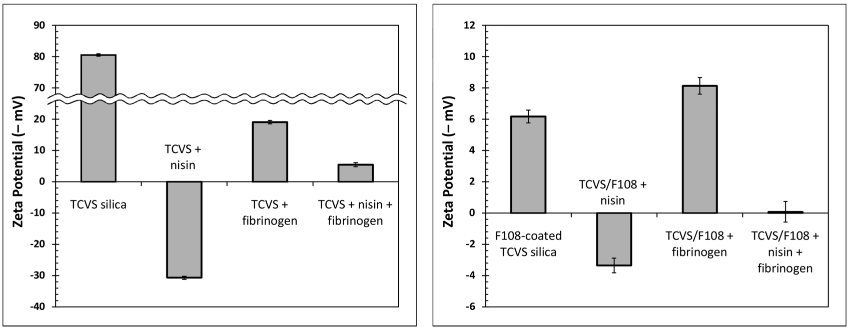

Figure 5. Zeta potential of hydrophobic silica microspheres with and without immobilized F108 triblocks, after individual or sequential adsorption of nisin and fibrinogen. Loss of positive charge upon challenge with fibrinogen is consistent with partial elution or competitive desorption of nisin. Adapted with permission from reference (20). Copyright © 2010 Elsevier, Inc.

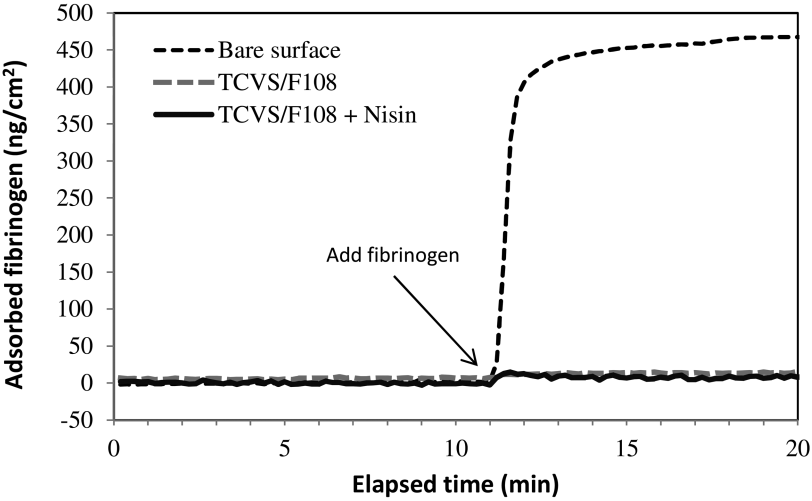

Figure 6. Fibrinogen adsorption on TCVS-modified OWLS sensors with and without a Pluronic® F108 coating stabilized by γ-irradiation. Adsorption of fibrinogen is completely abolished on the F108-coated surface, and is not affected by the presence of entrapped nisin in the brush.

These results clearly indicate that the PEO layer retains its ability to repel fibrinogen, independent of the presence of nisin. Importantly, these results support the notion that the elution profile of a peptide entrapped in PEO and placed in the presence of blood protein may be accurately described as a function of peptide properties and PEO layer thickness, and is not strongly affected by interaction with blood proteins. Further research on the integration and function of nisin and other small peptides in PEO is continuing in our lab.

We are currently quantifying the kinetics of nisin adsorption, desorption and clustering in PEO, and evaluating the retention of antibacterial activity at nisin-loaded PEO layers. However, in order to characterize the molecular origins of peptide entrapment among PEO chains, and thus enable the broader application of this effect for peptide drug storage and release strategies, we are turning to the use of well-characterized synthetic peptides with highly-controllable structural attributes.

Molecular Origins of Peptide Entrapment within Pendant PEO Layers

Background and Approach

It is reasonable to expect that, for a peptide size giving rise to the possibility of adsorption to a PEO brush layer, the molecular structure and amphiphilic character of the peptide will primarily determine its adsorption affinity for the PEO layer. In particular, at sufficiently high PEO chain density, protein rejection capacity is determined by protein size relative to the average distance between PEO chains (*4*, *10*). Thus we expect that a well-ordered, compact protein will enter the PEO brush more readily than a protein of similar size which adopts a less ordered, less compact form.

However, we do not expect that *retention* of a peptide or protein in the PEO phase is solely determined by size. Experimental and theoretical evidence described above indicates a potential for favorable protein-PEO associations within a PEO brush, due to the formation of a more hydrophobic phase in the brush. While a stable, compact solution structure may facilitate peptide insertion into the PEO layer, we expect that stability of that integration will be increased for more amphiphilic peptides, due to favorable associations between the peptide and the semi-hydrophobic interior of the brush (Figure 7).

Also depicted in Figure 7 is the possibility that transitions of an entrapped peptide from an ordered to a disordered form could be used to alter the rate of elution from the brush. Such a transition could be caused by a natural conformational change in a peptide as it interacts with the PEO brush, or could be engineered by conjugation of a responsive polymer to an otherwise stable therapeutic peptide. Various novel “smart” drug storage strategies could be developed based on induced structural transitions. For example, a peptide drug might be loaded into a PEO layer as a brush-penetrating helix, then “switched” into a bulky, disordered coil to hold it in place.

Later, another stimulus (e.g. a pH or temperature change) could reverse this transition, and rapidly release the peptide; alternatively, hindered desorption of the disordered form could provide a controlled, slow release. Studies to characterize such techniques are currently underway in our laboratory, and some early results are briefly summarized below.

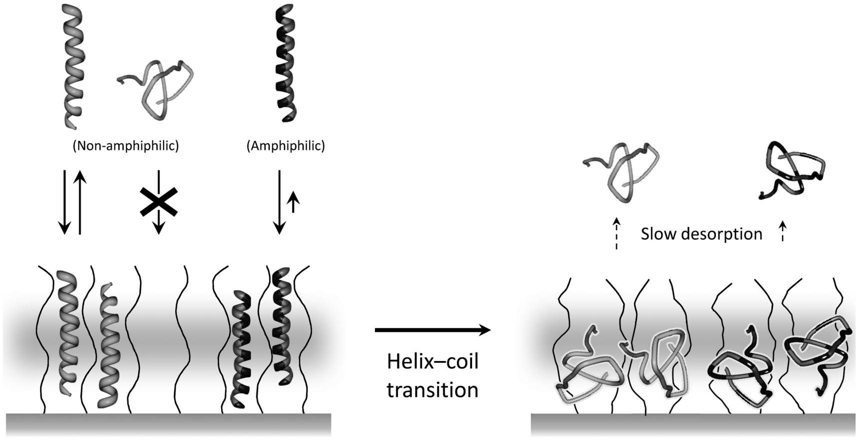

Figure 7. Schematic illustration of proposed effects of peptide structure and amphiphilicity on brush integration and desorption. More compact peptide conformations are expected to integrate and desorb readily, while less compact forms will be excluded. Amphiphilic peptides are expected to be entrapped more stably in the more hydrophobic inner region of the brush (shaded gray). Helix-coil transitions of responsive peptides may anchor them in the brush and substantially slow the rate of desorption, potentially enabling novel storage and release strategies for peptides or other molecules conjugated to peptide anchors.

We can begin to test these concepts by quantifying the rate and extent of adsorption and elution of selected natural and synthetic peptides, of similar size and well characterized structure, at an immobilized PEO brush layer. Peptide affinity for the PEO layer can be quantified in each case by application of a history dependent model (*24*), as described above. Using this model, several kinetic parameters can be determined, including the intrisnsic rate of peptide adsorption to the PEO layer, and a "cavity function" from which the relative mobility of the peptides within the PEO layer can be derived.

We expect that a peptide which is associated with the PEO chains will show less lateral mobility ("clustering") than a peptide exhibiting weaker interactions with the brush. The rates of peptide desorption (elutability) from loosely and tightly bound states within the PEO layer can also be derived using this model. A fundamental knowledge of these kinetic parameters will support the deliberate design of peptide/brush systems that exhibit desirable elution profiles or other properties.

Current Work

With a view toward gaining a better quantitative understanding of the molecular origins of peptide entrapment among PEO chains, we are investigating the adsorption and elution of three synthetic, 24-residue peptides with well-characterized, controllable structural attributes (Figure 8). The synthetic peptides $(Glu)_{24}$ and $(Lys)_{24}$ are homopolymers with regular structures that can extend the full length of the peptide (*29*). As with natural proteins, the solution pH, ionic strength, polarity, and peptide concentration can be modulated to adjust the homopolymer conformation from compact α-helix to a variety of "disordered" states (*30*, *31*).

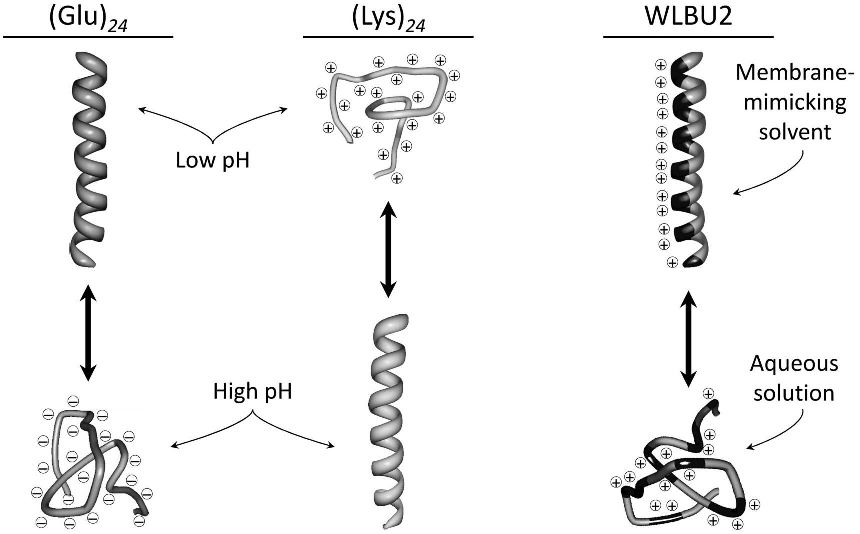

Figure 8. Schematic diagram of helix-coil transitions of synthetic polypeptides currently being studied in our laboratory. Depending on solution conditions, the $(Glu)_{24}$ and $(Lys)_{24}$ will adopt compact α-helical forms or disordered, highly-charged conformations. WLBU2 carries a high net positive charge, and adopts helical or disordered conformations in response to the solution polarity.

However, very recent advances in molecular modeling and analytical instrumentation (e.g. UV resonance Raman spectroscopy) indicate the existence of complex and fluid mixtures of regular structures in "random" coil peptides under different solution conditions (*30–33*). All peptide integration and elution experiments must be mindful of the potential confounding effects caused by regular structures which may be found in some "random" conformations.

WLBU2 is an engineered, cationic amphiphilic peptide (CAP) with 13 positively-charged arginine residues, and 11 hydrophobic valine or tryptophan residues. It shows substantial promise for clinical applications, due to its wide spectrum antimicrobial activity against both Gram-negative and Gram-positive bacteria under physiological conditions (*34–37*). Segregation of the positively-charged and hydrophobic groups onto opposing faces of an

α-helix confers the ability to disrupt bacterial cell membranes, physically killing the bacteria in a manner similar to nisin. Moreover, in addition to its high, broad-spectrum potency in blood, it has been shown to retain its antimicrobial activity when immobilized by a number of methods at solid surfaces (*38–41*).

While it shows no appreciable stable structure in phosphate buffer, WLBU2 exhibits 81% α-helix in membrane-mimetic solvents (e.g., 30% trifluoroethanol in phosphate buffer). Unlike WLBU2, which is highly amphiphilic, neither $(Lys)_{24}$ nor $(Glu)_{24}$ are amphiphilic. Thus, WLBU2 serves both as a good control for the effects of amphilicity on peptide integration into brush layers, and as a clinically-relevant application for this research. We are currently studying the elution kinetics and antimicrobial activity of WLBU2 entrapped in PEO brushes. Results of these experiments will contribute to the subject of future reports.

Conclusions

Information relating peptide structure and amphiphilicity to peptide adsorption, desorption and lateral mobility within PEO will form a quantitative basis for testing new hypotheses and new strategies for drug loading and release from polymer brush layers. An experimentally-based, quantitative understanding of the adsorption and function of peptides at PEO layers does not currently exist, but well-controlled studies are currently underway in our laboratory.

Possible applications of brush-integrated peptides may include novel biofunctional surface coatings for medical devices, peptide-anchored drug release applications, and molecular sorting and purification systems for small molecules and peptides. This research will also directly support further discoveries and an improved understanding of the interactions between peptides or small proteins and otherwise protein-repellent pendant polymer brush layers.

Acknowledgments

The authors thank Julie Auxier, Justen Dill and Marsha Lampi of Oregon State University for experimental contributions and useful discussions. We also thank Allvivo Vascular Inc. for invaluable assistance on this research over the last several years. This work was supported in part by the National Institute of Biomedical Imaging and Bioengineering (Grant No. R01EB011567). The content is solely the responsibility of the authors and does not necessarily represent the official views of NIBIB or the National Institutes of Health.

References

1. McPherson, T. B.; Shim, H. S.; Park, K. *J. Biomed. Mater. Res.* **1997**, *38*, 289–302.
2. McPherson, T.; Kidane, A.; Szleifer, I.; Park, K. *Langmuir* **1998**, *14*, 176–186.
3. Archambault, J. G.; Brash, J. L. *Colloids Surf., B* **2004**, *33*, 111–120.

4. Unsworth, L. D.; Sheardown, H.; Brash, J. L. *Biomaterials* **2005**, *26*, 5927–5933.
5. Unsworth, L. D.; Sheardown, H.; Brash, J. L. *Langmuir* **2008**, *24*, 1924–1929.
6. de Gennes, P. G. *Adv. Colloid Interface Sci.* **1987**, *27*, 189–209.
7. Tseng, Y.-C.; McPherson, T.; Yuan, C. S.; Park, K. *Biomaterials* **1995**, *16*, 963–972.
8. Malmsten, M.; Emoto, K.; Van Alstine, J. M. *J. Colloid Interface Sci.* **1998**, *202*, 507–517.
9. Rovira-Bru, M.; Giralt, F.; Cohen, Y. *J. Colloid Interface Sci.* **2001**, *235*, 70–79.
10. Katira, P.; Agarwal, A.; Hess, H. *Adv. Mater.* **2009**, *21*, 1599–1604.
11. Halperin, A. *Langmuir* **1999**, *15*, 2525–2533.
12. Sheth, S. R.; Leckband, D. *Proc. Natl. Acad. Sci. U.S.A.* **1997**, *94*, 8399–8404.
13. Fang, F.; Satulovsky, J.; Szleifer, I. *Biophys. J.* **2005**, *89*, 1516–1533.
14. Wiedemann, I.; Breukink, E.; van Kraaij, C.; Kuipers, O. P.; Bierbaum, G.; de Kruijff, B.; Sahl, H.-G. *J. Biol. Chem.* **2001**, *276*, 1772–1779.
15. Breukink, E.; de Kruijff, B. *Nat. Rev. Drug Discovery* **2006**, *5*, 321–323.
16. Sun, Z.; Zhong, J.; Liang, X.; Liu, J.; Chen, X.; Huan, L. *Antimicrob. Agents Chemother.* **2009**, *53*, 1964–1973.
17. Tai, Y.-C.; Joshi, P.; McGuire, J.; Neff, J. A. *J. Colloid Interface Sci.* **2008**, *322*, 112–118.
18. Tai, Y.-C.; McGuire, J.; Neff, J. A. *J. Colloid Interface Sci.* **2008**, *322*, 104–111.
19. Li, J.-T.; Caldwell, K. D. *Colloids Surf., B* **1996**, *7*, 9–22.
20. Ryder, M. P.; Schilke, K. F.; Auxier, J. A.; McGuire, J.; Neff, J. A. *J. Colloid Interface Sci.* **2010**, *350*, 194–199.
21. Schilke, K. F.; McGuire, J. *J. Colloid Interface Sci.* **2011**, *358*, 14–24.
22. Calonder, C.; Tie, Y.; Van Tassel, P. R. *Proc. Natl. Acad. Sci. U.S.A.* **2001**, *98*, 10664–10669.
23. Calonder, C.; Van Tassel, P. R. *Langmuir* **2001**, *17*, 4392–4395.
24. Tie, Y.; Calonder, C.; Van Tassel, P. R. *J. Colloid Interface Sci.* **2003**, *268*, 1–11.
25. Joshi, O.; Lee, H. J.; McGuire, J.; Finneran, P.; Bird, K. E. *Colloids Surf., B* **2006**, *50*, 26–35.
26. Park, K.; Shim Hong, S.; Dewanjee Mrinal, K.; Eigler Neal, L. *J. Biomater. Sci., Polym. Ed.* **2000**, *11*, 1121–1134.
27. Popat, K. C.; Johnson, R. W.; Desai, T. A. *Surf. Coat. Technol.* **2002**, *154*, 253–261.
28. Kidane, A.; McPherson, T.; Shim, H. S.; Park, K. *Colloids Surf., B* **2000**, *18*, 347–353.
29. Adiga, S. P.; Brenner, D. W. *Macromolecules* **2007**, *40*, 1342–1348.
30. Finke, J. M.; Jennings, P. A.; Lee, J. C.; Onuchic, J. N.; Winkler, J. R. *Biopolymers* **2007**, *86*, 193–211.
31. Ma, L.; Ahmed, Z.; Asher, S. A. *J. Phys. Chem. B* **2011**, *115*, 4251–4258.

32. Mikhonin, A. V.; Myshakina, N. S.; Bykov, S. V.; Asher, S. A. *J. Am. Chem. Soc.* **2005**, *127*, 7712–7720.
33. Oladepo, S. A.; Xiong, K.; Hong, Z.; Asher, S. A. *J. Phys. Chem. Lett.* **2011**, *2*, 334–344.
34. Deslouches, B.; Gonzalez, I. A.; DeAlmeida, D.; Islam, K.; Steele, C.; Montelaro, R. C.; Mietzner, T. A. *J. Antimicrob. Chemother.* **2007**, *60*, 669–672.
35. Deslouches, B.; Islam, K.; Craigo, J. K.; Paranjape, S. M.; Montelaro, R. C.; Mietzner, T. A. *Antimicrob. Agents Chemother.* **2005**, *49*, 3208–3216.
36. Deslouches, B.; Phadke, S. M.; Lazarevic, V.; Cascio, M.; Islam, K.; Montelaro, R. C.; Mietzner, T. A. *Antimicrob. Agents Chemother.* **2005**, *49*, 316–322.
37. Skinner, M. C.; Kiselev, A. O.; Isaacs, C. E.; Mietzner, T. A.; Montelaro, R. C.; Lampe, M. F. *Antimicrob. Agents Chemother.* **2010**, *54*, 627–636.
38. Costa, F.; Carvalho, I. F.; Montelaro, R. C.; Gomes, P.; Martins, M. C. L. *Acta Biomater.* **2011**, *7*, 1431–1440.
39. Gonzalez, I. A.; Wong, X. X.; De Almeida, D.; Yurko, R.; Watkins, S.; Islam, K.; Montelaro, R. C.; El-Ghannam, A.; Mietzner, T. A. *Nature Precedings* **2008**.
40. Montelaro, R. C.; Mietzner, T. A. U.S. Patent 6,887,847, 2005.
41. Onaizi, S. A.; Leong, S. S. J. *Biotechnol. Adv.* **2011**, *29*, 67–74.

Chapter 30

Polyacrylamide: Evaluation of Ultralow Fouling Properties of a Traditional Material

Lingyun Liu,* Qingsheng Liu, and Anuradha Singh

Department of Chemical and Biomolecular Engineering,
University of Akron, Akron, Ohio 44325
***E-mail: lliu@uakron.edu. Phone: (330) 972-6187. Fax: (330) 972-5856**

Publication Date (Web): December 12, 2012 | doi: 10.1021/bk-2012-1120.ch030

Antifouling properties of a traditional material, polyacrylamide, were evaluated comprehensively in this work to answer two questions: 1. Can polyacrylamide achieve ultralow fouling surfaces (< 50 pg/mm^2 protein adsorption)? 2. How robust is the antifouling ability of the polyacrylamide coating when the environment factors (pH, ionic strength, complex media) change? Polyacrylamide brushes were grafted on gold surfaces via surface-initiated atom transfer radical polymerization. Protein adsorption from single protein solutions of fibrinogen, bovine serum albumin, and lysozyme, diluted and undiluted human blood serum, diluted and undiluted human blood plasma, was studied by surface plasmon resonance. With the optimized polymer film thickness, the adsorption amount of all three single proteins on polyacrylamide-grafted surfaces was < 3 pg/mm^2. The nonspecific adsorptions from 10% plasma, 10% serum, 100% plasma, and 100% serum onto the polyacrylamide-grafted surfaces were 5, 6.5, 17, and 28 pg/mm^2, respectively. The grafted surfaces remained highly resistant to protein adsorption in a wide range of tested pH values (5.2-8.4) and ionic strengths (10-150 mM). The polyacrylamide-grafted surfaces were also strongly resistant to adhesion from bovine aortic endothelial cells. This work demonstrates that polyacrylamide is a robust ultralow fouling material and it is a promising alternative to the traditional ethylene glycol-based antifouling materials.

In Proteins at Interfaces III State of the Art 2012; Horbett, T., et al.;
ACS Symposium Series; American Chemical Society: Washington, DC, 2012.

Introduction

Antifouling materials and surfaces are critical to many biomedical and engineering applications (*1*). Initial protein adsorption on implanted medical devices may lead to the formation of fibrous capsules around implants and the eventual device failure. Adsorption of blood proteins on drug-carrying nanoparticles leads to recognition and fast clearance by the body, resulting in reduced circulation time and poor therapeutic efficiency. Nonspecific adsorption on biosensor chips may cause false alarm and decrease the sensor sensitivity. Marine biofouling on ship hulls may significantly increase hydrodynamic drag force when ships move through water and decrease their speed. Fibrinogen adsorption on material surfaces, even at low levels, was able to mediate platelet adhesion, potentially leading to thrombosis (*2*, *3*). A fibrinogen (Fg) adsorption level below 50 pg/mm^2 is essential to inhibit platelet adhesion and improve hemocompatibility of biomaterials; such surfaces were defined as ultralow fouling surfaces (*4*).

Currently the most commonly used antifouling materials are poly(ethylene glycol) (PEG), oligo(ethylene glycol) (OEG), and their derivatives (*4–7*). The major limitation of the ethylene glycol-based materials is their susceptibility to oxidative degradation, especially in the presence of transition metal ions (*8–11*), thus limiting their long-term or *in vivo* applications. Previous work reported that the surfaces modified with or without PEG polymers exhibited same degree of fouling *in vivo* (*12*). The tri(ethylene glycol)-terminated self-assembled monolayers (SAMs) failed to resist fibroblast adhesion after 7 days in culture (*13*). Other alternative antifouling materials include hydrophilic polymers such as polysaccharides (*13*, *14*), polypeptoids (*15*), and poly(β-peptoid)s (*16*), and zwitterionic polymers such as poly(sulfobetaine methacrylate) (pSBMA) (*17*), poly(carboxybetaine methacrylate) (pCBMA) (*18*), poly(2-methacryloyloxyethyl phosphorylcholine) (*19*), and polyampholyte (*20*).

The purpose of this work is to investigate anti-biofouling properties of polyacrylamide, a traditional material that has been used in sodium dodecyl sulfate polyacrylamide gel electrophoresis (SDS-PAGE) for a long time. Besides protein separation, polyacrylamide hydrogel has been used for other applications such as drug release and water-oil separation, due to its hydrophilic nature (*21–23*). Only a few work used polyacrylamide as a surface coating material to reduce biofouling, as summarized in Table 1 (*24–28*). These studies show that the polyacrylamide surface coating was low-fouling, being able to suppress protein adsorption from single proteins such as bovine serum albumin (BSA), lysozyme (Lyz), fibrinogen (Fg), and immunoglobulin. However, the potential of polyacrylamide as an antifouling coating has not been fully explored. It is not clear whether polyacrylamide can realize ultralow fouling surfaces (i.e., < 50 pg/mm^2 protein adsorption) and how robust the antifouling ability of the polyacrylamide coating is when the environment factors (e.g., pH, ionic strength, complex media) change. For instance, many biomedical applications require material surfaces in direct contact with complex media such as blood serum or plasma. It is important to note that resistance to protein adsorption from complex media is much more demanding than from single protein solutions. Surfaces that can resist protein adsorption from single protein solutions may not be as resistant to adsorption from complex media (*29*).

Table 1. Polyacrylamide as an Antifouling Coating[a]

substrate	*method of coating*	*antifouling properties*	*method of characterization*
poly-urethane (*24*)	glow-discharge treatment and graft polymerization	reduced adsorption of BSA and IgG; suppressed platelet adhesion	^{125}I -protein adsorption assay LDH assay, SEM
PDMS (*25*)	ATRP	lysozyme adsorption reduced by ~ 20-fold	FTIR
silicon wafer (*26*)	ATRP	strong reduction in microbial adhesion	count number
silicon rubber (*27*)	photochemical immobilization	reduced adsorption of Fg and IgG; inhibited fibroblast adhesion; no difference in thickness of fibrous capsule	^{3}H-protein adsorption assay MTT assay subcutaneous implant in rat for 2 or 6 wk
ethylene-propylene rubber (*28*)	laser-induced grafting	reduced macrophage adhesion in vivo; thinner fibrous capsule around the implant	SEM, implant in rabbit deep intramuscular and peritoneal layers for 8 wk

[a] BSA: bovine serum albumin, IgG: immunoglobulin G, LDH: lactic acid dehydrogenase, SEM: scanning electron microscopy, PDMS: poly(dimethylsiloxane), ATRP: atom-transfer radical polymerization, FTIR: Fourier transform infrared spectroscopy, MTT: 3-(4,5-dimethylthiazol-2-yl)-2,5-diphenyl tetrazolium bromide

Here we report the ultralow biofouling properties of polyacrylamide brushes grafted on gold surfaces via surface-initiated atom-transfer radical polymerization (ATRP). Protein adsorptions from single protein solutions of Fg, BSA, and Lyz, complex media including diluted serum, undiluted serum, diluted plasma, and undiluted plasma were studied by a surface plasmon resonance (SPR) sensor. We further investigated the effect of pH and ionic strength on protein resistance of the polyacrylamide-grafted surfaces. Mammalian cell adhesion on the polyacrylamide-grafted gold surfaces was also studied.

Self-assembled monolayer (SAM) of thiol on gold is a well-established model system to engineer surface properties at the molecular level. In this work, gold surfaces coupled with SAMs of the ATRP initiator, were used to graft polyacrylamide brushes on surfaces. Development of ultralow fouling coatings on gold is also practically very important. Gold has been applied for applications such as electrodes for a drug delivery microchip and for neural implants (*30*, *31*). For the drug delivery microchip, active drug is stored in a microreservoir covered with a gold membrane electrode and released by electrochemical dissolution of the thin gold membrane. Significant biofouling *in vivo*, however, may affect drug-eluting capability of the device (*32*). For the neural device application, biofouling on electrodes causes increased impedance, which makes it difficult to record electrical signals (*31*). Biofouling on gold hence presents major concerns for both applications.

Materials and Methods

Materials

Acrylamide (99.9%) was obtained from Alfa Aesar. 1,1,4,7,7-pentamethyldiethylenetriamine (PMDETA, 99+%) and copper(I) bromide (CuBr, 98%) were purchased from Acros Organics. 2-bromoisobutyryl bromide (BIBB, 98%), 11-mercapto-1-undecanol (99%), tetrahydrofuran (THF, 99%), and methanol (99.8%) were purchased from Sigma-Aldrich. The absolute 200 proof ethanol was obtained from PHARMCO-AAPER. Phosphate-buffered saline (PBS, pH 7.4, 10 mM, 138 mM NaCl, 2.7 mM KCl), sodium phosphate dibasic (Na_2HPO_4), sodium chloride, and potassium chloride were obtained from Sigma-Aldrich. Potassium phosphate monobasic (KH_2PO_4) was purchased from Fluka. Human plasma fibrinogen (Fg) was purchased from EMD Biosciences. Bovine serum albumin (BSA) and chicken egg white lysozyme (Lyz) were obtained from Sigma-Aldrich. Pooled human blood plasma and serum were obtained from BioChemed Services (Winchester, VA). Bovine aortic endothelial cells (BAECs) were kindly supplied by Prof. Shaoyi Jiang (University of Washington). Water used in all experiments, with a minimum resistivity of 18.0 MΩ·cm, was purified using a Millipore system. Dulbecco's modified Eagle medium (DMEM, with 4500 mg/L glucose, 4.0 mM L-glutamine, and 110 mg/L sodium pyruvate) was obtained from Thermo Scientific. All other cell culture reagents were purchased from Invitrogen.

Surface-Initiated ATRP of Acrylamide

ω-Mercaptoundecyl bromoisobutyrate, the ATRP initiator, was synthesized by the reaction of 11-mercapto-1-undecanol and 2-bromoisobutyryl bromide using a previously published method (*33*). The initiator structure was confirmed by ^1H NMR.

Polyacrylamide brushes were grafted on SPR sensing chips by a two-step procedure: formation of SAMs of ω-mercaptoundecyl bromoisobutyrate on gold and surface-initiated ATRP of acrylamide. SPR sensing chips were prepared on clean glass slides by deposition of an adhesion-promoting chromium layer (2 nm) followed by a surface plasmon-active gold layer (48 nm) using e-beam evaporation. To form the initiator SAMs on gold, SPR chips were rinsed by acetone, ethanol and water, treated under UV/ozone for 20 min, cleaned by water and ethanol, dried, and finally soaked in 1 mM ω-mercaptoundecyl bromoisobutyrate in ethanol overnight. Chips were then rinsed sequentially with THF and ethanol, and dried with a gentle stream of air. For the ATRP procedure, CuBr (0.45 mmol) and two SPR chips modified with initiator SAMs were placed in a 50 mL reaction tube, protected under N_2, and sealed with a rubber septum stopper. A degassed solution (mixture of 3 ml water and 7 ml methanol) with PMDETA (1.34 mmol) and acrylamide (28.14 mmol) was then transferred to the tube under N_2 protection. After polymerization, the chips were rinsed with ethanol, PBS, and water, and kept in PBS before use.

Surface Characterization

The dry film thickness of the polyacrylamide layer on gold was measured in air by an α-SE ellipsometer (J. A. Woollam Co., Lincoln, NE) with a 632.8 nm He-Ne laser. Before the ellipsometry measurements, polyacrylamide-grafted chips were washed in water and dried with an air flow. A refractive index of 1.45 was used for the polymer layer. Static contact angles of water on the initiator SAM or polyacrylamide-grafted gold surfaces were measured under ambient conditions, using a Rame-Hart goniometer (model 100-00, Mountain Lakes, NJ). Ellipsometry, which averages the response over a macroscopic area, is a commonly used method to measure thickness of polymer brushes grafted on surfaces via ATRP (*34*, *35*).

Protein Adsorption

A custom-built four-channel SPR sensor was used to evaluate protein adsorption. Our SPR sensor measures change in the resonant wavelength at a fixed light incident angle. During an SPR experiment, the polyacrylamide-grafted SPR chip was attached to the base of the prism, with a layer of refractive index matching fluid (Cargille) in-between to ensure optical contact. A pre-adsorptive baseline of the sensorgram was first established by flowing PBS buffer over the chip surface for 5-10 min. Single protein solution (1mg/mL) of Fg, BSA, or Lyz, 10% serum in PBS, 100% serum, 10% plasma in PBS, or 100% plasma was then run through different channels for 10 min. The chip surface was finally flushed with buffer for 5 min to establish the post-adsorptive baseline. A flow rate of 0.05 mL/min was used for all experiments. Bare gold surfaces without any modification were used as control for comparison.

To study the pH and ionic strength effect on protein adsorption, phosphate buffers with different pH values (5.2, 6.4, 7.4, and 8.4) and ionic strengths (10 mM and 150.7 mM) were used to prepare Fg solutions. SPR experiments follow the same procedure as described above except using customized buffers. The 10 mM phosphate buffers with different pH values were prepared by mixing Na_2HPO_4 and KH_2PO_4 solutions with appropriate ratios. Buffers with high ionic strength of 150.7 mM were prepared by adding 138 mM NaCl and 2.7 mM KCl into the 10 mM buffers.

Wavelength shift between pre-adsorptive and post-adsorptive baselines was finally converted to the amount of the adsorbed protein. A 1-nm SPR wavelength shift at 750 nm for our sensor is equivalent to 150 pg/mm^2 adsorbed proteins

(*16*). The same conversion factor was used when evaluating adsorption from different protein solutions, under the widely accepted recognition that different proteins generally do not have very different refractive index increments (dn/dc) (*36*). A consensus dn/dc value (0.18–0.19 mL/g), verified by many experimental and simulation work, has been commonly adopted and also used in our studies to derive the conversion factor for our SPR sensor (*16*, *36*).

Cell Adhesion

BAECs were passaged once a week and maintained in continuous growth in tissue culture polystyrene flasks at 37 °C in a 5% CO_2 humidified atmosphere. The culture medium consists of DMEM, 10% fetal bovine serum (FBS), 1% nonessential amino acids, 1% sodium pyruvate, and 2% penicillin streptomycin. The polyacrylamide-grafted or bare gold-coated glass substrates were placed in individual wells of a 24-well plate and rinsed with sterile PBS three times. Cells were harvested by trypsinization with trypsin/ethylenediaminetetraacetic acid (0.05%/0.53 mM) and washed once with PBS. The cell pellet was then diluted in the culture medium to reach a final concentration of 10^5 cells/mL. Two milliliters of cell suspension were subsequently added into each well and incubated with the samples for 24 h, 48 h, 7 d, or 14 d at 37°C. For the 1- or 2-wk incubation, culture medium was refreshed every 3 days. Phase-contrast micrographs were acquired using an Olympus IX81 inverted microscope (10 ×).

Results and Discussion

Polyacrylamide coatings on gold surfaces were prepared following a 2-step procedure (Scheme 1). First, initiator SAMs of ω-mercaptoundecyl bromoisobutyrate (Br-thiol) were formed on gold surfaces. Second, polyacrylamide brushes were synthesized via surface-initiated atom-transfer radical polymerization (ATRP), an effective and convenient approach to achieve polymer brushes on surfaces with controlled thickness and well-defined structure (*37*). The bromine-based initiator was chosen for this work since bromide-carbon bond can be easily cleaved thus ensure fast initiation (*38*). As a controlled living method, ATRP provides much more uniform polymer chains compared to the conventional radical polymerization methods. For example, the polydispersity index (PDI) of poly (methyl methacrylate) synthesized from ATRP is much smaller (PDI < 2) compared to those synthesized from conventional radical polymerization (PDI > 6) (*39*).

Previous reports show that the thickness of polymer brushes of an antifouling material significantly affects its antifouling properties (*34*, *40*). To determine the optimal polyacrylamide film thickness with the best antifouling performance, polyacrylamide brushes with different thicknesses were prepared by controlling the ATRP polymerization time. Figure 1a shows the dependence of polyacrylamide film thickness on the polymerization time. The thickness of film, measured by ellipsometry, increased dramatically in the early stages of the reaction and rose up slowly later in the reaction. The insensitiveness of polyacrylamide layer thickness to reaction time at later stages of polymerization may result from termination caused by radical combination, loss of active catalyst, or hindered mass transport of monomer to radical. Radical combination is particularly a problem for surface polymerization because the reactive groups are in close proximity on surfaces (*41*). Similar phenomena have been observed by many other studies (*34*, *35*, *40*, *41*). It has to be noted that the coating thickness reported here is the dry film thickness. In an aqueous environment, polymer chains will become more extended and the film thickness will increase, due to strong polymer-water interactions.

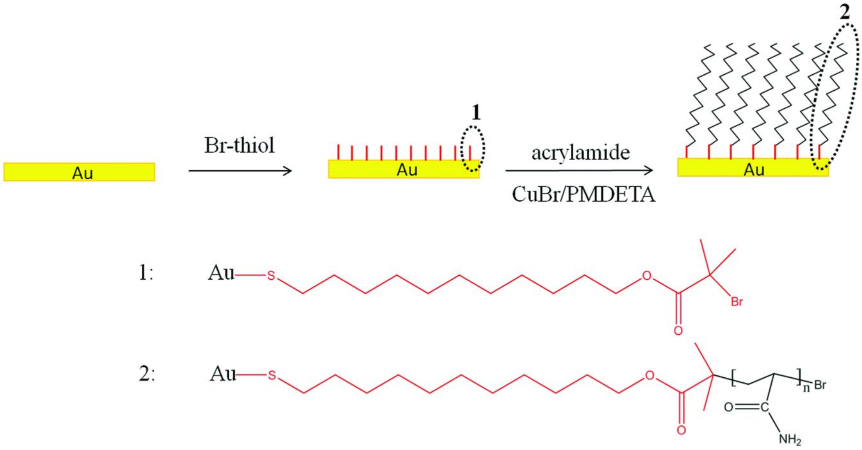

Scheme 1. Polyacrylamide grafted on gold via surface-initiated atom transfer radical polymerization.

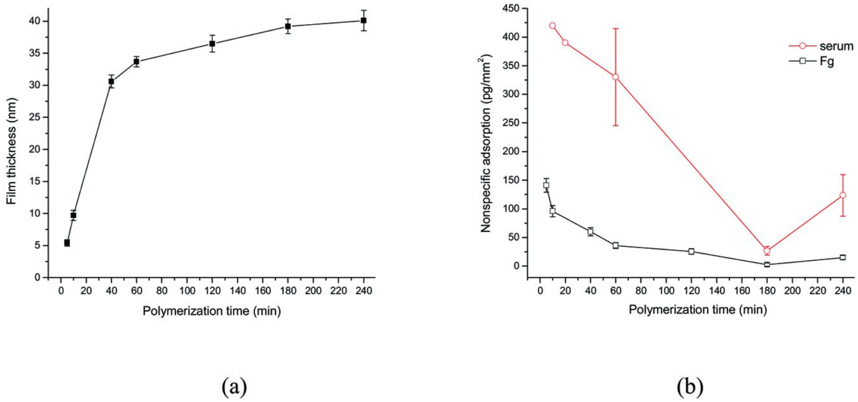

Figure 1. (a) Dependence of polyacrylamide film thickness on the polymerizaton time. Data are from reference (38). (b) Adsorption of 1 mg/mL fibrinogen in PBS and 100% human blood serum on the polyacrylamide-grafted surfaces with different film thicknesses.

Figure 1b shows nonspecific adsorption from 1mg/mL Fg solution or full serum as a function of polymerization time. As the reaction time increased from 5 min to 40 min, 1 h, 3 h, to 4 h, the amount of adsorbed Fg was 141, 60, 36, 2.5, and 15 pg/mm^2, respectively; meanwhile, the polyacrylamide film thickness was 5.4, 30.6, 33.7, 39.2, and 40.8 nm, respectively (*42*). Minimal Fg adsorption of 2.5 pg/mm^2 was found at the polymerization time of 3 h, with a medium film thickness of ~ 39.2 nm. The trend was even more obvious for nonspecific adsorption from serum, similarly with a minimal adsorption level observed at 3-h-polymerization.

For the thin polyacrylamide films, short polymer chains may not be able to form a surface hydration layer strong enough to resist protein adsorption. On the other hand, since polyacrylamide possesses both hydrogen donors and hydrogen acceptors, if polymer coatings are too thick, the long polyacrylamide chains may conformationally self-condense via inter- or intra-molecular hydrogen bonding. As a result, the polymer-water interactions were decreased, leading to weaker surface hydration and higher protein adsorption. Previous work by Zhao et al. shows that the similarly grafted poly(hydroxypropyl methacrylate) film on gold was very smooth and uniform at an intermediate polymer film thickness but becoming much rougher and less protein-resistant when the grafted film was thicker (*35*). From now on, unless otherwise specified, the polymerization time was fixed to 3 h to prepare polyacrylamide-grafted samples for studying contact angle, protein adsorption, and cell attachment.

Water contact angle of the initiator SAMs of the Br-thiol was 82°. After ATRP for 3 h, the polyacrylamide-grafted surfaces became much more hydrophilic, with a water contact angle of 14.8°, resulting from strong hydrogen bonding between amide groups of polyacrylamide and water molecules.

Protein adsorption on polyacrylamide-grafted gold surfaces was evaluated using a SPR sensor. Fg (340 kD, pI = 5.5), BSA (67 kD, pI = 4.7), and Lyz (14 kD, pI = 11.1), were used as model proteins in this work to study the adsorption from single protein solutions. These proteins cover a range of molecular weight, isoelectric point, and structural stability, and have been widely used to evaluate antifouling performance of a variety of materials (*4*, *6*, *16–18*). Representative SPR sensorgrams for adsorption of three proteins on polyacrylamide-grafted or bare gold surfaces were shown in Figure 2. The amounts of the adsorbed Fg, BSA, and Lyz on two surfaces were summarized in Table 2. It is evident that polyacrylamide-grafted surfaces strongly resist protein adsorption from single protein solutions, with the adsorbed mass for any of the three proteins less than 3 pg/mm^2, which is far below the ultralow fouling surface criteria of <50 pg/mm^2 protein adsorption (*4*). Fg adsorption on other existing antifouling materials such as PEG/OEG-based or zwitterionic pSBMA-grafted materials ranges from a few to 10 pg/mm^2, as determined by a similar SPR method (*18*, *43*, *44*). Therefore we conclude that polyacrylamide is as effective as PEG or pSBMA in suppressing protein adsorption from single protein solutions.

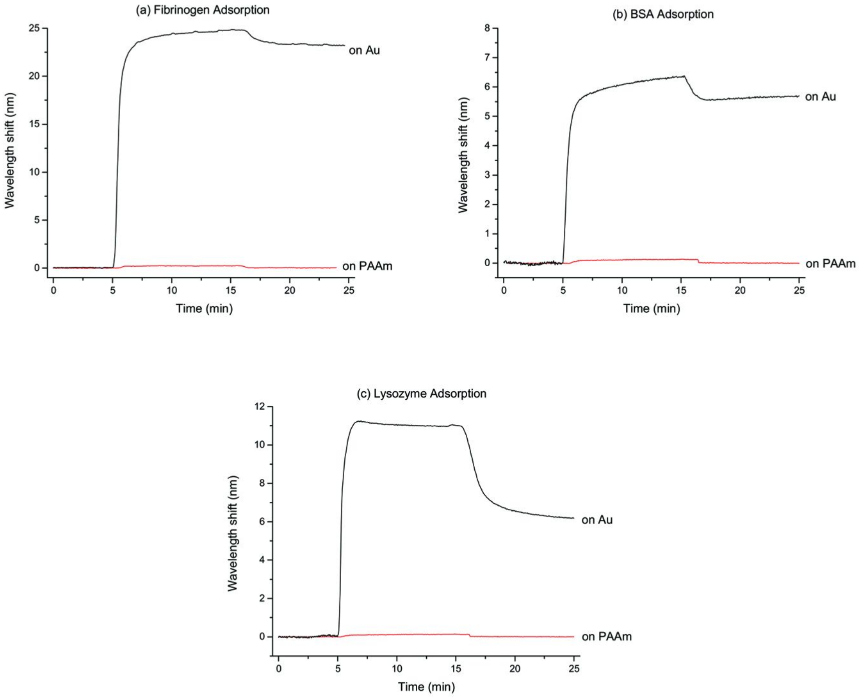

Figure 2. SPR sensorgrams showing protein adsorption onto the polyacrylamide (PAAm)-grafted or bare gold surfaces from (a) fibrinogen, (b) BSA, or (c) lysozyme solutions (1mg/mL, in PBS).

Table 2. Protein Adsorption Measured by SPR[a]

	adsorbed mass (pg/mm²)						
	single proteins [b]			*complex media*			
surface	*Fg*	*BSA*	*Lyz*	*10% plasma*	*10% serum*	*100% plasma*	*100% serum*
PAAm/ gold	2.5 (±1)	0 (±2)	2 (±2)	5 (±4)	6.5 (±6)	17 (±7)	28 (±9)
gold	3488 (±261)	833 (±177)	945 (±132)	1470 (±212)	1548 (±261)	1503 (±314)	1662 (±322)

[a] Average and standard deviation of three or more measurements. [b] Data are from reference (*38*).

To further evaluate the robustness of antifouling properties of the polyacrylamide-grafted gold surfaces, we studied how changes in pH value and ionic strength affected protein resistance of the polyacrylamide surfaces. Figure 3 shows that within the tested ranges of pH (5.2-8.4) and ionic strength (10-150mM), the polyacrylamide-grafted surfaces remained ultralow fouling, with protein adsorption levels all less than 10 pg/mm^2. PH value and ionic strength had no significant influence on protein adsorption on polyacrylamide-grafted surfaces. From this aspect, the polyacrylamide coating is advantageous compared to the coatings of zwitterionic polymers such as pCBMA, which presents significant pH and ionic strength dependence of protein adsorption due to the antipolyelectrolyte behavior of zwitterionic polymer and acid-base equilibrium at different pH values (*45*). For example, the pCBMA-grafted gold surface was nonfouling at pH 7.4 and ionic strength of 150 mM, but presented Fg adsorption of 256 pg/mm^2 at low ionic strength (10 mM, pH 7.4) and 160 pg/mm^2 at low pH (pH 5, ionic strength of 200 mM) (*45*). Considering that a primary amide does not become protonated or deprotonated under normal conditions (pKa < 1 for protonation; pKa > 15 for deprotonation), we expect our polyacrylamide coatings remain highly protein-resistant in a much wider range of pH values.

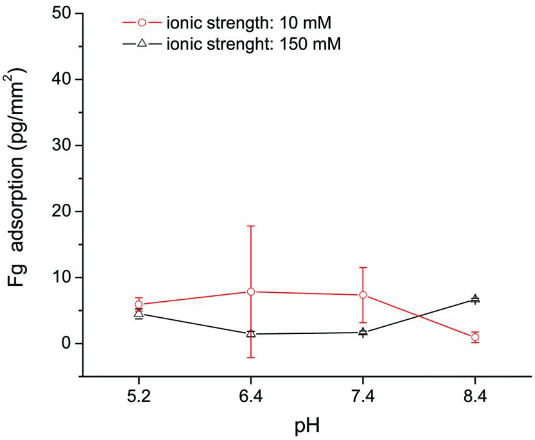

Figure 3. Effect of pH and ionic strength on fibrinogen adsorption on polyacrylamide-grafted gold surfaces.

The strong resistance of polyacrylamide surfaces to single protein adsorptions prompted us to study their resistance to adsorption from complex media. Blood plasma and serum contain hundreds of proteins, amino acids, sugars, and fat (*46*). Resistance to nonspecific adsorption from plasma and serum is much more demanding than to the single protein adsorption (*18*, *47*). The 10% serum and plasma are often utilized for medical diagnostics. Therefore, in this work we chose to test four complex media including 10% human blood serum, 100% human blood serum, 10% human blood plasma, and 100% human blood plasma. Representative SPR sensorgrams of complex media adsorption on polyacrylamide-grafted gold surfaces were shown in Figure 4. The nonspecific adsorption amounts on the polyacrylamide-grafted or bare gold surfaces were summarized in Table 2. Clearly, polyacrylamide-grafted surfaces strongly resist nonspecific adsorption from complex media, with the adsorbed mass from diluted or undiluted plasma or serum all below 50 pg/mm^2, indicating that the polyacrylamide-grafted gold surfaces are ultralow fouling to adsorption from complex media.

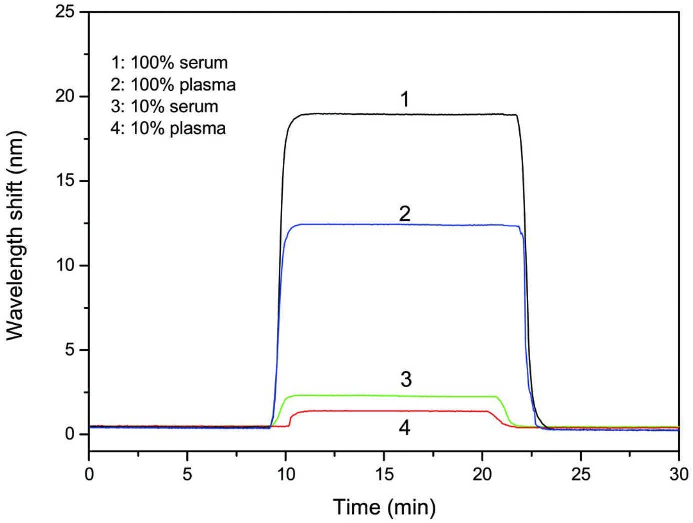

Figure 4. SPR sensorgrams showing nonspecific adsorption onto the polyacrylamide-grafted gold surfaces from 10% serum in PBS, 10% plasma in PBS, 100% serum, and 100% plasma. All serum and plasma are from human blood.

Here, the nonspecific adsorptions from full plasma and serum onto the polyacrylamide-grafted surfaces were 17 and 28 pg/mm^2 respectively, which are lower than those on the conventional OEG- or PEG-based surfaces (*18*, *47*) while comparable (if not better) than the zwitterionic pSBMA (*40*). It was reported previously that the poly(OEG-methacrylate)-grafted gold surfaces, produced via a similar SI-ATRP method, had ~ 100 pg/mm^2 and ~ 300 pg/mm^2 adsorption from human plasma and human serum, respectively, although they exhibited ultralow Fg adsorption (< 3 pg/mm^2) (*18*). The lowest adsorption on optimized zwitterionic pSBMA-grafted surfaces was 23.1 pg/mm^2 from human plasma and 60.9 pg/mm^2 from human serum (*40*).

Endothelial cells were cultured with polyacrylamide-grafted or bare gold-coated glass substrates in culture medium containing 10% FBS. On bare gold surfaces, cells attached, proliferated, developed into confluent monolayers after 1-wk culture, and remained confluent afterwards; In contrast, the polyacrylamide-grafted gold surfaces remained resistant to cell attachment even after culturing for 2 weeks (Figure 5). Cell resistance of the polyacrylamide coatings correlates well with their ultralow protein fouling feature. Attachment of anchorage-dependent cells on surfaces is dictated by the interactions between integrins on cell membranes and adhesive proteins on surfaces. Polyacrylamide-grafted surfaces do not support protein adsorption on surfaces, thus suppress cell attachment. It is also indicated from the results that the grafted polyacrylamide brushes were stable in the culture medium for at least 2 weeks.

Surface hydration is the key factor responsible for the surface resistance to nonspecific protein adsorption. The ultralow fouling properties of polyacrylamide brushes may be attributed to the strong surface hydration layer, formed via hydrogen bond between primary amide groups of polyacrylamide and water. The possible reason why lower adsorption amounts from serum and plasma were observed on polyacrylamide-grafted surfaces than those on the PEG (polyether) surfaces might be because polyacrylamide forms stronger hydrogen bond with water compared to PEG. The functional groups responsible for the hydration layer formation of polyacrylamide and PEG are primary amide and ether, respectively. Primary amides are stronger bases than ethers (pKa = 0.63 for protonated acetamide (*48*); pKa = -2.4 for protonated diethyl ether (*49*)). Therefore, hydrogen bond between primary amide and water is expected to be significantly stronger than that of ether with water. It is also worth to note that since the nitrogen lone pair of electrons in amide is extensively pulled by the strongly electron-withdrawing carbonyl group, amides have stronger dipole moment than ether (3.76D and 1.18D, for acetamide and ethyl ether, respectively) (*48*), which should lead to stronger hydrogen bond of amide with water than that of ether, although both realize surface hydration via hydrogen bond. Recent experimental evidences show that different antifouling materials have significantly different water-binding abilities. One sulfobetaine unit (responsible for antifouling behavior of pSBMA) can tightly bind eight water molecules, while one ethylene glycol unit (responsible for antifouling behavior of PEG) can only tightly bind one water molecule, demonstrating possible reason for higher protein resistance of zwitterionic materials compared to PEG (*50*, *51*). It remains interesting to experimentally investigate and compare the water-binding ability of acrylamide and ethylene glycol in the future, to better understand different antifouling behavior of polyacrylamide and PEG. Besides the hydration property, there might be other contributing factors contributing to different antifouling behavior of the two polymers, such as polymer film thickness, or polymer-free holes left on surfaces due to random distribution of polymer chains on the surface (*52*).

Taking further into consideration the commercial availability and low cost of acrylamide, polyacrylamide is a promising alternative to the traditional PEG-based antifouling materials. One other interesting feature to note is that polyacrylamide contains both hydrogen-bond acceptors and hydrogen-bond donors. It is commonly accepted that the functional groups resistant to protein adsorption should exhibit four molecular-level characteristics: hydrophilic, overall electrically neutral, include hydrogen-bond acceptors, have no hydrogen-bond donors (*43*). Polyacrylamide appears to be an exception to these criteria, being ultralow fouling while containing hydrogen-bond donors. Recent literatures have reported other materials such as poly(carboxybetaine acrylamide) which exhibits superior antifouling properties while also possessing hydrogen-bond donors (*53*).

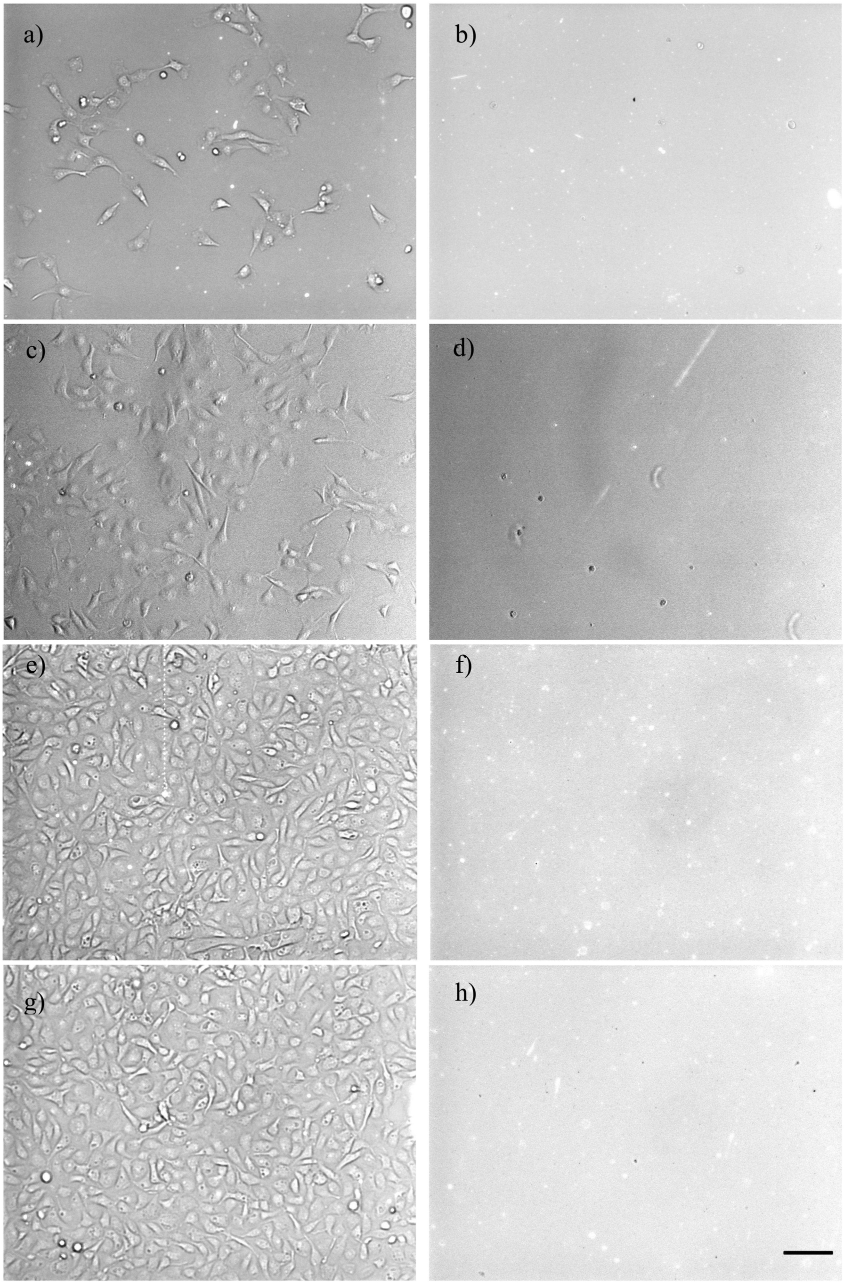

Figure 5. Cell attachment on (a, c, e, g) uncoated gold and (b, d, f, h) polyacrylamide-grafted gold surfaces after culturing for 24 h (a, b), 48 h (c, d), 7 d (e, f), or 14 d (g, h). Bar = 100 μm.

Conclusions

Polyacrylamide brushes were successfully grafted onto gold surfaces via surface-initiated ATRP to achieve ultralow fouling surfaces. At the optimal film thickness, polyacrylamide-grafted surfaces resist adsorptions from single protein solutions, diluted and undiluted human blood serum, and diluted and undiluted human blood plasma. The grafted surfaces remain resistant to protein adsorption in a wide range of pH values and ionic strengths. The grafted surfaces also highly resist the mammalian cell attachment.

Acknowledgments

We greatly appreciate supports from Prof. Shaoyi Jiang at the University of Washington for providing SPR chips and Prof. Stephen Z. D. Cheng for the use of ellipsometer. We are also thankful for support from NSF-MRI (CMMI-0923053), University of Akron Faculty Research Grant, and Firestone Research Initiative Fellowship.

References

1. Ratner, B. D.; Bryant, S. J. *Annu. Rev. Biomed. Eng.* **2004**, *6*, 41–75.
2. Tsai, W.-B.; Grunkemeier, J. M.; McFarland, C. D.; Horbett, T. A. *J. Biomed. Mater. Res.* **2001**, *60*, 348–359.
3. Kwak, D.; Wu, Y.; Horbett, T. A. *J. Biomed. Mater. Res.* **2005**, *74A*, 69–83.
4. Cao, L.; Sukavaneshvar, S.; Ratner, B. D.; Horbett, T. A. *J. Biomed. Mater. Res.* **2006**, *79A*, 788–803.
5. Zhang, M. Q.; Desai, T.; Ferrari, M. *Biomaterials* **1998**, *19*, 953–960.
6. Li, L. Y.; Chen, S. F.; Zheng, J.; Ratner, B. D.; Jiang, S. Y. *J. Phys. Chem. B* **2005**, *109*, 2934–2941.
7. Schwendel, D.; Dahint, R.; Herrwerth, S.; Schloerholz, M.; Eck, W.; Grunze, M. *Langmuir* **2001**, *17*, 5717–5720.
8. Herold, D. A.; Keil, K.; Bruns, D. E. *Biochem. Pharmacol.* **1989**, *38*, 73–76.
9. Branch, D. W.; Wheeler, B. C.; Brewer, G. J.; Leckband, D. E. *Biomaterials* **2001**, *22*, 1035–1047.
10. Kawai, F. *Appl. Microbiol. Biotechnol.* **2002**, *58*, 30–38.
11. Sharma, S.; Johnson, R. W.; Desai, T. A. *Langmuir* **2004**, *20*, 348–356.
12. Shen, M. C.; Martinson, L.; Wagner, M. S.; Castner, D. G.; Ratner, B. D.; Horbett, T. A. *J. Biomater. Sci., Polym. Ed.* **2002**, *13*, 367–390.
13. Luk, Y. Y.; Kato, M.; Mrksich, M. *Langmuir* **2000**, *2000*, 9604–9608.
14. Holland, N. B.; Qiu, Y. X.; Ruegsegger, M.; Marchant, R. E. *Nature* **1998**, *392*, 799–801.
15. Statz, A. R.; Barron, A. E.; Messersmith, P. B. *Soft Matter* **2008**, *4*, 131–139.
16. Lin, S. H.; Zhang, B.; Skoumal, M. J.; Ramunno, B.; Li, X. P.; Wesdemiotis, C.; Liu, L. Y.; Jia, L. *Biomacromolecules* **2011**, *12*, 2573–2582.
17. Jiang, S. Y.; Cao, Z. Q. *Adv. Mater.* **2010**, *22*, 920–932.
18. Ladd, J.; Zhang, Z.; Chen, S. F.; Hower, J. C.; Jiang, S. Y. *Biomacromolecules* **2008**, *9*, 1357–1361.

19. Kyomoto, M.; Moro, T.; Takatori, Y.; Kawaguchi, H.; Nakamura, K.; Ishihara, K. *Biomaterials* **2010**, *31*, 1017–1024.
20. Bernards, M. T.; Cheng, G.; Zhang, Z.; Chen, S. F.; Jiang, S. Y. *Macromolecules* **2008**, *41*, 4216–4219.
21. Hochstrasser, D. F.; Patchornik, A.; Merril, C. R. *Anal. Biochem.* **1988**, *173*, 412–423.
22. Mandal, B. B.; Kapoor, S.; Kundu, S. C. *Biomaterials* **2009**, *30*, 2826–2836.
23. Xue, Z. X.; Wang, S. T.; Lin, L.; Chen, L.; Liu, M. J.; Feng, L.; Jiang, L. *Adv. Mater.* **2011**, *23*, 4270–4273.
24. Fujimoto, K.; Tadokoro, H.; Ueda, Y.; Ikada, Y. *Biomaterials* **1993**, *14*, 442–448.
25. Xiao, D. Q.; Zhang, H.; Wirth, M. *Langmuir* **2002**, *18*, 9971–9976.
26. Cringus-Fundeanu, I.; Luijten, J.; van der Mei, H. C.; Busscher, H. J.; Schouten, A. J. *Langmuir* **2007**, *23*, 5120–5126.
27. DeFife, K. M.; Shive, M. S.; Hagen, K. M.; Clapper, D. L.; Anderson, J. M. *J. Biomed. Mater. Res.* **1999**, *44*, 298–307.
28. Mirzadeh, H.; Katbab, A. A.; Khorasani, M. T.; Burford, R. P.; Gorgin, E.; Golestani, A. *Biomaterials* **1995**, *16*, 641–648.
29. Horbett, T. A. *Cardiovasc. Pathol.* **1993**, *2*, S137–S148.
30. Santini, J. T. J.; Cima, M. J.; Langer, R. *Nature* **1999**, *397*, 335–338.
31. Frommhold, A.; Tarte, E. *Electrochim. Acta* **2011**, *56*, 6001–6007.
32. Voskerician, G.; Shive, M. S.; Shawgo, R. S.; von Recum, H.; Anderson, J. M.; Cima, M. J.; Langer, R. *Biomaterials* **2003**, *24*, 1959–1967.
33. Jones, D. M.; Brown, A. A.; Huck, W. T. S. *Langmuir* **2002**, *18*, 1265–1269.
34. Zhao, C.; Li, L. Y.; Wang, Q. M.; Yu, Q. M.; Zheng, J. *Langmuir* **2011**, *27*, 4906–4913.
35. Zhao, C.; Li, L. Y.; Zheng, J. *Langmuir* **2010**, *26*, 17375–17382.
36. Zhao, H. Y.; Brown, P. H.; Schuck, P. *Biophys. J.* **2011**, *100*, 2309–2317.
37. Barbey, R.; Lavanant, L.; Paripovic, D.; Schuwer, N.; Sugnaux, C.; Tugulu, S.; Klok, H. A. *Chem. Rev.* **2009**, *109*, 5437–5527.
38. Matyjaszewski, K.; Shipp, D. A.; Wang, J.-L.; Grimaud, T.; Patten, T. E. *Macromolecules* **1998**, *31*, 6836–6840.
39. Min, K.; Matyjaszewski, K. *Macromolecules* **2005**, *38*, 8131–8134.
40. Yang, W.; Chen, S. F.; Cheng, G.; Vaisocherova, H.; Xue, H.; Li, W.; Zhang, J. L.; Jiang, S. Y. *Langmuir* **2008**, *24*, 9211–9214.
41. Xiao, D. Q.; Wirth, M. J. *Macromolecules* **2002**, *35*, 2919–2925.
42. Liu, Q. S.; Singh, A.; Lalani, R.; Liu, L. Y. *Biomacromolecules* **2012**, *13*, 1086–1092.
43. Ostuni, E.; Chapman, R. G.; Holmlin, R. E.; Takayama, S.; Whitesides, G. M. *Langmuir* **2001**, *17*, 5605–5620.
44. Zhang, Z.; Chen, S. F.; Chang, Y.; Jiang, S. Y. *J. Phys. Chem. B* **2006**, *110*, 10799–10804.
45. Zhang, Z.; Vaisocherova, H.; Cheng, G.; Yang, W.; Xue, H.; Jiang, S. Y. *Biomacromolecules* **2008**, *9*, 2686–2692.
46. Adkins, J. N.; Varnum, S. M.; Auberry, K. J.; Moore, R. J.; Angell, N. H.; Smith, R. D.; Springer, D. L.; Pounds, J. G. *Mol. Cell. Proteomics* **2002**, *1*, 947–955.

47. Benesch, J.; Svedhem, S.; Svensson, S. C. T.; Valiokas, R.; Liedberg, B.; Tengvall, P. *J. Biomater. Sci., Polym. Ed.* **2001**, *12*, 581–597.
48. Nakai, S.; Modler, H. W. *Food Proteins: Properties and Characterization*; Wiley-VCH: Canada, 1996.
49. Sorensen, P. E.; Jencks, W. P. *J. Am. Chem. Soc.* **1987**, *109*, 4675–4690.
50. Wu, J.; Chen, S. F. *Langmuir* **2012**, *28*, 2137–2144.
51. Wu, J.; Lin, W. F.; Wang, Z.; Chen, S. F.; Chang, Y. *Langmuir* **2012**, *28*, 7436–7441.
52. Katira, P.; Agarwal, A.; Hess, H. *Adv. Mater.* **2009**, *21*, 1599–1604.
53. Yang, W.; Xue, H.; Li, W.; Zhang, J. L.; Jiang, S. Y. *Langmuir* **2009**, *25*, 11911–11916.

Chapter 31

Protein-Repellent Functionalizable Surfaces Based on Covalently Bonded Phospholipids with Phosphorylcholine Head

Lynda Ferez,[1] Thierry Thami,[1] Lara Tauk,[1] Edefia Akpalo,[1] Valérie Flaud,[2] Armagan Kocer,[3] Jean-Marc Janot,[1] and Philippe Déjardin*,[1]

**[1]Institut Européen des Membranes, Université Montpellier 2
(ENSCM, UM2, CNRS), CC047, 2 Place Eugène Bataillon,
F-34095 Montpellier Cedex 5, France
[2]XPS Technologique Platform, Institut Charles Gerhardt,
Université Montpellier 2, 2 Place Eugène Bataillon,
F-34095 Montpellier Cedex 5, France
[3]Department of Biochemistry, Groningen Biomolecular Sciences
and Biotechnology Institute, University of Groningen, Nijenborgh 4,
9747 AG, Groningen, The Netherlands
*E-mail: Philippe.Dejardin@iemm.univ-montp2.fr**

Surface anchored poly(methylhydrosiloxane) (PMHS) films (≈ 10 nm – 1μm) were functionalized with 1,2-dilinoleoyl-sn-glycero-3-phosphorylcholine (18:2 Cis). The surface was characterized by X-ray photoelectron spectroscopy, contact angle measurements, atomic force microscopy, and scanning electron microscopy. The interface was very hydrophilic and repellent toward avidin, bovine serum albumin, bovine fibrinogen, lysozyme, cytochrome C and α-chymotrypsin at pH 7.4 as observed by quantitative normal scanning confocal fluorescence. The surface is also repellent to liposomes (400 nm diameter) of L-α-phosphatidylcholine (Soy-20%). Further possibilities of functionalization on the surface remain available owing to the formation of interfacial SiOH groups.

In Proteins at Interfaces III State of the Art 2012; Horbett, T., et al.;
ACS Symposium Series; American Chemical Society: Washington, DC, 2012.

1. Introduction

In many biomedical applications, non specific adsorption is a recurrent problem, as neutrality of the interface with respect to biological fluids is required, whereas additional functionalities may be needed on such a neutral background. This situation especially occurs in the design of biosensors. Blocking buffers are proposed in diagnostic kits with for instance albumin (*1*, *2*) to reduce non specific adsorption on functionalized surfaces. This corresponds to the usual strategy of production of biosensors. However, two strategies can be considered to create functionalized surfaces: (i) functionalize first the surface and then block the void surface with some inert material, (ii) block first the surface and then add desired functionalities. We are considering in the present work the second strategy by creating first a protein-repellent background surface rich in phosphorylcholine groups over which functionalities can be grafted thereafter.

Several routes were considered to create surfaces with neutral behavior. They can be roughly classified into two categories (*3*): the first being based on poly(ethylene oxide) –PEO– (*4–16*), and the second on zwitterionic groups (*17–19*), especially the phosphorylcholine head. They correspond to the two main classes of available effective protein-repellent surfaces whose main characteristics is their high hydrophilicity (*20*).

Poly(ethylene glycol) (PEG) and oligo(ethylene glycol) (OEG) have been widely used to resist nonspecific protein adsorption (*4*, *21*). Both are able to form a hydration layer via hydrogen bonds. However, as the temperature increases, the strength of these bonds decreases (*22*). Moreover, in the presence of oxygen and transition metal ions PEG or OEG can decompose (*23*).

The choice of the zwitterionic phosphorylcholine (PC) head is inspired by the large number of phospholipids bearing that head on the external side of the bilayer membrane of cells (*24*). PC-phospholipid polymers were developed many years ago by the group of D. Chapman (*25–29*) and later by others (*30*). Chemical transformation of the phospholipids was then necessary to obtain first the polymerizable functional group as was the case when individual surface grafting was carried out (*31*). Other zwitterionic (sulfobetaine; carboxybetaine) materials have been found to exhibit ultralow protein adsorption (*32*, *33*) (fibrinogen adsorption < 5 ng cm^{-2}). Such an efficiency is due to the zwitterion structure which retains a large amount of water independent of temperature because of hydration via ionic solvation (*18*). With phosphate and sulfonate zwitterions, the interface is expected to be electrically neutral over a wide pH range (5-9), whereas carboxy zwitterions offer variations with pH which can be exploited. High resistance to protein adsorption was observed for surfaces coated with zwitterionic phospholipids (*25*). It was suggested that in the presence of interfacial high water content the surface contact does not induce significant conformational changes of the protein (*34–37*).

The availability of 2-methacryloyloxyethyl phosphorylcholine (MPC) monomer, first introduced by the group of K. Ishihara, has resulted in numerous studies with polymers based on this monomer (*38–47*). Recently the reaction of the monomer with triethoxysilane was carried out to treat titanium alloy (*48*). Chemistry on existing polymers in polyelectrolyte multilayer applications (*49*) or on hydroxylated gold in studies on leukocyte adhesion (*50*) allowed to obtain PC side chains.

Besides these different routes to obtaining PC rich interfaces, we looked at the strategy to creating first soft structures aimed at covalent bonding of PC in high density, then to functionalize with PC. Moreover, rather than using small molecules with PC head like in the MPC monomer, we used phospholipids with long fatty chains like in the biological cells. From this point of view, the method has similarities with the Chapman strategy, one noticeable difference being a final interface without carbon-carbon unsaturated bonds.

We consider the building of a poly(methylhydrosiloxane) (PMHS) scaffold which can be viewed as a large reservoir of SiH functions (*51*, *52*). Then 1,2-dilinoleoyl-sn-glycero-3-phosphorylcholine (18:2 Cis) bearing double bonds can react by hydrosilylation reaction leading to a PL-PMHS interface. The process is schematically represented in Figure 1 with the phospholipid (PL) structure. Moreover, the side reaction with water produces some silanols which are available for subsequent functionalization over a background of phosphorylcholine groups.

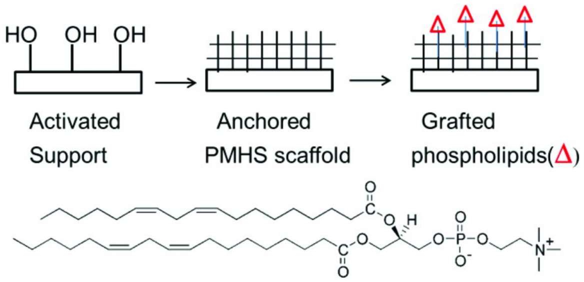

Figure 1. Schematic representation of the successive steps to build an anchored PMHS network functionalized with phospholipids. Structure of 1,2-dilinoleoyl-sn-glycero-3-phosphorylcholine (18:2 Cis).

The present chapter gathers studies performed recently in our laboratory with thick (1 µm order of magnitude) (*53*) and thin (7-180 nm) layers (*54*) of PMHS. The protein-repellent character of such surfaces was checked at physiological pH 7.4 from solutions of bovine serum albumin (BSA), bovine fibrinogen, avidin, α-chymotrypsin, cytochrome C and lysozyme by means of quantitative normal scanning confocal fluorescence. A method of calibration from the solution signal is proposed to extract the interfacial concentration. By the same technique the repellency of such surfaces to liposomes of L-α-phosphatidylcholine is also demonstrated.

The presentation is structured in three sections: (i) Materials and methods, (ii) Results and discussion, (iii) Conclusion. The Materials and Methods section has six subsections: chemicals, proteins and labeling, liposome preparation and labeling, methods of preparation of the support, techniques of characterization of the support and finally adsorption: determination of the interfacial concentration. The Results and Discussion section comprises four subsections: material characterization, protein adsorption, liposome adsorption/spreading and finally functionalization of PL-PMHS surface.

2. Materials and Methods

2.1. Chemicals

Both precursors methyldiethoxysilane $HSi(CH_3)(OCH_2CH_3)_2$ (DH) and triethoxysilane $HSi(OCH_2CH_3)_3$ (TH) were purchased from ABCR (Karlsruhe, Germany) and used as received. Water for substrate cleaning was obtained from a Milli-Q water purification apparatus (Millipore). Absolute ethanol for sol−gel synthesis was of synthesis grade purity. The sol-gel catalyst trifluoromethanesulfonic acid CF_3SO_3H was purchased from Aldrich. Toluene for thin film hydrosilylation was distilled before use. The platinum-divinyltetramethyldisiloxane complex in xylene (platinum concentration *ca.* 0.1 M assuming 2.4% (w) Pt in xylene), also known as Karstedt's catalyst, was purchased from ABCR (PC072). 1,2-dilinoleoyl-sn-glycero-3-phosphorylcholine (18:2 Cis) (PL) was purchased from AvantiPolarLipids.

Other chemicals were used as received: 3-(ethoxydimethylsilyl)-propyl amine (Aldrich, 588857), Alexa Fluor® 594 succinimidyl ester (labelling kit A10239, InvitroGen), biotin-ethylenediamine hydrobromide (Sigma B9181).

2.2. Proteins and Labeling

Bovine serum albumin (A-7638), bovine fibrinogen (F-8630), cytochrome C (C-2506), lysozyme (62971-Fluka), α-chymotrypsin (C-4129) and avidin (A9275) were purchased from Sigma-Aldrich; some avidin from Fluka (No. 11368). Labeling of proteins was performed with Alexa-fluor-594 succinimidyl ester (InvitroGen, A30008). The procedure of labeling was previously described (*53*).

2.3. Liposome Preparation and Labeling

One hundred milligrams of L-α-Phosphatidylcholine (Soy-20%) (Avanti Polar Lipids Inc. 541601) was dissolved in 5mL of chloroform containing 100μL of a 1,1′-dioctadecyl-3,3,3′,3′-tetramethylindodicarbocyanine perchlorate solution (Invitrogen Inc.) (1mg/mL in methanol). After chloroform was thoroughly removed by vacuum, phosphate buffered saline (PBS, 10mM, pH 8.1, 150mM NaCl) was added and mixed. Details of the preparation, using polycarbonate membrane filters (Avestin Inc.) with pore diameter of 400nm mounted in a mini-extruder (Avestin Inc.), can be found elsewhere (*54*).

2.4. Methods of Preparation of the Support

2.4.1. Substrate Cleaning and Activation

Silicon wafers Si(100) (ACM, France) cut into square strips of 2 × 2 cm^2 or thin microscope glass slides (see below) were used as substrates for spin-coating deposition. The square was cut into four pieces of 1 cm^2 area for phospholipid reaction with the PMHS layer. To bond covalently the PMHS thin films to native oxide silica (thickness ~ 2 nm), the silicon wafers were first cleaned and activated using the previously described procedure with "piranha" solution H_2SO_4/H_2O_2-30%w (70/30 vol); 90°C; 30 min (*55*). *Caution: piranha solution must be handled extremely carefully.* For fluorescence adsorption measurements, the substrates were wafers or thin microscope glass slides (Menzel-Glazer, Germany) of 2.5 × 6 cm^2 submitted to the same treatment to bond PMHS. However, for protein adsorption to glass (without subsequent PMHS bonding), the substrate was previously treated with sulfochromic acid and rinsed carefully just before adsorption experiment.

2.4.2. PMHS Films

PMHS thin films were prepared at 22 ± 1 °C by sol–gel polymerization of DH and TH as crosslinker. DH/TH 95/5 (mol%) sol mixtures were deposited by spin-coating on freshly activated substrates according to the procedure (*51, 52*) summarized as follows. Trifluoromethanesulfonic acid CF_3SO_3H (1.0 M in absolute ethanol) was used as catalyst (0.5 mmol/mol of monomers). The mixture of monomers (4.0 M in EtOH; molar ratio [EtOH]/[Si] = 1) was polymerized with hydrolysis ratio $h = [H_2O]/[SiOEt] = 0.5$. The content of trifluoromethanesulfonic acid was not higher than 0.05% to control the kinetics of gelation of the liquid mixture. The resulting clear sols were allowed to age for ~30 minutes with magnetic stirring before spin-coating deposition. The freshly cleaned silicon wafer was purged (2 min) in the spin-coater (Spin150, SPS Europe) under a stream of nitrogen (2 L/min) to avoid air moisture. For all samples, the speed of rotation was 4000 rpm (spin acceleration 2000 rpm/s) and the rotation time 30 s. The samples were finally cured at 110°C in an oven for 15 minutes. This procedure gave layers of reproducible homogeneity and thickness as verified by electron microscopy and infrared analysis.

2.4.3. Grafting PMHS with Phospholipid To Afford PL-PMHS

After spin-coating PMHS layer onto pieces of oxidized silicon wafer, the hydrosilylation reaction between the dilinoleoyl phospholipid (PL) and the PMHS SiH functional group was performed in air by casting solutions (20 mg PL in 1 mL of toluene (25.5 mM), with an additional 2 µL of the xylene solution of the platinum divinyltetramethyldisiloxane complex, Karstedt's catalyst) or by immersion of the plates in the PL solution. The reaction was then allowed to proceed at room temperature (~ 20°C) or 40°C, before the sample was rinsed with toluene/chloroform mixtures ranging from 100% to 0% to remove any physisorbed material, and finally dried under a stream of nitrogen for 5 minutes. Then the samples were immersed in water for two hours and finally re-dried. Transmission infrared (IR) absorption spectra of the 1 µm thick films before and after hydrosilylation were used to ascertain the reaction yield after solvent and water rinsing, XPS spectra was used for thick and very thin films. The air captive

In Proteins at Interfaces III State of the Art 2012; Horbett, T., et al.;
ACS Symposium Series; American Chemical Society: Washington, DC, 2012.

bubble contact angle in water was finally measured in order to characterize the sample surface hydrophilicity. We used the notation PL-PMHS(x nm) to signify that PL reaction occurred on an initial PMHS layer of thickness x nm.

2.4.4. Synthesis of Monoethoxysilane Bearing Alexa. Grafting on PL-PMHS

To a solution of Alexa Fluor® 594 succinimidyl ester (12.2 nmol) in dry ethanol (100 µL) under an argon atmosphere, was added 3-(ethoxydimethylsilyl)-propyl amine (12.2 nmol). The reaction mixture was vigorously stirred for two hours at room temperature. The resulted mixture was then divided into ten parts. The solvent was evaporated under reduced pressure and the product alexa-monoethoxysilane thus obtained was used without further purification. HRMS (Q-Tof) : Calcd for $C_{35}H_{35}N_3O_{10}S_2$ 721.1745 (M^- - $C_4H_{11}SiO$); found: 721.1764.

PL-PMHS functionalization: Each part of the divided alexa-monoethoxysilane (~ 1 nmol) was dissolved in a mixture of toluene/dry ethanol (700µL/300µL). The PL-PMHS coated surfaces were then soaked in the solution for one hour. The substrates were further rinsed with ethanol, dried under a stream of argon, then kept overnight in Milli-Q water in order to remove any trace of physically adsorbed alexa before characterisation by confocal microscopy.

PL-PMHS passivation with hexamethyldisilazane (HMDS): The substrate with a PL-PMHS layer was dried under a stream of argon and treated with a solution of 95-5 % (vol.) of dry toluene-HMDS for 30 min at room temperature. After rinsing with toluene, and drying under a stream of argon, the substrate was soaked in alexa-monoethoxysilane solution as described above.

2.5. Techniques of Characterization of the Support

2.5.1. X-ray Photoelectron Spectroscopy (XPS)

The surface elemental composition of the PMHS and PL-PMHS surfaces were analysed by XPS, as previously described (*53*). The spectra were obtained by means of a spectrophotometer (ESCALAB 250, Thermo Electron, UK) equipped with a monochromatic Al Kα (1486.6 eV) radiation source. The acceleration tension and power of the X-ray source were 15 kV and 100 W, respectively. Survey scans (0-1350 eV) at low resolution were performed to identify the constitutive elements. High resolution C_{1s}, Si_{2p}, O_{1s}, N_{1s} and P_{2p} spectra were recorded to obtain more detailed information on the nature of the surface.

2.5.2. Captive Air Bubble Contact Angle Measurements in Water

Air captive bubble contact angles in water were measured (GBX - Digidrop, Romans, France) by applying an air bubble of about 25 µL to the surface. The contact angle through air was calculated using computerized image analysis. The data dicussed are relative to the complement angle to 180° through the liquid as generally defined (*56*), in opposition to the angle through air as used in a previous work (*53*).

2.5.3. AFM and SEM

Atomic Force Microscopy (AFM) experiments were performed using a Dimension 3100 microscope equipped with a Nanoscope IIIa controller system (Digital Instruments, Veeco Metrology Group). AFM images were obtained by scanning in tapping mode in water or under air ambient conditions using silicon SPM probes (stiffness $k \approx 2$ N/m, resonance frequency of 67 kHz, pointeprobeplus, Nanosensors). The root mean square average roughness (R_q) was analyzed by the Nanoscope software (version 5.31r1). Scanning electron microscopy (SEM) pictures were obtained with a Hitachi S4800 instrument. The MeX software (version 5.1) was used for the construction of the 3D SEM image and z-profile (±10 nm) from differently tilted SEM images.

2.6. Adsorption: Determination of Interfacial Concentration

The experiments were performed at T = 19°C in a slit flow cell of thickness 63 or 105 µm and flow rate corresponding to wall shear rate 1000 s^{-1}. Entrance design leads to a sharp transition between the flows of buffer and solution. Confocal measurements were performed at 3 cm from the slit entrance.

The interfacial concentration was evaluated as follows: the fluorescence signal F_{sol} from the solution at concentration C is relative to an effective volume V while the signal F_{surf} at the surface concerns the interfacial concentration Γ over area A. $F_{surf} \propto \Gamma A$ and $F_{sol} \propto C V$ therefore $\Gamma = (V/A)(F_{surf}/F_{sol})\,C$. In a previous paper (*57*) the order of magnitude of V/A was estimated from the focus radius for A and 1 µm^3 taken as the confocal volume V. We proposed recently (*53*) the experimental determination of V/A and we will recall shortly the argument. The normal scanning of the laser beam through a flat fluorescent interface leads to a peak $F_i(y)$ which can be viewed as the convolution of the laser beam with a Dirac function (Figure 2).

Considering the same beam scanning in fluorescent solution viewed as a contiguous series of thin slabs treated like Dirac functions, and summing all contributions when focusing at one point in solution, it is deduced that V/A is the area under the peak of the interface normalized to its maximal value. The width $w_D = V/A$ was in the range 2 -2.5 µm.

$$\frac{V}{A} = w_D = \int_{-\infty}^{+\infty} \frac{F_i(y)}{F_i(0)}\,dy$$

The presence of solution (step function at interface) leads to a contribution when focusing at interface which is half the signal in bulk solution. We used then as surface signal F_{surf} the raw signal minus half the solution signal. This correction was negligible when a strong adsorption occurred at small solution concentrations.

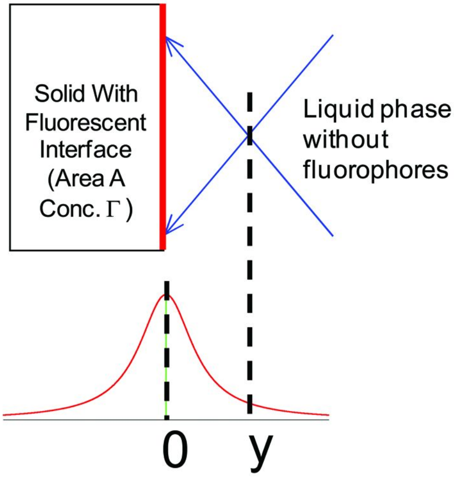

Figure 2. (top) Scheme of focused laser beam at some distance from an interface occupied by fluorescent molecules. No fluorescent molecules in solution. (bottom) Resulting peak $F_i(y)$ from normal scanning to the interface. Adapted with permission from ref. (53). Copyright 2011 American Chemical Society.

3. Results and Discussion

3.1. Material Characterization

The two interfaces of PMHS and PL-PMHS were examined by AFM, air bubble contact angle and SEM (Figure 3).

The PMHS layer presented always a small roughness of some tenths of nanometer and a hydrophobic character with a 90° air bubble contact angle. Reaction with phospholipid (PL) induced the creation of ~ 2 µm large grooves on thick (~ 1 µm) PMHS, with a depth of 100 nm. The reaction led to a very hydrophilic material as we observed a contact angle close to 0° and rolling bubbles. SEM exhibited the swelling of PMHS under reaction with PL, as previously observed under reaction with linear olefins (*51*). The grooves and generally the structures observed after reaction with PL were mainly attributed to the reticulation induced by side reaction with water. Such reaction was suggested by Si_{2p} XPS spectra which exhibited an unexpected increase of the component of silicon surrounded by three oxygens under reaction of PMHS with PL (Figure 4). In addition, streaming potential showed an interfacial behavior consistent with the presence of silanols (*53*).

With smaller PMHS thicknesses (10-200 nm) we did not observe such large grooves, the roughness R_q being of the order of a few nanometers with a minimum less than 1 nm for PMHS thickness of 20 nm (*54*).

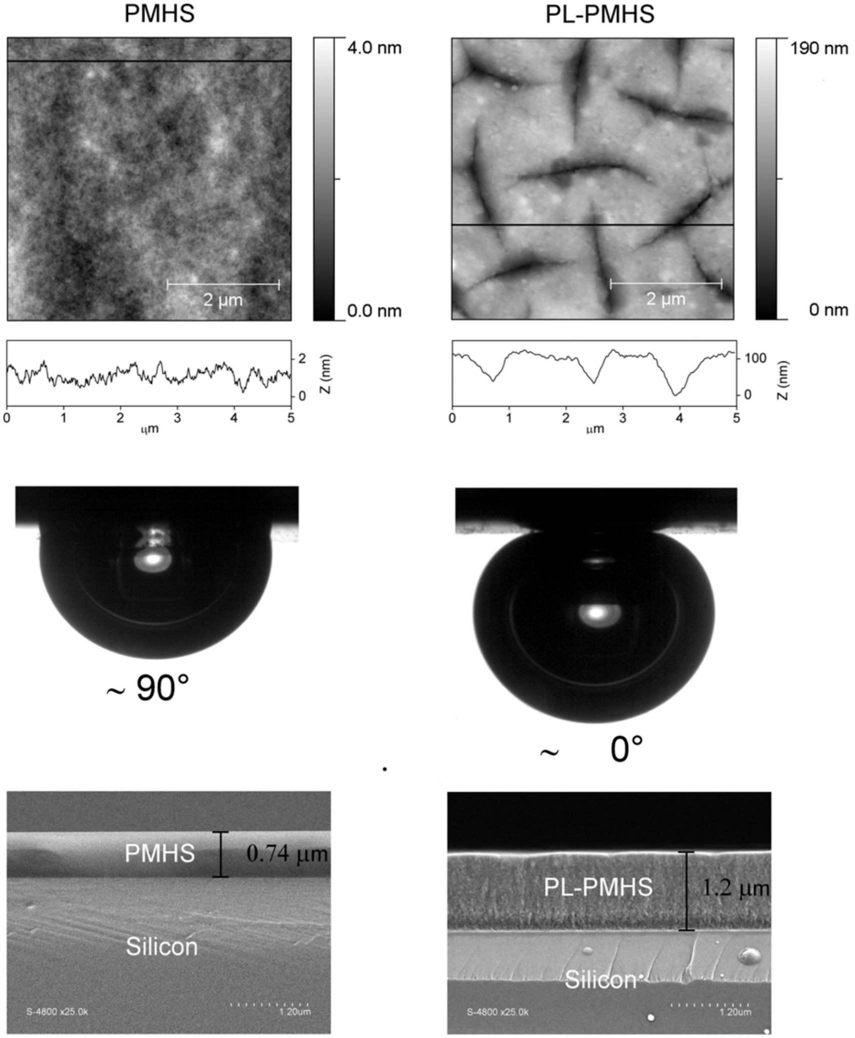

Figure 3. Comparison of PMHS (left) and PL-PMHS (right) analysis by- from top to bottom - atomic force microscopy (AFM; 5μm ×5 μm), captive air bubble contact angle and scanning electron microscopy (SEM). Adapted with permission from ref. (53). Copyright 2011 American Chemical Society.

3.2. Protein Adsorption

The adsorption of several proteins was checked on PL-PMHS(1 μm) surfaces prepared at room temperature (Figure 5). Very low interfacial concentrations, clearly below 1 ng cm^{-2}, were obtained for all proteins, except for the fibrinogen at 100 μg/mL. BSA presented the peculiar behavior of slow desorption over 10 min while rinsing with buffer.

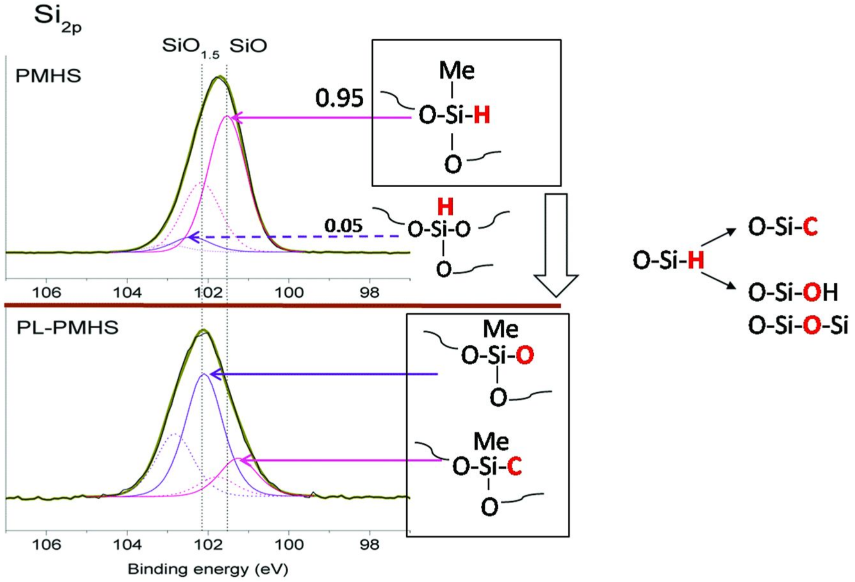

Figure 4. XPS spectra of Si_{2p} for PMHS (top) and PL-PMHS (bottom).

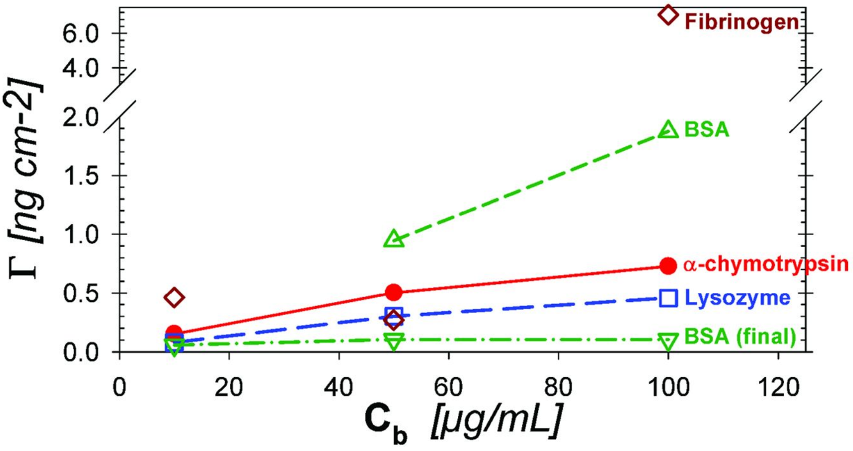

Figure 5. Interfacial concentration on PL-PMHS(1 µm) as a function of protein solution concentration. Higher values for BSA (1-2 ng cm^{-2}) correspond to the beginning of rinsing.

The same kind of behavior was observed with interfaces prepared from much smaller thicknesses of the initial PMHS network (Figure 6). The mean values were for avidin (5 µg/mL) $\Gamma = 0.1 \pm 0.9$ ng cm^{-2} on PL-PMHS(180 nm) and (10 µg/mL) 1.2 ± 0.9 ng cm^{-2} on PL-PMHS(7 nm); for BSA (10 µg/mL), $\Gamma = 0.5 \pm 0.3$ ng cm^{-2} on PL-PMHS(20 nm). Taking into account the transport contribution in the analysis of the initial kinetics (*58*, *59*) on glass, we obtained $k_a = 0.97 \times 10^{-4}$ cm s^{-1} for avidin from the initial raw kinetic constant $k = 0.74 \times 10^{-4}$ cm s^{-1}, and 0.060×10^{-4} cm s^{-1} for BSA where transport contribution was negligible. Indeed, with $D \approx 6 \times 10^{-7}$ cm^2 s^{-1}, $x = 3$ cm and wall shear rate 1000 s^{-1}, the transport limited constant k_{Lev} is 2.65 10^{-4} cm s^{-1} and $u = k/k_{Lev} = 0.28$ for avidin and 0.022 for BSA. The k_a, value, illustrated by the graphical interpolation in Figure 7, is determined by applying accurate approximations (*58*, *59*), as the two parameters expression $k_a = k\,(\mathrm{b}\,u + 1)/((u\text{-}1)\,(\mathrm{a}\,u\text{-}1))$, where a = 0.452, b = -0.625 (*58*).

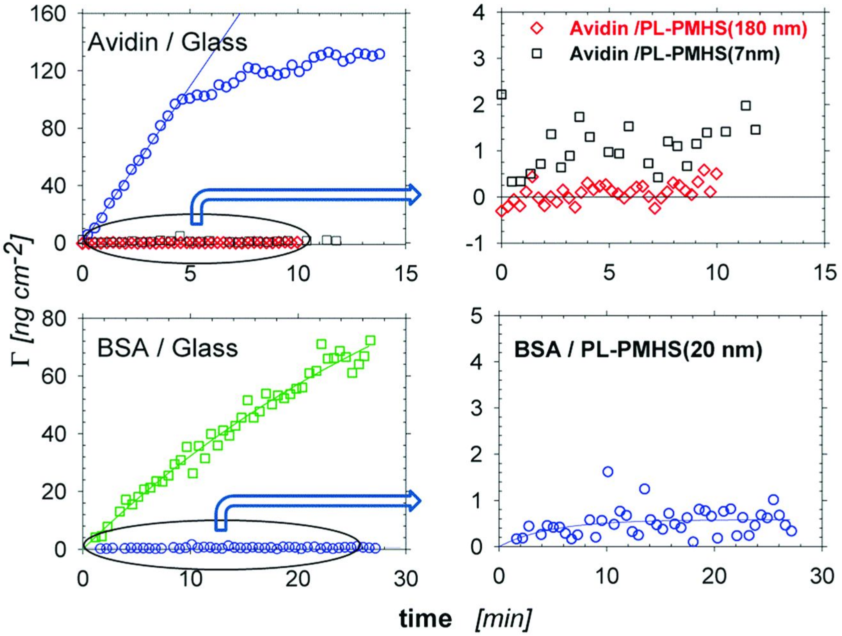

Figure 6. Passivation of PL-PMHS interfaces with respect to BSA and avidin adsorption, compared to glass. Enlargement of scales (graphs on the right) allows to show the order of magnitude of the interfacial concentration. Adapted with permission from ref. (54). Copyright 2012 Elsevier.

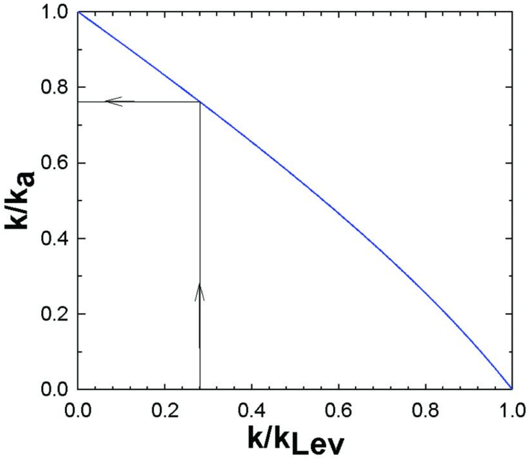

Figure 7. Graphical determination of adsorption kinetic constant k_a from raw kinetic constant k and transport-limited constant $k_{Lev} = 0.538\ (D^2\ \gamma\ /\ x)^{1/3}$.

3.3. Liposome Adsorption/Spreading

Adsorption of labeled (DiD) liposomes of L-α-Phosphatidylcholine (diameter 400 nm) was measured by scanning confocal fluorescence as for the proteins. Based on an average area per head of 0.5 nm^2 or diameter per head of 0.8 nm, the adsorption at different interfaces (Figure 8) illustrates the neutral nature of the PL-PMHS interface as no adsorption/spreading was observed, contrary to the other interfaces of glass and PMHS.

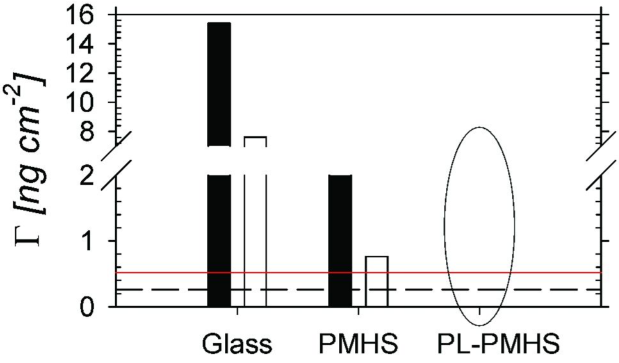

Figure 8. Adsorption/spreading of labeled liposomes on piranha treated glass, PMHS and PL-PMHS. After (full bar) one and (empty bar) a few rinsings. Horizontal lines correspond to estimated (dashed line) monolayer and (full line) bilayer coverage. Adapted with permission from ref. (54). Copyright 2012 Elsevier.

3.4. Functionalization of PL-PMHS Surface

The interfacial silanol groups revealed by the XPS analysis after PL reaction with PMHS could be available for subsequent reaction. Their presence was checked by reaction of a monoethoxy silane coupling agent bearing alexa as fluorescent probe (*53*). The high fluorescence signal confirmed the possibilities of chemical functionalization at such surfaces, whereas pretreatment of PL-PMHS with hexamethyldisilazane (HMDS) led to no coupling reaction as the silanols were neutralized by bulky trimethylsilyl groups.

Quantitative analyze of fluorescence led to a mean degree of functionalization of PL-PMHS layer of 3.0×10^{-2} nm^{-2}. Therefore an order of magnitude of the mean distance between sites on the assumed flat surface was estimated to be 5.7 nm. Such sites can be provided with amino groups available for amide junctions (*54*).

4. Conclusion

Polymethylhydrosiloxane anchored on an activated oxidized silicon wafer or glass can be deposited as a thick (~ 1 µm) or very thin (7-180 nm) film and provided with covalently bonded phospholipids bearing a phosphorylcholine head. A 20 nm thin PMHS layer led to very flat surfaces with roughness less than 1 nm, whereas thick PMHS layers led to final PL-PMHS surface with large grooves of depth 100 nm.

Whatever the initial PMHS thickness, the resulting PL-PMHS interface was protein-repellent at neutral pH in phosphate saline buffer with side reaction silanols available for appropriate functionalization. The repellent character was also observed with 400 nm L-α-Phosphatidylcholine liposomes. Therefore adequate functionalization could help to fix specific cells to the interface. However, the control of the pertinent character of softness in cell spreading (*60*), through the ratio DH/TH in the synthesis of the PMHS films would require a better control of water in subsequent grafting.

Finally the protein-repellent interface can be easily provided with amine functional group. Therefore such protein-repellent interface can be useful in the biomedical domain, e.g. for biosensors, biomaterials and cell culture, by reducing strongly the non-specific adsorption, on the one hand, and offering in addition the possibilities for grafting desired functions, on the other hand. Moreover the covalent coverage with phospholipids and the silanol sites for further functionalization are generated simultaneously in a one step process.

Let us note also that the strategy of first anchoring a PMHS network opens the possibility to graft thereafter different compositions of phospholipids, provided they possess at least one double bond in their fatty chains. With respect to other surfaces prepared with covalent bonding of phospholipids the present method provides surfaces without carbon – carbon double bonds and therefore diminishes strongly the probability of autoxidation.

Acknowledgments

This work was especially supported by FP7 European grant NMP-214538 (BISNES project; Coord. D. Nicolau). We are grateful to M. Ramonda (LMCP, UM2) for the AFM pictures, to D. Cot (IEM, UM2) for SEM pictures, and to F. Pichot (UM2) for access to clean room and ellipsometry.

References

1. Ogi, H.; Fukunishi, Y.; Nagai, H.; Okamoto, K.; Hirao, M.; Nishiyama, M. *Biosens. Bioelectron.* **2009**, *24*, 3148–3152.
2. Holmberg, M.; Hou, X. L. *Colloids Surf., B* **2011**, *84*, 71–75.
3. Vermette, P.; Meagher, L. *Colloids Surf., B* **2003**, *28*, 153–198.
4. Yan, F.; Dejardin, P.; Mulvihill, J. N.; Cazenave, J. P.; Crost, T.; Thomas, M.; Pusineri, C. *J. Biomater. Sci., Polym. Ed.* **1992**, *3*, 389–402.
5. Lee, J.; Kopecek, J.; Andrade, J. *J. Biomed. Mater. Res.* **1989**, *23*, 351–368.
6. Wu, Y. J.; Timmons, R. B.; Jen, J. S.; Molock, F. E. *Colloids Surf., B* **2000**, *18*, 235–248.
7. Maste, M. C. L.; van Velthoven, A. P. C. M.; Norde, W.; Lyklema, J. *Colloids Surf., A* **1994**, *83*, 255–260.
8. Archambault, J. G.; Brash, J. L. *Colloids Surf., B* **2004**, *39*, 9–16.
9. Du, Y. J.; Brash, J. L. *J. Appl. Polym. Sci.* **2003**, *90*, 594–607.
10. Cecchet, F.; De Meersman, B.; Demoustier-Champagne, S.; Nysten, B.; Jonas, A. M. *Langmuir* **2006**, *22*, 1173–1181.
11. Unsworth, L. D.; Sheardown, H.; Brash, J. L. *Langmuir* **2008**, *24*, 1924–1929.
12. Tan, J.; McClung, W. G.; Brash, J. L. *J. Biomed. Mater. Res., Part A* **2008**, *85A*, 873–880.
13. Tan, J.; Brash, J. L. *J. Appl. Polym. Sci.* **2008**, *108*, 1617–1628.
14. Holmberg, M.; Hou, X. L. *Langmuir* **2010**, *26*, 938–942.
15. Ionov, L.; Synytska, A.; Kaul, E.; Diez, S. *Biomacromolecules* **2010**, *11*, 233–237.
16. Trmcic-Cvitas, J.; Hasan, E.; Ramstedt, M.; Li, X.; Cooper, M. A.; Abell, C.; Huck, W. T. S.; Gautrot, J. E. *Biomacromolecules* **2009**, *10*, 2885–2894.
17. Su, Y. L.; Li, C. *React. Funct. Polym.* **2008**, *68*, 161–168.
18. Yang, W.; Xue, H.; Li, W.; Zhang, J. L.; Jiang, S. Y. *Langmuir* **2009**, *25*, 11911–11916.
19. Liu, P. S.; Chen, Q.; Liu, X.; Yuan, B.; Wu, S. S.; Shen, J.; Lin, S. C. *Biomacromolecules* **2009**, *10*, 2809–2816.
20. Prime, K.; Whitesides, G. *Science* **1991**, *252*, 1164.
21. Li, L. Y.; Chen, S. F.; Jiang, S. Y. *J. Biomater. Sci., Polym. Ed.* **2007**, *18*, 1415–1427.
22. Dormidontova, E. E. *Macromolecules* **2002**, *35*, 987–1001.
23. Ostuni, E.; Chapman, R. G.; Holmlin, R. E.; Takayama, S.; Whitesides, G. M. *Langmuir* **2001**, *17*, 5605–5620.
24. Zwaal, R. *Nature* **1977**, *268*, 358.
25. Chapman, D. *Langmuir* **1993**, *9*, 39–45.

26. Hall, B.; Bird, R. L.; Chapman, D. *Angew. Makromol. Chem.* **1989**, *166*, 169–178.
27. Leaver, J.; Alonso, A.; Durrani, A. A.; Chapman, D. *Biochim. Biophys. Acta* **1983**, *732*, 210–218.
28. Albrecht, O.; Johnston, D. S.; Villaverde, C.; Chapman, D. *Biochim. Biophys. Acta* **1982**, *687*, 165–169.
29. Johnston, D. S.; Sanghera, S.; Pons, M.; Chapman, D. *Biochim. Biophys. Acta* **1980**, *602*, 57–69.
30. Marra, K. G.; Winger, T. M.; Hanson, S. R.; Chaikof, E. L. *Macromolecules* **1997**, *30*, 6483–6488.
31. Kohler, A. S.; Parks, P. J.; Mooradian, D. L.; Rao, G. H. R.; Furcht, L. T. *J. Biomed. Mater. Res.* **1996**, *32*, 237–242.
32. Yang, W.; Chen, S. F.; Cheng, G.; Vaisocherova, H.; Xue, H.; Li, W.; Zhang, J. L.; Jiang, S. Y. *Langmuir* **2008**, *24*, 9211–9214.
33. Zhang, Z.; Chen, S. F.; Jiang, S. Y. *Biomacromolecules* **2006**, *7*, 3311–3315.
34. Ishihara, K.; Takai, M. *J. R. Soc. Interface* **2009**, *6*, S279–S291.
35. Ishihara, K.; Nomura, H.; Mihara, T.; Kurita, K.; Iwasaki, Y.; Nakabayashi, N. *J. Biomed. Mater. Res.* **1998**, *39*, 323–330.
36. Sheng, Q.; Schulten, K.; Pidgeon, C. *J. Phys. Chem.* **1995**, *99*, 11018–11027.
37. Goda, T.; Watanabe, J.; Takai, M.; Ishihara, K. *Polymer* **2006**, *47*, 1390–1396.
38. Ishihara, K.; Ziats, N. P.; Tierney, B. P.; Nakabayashi, N.; Anderson, J. M. *J. Biomed. Mater. Res.* **1991**, *25*, 1397–1407.
39. Ishihara, K.; Takayama, R.; Nakabayashi, N.; Fukumoto, K.; Aoki, J. *Biomaterials* **1992**, *13*, 235–239.
40. Furuzono, T.; Ishihara, K.; Nakabayashi, N.; Tamada, Y. *Biomaterials* **2000**, *21*, 327–333.
41. Konno, T.; Kurita, K.; Iwasaki, Y.; Nakabayashi, N.; Ishihara, K. *Biomaterials* **2001**, *22*, 1883–1889.
42. Jang, K.; Sato, K.; Mawatari, K.; Konno, T.; Ishihara, K.; Kitamori, T. *Biomaterials* **2009**, *30*, 1413–1420.
43. Xu, Y.; Takai, M.; Ishihara, K. *Biomacromolecules* **2009**, *10*, 267–274.
44. Goda, T.; Konno, T.; Takai, M.; Moro, T.; Ishihara, K. *Biomaterials* **2006**, *27*, 5151–5160.
45. Chen, M.; Briscoe, W. H.; Armes, S. P.; Klein, J. *Science* **2009**, *323*, 1698–1701.
46. Cheng, G.; Li, G. Z.; Xue, H.; Chen, S. F.; Bryers, J. D.; Jiang, S. Y. *Biomaterials* **2009**, *30*, 5234–5240.
47. Feng, W.; Brash, J. L.; Zhu, S. P. *Biomaterials* **2006**, *27*, 847–855.
48. Ye, S. H.; Johnson, C. A.; Woolley, J. R.; Murata, H.; Gamble, L. J.; Ishihara, K.; Wagner, W. R. *Colloids Surf., B* **2010**, *79*, 357–364.
49. Reisch, A.; Voegel, J. C.; Decher, G.; Schaaf, P.; Mesini, P. J. *Macromol. Rapid Commun.* **2007**, *28*, 2217–2223.
50. Tegoulia, V. A.; Cooper, S. L. *J. Biomed. Mater. Res.* **2000**, *50*, 291–301.
51. Thami, T.; Nasr, G.; Bestal, H.; van der Lee, A.; Bresson, B. *J. Polym. Sci., Part A: Polym. Chem.* **2008**, *46*, 3546–3562.

52. Nasr, G.; Bestal, H.; Barboiu, M.; Bresson, B.; Thami, T. *J. Appl. Polym. Sci.* **2009**, *111*, 2785–2797.
53. Ferez, L.; Thami, T.; Akpalo, E.; Flaud, V.; Tauk, L.; Janot, J. M.; Dejardin, P. *Langmuir* **2011**, *27*, 11536–11544.
54. Tauk, L.; Thami, T.FerezL.; Kocer, A.; Janot, J.-M.; Dejardin, P. *Colloids Surf., B* **2012**, *101*, 189–195.
55. Thami, T.; Bresson, B.; Fretigny, C. *J. Appl. Polym. Sci.* **2007**, *104*, 1504–1516.
56. Hong, S. J.; Chang, F. M.; Chou, T. H.; Chan, S. H.; Sheng, Y. J.; Tsao, H. K. *Langmuir* **2011**, *27*, 6890–6896.
57. Janot, J.-M.; Boissiere, M.; Thami, T.; Tronel-Peyroz, E.; Helassa, N.; Noinville, S.; Quiquampoix, H.; Staunton, S.; Dejardin, P. *Biomacromolecules* **2010**, *11*, 1661–1666.
58. Dejardin, P.; Vasina, E. N. *Colloids Surf., B* **2004**, *33*, 121–127.
59. Noinville, S.; Vidic, J.; Dejardin, P. *Colloids Surf., B* **2010**, *76*, 112–116.
60. Ren, K. F.; Fourel, L.; Rouviere, C. G.; Albiges-Rizo, C.; Picart, C. *Acta Biomater.* **2010**, *6*, 4238–4248.

Chapter 32

High-Throughput Study of Protein–Surface Interactions Using a Surface Plasmon Resonance Imaging Apparatus

Yusuke Arima,[1] Rika Ishii,[1] Isao Hirata,[2] and Hiroo Iwata*,[1]

[1]Institute for Frontier Medical Sciences, Kyoto University, 53 Kawahara-cho, Shogoin, Sakyo-ku, Kyoto 606-8507, Japan
[2]Department of Biomaterials Science, Graduate School of Biomedical Sciences, Hiroshima University, 1-2-3, Kasumi, Minami-ku, Hiroshima 734-8553, Japan
***E-mail: iwata@frontier.kyoto-u.ac.jp**

Protein adsorption at the liquid–solid interface is critically important for the development of biomedical materials. Surface plasmon resonance (SPR) has been widely used in real-time monitoring of protein adsorption behavior on surfaces. However, the number of combinations of protein–surface interactions that can be measured in a single experiment is limited by a conventional SPR apparatus. We assembled an SPR imaging apparatus for high-throughput studies of many sets of protein–surface interactions. In addition, SPR sensor surfaces with arrayed spots carrying different surface properties were prepared by taking advantage of self-assembled monolayers of alkanethiols. The combination of the SPR imaging apparatus and the arrayed sensor surfaces allows for multiple and real-time monitoring of protein–surface interactions.

Introduction

Protein adsorption at the liquid–solid interface is of critical importance in a number of fundamental fields and applications, such as development of biomaterials, medical devices, and biosensors, and thus has been extensively studied. However, many questions remain to be addressed to better understand the phenomena of protein adsorption on artificial surfaces.

In Proteins at Interfaces III State of the Art 2012; Horbett, T., et al.;
ACS Symposium Series; American Chemical Society: Washington, DC, 2012.

Various surface-sensitive methods have been introduced to study protein adsorption on artificial surfaces, including ellipsometry (*1–3*), Fourier transform infrared reflection adsorption spectroscopy (FTIR-RAS) (*4*, *5*), sum frequency generation spectroscopy (*6*, *7*), atomic force microscopy (*8*, *9*), quartz crystal microbalance (*5*, *10*), optical waveguide light mode spectroscopy (*11*), and surface plasmon resonance (SPR) (*12–15*). SPR can offer real-time and label-free analysis of the interfacial events that occur on the surface of thin films formed on a metal (usually gold or silver) layer under physiological conditions (*16*). Thus, it coordinates well with self-assembled monolayers (SAMs) of alkanethiols easily formed on metal surfaces. We have examined protein–surface interactions including non-specific protein adsorption and complement activation using SPR (*17–19*). However, the number of studies of protein–surface interaction that can be performed by a conventional SPR apparatus is limited, leading to time-consuming series of analyses for comprehensive study of these interactions. Therefore, a high-throughput method is required.

Recently, a technique of SPR imaging (also designated as SPR microscopy) has been developed and applied to monitor adsorbing organic materials and biomolecules in a spatially resolved manner (*20*, *21*). The combination of SAMs of alkanethiols and the SPR imaging technique is expected to result in a high-throughput, real-time, label-free, and highly sensitive method to study protein–surface interactions. In this study, SPR sensors with arrays of spots carrying SAMs of alkanethiols with different terminal functional groups were made on a gold thin film. We examined the efficacy of the SPR imaging technique using an SPR imaging apparatus that we developed for quantitative analyses of protein adsorption on the functionalized SAM surfaces.

Surface Plasmon Resonance (SPR) Imaging Apparatus

Principle of SPR

A surface plasmon is a longitudinal charge density wave that is propagated in a parallel manner along the interface of two media, where one surface is a metal and the other is a dielectric layer (*22*). A metal with a free electron is an essential component, as described by the free electron model of the SPR phenomenon. Most experimental work has been performed using gold and silver thin layers. The surface plasmon is excited by a light wave in SPR sensors. The Kretchmann configuration based on the total internal reflection of light has been employed for development of an SPR optical unit (*23*).

The evanescent wave of the incident light can couple with a surface plasmon at a specific incident angle, θ_{SPR}; that is, the wave vector k_{sp} for the propagating surface plasmon is coupled with the wave vector of the evanescent field k_{ev}, resulting in energy loss of the incident light to the metal film, observed as a minimum in the reflected light intensity (Figure 1 (b)). The electromagnetic field of a surface plasmon is confined at the metal–dielectric boundary and decays exponentially with ~200 nm of a typical penetration depth in common (*24*). The SPR angle (θ_{SPR}) thus sensitively depends on the refractive index of the medium in the vicinity of the metal film. Changes in the refractive index above the metal surface caused by various biological processes, such as adsorption of proteins, result in a change in θ_{SPR}.

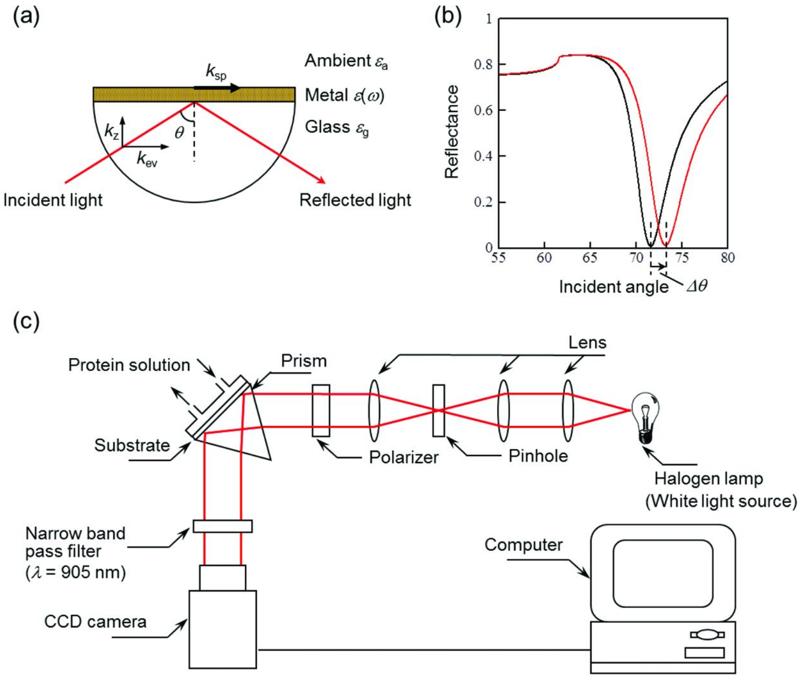
(a)
k_{sp}
Ambient ε_a
Metal $\varepsilon(\omega)$
Glass ε_g
k_z
θ
k_{ev}
Incident light
Reflected light
(b)
Reflectance
1
0.8
0.6
0.4
0.2
0
55
60
65
70
75
80
Incident angle
$\Delta\theta$
(c)
Protein solution
Prism
Lens
Substrate
Polarizer
Pinhole
Halogen lamp
(White light source)
Narrow band pass filter
(λ = 905 nm)
Computer
CCD camera

Figure 1. (a) Schematic illustration of the Kretschmann configuration for SPR. The surface plasmon is excited at the metal–ambient interface when the evanescent component of a wave vector of incoming light (k_{ev}) is equal to the wave vector of the propagating surface plasmon (k_{sp}). (b) Reflectance as a function of incident angle before (black) and after (red) adsorption of substances. (c) Schematic representation of an SPR apparatus. Reprinted with permission from reference (25).

SPR Imaging Apparatus

The optical construction of our SPR imaging apparatus is simple, as shown schematically in Figure 1 (c) (*25*). The SPR sensor is a glass plate coated with gold (~44 nm), with an underlayer of chromium (~1 nm) as an adhesive layer. The plate is optically coupled to a glass prism using an index-matching fluid. A collimated and *p*-polarized laser beam is directed to the back side of a sample plate through a glass prism, and reflected light is captured by a CCD camera. Near-infrared light ($\lambda = 905 \pm 5$ nm) was used to improve sensitivity for the SPR imaging experiment (*26*). By changing the incident angle of the collimated light, we can determine the SPR angle (θ_{SPR}) as the minimum in reflectance (Figure 1 (b)). When the angle of incident light is fixed, the intensity of the reflected light changes due to a shift in θ_{SPR} that occurs ($\Delta\theta_{SPR}$) in a manner dependent on the amount of the deposited substances. Detection of light intensity allows for monitoring of protein adsorption behavior on the sensor surface in real time. The light intensity change can be converted to the amount of protein adsorbed using Fresnel fits for the system glass/Cr/Au/protein/water (*27*, *28*).

Model Surfaces

Self-Assembled Monolayers of Alkanethiols

We employed alkanethiols, $HS(CH_2)_nX$, which form SAMs on the SPR sensor surface, to prepare model surfaces presenting functional group “X.” Alkanethiols chemisorb from a solution onto a metal surface such as gold, silver, or platinum. A gold thin layer on a glass plate is commonly used to form SAMs because it is easy to prepare and is stable in the ambient environment. The gold–sulfur bond is relatively stable with $\Delta H^\circ \approx 28$ kcal/mol (*29*, *30*). In addition, van der Waals interactions between each long alkyl chain lead to self-assembly of the molecules. Alkanethiols carrying a long alkyl chain ($n > 11$) form closely packed SAMs with approximately 21.4 Å^2 of occupied area per molecule (*31*, *32*). Due to anchoring of the thiol to gold and the close packing of the alkyl chain, a functional group, X, at another terminal end is effectively displayed at the surface of the SAM. Alkanethiols with various functional groups, X, are commercially available. It is easy to prepare SAMs displaying various functional groups.

In addition, the surface properties of SAMs can be finely controlled by coadsorption from a mixture of alkanethiols with different functional groups. The composition of alkanethiols in SAMs reflects the mole fraction of alkanethiols in solution but is not the same as their composition in the solution. The composition of SAMs can be determined by spectroscopic methods such as FTIR-RAS and X-ray photoelectron spectroscopy. Figure 2 summarizes mixed SAMs, which are prepared from a mixture of hydroxyl-terminated alkanethiols (11-mercapto-1-undecanol) and methyl-terminated alkanethiols with different alkyl chain lengths (*33*). The surface composition of the alkanethiol in the mixed SAM was determined from the FTIR-RAS spectra using an absorption band assigned to the asymmetric stretching mode of the methyl groups. The surface fraction of the alkanethiols in the mixed SAM does not linearly reflect the mole fraction in the original solution (Figure 2 (a)). Rather, it is highly dependent on the alkyl chain length of alkanethiols and the terminal functional groups (*18*, *34*). The water contact angle reflects hydroxyl content in the mixed SAMs (Figure 2 (b)). Thus, the preparation of mixed SAMs from a mixture of different alkanethiols allows us to systematically change surface properties and provides different kinds of model surfaces for studies of protein adsorption on artificial materials.

Arrays for SPR Imaging Experiment

Protein adsorption onto surfaces with different surface properties can be simultaneously monitored using the SPR imaging apparatus and a sensor chip with arrayed spots with different SAMs. We prepared the sensor chip using photo-patterning of SAMs. Other techniques such as microcontact printing (*35*) and inkjet printing (*36*) are also available for preparing the arrays.

Preparation of the array is schematically depicted in Figure 3. A gold-coated glass substrate was immersed in an ethanol solution of methyl-terminated alkanethiol to form a hydrophobic SAM. The SAM was photo-oxidized by UV irradiation through a photomask, and then the oxidized SAM was removed by rinsing with ethanol. Droplets of ethanol solutions of alkanethiols (300 nL) were subsequently placed on the oxidized spots to form the SAM. A hydrophobic SAM of the methyl-terminated alkanethiol was employed as a base SAM to prevent spreading of ethanol solution placed on each spot. The surface properties of the spots were controlled by varying the terminal functional group of the alkanethiol or by mixing two kinds of alkanethiols.

High-Throughput Protein Adsorption Studies Using the SPR Imaging Apparatus

Non-Specific Protein Adsorption

When artificial materials are brought into contact with biological fluids, non-specific protein adsorption occurs at the initial phase and affects subsequent biological responses, including blood coagulation, complement activation, and cell adhesion. Therefore, it is of critical importance to understand and control non-specific protein adsorption to develop materials for biomedical uses. We employed the SPR imaging apparatus to examine the effect of surface functional groups on non-specific protein adsorption.

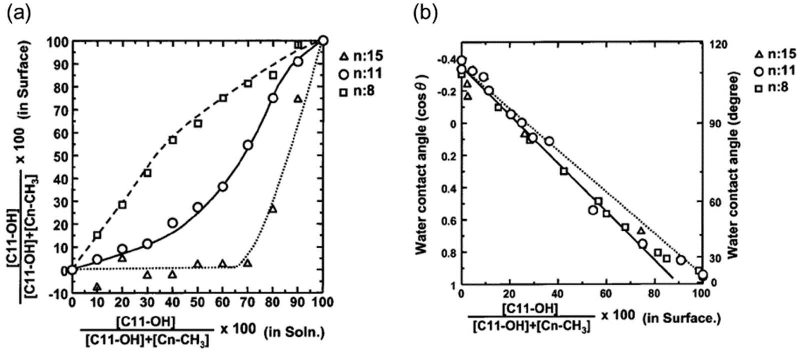

Figure 2. Composition (a) and water contact angles (b) of SAMs formed from various reaction mixtures of 11-mercapto-1-undecanol and several methyl-terminated alkanethiols with different alkyl chain lengths. The composition of SAMs was determined by FTIR-RAS spectra. Reprinted with permission from reference (33). Copyright 2003 John Wiley & Sons.

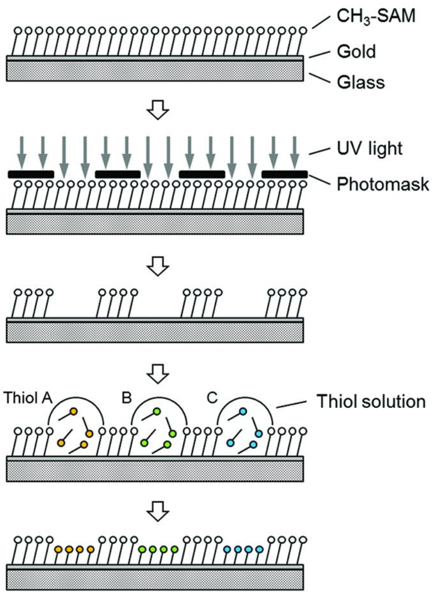

Figure 3. Scheme for fabrication of an array of SAMs carrying different functional groups.

Spots carrying alkanethiols with different functional groups, e.g., methyl (CH_3), hydroxyl (OH), carboxylic acid (COOH), amine (NH_2), or poly(ethylene glycol) (PEG)-coupled amine (PEG) groups, were formed in an array format on the SPR sensor as depicted in Figure 4 (c) (*25*). PEG-tethered spots were prepared by reacting the *N*-hydroxysuccinimidyl ester of methoxy–PEG propionic acid (PEG-NHS; MW of PEG: 2,000) with spots of an amine-terminated alkanethiol. In our SPR imaging apparatus, spots appeared as ellipses because images of the arrayed spots were observed at an oblique angle as schematically shown in Figure 1(c). Spots except the PEG-tethered spots were darker than background (Figure 4(a)). The number of repeating methylene units in an alkanethiol molecule on spots (n = 11) was smaller than that on the surrounding area (n = 15). Supporting the notion that refractive indices of all alkanethiols are the same (i.e., 1.45) (*37*), the brightness in the CCD image reflects the thickness of the monolayer. The difference in thickness between spots and background is expected to be 0.5 nm. This caused darkness in the SPR images for spots with alkanethiols with methyl (CH_3), hydroxyl (OH), carboxylic acid (COOH), and amine (NH_2) groups. These results demonstrated the high vertical resolution of the SPR imaging apparatus. The PEG-tethered spots, where PEG-NHS (MW = 2,000) was reacted with NH_2 spots, appear to be the same brightness as the background. The brightness in the SPR image depends on the effective refractive index near the metal surface. This association might be due to hydration of the surface-bound PEG chains. The effective refractive index of hydrated chains is much lower than that of ethylene glycol (n = 1.4306) and dehydrated PEG film (high molecular weight poly(oxyethylene), n = 1.4563) (*38*).

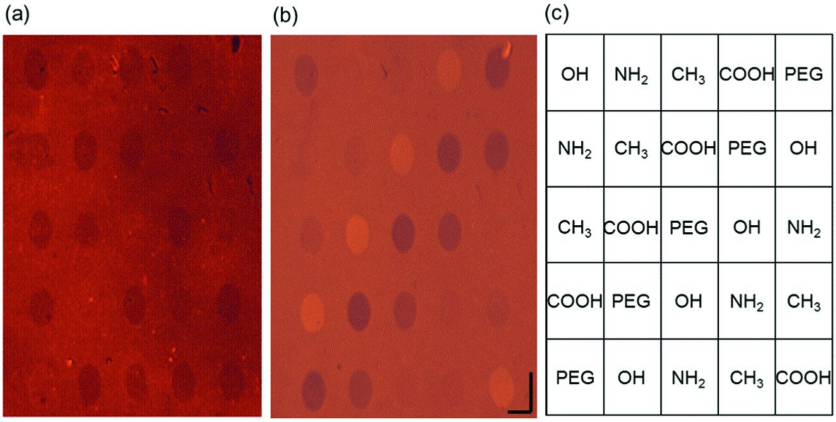

OH	NH_2	CH_3	COOH	PEG
NH_2	CH_3	COOH	PEG	OH
CH_3	COOH	PEG	OH	NH_2
COOH	PEG	OH	NH_2	CH_3
PEG	OH	NH_2	CH_3	COOH

Figure 4. SPR image of the array in buffer (a) before and (b) after BSA adsorption. The surface functional group of each spot is shown in (c). Image (b) was acquired by subtraction of the image from image (a). Scale bar, 1 mm. Reprinted with permission from reference (25).

We examined adsorption of bovine serum albumin (BSA) on the SAM array. Figure 4(b) shows a CCD image acquired by subtraction of the two images collected before and after exposure of the array to a BSA solution for 2 hours. Brightness of spots is related to the amount of adsorbed protein. It is noted that BSA adsorption also occurs onto the background surface, which carries a methyl-terminated alkanethiol. Therefore, contrasted in Figure 4 (b) are results from the difference in the adsorbed amount of BSA between spots and the background. The observed pattern allows for qualitative analysis of protein adsorption.

The intensities of reflected light averaged for 7 × 7 pixels in each spot were continuously monitored during the entire period of the flowing solutions. Figure 5 shows the time course of BSA adsorption for multiple regions of the array. First, Dulbecco's phosphate buffered saline (DPBS) was introduced in a flow cell to establish baselines, and then a BSA solution in DPBS (1 mg/mL) was introduced. The SPR signal sharply increased upon introduction of the BSA solution. Change in reflected light intensity was caused by the combination effects of the refractive index increase of the solution containing BSA and BSA adsorption onto the surface. Net SPR signal increase due to the BSA adsorption could be seen after replacement with DPBS. After a 2-hour exposure, the BSA solution was replaced with DPBS. For protein adsorption studies, the change in the intensity of reflected light (ΔI) should be converted to the adsorbed amount of proteins (Γ) by the following equation according to a calibration curve of the SPR signal (*25*),

$$\Gamma = 0.91 \text{ x } 10^{-2} \, \Delta I$$

The adsorbed amounts of proteins are depicted at the right vertical line.

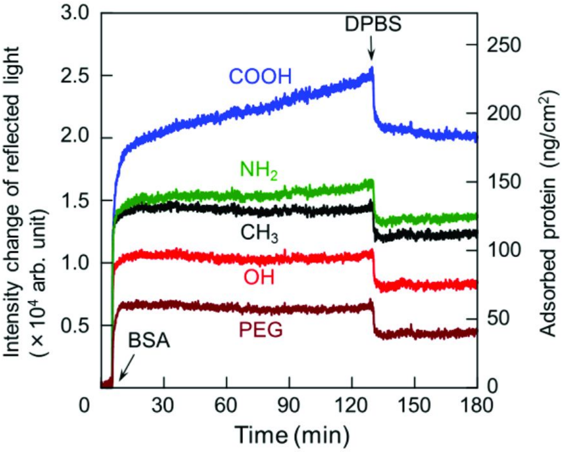

Figure 5. Parallel monitoring of BSA adsorption onto an array carrying different functional groups. BSA concentration: 1 mg/mL. Reprinted with permission from reference (25).

We further examined the effect of protein type and the pH of buffers on protein adsorption (Figure 6). We employed BSA, γ-globulin, and lysozyme for model proteins and buffers of pH 3–11 (McIlvaine buffer for pH 3, 5, and 7, and 0.2 M carbonate buffer for pH 9 and 11). As expected, coupling of PEG reduced non-specific adsorption for all proteins and at all pH values examined. For BSA and γ-globulin, the amounts of adsorbed proteins showed the maximum at pH 5 regardless of the surface functional group of SAM spots. This pH value is close to the isoelectric points (IEPs) of the proteins (BSA: 4.8, γ-globulin: ~6) (*39*). The maximum in adsorbed protein around its IEP is in agreement with previous studies on pH-dependent adsorption (*40–42*). Intermolecular and intramolecular electrostatic repulsions of proteins are minimized at this pH value. These results suggest that the protein property resulting from the electrostatic interaction plays important roles in protein adsorption. According to the dimensions of BSA (14 × 4 × 4 nm), the amounts of adsorbed proteins are estimated to be 250 ng/cm^2 for side-on and 600 ng/cm^2 for end-on orientations (*39*). Our results suggest that BSA adsorbs onto the surfaces in side-on orientation even at pH 5. For γ-globulin (24 × 4.4 × 4.4 nm), the adsorbed amounts are calculated to be 270 ng/cm^2 for side-on and 1480 ng/cm^2 for end-on orientations (*39*), suggesting that γ-globulin adsorbs onto SAM surfaces partially in end-on orientation. As the solution pH became alkali, the amount of adsorbed proteins decreased. Especially, the amounts of adsorbed proteins drastically decreased at pH 9 and 11 for COOH-SAM. At this pH, both COOH-SAM surface and proteins are negatively charged. Therefore, electrostatic repulsion plays an important role in reducing the non-specific adsorption to the COOH-SAM surface at this pH range.

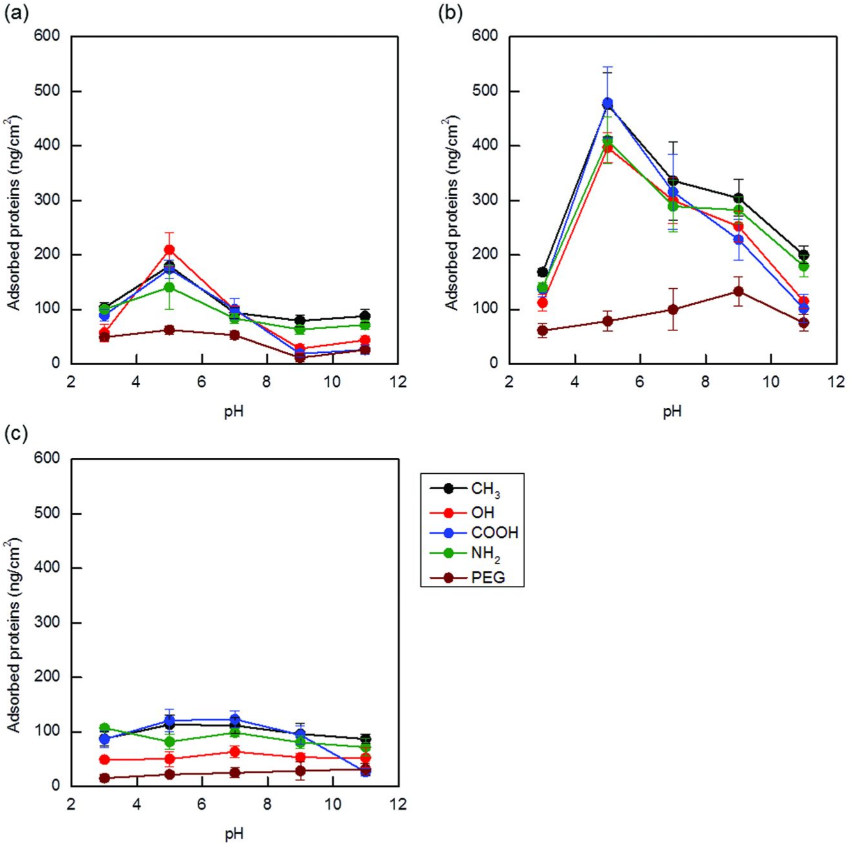

Figure 6. Effect of solution pH on the amount of BSA (a), γ-globulin (b), or lysozyme (c) adsorbed onto SAMs carrying different terminal groups. Protein concentration: 1 mg/mL. Data shown are means ± SD (n = 5).

These results demonstrate the usefulness of the SPR imaging apparatus for real-time and parallel analysis (high-throughput) of protein adsorption on many spots presenting different surface functional groups. Ostuni et al (*43*) examined the relationship between characteristics of functional groups and the ability to resist the non-specific adsorption of proteins on 58 kinds of surfaces on gold by SPR analysis in a one-spot format. However, their method requires large numbers of measurements, one for each sample surface. In our system, protein adsorption on 25 different surfaces can be simultaneously examined. Thus, parallel sensing using the SPR imaging apparatus has great advantages in its ability to allow label-free, high-sensitivity, and real-time detection of interfacial events.

Complement Activation

The complement system is composed of approximately 30 fluid-phase and cell-membrane–bound proteins. It is activated through a cascade of enzyme reactions and plays an important role in the body's defense systems against pathogenic xenobiotics (*44*, *45*). It is also non-specifically activated by artificial polymeric materials. For example, hemodialysis membranes made of cellulose or its derivatives strongly activate the complement system, and this process has been extensively studied (*46*, *47*). The complement activation by artificial materials also has been seen in various clinical settings, such as open heart surgery, blood transfusion medicine, and extracorporeal immunotherapies (*48–50*). Understanding the complement activation by artificial materials is important to the rational design of biocompatible surfaces of synthetic materials.

We examined the effect of surface functional groups on complement activation using the SPR imaging apparatus. Human serum (10%) was exposed to the array with the pattern shown in Figure 4, and deposition of serum proteins was monitored in real time. Deposition of serum proteins occurred for all spots. The largest amount of deposited proteins was observed for the spots carrying hydroxyls and PEG (Figure 7(a)). This behavior greatly differs from that in a single protein solution of BSA, γ-globulin, or lysozyme, as shown in Figure 5. After the array was rinsed with buffer, the surfaces carrying layers of adsorbed serum protein were further characterized by exposure to an anti-human C3b antiserum solution. Anti-C3b antibody was expected to be bound to C3b or C3 convertase (C3bBb) deposited on the SAM surfaces. A much larger amount of anti-C3b antibody was bound to the protein layers deposited on hydroxyl and PEG spots (Figure 7(b)), indicating that a major component in the protein adsorbed layer is C3b or C3bBb. These results demonstrated that the surface carrying the hydroxyl groups and PEG strongly activated the complement system, resulting in C3b or C3bBb deposition. When C3b is deposited on the material surface, it forms C3bBb, which cleaves C3 in the vicinity of the surface into C3a and C3b. The rate of C3b deposition onto the surface is accelerated by an autocatalytic positive feedback mechanism after C3 convertase has been generated once.

The above inference was supported by results from enzyme-linked immunosorbent assay (ELISA) of the fragments of complement proteins produced during the complement activation. Human serum was incubated with surfaces, and concentrations of complement fragments or complexes (C3a, Bb, or SC5b-9) in the serum samples were then determined by ELISA. Surfaces on which a large amount of anti-C3b antibody was deposited also produced fragments of complement proteins, such as Bb, C3a, and SC5b-9, in serum (*51–53*). The combination of SPR and ELISA thus provides coordinated information about complement activation behavior on material surfaces, but SPR is superior for rapid and real-time monitoring of complement activation compared to ELISA.

Strong complement activation by a SAM carrying a hydroxyl group is consistent with our previous work (*51*). It has also been reported that materials surfaces carrying hydroxyl groups, such as a hemodialysis membrane made from cellulose, strongly activate the complement system (*46*, *47*). Of interest, a large amount of C3b was deposited on a PEG-tethered amine surface. Based on our previous studies, this result suggests that the complement system is strongly activated by a PEG-tethered amine surface even though we did not quantify concentrations of complement fragments generated in human serum after incubation with the surface. We reported that methoxy-terminated PEG surfaces do not activate the complement system although long-term storage makes the surface a strong activator for the complement system (*54*, *55*). PEG, which was used in this study, carries a methoxy group at its terminus. The PEG might be degraded during storage, or the mixed surface of PEG and amine groups might affect triggers for complement activation. Further study is needed to understand the mechanism in detail.

We also examined the effect on complement activation of the density of hydroxyl groups. Spots carrying different hydroxyl contents were prepared by mixing two kinds of alkanethiols: 1-nonanethiol ($CH_3(CH_2)_8SH$) and 11-mercapto-1-undecanol ($HO(CH_2)_{11}SH$). Alkanethiol solutions (mole percent of $HO(CH_2)_{11}SH$: 0, 25, 50, 75, 100%; total thiol concentration: 1 mM) were placed on a photo-patterned SAM surface for 1 hour. Methyl-terminated alkanethiols with shorter alkyl chains were used so that the hydroxyl contents on the surface became nearly identical to those in solution (see Figure 2(a)) (*33*). The amount of deposited proteins increased with an increase in hydroxyl content (Figure 8a). The amount of bound anti-C3b antibody also increased with increasing hydroxyl content (Figure 8b), consistent with our previous report (*33*). These results clearly demonstrate that the surface density of hydroxyl groups greatly modulates the complement behavior.

To further investigate complement activation behavior on material surfaces, a combination study of SPR and ELISA is needed. The SPR imaging apparatus is still useful for screening complement behavior on materials surfaces.

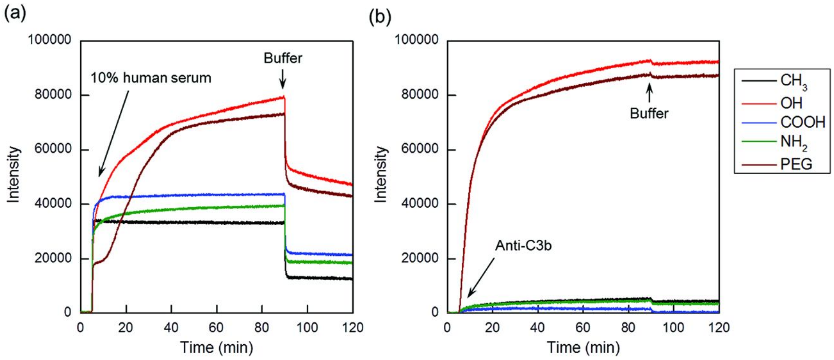

Figure 7. Time course of protein adsorption from 10% human serum (a) and subsequent binding of anti-C3b antiserum onto SAMs carrying different functional groups.

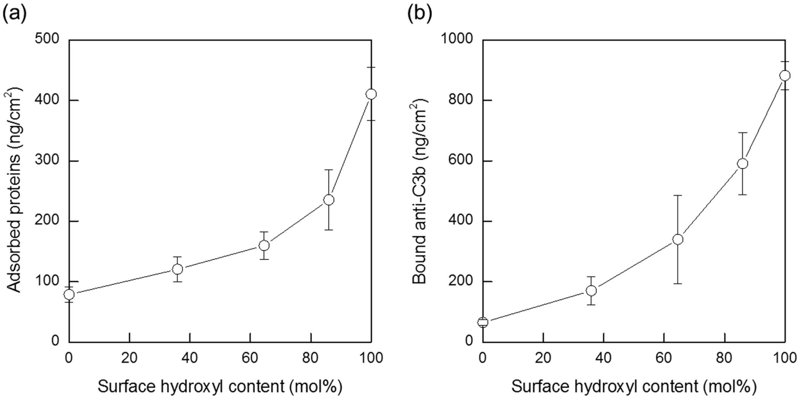

Figure 8. Relationship between hydroxyl content on SAM surface and the amount of adsorbed serum proteins (a) and bound anti-C3b antiserum (b). Data shown are means ± SD (n = 5).

Summary

We described a high-throughput method using an SPR imaging apparatus and a sensor with arrayed spots for quantitative and parallel analysis of protein–surface interactions, including non-specific protein adsorption and complement activation. The array presenting spots with different surface characteristics was fabricated by photo-patterning of SAMs, which has the great advantage of stable and well-defined surfaces. A large number of spots with various surface properties is displayed on a sensor chip. Thus, our method is a powerful tool for screening of protein–surface interactions in designing biomaterials with desired functions.

Acknowledgments

This work was supported by a Grant-in-Aid for Scientific Research on Innovative Areas “Nanomedicine Molecular Science” (No. 2306) and a Grants-in-Aid for Young Scientists (B) (No. 23700559) from the Ministry of Education, Culture, Sports, Science, and Technology of Japan.

References

1. Elwing, H. *Biomaterials* **1998**, *19*, 397–406.
2. Lestelius, M.; Liedberg, B.; Tengvall, P. *Langmuir* **1997**, *13*, 5900–5908.
3. Herrwerth, S.; Eck, W.; Reinhardt, S.; Grunze, M. *J. Am. Chem. Soc.* **2003**, *125*, 9359–9366.
4. Chittur, K. K. *Biomaterials* **1998**, *19*, 357–369.
5. Roach, P.; Farrar, D.; Perry, C. C. *J. Am. Chem. Soc.* **2005**, *127*, 8168–8173.
6. Kim, J.; Somorjai, G. A. *J. Am. Chem. Soc.* **2003**, *125*, 3150–3158.
7. Clarke, M. L.; Wang, J.; Chen, Z. *J. Phys. Chem. B* **2005**, *109*, 22027–22035.
8. Kidoaki, S.; Matsuda, T. *Langmuir* **1999**, *15*, 7639–7646.

9. Sethuraman, A.; Han, M.; Kane, R. S.; Belfort, G. *Langmuir* **2004**, *20*, 7779–7788.
10. Höök, F.; Rodahl, M.; Kasemo, B.; Brzezinski, P. *Proc. Natl. Acad. Sci. U.S.A.* **1998**, *95*, 12271–12276.
11. Vörös, J.; Ramsden, J. J.; Csúcs, G.; Szendrő, I.; De Paul, S. M.; Textor, M.; Spencer, N. D. *Biomaterials* **2002**, *23*, 3699–3710.
12. Mrksich, M.; Sigal, G. B.; Whitesides, G. M. *Langmuir* **1995**, *11*, 4383–4385.
13. Sigal, G. B.; Mrksich, M.; Whitesides, G. M. *J. Am. Chem. Soc.* **1998**, *120*, 3464–3473.
14. Green, R. J.; Davies, M. C.; Roberts, C. J.; Tendler, S. J. B. *Biomaterials* **1999**, *20*, 385–391.
15. Ostuni, E.; Chapman, R. G.; Holmlin, R. E.; Takayama, S.; Whitesides, G. M. *Langmuir* **2001**, *17*, 5605–5620.
16. Green, R. J.; Frazier, R. A.; Shakesheff, K. M.; Davies, M. C.; Roberts, C. J.; Tendler, S. J. B. *Biomaterials* **2000**, *21*, 1823–1835.
17. Arima, Y.; Iwata, H. *J. Mater. Chem.* **2007**, *17*, 4079–4087.
18. Arima, Y.; Iwata, H. *Biomaterials* **2007**, *28*, 3074–3082.
19. Arima, Y.; Toda, M.; Iwata, H. *Adv. Drug. Delivery Rev.* **2011**, *63*, 988–999.
20. Rothenhausler, B.; Knoll, W. *Nature* **1988**, *332*, 615–617.
21. Brockman, J. M.; Nelsen, B. P.; Corn, R. M. *Annu. Rev. Phys. Chem.* **2000**, *51*, 41–63.
22. Raether, H. *Surface plasmons on smooth and rough surfaces and on gratings*; Springer: Berlin, 1988; pp 4−7.
23. Kretchmann, E. *Z. Phys.* **1971**, *241*, 313–324.
24. Liedberg, B.; Lundström, I.; Stenberg, E. *Sens. Actuators, B* **1991**, *63*, 63–72.
25. Arima, Y.; Ishii, R.; Hirata, I.; Iwata, I. *e-J. Surf. Sci. Nanotechnol.* **2006**, *4*, 201–207.
26. Nelson, B. P.; Frutos, A. G.; Brockman, J. M.; Corn, R. M. *Anal. Chem.* **1999**, *71*, 3928–3934.
27. Azzam, R. M. A.; Bashara, N. M. *Ellipsometry and polarized light*; North-Holland Publishing Company: Amsterdam, 1977; pp 269−363.
28. Knoll, W. *Makromol. Chem.* **1991**, *192*, 2827–2856.
29. Nuzzo, R. G.; Zegarski, B. R.; Dubois, L. H. *J. Am. Chem. Soc.* **1987**, *109*, 733–740.
30. Nuzzo, R. G.; Dubois, L. H.; Allara, D. L. *J. Am. Chem. Soc.* **1990**, *112*, 558–569.
31. Porter, M. D.; Bright, T. B.; Allara, D. L.; Chidsey, C. E. D. *J. Am. Chem. Soc.* **1987**, *109*, 3559–3568.
32. Strong, L.; Whitesides, G. M. *Langmuir* **1988**, *4*, 546–558.
33. Hirata, I.; Hioki, Y.; Toda, M.; Kitazawa, T.; Murakami, Y.; Kitano, E.; Kitamura, H.; Ikada, Y.; Iwata, H. *J. Biomed. Mater. Res.* **2003**, *66A*, 669–676.
34. Bain, C. D.; Evall, J.; Whitesides, G. M. *J. Am. Chem. Soc.* **1989**, *111*, 7155–7164.
35. Xia, Y.; Whitesides, G. M. *Annu. Rev. Mater. Sci.* **1998**, *28*, 153–184.
36. Sakurai, K.; Teramura, Y.; Iwata, H. *Biomaterials* **2011**, *32*, 3596–3602.

37. Bain, C. D.; Troughton, E. B.; Tao, Y. T.; Evall, J.; Whitesides, G. M.; Nuzzo, R. G. *J. Am. Chem. Soc.* **1989**, *111*, 321–335.
38. Seferis, J. C. In *Polymer handbook*, 4th ed.; Brandrup, J., Immergut, E. H., Grulke, E. A., Eds.; John Wiley & Sons: New York, 1999; pp 571−582.
39. Soderquist, M. E.; Walton, A. G. *J. Colloid Interface Sci.* **1980**, *75*, 386–397.
40. Norde, W. *Adv. Colloid Interface Sci.* **1986**, *25*, 267–340.
41. Shirahama, H.; Suzuwa, T. *Colloid Polym. Sci.* **1985**, *263*, 141–146.
42. Kondo, A.; Higashitani, K. *J. Colloid Interface Sci.* **1992**, *150*, 344–351.
43. Ostuni, E.; Chapman, R. G.; Holmlin, R. E.; Takayama, S.; Whitesides, G. M. *Langmuir* **2001**, *17*, 5605–5620.
44. Walport, M. J. *N. Engl. J. Med.* **2001**, *344*, 1058–1066.
45. Ricklin, D.; Hajishengallis, G.; Yang, K.; Lambris, J. D. *Nat. Immunol.* **2010**, *11*, 785–797.
46. Chenoweth, D. E. *Artif. Organs* **1984**, *8*, 281–290.
47. Wegmuller, E.; Montandon, A.; Nydegger, U.; Descoeudres, C. *Int. J. Artif. Organs* **1986**, *9*, 85–92.
48. Chenoweth, D. E.; Cooper, S. W.; Hugli, T. E.; Stewart, R. W.; Blackstone, E. H.; Kinklin, J. W. *N. Engl. J. Med.* **1981**, *304*, 497–503.
49. Gu, Y. J.; van Oeveren, W. *ASAIO J.* **1994**, *40*, 598–601.
50. Maillet, F.; Petitou, M.; Choay, J.; Kazatchkine, D. *Mol. Immunol.* **1988**, *25*, 917–923.
51. Hirata, I.; Morimoto, Y.; Murakami, Y.; Iwata, H.; Kitano, E.; Kitamura, H.; Ikada, Y. *Colloids Surf., B* **2000**, *18*, 285–292.
52. Toda, M.; Kitazawa, T.; Hirata, I.; Hirano, Y.; Iwata, H. *Biomaterials* **2008**, *29*, 407–417.
53. Toda, M.; Iwata, H. *ACS Appl. Mater. Interfaces* **2010**, *2*, 1107–1113.
54. Arima, Y.; Toda, M.; Iwata, H. *Biomaterials* **2008**, *29*, 551–560.
55. Toda, M.; Arima, Y.; Iwata, H. *Acta Biomater.* **2010**, *6*, 2642–2649.

Chapter 33

Probing Protein Association with Nano- and Micro-Scale Structures with ToF-SIMS

Ivan M. Kempson,*,[1,2] Yeukuang Hwu,[1] and Clive A. Prestidge[2]

**[1]Institute of Physics, Academia Sinica, Academia Road,
Nankang, Taipei, 11529, Taiwan
[2]Ian Wark Research Institute, University of South Australia,
Mawson Lakes, S.A., 5095, Australia
*E-mail: Ivan.Kempson@unisa.edu.au**

Time-of-Flight Secondary Ion Mass Spectrometry (ToF-SIMS) can be used for mass spectrometry and imaging of inorganic and organic components on surfaces. Full spectral information for each pixel down to sub-micron resolution provides a means to study protein interactions with interfaces in highly heterogeneous structures, assemblies and mixtures; patterned arrays; or simultaneous correlation with other chemical features (gradients, spatial arrangements etc). With careful spectral analysis and interpretation, indications of protein orientation, bonds and structural changes can be investigated. ToF-SIMS, with highly sensitive mass fragmentation patterns and high spatial resolution provides complementary information in systems with structurally complex arrangements, chemical heterogeneity and multicomponent mixtures. ToF-SIMS analysis of proteins at interfaces offers unique complementary information which is described here in the context of understanding protein interactions at interfaces with examples of nano- and micro-scale structures. The use for complementary characterization of surface chemical properties which relate to protein interactions is also emphasized.

In Proteins at Interfaces III State of the Art 2012; Horbett, T., et al.;
ACS Symposium Series; American Chemical Society: Washington, DC, 2012.

1. Introduction

Time-of-Flight Secondary Ion Mass Spectrometry (ToF-SIMS) can be used for mass spectrometry and imaging of inorganic and organic components on surfaces. Full spectral information for each pixel down to sub-micron resolution provides a means to study protein interactions with interfaces in highly heterogeneous structures, assemblies and mixtures; patterned arrays; or simultaneous correlation with other chemical features (gradients, spatial arrangements etc). With careful spectral analysis and interpretation, indications of protein orientation, bonds and structural changes can be investigated.

Protein association with interfaces is an absolutely fundamental phenomenon with implications in numerous areas of fundamental biological processes, homeostasis, disease and associated research for mechanistic understandings, sensors, pharmaceutics etc, as described throughout this book. Many aspects of protein interactions with interfaces are well characterized with methods to deduce gross information such as adsorption isotherms, nature of bonds or layer thickness; however these typically rely on a homogenous and often ‘flat’ interface, or provide an ensemble average over the analysis area/volume. Within many realistic systems in which a protein is interacting at an interface, there are localized physical and chemical features which can affect the nature and impact of the interaction. For example; radii of curvature of cellular compartments and materials, bio-interactions with nanoparticulate material, porous drug delivery substrates, competitive mechanisms, crystallographic orientations and faces all impact protein-substrate interactions. In these instances it is often difficult to establish a model system suitable for analyses and to discriminate relevant variables. This is of great consequence for research into systems where a large extent of heterogeneity in both physical and chemical properties exist (both within the properties themselves and spatially).

Analytical approaches for investigating protein adsorption are highly varied, each adding components of information to piece together an understanding of the protein interaction in the system. ToF-SIMS, with highly sensitive mass fragmentation patterns and high spatial resolution provides complementary information in systems with structurally complex arrangements, chemical heterogeneity and multicomponent mixtures (summarized in Figure 1). ToF-SIMS analysis of proteins at interfaces offers unique complementary information which is described here in the context of understanding protein interactions at interfaces with examples of nano- and micro-scale structures. The use for complementary characterization of surface chemical properties which relate to protein interactions is also emphasized.

2. ToF-SIMS

Time-of-Flight Secondary Ion Mass Spectrometry (ToF-SIMS) is a valuable instrumental technique for studying surface composition of elements, isotopes, molecules and associated fragments (Figure 2). Subsequently, ToF-SIMS has broad application (*1–5*). For thorough descriptions of the principals, instrumentation, sample preparation and other technical details, readers are refered to other books dedicated to such instruments (*6*, *7*). It operates via the focusing and rastering of a primary ion beam (often Ga^+, Bi cluster, Au cluster or C_{60} as examples) upon a sample surface. The impact and momentum transfer of the primary ions leads to ejection from the surface of its constituents as elemental species, molecular fragments or partial fragments due to bond breakage in the impact and emission process. Charged species within the sputter plume can be extracted, accelerated and transported to a spatially and temporally resolved detector via ion optics. Within the analyser and prior to the secondary ions reaching the detector, the ions navigate a time-of-flight region. Over this well-defined distance, an ions' transit time is measured and due to the relation between kinetic energy (known from the ion extraction and acceleration process) and velocity, a mass-to-charge ratio can be determined. Thus for each primary ion pulse, an entire mass spectrum is generated. The spatial arrangement is preserved in the detector plane and images of windowed spectral features are formed. The nature of this probe is highly surface sensitive and for larger molecules such as proteins, may probe sub-monolayer depths. The typical sub-micron spatial resolution achieved with Liquid Metal Ion Guns (LMIG) enables highly detailed imaging. Isotopic imaging has been particularly well exemplified by Metzner et al. with cryo-fixed images of potassium isotope ratios in plant tissue sections (*8*). Similar potential exists for isotope labeled biologically relevant molecules.

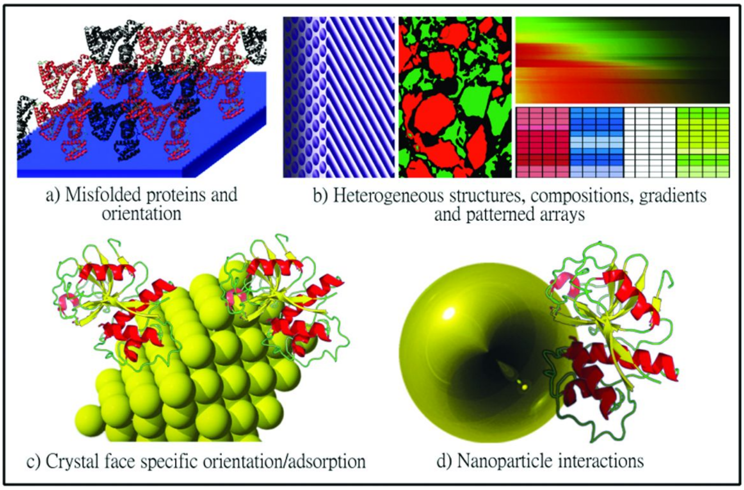
a) Misfolded proteins and orientation
b) Heterogeneous structures, compositions, gradients and patterned arrays
c) Crystal face specific orientation/adsorption
d) Nanoparticle interactions

Figure 1. Areas of protein adsorption research relevant to ToF-SIMS.

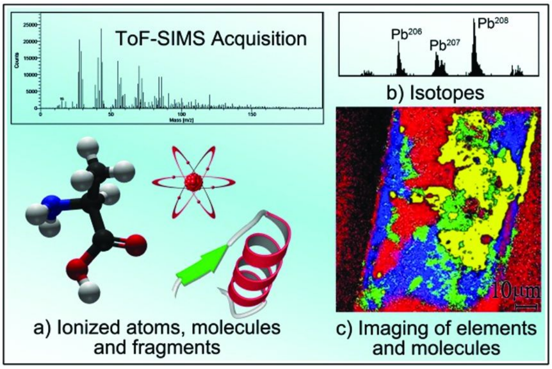

Figure 2. An example of a ToF-SIMS positive ion spectrum with representative information provided. The acquisition detects: (a) elemental composition, molecular ions (up to approximately 500-5,000 daltons depending on instrumentation) and compositional fragments; (b) isotopic information; and (c, adapted from Kempson et al. (9)) can image their distributions with sub-micron resolution; the image of a hair shows a Si-based compound (red), typical (blue) and oxidized (green) protein, and chloride based salts (yellow).

2.1. Primary Ion Sources

Often, the specific scientific question under investigation will determine the most appropriate primary ion source. The primary ion imparts major influence on the sputtering process. Due to these effects, the following questions may be asked in determining the optimal choice: What spatial resolution (if any) is needed? What mass resolution is needed to resolve peaks of interest? Will depth profiling be performed? Are the secondary ions of interest negatively or positively charged? The answer to such or similar questions will determine what primary ion source is most appropriate as well as it's mode of operation (primary ion bunching, dose, energy etc). The secondary ion yield can vary by orders of magnitude from one secondary ion to another and due to the primary source used, thus the surface density of the molecule of interest can also determine what is feasible from one ion source to another. With specific regard to protein analysis, each primary ion can influence fragmentation patterns (or protein 'finger-printing') and needs to be suited to the scientific question at hand (*10*).

Most commonly, primary ion sources will be either LMIG, polyatomic or cluster sources. Each primary ion (of which there are many options), its composition and energy, will have specific advantages in approaching specific analytical requirements. Many publications have subsequently resulted in comparing ion sources with particular regard to biologically relevant samples (*11*, *12*). There are many intricacies in attempting to make direct comparisons between ion sources and as such the discussion here is kept to generalised information and will ultimately primarily depend on what is available to the investigator. Many ToF-SIMS instruments will be installed with two or more ion sources to gain their respective benefits. Some examples of reported comparisons between ion sources are included in the following paragraphs to demonstrate variability and options in ion sources. This is by no means complete, but rather serves as an indication of the need to assess available primary ions on the basis of the analytical requirements.

LMIG ion sources (such as Ga^+, Au^+, Bi^+ etc) are likely to be the most common ion sources, especially in older instruments. In more recent years however, the analysis of proteins has largely evolved with the development of polyatomic and cluster ion sources which have higher secondary ion yields and greater mass range, but at the expense of spatial resolution. Ga^+ primary ions have achieved impressive spatial resolutions to detect 50nm features (*13*). However, Au+ and Au_3^+ can enhance secondary ion yields over Ga^+ while maintaining good spatial resolution (*14*). Larger primary ions have further advantages for biological and protien imaging (*15–18*). Bi_3^+ can have better surface sensitivity than Bi_1^+ and C_{60}^+ (*19*), and can achieve good currents for large area mapping while Bi_5^{2+} may be desired for maintaining better spatial resolutions <400nm (*20*).

More recently, C_{60} has emerged with beneficial properties for depth profiling and extending mass range sensitivity (*21*). The sputtering process reduces fragmentation compared to other ion sources and enables depth profiling in complex samples while retaining a good degree of sample integrity. This is particularly well illustrated by depth profiling and 3D chemical reconstruction of an individual cell by Fletcher et al. (*22*), but so far is best demonstrated for lipids. C_{60}^+ can generally provide better surface sensitivity than gold and gold clusters (*23*). However, a 520keV Au_{400}^{4+} source increased secondary ion yield 100 fold compared to 130 keV Au_3^+ and 43 keV C_{60} (*17*). At the time of publication this was limited to 10x10 micron focal spots. Conversely, for deuterated labels, clusters may not provide advantage over Bi^+ ions (*18*). C_{60} analysis more recently has been incorporated with Ar^+ sputtering to quantitatively depth profile peptide mixtures (*24*). Ar^+ and in particular the newly emerging argon cluster technology are looking to provide new opportunities for protein analysis due to simpler fragmentation patterns (*25*). The generalised advantages and disadvantages of the classes of primary ions are included in Table I.

2.2. Challanges and Other Considerations

ToF-SIMS, as with any other analytical technique, is not without its limitations and challenges. Of particular note is the limited mass range which varies between ion sources. This is often limited to a few hundred mass units for LMIG sources or ~2,000 for cluster sources. This means unique protein fragments are rarely detected and fragmentation patterns are required for the analysis of large molecules. Its extreme surface sensitivity means contamination (particularly siloxane and hydrocarbon contamination) can severely impede data analysis and interpretation. However on the other hand, it forces investigators to maintain high standards in sample preparation, purity and handling. The experimental nature of mass spectrometry also requires samples to be held under vacuum. As such, the protein is no longer technically at an interface but rather forms a surface (a surface being the interface between matter and vacuum). In many circumstance this is detrimental to the native protein state as is the case for all dehydrating procedures, however it does not moot the usefulness of the method. The nature of a hydrated

In Proteins at Interfaces III State of the Art 2012; Horbett, T., et al.;
ACS Symposium Series; American Chemical Society: Washington, DC, 2012.

interaction can lead to different spectral manifestations after dehydration. Other opportunities still exist in the use of cryo- prepared specimens where a vitrified hydrated protein at an interface may be preserved. There is little demonstration of this in the literature however. Topography can also cause analytical artefacts and features greater than ~20 microns in height can become difficult to effectively image and has impact on spectral resolution and peak identification. Due to the electrostatic nature of the analysis, the samples subsequently require charge transfer to maintain neutrality; otherwise surface charging will lead to severe distortion of imaging and spectra. Data analysis is often not straight forward and requires statistical approaches for handling large amounts of complex spectral information. In particular, multivariate analyses such as principal component analysis are powerful statistical tools to reduce highly complex data to easily managed variables that distinguish discriminating fragments (*10*, *26*, *27*). These approaches have substantially enhanced ToF-SIMS spectral analysis and interpretation over recent years (*10*, *19*, *28–31*). Additionally, spectral interpretation is not always obvious and experience can be needed for correct peak identification and confirmation.

Spectral quality is limited by secondary ion yields. While yields are dependent on instrumentation, they are also limited by the actual quantity of material in the sample. For sampling 1-2 nm of the sample surface, this can translate to very little material and compromises spectra, particularly for high mass fragments. This is compounded by remaining within static limits, which describe the maximum primary ion dose the sample can receive before spectral artefacts are induced by damage to the surface. For ion beams such as LMIGs, this can be as low as bombarding less than 1% of the surface monolayer. However, C_{60} and Ar cluster dramatically improve and can even eliminate static limitations.

Table I. Some of the more common ion sources and their advantages and disadvantages. The complementarity of different ion sources often results in multiple options installed on one instrument.

Ion Sources	*Monatomic LMIG*	*Polyatomic / Cluster*
Examples	Ga^+, In^+, Bi^+, Au^+ ...	SF_5^+, Au_n^+ cluster, Bi_n^+ cluster, C_{60}^+, Ar cluster...
Advantages	High spatial resolution	Improved ion yields and mass range
Disadvantages	Low mass range and protein fragment yields	Low image resolution

3. Characterizing Porous Materials and Protein Loading Phenomena

Micro-, meso- and macro-porous materials are manufactured with pores ranging from sub-nanometer diameter upwards and can have immense surface area. They have particular importance regards loading of functional molecules for use in a range of applications, including; optical (*32*, *33*), bio- and chemical-sensing (*34*, *35*), brachytherapy (*36*), molecular separation (*37*), catalysis (*38*, *39*) and the delivery of active pharmaceutical ingredients (*40*, *41*). The ongoing interest for use as therapeutic delivery systems is due to the large internal surface area available and readily modified surface chemistry (*42*). The loading dynamics of proteins into a porous matrix is dependent on surface chemistry (charge, wetting etc) and the size of the pores. Subsequently, characterization of the nature of distributions and interactions with surface chemistry of the pores provides valuable understanding. Enhanced control over the surface properties of porous materials is of particular importance in these applications. Recent research has made progress in this area, devising experimental strategies towards surface manipulation and characterization of porous materials with ToF-SIMS, as described in this section.

ToF-SIMS is able to analyse the outer surface of a porous substrate, or through cleavage, study pore cross-sections to characterise surface chemistry and functionalization, protein loading and aspects of molecular binding. Loading dynamics as a function of time, concentration and pore structure can be studied. In addition, due to the detection of organic, inorganic and molecular fragments with ToF-SIMS, complimentary data can enhance understanding of the chemical mechanisms for adsorption. The following results assist in understanding the interaction between probe molecules and proteins with the internal nano-porous network structures and provide information about the chemical versus physical binding. This helps optimise loading of porous substrates with active pharmaceuticals and proteins for biologic delivery. This section summarises our previous publications (*43*–*46*) in a step-wise fashion from characterizing fabricated pores, their functionalization and loading with a small model molecule before demonstrating the loading of proteins. These examples demonstrate the versatility of ToF-SIMS analysis to extend from a simple surface characterization tool to a powerful means for comprehending functional surfaces. The advantageous aspects of ToF-SIMS analysis will see progressing research in understanding proteins at interfaces as they relate to numerous aspects of physical-chemistry and bio-chemistry.

3.1. Analysis for Internal Pore-Surface Chemistry

In a cross section of a porous silicon wafer cleaved in air (Figure 3), peaks in the negative and positive ion spectra indicate the silicon substrate and surface modification after reaction with oxygen (i.e. Si^+, SiO^+, SiO_2^-, and SiO_3^- as expected for silica materials (*47*)). Conversely however for the porous silicon region, $SiOH^+$, SiO_2H^-, and SiO_3H^- peaks were prominent. This effect was ascribed to the hydrolysis of the silicon surface and formation of silanol functional groups during exposure to aqueous environments during sample preparation. There was also evidence of fluorination of the surface from the etching process by way of signals due to SF^- (hydrofluoric acid was used in the structure fabrication).

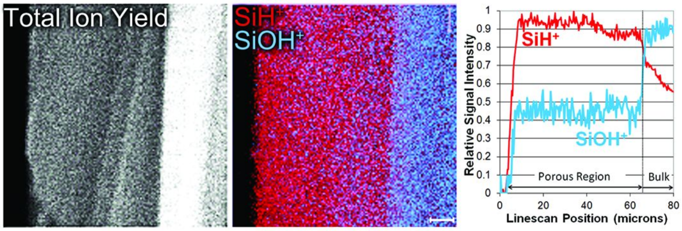

Figure 3. Positive ion images and cross-sectional profiles indicating different surface chemistry from an unloaded porous silicon wafer. Bar = 10 microns. Adapted from Kempson et al. (45)

The total ion yield (TIY) in Figure 3 indicates some topographical features of the surface which need to be taken into account during interpretation due to the ToF-SIMS secondary ion yield sensitivity to localized changes in topography and chemistry. Most secondary ion yield effects are normalized out for abundant species such as Si^+. For low yielding species, some of these topographically induced features can remain. The linescans show a subtle decrease in the relative signal of SiH^+ and could indicate a slight change in the silicon chemistry at the base of the pore. Such chemical characterization is critical in interpreting functionalization and protein loading of material to assess quality control of the pores. For example, an additional aspect noteworthy was the presence of Cl^- in the negative ion spectra in the porous region. Cl^- was observed in the blank wafer as well as the loaded wafer. This can originate from HCl existing in small quantities in the HF used for the silicon anodization process. Additionally, further Cl could originate from molecular chloride salts. Free anionic chloride ions could interact with the substrate and impose competitive processes, changes in surface energy or act to obscure the porous surface and inhibit protein adsorption. A small $SiCl^-$ peak indicated the presence of chloride ions which could exist at the expense of hydroxyl groups from silica surfaces (*48*).

3.2. Spatial Assessment of Pore-Surface Functionalization for Loading Applications

Increasingly stringent device requirements for advanced applications of porous media demand development of multi-phasic multi-functional materials. Adequate control and characterization of internal pore chemistry is complex and often poorly understood despite the fact that the functionality on the pore surface is a key determinant for device performance. For example, the selectivity and efficiency of molecular transport and separation through Anodized Aluminium Oxide (AAO) membranes are not only effectively modulated by changing the size, but also by the charge (*46*, *49*) and polarity (*50*) of the porous layer and the engineered affinity towards the species of interest (*43*).

Shown in Figure 4 is an AAO membrane having pores with spatially controlled multilayered surface functionalities. Membranes with layered surface functionalities inside the pore channel were prepared by a series of anodization and silanization cycles with pentafluorophenyldimethylpropylchlorosilane (PFPTES) and 3-aminopropyltriethoxysilane (APTES), achieving variations in surface functionalities and wettabilities. Each of the deposited layers was distinguishable by ToF-SIMS imaging with the exemplar negative-ion image of a membrane cross-section. An advantage here with the ToF-SIMS imaging is clear distinction of chemical layer boundaries. This is due to the surface sensitivity which minimizes distortion arising from depth effects such as observed with instruments which probe a greater volume (*51*).

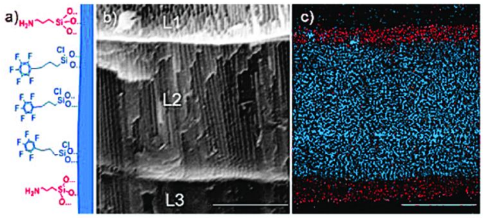

Figure 4. A cross-sectional schematic (a), SEM (b) and ToF-SIMS images (c) of a freestanding tri-layered AAO membrane functionalized with APTES and PFPTES. The negative ion ToF-SIMS image directly visualizes the spatial arrangement of the surface functionalization through N$^-$ (red) and F$^-$ (blue) ions. Bar = 10 micron. Adapted with permission from Md Jani et al. (43).

3.3. Understanding Molecule-Substrate Interaction and Loading with a Model Compound

Methylene blue was used as a model molecule for initial appreciation of ToF-SIMS analysis of loading porous substrates (*45*). This molecule was chosen for its convenient molecular weight, range of functional groups, use in surface adsorption studies and to confirm fragment ions from an organic molecule (rather than a molecular ion) could accurately reflect the distribution of the parent molecule of interest. This is important due to the limited mass range with ToF-SIMS which will not indicate a molecular ion of proteins. Methylene blue was indicated by a group of fragments dominated by a peak at 285 Da. The cationic molecular ion occurs at 284 Da ([MB]$^+$), but the 285 Da ([MB + H]$^{+\bullet}$) peak had a factor of ~2 more counts. This was ascribed to a combination of (MH)$^+$ and/or (M)H$^+$ due to a reductive process and isotopic M$^+$ (*52*). The 284, 285 and 286 Da peak intensities are highly dependent upon matrix effects. Such fragment intensities can also depend on the micro-structure of the fractured surface (*53*) and primary ion properties (*54*, *55*). An image of organic peaks in a mass range of 235-290 Da indicated methylene blue distribution (Figure 5). The distribution of methylene blue and the associated organic fragments were found to deposit at the deepest pore regions of the substrate. Such a distribution could be induced by either different chemistry in the deeper region (which was not obviously apparent), or as an artefact due to the loading dynamics of the Methylene Blue procedure.

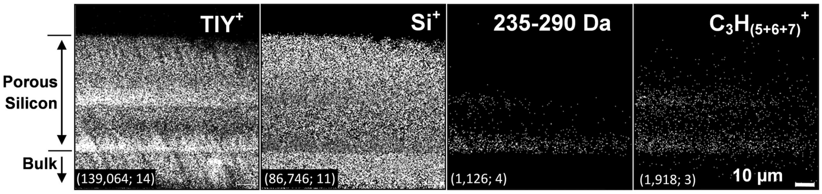

Figure 5. Positive ion images of a methylene blue loaded porous Si wafer cross-section. The total ion yield demonstrates some topographical effects, while the Si^+ image highlights the porous and bulk region of the wafer. Images of organic peaks demonstrate methylene blue penetration and adsorption into the deepest regions of the porous layer. Numbers in parentheses indicate: (total ion counts; maximum count per pixel). Reproduced with permission from reference (45). Copyright 2010 Elsevier.

An added benefit of analysing such systems with ToF-SIMS is the potential for gaining chemical information identifying the association of specific functional groups involved in any chemical bonding. Molecular ions, for instance, can reveal fragments generated from a combination of the substrate and deposited material. An interesting peak, for instance, occurred at 313 Da, ascribed to $(MSi)H^+$ or $(MSiH)^+$ suggesting that methylene blue had chemically interacted and bound to the substrate. The presence of $SiCH_3^+$ as a prominent peak suggested this interaction occurred with the dye's methyl groups. In addition, sulphur-containing peaks ascribed most likely to be $SiOSH_3^-$ and SiO_2SCH^- appeared to indicate further possible orientations and interactions with the surface. These fragments suggest bridging of the Si substrate and the positively charged methylene blue sulphur via a surface hydroxyl group. In aqueous solution methylene blue exists as a positive ion. In a neutral pH environment, the acidic nature of the hydroxylated substrate surface leads to deprotonation of the silanol termini, thus providing SiO^- groups that can readily interact with cationic species. Hence, chemisorption via oxygen bridging of the substrate silicon and the methylene blue's sulphur may be feasible but requires confirmation, for example with NMR (*56*) or infrared spectroscopy (*57*). These results indicated a mixture of molecular arrangements at the surface. Positive ions (e.g. $SiCH_3^+$) suggested methylene blue bound to the substrate via its methyl groups. Negative fragments ($SiOSH_3^-$ and SiO_2SCH^-) also suggested chemisorption via O bridging of the substrate Si and methylene blue S.

3.4. Understanding Protein Loading in Porous Material Cross-Sections

In contrast to methylene blue, proteins are much larger molecules. Papain for instance comprises 212 residue units in 2 domains giving a molecular weight of 23,406 g/mol (*58*). Papain is a cysteine protease hydrolase enzyme present in papaya. This molecular weight is far greater than can be detected with ToF-SIMS, however fragmentation products can be detected and represent the larger protein molecule (Figure 6). Numerous peaks were observed with ToF-SIMS, as is normal for the complex spectra obtained from large molecule fragmentation. For many of the peaks, due to their position relative to the nominal mass units, they were identified to be a combination of C_xH_ySi as well as C_xH_y and other N, O and S containing fragments consistent with protein material and forming through similar interactions with the substrate via methyl groups as observed with methylene blue described in the previous section. For the same substrate material, Gramicidin A protein was also found to load in the same manner as papain (Figure 7). The rise in the silicon signal at the surface of the porous wafer is an indication of a change in secondary ion yields due to matrix effects. The fragmentation is highly sensitive to local environment and changes such as this need careful consideration when interpreting ToF-SIMS data. In this case, it may originate from subtle changes in the oxidised structure or altered surface energetics due to adsorbed atoms or molecules in this region.

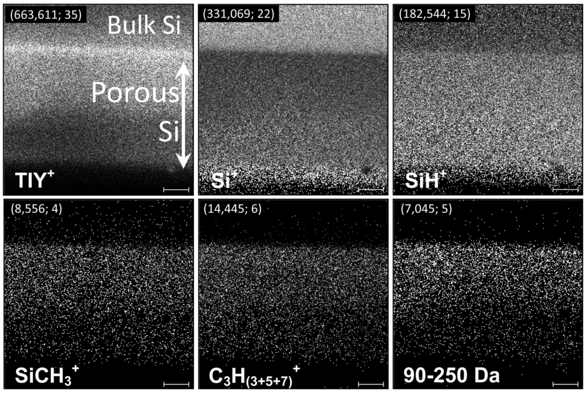

Figure 6. Positive ion ToF-SIMS images of the porous region of a papain loaded wafer. Si^+ and SiH^+ highlight the bulk and prous regions while the organic fragments reveal the distribution of papain. Numbers in parentheses indicate: (total ion counts; maximum count per pixel). Bar = 10 micron. Reproduced with permission from reference (45). Copyright 2010 Elsevier.

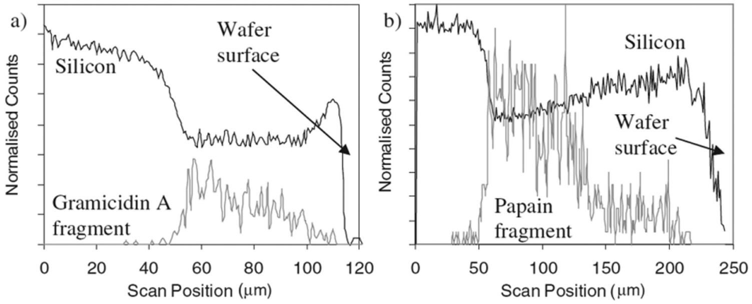

Figure 7. Line scans obtained from ToF-SIMS cross-section imaging depicting the distribution of specific organic mass fragments from a) Gramicidin A and b) Papain within a porous silicon layer. Reproduced with permission from reference (44). Copyright 2008 Wiley.

4. Protein Interactions with Nanoparticles

4.1. Misfolded-Protein Analysis. Towards Bio-Sensing with Plasmonic Structures

Protein adsorption on nanostructures can lead to plasmonic and fluorescent changes (*59*). Due to ToF-SIMS' extreme surface sensitivity and related aspects of surface energetics during the sputtering process, spectral signatures are sensitive to the orientation or subtle changes in conformation in proteins adsorbed at a surface (*60–63*). In this regard, ToF-SIMS has been employed quite successfully in differentiation of protein mixtures, distributions and orientations based on small (~sub 500 amu) protein fragments (*62*, *64*, *65*). Protein misfolding is a fundamental aspect of numerous diseases which lead to protein inactivity, disruption of signalling pathways and in severe cases, aggregation. Obviously the consequence of such anomalies is manifestation of diverse morbidities including brain degenerative diseases. With particular regard to blood serum, differences in structures due to ovarian cancer, prostate cancer, prostate inflammation, mammary cancer and rheumatic inflammation have all been detected (*66*). In cancer, solubilized-protein structural changes have been identified (*67*), due to conformational changes increasing interactions between water molecules and polar functional groups, with greater disturbance correlated with progression. In the solid phase, changes in lyophilized serum samples were detected from cirrhosis and hepatocellular carcinoma patients (*68*). The progression of the carcinoma results in phenotypic changes in proteins and other structural alterations in proteins produced in the liver. These differences were attributed to protein tertiary structural changes.

In a particular study described here, ToF-SIMS was used in conjunction with multivariate statistics to differentiate low levels of misfolded proteins in adsorbed mono-layers (specifically, Human Serum Albumin (HSA) on oxidised silicon substrates) to assess differences in protein interactions at interfaces which could relate to bio-sensing applications. In the study of Human Serum Albumin, misfolding was induced by thermal denaturing of the molecule (*69*, *70*). Above approximately 70°C, severe misfolding induces aggregation. This is easily observable by measuring molecular diameter as a function of temperature with Dynamic Light Scattering (DLS), shown in Figure 8. Such a transition in protein interaction is also shown through HSA adsorption with gold core, silica shell nanoparticles with UV-Vis spectroscopy. Monitoring of the peak position of the UV-Vis absorption spectrum detected no difference until the gross morphological change in the HSA molecule correlated with the DLS data. At room temperature, HSA was confirmed to adsorb to the nanoparticles with negative staining electron microscopy (Figure 9).

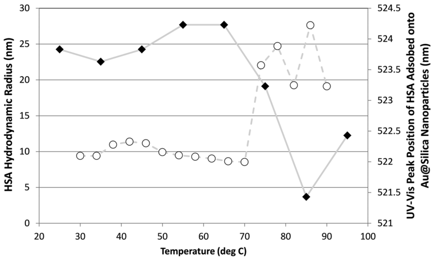

Figure 8. Temperature induced misfolding of Human Serum Albumin leads to protein aggregation above ~70°C, observed as a dramatic increase in hydrodynamic radius (open circles). Correlating with this is the induction of a UV-Vis spectroscopy peak shift due to changed interaction of HSA with gold core, silica shell nanoparticles (filled diamonds). Reproduced with permission from reference (70). Copyright 2010 American Chemical Society.

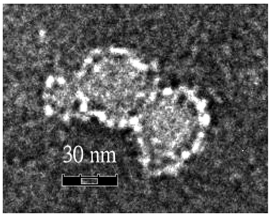

Figure 9. Negative stained electron microscopy micrograph of individual HSA molecules (white dots) adsorbed onto gold-core, silica-shell nanoparticles at room temperature.

Below 70°C, no discernable difference in the protein interaction was observed with these approaches. Analysis with Circular Dichroism (CD), which gives a good measure of secondary structure, comparing HSA in solution at room temperature and 65°C could only detect a very slight difference (*70*).

ToF-SIMS was explored for its ability to semi-quantitatively differentiate misfolded protein mixtures to assist in understanding the changing nature of protein interaction as a function of temperature induced misfolding. The work described below applied ToF-SIMS analysis to studying mixtures of human serum albumin, in native and denatured/misfolded states, in serum adsorbed onto oxidised silicon wafers. Differences discerned by Principal Component Analysis (PCA) from the analysis of the amino acid fragments can indicate several phenomena regarding the protein molecule. Such multivariate statistical approaches (as mentioned in Section 2.2.) are necessary for identifying correlations in changes in peak intensities. The correlation of fragments is used to identify a spectral component in a complex mixture, as compared to having a uniquely identifiable mass fragment (such as a protein molecular ion). The varying influence of one amino acid over another contributing to differentiating proteinaceous samples indicates compositional, conformational or orientational discriminators. Different protein mixtures are distinctly differentiated due to different compositions (*64*). In the case of the native versus denatured HSA, the fundamental amino acid composition does not change. However, the concentration of exposed functional groups and residue units visible to ToF-SIMS and corresponding fragmentation patterns, can change with denaturing or protein orientation (*71*). When a protein interacts at an interface it can orientate itself to facilitate adsorption depending upon the exposed functional groups of the protein and the interface it is orientated from. This can be altered by the protein functionality (such as through misfolding) or changing properties of the substrate (*72*).

PCA was successfully used to distinguish mixtures of misfolded HSA in native HSA based on ToF-SIMS spectra. Due to slight differences in how the protein molecules were folded, subtle changes in the fragmentation pattern were deduced by the multivariate analysis. Even though the same fragments were produced from native and misfolded HSA, there were detectable differences in the correlations of the fragment peaks. The degree of the primary principal component was subsequently used as a semi-quantitative measure of the proportion of misfolded HSA in serum (i.e. a complex biological mixture), shown in Figure 10.

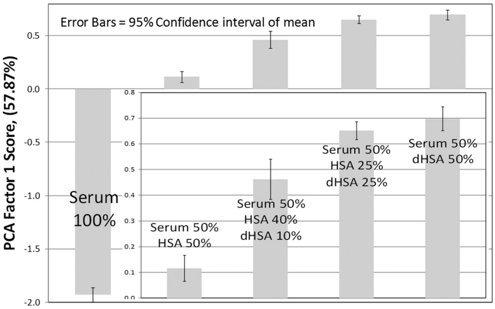

Figure 10. Principal Component Analysis factor 1 scores based on analysis of ToF-SIMS spectra plotted as a function of amount of misfolded HSA (denoted as dHSA) added to serum. The inner graph is an expanded view of the mixed samples to aid in visualization. Reproduced with permission from reference (70). Copyright 2010 American Chemical Society.

A non-linear response was observed and a 2 degree polynomial function fitted the trend with good precision. In the original solution, the absolute quantity of each component was a linear sum and hence varies linearly. However, adsorption rates of each component can differ. Quartz Crystal Microbalance (QCM) measurements indicated that denatured HSA exhibited a greater affinity for the substrate than the native form. It was also proven they both formed monolayer coverage over the surface. Therefore a greater relative coverage of the surface was presumably achieved by the denatured HSA in competition with the native HSA for equivalent concentrations. This phenomenon justifies a polynomial fit and less substantial distinction between samples of higher denatured HSA concentrations. The nature of this competition for binding to the substrate results in larger differences observed at low concentrations of denatured HSA enhancing the ability to detect lower concentrations of denatured HSA. Figure 10 indicates that this approach can detect even just a few percent of a subtly denatured protein in a complex protein solution.

Data presented here demonstrates an ability to easily differentiate HSA due to misfolding and varying relative concentrations with ToF-SIMS. Even though adsorbed monolayers were compositionally equivalent, analysis of molecular fragments by ToF-SIMS clearly discriminated native and misfolded samples. The fragmentation pattern is highly sensitive to protein conformation, allowing assessment of relative amounts of proteins in mixtures and quantifying amounts of denatured protein in a sample. Taken as a whole, these data suggest slight misfolding of proteins can lead to interactions with substrates that could lead to plasmonic changes in nanostructures. So far we have shown this for severe denaturation but it is conceivably possible for more subtly misfolding as deduced by the ToF-SIMS data. This has implications for detecting misfolded protein in biotechnology and medical applications.

4.2. Evolution of Bonds with Au Nanoparticle Surface

Protein interaction with nanoparticles is invigorating much research as development continues for biosensors, appreciating nanoparticle toxicology and interactions in biological contexts. Figure 10 shows how a misfolded protein mixture adsorbed on a silica surface manifested in semiquatitative analysis with ToF-SIMS. Figure 9 shows protein molecules adsorbing with a nanoparticle's silica surface which can result in plasmonic shifts. ToF-SIMS has potential in contributing additional information regarding protein interactions with nanoparticle interfaces. Figure 11 shows evolution of gold-based fragments during the synthesis of gold nanoparticles in the presence of 11-mercaptoundecanoic acid (MUA), a sulfhydryl terminated 11-carbon linear molecule. The sulfhydryl group is of particular relevance due to its prevalent role as a functional group of proteins and for ligation with gold nanoparticles. This synthesis method utilizes a highly reactive aqueous environment and water-dissociated-based radicals for redox processes (*73–75*). ToF-SIMS analysis of the nanoparticles at varying stages of synthesis indicate the first bonds to form were with ethyl groups; subsequently sulfhydryl interactions follow and ultimately predominate. Similar analysis can be extended to the study of peptide and protein interactions with nanoparticles.

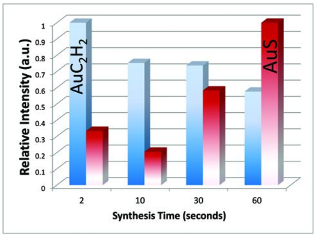

Figure 11. Evolution of gold based fragments with time from gold nanoparticles during synthesis in the presence of a thiol-terminated polymer.

5. Further Opportunities

Taking advantage of the sub-micron spatial resolution of ToF-SIMS, protein adsorption can be studied in complex mixtures of particles or patterned arrays. This section briefly highlights research which demonstrate areas where future ToF-SIMS-based research will likely contribute important information in understanding protein interactions at interfaces.

5.1. Crystal Face- and Particle-Specific Analysis

The gross behavior of a heterogenous system will be a sum and average of the behavior of all the components of the system. Analysis of the individual components (such as facets, grains, partitions etc) can elude to the bulk response. Examples have been shown where microscopic chemistry deduced by ToF-SIMS has been able to infer macroscopic behavior. Two key papers in this area were able to infer wettability of a surface based on hydrophobic and hydrophilic fragment ions (*76*) and contact angle measurements of particulate systems (*77*).

In other research, analysis of specific crystal faces of a pharmaceutical particle product were shown to infer physico-chemical traits. Molecular arrangement at specific pharmaceutical crystal faces influenced surface energetics and subsequently physico-chemical properties (*78*). Coupling this type of information with effects of peptide and protein adsorption could provide valuable interpretation for nano-scale structure interactions with protein, including nanoparticles, clusters, and pharmaceutical products and delivery platforms.

5.2. Patterned Arrays

Biomimetic and biocompatible surfaces are more likely to present accurate and effective properties if they are heterogeneous, such as in nature. In this regard spatial scales will replicate cellular size and compartment and structure scales, i.e. 100’s of nanometers to 10’s of microns. Additionally, it is the surface chemistry and behavior which impart protein interactions. Over this spatial scale and for relevant information on surface chemical properties and protein interactions, ToF-SIMS is highly appealing. Examples of the application of ToF-SIMS in such areas of research (i.e. patterned arrays and protein patterning) have generated exciting data in spatial characterization of patterned protein surfaces (*19*), and chemical and biomolecule arrangement (*79*). Such application is particularly well demonstrated in Figure 12 which shows surface functionalization in the pursuit of fabricating bio-compatible and bio-functional materials.

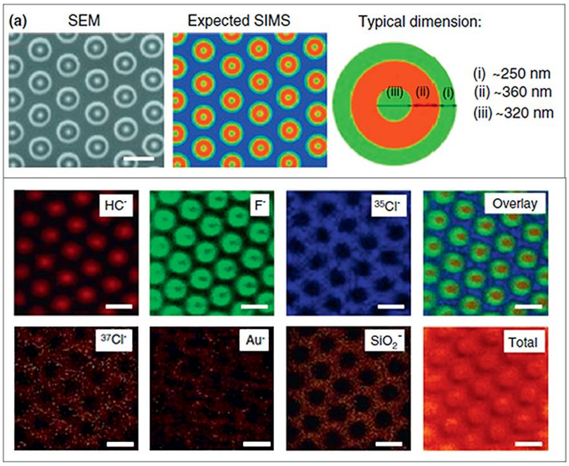

Figure 12. ToF-SIMS imaging of submicron patterning for bio-interfaces. The example shows a Au substrate onto which 2 mm colloidal masks were deposited and etched, followed by deposition of a plasma polymer, followed by sputtering of Au and evaporation of SiO_2 to create four chemical contrasts for chemical functionalisation. The contrasts are represented by a fluorinated thiol (green), a chlorinated silane (blue) on SiO_2 and hydrocarbon peaks from a plasma polymer (red). Bar = 2 microns. Reproduced with permission from reference (80). Copyright 2011 Elsevier.

6. Concluding Remarks

The examples of ToF-SIMS surface analysis provided in this chapter have demonstrated the unique aspects of this analytical approach to further research into protein interactions at interfaces on the nano- and micro-scale. With further instrumental and analytical development there is immense promise in directly probing physical and chemical properties of surfaces in highly heterogenous systems with ToF-SIMS and directly relating these to protein interactions and behavior. A key aspect in this regard will be greater elucidation of fragmentation patterns and how they relate to protein bonding, structure and orientation.

References

1. Denman, J. A.; Kempson, I. M.; Skinner, W. M.; Kirkbride, K. P. *Forensic Sci. Int.* **2008**, *175*, 123–129.
2. Denman, J. A.; Skinner, W. M.; Kirkbride, K. P.; Kempson, I. M. *Appl. Surf. Sci.* **2010**, *256*, 2155–2163.

3. Kempson, I. M.; Skinner, W. M. *Sci. Total Environ.* **2005**, *338*, 213–227.
4. Kempson, I. M.; Skinner, W. M.; Kirkbride, P. K. *Biochim. Biophys. Acta (G)* **2003**, *1624*, 1–5.
5. Barnes, T. J.; Kempson, I. M.; Prestidge, C. A. *Int. J. Pharm.* **2011**, *417*, 61–69.
6. *Surface Analysis: The Principal Techniques*, 2nd ed.; Wiley: 2009.
7. *ToF-SIMS surface analysis by mass spectrometry*; IM Publications and SurfaceSpectra Limited: 2001.
8. Metzner, R.; Schneider, H. U.; Breuer, U.; Schroeder, W. H. *Plant Physiol.* **2008**, *147*, 1774–1787.
9. Kempson, I. M.; Skinner, W. M.; Kirkbride, P. K.; Nelson, A. J.; Martin, R. R. *Eur. J. Mass Spectrom.* **2003**, *9*, 589–597.
10. Muramoto, S.; Graham, D. J.; Wagner, M. S.; Lee, T. G.; Moon, D. W.; Castner, D. G. *J. Phys. Chem. C* **2011**, *115*, 24247–24255.
11. Michel, R.; Castner, D. G. *Surf. Interface Anal.* **2006**, *38*, 1386–1392.
12. Mas, S.; Perez, R.; Martinez-Pinna, R.; Egido, J.; Vivanco, F. *Proteomics* **2008**, *8*, 3735–3745.
13. Whitby, J. A.; Östlund, F.; Horvath, P.; Gabureac, M.; Riesterer, J. L.; Utke, I.; Hohl, M.; Sedláček, L.; Jiruše, J.; Friedli, V.; Bechelany, M.; Michler, J. *Adv. Mater. Sci. Eng.* **2012**, *2012*.
14. Aimoto, K.; Aoyagi, S.; Kato, N.; Iida, N.; Yamamoto, A.; Kudo, M. *Appl. Surf. Sci.* **2006**, *252*, 6547–6549.
15. Brunelle, A.; Touboul, D.; Laprévote, O. *J. Mass Spectrom.* **2005**, *40*, 985–999.
16. Brunelle, A.; Laprévote, O. *Curr. Pharm. Des.* **2007**, *13*, 3335–3343.
17. Fernandez-Lima, F. A.; Post, J.; Debord, J. D.; Eller, M. J.; Verkhoturov, S. V.; Della-Negra, S.; Woods, A. S.; Schweikert, E. A. *Anal. Chem.* **2011**, *83*, 8448–8453.
18. Zhu, Z.; Shutthanandan, V. *Surf. Interface Anal.* **2012**, *44*, 89–93.
19. Dubey, M.; Brison, J.; Grainger, D. W.; Castner, D. G. *Surf. Interface Anal.* **2011**, *43*, 261–264.
20. Touboul, D.; Kollmer, F.; Niehuis, E.; Brunelle, A.; Laprevote, O. *J. Am. Soc. Mass. Spectrom.* **2005**, *16*, 1608–1618.
21. Fletcher, J. S.; Lockyer, N. P.; Vickerman, J. C. *Surf. Interface Anal.* **2006**, *38*, 1393–1400.
22. Fletcher, J. S.; Vickerman, J. C.; Winograd, N. *Curr. Opin. Chem. Biol.* **2011**, *15*, 733–740.
23. Baker, M. J.; Fletcher, J. S.; Jungnickel, H.; Lockyer, N. P.; Vickerman, J. C. *Appl. Surf. Sci.* **2006**, *252*, 6731–6733.
24. Chang, C. J.; Chang, H. Y.; You, Y. W.; Liao, H. Y.; Kuo, Y. T.; Kao, W. L.; Yen, G. J.; Tsai, M. H.; Shyue, J. J. *Anal. Chim. Acta* **2012**, *718*, 64–69.
25. Kayser, S.; Rading, D.; Moellers, R.; Kollmer, F.; Niehuis, E. *Surf. Interface Anal.* **2012**.
26. Wagner, M. S.; Graham, D. J.; Castner, D. G. *Appl. Surf. Sci.* **2006**, *252*, 6575–6581.
27. Lee, J. L. S.; Gilmore, I. S. The Application of Multivariate Data Analysis Techniques in Surface Analysis. In *Surface Analysis: The Principal*

Techniques; Vickerman, J. C., Gilmore, I. S., Eds.; John Wiley & Sons: 2009.

28. Anderton, C. R.; Vaezian, B.; Lou, K.; Frisz, J. F.; Kraft, M. L. *Surf. Interface Anal.* **2012**, *44*, 322–333.
29. Mouhib, T.; Delcorte, A.; Poleunis, C.; Henry, M.; Bertrand, P. *Surf. Interface Anal.* **2010**, *42*, 641–644.
30. Park, J. W.; Cho, I. H.; Moon, D. W.; Paek, S. H.; Lee, T. G. *Surf. Interface Anal.* **2011**, *43*, 285–289.
31. Wu, L.; Felton, J. S.; Wu, K. J. J. *Methods Mol. Biol.* **2010**, *656*, 267–281.
32. Charrier, J.; Kloul, M.; Pirasteh, P.; Bardeau, J. F.; Guendouz, M.; Bulou, A.; Haji, L. *Opt. Mater.* **2007**, *30*, 431–437.
33. Kilian, K. A.; Böcking, T.; Gaus, K.; King-Lacroix, J.; Gal, M.; Gooding, J. J. *Chem. Commun.* **2007**, *19*, 1936–1938.
34. Pacholski, C.; Sartor, M.; Sailor, M. J.; Cunin, F.; Miskelly, G. M. *J. Am. Chem. Soc.* **2005**, *127*, 11636–11645.
35. Bohn, P. W. *Annu. Rev. Anal. Chem.* **2009**, *2*, 279–296.
36. Goh, A. S.-W.; Chung, A. Y.-F.; Lo, R. H.-G.; Lau, T.-N.; Yu, S. W.-K.; Chng, M.; Satchithanantham, S.; Loong, S. L.-E.; Ng, D. C.-E.; Lim, B.-C.; Connor, S.; Chow, P. K.-H. *Int. J. Radiat. Oncol., Biol., Phys.* **2007**, *67*, 786–792.
37. Fu, J.; Mao, P.; Han, J. *Trends Biotechnol.* **2008**, *26*, 311–320.
38. Kaur, P.; Hupp, J. T.; Nguyen, S. T. *ACS Catal.* **2011**, *1*, 819–835.
39. Kim, K.; Banerjee, M.; Yoon, M.; Das, S. *Top. Curr. Chem.* **2010**, *293*, 115–153.
40. Prestidge, C. A.; Barnes, T. J.; Mierczynska-Vasilev, A.; Kempson, I.; Peddie, F.; Lau, C. H. *Phys. Status Solidi A* **2008**, *205*, 311–315.
41. Salonen, J.; Laitinen, L.; Kaukonen, A. M.; Tuura, J.; Bjorkqvist, M.; Heikkila, T.; Vaha-Heikkila, K.; Hirvonen, J.; Lehto, V. P. *J. Controlled Release* **2005**, *108*, 362–374.
42. Prestidge, C. A.; Barnes, T. J.; Lau, C.-H.; Barnett, C.; Loni, A.; Canham, L. *Exp. Opin. Drug Delivery* **2007**, *4*, 101–110.
43. Jani, A. M. M.; Kempson, I. M.; Losic, D.; Voelcker, N. H. *Angew. Chem., Int. Ed.* **2010**, *49*, 7933–7937.
44. Prestidge, C. A.; Barnes, T. J.; MierczynsKa-Vasilev, A.; Kempson, I.; Peddie, F.; Barnett, C. *Phys. Status Solidi A* **2008**, *205*, 311–315.
45. Kempson, I. M.; Barnes, T. J.; Prestidge, C. A. *J. Am. Soc. Mass. Spectrom.* **2010**, *21*, 254–260.
46. Jarvis, K. L.; Barnes, T. J.; Prestidge, C. A. *J. Colloid Interface Sci.* **2011**, *363*, 327–333.
47. Chiba, K.; Nakamura, S. *Appl. Surf. Sci.* **2006**, *253*, 412–416.
48. Unger, K. K. Surface chemistry of porous silica. *Porous Silica Its properties and use as support in column liquid chromatography*; Elsevier Science: Amsterdam, 1988; pp 57−146.
49. Wu, C.; Xu, T.; Yang, W. *J. Membr. Sci.* **2003**, *224*, 117–125.
50. Kyotani, T.; Xu, W.; Yokoyama, Y.; Inahara, J.; Touhara, H.; Tomita, A. *J. Membr. Sci.* **2002**, *196*, 231–239.

51. Martin, R. R.; Naftel, S. J.; Nelson, A. J.; Feilen, A. B.; Narvaez, A. *J. Environ. Monit.* **2004**, *6*, 783–786.
52. Okuno, S.; Nakano, M.; Matsubayashi, G.; Arakawa, R.; Wada, Y. *Rapid Commun. Mass Spectrom.* **2004**, *18*, 2811–2817.
53. Alimpiev, S.; Nikiforov, S.; Karavanskii, V.; Minton, T.; Sunner, J. *J. Chem. Phys.* **2001**, *115*, 1891–1901.
54. Delcorte, A. *Phys. Chem. Chem. Phys.* **2005**, *7*, 3395–3406.
55. Weibel, D.; Wong, S.; Lockyer, N. P.; Blenkinsopp, P.; Hill, R.; Vickerman, J. C. *Anal. Chem.* **2003**, *75*, 1754–1764.
56. Hayashi, A.; Iio, K.; Morimoto, H.; Minami, T.; Tatsumisago, M. *Solid State Ionics* **2004**, *175*, 637–640.
57. Wang, R.; Zhang, D.; Liu, C. *Chem. Phys. Lett.* **2005**, *404*, 237–243.
58. Mitchel, R. R.; Chaiken, I. M.; Smith, E. L. *J. Biol. Chem.* **1970**, *245*, 3485–3492.
59. Shang, L.; Brandholt, S.; Stockmar, F.; Trouillet, V.; Bruns, M.; Nienhaus, G. U. *Small* **2012**, *8*, 661–665.
60. Baio, J. E.; Weidner, T.; Baugh, L.; Gamble, L. J.; Stayton, P. S.; Castner, D. G. *Langmuir* **2012**, *28*, 2107–2112.
61. Cheng, F.; Gamble, L. J.; Castner, D. G. *Anal. Chem.* **2008**, *80*, 2564–2573.
62. Cho, I. H.; Park, J. W.; Lee, T. G.; Lee, H.; Paek, S. H. *Analyst* **2011**, *136*, 1412–1419.
63. Aoyagi, S.; Okada, K.; Shigyo, A.; Man, N.; Karen, A. *Appl. Surf. Sci.* **2008**, *255*, 1096–1099.
64. Wagner, M. S.; Shen, M.; Horbett, T. A.; Castner, D. G. *Appl. Surf. Sci.* **2003**, *203−204*, 704–709.
65. Liu, F.; Dubey, M.; Takahashi, H.; Castner, D. G.; Grainger, D. W. *Anal. Chem.* **2010**, *82*, 2947–2958.
66. Surma, M. *Phys. Chem. Liq.* **2007**, *45*, 271–279.
67. Mikusinska-Planner, A.; Surma, M. *Spectrochim. Acta, Part A* **2000**, *56*, 1835–1841.
68. Elshemey, W. M.; Desouky, O. S.; Mohammed, M. S.; Elsayed, A. A.; El-houseini, M. E. *Phys. Med. Biol.* **2003**, *48*, N239–N246.
69. Chodankar, S.; Aswal, V. K.; Kohlbrecher, J.; Vavrin, R.; Wagh, A. G. *Phys. Rev. E* **2008**, *77*, 031901–031909.
70. Kempson, I. M.; Martin, A. L.; Denman, J. A.; French, P. W.; Prestidge, C. A.; Barnes, T. J. *Langmuir* **2010**, *26*, 12075–12080.
71. Wagner, M. S.; Castner, D. G. *Appl. Surf. Sci.* **2004**, *231−232*, 366–376.
72. Tidwell, C. D.; Castner, D. G.; Golledge, S. L.; Ratner, B. D.; Meyer, K.; Hagenhoff, B.; Benninghoven, A. *Surf. Interface Anal.* **2001**, *31*, 724–733.
73. Lai, S. F.; Chen, W. C.; Wang, C. L.; Chen, H. H.; Chen, S. T.; Chien, C. C.; Chen, Y. Y.; Hung, W. T.; Cai, X.; Li, E.; Kempson, I. M.; Hwu, Y.; Yang, C. S.; Tok, E. S.; Tan, H. R.; Lin, M.; Margaritondo, G. *Langmuir* **2011**, *27*, 8424–8429.
74. Cai, X. Q.; Wang, C. L.; Chen, H. H.; Chien, C. C.; Lai, S. F.; Chen, Y. Y.; Hua, T. E.; Kempson, I. M.; Hwu, Y.; Yang, C. S.; Margaritondo, G. *Nanotechnology* **2010**, *21*, 335604.

75. Tung, H.-T.; Hwu, Y.; Chen, I.-G.; Tsai, M.-G.; Song, J. M.; Kempson, I. M.; Margaritondo, G. *Chem. Commun.* **2011**, *47*, 9152–9154.
76. Priest, C.; Stevens, N.; Sedev, R.; Skinner, W.; Ralston, J. *J. Colloid Interface Sci.* **2008**, *320*, 563–568.
77. Brito E Abreu, S.; Brien, C.; Skinner, W. *Langmuir* **2010**, *26*, 8122–8130.
78. Muster, T. H.; Prestidge, C. A. *J. Pharm. Sci.* **2002**, *91*, 1432–1444.
79. Al-Bataineh, S. A.; Szili, E. J.; Desmet, G.; Ruschitzka, P.; Gruner, P. J.; Priest, C.; Voelcker, N. H.; Steele, D. A.; Short, R. D.; Griesser, H. J. *Proc. SPIE-Int. Soc. Opt. Eng.* **2011**, *8204*, 82043H, DOI:10.1117/12.903304.
80. Kingshott, P.; Andersson, G.; McArthur, S. L.; Griesser, H. J. *Curr. Opin. Chem. Biol.* **2011**, *15*, 667–676.

Chapter 34

Soft X-ray Spectromicroscopy of Protein Interactions with Phase-Segregated Polymer Surfaces

**Adam P. Hitchcock,[*,a] Bonnie O. Leung,[b] John L. Brash,[c]
Andreas Scholl,[d] and Andrew Doran[d]**

**[a]Chemistry and Chemical Biology, BIMR, McMaster University,
Hamilton, Ontario, Canada L8S 4M1
[b]Alberta Environment and Sustainable Resource Development,
Edmonton, Alberta, Canada T5K 2J6
[c]School of Biomedical Engineering, McMaster University,
Hamilton, Ontario, Canada L8S 4M1
[d]Advanced Light Source, Berkeley Lab, Berkeley, California 94720, U.S.A.
[*]E-mail: aph@mcmaster.ca**

Quantitative spectro-microscopic characterization of the interfaces between polymers and relevant proteins helps understand fundamental issues of protein – polymer interactions and can provide insights into biocompatibility. Synchrotron based X-ray photoemission electron microscopy (X-PEEM) and scanning transmission X-ray microscopy (STXM) are being used to study distributions of proteins adsorbed on chemically heterogeneous polymer surfaces with ~30 nm spatial resolution. The relevant contrast in each technique is X-ray absorption spectroscopy which provides speciation and quantitation of both adsorbed proteins or peptides (and in combinations), simultaneously with chemically sensitive imaging of the underlying polymer substrate. An overview of recent progress in this field is given, along with some comparisons to complementary techniques (AFM and TOF-SIMS) for investigating protein-polymer interfaces.

In Proteins at Interfaces III State of the Art 2012; Horbett, T., et al.;
ACS Symposium Series; American Chemical Society: Washington, DC, 2012.

Keywords: photoemission electron microscopy; X-PEEM; scanning transmission X-ray microscopy; STXM; NEXAFS; AFM; TOF-SIMS; mapping; protein adsorption; HSA; polystyrene; poly(methyl methacrylate)-b-polyacrylic acid; blend

Introduction

Understanding and controlling protein interactions with surfaces are important aspects of biomaterials optimization for medical applications. Polymers are often used in medical technology. Typically the polymers chosen are ones whose surface chemistry and morphology are optimal for specific medical applications, either in their pure form or with suitable surface coatings (*1*). The nature and spatial arrangements of surface chemical motifs can lead to a biocompatible surface, or lead to adverse interactions, ultimately triggering the foreign body response (*2*), thrombus formation etc. In general, proteins are the first species to adsorb to biomaterials and thus much of biomaterials optimization involves controlling protein surface interactions. In this context control may refer to complete prevention or minimization of adsorption (protein resistance, antifouling) or it may refer to the selective promotion of adsorption of one specific protein relative to all others from the complex mix of species present in the biological tissue or fluid with which the biomaterial is in contact.

Reduction or elimination of protein adsorption is often the goal for medical devices, while controlled protein adsorption may be important for biochemical sensors (*3*, *4*) and nanofluidic systems (*5*). Reduction of protein adsorption or controlled adsorption of proteins may be possible by exploiting electrostatic interactions. For instance, nanopatterning of carboxyl-terminated self assembled monolayers (SAMs) with lysozyme for biosensor applications gives protein patterns based on the interaction of the positively charged protein with the negatively charged surface (*6*). Repulsive electrostatic interactions can reduce protein adsorption (*7*) but cannot prevent it entirely (*8*). Other major driving forces for protein adsorption include hydrogen bonding, van der Waals forces, and hydrophobic interactions (*9*).

For the past decade we have been systematically exploring the use of synchrotron based soft X-ray spectromicroscopy to study the surface chemistry of polymeric biomaterials and their interactions with relevant proteins and peptides. Most of our work in this area has involved development and exploitation of X-ray photoemission electron microscopy (X-PEEM), although a number of studies have also been carried out using scanning transmission X-ray microscopy (STXM). A comprehensive review of X-PEEM research on biomaterials up to 2009 was recently published (*10*) while recent reviews of the field of soft X-ray microscopy (*11–13*) place these studies in a broader context. In this chapter, we describe the X-PEEM and STXM techniques as applied to studies of proteins at interfaces. We compare the advantages and limitations of each technique, in some cases relative to other frequently used protein-polymer interface probes such as atomic force microscopy (AFM) and time-of-flight secondary ion mass spectrometry (TOF-SIMS). We illustrate the capabilities of these techniques by summarizing selected recent studies including:

- the effect of pH on adsorption of human serum albumin (HSA) and a cationic antimicrobial peptide, RWWKIWVIRWWR-NH_2 (sub-6) to the surface of a phase segregated blend of polystyrene (PS) and a copolymer, poly(methyl methacrylate)-b-polyacrylic acid (PMMA-PAA) (X-PEEM) (*14*)
- the effect of buffer on the adsorption of HSA to the surface of a phase segregated blend of PS and polylactide (PLA) (X-PEEM) (*15*)
- The effect of an aqueous environment on the adsorption of HSA to the surface of a phase segregated blend of PS/PMMA (X-PEEM, STXM) (*16*)
- the selective adsorption of fibrinogen (Fg) to the interfaces of styrene-b-acrylonitrile (SAN) and the polyether-rich matrix of a complex multi-component reinforced polyurethane (*17*). In this study the interface adsorption was measured in the presence of the protein solution (STXM)
- adsorption of Ac-LKKLLKLLKKLLKL-OH, a model α-helix peptide, on to a patterned micro-array of alcohol and carboxylate terminated self-assembled monolayers (SAM) (X-PEEM, TOF-SIMS)
- adsorption of ubiquitin on plasma polymerized polymers patterned using e-beam lithography (X-PEEM) (*18*)

Soft X-ray Spectromicroscopy Methods

X-PEEM Applied to Protein–Polymer Interactions

Photoemission electron microscopy (PEEM) is a full field technique which provides a magnified image of an illuminated area, derived from the lateral spatial distribution of electrons emitted from the surface. PEEM can be performed using a variety of photoionization light sources, from laser or Hg lamp illumination in laboratory implementations, where topography and work function contrast dominate, to synchrotron X-ray illumination (X-PEEM), where chemical (from NEXAFS or photoemission) and magnetic (from X-ray magnetic circular dichroism) contrast are additional contrast mechanisms. Figure 1 presents a schematic of the X-ray optics (Figure 1a) and electron microscope (Figure 1b) components of the PEEM-2 instrument (*19*) at the Advanced Light Source (ALS), where most of our measurements have been performed. Samples are typically a thin (< 100 nm, to avoid charging) polymeric layer on a Si wafer, which has been exposed to a protein or peptide solution under a well defined regime, thoroughly rinsed prior to drying to remove non-adhering protein, and introduced into the ultrahigh vacuum of the X-PEEM via a load-lock.

In Proteins at Interfaces III State of the Art 2012; Horbett, T., et al.;
ACS Symposium Series; American Chemical Society: Washington, DC, 2012.

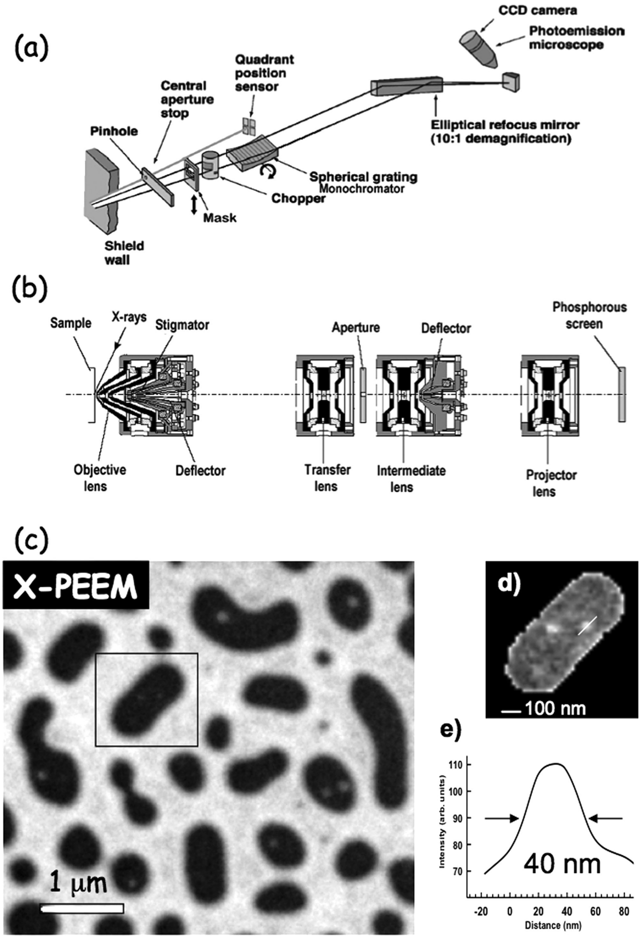
(a)
CCD camera
Photoemission microscope
Quadrant position sensor
Central aperture stop
Pinhole
Elliptical refocus mirror (10:1 demagnification)
Spherical grating Monochromator
Chopper
Mask
Shield wall
(b)
Sample
X-rays
Stigmator
Aperture
Deflector
Phosphorous screen
Objective lens
Deflector
Transfer lens
Intermediate lens
Projector lens
(c)
X-PEEM
1 µm
d)
100 nm
e)
Intensity (arb. units)
110
100
90
80
70
40 nm
-20
0
20
40
60
80
Distance (nm)

Figure 1. a) Layout of the 7.3.1 bend magnet beam line at the Advanced Light Source (ALS, Berkeley, CA) (19) where most of the X-ray photoemission electron microscope (X-PEEM) results presented in this chapter were obtained. b) schematic of the PEEM-2 microscope (19). c) Image recorded with the ALS PEEM-3 (without the aberration corrector) of a polystyrene - polymethyl-methacrylate (PS/PMMA) (30/70) blend sample, using a photon energy of 285.15 eV, the C 1s $\rightarrow\pi^*$ peak of PS. The logarithm of the intensity is presented to visualize the PS microdomains present in the PMMA macrodomains. d) expanded image of the single PMMA domain indicated in (a). e) line profile across the PS microdomain indicating a flat topped character of the 40 nm wide microdomain. The effective spatial resolution is estimated from the edge sharpness to be 30 nm.

Figure 1 also presents images from the recently developed PEEM-3 instrument (*20*) on ALS beamline 11.0.1, which has somewhat superior spatial resolution to that of the PEEM-2 microscope, much higher flux and flux density, a wide spectral range and full capabilities for control of the photon polarization. Figure 1c shows the macro-domain structure of a polystyrene - polymethylmethacrylate (PS/PMMA) (30/70) blend sample, recorded using a photon energy of 285.15 eV, the C 1s → π* peak of PS. The bright continuous signal is PS while the dark discrete domains are PMMA. Due to the high molecular weight (1 MD for PS, 300 kD for PMMA) there is incomplete phase separation, such that the discrete PMMA domains incorporate microdomains of PS with sizes in the 10-200 nm range. Figure 1d is a magnification of a single PMMA domain while Figure 1e is a line profile across one of the smallest PS microdomains in this image, demonstrating a spatial resolution better than 40 nm. This is typical of the spatial resolution capabilities of X-PEEM instruments which do not employ an energy filter or aberration compensation. X-PEEMs with energy filters provide somewhat better energy resolution (*21*). Recently aberration compensation optics that reduce spherical aberrations have been developed for X-PEEM (*20*, *22*). These promise to further improve spatial resolution while also improving the efficiency of the electron optics. The latter is critical for studies of soft matter samples like biomaterials and proteins which are highly sensitive to radiation damage.

Figure 2 presents an experimental measurement of the sampling depth and outlines the analysis of a typical X-PEEM data set from a study of protein (human serum albumin, HSA) adsorbed to a phase segregated polymer (PS/PMMA). We have measured the sampling depth for X-PEEM as applied to proteins on a polymer surface to be 4±1 nm for the 1/e fall-off of the signal based on analysis of the C 1s spectra of uniform PS thin films on a Si wafer (Figure 2a) (*23*) which means the total sampling depth is 10 nm. While the sampling depth does vary with material, due to changes in work function and electron transport in the near surface region, the electronic character of organic polymers and bio-polymers are rather similar and thus both the transport and the work function are likely to be similar in the materials we are studying. The X-PEEM sampling depth of 10 nm can be up to ~ 5 times larger than that of XPS. This is very advantageous for studies of protein-polymer interactions since, at sub-monolayer coverages that are the focus of this work, the protein or peptide adsorbate layer is sufficiently thin (0.5-5 nm) that the underlying polymer biomaterial also contributes significantly to the detected signal. Thus, X-PEEM is an ideal tool for studies of the interface between proteins and solid surfaces since it can simultaneously detect, quantify and map both adsorbate and substrate.

Figures 2b-2g document a typical X-PEEM study, in this case of a PS/PMMA blend exposed for 20 minutes to an aqueous solution of human serum albumin (HSA) at a very low concentration (0.005 mg/mL) (*24*). The PS/PMMA blend was prepared by dissolving PS and PMMA in dichloromethane in a 30:70 weight ratio at a 1 wt% level, then spin casting (4000 rpm, 40 s) onto clean 0.8 cm x 0.8 cm native oxide silicon wafers. The substrates were placed in 50 mL beakers and covered with 5 mL of protein solution. After 20 min, the solutions were diluted with at least 50 mL of distilled, deionized water (DDI), vigorously rinsed and the overlayer water replaced 3 times, while continuously keeping the Si chip covered with water. This avoids passing the substrate through the air-water interface of the original protein solution, which is important since protein typically locates preferentially at the air-water interface. After rinsing, the remaining water was removed by touching the edge of the Si wafer with lens paper. Since the samples are introduced into the ultrahigh vacuum (UHV) of the X-PEEM via a turbo-pumped load lock, all of the water is ultimately removed and the samples are examined in a dry state.

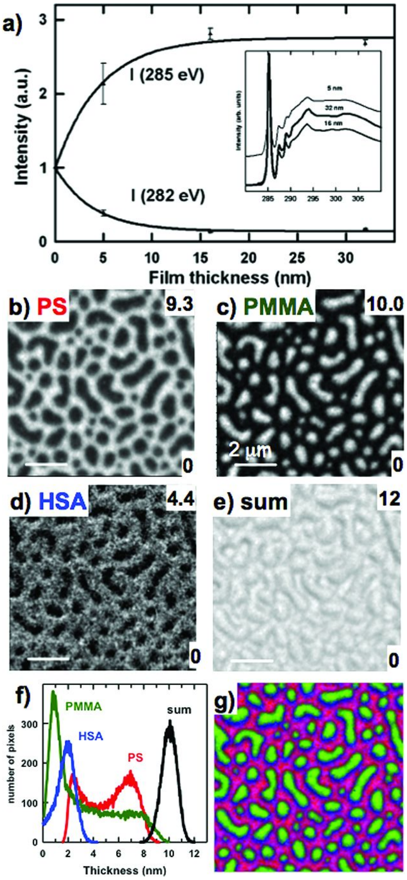

Figure 2. a) Plot of intensity at 282 eV (pre-C 1s, sensitive to the Si substrate) and 285 eV (PS peak) as a function of the thickness of spun-coat films of PS (23).The film thicknesses were measured by atomic force microscopy (AFM) from the profile across a scratch. (b-d) Components maps of a fit of the spectra of PS, PMMA and human serum albumin (HSA) to a C 1s image sequence of a PS/PMMA blend exposed for 20 minutes to a 0.005 mg/ml aqueous solution of HSA. The number at the top right of each map is the maximum of the gray scale for each component map (in each case the minimum is 0). e) Sum of the component maps. The quantitative thickness scales were established by setting the mean of the sum signal to 10 nm. f) histograms of the individual and sum of component maps. g) Rescaled, color coded composite of the PS (red), PMMA (green) and HSA (blue) maps. (see color insert)

This X-PEEM measurement consisted of a sequence of 43 images, each recorded with a 2 sec exposure, with photon energies between 281 and 297 eV. The X-ray beam was shuttered in the 2-3 second interval between each image acquisition in order to reduce radiation damage. After energy calibration (by assigning the C 1s → $\pi^*_{C=C}$ transition of PS to 285.15 eV), the image sequence was normalized to the incident photon flux spectrum which was recorded from a clean Si wafer, with correction for the Si X-ray adsorption and a bolometric term relating to the photon energy dependence of the detector. Reference spectra of PS, PMMA and HSA (*25*) were obtained in separate measurements of the pure materials and placed on absolute intensity scales, as outlined elsewhere (*10*, *12*, *13*). The C 1s image sequence was fit to these quantitative C 1s reference spectra, which results in maps of the spatial distribution of the 3 components (Figures 2b, 2c, 2d). The grayscale range of each component map (indicated by the number at the lower and upper left of each map) indicates the thickness in nm, determined by setting the mean of the sum of all component maps (Figure 2e) to the total sampling depth (10 nm). Figure 2f displays histograms of the quantitative component maps and the sum. The map of the sum has much lower contrast variation than the individual component maps, and the histogram of the sum is relatively narrow, consistent with our assumption that the electron yield and sampling depth are independent of the exact surface composition. Figure 2g is a color coded composite of the 3 component maps with the intensity of each color set to span the full range of each component map. This display clearly shows that the preferred adsorption sites of the HSA protein are the interphase region (the ~100-300 nm band between the PS and PMMA domains), followed by PS, with relatively little protein adsorbed on the PMMA domains, as visualized by a relatively pure green color in those areas. While this example is presented mainly to illustrate the X-PEEM method, data analysis and presentation, the results are very typical of the many protein – polymer blend surfaces we have examined. Except in cases where interactions with a specific domain type are favored by engineered electrostatic interactions (cf the pH dependent results for HSA and sub-6 adsorption to PS/PMMA-PAA (*14*), where the positively charged sub-6 peptide is electrostatically attracted to the negatively charged PAA polymer), we have found that proteins and peptides preferentially adsorb to the interphase (region where domains of different character meet) – polar/non-polar or more/less hydrophobic. We interpret this in terms of more favorable interactions with the more complex environment of the interphase, which allows a wider range of interactions with the multi-functional nature of proteins. Since the adsorption regime (concentrations, time of interactions) is one where the adsorption is partially reversible, the actual surface distributions depend on the length of time of interaction (*24*) and thus both kinetic and thermodynamic factors play a role.

Radiation damage is a severe challenge when applying X-PEEM to protein-polymer interactions. Despite being a full field technique, we estimate the rate of damage relative to signal generation is about 1 order of magnitude higher in X-PEEM than in STXM (*23*). To reduce radiation damage, a shutter with a 0.1 second response time is used to block the X-ray beam during each photon energy step as well as the period of transfer of images from the CCD camera to the acquisition computer. The photon beam is masked upstream of the monochromator to reduce the incident flux to less than 10% of the maximum. A variable point spacing is used and the number of photon energies is restricted to that which will capture the spectral aspects that differentiate the components of the system studied. Very short exposure times (1 – 2 s) are used to further minimize radiation damage. The relatively rapid radiation damage, combined with the very weak signal from ultra-thin systems such as self-assembled monolayers (SAM) makes such systems very challenging to study – however results have been obtained as indicated below.

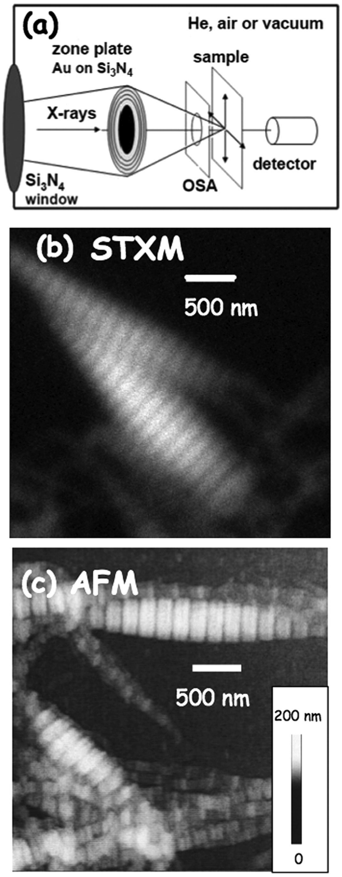

Figure 3. a) schematic of a scanning transmission X-ray microscope (STXM). b) STXM image (OD representation) of a collagen fibril recorded at 288.2 eV, peak of the C 1s → π^*_{amide} transition of collagen. The spatial resolution, as judged by the sharpness of the structure and a Fourier spatial frequency analysis, is 35 nm. c) AFM height image of collagen fibrils in another area on the same sample examined by STXM. (collagen sample and AFM image courtesy of J. Goh)

STXM Applied to Protein–Polymer Interactions

Scanning Transmission X-ray Microscopy (STXM) is a point probe method in which images are obtained serially by mechanically raster scanning the sample though the focal point of a zone plate X-ray lens or (in a few cases) by scanning the zone plate (ZP) and order sorting aperture (OSA) synchronously while the sample is stationary. Figure 3a is a schematic of the functional components of a STXM. The X-ray beam is focused using a Fresnel zone plate (ZP) which is a circular diffraction grating. ZPs have a focal length (f) given by $f = D\delta r/\lambda$ where D is the diameter of the ZP, δr is the width of the outermost zone, and λ is the X-ray wavelength (*11*). The ZPs used in the work reported here had D=240 µm, δr = 25 nm, which gives focal lengths from 1 – 4 mm between 250 and 1000 eV. The focused spot contains only 5-15 % of the X-rays incident on the ZP and thus a scheme to block the un-diffracted (and higher order diffracted) X-rays is needed. This is provided by the combination of a central stop (95 µm diameter, 2 µm thick Au circle at the centre of the ZP), and an order sorting aperture (40-70 µm), which, when properly aligned, blocks all but the first order light. The properties and quality of the zone plate determine the spatial resolution and efficiency of STXM. Over the past 20 years there have been major advances in the fabrication technology such that the present state-of-the-art systems can provide 10 nm spatial resolution with a high contrast test structure (*26*). Figure 3b presents a STXM image of a bundle of collagen. The transverse banding is a well known superstructure in collage (*27*, *28*). Analysis of the Fourier spatial frequencies of this image indicates a spatial resolution of 35 nm. For comparison, Figure 3c presents an atomic force microscopy (AFM) image from elsewhere on the same sample (presented on the same spatial scale).

Comparison of X-PEEM and STXM for Studies of Protein–Polymer Interactions

Although techniques such as atomic force microscopy (AFM) (*29*, *30*) and transmission electron microscopy (TEM) (*31*) have better spatial resolution, X-PEEM and STXM provide much more detailed chemical information through spatially resolved near-edge X-ray absorption fine structure (NEXAFS) spectroscopy (*32*). X-PEEM is an ideal tool to map the distribution of protein on polymeric surfaces since this technique has an optimal near surface sensitivity with a spatial resolution better than 50 nm. Scanning Transmission X-ray Microscopy (STXM) has comparable or perhaps slightly better spatial resolution, and excellent quantitative speciation capabilities, with fewer limitations in terms of this application. A major advantage of STXM over X-PEEM is the ability to examine protein adsorption in the presence of a thin aqueous over layer, thus under conditions much closer to real-world situations than is the case for the UHV, high applied electric field environment of the X-PEEM. However, STXM operates in transmission mode, which integrates the signal through the entire thickness of the sample, and thus it is much less surface sensitive.

For quantitative analyses of surface-adsorbed molecules where the underlying substrate can be mapped simultaneously, X-PEEM is the premier technique. It probes the top 10 nm of the sample, with a sensitivity to adsorbates in the range of 0.1 monolayer or less. Of course there are limitations to X-PEEM as applied to studies of protein interfaces. *In situ* biological experiments using X-PEEM are not possible since relevant biological interactions must be established in an aqueous environment, which is incompatible with the ultra-high vacuum requirement of X-PEEM. To avoid charging artifacts, X-PEEM requires ultra-thin samples of the biomaterial, which can be difficult to prepare. For example polyurethanes are a common medical biomaterial (*33*) but they, along with other cross-linked polymers, are very difficult to spin coat, which is the preferred technique to prepare polymer films sufficiently flat (to avoid topography artifacts) and sufficiently thin (<50 nm) to avoid charging in X-PEEM. In principle it may be possible to use ultramicrotomy to solve this problem, although X-PEEM does require very flat surfaces for optimal imaging. An alternative approach would be to prepare a relevant protein exposed biomaterial on a thick substrate, and then sputter-coat that surface with a layer of metal (Pd, or Pt) that is sufficiently thin to allow the photoelectrons to escape the surface but which is also thick enough to be nearly continuous and sufficiently conducting so as to avoid charging. Gilbert et al. (*34*, *35*) have perfected this approach and applied it to many insulating materials, so as to allow studies of thick sections or bulk samples, including many studies of $CaCO_3$ based biominerals. However it is not clear how well adsorbed proteins and delicate organic substrates would survive the energetic sputter coating process. Further, it would not be possible to study the same substrate before and after protein adsorption.

It is difficult to use NEXAFS spectroscopy to identify different types of proteins in a mixture. One might expect this to be feasible since each amino acid has a unique NEXAFS spectrum (*36*). However, the NEXAFS spectra of all proteins and most peptides tend to be very similar, since they are the average over relatively similar distributions of amino acid residues (*37*). Even so, we have successfully studied competitive protein-peptide adsorption in cases where the peptide contains a special spectral signature arising from an abundance of a specific amino acid, in this case, arginine (*25*). It may be possible to use metal- or quantum-dot-labeled proteins to achieve differentiation of specific components in a mixture of biological adsorbates, although one is always concerned that the label may alter adsorption behavior, and there are sensitivity limitations to soft X-ray microscopy techniques.

Radiation damage is of considerable concern in these experiments due to the high flux of X-rays. Direct comparison of doses in X-PEEM and STXM (*23*) have shown that the dose per spectrum is much larger in X-PEEM than in STXM despite the much more concentrated beam in a STXM (typically a spot size of 30 nm diameter with ~10^7 X-ray/s) than in X-PEEM (typically a spot size of 30 μm diameter with ~10^9 X-ray/s) because the exposure times in STXM (50-100 ms total per spectrum) are much shorter than in X-PEEM (50-500 s per spectrum). In both types of X-ray microscopes it is now routine to shutter the photon beam except during the actual acquisition step. For X-PEEM the shutter is closed between successive images, a period of a few seconds in which the

In Proteins at Interfaces III State of the Art 2012; Horbett, T., et al.;
ACS Symposium Series; American Chemical Society: Washington, DC, 2012.

image is transferred from the camera to the acquisition computer and the photon energy is changed to the next value. There are clearly improvements that can be made, such as more sensitive cameras, faster data transfer, and more rapid photon shutters. In our measurement protocol on PEEM-2 at the ALS we minimize the exposure by preferentially using the 2-bunch mode which has 1/15th the flux of the normal multi-bunch mode operation. We also mask the incident beam to reduce the flux, and keep the dwell times and number of images measured as low as possible, consistent with spectroscopic differentiation. With the undulator based PEEM3 at the ALS we must extensively detune the EPU to keep the incident flux within the levels that the sensitive PMMA and protein materials can tolerate. Sample preparation must also be performed carefully to avoid sharp particulates such as silicon dust from cutting the Si substrate, since particles can cause charging and field emission. Finally, despite the zero cost for peer-reviewed access, synchrotron-based techniques are not readily available for many academic or industrial laboratories, due to the limited number of synchrotron facilities and X-PEEM beamlines.

Despite the aforementioned challenges, X-PEEM and STXM spectromicroscopy methods are providing useful information in the biomaterials area. New developments such as aberration correction (*38–40*) are expected to improve the spatial resolution to ~10 nm in the near future. With 10 nm spatial resolution, imaging individual proteins will become possible. Perhaps more beneficial for this research area, correction of spherical aberration is predicted to increase the transmission of the electron imaging column up to 100-fold which would allow use of smaller apertures in the PEEM column to improve spatial resolution, or enable lower incident fluxes to be used for the same spatial resolution.

For experimental details of materials, sample preparation, data analysis etc, the reader is referred to the original literature cited for each example. All data processing was performed using aXis2000 (*41*).

Examples of Soft X-ray Spectromicroscopy Studies of Protein–Polymer Interfaces

pH-Dependent Protein and Peptide Adsorption to PS-PMMA/PAA

Our studies of albumin, fibrinogen and peptide adsorption to polystyrene-poly(methyl methacrylate) (PS-PMMA) (*24*, *42*, *43*) or PS-polylactide (PLA) films (*15*, *25*, *44*) indicate that hydrophobic interactions are the dominant force determining the preferred sites of adsorption. However, most surfaces analyzed to date using our approach have been neutral and hydrophobic. Recently (*14*) we have explored protein and peptide adsorption to a surface prepared by blending PS with a block co-polymer of poly(methyl methacrylate) and polyacrylic acid (PMMA-b-PAA) to form a phase segregated patterned surface that is negatively charged at neutral pH but which can have the surface charge modified by adjusting the pH, thereby probing the effect of electrostatic interactions with a negatively charged protein and a positively charged peptide as a function of pH. Ultimately our intent is the use the acrylic acid surface groups in order to chemically functionalize the surface in order to tailor its surface adsorption properties for proteins and peptides.

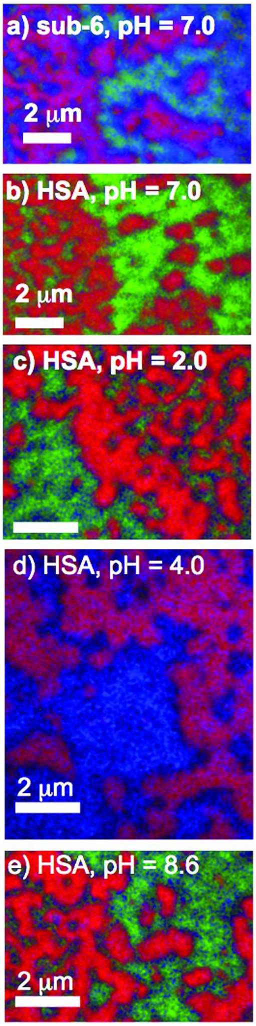

Figure 4. X-PEEM derived color coded composite maps (14) of PS/PMMA-PAA 60:40 exposed to (a) sub-6 protein at pH=7.0; (b-e) 0.05 mg/mL HSA at pH=7.0, 2.0, 4.0 and 8.6. PS is coded red, PMMA-PAA is coded green and HSA or sub-6 is coded blue. In each color coded composite map, the mapping of each color to amount perseveres the overall thickness scale – i.e. the zero of each color scale is set to the minimum over all 3 component maps while the 255 of each color scale is set to the maximum over all 3 component maps (called an 'absolute' presentation). (see color insert)

Figure 4 presents color coded composite images (red = PS, green = PMPA, blue = peptide (Figure 4a) or albumin (Figures 4b-4e)) for surfaces prepared by a 20 minute exposure of a 60:40 (wt %) PS/PMMA-PAA blend to a 0.005 mg/mL aqueous solution of sub-6 peptide and albumin at pH=7.0. Peptide concentrations of 0.005 mg/mL were used for direct comparison to our previous study of SUB-6 adsorption to PS-PMMA (*25*). For each composite map an absolute color coding is used (see caption for details). At neutral pH, SUB-6 is positively charged (+5) while HSA is negatively charged (-15) (*24*). Thus, if electrostatic interactions were a significant factor, one would expect much larger amounts of positively charged peptide to be adsorbed at neutral pH than negatively charged albumin. This is indeed what is found, as seen by comparing Figures 4a and 4b. HSA adsorption is the strongest on the interdomainal interphase between PS and PMMA-PAA, while the central parts of both the PS and PMMA-PAA domains are relatively pure red and green respectively, indicating very little HSA adsorption. The interdomainal interphase is expected to be region with the highest binding capability due to an amphiphillic character and this would explain these observations if thermodynamics controls the interactions. Alternatively it may be that the interphase is the most “kinetically accessible” at short exposure times, where kinetic factors such as the rates of transformation of proteins from less favorable to more favorable conformations/ orientations for bonding may play a role (*24*, *43*).

The much stronger blue color in the composite for SUB-6 adsorption to the PS/PMMA-PAA surface (Figure 4a) indicates the amount of peptide adsorbed is much larger than the amount of protein adsorbed (Figure 4b). The highest intensity is at the interphase between PS and PMMA-PAA. Both the PS and PMMA-PAA domains show peptide adsorption (pink and teal colors) indicating there is significant adsorption of peptide on these regions. The quantitative analysis of these results is presented elsewhere (*14*). Since both HSA and the surface are net negatively charged, repulsive interactions are expected. In fact, adsorption of HSA to the negatively charged PS/PMMA-PAA surface was more than 50% less than to an uncharged PS-PMMA surface at the same concentration (*24*). The positively charged SUB-6 peptide shows the opposite adsorption behavior to HSA with a large peptide thickness at the interphase and negatively charged PMMA-PAA domains. Peptide adsorption to the PS/PMMA-PAA surface was much higher than to an uncharged PS-PMMA surface (*43*). The increased adsorption of SUB-6 on the PS domains of the charged surface compared to neutral surface is most likely due to adsorption to microdomains of PMMA-PAA embedded within the PS domains.

Figure 4c – 4e are color coded composites for 20 minute exposure of a 60:40 (wt %) PS/PMMA-PAA blend surface to a 0.005 mg/mL albumin solution at pH values of 2.0 (c), 4.0 (d) and 8.6 (e). By changing the pH to acid conditions the surface charge is reduced by protonating the carboxylate sites on the PAA domains. At pH 2, HSA is positively charged while the surface is close to neutral. This modified the adsorption of both the protein and the peptide. At the same time as changing the charge at the surface, pH changes the charge and conformation of the albumin in solution. The quantitative chemical maps of the albumin distribution on the pH-modified PS/PMMA-PAA surfaces (Figure 4b-e) reflect

both effects. At pH 4.0, close to the isoelectric point (IP = 4.7 – 5.3) (*45*), HSA is slightly positive while the surface is negatively charged. At pH 8.6, both protein and surface are negatively charged. Due to intramolecular charge interactions HSA exists in five different conformations depending on the pH. These are designated E, F, N, B, and A (*45*). At lower pH, HSA exists in an unfolded and expanded conformation, while at higher pH it is more compact. The maps at pH 2.0 (Figure 4c) and 8.6 (Figure 4e) show a strongly blue interphase region, indicating the highest protein adsorption. Similar amounts were adsorbed at pH 2.0 and 8.6 as shown by similar shades of pink PS and teal PMMA-PAA in both maps. Close to the isoelectric point, at pH 4.0, adsorption to the PMMA-PAA region was so high that almost no green PMMA-PAA color was visible (Figure 4d). The PS region was also strongly pink showing that adsorption was at a maximum at pH 4.0. Previous studies have shown that maximum levels of protein adsorption tend to occur at the isoelectric point where the protein carries no charge and thus exhibits least electrostatic repulsion. HSA adsorption at pH 2.0 and 8.6 was significantly less than at pH 4.0. At pH 4.0, adsorption on PS/PMMA-PAA was significantly higher presumably due to attractive electrostatic interactions. Compared to the (uncharged) PS/PMMA surface (*24*), adsorption on PS/PMMA-PAA was two- to three-fold greater (*14*). At pH 8.6, where HSA is negative, adsorption to the negative PS/PMMA-PAA surface was much greater than to the uncharged PS/PMMA surface. The X-PEEM results for HSA and SUB-6 adsorption on PS/PMMA-PAA spun cast thin films indicate that the adsorption propensity is determined, at least in part, by electrostatic interactions as indicated by the results of adsorption at varying pH.

Effect of Ionic Strength on Adsorption of Albumin to a Polystyrene-Polylactide Blend

Polylactide (PLA), synthesized by ring-opening polymerization of lactide, is a biocompatible and biodegradable synthetic polyester commonly used in tissue engineering and for drug delivery. For scaffold engineering and drug microcapsules, the rate of degradation and controlled release, respectively, can be greatly impacted by combining a non-biodegradable polymer such as polystyrene (PS) (*46*) or polyethylene glycol (PEG) (*47*) with a biodegradable material. Such combinations of biodegradable and nonbiodegradable polymers, known as bioblends, can be a simple, cost-effective means of obtaining a composite with tunable physical or chemical properties (*48*).

Recently we have investigated the adsorption of HSA to the PS/PLA bioblend platform (*15*). That study showed that phase inversion induced by changing the composition of the PS/PLA substrate, did not affected protein adsorption properties. It also showed that surface topography was not a major factor in controlling adsorption, over a range of 35 to 90 nm rms rugosity. Here we summarize the results from that study on the effect of ionic strength on HSA adsorption to PS/PLA, which was investigated by comparing the adsorption of HSA from distilled deionized (DDI) water and phosphate-buffered saline (PBS) solutions.

HSA at concentrations of 0.005, 0.01 and 0.05 mg/mL was adsorbed from DDI water and PBS buffer solutions onto a polystyrene (PS) – polylactide (PLA) 40:60 film that was annealed for 1h at 70 °C. Figure 5 a-f presents the absolute color coded maps for the six films. For the films exposed to HSA in DDI water, the color coded composite maps show that at the highest concentration (Figure 5a), the amount of protein adsorbed is greatest at the interface between the PS and PLA domains. Furthermore, at higher concentrations the maps exhibit more turquoise and pink colors, suggesting slightly higher protein adsorption, while at the lowest concentration (Figure 5c, 5f), there are more green pixels which suggest a more uneven adsorption. For the PBS buffer system (Figure 5 d-f), the composite images show a strong blue color for the 0.05 mg/mL surface. This indicates a high amount of adsorbed protein. The blue color is not as strong for the other images, showing that less HSA adsorbs to the surface as the HSA concentration decreases, or when the adsorption takes place from DDI water.

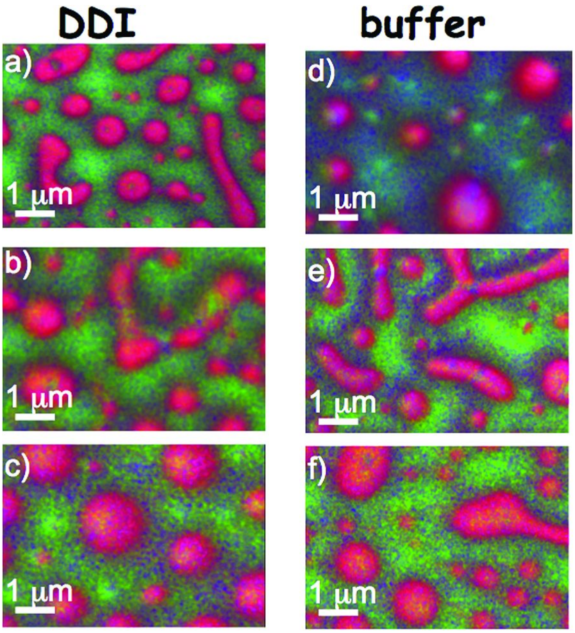

Figure 5. X-PEEM color coded composite maps of 40:60 PS/PLA films (0.7 wt % loading), annealed 1 h at 70 °C exposed to HSA solutions of varying concentrations and from distilled deionized water (DDI) or phosphate saline buffer (PBS) solutions (15): (a, d) 0.05 mg/mL HSA , (b,e) 0.01 mg/mL HSA (rescaled), (c,f) 0.005 mg/mL. The maps on the left (a, b, c) correspond to samples where the solvent was distilled water; the maps on the right (d, e, f) are for samples where the solvent was phosphate buffered saline. PS is coded red, PLA is coded green, and HSA is coded, and the signal from each component is presented on an overall absolute intensity. (see color insert)

Table 1. Thickness (nm) of PS, PLA, and HSA in the PS, PLA and interface regions from PS:PLA 40:60 (0.7 wt%) films annealed 1h at 70 °C exposed to 0.05, 0.01, and 0.005 mg/mL HSA from either DDI water of PBS buffer. Uncertainty ±0.5 nm (*25*)

Region	*Composite*	*HSA adsorbed from DDI*			*HSA adsorbed from PBS*		
	Thickness (nm)	*0.05 mg/mL*	*0.01 mg/mL*	*0.005 mg/mL*	*0.05 mg/mL*	*0.01 mg/mL*	*0.005 mg/mL*
PS	PS	8.1	8.0	9.0	7.8	8.3	9.2
	PLA	0.0	0.9	0.2	0.2	0.3	0.2
	HSA	1.9	1.1	0.8	2.0	1.4	0.7
PLA	PS	2.5	3.0	3.0	2.6	2.5	2.7
	PLA	5.1	6.1	6.7	4.7	6.0	6.5
	HSA	2.4	0.9	0.3	2.8	1.5	0.8
Inter-face	PS	6.5	5.1	3.8	3.9	4.6	4.6
	PLA	0.7	3.1	4.5	2.0	2.5	2.7
	HSA	2.7	1.8	1.7	4.1	3.5	2.8

The quantitative results from the curve fitting of the C 1s spectra extracted from the PS, PLA and interphase domains are summarized in table 1. This analysis show that at all concentrations examined, HSA adsorption occurs most strongly at the interface between PS and PLA. As the protein concentration decreases the average thickness of HSA on the surface also decreases. The quantitative results for the PBS buffer system also show preferential HSA adsorption to the interface between PS and PLA domains. However, the extracted average thickness values of the adsorbed HSA in the interfacial region are almost twice as large compared to adsorption from DDI water for all three concentrations. The X-PEEM results show a correlation between the thickness of the adsorbed protein layer and the ionic strength. This seemingly conflicts with literature reports which show the amount of adsorbed protein decreases with increasing salt concentration on silica, pegylated Nb_2O_5 and $Si(Ti)O_2$ surfaces, as examined with neutron reflectivity (*49*), optical waveguide light mode spectroscopy (*50*) and integrated optical methods (*51*), respectively. Importantly, according to the integrated optical methods, although the number of adsorbed protein molecules decreased with increasing ionic strength, the area occupied by the adsorbed molecules increased with increasing salt concentration. Thus, the increased HSA thickness detected by X-PEEM for PBS buffer system may reflect a conformational change resulting in an increase in the adsorbed protein size without changing the number of adsorbed HSA molecules.

To further investigate this system and to verify if a conformational change was present, the same systems were investigated with ^{125}I radiolabeled HSA which provides a means of measuring the number of adsorbed molecules on the polymer surface. Figure 6 presents a comparison of the X-PEEM and ^{125}I radiolabeling results, while the data from the radiolabeling experiments are presented in table 2. We used the values for the X-PEEM interfacial region to clearly highlight that there is a difference between adsorption from DDI and PBS using both methods. This comparison shows that at the two higher HSA concentrations (0.05 and 0.01 mg/mL) the number of protein molecules adsorbed from DDI water was almost double that from buffer, while at lower HSA concentration (0.005 mg/mL) the numbers of adsorbed HSA were similar. These results contrast strikingly with the X-PEEM data which showed increasing thickness with increasing ionic strength. Thus, using a combination of X-PEEM and radiolabeling experiments, we concluded that the conformation of HSA adsorbed from buffer is extended relative to that adsorbed from DDI water.

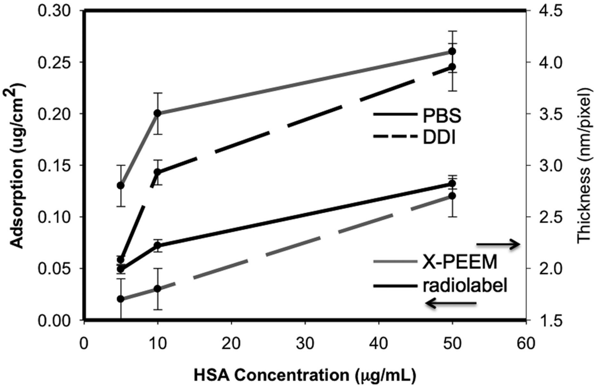

Figure 6. Adsorption isotherms for albumin adsorption from DDI and buffer on 40:60 PS/PLA films (0.7 wt % loading), measured by X-PEEM and ^{125}I radiolabelling (15). PBS is solid and DDI is dashed. X-PEEM detected thickness (right y-axis) is plotted in gray, radiolabeling (left y-axis) in black.

Effect of Hydration on Adsorption of HSA to PS/PMMA

There are concerns that the lateral spatial distributions measured in the dry, UHV conditions in X-PEEM could be different from those which may exist at the fully hydrated polymer surface. This could be a result of modifications of surface distributions in the last stages of drying for example. Although it has lower surface sensitivity than X-PEEM it is possible to measure proteins at polymer surfaces in STXM, since the polymer films have to be quite thin (<100 nm) to allow for partial penetration of the soft X-rays. In order to investigate the effect of surface hydration, we used STXM to image a HSA hydrated sample formed by sandwiching a thin film of PS-PMMA between two X-ray transparent silicon nitride windows (*16*). This system was examined under completely hydrated, washed and hydrated, and completely dried conditions. Figure 7a-c shows the component maps of PS, PMMA and HSA in the fully hydrated sample, while Figure 7d presents a color coded composite of these component maps (PS, PMMA and HSA are color coded in red, green and blue, respectively;). The lighter pixels in Figure 7c reveals the areas that correspond to high adsorption of HSA. There is a strong correlation between the areas of high protein and the PMMA domains. Also, the color coded composite shows there is a high density of adsorbed HSA is seen at the interphase between PS and PMMA domains. Figures 7e-h present the corresponding results for the washed, dried and rehydrated system. The results are rather similar to those for the fully hydrated sample.

Table 2. Adsorption of albumin from ^{125}I radiolabelling measurements on PS-PLA (µg/cm^2) from distilled water (DDI) versus phosphate buffered saline (PBS). Data shown are the mean of 4 replicates with standard deviation in parentheses (sd, n = 4) (*25*)

	Surface density *(µg/cm^2) (sd)*	
Solution concentration (mg/mL)	*DDI*	*PBS*
0.005	0.058 (0.004)	0.049 (0.004)
0.01	0.143 (0.012)	0.072 (0.006)
0.05	0.245 (0.023)	0.132 (0.005)

Figure 7i-k displays the images for the dry system. Compared to the completely wet system, the color coded composite map of the dry surface (Figure 7k) shows a much pinker map, indicating there is more protein on the PS region. The quantitative results show that for the dehydrated system, the spatial distribution of the adsorbed protein is: interdomainal > PS > PMMA. This trend is similar to that observed for HSA adsorption on PS-PMMA as imaged with X-PEEM (*42*). Since X-PEEM probes only the top 10 nm of the surface while STXM samples through the entire film the percentages of adsorbed HSA are higher in the X-PEEM data. The data between STXM and X-PEEM cannot be directly compared, however the relative ratios of the amount of HSA adsorbed to the PS region, PMMA region and interface can be compared. Similar ratios are seen for STXM and X-PEEM dry samples, but the distributions on the washed and fully hydrated samples are different, with a greater amount of HSA adsorbed to the PMMA domains.

The quantitative results for the hydrated system (see table 3) show adsorbed protein thicknesses in excess of 10 nm on the PMMA domains which suggest that there may possibly be bilayer adsorption since the crystallographic dimensions of HSA are 8x8x3 nm. Nonetheless, this adsorbed HSA is only loosely bound to the PMMA domains since a large percentage of the protein was removed upon washing. Washing with 30 uL of DDI water reduced the thickness of HSA adsorbed on the PMMA domains by 50%. By using X-ray spectromicroscopy to examine HSA adsorption under wet and dry conditions, qualitative insight was gained into the adsorption behavior of HSA on chemically heterogeneous surfaces. Moreover, by washing the HSA system, further information on the strength of HSA adsorption was also elucidated.

Table 3. Average thickness (nm) of HSA on PS, PMMA and PS/PMMA interdomainal regions (*16*)

	Component	*Hydrated (STXM)*		*Washed (STXM)*		*Dry (STXM)*		*Dry (X-PEEM)*
Region		*(nm/pixel)*	*(%)*	*(nm/pixel)*	*(%)*	*(nm/pixel)*	*(%)*	*(%)*
PS	PS	19.5	50	16.7	51	13.9	60	65
	PMMA	14.5	37	11.5	35	6.6	28	14
	HSA	4.7	12	4.6	14	2.7	12	21
PMMA	PS	7.5	15	7.1	18	1.9	8	23
	PMMA	31.9	64	27.4	69	19.4	82	64
	HSA	10.6	21	5.4	14	2.3	10	13
Interdomainal region	PS	4.3	10	9.2	26	4.6	18	38
	PMMA	27.6	66	19.5	55	16.1	63	37
	HSA	10.2	24	6.7	19	4.8	19	25
(HSA ratios PS/PMMA/Interphase)		0.4/1.0/1.0		1.1/1.0/1.2		1.2/1.0/1.9		1.6/1.0/1.9

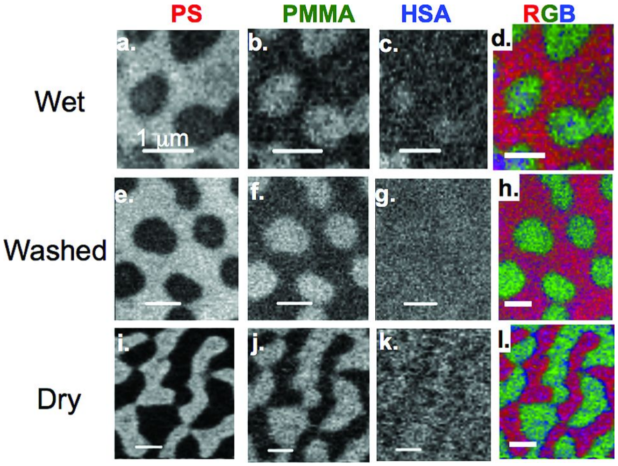

Figure 7. (top) Component maps derived from C 1s STXM image sequences measured from (16): fully hydrated wet cell of HSA adsorbed to a PS-PMMA thin film: (a) PS, (b) PMMA, (c) HSA, and (d) rescaled color composite map. (center) Component maps from a fully hydrated sample, but washed repeatedly with DDI water prior to sealing the wet cell: (e) PS, (f) PMMA, (g) HSA, and (h) rescaled color composite map. (bottom) Component maps from HAS adsorbed to PS-PMMA, washed with DDI water after 20 min exposure and air-dried: (i) PS, (j) PMMA, (k) HSA, and (l) rescaled color composite map. In each case, the color coding for the composite maps is: red, PS; green, PMMA; blue, HSA. HSA = 0.005 mg/mL. (see color insert)

STXM Study of Fibrinogen Adsorption on a Reinforced Polyurethane under Fully Hydrated Conditions

Polyurethanes are commonly used in medical applications due to their favourable mechanical and chemical properties. In a very early exploration of the potential for soft X-ray microscopy to contribute to the field of protein-polymer interface studies (*17*), we investigated the adsorption of fibrinogen to a complex multi-component polyurethane in which the polyether-rich toluene-di-isocyante (TDI) polyurethane matrix was reinforced with two types of more rigid polymer particles, styrene-b-acrylonitrile (SAN) particles and poly-isocyanate poly-addition product (PIPA, a methylene diphenyl diisocyanate

(MDI)-based hard segment-like material) particles. STXM studies of the chemistry and morphology of the polyurethane was reported separately (*52*). In this study the protein distributions determined after the sample was rinsed and dried were compared to those determined with a pure aqueous overlayer (the sample was dried then rehydrated), and with the protein solution as the overlayer (i.e. an '*in situ*' measurement).

Figure 8a displays the color coded composite of component maps derived from a C 1s image sequence of the dry sample. The substrate was a microtomed polyurethane sample embedded with poly(styrene-co-acrylonitrile) (SAN) and poly-isocyanate poly-addition product (PIPA) nanoparticles imaged with STXM. The surface was exposed to 0.1 mg/mL of fibrinogen for 20 min and then rinsed and air dried. SAN, PIPA, Fg and polyurethane are color coded as red, green, blue and black respectively. Figure 8a shows that Fg strongly prefers to adsorb at the interface between SAN and the polyurethane matrix. Figure 8b shows the fit of the C 1s spectrum extracted from those pixels with relatively large Fg content. A distinct shoulder is observed at 288.2 eV, the energy of the dominant C 1s → π^*_{amide} transition of the protein. Also, the quality of the fit without including the Fg reference spectrum is significantly worse.

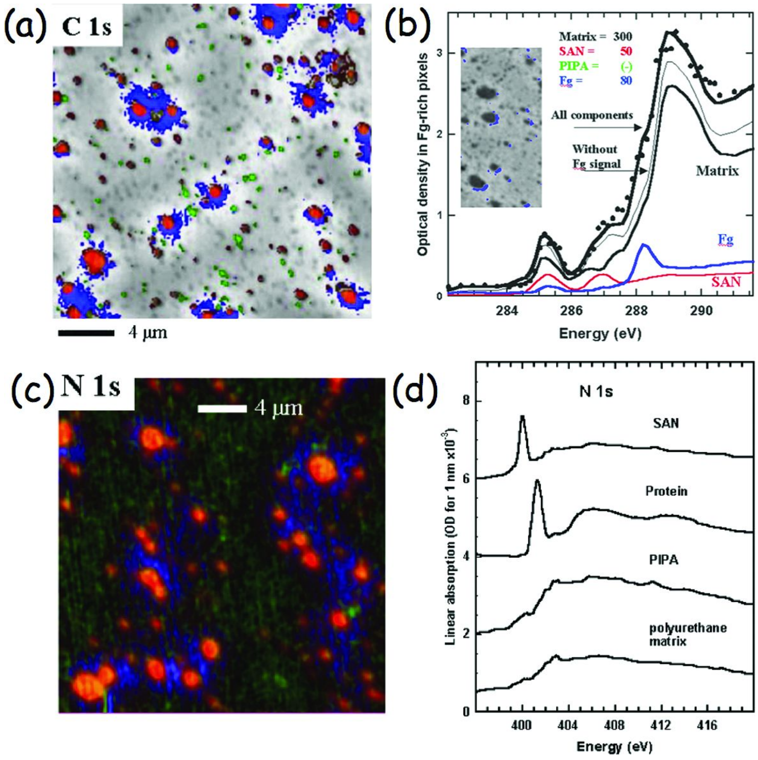

Figure 8. (a) color coded composite of the component maps of the matrix and reinforcing particles in a polyurethane (red = SAN , green = PIPA; grey-scale = matrix) and the adsorbed fibrinogen (Fg, blue), derived from fits to a C 1s image sequence recorded with STXM from a 0.1 mg/mL solution of Fg in phosphate buffer (17). The measurements were performed with the sample in a wet state covered in the buffer solution of the protein. (b) Fit of the C 1s spectrum of the blue pixels. (c) color composite of maps of SAN, PIPA and Fg derived from fits to a C 1s image sequence. (d) Fit of the N 1s spectrum of the blue pixels. (see color insert)

A second sample with the dried Fg rehydrated with water and imaged under fully hydrated conditions showed that Fg preferred to adsorb to the matrix over the SAN. Figure 8c shows the color coded composite derived from a N 1s image sequence. The N 1s edge is particularly sensitive to protein since only the SAN particles have significant amount of nitrogen. The N 1s spectrum of the nitrile component is very different from that of the protein (Figure 8d) and thus the protein is clearly differentiated. As found for the dried sample, the fibrinogen has a very strong affinity for the interface between SAN and the polyurethane matrix. Since Fg has dimensions of 45 x 9 x 6 nm, determined by electron microscopy (*53*), the Fg may be adsorbed end-on to the surface rather than side-on. While the mechanism of Fg adsorption to the interface is not clear, the surface topography may be playing a role since the SAN particles protrude up to 50 nm from the surface. Previous studies by Rechendorff et al. (*54*) found a correlation between surface roughness and increased Fg adsorption.

X-PEEM and TOF-SIMS Study of Peptide Adsorption to a SAM Microarray

Castner and co-workers (*55*) are exploring methods to create surface patterned chemistry for micro-array based medical diagnostics (*56*). One approach is to use a focused ion beam (or irradiation through a mask) to remove parts of a uniform self-assembled monolayer (SAM), followed by filling the removed regions with a second type of SAM. Surface and interface sensitive methods are needed to examine the fidelity of these SAM micro-arrays, as well as the specificity of protein or peptide adsorption to them. In collaboration with Castner and Weidner, we have used X-PEEM to examine adsorption of LKα14 (Ac-LKKLLKLLKKLLKL-OH, a model α-helix peptide) on to a patterned micro-array consisting of alternating squares of an alcohol-terminated SAM (1-thiol-undecanol MCU) and a carboxylate terminated SAM (1-thiol-dodecylcarboxylate, MUDA). Similar samples were also examined using TOF-SIMS. Figure 9a shows a TOF-SIMS image based on the $C_3H_5^+$ ion. The brighter areas correspond to alcohol-rich MCU, while the darker areas correspond to the carboxylate-rich MUDA. For most of the pattern the individual squares are 10 μm x 10 μm while the upper left square has a finer scale pattern (1 μm x 1 μm). Figure 9b shows a TOF-SIMS image derived from the $C_5H_{10}N^+$ ion, which can only have originated from the peptide. The reversal of contrast between these two TOF-SIMS images indicates the peptide is predominantly adsorbed to the MUDA domains. Figure 9c is the ratio of X-PEEM images recorded at 400 eV and 280 eV, which samples net carbon. The bright regions in the X-PEEM image are the carbon-rich MCU domains and the image contrast is similar to that in Figure 9a. A C 1s image sequence was recorded from the intersection of four of the large squares. Preliminary X-PEEM results are shown in Figure 9e-h. Fitting to C 1s reference spectra of MCU, MUDA and the LKα14 peptide (Figure 9d, measured from pure thin films using electron yield NEXAFS at NSLS I) gave the component maps shown in Figures 9e-g. Figure 9h is the peptide component map from fitting a N 1s image sequence to the N 1s spectrum of LKα14 and a constant (the constant represents the C 1s signal of the underlying SAM materials, and has a mapsimilar to that of Figure 9e). The X-PEEM results support the conclusion from TOF-SIMS that the peptide is adsorbed predominantly on the MUDA, carboxylate-terminated domains. However, these early results also suggest that the underlying SAM domains are not pure, but exists as a mixture of both types of SAMs. This suggests that the Bi^+ bombardment used to remove the MCU was only partly successful and / or the MCU SAM molecules can redistribute during the preparation of the MUDA SAM component.

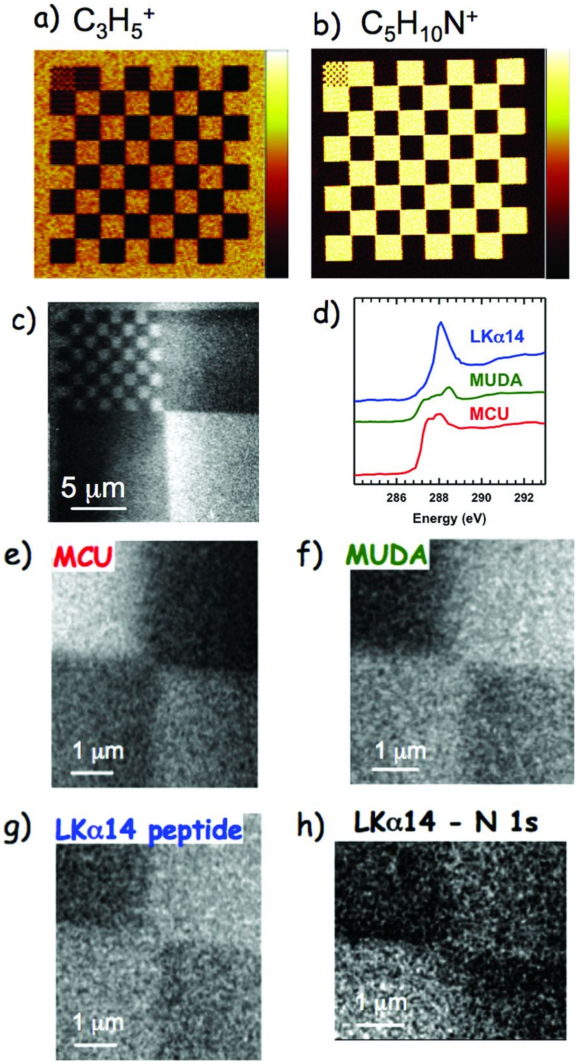

Figure 9. (a) TOF-SIMS image of the surface distribution of $C_3H_5^+$ from a patterned micro-array consisting of alternating squares of an alcohol-terminated SAM (MCU) and a carboxylate terminated SAM (MUDA), exposed to a 0.05 mg/mL solution of LKα14, an alternating leucine (L), lysine (K) peptide, Ac-LKKLLKLLKKLLKL-OH, which is a model α-helix peptide. The brighter pads correspond to the carboxylate terminated MUDA domains while the darker

pads correspond to the alcohol terminated MCU domains. (b) TOF-SIMS image of surface distribution of $C_5H_{10}N^+$ which originates from the peptide. The contrast indicates the peptide is predominantly adsorbed to the MUDA domains. (c) X-PEEM image from the C 1s signal [I(400 eV) – I(280 eV)]. The contrast is the same as that in the TOF-SIMS image of $C_3H_5^+$ indicating it is dominated by substrate signals. (d) C 1s NEXAFS spectra of MCU, MUDA and LKα14 indicting the characteristic features of alcohols, carboxylates and amides in the 287-290 eV region. (e-g) Component maps of MCU, MUDA and LKα14 derived from a fit to a C 1s image sequence (282-293 eV). (h) Map of LKα14 derived from a fit to a N 1s image sequence (396-420 eV). (see color insert)

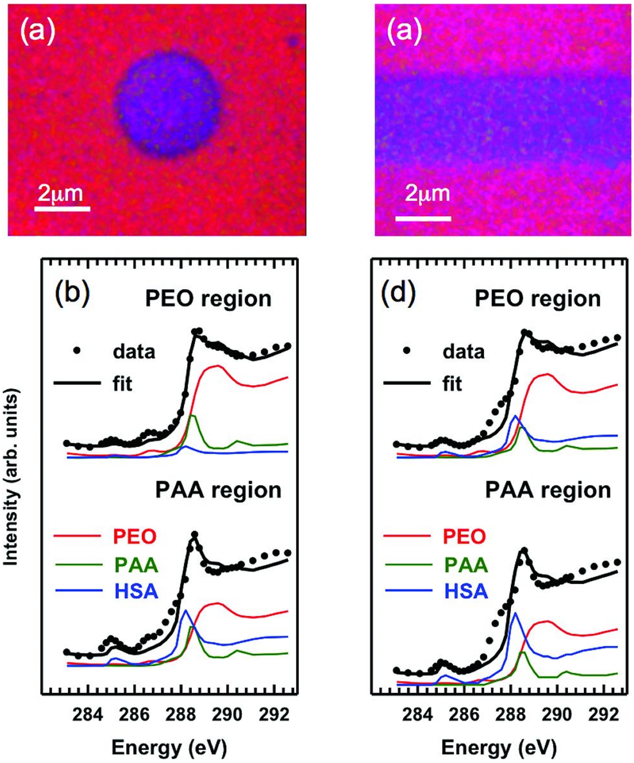

Figure 10. (a) Absolute color component maps for 0.002 mg/ml ubiquitin adsorbed to a PEO-like/ppAA circular microstructure (18). (b) Spectral fitting for the PEO-rich region (top) and ppAA-rich region (bottom). (c) Absolute color component maps for 0.002 mg/ml ubiquitin adsorbed to a PEO/ppAA linear microstructure (18). (d) Spectral fitting for the PEO-rich region (top) and ppAA-rich region (bottom). For all images and spectra, PEO-like is color-coded as red, ppAA is color-coded as green and ubiquitin is color-coded as blue. (see color insert)

X-PEEM Study of Ubiquitin Adsorbed to Microbeam-Patterned Polymeric Surfaces

Materials used for biological applications can be improved through surface modification which can selectively increase or reduce the interaction of the material with biological entities such as proteins, cells, or bacteria (*57–59*). Among the different surface functionalization methods, plasma deposition and plasma grafting techniques have gained considerable popularity for producing surfaces suitable for biomolecule immobilization to elicit specific biological responses (*60*, *61*). For example, surfaces containing COOH and NH_2 functionalities are widely used to bind protein (*62*) and for cell growth assays (*63*). In a recent study, X-PEEM was used to investigate protein adsorption on micro-structured polymers fabricated by e-beam lithography and plasma polymerization (*18*). Ubiquitin was used as model protein because of its relatively simple structure. Ubiquitin, is a highly ubiquitous protein present in all eukaryotes, while it is absent from prokaryotes. Ubiquitin is a 76 amino acid residue protein. It is the most highly conserved protein known thus far. It has a molecular weight of 8.564 kDa and an isoelectric point of 6.79. Ubiquitin labels proteins for proteosomal degradation. Through this means, ubiquitination controls the stability, function, and intracellular localization of a wide variety of proteins (*64*).

Micropatterned structures consisting of plasma polymerized acrylic acid (ppAA) circular domains within a background of a polyethylene oxide (PEO) -like protein resistant material were fabricated by electron beam lithography and plasma polymerization. 0.002 mg/mL ubiquitin was adsorbed to the surface and then imaged with X-PEEM. Figure 10 shows the absolute color coded composites of component maps derived from C 1s X-PEEM image sequences for a circular (Figure 10a) and a linear (Figure 10b) pattern. In these maps, PEO is color coded red, ppAA is color coded green and ubiquitin is color coded blue. The matrix is intensely red, which is indicative of low protein adsorption while the ppAA circular domains are purple, which arises from a roughly equal amount of red PEO and blue protein. These results show that PEO dominates the entire surface. Even under the thin layer of ppAA, a large amount of PEO can be detected. These mapping results were verified by quantitative curve fit analysis of spectra extracted from the two substrate domains (see Table 4). Only a small amount (22-25%) of ppAA was detected by X-PEEM. Nonetheless, even though the ppAA layer is thin, selective adsorption of ubiquitin is seen on the surface. On the protein resistant PEO-like surface, only 6% of protein is present, while on the ppAA-rich area, 32% of protein is found at the center of the circle. The spectral results show a good fit for the PEO-rich areas. However a poor fit is seen for the ppAA-rich region, where there seems to be a missing component below C1s → $\pi^*_{C=O}$ which may be the result of radiation damage or contamination. In the case of the line pattern, the quantitative spectral fitting (Figure 10d) shows poor fits for both the PEO-like and ppAA-rich regions. A missing component is clearly seen at ~287 eV. Based on our knowledge of C 1s NEXAFS spectroscopy, this missing component is indicative of a hydrocarbon (C-H) signal and is assumed arise from some source of contamination which is currently unidentified. This spectral mismatch may be the reason why ppAA is shown to be only a minor component while XPS results of the same system suggest that the ppAA layer is greater than 10 nm. Further investigations are required to clarify this discrepancy.

Table 4. Percentage of PEO-like, ppAA, and ubiquitin on PEO-like/ppAA microstructures for PEO-rich and PAA-rich areas for films exposed to 0.002 mg/mL ubiquitin. Uncertainty ±5% (*18*)

		Percentage	
Region	*Component*[(a)]	*Circle*	*Line*
PEO-like	PEO	69%	59%
	ppAA	25%	17%
	Ubiquitin	6%	24%
ppAA	PEO	46%	36%
	ppAA	22%	14%
	Ubiquitin	32%	50%

(a) reference spectra used to derive these results were: PEO-like, ppAA as ppAA and ubiquitin as albumin.

Summary

Through these examples it is clear that soft X-ray spectromicroscopy is making significant contributions to our understanding of protein and peptide interactions with spontaneously or artificially phase segregated polymer surfaces, of the type frequently encountered in biomaterials used for medical and other applications. While this chapter has focused on recent results from our group, there are others using these techniques. For example, Turgeon and coworkers (*65*, *66*) have applied X-PEEM to investigate the integrity of fluorocarbon coatings on stents, while Kappen et al. (*67*) have used X-PEEM to study copper and polypyrrole micro-patterns deposited on fluorocarbon substrates, in order to elucidate growth mechanisms, elemental distributions, topography, local conductivity and thin film orientation. An up-to-date listing of current and projected soft X-ray microscopes has recently been published (*13*) – there are about 50 such facilities world-wide, all of which are publically accessible, with access determined on a peer-reviewed competitive basis. With ever increasing numbers of 3rd generation synchrotron facilities, almost all of which feature beamlines dedicated to X-PEEM and STXM, the potential for applying soft X-ray microscopy to studies of protein interfaces is enormous.

Acknowledgments

We thank the Hancock Research Group from UBC for providing the SUB-6 peptide. We thank J. Goh for providing the collagen sample and AFM images. We thank D. Castner and T. Weidner for providing the SAM micro-array samples, the C 1s reference spectra and the TOF-SIMS results. This research was supported by the Natural Sciences and Engineering Research Council (NSERC, Canada), AFMNet and the Canada Research Chairs program. X-ray microscopy was carried out using PEEM2, PEEM3 and STXM5322 at the ALS and the CaPeRS PEEM and STXM at the CLS. The ALS is supported by the US Department of Energy under Contract DE-AC03-76SF00098. The CLS is supported by NSERC, CIHR, NRC and the University of Saskatchewan. We thank the staff scientists, David Kilcoyne and Tolek Tyliszczak (ALS) and Jian Wang, Uday Lanke and Chithra Karunakaran (CLS) for their expert support of the beamlines and microscopes.

References

1. Castner, D. G.; Ratner, B. D. *Surf. Sci.* **2002**, *500*, 28–60.
2. Anderson, J. M.; Rodriguez, A. D.; Chang, T. *Semin. Immunol.* **2008**, *20*, 86–100.
3. Frey, B. L.; Jordan, C. E.; Komguth, S.; Com, R. M. *Anal. Chem.* **1995**, *67*, 4452–4457.
4. Veiseh, M.; Zareie, M. H.; Zhang, M. *Langmuir* **2002**, *18*, 6671–6678.
5. Roach, L. S.; Song, H.; Ismagilov, R. F. *Anal. Chem.* **2005**, *77*, 785–796.
6. Wadu-Mesthrige, K.; Xu, S.; Amro, N. A.; Liu, G. Y. *Langmuir* **1999**, *15*, 8580–8583.
7. Rezwan, K.; Meier, L. P.; Gauckler, L. J. *Biomaterials* **2005**, *26*, 4351–4357.
8. Norde, W.; Lyklema, J. *J. Biomater. Sci., Polym. Ed.* **1991**, *2*, 183–202.
9. Haynes, C. A.; Norde, W. *Colloids. Surf., B* **1994**, *2*, 517–566.
10. Leung, B. O.; Brash, J. L.; Hitchcock, A. P. *Materials* **2010**, *3*, 3911–3938.
11. Howells, M.; Jacobsen, C.; Warwick, T. Principles And Applications of Zone Plate X-Ray Microscopes. In *Science of Microscopy*; Hawkes, P. W., Spence, J. C. H., Eds.; Springer, New York, 2007.
12. Ade, H.; Hitchcock, A. P. *Polymer* **2008**, *49*, 643–675.
13. Hitchcock, A. P. Soft X-ray Imaging and Spectromicroscopy. In *Handbook on Nanoscopy*; Van Tendeloo, G., Van Dyck, D., Pennycook, S. J., Eds.: Wiley: New York, 2012; Volume 2, pp 745−791.
14. Leung, B. O.; Hitchcock, A. P.; Cornelius, R. M.; Brash, J. L.; Scholl, A.; Doran, A. *J. Electron Spectrosc. Relat. Phenom.* **2012** DOI: 0.1016/j.elspec.2012.06.004.
15. Leung, B. O.; Hitchcock, A. P.; Brash, J. L.; Scholl, A.; Doran, A. *Biomacromolecules* **2009**, *10*, 1838–1845.
16. Leung, B. O.; Wang, J.; Brash, J. L.; Hitchcock, A. P. *Langmuir* **2009**, *25*, 13332–13335.
17. Hitchcock, A. P.; Morin, C.; Heng, Y. M.; Cornelius, R. M.; Brash, J. L. *J. Biomater. Sci., Polym. Ed.* **2002**, *13*, 919–938.

18. G. Ceccone, G.; Leung, B. O.; Perez-Roldan, M. J.; Valsesia, A.; Colpo, P.; Rossi, F.; Hitchcock, A. P.; Scholl, A. *Surf. Interface Anal.* **2010**, *42*, 830–834.
19. Anders, S.; Padmore, H. A.; Duarte, R. M.; Renner, T.; Stammler, T.; Scholl, A.; Scheinfein, M. R; Stohr, J.; Seve, L.; Sinkovic, B. *Rev. Sci. Instrum.* **1999**, *70*, 3973–3981.
20. Feng, J.; Forest, E.; MacDowell, A. A.; Marcus, M.; Padmore, H.; Raoux, S.; Robin, D.; Scholl, A.; Schlueter, R.; Schmid, P.; Stöhr, J.; Wan, W.; Wei, D. H.; Wu, Y. *J. Phys C: Condens. Matter* **2005**, *17*, S1339–S1350.
21. Christensen, S. L.; Haines, B. M.; Lanke, U. D.; Paige, M. F.; Urquhart, S. G. *IBM J. Res.* **2011**, *55*, 5:1–5:6.
22. Schmidt, Th.; Marchetto, H.; Lévesque, P. L.; Groh, U.; Maier, F.; Preikszas, D.; Hartel, P.; Spehr, R.; Lilienkamp, G.; Engel, W.; Fink, R.; Bauer, E.; Rose, H.; Umbach, E.; Freund, H.-J. *Ultramicroscopy* **2010**, *110*, 1358–1361.
23. Wang, J.; Li, L.; Morin, C.; Hitchcock, A. P.; Doran, A.; Scholl, A *J. Electron Spectrosc.* **2009**, *170*, 25–36.
24. Li, L.; Hitchcock, A. P.; Robar, N.; Cornelius, R.; Brash, J. L.; Scholl, A.; Doran, A. *J. Phys. Chem B* **2006**, *110*, 16763–16773.
25. Leung, B. O.; Hitchcock, A. P.; Brash, J. L.; Scholl, A.; Doran, A.; Henklein, P.; Overhage, J.; Hilpert, K.; Hale, J. D.; Hancock, R. E. W. *Biointerphases* **2008**, *3*, F27–F35.
26. Chao, W.; Fischer, P.; Tyliszczak, T.; Rekawa, S.; Anderson, E.; Naulleau, P. *Opt. Express* **2012**, *20*, 9777–9783.
27. Wen, C. K.; Goh, M. C. *Proteins* **2006**, *64*, 227–233.
28. Shoulders, M. D; Raines, R. T. *Ann. Rev. Biochem.* **2009**, *78*, 929–958.
29. Siedlecki, C. A.; Marchant, R. E. *Biomaterials* **1998**, *19*, 441–454.
30. Ta, T. C.; McDermott, M. T. *Anal. Chem.* **2000**, *72*, 2627–2634.
31. Sousa, A.; Sengonul, M.; Latour, R.; Kohn, J.; Libera, M. *Langmuir* **2006**, *22*, 6286–6292.
32. Stöhr, J. NEXAFS Spectroscopy. In *Springer Tracts in Surface Science*; Springer: Berlin, 1992; Vol. 25.
33. Xu, L.-C.; Runt, J.; Siedlecki, C. A. *Acta Biomater.* **2010**, *6*, 1938–1947.
34. Gilbert, B.; Margaritondo, G.; Douglas, S.; Nealson, K. H.; Edgerton, R. F.; Rempfer, G.; De Stasio, G. *J. Electron.. Spectrosc. Relat. Phenom.* **2001**, *114/116*, 1005–1009.
35. De Stasio, G.; Frazer, B. H.; Gilbert, B.; Richter, K. L.; Valley, J. W. *Ultramicroscopy* **2003**, *98*, 57–62.
36. Zubavichus, Y.; Shaporenko, A.; Grunze, M.; Zharnikov, M. *J. Phys. Chem. Lett.* **2005**, *109*, 6998–7000.
37. Stewart-Ornstein, J.; Hitchcock, A. P.; Hernàndez-Cruz, D.; Henklein, P.; Overhage, J.; Hilpert, K.; Hale, J.; Hancock, R. E. W. *J. Phys. Chem. B* **2007**, *111*, 7691–7699.
38. Wichtendahl, R.; Fink, R.; Kuhlenbeck, H.; Preikszas, D.; Rose, H.; Spehr, R.; Hartel, P.; Engel, W.; Schlögl, R.; Freund, H.-J.; Bradshaw, A. M.; Lilienkamp, G.; Schmidt, Th.; Bauer, E.; Brenner, G.; Umbach, E. *Surf. Rev. Lett.* **1998**, *5*, 1249–1256.

39. Schmid, P.; Feng, J.; Padmore, H. A.; Robin, D.; Rose, H.; Schlueter, R.; Wan, W.; Forest, E.; Wu, Y. *Rev. Sci. Instrum.* **2005**, *76* (1-14), 023302.

40. MacDowell, A. A.; Feng, J.; DeMello, A.; Doran, A.; Duarte, R.; Forest, E.; Kelez, N.; Marcus, M. A.; Miller, T.; Padmore, H. A.; Raoux, S.; Robin, D.; Scholl, A.; Schlueter, R.; Schmid, P.; Stöhr, J.; Wan, W.; Wei, D. H.; Wu, Y. *AIP Conf. Proc.* **2007**, 1341–1344.

41. Hitchcock, A. P. aXis2000 is free for non-commercial use. It is written in Interactive Data Language (IDL) and available from http://unicorn.mcmaster.ca/aXis2000.html, 2012.

42. Morin, C.; Hitchcock, A. P.; Cornelius, R. M.; Brash, J. L.; Scholl, A.; Doran, A. *J. Electron. Spectrosc. Relat. Phenom.* **2004**, *137-140*, 785–794.

43. Li, L.; Hitchcock, A. P.; Cornelius, R.; Brash, J. L.; Scholl, A.; Doran, A. *J. Phys. Chem B* **2008**, *112*, 2150–2158.

44. Leung, B. O.; Hitchcock, A. P.; Brash, J. L.; Scholl, A.; Doran, A. *Macromolecules* **2009**, *42*, 1679–1684.

45. Foster, J. F. In *Albumin Structure, Function and Uses*; Rosenoer, V. M., Oratz, M., Rothschild, M. A., Eds.; Pergamon: Oxford, 1977; pp 53−84.

46. Saravanan, M.; Bhaskar, K.; Srinivasa, R. G.; Dhanaraju, M. D. *J. Microencapsulation* **2003**, *20*, 289–302.

47. Cai, Q.; Bei, J.; Wang, S. *Polym. Adv. Technol.* **2002**, *13*, 534–540.

48. Zhang, G.; Zhang, J.; Wang, S.; Shen, D. *J. Polym. Sci., Part B: Polym. Phys.* **2003**, *41*, 23–30.

49. Su, T. J.; Lu, J. R.; Thomas, R. K.; Cui, Z. F.; Penfold, J. *J. Colloid Interface Sci.* **1998**, *203*, 419–429.

50. Pasche, S.; Voros, J.; Griesser, H. J.; Spencer, N. D.; Textor, M. *J. Phys. Chem. B* **2008**, *109*, 17545–17552.

51. Ramsden, J. J.; Prenosil, J. E. *J. Phys. Chem.* **1994**, *98*, 5376–5381.

52. Rightor, E. G.; Urquhart, S. G.; Hitchcock, A. P.; Ade, H.; Smith, A. P.; Mitchell, G. E.; Priester, R. D.; Aneja, A.; Appel, G.; Wilkes, G.; Lidy, W. E. *Macromolecules* **2002**, *35*, 5873–5882.

53. Hook, F.; Voros, J.; Rodahl, M.; Kurrat, R.; Boni, P.; Ramsden, J. J.; Textor, M.; Spencer, N. D.; Tengvall, P.; Gold, J.; Kasemo, B. *Colloids Surf., B* **2002**, *24*, 155–170.

54. Rechendorff, K.; Hovgaard, M. B.; Foss, M.; Zhdanov, V. P.; Besenbacher, F. *Langmuir* **2006**, *22*, 10885–10888.

55. Weidner, T.; Ballav, N.; Siemeling, U.; Troegel, D.; Walter, T.; Tacke, R.; Castner, D. G.; Zharnikov, M. *J. Phys. Chem. C* **2009**, *113*, 19609–19614.

56. Diaz-Mochon, J. J.; Tourniaire, G.; Bradley, M. *Chem. Soc. Rev.* **2007**, *36*, 449–457.

57. Lahann, J.; Langer, R. *MRS Bull.* **2005**, *30*, 185–188.

58. Kingshott, P.; Griesser, H. J. *Curr. Opin. Solid State Mater. Sci.* **1999**, *4*, 403–412.

59. Chen, C. S.; Jang, X.; Whitesides, G. M. *MRS Bull.* **2005**, *30*, 194–201.

60. Bretagnol, F.; Valsesia, A.; Ceccone, G.; Colpo, P.; Gilland, D.; Ceriotti, L.; Hasiwa, M.; Rossi, F. *Plasma Proc. Polym.* **2006**, *3*, 443–455.

61. Sardella, E.; Favia, P.; Gristina, R.; Nardulli, R.; D'Agostino, R. *Plasma Processes Polym.* **2006**, *3*, 456–459.

In Proteins at Interfaces III State of the Art 2012; Horbett, T., et al.;
ACS Symposium Series; American Chemical Society: Washington, DC, 2012.

62. Dewez, J. L.; Doren, A.; Schneider, Y.; Rouxhet, P. G. *Biomaterials* **1999**, *20*, 547–559.
63. Morra, M. *Biomacromolecules* **2005**, *6*, 1205–1223.
64. Pickard, C. M. In *Ubiquitin and biology of the cell*; Peters, J. M., Harris, J. R., Finley, D., Eds.; Kleuwer Academic Press: New York, 1998.
65. Hale, P.; Turgeon, S.; Horny, P.; Lewis, F.; Brack, N.; Van Riessen, G.; Pigram, P.; Mantovani, D. *Langmuir* **2008**, *24*, 7897–7905.
66. Chevallier, P.; Holvoet, S.; Turgeon, S.; Horny, P.; Pireaux, J. J.; Mantovani, D. *J. Appl. Polym. Sci.* **2010**, *118*, 3176–3186.
67. Kappen, P.; Hale, P. S.; Brack, N.; Prissanaroon, W.; Pigram, P. J. *Appl. Surf. Sci.* **2006**, *253*, 1473–1479.

Chapter 35

Characterizing the Structure of Surface-Immobilized Proteins: A Surface Analysis Approach

Joe E. Baio,[1,2] Tobias Weidner,[1,2] and David G. Castner*,[1]

[1]National ESCA and Surface Analysis Center for Biomedical Problems (NESAC/BIO), Departments of Bioengineering and Chemical Engineering, University of Washington, Seattle, Washington, U.S.A.
[2]Max Planck Institute for Polymer Research, Mainz, Germany
***E-mail: castner@uw.edu**

There are many techniques that allow surface scientists to study interfaces. However, few are routinely applied to probe biological surfaces. The work presented here demonstrates how detailed information about the conformation, orientation, chemical state, and molecular structure of biological molecules immobilized onto a surface can be assessed by electron spectroscopy, mass spectrometry, and nonlinear vibrational spectroscopy techniques. This investigation began with the development of simple model systems (small proteins, and peptides) and has evolved into a study of more complex – real world systems. Two model systems based on the chemical and electrostatic immobilization of a small rigid protein (Protein G B1 domain, 6kDa) were built to develop the capabilities of time-of-flight secondary ion mass spectrometry (ToF-SIMS), near edge X-ray absorption fine structure spectroscopy (NEXAFS) and sum frequency generation (SFG) spectroscopy as tools to probe the structure of surface immobilized proteins. ToF-SIMS sampled the amino acid composition of the exposed surface of the protein film. Within the ToF-SIMS spectra, an enrichment of secondary ions from amino acids

In Proteins at Interfaces III State of the Art 2012; Horbett, T., et al.;
ACS Symposium Series; American Chemical Society: Washington, DC, 2012.

located at opposite ends of the proteins were used to describe protein orientation. SFG spectral peaks characteristic of ordered α-helix and β-sheet elements were observed for both systems and the phase of the peaks indicated a predominantly upright orientation for both the covalent and electrostatic configurations. Polarization dependence of the NEXAFS signal from the N 1s to π* transition of the peptide bonds that make up the β-sheets also indicated protein ordering at the surface.

Introduction

Wolfgang Pauli once lamented that "God made the bulk; the surface was invented by the devil." His frustration, implied by this famous quote, stems from the inherent difficulties associated with characterizing and explaining the heterogeneous nature of surfaces. Since Pauli's time, surface scientists, in their quest for novel explanations of surface phenomena have made some headway (*1*). This progress has been made in part due to the development of a range of techniques that involve bombarding the surface with photons, electrons or ions (*2*). Yet, most of these techniques have been developed to look at simple systems – single, small molecules interacting with a model surface. For example, fifty years after Pauli's death, surface scientists are still trying to characterize the structure of a single water molecule interacting with a Pt 111 surface (*3*). In comparison to these non-organic systems - biological molecules are orders of magnitude more complex. Protein–surface mediated phenomena are directly influenced by the conformation, orientation, activity, organization and surface concentrations of the adsorbed proteins (*4*). Then combine this with the fact that most traditional surface analysis tools perform only under ultra high vacuum conditions (*2*) and accurately characterizing the structure of a surface bound biomolecule quickly becomes a Herculean affair.

Proteins at a surface or interface mediate most biological interactions. The capsulation of an implanted surface, affinity chromatography of a protein, cellular signaling or the analyte capture performance of a biological sensor - are all influenced by the structure of proteins at a surface (*4*–*7*). Yet, of the 70,000+ protein structures solved and uploaded to the protein database, not a single one describes the structure of the protein at a surface (*8*). This despite research that has demonstrated that the structure of a protein changes when it comes in contact with a surface (*9*–*11*). Therefore, do these reported crystal structures accurately define the structure of the protein at the surface? For example, hydrophobic effects between the protein and a substrate may drive the protein to expose hydrophobic domains– inducing conformational changes (*12*, *13*). Typically, changes in conformation are then probed by assessing the activity of the surface, where a qualitative view of protein orientation and conformation can be provided by some sort of binding assay. Observed changes in binding are then assumed to be a direct result of orientation or the exposure of different domains within the protein (*9*, *11*, *14*, *15*). Yet, a detailed, atomic-level picture of protein orientation or structural changes induced by the surface still does not exist.

In response to this explosion of interest centered around the construction of biological based immunosensors, chemists have proposed a range of possible protein immobilization schemes based on coordination complexes (*16–19*), ligand-reception (*20*), covalent conjugation (*19*, *21–26*), hydrophobic/hydrophilic driving forces (*27–29*) and electrostatic interactions (*30–32*). The ability of these biological devices to bind specific targets is directly related to the accessibility of capture groups at the sensor surface (*14*). For devices based on proteins and antibodies, these immobilization schemes must preserve the conformation of the protein and successfully orient binding sites so that they are accessible. To avoid a trial and error approach, and truly the design these devices at the molecular level, high-resolution techniques are needed to assess the structure, the activity and the orientation of these proteins.

While methods like x-ray diffraction (XRD) and nuclear magnetic resonance (NMR) do provide angstrom level resolution of atomic positions of proteins in crystals or solutions (*33*, *34*) – they do not provide the sensitivity required to characterize the structure of monolayer or sub-monolayer concentrations of proteins interacting with a surface. As a result, a single technique that provides a high-resolution picture of complex organic molecules at a surface, is still elusive. Currently, biological assays like ELISA provide qualitative insights into changes in activity of surface bound proteins (*35*). Scanning probe techniques can provide images and force curves of proteins unfolding at a surface (*36*). Optical techniques like surface plasmon resonance (SPR) can monitor changes at a surface by providing quantitative measures of kinetics (*37*, *38*). Yet, even together, these techniques all fail to fully bridge the current gap between characterizing simple molecules on non-organic surfaces to providing structural details of proteins at a complex biointerface.

The overarching goal of the work presented here - is the development of a suite of high-resolution surface analytical techniques to fully explore the structure, orientation and ordering of proteins at an interface. The hope is that the complementary techniques developed here will provide molecular information that can then be applied to the design and characterization of biomaterial surfaces. The strategy we have adopted is to began with the development of some simple model systems (small proteins and peptides), use these systems to test our surface analytical methods, and then evolve into a study of some more complex, real world systems.

The Protein G B1 Model System

This initial work involved inducing the B1 domain of Protein G into two different orientations by creating two versions of the protein by site directed mutagenesis (*39*). This small barrel shaped protein is 3nm in height and contains just a single alpha helix and four anti-parallel beta-sheets. To immobilize this B1 domain, we took advantage of the large body of work in the literature, where researchers have reported reproducible multiplexed biomolecular surfaces by attaching proteins and DNA (*40*, *41*) via bioactive ligands (*16–18*, *20*, *22–25*, *42*, *43*), Originally, a single cysteine was introduced onto the exposed loop at either end of the protein (V21C and T11C) (*39*). This cysteine presented a thiol group which drove binding to a maleimide-oligo(ethylene glycol)-functionalized (MEG) substrate (Figure 1). On both of these substrates we expected that the two variants of this protein should induce itself into two different end-on orientations.

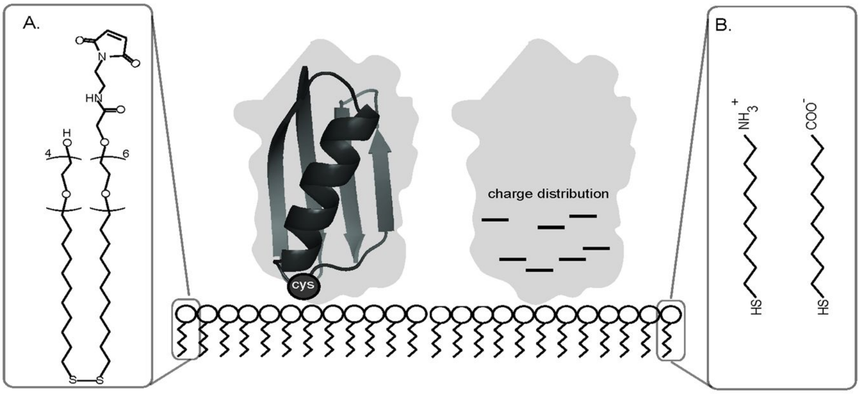

Figure 1. Protein G B1 immobilization schemes: ***A****. Protein G B1 variants, V21C and T11C, with cysteines introduced at opposite ends of the protein, were immobilized via the cysteine thiol onto maleimide-oligo(ethylene glycol)-functionalized gold.* ***B****. The charge variant of Protein G B1, D4', was immobilized via electrostatic interactions onto amine and carboxyl functionalized gold.*

We then characterized these different systems with a suite of surface analysis tools. We set out to probe ordering of secondary structures within these protein films by Sum Frequency Generation spectroscopy (SFG); determine the geometry of specific bonds within these surface bound proteins with Near Edge X-ray Adsorption Fine Structure (NEXAFS) spectroscopy; and asses the orientation induced by these conjugation schemes with Time-of-Flight Secondary Ion Mass Spectrometry (ToF-SIMS).

Characterizing Ordering of Secondary Structure

Just like other vibrational spectroscopic techniques N-C=O, N-H, C-H, and O-H vibrational modes observed within SFG spectra are all used to identify secondary structures (ie. α-helices, β-sheets and β-turns) and amino acid side chains. However, the SFG selection rules dictate that these N-C=O, N-H, C-H, and O-H vibrational modes will only start to appear if secondary structures, amino acid side chains, or water are ordered at the interface (*44–47*). During an SFG experiment, one incident photon source is kept at a fixed frequency within the visible range, while the other is a tunable or broad-band IR source. When the sum of the frequencies of the incident photons is equal to a frequency of the resonance modes of the specimen, a non-linear susceptibility term, $X^{(2)}$, exhibits a sudden change in magnitude (*48*). The square of the magnitude of $X^{(2)}$ is proportional to the intensity of the reflected summed beam. No change in the SFG response will be observed in a medium with inversion symmetry ($X^{(2)}=0$) (*48*), but inversion symmetry is always broken at interfaces. As a result of these selection rules, we expect that any signal observed in the amide I stretching region will only originate from ordered secondary structures within this surface immobilized protein.

This B1 domain contains just a single alpha helix and four anti-parallel beta-sheets and within the amide I SFG spectra (Figure 2A), collected from the two cysteine mutants bound to the maleimide functionalized Au, we observe three peaks at 1626, 1645 and 1675cm^{-1} (*39*). The peak near 1645 cm^{-1} is characteristic of ordered alpha helices while the two peaks at 1626 and 1675 cm^{-1} originate from beta-sheets. However, in contrast, the spectrum collected from a protein film made up of the wild-type version of the protein does not contain these spectral features (Figure 2A). Thereby implying that without the thiol group, inserted by the cysteine mutation, this protein adsorbs onto the maleimide with a random distribution of orientations (*39*).

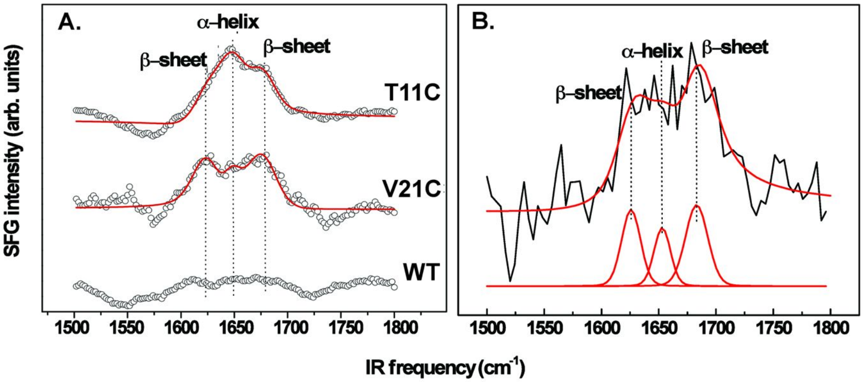

*Figure 2. **A**. SFG amide I spectra of Protein G B1 wild type and cysteine mutants (V21C and T11C) on maleimide-oligo(ethylene glycol)- functionalized gold (39). **B.** SFG amide I spectra of a monolayer of D4' Protein G B1 on amine functionalized gold (51). The amide I peak near 1645 cm^{-1} is characteristic of ordered α-helices, while those near 1630 and 1680 cm^{-1} are characteristic of ordered β-sheet structures. These features are absent from data taken from a monolayer of wild-type protein on the same substrate.*

The phase of these peaks, with respect to the Au nonresonant background, can also shed some light on the overall orientation of these secondary structures. Previous work examining a helical peptide adsorbed onto functionalized Au demonstrate that when the spectral feature at 1645 cm^{-1} is out of phase with the nonresonant Au background (peak amplitude is negative) the peptide backbone is oriented parallel to the substrate (*49*). The phase of the peaks found in Figure 2A are in phase with the nonresonant background (positive amplitude) therefore we can conclude that that helix within the B1 domain is pointing in an orthogonal direction to the surface. Based on the location of the cysteine mutation we expect that the helix orientation should be more upright for the T11C compared to the V21C system, which is consistent with the SFG spectra (Figure 2A) that show a more prominent amide resonance at 1645 cm^{-1}. This qualitative view of orientation can be expanded to include a more quantitative analysis by comparing spectra across different polarization combinations (i.e., ppp versus ssp) (*50–52*). For example, Nguyen *et. al.*, probing the orientation of a α-helix inserted within a membrane, demonstrated that changes in tilt angle across the long axis of the helix can be directly calculated from the dichroism of the signal strength between the ppp and ssp spectra (*50*).

NEXAFS, as a technique, can offer detailed information about the bonding environment of molecules at a surface and provide additional information about the orientation and order of bonds within a protein film (*19*, *39*, *51*). During a NEXAFS experiment, polarized synchrotron x-rays are absorbed by electrons at the core levels exciting photoelectrons. The resulting holes at the core levels are filled by an electron at a higher energy level, which induces the emission of either an Auger electron or a photon. As these electrons travel to the surface they typically encounter an inelastic scattering processes. Therefore, detection of partial electron yield is dictated by the electron scattering cross section and for organic thin films is typically ~10nm (*52*).

The orientation and tilt angles of ordered molecular bonds can be determined by simply following the change in the x-ray absorption as the incident angle of the electric field vector of the x-rays is varied. Based on this polarization dependence, groups have used NEXAFS to determine tilt angles of specific bonds within DNA oligomers, model peptides and proteins immobilized to a surface (*16*, *17*, *19*, *24*, *25*, *39*, *43*, *51*, *53*).

To complement the SFG characterization, ordering of the two immobilized Protein G variants were also described by the polarization dependence of the π* feature, within the carbon and nitrogen K-edges (Figure 3). Partial electron yield NEXAFS N K-edge spectra collected from the two Protein G variants can be found in Figure 3 (*39*). Assuming a well ordered protein film - any observable polarization dependence of the π* feature, at 400.6 eV, can be related to the ordering of the amide bonds within the protein backbone. Tilt angles of the π* molecular orbitals were then calculated from the magnitude of this polarization dependence. The estimated tilt angles of inner β-strands were 40-50° for both variants - one variant is more tilted than the other. If we assume that both the helix and the β-sheets point in the same direction, then these tilt angles of the β-strands are consistent with the SFG results which demonstrate that the helix is also pointing upright, with respect to the substrate (*39*).

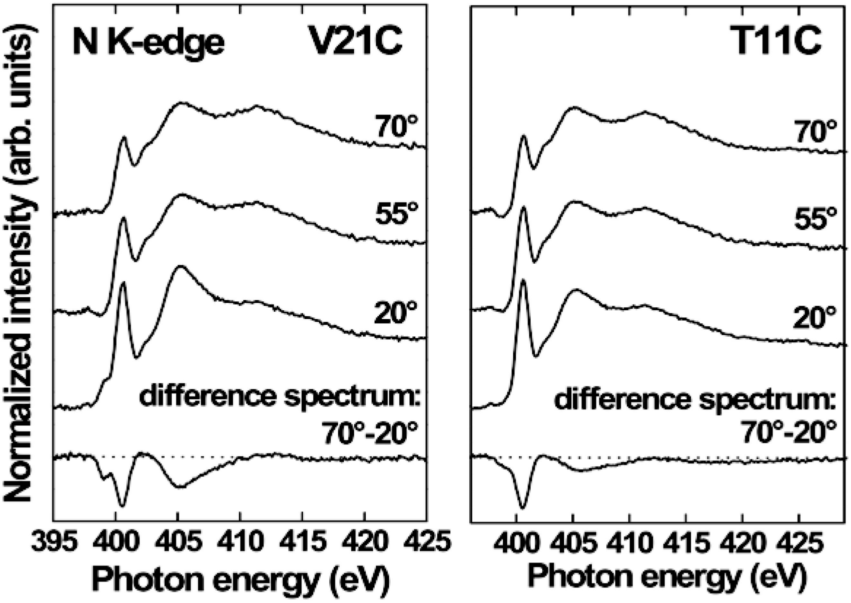

Figure 3. Partial electron yield NEXAFS spectra of the nitrogen K-edge for the two cysteine variants (V21C and T11C) immobilized onto maleimide-oligo(ethylene glycol)-functionalized gold, acquired at angles of 20° and 70°, along with the difference between 70°, 55° and 20° spectra. The prominent dichroism observed at 400.6 eV in the difference spectra (70°-20°) is attributed to peptide bonds of the four anti-parallel β-sheets. Reproduced with permission from ref. (39). Copyright 2010 American Chemical Society.

Characterizing Protein Orientation

Following the protein adsorption step any changes in overall end-on orientation, induced by our immobilization schemes, were characterized by ToF-SIMS. ToF-SIMS involves bombarding a surface with a pulsed primary ion beam that sputters molecular fragments. The primary ion hits the surface inciting a collision cascade and within this energized region many processes are occurring, including post emission ionization, recombination, etc (*54*). The small fraction of these fragments (<1%) that are ionized – the secondary ions – are then extracted into a time-of-flight mass analyzer. Both positive and negative secondary ions can be collected and the result is a comprehensive mass analysis of all secondary ions ejected from the surface (*54*).

The mechanics of how secondary ions originate within the collision cascade is complicated, dependent on the type and size of primary ion, the material of interest and the substrate that material is resting in or on (so called matrix effects) (*55*). In metals, secondary ion formation is strongly influenced by an electron transfer process, which is illustrated by the large variance in elemental secondary ions across the periodic table and oxidation state (*2*). For organics the possible mechanisms leading to the formation of secondary ions are even more complex. Ejected ions can reform into new molecular fragments, undergo acid base reactions, or a complex mix of cationization/anionization processes (*2*, *54*).

One method of extracting useful information out of the hundreds of peaks in a typical spectrum is multivariate methods like principle component analysis (PCA). Details of the mathematics behind PCA can be found else where (*56*), but the basic idea is that PCA can quickly identify the sources of variance between two sets of spectra. Two recent reviews highlight how PCA can be used to analyze ToF-SIMS data taken from biological samples (*57*, *58*).

Within SIMS data collected from protein films we rarely see ions that represent whole amino acids or groups of amino acids. As a result, the composition of the surface must be reconstructed from low mass fragment products. Thankfully, the structure of these low mass fragments is directly related to the amino acid's side chain chemistry and all of the ToF-SIMS data analysis presented here is based on tables of spectral fingerprints. Fingerprints were distilled from spectra collected from films of homo-peptides (*59*).

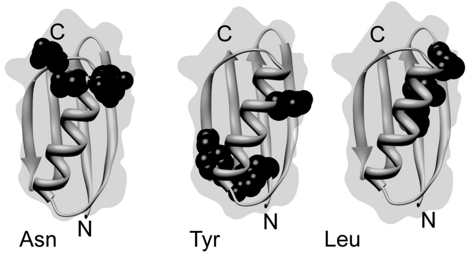

AA	Mass (*m/z*)	Secondary ion
Asn	70	C_3H_4NO+
Asn	87	$C_3H_7N_2O+$
Asn	98	$C_4H_4NO_2+$
Leu	86	$C_5H_{12}N+$
Tyr	107	C_7H_7O+
Tyr	136	$C_8H_{10}NO+$

Figure 4. Amino acids with asymmetric distributions used in ToF- SIMS analysis (shown in black). Table inset - secondary ion fragments used in ToF-SIMS analysis.

Despite the complexities, ToF-SIMS offers both high chemical specificity (mass resolution of ~5000 *m/Δm* and higher) and extreme surface sensitivity (sampling depths typically 1-3 nm) (*2*, *54*, *60*) thereby, allowing subtle changes in protein conformation and orientation to be observed. For example, changes in the intensities of secondary ions emitted from hydrophobic and hydrophilic amino acids can be related to the unfolding of a protein. As the conformation of a protein changes (e.g., unfolding as it denatures), different amino acid side chains are brought into the ToF-SIMS sampling region (*61*, *62*).

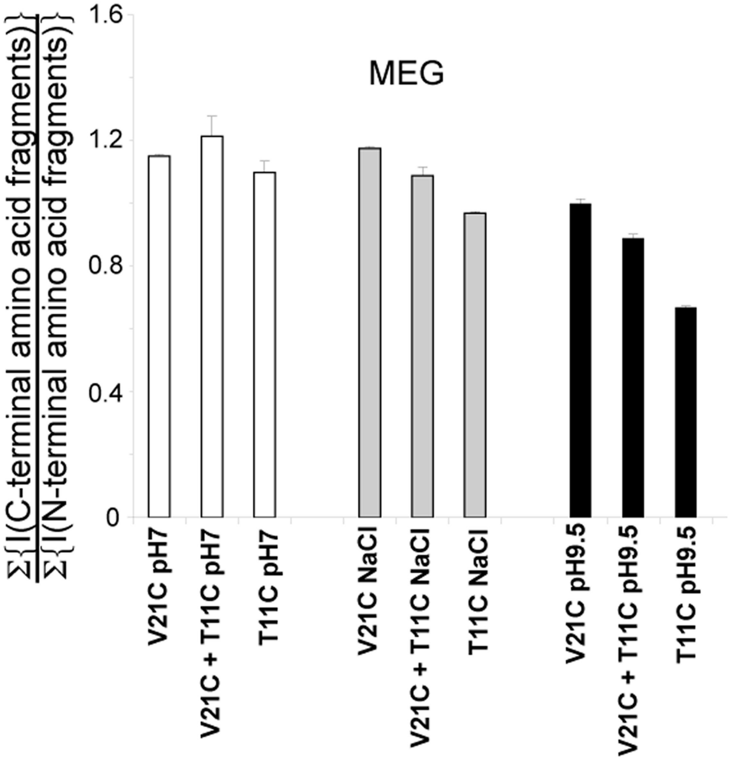

*Figure 5. ToF-SIMS peak ratios calculated as the sum of intensities of C-terminal peaks – 70, 87 and 98 from asparagine and 86 from leucine/isoleucine – divided by the sum of intensities of N-terminal peaks – 107 and 136 from tyrosine. Moving from left to right graphs represent films immobilized with the following buffer conditions: at pH 7 with 0 M NaCl (**pH7**), at pH 7 with 1.5 M NaCl (**NaCl**), and at pH 9.5 with 0 M NaCl (**pH9.5**). The trend, V21C > equimolar mixture ("V + T") > T11C, is expected for end-on orientations of the two mutants. Reproduced with permission from ref. (39). Copyright 2010 American Chemical Society.*

Similarly, if amino acids are asymmetrically distributed about the protein – intensities of secondary ions originating from these amino acids can be directly related to conformation and orientation (*32*, *63–65*). The B1 domain of Protein G has an asymmetric distribution of amino acids. The N-terminus is rich in tyrosine while at the opposite end of the protein, the C-terminus, is rich in leucine and asparagine (Figure 4). ToF-SIMS data from the T11C and V21C variants showed an enrichment of secondary ions originating from asymmetric amino acids (Asparagine: 70, 87, and 98 m/z; Leucine: 86 m/z; Tyrosine: 107 and 136 m/z) concentrated in the opposite end of the protein from the cysteine (Figure

4). For a semi-quantitative assessment of orientation, we created a ratio relating the intensities of these secondary-ions originating from either end of the protein (Figure 5) (*26*, *39*). Observed changes in this ratio, for the two variants on both substrates, indicate two distinct end-on orientations. This was in spite of the fact that the thickness of this protein layer is similar to the SIMS sampling depth. These intensity ratios were also compared with 50:50 mixtures of the variants and with nonspecifically immobilized proteins in random orientations. Additionally, we explored a range of conjugation protocols and found that for immobilization onto the MEG substrates, orientation was enhanced by increasing both the pH (7.0 to 9.5) and salt concentration (0 to 1.5 M NaCl) of the protein-buffer solution (Figure 5) (*39*). These ratios illustrate a transition from a randomly oriented protein film at a neutral pH (Figure 5; pH 7) to an oriented film as we increase the salt concentration to 1.5M NaCl (Figure 5; NaCl). The addition of the NaCl at pH 7 may inhibit the charge-charge interactions of adjacent proteins, thereby, improving the packing and orientation of the film.

Electrostatic Conjugation

This initial Protein G B1 model system, based on the cysteine-maleimide bond, helped us develop and highlight the capabilities of ToF-SIMS, NEXAFS spectroscopy and SFG as tools to probe the structure of surface immobilized proteins. Information about the orientation was provided by the intensities of secondary-ions originating from amino acids asymmetrically distributed within the protein's three-dimensional structure. NEXAFS and SFG experiments illustrated how we can define the geometry of molecular bonds, thus, complementing the ToF-SIMS characterization of overall protein orientation. So with this newly constructed toolbox in hand – we expanded this work to include proteins induced into different orientations by pairing electrostatic dipoles within the protein to charged substrates (Figure 1B). This expansion was focused around the same Protein G B1 domain, but instead of inserting cysteines, a charge distribution was created within the protein. Negatively charged amino acids are uniformly distributed throughout wild-type Protein G B1, so at one end of the protein a neutral region was created by replacing negatively charged amino acids with neutral residues (Figure 1B). This mutant (D4′) was then immobilized onto two oppositely charged substrates (COO^- and NH_3^+ functionalized gold) (*51*).

Within the amide I SFG spectra, acquired for the D4′ variant immobilized onto a NH_3^+ functionalized surface, are spectral features related to ordered α-helicies (1645 cm^{-1}) and β-sheets (1630 and 1680 cm^{-1}) within the amide I SFG spectrum (Figure 2b) (*51*). This implies that the electrostatic interaction between the protein and the surface drives the protein into an ordered monolayer. This also corresponded to the observed polarization dependence of the N_{1s} to π^* transition, within the N K-edge NEXAFS spectra, related to the β-sheet peptide bonds present within the protein film. Finally, ToF-SIMS data, taken from the D4′ adsorbed onto COO^- and NH_3^+ functionalized gold demonstrated a well-defined separation between the two samples. The observed two-fold increase in the ratio of secondary-ion intensities originating from opposite ends of the protein indicates opposite orientations of the Protein G B1 fragment on the two different surfaces (see Figure 6) (*51*). Again, a charge distribution was created at opposite ends of the protein by substituting specific negatively charged amino acids with neutral residues. As a result, asparagine was no longer asymmetrically distributed within the protein and peaks originating from asparagine were not included in the calculation ratio of secondary-ion intensities.

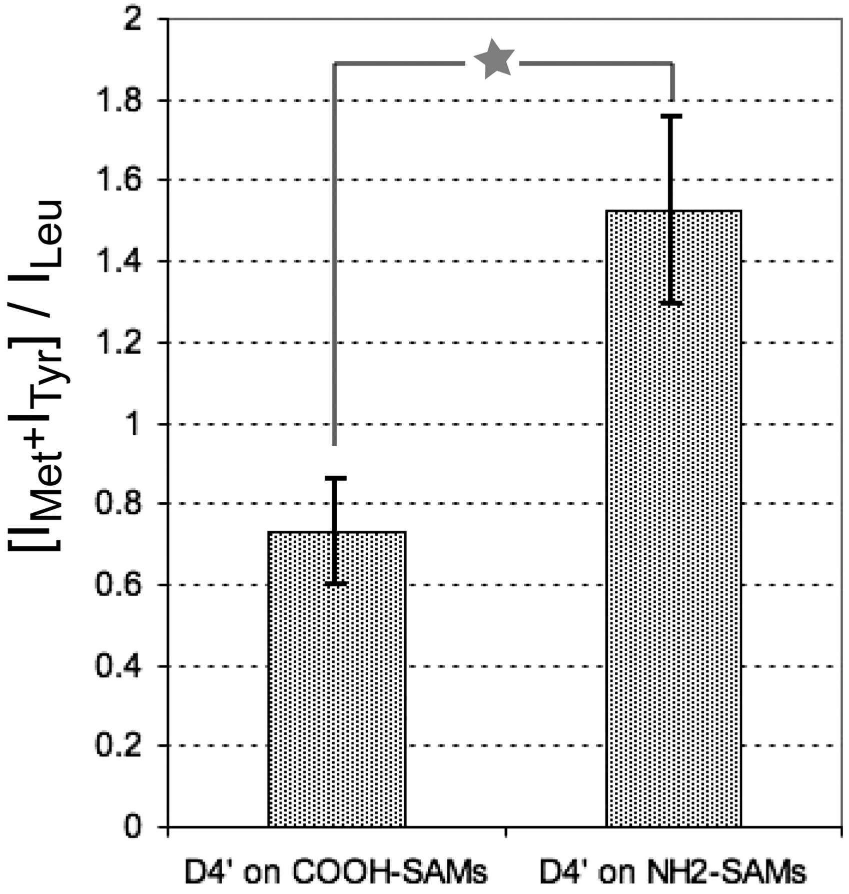

Figure 6. ToF-SIMS peak ratios calculated as the sum of intensities of secondary ions from methionine (62 and 105 m/z) and tyrosine (107 and 136 m/z) divided by the sum of intensities of secondary ions from the leucine/isoleucine residues (86 m/z). Error bars represent the standard deviation across fifteen analysis spots over three distinct samples. Reproduced with permission from ref. (51). Copyright 2012 American Chemical Society.

Future Approaches: Amino Acid Labeling Strategies

Information about the end-on orientation and secondary structure of proteins immobilized onto surfaces is, as discussed above, useful for a number of practical bioengineering problems. However, important phenomena regarding the molecular mechanisms of protein–surface interactions and the structure of surface proteins can only be understood in detail by probing individual side chains with Ångstrom resolution. We have shown that isotope labels at specific protein sites in combination with SFG spectroscopy is a promising route towards high-resolution protein structures on surfaces (*66*, *68*). Deuteration of C–H bonds leads to a red shift of nearly 800 cm^{-1} of that particular resonance. Therefore one can measure SFG spectra of the deuterium labeled amino acid without spectral confusion with C-H containing side chains. Established procedures for SFG orientation analysis of aromatic and aliphatic groups can then be applied to probe the side chain orientation. In an earlier study, we have determined the orientations of the entire set binding side chains of an amphiphilic model peptide containing lysine and leucine side chains on a polystyrene surface in situ (*66*). We also determined the orientation of individual phenylalanine side chains in the binding domain of statherin on its native mineral hydroxyapatite (*53*). Both studies allowed the determination of both tilt and torsion angles for the respective side chains.

One challenge in the context of single amino acid detection is the extremely low surface density of labeled species. The surface area of a small 15 amino-acid peptide is on the order of 400 $Å^2$. This means a single side chain has an approximately 15-20 times lower surface density than terminal groups in typical self-assembled monolayers with a footprint of around 20-27 $Å^2$ per molecule. For larger proteins the surface density of individual labeled sites quickly drops to a hundredth of a monolayer or less.

To test the feasibility of extending our labeling approach from peptides to proteins, we collected SFG spectra of deuterium labeled tyrosine (Tyr45) and isoleucine (Ile6) sites in the T11C mutant of the B1 domain of protein G (*v.s.*). Again, T11C was immobilized via cysteine onto a MEG self-assembled monolayer (SAM) on gold (Figure 7). T11C covers a surface area of ca. 800 $Å^2$, leading to a surface density of the labeled amino acids of the equivalent of 2-3% of a monolayer. The aliphatic and aromatic groups have spectrally distinct resonance positions, labeling aromatic and aliphatic species in a single protein causes no spectral overlap and two species can be probed in a single experiment.

A C–D stretching range SFG spectrum collected in ppp polarization of the surface bound protein is shown in figure 7. There is a clear signature of both the aromatic tyrosine and the aliphatic isoleucine above and below 2230 cm^{-1}, respectively. Isoleucine resonances are visible near 2150 cm^{-1}, assigned to the methylene Fermi resonance and near 2220 cm^{-1}, assigned to the asymmetric CD_3 stretching mode. From the positive polarity of the peaks we can conclude that the methyl vibrations are in phase with the non-resonant SFG gold background. It has been shown that a constructive interference of methyl resonances with the gold background signal is indicative of isopropyl methyl groups pointing towards the surface (*67*, *68*). From the absence of a symmetric CH_3 mode we can conclude that the average orientation of the methyl units is strongly tilted (*69*). At higher wavenumbers there is a strong mode near 2290 cm^{-1} related to a ν_2 ring mode and two overlapping ring resonances at 2240 cm^{-1} and 2276 cm^{-1} visible in the spectrum which can be assigned to ν_7 and ν_{13} ring vibrations, respectively. This data clearly confirms, that labeling of individual protein sites for surface protein structure analysis is a concept that can be extended to proteins.

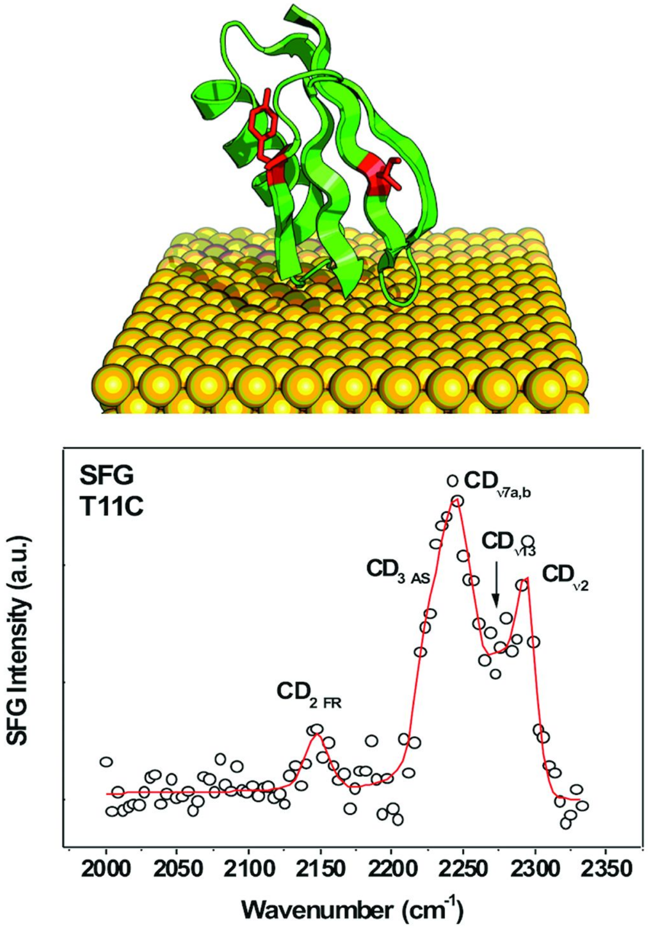

Figure 7. A SFG spectrum of the labeled T11C protein immobilized onto maleimide-oligo(ethylene glycol)-functionalized gold acquired at ppp polarization. Signature peaks of both the aromatic tyrosine and the aliphatic isoleucine above and below 2230 cm^{-1}, respectively. Isoleucine resonances are visible near 2150 cm^{-1}, assigned to the methylene Fermi resonance and near 2220 cm^{-1}, assigned to the asymmetric CD_3 stretching mode.

Summary

One major hurdle in the design of biomaterial interfaces it the accurate characterization of the protein – surface interactions. Here we have applied three techniques to probe and describe the orientation, chemical state, and molecular structure of proteins immobilized onto a surface. We believe that this set of tools has now reached a state of development where ToF-SIMS, NEXAFS, and SFG can be routinely applied to the characterization of protein films. The models systems described here provided straightforward examples of how overall protein orientation is characterized by ToF-SIMS and a molecular level picture of bond orientation is provided by NEXAFS and SFG experiments.

Acknowledgments

The authors acknowledge support from NIH grants EB-2027 (NESAC/BIO), GM-074511 and DE-012554 during preparation of this manuscript as well as for some of the results reported in it. J.E.B. and T.W are grateful to the Max Planck Society for financial support of this work.

References

1. Somorjai, G. *Chemistry In Two Dimensions: Surfaces*; Cornell University Press: Ithaca, New York, 1981.
2. Vickerman, J.; Gilmore, I. *Surface Analysis: The Principal Techniques*, 2nd ed.; John Wiley and Sons: West Sussex, U.K., 2009.
3. Arnadottir, L.; Stuve, E. M.; Jonsson, H. Adsorption of water monomer and clusters on platinum(111) terrace and related steps and kinks I. Configurations, energies, and hydrogen bonding. *Surf. Sci.* **2010**, *604* (21-22), 1978–1986.
4. Horbett, T. Proteins: Structure, Properties and Adsoption to Surfaces. In *Biomaterial Science: An Introduction to Materials in Medicine*; Ratner, B., Hoffman, A., Schoen, F., Lemons, J., Eds.; Academic Press: New York, 1996; pp 133−141.
5. Nakanishi, K.; Sakiyama, T.; Imamura, K. On the adsorption of proteins on solid surfaces, a common but very complicated phenomenon. *J. Biosci. Bioeng.* **2001**, *91* (3), 233–244.
6. Hynes, R. Molecular-Biology of Fibronectin. *Annu. Rev. Cell Biol.* **1985**, *1*, 67–90.
7. Hynes, R. O.; Yamada, K. M. Fibronectins - Multifunctional Modular Glycoproteins. *J. Cell Biol.* **1982**, *95* (2), 369–377.
8. RCSB Protein Data Bank. 2011.
9. Butler, J. E.; Ni, L.; Nessler, R.; Joshi, K. S.; Suter, M.; Rosenberg, B.; Chang, J.; Brown, W. R.; Cantarero, L. A. The Physical And Functional-Behavior Of Capture Antibodies Adsorbed On Polystyrene. *J. Immunol. Methods* **1992**, *150* (1-2), 77–90.

10. Plant, A. L.; Locasciobrown, L.; Haller, W.; Durst, R. A. Immobilization Of Binding-Proteins On Nonporous Supports - Comparison Of Protein Loading, Activity, And Stability. *Appl. Biochem. Biotechnol.* **1991**, *30* (1), 83–98.
11. Baugh, L.; Vogel, V. Structural changes of fibronectin adsorbed to model surfaces probed by fluorescence resonance energy transfer. *J. Biomed. Mater. Res., Part A* **2004**, *69A* (3), 525–534.
12. Haynes, C. A.; Sliwinsky, E.; Norde, W. Structural And Electrostatic Properties Of Globular-Proteins At A Polystyrene Water Interface. *J. Colloid Interface Sci.* **1994**, *164* (2), 394–409.
13. Phillips, D. C.; York, R. L.; Mermut, O.; McCrea, K. R.; Ward, R. S.; Somorjai, G. A. Side chain, chain length, and sequence effects on amphiphilic peptide adsorption at hydrophobic and hydrophilic surfaces studied by sum-frequency generation vibrational spectroscopy and quartz crystal microbalance. *J. Phys. Chem. C* **2007**, *111* (1), 255–261.
14. Tajima, N.; Takai, M.; Ishihara, K. Significance of Antibody Orientation Unraveled: Well-Oriented Antibodies Recorded High Binding Affinity. *Anal. Chem.* **2011**, *83* (6), 1969–1976.
15. Michael, K. E.; Vernekar, V. N.; Keselowsky, B. G.; Meredith, J. C.; Latour, R. A.; Garcia, A. J. Adsorption-induced conformational changes in fibronectin due to interactions with well-defined surface chemistries. *Langmuir* **2003**, *19* (19), 8033–8040.
16. Cheng, F.; Gamble, L. J.; Castner, D. G. XPS, TOF-SIMS, NEXAFS, and SPR characterization of nitrilotriacetic acid-terminated self-assembled monolayers for controllable immobilization of proteins. *Anal. Chem.* **2008**, *80* (7), 2564–2573.
17. Huang, Z. H.; Park, J. I.; Watson, D. S.; Hwang, P.; Szoka, F. C. Facile synthesis of multivalent nitrilotriacetic acid (NTA) and NTA conjugates for analytical and drug delivery applications. *Bioconjugate Chem.* **2006**, *17* (6), 1592–1600.
18. Wegner, G. J.; Lee, N. J.; Marriott, G.; Corn, R. M. Fabrication of histidine-tagged fusion protein arrays for surface plasmon resonance imaging studies of protein-protein and protein-DNA interactions. *Anal. Chem.* **2003**, *75* (18), 4740–4746.
19. Baio, J.; Cheng, F.; Ratner, D.; Stayton, P.; Castner, D. Probing orientation of immobilized humanized anti-lysozyme variable fragment by time-of-flight secondary-ion mass spectrometry. *J. Biomed. Mater. Res., Part A* **2011**, *97A* (1), 1–7.
20. Jung, L. S.; Nelson, K. E.; Stayton, P. S.; Campbell, C. T. Binding and dissociation kinetics of wild-type and mutant streptavidins on mixed biotin-containing alkylthiolate monolayers. *Langmuir* **2000**, *16* (24), 9421–9432.
21. Xia, N.; Hu, Y.; Grainger, D. W.; Castner, D. G. Functionalized Poly(ethylene glycol)-Grafted Polysiloxane Monolayers for Control of Protein Binding. *Langmuir* **2002**, *18* (8), 3255–3262.
22. Cheng, F.; Gamble, L. J.; Grainger, D. W.; Castner, D. G. X-ray Photoelectron Spectroscopy, Time-of-flight Secondary Ion Mass Spectrometry and Principal Component Analysis of the Hydrolysis,

Regeneration and Reactivity of NHS-containing Organic Thin Films. *Anal. Chem.* **2007**, *79*, 8781–8788.

23. Huang, W.; Wang, J. Q.; Bhattacharyya, D.; Bachas, L. G. Improving the activity of immobilized subtilisin by site-specific attachment to surfaces. *Anal. Chem.* **1997**, *69* (22), 4601–4607.
24. Lee, C. Y.; Gamble, L. J.; Grainger, D. W.; Castner, D. G. Mixed DNA/oligo (ethylene glycol) functionalized gold surfaces improve DNA hybridization in complex media. *Biointerphases* **2006**, *1* (2), 82–92.
25. Lee, C. Y.; Gong, P.; Harbers, G. M.; Grainger, D. W.; Castner, D. G.; Gamble, L. J. Surface coverage and structure of mixed DNA/alkylthiol monolayers on gold: Characterization by XPS, NEXAFS, and fluorescence intensity measurements. *Anal. Chem.* **2006**, *78* (10), 3316–3325.
26. Baio, J. E.; Weidner, T.; Samuel, N. T.; McCrea, K.; Baugh, L.; Stayton, P. S.; Castner, D. G. Multi-technique Characterization of Adsorbed Peptide and Protein Orientation: LK310 and Protein G B1. *J. Vac. Sci. Technol., B* **2010**, *28* (4), C5D1–C5D8.
27. Bos, M. A.; Kleijn, J. M. Determination of the Orientation Distribution of Adsorbed Fluorophores Using TIRF. 2. Measurements On Porphyrin And Cytochrome-c. *Biophys. J.* **1995**, *68* (6), 2573–2579.
28. Fraaije, J.; Kleijn, J. M.; Vandergraaf, M.; Dijt, J. C. Orientation of Adsorbed Cytochrome-c as a Function of the Electrical Potential of the Interface Studied by Total Internal-Reflection Fluorescence. *Biophys. J.* **1990**, *57* (5), 965–975.
29. Lee, J. E.; Saavedra, S. S. Molecular orientation in heme protein films adsorbed to hydrophilic and hydrophobic glass surfaces. *Langmuir* **1996**, *12* (16), 4025–4032.
30. Chen, S. F.; Liu, L. Y.; Zhou, J.; Jiang, S. Y. Controlling antibody orientation on charged self-assembled monolayers. *Langmuir* **2003**, *19* (7), 2859–2864.
31. Chi, Q. J.; Zhang, J. D.; Andersen, J. E. T.; Ulstrup, J. Ordered assembly and controlled electron transfer of the blue copper protein azurin at gold (111) single-crystal substrates. *J. Phys. Chem. B* **2001**, *105* (20), 4669–4679.
32. Wang, H.; Castner, D. G.; Ratner, B. D.; Jiang, S. Y. Probing the orientation of surface-immobilized immunoglobulin G by time-of-flight secondary ion mass spectrometry. *Langmuir* **2004**, *20* (5), 1877–1887.
33. Cavanagh, J. *Protein NMR spectroscopy : principles and practice*; Academic Press: San Diego, 1996.
34. Rupp, B. *Biomolecular crystallography : principles, practice, and application to structural biology*; Garland Science: New York, 2009.
35. Clark, M. ELISA Techniques. In *Plant Molecular Biology*; Weissbach, A., Weissbach, H., Eds.; Academic Press: New York, 1986; pp 742−766.
36. Li, M. Q. Scanning probe microscopy (STM/AFM) and applications in biology. *Appl. Phys. A: Mater. Sci. Process.* **1999**, *68* (2), 255–258.
37. Apte, J.; Gamble, L.; Castner, D.; Campbell, C. Kinetics of leucine-lysine peptide adsorption and desorption at -CH3 and -COOH terminated alkylthiolate monolayers. *Biointerphases* **2010**, *5* (4), 97–104.

38. Green, R. J.; Frazier, R. A.; Shakesheff, K. M.; Davies, M. C.; Roberts, C. J.; Tendler, S. J. B. Surface plasmon resonance analysis of dynamic biological interactions with biomaterials. *Biomaterials* **2000**, *21* (18), 1823–1835.
39. Baugh, L.; Nguyen, P.-C.; Baio, J. E.; Weidner, T.; Gamble, L. J.; Castner, D. G.; Stayton, P. S. Probing the Orientation of Surface-Immobilized Protein G B1 using ToF-SIMS, Sum Frequency Generation, and NEXAFS Spectroscopy. *Langmuir* **2010**, *26* (21), 16434–16441.
40. Seidel, M.; Niessner, R. Automated analytical microarrays: a critical review. *Anal. Bioanal. Chem.* **2008**, *391* (5), 1521–1544.
41. Laurent, N.; Voglmeir, J.; Flitsch, S. L. Glycoarrays - tools for determining protein-carbohydrate interactions and glycoenzyme specificity. *Chem. Commun.* **2008** (37), 4400–4412.
42. Nam, J. M.; Han, S. W.; Lee, K. B.; Liu, X. G.; Ratner, M. A.; Mirkin, C. A. Bioactive protein nanoarrays on nickel oxide surfaces formed by dip-pen nanolithography. *Angew. Chem., Int. Ed.* **2004**, *43* (10), 1246–1249.
43. Nelson, K. E.; Gamble, L.; Jung, L. S.; Boeckl, M. S.; Naeemi, E.; Golledge, S. L.; Sasaki, T.; Castner, D. G.; Campbell, C. T.; Stayton, P. S. Surface characterization of mixed self-assembled monolayers designed for streptavidin immobilization. *Langmuir* **2001**, *17* (9), 2807–2816.
44. Kim, J.; Opdahl, A.; Chou, K. C.; Somorjai, G. A. Hydrophobic-interaction-induced alignment of polymers at the solid/liquid interface studied by infrared-visible sum frequency generation. *Langmuir* **2003**, *19* (23), 9551–9553.
45. Chen, X. Y.; Wang, J.; Sniadecki, J. J.; Even, M. A.; Chen, Z. Probing alpha-helical and beta-sheet structures of peptides at solid/liquid interfaces with SFG. *Langmuir* **2005**, *21* (7), 2662–2664.
46. Chen, X. Y.; Clarke, M. L.; Wang, J.; Chen, Z. Sum frequency generation vibrational spectroscopy studies on molecular conformation and orientation of biological molecules at interfaces. *Int. J. Mod. Phys. B* **2005**, *19*, 691–713.
47. Mermut, O.; Phillips, D. C.; York, R. L.; McCrea, K. R.; Ward, R. S.; Somorjai, G. A. In Situ Adsorption Studies of a 14-Amino Acid Leucine-Lysine Peptide onto Hydrophobic Polystyrene and Hydrophilic Silica Surfaces Using Quartz Crystal Microbalance, Atomic Force Microscopy, and Sum Frequency Generation Vibrational Spectroscopy. *J. Am. Chem. Soc.* **2006**, *128* (11), 3598–3607.
48. Lambert, A. G.; Davies, P. B.; Neivandt, D. J. Implementing the Theory of Sum Frequency Generation Vibrational Spectroscopy: A Tutorial Review. *Appl. Spectrosc. Rev.* **2005**, *40*, 103–145.
49. Weidner, T.; Apte, J. S.; Gamble, L. J.; Castner, D. G. Probing Orientation and Conformation of α-Helix and β-Strand Model Peptides on Self-Assembled Monolayers Using Sum Frequency Generation and NEXAFS Spectroscopies. *Langmuir* **2010**, *26* (5), 3433–3440.
50. Nguyen, K. T.; Soong, R.; Im, S. C.; Waskell, L.; Ramamoorthy, A.; Chen, Z. Probing the Spontaneous Membrane Insertion of a Tail-Anchored Membrane Protein by Sum Frequency Generation Spectroscopy. *J. Am. Chem. Soc.* **2010**, *132* (43), 15112–15115.

51. Baio, J. E.; Weidner, T.; Baugh, L.; Gamble, L. J.; Stayton, P. S.; Castner, D. G. Probing the Orientation of Electrostatically Immobilized Protein G B1 by Time-of-Flight Secondary Ion Spectrometry, Sum Frequency Generation, and Near-Edge X-ray Adsorption Fine Structure Spectroscopy. *Langmuir* **2012**, *28* (4), 2107–2112.
52. Stöhr, J. *NEXAFS Spectroscopy*; Springer-Verlag: Berlin, 1992; Vol. 25.
53. Weidner, T.; Dubey, M.; Breen, N. F.; Ash, J.; Baio, J. E.; Jaye, C.; Fischer, D. A.; Drobny, G. P.; Castner, D. G. Direct Observation of Phenylalanine Orientations in Statherin Bound to Hydroxyapatite Surfaces. *J. Am. Chem. Soc.* **2012**, *134* (21), 8750–8753.
54. Vickerman, J. C.; Brown, A. A.; Reed, N. M. *Secondary ion mass spectrometry: principles and applications*; Oxford University Press: New York, 1989.
55. Garrison, B. J.; Postawa, Z. Computational View of Surface Based Organic Mass Spectrometry. *Mass Spectrom. Rev.* **2008**, *27*, 289–315.
56. Jackson, J. E. Principal Components And Factor-Analysis .1. Principal Components. *J. Qual. Technol.* **1980**, *12* (4), 201–213.
57. Graham, D. J.; Wagner, M. S.; Castner, D. G. Information from complexity: Challenges of TOF-SIMS data interpretation. *Appl. Surf. Sci.* **2006**, *252* (19), 6860–6868.
58. Wagner, M. S.; Graham, D. J.; Ratner, B. D.; Castner, D. G. Maximizing information obtained from secondary ion mass spectra of organic thin films using multivariate analysis. *Surf. Sci.* **2004**, *570* (1-2), 78–97.
59. Mantus, D. S.; Ratner, B. D.; Carlson, B. A.; Moulder, J. F. Static Secondary-Ion Mass-Spectrometry of Adsorbed Proteins. *Anal. Chem.* **1993**, *65* (10), 1431–1438.
60. Wagner, M. S.; Castner, D. G. Analysis of adsorbed proteins by static time-of-flight secondary ion mass spectrometry. *Appl. Surf. Sci.* **2004**, *231*, 366–376.
61. Tidwell, C. D.; Castner, D. G.; Golledge, S. L.; Ratner, B. D.; Meyer, K.; Hagenhoff, B.; Benninghoven, A. Static ToF SIMS and XPS Characterization of Adsorbed Albumin and Fibronectin Films. *Surf. Interface Anal.* **2001**, *31*, 724–733.
62. Xia, N.; May, C. J.; McArthur, S. L.; Castner, D. G. Time-of-flight secondary ion mass spectrometry analysis of conformational changes in adsorbed protein films. *Langmuir* **2002**, *18* (10), 4090–4097.
63. Lhoest, J. B.; Detrait, E.; van den Bosch de Aguilar, P.; Bertrand, P. Fibronectin adsorption, conformation, and orientation on polystyrene substrates studied by radiolabeling, XPS, and ToF SIMS. *J. Biomed. Mater. Res.* **1998**, *41* (1), 95–103.
64. Lhoest, J. B.; Wagner, M. S.; Tidwell, C. D.; Castner, D. G. Characterization of adsorbed protein films by time of flight secondary ion mass spectrometry. *J. Biomed. Mater. Res.* **2001**, *57* (3), 432–440.
65. Apte, J. S.; Collier, G.; Latour, R. A.; Gamble, L. J.; Castner, D. G. XPS and ToF-SIMS Investigation of alpha-Helical and beta-Strand Peptide Adsorption onto SAMs. *Langmuir* **2010**, *26* (5), 3423–3432.
66. Weidner, T.; Breen, N. F.; Li, K.; Drobny, G. P.; Castner, D. G. Sum frequency generation and solid-state NMR study of the structure, orientation,

and dynamics of polystyrene-adsorbed peptides. *Proc. Natl. Acad. Sci. U.S.A.* **2010**, *107* (30), 13288–13293.

67. Ward, R. N.; Davies, P. B.; Bain, C. D. Orientation of Surfactants Adsorbed on a Hydrophobic Surface. *J. Phys. Chem.* **1993**, *97* (28), 7141–7143.
68. Breen, N. F.; Weidner, T.; Li, K.; Castner, D. G.; Drobny, G. P. A Solid-State Deuterium NMR and Sum-Frequency Generation Study on the Side-Chain Dybamics of Peptides Adsorbed onto Surfaces. *J. Am. Chem. Soc.* **2009**, *131* (40), 14148–14149.
69. Nishi, N.; Hobara, D.; Yamamoto, M.; Kakiuchi, T. Chain-length-dependent change in the structure of self-assembled monolayers of n-alkanethiols on Au(111) probed by broad-bandwidth sum frequency generation spectroscopy. *J. Chem. Phys.* **2003**, *118* (4), 1904–1911.

Chapter 36

Protein Patterns Fabricated by Affinity-Based Surface Ligand Selection from Protein Solution Mixtures on a Polymer Hydrogel Substrate

Hironobu Takahashi,[1] David G. Castner,[2] and David W. Grainger*,[3]

[1]Institute of Advanced Biomedical Engineering and Science Tokyo Women's Medical University (TWIns), 8-1 Kawadacho Shinjuku, Tokyo 162-8666, Japan
[2]National ESCA and Surface Analysis Center for Biomedical Problems, Departments of Chemical Engineering and Bioengineering, Box 351750, University of Washington, Seattle, Washington 98195-1750 U.S.A.
[3]Departments of Pharmaceutics and Pharmaceutical Chemistry, and Bioengineering Health Sciences, University of Utah, Salt Lake City, Utah 84112-5820 U.S.A.
***E-mail: david.grainger@utah.edu. Phone: +1 801-585-7824.**
Fax: +1 801-5813674

We review a recent surface patterning, modification and protein-surface affinity selection strategy that yields high-fidelity protein patterns by protein-ligand selection from solutions at surfaces – so-called affinity-based surface "protein sorting". The approach exploits pre-patterned high affinity ligands immobilized on polymer surface chemistry known to effectively inhibit non-specific protein adsorption and cell adhesion, while providing a reliable capacity for specific, dense, uniform immobilization of desired molecules to pre-designed patterns of reactive chemistry. Soluble proteins select ligands at these surfaces from solution by affinity-matched surface engagement, producing two distinct types of protein monolayer organization on surfaces: spatial (e.g., two different proteins selecting their respective ligands in spatial patterns on surfaces) and orientational (e.g., antibody binding to ligands specific to their Fab versus Fc domains). These ligand patterns and surface-protein interactions are analyzed, and spatially and

In Proteins at Interfaces III State of the Art 2012; Horbett, T., et al.;
ACS Symposium Series; American Chemical Society: Washington, DC, 2012.

orientationally verified using time-of-flight secondary ion mass spectrometry (TOF-SIMS). Photolithographic patterning of reactive ester groups on a non-fouling PEG-coated surface facilitate ligand coupling with high fidelity or patterns of peptides, proteins, and mammalian cells. Furthermore, two different surface-patterned affinity ligands, facilitate binding of two different proteins (e.g., streptavidin and HaloTag®), co-patterned self-selectively from their mixed solution on the non-fouling surface. As a unique label-free chemically selective surface imaging technique, TOF-SIMS analysis can distinguish differences in amino acid composition between bound streptavidin and HaloTag® proteins, and also between Fab and Fc domains on surface-immobilized antibodies. Since antibody orientation and spatial patterning remains important to antibody-based surface capture assays, TOF-SIMS imaging is useful to correlate immobilized biomolecule bioactivity. Patterned RGD peptides can also be imaged, and maintain high-fidelity cell patterns in long-term serum-containing cultures.

Keywords: TOF-SIMS imaging; protein sorting; affinity ligands; Surface Analysis; antibody orientation; protein mixtures; protein patterning; multivariate analysis; principal component analysis

1. Introduction

Surface patterning techniques are often used to spatially regulate local chemical reactions with immobilized biomolecules such as oligonucleotides, proteins, and peptides for bioassays and to create microenvironments for organizing surface cell and bacterial activities (*1–5*). DNA microarray technology in particular has asserted its value in genomic research in diverse forms (*6*, *7*). However, genomic message and transcriptional information is several steps away from direct information regarding target proteins. With validated performance and validation, protein microarrays provide new potential for exploitation in a variety of biomedical and biotechnological applications including biosensors, drug screening, and fundamental studies involving proteomics in pathogenesis and aspects of cell biology (*4*, *8–13*). Unlike oligonucleotides, however, proteins are highly diverse in terms of charge, hydrophobic character, structure and other biochemical factors that affect their stability and behavior at interfaces. Protein microarrays therefore require well-defined immobilization methods that preserve protein structure-property relationships, with surface chemistry and fabrication techniques that accommodate wide varieties of different proteins.

Routine surface patterning technologies and microcontact printing methods are frequently used to produce nano- or micro-patterns of biomolecules on surfaces (*14*, *15*). A number of such techniques (e.g., photolithography) have demonstrated spatio-selective bio-immobilization on a variety of substrates (*16–19*). These are then commonly used to pursue cell patterning methods (*20–22*) for applications biochips (*23–25*), co-cultures (*26–28*), tissue engineering (*29*, *30*), cell-based biosensors (*9*). Successful performance in these applications requires that protein-immobilized platforms exhibit reliable specific immobilization together with general background resistance to non-specific protein adsorption (fouling) to these surfaces. Few surfaces reliably yield these properties. One convenient protein immobilization commercial method coats glass substrates with nitrocellulose or poly-L-lysine such that proteins passively adsorb through non-specific binding interactions (*31*, *32*). While high densities of proteins can be physisorbed on these surfaces, these platforms are limited in their ability to obtain high capture sensitivity and selectivity in bioassay systems due to high surface population fractions of randomly oriented and partially denatured adsorbed proteins (*10*). Retention of immobilized bioactivity of surface-resident proteins requires careful surface chemistry designs that maximize immobilization density, retain protein function and eliminate non-specific capture, often from complex mixtures containing thousands of components (e.g., serum or cell lysate).

2. Nonfouling Protein-Capture Polymer Surfaces

Inhibiting non-specific biomolecular binding and cellular adhesion to solid surfaces is critical to *in vitro* bioassay performance whose metric is specific analyte capture. Microarray formats often print proteins at high densities in micron-sized areas, often with no regard for printed area thickness. These pre-printed, surface-bound and dried spots are probed for various binding and biochemical activities. Traditional materials used for immunoassay and DNA microarraying (e.g., polystyrene, poly(vinylidene fluoride) (PVDF) and nitrocellulose) are often not compatible for protein microarrays (*10*, *32*). These surfaces often yield insufficient immobilized protein density and retained bioactivity, and can have unacceptable wetting or spotting properties limiting assay reproducibility, reliability and sensitivity. In contrast, thin hydrophilic coatings are commonly exploited to provide biologically "non-fouling" surface chemistries for biomedical and biotechnology applications (*13*, *33*, *34*). Among the many chemistries reported, poly(ethylene glycol) (PEG) polymers and PEG-like materials have an extensive history (*35–37*). Numerous surface treatment methods to produce PEG interfaces have been reported, including PEG grafting (*38*, *39*), adsorptive chemistries (*40*, *41*), and oligo-PEG-terminated self-assembled monolayers (*42*, *43*). Despite intensive work in this area, many surface chemistries suffer from limitations, hindering widespread adoption. Many coating methods require multiple, difficult-to-control processing steps to achieve a high-quality final films. Furthermore, these surface chemistries, when scaled beyond research production, often do not exhibit non-fouling performance required for biomedical utility in sensors, assays, and medical devices.

In Proteins at Interfaces III State of the Art 2012; Horbett, T., et al.;
ACS Symposium Series; American Chemical Society: Washington, DC, 2012.

Additionally, many coating formulations contain reactive chemistries necessary for immobilization (e.g., N-hydroxysuccinimide (NHS), sulfhydryl, maleimide, vinylsulfones, nitrophenylesters), often reactive with amine-based nucleophiles commonly found in a range of biomolecules including proteins, enzymes, chromophore dyes, and commercially derivatized oligonucleotides. Specifically, NHS is widely used as an activating reagent for carboxylic acid-based coupling in biochemistry (*44*), specifically in bioconjugation and bio-immobilization, as well as in a number of commercial chemistry kits and assay, including biodiagnostic arrays, biochips and biosensors (*9*, *12*, *23*, *24*, *45*). With these intrinsic, broad chemical reactivity, careful step-wise methods are necessary to immobilize desired molecules then remove residual reactivity across the surface and retain high resistance to non-specific background adsorption. Many coatings suffer performance reductions in these surface chemical sequences used for spatially controlled surface immobilization.

2.1. Patterning of Bioimmobilization Reactivity in Low-Background Polymer Coatings

Surface patterning methods extensively used to immobilize proteins and other bioactive molecules for biomedical applications (*1*, *25*, *46*) must spatially localize and control their immobilized targets, then remain passive against other species not targeted for immobilization. This is despite the chemical reactivity similarities between immobilization targets (e.g., antibodies or streptavidin) and non-targets (e.g., over 20,000 different proteins in human plasma samples or cell lysates). This is often discriminated using masking steps that cover unreacted surface chemistry with a sacrificial species (e.g., albumin), or by consuming the residual reactivity by a small molecule substitution that retains low non-specific binding (e.g., eliminating NHS with methoxyethylamine providing methoxy (MeO)-capping of NHS groups) (*47*). In microarraying methods, immobilized molecules are spatially printed using contact or non-contact printing methods into designated surface locations and chemical immobilization ensues spontaneously within seconds as the aqueous solution droplet evaporates rapidly. Subsequent stringency rinsing and processing steps over the entire surface allow masking or capping of residual surface reactive chemistry in unprinted spatial areas (*48*). Additionally, routine photolithography techniques can also be used to micropattern NHS surface chemistry directly, allowing spatial deactivation of chemistry prior to desired spatial bio-immobilization, or sequential protection/deprotection of NHS groups in different spatial areas for different pattern exposures (*49–51*). Using this process, NHS (reactive) and MeO-terminated (deactivated) surface patterns are obtained and a variety of biomolecule patterns can be produced in different designs for different purposes.

For protein immobilization purposes, we and many others have used a commercial multi-component PEG-based coating formulation supplied on low-fluorescence glass slides (Optichem®, Accelr8 Technologies, USA, marketed as Slide H™, Schott-Nexterion, Germany, see http://www.us.schott.com/nexterion/english/products/coated_slides/thin_film.html for application notes and updated technical publication bibliography for this chemistry use). The

In Proteins at Interfaces III State of the Art 2012; Horbett, T., et al.;
ACS Symposium Series; American Chemical Society: Washington, DC, 2012.

polymer chemistry and coating is unique in that it: (1) is applied in a single, reproducible, solution-based coating step; (2) can be applied to diverse substrate materials without the use of special primers; and (3) is readily functionalized to provide several known specific immobilization chemistries. The polymer base coating formulation comprises a single mixture of three components: (1) the active immobilization component, (2) matrix-forming component, and (3) cross-linking component (*52*). Figure 1 shows the active component as a heterobifunctional PEG polymer (NHS-PEG-aminosilane) bearing NHS end groups that serve as the reactive PEG-tethered functional groups in the final coating. The other PEG terminal group (aminosilane) provides covalent crosslinking capabilities and both attachment within the coating matrix and to certain substrates. Added polyoxyethylene sorbitan tetraoleate serves as the matrix-forming film component, and in some formulations, an azidosilane is used as a thermally or photochemically reactive cross-linker for the matrix and surface anchoring. The azide converts to a reactive nitrene that rapidly and non-specifically inserts into aliphatic or aromatic bonds within the coating matrix and into organic surfaces such as polystyrene, polycarbonates, or polypropylene. The multiple reaction pathways convert the soluble three-component mixture to a stable, resilient functional coating through diverse cross-linking, adhesion, and covalent attachment mechanisms upon curing. Importantly, both film uniformity and swelling properties as well as intrinsic NHS activity in the final film can be adjusted by changing component ratios and concentrations.

2.2. Polymer Background Nonspecific Adsorption Properties

After fabrication, NHS groups are easily converted to MeO-terminated groups by slide immersion into a 2-methoxyethylamine solution (50 mM in 50 mM borate buffer at pH 9 for 1 hour (*47*). The deactivated polymer film provides significant inhibition of non-specific serum protein adsorption and also PCR reagent uptake under rigorous in vitro testing conditions. Exposed to 10% goat serum as a model for in vitro bioassay formats, the polymer provides 97% reduction in non-specifically adsorbed serum components over controls. Single proteins such as fibrinogen and lysozyme are also inhibited significantly in binding non-specifically to the surface. As a functional assay, serum protein adsorption is low enough that no adhesion-dependent mammalian cell lines tested in 10% fetal bovine serum (e.g., macrophage, fibroblast, endothelial phenotypes) will attach to the surface (unpublished data) (*49*, *52*). Bacteria adhesion - a critical first step in the cascade of processes from surface colonization to biofilm formation – is also severely inhibited. OptiChem® is shown effective in vitro in reducing the adhesion of different clinical bacterial isolates by several orders of magnitude in several different flowing actual biological media such as saliva, urine, and plasma, and delaying ultimate biofilm formation in flow-cell extended cultures (*53*). Additionally, two model bacterial strains (clinical strains of *Staphylococcus aureus* as model Gram-positive cocci and *Klebsiella pneumoniae* as model Gram-negative rods were easily removed at the lowest shear rate (4.6 sec^{-1}) in a microfluidic flow cell, reflecting their poor adhesion in biological fluids. For these representative strains, surface performance is qualitatively comparable to that seen on ethylene oxide-terminated SAMs (*43*) and long chain-length PEG brushes (*54*). Lastly, the OptiChem® coating effectively inhibited biofilm formation *in vitro* during 960 min of growth in a well-characterized flow chamber, while the adsorption of plasma proteins produced a small loss of the anti-adhesive coating activity. Biofilms produced *in vitro* were slightly less viable on the coating than on glass. In a mouse *in vivo* pocket implant infection model, OptiChem®-coated silicone rubber discs were not colonized by staphylococci, while bare silicone rubber discs were consistently colonized (*55*). This is a collective, consistent functional and in vitro/in vivo correlating testament to the low non-specific binding properties of this polymer coating – a critical pre-requisite for patterned applications (Figure 2).

3. Time-of-Flight Secondary Ion Mass Spectrometry (TOF-SIMS) Chemical State Imaging Techniques for Surface Analysis of Immobilized Proteins

TOF-SIMS is a widely used surface analysis technique for characterization of biomaterial surfaces (*56*, *57*). Specifically, TOF-SIMS chemical state imaging is a powerful tool for visualizing the distribution of surface chemical compositions at micron resolution (*24*, *58*). Although X-ray photoelectron spectroscopy (XPS) is also extremely useful for surface chemistry analysis, it does not have sufficient molecular specificity (*59*). Particularly for this PEG-based polymer coating, the atomic percentage of XPS-detected nitrogen signals cannot be used to uniquely quantify the NHS chemistry on the polymer surface due to the presence of more than one nitrogen-containing species in the composition (see Figure 1) (*45*). With its high detection sensitivity and specificity to selected chemical groups, TOF-SIMS has been shown to provide semi-quantitative analysis of NHS-conjugated PEG surfaces in combination with multivariate analysis statistical methods such as principal component analysis (PCA) (*59*). In fact, TOF-SIMS methods have been shown to enable a method for understanding relative NHS density on surfaces as an important quality control feature to assess the known hydrolytic instability of this chemistry upon storage (*60*) and impact of this degradation on surface immobilization efficiencies (*49*, *59*).

TOF-SIMS data here were acquired using previously published methods (*49*, *59*, *61*): using an ION-TOF 5-100 instrument (ION-TOF GmbH, Münster, Germany) using a Bi_3^+ primary ion source with a pulsed 25 keV, 1.3 pA primary ion beam in high current bunched mode (i.e., high mass resolution mode) from 500 µm x 500 µm areas on the sample surfaces. All images contain 128 x 128 pixels. These analysis conditions result in spatial resolution of approximately 4 microns. All data were collected using an ion dose below the static SIMS limit of 1 x 10^{12} ions/cm^2. A low-energy electron beam was used for charge compensation on the polymer-coated glass slides. The mass resolutions ($m/\Delta m$) for the negative secondary ion spectra are typically between 6000 and 7500 for the (m/z) 25 peak. The mass resolutions ($m/\Delta m$) for the positive secondary ion spectra are typically between 7000 and 8500 for the (m/z) 27 peak. PCA was performed on this dataset as described previously using a series of scripts written by NESAC/BIO for MATLAB (MathWorks, Inc., Natick, USA) to build PCA scores images of the surfaces from chemical fragment data (*62*, *63*). TOF-SIMS image line resolution can be calculated to be 6.0 ± 0.4 µm as derived from multiple line scans, approximately the same resolution as the photomask used for surface patterning.

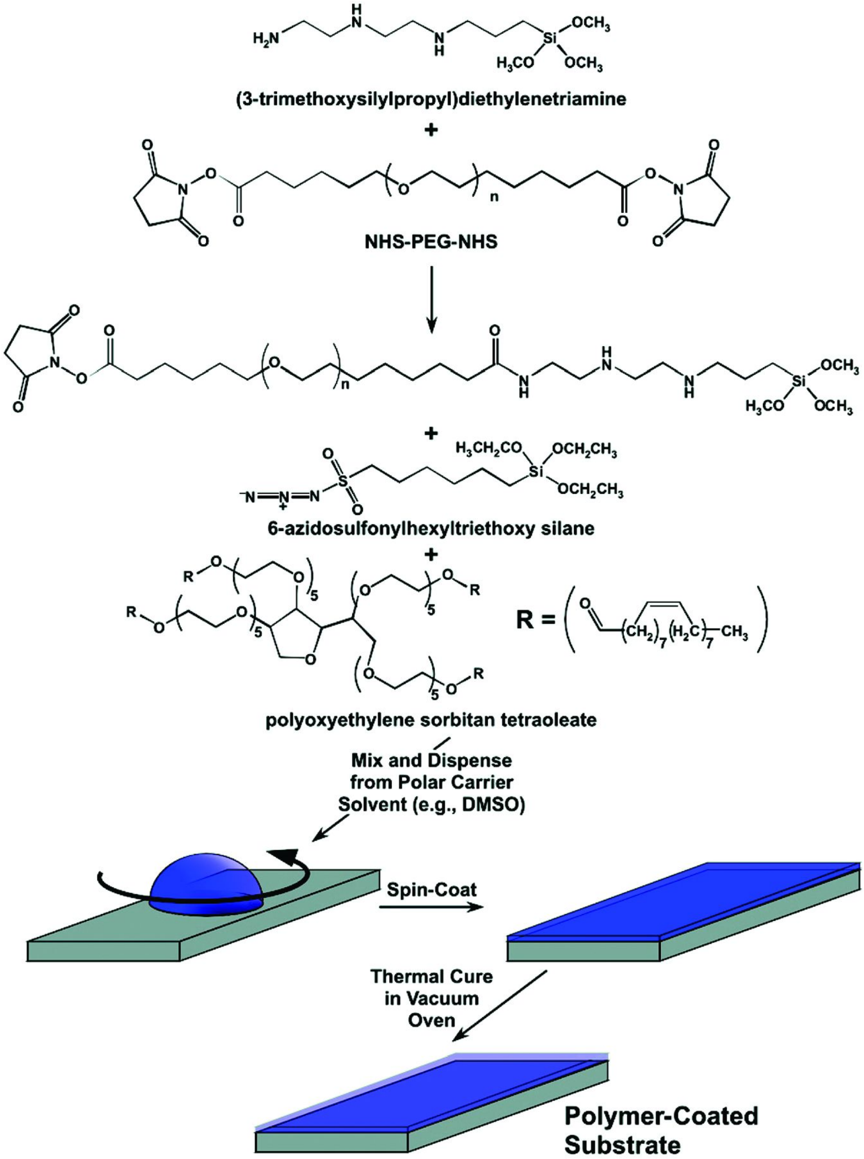
(3-trimethoxysilylpropyl)diethylenetriamine
+
NHS-PEG-NHS
+
6-azidosulfonylhexyltriethoxy silane
+
polyoxyethylene sorbitan tetraoleate
R =
Mix and Dispense from Polar Carrier Solvent (e.g., DMSO)
Spin-Coat
Thermal Cure in Vacuum Oven
Polymer-Coated Substrate

Figure 1. Schematic illustration of NHS-containing PEG-based crosslinked polymer coating process. Reproduced with permission from Ref. (52). Copyright 2007 American Chemical Society.

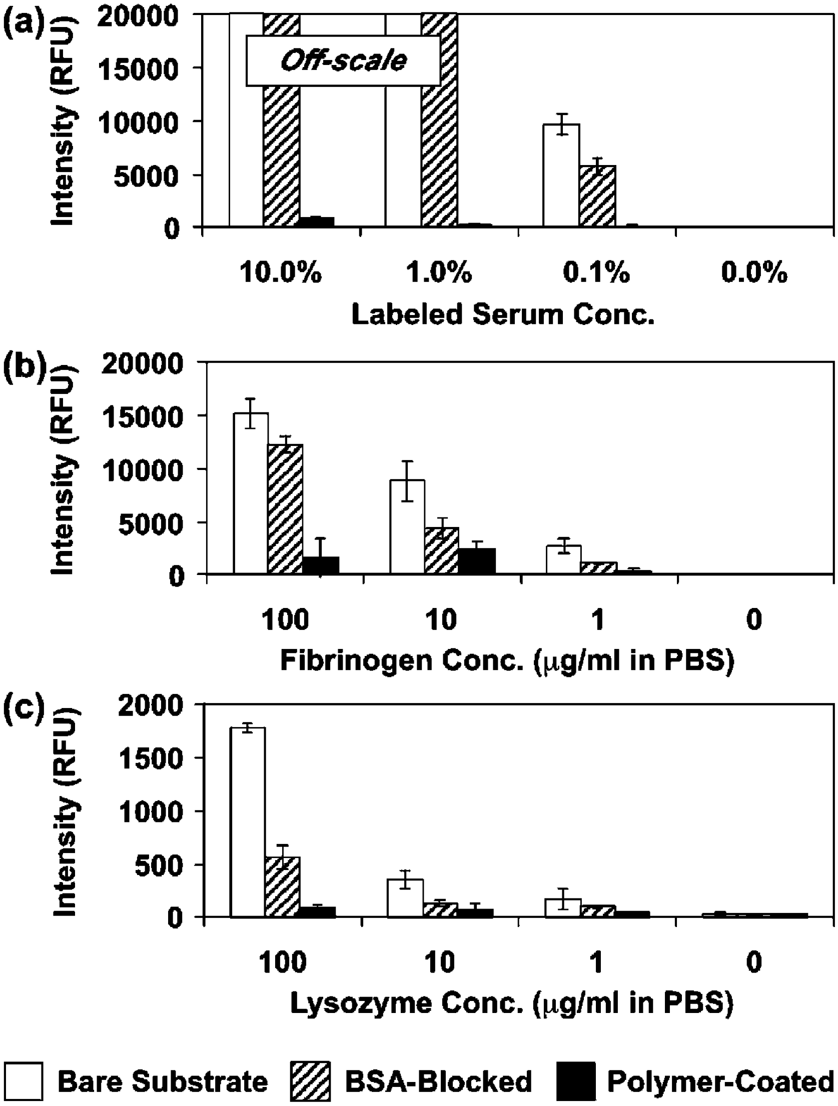

Figure 2. Relative non-specific protein adsorption on bare glass, bovine serum albumin (BSA)-blocked substrates, and the PEG-based polymer-coated substrate. Fluorescently-labeled proteins (a: goat serum, b: human fibrinogen, c: human lysozyme). Fluorescence intensity was detected by a commercial array laser scanner and calculated as relative fluorescence unit (RFU) under identical conditions. Reproduced with permission from Ref. (52). Copyright 2007 American Chemical Society.

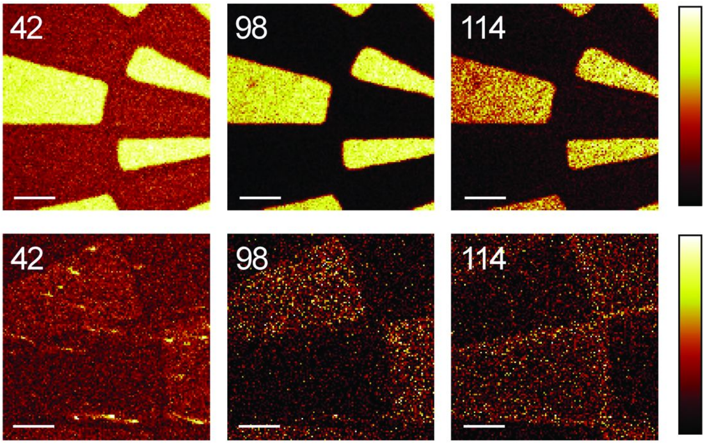

Figure 3. Chemically specific NHS surface mapping using TOF-SIMS. Negative TOF-SIMS ion images for patterned NHS-co-methoxy capped patterned PEG polymer surfaces showing areas from TOF-SIMS analysis selected for fragments m/z 42, 98, and 114 from fresh NHS patterned (top, raw ion images) and hydrolyzed PEG-NHS surfaces (bottom, raw ion images). Scale bar: 100 µm. Reproduced with permission from Ref. (64). Copyright 2009 John Wiley & Sons, Ltd.

3.1. TOF-SIMS Imaging of Chemical and Protein Patterns on Polymer Surfaces

NHS groups undergo well-known hydrolysis both under ambient atmospheric humidity and rapidly in bulk water with both temperature and pH dependence (*44*, *49*, *59*). While NHS coupling chemistry is utilized in thousands of publications and many commercial kits and technologies, quality control methods to assess NHS presence, activity and hydrolysis on surfaces for controlling surface immobilization reaction efficiency are not readily available. TOF-SIMS analysis of chemical fragments derived from NHS-polymer surfaces after various treatments exploited PCA methods to distinguish resident NHS presence and activity between fresh NHS-containing, NHS-aged and hydrolyzed surfaces (*59*, *64*). Principal component (PC1) scores and loadings plot for negative ion surface data shows that these polymer samples are clearly differentiated (*64*). Peaks from fragments at m/z 98 ($C_4H_4NO_2^-$) and 114 ($C_4H_4NO_3^-$) among others are characteristic of the NHS five-member ring. TOF-SIMS analysis clearly shows remarkable decreases in these ion peaks from NHS-hydrolyzed surfaces. Subsequently, NHS hydrolysis results in increasing intensity of peaks at m/z 58 ($C_2H_2O_2^-$) and 43 ($C_2H_3O^-$) from the hydrolyzed NHS ring-opened fragment and resulting surface carboxylate group. TOF-SIMS analysis is therefore capable of producing a quality control metric for NHS surface states, and produce surface images for this chemistry and hydrolytic changes on surfaces (Figure 3) (*59*, *64*). This method of "chemical mapping" of surface reactivity can then be used further to follow sequential reactions at surfaces by following the changes in TOF-SIMS fragment profiles and resulting surface chemical maps, especially valuable for validating approaches that involve surface patterns for spatial control of immobilization.

TOF-SIMS can be exploited to provide chemical fragment images for immobilized proteins by mapping specific ion fragments originating from constituent surface-derived amino acids (*65–67*). The use of fluorescently-labeled proteins on surface patterns confirms the validity of this approach. Figure 4 shows that the fluorescence image for streptavidin forms micropatterns only on NHS-bearing surface regions through solution phase protein immobilization (Figure 4a). The corresponding chemical state TOF-SIMS confirms these protein patterns by detecting and mapping the mass fragments from amino acids in the immobilized protein (m/z 110, 120, 130, 136, 159, and 170) (Figure 4b) (*49*).

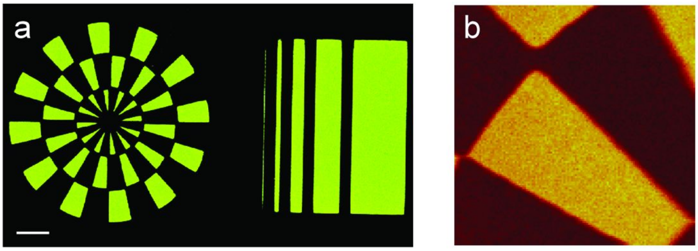

Figure 4. (a) Fluorescence image of a NHS-patterned surface treated with solution phase streptavidin and then exposed to biotinylated BSA labeled with Alexa555. Scale bar left: 500 µm. (b) TOF-SIMS image generated from PC-1 score map of TOF-SIMS positive ion analysis of the streptavidin-immobilized surface pattern (image: 500 µm x 500 µm, streptavidin ion fragments mapped to lighter PCA score regions). Reproduced with permission from Ref. (49). Copyright 2008 WILEY-VCH Verlag GmbH & Co. KGaA, Weinheim.

4. Affinity-Based Protein Immobilization: Self-Selecting Ligand Patterns

Traditional affinity chromatography exploits highly specific, unique binding interactions between a desired target, typically a protein, and its paired ligand bound at sufficient surface density to a separation matrix (i.e., a solid phase filter, suspended particles, or a stationary phase chromatography support). This method is used to separate proteins from mixed solutions using protein-ligand affinities (K_d ~nM) that provide reliable selectivity and specificity for target removal from complex samples (*68*). We have adapted these affinity selection methods to planar surfaces by tethering high affinity ligands in patterns to polymer surface chemistry that exhibits very low background non-specific capture. The patterning process can be followed step-wise using ToF-SIMS to validate each derivatization, and can reliably bind target proteins to patterns from mixed aqueous solutions.

4.1. Dual Protein Patterning by Ligand Self-Selection at Interfaces

A variety of patterning techniques now allow multiple different proteins to be co-patterned on the same surface by soft lithography (*69*, *70*), masked stencils (*71*, *72*), and other methods (*73*, *74*). However, many studies on protein patterning are still based on sequential strategies immobilizing different proteins stepwise in series. These strategies typically utilize serial processing methods to immobilize one protein at a time from pure, single component solutions onto surfaces by physical adsorption, covalent attachment, or affinity ligand capture (*1*). Capture using affinity ligands is promising to facilitate protein selection and immobilization from mixed solution phases (*10*, *75*). Self-selection of ligands as a co-patterning technique is intuitive but characterizing this pattern for properties beyond confocal imaging is challenging.

As affinity ligand models, biotin and chloroalkane were co-patterned using lithography-generated NHS patterned chemistry on PEG hydrogel surfaces (*61*). As shown in Figure 3, NHS groups can be patterned site-selectively. Photoresist can be selectively retained in regions to mask and protect NHS chemistry while exposed groups are reacted with a ligand (*49*). NHS groups in the exposed regions are coupled with a first ligand (biotin) by incubation with hydrazine-derivatized biotin. The photoresist in the second pattern is then removed and the second ligand, amino-chloroalkane, can be further immobilized onto the biotin/NHS-patterned surface, yielding biotin/chloroalkane co-patterned slides. The chloroalkane ligand is specific to HaloTag® protein (Promega, USA) a 34kDa modified hydrolase enzyme that rapidly forms specific, covalent bonds with chloroalkane ligands (*76*). Each region of this dual ligand-immobilized surface has high binding affinity in principle for one of two proteins, allowing self-selecting co-patterning solely by exposure of protein solutions comprising streptavidin and HaloTag® proteins.

4.2. Fluorescence Imaging of Protein Co-Patterned Surfaces

Fluorescence detection of pattern recognition by labeled proteins is a simple, direct confirmation of site-specific binding. Detection of fluorescently labeled proteins on substrates using common microarray scanners is standard protocol (*8*, *31*, *45*, *71*). After exposure to mixed protein solutions where both proteins bear different fluorophores, resulting fluorescence patterns exhibit images corresponding to the lithographed dual-ligand co-patterning. The approach is schematically shown in Figure 5. High fidelity of the protein-ligand surface interactions in respective side-by-side spatial zones using paired ligand-protein interactions on PEG-based hydrogel surface with its intrinsically low non-specific protein adsorption is expected (*52*). Patterned NHS groups are converted to spatially controlled areas of ligand-immobilized chemistry and facilitate reliable immobilization of streptavidin and HaloTag® from aqueous mixed solutions (Figure 5). Fluorescence images reveal that two different proteins, streptavidin and HaloTag®, bind specifically and are exclusively captured on the surface through specific interactions with their respective partner molecules, biotin and chloroalkane (*61*). These data are then conveniently correlated with TOF-SIMS chemical state images for the same samples.

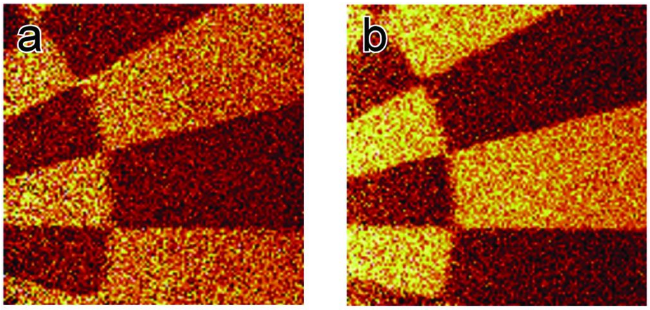

Figure 5. Schematic illustration for self-sorting of two different proteins, streptavidin (green) and HaloTag® (red), onto biotin and chloroalkane ligand-patterned low-background polymer surfaces. Fluorescence imaging of co-patterned surfaces after exposure to solutions of mixed streptavidin-Alexa555 and HaloTag®-Alexa647 demonstrates high fidelity of each protein to their respective surface ligand patterns. Reproduced with permission from Ref. (61). Copyright 2009 WILEY-VCH Verlag GmbH & Co. KGaA, Weinheim.

4.3. TOF-SIMS Chemical State Imaging of Protein Co-Patterned Surfaces

TOF-SIMS chemical imaging with PCA provides a “label-free” surface mapping technique to corroborate fluorescence surface patterns and confirm successful co-patterning of streptavidin and HaloTag® using the affinity-ligand self-sorting solution approach (*61*). TOF-SIMS has been widely used to characterize proteins and peptides on various substrates by exploiting specific ion fragments originating from constituent amino acids (*65*, *66*, *77*). The overall amino acid composition for proteins is generally restricted to the canonical natural amino acid population, where most proteins exhibit relatively small differences in their amino acid composition that manifest much more substantial and diverse distinctions in size, folded shapes, domains and therefore respective functions. The ability of TOF-SIMS to readily discriminate and then image 2 different unlabeled proteins in adjacent surface-patterned areas was the idea pursued in this study. Moreover, as minute amounts of albumin were mixed into the protein mixtures to limit non-specific protein adsorption to the surface, this represented an additional confounding protein signal source for TOF-SIMS to overcome.

Compositional differences in amino acids between these three proteins are listed in Table 1. Cysteine and methionine are two amino acids not present in streptavidin, so the characteristic sulfur-containing fragments from these amino acids (i.e., CHS, 45 m/z, and C_2H_5S, 61 m/z) provide specific indications for where streptavidin is absent. By contrast, amino acids threonine (16%), tryptophan (9%) and tyrosine (8%) are present in higher concentrations in streptavidin compared to either HaloTag® or BSA, so TOF-SIMS images corresponding to the characteristic fragments from these three amino acids (e.g., C_3H_8NO, 74 m/z; C_9H_8N, 130 m/z; C_7H_7O, 107 m/z; and $C_8H_{10}NO$,136 m/z) should indicate streptavidin presence.

Table 1. Protein amino acid composition comparisons for streptavidin, HaloTag® and bovine serum albumin (BSA) (*61*)

Amino acid	*% composition in protein*		
	Streptavidin	*HaloTag®*	*BSA*
Lys	3.96	5.74	11.35
His	2.20	3.15	3.26
Arg	4.85	5.37	5.74
Asp	3.53	8.15	6.09
Asn	5.95	2.59	2.96
Thr	16.08	2.96	4.26
Ser	5.67	3.52	3.13
Pro	0.96	7.96	3.65
Gly	6.72	7.04	0.96
Glu	4.32	7.41	12.13
Gln	3.08	1.67	3.91
Ala	8.79	6.48	6.63
Cys	0	1.30	4.57
Val	5.01	5.74	6.24
Met	0	2.96	1.04
Ile	2.63	6.30	1.39
Leu	6.61	10.74	10.26
Tyr	7.93	3.89	4.69
Phe	2.42	4.63	7.41
Trp	9.25	2.41	0.30
Total	**100**	**100**	**100**

Despite theoretical challenges for discriminating different proteins patterned on the same surface using subtle amino acid compositional differences, TOF-SIMS imaging clearly indicates its capabilities to discriminate streptavidin from HaloTag® proteins on the ligand-patterned surface. TOF-SIMS chemical fragment images generated by selecting specific ion fragments clearly distinguishes co-patterning of streptavidin and HaloTag® on a PEG-based hydrogel film, consistent with both the NHS patterns and fluorescence images from labeled protein patterns (see Figure 6). The sensitive and selective protein chemical discrimination of surface patterns shown here by these methods is unprecedented. Furthermore, the co-patterning study also exhibit a potential of

TOF-SIMS analysis for distinguishing different proteins immobilized onto the same surface.

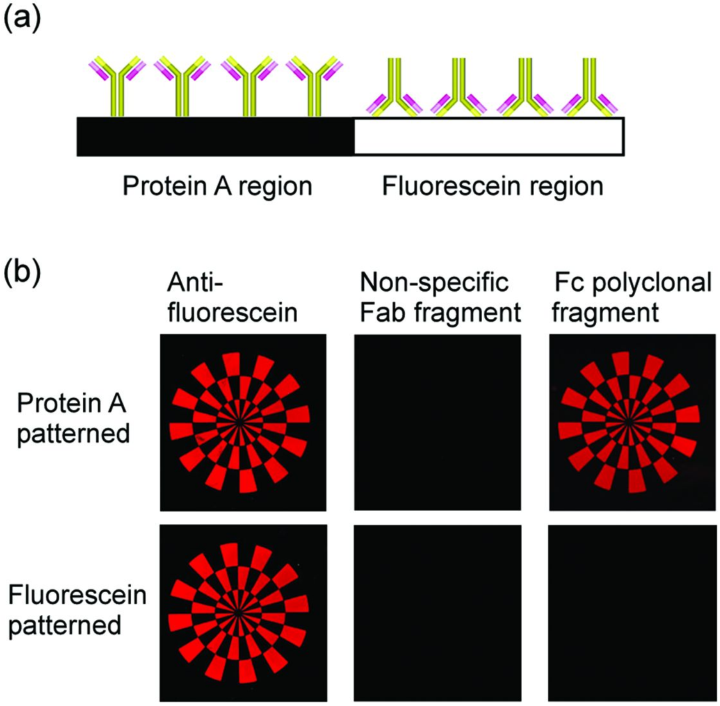

Figure 6. TOF-SIMS images of identical sample areas for an affinity ligand-selected protein co-patterned surface using biotin/chloroalkane, generated by selecting protein-specific ion fragments identified in the PCA loadings plot for both streptavidin and HaloTag®. Bright patterned regions in each image are generated from chemical state maps derived from (a) Cys+Met ion-specific fragments characteristic of HaloTag® protein, and (b) Tyr+Thr+Trp ion-specific fragments characteristic of streptavidin. Reproduced with permission from Ref. (61). Copyright 2009 WILEY-VCH Verlag GmbH & Co. KGaA, Weinheim.

5. Using TOF-SIMS Chemical Imaging To Demonstrate Orientational Control of Immobilized Proteins at Interfaces (*78*)

Surface capture-based technologies and proteomics tools in high-throughput formats have been an on-going interest for biosensing, clinical chemistry, and fundamental work analyzing protein expression patterns, protein-protein interactions, and processes underlying cellular functions. As a central component, immobilized antibody surface capture is central to more traditional enzyme-linked immunosorbent assays (ELISAs) (*79*, *80*), affinity chromatography separations

(*81*, *82*), lateral flow assays (*83*), antibody-based diagnostics (*84*), antibody microarray assay formats (*85*, *86*), and biosensors (*87*). Improvements in antibody surface-immobilized stability, sensitivity, density, and shelf-life, reduced cross-reactivity remain as a long-standing issue limiting performance in numerous applications. Surface-immobilized antibody orientation is frequently a focus since mis-oriented antibodies conceivably are compromised in their antigen binding capacity (*85*, *88*, *89*). Random antibody surface orientation results in limited access to bind analytes if the antigen-binding domains of the antibody (i.e., Fv variable domains within the antigen-binding Fab domains) are immobilized against the surface (*10*). In additional to surface immobilization methods that might reliably improve antibody immobilized orientations, methods to actually analyze this as a quality control measure in situ on surfaces are challenging (*90*). The affinity-based protein self-selecting strategy, using surfaces patterned with ligands with preference for specific antibody sites, offers an opportunity for TOF-SIMS discrimination (*78*).

5.1. Fluorescent Protein Imaging for Visualizing Antibody Patterning Specificities

To validate TOF-SIMS as a new method to analyze protein orientation, we exploited our previous surface co-patterning strategy, using lithography of commercial NHS-bearing PEG polymer surfaces to attach two different ligands into adjacent regions with spatial selectively. Unlike the previous example where two different proteins selected two different surface affinity ligands by self-selection from mixed aqueous solutions (*61*), the antibody orientation approach involved a dual ligand co-patterning method to facilitate antibody orientation selection on adjacent surface patterns. To achieve this, a bacterial membrane protein, Protein A, well-known to specifically bind the antibody Fc domain (*91*, *92*) and extensively used as a surface affinity ligand to bind and orient antibodies for solid-phase affinity use (*93*) was patterned. The antibody Fc-Protein A interaction pairing at the solid surface allows a preference for orientation of the antigen-binding domain Fab fragment to be exposure to reaction solution. While this is not absolute certain orientation, given finite possibilities for surface mis-orientation and non-specific surface adsorption, the method does improve antigen capture, reflecting surface orientation with more antibody Fab domain exposure/accessibility away from the surface (*93*). Second, fluorescein, a known high affinity antigen for several anti-fluorescein monoclonal antibodies (e.g., MAb 4-4-20) (*94*), was surface-immobilized using amino-fluorescein, producing specific antigen ligands to orient anti-fluorescein antibodies with Fab domains down against the surface by antigen binding. Co-patterning of fluorescein haptens in adjacent regions co-planar with protein A using the NHS patterning strategy defined here (vida supra) provides an approximate 2-state surface selection model. This was intended to produce patterned regions on surfaces where antibodies select an antibody Fab upwards surface orientation using protein A capture (i.e., “heads-up”), and an antibody Fab downwards surface orientation using fluorescein hapten binding (i.e., “tails-up”) (*78*). Figure 7a depicts this desired result. This strategy provides a basis for analyzing antibody surface selection and orientational control. Both convenient capabilities for dual ligand-patterning (in this case, dual protein A and fluorescein adjacent patterns) combined with low non-specific background binding already shown for this surface (*52*), provide a suitable model system to assess the abilities of fluorescence mapping and TOF-SIMS chemical state imaging to validate this approach.

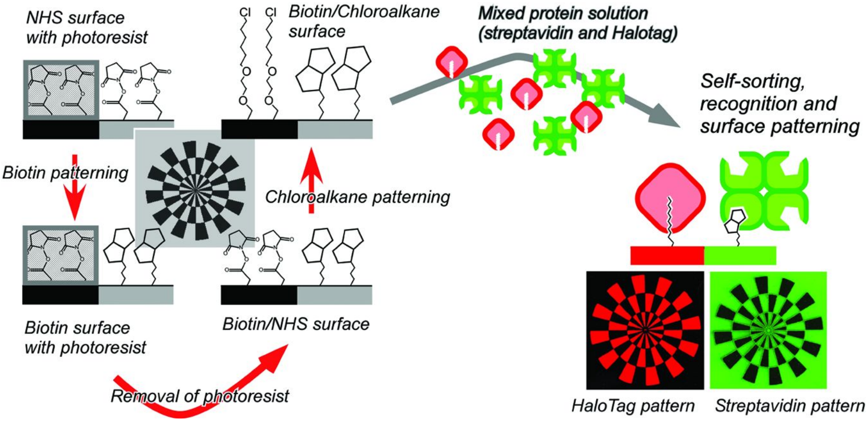
NHS surface
with photoresist
Cl
Cl
Biotin/Chloroalkane
surface
Mixed protein solution
(streptavidin and Halotag)
Self-sorting,
recognition and
surface patterning
Biotin patterning
Chloroalkane patterning
Biotin surface
with photoresist
Biotin/NHS surface
Removal of photoresist
HaloTag pattern
Streptavidin pattern

Figure 7. Antibody self-selection of 2-state ligand patterns on surfaces from solution. (a) Schematic illustration showing the intended 2-state immobilized antibody orientations using co-patterned protein A- and fluorescein- immobilized regions to selectively bind antibodies in "heads-up" (Fab domain exposed) and "tails-up" (Fc domain exposed) orientations on ligand-patterned surfaces known to select these states; (b) Fluorescence images of Alexa647-labeled anti-fluorescein antibody, non-specific murine Fab fragments, and Fc polyclonal fragments captured on protein A- and fluorescein-patterned surfaces, respectively, showing surface specificities for each species and the designed patterned surface ligand. Reproduced with permission from Ref. (78). Copyright 2010 American Chemical Society.

First, domain-specific antibody reactions were confirmed indirectly using fluorescence imaging (see Figure 7b). AlexaFluor-labeled MAb 4-4-20 exhibits the anticipated selection of either protein A or fluorescein on single-ligand patterned surface controls (i.e., either protein A/MeO-capped or fluorescein hapten/MeO-capped patterns). No antibody signal from exposure of fluorescently-labeled Fab fragment to the protein A-patterned surface supports specific reaction of the full antibody on regions where protein A is immobilized (Figure 7b). In contrast, Alexa-labeled Fc fragments bind selectively to the protein A-patterned surfaces, similar to the full antibody. These images indicate that anti-fluorescein 4-4-20 antibody specifically interacts with surface-immobilized protein A through Fc recognition. Thus, when this antibody binds to protein A-immobilized regions, a predominantly “heads-up” orientation is expected in these regions. By contrast, when the fluorescein-patterned surface is exposed to non-specific murine Fab and Fc polyclonal fragments lacking specificity for the immobilized fluorescein, neither of these two antibody fragments bind to this surface (Figure 7b). This supports specific anti-fluorescein antibody binding with patterned fluorescein ligands through specific antigen-Fab domain interactions, providing the desired “tails-up” orientation (*78*).

5.2. TOF-SIMS Imaging for Visualizing Antibody Orientation

TOF-SIMS has proven to be an effective surface analytical method for providing information on the orientation and other aspects of surface-bound proteins (*59*, *95–98*). While fluorescence imaging shows site-specific high-fidelity antibody selection of ligand patterns on surfaces, protein-surface orientation cannot be distinguished from data in Figure 7b. Even commonly employed analytical methods (e.g., SPR, TIRF, AFM) have difficulties asserting conformational or orientational differences on antibody-immobilized surfaces (*99*). Importantly, TOF-SIMS methods provide new chemical information capable of discerning protein orientations on surfaces. Since the TOF-SIMS sampling depth is generally ~2 nm, the ion yields reflect only the outermost amino acids of the exposed protein regions on these surfaces (*100*). Antibody orientation therefore is selectively detectable if: (1) these amino acids in the surfaces of these different antibody domains are sufficiently compositionally distinct in different orientations (i.e., Fab domain oriented toward ambient interface versus Fc domain oriented toward ambient interface), (2) antibody orientation is relatively consistent across the sampling area of the TOF-SIMS analysis, and (3) the method is capable of sorting the complex surface mass spectra to provide these distinguishing features. Table 2 shows specific amino acids for antibody domains, showing the relative enrichment between Fab versus Fc domains, and the basis for predicting whether amino acid TOF-SIMS fragments originating from antibodies selecting protein A versus fluorescein patterns could show pattern-specific signals.

With such analytical performance, the co-patterning strategy using TOF-SIMS analysis distinguishes “heads-up” from “tails-up” antibody orientations shown in Figure 7(a) (*78*). Fab/Fc amino acid ratios less than unity in Table 2 have these amino acids enriched in the Fc region and therefore would be predicted to have lower TOF-SIMS intensities from these amino acids if the antibody is bound “tails-up” in fluorescein hapten regions. Correspondingly, Fab/Fc amino acid ratios greater than unity in Table 2 have these amino acids enriched in their Fab domains and therefore would be predicted to have higher TOF-SIMS intensities from these amino acids if the antibody is bound “heads-up” on protein A patterns. This experimental design is conceptually captured in Figure 8 (*78*).

Table 2. Comparisons of relative amino acid enrichment in Fab versus Fc antibody domains and predicted TOF-SIMS PCA loadings based on affinity immobilization to protein A versus fluorescein surface patterns (*78*)

Amino Acid	*Compositional ratio (F_{ab}/F_c)*	*Predicted PCA loading region*
Cys	0.70	Fluorescein
His	0.42	Fluorescein
Pro	0.53	Fluorescein
Leu	1.57	Protein-A
Arg	1.21	Protein-A
Gln	1.18	Protein-A

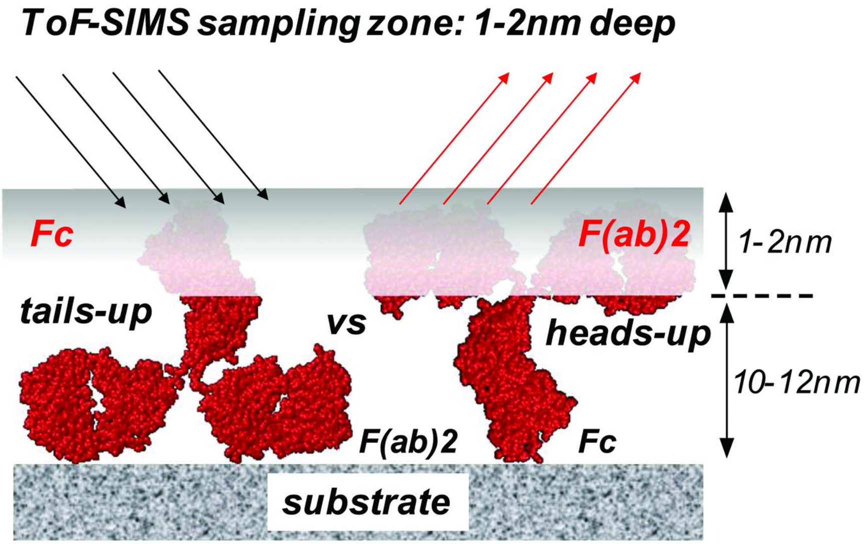

Figure 8. Schematic for the orientation-dependence of TOF-SIMS amino acid signals from antibodies oriented in a theoretical 2-state surface model (i.e., "heads-up" versus "tails-up" orientations) on antibody regio-specific affinity-capture ligand co-patterned surfaces (78).

Based on this predicted amino acid signal enrichment and the opportunity for TOF-SIMS to detect this enrichment, TOF-SIMS images generated from peptide fragments specific to either the antibody Fab or Fc regions were used to validate this method. Surface images generated from summing all amino acid fragment m/z signals for antibody patterns on surfaces show clear surface patterns consistent with the lithographic patterning and its characterization. This contrast must arise from differences in total immobilized antibody densities between both surface regions. This reflects possible intrinsic differences between protein A-Fc recognition and fluorescein antigen-antibody surface interactions, as well from the presence of photoresist residue in the UV exposed regions. Figure 9(a) shows the total amino acid ion intensities, with the pattern contrast consistent with more antibody residing on the protein A region than on the fluorescein region. However, compositional "mapping" of the selected amino acid fragments known for Fab (i.e., "heads-up" orientation) versus Fc (i.e., "tails-up" orientation) across the surface (Figure 9(b)) clearly indicates greater ion intensity for fragments associated with Fc domains originate from the fluorescein-patterned region. Complete analysis of surface patterned antibody capture for each affinity ligand is consistent with different pattern specificity for antibody Fab versus Fc domain binding as depicted in Figure 7(a). This prompted our conclusion that antibody orientation could be produced on each pattern by ligand-based orientational influences on immobilization (*78*).

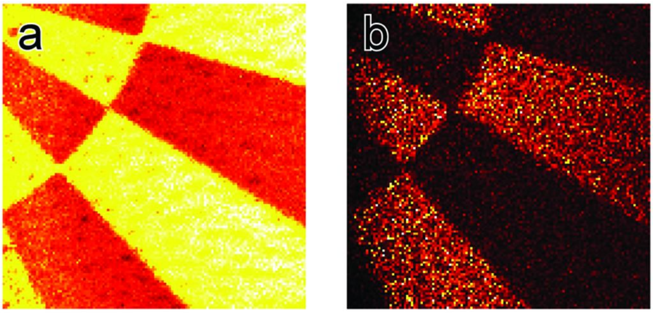

Figure 9. TOF-SIMS-generated images of antibody-patterned surfaces produced from solution phase binding with co-patterned protein A/fluorescein. Contrast in identical images is generated from TOF-SIMS surface analysis data from (a) summing all amino acid ion fragments detected, and (b) amino acid enrichment ratio characteristic of Fab versus Fc domain amino acid compositions as defined in Table 2. Reproduced with permission from Ref. (78). Copyright 2010 American Chemical Society.

Direct evidence of surface-immobilized orientation is seldom directly shown in similar antibody studies: the complexity of the problem at surfaces with immobilized proteins is not easily interrogated and few methods exist to assert orientation of protein monolayers. TOF-SIMS chemical state imaging reveals antibody orientation regulated by site-specific protein A-Fc and antigen-antibody Fab interactions, respectively. The dual ligand co-patterning technique elicits antibody sorting at surfaces into "heads-up" and "tails-up" oriented antibodies validated by TOF-SIMS imaging based on differences in oriented antibody amino acid compositions. Importantly, this approach could lead to both understanding of and control over surface antibody orientations required for improved bioassay performance (i.e., assay precision, sensitivity and accuracy) with impact to protein microarrays, biosensors, affinity chromatography and immunoassays.

6. Cell Culture Patterning through Cell Adhesion Peptide Patterns

Cell patterning techniques facilitate local control over adherent cellular shapes, footprint or adhered size, cell density, cell-cell interactions and cell communication, influencing cell function, phenotype, and metabolism at surfaces (*29*, *71*, *101*). Additionally, micropatterned viable cells on a chip represent a promising micro-sensor in the field of medical diagnostics (*23–25*). The PEG-based crosslinked polymer coating described in Figures 1-3 and previous work exhibits sufficiently reliable non-fouling properties in cell culture serum-containing media to both mammalian cell and bacterial adhesion to these surfaces (vida supra) (*49*, *52*). This low background protein binding is critical for cell patterning. With its pattern-capable amine-reactive NHS groups, the surface is conveniently patterned with proteins and peptides known to promote cell adhesion even on non-adhesive surfaces. Because peptides are much shorter, less expensive and more stable than longer proteins, high-density peptide microarrays can be fabricated by peptide conjugation to surfaces (*102*, *103*).

Short RGD-containing peptides are most commonly used to promote specific cell-surface immobilization (*104*, *105*). These can be immobilized on NHS patterns on the PEG hydrogel surface coating through bulk aqueous immobilization (*49*). Figure 10 shows the RGD peptide and its ion fragments detected by TOF-SIMS in analysis. Chemical fragment images from solution-immobilized RGD to NHS patterned surfaces show the anticipated pattern for NHS-specific peptide immobilization (compare Figure 3). This is consistent with previous data (vida supra) showing the chemical specificity of this surface chemistry for bulk peptide solution chemical immobilization to NHS patterns (*49*, *52*).

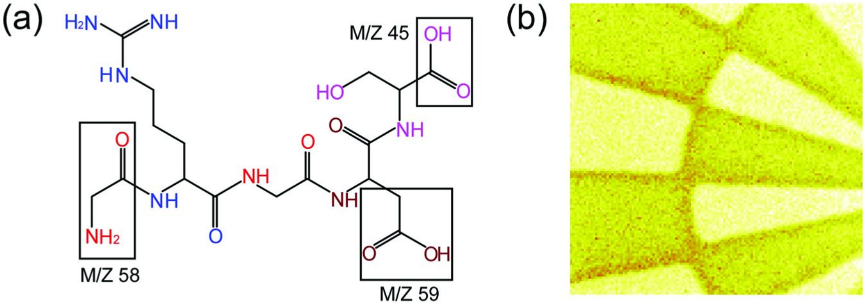

Figure 10. (a) Cell adhesion peptide RGD with characteristic TOF-SIMS fragments (boxes). (b) TOF-SIMS chemical fragment image generated from characteristic RGD fragments m/z 45 + 58 + 59, showing the ability to co-pattern RGD from solution to patterned NHS chemistry on the PEG crosslinked coating. Reproduced with permission from Ref. (49). Copyright 2008 WILEY-VCH Verlag GmbH & Co. KGaA, Weinheim.

Figure 11(a) shows that mammalian fibroblast cultures in 10% serum cannot adhere or grow on the PEG coating without adhesion peptides. Figure 11(b) shows that uniform RGD peptide immobilization to the unpatterned PEG-NHS surface endows this non-adhesive PEG chemistry with the uniform ability to adhere fibroblasts in serum-based culture. Figure 11(c) demonstrates that line patterns of various widths using photolithographically patterned NHS and bulk solution RGD modification readily adhere fibroblasts from serum-based cultures with high fidelity to these same patterns. This is consistent with the TOF-SIMS chemical image mapping also clearly showing the same RGD peptide patterning (see Figure 10) (*49*).

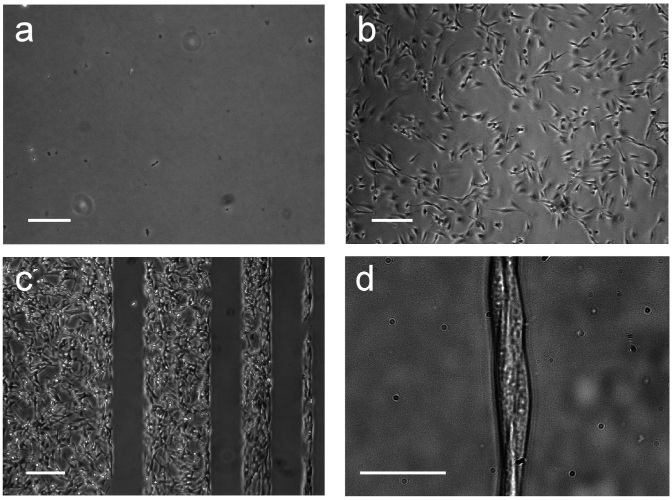

Figure 11. Phase contrast microscopic images of cultured fibroblast adhesion on RGD-patterned PEG-based surfaces in serum-containing culture at 48 h after cell seeding: unpatterned NHS-PEG coating surface without (a) and with (b) RGD peptide solution phase modification; Variable-width line RGD-immobilized peptide patterns on PEG surfaces cultured with fibroblasts (c) after 3 days of continuous serum-based cell seeding and culture; and (d) a single narrow patterned line after 15 days in serum-containing culture showing single cell-width patterns. Scale bars: (a, b, c) 200 microns, (d) 50 microns. Reproduced with permission from Ref. (49). Copyright 2008 WILEY-VCH Verlag GmbH & Co. KGaA, Weinheim.

Fibroblasts remain confined with high fidelity to these RGD patterns on the PEG hydrogel surface in continuous 10% serum-containing media to 15 days (Figure 11(d)). This performance reflects the high on-pattern peptide adhesion signal/low off-pattern background protein deposition, despite continuous competition from serum proteins (*49*). Typically, endogenous cell extracellular matrix production, proliferation and migration contribute ultimately to cell pattern failure in cultures over time within a few days (*20*, *106*, *107*). That all RGD patterns on this chemistry show no cell exit from these patterns and invasion of adjacent inert surface areas for at least 15 days after cell seeding in serum-containing media is a testament to the selective surface patterned chemical reactivity that produces cell-specific adhesion domains and non-specific binding in off-pattern areas.

7. Conclusions

Given PEG's current popularity as a chemistry of choice in diverse biotechnology and biomaterials applications, this study validates some of the practical value for a commercial chemically reactive PEG surface coating and accompanying analytical value of TOF-SIMS methods in asserting this value. TOF-SIMS methods were enabled by 1) the versatile patterning capability for reactive chemistry on this surface, and 2) the resulting on-pattern high signal, off-pattern low noise for desired modification using solution phase reagents. This signal:noise contrast for patterned surface immobilization facilitated high-fidelity co-patterning of high affinity ligands for specific proteins that demonstrated the ability to 1) producing self-sorting surfaces capable of selecting proteins immobilized to specific surface regions from mixed protein solutions by ligand selection, and 2) immobilized antibody orientational control on surfaces. TOF-SIMS chemical state imaging clearly demonstrated its utility to discriminate these patterns and validate both the approach and the operating hypothesis for controlling and monitoring surface-protein interfacial behaviors. Highly specific surface patterning and surface analysis tools for both site- and orientation selective protein immobilization is one impact. Extension of the surface patterning approach to validate surface control of subsequent interfacial events including cell and bacterial adhesion in complex physiological fluids is a second demonstrated impact. As described, these features are particularly relevant for improving *in vitro* bioassay applications in microarrays and biosensors. In addition, chemical imaging-based TOF-SIMS analysis combined with PCA can be a very useful tool to understand surface chemical reactivity including patterning and orientation of immobilized biomolecules when high signal-to-noise ratio can be specifically maintained by design.

Acknowledgments

This research was supported by the National ESCA and Surface Analysis Center for Biomedical Problems (NIH Grant EB-002027) and NIH Grant EB-001473. Note: Author DWG discloses financial interests in Accelr8 Technologies, Inc (USA), commercial vendor for one polymer coating described in this manuscript, representing a possible conflict of interest (either real or perceived).

References

1. Blawas, A. S.; Reichert, W. M. *Biomaterials* **1998**, *19*, 595–609.
2. Demers, L. M.; Ginger, D. S.; Park, S. J.; Li, Z.; Chung, S. W.; Mirkin, C. A. *Science* **2002**, *296*, 1836–1838.
3. West, J. L. *Nat. Mater.* **2011**, *10*, 727–729.
4. Christman, K. L.; Enriquez-Rios, V. D.; Maynard, H. D. *Soft Matter* **2006**, *2*, 928–939.
5. Weibel, D. B.; Diluzio, W. R.; Whitesides, G. M. *Nat. Rev. Microbiol.* **2007**, *5*, 209–218.
6. Schena, M.; Shalon, D.; Davis, R. W.; Brown, P. O. *Science* **1995**, *270*, 467–470.
7. Brown, P. O.; Botstein, D. *Nat. Genet.* **1999**, *21*, 33–37.
8. Zhu, H.; Bilgin, M.; Bangham, R.; Hall, D.; Casamayor, A.; Bertone, P.; Lan, N.; Jansen, R.; Bidlingmaier, S.; Houfek, T.; Mitchell, T.; Miller, P.; Dean, R. A.; Gerstein, M.; Snyder, M. *Science* **2001**, *293*, 2101–2105.
9. Falconnet, D.; Csucs, G.; Grandin, H. M.; Textor, M. *Biomaterials* **2006**, *27*, 3044–3063.
10. Zhu, H.; Snyder, M. *Curr. Opin. Chem. Biol.* **2003**, *7*, 55–63.
11. MacBeath, G.; Schreiber, S. L. *Science* **2000**, *289*, 1760–1763.
12. Lahiri, J.; Isaacs, L.; Tien, J.; Whitesides, G. M. *Anal. Chem.* **1999**, *71*, 777–790.
13. Wu, P.; Castner, D. G.; Grainger, D. W. *J. Biomater. Sci., Polym. Ed.* **2008**, *19*, 725–753.
14. Barbulovic-Nad, I.; Lucente, M.; Sun, Y.; Zhang, M.; Wheeler, A. R.; Bussmann, M. *Crit. Rev. Biotechnol.* **2006**, *26*, 237–259.
15. Renault, J. P.; Bernard, A.; Juncker, D.; Michel, B.; Bosshard, H. R.; Delamarche, E. *Angew. Chem., Int. Ed.* **2002**, *114*, 2426–2429.
16. Sorribas, H.; Padeste, C.; Tiefenauer, L. *Biomaterials* **2002**, *23*, 893–900.
17. Carrico, I. S.; Maskarinec, S. A.; Heilshorn, S. C.; Mock, M. L.; Liu, J. C.; Nowatzki, P. J.; Franck, C.; Ravichandran, G.; Tirrell, D. A. *J. Am. Chem. Soc.* **2007**, *129*, 4874–4875.
18. Martin, T. A.; Herman, C. T.; Limpoco, F. T.; Michael, M. C.; Potts, G. K.; Bailey, R. C. *ACS Appl. Mater. Interfaces* **2011**, *3*, 3762–3771.
19. Kane, R. S.; Takayama, S.; Ostuni, E.; Ingber, D. E.; Whitesides, G. M. *Biomaterials* **1999**, *20*, 2363–2376.
20. Rozkiewicz, D. I.; Kraan, Y.; Werten, M. W. T.; de Wolf, F. A.; Subramaniam, V.; Ravoo, B. J.; Reinhoudt, D. N. *Chem.−Eur. J.* **2006**, *12*, 6290–6297.
21. Yang, Z. P.; Chilkoti, A. *Adv. Mater.* **2000**, *12*, 413–417.
22. Tan, W.; Desai, T. A. *Tissue Eng.* **2003**, *9*, 255–267.
23. Houseman, B. T.; Gawalt, E. S.; Mrksich, M. *Langmuir* **2003**, *19*, 1522–1531.
24. Lee, C. Y.; Harbers, G. M.; Grainger, D. W.; Gamble, L. J.; Castner, D. G. *J. Am. Chem. Soc.* **2007**, *129*, 9429–9438.
25. Xu, G.; Goldberg, M. U.S. Patent 20040023367, 2004.

In Proteins at Interfaces III State of the Art 2012; Horbett, T., et al.;
ACS Symposium Series; American Chemical Society: Washington, DC, 2012.

26. Bhatia, S. N.; Balis, U. J.; Yarmush, M. L.; Toner, M. *FASEB J.* **1999**, *13*, 1883–900.
27. Khademhosseini, A.; Suh, K. Y.; Yang, J. M.; Eng, G.; Yeh, J.; Levenberg, S.; Langer, R. *Biomaterials* **2004**, *25*, 3583–3592.
28. Hui, E. E.; Bhatia, S. N. *Langmuir* **2007**, *23*, 4103–4107.
29. Tsuda, Y.; Kikuchi, A.; Yamato, M.; Chen, G.; Okano, T. *Biochem. Biophys. Res. Commun.* **2006**, *348*, 937–944.
30. Tsuda, Y.; Shimizu, T.; Yamato, M.; Kikuchi, A.; Sasagawa, T.; Sekiya, S.; Kobayashi, J.; Chen, G.; Okano, T. *Biomaterials* **2007**, *28*, 4939–4946.
31. Haab, B. B.; Dunham, M. J.; Brown, P. O. *Genome Biol.* **2001**, *2*, 0004.1–0004.13.
32. Balboni, I.; Limb, C.; Tenenbaum, J. D.; Utz, P. J. *Proteomics* **2008**, *8*, 3443–3449.
33. Gong, P.; Grainger, D. W. *Methods Mol. Biol.* **2007**, *381*, 59–92.
34. Grainger, D. W.; Greef, C. H.; Gong, P.; Lochhead, M. J. *Methods Mol. Biol.* **2007**, *381*, 37–57.
35. Harris, J. M. *Poly(ethylene glycol) chemistry : biotechnical and biomedical applications*; Plenum: New York, 1992.
36. Hoffman, A. S. *J. Biomater. Sci., Polym. Ed.* **1999**, *10*, 1011–1014.
37. Ostuni, E.; Chapman, R. G.; Holmlin, R. E.; Takayama, S.; Whitesides, G. M. *Langmuir* **2001**, *17*, 5605–5620.
38. Gombotz, W. R.; Wang, G. H.; Horbett, T. A.; Hoffman, A. S. *J. Biomed. Mater. Res.* **1991**, *25*, 1547–1562.
39. Emoto, K.; Van Alstine, J. M.; Harris, J. M. *Langmuir* **1998**, *14*, 2722–2729.
40. Lee, J. H.; Kopecek, J.; Andrade, J. D. *J. Biomed. Mater. Res.* **1989**, *23*, 351–368.
41. Huang, N. P.; Michel, R.; Voros, J.; Textor, M.; Hofer, R.; Rossi, A.; Elbert, D. L.; Hubbell, J. A.; Spencer, N. D. *Langmuir* **2001**, *17*, 489–498.
42. Mrksich, M.; Whitesides, G. M. *ACS Symp. Ser.* **1997**, *680*, 361–373.
43. Ostuni, E.; Chapman, R. G.; Liang, M. N.; Meluleni, G.; Pier, G.; Ingber, D. E.; Whitesides, G. M. *Langmuir* **2001**, *17*, 6336–6343.
44. Hermanson, G. T. *Bioconjugate Techniques*; Academic Press: London, U.K., 1996.
45. Gong, P.; Harbers, G. M.; Grainger, D. W. *Anal. Chem.* **2006**, *78*, 2342–2351.
46. Revzin, A.; Tompkins, R. G.; Toner, M. *Langmuir* **2003**, *19*, 9855–9862.
47. Metzger, S. W.; Lochhead, M. J.; Grainger, D. W. *In Vitro Diagn. Technol.* **2002**, *8*, 39–45.
48. Taylor, S.; Smith, S.; Windle, B.; Guiseppi-Elie, A. *Nucleic Acids Res.* **2003**, *31*, e87.
49. Takahashi, H.; Emoto, K.; Dubey, M.; Castner, D. G.; Grainger, D. W. *Adv. Funct. Mater.* **2008**, *18*, 2079–2088.
50. Pathak, S.; Dentinger, P. M. *Langmuir* **2003**, *19*, 1948–1950.
51. Petrou, P. S.; Chatzichristidi, M.; Douvas, A. A.; Argitis, P.; Misiakos, K.; Kakabakos, S. E. *Biosens. Bioelectron.* **2007**, *22*, 1994–2002.

52. Harbers, G. M.; Emoto, K.; Greef, C.; Metzger, S. W.; Woodward, H. N.; Mascali, J. J.; Grainger, D. W.; Lochhead, M. J. *Chem. Mater.* **2007**, *19*, 4405–4414.
53. Saldarriaga Fernandez, I. C.; van der Mei, H. C.; Lochhead, M. J.; Grainger, D. W.; Busscher, H. J. *Biomaterials* **2007**, *28*, 4105–4112.
54. Roosjen, A.; Boks, N. P.; van der Mei, H. C.; Busscher, H. J.; Norde, W. *Colloids Surf., B* **2005**, *46*, 1–6.
55. Saldarriaga Fernandez, I. C.; Mei, H. C.; Metzger, S.; Grainger, D. W.; Engelsman, A. F.; Nejadnik, M. R.; Busscher, H. J. *Acta Biomater.* **2010**, *6*, 1119–1124.
56. Castner, D. G.; Ratner, B. D. *Surf. Sci.* **2002**, *500*, 28–60.
57. Belu, A. M.; Graham, D. J.; Castner, D. G. *Biomaterials* **2003**, *24*, 3635–3653.
58. Barnes, T. J.; Kempson, I. M.; Prestidge, C. A. *Int. J. Pharm.* **2011**, *417*, 61–69.
59. Cheng, F.; Gamble, L. J.; Grainger, D. W.; Castner, D. G. *Anal. Chem.* **2007**, *79*, 8781–8788.
60. Gong, P.; Grainger, D. W. *Surf. Sci.* **2004**, *570*, 67–77.
61. Dubey, M.; Emoto, K.; Takahashi, H.; Castner, D. G.; Grainger, D. W. *Adv. Funct. Mater.* **2009**, *19*, 3046–3055.
62. Graham, D. J.; Wagner, M. S.; Castner, D. G. *Appl. Surf. Sci.* **2006**, *252*, 6860–6868.
63. Wickes, B. T.; Kim, Y.; Castner, D. G. *Surf. Interf. Anal.* **2003**, *35*, 640–648.
64. Dubey, M.; Emoto, K.; Cheng, F.; Gamble, L. J.; Takahashi, H.; Grainger, D. W.; Castner, D. G. *Surf. Interf. Anal.* **2009**, *41*, 645–652.
65. Aoyagi, S.; Kudo, M. *Biosens. Bioelectron.* **2005**, *20* (8), 1626–30.
66. Bernsmann, F.; Lawrence, N.; Hannig, M.; Ziegler, C.; Gnaser, H. *Anal. Bioanal. Chem.* **2008**, *391*, 545–554.
67. Mantus, D. S.; Ratner, B. D.; Carlson, B. A.; Moulder, J. F. *Anal. Chem.* **1993**, *65*, 1431–8.
68. Cutler, P. *Methods Mol. Biol.* **2004**, *244*, 139–49.
69. Yap, F. L.; Zhang, Y. *Biosens. Bioelectron.* **2007**, *22*, 775–88.
70. Coyer, S. R.; Garcia, A. J.; Delamarche, E. *Angew. Chem., Int. Ed.* **2007**, *46*, 6837–6840.
71. Wright, D.; Rajalingam, B.; Karp, J. M.; Selvarasah, S.; Ling, Y.; Yeh, J.; Langer, R.; Dokmeci, M. R.; Khademhosseini, A. *J. Biomed. Mater., Res. A* **2008**, *85*, 530–538.
72. Atsuta, K.; Noji, H.; Takeuchi, S. *Lab Chip* **2004**, *4*, 333–336.
73. Lee, L. M.; Heimark, R. L.; Guzman, R.; Baygents, J. C.; Zohar, Y. *Lab Chip* **2006**, *6*, 1080–1085.
74. Jang, C. H.; Stevens, B. D.; Phillips, R.; Calter, M. A.; Ducker, W. A. *Nano Lett.* **2003**, *3*, 691–694.
75. Hodneland, C. D.; Lee, Y.-S.; Min, D.-H.; Mrksich, M. *Proc. Natl. Acad. Sci. U.S.A.* **2002**, *99*, 5048–5052.
76. Urh, M.; Hartzell, D.; Mendez, J.; Klaubert, D. H.; Wood, K. *Methods Mol. Biol.* **2008**, *421*, 191–209.
77. Wagner, M. S.; Castner, D. G. *Langmuir* **2001**, *17*, 4649–4660.

78. Liu, F.; Dubey, M.; Takahashi, H.; Castner, D. G.; Grainger, D. W. *Anal. Chem.* **2010**, *82*, 2947–58.
79. de Wildt, R. M. T.; Mundy, C. R.; Gorick, B. D.; Tomlinson, I. M. *Nat. Biotechnol.* **2000**, *18*, 989–994.
80. Orosz, F.; Ovadi, J. *J. Immunol. Methods* **2002**, *270*, 155–162.
81. Berry, M. J.; Davies, J.; Smith, C. G.; Smith, I. *J. Chromatogr.* **1991**, *587*, 161–169.
82. Muronetz, V. I.; Korpela, T. *J. Chromatogr., B: Anal. Technol. Biomed. Life Sci.* **2003**, *790*, 53–66.
83. Chan, C. P.; Sum, K. W.; Cheung, K. Y.; Glatz, J. F.; Sanderson, J. E.; Hempel, A.; Lehmann, M.; Renneberg, I.; Renneberg, R. *J. Immunol. Methods* **2003**, *279*, 91–100.
84. Saengjaruk, P.; Chaicumpa, W.; Watt, G.; Bunyaraksyotin, G.; Wuthiekanun, V.; Tapchaisri, P.; Sittinont, C.; Panaphut, T.; Tomanakan, K.; Sakolvaree, Y.; Chongsa-Nguan, M.; Mahakunkijcharoen, Y.; Kalambaheti, T.; Naigowit, P.; Wambangco, M. A.; Kurazono, H.; Hayashi, H. *J. Clin. Microbiol.* **2002**, *40*, 480–489.
85. Peluso, P.; Wilson, D. S.; Do, D.; Tran, H.; Venkatasubbaiah, M.; Quincy, D.; Heidecker, B.; Poindexter, K.; Tolani, N.; Phelan, M.; Witte, K.; Jung, L. S.; Wagner, P.; Nock, S. *Anal. Biochem.* **2003**, *312*, 113–124.
86. Kato, K.; Toda, M.; Iwata, H. *Biomaterials* **2007**, *28*, 1289–1297.
87. D'Orazio, P. *Clin. Chim. Acta* **2003**, *334*, 41–69.
88. Spitznagel, T. M.; Clark, D. S. *Biotechnology (N.Y.)* **1993**, *11*, 825–829.
89. Ahmed, S. R.; Kelly, A. B.; Barbari, T. A. *J. Membr. Sci.* **2006**, *280*, 553–559.
90. Hurst, R.; Hook, B.; Slater, M. R.; Hartnett, J.; Storts, D. R.; Nath, N. *Anal. Biochem.* **2009**, *392*, 45–53.
91. Ogi, H.; Motohisa, K.; Hatanaka, K.; Ohmori, T.; Hirao, M.; Nishiyama, M. *Biosens. Bioelectron.* **2007**, *22*, 3238–3242.
92. Lee, W.; Oh, B. K.; Bae, Y. M.; Paek, S. H.; Lee, W. H.; Choi, J. W. *Biosens. Bioelectron.* **2003**, *19*, 185–192.
93. Jung, Y.; Lee, J. M.; Jung, H.; Chung, B. H. *Anal. Chem.* **2007**, *79*, 6534–6541.
94. Ahlers, M.; Grainger, D. W.; Herron, J. N.; Lim, K.; Ringsdorf, H.; Salesse, C. *Biophys. J.* **1992**, *63*, 823–838.
95. Tyler, B. J.; Rayal, G.; Castner, D. G. *Biomaterials* **2007**, *28*, 2412–2423.
96. Wagner, M. S.; Castner, D. G. *Appl. Surf. Sci.* **2004**, *231-2*, 366–376.
97. Xia, N.; May, C. J.; McArthur, S. L.; Castner, D. G. *Langmuir* **2002**, *18*, 4090–4097.
98. Wang, H.; Castner, D. G.; Ratner, B. D.; Jiang, S. Y. *Langmuir* **2004**, *20*, 1877–1887.
99. Bilitewski, U. *Anal. Chim. Acta* **2006**, *568*, 232–247.
100. Tidwell, C. D.; Castner, D. G.; Golledge, S. L.; Ratner, B. D.; Meyer, K.; Hagenhoff, B.; Benninghoven, A. *Surf. Interface Anal.* **2001**, *31*, 724–733.
101. Mei, Y.; Cannizzaro, C.; Park, H.; Xu, Q.; Bogatyrev, S. R.; Yi, K.; Goldman, N.; Langer, R.; Anderson, D. G. *Small* **2008**, *4*, 1600–1604.

102. Usui, K.; Tomizaki, K.-y.; Ohyama, T.; Nokihara, K.; Mihara, H. *Mol. BioSyst.* **2006**, *2*, 113–121.
103. Antohe, B. V.; Cooley, P. W. *Methods Mol. Biol.* **2007**, *381*, 299–312.
104. Mrksich, M. *Chem. Soc. Rev.* **2000**, *29*, 267–273.
105. Houseman, B. T.; Mrksich, M. *Biomaterials* **2001**, *22*, 943–955.
106. Sharma, S.; Tan, W.; Desai, T. A. *Bioconjugate Chem.* **2005**, *16*, 18–22.
107. Luk, Y. Y.; Kato, M.; Mrksich, M. *Langmuir* **2000**, *16*, 9604–9608.

Chapter 37

Proteomic Approaches To Characterize Surface-Bound Proteins and Material-Mediated Cellular Proteins

Yao Fu[1] and Weiyuan John Kao*[,1,2,3]

[1]School of Pharmacy, School of Medicine and Public Health,
University of Wisconsin-Madison, Madison, Wisconsin 53705
[2]Department of Biomedical Engineering, College of
Engineering, and School of Medicine and Public Health,
University of Wisconsin-Madison, Madison, Wisconsin 53705
[3]Department of Surgery, School of Medicine and Public Health,
University of Wisconsin-Madison, Madison, Wisconsin 53705
***E-mail: wjkao@pharmacy.wisc.edu**

Proteins at the biomaterial interface include surface-adsorbed proteins and soluble proteins secreted by cells adherent or attached to biomaterial interfaces. These proteins carry multiple functions such as directing cell adhesion, proliferation, differentiation, and migration. The identification of proteins at the material interface will help elucidate the impact of proteins in mediating cell-material interaction, host response, and cell signaling pathway. The aim of this chapter is to provide an overview of the application of proteomic tools to analyze proteins at the material interface. Two main analytical methods, protein microarrays and mass spectrometry (MS), have been reviewed and their applications in proteomic study of biomaterial-related proteins were discussed in case studies. In sum, proteomics provides a viable approach to survey global proteome of surface-adsorbed proteins and soluble proteins from adherent cells at the biomaterial interface.

In Proteins at Interfaces III State of the Art 2012; Horbett, T., et al.;
ACS Symposium Series; American Chemical Society: Washington, DC, 2012.

Introduction

Early works on protein adsorption onto synthetic surfaces can be traced back to the 1930s (*1*). In the 1960s, Dr Vroman and his colleagues observed that the adsorption and desorption of serum proteins onto material surfaces followed a sequential and competitive process using ellipsometry methods (*2–5*). The initial adsorbed proteins such as fibrinogen were replaced by high molecular weight kininogen of higher affinity to the material surface in a time- and concentration- dependent fashion. Proteins at the biomaterial interface carry multiple functions such as directing cell adhesion, proliferation, differentiation, and migration. However, the adsorbed proteins may undergo structural changes (*6–8*), which may impact the subsequent cellular responses to the biomaterial. As such, materials that displayed a low degree of conformational changes (*i.e.*, secondary structure changes) of adsorbed proteins and a low platelet adhesion are considered better candidates for blood-contacting biomedical devices (*9*). Bacteria adhesion onto material surfaces is also mediated by adsorbed proteins such as fibrinogen and vitronectin (*10*). Thus, controlling the non-specific adsorption of proteins is of crucial importance for the development of non-fouling medical devices (*11*). Moreover, studies showed natural killer (NK) cell-mediated mesenchymal stem/stromal cell (MSC) recruitment was modulated by fibrinogen adsorption. Thus, the incorporation of pro-inflammatory proteins such as fibrinogen into biomaterials was conducted to facilitate the rational modulation of the inflammatory response and stem cell recruitment in regulating tissue repair and regeneration (*12*). In addition to adsorbed proteins, soluble proteins that are secreted from adherent cells on the biomaterial surface also play an important role in directing cellular responses to the material. Macrophages for instance are one of the key players in the host inflammatory response to implanted biomaterials. Our studies revealed the effect of surface-adsorbed proteins on the intracellular protein expression in adherent macrophages, providing insights into the intracellular signaling pathways mediated by different surface adsorbed ligands through extracellular matrix (ECM)-integrin interactions (*13*). Therefore, detailed analysis of proteins at the material interface will help elucidate the impact of proteins in mediating cell-material interaction, host response, and cell signaling pathway.

Traditional analytical methods for proteins include ellipsometry, gel electrophoresis, Fourier transform infrared spectroscopy (FT-IR), spectrophotometry, nuclear magnetic resonance (NMR), western blot, immunoprecipitation, and immunostaining. These methods can be divided into two groups: i) qualitative methods that provide composition, molecular weight and structural information, *e.g.*, western blot, ellipsometry, FT-IR, NMR, immunoprecipitation, immunostaining, immunoblotting; and ii) quantitative methods that determine the concentration of proteins, *e.g.*, spectroscopic methods, colorimetry, radiolabeling of proteins, and reversed phase high performance liquid chromatography (RP-HPLC). For these analytical methods, *a priori* knowledge of the proteins under investigation is usually required. Thus, identifying and quantifying unknown proteins using these aforementioned analytical methods is difficult and cannot be carried out efficiently in a large scale. The emergence and development of mass spectrometry (MS) provides a powerful tool to characterize and sequence proteins without *a priori* knowledge of the protein identity (*14*). This leads to the burgeoning of a novel research field - proteomics. The term proteome was first mentioned by Marc Wilkins in 1994 in a symposium on “2D Electrophoresis: from protein maps to genomes” (*15*). Gygi and Aebersold defined proteomics as “the ability to systematically identify every protein expressed in a cell or tissue as well as to determine the salient properties of each protein such as abundance, state of modification, and involvement in multiprotein complexes” (*16*). The system-wide study of proteins thus provides an integrated understanding of biological systems (*17*). Its high throughput screening capability has found broad applications in the identification of biomarkers for diseases and drugs (*18*). Therefore, using proteomics to study proteins at the material interface may help identify important biomarkers in mediating cell-material interactions. In general, two types of proteomic analysis are involved: quantitative and functional proteomics. Specifically, a quantitative ‘proteomic analysis’ may involve measuring the abundance, modification, activity, localization and interaction of all proteins in a sample (*19*). While a functional proteomics aims to seek functional proteins that are involved in identifying putative substrates for enzymes or putative interactions between proteins (*19*).

The aim of this chapter is to provide an overview of the application of proteomic tools to analyze proteins at the material interface. Protein microarrays and MS are the two main analytical methods that are extensively used. Proteins at the interface can be classified into surface-adsorbed proteins and soluble cellular proteins, and case studies for each will be provided. The challenges and limitations with current technologies in biomaterial applications will also be commented.

Proteomics and Protein Analytical Technologies

Protein Microarrays

A protein microarray is an affinity-based multiplex approach to identify protein-protein interactions. A microarray comprises different affinity antibodies arrayed at high spatial density on a solid support (*19*). Through specific binding interactions, each antibody captures its target protein from a complex mixture, and the captured proteins are subsequently detected and quantified (*19*). Briefly, protein microarrays can be classified into target microarrays, reverse phase protein arrays (RPP), and *in situ* expressed arrays (*20*). Two immunoassays that are commonly used in the targeted protein microarray technology are: (i) sandwich immunoassay where a primary antibody is immobilized on the solid substrate and a second labeled antibody is required for detection; (ii) antigen capture assay where an antibody is immobilized on the solid substrate and prelabeled proteins are used for detection. Such approaches are effective in determining protein expression levels, *i.e.*, protein profiling. However, major drawbacks with target arrays include the cross-reactivity and the loss of antibody activity upon immobilization (*20*). The RPP array is a direct assay that does not require primary antibody immobilization, but allows target proteins to be adsorbed and then are subjected to specific antibody binding for detection. The RPP approach has been applied to the study of post-translational modifications and signal transductions *ex vivo* (*20*). Recently, protein microarrays can be fabricated through *in situ* cell-free synthesis directly from corresponding DNA arrays. The *in situ* protein array format is mainly based on cell-free eukaryotic expression systems such as *Escherichia coli* 30s, rabbit reticulocyte lysates and wheat germ extracts (*20*, *21*). Regarding content for protein *in situ* arrays, a library of open reading frames (ORFs) is required (*20*). Many different *in situ* protein arrays have been developed recently to improve the protein availability and long term storage, for example: Protein *in situ* arrays (PISA) arrays (*22*), printing protein arrays from DNA (DAPA) arrays and nucleic acids programmable protein arrays (NAPPA) arrays (*23*).

Advantages with protein microarray technologies include high sensitivity, small sample volume, and high screening capability. Arrays fabricated at a high density can ensure simultaneous analysis of large numbers of immobilized proteins in a time- and cost-effective manner (*24*). Recently, the production of large collections of pure recombinant proteins can be achieved *via in situ* cell free approaches. One limitation with this technology is the competing binding from proteins of high abundance that may prevent binding of target proteins of very low abundance. Protein concentrations in biological samples display a broad dynamic range by a factor of 10^8 - 10^{10} (*25*, *26*), which presents an analytical challenge on developing robust methods for protein identification and quantification. Thus, pretreatment of biological samples is often required to separate and enrich proteins of low abundance for proteomic study. Method sensitivity is another limitation. Protein microarrays rely on signal amplification strategies to reach sensitivity levels for application, and common amplification methods include quantum dots, fluorescence and colorimetric signals (*27*, *28*). The sensitivity is thus affected by the complex components in the biologic samples. For example, biotin, peroxidases, alkaline phosphatases, fluorescent proteins, and immunoglobulins may substantially reduce the yield of amplification reactions (*25*).

MS Technology

MS technology is one of the most important developments in Anal. Chem. of the 20th century. MS is a highly sensitive analytical technique that has been successfully applied to analyze complex protein samples. An MS system is comprised of three major components: an ion source, a mass analyzer and a detector. MS is based upon detecting charged ions in the gas phase thus allowing the calculation of the overall molecular weight (*13*). Electrospray ionization (ESI) and matrix-assisted laser desorption/ionization (MALDI) are the two most commonly used ionization methods in MS measurements and both are considered as "soft" ionization methods that minimize protein or peptide degradation (*13*). ESI ionizes analytes in solution that can be coupled on-line to liquid chromatographic separation systems (LC), while MALDI ionizes samples from a dry, crystalline matrix *via* laser pulses (*29*, *30*). ESI-MS is usually used for the analysis of more complex samples, and MALDI-MS has been applied to analyze relatively simple peptides (*29*). ESI instruments coupled with LC systems (LC/MS) provide a good resolution of complex peptide mixtures before ionization. In addition, two-dimensional gel electrophoresis, a highly resolving separation technique, is also used to fractionate protein mixtures prior to MS analysis (*31*). As for mass analyzers, four basic types currently in use are: ion trap, time-of-flight (TOF), quadrupole, and Fourier transform ion cyclotron (FT-MS) analyzers. Often, an ion trap analyzer is included in the ESI to capture specific peptide ions by collision-induced dissociation (CID) with an inert gas (*32*). CID enables compilation of detailed peptide sequence data (*33*). Each has its advantages and disadvantages, and therefore can be used independently or together (Table I). Although MALDI-MS cannot be used to sequence peptides directly, it allows rapid and sensitive analysis of peptide masses (*13*). MALDI coupled to TOF analyzers (MALDI-TOF) is usually used to measure intact peptides. Due to its excellent mass accuracy, high resolution and sensitivity, peptide mass mapping/fingerprinting *via* MALDI-TOF can be used to identify proteins. For peptide sequencing purposes, CID tandem mass-based spectrometry is frequently used in proteomics. In MS-based proteomics studies, two methods in use are the “bottom-up” and “top-down” strategies. The “bottom-up” strategy identifies and characterizes proteins by proteolytic and enzymatic digestion of proteins prior to MS analysis, which is now commonly used to identify protein localization, expression, and modifications (*34–36*). A technique, known as “shotgun proteomics”, is a method using high performance liquid chromatography (HPLC) coupled with MS or tandem MS to identify proteins (*37*). Usually, proteins in complex biological mixtures are digested into a collection of peptides and subjected to LC/MS/MS analysis. In contrast, the “top-down” strategy uses an ion trapping mass spectrometer to store an isolated protein ion for mass measurement and tandem MS analysis (*38*, *39*). Unlike bottom-up methods using proteolytic digestion, protein fragmentation is accomplished *via* gas phase dissociation in the “top-down” approach. Thus, the “top-down” approach is a direct profiling method to identify and characterize proteins that provides critical information such as protein post-translational modifications, which might be obscured by shotgun digestion of a complex protein mixture (*39*). However, the application of top-down strategy is largely limited by instrument, *e.g.*, sensitivity and the broad dynamic range. Using ESI and MALDI, protein standards were analyzed with ultrahigh sensitivity and fast acquisition of fragmentation data, but wild-type proteins were proven difficult to be analyzed (*39*, *40*).

Overall procedures for a MS-based proteomic study include sample collection, purification, separation, MS analysis, generation of an identified peptide list, and protein identification *via* matching with sequence database. Samples that are commonly used in proteomic studies are cell lysates and tissue homogenates that have complex components. Sample pretreatment thus provides a mean to reduce the complexity of the sample proteome and to decrease the dynamic range (*41*). The two main purposes of sample pretreatment for MS analysis are: (i) purification, to remove interfering components; (ii) enrichment, to increase the concentration of the target analyte that is of low abundance. For cell lysates, tissue fluids, or other biological samples, they may contain non-proteinaceous compounds which may interfere with downstream procedures (*42*). Thus, proteins need to be extracted from the crude biological sample.

A common procedure is desalting, which can be accomplished *via* dialysis, ultrafitration, gel filtration or electrophoresis, precipitation with acids or organic solvents, or solid-phase extraction (*43*). Organic solvents used for protein precipitation include acetone, trichloroacetic acid (TCA), ethanol, isopropanol, chloroform/methanol, and ammonium sulfate (*44*). Following extraction, proteins are fractionated before being subjected to MS analysis. In general, protein fractionation can be performed at either protein or peptide level. At the protein level, pre-fractionation of proteins *via* chromatographic methods or gel electrophoresis can help reduce the complexity of the sample (*41*, *45*). Removing proteins of high abundance may also improve the detection sensitivity for proteins of low abundance (*45*, *46*). For peptide-level pretreatment methods, fractionated peptides can be generated *via* proteolytic digestion. Furthermore, representative peptides containing rare amino acids or terminal peptides can be enriched *via* pre-fractionation approaches. For examples, cysteine (Cys) containing peptides can be isolated using Cys-specific tags that can specifically react with the thiol group of Cys, *e.g.*, isotope-coded affinity tag (ICAT) (*47*). The Methionine (Met) containing peptides were isolated and enriched *via* covalently binding to Met-specific beads containing bromoacetyl functional groups (*48*). A specific tagging method was developed for selectively enriching peptides containing tryptophan (Trp) (*49*). Besides amino acid-specific tagging methods, immobilized metal affinity chromatography (IMAC), metal oxide, ion-exchange chromatography, chip-based methods, chemical modifications, and centrifugal ultrafiltration have been used for peptide enrichment (*41*). For example, histidine (His) containing peptides were enriched from complex peptide mixtures using (IMAC) loaded with copper II (Cu^{2+}) (*50*). To sum up, the aforementioned pretreatment methods are efficient approaches to isolate and to fractionate target peptides of interests. However, it is critical to select a pretreatment method that can reduce the sample complexity yet retain the integrity of the proteome for the subsequent proteomic analysis.

Table I. Comparison of four basic mass analyzers (*16*, *29*)

Mass analyzer	*Advantages*	*Disadvantages*	*Upper mass range (m/z)*
The ion trap	Robust, sensitive, inexpensive, medium resolution, well-suited for tandem mass spectrometry	Low mass accuracy, limited mass range	2000
Time-of-flight (TOF)	High sensitivity, mass accuracy, resolution, fast scan speed, adaptation to MALDI	Low resolution, difficulty of adaptation to ESI	Unlimited

Continued on next page.

Table I. (Continued). Comparison of four basic mass analyzers (*16*, *29*)

Mass analyzer	*Advantages*	*Disadvantages*	*Upper mass range (m/z)*
Quadrupole	High pressure-tolerant, ease of switching between positive/negative ions, small size	Poor adaptability to MALDI	4000
Fourier transform ion cyclotron resonance mass spectrometer (FT-MS)	High sensitivity, mass accuracy, resolution and dynamic range, well-suited for tandem mass spectrometry	High cost, operational complexity, low peptide-fragmentation efficiency	10,000

Proteomic Studies of Proteins at Biomaterial Interfaces

Protein adsorption has long been a subject of interest to researchers in the biomaterial field. Traditionally, SDS-PAGE, radiolabeling, and Western blot were approaches extensively used to study protein adsorption on materials for biomedical applications including Cuprophane dialysis membranes and hemodialyzers (*51–53*). With the rapid development in the analytical technique, more and more proteomic studies on proteins at the biomaterial interface have been reported. A thorough discussion was given by Elbert DL regarding the unbiased approaches to study protein adsorption before and after the field of proteomics emerged (*54*). Power KA *et al* discussed the application of proteomic technology to biomaterials when providing leading opinions on examination of cell-host-biomaterial interactions *via* high-throughput technologies (*55*). Griesser HJ *et al* presented a good review on surface-MALDI-MS in biomaterials research demonstrating its potency as a powerful tool to analyze surface-adsorbed proteins in biomaterials (*56*). In the following sections, proteomic studies on surface-associated proteins and soluble proteins at the biomaterial interface are reviewed. These studies generated some viable approaches on how to identify proteins and to elucidate the roles of specific protein biomarkers in implementing cell adhesion, cell activation post-adhesion, and intracellular signaling pathways involved in cell-material interaction.

Surface-Associated Proteins

It is well appreciated that serum proteins adsorbed on blood-contacting biomaterials play a key role in mediating cell adhesion, activation, and thrombosis and affecting the outcome of host responses to materials (*14*, *57*). The surface adsorption of albumin, complement components, vitronectin, and fibrinogen onto various polymer-based substrates have been extensively studied (*58–61*). Material composition, surface properties such as hydrophobicity and ion charges, protein structure and the competitive adsorption amongst proteins are deemed major factors that impact protein adsorption isotherm (*14*). Using proteomic analysis, complete adsorbed serum proteome information can be generated to provide insights into the material blood compatibility and further benefit the development of materials.

Wang X *et al* applied MS-based proteomics to study serum protein adsorption/absorption and complement C3 activation of poly(ethylene glycol) (PEG) hydrogels (*14*). PEG, a hydrophilic linear polymer, is well known for its "non-fouling" and low protein adsorption properties. It is widely used in surface modifications to increase material surface hydrophilicity and improve material biocompatibility. Primary human monocytes were found to adhere onto PEG hydrogel surfaces, and considered to be mediated by serum protein adsorption (*62*). Thus, a thorough understanding of the adsorbed proteome on PEG hydrogels will provide significant insights into the mechanisms of the observed cellular behavior. In this study, human serum was collected from human blood and subjected to fractionation using PEG (4 kDa) to reduce proteins of high abundance, *e.g.*, albumin. Distribution of plasma proteins using PEG fractionation method was shown in Table II.

Table II. Distribution of human serum proteins in PEG fractionsas determined by ELISA[*]

Serum protein	***Protein distribution (%)***		
	Fraction I (0-10% PEG)	*Fraction II (10-20% PEG)*	*Fraction III (20% PEG)*
Albumin	13.4 ± 3.7	16.5 ± 4.6	70.1 ± 4.2
Thrombin	43.1 ± 6.1	51.2 ± 10.4	5.8 ± 5.0
Fibrinogen	98.3 ± 9.0	1.3 ± 0.3	0.4 ± 0.3
Complement C3	99.7 ±1.5	0.3 ± 0.0	0.1 ± 0.0
Vitronectin	31.1± 0.7	38.0 ± 0.7	30.9 ± 0.5

[*] Reproduced with permission from reference (*14*). Copyright 2011 Taylor & Francis.

The procedures for serum protein adsorption study and MS analysis are shown in Figure 1. Based upon these procedures, different spectra of adsorbed proteins between PEG hydrogels and tissue culture polystyrene surface (TCPS) *via* MALDI-MS were generated (Table III). Using fractionated serum, the number of albumin hits on TCPS was lower compared to samples treated with whole serum. Vitronectin, fibrinogen and thrombin were demonstrated with top scores on TCPS incubated with fractionated serum. In contrast, a low number of hits for these proteins was observed for TCPS treated with whole serum due to the presence of albumin. However, PEG hydrogels incubated with fractionated serum displayed a high number of hits for albumin, and no vitronectin or thrombin was detected, indicating the adsorption of vitronectin and thrombin was inhibited by PEG hydrogels. In addition, the detection of α_2-macroglobulin and α_1-acid glycoprotein 1 on PEG hydrogels further demonstrated that the lectin pathway could be involved in the macrophage response to PEG (*63*), which is in accordance with literature. The presence of serum amyloid P component on PEG hydrogels suggests the classic complement pathway (*64*). However, the presence of complement factor C3 was not detected in MALDI-MS results, which is most likely due to the low abundance of the adsorbed C3 protein and the relatively low affinity of C3 to TCPS and PEG hydrogels. Thus, the adsorption of vitronectin, thrombin, fibrinogen and complement factor C3 was further verified by enzyme linked immunosorbent assay (ELISA).

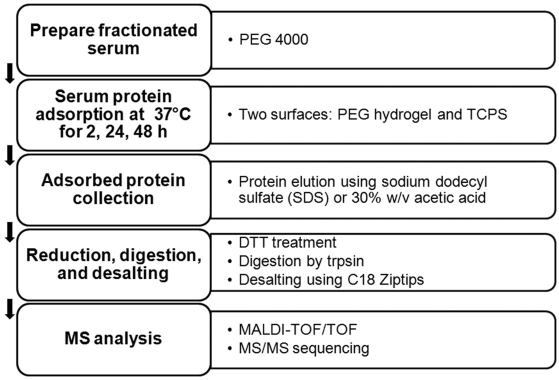
Prepare fractionated serum
• PEG 4000
Serum protein adsorption at 37°C for 2, 24, 48 h
• Two surfaces: PEG hydrogel and TCPS
Adsorbed protein collection
• Protein elution using sodium dodecyl sulfate (SDS) or 30% w/v acetic acid
Reduction, digestion, and desalting
• DTT treatment
• Digestion by trpsin
• Desalting using C18 Ziptips
MS analysis
• MALDI-TOF/TOF
• MS/MS sequencing

Figure 1. Schematic procedures for serum protein adsorption study via MS based proteomics. Adapted from reference (14).

Oughlis S *et al* developed a similar proteomic method to study protein adsorption on titanium (Ti) grafted with poly(sodium styrene sulfonate) (polyNaSS), which utilized 2D gel electrophoresis coupled with MS to analyze adsorbed proteins on various surfaces (*65*). Platelets rich plasma (PRP) sample was used to study protein adsorption on various titanium materials and the adsorption experiment was conducted using an affinity chromatography set-up. Specifically, various Ti-based granules were packed into columns and equilibrated with phosphate buffer saline (PBS, pH 7.4). PRP samples were first loaded and allowed to pass through the column at a flow rate of 0.3 mL/min. UV absorbance of the mobile phase was monitored at the wavelength of 280 nm. The column was then washed with PBS until stable baseline was observed. To elute the adsorbed proteins, PBS containing 3M sodium chloride (NaCl) was then used as the mobile phase. The results showed polyNaSS grafted Ti phase displayed two peaks corresponding to the flowthrough and the eluate, while non-grafted Ti phase displayed one peak corresponding to the flowthrough (Figure 2). The eluted protein fractions were further subjected to 2D gel electrophoresis and LC/MS/MS analysis (Figure 3). The results demonstrated the grafted polyNaSS/Ti surface had a higher level of protein adsorption than un-grafted titanium. The selective adsorption of complement factor B and serum albumin onto polyNaSS/Ti surface were not affected by high abundance plasma proteins such as immunoglobulin G (IgG) and α1 antitrypsin.

Table III. Comparison of adsorbed proteins on PEG hydrogel (3400 Da) and TCPS incubated with fractionated (Fraction I+II) and whole human serum. (Reproduced with permission from reference (*14*). Copyright 2011 Taylor & Francis.)

Substrate	0.2% SDS			30% Acetic acid			No elution		
	Protein	**Accession number**	**No. of hits**	**Protein**	**Accession number**	**No. of hits**	**Protein**	**Accession number**	**No. of hits**
PEG hydrogel [a]	Albumin	gi|11493459 gi|168988718 gi|31615331 gi|122920512 gi|3212456 gi|158258947 gi|119626071 gi|4502027 gi|28592 gi|178345	30	Fibrinogen	gi|2781209 gi|119625310 gi|223170 gi|119625326 gi|78395029 gi|119625339 gi|220702427 gi|2781208 gi|119625338 gi|119625340 gi|300313	27	Albumin	gi|119626065 gi|11493459 gi|168988718 gi|3212456 gi|122920512 gi|763431	11
	Fibrinogen	gi|119625340 gi|2781208 gi|70906435 gi|78395029 gi|119625342 gi|220702427 gi|182439	17	Fibrinogen precursor	gi|70906437 gi|70906439 gi|70906435 gi|182430 gi|4503689 gi|182424	6	Fibrinogen precursor	gi|182424 gi|13591823 gi|4503689	3
	Fibrin	gi|223002 gi|159795715	2	Fibrin	gi|223002 gi|223057 gi|159795715 gi|28373950	4	Fibrin	gi|223057	1
	Immunoglobulin	gi|21669337 gi|229526	2				Fibrinogen	gi|300313	1
	Alpha2-macroglobulin	gi|224053	1						
	Phosphatidylserine-binding phosphoprotein	gi|107288	1						
	serum amyloid P component precursor	gi|4502133	1						
	syntaxin 11	gi|3248918	1						
	0.2% SDS			1% SDS			No elution		
	Protein	**Accession number**	**No. of hits**	**Protein**	**Accession number**	**No. of hits**	**Protein**	**Accession number**	**No. of hits**
TCPS [b]	Albumin	gi|168988718 gi|11493459 gi|119626071 gi|27692693 gi|78101694 gi|62113341 gi|119626074 gi|3212456 gi|6650826	22	Immunoglobulin	gi|184747 gi|229601 gi|21757089 gi|21757086 gi|2765421 gi|29726970 gi|20664303 gi|49065860 gi|23683338 gi|19717684	52	Albumin	gi|168988718 gi|31615331 gi|28592 gi|122920512 gi|3212456 gi|178345 gi|4502027 gi|62113341 gi|23307793	36
	Fibrinogen	gi|223170 gi|47168756 gi|2781209 gi|119389654 gi|119625310	12	Albumin	gi|189054552	1	Vitronectin	gi|13477169 gi|36575 gi|36573 gi|221042224	4
	Immunoglobulin	gi|1799560 gi|50301691 gi|33319302 gi|17902604 gi|17902616	7	Fibrinogen	gi|4503689	1	Thrombin	gi|118137345 gi|11514286 gi|34810002 gi|6980506	4
	Tigger transposable element derived 3	gi|23312394	1	Fibrin	gi|223002 gi|28373950	2	Kininogen	gi|4504893 gi|62898910 gi|156231037	3
	Haptoglobin preproprotein	gi|186910296	1	Haptoglobin preproprotein	gi|186910296	1	Fibrinogen	gi|300313 gi|2781209	2
	Zinc finger protein	gi|111306532	1	serum amyloid P component precursor	gi|4502133	1	Heat shock protein 60	gi|77702086	1
	Thyroid receptor interactor	gi|703108	1	Golgi phosphoprotein	gi|11545859	1	Nck-2	gi|3930217	1
	Heat shock protein 60	gi|77702086	1	Thyroid receptor interactor	gi|703108	1	Cytosolic phosphoprotein DP58	gi|119616263	1
	Nck-2	gi|3930217	1	Host cell factor 1	gi|98986457	1	Fibrin	gi|223002	1
				Heat shock protein 60	gi|77702086	1	p51 isoform delNdelta	gi|7248452	1
				Nck-2	gi|3930217	1	Nestin	gi|119573309	1
				Vitronectin precursor	gi|88853069	1	Syntaxin 11	gi|3248918	1

[a] PEG hydrogels (3,400 Da) were incubated 2 hours with DMEM supplemented with 10% fractionated (Fraction I+II) human serum, and proteins were eluted by 0.2% SDS or 30% acetic acid followed by urea/DTT denaturation.

[b] TCPS samples were prepared by incubating with DMEM supplemented with 10% whole human serum for 24 hours, and proteins were eluted by 0.2% SDS or 1% SDS followed by urea/DTT denaturation. Sample without elution of proteins and denatured by urea/DTT directly served as control.

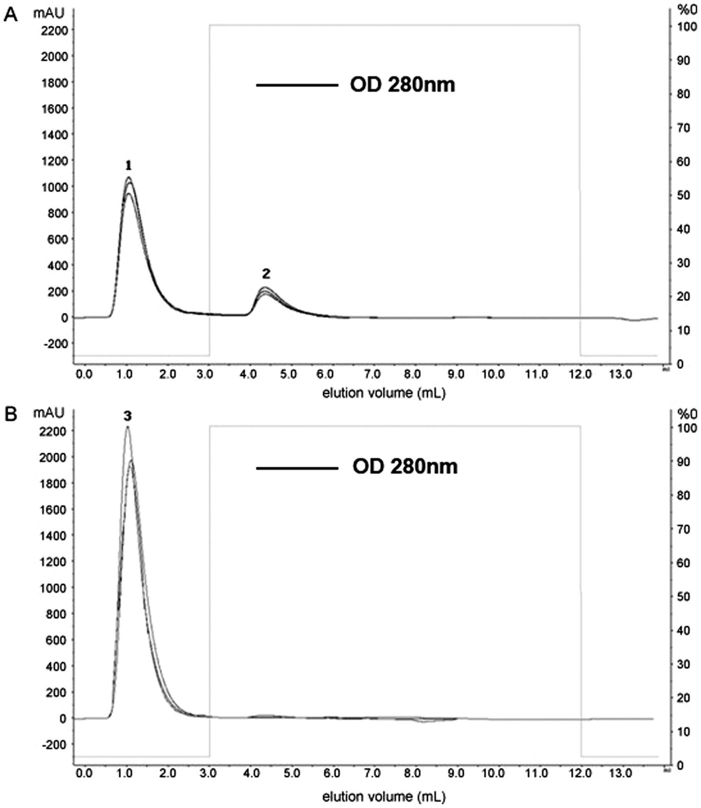

Figure 2. Affinity chromatography profiles. Separation of PRP proteins on NaSS/Ti column (A) or TiOx column (B) equilibrated with PBS pH 7.4 at a flow rate of 0.3 mL/min. Peaks are assigned as followed: 1, 3. flowthrough, and 2. eluate. (Reproduced with permission from reference (65). Copyright 2011 Elsevier.)

To evaluate protein adsorption in a physiology-relevant condition, adherent cells should unarguably be included in the experimental setup. The extracellular matrix (ECM) mainly functions as the supporting substrates for cell adhesion, growth and proliferation, which is composed of collagen fibers, elastin fibers, glycosaminoglycans (GAGs), and water. ECM is involved in directing extensive cell-cell and cell-matrix interactions. Thus, it is of great significance to characterize ECM components at the cell-biomaterial interface both qualitatively and quantitatively. Regarding cell-material interactions, the adherence surface (AS) is defined as a biochemical structure present at the cell-material interface (*66*). AS is composed of the basal plasma membrane with associated structures such as the ECM on one side and the focal adherence complexes on the other, which mediates the communication of mechanical and tectonic signals from the material to the biochemical transducers in the cells (*66*). The AS of mammalian cells can be isolated using techniques such as wet cleaving (*67*), sonication (*68*), controlled lysis squirting (*69*), isolation on poly(L-lysine)-coated beads (*70*), and sandwiching (*71*, *72*). Derhami *et al* conducted some interesting proteomic studies on skin fibroblasts grown on titanium substrates (*73*, *74*). In their study, human skin fibroblasts adhered to titanium substrates. The AS material was thus obtained after detachment of fibroblasts which represented the remnants of focal adhesions. A proteomic analysis was then conducted using 2D-PAGE combined with MALDI-MS. A total of 40 proteins were identified and several proteins such as albumin, α2-HS-glycoprotein, α-fetoprotein, plasminogen, thrombospondin 1, and serotransferrin were found to adsorb onto titanium substrates in relatively high concentrations as compared to TCPS. Tong W *et al* developed a method that can achieve large-scale isolation of AS and a quantitative proteomic method to characterize the Madin-Darby canine kidney cell (MDCK)-biomaterial interface (*66*). Their study provided a robust method to enrich extracellular matrix proteins, membrane and stress fiber proteins from the adherence surface (AS). Specifically, the AS purification was conducted as shown in Figure 4.

1D gel electrophoresis and LC/MS/MS were used to separate and characterize proteins enriched in the AS preparation. Stable isotope labeling with amino acids in cell culture (SILAC) is a metabolic labeling technique to quantify and compare proteome changes between biological samples (*75*). Two isotopes, SILAC "heavy" R6 K4 and "light" R0 K0, generated peptides labeled with isotopes of different intensities. The intensity ratio between each heavy isotope-labeled peptide and its light isotope counterpart could be measured. A total of 3478 unique peptide and 204 proteins were identified in the study. SILAC ratio was further used to classify proteins into AS-associated and non-AS associated proteins. The results showed proteins enriched in the AS at cell-biomaterial interfaces were classic ECM proteins such as laminin and fibronectin. Proteins that regulate cell adhesion and motility were also identified, *e.g.*, the chondroitin sulfate proteoglycan and nebulin.

Backovic A *et al* selected silicone as the material platform to study surface-adsorbed proteins both *in vitro* and *in vivo* (*76*). Protein identification was conducted with MS analysis, database matching, and Western blots. Silicone implant samples were collected from patients undergoing implant replacements or removal. Explanted silicone implants were washed with PBS and water at 4°C, and eluted in buffer solutions for appropriate downstream analyses. Proteins eluted were primarily analyzed by 2D gel electrophoresis. Spots of interest were then excised, proteins were digested with trypsin and analyzed by MALDI-TOF and LIFT-TOF/TOF MS/MS. A total number of 30 most abundant proteins was identified on the surface of silicone. The study provided significant insights into protein adherence to implanted silicone materials that is of great practical medical relevance. For example, the abundant presence of heat shock protein 60 (HSP60) most likely reflected the response of tissues surrounding silicone implants to mechanical stress under physiological conditions. The presence of MMP-2 is indicative of prominent remodeling processes in the protein layer.

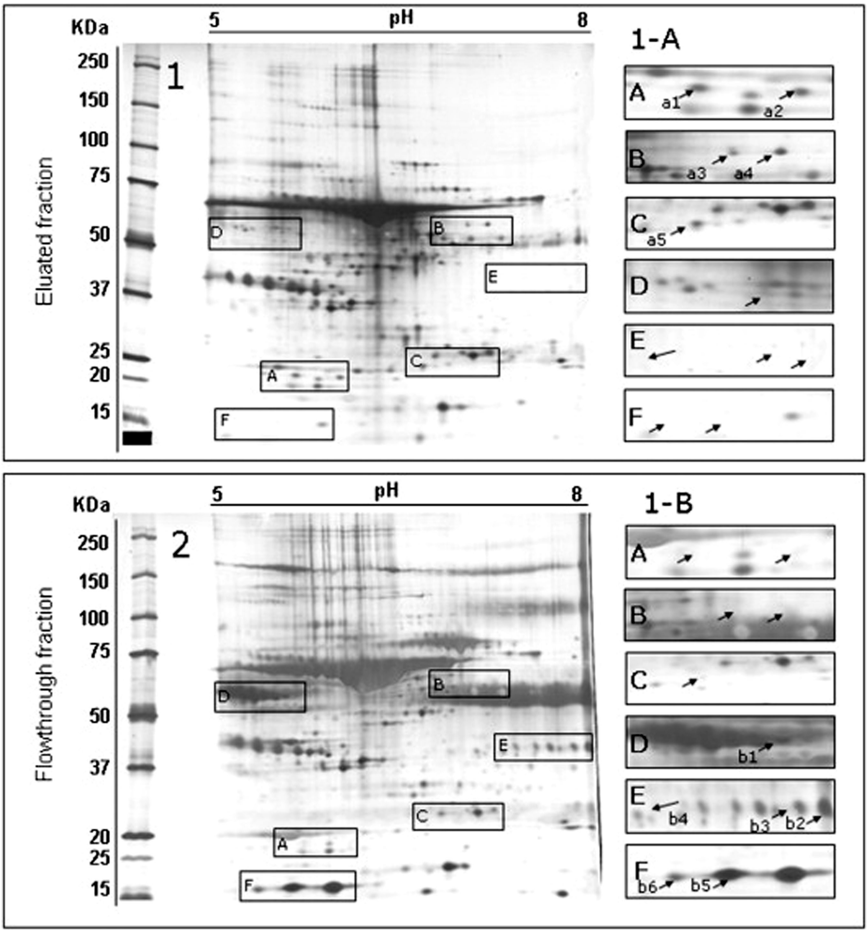
KDa
pH
5
8
1
1-A
Eluated fraction
250
150
100
75
50
37
25
20
15
A
B
C
D
E
F
a1
a2
a3
a4
a5
KDa
pH
5
8
2
1-B
Flowthrough fraction
250
150
100
75
50
37
20
25
15
A
B
C
D
E
F
b1
b2
b3
b4
b5
b6

Figure 3. 2-DE profiles of PRP proteins adsorbed on polyNaSS/Ti chromatography. Proteins were separated on a linear pH 5–8 IPG strip, followed by a 8–18.5% SDS-polyacrylamidegel. Proteins were stained with silver nitrate. (1-A) 2-DE map of the eluted fraction. (1-B) 2-DE map of the flowthroughed fraction. A–F windowscorrespond to interesting areas with polypeptides interacting or not with the bioactivated biomaterial. Spots are indicated by labelled arrows for polypeptides present only in gel 1 or only in gel 2. The spots were excised and analysed by nanoLC–MS/MS. (Reproduced with permission from reference (65). Copyright 2011 Elsevier.)

As discussed previously, MALDI-MS analyzes protein samples in solution. In contrast, surface-MALDI-MS has appeared as a unique method for analyzing adsorbed proteins at the material surface. Regarding proteomic studies of adsorbed proteins on biomaterials, sample preparation for MALDI-MS analysis invovles collecting adsorbed proteins *via* washing steps. For surface-MALDI-MS, the analyte molecules are pre-adsorbed on the solid substrate and the matrix solution is then added to the sample to aid matrix crystal formation (*56*). Kingshott P *et al* applied surface-MALDI-MS to directly dectect proteins adsorbed on contact lenses (*77*). Lysozyme and several other smaller proteins were identified on different contact lenses worn by human volumteers. McArthur S *et al* also characterized the worn HEMA-based contact lenses using surface-MALDI-MS (*78*). The presence of surface-adsorbed species were detected with molecular weights < 15 kDa and some of them were not identified as ocular proteins. This may indicate a potential conversion of proteins upon adsorption onto synthetic surfaces.

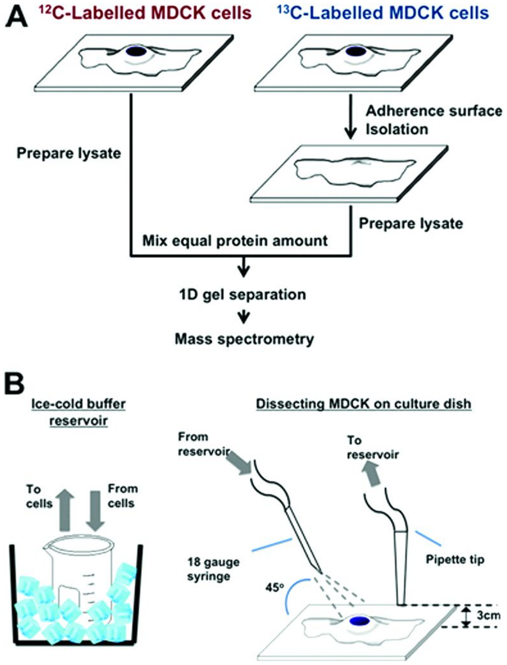
A
^{12}C-Labelled MDCK cells
^{13}C-Labelled MDCK cells
Adherence surface Isolation
Prepare lysate
Prepare lysate
Mix equal protein amount
1D gel separation
Mass spectrometry
B
Ice-cold buffer reservoir
Dissecting MDCK on culture dish
From reservoir
To reservoir
To cells
From cells
18 gauge syringe
Pipette tip
45°
3cm

Figure 4. Experiment setup and schematic diagram of machinery used to isolate adherence surface (AS) at cell-biomaterials interface. (Reproduced with permission from reference (66). Copyright 2010. The American Society for Biochemistry and Molecular Biology.)

In addition to MS-based proteomic analysis, protein or polymer microarrays were also used to conduct studies on protein adsorption. Neto AI *et al* reported a new platform for high-throughput analysis of interactions between biomaterials, proteins and cells using patterned superhydrophobic substrates (*79*). In their study, they designed superhydrophobic flat substrates with controlled wettable spots for producing microarray chips. The platform was applied to quantitative protein adsorption analysis. Moreover, different media, different numbers/types of cells, different polymeric biomaterials could be arrayed on the platform substrate to achieve high-throughput screening. Taylor M *et al* also reported a methodology for investigating protein adhesion and adsorption to microarrayed combinatorial polymers (*80*). Fluorescently labelled proteins were used to study protein adsorption on microarrayed synthetic polymers. However, these types of experiments cannot identify unknown proteins or characterize the complete proteome, but probe the specific material-protein interaction using known protein probes.

In sum, different experimental settings were used to generate proteome samples from surface adsorbed proteins. To study protein samples in the solution, adsorbed proteins need to be washed off from material surfaces using various buffer solutions to facilitate protein recovery particularly those of relatively low abundance. Thus, protein fractionation is necessary to remove proteins of high abundance and enable detection of proteins of low abundance. In addition, adsorbed proteins on the biomaterial substrate can be mixed with the matrix solution to ensure direct analysis *via* surface-MALDI-MS. Compared to the array-based method, MS-based methods are potentially powerful tools to conduct comprehensive proteome survey.

Soluble Proteins

Cells on or adjacent to a biomaterial implant can further mediate the host response through the release of soluble chemical mediators. Monocytes, macrophages, and foreign body giant cells are known to play critical roles during the host response to the biomaterial implants. These cells can produce reactive oxygen species (ROS) to degrade the biomaterial, chemokines to recruit additional inflammatory and wound healing cells (*e.g.*, lymphocytes, neutrophils, macrophages, and fibroblasts) to the injury site, and cytokines to activate or deactivate the inflammatory cells (*81*). Cytokines are known to have overlapping and redundant activities, and are frequently involved in complex intra/inter-cellular cross-talks. Therefore, a proteomic approach provides a robust way to investigate the cytokine network. Using protein microarray or MS-based technologies, functional proteins, chemokines, and cytokines secreted from cells can be identified and their release profiles can be generated *via* appropriate quantification methods. Jones J *et al* studied the cytokines and chemokines released from biomaterial surface-adherent macrophages and foreign body giant cells using array-based proteomic analysis (*81*). Biomaterials with varying surface properties such as hydrophilicity/hydrophobicity, cationic/anionic were included and subjected to culture with primary human monocytes. Cytokine screening of the cell culture supernatants was conducted using an array system of 77 cytokines/chemokines. Results showed 24 cytokines and chemokines were detected using antibody-bound membrane protein arrays. The array-based assay provided multiple cytokine/chemokine information from a single qualitative assay, but the results generated were only qualitative. Direct signal comparison between signal intensities cannot represent differences in cytokine production level due to the fact that different proteins have different concentration ranges for detection. Thus, quantification of selected proteins *via* ELISA was conducted to provide complementary information.

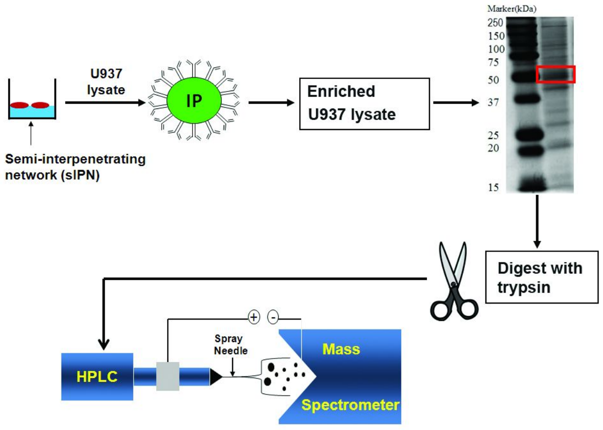
U937
lysate
IP
Enriched
U937 lysate
Semi-interpenetrating
network (sIPN)
Marker(kDa)
250
150
100
75
50
37
25
20
15
Digest with
trypsin
HPLC
Spray
Needle
Mass
Spectrometer

A. SDS-PAGE and LC/MS

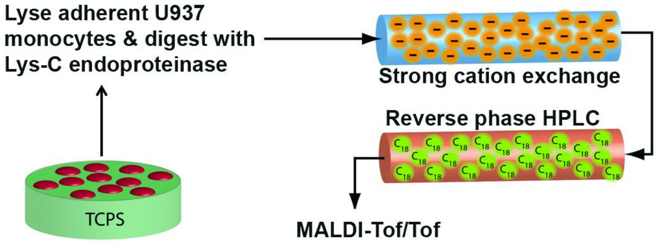
Lyse adherent U937
monocytes & digest with
Lys-C endoproteinase
Strong cation exchange
Reverse phase HPLC
TCPS
MALDI-Tof/Tof

B. 2D-liquid chromatography and MALDI-Tof/Tof

Figure 5. Optimized workflow for proteomic analysis of adherent monocytic U937 cell lysates on sIPN and TCPS using (A) SDS-PAGE and LC/MS and (B) 2D-liquid chromatography and MALDI-Tof/Tof. Adapted from reference (13, 68, 91, 92).

Monocytes interact with materials through adsorbed proteins, which leads to monocyte adhesion (*82*), activation (*83*, *84*), fusion to form foreign body giant cells (*85*, *86*), and secretion of inflammatory cytokines (*87*). The interaction between surface adsorbed proteins and cell surface receptors such as integrin is critical to the extent and duration of the host inflammatory response to biomaterials (*88–90*). To address how surface-adsorbed proteins and phosphorylation inhibitor may affect adherent monocytes, Zuckerman S *et al* (*13*, *91*) applied nanospray LC/MS based proteomic approaches to study the cell-material interaction (Figure 5A). The model surface was TCPS with or without pre-adsorbed proteins including albumin (Alb) or fibronectin (Fn). Cell lysates were prepared and subjected to SDS-PAGE analysis. Then, gel bands of interest were excised and peptides were collected, desalted, purified and enriched before LC/MS analysis. Studies showed phosphorylation inhibitor AG18 up- or down- regulated the expression of a set of proteins with molecular weight ranging from ~200 to ~23 kDa. Without AG18 and ligand treatment, five proteins at ~65/70 kDa, and 12 proteins at ~42 kDa were identified in cells. With 20 μM AG18 treatment, only one phosphorylation related protein titin at ~65/70 kDa was found. No proteins at ~42 kDa was identified in cells with 20, 40, 60 µM AG18 treatment. Thus, AG18 displayed a down-regulation effect on 12 proteins in adherent cells on TCPS. At ~23kDa, 60 and 80 µM of AG18 up-regulated the expression of proteins in cells that are not present in cells treated with 0, 20, or 40 µM AG18. Cells adherent to Fn-adsorbed TCPS were further compared to cells on PBS-adsorbed TCPS to determine the effect different ligand-receptor interactions have upon intracellular protein expression. Six unique proteins were identified in cells on the Fn pre-adsorbed samples at ~42 kDa; nine proteins were identified only in cells on PBS-adsorbed TCPS at ~42 kDa. Peroxiredoxin 1, histone H1.4 and testicular H1 histone were found in the ~23 kDa samples from cells on Fn-adsorbed TCPS (Table IV). No proteins were identified from cells adherent to PBS-adsorbed TCPS at ~23 kDa. Thus, surface-adsorbed Fn was involved in regulating a particular set of proteins in the adherent U937 cells at molecular weight ranging from ~160 to ~23 kDa, demonstrating a change in cellular signaling pathway mediated by surface-adsorbed ligand.

Table IV. The effect of Fn-adsorbed TCPS upon protein expression in adherent U937 cells[*]

Surface ligand	*Protein*	*Molecular weight (Da)*
Comparison of ~160 kDa proteins from cells on PBS- or FN-adsorbed TCPS without AG18		
PBS	DNA dependent protein kinase catalytic subunit (DNA-dependent protein kinase)	99,816
FN	N/D[b]	—
Comparison of ~130 kDa proteins from cells on PBS- or FN-adsorbed TCPS without AG18		
PBS	DNA topoisomerase II beta	180,501
	Dedicator of cytokinesis protein 2 (DOCK2 protein)	38,436
FN	N/D[b]	—
Comparison of ~100 kDa proteins from cells on PBS- or FN-adsporbed TCPS without AG18		
PBS	N/D[b]	—
FN	DNA topoisomerase II beta	182,578
	DNA dependent protein kinase catalytic subunit	465,266

Continued on next page.

Table IV. (Continued). The effect of Fn-adsorbed TCPS upon protein expression in adherent U937 cells*

Surface ligand	*Protein*	*Molecular weight (Da)*
Comparison of ~52 kDa proteins from cells on PBS- or FN-adsorbed TCPS without AG18		
PBS	**TPO autoantibody immunoglobulin heavy chain, V-region (TR1.41)**	**13,367**
	Anti-colorectal carcinoma heavy chain	**50,570**
	HLA-B-associated transcript 1 (BAT1 gene product)	33,121
	Growth regulated nuclear 68 protein	**66,881**
FN[b]	**TPO autoantibody immunoglobulin heavy chain, V-region (TR1.41)**	**13,367**
	Anti-colorectal carcinoma heavy chain	**50,570**
	Vimentin	53,653
	Mitochondrial ATP synthase beta chain	34,026
	Growth regulated nuclear 68 protein	**66,881**
Comparison of ~42 kDa proteins from cells on PBS- or FN-adsorbed TCPS without AG18		
PBS	CTCL tumor antigen se2-2	88,383
	Mutant beta-actin (beta'-actin)	41,786
	Desmoglein type 1	113,644
	Glyceraldehyde-3-phosphate dehydrogenase	36,031
	Alpha enolase	47,079
	Hqp0256 protein	31,162
	Apolipoprotein B precursor	187,126
	Sulfide:quinone oxidoreductase, Mitochondrial	49,917
	Vimentin	**53,653**
	Ribosomal protein L3	45,440
	NCL protein	**50,920**
	Eukaryotic translation elongation factor 1 gamma	**50,115**

Continued on next page.

Table IV. (Continued). The effect of Fn-adsorbed TCPS upon protein expression in adherent U937 cells*

Surface ligand	*Protein*	*Molecular weight (Da)*
FN	Beta actin variant	41,738
	Lamin A/C	53,219
	Vimentin	**53,653**
	40S ribosomal protein SA (laminin-binding protein)	31,774
	NCL protein	**50,920**
	Muscle specific enolase	46,957
	Eukaryotic translation initiation factor 2, subunit 3 gamma, 52 kDa	51,077
	Eukaryotic translation elongation factor 1 gamma	50,115
	Plasminogen activator inhibitor 2	46,615
Comparison of ~23 kDa proteins from cells on PBS- or FN-adsorbed TCPS without AG18		
PBS	N/D[b]	—
FN	Peroxiredoxin 1	22,096
	Histone H1.4 (histone H1b)	21,721
	Testicular H1 histone	22,020

[a] Common proteins are in bold text. [b] None detected. * Reproduced with permission from reference (*13*). Copyright 2006 Elsevier.

An in-depth study was conducted to identify intracellular cytoskeletal and inflammatory proteins from adherent U937 cells on surface with pre-adsorbed Fn-derived peptides (*91*). The tripeptide arginine-glycine-aspartic acid (RGD) is a cell adhesion sequence in Fn and the synergistic sequence proline-histadine-serine-arginine-asparagine (PHSRN) is known to increase cell adhesion to RGD (*93*). Thus, the study utilized oligopeptides G3RGDG and G3PHSRNG to investigate the effect of these pre-adsorbed peptides on the intracellular signaling of adherent monocytes. Nanospray LC/MS was used to survey and identify proteins from adherent monocytes mediated by surface-adsorbed peptide ligands. Twelve adhesion and inflammatory-related proteins were identified including moesin, heat shock protein 90-β, α- and β-tubulin, elongation factor 1α, β-actin, vimentin, PAI-2, hnRNP A2, HMGB1, CARD5, gp96, and hnRNP D0. The functions of these proteins are summarized in Table V.

Table V. Twelve identified proteins and the related cellular functions[*]

Proteins	***Functions***
moesin	Couple the actin cytoskeleton to the plasma membrane
heat shock protein 90-β	Bind to tubulin and retard polymerization
α- and β-tubulin	Cytoskeleton proteins
α- and β-tubulin	Localize mRNA to cell protrusions
β-actin and vimentin	Cytoskeleton proteins
PAI-2	Inhibit inflammatory cell migration in ECM remodeling
hnRNP A2	Aid ECM remodeling through collagen folding
HMGB1	Stimulate release of inflammatory cytokines
CARD5	Increase cellular metabolism of pro-IL-1β
gp96	Antigen presentation and $CD8^+$ T-cell activation
hnRNP D0	Initiate complement receptor 2 (CR2) transcription

[*] Adapted from reference (*91*).

Above studies utilized TCPS as the model system to identify proteins expressed by adherent U937 monocytes. However, protein expression from adherent cells on TCPS may vary significantly from that of adherent cells on surfaces such as hydrogels or other tissue-engineering constructs (*92*). Therefore, Zuckerman S *et al* further explored the study in soluble proteins from adherent monocytes on PEG containing hydrogel matrices using the aforementioned proteomic approach. As shown in Figure 5B, cell lysates from adherent U937 cells on TCPS was subjected to LC-MALDI analysis and 43 proteins of interest relevant to monocyte-mediated host inflammatory response were identified and refined. The Src family hematopoietic cell kinase (Hck) and plasminogen activator inhibitor-2 (PAI-2) were selected for an additional study using a small molecule inhibitor and exogenous protein addition, respectively. The study investigated the effect of Hck and PAI-2 on inflammatory cytokine secretion, matrix metalloproteinase (MMP) expression, and the plasminogen system in monocytes adherent to TCPS, RGD-modified semi-interpenetrating networks (sIPNs) containing gelatin and PEG, and PEG-only hydrogels. Interestingly, monoctye chemotactic protein-1 (MCP-1) secretion showed Src-dependence in monocytes on TCPS but not on PEG-only hydrogels. Secretion of the gelatinase matrix metalloproteinase 9 (MMP-9) from monocytes on PEG-only hydrogels was similar to that observed from monocytes on TCPS. Low levels of MMP-9, PAI-2, and MCP-1 were observed from monocytes on sIPNs. These results showed significant surface-dependent secretion of proteins from adherent monocytes.

In sum, the combination of high-resolution separation techniques and powerful mass spectrometric analysis were developed to efficiently study the proteome of adherent cells on biomaterials without *a priori* knowledge. However, the techniques discussed above are not quantitative thus cannot provide direct comparisons between proteins. Thus, complementary analyses such as western blot, ELISA, and polymerase chain reaction (PCR) should be performed to obtain more quantitative information.

Limitations and Challenges in Biomaterials Research

The essence of proteomics is performing sensitive analysis on specific proteins/peptides in a complex sample. Traditional protein analysis techniques focus only on a few target proteins per analysis, whereas proteomics conducts a global proteome analysis in a high throughput manner (*94*). For proteomic studies, protein identification is the primary goal and quantitative proteome profiling is another goal. Regarding proteins at the material interface, quantitative protein information is important for comparative analysis of proteins adsorbed or expressed by adherent cells. However, quantification is one of the major challenges for both protein microarrays and MS-based technologies thus requires additional complementary tools for quantification. Labeling technologies have been developed to conduct relative quantitative proteomics, *e.g.*, isotope-coded affinity tags (ICAT) (*95*), tandem mass tags (TMT) (*96*, *97*), isobaric tags for relative and absolute quantitation (iTRAQ) (*98*), and SILAC (*99*, *100*). Using LC-MS/MS with spiked internal standards, *e.g.*, a known concentration of isotope-labeled peptides, provides a possible approach to conduct an absolute proteomic quantitation (*101*, *102*). As discussed previously, the competing binding from high abundance proteins and the dynamic range of protein concentrations present a major challenge on both protein microarray and MS-based proteomics. The use of nanocapillary LC/MS to identify phosphotyrosine enriched proteins from cells adherent on peptide- and protein-adsorbed substrates illustrated the difficulty of identifying proteins with very low expression profiles (*13*, *91*). In addition, a limited sample quantity presents another challenge to biomaterial studies. For example, cell lysates obtained from adherent cells on TCPS was around 500 µg and the proteins of interest were on the nanogram scale, *e.g.*, phosphotyrosine protein (~275 ng) (*68*). Sample pretreatment is thus critical in developing analytical methods of high sensitivity and consistency.

Conclusion

Proteomics provides a viable approach to survey global proteome of surface-adsorbed proteins and soluble proteins from adherent cells. MS-based proteomics provides a powerful tool to identify proteins that are involved in extensive cell-material interactions without a priori knowledge. However, biomaterials present unique challenges to proteomic study, namely scarcity of the amount of proteome samples.

References

1. Castner, D. G.; Ratner, B. D. Biomedical Surf. Sci.: Foundations to frontiers. *Surf. Sci.* **2002**, *500* (1-3), 28–60.
2. Vroman, L.; Adams, A. L. Findings with recording ellipsometer suggesting rapid exchange of specific plasma proteins at liquid/solid interfaces. *Surf. Sci.* **1969**, *16*, 438.
3. Vroman, L.; Adams, A. L. Possible involvement of fibrinogen and proteolysis in surface activation - a study with recording ellipsometer. *Thromb. Diath. Haemorrh.* **1967**, *18* (3-4), 510&.
4. Vroman, L. Effects of hydrophobic surfaces upon blood coagulation. *Thrombosis et diathesis haemorrhagica* **1964**, *10*, 455–93.
5. Vroman, L.; Adams, A. L.; Fischer, G. C.; Munoz, P. C. Interaction of high molecular-weight kininogen, factor-xii, and fibrinogen in plasma at interfaces. *Blood* **1980**, *55* (1), 156–159.
6. Sivaraman, B.; Latour, R. A. Time-dependent conformational changes in adsorbed albumin and its effect on platelet adhesion. *Langmuir* **2012**, *28* (5), 2745–2752.
7. Hylton, D. M.; Shalaby, S. W.; Latour, R. A. Direct correlation between adsorption-induced changes in protein structure and platelet adhesion. *J. Biomed. Mater. Res. Part A* **2005**, *73A* (3), 349–358.
8. Lehnert, M.; Gorbahn, M.; Rosin, C.; Klein, M.; Koeper, I.; Al-Nawas, B.; Knoll, W.; Veith, M. Adsorption and conformation behavior of biotinylated fibronectin on streptavidin-modified TiOX surfaces studied by SPR and AFM. *Langmuir* **2011**, *27* (12), 7743–7751.
9. Tanaka, M.; Motomura, T.; Kawada, M.; Anzai, T.; Kasori, Y.; Shiroya, T.; Shimura, K.; Onishi, M.; Mochizuki, A. Blood compatible aspects of poly(2-methoxyethylacrylate) (PMEA) - relationship between protein adsorption and platelet adhesion on PMEA surface. *Biomaterials* **2000**, *21* (14), 1471–1481.
10. Katsikogianni, M.; Missirlis, Y. F. Concise review of mechanisms of bacterial adhesion to biomaterials and of techniques used in estimating bacteria-material interactions. *Eur. Cells Mater.* **2004**, *8*, 37–57.
11. Francolini, I.; Crisante, F.; Martinelli, A.; D'Ilario, L.; Piozzi, A. Synthesis of biomimetic segmented polyurethanes as antifouling biomaterials. *Acta Biomater.* **2012**, *8* (2), 549–558.
12. Almeida, C. R.; Vasconcelos, D. P.; Goncalves, R. M.; Barbosa, M. A. Enhanced mesenchymal stromal cell recruitment via natural killer cells by incorporation of inflammatory signals in biomaterials. *J. R. Soc. Interface* **2012**, *9* (67), 261–271.
13. Zuckerman, S. T.; Kao, W. J. Effect of surface-adsorbed proteins and phosphorylation inhibitor AG18 on intracellular protein expression in adherent macrophages. *Biomaterials* **2006**, *27* (20), 3745–57.
14. Wang, X.; Schmidt, D. R.; Joyce, E. J.; Kao, W. J. Application of MS-based proteomics to study serum protein adsorption/absorption and complement C3 activation on poly(ethylene glycol) hydrogels. *J. Biomater. Sci., Polym. Ed.* **2011**, *22* (10), 1343–1362.

15. Wilkins, M. Proteomics data mining. *Expert Rev. Proteomics* **2009**, *6*, 599–603.
16. Gygi, S. P.; Aebersold, R. Mass spectrometry and proteomics. *Curr. Opin. Chem. Biol.* **2000**, *4* (5), 489–494.
17. MacBeath, G.; Schreiber, S. L. Printing proteins as microarrays for high-throughput function determination. *Science* **2000**, *289* (5485), 1760–1763.
18. Hale, J. E.; Gelfanova, V.; Ludwig, J. R.; Knierman, M. D. Application of proteomics for discovery of protein biomarkers. *Briefings Funct. Genomics Proteomics* **2003**, *2* (3), 185–93.
19. MacBeath, G. Protein microarrays and proteomics. *Nat. Genet.* **2002**, *32*, 526–532.
20. Gonzalez-Gonzalez, M.; Jara-Acevedo, R.; Matarraz, S.; Jara-Acevedo, M.; Paradinas, S.; Sayagues, J. M.; Orfao, A.; Fuentes, M. Nanotechniques in proteomics: Protein microarrays and novel detection platforms. *European Journal of Pharm. Sci.* **2012**, *45* (4), 499–506.
21. Zarate, X.; Henderson, D. C.; Phillips, K. C.; Lake, A. D.; Galbraith, D. W. Development of high-yield autofluorescent protein microarrays using hybrid cell-free expression with combined Escherichia coli S30 and wheat germ extracts. *Proteome Sci.* **2010**, *8*.
22. Nand, A.; Gautam, A.; Perez, J. B.; Merino, A.; Zhu, J. Emerging technology of in situ cell free expression protein microarrays. *Protein Cell* **2012**, *3* (2), 84–8.
23. Tang, C. K.; Vaze, A.; Rusling, J. F. Fabrication of immunosensor microwell arrays from gold compact discs for detection of cancer biomarker proteins. *Lab Chip* **2012**, *12* (2), 281–286.
24. Stoevesandt, O.; Taussig, M. J.; He, M. Y. Protein microarrays: high-throughput tools for proteomics. *Exp. Rev. Proteomics* **2009**, *6* (2), 145–157.
25. Liotta, L. A.; Espina, V.; Mehta, A. I.; Calvert, V.; Rosenblatt, K.; Geho, D.; Munson, P. J.; Young, L.; Wulfkuhle, J.; Petricoin, E. F. Protein microarrays: meeting analytical challenges for clinical applications. *Cancer Cell* **2003**, *3* (4), 317–325.
26. Talapatra, A.; Rouse, R.; Hardiman, G. Protein microarrays: challenges and promises. *Pharmacogenomics* **2002**, *3* (4), 527–536.
27. Bally, M.; Syed, S.; Binkert, A.; Kauffmann, E.; Ehrat, M.; Voros, J. Fluorescent vesicles for signal amplification in reverse phase protein microarray assays. *Anal. Biochem.* **2011**, *416* (2), 145–151.
28. Alivisatos, P. The use of nanocrystals in biological detection. *Nat. Biotechnol.* **2004**, *22* (1), 47–52.
29. Aebersold, R.; Mann, M. Mass spectrometry-based proteomics. *Nature* **2003**, *422* (6928), 198–207.
30. Strupat, K.; Karas, M.; Hillenkamp, F. 2,5-dihydroxybenzoic acid - a new matrix for laser desorption ionization mass-spectrometry. *Int. J. Mass Spectrom. Ion Processes* **1991**, *111*, 89–102.
31. Liu, H. B.; Sadygov, R. G.; Yates, J. R. A model for random sampling and estimation of relative protein abundance in shotgun proteomics. *Anal. Chem.* **2004**, *76* (14), 4193–4201.

32. Wu, S. L.; Huehmer, A. F. R.; Hao, Z. Q.; Karger, B. L. On-line LC-MS approach combining collision-induced dissociation (CID), electron-transfer dissociation (ETD), and CID of an isolated charge-reduced species for the trace-level characterization of proteins with post-translational modifications. *J. Proteome Res.* **2007**, *6* (11), 4230–4244.
33. Samgina, T. Y.; Vorontsov, E. A.; Gorshkov, V. A.; Artemenko, K. A.; Nifant'ev, I. E.; Kanawati, B.; Schmitt-Kopplin, P.; Zubarev, R. A.; Lebedev, A. T. Novel cysteine tags for the sequencing of non-tryptic disulfide peptides of anurans: ESI-MS study of fragmentation efficiency. *J. Am. Soc. Mass Spectrom.* **2011**, *22* (12), 2246–2255.
34. Schirmer, E. C.; Florens, L.; Guan, T. L.; Yates, J. R.; Gerace, L. Nuclear membrane proteins with potential disease links found by subtractive proteomics. *Science* **2003**, *301* (5638), 1380–1382.
35. Cheeseman, I. M.; Anderson, S.; Jwa, M.; Green, E. M.; Kang, J.-s.; Yates, J. R., III; Chan, C. S. M.; Drubin, D. G.; Barnes, G. Phospho-regulation of kinetochore-microtubule attachments by the Aurora kinase Ipl1p. *Cell* **2002**, *111* (2), 163–172.
36. Leng, J.; Wang, H.; Zhang, L.; Zhang, J.; Wang, H.; Cai, T.; Yao, J.; Guo, Y. Integration of high accuracy n-terminus identification in peptide sequencing and comparative protein analysis via isothiocyanate-based isotope labeling reagent with ESI Ion-trap TOF MS. *J. Am. Soc. Mass Spectrom.* **2011**, *22* (7), 1204–1213.
37. Domon, B.; Aebersold, R. Options and considerations when selecting a quantitative proteomics strategy. *Nat. Biotechnol.* **2010**, *28* (7), 710–721.
38. Sze, S. K.; Ge, Y.; Oh, H.; McLafferty, F. W. Top-down mass spectrometry of a 29-kDa protein for characterization of any posttranslational modification to within one residue. *Proc. Natl. Acad. Sci. U.S.A.* **2002**, *99* (4), 1774–1779.
39. Kelleher, N. L. Top-down proteomics. *Anal. Chem.* **2004**, *76* (11), 197A–203A.
40. Valaskovic, G. A.; Kelleher, N. L.; McLafferty, F. W. Attomole protein characterization by capillary electrophoresis mass spectrometry. *Science* **1996**, *273* (5279), 1199–1202.
41. Jiang, X. G.; Ye, M. L.; Zou, H. F. Technologies and methods for sample pretreatment in efficient proteome and peptidome analysis. *Proteomics* **2008**, *8* (4), 686–705.
42. Paulo, J. A.; Kadiyala, V.; Banks, P. A.; Steen, H.; Conwell, D. L. Mass spectrometry-based proteomics for translational research: a technical overview. *Yale J. Biol. Med.* **2012**, *85* (1), 59–73.
43. Ward, W. W.; Swiatek, G. Protein Purification. *Curr. Anal. Chem.* **2009**, *5* (2), 85–105.
44. Jiang, L.; He, L.; Fountoulakis, M. Comparison of protein precipitation methods for sample preparation prior to proteomic analysis. *J. Chromatogr., A* **2004**, *1023* (2), 317–320.
45. Azarkan, M.; Huet, J.; Baeyens-Volant, D.; Looze, Y.; Vandenbussche, G. Affinity chromatography: A useful tool in proteomics studies. *J. Chromatogr., B* **2007**, *849* (1-2), 81–90.

46. Lescuyer, P.; Hochstrasser, D. F.; Sanchez, J. C. Comprehensive proteome analysis by chromatographic protein prefractionation. *Electrophoresis* **2004**, *25* (7-8), 1125–1135.
47. Leitner, A.; Lindner, W. Current chemical tagging strategies for proteome analysis by mass spectrometry. *J. Chromatogr., B* **2004**, *813* (1-2), 1–26.
48. Weinberger, S. R.; Viner, R. I.; Ho, P. Tagless extraction-retentate chromatography: a new global protein digestion strategy for monitoring differential protein expression. *Electrophoresis* **2002**, *23* (18), 3182–3192.
49. Kuyama, H.; Watanabe, M.; Toda, C.; Matsuo, E.-i.; Ando, E.; Tanaka, K.; Nishimura, O. An approach to quantitative proteome analysis by labeling tryptophan residues. *Mol. Cell. Proteomics* **2004**, *3* (10), S289–S289.
50. Ji, J. Y.; Chakraborty, A.; Geng, M.; Zhang, X.; Amini, A.; Bina, M.; Regnier, F. Strategy for qualitative and quantitative analysis in proteomics based on signature peptides. *J. Chromatogr., B* **2000**, *745* (1), 197–210.
51. Limber, G. K.; Mason, R. G. Studies of proteins elutable from cuprophane exposed to human plasma. *Thrombosis Res,* **1975**, *6* (5), 421–430.
52. Weathersby, P. K.; Horbett, T. A.; Hoffman, A. S. New method for analysis of adsorbed plasma-protein layer on biomaterial surfaces. *Trans. - Am. Soc. Artif. Intern. Organs* **1976**, *22*, 242–252.
53. Mulzer, S. R.; Brash, J. L. Identification of plasma-proteins adsorbed to hemodialyzers during clinical use. *J. Biomed. Mater. Res.* **1989**, *23* (12), 1483–1504.
54. Elbert, D. L. Proteomic and advanced biochemical techniques to study protein adsorption. In *Comprehensive Biomaterials*, 1st ed.; Elsevier: New York, 2011; Vol. 3.
55. Power, K. A.; Fitzgerald, K. T.; Gallagher, W. M. Examination of cell-host-biomaterial interactions via high-throughput technologies: A re-appraisal. *Biomaterials* **2010**, *31* (26), 6667–6674.
56. Griesser, H. J.; Kingshott, P.; McArthur, S. L.; McLean, K. M.; Kinsel, G. R.; Timmons, R. B. Surface-MALDI mass spectrometry in biomaterials research. *Biomaterials* **2004**, *25* (20), 4861–4875.
57. Hu, W. J.; Eaton, J. W.; Tang, L. P. Molecular basis of biomaterial-mediated foreign body reactions. *Blood* **2001**, *98* (4), 1231–1238.
58. Nakanishi, K.; Sakiyama, T.; Imamura, K. On the adsorption of proteins on solid surfaces, a common but very complicated phenomenon. *J. Biosci. Bioeng.* **2001**, *91* (3), 233–244.
59. Higuchi, A.; Sugiyama, K.; Yoon, B. O.; Sakurai, M.; Hara, M.; Sumita, M.; Sugawara, S.; Shirai, T. Serum protein adsorption and platelet adhesion on pluronic (TM)-adsorbed polysulfone membranes. *Biomaterials* **2003**, *24* (19), 3235–3245.
60. Chen, H.; Yuan, L.; Song, W.; Wu, Z. K.; Li, D. Biocompatible polymer materials: Role of protein-surface interactions. *Progr. Polym. Sci.* **2008**, *33* (11), 1059–1087.
61. Welle, A.; Grunze, M.; Tur, D. Plasma protein adsorption and platelet adhesion on poly bis(trifluoroethoxy)phosphazene and reference material surfaces. *J. Colloid Interface Sci.* **1998**, *197* (2), 263–274.

62. Schmidt, D.; Joyce, E. J.; Kao, W. J. Fetal bovine serum xenoproteins modulate human monocyte adhesion and protein release on biomaterials in vitro. *Acta Biomater.* **2011**, *7* (2), 515–25.
63. Hamada, I.; Hunter, A. C.; Szebeni, J.; Moghimi, S. M. Poly(ethylene glycol)s generate complement activation products in human serum through increased alternative pathway turnover and a MASP-2-dependent process. *Mol. Immunol.* **2008**, *46* (2), 225–232.
64. Ying, S. C.; Gewurz, A. T.; Jiang, H. X.; Gewurz, H. Human serum amyloid-p component oligomers bind and activate the classical complement pathway via residue-14-26 and residue-76-92 of the a-chain collagen-like region of C1Q. *J. Immunol.* **1993**, *150* (1), 169–176.
65. Oughlis, S.; Lessim, S.; Changotade, S.; Bollotte, F.; Poirier, F.; Helary, G.; Lataillade, J. J.; Migonney, V.; Lutomski, D. Development of proteomic tools to study protein adsorption on a biomaterial, titanium grafted with poly(sodium styrene sulfonate). *J. Chromatogr., B* **2011**, *879* (31), 3681–3687.
66. Tong, W. Y.; Liang, Y. M.; Tam, V.; Yip, H. K.; Kao, Y. T.; Cheung, K. M.; Yeung, K. W.; Lam, Y. W. Biochemical characterization of the cell-biomaterial interface by quantitative proteomics. *Mol. Cell. Proteomics* **2010**, *9* (10), 2089–98.
67. Feltkamp, C. A.; Pijnenburg, M. A. P.; Roos, E. Organization of talin and vinculin in adhesion plaques of wet-cleaved chicken-embryo fibroblasts. *J. Cell Sci.* **1991**, *100*, 579–587.
68. Drees, F.; Reilein, A.; Nelson, W. J. Cell-adhesion assays: fabrication of an E-cadherin substratum and isolation of lateral and Basal membrane patches. *Methods Mol. Biol.* **2005**, *294*, 303–20.
69. Cattelino, A.; Albertinazzi, C.; Bossi, M.; Critchley, D. R.; de Curtis, I. A cell-free system to study regulation of focal adhesions and of the connected actin cytoskeleton. *Mol. Biol. Cell* **1999**, *10* (2), 373–391.
70. Cohen, C. M.; Kalish, D. I.; Jacobson, B. S.; Branton, D. Membrane isolation on polylysine-coated beads - plasma-membrane from hela-cells. *J. Cell Biol.* **1977**, *75* (1), 119–134.
71. Aggeler, J.; Werb, Z. Initial events during phagocytosis by macrophages viewed from outside and inside the cell - membrane-particle interactions and clathrin. *J. Cell Biol.* **1982**, *94* (3), 613–623.
72. Jacobson, B. S.; Branton, D. Plasma-membrane - rapid isolation and exposure of cytoplasmic surface by use of positively charged beads. *Science* **1977**, *195* (4275), 302–304.
73. Derhami, K.; Wolfaardt, J. F.; Wennerberg, A.; Scott, P. G. Quantifying the adherence of fibroblasts to titanium and its enhancement by substrate-attached material. *J. Biomed. Mater. Res.* **2000**, *52* (2), 315–322.
74. Derhami, K.; Zheng, J.; Li, L.; Wolfaardt, J. F.; Scott, P. G. Proteomic analysis of human skin fibroblasts grown on titanium: novel approach to study molecular biocompatibility. *J. Biomed. Mater. Res.* **2001**, *56* (2), 234–244.
75. Ong, S.-E.; Mann, M. A practical recipe for stable isotope labeling by amino acids in cell culture (SILAC). *Nat. Protoc.* **2006**, *1* (6), 2650–2660.

76. Backovic, A.; Huang, H. L.; Del Frari, B.; Piza, H.; Huber, L. A.; Wick, G. Identification and dynamics of proteins adhering to the surface of medical silicones in vivo and in vitro. *J. Proteome Res.* **2007**, *6* (1), 376–381.
77. Kingshott, P.; St John, H. A. W.; Griesser, H. J. Direct detection of proteins adsorbed on synthetic materials by matrix-assisted laser desorption ionization-mass spectrometry. *Anal. Biochem.* **1999**, *273* (2), 156–162.
78. McArthur, S. L.; McLean, K. M.; St John, H. A. W.; Griesser, H. J. XPS and surface-MALDI-MS characterisation of worn HEMA-based contact lenses. *Biomaterials* **2001**, *22* (24), 3295–3304.
79. Neto, A. I.; Custodio, C. A.; Song, W. L.; Mano, J. F. High-throughput evaluation of interactions between biomaterials, proteins and cells using patterned superhydrophobic substrates. *Soft Matter* **2011**, *7* (9), 4147–4151.
80. Taylor, M.; Urquhart, A. J.; Anderson, D. G.; Williams, P. M.; Langer, R.; Alexander, M. R.; Davies, M. C. A methodology for investigating protein adhesion and adsorption to microarrayed combinatorial polymers. *Macromol. Rapid Commun.* **2008**, *29* (15), 1298–1302.
81. Jones, J. A.; Chang, D. T.; Meyerson, H.; Colton, E.; Kwon, I. K.; Matsuda, T.; Anderson, J. M. Proteomic analysis and quantification of cytokines and chemokines from biomaterial surface-adherent macrophages and foreign body giant cells. *J. Biomed. Mater. Res.. Part A* **2007**, *83A* (3), 585–596.
82. Juliano, R. L. Signal transduction by cell adhesion receptors and the cytoskeleton: functions of integrins, cadherins, selectins, and immunoglobulin-superfamily members. *Annu. Rev. Pharmacol. Toxicol.* **2002**, *42*, 283–323.
83. MacEwan, M. R.; Brodbeck, W. G.; Matsuda, T.; Anderson, J. M. Monocyte/lymphocyte interactions and the foreign body response: in vitro effects of biomaterial surface chemistry. *J. Biomed. Mater. Res., Part A* **2005**, *74A* (3), 285–293.
84. Mograbi, B.; Rochet, N.; Emiliozzi, C.; Rossi, B. Adhesion of human monocytic THP-1 cells to endothelial cell adhesion molecules or extracellular matrix proteins via beta(1) integrins regulates heparin binding epidermal growth factor-like growth factor (HB-EGF) expression. *Eur. Cytokine Network* **1999**, *10* (1), 79–86.
85. Collier, T. O.; Anderson, J. M. Protein and surface effects on monocyte and macrophage adhesion, maturation, and survival. *J. Biomed. Mater. Res.* **2002**, *60* (3), 487–496.
86. Anderson, J. M.; Rodriguez, A.; Chang, D. T. Foreign body reaction to biomaterials. *Semin. Immunol.* **2008**, *20* (2), 86–100.
87. Maxeiner, H.; Husemann, J.; Thomas, C. A.; Loike, J. D.; El Khoury, J.; Silverstein, S. C. Complementary roles for scavenger receptor A and CD36 of human monocyte-derived macro-phages in adhesion to surfaces coated with oxidized low-density lipoproteins and in secretion of H_2O_2. *J. Exp. Med.* **1998**, *188* (12), 2257–2265.
88. Hamilton, J. A. Nondisposable materials, chronic inflammation, and adjuvant action. *J. Leukocyte Biol.* **2003**, *73* (6), 702–712.

89. Schmidt, D. R.; Kao, W. J. Monocyte activation in response to polyethylene glycol hydrogels grafted with RGD and PHSRN separated by interpositional spacers of various lengths. *J. Biomed. Mater. Res., Part A* **2007**, *83A* (3), 617–625.

90. Schmidt, D. R.; Kao, W. J. The interrelated role of fibronectin and interleukin-1 in biomaterial-modulated macrophage function. *Biomaterials* **2007**, *28* (3), 371–82.

91. Zuckerman, S. T.; Kao, W. J. LC/MS identification of 12 intracellular cytoskeletal and inflammatory proteins from monocytes adherent on surface-adsorbed fibronectin-derived peptides. *J. Biomed. Mater. Res., Part A* **2008**, *85* (2), 513–29.

92. Zuckerman, S. T.; Brown, J. F.; Kao, W. J. Identification of regulatory Hck and PAI-2 proteins in the monocyte response to PEG-containing matrices. *Biomaterials* **2009**, *30* (23-24), 3825–33.

93. Ruoslahti, E. RGD and other recognition sequences for integrins. *Annu. Rev. Cell Develop. Biol.* **1996**, *12*, 697–715.

94. Din, S.; Lennon, A. M.; Arnott, I. D. R.; Hupp, T.; Satsangi, J. Technology insight: the application of proteomics in gastrointestinal disease. *Nat. Clin. Pract. Gastroenterol. Hepatol.* **2007**, *4* (7), 372–385.

95. Sohn, C. H.; Lee, J. E.; Sweredoski, M. J.; Graham, R. L. J.; Smith, G. T.; Hess, S.; Czerwieniec, G.; Loo, J. A.; Deshaies, R. J.; Beauchamp, J. L. Click Chemistry Facilitates Formation of Reporter Ions and Simplified Synthesis of Amine-Reactive Multiplexed Isobaric Tags for Protein Quantification. *J. Am. Chem. Soc.* **2012**, *134* (5), 2672–2680.

96. Guo, J.; Prokai, L. To tag or not to tag: A comparative evaluation of immunoaffinity-labeling and tandem mass spectrometry for the identification and localization of posttranslational protein carbonylation by 4-hydroxy-2-nonenal, an end-product of lipid peroxidation. *J. Proteomics* **2011**, *74* (11), 2360–2369.

97. Coombs, K. M. Quantitative proteomics of complex mixtures. *Exp. Rev. Proteomics* **2011**, *8* (5), 659–677.

98. Chang, K.-P.; Yu, J.-S.; Chien, K.-Y.; Lee, C.-W.; Liang, Y.; Liao, C.-T.; Yen, T.-C.; Lee, L.-Y.; Huang, L.-L.; Liu, S.-C.; Chang, Y.-S.; Chi, L.-M. Identification of PRDX4 and P4HA2 as Metastasis-Associated Proteins in Oral Cavity Squamous Cell Carcinoma by Comparative Tissue Proteomics of Microdissected Specimens Using iTRAQ Technology. *J. Proteome Res.* **2011**, *10* (11), 4935–4947.

99. Austin, R. J.; Kuestner, R. E.; Chang, D. K.; Madden, K. R.; Martin, D. B. SILAC Compatible Strain of Pichia pastoris for Expression of Isotopically Labeled Protein Standards and Quantitative Proteomics. *J. Proteome Res.* **2011**, *10* (11), 5251–5259.

100. Datta, A.; Qian, J.; Khor, T. H.; Teo, M. T.; Heese, K.; Sze, S. K. quantitative neuroproteomics of an in vivo rodent model of focal cerebral ischemia/reperfusion injury reveals a temporal regulation of novel pathophysiological molecular markers. *J. Proteome Res.* **2011**, *10* (11), 5199–5213.

101. Huang, Z. L.; Wang, H. L.; Huang, H. L.; Xia, L. H.; Chen, C. S.; Qiu, X. X.; Chen, J. B.; Chen, S. S.; Liang, W. H.; Huang, M.; Lang, L.; Zheng, Q. L.; Wu, B. H.; Lai, G. C. iTRAQ-based proteomic profiling of human serum reveals down-regulation of platelet basic protein and apolipoprotein B100 in patients with hematotoxicity induced by chronic occupational benzene exposure. *Toxicology* **2012**, *291* (1-3), 56–64.

102. Xiong, Q.; Zhong, Q.; Zhang, J.; Yang, M.; Li, C.; Zheng, P.; Bi, L.-J.; Ge, F. Identification of novel mir-21 target proteins in multiple myeloma cells by quantitative proteomics. *J. Proteome Res.* **2012**, *11* (4), 2078–90.

Chapter 38

Structure and Stability of Proteins Interacting with Nanoparticles

Luigi Calzolai, Stefania Laera, Giacomo Ceccone, and Francois Rossi*

European Commission, Joint Research Centre, Institute for Health and Consumer Protection Via E. Fermi 2749, I-21027, Ispra (VA), Italy
***E-mail: francois.rossi@jrc.ec.europa.eu. Tel: +390332786561**

The behavior and toxicological properties of nanoparticles (NP) in biological medium depends heavily on their interactions with proteins. In return, the structure, stability and biological properties of the proteins that interact with the nanoparticles are strongly affected by this interaction. Unfortunately, the mechanisms of interaction and their structural consequences are very difficult to analyse. Here we show the use of advanced biophysical techniques to obtain information on the structure and stability of protein-nanoparticle complexes. By using circular dichroism spectroscopy it is possible to detect changes in the secondary structure and stability of proteins upon interaction with nanoparticles. Moreover, by using nuclear magnetic resonance experiments, it is even possible to detect the specific domain of proteins interacting with nanoparticles.

Introduction

Nanotechnology is having a large impact in very different scientific fields such as material sciences, photonics, nanomedicine and biotechnology. The uses of nanotechnology-based materials is not just limited to research laboratories, but has already been applied in several industrial sectors and into real products as disparate as medical diagnostic tools, drug delivery systems, cosmetics, and consumer products. In nanomedicine and nanotechnologies industries, the global market reached $63.8 billion in 2010 and $72.8 billion in 2011. The market is

In Proteins at Interfaces III State of the Art 2012; Horbett, T., et al.;
ACS Symposium Series; American Chemical Society: Washington, DC, 2012.

expected to grow to $130.9 billion by 2016 at a compound annual growth rate of 12.5% between years 2011 and 2016. (BCC Research Report, Nanotechnology in Medical Applications: The Global Market; April 2012).

There is a growing public concern about the safety of engineered nanoparticles (ENPs) since it has been demonstrated that those intended for industrial and medical applications could cause adverse effects in mammalians or aquatic organisms by specific mechanisms depending on their physical chemical properties (*1*).

Experiments have clearly shown that there are several factors that should be taken into account to understand the interaction of ENPs with organisms. While the physical chemical properties such as size distribution, composition, surface charge, and solubility influence cell viability, these effects are always mediated by biological entities adsorbed on the surface of the nanomaterial: in physiological environments, ENPs selectively absorb proteins to form NP-protein corona (*2*), a process governed by molecular interaction between chemical groups on the NP surface and the amino acids residues of the protein.

When proteins interact with nanoparticles, their native conformation can be altered, thus reducing their stability or exposing new epitopes on the protein surface giving rise to unexpected biological responses that ultimately can lead to adverse effects (*3*, *4*). In other cases, the binding of enzymes to nanoparticles can reduce (or increase) enzymatic activity then altering the normal cell homeostasis (*5*, *6*).

It is also becoming clear that the properties and fate of nanoparticles in biological systems, and ultimately the cellular responses to them, critically depends from the adsorbed biomolecule layer(s) (*7*, *8*). The identity of the proteins adsorbed on the nanoparticle surface will change the interface properties and strongly influence the interaction of the nanoparticles with cells, thus modifying both the cellular uptake and distribution (*9*).

In this chapter, we will focus on what happens to nanoparticles when entering biological systems and some of the available techniques to study in detail this complex problem. Finally we will show recent results from our experimental work on the use of biophysical techniques to analyze the changes in structure and stability of proteins in protein-nanoparticle complexes.

What Happens To NP in Biological Systems?

When nanoparticles enter into contact with biological systems (cells, tissues, or biological fluids) their size, stability, electrostatic potential, and surface chemical properties can change significantly. In fact, biological systems contain several components that can greatly influence the physico-chemical properties of nanoparticles and thus their interaction with living systems. Even simple biological fluids such as serum or complete cell culture medium contain various salts (for example NaCl, phosphates) in quite high concentrations, a multitude of different proteins, ligands (such as chloride ions, citrate, sulphides), reducing agents (such as glutathione) as well as oxidizing agents. Figure 1 schematically depicts the possible behaviour of NP in a typical *in-vitro* cell system. A NP (black spheres) of a well defined and monodispersed size can aggregate (red circle) due to the high ionic strength of the biological medium. Single Nanoparticles, or NP aggregates, can then bind to proteins present in the medium (yellow circle) and this NP-protein complex can enter inside cells. Inside the cell, the NP-protein complex will interact with different cell compartments (such as mitochondria, lysosome, and nucleus), possibly causing damages that ultimately lead to toxicity.

This broad and general picture is even more complex in the case of some metal and metal oxide nanoparticles where the oxidative release of metal ions seems to be the most significant contributor to the nanotoxicity, especially in the case of silver nanoparticles (*10*, *11*). For instance, the metallic atom present in silver nanoparticles can be oxidized to silver ions by dissolved oxygen molecules; in biological systems are present several compounds (such as cysteine, chloride, thiols, citrate) that can contribute to modulate the ion release rate over 4 orders of magnitude (*12*). This mechanism of cell nanotoxicity seems not to be limited to silver nanoparticles, but it has been recently shown to be active also in the case of zinc oxide and copper oxide (*13*).

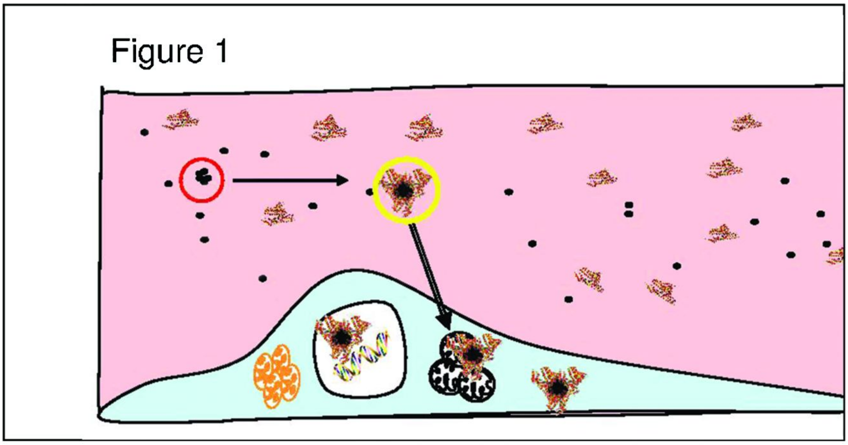

Figure 1. Nanoparticles in biological systems.

How To Study Protein−Nanoparticle Interactions

The interaction of nanomaterials with proteins is a difficult problem to study due both to the complexity of the system involving a solid/liquid interface (*14*) and low concentration of the proteins to be analyzed. The characterization of nanomaterials in biological systems (even relatively simple ones such as serum) is much more challenging due to the complexity and heterogeneity of biological medium *per se*.

The protein-nanoparticle interactions can be approached using a multistep process starting from the basic problem of measuring the changes in the size of nanoparticles, quantifying the amount of protein(s) adsorbed onto them, and to the more sophisticated identification of the proteins forming the protein corona, to measuring the structure and stability changes to the protein forming the NP-protein complexes.

To measure the size of NP, there are several techniques available, but none of them is completely suitable for measuring changes in the size of NP interacting with proteins in biological systems. Generally speaking, electron microscopy (either SEM or TEM) is one of the best methods for measuring the size of particles (especially in the case of NP containing heavy atoms) and is one of few that can address the problem of measuring sizes of NP agglomerates. Unfortunately, even this method is not very well suited to evaluate protein adsorption due to the requirements for sample preparation and poor contrast given by protein molecules. In fact, EM instruments work under high vacuum and proteins are mainly composed of atoms of low atomic number which generally do not provide enough contrast in the EM micrographs to obtain a clear image of the protein corona surrounding the metallic NP core.

To measure the size of NP in solutions, one of the most used techniques is dynamic light scattering, DLS, (sometimes referred as photon correlation spectroscopy). The technique measures the autocorrelation function of particles tumbling in solution and then by a Laplace-type transformation calculates the particle size distribution. The technique works quite well for NP made up by a single size but is not very reliable in the case of multiple sizes due to the fact that the intensity of signal of the various species is proportional to the 6th power of the size and thus the presence of even very small amounts of large aggregates would cover the signal from smaller particles (*15*). The technique is suitable for a careful use in well defined conditions with limited complexity. For example, Figure 2a shows the DLS data for free gold nanoparticles (AuNP) of around 20nm and then of the AuNP in complex with human serum albumin (HSA) of around 30nm that nicely fit with the presence of a single monolayer of albumin protein (HSA has a size of around 5nm) around the gold nanoparticles. It must be noted that such results can be obtained with DLS in carefully optimized experimental conditions (such as neutral pH and very low ionic strength) that minimizes the amount of aggregates.

In more complex (and potentially more relevant) cases such as the analysis of NP in serum medium, other techniques show a great potential. For example our group (*15*) and others (*16*) have found that the combination of a size separation technique such as flow field flow fractionation and size measurement with light scattering detectors (DLS or MALS) offers a very powerful combination for the characterization of the samples. Figure 2b shows an example of the use of FFF coupled with a light scattering detector to characterize SiO_2NP-protein corona. On the horizontal axis, the exit time from the separation channel is proportional to the size of the particles, with smaller particles exiting first, on the vertical axis the signal of the light scattering detector at 90° is related to the amount of material and to the size. The blue curve shows the SiO_2NP (size 50nm) in water, exiting at 28′, the orange curve is the plasma serum alone showing some small proteins exiting at

8′ and larger proteins at 18′. The red curve is the SiO_2NP sample in plasma serum: it shows peaks at around 9′ and 18′ (due to the free plasma proteins) and a peak at 34′ due to the SiO_2NP-protein corona complex.

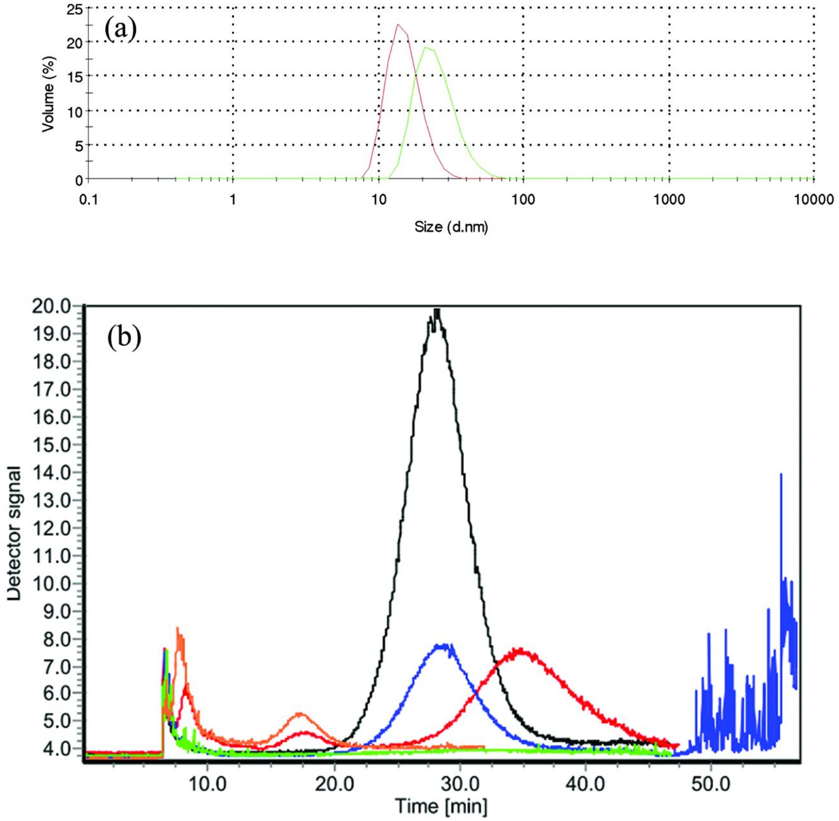

Figure 2. Measurement of the size of nanoparticle-protein complexes. (a) Dynamic light scattering measurement of free AuNP (red) and in complex with human serum albumin (green). (b) Field flow fractionation separation of SiO_2 nanoparticles in plasma serum with light scattering detector. Plasma serum alone (orange); free SiO_2NP (blue), SiO_2NP in plasma serum (red).

After separating the NP-protein corona system, it is possible to detect the proteins forming the corona by using proteomics approaches that identify each single protein using mass spectroscopy-based techniques (*17–19*). The results of such studies show that the protein corona surrounding nanoparticles is a dynamic system with a complex time evolution. In general the most abundant proteins in plasma serum do bind first to nanoparticles, while other less abundant proteins with stronger interaction with the NP replace them at later times (*20*, *21*). This effect reminds to the so called Vroman effect, that describes how blood serum proteins absorb to a surface: the highest mobility proteins generally arrive first and are later replaced by less motile proteins that have a higher affinity for the surface (*22*, *23*).

The studies performed so far have focused on the identification of the proteins forming the protein corona at different time points, and on the evaluation of the kinetic constants of the interaction of the different proteins with the nanoparticles (*2*, *9*, *20*, *24*). Various techniques have been used for measuring the affinity of proteins for different nanoparticles, such as isothermal titration calorimetry (*25*) and surface plasmon resonance (*2*). In addition, size exclusion chromatography has been used to determine the residence times of proteins (starting from a complex protein mixture) on nanoparticles (*2*). The effect of nanoparticle binding on the three dimensional structure and stability of the proteins is clearly an important issue, but up to now has received less attention, probably due to the inherent difficulties of the experimental system to be investigated.

How To Study the Structure of Proteins in NP−Protein Systems

The analysis of the structure, stability and function of proteins in protein−NP complexes is a key requirement to understand if and how the properties of the various proteins change when bound/interacting with NP.

In principle, the structural analysis of proteins in the complex formed with nanoparticles can be performed with the available techniques normally used in structural biology: in a sense, studying protein−NP interaction is not much different than studying protein-protein interaction. Unfortunately, in the case of NP−proteins complexes, there are major complications: the system can be dynamic, for example the protein corona is a very dynamic and heterogeneous system where the amounts and even the identities of the involved proteins changes over time. This thus rules out the use of crystals and X-ray spectroscopy that is somehow the workhorse of structural biology. On the other hand, nuclear magnetic resonance is well adapted to studying dynamic systems and later on, an example of the use of NMR in identifying the protein-gold nanoparticle interaction site will be provided.

Among the methods that can give low resolution structural information, circular dichroisms (CD) has several advantages: it can rapidly evaluate the secondary structure, folding, and binding properties of proteins (*26*, *27*) and, critically, the technique is very sensitive and CD spectra (under optimal conditions) can be acquired with just a few micrograms of sample.

The 180-250 nm region of the circular dichroism spectrum of a protein is sensitive to the secondary structure elements present in the protein. Alpha-helical regions have a typical spectrum with a double minimum at 222 and 208 nm and a maximum at 190nm, while beta-sheet structures have a single minimum at 215 nm and a maximum at 190nm. Using a basis set of CD spectra of secondary structures, it is possible to deconvolute the CD spectrum of a given protein and thus estimate the amount of each secondary structure elements present. Several open access programs are available to perform such deconvolution, and some of them (such as the dichroweb tool) are accessible via a web browser interface, thus providing an easy and simple access to such tools even to non specialists.

With “standard” CD, that uses a normal lamp as irradiation source, it is possible to detect the secondary structure of proteins and their changes upon interactions with nanoparticles. For example the black spectrum in Figure 3 shows the CD spectrum of human serum albumin (HSA). Using a 1cm long quartz cell, it is possible to measure the CD spectra of HSA with a low concentration of 5ug/mL (corresponding to a molar concentration of 100 nM). The red spectrum in Figure 3 shows the CD spectrum of HSA in the presence of silicon dioxide nanoparticles (SiO2-NP) of 50nm size. From the two spectra, it is clear that upon interaction with SiO2-NP, the HSA protein changes its secondary structure. Using the dichroweb program to estimate the amount of secondary structure elements present in the protein, it is found that when HSA interacts with SiO_2NP, the amount of alpha-helix decreases by around 12%, while the β-sheet and turn content increase by 8% and 3%, respectively.

One of the problem of measuring CD spectra in the far UV region at the lowest possible concentrations, is represented by the absorbance of buffers and salts present in the sample that do not allow the collection of meaningful data below the 190 nm wavelength. This causes even more problems when measuring protein−NP complexes, where the NP (especially silver, gold, and silicon dioxide) show strong absorbance below 190nm. This effect could be minimized by reducing the cell pathlenght, but in this case higher protein concentrations should be used, which would change the protein NP ratio and produce agglomeration.

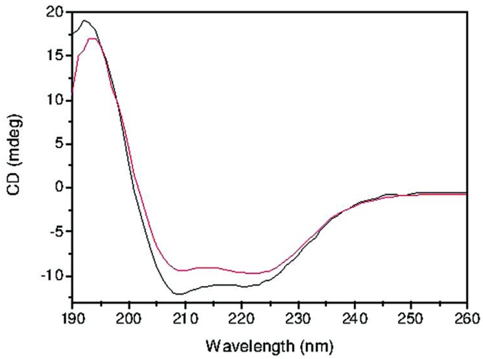

Figure 3. CD spectra acquired with standard bench top instrument. CD spectrum of HSA (black) and HSA-SiO_2NP (red).

To be able to measure CD spectra of even less concentrated proteins, long path measuring cells should be used, but to accomplish this there is the need of high flux and highly collimated excitation sources. Synchrotron radiation (SR) has these characteristics and the use of such sources to perform CD experiments (SRCD) presents several advantages compared to conventional CD techniques.

Using the B23 beam line of Diamond Light Source, we have recently shown that it is possible to collect high quality CD spectra of proteins with just 1 µg/mL samples (*28*). Figure 4 shows the CD spectra of HSA and lysozyme collected using a cell with a 10cm long pathway and 800 µL volume sample. The spectrum of HSA has been collected with a concentration of 20nM, and given its quality, it would be possible to collect CD spectra with concentration as low as 8nM with still a good signal to noise ratio by increasing the number of scans from 4 to 16.

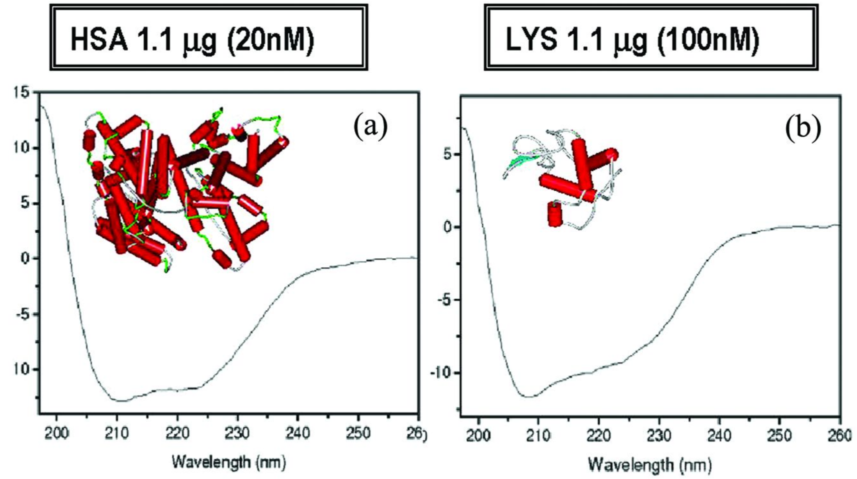

Figure 4. SRCD spectra of low concentration proteins acquired with a 10cm pathlenght cell. Insets: cartoon picture of the protein secondary structures with alpha-helices in red and beta-sheets in cyan. (a) Human serum albumin. (b) Human Lysozyme. Reproduced with permission from ref. (28). Copyright 2011 American Chemical Society.

The possibility of working at such a low protein concentration with SRCD allows measuring the changes in secondary structure associated with proteins bound noncovalentely to metallic nanoparticles with a protein-particle ratio in the range corresponding to a monolayer. Figure 5a shows the CD spectra of free HSA (black spectrum) and in complex with silver nanoparticles (red spectrum) in a molar ratio of 44:1 and that of lysozyme free (black) and in complex with silver nanoparticles (red) in a molar ratio of 200:1. The CD spectrum of HSA-AgNP shows that human serum albumin does not change its overall secondary structure upon interaction with silver nanoparticles. On the contrary, the CD spectrum of lysozyme-AgNP complex in Figure 5b clearly indicates a significant change in the intensity and shape. The data suggests that part of the lysozyme protein precipitates upon interaction with AgNP. This is confirmed also by the shift towards bluish colour of silver nanoparticles (indicative of the formation of particles larger than 80-100nm) and by DLS measurements that indicate the formation of large aggregates in the lysozyme-AgNP sample.

This different behaviour between serum albumin and lysozyme upon interaction with silver nanoparticles can be explained by the different electrostatic surface potential properties of the two proteins. Serum albumin has an isoelectric point of 5.5 and thus in the experimental conditions of pH 7.0, its charge is overall negative (with some positive patches, see inset in Figure 5a). On the contrary lysozyme has an isoelectric point of 9.5 and at pH 7.0 it is almost completely positively charged (inset in Figure 5b), thus greatly enhancing its interaction with the negatively charged silver nanoparticles, that will cause the nanoparticles to loose their repulsive forces leading to aggregation and partial precipitation of the system.

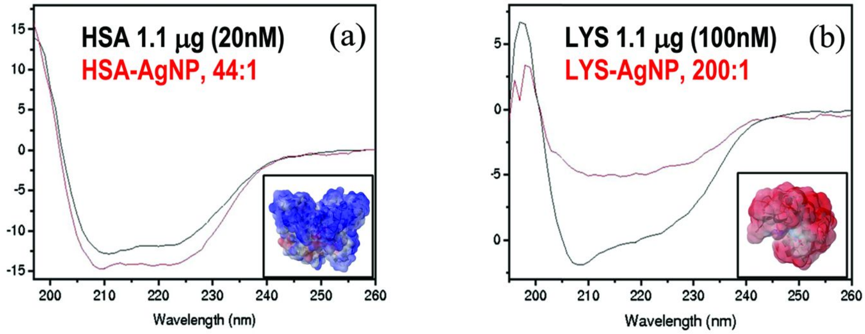

Figure 5. Changes in protein structure due to protein-silver nanoparticles interaction. (a) CD spectrum of free HSA (black) and HSA-AgNP (red). (b) CD spectra of lysozyme (black) and lysozyme-AgNP (red). Reproduced with permission from ref. (28). Copyright 2011 American Chemical Society.

Measuring Stability Changes of Protein−NP Systems

Circular dichroism can also be used to assess the thermal stability of proteins, and, in the case of reversible thermal unfolding, it is possible to calculate the Gibbs free energy of the unfolding process. The technique is quite sensitive and can be used to assess subtle differences in the stability of proteins in different conditions, for example the destabilization of human prion proteins in acidic conditions, as compared to neutral pH (*29*).

Using SRCD, we have studied the thermal unfolding process of serum albumin in the presence of different metallic nanoparticles. The whole CD spectrum of the protein has been collected varying the temperature from 20° C to 90° C at intervals of 2° C; a subset of the CD spectra at variable temperatures is shown in Figure 6a.

This ensemble of spectra has been analyzed by singular value decomposition to identify the singular vectors that have the highest singular values (*30*). This analysis indicated that the whole dataset could be described by the combination of just two singular vectors, while attempt to involve a third vector resulted in it giving a negligible contribution. The CD spectra corresponding to the two components identified by the singular value decomposition of the thermal unfolding process of free HSA are shown in Figure 6b: component 1 (black spectrum) corresponds to the completely folded spectrum of HSA, while the component 2 (red spectrum) is clearly the CD spectrum of a random coil protein devoided of any secondary structure. This indicates that the thermal unfolding process of HSA can be described as a two-states process going from a fully folded to a fully unfolded structure. Each one of the CD spectra acquired at variable temperatures is thus a linear combination of the two components with different weightings of the two basis spectra. Plotting the percentage of component 1 presents in each CD spectrum as a function of temperature gives a typical sigmoid curve shown in Figure 6c.

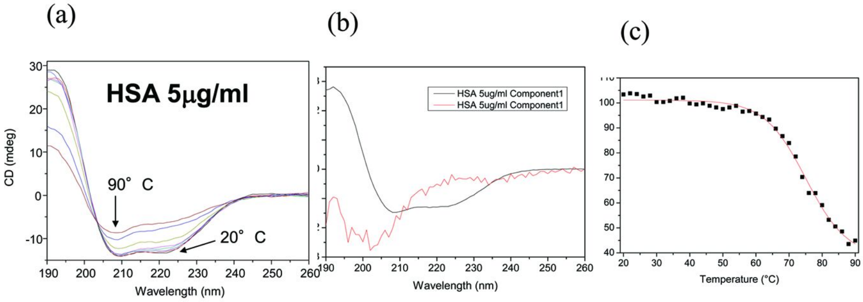

Figure 6. Measuring the thermal unfolding of HSA at 5ug/mL by SRCD. (a) CD spectra collected at variable temperatures from 20 C to 90 C. (b) CD spectra of the two components identified by singular value decomposition. (c) Non-linear square fitting (red curve) of % of folded structure as a function of temperature (black squares). Reproduced with permission from ref. (28). Copyright 2011 American Chemical Society.

Using the same approach we have then measured the thermal unfolding process of HSA in the presence of gold nanoparticles (AuNP) and silver nanoparticles (AgNP). Due to the use of SRCD we have been able to measure high quality data using quite low concentrations of proteins, and a molecular ratio of 22:1 for the HSA-AuNP system and 18:1 for the HSA-AgNP system. Figure 7 shows the thermal unfolding data for the three systems. The melting temperature (T_M) of HSA in complex with gold nanoparticles is 74.8±1.3°C, thus experimentally indistinguishable from the T_M of the protein alone, 75.2±0.6°C. In contrast, the T_M of the HSA-AgNP system is 69.1±1.0°C, significantly lower than that of the protein alone or in complex with gold nanoparticles. The shape of the three sigmoid thermal unfolding curves indicate that in the case of the HSA-AgNP complex the unfolding transition is less steep and less cooperative compared to the free protein.

The thermal unfolding process of serum albumin is not reversible and thus it is not possible to extract real thermodynamic parameters from the data, but it is possible to use the values of the melting temperatures to evaluate the relative stability of HSA interacting with gold and silver nanoparticles. Analyzing the

CD spectra and the thermal unfolding of the protein in the three conditions (free, +AuNP, +AgNP) it can be concluded that upon interaction with silver nanoparticles, the protein significantly reduces its thermal stability and seems to adopt a less compact folded state. On the contrary, the interaction with gold nanoparticles does not alter the stability of the protein and its overall folded state.

In summary, the use of SRCD allows measuring the changes in the secondary structure of proteins at unprecedented low concentration (as low as a few nanomolar concentration) and provides a unique tool for characterizing the structural properties of proteins at bio-nonbio interfaces. In addition, the analysis of CD-detected thermal unfolding allows to measure changes in the relative stability of proteins interacting with different nanomaterials and gives access to information that are difficult to obtain with other techniques, especially at these very low concentrations.

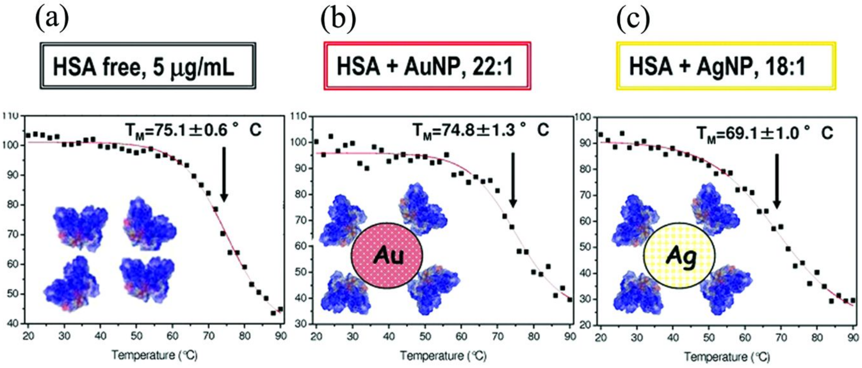

Figure 7. Destabilization of HSA-AgNP system. SRCD detected HSA thermal unfolding. Plot of % of folded protein as a function of temperature (black squares), fitted to Boltzmann equation (red curve). (a) free HSA protein. (b) HSA-AuNP. (c) HSA-AgNP. Reproduced with permission from ref. (28). Copyright 2011 American Chemical Society.

High-Resolution Structure of Protein−NP Complexes

High resolution informations on the structure of proteins bound to nanoparticles are very sparse and very difficult to obtain due to the challenges imposed by system involving the bio/non-bio interfaces. The protein−NP system is, in general, quite dynamic, and this makes the use of X-ray diffraction almost impossible, as usually dynamic systems do not crystallize and well behaving crystals are a prerequisite for X-ray protein crystallography. Nuclear Magnetic Resonance (NMR) is a well established technique to obtain high resolution three dimensional structures of proteins in solution (*31*), and is particularly well suited to obtain information on weak protein-protein interactions (*32*, *33*). NMR has been used to detect the interaction of nanoparticles with proteins by using either hydrogen-deuterium exchange experiments or two-dimensional NMR spectroscopy (*17*, *34*). By using 2D NMR spectroscopy and chemical shift perturbation we have shown that it is possible to characterize at the amino acid level the interaction between the ubiquitin protein and gold nanoparticles (*35*). Our approach relied on the measurement of two dimensional NMR spectra that are able to detect the ^{1}H and ^{15}N chemical shifts (technically ^{15}N-^{1}H heteronuclear single quantum correlation, [^{15}N-^{1}H]-HSQC) of each N-H group present in a ^{15}N-labelled protein. A typical HSQC spectrum for human ubiquitin is shown in Figure 8 with highlighted one amide N-H group of the backbone of the protein that gives rise to a single 2D peak on the two-dimensional spectrum. With modern NMR instruments equipped with cryoprobe it is possible to measure 2D NMR experiments with protein samples with concentrations of the order of 10-20 μM, that for NMR experiments are remarkably low.

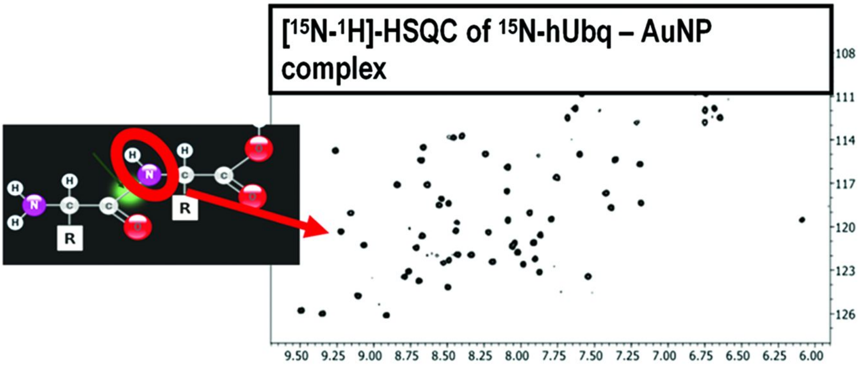

Figure 8. Two dimensional (^{15}N-^{1}H)-HSQC spectrum of ^{15}N-labelled human Ubiquitin in complex with gold nanoparticles. Each peak on the spectrum represents one N-H chemical group of the protein, mainly from the amide backbone (left inset). Reproduced with permission from ref. (35). Copyright 2010 American Chemical Society.

With some effort and the acquisition of several NMR experiments each one of the 2D peaks present in the HSQC spectrum can be sequence-specifically assigned to each amino acid present in the protein. The position (^{1}H and ^{15}N chemical shifts) of each peak is very sensitive to the chemical environment and somehow represents the environment "sensed" by each amino acid in the protein. By collecting 2D HSQC NMR experiments of two samples, one of the free protein and one of the protein in the presence of nanoparticles, it is thus possible to map the "chemical perturbation" induced by nanoparticles on the protein side at the amino acid level. These effects can be monitored by quantifying the chemical shift changes in terms of the chemical shift perturbation (CSP), defined as (*33*):

$$CSP = [\surd(\Delta_{1H})^{2} - (\Delta_{15N} / 5)^{2}]/2$$

where Δ_{1H} is the difference in chemical shift on the ^1H dimension between free protein and bound protein for each amino acid and Δ_{15N} is the corresponding chemical shift difference for the ^{15}N dimension.

Figure 9a shows the CSP for the interaction of ubiquitin with gold nanoparticles of 10nm size, mapped onto the amino acid sequence of the protein. The data shows that the vast majority of the amino acids show changes smaller than 0.02 ppm that are almost negligible. Two peptide fragments (Gln2-Ile3, and Leu15-Glu18) show substantial changes. The fact that the biggest changes are not isolated, but cluster in groups of more than 1 amino acid gives confidence that the detected changes are not artefacts due for example to incorrect assignment of the NMR peaks.

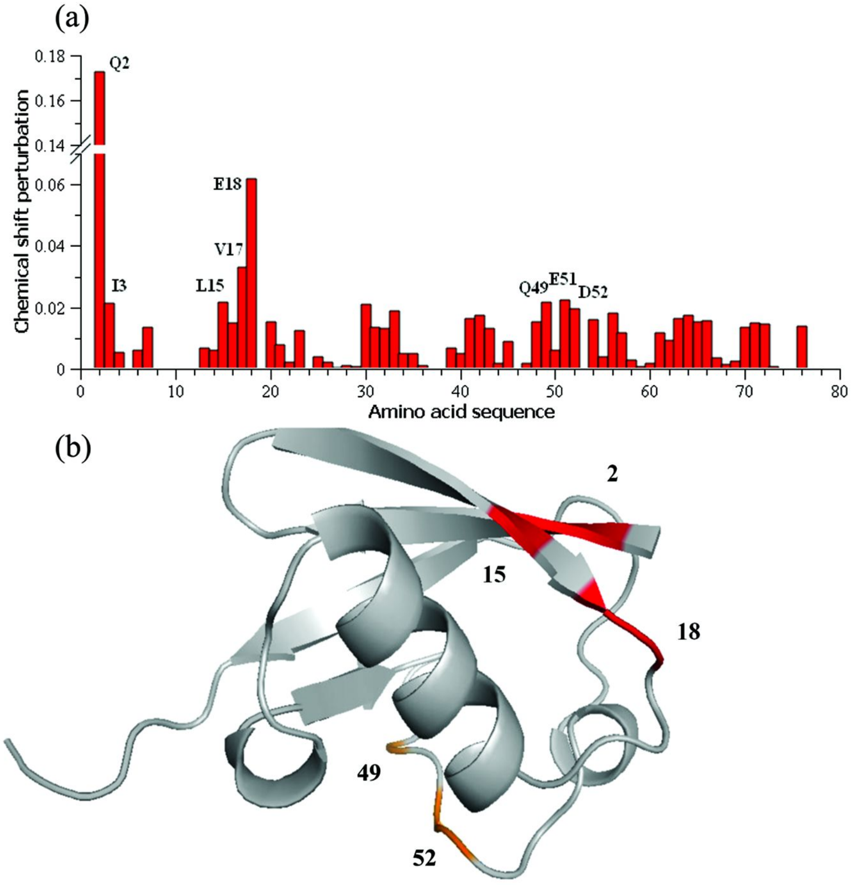

Figure 9. Chemical shift perturbation data of interaction of ubiquitin with gold nanoparticles. (a) CSP mapped onto the amino acid sequence of the protein. (b) CSP mapped onto the three dimensional cartoon structure of the protein. Reproduced with permission from ref. (35). Copyright 2010 American Chemical Society.

These results become much more interesting when mapped onto the well known three dimensional structure of the protein. Figure 9b shows the cartoon structure of the backbone of human ubiquitin, with the two peptide fragments showing the largest CSP changes coloured in red. The two fragments formed by the amino acids 2-3 and 15-18 are apart in the amino acid sequence, but are actually close in space due to the globular folding of the protein. They partially belong to the beta strand 1 and beta strand 2 that form the first β-sheet of ubiquitin.

The fragments Gln2-Ile3 and Leu15-Glu18, identified by CSP using NMR, are a well defined part of the ubiquitin protein that interacts with gold nanoparticles, thus forming a gold-nanoparticle interaction domain.

A similar experimental approach can be applied to other protein-nanoparticle systems to identify specific interacting or binding domains on the protein side. The main requirements for such studies is the use of modern NMR instruments equipped with cryoprobes and the availability of recombinant proteins labelled with ^{15}N (and eventually ^{13}C).The use of cryoprobes enhances the signal to noise ratio of NMR experiments of a factor 8 to 10 and thus allows to collect 2D spectra of protein samples with concentration as low as 10-20 μM and sample volumes of a minimum of 300μL (with the use of specialized NMR tubes).

One of the main drawbacks of NMR is posed by the maximum size of the proteins and of the protein-nanoparticle complex that can be reasonably measured. Recording NMR data of proteins of up to 50KDa in size (corresponding to around 500 amino acids) is quite standard nowadays (*36*) and it is also possible to measure 2D experiments of protein-antibody complexes of around 200 KDa (*37*).

Our results show that the interaction of a small protein such as ubiquitin with gold nanoparticles is quite specific and that by using NMR it is possible to obtain high resolution structural information, at the amino acid level of detail, on protein-nanoparticle complexes. The availability of such detailed experimental information will allow a better understanding of the structural signatures that guide the interaction of proteins with nanoparticles and will also open up new avenues of research in the detailed modelling and eventual prediction of such interactions.

References

1. Oberdorster, G.; Oberdorster, E.; Oberdorster, J. Nanotoxicology: an emerging discipline evolving from studies of ultrafine particles. *Environ. Health Perspect.* **2005**, *113* (7), 823–39.
2. Cedervall, T.; Lynch, I.; Lindman, S.; Berggard, T.; Thulin, E.; Nilsson, H.; Dawson, K. A.; Linse, S. Understanding the nanoparticle-protein corona using methods to quantify exchange rates and affinities of proteins for nanoparticles. *Proc. Natl. Acad. Sci. U.S.A.* **2007**, *104* (7), 2050–5.
3. Lynch, I.; Dawson, K. A.; Linse, S. Detecting cryptic epitopes created by nanoparticles. *Sci. STKE* **2006**, *2006* (327), pe14.
4. Deng, Z. J.; Liang, M.; Monteiro, M.; Toth, I.; Minchin, R. F. Nanoparticle-induced unfolding of fibrinogen promotes Mac-1 receptor activation and inflammation. *Nat. Nanotechnol.* **2011**, *6* (1), 39–44.

5. Wu, Z.; Zhang, B.; Yan, B. Regulation of Enzyme Activity through Interactions with Nanoparticles. *Int. J. Mol. Sci.* **2009**, *10* (10), 4198–4209.
6. Speshock, J.; Braydich-Stolle, L.; Szymanski, E.; Hussain, S. Silver and Gold Nanoparticles Alter Cathepsin Activity In vitro. *Nanoscale Res. Lett.* **2011**, *6* (1), 17.
7. Gray, J. J. The interaction of proteins with solid surfaces. *Curr. Opin. Struct. Biol.* **2004**, *14* (1), 110–5.
8. Norde, W.; Lyklema, J. Why proteins prefer interfaces. *J. Biomater. Sci.: Polym. Ed.* **1991**, *2* (3), 183–202.
9. Walczyk, D.; Bombelli, F. B.; Monopoli, M. P.; Lynch, I.; Dawson, K. A. What the cell “sees” in bionanoscience. *J. Am. Chem. Soc.* **2010**, *132* (16), 5761–8.
10. Lok, C. N.; Ho, C. M.; Chen, R.; He, Q. Y.; Yu, W. Y.; Sun, H.; Tam, P. K.; Chiu, J. F.; Che, C. M. Silver nanoparticles: partial oxidation and antibacterial activities. *J. Biol. Inorg. Chem.* **2007**, *12* (4), 527–34.
11. Liu, J.; Hurt, R. H. Ion release kinetics and particle persistence in aqueous nano-silver colloids. *Environ. Sci. Technol.* **2010**, *44* (6), 2169–75.
12. Liu, J.; Sonshine, D. A.; Shervani, S.; Hurt, R. H. Controlled release of biologically active silver from nanosilver surfaces. *ACS Nano* **2010**, *4* (11), 6903–13.
13. Zhang, H.; Ji, Z.; Xia, T.; Meng, H.; Low-Kam, C.; Liu, R.; Pokhrel, S.; Lin, S.; Wang, X.; Liao, Y. P.; Wang, M.; Li, L.; Rallo, R.; Damoiseaux, R.; Telesca, D.; Madler, L.; Cohen, Y.; Zink, J. I.; Nel, A. E. Use of Metal Oxide Nanoparticle Band Gap To Develop a Predictive Paradigm for Oxidative Stress and Acute Pulmonary Inflammation. *ACS Nano* **2012**, *6* (5), 4349–4368.
14. Nel, A. E.; Madler, L.; Velegol, D.; Xia, T.; Hoek, E. M.; Somasundaran, P.; Klaessig, F.; Castranova, V.; Thompson, M. Understanding biophysicochemical interactions at the nano-bio interface. *Nat. Mater.* **2009**, *8* (7), 543–57.
15. Calzolai, L.; Gilliland, D.; Garcia, C. P.; Rossi, F. Separation and characterization of gold nanoparticle mixtures by flow-field-flow fractionation. *J. Chromatogr., A* **2011**, *27*, 1218.
16. Schmidt, B.; Loeschner, K.; Hadrup, N.; Mortensen, A.; Sloth, J. J.; Koch, C. B.; Larsen, E. H. Quantitative characterization of gold nanoparticles by field-flow fractionation coupled online with light scattering detection and inductively coupled plasma mass spectrometry. *Anal. Chem.* **2011**, *83* (7), 2461–8.
17. Lundqvist, M.; Stigler, J.; Elia, G.; Lynch, I.; Cedervall, T.; Dawson, K. A. Nanoparticle size and surface properties determine the protein corona with possible implications for biological impacts. *Proc. Natl. Acad. Sci. U.S.A.* **2008**, *105* (38), 14265–70.
18. Lundqvist, M.; Stigler, J.; Cedervall, T.; BerggÃ¥rd, T.; Flanagan, M. B.; Lynch, I.; Elia, G.; Dawson, K. The Evolution of the Protein Corona around Nanoparticles: A Test Study. *ACS Nano* **2011**, *5* (9), 7503–7509.
19. Casals, E.; Pfaller, T.; Duschl, A.; Oostingh, G. J.; Puntes, V. Time Evolution of the Nanoparticle Protein Corona. *ACS Nano* **2010**, *4* (7), 3623–3632.

20. Cedervall, T.; Lynch, I.; Foy, M.; Berggard, T.; Donnelly, S. C.; Cagney, G.; Linse, S.; Dawson, K. A. Detailed identification of plasma proteins adsorbed on copolymer nanoparticles. *Angew. Chem., Int. Ed.* **2007**, *46* (30), 5754–6.
21. Dobrovolskaia, M. A.; Patri, A. K.; Zheng, J.; Clogston, J. D.; Ayub, N.; Aggarwal, P.; Neun, B. W.; Hall, J. B.; McNeil, S. E. Interaction of colloidal gold nanoparticles with human blood: effects on particle size and analysis of plasma protein binding profiles. *Nanomedicine* **2009**, *5* (2), 106–17.
22. Vroman, L. Effect of absorbed proteins on the wettability of hydrophilic and hydrophobic solids. *Nature* **1962**, *196*, 476–7.
23. Vroman, L.; Adams, A. L.; Fischer, G. C.; Munoz, P. C. Interaction of high molecular weight kininogen, factor XII, and fibrinogen in plasma at interfaces. *Blood* **1980**, *55* (1), 156–9.
24. Monopoli, M. P.; Walczyk, D.; Campbell, A.; Elia, G.; Lynch, I.; Bombelli, F. B.; Dawson, K. A. Physical-chemical aspects of protein corona: relevance to in vitro and in vivo biological impacts of nanoparticles. *J. Am. Chem. Soc.* **2011**, *133* (8), 2525–34.
25. Lindman, S.; Lynch, I.; Thulin, E.; Nilsson, H.; Dawson, K. A.; Linse, S. Systematic investigation of the thermodynamics of HSA adsorption to N-iso-propylacrylamide/N-tert-butylacrylamide copolymer nanoparticles. Effects of particle size and hydrophobicity. *Nano Lett.* **2007**, *7* (4), 914–20.
26. Fasman, G. D. *Circular dichroism and the conformational analysis of biomolecules*; Plenum Press: New York, 1996; p ix, 738 p.
27. Greenfield, N. J. Using circular dichroism spectra to estimate protein secondary structure. *Nat. Protoc.* **2006**, *1* (6), 2876–90.
28. Laera, S.; Ceccone, G.; Rossi, F.; Gilliland, D.; Hussain, R.; Siligardi, G.; Calzolai, L. Measuring protein structure and stability of protein-nanoparticle systems with synchrotron radiation circular dichroism. *Nano Lett.* **2011**, *11* (10), 4480–4.
29. Calzolai, L.; Zahn, R. Influence of pH on NMR structure and stability of the human prion protein globular domain. *J. Biol. Chem.* **2003**, *278* (37), 35592–6.
30. Konno, T. Conformational diversity of acid-denatured cytochrome c studied by a matrix analysis of far-UV CD spectra. *Protein Sci.* **1998**, *7* (4), 975–82.
31. Wüthrich, K. *NMR of proteins and nucleic acids*; Wiley: New York, 1986; p xv, 292.
32. Vaynberg, J.; Qin, J. Weak protein-protein interactions as probed by NMR spectroscopy. *Trends Biotechnol.* **2006**, *24* (1), 22–7.
33. Zuiderweg, E. R. Mapping protein-protein interactions in solution by NMR spectroscopy. *Biochemistry* **2002**, *41* (1), 1–7.
34. Engel, M. F.; Visser, A. J.; van Mierlo, C. P. Conformation and orientation of a protein folding intermediate trapped by adsorption. *Proc. Natl. Acad. Sci. U.S.A.* **2004**, *101* (31), 11316–21.
35. Calzolai, L.; Franchini, F.; Gilliland, D.; Rossi, F. Protein--nanoparticle interaction: identification of the ubiquitin--gold nanoparticle interaction site. *Nano Lett.* **2010**, *10* (8), 3101–5.
36. Horst, R.; Bertelsen, E. B.; Fiaux, J.; Wider, G.; Horwich, A. L.; WÃ¼thrich, K. Direct NMR observation of a substrate protein bound to

the chaperonin GroEL. *Proc. Natl. Acad. Sci. U.S.A.* **2005**, *102* (36), 12748–12753.

37. Simonelli, L.; Beltramello, M.; Yudina, Z.; Macagno, A.; Calzolai, L.; Varani, L. Rapid structural characterization of human antibody-antigen complexes through experimentally validated computational docking. *J. Mol. Biol.* **2010**, *396* (5), 1491–507.

Downloaded by UNIV OF SUSSEX on December 13, 2012 | http://pubs.acs.org
Publication Date (Web): December 12, 2012 | doi: 10.1021/bk-2012-1120.ix002

Subject Index

A

- Adhesion protein functional activity variations, 15
- Adsorbed antibodies, 13
- Adsorbed antibody orientation
  - ELISA assay, 459
  - experimental observations vs modeling outputs, 465
  - IgG orientation, 463, 463*f*, 464*f*
  - materials, 680
  - overview, 453
  - QCM experiments, 456, 460*f*, 461*f*, 462*f*
  - random sequential adsorption modeling, 457
  - RSA modeling, 458*f*, 463, 465
- Adsorbed enzymes, 11
- Adsorbed proteins
  - biological functions, 11
    - adsorbed antibodies, 13
    - adsorbed enzymes, 11
- Adsorbed salivary films, 144, 145*f*, 146*f*, 148*f*
- Affinity-based protein immobilization, 790, 792*f*
- AFM-based friction force spectroscopy
  - adsorbed salivary films, 144, 145*f*, 146*f*, 148*f*
  - FFS sensitivity, 140, 141*f*, 143*f*
  - film strength quanitification, 138
  - monolayers, model proteins, 132
    - β-casein, 135
    - BSA, 132, 133*f*, 134*f*
    - BSA vs β-casein, 136, 137*f*
  - overview, 129
  - proteinaceous film scratching, 131*f*
- Albumin adsorption effect
  - adsorption studies, 500
  - AFM, 501, 510*f*
  - coated joint materials, 513, 514*f*, 516*f*, 518*f*
  - joint material behavior, 502, 503*f*, 504*f*
  - overview, 497
  - prosthetic materials, 505, 507*f*, 509*f*, 512*f*
  - SEM, 501, 505*f*
  - tribological tests, 499
- Amino acid enrichment, 798*t*
- Amino acid labeling strategies, surface-immobilized proteins, 772, 773*f*
- Annexin A5, 419, 422*f*
- Antibody adsorption
  - antibody immobilization, antigen detection, 547, 569
    - adsorption dynamics, 549
    - antigen binding, 557, 559*f*
    - concentration effect, 549
    - immobilized antibody stability, 560
    - interfacial orientation, 549, 550*f*
    - orientation, 547, 547*f*, 548*f*
    - pH effect, 551, 554*f*, 556*f*
    - salt effect, 555
  - anti-hPSA antibody layers, 552*t*, 555*t*
  - immunochemical probing, 560
  - overview, 543
  - protein adsorption, 545
    - characterization, 546
  - proteins surface conformations, 560, 562*f*
    - fibrinogen polypeptide surface conformations, 563, 564*f*, 565*f*, 566*f*
    - fibronectin surface conformations, 566, 568*f*

B

- β-casein, 135
- β-casein/SDS mixtures
  - adsorption isotherm, 164, 165*f*, 166*f*
  - adsorption routes, 157, 158*f*, 159*s*, 160*s*
  - fluid dynamics, drop exchange, 161, 161*f*, 162*f*, 163*f*, 164*f*
  - overview, 153
  - protein displacement, 174*s*
  - protein/surfactant complex formation, 175*s*
  - water/air vs water/hexane interfaces, 166, 167*f*, 168*f*, 169*f*, 170*f*, 171, 171*f*
- Bioaffinity interaction, His-tag proteins & Ni(II) surface sites
  - His-tag H49 adsorption, 43
    - desorption, 48, 48*f*
    - mechanism, 45, 45*f*, 47*f*
    - physical adsorption vs bioaffinity interaction, 44, 44*f*
    - surface biofunctionality, 49, 50*f*
  - His-tag H49 antigen, 40
  - His-tag redox enzyme, 49, 51*f*
  - Ni(II)-modified substrate, 41, 42*f*, 43*f*
  - overview, 37

Downloaded by UNIV OF SUSSEX on December 13, 2012 | http://pubs.acs.org
Publication Date (Web): December 12, 2012 | doi: 10.1021/bk-2012-1120.ix002

Biocompatibility
  antithrombin, 293
  blood, adsorption, 280
  control, 289
  desorption, 279*f*
  factor XIIa, 294
  fibrinolytic surfaces, 290, 290*f*
  immunoblots, 284*f*
  overview, 277
  plasma, adsorption, 280, 281*f*, 283*f*
  resistance, adsorption, 285, 287*f*, 288*f*
  simple mixtures, 278
  single proteins, 278
  thrombin scavenging surfaces, 292
Biomineralization, solid-state NMR studies
  biosilicification peptides, 85, 87*f*, 88*f*, 89*f*, 91*f*
  magic angle spinning, 81*f*
  overview, 77
  principles, 79, 80*f*
  salivary statherin, HAP crystal surfaces, 82, 84*f*, 86*f*
Blood, adsorption, 280
Blood coagulation, 595*f*, 599
Bovine serum albumin (BSA), 132, 133*f*, 134*f*
BSA. *See* bovine serum albumin (BSA)

C

Calcium phosphate
  biological properties, 69
  Ca/P ratio, 57*t*
  hydrophobicity, 65
Carbohydrate-containing monomer, 596
Carbohydrate-recognizing protein, 585, 587*f*
Cell adhesion peptide patterns, 800, 800*f*, 801*f*
Cell culture patterning, 800
Circular dichroism, 630, 631*f*, 637*f*, 638*f*
Competitive protein adsorption, 69
Computer simulation, protein adsorption, 8
  computational prediction, adsorbed proteins, 8
  Corni group, 10
  Latour group, 9
  Raffaini and Ganazzoli, 10
  structure prediction, 9
Cysteine/Au(III), 231, 233*f*

E

Electrostatic conjugation, surface-immobilized proteins, 770, 771*f*

F

FBR. *See* foreign body response (FBR)
Fibrinogen adsorption, 653*f*
Fibrinogen adsorption mechanisms, mica
  hydrodynamic radii, 103*t*
  hydrophilic surfaces, 115*t*
  intrinsic viscosities, 103*t*
  model shapes, 99*t*
  overview, 97
  predicted conformations, 106*t*
  theoretical modeling, 102
    bulk hydrodynamic properties calculation, 102
    colloid deposition, 118, 120*f*, 121*f*, 122*f*, 124*f*
    experimental evidences, 113, 114*f*, 116*f*
Fibrinolytic surfaces, 290, 290*f*
Fibronectin-absorbed TCPS, 825*t*
Foreign body response (FBR)
  adsorbed fibrinogen, 323, 326*f*, 327*f*, 328*f*
  complement system, 328, 330*f*, 331*f*
  overview, 321

G

Gas embolism, surfactants role
  interface fluid mechanics, 398, 401*f*
  mass transport, 398, 404*f*
  numerical modeling, 398, 403*f*
  overview, 395
  protein adsorption, 405, 408*t*, 409*f*, 410*f*, 411*f*, 413*f*
Glycocalyx-mimetic surface synthesis
  blood coagulation, 595*f*, 599
  blood collection, 598
  carbohydrate-containing monomer, 596
  carbohydrate-recognizing protein, 585, 587*f*
  characterization, 599
  chemical structures, 580*s*
  glycocalyx-mimicking polymer brushes, 588, 589*f*
  glycopolymer brushes, 580, 583*t*, 596
  grafting density, 585

overview, 577
platelet activation, 592*f*, 598
platelet adhesion, 593*f*, 598
poly(2′-acrylamidoethyl-α-D-mannopyranoside) brush, 596
scheme, 582*s*
surface plasmon resonance analysis, 596, 598
Glycocalyx-mimicking polymer brushes, 588, 589*f*
Glycopolymer brushes, 580, 583*t*, 596
Gold surfaces
  ab initio computational methods, 231
    cysteine/Au(III), 231, 233*f*
    histidine/Au(III), 233, 234*f*, 235*f*
    polyserine/Au(III), 235, 236*f*
  atomistic MD, 237, 240*f*
  coarse-grained protein models, 243, 243*f*, 246*f*
  overview, 229
  rigid-body docking, 240, 242*f*
Growth factor delivery, starPEG-heparin hydrogels
  experimental parameters, 532*t*
  hydrogel interaction, 528*f*
  overview, 525
  presentation, 532, 533*f*
    cytokine concentration, 534, 536*f*
    physicochemical network properties, 532
  specific cell behavior, 536, 537*f*, 538*f*

H

Helix-coil transitions, 656*f*
His-tag H49 adsorption, 43
  desorption, 48, 48*f*
  mechanism, 45, 45*f*, 47*f*
  physical adsorption vs bioaffinity interaction, 44, 44*f*
  surface biofunctionality, 49, 50*f*
His-tag H49 antigen, 40
His-tag redox enzyme, 49, 51*f*
Histidine/Au(III), 233, 234*f*, 235*f*
Hydrophilic polymers, 20

I

IgG molecule relaxation, 7*f*
Immunoblots, 284*f*
Interfacial protein effect, apatite growth, 70

M

Mass analyzers, 814*t*
Material-driven fibronectin fibrillogenesis
  biological activity, 483, 484*f*, 488*f*
  cell-driven, 472
    essential domains, 474
    matrix assembly regulation, 474
    structure, 472
  cell-free assembly, 475
  glass transition temperature, 490*f*
  matrix proteolytic degradation, 486*f*
  molecular structure, 473*f*, 483*f*
  myogenic differentiation, 487*f*
  overview, 471
  physiological organization, 479, 480*f*, 482*f*
  water contact angle measurements, 491*f*
Material-mediated cellular proteins, 809
Mica, fibrinogen adsorption mechanisms. *See* fibrinogen adsorption mechanisms, mica
Microtopography effect
  collagen alignment, 348, 349*f*
  implant topography, 341
  implications/applications, 350
  overview, 339
  surface modifications, cellular responses, 340
  surface topography, implant tissue compatibility, 342, 344*f*
  surface topography effect, 345, 346*f*, 347*f*
Mixed phospholipid monolayers
  AFM measurement, 423, 428*f*, 429*f*
  annexin A5, 422*f*
  Langmuir trough, 421, 424*f*
  materials, 421
  monolayer preparation, 421
  overview, 419
  SPR measurement, 423, 425
  surface pressure, 425*f*
Mixed polymer brushes, protein adsorption/cell adhesion
  dry layer thickness, 183*t*
  grafting-to mechanism, 632*f*
  materials, 183
  null-ellipsometry setup, 185*f*
  overview, 179
  physico-chemical surface properties, 186
  preparation, 184
  P2VP-PNIPAAM brushes, cell adhesion, 186*f*, 187*f*, 189*f*, 190, 190*f*, 191*f*
  refractive index, 183*t*
  stimuli responsive protein adsorption, 188

Downloaded by UNIV OF SUSSEX on December 13, 2012 | http://pubs.acs.org
Publication Date (Web): December 12, 2012 | doi: 10.1021/bk-2012-1120.ix002

Downloaded by UNIV OF SUSSEX on December 13, 2012 | http://pubs.acs.org
Publication Date (Web): December 12, 2012 | doi: 10.1021/bk-2012-1120.ix002

- surface analysis methods, 184
- switching behaviour, 181*f*
- tethered polymer chains, 180*f*

MS technology, 812
Multiple protein system, 27

N

Nanoparticles
- biological systems, 840, 841*f*
- CD spectra, 845*f*, 846*f*, 847*f*, 848*f*
- chemical shift perturbation, 851*f*
- high-resolution structure, 849, 850*f*
- overview, 839
- protein complexes, 843*f*
- protein interactions, 841
- protein structure, 844
- stability changes, 847, 849*f*

Ni(II)-modified substrate, 41, 42*f*, 43*f*
Nisin entrapment, 648, 649*f*, 651*f*
- silanized silica surfaces, 648, 653*f*

Non-fouling architecture
- adsorbed film properties, 629
- circular dichroism, 630, 631*f*, 637*f*, 638*f*
- film hydration effect, 635, 636*t*
- poly(carboxy betaine), 705*f*
- poly(ethylene glycol), 624
- protein adsorption structure, 629
- quartz crystal microbalance, 631, 632*f*, 634*f*

Nonfouling protein-capture polymer surfaces, 783
- bioimmobilization reactivity, 784, 787*f*
- polymer background nonspecific adsorption properties, 785, 788*f*

O

Orientational control, 794, 796*f*, 798*f*

P

Peptide adsorption, PEO brush layers
- fibrinogen adsorption, 653*f*
- helix-coil transitions, 656*f*
- molecular origins, 654
- nisin entrapment, 648, 649*f*, 651*f*
  - silanized silica surfaces, 648, 653*f*
- overview, 645
- peptide structure, 655*f*
- protein adsorption, 646, 650*f*, 679*f*
- protein repulsion, 646

Phospholipids, 677
Phosphorylcholine, 677
Platelet activation, 592*f*, 598
Platelet adhesion, 593*f*, 598
Pluronic F-127 blocks protein adsorption, 412*f*
Polyacrylamide
- antifouling coating, 663*t*
- cell adhesion, 666
- cell attachment, 673*f*
- film thickness, 667*f*
- gold grafted, 667*s*
- ionic strength, 670*f*
- materials, 664
- overview, 661
- pH effect, 670*f*
- protein adsorption, 665, 669*t*
- SPR sensorgrams, 669*f*, 671*f*
- surface characterization, 665
- surface-initiated ATRP, 664

Poly(2′-acrylamidoethyl-α-D-mannopyranoside) brush, 596
Poly(carboxy betaine), 621, 626
- antifouling properties, 628*t*

Poly(ethylene glycol), 621, 624
- antifouling properties, 626*t*

Polyserine/Au(III), 235, 236*f*
Prion diseases, 433
- environmental transmission, 435

Prion protein, 433
- soil binding, 445, 446*f*, 447*f*, 449*t*
- soil interaction, 435
  - literature, 441*t*
  - N-terminal truncation, 442
  - protein degradation, 445*f*
  - PrP sorption, 438, 438*f*, 439*f*, 443*f*
  - sorption kinetics, 435, 436*t*
  - strain influence, 442

Proteinaceous film scratching, 131*f*
Protein adsorption
- absorbed antibodies, 13
- adhesion proteins, 14
- adsorbed enzymes, 11
- biological function, 11
- cell interactions, 16, 17*f*
- computer simulation, 8
  - computational prediction, adsorbed proteins, 8
  - Corni group, 10
  - Latour group, 9
  - Raffaini and Ganazzoli, 10
  - structure prediction, 9
- longer-term events, 19
- resistance, 19
  - mechanisms, 23

In Proteins at Interfaces III State of the Art 2012; Horbett, T., et al.;
ACS Symposium Series; American Chemical Society: Washington, DC, 2012.

Downloaded by UNIV OF SUSSEX on December 13, 2012 | http://pubs.acs.org
Publication Date (Web): December 12, 2012 | doi: 10.1021/bk-2012-1120.ix002

    - surface design, 20
  - surface chemistry effects, 18
- Protein adsorption, polymer brush surfaces
  - biological analysis, 610
  - chemical structure, 608*f*
  - initiator-immobilized substrates
    - preparation, 607
  - materials, 607
  - overview, 605
  - physicochemical surface
    - characterization, 608
  - physicochemical surface properties, 611, 612*f*
  - polymer brush layers preparation, 607
  - protein adsorption behavior, 613, 614*f*, 615*f*
  - water structure, 615, 616*f*, 617*f*
  - water structure analysis, 609, 610*f*
- Protein amino acid composition, 793*t*
- Protein-bioceramic interactions
  - calcium phosphate
    - biological properties, 69
    - hydrophobicity, 65
  - chemical characteristics, 63, 64*f*
  - competitive protein adsorption, 69
  - incubation solution characteristics, 66
  - interfacial protein effect, apatite growth, 70
  - overview, 55
  - physiochemical characteristics, 59
  - protein adsorption affecting factors, 58
    - ceramics, 59*f*, 66*f*
    - characterisation techniques, 62*t*
- Protein-carbohydrate interactions, glycosylated membranes surfaces
  - cluster glycoside effect, 256, 267, 268*f*
    - molecular mechanism, 258
  - construction, 262, 263*f*
    - graft from, 263
    - graft to, 264
    - immobilization, 265
  - cyclic saccharides, 266
  - evaluation, 261
  - glycobiology, 253
  - glycopolymer chains, 270, 270*f*
  - glycosylation, 261
  - linear chain saccharides, 265
  - mutilayer adsorption, 268, 269*f*
  - oligosaccharides recognition, 269
  - overview, 253
  - specificity, 266
  - transference mechanism, 268
- Protein G B1 model system, 763, 764*f*
- Protein microarrays, 811
- Protein orientation, surface-immobilized proteins, 767, 768*f*, 769*f*
- Protein patterns fabrication, affinity-based surface ligand selection
  - affinity-based protein immobilization, 790, 792*f*
  - amino acid enrichment, 798*t*
  - cell adhesion peptide patterns, 800, 800*f*, 801*f*
  - cell culture patterning, 800
  - nonfouling protein-capture polymer surfaces, 783
    - bioimmobilization reactivity, 784, 787*f*
    - polymer background nonspecific adsorption properties, 785, 788*f*
  - orientational control, 794, 796*f*, 798*f*
  - overview, 781
  - protein amino acid composition, 793*t*
  - ToF-SIMS, 786, 789*f*, 790*f*, 794*f*, 799*f*
- Protein-repellent functionalizable surfaces
  - adsorption kinetic constant, 688*f*
  - chemicals, 680
  - focused laser beam, 684*f*
  - interfacial concentration, 686*f*
  - liposome adsorption/spreading, 688
  - liposome preparation, 680
  - liposomes, 688*f*
  - material characterization, 684
  - overview, 677
  - passivation, 687*f*
  - PL-PMHS surface functionalization, 689
  - PMHS films, 681
  - PMHS network, 679*f*
  - PMHS vs PL-PMHS, 685*f*
  - preparation, 680
  - protein adsorption, 685
  - XPS spectra, 686*f*
- Protein repulsion, 646
- Proteins, physicochemical aspects, 1
  - adsorption affinity, 2
  - adsorption dynamics, 4
  - adsorption kinetics, 4
- Proteins at interfaces, 24
  - experimental techniques, 24
    - conformation, 28
    - orientation, 28
    - physical status, 28
    - quantity adsorbed, 25
- Protein/surface interaction regulation
  - chemical modification, 302
    - bioactive surfaces, 303*f*, 304*f*, 306, 307*f*, 308*f*, 309*f*
    - bioinert surfaces, 303
  - overview, 301
  - topographical design, 310, 312*f*, 313*f*, 314*f*
- Protein-surface interactions

Downloaded by UNIV OF SUSSEX on December 13, 2012 | http://pubs.acs.org
Publication Date (Web): December 12, 2012 | doi: 10.1021/bk-2012-1120.ix002

  adsorbed protein orientation, 219
    CD spectroscopy, 219, 220*f*
    characterization, 221, 222
  advanced sampling methods, 216
  AFM tip linkage, 207*f*
  BSA adsorption, 702*f*
  computational methods, 208*f*
  force field parameter adjustment, 213, 214*f*, 216*f*
  free energy, 202
    adsorbent surfaces, 202
    ΔG°ads determination, 203, 205*f*, 206*t*, 208*f*, 212*f*
    host-guest peptide model, 203
  hydroxyl content, 706*f*
  Kretschmann configuration, 697*f*
  molecular simulations, 201*f*
  overview, 197, 695
  pH effect, 703*f*
  protein adsorption studies, 699
    complement activation, 704
    non-specific protein adsorption, 699
    time course, 705*f*
  self-assembled monolayers, alkanethiols, 698
    array fabrication, 700*f*
    composition, 699*f*
    water contact angle, 699*f*
  SPR imaging, 698, 701*f*
  surface plasmon resonance, 696
  TGTG-V-GTGT peptide, 209*f*
Proteomics, 811, 815
PRP proteins, 819*f*, 821*f*
P2VP-PNIPAAM polymer brushes, 186*f*, 187*f*, 189*f*, 190, 190*f*, 191*f*

Q

Quartz crystal microbalance, 631, 632*f*, 634*f*

S

Saliva proteins/streptococcus mutans interactions
  adhering bacteria, 365*t*
  adhesion force distribution, 364*f*
  adhesion kinetics, 364*f*
  adhesion strength, 359, 360*f*
  adsorption enthalpy, 368*f*
  adsorption isotherms, 361, 366*f*
  antigen, 357*f*
  bacterial adhesion, 359
  buffer solution, 359
  culturing, 358
  harvesting conditions, 358
  initial deposition rate, 365*t*
  overview, 355
  repulsive force, 363*t*
  saliva, 358
  saliva-bacterium interaction enthalpy, 361
  statistical analysis, 362
Serum proteins, 816*t*, 817*f*, 818*t*
Soft X-ray spectromicroscopy
  albumin adsorption, 747*f*, 748*t*
  fibrinogen adsorption, 750
  microbeam-patterned polymeric surfaces, 755
  overview, 731
  polystyrene-polylactide blend, 744
  PS/PMMA, 747
  PS-PMMA/PAA, 741, 742*f*
  SAM microarray, 752, 753*f*
  STXM, 738*f*, 739, 750*f*, 751*f*
  ubiquitin adsorption, 755, 756*t*
  X-PEEM, 733, 734*f*, 736*f*, 742*f*, 745*f*
  X-PEEM vs STXM, 739
Soil binding, prion protein, 445, 446*f*, 447*f*, 449*t*
Soil interaction, prion protein, 435
  literature, 441*t*
  N-terminal truncation, 442
  protein degradation, 445*f*
  PrP sorption, 438, 438*f*, 439*f*, 443*f*
  sorption kinetics, 435, 436*t*
  strain influence, 442
Soluble proteins, 823
StarPEG-heparin hydrogels, 525
  characteristics, 528, 531*f*
  design, 528, 528*f*
Surface-associated proteins, 815
Surface-bound proteins, 809
Surface-immobilized proteins
  amino acid labeling strategies, 772, 773*f*
  electrostatic conjugation, 770, 771*f*
  overview, 761
  protein G B1 model system, 763, 764*f*
  protein orientation, 767, 768*f*, 769*f*
  secondary structure, 764, 765*f*, 767*f*

T

Thrombin scavenging surfaces, 292
Time-dependent functional
  activity measurement, adsorbed fibrinogen/platelet adhesion

    AFM data analysis, 378, 378*f*, 379*f*
    AFM probe functionalization, 376
    Boltzmann equation, 390*t*
    functional activity measurement, 377
    immuno-atomic force microscopy, 375
    mica surfaces, 379, 380*f*, 381*f*, 382*f*
    overview, 373
    polymeric biomaterial surfaces, 386, 387*f*, 388*f*, 389*f*
    protein solution composition effects, 383, 384*f*, 385*f*
Time-of-flight secondary ion mass spectrometry (ToF-SIMS), 786, 789*f*, 790*f*, 794*f*, 799*f*
    crystal face analysis, 724
    overview, 709
    particle-specific analysis, 724
    patterned arrays, 724, 725*f*
    primary ion sources, 712, 712*f*, 714*t*
    protein adsorption, 711*f*
    protein interactions, 720
        Au nanoparticle surface, 723, 724*f*
        misfolded-protein analysis, 720, 721*f*, 722*f*
    protein loading, 715
        internal pore-surface chemistry, 715, 716*f*
        molecule-substrate interaction, 717, 718*f*
        pore-surface functionalization, 716, 717*f*
        porous material cross-sections, 719, 719*f*, 720*f*

U

U937 cell lysates, 824*f*

Z

Zwitterion, 22

Downloaded by UNIV OF SUSSEX on December 13, 2012 | http://pubs.acs.org
Publication Date (Web): December 12, 2012 | doi: 10.1021/bk-2012-1120.ix002